

**NASA TECHNICAL  
TRANSLATION**



**NASA TT F-389**

**NASA TT F-389**

**LOAN COPY: RE**  
AFWL (WLIB)  
KIRTLAND AFB,  
0068817



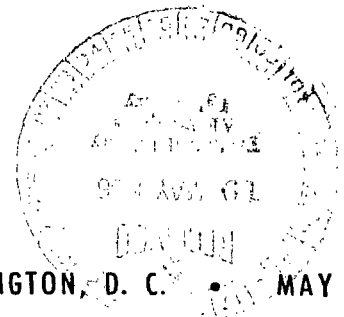
**TECH LIBRARY KAFB, NM**

**SPACE RESEARCH**

**TRANSACTIONS OF THE ALL-UNION  
CONFERENCE ON SPACE PHYSICS**

*Edited by G. A. Skuridin, et al.*

*Science Publishing House,  
Moscow, June 10-16, 1965*



**NATIONAL AERONAUTICS AND SPACE ADMINISTRATION • WASHINGTON, D. C. • MAY 1966**



**SPACE RESEARCH**

**TRANSACTIONS OF THE ALL-UNION**

**CONFERENCE ON SPACE PHYSICS**

**Edited by G. A. Skuridin, Ya. L. Al'pert,  
V. I. Krasovskiy, V. V. Shvarev**

**Translation of "Issledovaniya Kosmicheskogo Prostranstva."  
Trudy Vsesoyuznoy Konferentsii po Fizike Kosmicheskogo Prostranstva.  
Izdatel'stvo "Nauka," Moscow, June 10-16, 1965**

**NATIONAL AERONAUTICS AND SPACE ADMINISTRATION**

---

**For sale by the Clearinghouse for Federal Scientific and Technical Information  
Springfield, Virginia 22151 - Price \$8.35**





## TABLE OF CONTENTS

	<u>Page No.</u>
Introduction . . . . .	1
Introductory Remarks by the President of the Commission on the Research and Utilization of Space by the USSR Academy of Sciences . . . . .	4
Academician A. A. Blagonravov	
I. UPPER ATMOSPHERE OF THE EARTH	
Certain Problems of Upper Atmosphere Physics and Space Near the Earth . . . . .	8
V. I. Krasovskiy	
Density and Temperature of the Atmosphere Based on Measurement Results Obtained on High Altitude Geophysical Automatic Stations in 1963 . . . . .	25
V. V. Mikhnevich	
Certain Problems Entailed in Studying the Structure of the Upper Atmosphere . . . . .	35
M. N. Izakov	
Diurnal Variations in Density, Pressure and Temperature in the Atmosphere (Summary) . . . . .	49
R. S. Zhantuarov	
Dynamic Nature of Atmospheric Density at Altitudes of 200-300 km . . . . .	53
M. Ya. Marov	
Composition of the Atmosphere in the 100-200 km Region . . . . .	62
A. D. Danilov	
Problem of the Total Amount of Neutral Hydrogen in the Upper Atmosphere of the Earth (Summary) . . . . .	66
V. G. Kurt	
Utilization of Artificial Earth Satellite Orbital Data to Determine the Wind Velocity in the Thermosphere . . . . .	66
B. N. Trubnikov	

	<u>Page No.</u>
Determining the Ozone Concentration at Altitudes of 44-102 km Based on Data Obtained From Nocturnal Launches of Geophysical Rockets (Summary) . . . . .	74
A. Ye. Mikirov	
Aerodynamics of Manometers and Mass Spectrometers Carried on Rockets and Satellites . . . . .	74
A. I. Ivanovskiy	
Stratosphere Aerosol Based on Spacecraft Measurements (Summary) . . . . .	81
G. V. Rozenberg, V. V. Tereshkova	
Results Derived from Optical Observations with the Spacecraft "Voskhod" . . . . .	82
K. P. Feoktistov, G. V. Pozenberg, A. B. Sandomirskiy, V. N. Sergeyevich, D. M. Sonechkin	
Results Derived from Rocket Research on the Earth's Upper Atmosphere Between 1960-1964 (Summary) . . . . .	86
S. M. Poloskov	
Infrared Spectrophotometry of the Earth's Thermal Radiation . . .	88
A. I. Lebedinskiy, D. N. Glovatskiy, V. I. Tulupov, B. V. Khlopov, A. A. Fomichev, G. I. Shuster	
Investigating the Earth's Atmospheric Radiation in the Visible and Ultraviolet Regions . . . . .	105
A. I. Lebedinskiy, V. A. Krasnopol'skiy, A. P. Kuznetsov, V. A. Iozenas	
Eigen Radiation of the Atmosphere (Summary) . . . . .	120
T. M. Tarasova	
Study of the Angular Radiation Distribution of the Earth and the Earth's Atmosphere from Geophysical Rockets and Balloons . . . . .	122
M. N. Markov, Ya. I. Merson, M. R. Shamilev	
Angular and Spectral Radiation Distribution of the Earth in the Infrared Spectral Region . . . . .	126
P. A. Bazhulin, A. V. Kartashev, M. N. Markov	

Determining Temperature and Moisture of the Earth's Atmosphere Based on Satellite Measurements of the Earth's Atmosphere . . . . .	140
M. S. Malkevich, V. I. Tamarskiy	
Ultraviolet Radiation Scattering ( $\lambda 1300 \text{ \AA}$ ) in the Upper Atmosphere of the Earth (Summary) . . . . .	152
S. A. Kaplan, V. G. Kurt	
Upper Atmosphere Layers which Radiate in the Infrared Spectral Region . . . . .	153
M. N. Markov, Ya. I. Merson, M. P. Shamilev	
I . IONOSPHERE OF THE EARTH	
Altitudinal-Time Distribution of the Electron Concentration and Nonuniform Formations of the Outer Ionosphere . . . . .	166
Ya. L. Al'pert, V. M. Sinel'nikov	
Certain Results of Ionosphere Studies Using Artificial Earth Satellites and Geophysical Rockets . . . . .	185
V. A. Misyura, G. K. Solodovnikov, Ye. B. Krokhmal'nikov, V. M. Migunov	
Ionosphere Studies by Receiving AES Radio Emission on the Earth . . . . .	196
L. M. Yerukhitov, N. A. Mityakov, E. Ye. Mityakova	
Brief Survey of the Results of Physical Experiments on the Satellite "Kosmos-2" in the Ionosphere . . . . .	202
V. V. Afonin, T. K. Breus, G. L. Gdalevich, B. N. Gorozhankin, K. I. Gringauz, R. Ye. Rybchinskiy,	
Results of Ionosphere Research by Rockets and Satellites in 1960-1964 . . . . .	225
B. N. Gorozhankin, V. A. Rudakov	
The Outer Region of the Earth's Ionosphere (from 2000 to 200,000 km) . . . . .	238
V. V. Bezrukikh, K. I. Gringauz	

	<u>Page No.</u>
Rocket Data on the Behavior of Electron Concentration in the Ionosphere at Altitudes of 100-300 km . . . . .	248
T. V. Kazachevskaya, G. S. Ivanov-Kholodnyy	
Electron and Ion Temperatures in the Ionosphere (Summary) . . . .	254
T. K. Breus, G. L. Gdalevich	
Composition of the Outer Ionosphere of the Earth Based on Measurement Data from the "Elektron" Satellites . . . . .	259
V. G. Istomin	
One Anomaly in Electron Pitch-Distributions . . . . .	273
O. L. Vaysberg, F. K. Shuyskaya	
Variations in the Soft Component of the Electron Energy Spectrum . . . . .	277
T. M. Mulyarchik	
Spatial Distribution of Different Groups of Trapped Corpuscles Based on Data from the Satellites "Kosmos-3" and "Kosmos-5" . . . . .	281
V. V. Temnyy	
Measurement of Soft Electron Streams in the Upper Atmosphere at Altitudes to 500 km . . . . .	288
L. A. Antonova, T. V. Kazachevskaya	
Variations in Atmospheric Ion Composition at Altitudes of 100-200 km (Summary) . . . . .	291
G. S. Ivanov-Kholodnyy, A. D. Danilov	
Characteristics of Shortwave Communication with Spacecrafts . . .	295
F. I. Berbasov, T. S. Kerblay, Ye. M. Kovalevskaya, L. N. Lyakhova	
Radiowave Propagation in Interplanetary and Circumsolar Space . . . . .	305
M. A. Kolosov, O. I. Yakovlev, A. I. Yefimov	
The Passage of Electromagnetic Waves Having Superlow Frequency (SLF) Through Ionosphere Plasma (Summary) . . . .	314
V. I. Aksenov	

III. INTERACTION OF ARTIFICIAL EARTH SATELLITES  
WITH THE IONOSPHERE

Interaction of Moving Bodies with a Plasma (Introductory Remarks) . . . . .	317
Ya. L. Al'pert	
Braking of Bodies Moving in a Rarefied Plasma . . . . .	322
A. V. Gurevich, A. M. Moskalenko	
Asymptotic Form of the Trail of a Body Moving in a Rarefied Plasma . . . . .	342
Yu. M. Panchenko	
Perturbed Zone Structure in the Vicinity of a Cylindrical Body in a Plasma . . . . .	355
A. M. Moskalenko	
Intensification of the Outer Electric Field on the Surface of a Large Body in the Ionosphere . . . . .	360
L. L. Goryshnik, A. N. Dyukalov	
Discrete Model of Matter in the Problem Concerning the Interaction of Rapidly Moving Bodies with a Rarefied Plasma (Summary) . . . . .	365
M. V. Maslennikov, Yu. S. Sigov	
Electric Fields in the Ionosphere Based on Data from Direct Measurements on Geophysical Rockets . . . . .	367
G. L. Gdalevich, I. M. Imyanitov	

IV. CORPUSCULAR STREAMS AND THEIR INTERACTION WITH  
THE GEOMAGNETIC FIELD. MAGNETOSPHERE AND  
RADIATION ZONES OF THE EARTH.

State of and Prospects for Studying the Radiation Zones of the Earth . . . . .	375
S. N. Vernov	
Penetration Processes into the Magnetosphere of the Earth, Capture and Acceleration of Solar Stream Particles, and Their Role in the Dynamics of the Geomagnetic Trap . . . . .	386
V. D. Pletnev, G. A. Skuridin, V. P. Shalitov, I. N. Shvachvonov	

	<u>Page No.</u>
Anomalous Diffusion of Charged Particles in the Radiation Zones of the Earth . . . . .	426
B. A. Tverskoy	
The Formation of Radiation Zones as a Result of Particle Drift in the Depths of the Magnetosphere . . . . .	442
A. Ye. Antonova, A. I. Yershkovich, V. P. Shabanskiy	
Interplanetary Plasma (Solar Wind) (Summary) . . . . .	454
K. I. Gringauz	
Comparison of Simultaneous Measurements of the Magnetic Field and Positive Ion Streams Within the Earth's Magnetosphere, Performed on the Satellite "Elektron-2" . .	457
K. I. Gringauz, Sh. Sh. Dolginov, V. V. Bezrukikh, Ye. G. Yeroshenko, L. N. Zhuzgov, L. S. Musatov, E. K. Solomatina, U. V. Pastovskiy	
Investigation of the Earth's Magnetosphere in the Radiation Zone Region (3-6R <sub>e</sub> ), February-April, 1964 . . . .	464
Sh. Sh. Dolginov, Ye. G. Yeroshenko, L. N. Zhuzgov	
Study of the Earth's Magnetosphere at a Distance of 7-11.7 R <sub>e</sub> on the "Elektron" Satellites . . . . .	483
Ye. G. Yeroshenko	
Structure of the Solar Corpuscular Stream and its Interaction with the Magnetosphere of the Earth . . . . .	499
Yu. D. Kalinin, E. I. Mogilevskiy	
Recording Charged Particles with an Energy of 0.1-10 kev with a Spherical Electrostatic Analyzer . . . . .	518
S. N. Vernov, V. V. Mel'nikov, I. A. Savenko, B. I. Savin, T. I. Pervaya	
Physical Picture of the Formation of an Artificial Radiation Zone During the High-Altitude, American Thermonuclear Explosion on July 9, 1962 . . . . .	526
Yu. I. Gal'perin	

Radiation Research on the Satellite "Kosmos-17" (Summary) . . . . .	534
P. V. Vakulov	
Results Derived from Studying the Geometric Position and Particle Composition of Radiation Zones of the Earth Based on Data from the Satellites "Elektron-1" and "Elektron-2" . . . . .	535
S. N. Vernov, A. Ye. Chudakov, P. V. Vakulov, Ye. V. Gorchakov, S. N. Kuznetsov, Yu. I. Logachev, A. G. Nikolayev, E. N. Sosnovets, I. A. Rubinshteyn, V. G. Stolpovskiy, V. A. El'tekov	
Preliminary Results Derived for Corpuscle Investigations on the Satellite "Elektron-1" . . . . .	551
A. D. Bolyunova, O. L. Vaysberg, Yu. I. Gal'perin, B. P. Potapov, V. V. Temnyy, F. K. Shuyskaya	
Possible Existence of a Soft Electron Component in the Outer Radiation Zone and its Variations . . . . .	566
V. V. Bezrukikh, K. I. Gringauz, L. S. Musamov, E. K. Solomatina	
Time Changes in the Outer Radiation Zone of the Earth Based on Data from the "Elektron" Satellites . . . . .	569
S. N. Kuznetsov, E. N. Sosnovets, V. G. Stolpovskiy	
Irregular High-Energy Electron Streams Near the Boundary of the Radiation Zones of the Earth . . . . .	576
S. N. Vernov, A. Ye. Chudakov, P. V. Vakulov, S. N. Kuznetsov, Yu. I. Logachev, E. N. Sosnovets, V. G. Stolpovskiy	
Pulsations of the Magnetic Field According to Measurements on the Satellite "Elektron-3" (Summary) . . . . .	587
S. N. Vernov, A. Ye. Chudakov, P. V. Vakulov, Ye. V. Gorchakov, Yu. I. Logachev, A. G. Nikolayev, I. A. Rubinshteyn, E. N. Sosnovets, M. V. Ternovskaya	



Study of the Earth's Outer Radiation Zone at Low Altitudes During Spacecraft-Satellite Flights and the "Kosmos" AES Flights Between 1960 and 1963 . . . . .	588
S. N. Vernov, V. Ye. Nesterov, N. F. Pisarenko, I. A. Savenko, L. V. Tverskaya, P. I. Shavrin	
Study of the Inner and Artificial Radiation Zones of the Earth at Low Altitudes in 1960-1964 . . . . .	607
V. Ye. Nesterov, N. F. Pisarenko, I. A. Savenko, M. V. Tel'tsov, P. I. Shavrin, K. N. Sharvina	
Outer Radiation Zone of the Earth and Bursts of X-Ray Radiation in the Stratosphere . . . . .	616
S. N. Vernov, L. L. Lizumin, A. N. Charakhch'yan, T. N. Charakhch'yan	
Measurement Results of the Satellite "Kosmos-41" in the Outer Radiation Zone . . . . .	623
S. N. Vernov, I. A. Savenko, M. V. Tel'tsov, P. I. Shavrin	
Study of Radiation Intensity in the Radiation Zones of the Earth on the "Kosmos-17" AES (Summary) . . . . .	629
G. A. Kirdina, Yu. M. Kulagin, A. B. Malyshev, M. N. Nazarova, P. M. Svidskiy, I. S. Yudkevich	
The Problem of Corpuscular Radiation in Pre-Equatorial Regions at Low Altitudes (Summary) . . . . .	630
I. A. Savenko, P. I. Shavrin, L. V. Tverskaya	
Interaction of Solar Wind and Geomagnetic Field (Summary) . . .	632
M. V. Samokhin	
Structure of the Boundary Layer Between a Rarefied Plasma and a Magnetic Field (Summary) . . . . .	633
Yu. S. Sigov	
The Outermost Zone of Charged Particles . . . . .	633
K. I. Gringauz, M. Z. Khokhlov	

# V. COSMIC RAYS

Problems of and Prospects for the Study of High and Ultrahigh-Energy Cosmic Ray Particles (Summary) . . . . .	655
N. L. Grigorov, I. D. Rapoport, I. A. Savenko, G. A. Skuridin	
Problems of and Prospects for Primary Cosmic Ray Research . . .	657
V. L. Ginzburg, L. V. Kurnosova, L. A. Razorenov, S. I. Syrovatskiy, M. I. Fradkin	
Experimental Studies of the Composition of Primary Cosmic Rays (Summary) . . . . .	678
L. V. Kurnosova, L. A. Razorenov, V. I. Logachev, M. I. Fradkin	
Studies of Primary Cosmic Radiation on the Satellites "Elektron-2" and "Elektron-4" . . . . .	678
S. N. Vernov, P. V. Vakulov, V. I. Zatsepin, Yu. I. Logachev, V. P. Okhlopkov, A. Ye. Chudakov	
Study of Cosmic Rays During Flights of Spacecrafts- Satellites and the "Kosmos" AES . . . . .	684
R. N. Vasilova, V. Ye. Nesterov, N. F. Pisarenko, I. A. Savenko, P. I. Shavrin	
Recording Cosmic Rays on the "Kosmos-17" AES (Summary) . . . . .	688
S. I. Avdyushin, R. M. Kogan, M. N. Nazarova, N. K. Pereyaslova, I. Ye. Petrenko, P. M. Svidskiy	
Ionizing Radiation Intensity Based on Measurements on "Zond-1" (Summary) . . . . .	689
S. I. Avdyushin, N. K. Pereyaslova, I. Ye. Petrenko	
Effects of Solar and Geophysical Phenomena in Primary Radiation, Recorded by Equipment on the Artificial Earth Satellite "Kosmos-19" (Summary) . . . . .	692
Yu. G. Shafer, B. M. Kuzhevskiy, A. G. Kulagin, N. G. Skryabin	

	<u>Page No.</u>
Results Derived from Studying the Cosmic Ray Nuclear Component on the Satellite "Elektron-2" . . . . .	693
Ya. L. Blokh, L. I. Dorman, L. V. Kurnosova, V. I. Logachev, G. F. Platonov, L. A. Razorenov, V. G. Sinitsina, A. A. Suslov, M. I. Fradkin	
VI. SUN	
X-Ray Radiation of the Sun (Summary) . . . . .	712
S. L. Mandel'shtam	
Image of the Sun in the Far Shortwave Region of the Spectrum (Summary) . . . . .	714
I. A. Zhitnik, V. V. Krutov, L. P. Malyavkin, S. L. Mandel'shtam	
Measurement of Solar X-Ray Radiation Intensity by Means of the Cosmic Station "Elektron-2" . . . . .	714
I. P. Tindo	
Cosmic Ray Generation on the Sun . . . . .	732
A. N. Charakhch'yan, T. N. Charakhch'yan	
VII. VARIOUS PROBLEMS	
Interpretation of Radiation Data from Meteorological Satellites . . . . .	741
K. Ya Kondrat'yev	
Radiation Safety Problems in Space Flights . . . . .	758
V. Ye. Nesterov, N. F. Pisarenko, I. A. Savenko, P. I. Shavrin	
Study of Meteoric Matter . . . . .	763
T. N. Nazarova	
Measurement of Scattered $L\alpha$ - Radiation in the Vicinity of the Earth and in Interplanetary Space . . . . .	769
V. G. Kurt	

Results of Radio Emission Strength Measurements at 725 and 1525 kc by Equipment on the Satellite "Elektron-2" . . . . .	776
Ye. A. Benediktov, G. G. Getmantsev, N. A. Mityakov, V. O. Rapoport, Yu. A. Sazonov, A. F. Tarasov	
Experiments Under the Program of the World Magnetic Survey . .	806
Sh. Sh. Dolginov, V. I. Nalivayko, A. V. Tyurmin, M. N. Chincevoy	
Influence of Satellites on Radiation Intensity in the Radiation Zones . . . . .	817
P. V. Vakulov	

# S P A C E   R E S E A R C H

## INTRODUCTION

The first All Union Conference on Space Physics, organized by the Commission on Research and Utilization of Cosmic Space of the USSR Academy of Sciences, was held in Moscow between June 10-16. The main purpose of the conference was to summarize the research performed primarily by rockets and artificial Earth satellites.

/3\*

On October 4, 1957, the first artificial Earth satellite in the world was launched in the USSR; this marked the advent of man's direct penetration of space. Since that time, space rockets have been sent to the Moon, manned spacecrafts-satellites have been launched, and man's entry into space has been accomplished. These successes belong primarily to our country. Our scientists have obtained many new and interesting results by means of modern satellites in the "Kosmos" and "Elektron" series, and also by means of other space vehicles.

The conference included about 100 reports<sup>1</sup>, whose contents encompassed the majority of disciplines included in space physics: The upper atmosphere, the ionosphere, radiation zones, interaction of solar corpuscular streams with the geomagnetic field, physics of the Sun and cosmic rays.

Several experimental and theoretical reports summarized research on the Earth's upper atmosphere, its structure and dynamics, and chemical composition.

Some of them were devoted to studying infrared radiation both of the Earth, and of the upper atmosphere. The stratified intensity distribution of atmospheric infrared radiation in the 0.8-40 micron spectral region, with maxima at altitudes of 260, 420, and 500 km, was discovered - this distribution was previously unknown. Interesting <sup>/4</sup> data on lower atmospheric luminosity and data derived from analyzing it, which were obtained during the flights of the spacecrafts "Vostok" and "Voskhod", were discussed in the reports compiled with the participation of cosmonauts V. V. Tereshkova-Nikolayev and K. P. Feoktistov. On the basis of these data, the existence of a dust layer around the Earth at an altitude of ~ 19 km was postulated.

Ionosphere research by means of mass spectrometers, different types of probes, and radio methods has provided new information on the structure of ionized outer ionosphere regions and on the electromagnetic phenomena taking place within the ionosphere. It was found that above 1000-1200 km the ionosphere primarily consists of protons - ionized hydrogen atoms. Only a very small amount of ionized helium, which was discovered previously in

<sup>1</sup> It should be noted that the manuscripts for the majority of the reports were obtained in October-November, 1964.

\* Note: Numbers in the margin indicate pagination in the original foreign text.

other experiments at altitudes of 700-1000 km, was observed during the 1964 measurements by the scientific station "Elektron". When the data derived from studying coherent radio frequencies emitted from the artificial Earth satellites were examined, several electron concentration maxima were discovered for a prolonged period of time in the outer ionosphere. These maxima were apparently caused by the complex, horizontally nonuniform structure of the ionosphere, by the dynamics of ionized particles, by plasma fluctuations, and by similar phenomena. The mean altitudinal dependence was obtained for the electron concentration in the outer ionosphere; this concentration did not exhibit any unusual features in the 1000-2000 km altitudinal region, which was observed previously in other studies.

Several reports were devoted to a theoretical examination of the interaction between artificial satellites and the ionosphere. The theory of kinetic flow around bodies in a plasma plays an important role in artificial Earth satellite research. It makes it possible to study the phenomena produced in the vicinity of the body. If these phenomena are not taken into consideration (angular particle distribution, effect of electric and magnetic fields), it is impossible to provide a correct interpretation of the results derived from many measurements of different parameters of an unperturbed plasma. Electromagnetic friction also becomes significant at altitudes of 700-800 km and above. The future study of plasma stability in the vicinity of a moving body and the formulation of a probe theory, with allowance for the magnetic field, are of great importance.

Several reports examined different results derived from measuring the structure of the magnetosphere, the radiation zones, the magnetic field of the Earth, and corpuscular streams.

It can be seen from these studies that there is a close connection between the behavior of the radiation zones and several geophysical phenomena (variations of the Earth's magnetic field, behavior of the polar ionosphere, etc.). In spite of the great abundance of experimental data, it is still impossible to formulate a definite picture of the radiation fields and the radiation streams surrounding the Earth. There is still no comprehensive, established theory for these phenomena. The results of different experiments still do not agree, and sometimes diverge considerably in quantitative terms.

The nature and mechanisms of radiation zone formation will no doubt be reconsidered in the near future. There has been an active tendency to explain the zone structure by considering the dynamics of plasma protons entering the magnetic field of the Earth, particle capture in the geomagnetic trap, and subsequent particle acceleration. This picture encounters no contradictions from the energy point of view. /5

Electron streams, which were discovered in different experiments outside of the radiation zones on the magnetosphere boundary, were

observed in the zones of radiation capture in the geomagnetic trap. This is the plasma electron component which advances toward the Earth and which is distributed around the Earth in a certain manner. Experimental data, as well as the general physical picture of the magnetosphere structure, provide no basis for assuming that there is even one so-called outermost radiation zone.

The results derived from X-ray solar radiation research, which were presented at the conference, present a fairly lucid picture of its properties and the energy spectrum of this radiation during a quiet Sun period. Several new data characterize bursts of this radiation and their connection with other phenomena.

It is interesting that during cosmic ray bursts, which are generated on the Sun, their intensity in the interplanetary medium sometimes increases by hundreds and thousands of times.

Measurements of cosmic radio emission intensity on the scientific station "Elektron", in the low-frequency wave range (725 and 1525 kc), which can be performed only on satellites, revealed several interesting properties of this radiation, the nature of which will only be understood in the future.

Cosmic ray research performed on satellites provided data on the chemical composition of their nuclear component, cosmic ray intensity at different distances from the Sun, etc. One of these reports investigated - as one of the main problems of future research - the possibility of studying processes produced by very high-energy particles, which are included in the composition of cosmic rays, in experiments on artificial Earth satellites. This report also discussed the search for fundamental elementary particles, particularly the so-called quarks predicted by theory - i.e., particles with a charge which is  $1/3$  and  $2/3$  of the electric electron charge.

Individual reports were also devoted to the problem of satellite meteorology, radiation safety of space flights, propagation of radiowaves over millions of kilometers or in communication with cosmonauts, and several other problems.

The scale and extent of research on space physics has increased considerably in recent years. The scale of research being carried out still leaves much to be desired. There is an obvious necessity of improving the quality of experiments, the formulation of complex investigations, and their comprehensive analysis. A search for more modern and comprehensive theories of the phenomena being studied is requisite. There must be an accelerated development of planetary research by means of space rockets, expansion of experiments studying the galactic  $\gamma$ -radiation which has been recently discovered, important research on the spectra of the eigen electromagnetic radiation of the interplanetary medium and of the planets, and the solution of other space problems which are literally introduced by science each day. The abundant information which we have obtained from 6

experiments on artificial satellites and rockets provide the basis for assuming that the time is approaching when we shall be able to formulate a new, more modern and comprehensive theory for the formation of the atmosphere and the ionosphere of the Earth, to understand the dynamics of the interplanetary plasma, to create a theory for the formation of the magnetosphere and the radiation zones, and to clarify the nature of the most interesting phenomena which have been discovered in space.

---

INTRODUCTORY REMARKS BY THE PRESIDENT OF THE  
COMMISSION ON THE RESEARCH AND UTILIZATION OF  
SPACE BY THE USSR ACADEMY OF SCIENCES

Academician A. A. Blagonravov

Comrades! The first All Union Conference on Space Physics opens today. 7

Due to advances in rocket technology, today space physics has unprecedented possibilities for development. Tens of satellites have been launched into circumterrestrial space in the short period of time which has elapsed since the first artificial Earth satellite in the world was launched in the USSR. The weight of these satellites has constantly increased, making it possible to deliver more up-to-date scientific equipment into space.

The satellite orbits have become more diverse and complex, and scientific equipment can be carried into new, previously inaccessible regions of space. Measurements can be performed simultaneously on several satellites, which can change their orbit during flight. Space rockets have been launched into far-removed regions of space. The possibilities for investigating the Moon and other planets are constantly expanding.

Advances in radioelectronics and equipment design have increased the amount of information which can be transmitted from the space vehicles.

Finally, man's flights into space and man's entry into the cosmos have unfolded new possibilities for scientific research. The accuracy, reliability, and authenticity of experiments have been augmented considerably due to the participation of man. Problems which were inaccessible to the automats can be solved: These problems range from analyzing data obtained and reformulating the observational program, up to the most precise regulation of scientific equipment directly on board the spacecraft.



Advances in Soviet science and technology have opened up a wide vista before space physics, and our problem is to successfully utilize all of the possibilities for developing this new area of knowledge.

The problems of space research are attracting more and more attention from scientists in every country. The circle of countries directly participating in space physics research is expanding. New research methods are being developed. For example, in France the rocket-carriers "Diamant" are being developed; they are designed to launch satellites. The Japanese rockets "Lambda" make it possible to probe the Earth's atmosphere up to an altitude of 1000 km; the rocket "Mu" is being developed to launch satellites. Firing ranges for sounding rockets are being constructed in such countries as Pakistan and Argentina.

The results derived from measurements on satellites and space rockets have provided science with a great deal of new information regarding physical phenomena in circumterrestrial space and at considerable distances in interplanetary space. The data obtained point to a very close connection /8 between processes occurring on the Sun and those observed near the Earth, in its atmosphere.

Our concepts of circumterrestrial space have changed significantly due to such discoveries as a constant solar wind, its interaction with the Earth's magnetic field, and the existence of a gigantic charged particle trap near the Earth. Such phenomena as magnetic storms, the aurorae polaris, and the radiation zones of the Earth are closely connected with processes occurring on the Sun. Important data have been obtained on magnetism in the solar system. They have shown that the Moon and Venus apparently have very weak magnetic fields. At the same time, due to the solar wind the geomagnetic field is localized in a limited area of space, which can be called the magnetosphere of the Earth. Many other data and important new information have also been obtained on space.

The All Union Conference on Space Physics which opens today must summarize all of the research which has been performed and must investigate the prospects for, and problems of, future research.

I  
UPPER ATMOSPHERE OF  
THE EARTH

With certain exceptions, the section "Upper Atmosphere of the Earth"/10 is primarily devoted to problems related to upper atmosphere properties and to the processes occurring within it..

This section is opened by a report which discusses in random order the concepts regarding the interconnection between different upper atmospheric processes and processes in circumterrestrial space, and regarding the necessity of investigating them concurrently.

Many reports are devoted to determining and analyzing theoretically the structural parameters of the upper atmosphere. Data are cited which indicate the possibility of temperature inversion at an altitude of 150-170 km. However, it must be noted that this problem requires further study in order to clarify the heat outflow mechanisms.

A portion of the reports is devoted to atmospheric optics and to investigating atmospheric emission. In certain reports, optical observations or the spectral composition and atmosphere emission intensities are employed to formulate a judgement regarding the lowest atmospheric layers close to the Earth.

The volume of experimental information presented in the different reports is quite extensive. However, there are still not enough data to make a precise determination of all the different parameters and properties of the upper atmosphere. Further research and the compilation of more extensive information are requisite; as a result of this, the results obtained can be refined and it will be possible to compile a definitive summary of our information regarding the upper atmosphere. This lack of data also imposes an element of uncertainty in the theoretical interpretation of different phenomena occurring in the upper atmosphere. Therefore, many theoretical studies, particularly those presented at the Conference, purely reflect the opinions of the authors, and necessitate further refinement.

CERTAIN PROBLEMS OF UPPER ATMOSPHERE PHYSICS  
AND SPACE NEAR THE EARTH

V. I. Krasovskiy

In a very brief summary, it is impossible to even lightly touch /11  
upon all the very basic problems entailed in the physics of the upper atmosphere and space near the Earth. We shall examine only one general portion of these various problems here, which will illustrate the close interrelationship between phenomena which are usually examined, analyzed, and studied completely separately. Warming and circulation of the atmosphere, photochemical conversions and ionization, atmospheric emissions, atomic and allotropic composition, periodic and sporadic geomagnetic variations, aurorae polaris and outer corpuscular streams, and particularly the phenomenon of "radiation zones or bands" (which has been artificially elevated to the rank of the most important and key phenomenon), etc. - all of these phenomena will no longer appear to be even conditionally separated after the comparison is completed. In order to evaluate the methodological aspect of the problem, it is important to note that important factual material which can be used to evaluate these problems has been obtained, not only by means of rockets and satellites, but also to a lesser extent by means of numerous observations and studies performed on the Earth.

In practical terms, the total, general composition of the Earth's atmosphere is conserved to a sufficient extent. All the various conversion processes and processes of motion in the atmosphere are primarily caused by energy transmitted by radiant and corpuscular radiation of the sun. Above the equatorial and the mean latitudes, the main photochemical and ionization conversions and heating are related to radial radiation. It should be noted, however, that - although the absorption process of this agent is sufficiently clear at the present time - data on this process are still inadequate for formulating a definitive judgement on such finite phenomena as heating and degree of ionization.

The essential factor is that a significant portion of the heat is liberated during inverse recombination processes, occurring with a certain delay, which disturbs the cophasal relationship with the process of radiation absorption. There are many gaps in this area. They can be eliminated by means of direct observations in the outer atmosphere, by observations performed on the Earth regarding its emission and ionization, and also by additional laboratory studies of the corresponding elementary processes.

In the high latitudinal regions, a significant amount of energy is sporadically introduced into the Earth's atmosphere, particularly during the years of maximum solar activity. This energy is caused by streams of energetic corpuscles which are apparently primarily particles of solar corpuscular streams which change their energy. This factor causes particularly intense heating, chemical conversions, and ionization.

Verification has also now been provided for the phenomenon of outer atmosphere heating due to magneto-hydrodynamic waves formed during the interaction of solar corpuscular streams with the magnetic field of the Earth. Basic, up-to-date information on the phenomenon of corpuscular influx, accompanying the aurorae polaris and contributing to their geomagnetic perturbation, is constantly being obtained, not only by means of rockets and satellites, but also by means of numerous observations performed on the Earth.

It is our purpose to draw attention to the circulation processes in the upper atmosphere at levels above 100-150 km, which have barely been studied. However, as will be shown below, these processes have a significant influence on all processes occurring in the outer atmosphere and circumterrestrial space. The circulation process is directly related to the process by which the outer atmosphere is irregularly heated; in addition to a certain tidal action, this is the primary source of circulation.

Present day information on circulation of the atmosphere is very /12 limited. We should first point out the generally-known diurnal solar variations and the geomagnetic field, which are due to the variable influence of solar heating and tidal forces (Ref. 1). Unfortunately, data on geomagnetic variations provide only a certain amount of information on the strongly-averaged changes in atmospheric circulation on levels which have not been established accurately, and do not provide any information on the constant component of this circulation. The movement of ionosphere nonuniformities (Ref. 2) apparently points to intense circulation in the upper atmosphere with enormous dispersion of velocity and direction. They seem to indicate that at altitudes of about 200 km, at low latitudes on the average, winds predominate which coincide with the rotational direction of the Earth. At latitudes of greater than 30-40° on the average, winds predominate which have the opposite direction. However, data on the wind direction do not exclude, on the average, winds of any meridional direction. After analyzing the evolution of the satellite orbits recently, King-Hele (Ref. 3) discovered the existence of considerable systematic wind movements at altitudes of 200-300 km in the rotational direction of the Earth.

According to Chamberlain (Ref. 4), in the zone of the aurorae polaris the regions of increased ionization are usually distributed more equatorially than the luminescent formations. To a certain extent, this points to the existence of a wind going from the poles to the equator at this time, since the conservation of ionization is a much longer process than is radiation.

As is known, variations in the upper atmosphere density, caused by a change in its heating (Ref. 5, 6), were determined by analyzing the braking of the satellites. In a study by M. Ya. Marov (Ref. 7) which was performed by means of this same method, variations in the atmospheric density at an altitude of 170-300 km with the diurnal period and as a function of solar activity - including the time interval encompassing its minimum - were

clearly discovered on the basis of the braking of several Soviet satellites. Even in 1958 (Ref. 8), when analyzing processes in the region of the aurorae polaris, we showed that during the development of the aurorae polaris, there is intense heating and "inflation" of the upper atmosphere in this region. This primarily points to an increase in the altitudinal extension of the region with intense emission of ionized nitrogen molecules. An increase in the upper atmosphere temperature should be pointed out in the region of the aurorae polaris red spots (Ref. 9-11), determined on the basis of the Doppler width of the red oxygen emission. Temperatures extending up to  $3500^{\circ}$  K were recorded. Very intense, red oxygen emission also points to a high upper atmospheric temperature during several aurorae polaris. Aurorae were also recorded in which, above the 300-kilometer level, the majority of oxygen atoms occurred in a metastable state, whose energy of excitation was about 2 eV (Ref. 12). Although this assumption was met with a very sceptical attitude in 1958, nevertheless there is now no doubt after Jacchia (Ref. 13) discovered a density increase in the upper atmosphere at about 200 km during geomagnetic storms, on the basis of the orbital evolution of the satellite with the polar orbit.

Thus, it can now be confidently asserted that there is intense circulation in the upper atmosphere and that there are processes which stimulate it. Apparently, there are winds having very different directions, with velocities ranging from zero to  $3 \cdot 10^4$  cm·sec<sup>-1</sup>. However, the scheme of general planetary circulation, its zonal sectional structure with vertical ascending and descending currents, is not completely clear. Such details are very significant for many geophysical processes. Horizontal circulation is indicated by local variations in the distribution of density and pressure, particularly at high altitudes. The vertical agitation /13 disturbs the normal molecular composition. The upward impact of a large amount of molecules leads to an increase in the ion recombination coefficient, and therefore changes the degree of ionization and electro-conductivity of the ionosphere. The vertical and horizontal motion of the atmosphere is essentially reflected in emissions of the upper atmosphere representing these processes.

During the last five to ten years, new upper atmosphere emissions have been discovered and regularly observed in the Soviet Union (Ref. 14). Among these, those of the greatest interest are the hydroxyl, atomic hydrogen<sup>1</sup>, and helium<sup>2</sup> emission. It has now been established that helium emission is

<sup>1</sup> This pertains to the emission of atomic-hydrogen with a narrow Doppler emission contour, in contrast to the previously known atomic hydrogen emission of the aurorae polaris with a wide contour.

<sup>2</sup> The discovery of crepuscular helium emission, and the determination of its excitation mechanism which is only possible for a large helium concentration in the upper atmosphere (Ref. 15), preceded the development of the newest atmospheric models with a large helium content at high altitudes (Ref. 16).

caused by fluorescence in solar radiation of metastable helium atoms excited by "fresh" photoelectrons formed during the ionization of the upper atmosphere (Ref. 17). An analysis of this process shows that at altitudes of about 500 km, the concentration of the neutral helium - taking into account the altitudinal temperature distribution and separation by diffusion - closely coincides with its concentration on Earth (Ref. 18). However, an analysis of the hydrogen emission intensity shows that at levels of about 100-200 km, the hydrogen concentration is significantly less than those values which are provided by data on hydroxyl emission at levels below 100 km. Therefore, we must assume that atomic hydrogen disappears very rapidly from the upper atmosphere due to a very high temperature, which is nevertheless insufficient for similar dissipation of the heavier helium atoms. The dissipation of hydrogen will be most intense in regions with a higher temperature. Atmospheric circulation supplies hydrogen reserves to this region from other regions, and therefore it is very important in an analysis of the general planetary distribution of atomic hydrogen in the upper atmosphere.

As we have already reported (Ref. 19-23), as a result of analyzing results obtained by means of the satellites "Kosmos-3" and "Kosmos-5", we arrived at the assumption that there is an electric field in the magnetosphere. Ionosphere circulation, having a velocity amounting to several hundreds of meters per second in a direction which is perpendicular to the geomagnetic field (having an intensity of 0.3 to 0.6 oe), creates an electromotive force amounting to  $10^{-4} \text{ v} \cdot \text{cm}^{-1}$ . As a result, each section of the ionosphere acquires a certain eigen electric potential which is transmitted to the plasma occupying the geomagnetic tube operating in this section, since the electroconductivity of the plasma along the geomagnetic force lines is large. The electric field strength, which is less than  $10^{-4} \text{ v} \cdot \text{cm}^{-1}$ , is significantly less than the values indicated by certain authors (Ref. 24-26) as a result of their direct measurements in the ionosphere. The impression is gained that these results are erroneous. Nevertheless, even values from  $10^{-4} \text{ v} \cdot \text{cm}^{-1}$  and less open up new possibilities for interpreting the phenomenon of the aurorae polaris and their so-called radiation zones. In the preliminary summary presented below, which attempts to consider new possibilities, we have neglected the fact that in the real ionosphere, the wind velocities and direction, as well as the electroconductivity, change with altitude.

Figure 1,a, shows schematically a certain meridional band of the ionosphere (solid line). As a result of circulation, the electromotive /14 force  $\Delta V$  is excited between its points  $A_1$  and  $B_1$ . At the points  $A_1$  and  $B_1$  the geomagnetic force lines enter the ionosphere, leaving points  $A_2$  and  $B_2$  in the same ionosphere zone in another hemisphere. These points are designated schematically by the dashed lines. However, there is no electromotive force in the  $A_2$  and  $B_2$  section. The electric resistance of the corresponding sections is indicated by the letter R with different indexes. Figure 1,b, schematically presents an approximate scheme of the electric charge. The resistance  $R_0$  models the total resistance of the ionosphere between points  $B_1$  and  $B_2$ . Since the electric resistance along the geomagnetic force line is too small, the voltage decrease will be determined only by the

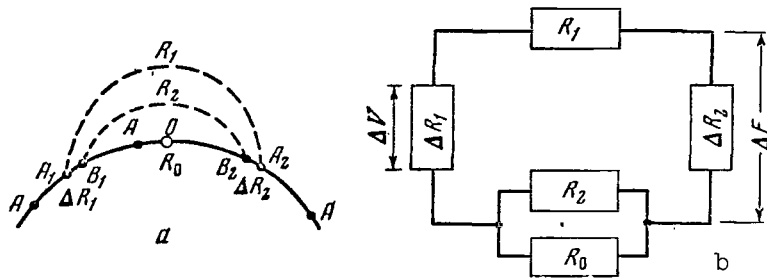


Figure 1

resistances  $\Delta R_1$  and  $\Delta R_2$ . On the average, these resistances are approximately the same. Therefore, the potential difference between the adjacent geomagnetic force lines will be approximately equal to  $\Delta V/2$ . If there is an electromotive force  $\Delta V$  in the  $A_2$  and  $B_2$  section, having a direction which is symmetrical with respect to the point  $O$  at the equator, then the potential difference between the adjacent geomagnetic lines will equal  $\Delta V$ . Usually the electromotive forces in both hemispheres always tend toward being symmetrical. Therefore, irregardless of whether there is no electromotive force in one hemisphere, the potential difference between adjacent geomagnetic lines will not be less than  $V/2$ . Thus, the possible values for the potential difference  $\Delta E$  will range from  $\Delta V$  to  $\Delta V/2$ .  $\Delta E$  can be calculated according to the formula

$$\Delta E = \frac{\Delta V \Delta R_1}{\Delta R_1 + R_1 + \Delta R_2 + \frac{\Delta R_2 R_0}{\Delta R_2 + R_0}} \sim \frac{\Delta V \Delta R_1}{\Delta R_1 + \Delta R_2} \sim \frac{\Delta V}{2}$$

( $\Delta R_1 \sim \Delta R_2$ ).

The potential difference  $E$  between the point  $O$  at the equator and any geomagnetic line, operating at any point  $A$ , will be determined by the total of the individual potential differences throughout the entire length from  $O$  to  $A$ . This system of electromotive forces is produced by wind motion along the parallels. If the wind direction is from the west to the east, then the outermost geomagnetic tubes will have a more negative potential with respect to the equatorial ionosphere, and vice versa. The electric field strength around the apex of the geomagnetic force lines will be less than the intensity of the electric field in the ionosphere by a factor approximately equal to the square of the ratio of the distance of the geomagnetic force line apex from the center of the geomagnetic dipole to the Earth's radius.

Figure 2, a, schematically shows by means of heavy lines two adjacent meridional zones of the ionosphere. The thinner perpendicular lines represent the position of the geomagnetic parallels in both hemispheres. The 15 dashed lines represent the geomagnetic force lines. The electric resistances of different sections are designated by the letter  $R$  with different indices.



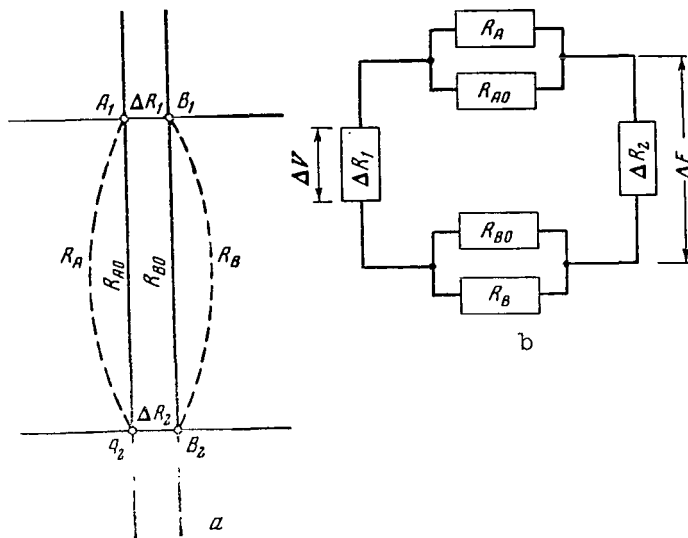


Figure 2

The electromotive force  $\Delta V$  can occur either in both  $A_1, B_1$  and  $A_2, B_2$  sections symmetrically with respect to the equator, or in one of the sections. Figure 2, b, presents an approximate scheme of the electric loading for this case. Resistances  $R_A$  and  $R_B$  model the total resistance of the ionosphere between the points  $A_1, A_2$  and  $B_1, B_2$ , respectively. If the same line of reasoning is pursued as in the case of circulation along the parallels, we find that in this case, the potential difference  $\Delta E$  between adjacent geomagnetic force lines will range from  $\Delta V$  to  $\Delta V/2$ . In this case,  $\Delta E$  can be calculated according to the following formula:

$$\Delta E = \frac{\Delta V \Delta R_1}{\Delta R_1 + \frac{R_A R_{AO}}{R_A + R_{AO}} + \Delta R_2 + \frac{R_{BO} R_B}{R_{BO} + R_B}} \sim \frac{\Delta V}{2}$$

$$\left( R_{AO} \ll R_A, R_{BO} \ll R_B, \Delta R_1 \sim \Delta R_2 \right).$$

This system of electromotive forces is created by the wind movements along the meridians. If the winds move from the equator to the poles, then the induced electric field will be directed from the east to the west, perpendicularly to the meridional planes, and vice versa. The intensity of the electric field between adjacent apexes of the geomagnetic force lines will be less at different longitudes than the intensity of the electric field in the ionosphere, by a factor which approximately equals the ratio between the distance of the geomagnetic force line apex from the center of the geomagnetic dipole and the Earth's radius.

It should be noted that even for asymmetrical circulation of the upper atmosphere in both hemispheres of the Earth, similar electric fields occur due to the high electroconductivity of the geomagnetic force lines at their terminal points. This fact is very significant for explaining the identical structure of the northern and southern aurorae polaris and their development.

In the case of an electric field in the magnetosphere, an additional drift of charged particles will appear which will be combined with the drift caused by the magnetic field gradient and the curvature of the geomagnetic force lines (Ref. 27). The velocity of the additional drift in the electromagnetic field can be determined according to the well-known expression:

$$V' = \frac{10^{-8}E}{H} \text{ cm} \cdot \text{sec}^{-1},$$

/16

where  $E$  is the intensity of the electric field in  $\text{v} \cdot \text{cm}^{-1}$ ;  $H$  is the intensity of the magnetic field in oersteds. In the absence of an electric field, the velocity of the usual drift  $V_0$  can be approximately written as

$$V_0 \sim 1,6WR^2\alpha,$$

where  $W$  is the energy of a charged particle in electron volts;  $R$  is the ratio of the distance of the geomagnetic force line apex from the center of the geomagnetic dipole to the Earth's radius;  $\alpha$  is the dimensionality coefficient and has a numerical value of unity.

Since the drift velocity in an electromagnetic field is primarily determined by the wind velocity, the former can be expressed by the latter ( $H$  barely changes within very small limits from 0.3 to less than 0.6 oe in the ionosphere since the pre-polar regions are not considered). However, the drift velocity will be different for winds having a meridional direction and a direction which is perpendicular to it. In the case of meridional winds, we have

$$V'_\perp \sim V R^2 \sin J$$

and in the case of winds along the parallels we have

$$V'_\parallel \sim V_\parallel R,$$

where  $V_\parallel$  and  $V_\perp$  are the velocities of the corresponding winds in the ionosphere;  $R$  - the ratio of the distance from the geomagnetic force line apex to the center of the geomagnetic dipole to the Earth's radius;  $J$  - inclination. Both positive and negative particles will always drift with meridional winds directed from the equator to the poles, within the geomagnetic field and vice versa. For winds along the parallels, these particles will always drift along the parallels in a direction which is opposite that of these winds. The circulation system of the upper atmosphere and the system of electric fields created by it are complex in nature. In principle, it is always possible to regard both the meridional component

and the perpendicular component as constant in time and changing with different characteristic geophysical periods. Since we do not know the exact wind velocities and directions at high altitudes, we shall confine ourselves to approximate oriented examples, assuming that the wind velocity equals  $3 \cdot 10^4 \text{ cm} \cdot \text{sec}^{-1}$ .

At a distance of two radii from the center of the Earth, perpendicular winds will shift particles from the apexes of single drift areas to others with a velocity of 1,000 km/hour, which corresponds to a shift of  $4^\circ$  per hour along the geomagnetic latitude. At a distance of 7 earth radii - i.e., in the region corresponding to the aurorae polaris - winds having a similar direction will produce shifts with a velocity of 55,000 km per hour, which corresponds to a shift of  $40^\circ$  per hour along the geomagnetic latitude. A supplementary drift velocity caused by electromagnetic drift, produced by ionosphere winds along the parallels, will equal  $6 \cdot 10^4$  and  $2 \cdot 10^5 \text{ cm} \cdot \text{sec}^{-1}$  at a distance of 2 and 7 radii from the center of the Earth, respectively. We should point out that at these distances, charged particles having an energy of about 10 and 3 kev, respectively, will have this drift velocity in an electrically neutral geomagnetic field. These energies are most characteristic for electrons exciting the aurorae polaris.

In the case of combined drift, the energy of drifting, charged particles will change periodically or randomly, depending on the characteristics of the ionosphere circulation. Significant effects will result from drift related to winds having a meridional direction. For one drift rotation /17 of an energetic charged particle around the Earth, the mean intensity of the electric field - caused by a narrow band of meridional winds - will equal zero. When it moves above the system of winds passing from the equator to the poles, the particle will drift from the normal drift areas to the drift areas having smaller L, increasing its energy. When it moves outside of this system, the reverse process will occur. When it moves above a system of winds going from the poles to the equator, the particle will drift from the normal drift areas to drift areas with larger L, decreasing its energy. When it moves outside of this system, the reverse process will occur. An energy change at any section of the drift path in these cases will not depend significantly on the distance of the drift trajectory apex from the Earth. It will be determined by the total electric field change in the ionosphere, directed along the corresponding geomagnetic parallels. If even a small field strength is assumed in this direction - for example,  $10^{-5} \text{ v} \cdot \text{cm}^{-1}$  - then the energy change along the parallels above the 1,000 km section is 1 kev.

When the charged particles change from single drift areas to others, for winds of any direction the altitude of the specular points changes. When the particles move from larger L to smaller L, the specular points of the charged particles having any sign descend to lower altitudes, since the isolines of the magnetic field strength are located at smaller L below. When the particles move from smaller L to larger L, the opposite process will occur. In the first case, it is possible that the drifting particles

will pour out more intensely, if the specular points descend to the more dense portions of the atmosphere at smaller geomagnetic latitudes.

However, during these movements the energy, and consequently the pitch-angles, of the drifting charged particles change, which complicates the picture considerably. If there is a decrease in the pitch-angles, the specular points will descend to an additional extent, and if there is an increase in the pitch-angles, the specular points will increase to an additional extent. If the energy of a charged particle increases as a result of the combined drift in electric and magnetic fields, then the pitch-angles will increase, and vice versa. The wind component, directed along the parallels, forms radially-directed electric fields, which have a different influence upon the positive and negative particles. If these electric fields are formed by the wind component moving in the direction of the Earth's rotation, then the pitch-angles of the negative particles will increase when the charged particles descend from larger  $L$  to smaller  $L$ , while the pitch-angles of positive particles will decrease. With a rise in the charged particles, the reverse will be the case. If these electric fields are formed by the wind component moving in a direction which is opposite to the Earth's rotation, when the charged particles descend from larger  $L$  to smaller  $L$ , the pitch-angles of the negative particles will decrease, while the pitch-angles of the positive particles will increase. When the charged particles ascend, the reverse will be the case. Thus, diverse conditions are created for positive and negative particles pouring out, depending on the wind direction along the parallels. It is interesting to point out in this connection that during the aurorae polaris, small-energy protons pour out outside of the regions having the most intense electron streams (Ref. 4, 21, 23). Electric fields influence charged particles with small energies to the greatest extent. Such phenomena were very recently analyzed by foreign authors (Ref. 28-30).

Winds directed along the parallels could not lead to significant changes in the drift areas for a geomagnetic dipole which coincides with the center of the Earth. In this case, there would only be a certain acceleration or retardation of the charged particle drifts around the Earth. However, the picture is essentially different, since the geomagnetic dipole is actually shifted with respect to the center of the Earth <sup>/18</sup> from the longitude of the Atlantic to the longitude of Indonesia. As a result, the areas of normal drift in the geomagnetic field which is electrically neutral penetrate to small altitudes above the longitudes of the Atlantic, and to large altitudes above the longitudes of Indonesia. However, areas having identical potential difference with respect to the equatorial ionosphere penetrate to large altitudes above the longitudes of the Atlantic, and to small altitudes above the longitudes of Indonesia. As a result, the customary drift areas in an electrically neutral geomagnetic field are located at lower altitudes above the longitudes of the Atlantic, and at higher altitudes above the longitudes of Indonesia. However, areas with the same potential difference with respect to the equatorial ionosphere occur at higher altitudes above the longitudes of the Atlantic and at

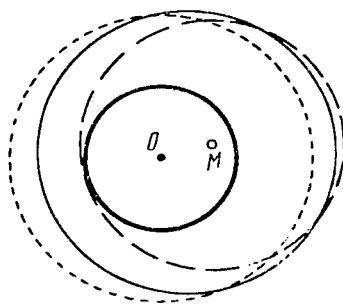


Figure 3

lower altitudes above the longitude of Indonesia. This takes place, due to the fact that in the ionosphere isolines, having identical electric potential with respect to the equator, are located at different distances from it due to dissimilar magnetic field strength. Due to the large strength of this field, these distances are smaller at the longitudes of Indonesia than they are at the longitudes of the Atlantic. However, magnetic tubes, operating on one and the same isolines, correspond to larger  $L$  above the longitudes of the Atlantic than they do above the longitudes of Indonesia. This is shown schematically in the cross section of the geomagnetic equator plane in Figure 3, in an exaggerated manner. The letter  $O$  designates the center of the Earth, while the letter  $M$  designates the center of the geomagnetic dipole. The small circle, drawn with the heavy line, indicates the distance from the center of the Earth, to which - in the case of a geomagnetic field which is electrically neutral - the apex of the drift area descends. The specular points of this drift area above the region of the Atlantic are located on those dense atmospheric regions where drifting particles perish. The cross section of this area is represented by the dashed line. It is impossible for charged particles to exist for a long period of time at the lower drift envelopes. The dot designates the point at which the geomagnetic force tubes having identical potential intersect the plane of the geomagnetic equator. Due to non-uniformity of the ionosphere winds, this cross section can actually be crooked. Charged particles having small energies will drift close to the areas of equal electrical potential, while charged particles having large energies will drift close to the drift areas in the geomagnetic field which is electrically neutral. The fine line represents the equatorial contour of a certain over-all drift trajectory corresponding to particles having average energy. It shows that, in the case of an electric field, other, lower drift areas are possible below the normal maximum drift. The locations of the specular points are shifted - with respect to the corresponding regions of the upper atmosphere, the rotational axes of the Earth, and the geomagnetic dipole - in a similar manner to the equatorial cross section of the drift areas shown above. Figure 3 shows that at low altitudes hard particles will predominate at longitudes of the Atlantic,

while soft particles will predominate at longitudes of Indonesia.

V. V. Temny (Ref. 31), as well as many other authors (Ref. 32), has confirmed the fact that the intensities of protons having energies greater than 50 Mev for L which are smaller than 3 can be expressed in the usual B,L-coordinates with small dispersion. However, V. V. Temny (Ref. 33), as well as O. L. Vaysberg and F. K. Shuyskaya (Ref. 34), could not clearly represent the intensities of electrons having energies of 50-150 keV in these usual B,L-coordinates, due to the large dispersion. The dispersion observed clearly depends on longitude and possibly on local time, since at longitudes corresponding to the data obtained by means of the satellites "Kosmos-3" and "Kosmos-5", there was a definite local time in the majority of cases. O. L. Vaysberg and F. K. Shuyskaya also observed an anomaly in the electron distribution with respect to pitch-angles at longitudes of East Africa. This anomaly consisted of the fact that at certain longitudes, at one and the same L and B, electrons having energies greater than 50 keV have a velocity distribution diagram which is flatter in a direction which is perpendicular to the geomagnetic force lines, and this anomaly is accompanied by a decrease in the stream intensity of these electrons. T. M. Mulyarchik (Ref. 35) showed that at certain altitudes very hard electrons having energies greater than 50 keV are observed at Atlantic longitudes, while softer electrons are observed at Indonesian longitudes. These facts, it seems to us, point to the existence of electric fields in the magnetosphere, as was postulated above. /19

The existence of an electric field in the magnetosphere with constant and variable components substantially changes the concepts which have existed up to the present regarding the almost stationary radiation zones. In view of the statements given above, the space around the Earth appears to be an almost ideal trap for energetic charged particles, although effective methods for these particles to penetrate this trap have not yet been found. Speaking figuratively, one could say that it is similar to a "sponge", which can "absorb" and "squeeze out" the energetic charged particles and thus change their individual energy. In those cases when the meridional winds, which pass from the equator to the poles, penetrate the geomagnetic latitudes at which the geomagnetic force lines of the boundary regions of the magnetosphere are at rest, canals appear for the penetration of the outer, interplanetary plasma, or of the solar wind, deep into the magnetosphere. When the meridional winds move in the reverse direction, the energetic charged particles are removed far beyond the limits of the magnetosphere. The random nature of the ionosphere wind structure is accompanied by energetic charged particles being scattered in the magnetosphere.

At one time, attempts were made to regard the radiation zones as the primary source of the aurorae polaris. However, from an energy point of view such an assumption is erroneous. In the so-called outer radiation zone, the energy flux of trapped particles does not exceed  $10 \text{ erg} \cdot \text{cm}^{-2} \cdot \text{sec}^{-1}$ , even in its center around the equatorial plane. A flux is implied which

equals  $10^8$  particles $\cdot$ cm $^{-2}$  $\cdot$ sec $^{-1}$  with a clearly exaggerated individual particle energy of about  $10^2$  kev, which is greater than the usual kev in the case of the aurorae polaris electrons. It could hardly be seriously expected that such fluxes create the powerful aurorae polaris having the intensity 4 on the international scale. The mean radiation flux of such aurorae amounts to 200 erg $\cdot$ cm $^{-2}$  $\cdot$ sec $^{-1}$  (Ref. 4), which is less than the energy flux of corpuscles causing this phenomenon. It should be kept in mind that the actual flux of liberated energy in individual concentrated formations - for example, rays - usually exceeds the mean value indicated above by a factor of two. For purposes of clarity, we should remember that very weak aurorae polaris, having an intensity of 1 on the international scale, are 1,000 times weaker than aurorae having an intensity of 4. Adjacent intensities differ from each other by a factor of 10.

It is also frequently stated that during the aurorae polaris an uninterrupted acceleration of the eigen Earth particles is initiated in the radiation zones, by a method which has still not been determined. Increasing the eigen energy, these particles penetrate the denser portion of the atmosphere and excite the aurorae polaris. However, this entire phenomenon is probably due to the absence of an adequate amount of low-energy charged particles, or an uninterrupted influx of them, in the corresponding equatorial regions of the magnetosphere. The low-energy charged particles in the central regions of magnetic tubes can be augmented only by a thermal plasma stream from the boundary of the exosphere. The inverse energy flux of such accelerated particles will always be less than  $2Unv/6$ , where  $U$  is the mean energy acquired after acceleration by these particles; this energy approximately equals  $10^{-8}$  erg ( $\sim 10$  kev).  $n$  represents the number of ion pairs per 1 cm $^3$  at the boundary of the exosphere;  $v$  is the thermal velocity of heavy ions. A helium ionosphere having a temperature of about 2,000° K usually predominates at the boundary of the exosphere. Therefore, the number of ion pairs will be on the order of  $10^4$  cm $^{-3}$ , and the velocity of heavy ions will be about  $3 \cdot 10^5$  cm $\cdot$ sec $^{-1}$ . Thus, the largest possible energy flux obtained in this way will be less than  $10$  erg $\cdot$ cm $^{-2}$  $\cdot$ sec $^{-1}$ . It cannot provide the aurorae polaris which are usually observed in actuality. /20

Particular attention must be called to the fact that the energy density of corpuscular streams in the region of the aurorae polaris frequently considerably exceeds the energy density of the geomagnetic field in the equatorial plane for the same geomagnetic force line. Actually, in aurorae polaris having an intensity of 4 on the international scale, the energy density of the corpuscles will be greater than  $10^{-7}$  erg $\cdot$ cm $^{-3}$ , since only the outflow of energy by means of radiation exceeds 200 erg $\cdot$ cm $^{-2}$  $\cdot$ sec $^{-1}$ , while the velocity of electrons having an energy close to 10 kev equals  $2 \cdot 10^9$  cm $\cdot$ sec $^{-1}$ . At the same time, the density of magnetic energy at the magnetosphere boundary for geomagnetic force lines operating in the aurorae polaris zones ( $L \sim 7$ ), equals approximately  $4 \cdot 10^{-8}$  erg $\cdot$ cm $^{-3}$ , since the magnetic field strength is close to  $10^{-3}$  oe at this point. Compression of

the charged particle streams by a factor of several tens, when they move from the equatorial plane to the polar ionosphere, is possible due to acceleration by the electric fields.

It is thus difficult to establish the fact that there is a regular dipole field (Ref. 36) during the aurorae polaris in the region which they occupy. However, the usual concepts based on the existence of this field have been formulated regarding the radiation zones formed by energetic charged particles which - figuratively speaking - are smoothly "wound around" the Earth and which form a solid frame around it. During the aurorae polaris, the variety of corpuscles observed fully corresponds to the variety of particles recorded in the radiation zones. This provides a basis for assuming that the predominant amount of particles in the radiation zones, as observed in the absence of the aurorae polaris, represents an insignificant surplus of the mass of particles discretely occupying certain locations in the magnetosphere during the aurorae polaris, and then scattering into more extensive regions. This assumption does not exclude the fact that the geomagnetic field may trap very energetic protons and electrons formed during the decomposition of albedo neutrons of cosmic rays. However, the role of this process is not important due to the small total density of particles having very high energy. The data obtained from the satellites "Kosmos-3" and "Kosmos-5" indicate that, even in the so-called inner zone, the total energy of electrons having small energy dominates (Ref. 19, 20).

Present day factual knowledge regarding the aurorae polaris has been enriched by numerous documents and examples of the penetration of charged particles from high latitudinal, geomagnetic force lines to low latitudinal, geomagnetic force lines (Ref. 23). The influx of corpuscles, which overlap in terms of latitude by several tens of degrees, has been recorded. Enormous irregular energy release in the ionosphere during the aurorae polaris leads to intense and irregular heating of it, as well as complex circulation. As a result, fluctuating magnetic and electric fields are formed in the corresponding regions of the magnetosphere. Under these conditions, the drift of energetic charged particles and of luminescent formations of the aurorae polaris, which are created by these particles, becomes possible at an enormous velocity and in very diverse directions. Due to the similarity mentioned above in the electric fields at the terminal points of one and the same geomagnetic force lines, the structure of the formations in the northern and southern aurorae polaris, as well as their development, is similar. As is known, luminescent elements of the aurorae polaris move at an altitude of 100-150 km in all directions with velocities of several  $\text{km} \cdot \text{sec}^{-1}$  (Ref. 23). This corresponds to a drift of charged particles in the equatorial plane, with velocities on the order of tens of  $\text{km} \cdot \text{sec}^{-1}$ , since the magnetic field strength in this region is on the order of  $10^{-3}$  oe. Thus, the observed drift points to electric fields with an intensity of approximately several tens of  $\text{mkv} \cdot \text{cm}^{-1}$ , which is very unlikely.

The lower boundary of the aurorae polaris, their spectrum, and the



position of their accompanying centers of ionosphere absorption provide valuable information on the nature and the energy of corpuscles creating the phenomenon of the aurorae polaris (Ref. 4, 23). It has been established from observations performed on Earth that the main energy liberation of the aurorae polaris is related to electrons having energies of about 10 kev. During the development of ray-like structures, there is a certain proportion of electrons with an enormous energy. Sometimes, both before and during the aurorae polaris, there is an influx of protons having energies of tens and hundreds of Mev into the Earth's atmosphere.

The phenomenon of the aurorae polaris also provides rich information regarding the nature of the interactions between the solar wind plasma and the magnetosphere, as well as the upper atmosphere (ionosphere) of the Earth. The electric field in the magnetosphere, which causes circulation of the upper atmosphere, cannot change the potential of the polar ionosphere with respect to the interplanetary plasma. The solar wind moves from the Sun to the Earth at velocities of several hundreds up to several thousands of  $\text{km}\cdot\text{sec}^{-1}$  (Ref. 37). However, it has been established on the basis of research that the contour of the hydrogen emission of the aurorae polaris at the magnetic zenith indicates that protons, penetrating the dense regions of the atmosphere, have velocities starting at zero and extending to thousands of  $\text{km}\cdot\text{sec}^{-1}$ ; the main portion of these protons has velocities corresponding to several hundreds of  $\text{km}\cdot\text{sec}^{-1}$  (Ref. 38-40).

This occurrence may possibly be explained by the fact that during the aurorae polaris the ionosphere acquires a positive potential, reaching tens of thousands of volts. As a result, braking of the primary solar protons occurs, after which particles having zero and small velocities appear. The positive recharging of the Earth's ionosphere is completely possible, since at the boundary of the magnetosphere the Larmor radius of the solar wind protons is greater than that of its electrons. In addition, such recharging provides for the acceleration of the solar wind electrons due to the energy loss of its protons. It follows from the geomagnetic disturbances that electric jet streams flow from the illuminated side to the nocturnal side in both the eastern and western portions of the aurorae polaris zones (Ref. 1). This also points to the fact that the sections of the ionosphere and the magnetosphere which face the Sun have a more positive potential than do their nocturnal sections.

It is difficult to observe any traces of the influence of weak eigen magnetic fields of solar wind in the complex picture of the aurorae polaris, which is determined by the diverse structure of the electric fields created by ionosphere circulation. However, a certain indication that they exist may be suspected in the fact that streams of more energetic electrons having small intensity - which is observed in ionosphere absorption (Ref. 23) - appear simultaneously with the development of ray-like structures and with an increase in aurorae polaris brightness produced by electrons having an energy of about 10 kev. It is improbable that two groups of

electrons having different energy spectra will appear simultaneously during the process by which energy is redistributed between protons and electrons of the solar wind at the boundary of the magnetosphere. However, charged particles having higher energy can be carried from the Sun to the "trap" formed by the eigen magnetic fields.

From this point of view, it is very interesting to recall the existence of two types of aurorae polaris. The first is primarily characterized by energy release caused by electrons having an energy of about 10 kev. The other type is characterized by very intense heating of the upper atmosphere due to magneto-hydrodynamic waves; this is not accompanied by significant energy release caused by low-energy corpuscles, although a certain amount of heavier particles, forming ionosphere absorption, penetrates into the lower regions of the atmosphere. It is very possible that the difference indicated above can be related to the degree of magnetization of solar corpuscular streams. However, this can be caused by the type of circulation in the upper atmosphere in the high latitudinal regions. As has already been pointed out, when the winds move from the equator to the poles, suction of the outer plasma within the magnetosphere is possible; when the winds move in the opposite direction - the reverse process occurs. It is fully possible that the variable wind structure in the polar ionospheres causes very significant fluctuations (by several orders of magnitude) in the intensity of the aurorae polaris (and the geomagnetic disturbances corresponding to them), whereas the recorded changes in the streams of solar wind particles are small (Ref. 37). A great deal of very important research must be carried out before definitive conclusions can be reached. Our working hypothesis, which is introduced for verification, assumes that the ionosphere circulation only produces factors which control the aurorae polaris. This distinguishes this hypothesis from the old, well-known "dynamo theory", in which ionosphere circulation was regarded as the energy source of the aurorae polaris (Ref. 41). /22

Satellites and rockets have still not been sufficiently and effectively utilized in studying such an important geophysical phenomenon as the aurorae polaris. The main reason for their ineffectiveness lies in the fact that they pass very rapidly through the very mobile and concentrated forms of the aurorae polaris, having a diameter which sometimes amounts to hundreds of meters. Therefore, it is very important to study the aurorae polaris simultaneously by means of equipment on the Earth. Rockets and satellites must study the most important problem of investigating the aurorae polaris during the daytime, when it is impossible to perform observations on the Earth. The dynamic morphology of the aurorae polaris contains many elements which have still not been studied and which undoubtedly are of general scientific interest. This is due to the fact that the behavior of the plasma in a magnetic field is clearly apparent in the phenomenon of the aurorae polaris, on scales which cannot be produced under laboratory conditions or cannot be observed in detail in space.

In summarizing all of the statements made above, we can affirm that only a complex study of all the diverse geophysical phenomena, employing both rockets and satellites as well as equipment on the Earth, will be most effective and productive. The material presented above has illustrated the direction in which our research has developed, the results produced by this research, and what appear to us to be the most advantageous elements in the performance of future research.

#### REFERENCES

1. Chapman, S., and Bartels, J. Geomagnetism, Oxford.
2. Narayana Rao, G. L., Ramachandra Rao, B. J. Atmos. and Terr. Phys., 26, 213, 1964.
3. King-Hele, D. G. Planet. Space Sci., 12, No. 9, 835, 1964.
4. Chamberlain, J. W. Physics of the Aurora and Airglow. (Acad. Press), 1961.
5. King-Hele, D. G. Nature, 198, No. 4883, 832, 1963.
6. Jacchia, L. G. Rev. Modern. Phys., 35, No. 4, 473, 1963.
7. Marov, M. Ya. Present Collection, p. 42.
8. Krasovskiy, V. I. Planet. Space Sci., 1, 14, 1959.
9. Mulyarchik, T. M. In "Issledovaniya polyarnykh siyaniy i svecheniya nochnogo neba". Izdatel'stvo AN SSSR, No. 1, p. 41, 1959.
10. Mulyarchik, T. M. Izvestiya AN SSSR, Seriya Geofizicheskaya, No. 3, 449, 1960.
11. Mulyarchik, T. M. and Shcheglov, P. V. Planet. Space Sci., 10, 215, 1963.
12. Manring, E. R. and Pettit, H. B. J. Geophys. Res., 64, 149, 1959.
13. Jacchia, L. G. J. Geophys. Res., 69, No. 5, 905, 1964. /23
14. Krasovskiy, V. I. Uspekhi Fizicheskikh Nauk, 75, 501, 1961; Translation: Planet. Space Sci., 8, 125, 1961.
15. Krasovskiy, V. I. Proc. 9 Internat. Astronaut. Congr., Stockholm, p. 518, 1960.
16. Nicolet, M. J. Geophys. Res., 66, 2263, 1961.

17. Krasovskiy, V. I. and Shefov, N. N. Planet. Space Sci., 12, No. 91, 1964.
18. Shefov, N. N. Ann. Geophys., 17, No. 4, 395, 1961.
19. Krasovskiy, V. I. et al. Geomagnetism i Aeronomiya, 3, 408, 1963.
20. Krasovskiy, V. I. et al. Kosmicheskiye Issledovaniya, 1, 132, 1963.
21. Krasovskiy, V. I. Space Res., 4, 114, 1964.
22. Krasovskiy, V. I. Gal'perin, Yu. I., Jorjio, N. V., Mulyarchik, T. M. and Bolunova, A. D. Space Res., 4, 572, 1964.
23. Krasovskiy, V. I. Space Sci. Rev., 3, 232, 1964.
24. Imyanitov, I. M., Shvarts, Ya. M. In "Iskusstvennyye Sputniki Zemli". Izdatel'stvo AN SSSR, No. 17, p. 59, 1963.
25. Johnson, D., Kavadas, A. Space Res., 4, 1964.
26. Imyanitov, I. M., et al. In "Iskusstvennyye Sputniki Zemli". Izdatel'stvo AN SSSR, No. 17, p. 66, 1963.
27. Spitzer, L. Physics of Fully Ionized Gases. London, 1956.
28. Dungey, J. W. J. Geophys. Res., 68, No. 11, 3540, 1963.
29. Maeda, H. J. Atmos. and Terr. Phys., 26, 1133, 1964.
30. Dewitt, E. N., Akasofu, S. I. Planet. Space Sci., 12, 1147, 1964.
31. Temnyy, V. V. Space Res., 5, 489, 1965.
32. O'Brien, R. J. Space Sci. Rev., 1, 415, 1963.
33. Temnyy, V. V. Present collection, p. 209.
34. Vaysberg, O. L., Shuyskaya, F. K. Present collection, p. 203.
35. Mulyarchik, T. M. Present collection, p. 205.
36. Heppner, J. P. et al. J. Geophys. Res., 69, No. 1, 1963.
37. Mustel, E. Space Sci. Rev., 3, 139, 1964.
38. Gal'perin, Yu. I. In "Issledovaniya polyarnykh siyaniy i svecheniya nochnogo neba". Izdatel'stvo AN SSSR, No. 1, p. 7, 1959.

39. Gal'perin, Yu. I. Planet. Space Sci., 1, 57, 1959.
40. Gal'perin, Yu. I. Planet. Space Sci., 10, 187, 1963.
41. Krasovskiy, V. I. Kosmicheskiye Issledovaniya (in press).

DENSITY AND TEMPERATURE OF THE ATMOSPHERE BASED ON  
MEASUREMENT RESULTS OBTAINED ON HIGH ALTITUDE  
GEOPHYSICAL AUTOMATIC STATIONS IN 1963

V. V. Mikhnevich

In order to study the properties of the upper atmosphere, on June 6 and 18, 1963, rockets were launched with high altitude geophysical automatic stations (AGAS). In addition to the scientific research equipment, the stations also included ionization and magneto-discharge manometers, with which density, pressure, and temperature of the atmosphere were determined. Preliminary results derived from determining densities have been published in (Ref. 1, 2).

Experiment Conditions and Processing Method

The conditions under which the experiments were performed were as follows:

- (1) Comparatively good vacuum frequency: the equipment was placed on the automatic station, far from the gas rocket; the AGAS was well pressurized; there were no structural elements, etc., in the way of the ionization manometer inputs;
- (2) The equipment was stabilized with respect to the Sun during the flight;
- (3) There was a relatively high ceiling to the ascent of the station (about 500 km); therefore, the velocity of the station was great below 350 km.

Measurements were performed during the ascent and descent of the station. The experiment conditions, as well as the main characteristics of the manometers and the boosters, are described in detail in the works /24 (Ref. 1-3).

The pressure and temperature of the atmosphere were determined on the basis of the pressure measured by the manometers, using the method of successive approximations. The following well-known relationship was thus employed (Ref. 4):

$$P_a = \sqrt{\frac{T_a}{T_n}} \frac{1}{\chi(\beta)} P_n \frac{K(0, l/r)}{K(\beta, l/r)},$$

where

$$\chi(\beta) = e^{-\beta^2} + \beta \sqrt{\pi} [1 + \operatorname{erf}(\beta)]; \quad \operatorname{erf}(\beta) = \frac{2}{\sqrt{\pi}} \int_0^\beta e^{-s^2} ds;$$

$$\beta = \frac{u}{v} \cos \theta; \quad T = \frac{Mg}{R} H,$$

where

$$H = \frac{h_1 - h_2}{\ln P_2/P_1}; \quad g = g_0 \frac{R_3^2}{(R_3 + h)^2};$$

$$N = \frac{P_a}{kT}.$$

Here  $T_a$  and  $T_n$  represent the temperatures of the atmosphere and the gas in the apparatus;  $P_a$  and  $P_n$  - pressure of atmosphere and gas in the apparatus;  $K(0, l/r)$  and  $K(\beta, l/r)$  - the Klausing coefficients for a tube having the length  $l$  and the radius  $r$  in the absence and presence of a directional stream;  $u$  - velocity of the directional stream;  $v$  - most probable velocity for the thermal motion of a particle;  $\theta$  - angle between the velocity vector of the stream and the manometer axis;  $M$  - molecular weight;  $R$  - gas constant;  $g$  - acceleration of the force of gravity;  $R_e$  - radius of the Earth;  $k$  - Boltzmann constant;  $h_1$  and  $h_2$  - altitudes at which the pressures  $P_1$  and  $P_2$  exist, respectively.

When the pressure was determined, corrections taking into account the change in the manometer sensitivity, due to an altitudinal variation in the gas composition and due to a nonuniform emission current, were introduced. In addition, a correction was introduced for gas removal in certain cases.

## Results

Figure 1 presents the atmospheric density on June 18, 1963, and on May 16, 1958.

On June 18, 1963, the rocket was launched at 4 hours 30 minutes local time. The radio emission flux of the Sun ( $\lambda = 10.7$  cm) was  $F = 82 \cdot 10^{-22} \text{ w} \cdot \text{m}^{-2} \cdot \text{cps}^{-1}$ , according to data from the observatory at Ottawa. On May 16, 1958, the measurements at different altitudes pertained to a different time (13-19 hours, local time). The data for May 16 were obtained by means of manometers on the third Soviet artificial Earth satellite (AES). The flux of solar radio emission was  $F = 194 \cdot 10^{-22} \text{ w} \cdot \text{m}^{-2} \cdot \text{cps}^{-1}$ .

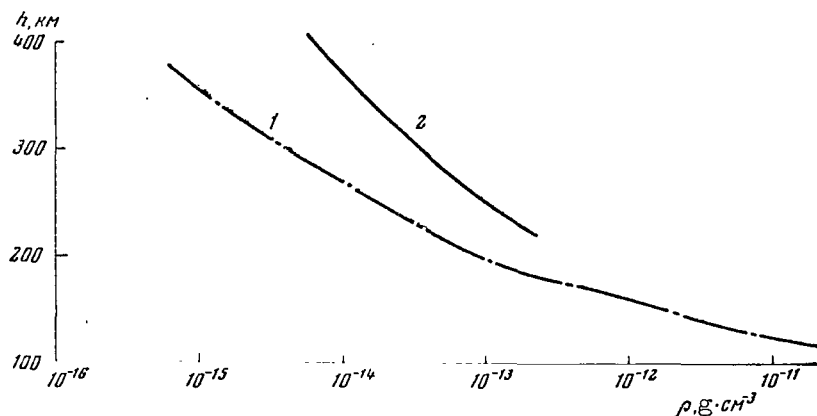


Figure 1

### Atmospheric Density

1 - June 18, 1963, 4 hours 30 minutes; mean latitudes of the European section of the USSR; AGAS, manometers; 2 - May 16, 1958, 13-19 hours; third Soviet AES, manometers.

A comparison of these data confirms the results obtained previously: the atmospheric density changes greatly at altitudes above 200 km. The change observed in atmospheric density was caused both by a decrease in solar activity, as well as by a diurnal effect. The atmospheric temperature above 200 km, recorded on May 18, also decreased considerably as compared with the years of maximum solar activity. During the years of maximum solar activity, according to data given in (Ref. 5), the temperature at 4 hours local time was 1159° K at an altitude of 300 km; at an altitude of 300 km\* - it was 1347° K. On June 18, 1963, at 4 hours 30 minutes, the temperature did not exceed ~775° K in the 200-300 km altitudinal region.

Figure 2 presents the altitude of a homogeneous atmosphere  $H$  and the atmospheric temperature  $T$  on June 18 (first and second approximations). As can be seen from the altitudinal pattern for the changes in  $H$  and  $T$ , in the altitudinal regions of ~165 and ~265 km, a temperature decrease was observed, while in the altitudinal regions of ~145 and ~215 km, a temperature increase was observed. On June 6, 1963, the temperature and altitude of the homogeneous atmosphere displayed a similar pattern with altitude (Figure 3). When  $P$ ,  $T$ ,  $\rho$ ,  $H$  were determined, values were used for the molecular weight and atmospheric composition which coincided with

/25

\*

Translator's note: This is an obvious misprint in the original foreign text.

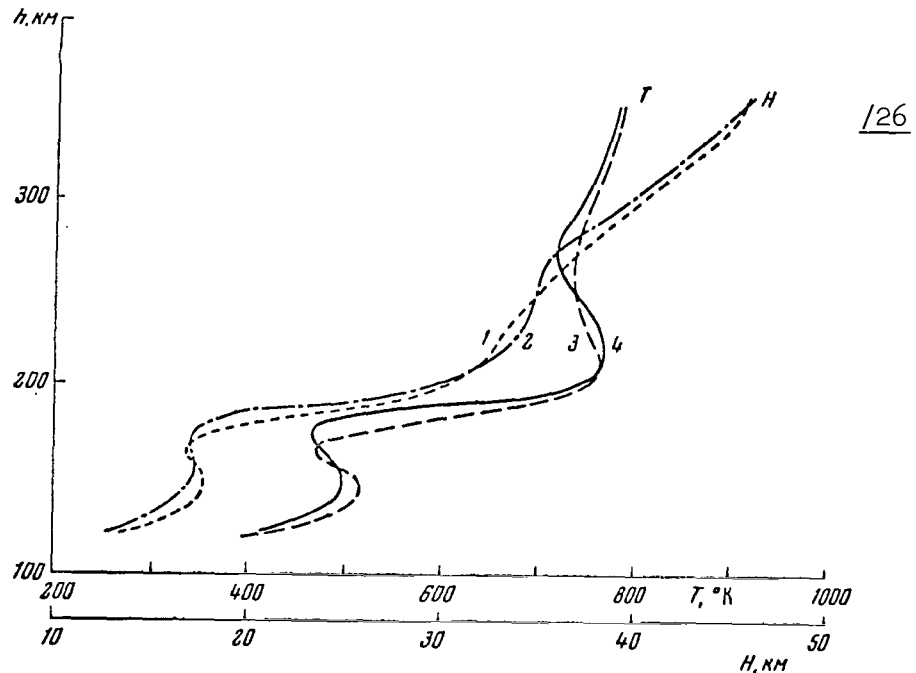


Figure 2

Altitude of Homogeneous Atmosphere and  
Atmospheric Temperature on June 18, 1963

1,3 - first; 2,4 - second approximation

those in (Ref. 5) for  $S = 100 \cdot 10^{-22} \text{ w} \cdot \text{m}^{-2} \cdot \text{cps}^{-1}$  (4 hours local time). The temperature corresponding to these tables was used as the zero approximation.

Is the observed change in  $H$  and  $T$  with altitude a result of measurement errors, or does it reflect a real change (which actually exists in the atmosphere) in the altitude of a homogeneous atmosphere and in temperature with altitude?

Let us examine the experimental data at our disposal to determine the density  $\rho$  of the atmosphere, using manometers and mass-spectrometers on rockets. Usually when experimental data are processed, taking into account a low measurement accuracy, the experimental points are greatly smoothed out. By way of an example, we can point to the works (Ref. 6, 7) and also (Ref. 1, 2). Figure 4 plots the experimental points and smoothed out curves based on data of Lagow and Horowitz (Ref. 6) and A. A. Pokhunkov (Ref. 7). As can be seen from the figure, the authors did not trust the



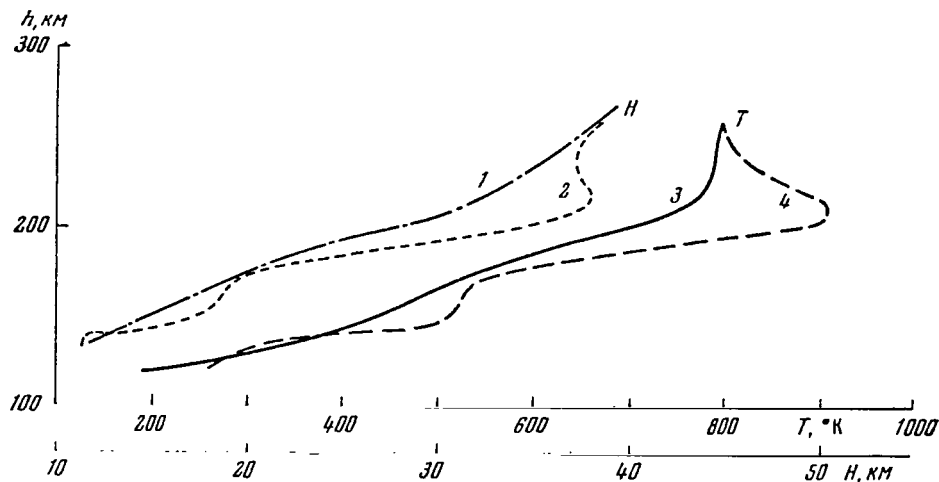


Figure 3

Temperature and Altitude of Homogeneous  
Atmosphere on June 6, 1963

Notation is the same as in Figure 2.

experimental points and smoothed them out, overlooking the systematic pattern of the points at certain altitudes.

A comparison of the primary, smoothed out experimental data on density (pressure), which have been obtained by different authors, shows that the deviations of the experimental points from the smoothed out curves are the same in nature. This compels us to reprocess the experimental data at our disposal. Thus, just as during the first processing, the curves were not drawn according to the points, but the smoothing out was performed by taking into account the systematic pattern of the points. The absolute values of  $H$  and  $T$  given below are not extremely accurate, since we did not strive for good congruence of the successive approximations in terms of absolute magnitude during the calculations.

The values for the altitude of the homogeneous atmosphere and of the temperature were calculated by the method described above, on the basis of pressure measured by manometers on February 21 and August 27, 1958, and October 18, 1962. The calculations were also based on the results derived from measuring partial nitrogen pressure by the mass-spectrometer on November 15, 1961 at 16 hours. In addition, the atmospheric temperature was determined on the basis of values for the altitude of a homogeneous atmosphere obtained from satellite braking (Ref. 8).

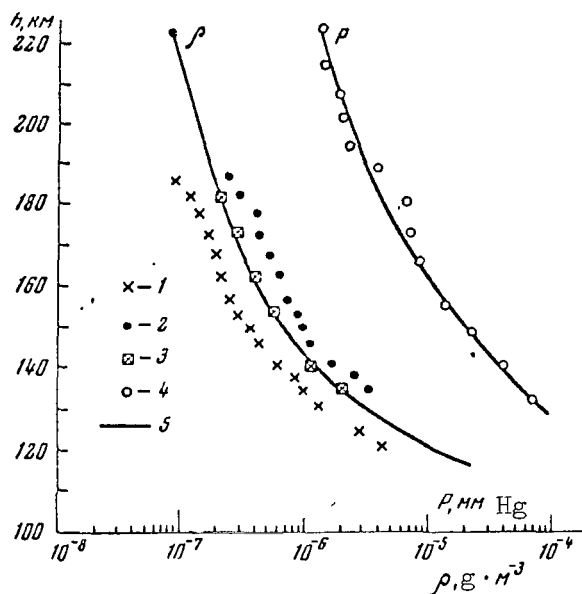


Figure 4

#### Atmospheric Density

August 7, 1951, 11 hours; manometers (Ref. 6). (1 - ascent; 2 - descent; 3 - averaged; 5 - smoothed-out curve.) November 15, 1961, 16 hours; mass spectrometer, nitrogen (Ref. 7). (4 - pressure inside the apparatus; 5 - smoothed-out curve.)

The results are shown in Figures 5 and 6. The atmospheric temperature, in accordance with the data in (Ref. 5), was used as the zero approximation. The values for the molecular weight and atmospheric composition are taken from these tables.

These results basically confirm the data obtained on June 18, 1963: the atmospheric temperature above 100 km does not increase monotonically; its inversion is observed. Primary, non-smoothed out data on density, obtained by Lagow and Horowitz (Ref. 6) on the rocket "Viking-7" on August 7, 1961 (see Figure 4), also point to the presence of temperature inversion in the altitudinal region of 150-180 km.

The results obtained by means of the mass spectrometer for nitrogen are particularly interesting from the point of view of determining temperature, since in this case no assumptions are made regarding the composition of atmospheric gas when determining the temperature. In accordance with these data (see Figure 6, curve 4), there is a temperature minimum at

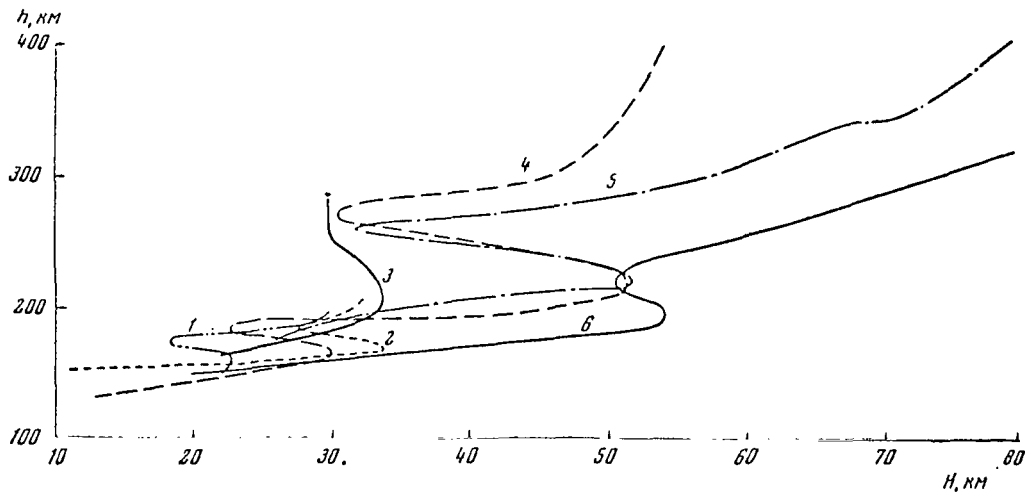


Figure 5

#### Altitude of Homogeneous Atmosphere

1 - August 27, 1958; 2 - February 21, 1958; 3 - October 18, 1962, manometers; 4 - November 15, 1962, mass spectrometer (Ref. 7); 5 - 1957-1959, satellite braking (Ref. 8); 6 - theoretical curve (Ref. 9).

altitudes of  $\sim 180$  and  $\sim 270$  km, and a temperature maximum at altitudes of  $\sim 160$  and  $\sim 220$  km. A similar pattern in the temperature change with two maxima and minima in the 100-300 km region was recorded - as was already shown - by manometers on June 18, 1963. In experiments on February 21 and August 27, 1958, the temperature minimum was observed at altitudes of  $\sim 175$  and  $\sim 185$  km, respectively.

In the dependence of the change in a homogeneous atmosphere altitude and the atmospheric temperature upon altitude - which was found from the braking of satellites - inversion was also observed in many cases.

As a result of observations on the braking of six satellites ("Explorer-4", "Discoverer-2", "Discoverer-5", "Discoverer-6", as well as the first and third Soviet satellites), King-Hele (Ref. 8) found that there is a maximum of the homogeneous atmosphere altitude at  $\sim 220$  km, and there is a minimum at  $\sim 260$  km. In accordance with these data on the composition of the atmosphere, according to (Ref. 5), there must be a temperature maximum and minimum at the indicated altitudes (see Figure 6, curve 5). In formulating a model of the atmosphere based on density values determined from satellite braking, Paetzold (Ref. 9) postulates the existence of temperature inversion (see Figure 6, curve 6). In his model, the value for

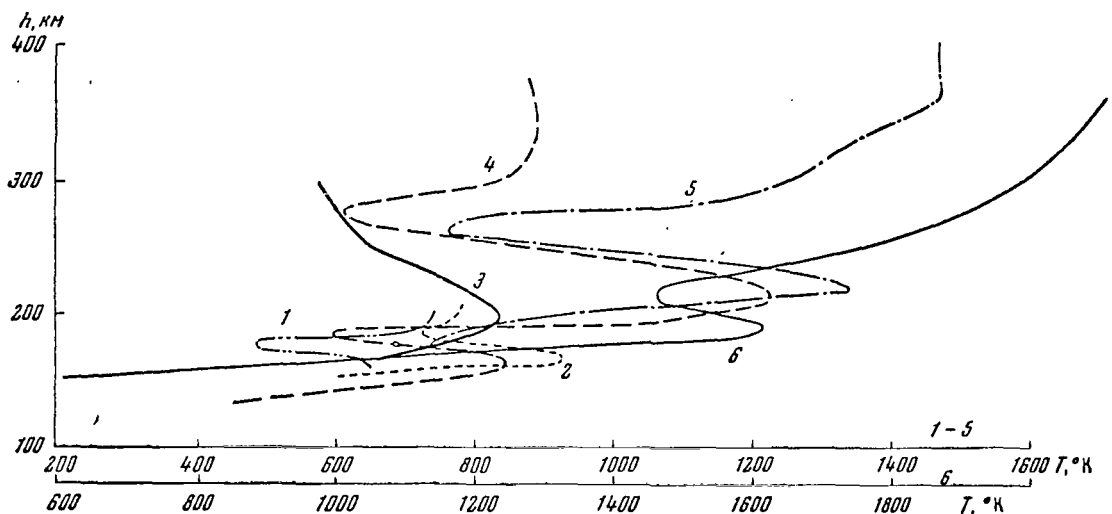


Figure 6

#### Atmospheric Temperature

Notation is the same as in Figure 5.

inversion during years of maximum solar activity is greater than during the period of the minimum.

The results derived from determining the altitude of the homogeneous atmosphere and the temperature were analyzed by different methods: measurements using manometers, mass spectrometers, satellites. This analysis provides a basis for assuming that above 100 km the temperature does not increase monotonically when there is diffusion equilibrium of the gas, but rather when there is temperature inversion. As is indicated by the measurement results using manometers and mass spectrometers, in the altitudinal region of 100-300 km there are two temperature maxima and minima. The altitude of the maxima and the minima is not constant. It is possible that temperature inversion does not always exist in this region. /29

The inversion of a homogeneous atmosphere, obtained from measurements of manometers and from satellite braking, can be explained by the inversion in the molecular weight change with altitude, which is less probable from our point of view.

It should be noted that Ya. L. Al'pert (Ref. 10) formulated an assumption regarding a temperature minimum at altitudes of 140-160 km, in order to explain the electron concentration distribution in the  $F_2$  region. The same assumption was expressed by Weeks and Wilkes (Ref. 11). At the same time, the works of Blamont (Ref. 12) and Nier (Ref. 13) make no mention of

temperature inversion. In particular, this may be due to the fact that, immediately during the years of minimum solar activity, the inversion may be significantly lower, and inversion is not observed as a result of experimental and methodological errors (particular, averaging).

At the present time, there have been very few rocket experiments to determine density and temperature of the atmosphere at altitudes of 100-400 km. Experimental errors are large, and due to this fact it is impossible to draw definite conclusions regarding the fine structure of the atmosphere from a single experiment in many cases. Considering the possible fine structure in temperature distribution, it would be desirable to increase measurement accuracy in future experiments.

The problem of temperature inversion in the 100-300 km altitudinal region requires additional study.

It is my pleasant duty to express my gratitude to G. N. Zlotin, M. I. Men'shikov, I. V. Meyzerov, and their coworkers for their participation in the preparation, for conducting the experiments, and for processing the results. I would also like to thank the coworkers in the laboratory in which I work.

#### REFERENCES

1. Mikhnevich, V. V. Space Res., 5, 1965.
2. Mikhnevich, V. V., Golubev, Ye. N., and Parfianovich, Yu. N. Kosmicheskiye Issledovaniya, 3, No. 3, 1965.
3. Kasatkin, A. M. In "Iskusstvennyye Sputniki Zemli". Izdatel'stvo AN SSSR, No. 15, p. 3, 1963.
4. Ivanovskiy, V. A. and Repnev, A. I. Space Res., 5, 1965.
5. Harris, I., and Priest, W. Theoretical Models of the Solar-Cycle-Variation of the Upper Atmosphere. Goddard Space Flight Center, NASA, V, 1962.
6. Lagow, H. E., Horowitz, R. J. Geophys. Res., 62, 57, 1957.
7. Pokhunkov, A. A. Space Research, North-Holland Publ., Amsterdam, 4, 325, 1964.
8. King-Hele, D. G. Nature, 184, No. 4695, 1267, 1959.
9. Paetzold, H. K., Zschörner, H. Space Res., 2, 958, 1961.
10. Al'pert, Ya. L. Zhurnal Eksperimental'noy i Teoreticheskoy Fiziki, 18, No. 10, 995, 1948.

11. Weeks, K., Wilkes, H. V. Proc. Roy. Soc., A192, 80, 1948.
12. Blamont, J. E., Chanin, M. L. et al. Space Res., 5, 1137, 1965.
13. Nier, A. O. Aeronomy Report, No. 1, 120, 1963.

CERTAIN PROBLEMS ENTAILED IN STUDYING THE STRUCTURE  
OF THE UPPER ATMOSPHERE <sup>1</sup>

M. N. Izakov

1. As a result of studies performed by means of rockets and satellites in recent years, great progress has been made regarding our knowledge of the structure of the upper atmosphere - i.e., regarding the distribution with respect to altitude of density, temperature, and composition of the atmosphere, as well as variations in these distributions. /30

A great portion of the existing data on the structure of the upper atmosphere has been summed up in the recently published COSPAR International Reference on the Atmosphere (CIRA-65) (Ref. 1). It can be assumed that the main variations in the structural parameters have already been determined, although - as will be shown below - their quantitative characteristics need to be defined more precisely. Certain assumptions were made in (Ref. 1-4) in summing up the experimental data and in formulating models, and these need to be verified.

The purpose of the present article is to determine the distribution of the structural parameters and their main variations, based directly on experimental data with a minimum of assumptions, and to compare the results obtained with other models.

For purposes of comparison, the model of Harris and Priester (Ref. 1, 2) was used; this model was used as the basis for describing the thermosphere in CIRA-65. The model of Jacchia (Ref. 3) which was also presented in the appendix to CIRA-65 (Ref. 1) was also used.

Harris and Priester (Ref. 1, 2) performed their calculations, using an equation of thermal balance and a barometric formula, with several

---

<sup>1</sup> The basic results of this study were presented at the Sixth Cospar Symposium (May, 1965, Argentina).

simplifying assumptions. The one-dimensional problem was examined, disregarding horizontal exchange. Constant boundary conditions were defined at an altitude of 120 km; the presence of gravitational-diffusion equilibrium was assumed above this point. An additional hypothetical heat source (which the authors attributed to corpuscular radiation) was introduced in order to have the solution agree with the experimental data. The magnitude of this heat source was assumed to be comparable with the magnitude of the main heat source due to absorption in the atmosphere of X-ray and ultraviolet solar radiation. It was assumed that this additional heat source was dependent on altitude, and that this dependence was similar to the dependence for the main source. The dynamics of the atmosphere was taken into account in a simplified manner by introducing a vertical velocity which was dependent on atmosphere heating. In spite of these simplifications, by means of a certain variation in the parameters introduced into the calculation, this scheme made it possible to provide a satisfactory description of the experimental data. In the model obtained, the experimental data on altitudinal density distribution coincided with the boundary conditions at 120 km (which were also obtained by averaging the experimental data). In addition, the data also agreed with the altitudinal temperature distribution, which corresponded to the assumed distribution of the heat source.

The starting point of the model formulated by Jacchia (Ref. 1, 3) was the altitudinal temperature distributions determined by Nicolet (Ref. 4), taking into account heating by solar ultraviolet, but from a stationary equation of thermal conductivity. The diurnal temperature variations in the exosphere are given by an empirical formula - a cosine to a certain extent, which is selected for the best description of the experimental data. The latitudinal temperature pattern, which is simply an interpolation between its diurnal and nocturnal values, is described by a similar formula with a different exponent, since there are still very few data on the latitudinal pattern of the structural parameters (Ref. 5). Just as in Harris and Priester, it is assumed that the boundary conditions are constant at an altitude of 120 km, and they are determined by averaged /31 experimental data. Simplifications introduced into the calculational scheme have the advantage that the obtained single-valued dependence of density and temperature distribution make it possible to take into consideration in a simplified way the latitudinal pattern of structural parameters, as well as the seasonal movement of the subsolar point.

On the other hand, the model of Harris and Priester, which takes into account thermal atmospheric inertia, points to certain additional effects (indeterminacy of the connection between density and temperature distribution, diurnal pattern which is asymmetrical with respect to the maximum, etc.), not provided by a stationary model. The main advantage of this model lies in the potential possibilities which it provides: this represents



the first step on the path toward creating a complete and representative physical model for the structure of the atmosphere, which is based on equations of thermohydrodynamics and which takes into account all the real sources and heat escapes.

The work by R. S. Zhantuarov (Ref. 6) can be regarded as a step along this path. By means of certain simplifications, this work attempts to take into account the influence of diurnal and semi-diurnal tidal movements on the structure of the atmosphere.

2. The computational scheme which we employed is given in (Ref. 7), and we shall only briefly summarize it here. The quantity, which is determined by the satellite braking and which equals the product of the density  $\rho$  by the square root of the scale height for the density  $H_\rho$ , is formulated as a function of the altitude  $h$ :  $\rho H_\rho^2 = F(h)$ . In this expression  $H_\rho$  is expressed in terms of  $\rho$ , and the differential equation obtained with respect to  $\rho$  is integrated over the altitude, which gives

$$\rho = \left[ \rho_0^{-2} + 2 \int_{h_0}^h \frac{dh}{F^2} \right]^{-1/2}, \quad (1)$$

where  $\rho_0$  is the density at the boundary altitude  $h_0$ . This equation is integrated numerically, and consideration is given to the variability of the coefficient of aerodynamical resistance  $C_D$ , on which  $F$  depends. The detailed derivation of the formulas for  $C_D$  is given in (Ref. 8). The pressure  $p$  is determined according to the density which is found:

$$p = p_1 + \int_{h_1}^h \rho g \, dh \quad (2)$$

(where  $p_1$  is the pressure at the boundary altitude  $h_1$ ;  $g$  is the acceleration of gravity), by numerical integration downward from the altitude  $h_1$ , in order to decrease the influence of errors at the boundary conditions. Finally, the scale height and the ratio of the temperature  $T$  to the molecular weight  $M$  is determined:

$$\frac{T}{M} = \frac{p}{R_0 \rho}, \quad (3)$$

where  $R_0$  is the universal gas constant.

In order to calculate the temperature, the method advanced by Kallmann-Bijl (Ref. 9) was applied, with the one difference that the boundary conditions are established at the altitude of 200 km, where satellite observations have provided adequate information regarding the density and where it can be assumed that the chemical reactions do not disturb gravitational-diffusion equilibrium. The equation arising from the assumption that there is gravitational-diffusion and thermal equilibrium was used (Ref. 7):

$$\sum_i p_i(h_0) e^{-M_i \int_{h_0}^h \frac{g \, dh}{R_0 T}} = p(h), \quad (4)$$

where  $p_i$ ,  $M_i$  is the partial pressure and molecular weight of the  $i$ th component of the atmosphere. /32

The quantities  $p(h)$  - which were determined according to formula (2) - as well as the quantities  $p_i(h_0)$  - determined according to experimental data on the composition - were substituted in this equation. After this, (4) was converted into an equation with respect to  $T$ , which was then solved on an IBM by the Newton method.

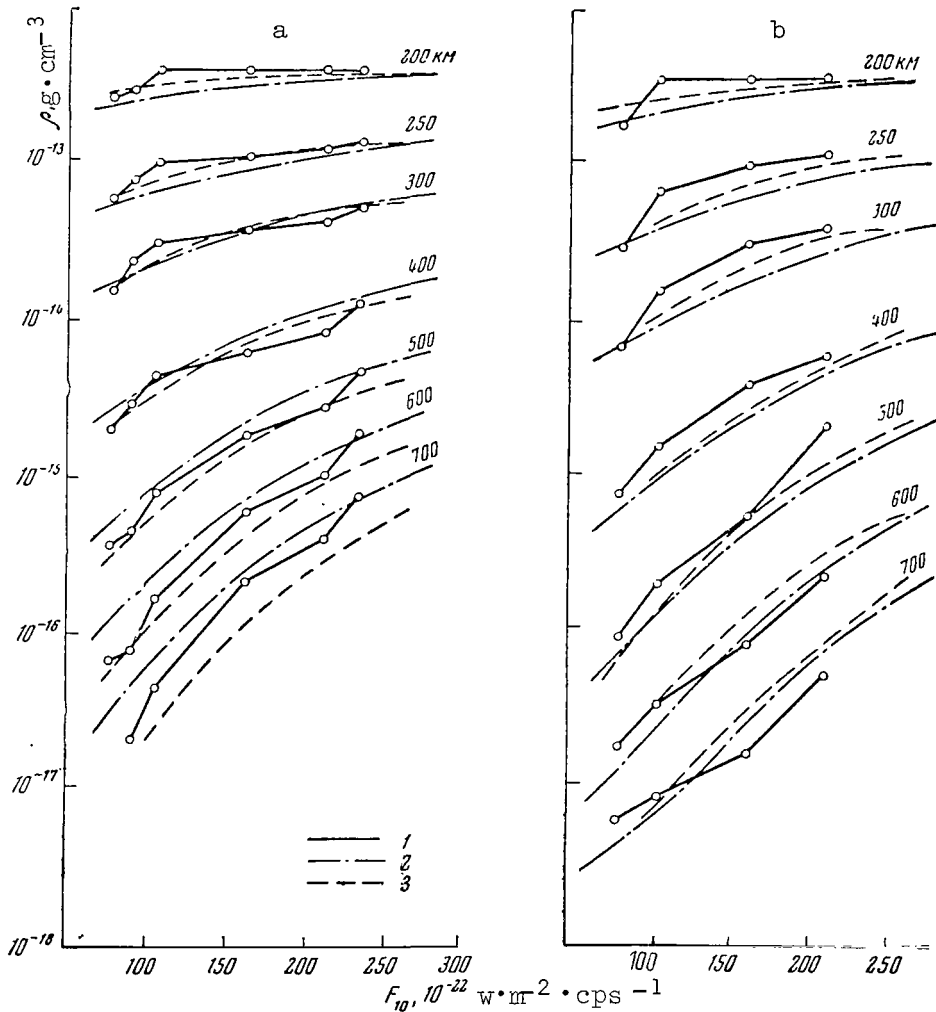


Figure 1

Dependence of Atmosphere Density  $\rho$  at Altitudes of 200-700 km on a Decimeter Flux of Solar Radio Emission  $F_{10}$

a - diurnal maximum; b - nocturnal minimum. 1 - Present article; 2 - according to Harris and Priester (Ref. 1); 3 - according to Jacchia (Ref. 3).

Numerical integration was used to determine the component concentration distribution according to calculated temperature distributions with respect

to altitude:

$$n_i(h) = n_i(h_0) \frac{T(h_0)}{T(h)} \exp\left(-M_i \int_{h_0}^h \frac{g dh}{R_0 T}\right), \quad (5)$$

according to which the molecular weight was then determined

$$M = \frac{\sum_i M_i n_i}{\sum_i n_i}. \quad (6)$$

3. For the specific application of this scheme, the mean yearly /33  
distributions of density with respect to altitude were used for the diurnal maximum and nocturnal minimum - determined by King-Hele (Ref. 10). At the present time a calculation based on the last work of King-Hele (Ref. 11) is being carried out, supplemented by data from Marov (Ref. 12).

The density values obtained differ from the original ones by 10-20%. An altitudinal pattern  $H_0$  was determined which was more complex than that given by other data, as was also the case for the ratio of temperature to molecular weight  $T/M$  (Ref. 7).

Figure 1 presents the maximum diurnal densities and the minimum nocturnal densities, determined in this way, at altitudes of 200-700 km, as a function of the flux of decimeter radio emission from the sun  $F_{10}$ . This figure also plots these dependencies according to Harris and Priester (Ref. 1) and Jacchia (Ref. 3). The mean annual values of the stream  $F_{10}$  were determined by averaging its mean monthly values.

It can be seen from Figure 1 that the over-all pattern of the curves is similar; however, certain differences can be observed. At altitudes less than 400 km, our dependencies are flatter for  $F_{10} > 100$ , and steeper for smaller  $F_{10}$ . According to our calculations, the density at these altitudes is almost everywhere somewhat greater than that given by other models, while its diurnal variations are considerably smaller. The magnitude of the diurnal variations increases somewhat with a decrease in  $F_{10}$ . For altitudes of 500-700 km, all of our diurnal curves are steeper than the others, ascending to the curves of Harris and Priester (Ref. 1) for  $F_{10} = 230$ , and descending to the curves of Jacchia (Ref. 3) for  $F_{10} = 80 - 90$ . Our nocturnal curves ascend higher for an altitude of  $h \leq 500$  km, for altitudes of 600-700 km they descend lower for  $F_{10} > 100$ , and for lower altitudes they are higher than that indicated by other models. It is true that the last points (for 600-700 km in the case of  $F_{10} < 100$ ) are unreliable, since there are not enough points on the original curves - as was shown in the work (Ref. 11) - and the curves are extrapolated substantially here. The difference in density values between our calculation and that provided by other models amounts to a factor of 1.5, and at several points this amounts to almost a factor of 2. In the majority of cases, our curves are somewhat closer to the curves of Jacchia than they are to the curves of Harris and Priester. We did not smooth out our curves  $\rho(F_{10})$ , in order to emphasize the fact that they have been determined on the basis of very few data, although the actual pattern of this dependence is apparently flatter. The determinations showed that the maximum error in the density values found amounts to  $\delta\rho = \pm 50\%$ .

Before the results derived from calculating the temperature are presented, we should touch in greater detail upon the selection of boundary conditions according to data on the composition. Figure 2 presents the concentrations of the main atmospheric components at an altitude of 200 km, according to measurements performed with mass spectrometers (Ref. 13-17) and monochromators (Ref. 18-20), as well as according to the calculation of Harris and Priester (Ref. 1), as a function of the decimeter stream of solar radio emission  $F_{10}$ , taken for the appropriate days according to data in (Ref. 21). It can be seen from the figure that, although there are very few data, the main dependences on the time of day and the solar cycle appear to agree in general with those used in the model (Ref. 1). However, the experimental data point to a somewhat large variation magnitude. It can also be pointed out that the first data (Ref. 13, 18) have a large scatter, while data obtained later coincide more closely with each other and with the model.

In the calculation, we took the main partial pressures at 200 km, determined according to temperature and concentrations obtained according to (Ref. 1). However, by varying the concentrations of the main components within limits determined by deviations of the experimental points in Figure 2 and by repeating the temperature calculation, we determined the error which might enter into the temperature determination due to an inaccurate knowledge of the composition at 200 km. This error amounts to  $30-50^\circ$  at altitudes less than 500 km, and increases significantly at higher altitudes. One should make immediate note of the fact that in the case of the indicated variations the over-all nature of the altitude dependences does not change significantly. The total error in the temperature caused by different factors may amount 34 to  $100-150^\circ$ .

Figure 3 presents the altitudinal temperature distributions determined by this method. Attention is called to certain differences in these distributions from the distributions obtained in other models (as was noted above, with definite assumptions regarding the altitudinal distribution of heat sources).

At altitudes of 400-500 km, the majority of the curves  $T(h)$  approaches the isotherms. Two diurnal curves represent an exception to this: For  $F_{10} = 232$ , which produces a temperature decrease above  $\sim 400$  km, and  $F_{10} = 105$ , which produces a temperature increase above  $\sim 500$  km. However, there is some doubt regarding the relationship between these two curves. The first curve was obtained in 1958 during the initial observational period with AES. The number of points was small, and they apparently include points which were not measured with respect to the diurnal maximum, but which distorted the curve somewhat in terms of nocturnal conditions. It should be pointed out, however, that certain arguments can be advanced in favor of the existence of such a temperature distribution in the case of large  $F_{10}$ . A definitive conclusion may be reached in the next year of maximum solar activity.

The second curve (diurnal maximum of 1961) compels us to point out that the original curve of  $\rho(h)$  (Figure 6, in the work [Ref. 11]) at altitudes of 500-700 km can be drawn somewhat lower in accordance with the measured points, which brings the temperature toward the isotherms.

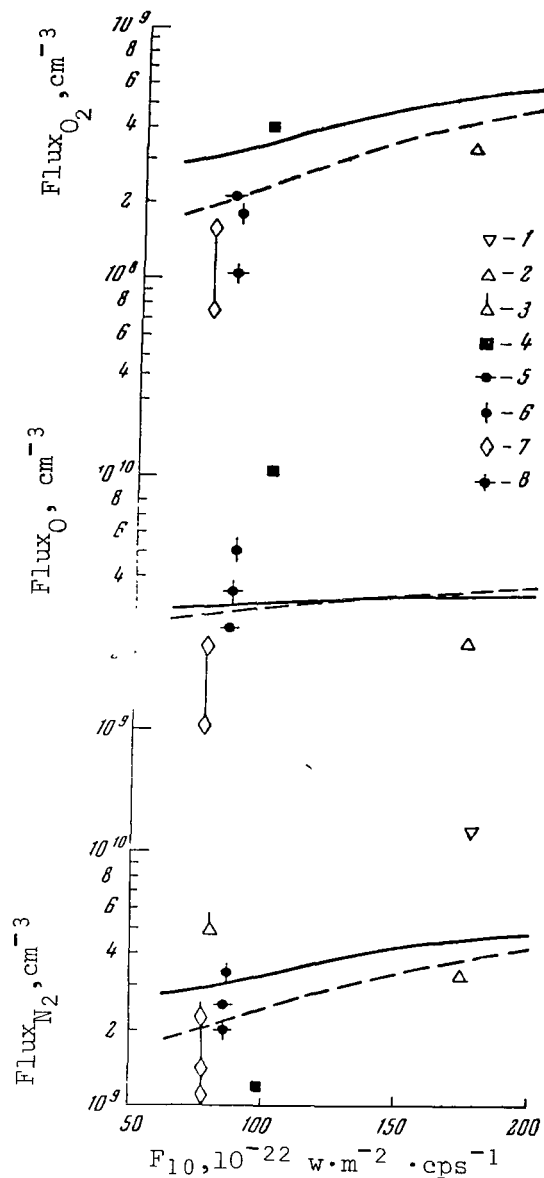


Figure 2

Dependence of Molecular Nitrogen Concentration As Well As Atomic and Molecular Oxygen Concentration On Decimeter Stream of Solar Radio Emission At An Altitude of 200 km

1 - July 22, 1959, 5 hours 15 minutes (Ref. 15); 2 - September 23, 1960, 0 hours 56 minutes (Ref. 16); 3 - November 15, 1961, 16 hours 00 minutes (Ref. 17); 4 - August 23, 1961, 10 hours 05 minutes (Ref. 20); 5 - June 5, 1962, 5 hours 45 minutes (Ref. 21); 6 - October 25, 1962, 16 hours 30 minutes (Ref. 21); 7 - June 6, 1963, 7 hours 30 minutes (Ref. 18, 19); 8 - July 10, 1963, 10 hours 00 minutes (Ref. 22). The light signs pertain to data from mass spectrometers; dark signs designate data from monochromators. The solid lines and dashed lines, respectively, designate data for diurnal maximum and nocturnal minimum, according to the model of Harris and Priester (Ref. 1).

In all the curves, there are temperature maxima in the lower thermosphere. In the case of large  $F_{10}$  during the day, these maxima are located at a lower point and, based on the diurnal curves, descend below 200 km for  $F_{10} = 160 - 230$ . For small  $F_{10}$  during the night, they are located at a higher point, reaching an altitude of  $h \approx 300$  km in the case of  $F_{10} \approx 80$ . It is <sup>/35</sup> true that, when there is a variation in the boundary conditions, the maxima close to 200 km disappear in the curves of  $F_{10} > 150$ . We should note that local temperature maxima in the lower thermosphere were also found by V. V. Mikhnevich (Ref. 22) in the case of rocket measurements.

Small maxima and minima on the curves for small  $F_{10}$  at altitudes of  $\sim 500-700$  km are apparently the result of a calculational error. The curves themselves for  $\rho(h)$  are quite unreliable (Ref. 11), and errors are more pronounced in the boundary conditions, particularly because of light components - helium and hydrogen. Finally, thermodiffusion (Ref. 23) and conditions in the exosphere, which make equation (4) inexact, influence the distribution of light components.

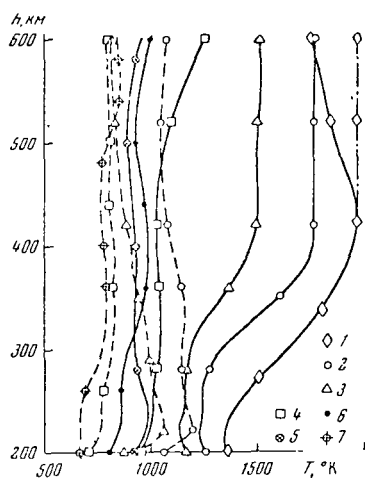


Figure 3

Altitudinal Temperature Distribution for Different Levels of Solar Activity (The Quantity  $F_{10}$  in Units of  $10^{-22} \text{ w} \cdot \text{m}^{-2} \cdot \text{cps}^{-1}$  is Used as a Characteristic of the Level)

1 -  $F_{10} = 232$ ; 2 -  $F_{10} = 210$ ; 3 -  $F_{10} = 161$ ; 4 -  $F_{10} = 105$ ;  
5 -  $F_{10} = 90$ ; 6 -  $F_{10} = 81$ ; 7 -  $F_{10} = 77$ .

Solid lines - diurnal maximum; dashed lines - nocturnal minimum.

Figure 4 clearly presents the main features of the temperature distribution determined. The temperature of the upper thermosphere in the region of the isotherm is expressed as a function of  $F_{10}$ . According to our calculation, we can see that an amplitude change in the diurnal temperature pattern with the solar cycle is found, which is larger than that provided by other models - from  $\Delta T_d \approx 100 - 150^\circ \text{ K}$  in the case of  $F_{10} \approx 80 - 90$  to  $\Delta T_d \approx 750^\circ \text{ K}$  for  $F_{10} \approx 210$ .

Particular attention must be given to the problem of the thermopause altitude  $h_c$  (either of the exosphere base, or of the critical level). The altitude of the thermopause  $h_c$  is calculated as the level at which the mean free path of  $\lambda$  equals the scale height for the concentration  $H_n: \frac{1}{H_n} = - \frac{d \ln n}{dn}$ , above which the role of collisions is small and molecules - having velocities close to the critical velocity - disperse from the atmosphere<sup>1</sup> :

$$\frac{\lambda(h_c)}{H_n(h_c)} = 1. \quad (7)$$

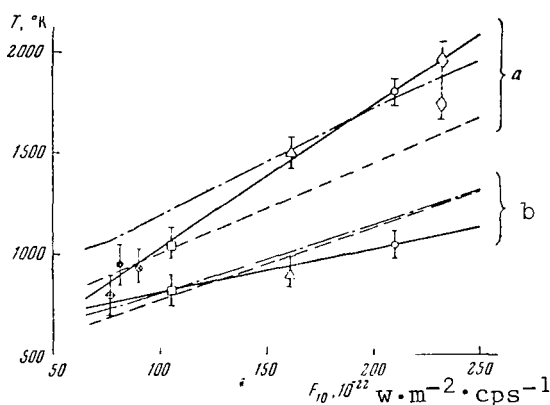


Figure 4

Dependence of the Temperature In the Upper Atmosphere and the Exosphere on the Decimeter Stream of Solar Radiation

a - diurnal maximum; b - nocturnal minimum. Solid curves - present article; dot dash lines, according to Harris and Priester (Ref. 1); dashed lines, according to Jacchia (Ref. 3). Notation for the points is the same as in Figure 3.

Figure 5 shows the change in the thermopause altitude  $h_c$  as a function of  $F_{10}$ . It can be seen from Figure 5 that, contrary to prevalent opinions, the thermopause altitude changes greatly with the solar cycle, from approximately  $h_c \approx 300$  km for small  $F_{10}$  up to  $h_c \approx 700$  km in the case of large  $F_{10}$ .

The altitudinal distribution of molecular weight, determined according to formula (6), is shown in Figure 6. Significant variations in

<sup>1</sup> The altitude of the thermopause is sometimes used to designate the altitude of the isotherm commencement in the thermosphere.

M at the given altitude with the solar cycle and the time of the day are apparent; these are similar to the variations based on the model in (Ref. 1). We should note that the amplitude of the diurnal variations M decreases with an increase in  $F_{10}$ .

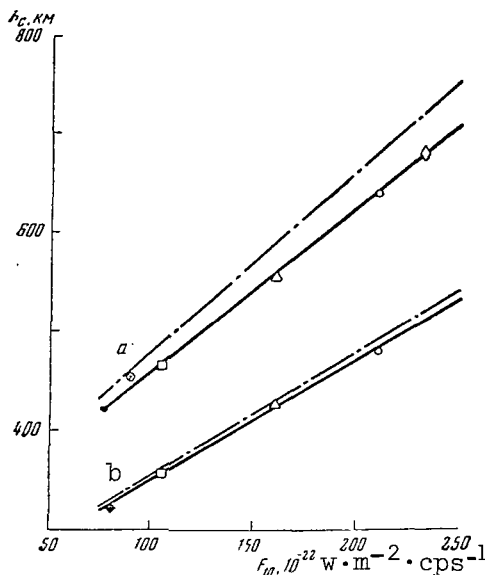


Figure 5

Dependence of Thermopause Altitude (Base of the Exosphere)  
 $h_c$  on Decimeter Stream of Solar Radio Emission

a - for diurnal maximum; b - for nocturnal minimum. Heavy lines designate calculation in our work; dot dash lines designate calculation in (Ref. 1). Notation of the points is the same as in Figure 3.

4. What can cause the difference in the dependences which are found and the real dependences? The comparatively small number of experimental data should first be pointed out: in the work (Ref. 11), ten curves are drawn on the basis of 146 points, i.e., about 15 points correspond on the average to each curve, and all of these data are obtained for half of one solar cycle (from the maximum in 1958 to the minimum in 1963-1964). An error is also caused by separate averaging of  $\rho$  and  $H_p$ , while we need the mean annual  $\rho H_p^2$ . In addition, it is known (Ref. 1) that 27-day variations, half-year variations, and variations related to the geomagnetic index are superimposed on the main variations considered here (11-day and diurnal variations). With a sufficiently large number of data, the secondary variations could be excluded with averaging, but since the number of points is small the error caused by this factor can enter into the dependences which are found. It should also not be forgotten that the magnitude of the stream of decimeter solar radio emission  $F_{10}$  is not a decisive parameter, but only an index. This index can be used to describe the manner in which the stream of ultraviolet and X-ray solar radiation, which heats the upper atmosphere, changes as a result of complex solar processes. It can be seen from experiments in (Ref. 24, 25) that  $F_{10}$  is closely correlated with certain intense



lines in the hard ultraviolet and roentgen, but that this index can hardly /37 provide an accurate description of the entire stream heating the thermosphere.

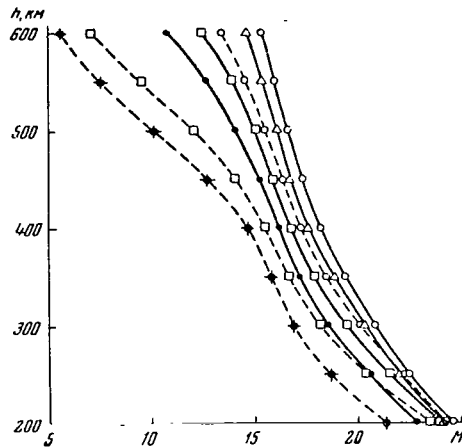


Figure 6

Altitudinal Distribution of Atmospheric Molecular Weight  
Notation is the same as in Figure 3.

It should finally be noted that the calculational scheme employed is only approximate, due to the utilization of a barometric formula - which, strictly speaking, is applicable in the presence of local thermodynamic equilibrium. Deviations from equilibrium can be caused by chemical reactions in the thermosphere. However, as was shown by A. I. Ivanovskiy (Ref. 26), under these conditions a barometric formula can be retained in the usual form, if an effective temperature  $T_*$  equalling

$$T_* = T - \frac{3}{2} \frac{Q}{k N_C}, \quad (8)$$

is used in it, where  $N_C = 8\sqrt{\pi} \sigma \left(\frac{kT}{m}\right)^{\frac{1}{2}} n^2$  is the number of collisions between molecules;  $Q$  - the difference between the absorbed and emitted radiation per unit volume;  $k$  - Boltzmann constant;  $\sigma$  - cross section of the collisions;  $m$  - mass of the molecule. Thus, in certain cases the temperature determined by the scheme which we have employed will be the effective temperature  $T_*$ . Estimates have shown that, for the distributions of the structural parameters determined here, the difference between the effective and the kinetic temperatures up to the boundary of the exosphere is small, and becomes significant only for large values of  $F_{10}$ . For these estimates,  $Q$  was based on data given in the work (Ref. 27).

In the exosphere, the barometric formula can also be retained with a correction for the absence of molecules, among those returning to the earth, having velocities larger than the critical velocities and dispersing from the atmosphere (see, for example, [Ref. 28]). Thus, the temperature in the exosphere equals the temperature at the critical level. This correction is significant only for concentrations of hydrogen and helium molecules, which -

in the altitudinal range under consideration up to 700 km - provides a correction of not more than 5-7% in the total atmospheric density, and about 9% at an altitude of 1,000 km.

In addition, thermal diffusion (Ref. 23) - which was not taken into consideration in the scheme which we employed - influences the distribution of hydrogen and helium in the thermosphere. However, since the proportion of light components in this altitudinal range is small and since isothermy occurs in the upper portion of the thermosphere, this simplification does not introduce significant errors into the determination of density and temperature - at least up to altitudes of about 500 km.

The following refinement of our scheme is possible: by determining the temperature distribution as was indicated above, one can then find the distribution of hydrogen and helium concentrations, taking into account thermodiffusion (Ref. 23):

$$n_{(H, He)}(h) = n_{(H, He)}(h_0) \left[ \frac{T(h_0)}{T(h)} \right]^{(1+\alpha)} \exp \left( -M_i \int_{h_0}^h \frac{g dh}{R_0 T} \right), \quad (9)$$

where  $\alpha$  is the thermodiffusion constant. Thus, the corresponding correction can be introduced into the concentration of all components in the exosphere - for example, the correction employed in the tables of work (Ref. 28). It may thus be assumed that the calculational scheme employed in the altitudinal range under consideration makes it possible to obtain the structural parameters of the upper atmosphere within satisfactory accuracy.

5. Certain conclusions may be drawn from the results presented above regarding the future development of research necessary for improving the structural model of the upper atmosphere.

We have seen that the over-all pattern of the dependences found is approximately the same for calculations based on different schemes, which substantiates to a certain extent the validity of the premises expressed in them. At the same time, the differences between the models point to the necessity of defining the dependence of the structural parameter variations on definite factors more precisely in the future.

At the present time, it is particularly important to compile data /38 on the latitudinal dependences of the structural parameters, on the structure of the atmosphere in the altitudinal range of 100-200 km, and on the concentrations of helium and hydrogen.

If we have data on the density of the atmosphere at different altitudes and on the composition at an altitude of about 200 km, we can then calculate all the structural parameters of the atmosphere for altitudes close to 200 km. The compilation of data makes it possible to apply the calculational scheme which we have employed to not just the mean annual data - as was done above - but also to data which are more local in time and space. This would make it possible to study the desired dependences in greater detail. Simultaneous measurements of density at different altitudes above one and the same point on the Earth's surface, together with measurements of the composition close to

200 km and measurements on short-wave and corpuscular radiation, absorption of hydromagnetic waves and other factors influencing the structure of the upper atmosphere, would be of the greatest value in solving these problems.

In order to study the actual dependence of structural parameters on definite factors, it would be of value to clarify the extent to which the parameter  $F_{10}$  reflects the change in the entire stream which heats and ionizes the upper atmosphere. If necessary, it would also be valuable to determine a more appropriate parameter.

The results of the present article are limited, due to the utilization of data on only satellite braking, since the problem was posed of comparing them with models (Ref. 1, 3) obtained on the basis of the same data by different computational methods. A more comprehensive picture will be obtained by the utilization of data from other methods - based on results derived from measurements of equipment located on AES and rockets, as well as from indirect methods, for example, meteoric methods. This presents the problem of matching data from different methods, which can be clearly seen from experiments on "Explorer-17", where the densities - which were measured simultaneously on the basis of braking and manometers - differed by approximately a factor of two (Ref. 29). In order to solve this problem, it is necessary to improve these methods, and to employ stricter theories for calculating atmospheric density based on readings of equipment on AES (Ref. 30).

Due to the fact that small variations occur, excluding main variations, the method of successive approximations is advantageous to employ in the total computational scheme: after the dependence for the main variations is found, it is excluded. Then the dependence for small variations is refined, after which the points are corrected for small variations. The main variations are again refined, etc. We would like to point out one problem pertaining to the consideration of small variations: certain of these variations - for example, 27-day variations and variations with the geomagnetic index - are not independent; a correlation can be observed between  $F_{10}$  and the geomagnetic index  $A_p$ . Consequently, they entail the problem of strict simultaneous calculation of different dependent variations.

The works mentioned above give several empirical dependences, which must be constantly compared with theoretical calculations. In the last analysis, this must make it possible to formulate a sufficiently complete and representative physical model of the upper atmosphere structure. This structure is based on the formulation and more accurate solution of a system of thermohydrodynamic equations, which takes into account all the significant sources and losses of heat and all reactions taking place in the atmosphere. Experiments on the determination and more precise definition of the transverse cross sections of these reactions are a necessary stage in the solution of this problem. Such a comprehensive model must naturally provide the distribution of not only neutral components, but also charged components, for which the interaction of the charged components and the difference of the electron temperature from the kinetic temperature must be defined more precisely.

1. COSPAR Internat. Reference on Atmosphere (CIRA-65), 1965.
2. Harris, I. and Priest, W. J. Atmos. Sci., 19, No. 4, 286, 1962.
3. Jacchia, L. Smithsonian Astrophys. Observ., Spec. Rept, No. 150, 170, 1964.
4. Nicolet, M. Smithsonian Astrophys. Observ., Spec. Rept., No. 75, 1961.
5. May, B. R. Planet. Space Sci., 12, No. 12, 1179, 1964.
6. Zhantuarov, R. S. Trudy Tsentral'noy Aerologicheskoy Laboratorii, 1965 (in press).
7. Izakov, M. N. Space Res., 5, 1191, 1965.
8. Izakov, M. N. Kosmicheskiye Issledovaniya, 3, No. 2, 297, 1965.
9. Kallmann-Bijl, H. K. and Sibley, W. L. Planet Space Sci., 11, No. 12, 1379, 1963.
10. King-Hele, D. G. and Rees, J. M. J. Atmos. and Terr. Phys., 25, No. 9, 495, 1963.
11. King-Hele, D. G. and Quinn, E. J. Atmos. and Terr. Phys., 27, No. 1, 197, 1965.
12. Marov, M. Ya. Kosmicheskiye Issledovaniya, 2, No. 6, 909, 1964.
13. Pokhunkov, A. A. In "Iskusstvennyye Sputniki Zemli". Izdatel'stvo AN SSSR, p. 89, No. 7, 1961.
14. Pokhunkov, A. A. In "Iskusstvennyye Sputniki Zemli. Izdatel'stvo AN SSSR, p. 110, No. 12, 1962.
15. Pokhunkov, A. A. Kosmicheskiye Issledovaniya, 1, No. 1, 147, 1963.
16. Nier, A. O. et al. J. Geophys. Res., 69, No. 5, 979, 1964.
17. Hedin, A. E. et al. J. Geophys. Res., 69, No. 21, 4637, 1964.
18. Hinteregger, H. E. J. Atmos. Sci., 19, No. 5, 351, 1962.
19. Hall, L. A. et al. J. Geophys. Res., 68, No. 24, 6413, 1963.
20. Hall, L. A. et al. J. Geophys. Res., 70, No. 1, 105, 1965.
21. Solar Geophysical Data, US NBS, 1960-1963.

22. Mikhnevich, V. V. Present collection, p. 23.
23. Kockarts, G. and Nicolet, M. Ann. Geophys., 19, 370, 1963.
24. Neupert, W. M. et al. Space Res., 4, 719, 1964.
25. Bourdeau, R. E. et al. J. Geophys. Res., 69, No. 21, 4531, 1964.
26. Ivanovskiy, A. I. Trudy Tsentral'noy Aerologicheskoy Observatorii, No. 40, 1, 1962; No. 46, 9, 1963.
27. Hinteregger, H. E. and Hall, L. A. Space Res., 5, 1175, 1965.
28. Chamberlain, J. W. Planet. Space Sci., 11, No. 8, 901, 1963.
29. Newton, G. et al. J. Geophys. Res., 69, No. 21, 4690, 1964.
30. Ivanovsky, A. I. and Repnev, A. I. Space Res., 5, 1101, 1965.

DIURNAL VARIATIONS IN DENSITY, PRESSURE AND TEMPERATURE  
IN THE ATMOSPHERE  
(Summary)

R. S. Zhantuarov

It is now known that the atmospheric parameters above 100 km undergo significant diurnal fluctuations. At an altitude of 600-700 km, the pressure changes by a factor of 8-10 between the nighttime and the daytime; the density changes by a factor of 6-8, and the temperature changes up to 600°K. Thus, the density maximum must be independent of the solar activity level at about 14 hours local time.

The theory of diurnal atmospheric fluctuations is unsatisfactory at the present time. One of the first theoretical models was formulated in 1962 by Harris and Priester. They started with the assumption that the energy balance of the upper atmosphere is determined by the absorbed solar radiation and by thermoconductivity. The horizontal movements, as well as the fact that the nature of atmospheric fluctuations depends significantly on frequency, were not taken into consideration. Consideration of only absorbed ultraviolet radiation led to fluctuation amplitudes which were too large and to an incorrect position of the density maximum: the maximum occurred at 17 hours local time. This led Harris and Priester to introduce an additional source (which they first called "corpuscular"), in order to make the results obtained concur with the observed results. In their last study in 1964, they rejected the initial interpretation of the additional source as a "corpuscular" source, and advanced another interpretation, which we have not yet substantiated. This interpretation assumed that an additional amount of heat can be supplied by horizontal convection. /40

This assumption introduces another method of solution based on the theory of tides. The theory of tides in the atmosphere for a rotating Earth - assuming that the fluctuations are small and, consequently, purely periodic - makes it possible to divide the variables in terms of latitude and altitude (the dependence on time and longitude is expressed in the form  $\exp\{-i\sigma t - i s \lambda\}$ , where  $\sigma$  is the fluctuation frequency;  $\lambda$  - longitude;  $s$  - wave number). The dependence on latitude will be determined by the tidal equation of Laplace, the solution of which provides a discrete series of eigen values and the eigen functions corresponding to them. The eigen values will thus be different for different frequencies. At first glance it appears that the tidal theory is inapplicable for an analysis of diurnal fluctuations in view of its purely linear nature. However, measurements have shown that up to an altitude of 250 km the fluctuations are rather small. In addition, according to measurements of Loven and also according to our preliminary calculations, it can be seen that the following law is in operation in the interval from 100 km and above. Up to approximately 160 km, the mechanism of thermoconductivity (molecular, and if the data of Letau are trusted, turbulent) does not play a significant role in heat transfer. Above 250 km, this mechanism is fundamental. Consequently, if the equation of heat transfer is employed in a linearized form, then at altitudes where the applicability of the equation is doubtful this will be unimportant, due to the fact that the fundamental process is thermoconductivity.

In addition, the function of the source has the form of a positive section of a cosine, with a maximum at 12 hours local time. Expanding it in Fourier series, we obtain harmonics with periods of 24, 12, 8, and 4 hours having amplitudes which decrease in the ratio 1/2, 1/15... - i.e., generally speaking, fluctuations must be excited in the atmosphere with periods of 24, 12, 8, and 4 hours.

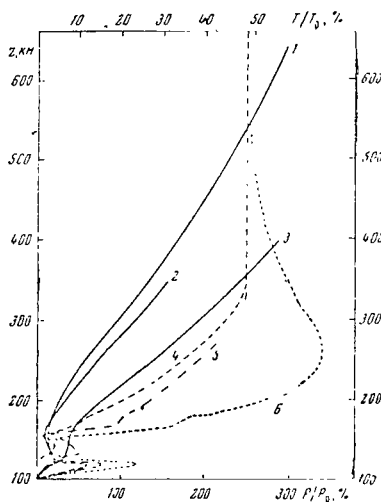


Figure 1

Dependence of Pressure and Temperature Variation on Altitude

Solid curves:  $p$  - pressure variation,  $p_0$  - mean model pressure; dashed curves:  $T$  - temperature variation,  $T_0$  - mean model temperature; 1 and 4 - calculation employing theory of tides; 3 and 6 - calculation with  $h = \infty$ .

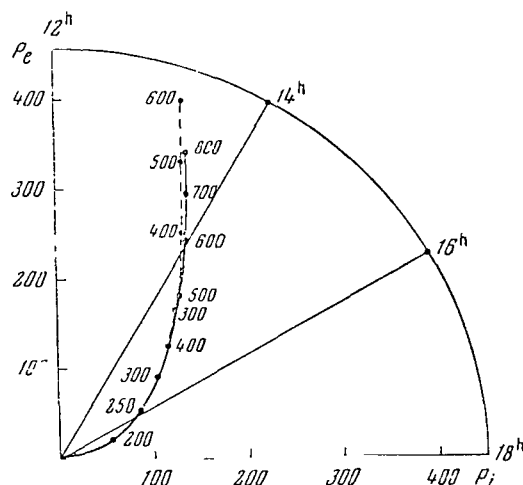


Figure 2

Pattern of Pressure Variation Phase With Altitude

$p_e$  and  $p_i$  - actual and imaginary parts of pressure variation; solid line - author's calculation; dashed line - calculation with  $h = \infty$ .

As was already indicated, the nature of the fluctuations depends significantly on frequency. /41

Preliminary calculations, performed on the basis of the tidal theory, have shown that the fluctuation amplitude with a period of 24 hours changes with altitude according to an increasing exponential-the one with a period of 12 hours changes periodically. If the fact is taken into consideration that the harmonic amplitude decreases with an increase in frequency, as well as the fact that the mean amplitude increases at least linearly when there is a periodic change in the fluctuation amplitude, the conclusion can then be drawn that fluctuations with periods of 12, 8, and 4 hours will have an insignificant influence on the fundamental 24-hour harmonics - i.e., unusual resonance occurs in the diurnal harmonics of the heating function (Figure 1). Thus, the fluctuation phase of the main harmonics behaves in the following way: The maximum is shifted from 18 hours at 100 km to 14 hours at 600 km, and slowly approaches 12 hours (Figure 2).

In order to verify the assumption that the results obtained by Harris and Priester stem from ignoring the fluctuational characteristics of the atmosphere, a calculation was performed with the eigen value of the Laplace tidal equation ( $h = \infty$ ) which was used by Harris and Priester, with the heating function in the form of the first harmonics. As a result, as was expected, an amplitude which was larger than necessary was obtained, but a correct phase: a maximum at 14 hours at an altitude of 400 km. The assumption then arises (which has not been verified yet, unfortunately) that the overall solution for both harmonics of the heating function with one and

the same eigen value (which is not clearly formulated in the model of Harris and Priester) will coincide with their solution even without taking nonlinearity into account.

The theory must be defined more precisely, but even preliminary results show the complex dependence of amplitude and phase on altitude in the 100-200 km range. This points to the fact that the dynamic characteristics of this atmospheric region significantly influence the processes occurring in the layers located above, creating "boundary conditions" for them -i.e., the energy balance of the upper atmosphere is determined not only by absorbed solar radiation and thermoconductivity, but also by the fluctuational properties of the atmosphere.



# DYNAMIC NATURE OF ATMOSPHERIC DENSITY AT ALTITUDES OF 200-300 km<sup>1</sup>

M. Ya. Marov

Data which have been recently processed on the orbital evolution of several Soviet artificial Earth satellites have provided definite experimental corroboration of theoretical assumptions (Ref. 1, 2) regarding the dynamic nature of density at altitudes of approximately 200-300 km. This has made it possible to derive more or less definite estimates of the atmospheric variation close to the thermosphere base for half of the solar cycle.

The results to be discussed were obtained by analyzing the braking of 14 satellites in the "Kosmos" series, the first Soviet spacecraft-satellite (e<sub>2</sub> 1960), its cabin (e<sub>3</sub> 1960), and also the third Soviet AES, for purposes of comparison. Several data have been published previously (Ref. 3-5) regarding the atmospheric density; these data resulted from 42 processing information from individual satellites out of the group indicated above by a similar method.

The current values of osculating ellipse elements of the AES motion were used as reference data. These values made it possible to determine individual discrete values of the parameter

$$\rho \sqrt{H} = K(t) \dot{P}, \quad (1)$$

where  $\rho$  is density;  $H$  - altitude of a homogeneous atmosphere for density;  $\dot{P}$  - secular acceleration reflecting variations in the satellite braking to the greatest extent;  $K(t)$  - coefficient, as a function of the osculating elements and ballistic parameters of the craft, which is quasi-constant on adjacent AES revolutions. The form of the coefficient  $K(t)$ , which in essence represents the normalizing factor for conversion from secular acceleration to values of  $\rho\sqrt{H}$ , is primarily determined by the magnitude of the eccentricity, and its complexity is determined by the degree of approximation when the integrals are replaced by finite relationships. In the graphoanalytical method used to determine  $\rho\sqrt{H}$  (Ref. 4), the error arising from computing  $K(t)$  - in accordance with certain dependences (Ref. 6, 7) for a chosen value of the aerodynamic resistance coefficient  $C_D = 2.1$  (Ref. 8) lies within the accuracy of the results given below.

The correctness of employing the values of  $\rho\sqrt{H}$ , calculated for relatively small intervals, is determined primarily by the quality of the reference data, and also by the dynamic scheme for the spatial orientation

---

<sup>1</sup> The main body of the report was presented at the sixth COSPAR symposium, May, 1965, Argentina.

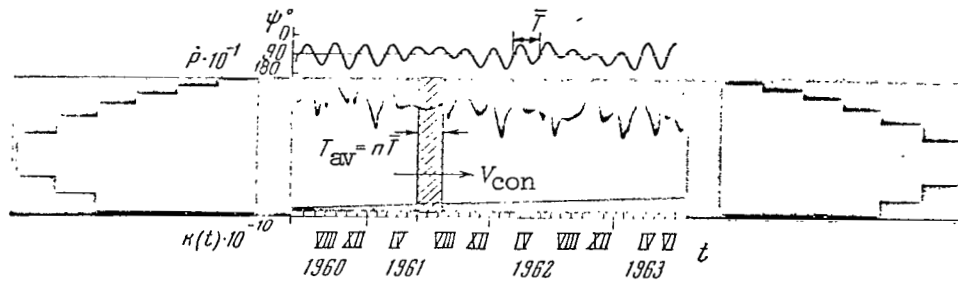


Figure 1

Example of Initial Graph Based on the 1960  $e_3$  Satellite,  
Used to Obtain Traces  $\rho\sqrt{H}$  by Photometric Measurement.

of non-oriented satellites with respect to the center of mass. The problem of determining the mean density values, as well as different long-period variations is thus related to averaging the individual discrete values of  $\rho\sqrt{H}$  with the corresponding values of grid. For this purpose, the method entailing photometric measurement of uniformly illuminated effective areas defined by the curves  $\dot{P}$  and  $K(t)$  was employed. Figure 1 shows an example of the initial graph of  $e_3$  1960 satellite, and Figure 2 shows an example of tracings obtained by the  $e_2$  1960 and  $e_3$  1960 satellites. The daily variations are excluded for the grid  $T = \bar{T}$  in Figure 2, where  $\bar{T}$  is one daily cycle (more accurately,  $\Psi$ -cycle;  $\Psi$  - the geocentric angle between the directions to the Sun and the satellite perigee). This made it possible to compare the changes in  $\overline{\rho\sqrt{H}}$  with the curve of decimeter solar radio emission as an index of solar activity (based on data from the observatory in Ottawa [Ref. 9]). The correlation coefficient throughout all of the curves is  $r_K = 0.86 \pm 0.05$ , and it corroborates the good agreement between changes in density at these altitudes and variations in solar radio emission during a period of intermediate and minimum solar activity.

Fluctuations in the parameter  $\rho\sqrt{H}$  from day to night at altitudes of 270-280 km are clearly apparent in the tracing obtained in a similar way on the  $e_3$  1960 satellite, but with the grid  $T = 0.2 \bar{T}$ . The examples of approximating curves in Figure 3, which were compiled as a function of local time of the perigee, based on data from the tracings for the satellites "Kosmos-2", "Kosmos-5", "Kosmos-3", and "Kosmos-11", point to daily variations also close to 200-230 km. The inclination of the tangents to the given curves, in a direction going from the morning hours through midnight into the day - which corresponds to precession of the orbital perigee - is caused by a decrease in the satellite perigee altitudes.

The data used from 16 Soviet AES, which were processed by an identical method, made it possible to trace the density changes in the 180-300 km altitudinal range for almost half of the solar activity cycle. More than 150 experimental values of the parameter  $\rho\sqrt{H}$  were calculated for the

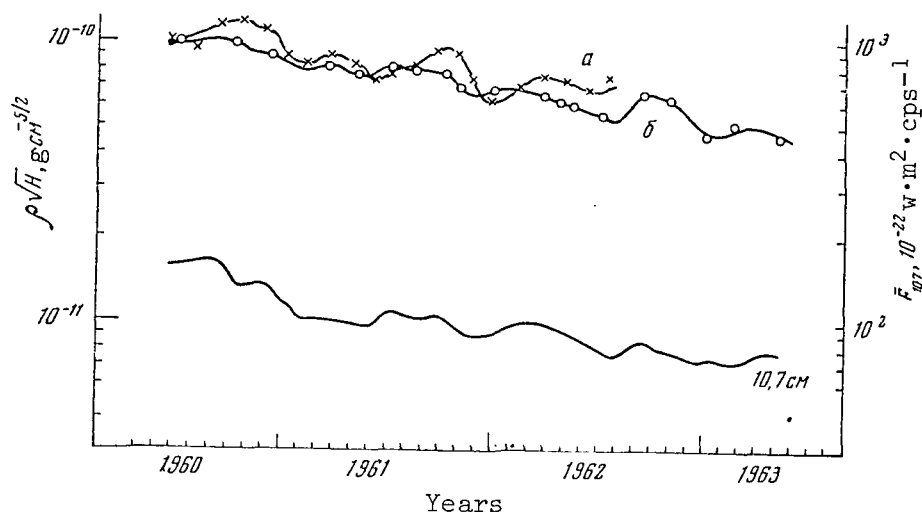


Figure 2

Traces According to the  $e_2$  Satellite of 1960 (a) and the  $e_3$  Satellite of 1960 (b), Compared With the Curve  $\bar{F}_{10.7}$

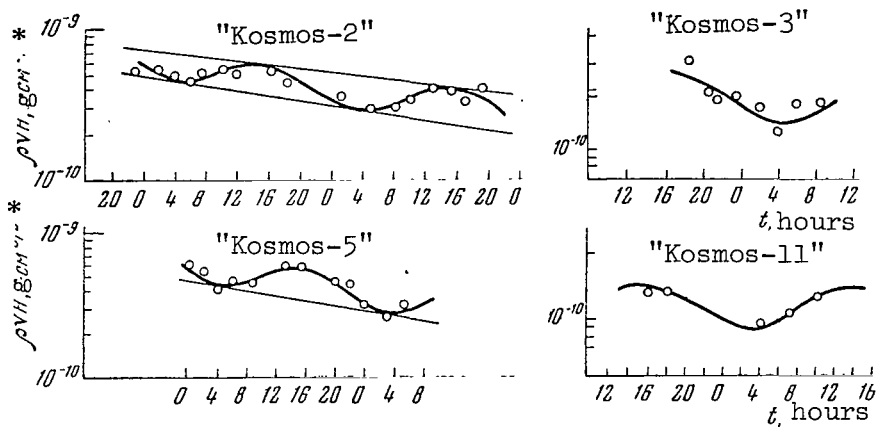
flux of decimeter solar radio emission  $\bar{F}_{10.7} \approx 85 \cdot 10^{-22} \text{ w} \cdot \text{m}^{-2} \cdot \text{cps}^{-1}$ ; these experimental values corresponded to the mean daily, maximum diurnal, and minimum nocturnal conditions (Figure 4). In order to obtain data pertaining to earlier periods of time, in accordance with other similar results, they were corrected up to the smoothed out values of the flux  $\bar{F}_{10.7} = 85 \cdot 10^{-22} \text{ w} \cdot \text{m}^{-2} \cdot \text{cps}^{-1}$  by employing the semiempirical relationship

$$\rho \sqrt{H} = \alpha \bar{F}_{10.7}^m \quad (2)$$

This method is approximately similar to that described in (Ref. 10). The mean values of the exponent  $m$  (in view of its dependence on local time [Ref. 11]) were calculated for several altitudes, assuming the proportionality coefficient was constant in the first approximation ( $\alpha = \text{const}$ ), utilizing experimental data on the braking of Soviet AES from 1957 to 1963 for values of  $\bar{F}_{10.7}$  from  $260 \cdot 10^{-22}$  to  $85 \cdot 10^{-22} \text{ w} \cdot \text{m}^{-2} \cdot \text{cps}^{-1}$ , respectively. Data were also employed from the CIRA tables of 1961 (Ref. 12) pertaining to a value of  $\bar{F}_{10.7} \approx 200 \cdot 10^{-22} \text{ w} \cdot \text{m}^{-2} \cdot \text{cps}^{-1}$  (Figure 5).

Figure 6 shows the curves compiled according to the calculated points. Along with the mean distribution of the parameter  $\rho \sqrt{H}$ , these curves give the range of maximum variations in one day. The mean quadratic error /45 entailed in determining the true altitudinal values, with allowance for dispersion of the experimental values, does not exceed 5 km, and is less than 18% of the absolute value for the parameter  $\rho \sqrt{H}$ .

It can be seen from the curves in Figure 6 that during years of



\*Note: Illegible in original foreign text.

Figure 3

### Daily Variations According to the Braking of the "Kosmos" Satellites

minimum solar activity the daily variations in the parameter  $\rho\sqrt{H}$ , which comprise approximately 60-70% at 200 km, amount to more than 200% close to 300 km. This does not occur at these altitudes during a period of maximum solar activity. This has been recently corroborated by results <sup>46</sup> obtained by foreign researchers, particularly Jacchia and Slowey (Ref. 13), and King-Hele and Quinn (Ref. 14). An analysis of these data leads to the conclusion that the most probable change in the level of regions warming up is due to the general cooling nature of the atmosphere during the present period, and due to a change in the altitudinal distribution of the main components. This process, which is accompanied by a re-distribution in terms of altitude of such basic parameters as the density  $\rho$  and the altitude of a homogeneous atmosphere for the density  $H$ , is thus responsible for fluctuations in these parameters with a significant amplitude at low altitudes, as compared with a period of maximum solar activity.

Based on the curves shown in Figure 6 and taking the fact into account that

$$\frac{d}{dh} \left[ \ln \frac{(\rho\sqrt{H})_{n+1}}{(\rho\sqrt{H})_n} \right] \approx -\frac{1}{H}, \quad (3)$$

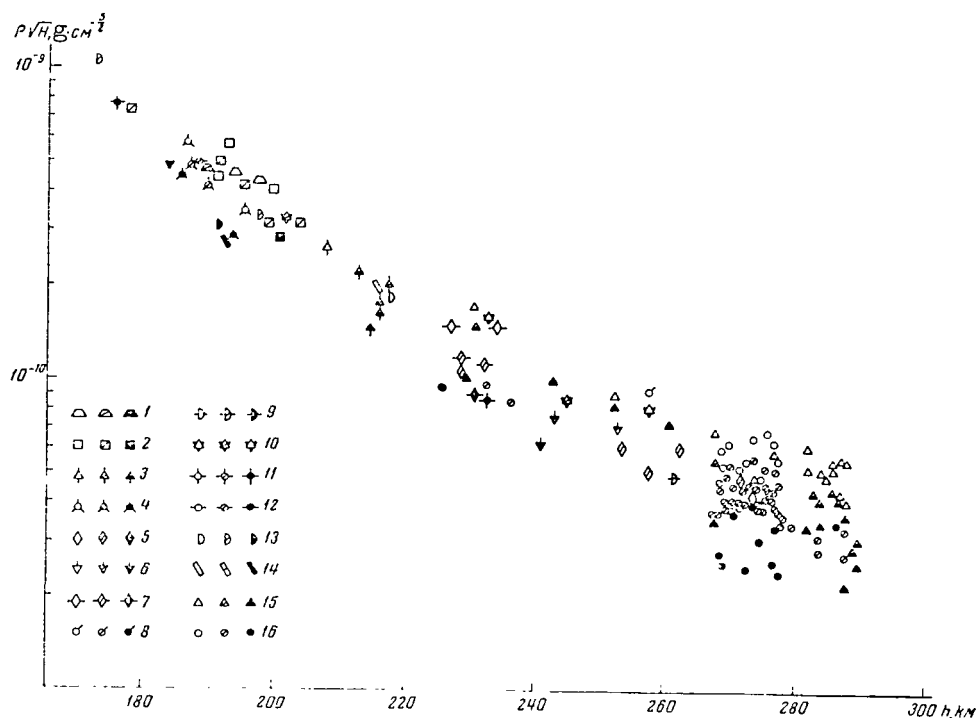


Figure 4

Experimental Values of  $\rho\sqrt{H}$ , Obtained by the Braking of  
16 Soviet AES for the Mean Daily, Maximum Daily, and  
Minimum Nocturnal Conditions.

1 - "Kosmos-1"; 2 - "Kosmos-2"; 3 - "Kosmos-3"; 4 - "Kosmos-5";  
5 - "Kosmos-6"; 6 - "Kosmos-8"; 7 - "Kosmos-11"; 8 - "Kosmos-17";  
9 - "Kosmos-19"; 10 - "Kosmos-25"; 11 - "Kosmos-26"; 12 - "Kosmos-31";  
13 - "Kosmos-38"; 14 - "Kosmos-39"; 15 - e<sub>2</sub> 1960 (first Soviet spacecraft-satellite); 16 - e<sub>3</sub> 1960 (cabin of the first Soviet spacecraft-satellite). The light symbols correspond to diurnal maximum values; dark symbols correspond to nocturnal minimum values; the symbols with crosshatched lines designate mean daily values.

we can determine with acceptable accuracy the altitude of the homogeneous atmosphere and can thus compute the density distribution between 180-300 km.

As a result of these computations, Figure 7 shows the curve for the mean atmospheric density at these altitudes. A comparison of these curves with certain estimates obtained during a period of maximum solar activity, and particularly with the value of  $\rho$  determined according to the method advanced from data on the braking of the third Soviet satellite, makes it possible to trace the variations for half of the solar cycle. The mean density decrease, as compared with 1958, is about 2 times at 200 km, and

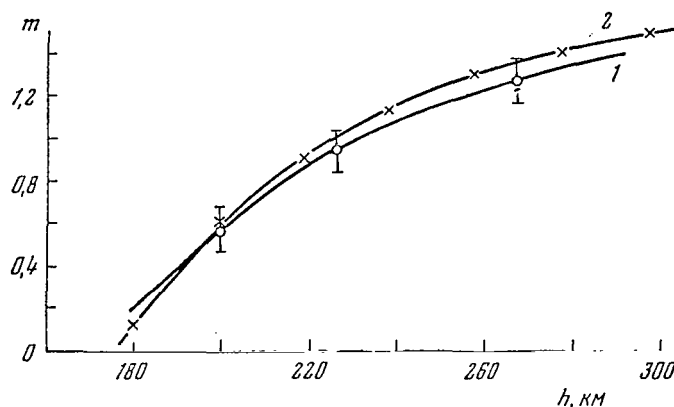


Figure 5

Exponent  $m$  as a Function of Geometric  
Altitude for  $\rho\sqrt{H} = \alpha\bar{F}_{10.7}^m$   
1 - according to Soviet AES data; 2 -  
utilizing the CIRA tables of 1961.

not less than 3.5 times close to 300 km.

The graphic indication of the very dynamic nature of the upper atmosphere density above approximately 180-200 km leads to the necessity of systematically obtaining the corresponding experimental data throughout the entire solar cycle. On the basis of experimental material on density, which has been compiled up to the present, based on the change in the curve for a stream of solar decimeter radio emission during preceding years (Ref. 9) it can be assumed that there is a gradual increase in atmospheric density above approximately 200 km, beginning in 1965. This increase will reach a maximum value which is close to the level of 1951-1958 in the next period of maximum solar activity (1968-1969).

We tried to predict the mean density between 180 and 300 km in individual periods of the solar cycle, based on the experimentally determined distribution of the parameter  $\rho\sqrt{H}$  for  $\bar{F}_{10.7} \approx 85 \cdot 10^{-22} \text{ W} \cdot \text{m}^{-2} \cdot \text{cps}^{-1}$  (Figure 4) as well as the expected change in the flux  $F_{10.7}$ , with allowance for the correlation (which has been verified for the given altitudinal range) between density and the decimeter solar radio emission. Relationship (2) was thus employed.

Figure 8 gives the values calculated on the assumption that

$$\alpha = \alpha_{\bar{F}_{10.7}} \simeq 85 \cdot 10^{-22} \text{ W} \cdot \text{m}^{-2} \cdot \text{cps}^{-1}$$

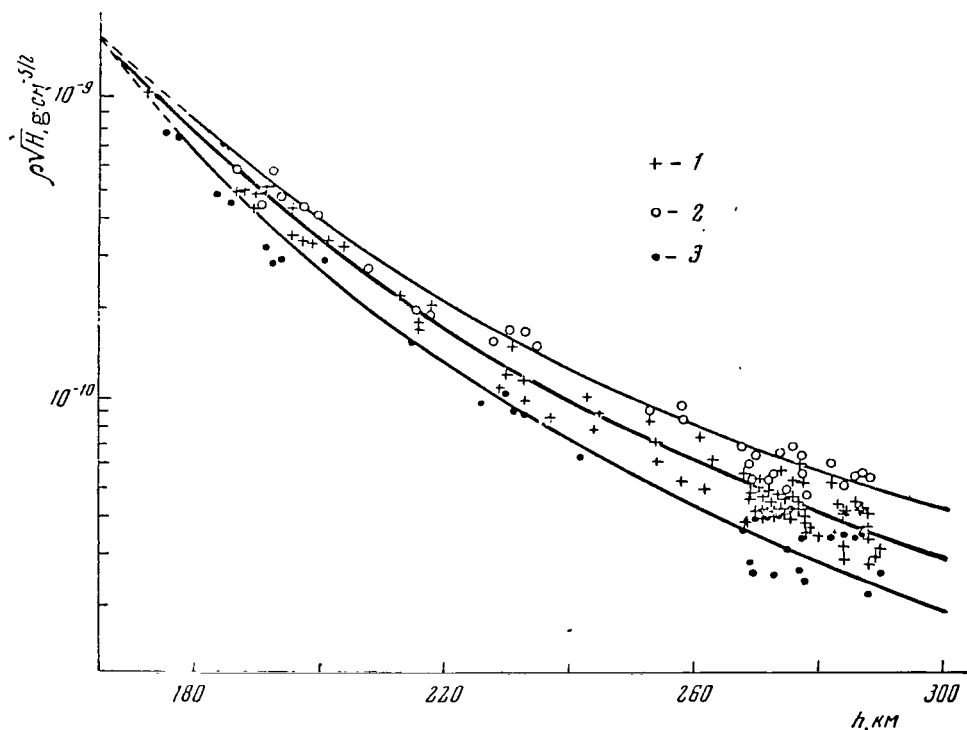


Figure 6

Curves of  $\rho\sqrt{H}$  as a Function of Geometric Altitude  
Based on Data in Figure 4, With the Daily Variation Range

1 - mean daily values; 2 - maximum diurnal values; 3 - minimum nocturnal values.

for atmospheric density as a function of the change in the solar activity level expected in the forthcoming years. This figure also plots the curves corresponding to the mean daily conditions, according to the model given by Harris and Priester (Ref. 15) for the model parameter of  $S = 70$  and 150, and also by the CIRA for 1961 (Ref. 12). Computations which employ forecasted values which take into account the most important factors in the dynamic nature of the upper atmospheric density provide correct results. These results are more correct than those obtained by employing certain statistical models which reflect, more or less correctly, only a comparatively small period of the actual change in structural parameters during the 11-year solar cycle. /48

The authors would like to take this opportunity to thank V. I. Krasovskiy for valuable comments and constant attention to this work.

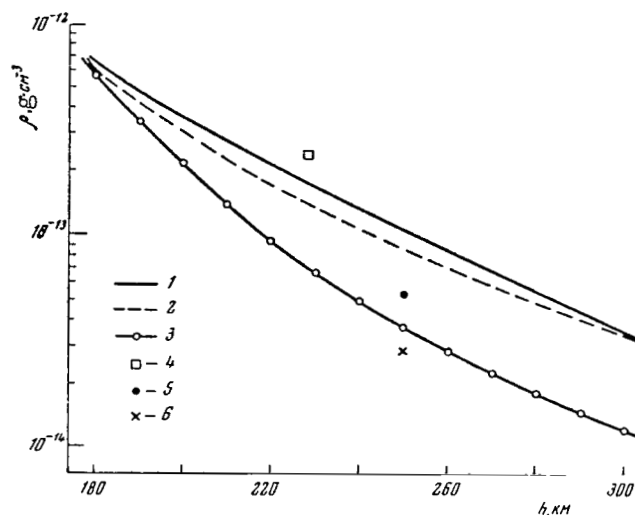


Figure 7

Mean Atmospheric Density at Altitudes of 180-300 km  
 1 - CIRA 1961; 2 - US Standard 1962; 3 - Marov, 1964;  
 4 - third satellite, 1958; 5 - Jacchia, 1963; (day, "Injun-3"); 6 - Jacchia, 1963 (night, "Injun-3").

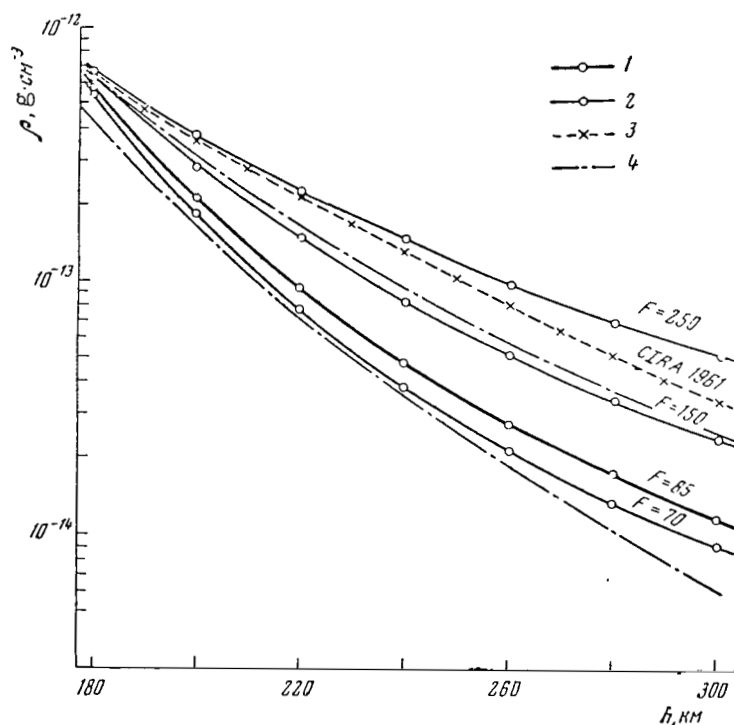


Figure 8

Calculated, Forecasted Density Distributions for  
 Values of  $F_{10}$  70, 150 and 250  $\text{w} \cdot \text{m}^{-2} \text{cps}^{-1}$   
 1 - reference curve; 2 - forecasted values; 3 -  
 CIRA 1961; 4 - Harris and Priester model ( $S=70$   
 and 150, 9 hours local time).



## REFERENCES

1. Nicolet, M. Planet Space Sci., 5, 1, 1961.
2. Harris, I., Priestler, W. Space Res., 3, 1963.
3. Marov, M. Ya. Kosmicheskiye Issledovaniya, 1, No. 1, 143, 1963.
4. Marov, M. Ya. Kosmicheskiye Issledovaniya, 2, No. 6, 909, 1964.
5. Marov, M. Ya. Space Res., 5, 1140, 1965.
6. Lidov, M. L. In "Iskusstvennyye Sputniki Zemli". Izdatel'stvo AN SSSR, No. 1, p. 9, 1957.
7. King-Hele, D. G. Planet. Space Sci., 11, 261, 1963.
8. Lidov, M. L. Izvestiya AN SSSR, Seriya Geofiz., No. 12, 1524, 1957.
9. Jacchia, L. G. Review prepared for the Inter-Union Commission on Solar and Terrestrial Relationships to be presented at the Tokyo (Japan) meeting in Sept., 1963.
10. Priestler, W. J. Geophys. Res., 66, 4143, 1961.
11. Jacchia, L. G. Nature, 192, No. 4808, 1147, 1961.
12. Kalmann-Bijl, H. K. et al. CIRA 1961, Cospar Internat. Reference Atmosphere, North-Holland Publ. Co., Amsterdam, 1961.
13. Jacchia, L. G., Slowey, J. J. Geophys. Res., 69, 905, 1964.
14. King-Hele, D. G., Quinn, E. Technical Note, No. Space 72, Royal Aircraft Establishment, 1964.
15. Harris, I., Priestler, W. J. Geophys. Res., 67, 4585, 1962.

## COMPOSITION OF THE ATMOSPHERE IN THE 100-200 km REGION

A. D. Danilov

The neutral composition of the atmosphere above 100 km represents one of the main problems in the physics of the upper atmosphere at the present time. Up until recently, our information on the concentrations of the main atmospheric components above 100-120 km was limited to theoretical models, which investigated the dissociation of oxygen and the gravitational division of gases above 110-140 km. These models pointed to the rapid decrease in the concentration of  $N_2$  and  $O_2$  molecules above this level. According to the majority of theoretical distributions of the main concentrations, the ratio  $[O]/[N_2]$  is considerably greater than unity at altitudes of 180-200 km. And above 200 km it was assumed that the atmosphere is purely atomic. At the same time, the problem of the concentration distribution of atomic and molecular components in the upper atmosphere is very important, since the solution of an entire series of problems, related to the support of the ionosphere, to the formation of eigen atmospheric emissions, etc., is based upon this problem.

In terms of methodology, experimental studies of the neutral atmospheric composition can be divided into two groups: optical and mass spectrometer. Optical studies were initiated in 1953 by Bleyram et al (Ref. 1). These experiments (Ref. 2, 3) included the study of solar radiation absorption in the 1400-1500 Å region, and it was found that molecular oxygen is not distributed in the upper atmosphere in the manner indicated by theoretical models of dissociation. It was found that there is a significant concentration of  $O_2$  molecules up to altitudes of 150-160 km, while - according to calculations of Pendorf (Ref. 4) - the transitional region between  $O$  and  $O_2$  is on the order of ten km wide, and lies at altitudes of about 100 km. /49

In order to solve the ionization problems of the lower ionosphere, it is extremely important to know the concentrations of nitric oxide. The experimental results obtained by Jursa et al (Ref. 5) showed that the NO concentration does not exceed  $10^6 \text{ cm}^{-3}$  at altitudes of 60-90 km.

The neutral composition of the atmosphere at altitudes of 100-180 km was found in experiments studying the spectrum of ultraviolet solar radiation. These experiments were conducted in 1960 and 1961 under the supervision of Hinteregger (Ref. 6, 7). The results of these experiments led the author (Ref. 7) to the conclusion that there is an equalization of the concentrations of atomic oxygen and molecular nitrogen at an altitude of 120 km, and above approximately 140 km the atmosphere can be regarded as purely atomic.

The results derived from mass spectrometer studies, carried out somewhat earlier, on the composition at the same altitudes led A.A. Pokhunkov (Ref. 8, 9) to a completely different conclusion. According to the work of A. A. Pokhunkov,

the proportion of molecular nitrogen in the over-all atmospheric density remains almost unchanged up to the investigated altitude of 210 km.

More recent studies with mass spectrometers, carried out in the Soviet Union (Ref. 10, 11) and abroad (Ref. 12-14), have shown that the first results of A. A. Pokhunkov (Ref. 9) were correct with respect to the high concentration of molecular nitrogen. However, they were incorrect with respect to the high value of  $[O]/[O_2]$ , which resulted from making an inaccurate allowance for recombination of O atoms on the walls of apparatus. The results derived from optical studies, carried out recently, on the atmospheric composition (Ref. 15, 16) have also shown that the conclusions of Hinteregger (Ref. 7) were incorrect regarding the small proportion of  $N_2$  at altitudes of 150-160 km. These results also showed that molecular nitrogen is the dominating atmospheric component at 200 km.

A comparison of the results derived by determining the molecular nitrogen concentration by different methods, which is shown in Figure 1, indicates that a mean curve may be drawn based on the results of the majority of measurements. This curve will differ from the experimental points by not more than a factor of 1.6. The curves obtained in the first experiment of A. A. Pokhunkov (Ref. 8) and obtained in the first work of Hinteregger (Ref. 7), are excluded from the general group of similar curves. /50

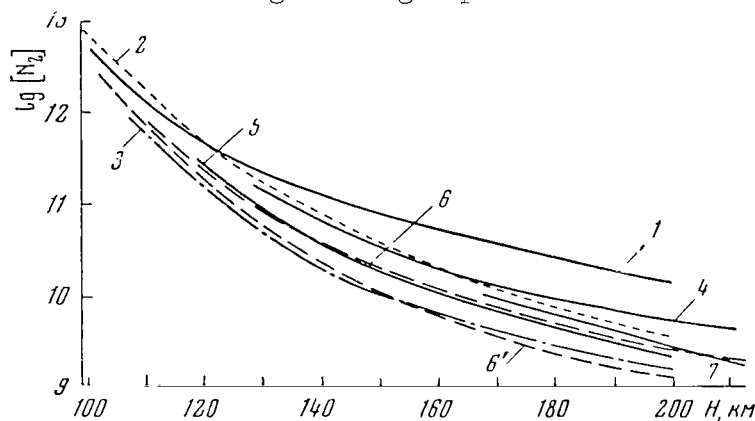


Figure 1

#### Results Derived from Determining the $N_2$ Concentration by Different Methods

1 - August, 1959, morning ; 2 - September 23, 1960, 0 hours 56 minutes; 3 - August 23, 1961, 10 hours 03 minutes; 4 - November 15, 1961, 16 hours; 5 - July 10, 1963, 10 hours; 6 - June 6, 1963, 7 hours 30 minutes; 7 - the mean of data obtained on June 5, 5 hours 45 minutes and October 25, 16 hours 30 minutes, 1962.

A comparison of the curves shown in Figure 1 with the time at which the experiments were conducted does not reveal any regular changes in the magnitude of  $[N_2]$  with the time of day or with the season. Apparently, the concentration of molecular nitrogen at altitudes of 100-200 km does not change

significantly. An investigation of similar curves for the distribution of  $O_2$  concentration also indicates that no significant variations in the amount of molecular oxygen is observed. This makes it possible to draw the mean curve for the change in  $[N_2]$  as a function of altitude. The  $O_2$  and  $N_2$  concentrations, obtained as the mean of all the values obtained experimentally, for altitudes of 100-200 km are given below:

H, km	100	110	120	130	140	150	160	170	180	190	200
$[N_2] \cdot 10^{-10}$	520	120	35	11	6	2.6	1.4	0.87	0.58	0.4	0.26
$[O_2] \cdot 10^{-9}$	1700	190	32	10	4.8	2.9	1.4	0.76	0.44	0.29	0.19

A comparison of the nature of the change in the  $[O]/[N_2]$  ratio in different experiments shows that there is a diurnal variation in this ratio, with an increase in  $[O]/[N_2]$  up until midday. Figure 2 shows the change in  $[O]/[N_2]$  at an altitude of 180 km as a function of time, with respect to the local midday. The similar change with respect to the  $[O]/[N_2]$  concentration is apparently related to the absolute increase in  $[O]$  at noon, because - as was shown above - rocket data do not indicate significant variations in the magnitude of  $[N_2]$ .

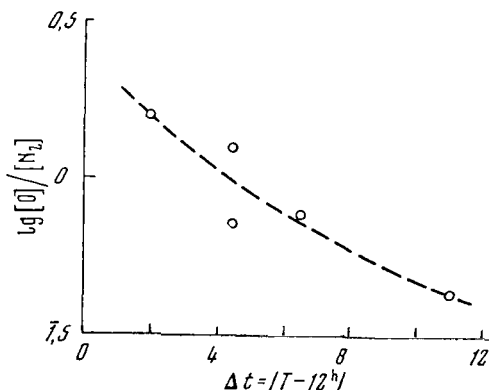


Figure 2

Dependence Of  $[O]/[N_2]$  On Time, With Respect To the  
Local Midday At An Altitude Of 180 km

It is thus apparent at the present time that molecular nitrogen is the main component of the atmosphere, at least up to an altitude of 200 km, which represents the maximum altitude of rocket studies on the neutral composition in most cases. The results of one experiment by A. A. Pokhunkov (Ref. 11), as well as recent studies on the satellite "Explorer-17", show that the  $N_2$  concentration can dominate in the atmosphere up to an altitude of 300-350 km.

#### REFERENCES

1. Byrame, E. T. et al. Phys. Rev., 98, 1594, 1955.
2. Friedman, H. Ann. Geophys., 11, 174, 1955.

3. Byrame, E.T. et al. In "At the Threshold to the Cosmos". Izdatel'stvo Inostrannoy Literatury (IL), 1960.
4. Pendorf, R. J. Geophys. Res., 54, 7, 1949.
5. Jursa, A.S. et al. In "A Study of the Upper Atmosphere by Means of Rockets and Satellites". IL, p. 372, 1961.
6. Hinteregger, H.E. J. Geophys. Res., 66, No. 8, 2367, 1961.
7. Hinteregger, H.E. J. Atmos. Sci., 19, No. 5, 351, 1962.
8. Pokhunkov, A.A. Izvestiya AN SSSR, Seriya Geofiziki, No. 11, 1649, 1960.
9. Pokhunkov, A.A. In "Iskusstvennyye Sputniki Zemli". Izdatel'stvo AN SSSR, No. 7, p. 89, 1961.
10. Pokhunkov, A.A. In "Iskusstvennyye Sputniki Zemli". Izdatel'stvo AN SSSR, p. 10, No. 13.
11. Pokhunkov, A.A. Kosmicheskiye Issledovaniya, 1, No. 1, 148, 1963.
12. Near, A.O. et al. J. Geophys. Res., 69, No. 5, 979, 1964.
13. Shaefer, E.J. J. Geophys. Res., 68, No. 4, 1173, 1963.
14. Shaefer, E.J., Nichols, M.H. Aeronaut. Rept., No. 1, 1963.
15. Hall, L.A. et al. J. Geophys. Res., 68, No. 24, 6913, 1963.
16. Hinteregger, H.E. et al. Rept. COSPAR, 1964.

# PROBLEM OF THE TOTAL AMOUNT OF NEUTRAL HYDROGEN IN THE UPPER ATMOSPHERE OF THE EARTH

(Summary)

V. G. Kurt

If the transfer equation of  $L_\alpha$ -radiation is solved for a spherical /51  
case, with allowance for shade, we obtain the dependence of the theoretical albedo ( $A_T$ ) of the Earth's atmosphere on the total optical thickness  $\tau_0$  (above 110 km) for the center of the line. The dependence of  $A_T$  on  $\tau$  is formulated within  $0 \leq \tau \leq \tau_0$  for  $\tau_0 = 1, 2, 3, 5, 10$ . The results derived from two observations are employed for the solar depression angle  $\sim 30^\circ$  at altitudes of 140 and  $70^\circ$  for 600 km. The observations were reduced for the background of the extraatmospheric component, equalling  $\sim 2 \cdot 10^{-4} \text{ erg} \cdot \text{cm}^{-2} \cdot \text{sec}^{-1} \cdot \text{sterad}^{-1}$ , and also for the temperature difference above and below the level under consideration. With allowance for these corrections, the albedo, which equals 0.42 for 140 km, increased to 0.65, and increased from  $\sim 0.65$  to 0.83 for 600 km. An altitude of 140 km corresponds to  $\tau/\tau_0 = 0.75$ ; 600 km - 0.52. Under the assumption that the temperature at the exosphere level is  $\sim 1000^\circ\text{K}$ , it is found that  $\tau_0 \approx 6-7$  for the conditions formulated above. This corresponds to the total hydrogen content above 110 km  $\sim 3.5 \cdot 10^{13} \text{ cm}^{-2}$ , and about 15 for the second case. Thus, the concentration is  $10^7 \text{ cm}^{-3}$  at an altitude of 100 km, and  $2.5 \cdot 10^5$  at an altitude of 200 km for a solar depression angle of about  $30^\circ$  - within the framework of the thermosphere model postulated by Bates-Patterson.

## UTILIZATION OF ARTIFICIAL EARTH SATELLITE ORBITAL DATA TO DETERMINE THE WIND VELOCITY IN THE THERMOSPHERE

B. N. Trubnikov

It is a well-known fact that several of the new scientific discoveries which have been made by artificial Earth satellites have resulted from analyzing their orbital variations, and not from measurements performed by on-board equipment. The processing of orbital AES data has clarified the functional dependence of the upper atmosphere parameters on solar activity. The purpose of this article is to illustrate the possibility of deriving information on movements in the thermosphere from orbital AES data, on the basis of existing studies.

Let us write the equations of the AES motion in the osculating elements:

$$\frac{da}{dt} = \frac{2}{m(1-e^2)^2} \sqrt{\frac{p^3}{\mu}} \left( Re \sin \vartheta + S \frac{p}{r} \right); \quad (1)$$

$$\frac{de}{dt} = \frac{1}{m} \sqrt{\frac{p}{\mu}} \left[ R \sin \vartheta + \left( 1 + \frac{r}{p} \right) S \cos \vartheta + S \frac{er}{p} \right]; \quad (2)$$

$$\frac{di}{dt} = W \frac{r \cos u}{m \sqrt{\mu p}}; \quad (3)$$

$$\frac{d\Omega}{dt} = W \frac{r \sin u}{m \sqrt{\mu p} \sin i}; \quad (4)$$

$$\frac{d\omega}{dt} = \frac{1}{me} \sqrt{\frac{p}{\mu}} \left[ -\dot{R} \cos \vartheta + \left( 1 + \frac{r}{p} \right) S \sin \vartheta - \frac{er}{p} W \operatorname{ctg} i \sin u \right]; \quad (5)$$

$$\frac{dt}{du} = \frac{\gamma r^2}{\sqrt{\mu p}}; \quad (6) \quad \underline{52}$$

$$\frac{1}{\gamma} = 1 - \frac{r^3}{m\mu p} W \operatorname{ctg} i \sin u, \quad (7)$$

where  $a$  - the main semiaxis of the orbit;  $e$  - eccentricity;  $i$  - orbital inclination;  $\Omega$  - longitude of the ascending node;  $\omega$  - perigee argument;  $u$  - latitudinal argument;  $m$  - AES mass;  $\vartheta$  - true anomaly;  $p$  - AES orbital parameter;  $\mu$  - product of constant gravitation by the mass of the Earth;  $R$ ,  $S$ ,  $W$  - projections of the disturbing acceleration on the radius vector, on the perpendicular to it in the plane of the osculating orbit, and on the normal to the osculating orbit;  $u = \omega + \vartheta$ ;  $r = p/(1 + e \cos \vartheta)$ ; the main disturbing accelerations arise due to deviation of the Earth's gravitational field from the central field and due to atmospheric resistance:  $S = S_1 + S_2$ ,  $R = R_1 + R_2$ ,  $W = W_1 + W_2$  where  $S_1$ ,  $R_1$ ,  $W_1$  are the projections of disturbing acceleration due to the eccentricity of the Earth's gravitation;  $S_2$ ,  $R_2$ ,  $W_2$  - projections of the disturbing acceleration created by the resistance of the rotating atmosphere.

If the axial asymmetry in the mass distribution is disregarded, the gravitational potential of the Earth is given by the formula

$$\Phi(r, \delta) = -\frac{\mu}{r} \left[ 1 - \sum_{n=2}^{\infty} \left( \frac{a_2}{r} \right)^n J_n P_n(\cos \delta) \right], \quad (8)$$

where  $P_n$  is the Legendre polynomial;  $\delta$  - the colatitude;  $J_n$  - the constants determined empirically. We then have

$$R_1 = -\frac{\partial \Phi}{\partial r}, S_1 = -\frac{\partial \Phi}{r \partial u}, W_1 = -\frac{\partial \Phi}{r \sin u \partial i}, \cos \delta = \sin i \sin u. \quad (9)$$

The solutions of (1) - (7), in the presence of the perturbations (8), (9) are known, and can be written, for example, in the form (Ref. 1):

$$i = i_0 + \frac{1}{8} J_2 \left( \frac{a_0}{p} \right)^2 \sin 2i \left[ 3e \cos(v + 2\omega) + 3 \cos(2v + 2\omega) + e \cos(3v + 2\omega) \right] - \dots; \quad (10)$$

$$a = a_0 + \frac{3}{2} \frac{J_2 a_0^2}{a(1-e^2)^3} \left\{ (2 - 3 \sin^2 i) \left[ e \left( 1 + \frac{1}{4} e^2 \right) \cos v + \frac{1}{2} e^2 \cos 2v + \frac{1}{12} e^3 \cos 3v \right] + \dots \right\}; \quad (11)$$

$$\Omega = \Omega_0 - \frac{3}{2} J_2 \left( \frac{a_0}{p} \right)^2 \cos i \, nt \left\{ 1 - \dots \right\} + \Delta\Omega_{lp} + \Delta\Omega_{sp}; \quad (12)$$

$$\omega = \omega_0 + \frac{3}{4} J_2 \left( \frac{a_0}{p} \right)^2 (4 - 5 \sin^2 i) \, nt \left\{ 1 + \dots \right\} + \Delta\omega_{lp} + \Delta\omega_{sp}. \quad (13)$$

As can be seen from (10) - (13), in the expressions for the elements the nonsphericity of the Earth produces short-, long- (ep, sp) and secular terms which depend secularly on time (Ref. 2). The tesseral harmonics of the Earth's potential can produce long-period effects, if the mean satellite motion is comparable with angular velocity of the Earth's rotation (Ref. 3). For AES orbits which are close to the Earth, these "resonance" effects of the ecliptic equator can be disregarded.

Let us also write, for example, according to (Ref. 4, 5) the components of the aerodynamic force influencing the AES:

$$\begin{aligned} R_2 &= -\rho CV u_r, \quad S_2 = -\rho CV (v_n - \alpha r \cos i), \\ W_2 &= -\rho CV \alpha r \sin i \cos u, \end{aligned} \quad (14)$$

where  $V$  is the velocity of the AES with respect to the atmosphere;  $C$  - /53  
the constant depending on the area of the effective cross section;  $\rho$  - the air density which changes exponentially as a function of the distance  $r$  from the center of the Earth;  $\alpha$  - angular rotational velocity of the atmosphere with respect to the Earth's axis;  $v$ ,  $v_n$  - components of the AES undisturbed velocity with respect to  $R$  and  $S$ . The AES velocity with respect to the atmosphere is  $V^2 = v_r^2 + v_n^2 - 2v_n \alpha r \cos i + \alpha^2 r^2 \cos^2 \varphi$ , where  $\varphi$  is the geocentric latitude of the satellite. It can be seen from (14) that in the case of a motionless atmosphere  $W_2 = 0$  for  $\alpha = 0$  - i.e., the force which is normal to the orbital plane and which is caused by the atmosphere is produced only when it rotates. Variations of only 2 parameters of the osculating orbit  $i$  and  $\Omega$  are caused by the normal component  $W_1$  of the Earth's gravity and by atmospheric braking  $W_2$ .

According to (10) and (12),  $W_1$  causes short- and long- period variations in  $\Omega$ , as well as secular behavior. As a result, the angle of



inclination  $i$  fluctuates, and the orbital plane rotates from the east to the west at a velocity of

$$-\frac{3}{2} J_2 \left( \frac{a_e}{p} \right)^2 \cos i. \quad (15)$$

Since the secular changes of the orbital elements can be determined most accurately, in order to study any geophysical factor it is expedient to concentrate on the parameter which displays a secular change as a function of the geophysical parameter being studied. According to (Ref. 15), the secular behavior of  $\Omega$  is entirely determined by the constant  $J_2$  in the gravitational potential of the Earth, so that the oblateness of the Earth can be determined by the secular behavior. Thus, if the rotation of the Earth's atmosphere with an angular velocity of  $\alpha$  produces a secular component, it should not be studied for  $\Omega$  - where there is secular motion due to flattening of the Earth - but for  $i$ , where the potential of the Earth produces only fluctuations, as was indicated above. The effect of the rotation of the Earth's atmosphere upon the AES motion has been studied by many authors. We would like to point out the influence of the atmosphere upon an AES moving along an elliptical orbit. According to (Ref. 4-6), almost all of the braking which the satellite moving along an elliptical orbit undergoes has an influence close to the perigee point, since the air density rapidly decreases with altitude and the perigee altitude changes slowly. Therefore, the air density measured according to orbital data from the AES is found completely at perigee, or close to it.

The change in  $i$  with time can be found from (3):

$$\frac{di}{dt} = -\frac{\rho C}{m \sqrt{p}} \propto \frac{r^2}{\sqrt{p}} V \sin i \cos^2 u.$$

This has been done by several authors on the basis of several assumptions with respect to  $\rho$ . Thus, it was found in (Ref. 7) that  $i$  has a secular component connected with the secular change in the period of rotation in the following way:

$$\frac{\Delta i}{\Delta T} = \frac{\alpha}{\alpha_e} \frac{\sin i}{3} \cos^2 \omega,$$

which coincides with the corresponding formula given by King-Hele (Ref. 6).

We find that  $\alpha/\alpha_3 = 1 + \sigma/\alpha_3$  when we introduce the angular velocity of the air with respect to the Earth's surface, which is not dependent on latitude  $\sigma$  - "the index of circulation". Thus, for  $\sigma = 0$  the atmosphere rotates along with the Earth, and there is no wind in it. Thus, we have

$$\frac{\Delta i}{\Delta T} = \left( 1 + \frac{\sigma}{\alpha_e} \right) \frac{\sin i}{3} \cos^2 \omega.$$

Employing the expression obtained, we can trace the secular changes in the orbit over long periods of time. With allowance for the monotonic nature of the orbital secular changes, according to (Ref. 8) we can write /54

$$di = \left(1 + \frac{\sigma}{\alpha_e}\right) \frac{\sin i}{3} \cos^2 \omega dT,$$

and can perform integration from several initial values  $i_0$ ,  $T_0$  up to the values  $i$  and  $T$ . Then

$$i - i_0 = \left(1 + \frac{\sigma}{\alpha_e}\right) \int_{T_0}^T \frac{\sin i}{3} \cos^2 \omega dT,$$

and we can find the index of circulation in the thermosphere, which is expressed by the variation of the orbital elements:

$$\frac{\sigma}{\alpha_e} = -1 + (i - i_0) \left/ \frac{1}{3} \int_{T_0}^T \sin i \cos^2 \omega dT \right. . \quad (16)$$

Formula (16) was used to compute the circulation indices based on data from the first Soviet and American Earth satellites, which are given in the literature (Table 1).

TABLE 1

Satellite	Date	Angle of Inclin- ation	Period of Rotation, minutes	Perigee Altitude, km	Perigee Argument	Perigee Latitude	Circula- tion Index
1957 $\beta$	11/3	65° 33	103.75	225	59°	52° N	0.5
	2/21	65 26	97.10	204	14	15 N	
1957 $\beta$	3/25	65. 23	93.78	192	359	2 S	-0.4
	4/9	65. 21	90.78	172	352	8 S	
1958 $\delta_2$	5/15	65. 19	105.95	226	58	52 N	-0.3
	10/1	65. 17	104.0	217	9	9 N	
1958 $\delta_2$	10/1	65. 17	104.0	217	9	9 N	0.45
	3/2	65. 13	100.75	211	310	44 S	
1958 e	8/26	50. 3	110.18	268	50	36 N	-1
	6/15	50. 3	107.06	265	23	18 N	

The use of formula (16) to compute the summer orbital data of five American satellites launched in 1963 (21-A, 21-B, 21-E, 25-A, 29-A) and the Soviet 1963-33A (Ref. 9) gives the mean circulation index (- 0.4). Thus, the opposite problem has been solved - determination of wind in the thermosphere based on data from orbital AES measurements.

The direct problem is usually solved in the literature - computation of atmospheric rotation for the AES motion. Thus, King-Hele (Ref. 6) compared the change in the orbital inclination of the second Soviet satellite 1957  $\beta$ , produced by atmospheric rotation, with experimental values. According to (Ref. 6), the calculation best corresponds to actual data in the case of a westerly wind of  $90 \text{ m} \cdot \text{sec}^{-1}$ . This corresponds to our calculations given in Table 1. However, for the equinox period the satellite indicates easterly winds close to the equator. According to (Ref. 7), the best agreement with observations of the second the third Soviet AES occurs for  $\sigma = 0$ , i.e., the upper atmosphere rotates with the Earth like a solid body. The estimates given in Table 1 coincide with the calculations of King-Hele for the perigee position in the winter season in the northern hemisphere. During the summer a strong easterly wind prevails in the thermosphere; in winter, it changes to a westerly wind. When predicting AES motion, many works assume that the atmosphere is at rest at perigee altitude. This is equivalent to the statement that an easterly wind prevails in the atmosphere, with respect to the terrestrial observer, and equals the Earth's rotational velocity at the corresponding latitude.

In the last work of King-Hele (Ref. 10), the angular rotational velocity of the atmosphere at perigee altitude was computed according to the formula /55

$$i_0 - i = 0,0398 \frac{\alpha}{\alpha_e} \int_{\dot{T}}^{T_0} M dT,$$

where

$$M = \frac{\sin i_0}{6} \left[ 1 - 4e + \left( 1 - 4e - \frac{2H}{ae} \right) \cos 2\omega + \dots \right].$$

This formula changes to (16) for  $H/ae \ll 1$ . We compiled a table showing the circulation indices based on the computations of King-Hele (Table 2)

Under the assumption that the westerly-easterly wind in the thermosphere can be described by a formula of thermal wind, King-Hele found that the temperature must be 10% higher above the equator than it is above the pole at altitudes of 150-200 km, in order that the wind which was found could exist. However, it is well-known that, according to rocket data, the temperature at these altitudes is higher ( $59^\circ\text{N}$ ) in the summer above Fort Churchill during the day than it is above White Sands ( $33^\circ\text{N}$ ) (Ref. 11).

TABLE 2

Satellite	Years	Perigee, km	Latitudinal Range	Circulation Index
1957 $\beta_1$	1958	210	48°N - 10°S	0.2
1958 $\alpha$	1957-1960	360	25 N - 25 S	0.36
1958 $\gamma$	1958	190	25 N - 25 S	0.16
1958 $\delta_1$	1958	210	40 N - 10 S	0.4
1958 $\delta_2$	1958-1960	220	40 N - 10 S	0.1
1961 $\zeta$	1961-1962	240	60 N - 60 S	0.8
1961 $\lambda_1$	1961-1962	300	60 N - 60 S	0.4
1961 $\lambda_2$	1961-1962	210	60 N - 60 S	0.4
1961* $\lambda_1$	1962-1963	200	37 N - 37 S	0.4
1961 $\nu$	1962-1963	190	37 N - 37 S	0.9

This lack of agreement between rocket data and information on the wind obtained from satellite data can apparently be interpreted by the fact that the wind is determined in the perigee sector by the AES. It can also be explained by the fact that the latitude and season of the atmospheric zone where the perigee is located must be taken into account during "wind" processing of orbital data.

In spite of the uncertainty of the first data obtained from AES, it can be assumed that wind observations by the AES were more representative than observations of noctilucent clouds and ionosphere drifts. This is due to the fact that the measured wind represents a quantity which is averaged over a rather extensive perigee section and which contains no random local fluctuations.

As was already noted above, in several cases the calculated prediction of AES orbits have been successful both for a "motionless" atmosphere and for an atmosphere rotating at a certain velocity. These variations can be interpreted by seasonal and daily atmospheric variations, and merit a more detailed study.

---

\* Note: Illegible in original foreign text.

1. Handbook of Astronautical Engineering, ed. H. Koelle, 1961.
2. Kovalevskiy, J. Development of the Dynamic Study of an Artificial Satellite. (Exploitation de l'étude dynamique d'un satellite artificiel.)- XI Astronaut. Congr., Stockholm, 1960.
3. Musen, P. J. Geophys. Res., 67, No. 1, 1962.
4. Taratynova, G. P. Uspekhi Fizicheskikh Nauk, 67, No. 1a, 1957.
5. Cook, G. E. Proc. Roy. Soc., A261, No. 1305, 1961.
6. King-Hele, D. Satellites and Scientific Research. London, 1960.
7. Cook, G. E., Plimmer, E. Proc. Roy. Soc., A261, No. 1295, 1960.
8. El'yasberg, P. Ye. Kosmicheskiye Issledovaniya, 2, No. 2, 1964.
9. King-Hele, D., Quinn, E. Planet. Space Sci., 12, No. 7, 1964.
10. King-Hele, D. Planet. Space Sci., 12, No. 9, 1964.
11. In "Experimental Study of Circumterrestrial Cosmic Space". IL, Moscow, 1961.

DETERMINING THE OZONE CONCENTRATION AT ALTITUDES OF 44-102 km  
BASED ON DATA OBTAINED FROM NOCTURNAL LAUNCHES OF GEOPHYSICAL ROCKETS  
(Summary)

A. Ye. Mikirov

This work discusses the results obtained at altitudes of 44-102 km /56  
when atmospheric brightness was measured by FIR equipment carried on an  
oriented spherical container.

One of the recorders was oriented toward the moon during the experi-  
ments. The ozone distribution at this altitude was obtained by  
measuring the lunar radiation intensity in the 5850 and 4200 Å spectrum  
region.

The ozone concentrations obtained are somewhat higher than those  
calculated theoretically by Nicolet and Goriukh, which were found from  
the condition of photochemical equilibrium.

The concentration was  $10^3$  times greater at night than it was during  
the day at an altitude of 85 km.

---

AERODYNAMICS OF MANOMETERS AND MASS SPECTROMETERS  
CARRIED ON ROCKETS AND SATELLITES

A. I. Ivanovskiy

The following relationship can be readily obtained from the  
balance of a flux falling on the input tube of the measurement device,  
which is shown in Figure 1, and the flux leaving it:

$$nv = n_0 v_0 \chi(\beta) \frac{K(\beta)}{K(0)}. \quad (1)$$

Formula (1) was obtained in the studies (Ref. 1, 2) for the case of a  
cavity connected with the atmosphere by an aperture. Here  $n$  is the density  
in the equipment;  $v$  - the most probable thermal velocity corresponding  
to the wall temperature of the equipment;  $n_0$ ,  $v_0$  - the corresponding  
quantities characterizing gas in the atmosphere;

$$\chi(\beta) = e^{-\beta^2} + \sqrt{\pi} \beta (1 + \Phi(\beta)); \quad \beta = u/v;$$

$K(\beta)$  is the Klausung factor of the coupling tube in the presence of an axial advancing stream,  $K(0)$  - in its absence. The ratio between the stream leaving the tube in a vacuum and the stream from the atmosphere /57 falling on the tube is called the Klausung factor for the tube. Thus, the problem of computing the equipment behavior in a stream of rarefied gas can be reduced to computing the Klausung factor for the tube.

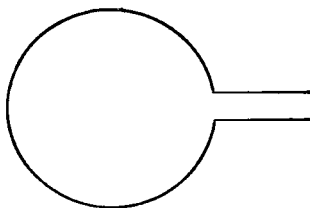


Figure 1

This problem has been solved under the following assumptions:

- (1) The gas in the atmosphere is a Maxwell gas;
- (2) The particle colliding against the wall acquires its temperature, and is reflected diffusely; the accommodation coefficient is 1;
- (3) The particle mean free path in the atmosphere is considerably greater than the linear dimensions of the equipment.

All of the particles entering the tube can be divided into two classes:

- (1) Primary particles - these particles do not collide even once with the wall;
- (2) Secondary particles, which may collide once with the wall and which assume the wall temperature.

The secondary particles can be characterized by the radiation intensity  $I$  - by the flux of a number of secondary particles from unit of wall surface per unit of solid angle. If the diffusion condition is taken into account, the following integral equation can be written

$$\int_{\Omega} I \frac{\cos \vartheta \cos \vartheta'}{R^2} ds + I_0 \int_{\mathcal{U}} \gamma(\vartheta) \frac{\cos \vartheta \cos \vartheta'}{R^2} ds = \pi I. \quad (2)$$

Here  $\vartheta$  and  $\vartheta'$  - are the angles between the radiation direction and the normal to the emitted and received radiation by elementary surfaces;  $\gamma(\vartheta)$  - the indicatrix characterizing the angular distribution by the mass stream in the presence of macroscopic velocity;  $\Omega$  - the index indicating integration over the equipment surface;  $\mathcal{U}$  - the index of

integration over the aperture into which the gas flows.

In the special case of a cylindrical tube, this equation can be reduced to the following:

$$\int_0^l \psi(|x-x'|) I(x') dx' + \frac{2I_0}{\pi} \int_0^{\arctg \frac{2k}{x}} \gamma(\vartheta) \sqrt{1 - \frac{\lg^2 \vartheta x^2}{4R^2}} \sin^2 \vartheta d\vartheta = I; \quad (3)$$

$$\psi = \frac{1}{2R} \left( 1 - \frac{|x| (x^2 + 6R^2)}{(x^2 + 4R^2)^{3/2}} \right).$$

If the solution of the integral equation I is known, the density of secondary particles at an arbitrary point and the flux of secondary particles through an arbitrary area can be computed:

$$\left. \begin{aligned} n_2 &= \frac{V\pi}{2} \int_{\Omega} I \frac{\cos \vartheta}{R^2 \vartheta} dS; \\ q &= \int I \frac{\cos \vartheta \cos \vartheta'}{R^2} dS. \end{aligned} \right\} \quad (4)$$

This problem was first solved by Klausning (Ref. 3) for the case of a static tube (a tube at rest in a gas). This problem was then solved in the work (Ref. 4-7) in the presence of an axial advancing stream.

/58

The method of solving equation (3) can be reduced to replacing the true kernel by a certain approximating function. After rather cumbersome calculations, we can obtain the formula

$$\frac{\chi(3) K(3)}{K(0)} = \frac{1}{R^2} \int_0^l \int_0^\infty f dx' dx'' + \frac{1}{R} \int_0^\infty f dx' + \frac{1}{R} \int_l^\infty f dx'. \quad (5)$$

Here  $f$  is the inhomogeneity of equation (3).

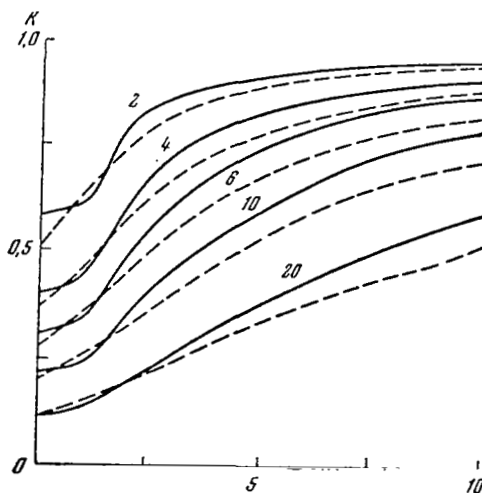


Figure 2



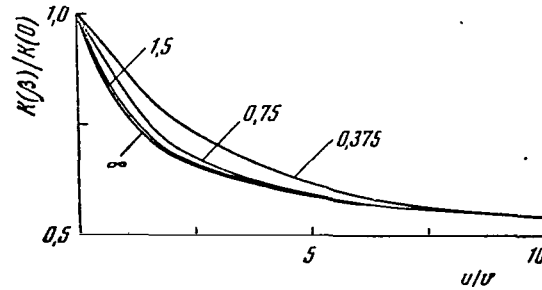


Figure 3

The results derived from the calculation according to formula (5) are shown in Figure 2. For a tube which is closed at the bottom, the following interesting theorem may be advanced: The intensity distribution  $I$  along such a tube is just the same as for an infinitely long tube. This indicates that only the geometry from the input section to the ionization region is important for mass spectrometers. The geometry of equipment located beyond the ionization region does not influence the particle density in the ionization region. For the region of the bottom vacuum, the following formula is obtained:

$$\frac{K(3)}{K(0)} \approx 1 + \frac{1}{2} \left( \frac{V\pi}{2p} - 1 \right) \left( 1 - e^{-\frac{2\beta}{V\pi} \frac{l}{R}} \right) \quad (6)$$

The computational results are shown in Figure 3.

/59

All of the preceding discussions pertain to particles which do not react chemically with the wall. However, atomic oxygen, which is the main component of the upper atmosphere, recombines into molecules at the walls. Therefore, an atomic oxygen concentration which is too low is recorded. For such particles, the concept of the loss coefficient  $\eta$  is introduced - the probability of particle loss during a single collision with the wall.

Equation (3) can thus be modified as follows:

/60

$$\int_0^l \psi(|x-x'|) I(x') dx' + f(x) = I/(1-\eta). \quad (7)$$

This solution is unusually cumbersome in this case; therefore, it is not given here (see [Ref. 6]).

One feature of this case lies in the fact that one Klausung factor is insufficient for the computations here. The factor of inverse conductance  $F$  plays an important role - the ratio of the stream reflected by the tube to the stream falling on the tube.

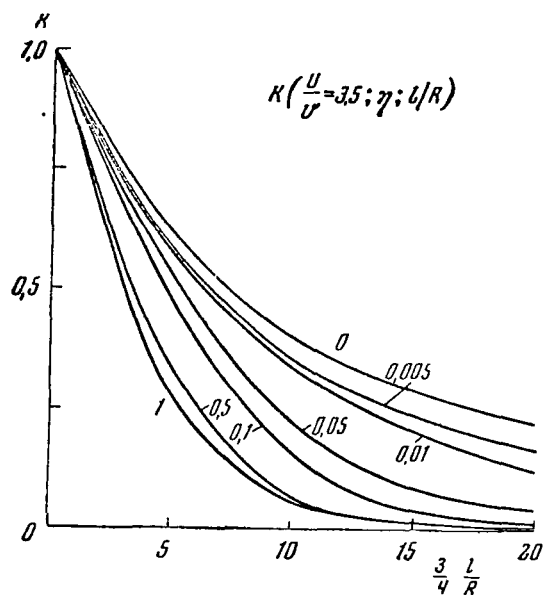


Figure 4

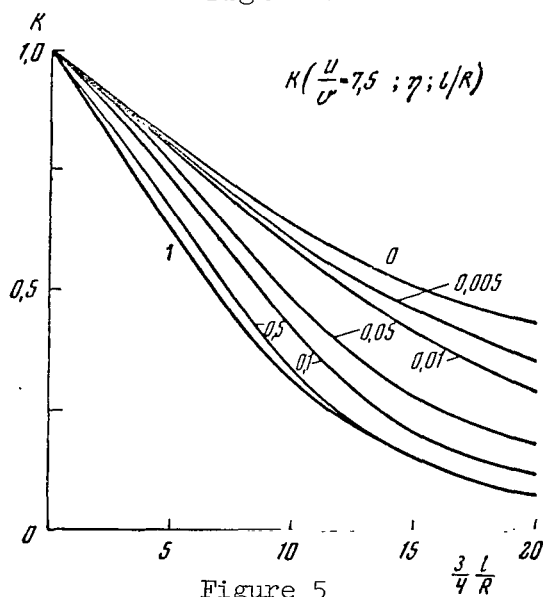


Figure 5

The inner density for the equipment (see Figure 1) is determined by the formula

$$nv = n_0 v_0 \frac{K(\beta)}{\Sigma + \frac{\eta}{1-\eta} \frac{S}{s}} \quad (8)$$

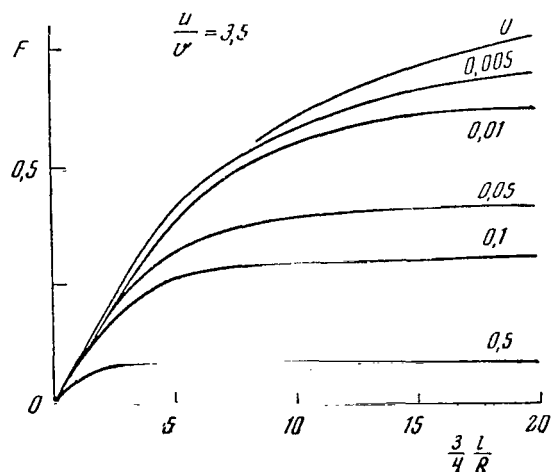


Figure 6

Here  $\Sigma = 1 - F(0)$ ;  $S$  - the cavity area;  $s$  - the area of the input tube aperture. In the case of  $\eta = 0$ , we obtain formula (1), since in this case  $K(0) = 1 - F(0)$ . Tables have been compiled for  $K(\beta)$  and  $F(\beta)$ , where these quantities are given as a function of  $l/R$ ,  $u/v$  and  $\eta$ . The nature of the dependences obtained can be seen in Figures 4-7.

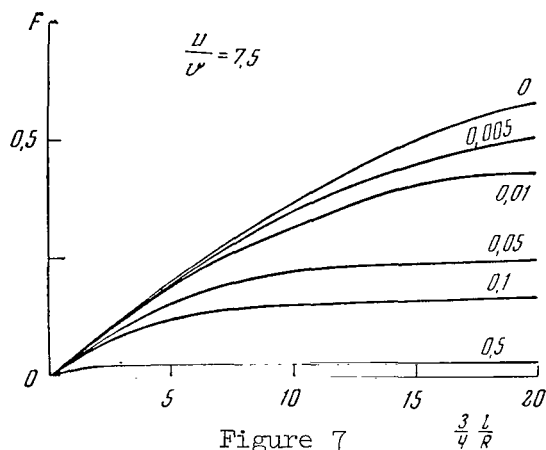


Figure 7

#### REFERENCES

1. Danilin, B. S., Mikhnevich, V. V., Repnev, A. I., Shvidkovskiy, Ye. G. Uspekhi Fizicheskikh Nauk, 63, No. 1B, 1957. /61
2. Horowitz, R., La Gow, H. E. J. Geophys. Res., 62, No. 1, 1957.
3. Klausing, P. Ann Phys., 12, 961, 1932.
4. Ivanovskiy, A. I., Repnev, A. I. Trudy Tsentral'noy Aerologicheskoy Observatorii (TsAO), No. 29, 1960.

5. Ivanovskiy, A.I., Kostko, O.K., Fedynskiy, A.V. Trudy TsAO, No. 46, 1962.
6. Ivanovskiy, A.I. Trudy TsAO, No. 56, 1964.
7. Hartly, L. Pond. J. Aerospace Sci., 29, No. 8, 1962.

# STRATOSPHERE AEROSOL BASED ON SPACECRAFT MEASUREMENTS

(Summary)

G. V. Rozenberg, V. V. Tereshkova

1. The spacecraft "Vostok-6" obtained photographs of the edge of the 61 Earth, with the twilight aureoles surrounding it extending for about 500 km, on June 17, 1963. The photographs were taken from the umbra region near the Atlantic Ocean with a "Konvas" motion picture camera on black and white film having photometric markings without light filters. The terminator line extended along the southern tip of Africa.

2. Two bands of decreased brightness could be clearly distinguished in the photographs; these bands indicated two sharply expressed layers of increased atmospheric turbidity. The altitudinal, photometric cross section of the photographs made it possible to determine the dependence of brightness, measured in relative units, on the perigee altitude in the sighting direction. On the basis of these data, the absolute values and the altitudinal behavior of the scattering coefficients  $\sigma$  were obtained for the aerosol, i.e., the altitudinal optical structure of aerosol layers in the stratosphere. It was found that the first thin aerosol layer was located at an altitude of  $11.5 \pm 1$  km. The second more powerful layer had a maximum at an altitude of  $19.5 \pm 1$  km; its half-thickness was 5 km, and  $\sigma = 5 \cdot 10^{-3} \text{ km}^{-1}$ .

3. The results obtained were compared with data from indirect and direct measurements of the aerosol concentration in the stratosphere - particularly, with data from airplane and balloon measurements, making it possible to determine the aerosol chemical composition (sulferous compounds of ammonium), the particle dimensions (0.1-1 micron), the concentration at the maximum ( $N = 1 \text{ cm}^{-3}$ ) and the volumetric concentration ( $v = 10^{-14}$ .) These comparisons indicated that the concentration obtained from the spacecraft coincides with data from airplane measurements; in both cases, it was determined with an accuracy of one order of magnitude. It was found that the volumetric concentration was one order of magnitude greater than that indicated by airplane measurements. This is due to the fact that gyroscopic aerosol particles in the stratosphere have an aqueous or icy cover. When particles were captured by the traps, only their dry state was examined, which was smaller in volume.

4. On the basis of the results obtained, assumptions were advanced stipulating that the altitudinal aerosol layer represents a source of condensation nuclei during the formation of nacreous clouds. The quantitative characteristics of the aerosol layer must be defined more precisely, particularly the nature of its horizontal nonuniformity.

RESULTS DERIVED FROM OPTICAL OBSERVATIONS  
WITH THE SPACECRAFT "VOSKHOD"

K. P. Feoktistov, G. V. Pozenberg, A. B. Sandomirskiy,  
V. N. Sergeyevich, D. M. Sonechkin

During the flight of the spacecraft "Voskhod", its crew performed 62 a group of optical observations which continued the experiments initiated on the "Vostok" spacecrafts.

Some preliminary results will be discussed here.

1. Photographs of the light mist surrounding the planet's edge in the diurnal hemisphere showed that this mist, which is more clearly expressed in the blue part of the spectrum than it is in the red part, not only veils the Earth's surface at the horizon, but also the troposphere cloudiness. The optical horizon of the planet was assumed to be the line of the maximum vertical brightness gradient, which can be clearly seen in Figure 1, a, representing the vertical photometric cross section of the horizon brightness (perigee altitude of the sighting line is plotted along the abscissa axis; brightness and altitude are expressed in relative units). The change in the color of the mist with altitude, which is characteristic for the vicinity of this line, can be readily explained by dispersion of the optical horizon altitudes, due to the spectral dependence of the scattering coefficient.

The rather sharply expressed indicatrix phenomenon and the fact that the optical horizon altitude does not depend on the azimuth are of particular interest. As a rule, the weakly expressed bands of increased brightness, which are parallel to the horizon and which have a white color, on the background of a monotonic decrease in the mist brightness (depending on the distance between the sighting line and the planet edge) are visually overlooked. The number of these bands, which are concentrated at below 30 km, varies from one to three. Figure 1, b shows an example of a 63 recording where  $x_1 \approx 7-10$  km is the altitude of the optically recorded planet edge above the Earth's surface.

2. When the spacecraft passed above the nocturnal hemisphere not too far from the terminator, color photographs were obtained of the sunset above the planet's edge. Figure 2, a, shows a reproduction of one of these photographs. The characteristic color change - from orange at the edge of the planet, into white, and then blue during the transition into space - was caused by selective attenuation of the light from the sunset as it passed toward the observer.

Attention should be called to the dark bands intersecting the sunset aureole parallel to the Earth's surface. This is a shadow due to the aerosol layers screening the sunset region and observed on the background of the diurnal horizon as weak light bands. These layers are more prominent

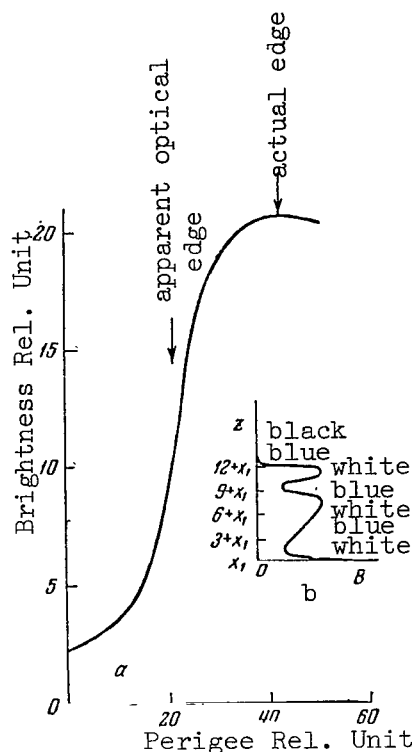


Figure 1

on the background of the sunset than they are on the diurnal horizon, and have a bluish color in addition to the color of the layers observed in the daytime. It can be seen from the visual recording of this horizon (shown sequentially in Figure 2, b) that this color is actually observed, and is not caused by color transmittal defects in the photograph. These pictures of the sunset and daytime horizons of the planet closely coincide with each other and with the picture expected theoretically.

From the geophysical point of view, it is important to stress the existence of extensive and comparatively stable aerosol layers, which were discovered previously by "Vostok-6". We established that their number fluctuates (from one to three), in addition to the fact that these layers were observed by "Voskhod" not only at twilight, but also during the daytime. Sometimes they were not present at all, as can be seen from the black and white photographs taken under different conditions. Figure 3 shows the altitudinal photometric cross sections of one of these photographs, corresponding to different azimuths. The strong azimuthal dependence of the aureole brightness can also be seen from the figure, as was already observed in photographs taken from "Vostok-6" and as was predicted theoretically.

3. During the flight of "Voskhod", the nocturnal hemisphere of the

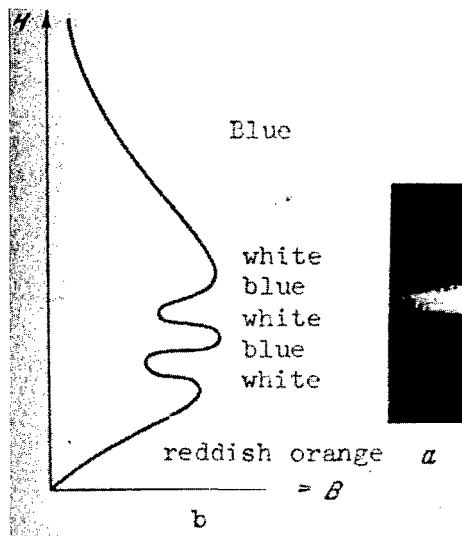


Figure 2

planet was illuminated by the moon, and during the observations it was close to the horizon. Under these conditions, a weak luminescent band, extending along the horizon and clearly distinguishable on the background of the aurora polaris, was observed above the edge of the planet at an altitude of about  $2.5-3^\circ$ . It was bluish-white, with a yellowish-green shade. At the sublunar point, the brightness was comparable with the brightness of troposphere clouds illuminated by the moon, and decreased considerably as one receded from the sublunar point (the band could be traced to  $30-35^\circ$  on both sides).

The altitudinal distribution of the luminescence (sharp upper boundary and blurred lower boundary) indicated that the luminescence was concentrated in a comparatively thin layer. When the spacecraft left the shade, the luminescent band "dissolved" in the daylight. /64

4. When the spacecraft left the shade (very rarely above the diurnal hemisphere) comparatively slowly moving luminescent points of white light appeared beyond the illuminator; these points curved toward the sun rays. This phenomenon was first observed by John Glenn, and then by many other cosmonauts. According to observations by the spacecraft "Voskhod", several particles with a brightness of between 0-2 stellar magnitude usually moved into the  $40-60^\circ$  field of view. The particles remained in the field of view for 10-15 seconds. Their direction of motion was different, and sometimes they changed before the eyes of the observer without any apparent external reasons.

The particles were located at 0.5-3 m from the spacecraft (at larger distances, they disappeared from the field of view). This provides a basis



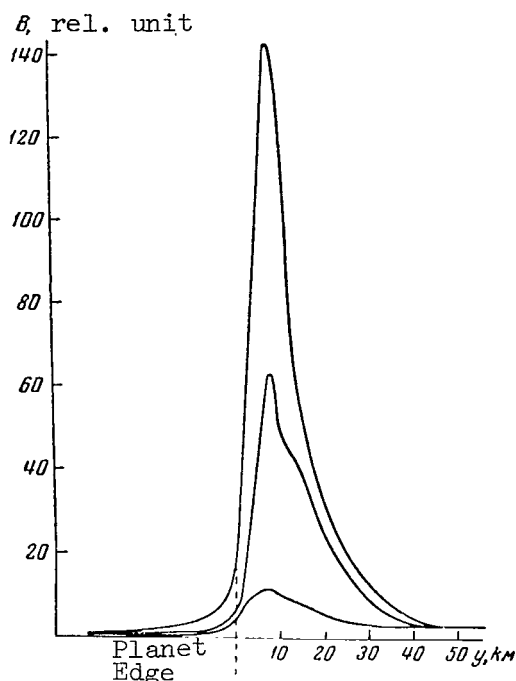


Figure 3

for assuming that the particles represent ordinary dust particles which are on the order of 10 microns in size; these dust particles are illuminated by the Sun and move with respect to the spacecraft at a velocity of 0.1-2 m/sec, i.e., they belong genetically to its system.

5. Among the photographs obtained, there are two series of photographs depicting cloudiness on the background of a water surface. One pertains to the periphery of a cyclone, and the other pertains to the periphery of an anticyclone.

A statistical analysis of the brightness structure of the cloud fields, which was performed on the results derived from photometric measurement of these photographs with a resolution of  $1 \text{ km}^2$ , has not only confirmed the connection between the statistical characteristics and the type of cloudiness, but also between the amount of cloudiness. Figure 4 shows examples of normalized correlation brightness functions for different types of cloudiness on the periphery of a cyclone (1 - small cloudiness  $A_c$ ; 2 - significant cloudiness  $A_c$ ; 3 - significant cloudiness  $A_c, C_i$ ; 4 - significant cloudiness  $C_i$ ). For these types of cloudiness (and for a water surface) the one-dimensional brightness distribution law differs from the normal law.

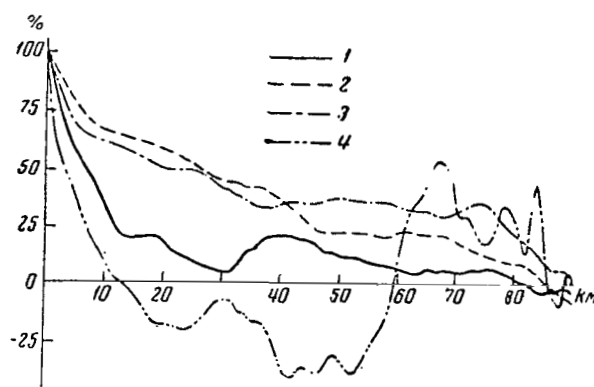


Figure 4

# RESULTS DERIVED FROM ROCKET RESEARCH ON THE EARTH'S UPPER ATMOSPHERE BETWEEN 1960-1964

(Summary)

S. M. Poloskov

This report includes:

1. The results derived from studying the neutral composition of the Earth's atmosphere by means of radio frequency mass spectrometers carried on geophysical rockets. Data are obtained on the distribution of all the 65 main neutral gases comprising the Earth's atmosphere, as well as small admixtures of non-atmospheric origin, at altitudes greater than 100 km. In addition to these data, the results derived from studying other structural (thermobaric) parameters of the upper atmosphere (pressure, temperature) by means of mass spectrometers are also presented.

2. Certain geophysical and astronomical results obtained by geophysical rockets during the total solar eclipse on February 15, 1961.

The outer corona brightness distribution in the 3000-6000 Å spectral region during the total solar eclipse on February 15, 1961, was obtained by an electrophotometer carried on a spherical container oriented in space. The results obtained do not indicate a smooth brightness distribution behavior at distances on the order of 11-33  $R_{\odot}$  from the Sun, which points to the existence of nonuniformities in the solar corona which have linear dimensions on the order of 300,000 km.

In addition, the ozone distribution at altitudes between 40-80 km before, during, and after the eclipse was obtained, based on absorption in the 2700 Å spectral region. A comparison of the results shows that there is an ozone concentration increase at these altitudes during an eclipse.

3. The results derived from a study of the scattered light of the sky, and - on the basis of these data - the results derived from studying the aerosol component distribution in the upper atmosphere up to an altitude of 450 km. The results derived from studying the upper atmosphere brightness at altitudes between 70-450 km are given. It is found that the upper atmosphere brightness values obtained cannot be explained by Rayleigh scattering or by eigen atmospheric luminescence.

An assumption is formulated regarding the aerosol nature of the brightness values obtained. Based on this, the scattering coefficient and the scattering (dust) matter concentration is computed. It is found that there is an aerosol layer at the Earth with a matter concentration maximum at an altitude of 80-85 km. It is also found that the aerosol layer continues to exist at altitudes greater than 500 km.

4. The results derived from studying the altitudes and intensities of the main terrestrial atmosphere emissions facilitate a determination of the intensity and altitude of the 5577 and 6300 Å luminescence lines, as well as the continuous background in the 5300 Å spectral region.

---

## INFRARED SPECTROPHOTOMETRY OF THE EARTH'S THERMAL RADIATION

A. I. Lebedinskiy, D. N. Glovatskiy, V. I. Tulupov,  
B. V. Khlopov, A. A. Fomichev, and G. I. Shuster

An essential role in meteorological processes is played by thermal radiation of the atmosphere and the underlying surface. By now rather extensive information has been amassed on the integral thermal radiation of the atmosphere and the underlying surface, as well as on radiation in narrow spectral intervals in the infrared region which can be recorded from artificial Earth satellites (Ref. 1-7). Information on colorimetric (Ref. 8) and spectral distribution of thermal radiation, however, is very sparse (Ref. 9).

An experiment was performed to study energy distribution in the thermal radiation spectrum of the Earth (atmosphere and underlying surface); preliminary processing of results from this experiment has provided the information presented in this report. The experiment employed a scanning diffraction spectrophotometer installed on the artificial Earth satellite "Kosmos-45". The orbital elements of this satellite are: angle of inclination of orbital plane to the equator -  $65^\circ$ ; period of revolution  $T = 89.69$  min.; perigee altitude - 206 km; apogee altitude - 327 km. The spectrometer uninterruptedly conducted measurements for 65 hr. Information was obtained which made it possible to compile a rather detailed chart of the Earth's thermal radiation field from  $65^\circ\text{N}$  to  $65^\circ\text{S}$ . /66

The optical axis of the instrument pointing toward the Earth was vertically oriented. Background comparison radiation (from space) entered the device horizontally. Measurements were made by the Earth-space method of modulation. Assuming that there is small radiation from space in the thermal region of the spectrum, we can obtain absolute readings of the Earth's thermal-radiation flux.

A photometer measuring brightness at the nadir in the waveband of  $6000\text{--}8000\text{ \AA}$  was employed to determine the nature of cloudiness in the sub-satellite region. Photometer resolution in this locality was about 30 km.

The spectrophotometer is an electron-opticomechanical instrument designed to measure the strength of the Earth's thermal radiation in a spectral range of  $7\text{--}38\text{ }\mu$ . The device has two spectral measurement ranges which are necessary for operation in a very wide spectral region without superposition of the third and higher spectral orders on the working spectrum of the first order. The spectral radiation intensity is measured in the first spectral range in the wavelength range from 7 to 20 microns; in the second - it is measured in the wavelength range from 14 to 38 microns.

The dispersing elements of the instrument's monochromators are plane reflecting diffraction grids of 24 lines per mm in the first spectral range, and 12 lines mm in the second, with maximum energy concentration in the spectrum of the first order at  $10\text{ }\mu$  wavelengths in the first

spectral range, and  $20\ \mu$  in the second spectral range.

Spectral resolution of the instrument is (a) from  $1.4\ \mu$  at a wavelength of  $7\ \mu$ , to  $1.1\ \mu$  at a wavelength of  $18\ \mu$  in the first range, and (b) from  $2.8\ \mu$  at a wavelength of  $14\ \mu$ , to  $2.1\ \mu$  at a wavelength of  $36\ \mu$  in the second.

The instantaneous visual field of view angle of the instrument's optical system is  $1^{\circ}46' \times 2^{\circ}20'$ . At average flight altitudes of 250 km at this field of view angle the inlet slits are filled with an image of a  $7.5 \times 10\ \text{km}^2$  portion of the radiating surface.

The instrument is capable of scanning with a visual field angle of  $\pm 8^{\circ}30'$ . During scanning, the spectral strength is measured in the wavelength ranges: (a)  $\lambda = 9.5 \pm 0.6\ \mu$  in the first, and (b)  $\lambda = 18.5 \pm 1.35\ \mu$  in the second range.

This mechanism was turned off in our experiment, and in measurements at the  $9.5$  and  $18.5\ \mu$  wavelengths there was only area scanning along the satellite's flight path caused by its orbital motion.

As radiation receivers, the instrument used semiconductor bolometers with a sensitive area of  $1 \times 1\ \text{mm}^2$ .

The instrument's operating cycle comprised the following sequentially performed operations:

(a) Measurement of energy distribution from  $7$  to  $20\ \mu$  in the spectrum for  $18.5\ \text{sec}$ ;

(b) Scanning along the satellite's path of motion for  $14.4\ \text{sec}$  at wavelength  $\lambda = 9.5\ \mu$ ;

(c) Measurement of energy distribution from  $14$  to  $38\ \mu$  in the spectrum for  $18.5\ \text{sec}$ ;

(d) Scanning at a wavelength of  $18.5\ \mu$  for  $14.4\ \text{sec}$ . The remainder /67 of the time in the cycle was occupied by transitions between operating regimes. The period of the instrument's complete operating cycle was  $81\ \text{sec}$ .

A six-channel oscillograph used  $35\ \text{mm}$  moving picture film to record information from (1) the infrared spectrophotometers described here, (2) a photometer for visible radiation, (3) the ultraviolet monochromator and colorimeter, which were on the same satellite and were described in an article (Ref. 10) which is being simultaneously published. Two channels registered the readings of the infrared spectrophotometers; one channel was used for the visible radiation photometer; two channels were switched on, depending on illumination at the subsatellite point. (The ultraviolet monochromator readings were recorded on the diurnal side, those of the colorimeter were recorded on the nocturnal side.) One channel was utilized via a 12-terminal switch to measure auxiliary parameters (instrument temperature, power supply voltage, etc.). The moving picture film traveled at

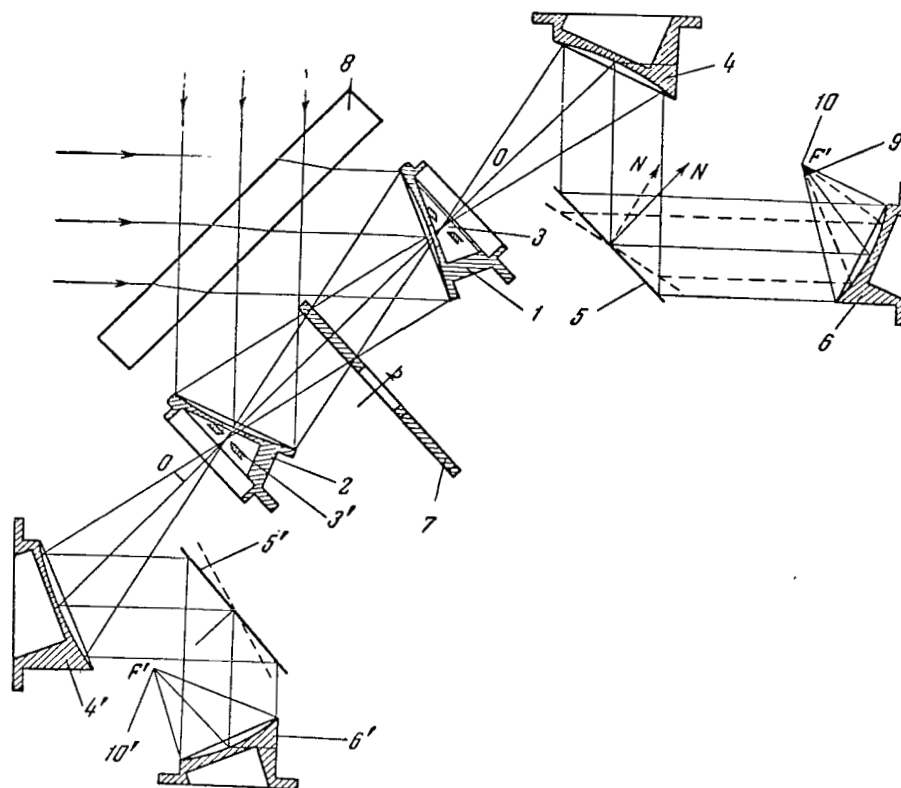


Figure 1

### Optical Diagram of Spectrophotometer

0.8 mm per sec. Every 112 sec the image of the dial of an electric clock was printed on the film. After termination of observation, the film container was returned to Earth, and the film was developed under laboratory conditions.

Figure 1 gives the optical diagram of the instrument. Light enters through inlet window 8, which provides a hermetic seal for the entire instrument complex. The window is made of KRS-5 crystal.

A specular, two-sided gold-plated modulator 7 with four blades successively replaces the luminous flux from the surface being studied by the flux from the background of comparison, and vice versa, at a rate of 27 cps at the input slits of the monochromators. /68

Mirror objective 1 reflects a section of the investigated surface to the inlet slits of monochromators 3 and 3'; the same objective 2 is

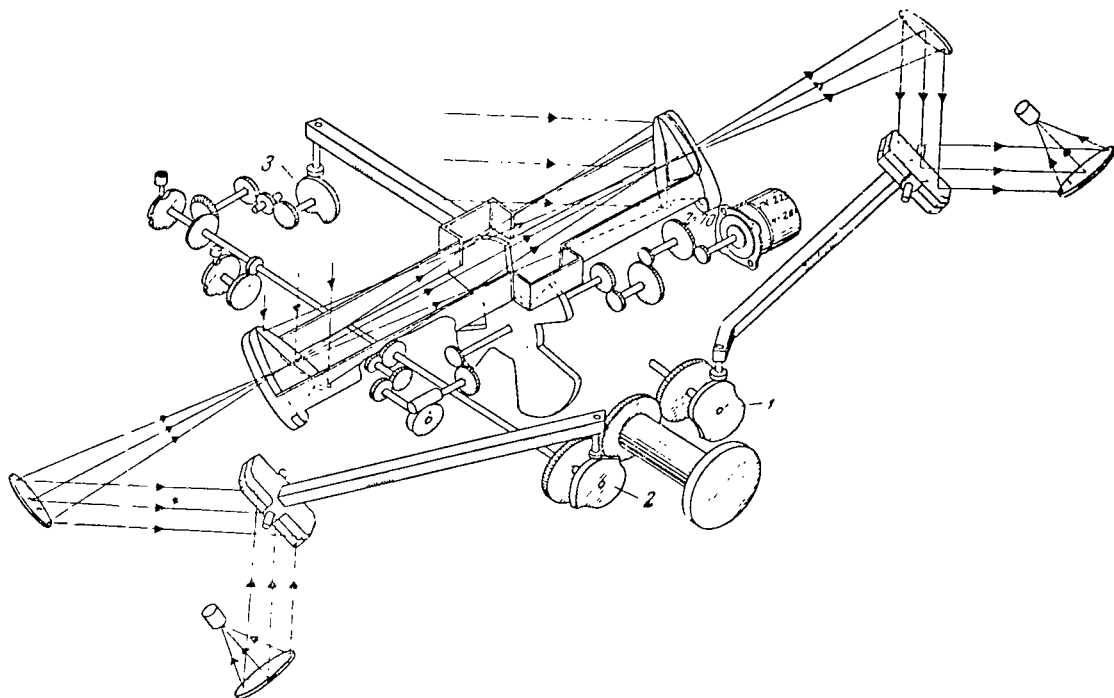


Figure 2

### Kinematic Diagram of Spectrophotometer

directed into space toward the comparison background; both objectives have focal lengths of 55 mm and aperture ratios of 1:2. Both diffraction monochromators are provided with collimators and cameras with identical mirror objectives (4 and 4', 6 and 6'); the camera objectives have focal lengths of 20 mm and aperture ratio of 1:1.

All the mirror objectives are extra-axial paraboloids and all are gold-plated, except for 4', which is made of uncoated lithium fluoride. Objectives 1 and 2 are so placed that the luminous fluxes from the investigated surface and the comparison background pass through the very same spot in the inlet window, thus eliminating noise from discontinuities in this window.

As cutoff filters, the optical system uses plate 9 in the first spectral range. This plate is made of indium antimonide 0.15 mm thick, which cuts off radiation shorter than  $7 \mu$ . There is no transparent light filter in the second spectral range, but the lithium fluoride crystal of which collimator objective 4' is made does not reflect radiation

shorter than  $14\ \mu$ , while giving good reflection in the entire range from  $14$  to  $38\ \mu$ .

The radiation fluxes from investigated surface and comparison background, which are distributed along the spectrum, are simultaneously focussed by objectives 6 and 6' onto the sensitive areas of the two radiation receivers in such a way that, when radiation from the investigated surface reaches the first spectral-band receiver, the comparison-background radiation arrives at the second spectral-band receiver, and vice-versa.

The spectrum is scanned by rotating the diffraction grids about axes parallel to the lines on the grids by means of the corresponding cam mechanisms (1 and 2, Figure 2). Area scanning at an angle of  $\pm 8^\circ 30'$  is accomplished by rotating the mirror objectives (1 and 2, Figure 1) about axis 00 at an angle of  $\pm 12^\circ$  by means of cam mechanism 3 (Figure 2). In the given experiment, cam 3 was removed and objectives 1 and 2 were rigidly attached. /69

The cam mechanisms and modulator disc are driven by a worm-cylinder reducing gear from a hysteresis synchronous motor, fed from the satellite power system through its own static converter.

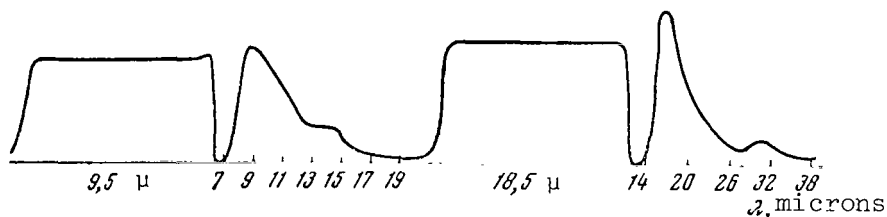


Figure 3

Sample of Calibration Trace of Radiation  
From Absolutely Black Body

The radiation acting on the bolometers is converted into 27-cps electrical signals which go to the input of the amplifying loop. In this loop they are amplified and converted into d.c. voltages proportional to the radiation fluxes.

To measure the radiation divided by the instrument's optical system into two spectral ranges, the amplifying loop accordingly contains two channels, each of which has its own preamplifier. In addition to their sensitive elements and preamplifiers, the channels share still another part - the amplifier. To increase the range of measurements, the amplifier is in turn divided into two subchannels with different amplification factors and separate outputs to two oscillograph loops with a sensitivity ratio of 1:2.5. The spectra were linked to the wavelength by the



absorption lines of polystyrene and the reflection lines of quartz, as well as by the familiar bands in the Earth's atmosphere - the ozone band at  $9.6\ \mu$  and the blend of carbon dioxide and ozone with its center near  $15\ \mu$ .

Before the start of the experiment, the instrument was calibrated by the radiation of a black body. This was done by using two identical black bodies set at a  $90^\circ$  angle to each other, in such a way that radiation from each of them filled the input aperture of the main channel and the comparison channel, respectively. The second black body (in front of the comparison channel) was at room temperature; the temperature of the first was changed. The temperature of both black bodies was measured with  $0.5^\circ$  accuracy.

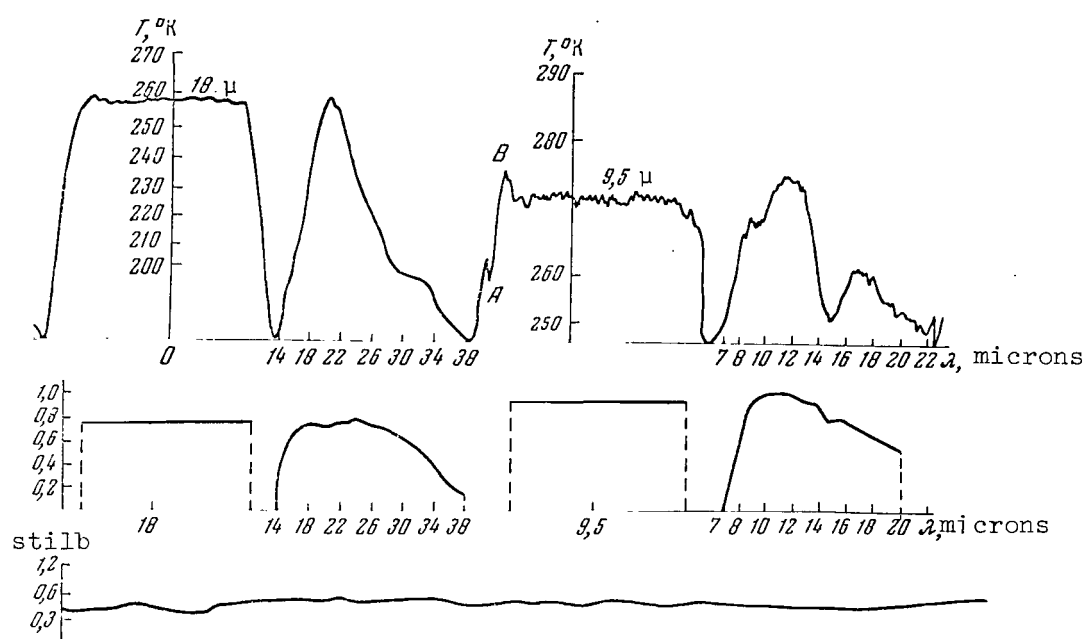


Figure 4

Sample Trace (Top) Obtained During Satellite Measurements;  
(Center) Spectral Transparency Curves of Instrument's Optics;  
and (Bottom) Photometer Trace for Visible Radiation

Radiation spectra were recorded with the first black body at different temperatures  $5^\circ$  apart, and with the second at a constant temperature. Figure 3 shows a specimen calibration trace of a complete spectrophotometer cycle for the difference in radiation between black bodies at temperatures  $T_1 = 336^\circ\text{K}$  and  $T_2 = 302^\circ\text{K}$ .

The top portion of Figure 4 gives a sample recording obtained during flight in space. In all, 2880 such traces were received while our equipment was in operation on satellite "Kosmos-45".

Overlaps of a second-order spectrum are clearly seen in the black-body laboratory spectra and in the longwave spectrum received from space. Overlap occurs in the longwave spectrum from 28 to 34  $\mu$ , and in the shortwave spectrum from 14 to 17  $\mu$ . At greater wavelengths, second-order /70 spectrum strength diminishes practically to zero, while the first-order spectrum still remains of satisfactory strength. At wavelengths shorter than 28  $\mu$  in the longwave spectrum, and shorter than 14  $\mu$  in the shortwave spectrum, there is no overlap at all, because the abovementioned cutoff filters with respective pass limits of 14 and 7  $\mu$  are used.

The spectral transmission coefficients of all instrument optical system elements, except diffraction grids, were measured on spectrophotometers. The center part of Figure 4 is a graph of the general transmission coefficient of the entire optical system; it is the product of the transmission coefficients of all optical system elements and is expressed in arbitrary units. When the spectrum was scanned, this coefficient changed as a function of wavelength; during area scanning, it remained constant. The breaks in the transmission coefficient curve in the intervals between spectrum and area scanning correspond to the periods of rapid motion of the diffraction grid from the position at the end of spectrum scanning to that at the beginning of area scanning - or, on the other hand, from the latter position to the one occupied before spectrum scanning. Some features of the trace in these transition sectors (particularly the ordinates of minimum A and maximum B noted on the shortwave scan) make it possible to check instrument operational accuracy and the constancy of its electric inertia.

We have used data from (Ref. 11) also in relative units to calculate distribution of light intensity over the spectrum, which is defined by the diffraction grid in the high-concentration region. With a knowledge of both instrument factors - spectral transmission coefficient and spectral reflecting capacity of the grid - we can convert the traces into curves /71 of relative intensity and can then change these data into absolute units by comparing them with results of black-body laboratory measurements with the same instrument.

In actual fact, the absolute calibration method is more complex because, when related to black-body radiation, the system of reference wavelengths is determined more accurately, as are also effective spectrophotometer resolution, the nonlinear characteristics of its scale, and the wavelength value of peak diffraction grid light concentration, which depends not only on the grid's geometric characteristics, but also on the degree to which the light is polarized.

After selecting optimum values for all parameters, we plotted calibration curves showing the dependence of trace ordinates on radiation flux expressed in absolute units every 1-2  $\mu$  for all wavelengths. These

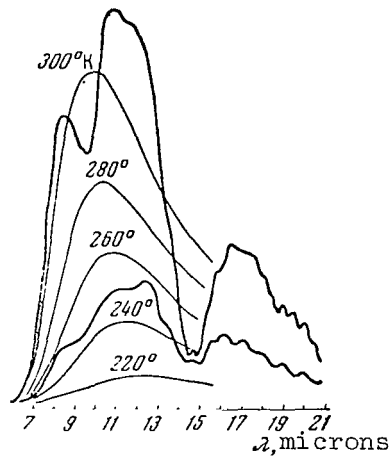


Figure 5

Energy Distribution in Typical Spectra in the 7 to 20  $\mu$  Range, and Comparison of it With Black-Body Curves

calibration curves were used to plot black-body radiation curves every  $10^\circ$  from 200 to  $300^\circ\text{K}$  on the same scale as the spectra being recorded. In large-scale processing of the spectra, it proved convenient to project the trace images on a screen, on which a family of black-body curves at different temperatures was plotted as a reference network. Figures 5 and 6 present samples of traces (dark lines) projected on such a network. The higher intensity curves match cases of clear weather, and the lower intensity curves - cases of cloudy weather.

The shortwave spectrum in Figures 4 and 5 clearly displays an ozone band with its center at  $\lambda = 9.6 \mu$  and a blend of carbon dioxide and ozone bands centered at  $15 \mu$ , sharply dividing the spectrum into two parts.

The longwave-spectrum peak occurs at a wavelength of  $18.5 \mu$ . It is at this same wavelength that area scanning occurred. The peaks of the black-body calibration curves of the corresponding temperatures occur at  $\lambda = 17 \mu$ . The peaks of the investigated spectra are shifted due to the effect of a strong absorption band in the atmospheric spectrum.

A number of curve irregularities, which are particularly noticeable /72 in the area scans, are caused by nonuniformity in the measured surface. In Figure 4 the satellite is flying over a rather uniform surface, as is evident from the photometer trace of the visible radiation given in the

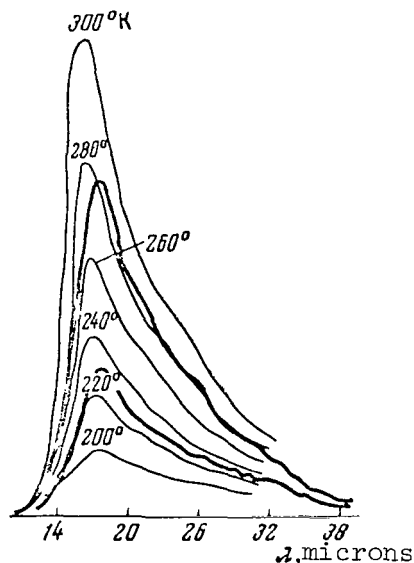


Figure 6

Energy Distribution in Typical Spectra in 14 to 38  $\mu$  Range, and Comparison of it With Black-Body Curves

lower part of this figure (brightness at the subsatellite point fluctuates within 0.35-0.55 sb). When cloudless regions alternate with clouds, the trace fluctuations are usually very strong.

The chief purpose of the visible-radiation photometer is to provide a method for distinguishing clouds from land and sea surfaces which is independent of infrared measurements. In 0.6-0.8  $\mu$  red light, the albedo of clouds reaches 60-70%, while water surfaces and dry-land regions covered by a forest seem almost black. Even deserts have an albedo which differs sharply from that of clouds, e.g., in the Sahara our measurements show that albedo varies from 15 to 25%.

In the so-called spectral "transmittance window," i.e., at wavelengths from 8 to 12  $\mu$ , the effective radiation temperature - when there are no clouds - is close to that of the ground. With clouds, however, it approaches the radiation temperature of their upper surface, often differing by 20-30° from ground temperature. There should therefore be, and in actual fact there is, a close negative correlation between intensities measured in this waveband by the infrared spectrophotometer and brightnesses at the subsatellite point measured by the visible-radiation photometer. A graphic illustration of this may be found in Figure 7, where a typical area scanning at 9.5  $\mu$  (curve 1) is compared to a visible-radiation photometer trace (curve 2). The scale of effective temperatures

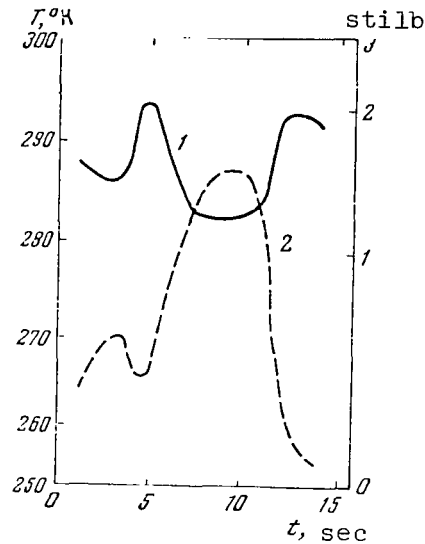


Figure 7

Area Scanning at a Wavelength of  $9.5 \mu$   
and in Visible Region of Spectrum

for curve 1 is given at the left; the scale of brightness for curve 2 is given at the right in stilbs. The time in seconds, computed from the start of scanning (15 sec corresponds to satellite travel of 120 km) is plotted along the abscissa axis.

It should be noted that, in spite of the fact that area scanning occurs in the ozone absorption band (centered at  $9.65 \mu$ ) the fluctuations of curve 1 in Figure 7 are explained principally by variations in radiation from the 73 underlying surface, not from changes in atmospheric ozone content, since bandwidth  $\Delta\lambda = 1.2 \mu$  registered by the instrument is wider than the ozone absorption band.

We could have easily predicted the finding shown in Figure 7, but the similar graph in Figure 8, where curve 1 represents a typical area scan at wavelength  $18.5 \mu$ , is far from trivial. The negative correlation in this case is just as close as in the preceding. However, wavelength  $18.5 \mu$  is not situated in the transmittance window, but in a region of rather strong water-vapor absorption bands, and the portion of radiation contributed by the lower tropospheric layers to the radiation flux emitted into outer space should be materially smaller here. The dependence of effective temperature of incoming radiation on cloudiness at greater wavelengths should be even weaker, since the mean water-vapor absorption coefficient increases significantly on the longwave side. In reality, this is not the case. The typical curve of spectral energy distribution in Figure 6 does not differ



Figure 8

Area Scanning at Wavelength of  $18.5 \mu$   
and in Visible Region of Spectrum

greatly from the black-body curve in the entire wavelength range from  $20$  to  $35 \mu$ . This deduction, based on an investigation of the typical curves, is corroborated by random statistical processing which still encompasses only a portion of the material at our disposal.

Figure 9 shows the latitudinal dependence of effective temperature at a wavelength of  $9.5 \mu$  from area scanning data on one of the revolutions. Time from the moment the satellite crosses the equator is plotted along the abscissa axis, and latitude  $\phi$  and longitude  $l$  of the subsatellite point are given every 8 min (longitude is assumed to be positive eastward from Greenwich).

The figure presents three curves: the upper corresponds to highest radiation intensities in every scan; the lower, to the smallest intensities; and the middle, to average intensities over the area delimited by the scanning curve. It is evident that the curves undergo abrupt changes which can be explained by cloudiness. It is clear from the figure that curve behavior varies - now the curves approach each other closely, now they diverge widely. The explanation of this lies in the varying degree of radiation field nonuniformity. In cases where the curves approach each other closely, the radiation field during the period of area scan ( $14.4$  sec) has not substantially changed. When, however, the curves

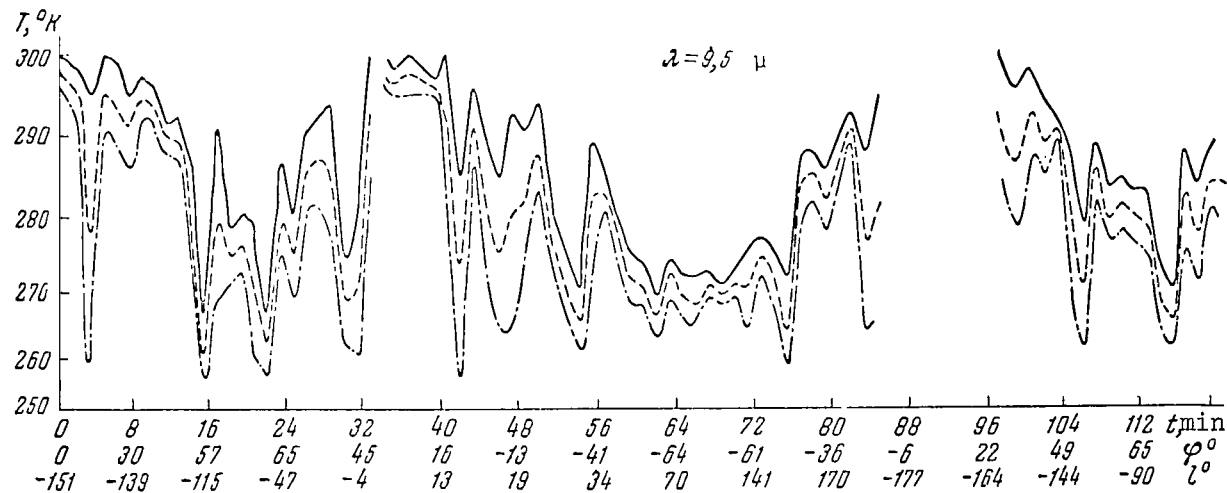


Figure 9

Latitudinal Dependence of, and Local Fluctuations in, Radiation at a Wavelength of  $9.5 \mu$

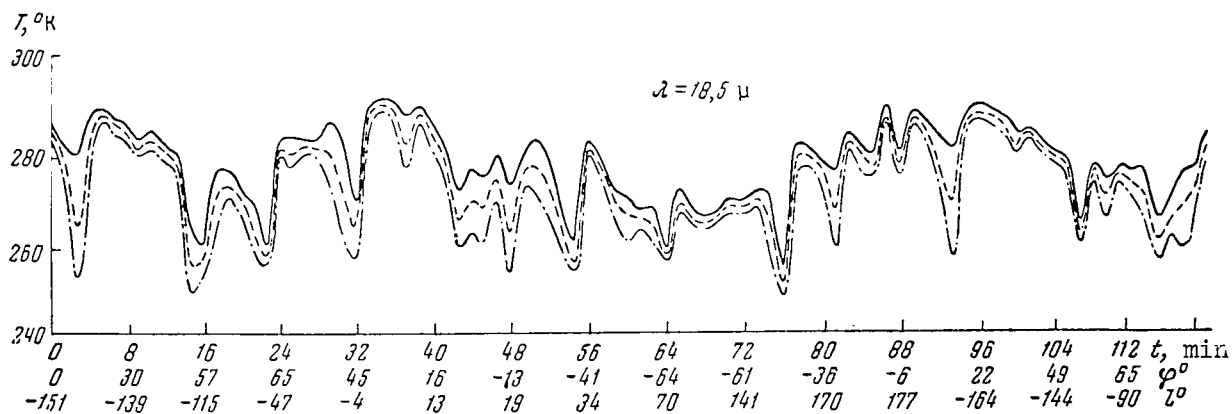


Figure 10

Latitudinal Dependence of, and Local Fluctuations in, Radiation at a Wavelength of  $18.5 \mu$

diverge, the radiation field is highly nonuniform, and the explanation lies in changes of the underlying surface - most often by alternation of clouds and spaces between them. Abrupt dips in radiation at  $9.5\ \mu$  are often observed, when effective radiation temperature drops to 250-260°K. At this moment the cloud cover has entered the instrument's field of view. The discontinuous segments of the curves indicate the instrument has gone off scale, i.e., effective radiation temperatures above 300°K.

The graphs in Figure 10, plotted just like those in Figure 9, also present a similar picture, but for a wavelength of  $18.5\ \mu$  and another revolution. The only essential difference is that the maximum temperatures here are somewhat lower.

Figure 11 compares the latitudinal relationships of the average effective temperatures during scans for wavelengths  $18.5\ \mu$  and  $9.5\ \mu$  (curves 1 and 2, respectively) with the photometer trace for visible radiation (upper curve) for a single revolution. The photometer readings are zero on the nocturnal side of the Earth (from 27 to 72 min) and closely coincide with both effective temperatures on the Earth's diurnal side.

The correlative graphs in Figure 12 were plotted from measurements on 180 consecutive intensity traces at five wavelengths:  $9.5$ ,  $18.5$ ,  $26$ , and  $34\ \mu$ , as well as at the minimum of the carbon-dioxide and ozone-band blend near  $15\ \mu$ . In the two graphs at the left the intensity at  $18.5\ \mu$  was measured from shortwave spectra, and in the two at the right - from <sup>76</sup>longwave spectra. All intensities are expressed in arbitrary units. Intensity in the minimum absorption band of about  $15\ \mu$  is almost constant, as has been previously noted (Ref. 6). A rather close correlation is detected between intensities at the other four wavelengths, and indicates that the spectra are fundamentally described by one parameter, i.e., the effective radiation levels do not differ too greatly in the various spectrum intervals from  $8$  to  $35\ \mu$ . Since all spectral intervals, in the first place, display a great cloudiness effect on strength of radiation leaving the atmosphere, and since, in the second place, the effective temperature is close to the temperature of the lower troposphere, it is probably precisely these layers which must be regarded as the main source of the radiation leaving Earth's atmosphere.

This conclusion is also confirmed by the latitudinal dependence of effective radiation temperature. The stratosphere is known to be colder at the equator than at high latitudes. Therefore, if the effective thermal-radiation level were in the stratosphere, the curves showing latitudinal dependence in Figures 10 and 11 would rise in the high latitudes and descend in the equatorial region. The actual course of these curves is just the reverse, i.e., the same as in Figure 9.

The essential characteristic of the derived spectra is the very large and highly variable intensity of the ozone band centered at  $9.6\ \mu$ . Figure 13



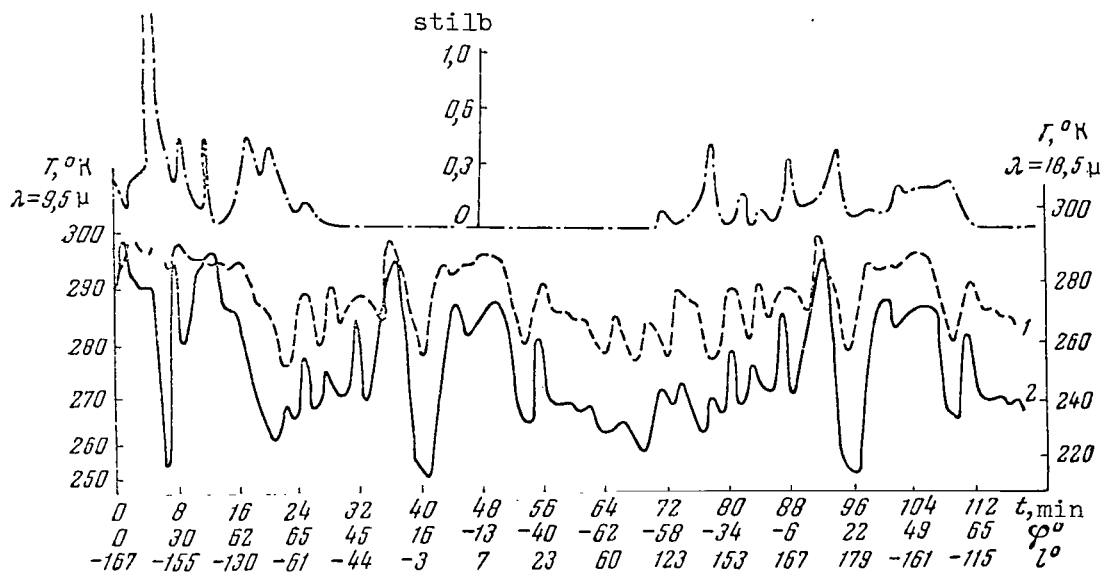


Figure 11

/75

Comparison of Geographical Distribution of  
Radiation at Wavelengths of  $9.5 \mu$ ,  $18.5 \mu$ ,  
and in Visible Region of Spectrum

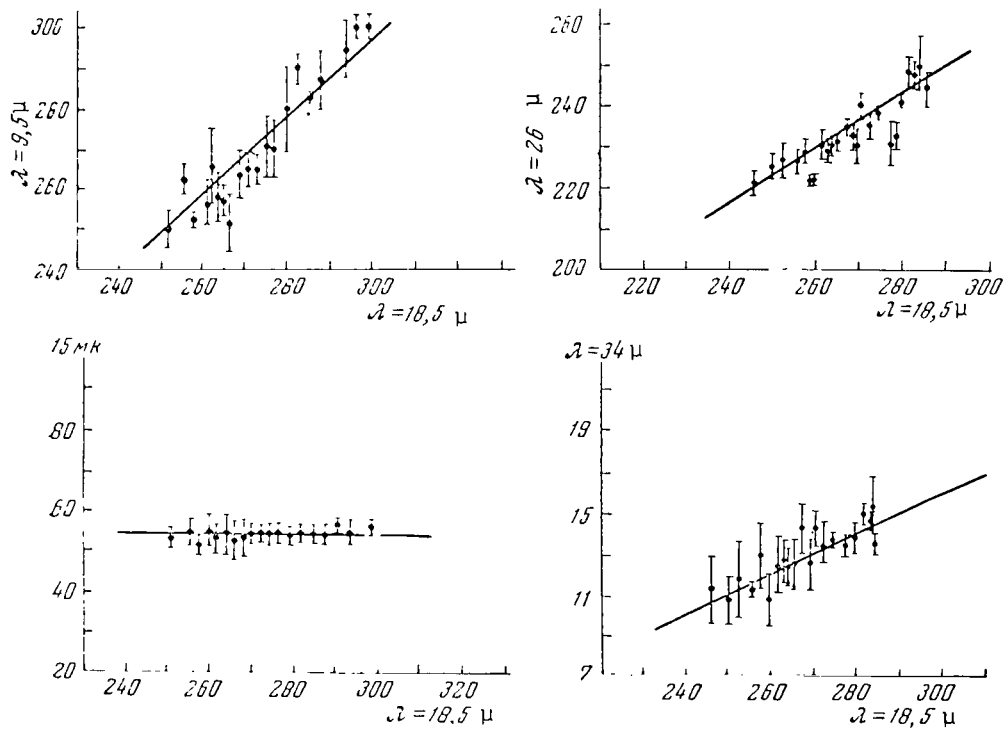


Figure 12

Correlative Dependences Between Radiation at Diverse Wavelengths

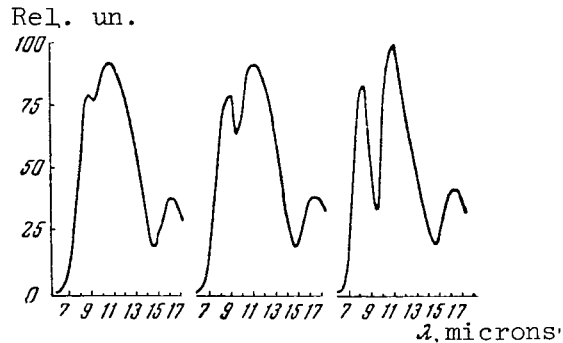


Figure 13

### Examples of Differing Intensity of Ozone Band at 9.6 $\mu$

presents examples of three spectral traces of this band at differing depths - all recorded in 10 min near a latitude of  $65^\circ$ . The actual depth of the ozone band must be even deeper, since the instrument which conducted the measurements had an effective resolving power of about 1.2  $\mu$ , which was substantially wider than the ozone band.

The latitudinal dependence of the relative depth of the ozone absorption lines was likewise plotted. The relative depth of these lines has been defined as the ratio  $\Delta h/h$ , where  $h = (h_1 + h_2)/2$ ,  $h_1$  is the height of the spectrum when  $\lambda = 8.5 \mu$ ;  $h_2$  is this height when  $\lambda = 11 \mu$ ;  $\Delta h = h - h_3$ , where  $h_3$  is spectrum height with  $\lambda = 9.6 \mu$ . Figure 14 presents this latitudinal dependence. As is evident from the figure, the amount of ozone in the atmosphere at high latitudes in September exceeds that in the equatorial region. The variations in absorption-band depth from place to place are clearly evident. /77

It has already been repeatedly observed that there are two components which absorb longwave radiation in the 14-15  $\mu$  region: The very strong carbon-dioxide absorption band from 12.9 to 17.1  $\mu$ , centered at  $\lambda = 14.7 \mu$ , and the ozone absorption band from 12.5 to 15.5  $\mu$ , centered at  $\lambda = 14.1 \mu$ . This ozone absorption band is often left out of consideration because it coincides with the very strong  $\text{CO}_2$  band. However, since the ozone absorption-band at 14.1  $\mu$  may be rather strong, as follows from examining the absorption band at 9.6  $\mu$ , the contribution made by ozone to the observed 14.5  $\mu$  band may be substantial.

When explaining the exceptionally high intensities of the carbon-dioxide and ozone absorption-bands, we should probably bear the fact in mind that, just as in stellar atmospheres, scattering in the rarefied layers above the region of local thermodynamic equilibrium may play an essential role in the formation of absorption lines in the Earth's atmosphere.

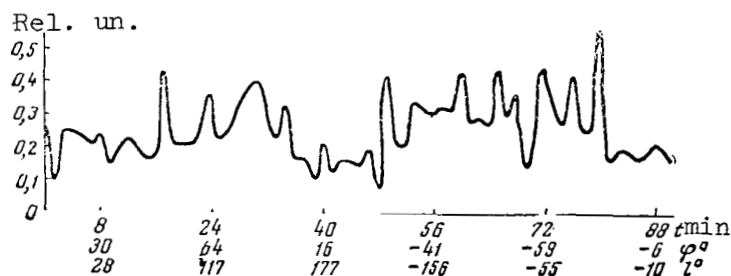


Figure 14

Latitudinal Dependence of, and Local Fluctuations in,  
Ozone Absorption Band at  $9.6 \mu$

The authors express their profound gratitude to G. I. Golubeva, Professor Ye. N. Tsarevskiy, F. M. Gerasimov, and N. G. Yaroslavskiy, who rendered repeated assistance with their valuable counsel in discussing the fundamental scientific principles of the present experiment.

#### REFERENCES

1. Astheimer, R. W., De Waard, R., Jackson, E. A. J. Opt. Soc. Amer., 5, No. 12, 1961.
2. Bandeen, W. R., Hanel, R. A., Licht, J., Stampfl, R. A., Sroond, W. G. J. Geophys. Res., 66, No. 10, 1961.
3. Bandeen, W. R., Hanel, R. A. Some Results From Tiros II. Sympos. on Radiation. Vienna, 1961.
4. Nordberg, W., Bandeen, W. R., Conrath, B. J., Kunde, V., Persano, J. J. Atmos. Sci., 19, No. 1, 1962.
5. Kondrat'yev, K. Ya. Weather Satellites (Meteorologicheskiye sputniki). Gidrometeoizdat, Leningrad, 1963.
6. Bandeen, W. R., Nordberg, W., McCulloch. Trans Amer. Geophys. Union 44, 875, 1963.
7. Erickson, C. Science, 143, No. 3606, 612, 1964.
8. Markov, M. N., Merson, Ya. I., Shamiliev, M. R. Kosmicheskiye Issledovaniya, 1, No. 2, 235, 1963; 3, No. 2, 268, 1965.

9. Block, L. C., Zachor, A. S. Appl. Opt., 3, 209, 1964.
10. Lebedinskiy, A. I., Krasnopol'skiy, V. A., Kuznetsov, A. P., Iozenas, V. A. Present collection, p. 77.
11. Yakovlev, E. A., Gerasimov, F. M. Optika i Spektroskopiya, 10, 104, 1961.

## INVESTIGATING THE EARTH'S ATMOSPHERIC RADIATION IN THE VISIBLE AND ULTRAVIOLET REGIONS

A. I. Lebedinskiy, V. A. Krasnopol'skiy,  
A. P. Kuznetsov, and V. A. Iozenas

The artificial Earth satellite "Kosmos-45" measured night airglow and scattered solar ultraviolet radiation. The satellite's orbit was inclined  $65^\circ$  to the equatorial plane; the experiment was conducted in September, 1964. An ultraviolet spectrophotometer, which was turned on only on the day side of the Earth, was used to register the scattered ultraviolet radiation. A colorimeter, operating only on the night side of the Earth, was employed to measure the night airglow. The instruments /78 were commutated on and the underlying surface checked by a recorder measuring illumination at wavelengths of  $0.6-0.85 \mu$ . The optical axes of the instruments were pointed at the nadir.

### Measurement Equipment

The ultraviolet spectrophotometer (Figure 1) is a double monochromator operating in the  $2250-3100 \text{ \AA}$  region. Light coming through the quartz window and condensing lens arrives at the spectrophotometer inlet slit and proceeds on to a concave diffraction grid (600 lines per mm) with a focal length of 125 mm. The diffraction grid lines are oriented for first-order dextrorotary reflection of the maximum amount of light at the wavelengths around  $2500 \text{ \AA}$ . A spectrum with a dispersion of  $67 \text{ \AA/mm}$  is received at the image plane of the inlet slit, where there is a moveable outlet slit which separates a narrow band of wavelengths from the spectrum. The output slit is moved by a step-type motor which is turned on by multi-vibrator pulses through a relay. In 150 steps the slit moves from the longwave to the extremely shortwave position, after which it returns to its original position. This cycle for recording one spectrum lasts about 30 sec.

After the outlet slit, the light passes through a lens which converts the diverging beam into a parallel one, which falls on a flat diffraction grid having  $2400 \text{ line/mm}$ . The linear dispersion of the monochromator with the flat diffraction grid is equal in magnitude to that of the concave grid and opposite to it in sign. Thus, regardless of wavelength, the light hits the same spot on the photomultiplier photocathode. /79

Double monochromatization is employed because of the need for maximum reduction of scattered light. For the same purpose, the spectrophotometer components are blackened, and the different parts of the optical system are photoinsulated from each other as much as possible.

The light flux is modulated at a frequency of 600 cps by a shutter situated immediately behind the quartz inlet window. Modulation frequency stability is about 1%.

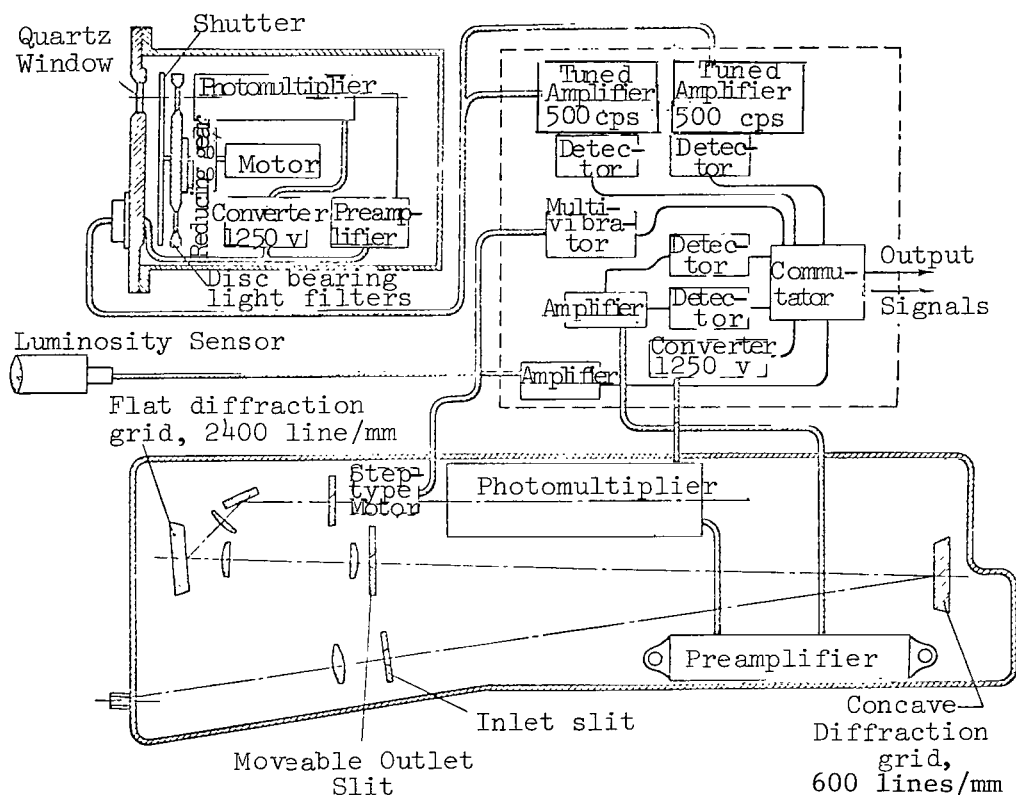


Figure 1

### Block Diagram of Equipment

The photomultiplier with an antimony-cesium photocathode on quartz had an amplification of around  $10^7$  and was fed from a converter giving a stabilized voltage of 1250 v. The photomultiplier output signal was amplified by a preamplifier with a tuned frequency of 600 cps and pass-band of 30 cps. It then went to the main amplifier and detector. The rectified signal was recorded. The preamplifier is situated within the optical unit of the spectrophotometer; a separate unit contains the main

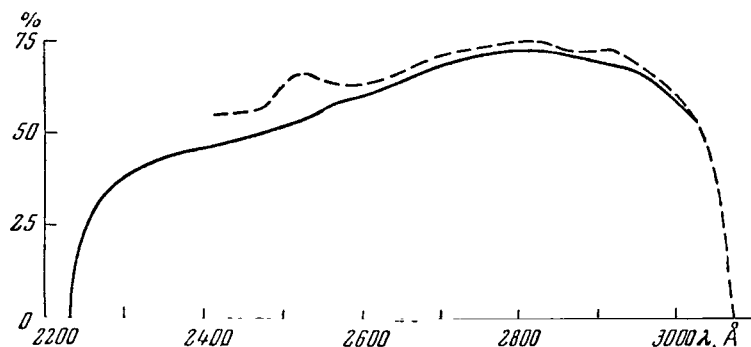


Figure 2

Dependence of Ultraviolet Spectrophotometer Sensitivity on Wavelength According to Data From Calibration Measurements with S18-200 Incandescent Lamp and DVS-25 Hydrogen Lamp

amplifier, detector, voltage converter, multivibrator, step-type starting motor, as well as the units ensuring instrument commutation and operation of colorimeter and luminosity sensor.

Instrument resolution was  $15 \text{ \AA}$  - the  $2393.5$  and  $2379 \text{ \AA}$  lines of the mercury spectrum were resolved by the instrument at the limit.

The visual field of the instrument covers an area of  $20 \text{ km}$ . The instrument was calibrated by mercury-spectrum wavelengths, and for sensitivity by means of the spectrum of a hydrogen lamp and a standard ribbon-filament incandescent lamp. The spectrum of the ribbon-filament incandescent lamp, in turn, was calibrated by a black body with 5% accuracy to  $2450 \text{ \AA}$ . For the hydrogen lamp the average spectrum for this type of lamp was used. Figure 2 shows the instrument sensitivity obtained by calibration as a function of wavelength. The agreement between results in calibrating the hydrogen and the ribbon-filament lamp was quite satisfactory.

A photoresistor of cadmium selenide situated at some distance from a lens of KS-10 glass acts as the luminosity sensor. The sensor's areal field of vision is  $25 \text{ km}$ . The KS-10 glass cuts off radiation of wavelength shorter than  $0.6 \mu$ , thus eliminating the effect of light scattered by the atmosphere. The infrared sensitivity-boundary of cadmium selenide is about  $0.85 \mu$ ; hence the luminosity sensor is a photometer in the  $0.6\text{-}0.85 \mu$  region. The sensor was calibrated by sunlight reflected from

a magnesium oxide screen. Neutral light filters were used for the calibration. Figure 3 gives the dependence of sensor readings on screen brightness. Sensor nonlinearity in low fluxes was caused by photoresistor nonlinearity; nonlinearity in large fluxes was created by the electric circuit for extending the range of sensor operation in high degrees of illumination.

The colorimeter (Figure 1) for measuring night airglow had a shutter and a disc with light filters arranged along one axis. The shutter modulated the light flux with a frequency of  $500 \pm 10$  cps. The disc with the light filters was rotated once in 12.5 sec through a reducer by the same motor which rotated the shutter. Directly behind the disc were two photomultipliers of the same type as the ultraviolet-spectrophotometer photomultiplier. Each photomultiplier had its own amplifying circuit. The sensitivities of these circuits differed by factors of approximately 30. The optical unit of the colorimeter also contained a converter (for powering the photomultipliers), input amplifiers, and noise-suppressing filters for eliminating motor-effect on the sensitive input circuits. The main amplifiers were located in an electronic unit. They had a resonance frequency of 500 cps and passband of 40 cps. The electrical units of the colorimeter did not essentially differ from analogous ones in the ultraviolet spectrophotometer. The areal field of vision of the colorimeter was 120 km.

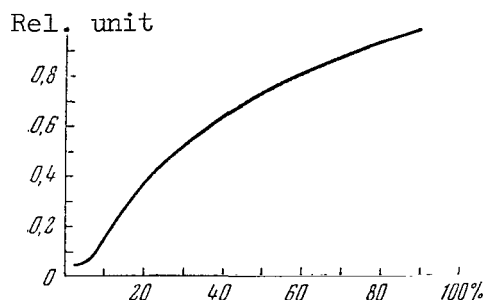


Figure 3

Dependence of Luminosity Sensor Readings on Screen  
Brightness (100% corresponds to a brightness of 3.0 stilbs)

Figure 4 gives the light-filter transmission curves. Light filter ZhS-4 cuts off ultraviolet radiation. On the longwave side the region separated out by this light filter is delimited by the longwave boundary of the antimony-cesium photocathode around 6000 Å. Light filter UFS-1 makes it possible to measure radiation in the 2500-4000 Å wavelength range. Two narrow-band light filters segregate emissions at 5577 and 3914 Å. The passbands of the narrow-band light filters are about 100 Å wide. An SFD-2



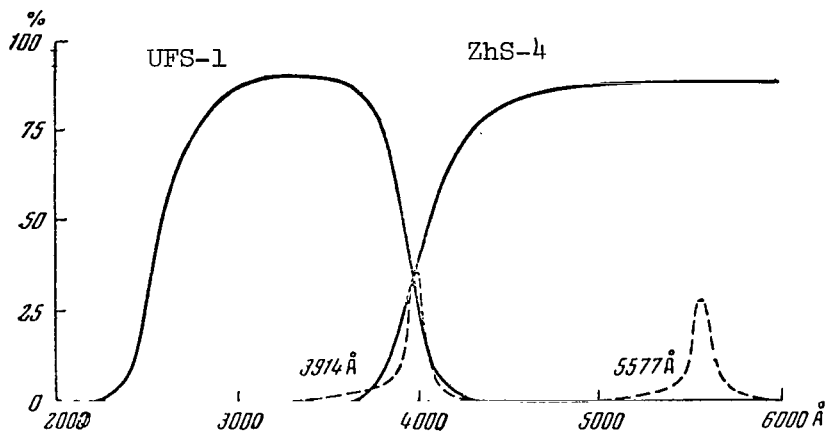


Figure 4  
Colorimeter Filter Transmission Curves

spectrophotometer was used to measure the light-filter transmission curves.

One of the five apertures for light filters in the disc is left open. <sup>/81</sup> The radiation arriving at the photomultiplier through this aperture is limited on the shortwave side by the quartz illuminator transmission. The engineering standards for the quartz set in this illuminator correspond to transmission no poorer than 20-40% for 1650 Å radiation.

Colorimeter calibration was accomplished by means of the same ribbon-filament lamp used to calibrate the ultraviolet spectrophotometer. A diaphragm 1.03 mm in diameter and a set of neutral light filters were employed to reduce the flux when calibrating effective instrument sensitivity with ZhS-4 and 5577 Å light filters. As a result of this calibration the instrument factor was determined in absolute units for radiation in the visible spectrum, which makes it possible to calculate instrument sensitivity for ultraviolet light-filters by means of the photomultiplier spectral-sensitivity curve and the light-filter transmission curves. This was also the means for determining instrument sensitivity in the absence of a light filter and for light filters 3914 Å and UFS-1. When instrument sensitivity with narrow-band light filters was determined, corrections were introduced for the dependence of the transmissivity of these filters on the incident angle of the light ray.

## Experimental Results

Figure 5 gives the typical aspect of an atmospheric spectrum recorded by the ultraviolet spectrophotometer. The ultraviolet spectrum of the Sun obtained by Rense (Ref. 1) by rocket on August 6, 1957 is also shown. The structure of both spectra is similar, but intensity decrease in the atmospheric spectrum as wavelength becomes shorter is substantially steeper than in the solar spectrum. This is caused by rising ozone absorption.

The computed spectra in (Ref. 2), in contrast to those observed, take a smoother course because a solar spectrum with the low resolution of  $\Delta\lambda = 50 \text{ \AA}$  (this spectrum was given, for example in [Ref. 3]) was used in this computation.

The spectrum depends on the zenith distance of the Sun. When the satellite was at different latitudes, the zenith distances of the Sun also varied. Therefore, this correlation involves not only an increase in the length of the solar ray's path through the absorptive ozone layer, but also the latitude dependence of the characteristics of this layer.

There also is a correlation between ultraviolet spectrophotometer readings and those of an infrared spectrophotometer in the  $9.65 \mu$  ozone band. An infrared spectrophotometer was part of the equipment aboard "Kosmos-45", and recorded thermal spectra of the atmosphere during the whole operating period of the ultraviolet spectrophotometer and the colorimeter (Ref. 4). The results obtained by the ultraviolet and infrared spectrophotometers may serve for mutual checks in evaluations of the ozone-layer characteristics.

A correlation between intensities near the longwave boundary of the ultraviolet spectrum at  $\lambda > 3000 \text{ \AA}$  and luminosity-sensor readings was detected. These readings depend greatly on cloudiness, since cloud albedo in the red region is substantially greater than that of the Earth's surface or of pure atmosphere. Therefore, the luminosity sensor does not give a bad estimate of cloudiness in the region measured. This correlation indicates that an appreciable part of atmospheric radiation is due to tropospheric scattering processes and reflection below the main ozone-layer mass when  $\lambda > 3000 \text{ \AA}$ .

A significant part of the data derived by the colorimeter is distorted by lunar illumination. The Moon's effect is particularly noticeable in wide-band light filters; the readings with the  $5577 \text{ \AA}$  light filter, on the contrary, do not essentially change their character when lunar illumination is not too strong. Figure 6 and 7 give instrument readings in revolutions covering regions of the Earth's surface and of the troposphere unilluminated by the moon (lunar zenith distance greater than  $92.5^\circ$ ). In these regions the strength of the Moon's light was on

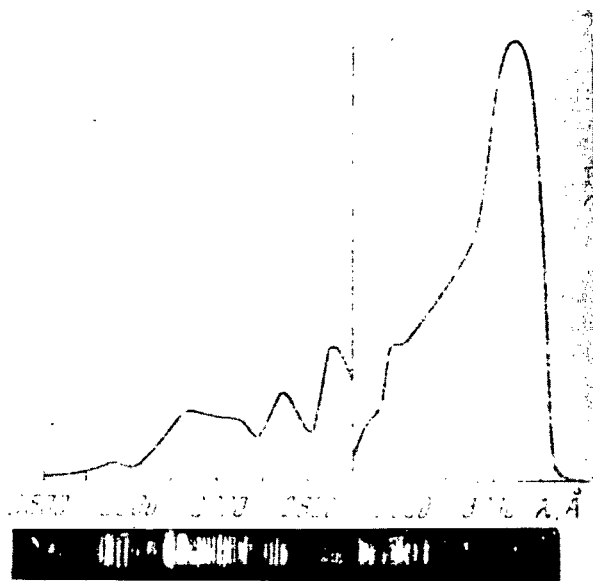


Figure 5

Typical Atmospheric Spectrum Recorded by  
Ultraviolet Spectrophotometer

Readings to the right and left of 2850 Å refer to different scales of instrument sensitivity (sensitivity ratio 1:3). Below is given the solar spectrum obtained by Rense in 1957 (Ref. 1).

the order of 5% of the night airglow in the visible part of the spectrum. In the moonless regions, the geomagnetic latitude is entered along the abscissa axis. The abscissa axis additionally indicates the local time at the point of measurement. Instrument readings during a completely moonlit revolution are given for purposes of comparison.

Artificial sources of light could exert no significant effect, since the moonless regions were in the Southwest Pacific Ocean and over the Indian Ocean. The results discussed below were obtained when processing the part of the material which was not influenced by the Moon.

In Figures 6 and 7 the reading 100 corresponds to a terrestrial atmospheric brightness of

$$9.2 \cdot 10^7 \text{ quantum} \cdot \text{cm}^{-2} \cdot \text{sec}^{-1} \cdot \text{sterad}^{-1} \text{ for filter } 5577 \text{ Å},$$

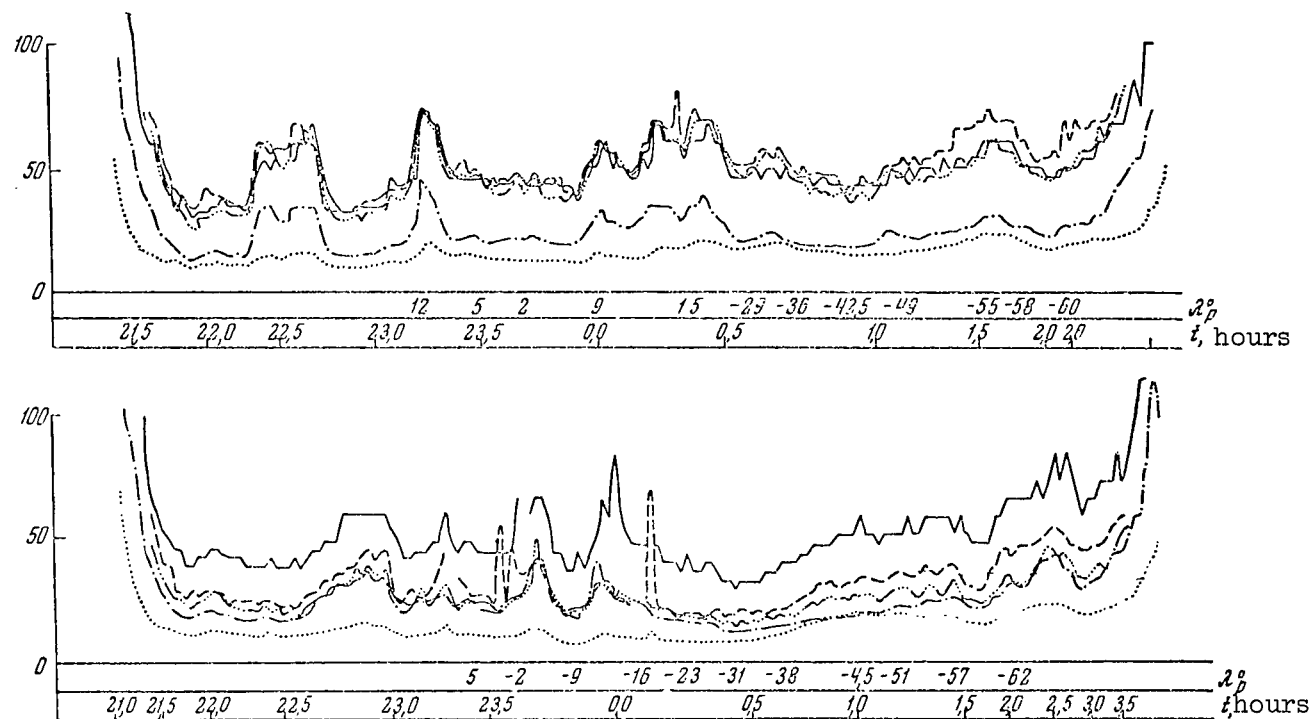


Figure 6

Colorimeter Readings on Several Revolutions

1 - Quartz window, 2 - ZnS-4, 3 - UFS-1, 4 - 3914 Å, 5 - 5577 Å. On the last revolution the Moon was 2-3° above the horizon.

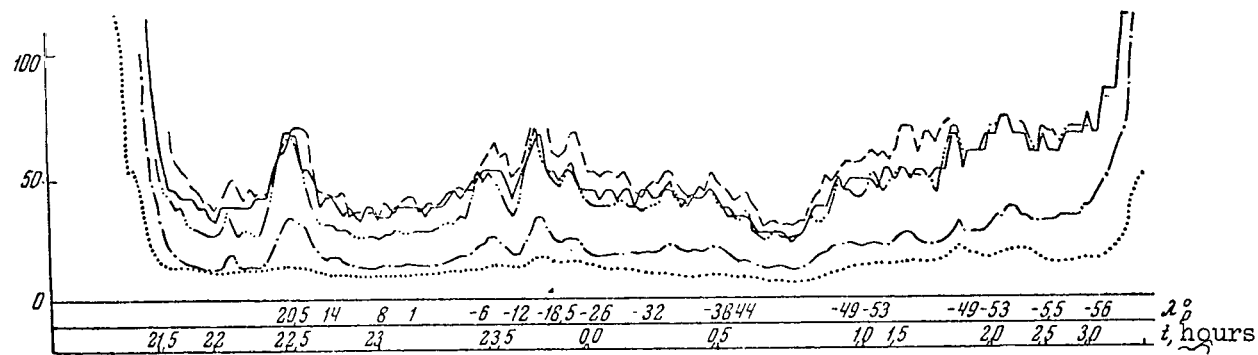
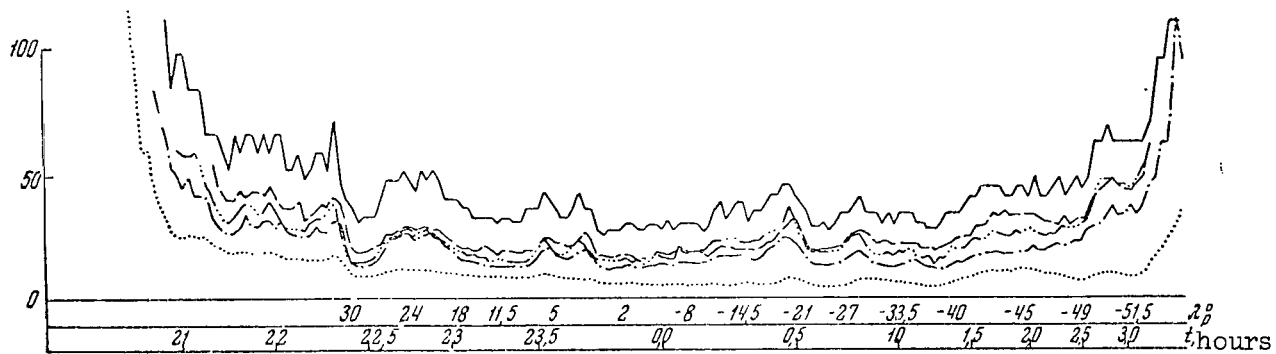
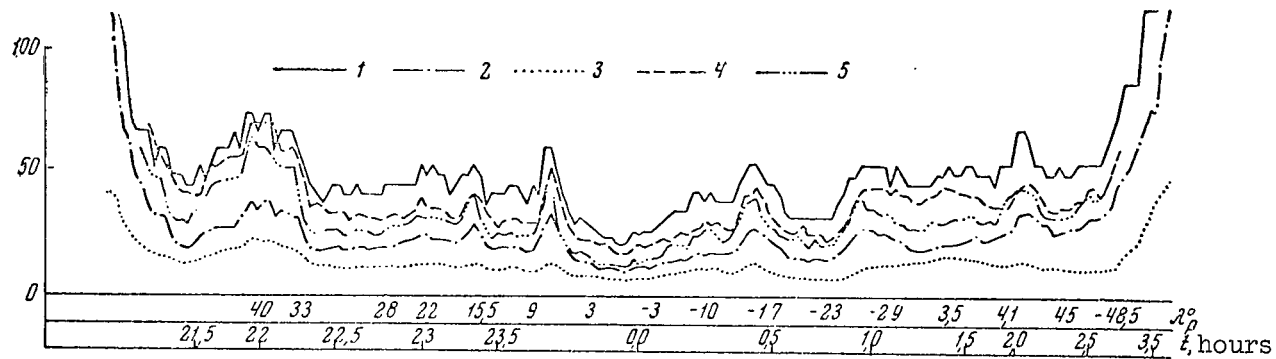


Figure 6 (Cont'd)

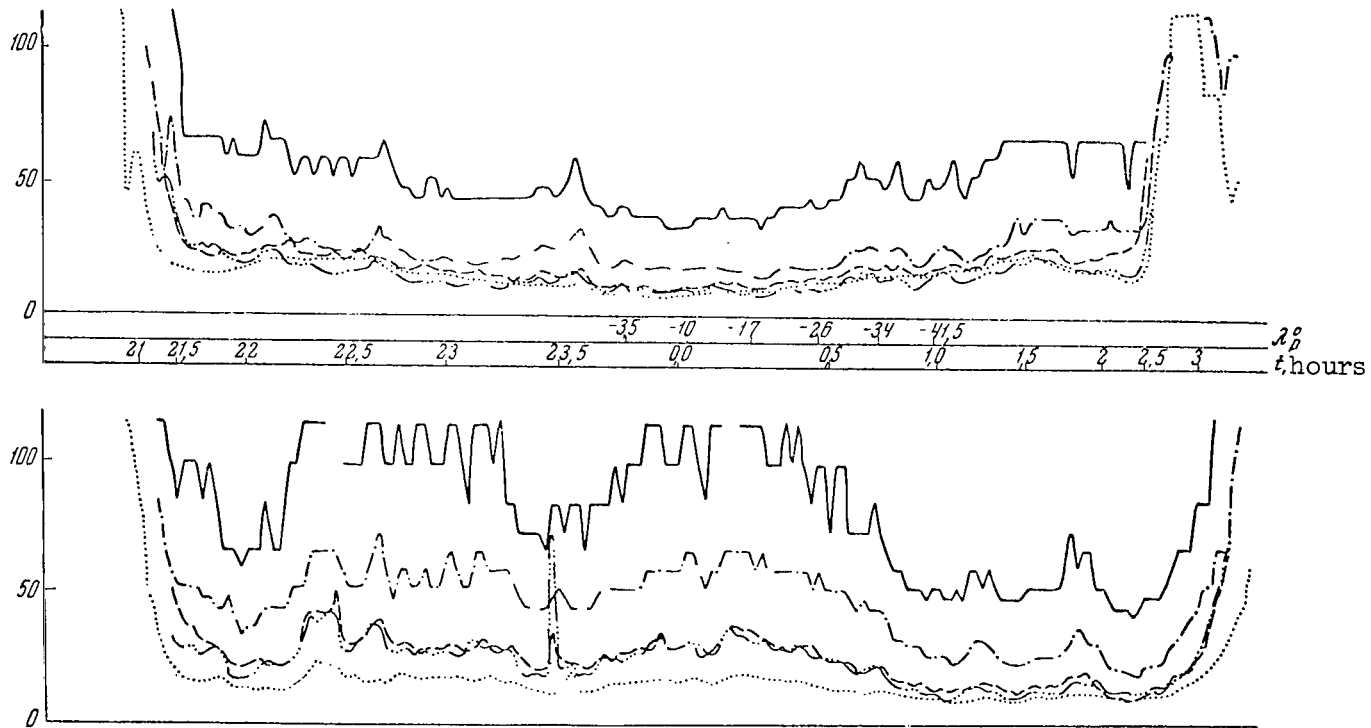


Figure 7

Colorimeter Readings on Several Revolutions

Notation is the same as in Figure 6.

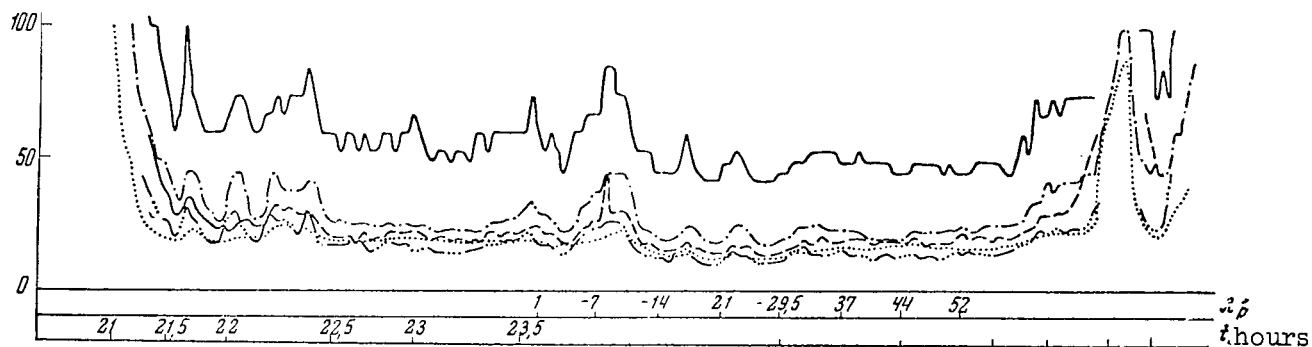
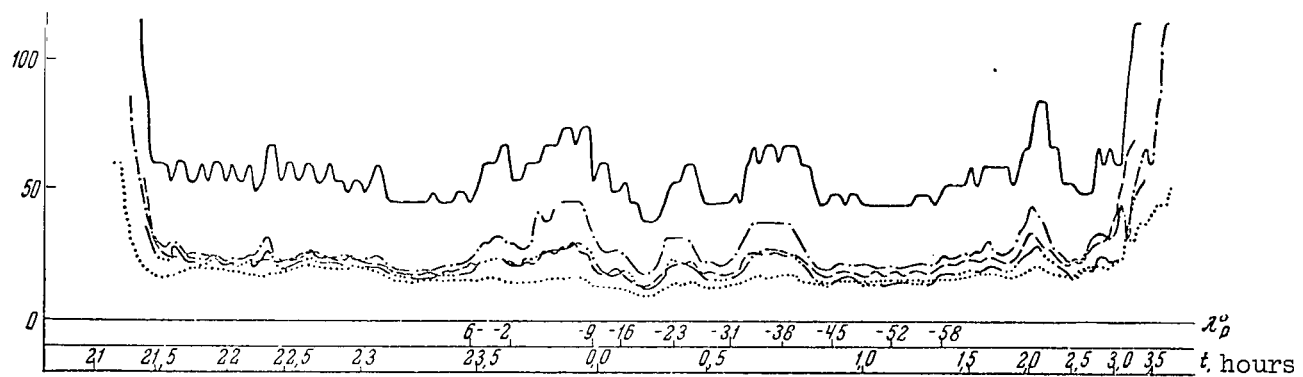


Figure 7 (Cont'd)

	$1.5 \cdot 10^7$	quantum	$\cdot \text{cm}^{-2}$	$\cdot \text{sec}^{-1}$	$\cdot \text{sterad}^{-1}$	for filter 3914 Å,
	$3.2 \cdot 10^8$	"	"	"	"	UFS-1, and
about	$6.5 \cdot 10^8$	"	"	"	"	ZhS-1.

Photomultiplier sensitivity in the visible region is highly dependent on quanta energy; therefore, the absolute value for filter ZhS-1 depends on the spectral distribution of radiation energy. The value of  $6.5 \cdot 10^8$  quantum  $\cdot \text{cm}^{-2} \cdot \text{sec}^{-1} \cdot \text{sterad}^{-1}$  for filter ZhS-1 was derived by computation for a uniform spectrum of radiation energy.

The correlation between readings taken with different light filters is very apparent. Cases of correlation disturbance are comparatively rare, and may therefore also be interesting (we can see, for example, a correlation disturbance in the first revolution at  $35^\circ$  south geomagnetic latitude as a certain decrease in the readings of all light filters accompanied by an increase in readings with filter UFS-1).

It would be interesting to draw a conclusion as to local, daily, and /83 latitudinal fluctuations in night airglow. The daily and latitudinal fluctuations are mutually related in observations from the satellite; only the difference in geographic and geomagnetic latitudes makes it possible to distinguish them. The chief difficulty in fluctuation analysis, however, is the dependence of the readings on cloudiness. Observations from the ground measure night airglow plus luminescence of astronomical origin (stellar and zodiacal light); both types of luminescence are somewhat reduced because of dispersion and reflection by the atmosphere. The state of the atmosphere has little effect on the result, for measurements are ordinarily made on clear nights.

Observations from space measure night airglow plus night airglow and luminescence of atmospheric origin reflected from the atmosphere. Consequently, depending on the state of the atmosphere, the result may vary by a factor of almost two, being at a minimum in cloudless weather and at a maximum during a complete overcast.

Albedo of the cloudless terrestrial atmosphere should be greatest in the near ultraviolet in the 3300 Å region, because ozone absorption here is relatively small and Rayleigh scattering is large. Therefore, variations in cloudiness should provoke the smallest changes in readings in the near ultraviolet. This is exactly what is observed - the UFS-1 readings are the least subject to fluctuation.

The attempt to utilize weather data to reconstruct the cloudiness picture gives limited results, because there are few weather stations in the Pacific and Indian Oceans. Great possibilities lie in the dependence of infrared spectrophotometer readings on cloudiness: cloud temperature is lower than that of the Earth's surface. Therefore, infrared spectrophotometer readings are lower over clouds. The correlation is particularly clear in the atmospheric transmittance window at 8-12  $\mu$ .



The climatological charts in (Ref. 5) may be used to determine average cloudiness in September for different regions.

Although the actual cloudiness at a specific point at the moment of measurement may differ significantly from the average, the average values over sufficiently large territories should be of adequate accuracy. Such averaging for mean cloudiness in September gives a result of approximately 0.5.

If we adopt an average cloud albedo of 0.75 regardless of wavelength, the average atmospheric albedo is 0.5 for the near ultraviolet and 0.4 for radiation in the visible region. The average intensity values given below were derived by dividing the result of averaging the curves in Figures 6 and 7 by unity, plus average atmospheric albedo. The maximum and minimum values were obtained by dividing the maximum and minimum readings by unity plus cloud albedo or clear atmosphere albedo, respectively. In this conversion the average intensity of the 5577 Å line measured by the instrument is 250 Rayleigh; maximum intensity, 430 Rayleigh; and minimum, 125 Rayleigh. These figures are in good agreement with the results of terrestrial observations. The 5577 Å emission line of the nocturnal sky is strongest in the visible region. Therefore, the contribution made by light from extraterrestrial sources to intensity measurements of this emission is small. Correlation of the readings from all the other light filters with those of the 5577 Å filter indicates that the portion of illumination from stars and zodiacal light is comparatively small in the instrument readings for the remaining light filters. In this respect, satellite measurements have advantages over ground measurements. Let us assume that the contribution made by light of astronomical origin to nocturnal light is 50% in ground observations; then in measurements from space this contribution will be 30% during complete overcast, about 20% in average cloudiness, and around 5% in cloudless weather.

The ratio of colorimeter readings with light filter 3914 Å to those with filter 5577 Å was very stable; its maximum deviation was no more than 20% of its average value. The interpretation of these readings is not unique; they may be attributed both to 3914 Å emission (in which case its average intensity is 45 Rayleigh) and to the pseudo-continuum (when its average intensity is 0.2 Rayleigh/Å). /88

Average radiation intensity in the 4000-6000 Å range (without deducting the 5577 Å line) was 1200 Rayleigh, with a lowest value of 750 Rayleigh and a highest value of 1800 Rayleigh. Thus, the readings with filters 3914 Å and ZhS-4 are less than might be expected from terrestrial measurements (Ref. 6-9). The difference may be principally due to the large portion of luminescence of astronomical origin in observations from the Earth and, in part, to measuremental errors.

Average intensity with light filter UFS-1 was 400 Rayleigh - minimum, 200 Rayleigh; maximum, 500 Rayleigh. The correlation between readings with this light filter and those with the other filters is looser, and there are

cases of correlation breakdown. Intensities corrected for atmospheric reflection would obviously be correlated even more loosely.

From the congruence of the average UFS-1 filter reading with the results of ground observations in the 3200-4000 Å range (Ref. 10-12), the inference may be drawn that radiation of the nocturnal sky in the 2500-3200 Å is small and does not exceed stellar luminescence and zodiacal light in the 3200-4000 Å region.

Atmospheric radiation in the 1700-2500 Å region may be derived from the difference between readings from the quartz window and filters ZhS-4 and UFS-1. This difference is very small. To increase its accuracy, an average was taken of the readings from 50 points where the readings were smallest and did not leave the region of essential instrumental nonlinearity. The accuracy of the readings at these points was comparatively high. In addition, the average difference for all other points in moonless regions was calculated. The result proved to be identical - in the 1700-2500 Å region there is no radiation from the nocturnal sky. The average difference was 5-10 Rayleigh. To be sure, since the transmission curves of filters UFS-1 and ZhS-4 are not rectangular, a systematic error could have occurred during subtraction. Nevertheless, it is very improbable that radiation intensity of the nocturnal sky exceeds 30 Rayleigh in the 1700-2500 Å region. Thus, the results of measurements in the 1700-2500 and 2500-4000 Å region corroborate the absence of high-energy excitation processes in the nocturnal sky.

The authors deem it their pleasant duty to express their sincere gratitude to A. K. Men'kov and Ye. N. Gerasimov for developing the optical mechanical units of the instruments, as well as to F. M. Gerasimov and I. V. Peysakhson for assistance in solving the basic problems of the optical system.

#### REFERENCES

1. Rense, W. A. Sky and Telescope, 17, No. 10, 1958.
2. Green, A. E. S. Appl. Opt., 3, No. 2, 1964.
3. Nicolet, M. Aeronomy.
4. Lebedinskiy, A. I., Glovatskiy, D. N., Tulupov, V. I., Khlopov, B. V., Fomichev, A. A., and Shuster, G. I. Present collection, p. 65.
5. Climatological and Oceanographic Atlas for Mariners. Washington, 1961.
6. Barbier, D. Ann. Astrophys., 17, 1954.
7. Barbier, D., Dufay, F., Williams, D. Ann. Astrophys., 14, 1951.

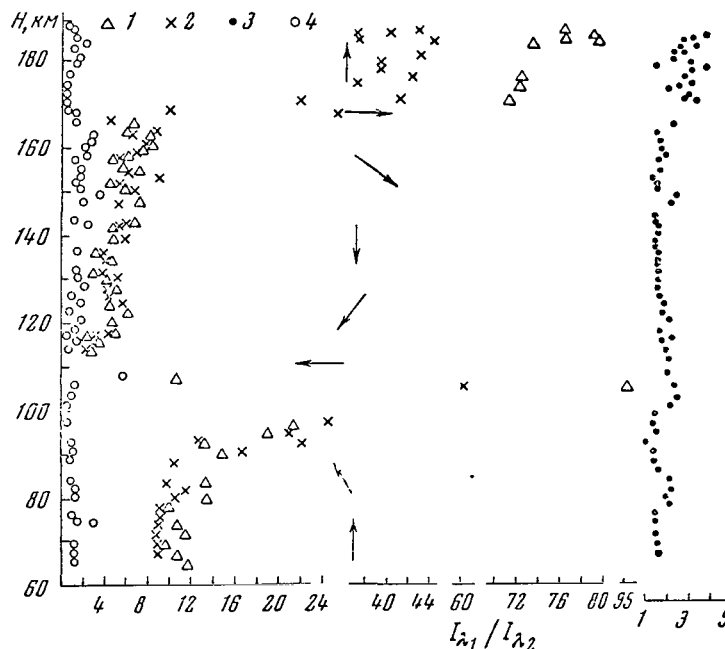
8. Chuvayev, K. K. Doklady Akademii Nauk SSSR (DAN SSSR), 87, No. 4, 1952.
9. Shefov, N. N. In: Spectral, Electrophotometric, and Radar Studies of the Aurorae Polaris and Night Airglow (Spektral'nyye, elektrofotometricheskiye i radiolokatsionnyye issledovaniya polyarnykh siyaniy i svecheniya nochnogo neba). No. 1. "International Geophysical Year Results" series (Seriya "Resul'taty MGG"), 1959.
10. Barbier, D. Comptes-rendus de l'Academie Francaise (C. R.), 238, 1954.
11. Barbier, D. "Preliminary Results of Eight-Color Photometry of the Night Airglow", "Resultats Préliminaires d'une Photométrie en Huit Couleurs de la Lumière du Ciel Nocturne". In "The Airglow and the Aurorae". London, Pergamon Press, 1956.
12. Rodionov, S. F., and Pavlova, Ye. N. Doklady Akademii Nauk SSSR, 79, No. 6, 1951.

# EIGEN RADIATION OF THE ATMOSPHERE

## (Summary)

T. M. Tarasova

The luminescence regions of several atmospheric components - /89  
hydroxyl, atomic and molecular oxygen, and other emissions (Ref. 1-4) -  
were determined by vertical rocket soundings. Data recorded during the  
rotation of the rocket photometer made it possible to study the lumines-  
cence distribution at levels above the ceiling of the photometer ascent.  
Thus, an analysis of material at the 6300 Å line for altitudes less than  
200 km assisted the author in reaching a preliminary conclusion regarding  
the luminescence distribution of the red oxygen line up to altitudes of  
1000 km (Ref. 5): Atomic oxygen luminescence was distributed over a  
large atmospheric thickness from 100-1000 km. This article investigates  
the behavior of sodium emission from material obtained in 1960 by means  
of a rocket photometer. The altitudinal range was 65-200 km, where the  
photometer completed a total 360° revolution (in the vertical plane) in



Dependence on Altitude of Emission Intensity Ratios  
Which are Free of Background and Hydroxyl Bands

1 -  $I_{5893}/I_{OH}$ ; 2 -  $I_{5893}/I_{8645}$ ; 3 -  $I_{5577}/I_{8645}$ ; 4 -  
 $I_{5893}/I_{6300}$ .

Arrows indicate photometer axis direction.

addition to its ascent.

According to data in (Ref. 2, 3), sodium luminescence is localized in a layer at an altitude of 85 km. The luminescence distribution of hydroxyl, molecular and atomic oxygen (5577 Å) has a stratified structure. It can be seen from the figure that there is a spatial correlation between the OH, O and O<sub>2</sub> emissions: For the 5577 and 8645 Å emissions, the ratio is almost constant when the radiation intensity of each of the emissions changes by a factor of 14-25.

The ratios  $I_{5577}/I_{OH}$  and  $I_{8645}/I_{OH}$  are also constant, which points to a similar spatial luminescence distribution of 5577, 8645 Å and hydroxyl: The radiation of all three emissions is concentrated in the form of layers at altitudes of 70-110 km.

According to (Ref. 2, 3), sodium radiation must also display a good 90 spatial correlation with these emissions.

However, the ratios  $I_{5893}/I_{OH}$ ,  $I_{5893}/I_{8645}$  (see the figure) and  $I_{5893}/I_{5577}$  do not remain constant when the equipment axis changes in space, and have a clearly expressed altitudinal dependence. This indicates that sodium luminescence is distributed in the upper atmosphere according to a law which differs essentially from the stratified structure of the 5577, 8645 Å and hydroxyl emissions.

There is no spatial correlation between the radiation of 6300 Å and the 5577, 8645 Å and OH emissions, which agrees with the data obtained previously (Ref. 5).

A comparison of sodium and atomic oxygen radiations at 6300 Å reveals an unexpected close spatial correlation: The ratio of the total light fluxes measured with filters with  $\lambda_{max} = 5893$  Å and  $\lambda_{max} = 6300$  Å, just like the intensity ratio of the  $I_{5893}/I_{6300}$  emissions, remains constant both in the ascending branch of the rocket trajectory (see the figure) and in the descending branch. It can thus be concluded that the laws governing the altitudinal luminescence distribution for sodium and atomic oxygen (6300 Å) are the same.

The discovery of a significant portion of sodium luminescence (~ 30%) at high altitudes makes it imperative that the existing concepts regarding the agent exciting sodium atoms be reexamined.

#### REFERENCES

1. Tarasova, T. M. Space Res., 3 (Washington, May 2-8, 1962), p. 162.
2. Heppner, J. P., Meredith, L. G. J. Geophys. Res., 63, 51, 1958.
3. Kumen, M. D., Skolnik, R., Tusi, R. In "On the Threshold to the Cosmos" II, 1960.
4. Tarasova, T. M. Astronomicheskii Tsirkulyar, No. 222, 31, 1961.
5. Tarasova, T. M. Space Res., 4 (Warsaw, June 4-10, 1963), Part II, p. 235.

# STUDY OF THE ANGULAR RADIATION DISTRIBUTION OF THE EARTH AND THE EARTH'S ATMOSPHERE FROM GEOPHYSICAL ROCKETS AND BALLOONS

M. N. Markov, Ya. I. Merson, M. R. Shamilev

Computations of the field of infrared radiation leaving the Earth coincide only approximately with reality, and therefore it is very important to obtain experimental data.

Beginning in 1958, we performed systematic studies of the infrared radiation of the planet. For this purpose, rocket and balloon equipment was constructed, and the angular radiation distribution of the Earth was measured in the 0.8-40 micron spectral region in rockets from altitudes of 100-500 km, and simultaneously from geophysical balloons from altitudes of up to 30 km.

During the experiments, the scanning apparatus was oriented in space along three axes with respect to the Earth, which was necessary in order to obtain the angular distribution.

Following are the main parameters of the apparatus: Scanning angle  $2\pi$ ; angular resolving power  $2 \cdot 10^{-3}$  rad; sensitivity threshold  $10^{-8}$ - $10^{-9}$  w.

The readings were recorded by independent systems and telemetry.

/91

Cloudiness Conditions	Computational Data w/m <sup>2</sup>		Experiment, w/m <sup>2</sup>			
	Simpson	Kondrat'yev and Filippovich	1958	1958	1962	1963
No clouds	220	--	90	--	--	--
Average Cloudiness	210	190	--	70	250	255 - 296

The rockets and balloons were launched during different times of the year, different times of the day, and under different geographical conditions within the Soviet Union. There were about 50 equipment launchings in all. Figure 1 shows the manner in which the experiment was performed. The results obtained up to the present time enable us to compile the properties of the radiating Earth-atmosphere system.

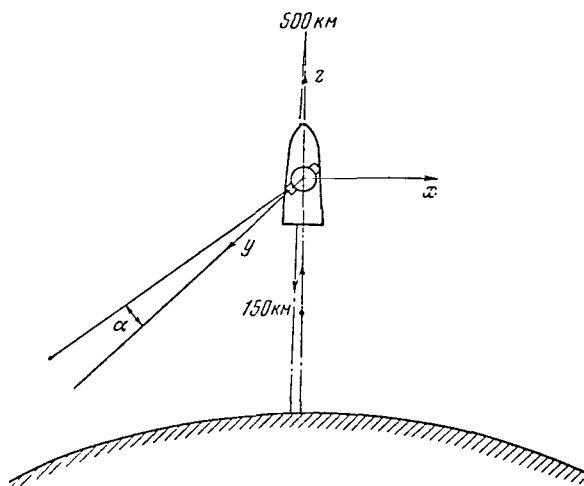


Figure 1

### Schematic Drawing of Experiment

1. Existing methods of computing the mean magnitude of radiation leaving the Earth (radiation at the zenith) enable us to determine this magnitude with sufficient accuracy. The table presents the results derived from calculating the outgoing radiation at the zenith as well as the magnitudes of this radiation obtained experimentally.

It can be seen from the table that the difference between the computed and measured values of outgoing radiation corresponds to the difference between the weather conditions during the experiment and the weather conditions assumed for the computations.

2. The contribution made by atmospheric radiation to the outgoing thermal flux is considerably greater than would be assumed on the basis of existing concepts (particularly for large thicknesses corresponding to a large zenith angle). This leads to the fact that the effective altitude of the emissive atmosphere is 150 km.

The altitudinal radiation distribution of the atmosphere is stratified in nature (clearly expressed at least at altitudes greater than 150 km). In particular, a radiation intensity increase primarily in the 2.5-8 micron spectral region is observed at altitudes of about 280, 430 and 500 km.

3. Small-scale nonuniformities are not present on the curve for the angular radiation distribution of the Earth. The nonuniformities recorded in one experiment are small, and are on a scale of about 100-200 km. There is a correlation between the change in radiation intensity and the change in the weather conditions in the corresponding regions of the Earth's atmosphere.

/92

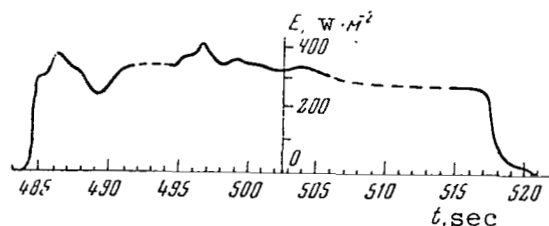


Figure 2

Angular Distribution of Infrared Radiation  
From an Altitude of 500 km

Figure 2 presents a typical curve for the angular radiation distribution of the Earth recorded from an altitude of  $\sim 500$  km for an equipment resolving power of  $2 \cdot 10^{-3}$  rad, which was indicated above.

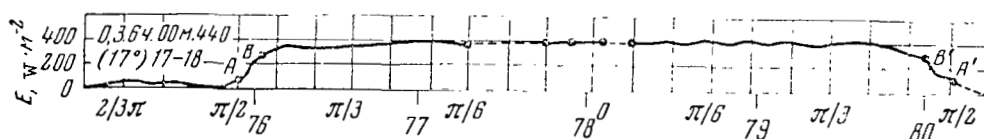


Figure 3

Angular Radiation Distribution of the Earth  
From an Altitude of 30 km

Figure 3, compiled from data obtained with a balloon, shows that the characteristic angular dimension of a nonuniformity is 0.5 rad, which corresponds to 200 km on the Earth's surface. Figure 4 gives a section of the Earth's surface with an indication of the weather conditions during the experiment, for which this angular distribution was obtained. The same numbers in Figures 3 and 4 designate the corresponding points of the angular radiation distribution curve on the surface of the Earth. A comparison of these two figures reveals a connection between the weather conditions and radiation intensity. In the cloudiness zone (region between points 76 and 77), the intensity is lower than in the non-cloudy region (point 79).

4. The daily variations in the angular radiation distribution curve of the Earth are also insignificant.

The measurement of radiation intensity at a different time of day only slightly increases those intensity changes which are recorded during one experiment, and is due to a change in the weather conditions in different regions of the Earth's surface.

Significant changes in the climato-geographic conditions lead to a more significant change in the recorded radiation intensity, just like the seasonal intensity variations.



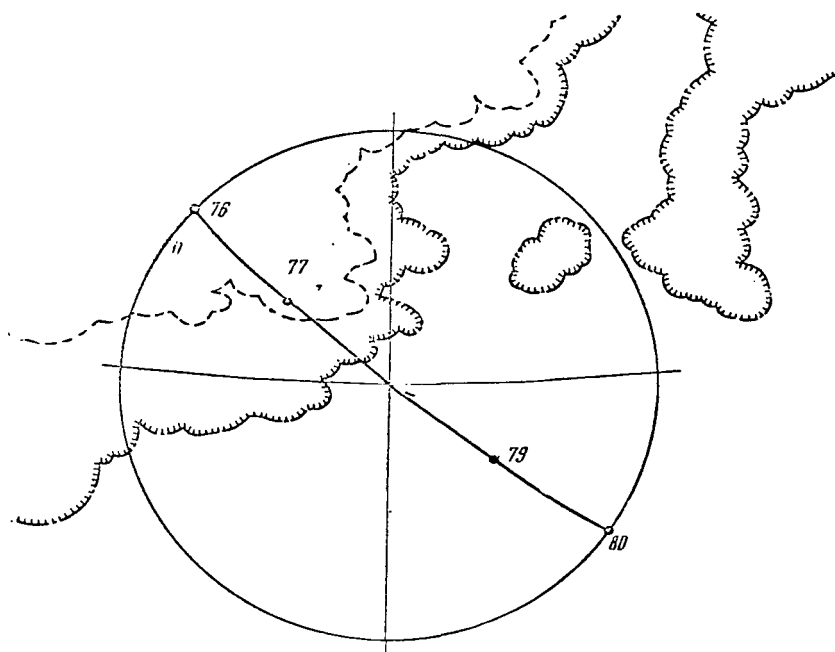


Figure 4

#### Weather Conditions During the Experiment

Dashed line - boundary of the multi-layered cloudiness zone, class 10-12; Solid line with shading - boundary of fine-layered cloudiness greater than class 1.

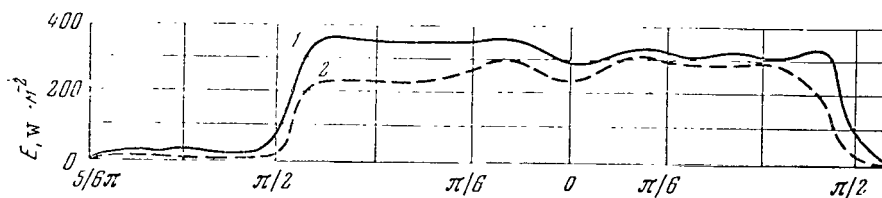


Figure 5

#### Seasonal Variations in Angular Radiation Distribution of the Earth

1 - Summer (daytime); 2 - Winter (daytime)

Figure 5 presents angular distribution curves obtained from altitudes of  $\sim 30$  km during a different time of the year.

The dependence of radiation intensity on a significant change in the climato-geographical conditions is illustrated in Figure 6. The different sections of these curves, recorded from altitudes of 300-500 km,

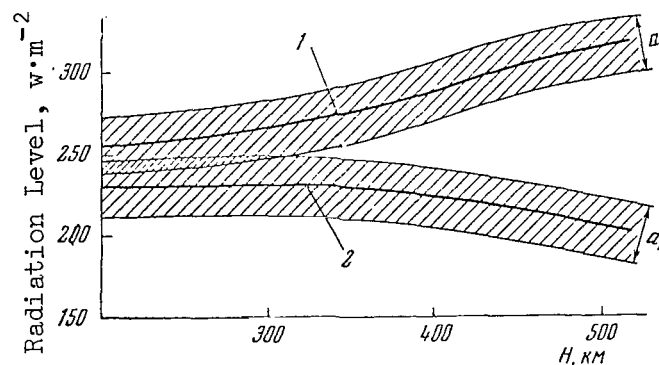


Figure 6

Dependence of Radiation Intensity on Geographic  
Position of Region Being Studied

$\alpha_1$ ,  $\alpha'$  - Mean square deviation of the level.

pertain to a north-west direction (1) in one section, and to a south-east direction (2) in another section.

#### ANGULAR AND SPECTRAL RADIATION DISTRIBUTION OF THE EARTH IN THE INFRARED SPECTRAL REGION

P. A. Bazhulin, A. V. Kartashev,  
M. N. Markov

1. The problem of the spectral distribution of radiation leaving the Earth has been repeatedly discussed in the literature. Its importance lies not only in the fact that the infrared radiation spectrum of the Earth is necessary in order to compute the energy balance of the planet, but also in the fact that this spectrum can be used directly to solve several applied problems: Determination of the molecular atmospheric composition at different altitudes, determination of temperature with respect to atmospheric altitude, etc. The computational methods for obtaining the infrared radiation spectrum of the Earth are primarily based on specific models of the emissive atmosphere. These models are only suitable for comparatively small optical thicknesses of the atmosphere, since only in this case can the absorption functions determined by laboratory methods be employed. In particular, we may point out computations carried out in (Ref. 1) for a model assuming an approximately 30-kilometer layer of the emissive atmosphere. /94

The infrared radiation spectrum of the Earth was first obtained from

the oriented satellite of the United States Air Force on September 21, 1962, with a resolution of 0.4-0.5 microns in the 1.8-1.5 micron region at the nadir (Ref. 2). The simultaneous determination of spectral and angular distribution is of greater interest, however. When the angular distribution is recorded, the contribution of the upper atmosphere can be quite significant when the sighting angles of the system deviate from the nadir, which contributes to the appearance of upper atmospheric characteristics in the infrared radiation spectrum of the Earth.

Consequently, such an experiment makes it possible, on the one hand, to obtain the characteristics of the radiating Earth which cannot generally be computed, and, on the other hand, to obtain more information on the properties of the upper atmosphere.

2. We made a simultaneous experimental determination of the angular and spectral distributions in the 4-38 micron spectral region in the  $\pm \pi/2$  angular region from the nadir during the launchings of oriented geophysical rockets of the USSR Academy of Sciences, at mean latitudes in the Soviet Union at an altitude of up to 500 km on October 18, 1962, and June 6 and 18, 1963. The manner in which the experiment was conducted is shown in Figure 1. An apparatus, containing a device for sighting in different directions in the plane passing through the rocket axis perpendicularly to the Earth's surface, scanned the narrow-angle optical system within the total angle during the ascent and descent of the rocket.

It is interesting to estimate the requisite sensitivity of the apparatus designed to record the angular and spectral distributions simultaneously. The time required to record the total scanning angle is connected with the rocket velocities in space, and also with the number of angular and spectral elements resolved as well as with the inertia of the radiation receiver. If a bolometer with a constant time of 5 msec is used as the radiation receiver, the time required to record one resolved element is about  $t_{cl} = 10$  msec; consequently, the system pass band must be  $\sim 100$  cps. For an angular resolving power of  $2 \cdot 10^{-3}$  rad and a mean observational altitude of 300 km, the minimum resolving linear dimension on the surface of the Earth will be 0.6 km (the minimum size of meteorological nonuniformities on this order is of interest). The mean spectral density of radiation reaching the receiver, with a lens diameter of  $\sim 40$  mm and an emitter temperature of  $250^\circ\text{K}$ , is about  $10^{-8} \text{ w} \cdot \text{micron}^{-1}$ . For a resolving power of 1 micron, this produces a signal equalling the mean square value of noise at the receiver having a threshold sensitivity of  $10^{-9} \text{ w} \cdot \text{cps}^{-1}$ . Such a signal will only exceed the peak noise value by 195 a factor of 2-3, for a receiver having a threshold of even  $10^{-10} \text{ w} \cdot \text{cps}^{-1}$ . In order to record radiation from the lower hemisphere with an angular resolving power of  $2 \cdot 10^{-3}$  rad, the time required to record 1800 angular resolution elements is 18 seconds ( $t_{el} = 10^{-2}$  sec). If ten spectral sections are recorded in each angular element, the total recording time is 180 seconds, or three scanning cycles can be performed during the flight time of the rocket (about 600 seconds). These rough estimates do not include loss during radiation monochromatization, and this decreases the effective

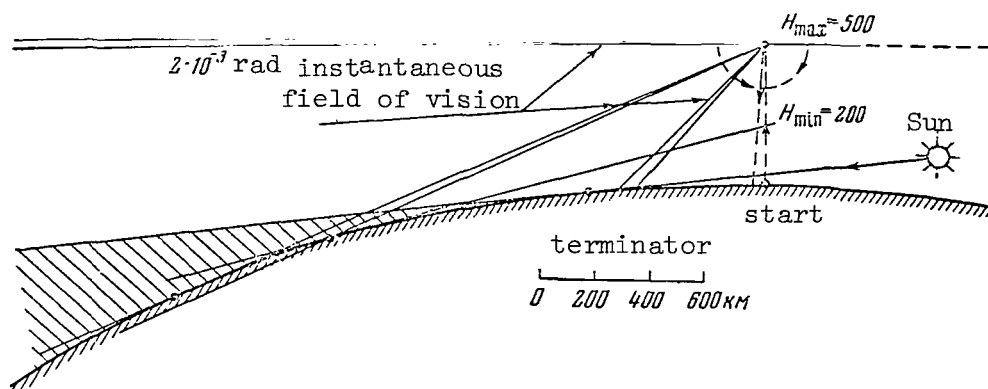


Figure 1

### Schematic Drawing of Experiment

signal by a factor of 2-3.

In this article, the flux increase was achieved by two methods: by increasing the angular dimensions of the field of vision in a direction perpendicular to the scanning plane (by using a slit-like diaphragm with a side ratio of 1:10, 1:30), by extending the spectral sections to be recorded up to several microns, and by employing the high-transmission methods of spectral resolution by means of modulating filters. Naturally, the first operation makes the spatial resolution poorer along one coordinate; however, a comparatively high, over-all spatial resolving power is retained ( $\alpha \sim 10^{-4} \text{ rad}^2$ ). A reasonable selection of spectral sections makes it possible to compensate for the deterioration in the spectral resolution to a certain extent.

Figure 2 shows the infrared spectrum of atmospheric transmission /96 when sighting is performed from the Earth's surface at the zenith; the absorption spectra of approximately equivalent thicknesses of the main absorbing atmospheric gases  $\text{H}_2\text{O}$ ,  $\text{CO}_2$  and  $\text{O}_3$  are given also. As can be seen, the structure of the infrared atmospheric spectrum ( $\lambda > 4$  micron) can be primarily characterized by comparatively wide regions of relative transmittance and absorption: 4-5 microns -  $\text{CO}_2$  absorption; 5-8 microns - absorption of  $\text{H}_2\text{O}$  vapors; 8-13 microns - the transparent section (9.5-10 microns -  $\text{O}_3$  absorption band); and, finally, for  $\lambda > 13\mu$  strong absorption of  $\text{CO}_2$  and  $\text{H}_2\text{O}$  vapors. Thus, almost all of the characteristic sections of the infrared spectrum are several microns wide.

3. It is most advantageous to perform spectral measurements under similar conditions by means of a filter system. The only infrared filter which has high transmission (up to 90%) and a passband which varies within wide limits is the modulation filter with transmission in the absorption band region of the material used as the radiation modulator. In order to

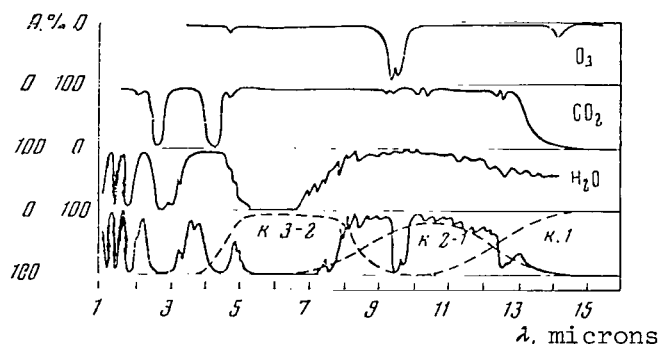


Figure 2

### Infrared Spectrum of Atmospheric Absorption and Transmission of Spectrometer Channels

obtain the spectral distribution in this case, a method of modulation spectrometry was developed, which utilizes materials having a different location of the absorption band edge as the modulators. In particular, certain alkali-haloid crystalline plates were employed.

The method is as follows. One absorbing crystal (the customary type) is replaced by  $n$  crystals in the radiation modulator (where  $n$  is the number of spectral intervals which can be distinguished directly). The selective amplifier is replaced by a wide-band amplifier with a pass-band which is adequate for transmitting impulses from each modulating crystal. The entire spectral region to be studied can be divided into  $n$  intervals, which are recorded consecutively in time by means of one optical and receiving-amplifying system. If the intervals which are distinguished are fairly wide (as in our case), the absorbing modulating crystals are made of different materials. When the intervals do not differ greatly, one material having a different thickness may be employed (for example, when the thickness of a plate made of lithium fluoride is changed from 0.1 to 10 mm, the absorption band edge changes from 11 to 6 microns [Ref. 3]).

It is interesting to note that in the limiting case this method changes into a spectral analysis method for absorption change, which was recently employed in the X-ray spectral region (Ref. 4) (the only difference being that in our method the sharp band edge and discrete readings are employed). The advantage of this method, as compared with the customary dispersion method (prism, lattice) lies in the high transmission, which is characteristic of systems with axial symmetry, and also in the rather large flux of radiation influencing the radiation receiver of the measurement device. When the recording is processed under laboratory conditions, individual spectral intervals are obtained as different quantities of two consecutive (or any, in general) signals from the modulating crystals. This is more suitable with respect to the signal/noise ratio when information is transmitted by telemetry, although it does impose great restrictions

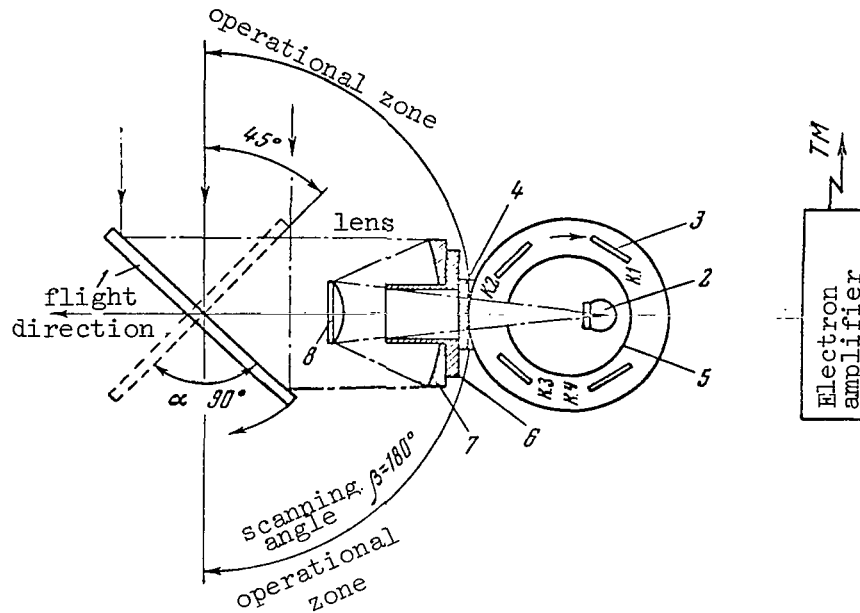


Figure 3

Block Diagram of Impulse, Infrared Rocket Spectrometer  
for Recording Angular Radiation Distribution

- 1 - scanning mirror; 2 - bolometer; 3 - modulator;  
4 - sealing window; 5 - slit diaphragm; 6 - inner tube;  
7 - spherical mirror 1; 8 - spherical mirror 2.

on the linearity of the transmittal and reproduction system. It is interesting to note that the number of spectral intervals which can be distinguished increases rapidly when the number of modulating crystals increases. Thus, for example, two crystals make it possible to distinguish three spectral intervals, 3-6, 4-10, 5-15, when two impulses are transmitted, and  $n$  crystals make it possible to distinguish  $n(n+1)/2$  spectral intervals. The rate at which modulating crystals are exchanged is connected with the rate at which the flux changes at the system input. In particular, in our case this change occurred approximately during the time when the sighting direction changed by the minimum resolving angle ( $2 \cdot 10^{-3}$  rad).

4. Figure 3 shows a block diagram of the impulse infrared spectro- /98  
meter for recording the angular distribution in different infrared spectra intervals. The flat scanning mirror rotates by an angle of  $\pi/2$ , scanning the total angle  $\pi$ . A spherical Cassegrain lens (effective diameter 33 mm, focusing distance 200 mm) concentrates the radiation onto a low-inertia bolometer. The bolometer has a sensitive area of  $0.3 \times 9 \text{ mm}^2$ , resistance of 1000 ohms, and a conversion factor of up to  $40 \text{ v} \cdot \text{w}^{-1}$  for a constant time of 5-7 msec. Thus, the bolometer has the detecting capacity

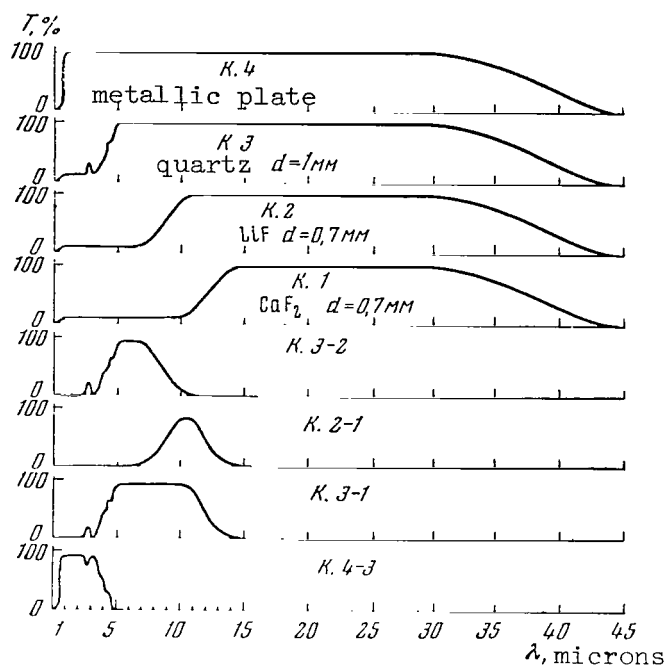


Figure 4

#### Transmission of Spectrometer Channels

D\* at a modulation frequency of 30-40 cps  $1.5 \cdot 10^9$ . The radiation bundle is intersected by the plates of the rotating modulator. Four plates are employed: A quartz plate which is 1 mm thick, a lithium fluoride plate and a fluorite plate 0.7 mm thick, and also a metallic plate which is generally opaque. The plates are distributed asymmetrically, in order to encode the signal position from the individual crystals on the time scale. The signals from the bolometer are amplified by the wide-band impulse amplifier (passband 0.5-200 cps, amplification factor greater than  $10^5$ ), and are transmitted to the Earth by telemetry. The modulator performs about 7 revolutions per second, and the scanning mirror requires about 100 seconds to examine the angle  $\pi$ .

Figure 4 gives the transmission of individual channels in accordance with the transmittance of the plates employed. The transmission of different spectral intervals is shown here. The manner in which these intervals are connected with the atmospheric absorption spectrum can be seen from Figure 2. It should be noted that the long-wave transmission boundary of the main channels is determined by the transmittance of the bolometer window (the plate made of potassium bromide, 1 mm thick). Figure 5 presents the real characteristics of the spectrometer angular resolving power in the sighting direction. As can be seen, its half-width is  $3 \cdot 10^{-3}$  rad, which is

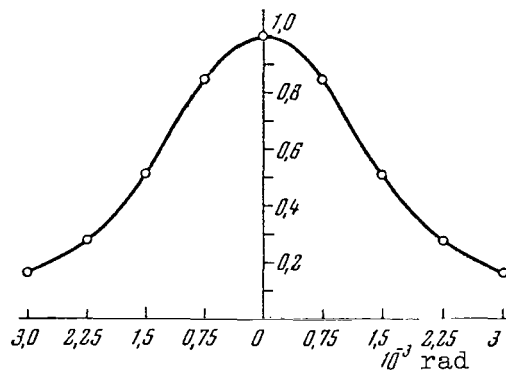


Figure 5

### Characteristics of Spectrometer Angular Resolving Power in the Scanning Plane

somewhat inferior due to the aberration of the geometric resolving power. Figure 6 shows the general form of the spectrometer.

All points on the equipment where there are rapidly moving elements are pressurized (constant current motor, reducer); the shaft for driving the slowly moving scanning mirror is brought out through a rubber gasket. The window for the radiation bundle entrance is made of a KRS-5 crystal. The spectrometer was calibrated with respect to the emitter with temperatures from 350-77°K. Thus, the sensitivity threshold under laboratory conditions for the 4.5-38 micron channel (effective lens diameter  $D_{\text{eff}} = 33 \text{ mm}$ ,  $\alpha = 10^{-4} \text{ rad}^2$ ) was  $2 \cdot 10^{-4} \text{ w} \cdot \text{cm}^{-2}$  for the object of radiation, while it increased up to  $1.5 \cdot 10^{-3} \text{ w} \cdot \text{cm}^{-2}$  during flights, due to a different type of additional interference (telemetry, etc.). This comprises effective temperatures of 0.36 and 2.7°K, respectively.

In contrast to several devices employed previously for recording infrared radiation of the Earth from geophysical rockets of the USSR Academy of Sciences (Ref. 5), in our case the differential method of recording was not employed, when the Earth-space level was continuously recorded. The quantity to be measured here was the difference between the fluxes of the Earth - modulator radiation. However, the modulator 99 temperature, and therefore the radiation flux, are undetermined, control cannot be affected with sufficient accuracy, and the flux can vary by a factor of approximately 3 for the possible temperature variations of the equipment within 233-313°K. It is true that allowance can best be made for the latter fact by expanding the linear scale region. The error, caused by indefinite modulator temperature, can be eliminated, and also allowance can be made for parasite window radiation, etc. in the scanning equipment by supplying a reference flux to the output one or more times during the scanning cycle. In particular, in this case radiation from



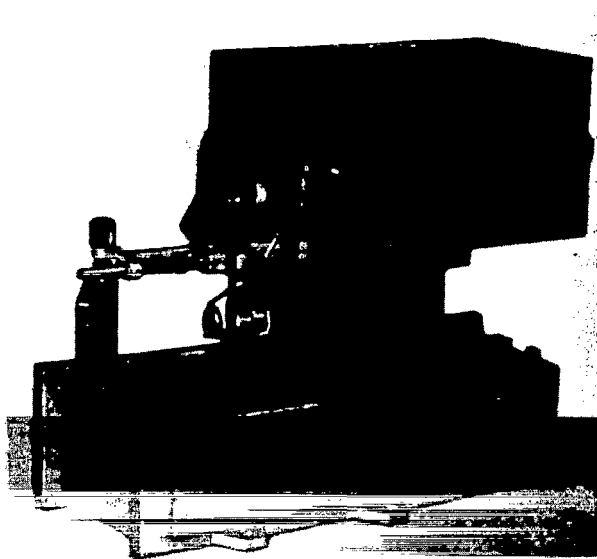


Figure 6

#### General View of the Spectrometer

space which is recorded in a direction close to the horizontal (in flights where ionosphere radiation was observed, the reference flux was recorded at an angle of  $\pi/4$  to the zenith) represents such a flux. When the results are processed, it is assumed that this radiation equals zero. Radiation from space reaches the input of an impulse spectrometer twice during one scanning cycle.

Consequently, the reference signal impulses are separated by a time interval of about 1 minute, which is sufficient to keep the zero level practically constant, due to the thermal inertia of the equipment (particularly the modulator).

However, a signal change at the spectrometer output is not only possible due to modulator temperature variations, but also due to fluctuations in the sensitivity of the receiver-amplifier system. In order to calibrate this system, a signal from a reference incandescent lamp periodically reaches its input. The level of this signal exceeds the modulator radiation level by one order of magnitude, and therefore it has practically no influence upon the resulting flux magnitude. The signal is supplied from the reference lamp at the moment when the scanning mirror is in a horizontal position (blind spot), and the amplifier sensitivity is decreased by a factor of 10 by the calibrated attenuator, in order that the reference signal amplitude at the output corresponds to the operational /100 signal scale.

5. The experiments were conducted under the following conditions. The position of the scanning plane with respect to the points of the compass was: In the experiment on October 18, 1962 - the E-N-E-W-S-W direction; on June 6, 1963 - in the E-W direction; on June 18, 1963 -

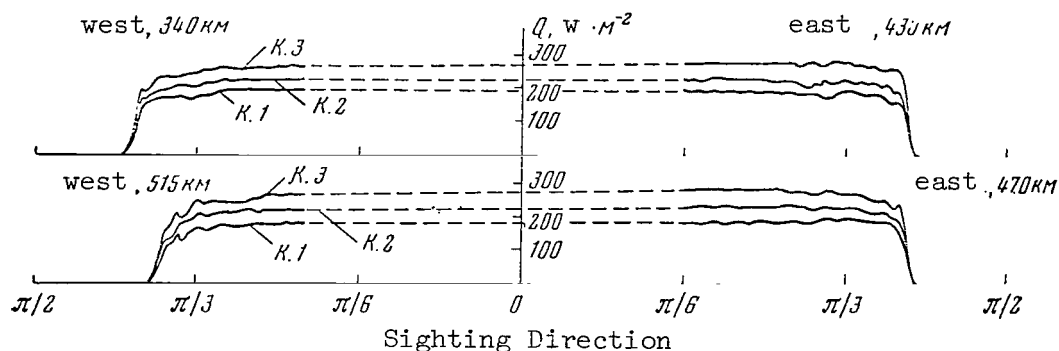


Figure 7

Angular Distribution of Infrared Terrestrial Radiation in Three Sections of the Spectrum;  
12.5-38 microns (k. 1), 8.5-38 microns (k. 2), and 4.5-38 microns (k. 3).

in the N-S direction. In the 1962 experiment, which was conducted close to the middle of the day, the conditions under which the Earth's surface was illuminated by the Sun did not differ significantly over all of the scanning direction. In the experiment on June 6, 1963, which was carried out at dawn, the eastern portion of the route was illuminated by the Sun (zenith angle of  $\pi/3$ ), while the atmospheric layer at an altitude of about 100 km to the west was in the shade.

It must be noted that the experiment on October 18, 1962, employed a modulator with three crystals (the 0.6-38 micron spectral interval was missing), in the experiment on June 6, 1963, a fourth filter separated the 2.5-38 micron spectral interval (glass plate), and in the experiment on June 18, 1963, the scanning route passed along regions in which the Sun was located very close to the horizon. Thus, there was practically no information on reflected solar radiation in all the experiments performed.

6. New scanning cycles from different altitudes and for different weather conditions were obtained in three flights. Figure 7 shows two such cycles pertaining to the flight on June 6, 1963. The angular distribution curves for three channels are given here - No. 3, 2 and 1 (4.5-38, 8.5-38 and 12.5-38 microns). The curves pertain to a flight time toward the trajectory apex, so that the altitude did not change significantly during the scanning process. The mean altitude from which the upper curve was obtained was about 400 km; the lower altitude - about 500 km. The energy threshold of the flux was 3-4%. Thus, the error of the different 3-2 (4.5-8.5 micron) and 2-1 (8.5-12.5 micron) channels was about 40%. We must note that the curves obtained in the angle  $10^{-2}$  rad were averaged in order to increase the accuracy.

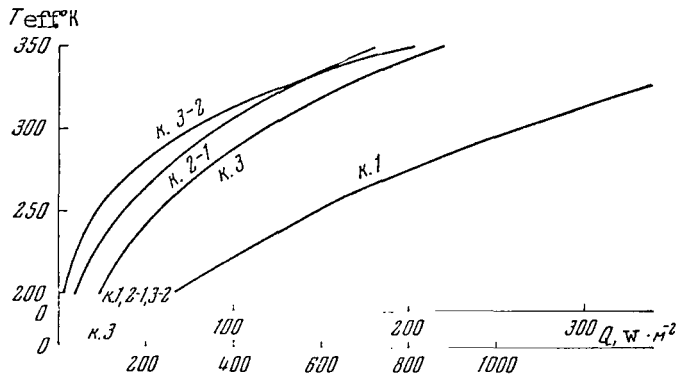


Figure 8

Dependence of Emitter Temperature on Flux Magnitude For Four Spectrometer Channels: For the Two Main Channels (1 and 3) and Two Different Channels; 4.5-8.5 Microns (3-2), 8.5-12.5 Microns (2-1).

The experimental angular distribution curves are represented on the scale of the fluxes ( $\text{w} \cdot \text{m}^{-2}$ ). However, they were processed for the analysis, in order to determine the effective temperatures and the spectral radiation density. In this case, averaging was performed with respect to the angle 0.1 rad, and therefore the measurement errors in the different channels decreased to 10-15%. The effective temperatures were determined as a function of the flux in the corresponding spectral interval, obtained by graphic integration of the product of the filter transmission curve and the Planck curve (Figure 8). The spectral radiation intensity density was determined for certain sighting directions as the ratio of the intensity in a given spectral interval to its width. Figure 3 shows the radiation intensity distribution with respect to three spectral intervals for two sighting directions - 0.5 and 1.2 rad from the nadir to the east and the west (the flight on June 6, 1963) and the north (the flight on June 18, 1963).

Table 1 lists the fluxes and effective temperatures for a sighting direction of about 0.6 rad from the nadir.

TABLE 1

Channel	East		West		North		Average	
	$Q_{2,2}$ $\text{w} \cdot \text{m}^{-2}$	$T, ^\circ\text{K}$	$Q_{2,2}$ $\text{w} \cdot \text{m}^{-2}$	$T, ^\circ\text{K}$	$Q_{2,2}$ $\text{w} \cdot \text{m}^{-2}$	$T, ^\circ\text{K}$	$Q_{2,2}$ $\text{w} \cdot \text{m}^{-2}$	$T, ^\circ\text{K}$
3(4.5-38 microns)	270	261	232	252	276	264	254	258
1(12.5-38 microns)	190	272	170	262	190	272	178	266
2-1(8.5-12.5 microns)	32	243	24	230	36	250	31	241
3-2(4.5-8.5 microns)	48	280	38	270	50	282	44.5	276

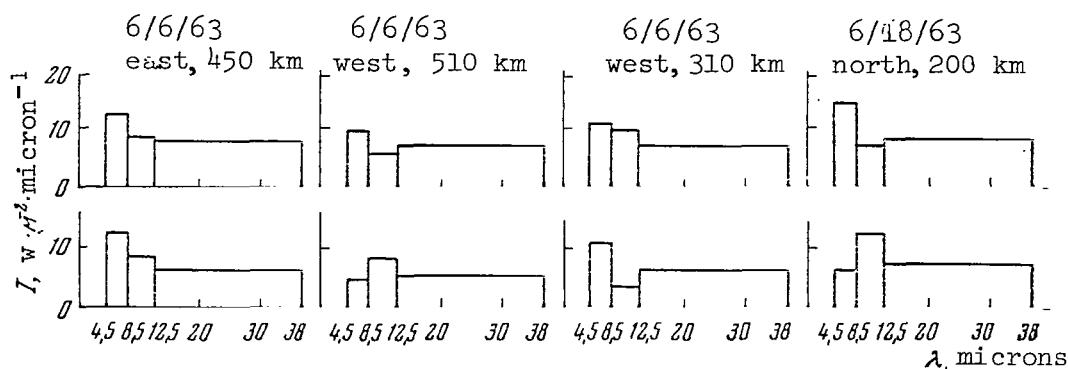


Figure 9

Spectral Distribution of Infrared Terrestrial Radiation  
Based on Flights on June 6 and 18, 1963, for Two Sight-  
Directions: 0.6 and 1.2 rad From the Nadir.

7. The results obtained can be examined from several points of view. /102

(a) Primarily with respect to the general form of the angular distribution curves. In wide intervals of the infrared spectrum the general form of the angular distribution curves corresponds to radiation from a comparatively isotropic object. Deviations from isotropy at the planet's edge during observations from an altitude of 400-500 km are less than during observations from an altitude of 25-30 km (Ref. 6). The structure of the radiation field is such that the contribution made by small-scale fluctuations ( $\sim 2 \cdot 10^{-2}$  rad) is small. In single measurements, practically no differences in thermal radiation intensity were detected under daytime and night time conditions (see, for example, Figure 8 - west and east). In the narrower spectral intervals corresponding to atmospheric conditions (4.5-8.5- $H_2O$  vapors; 8.5-12.5-"transmittance window"), the intensity fluctuations are much greater (up to 50%). We must point out the slight dependence of the general form for the angular distribution curves on the observational altitude between 200-500 km altitude.

(b) An examination of the spectral distribution, and also the effective temperatures determined according to the fluxes in different spectral intervals, shows that in the majority of cases the radiation maximum is located in the 4.5-8.5 micron spectral region, and the effective temperatures for this spectral region are higher than for other regions (including those for the transmittancy window), reaching 270-280°K. It should be noted that during all of the experiments performed in the extensive territory encompassed by the scanning route the cloudiness varied from class 1-2 to class 7-8, with a lower boundary altitude of 1-7 km. Thus, (with allowance for the sighting angle) the comparatively low effective temperature in the transmittance window (240°K) can be readily explained. Thus, for example, the mean meteorological conditions, characterized by

data given in Table 1, can be described by the following parameters, whose altitudinal distributions are given in Table 2 (pressure p, temperature T, and humidity q).

It is interesting to compare the effective temperatures (average), determined by the intensities in individual spectral intervals, with the atmospheric temperatures at different altitudes. It can be seen from Tables 1 and 2 that for integral radiation the altitude at which the effective temperature is close to the actual temperature is about 6 km ( $p \approx 500$  mbar); for radiation in the "transmittance window" of 8.5-12.5 microns, it is 7-8 km ( $p \approx 400$  mbar); and in the 4.5-8.5 micron range, it is 2 km ( $p \approx 800$  mbar).

TABLE 2

June 6, 1963, 3 hours, World Time								June 18, 1963, 3 Hours, World Time			
East, Cirrus Clouds, class 5 (Lower Boundary, 5-7 thousand m)				West, Altocumulus Clouds, class 2-3 (Lower Boundary, 2.5 thousand m)				North, Stratified Cumuliform Clouds, class 7-8 (Lower Boundary, 1 thousand m)			
H, m	p, mbar	T, °K	q, g·kg <sup>-1</sup>	H, m	p, mbar	T, °K	q, g·kg <sup>-1</sup>	H, m	p, mbar	T, °K	q, g·kg <sup>-1</sup>
0	1013	291	3.0	0	1018	287	8.0	0	1090	284	8.0
1500	850	287	2.7	1480	850	285	9.0	1440	850	284	7.0
3000	700	273	3.0	3100	700	273	3.5	3020	700	273	4.0
5700	500	260	0.5	5700	00	255	1.7	5670	500	255	1.0
9300	300	244	0.04	9300	300	227	--	9210	300	228	0.15
11900	200	231	0.07	11800	200	213	--	11890	200	224	0.1
16400	100	207	--	16400	100	222	--	16440	100	227	0.2
21000	50	216						20970	50	224	--
24300	30	218						24360	30	227	--
								27160	20	231	--
								31930	10	235	--

Thus, if the emissive layer altitude can be explained by the upper boundary of the cloudiness for the transmittance window, then the radiation level in the section of strong absorption by water, N<sub>2</sub>O and NO vapors - 4.5-8.5 microns - cannot be located at an altitude of 2 km. This is due to the fact that, according to existing information, above this level the vapor concentration is still large, and effective absorption

/103

occurs at rather high altitudes (up to 10 km) where the atmospheric temperature is low. However, at high altitudes (40-60 km), the temperature again decreases, and consequently the possibility cannot be excluded that radiation from these altitudes is responsible for the observed high effective temperatures in the 4.5-8.5 micron region. In this connection, we cannot overlook the results obtained in (Ref. 2), where a high radiation intensity was observed in several cases in the 6-8 micron region; in every case, this intensity was higher than that stipulated by the assumption of an atmospheric emissive layer concentrated in the 30-40 km layer near the Earth. We must note that the experiment, in which the angular radiation distribution of the Earth was recorded, provide a definite information regarding the transitional space-Earth region. In particular, it made it possible to directly obtain the altitude of the Earth's emissive atmosphere in different spectral intervals; for the experiment on June 6, 1963, in the 4.5-8.5 micron spectral region this altitude was 45 km to the east and 125 km to the west; for the experiment on June 18, 1963, it was 90 km to the north. A comparison of these data with the water vapor concentration near the Earth in these regions (see Table 2) indicates a definite correlation between the emissive atmosphere altitude and the vapor concentration near the Earth. The determination of small concentrations of emissive vapor is facilitated under the observational conditions, since the thickness of the optical path can amount to several hundred kilometers, when the sighting is performed by a narrow-angle optical system at large angles to the nadir. An increase in the amount of data and statistical processing of the information may possibly provide a more reliable basis for the assumption of vertical water vapor propagation. The radiation of nitric oxides cannot be excluded, although in this case variations with the underlying surface characteristics are less probable.

Since the experiments were performed by equipment having a narrow-angle optical system, it was possible to observe ionosphere infrared radiation from the oriented carrier in this series of launches (Ref. 7). It must be noted that, due to the very slow scanning motion of the optical system, when the rocket shifted by 50-70 km - during the sighting time of angles adjacent to the horizontal - the recorded layers were very diffuse. It was possible to observe ionosphere radiation by the change in the radiation spectral composition for the horizontal direction. In particular, the results derived from the launch on October 18, 1962, indicated that ionosphere radiation was concentrated in the 4.5-8.5 micron region. It is interesting to note that during the launch on June 6, 1963 (no perturbation in the ionosphere on the solar side) the infrared radiation in the horizontal direction was weak.

#### REFERENCES

1. Kondrat'yev, K. Ya., Yakushevskaya, K. Ye. In "Problemy Fiziki Atmosfery", No. 2, p. 48, 1963.
2. Block, L. C., Zachor, A. S. Appl. Opt., No. 2, 209, 1964.
3. Lekont, Zh. Infrared Radiation (Infrakrasnoye izlucheniye). Fizmatgiz, 1958.

4. Greening, I. R. Proc. Phys. Soc., A63, No. 371A, 227, 1950.
5. Aver'yanov, I. P., Kasatkin, A.M., Liventsov, A. V., Markov, M. N., Merson, Ya. I., Shamilev, M. R., Shervinskiy, V. Ye. In "Iskusstvennyye Sputniki Zemli". Izdatel'stvo AN SSSR, No. 14, p. 49, 1962.
6. Markov, M. N., Merson, Ya. I., Shamilev, M. R. Kosmicheskiye Issledovaniya, 1, No. 2, 235, 1963.
7. Markov, M. N., Merson, Ya. I., Shamilev, M. R. Present collection, p. 112.

# DETERMINING TEMPERATURE AND MOISTURE OF THE EARTH'S ATMOSPHERE BASED ON SATELLITE MEASUREMENTS OF THE EARTH'S ATMOSPHERE

M. S. Malkevich, V. I. Tamarskiy

Spectral measurements of radiation leaving the Earth in the region /104 of the carbon monoxide (15  $\mu$ k) and water vapor (6.3  $\mu$ k) absorption bands by satellites has made it possible to determine the vertical distribution of temperature and humidity in the Earth's atmosphere. A concurrent determination of these parameters in the following way is advantageous. The vertical temperature distribution  $T(p)$ , without allowance for the  $\text{CO}_2$  and  $\text{H}_2\text{O}$  bands overlapping ( $p$  is the pressure at standard levels) can be determined from radiation in the  $\text{CO}_2$  band, whose concentration in the atmosphere is known. Utilizing the  $T(p)$  thus obtained according to radiation in the  $\text{H}_2\text{O}$  band, we can determine the vertical distribution of specific humidity  $q(p)$ , and can then define  $T(p)$  more accurately, with allowance for the bands of both gases overlapping in the 15  $\mu$  region. An analagous problem can be solved by measuring the outgoing radiation of  $\text{O}_2$  and  $\text{H}_2\text{O}$  in the radio wave range of the spectrum.

The fact that the radiation leaving the Earth, which corresponds to different sections of the absorption bands under consideration, is produced in different layers of the Earth's atmosphere - and, consequently, reflects the thermal regime of these layers or the concentration of water vapor in them - provides a physical basis for solving this problem. It is clear that the outgoing radiation represents the superposition of radiation from all elementary atmospheric layers, and the incoming proportion of radiation from each of them is determined by the transmission function of the atmosphere  $\tau_\nu$ , which depends on the frequency  $\nu$ , the concentration of the absorbant substances, pressure, and temperature. If it is assumed that the underlying surface radiates like a black body at the temperature  $T(p_0)$ , then the intensity of radiation  $I_\nu$ , leaving the upper atmospheric boundary in a certain direction, (for example, in the zenith direction) is related to the desired functions by the following relationship:

$$I_\nu = B_\nu [T(p_0)] \tau_\nu [p_0, q(p_0)] - \int_0^{\tau_0} B_\nu [T(p)] d\tau_\nu [p, q(p)]. \quad (1)$$

Here  $B_\nu$  is the Planck function, and  $p_0$  is the pressure at the underlying surface. Expression (1) is an integral equation of the Fredholm type of the first kind (generally speaking, nonlinear).

Since it is necessary to obtain spatial and temporal variations of the functions  $T(p)$  and  $q(p)$ , i.e., deviations from certain mean distributions  $T(p)$  and  $q(p)$ , for the physics of the Earth's atmosphere, the solution of this problem must be based on precise measurements of the outgoing radiation. On the other hand, it is well-known (see, for example



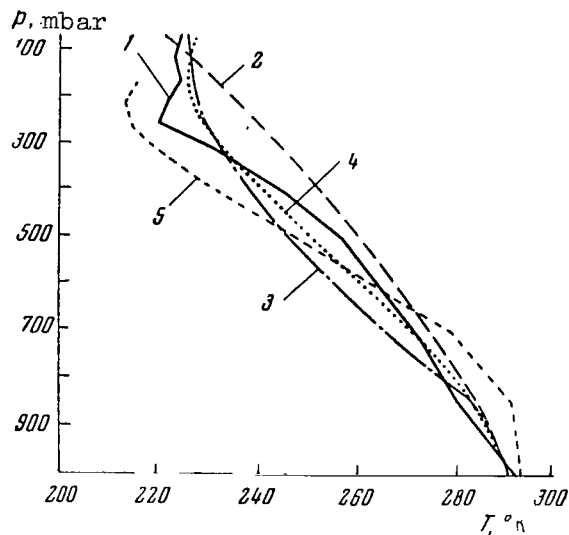


Figure 1

Reduction of Vertical Temperature Distribution by Yamamoto's Method  
(Ref. 9) Using Polynomials of Different Orders

$$T_n(p) = \sum_{k=0}^n t_k p_k; 1 - T(p); 2 - n=1; 3 - n=2; 4 - n=3; 5 - n=4$$

[Ref. 1]) that the opposite problems for equations of type (1) are incorrect, i.e., small errors in the measured quantities of  $I_v$  can lead to large errors in the functions determined  $T(p)$  and  $q(p)$ . This also necessitates a high measurement accuracy.

The conclusion can thus be drawn that, before formulating the physical experiment, it is necessary to establish what the errors in determining  $T(p)$  and  $q(p)$  will be for the existing possibilities of measuring  $I_v$ . We must also determine what requirements must be imposed on the experiment, in order to obtain the desired quantities with acceptable accuracy. Taking into account the difficulty entailed in measuring  $I_v$  from the satellite with high spectral resolution, it is advantageous to indicate the minimum number (which is sufficient for this purpose) of spectral intervals in which  $I_v$  must be measured. This article is devoted to clarifying some of these problems.

/105

## 1. Determining $T(p)$

Kaplan (Ref. 2) initiated the idea of determining  $T(p)$  by satellite measurements in the  $\text{CO}_2$  absorption band. The works of Wark (Ref. 3) and Yamamoto (Ref. 4) presented certain methods for solving this problem for the stratosphere, where water vapor absorption can be disregarded. In particular, Yamamoto developed a solution for equation (1), which only took into account the absorption of carbon monoxide, in the form of Legendre and Chebyshev polynomials expanded in powers of  $p$  and in the form of orthogonal polynomials. In his report to the symposium on radiation processes in Leningrad (August, 1964), Wark proposed the use of trigonometric functions for this purpose also. Examples of determining  $T(p)$  according to  $I_v$ , given in 4 sections of the spectrum, show that real variations of  $T(p)$  cannot be approximated identically in a satisfactory way on all levels being studied by polynomials of the first, second, and third order (Ref. 4). The utilization of additional expansion terms (even of the fourth order) impairs the approximation, since the incorrectness of the opposite problem is manifested (Figure 1). The methods which have been presently developed for regulating operators of the integral Fredholm equation types of the first kind (Ref. 1) still require more initial information on the defined function  $I_v$ .

It is necessary to perform an optimum approximation of  $T(p)$  in order to obtain a reliable solution of equation (1). Systems of statistically orthogonal functions provide such an approximation; a rigorous theory was developed for these functions by A. M. Obukhov (Ref. 5). This theory can be used to determine  $T(p)$ . If we represent  $T(p)$  in the form

$$T(p) = \bar{T}(p) + T'(p), \quad (2)$$

where  $T'(p)$  are random deviations from the norm  $T(p)$  ( $T' \ll T$ ) - which is 106 known for any region of the Earth and any time interval, or which can be determined according to aerological data - then we obtain an equation for determining  $T'(p)$  from (1) and (2):

$$f_v = \frac{\partial B_v[\bar{T}(p_0)]}{\partial T} \tau_v(p_0) T'(p_0) - \int_0^{p_0} \frac{\partial B_v[\bar{T}(p)]}{\partial T} T'(p) d\tau_v(p), \quad (3)$$

which is linear with respect to  $T'(p)$ . Here  $f_v = I_v - \bar{I}_v$ ;  $\bar{I}_v$  is the intensity of outgoing radiation for the mean profile. As has been shown in (Ref. 5), the optimum approximation of the random function - for example,  $T'(p)$  - is performed by a system of orthogonal functions which represent eigen functions of the corresponding correlation function, in the given case  $B_T$  (when  $T'$  is set at a discrete number of levels, this will be a basis system of vectors representing eigen vectors of the correlation matrix  $B_T(p_k, p_l)$ ).

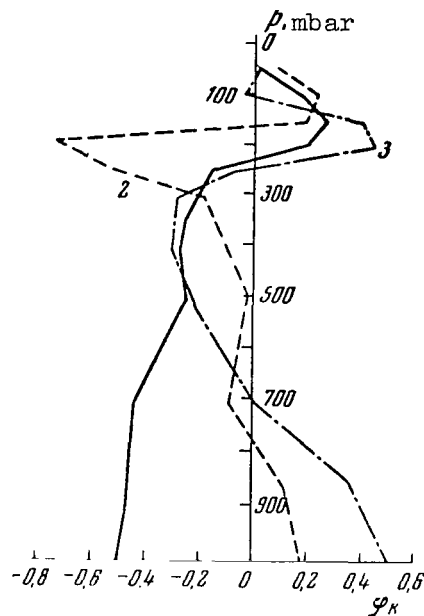


Figure 2

Examples of Eigen Vectors  $\phi_k(p_i)$  Calculated  
According to the Correlation Matrix  $B_T(p_k, p_l)$  for Bismarck

1 -  $\phi_1$ ; 2 -  $\phi_2$ ; 3 -  $\phi_3$ .

Figure 2 presents examples of 3 eigen vectors  $\phi_k(p_i)$  of the matrix  $B_T(p_k, p_l)$ . It is shown that any realization of  $T'(p_i)$  can be approximated by three-four eigen vectors with a mean quadratic error which does not exceed 10-15%. This error can be expressed by the eigen values of the matrix, representing the dispersion of the expansion coefficients. Thus, representing  $T'$  in form of the expansion

$$T'_n(p) = \sum_{k=1}^n t_k \phi_k(p) \quad (4)$$

and substituting in (3), we obtain a system of algebraic equations for determining  $t_k$ :

$$\sum_{k=1}^n D_{vk} t_k = f_v \quad (v = 1, 2, \dots; N \geq n), \quad (5)$$

Thus  $t_k = \sum_{v=1}^n D_{vk}^{-1} f_v$ . Here  $D_{vk}^{-1}$  represents elements of the inverse matrix of system (5).

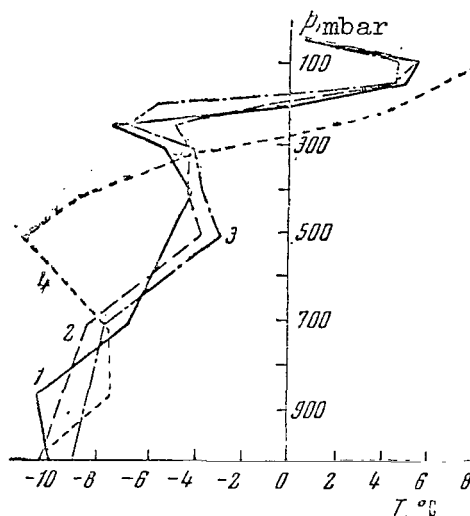


Figure 3

Reduction of Vertical Temperature Distribution by the Optimum Approximation Method Above Dry Land (Bismarck)

$$1 - T'(p); \quad 2 - T'_3(p_i) = \sum_{k=1}^3 \tilde{T}_k \varphi_k(p_i), \quad \tilde{T}_k = \sum_{i=1}^{10} T'(p_i) \varphi_k(p_i); \quad 3 - T'_3(p) = \sum_{k=1}^3 t_k \varphi_k(p);$$

$t_k$  are determined from the system (17); 4 - solution of equation (13) by Yamamoto's method (Ref. 9).

As was shown in (Ref. 6), the use of optimum systems does not eliminate the instability of the solution, related to the incorrect nature of the inverse problem for equation (9). But since these systems provide the best approximation by a small number of terms in the series (5), it is possible to solve equation (3) with satisfactory accuracy (Figure 3, 4), which is no worse than approximation in general. It is thus apparent that a satisfactory reduction of the vertical profiles for each of the cases examined (dry land, ocean) can also be performed by means of a "foreign" system of eigen vectors (Figure 4, curve 4).

The influence of the error entailed in measuring  $I_v$  or  $f_v$  upon the error in determining  $T'(p)$  is an important problem. It can be readily shown (Ref. 6) that, if the measurement errors are not correlated, the amplification factor of the mean quadratic error  $\delta f = \sqrt{f_v^2}$

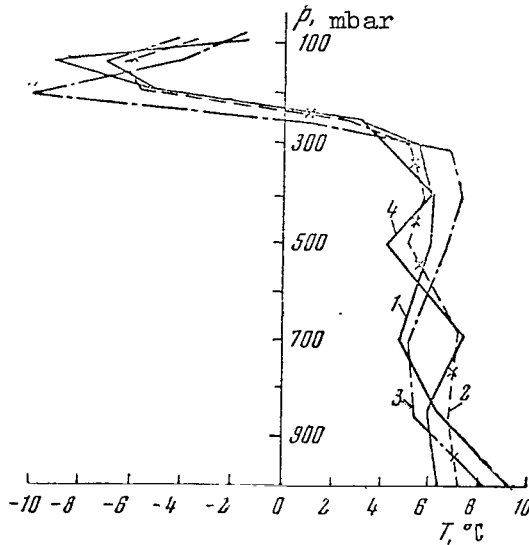


Figure 4

Reduction of Vertical Temperature Distribution by  
Optimum Parameterization Above the Ocean (On Ship Board "S")

Notation is the same as in Figure 3; curve 4 is obtained by means of  $\varphi_k(p_i)$  determined for the mainland.

$$K_T = \delta T / \delta f,$$

(where  $\delta T$  is the mean quadratic error entailed in determining  $T'$ ) can be expressed by the element  $D_{vk}^{-1}$  of the reverse matrix of system (5)

$$K_T(p) = \left[ \sum_{k=1}^n \sum_{l=1}^n \sum_{v=1}^n D_{vk}^{-1} D_{vl}^{-1} \varphi_k(p) \varphi_l(p) \right]^{1/2}. \quad (6)$$

The amplification factor of the error can be significantly reduced, if /107 we use the initial information on  $L_v$  for a large number  $N$  of spectral intervals exceeding the number  $n$  which takes into account the basis vectors. Then  $K_T$  can be reduced by a factor of approximately  $N/n$ . The amplification coefficients of  $K_T$  and  $K_q$  are given below for determining  $T'(p)$  and  $q'(p)$ :

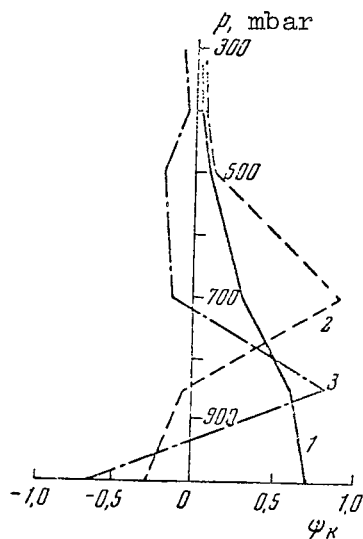


Figure 5

Examples of Eigen Vectors  $\Psi(p)$  Calculated  
According to the Correlation Matrix  $B_q(p_k, p_l)$  for Bismark  
1 -  $\Psi_1$ ; 2 -  $\Psi_2$ ; 3 -  $\Psi_3$

p, mb	1000	850	700	500	400	300	250	200	150	100
$K_T(n=N=2)$	3.1	1.1	5.3	2.0	4.7	7.1	17.2	21.3	8.2	8.8
$K_T(n=2; N=13)$	1.8	1.0	1.4	0.5	1.3	2.3	6.0	8.0	2.6	2.5
$K_q(n=3; N=3)$	6.2	7.6	5.0	0.61	0.4	0.1	-	-	-	-
$K_q(n=3; N=8)$	5.4	2.5	1.8	0.3	0.1	-	-	-	-	-

These results pertain to the case when the radiation of water vapor, whose band overlaps the  $CO_2$  band of  $15 \mu$ , is disregarded. Allowance for water vapor can be important in determining  $T(p)$ . Therefore, it is advantageous to solve these problems of determining the temperature profile concurrently with the problem of determining the vertical humidity distribution according to the outgoing radiation in the  $H_2O$  band (for example,  $6.3 \mu$ ).

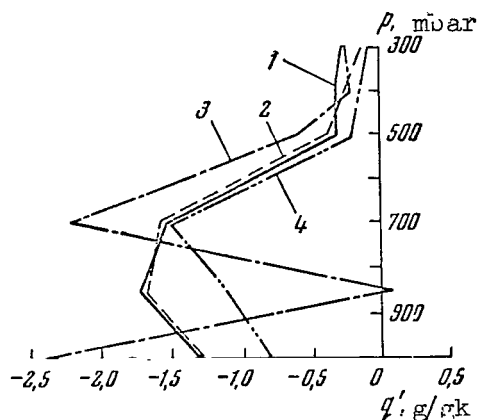


Figure 6

Reduction of Vertical Specific Humidity Distribution Above Bismarck

$$1 - q'(p); \quad 2 - q'_2(p_i) = \sum_{k=1}^3 \tilde{q}_k \psi_k(p_i); \quad \tilde{q}_k = \sum_{i=1}^6 q'(p_i) \psi_k(p_i); \quad 3 - q'_3(p) = \sum_{k=1}^n q_k \psi_k(p),$$

$q_1$  are determined from system (24); 4- second approximation  $q'(p)$  obtained from system (27).

## 2. Determination of $q(p)$

It is advantageous to determine  $T(p)$  and  $q(p)$  concurrently based on simultaneous measurements of  $I_V$  in the  $\text{CO}_2$  bands of  $15 \mu$  and the  $\text{H}_2\text{O}$  bands of  $6.3 \mu$ . This is due to the fact that it is necessary to know the rest in order to determine each of these parameters (the idea of such a complex was also advanced by Kaplan [Ref. 7]). By determining the first approximation of the vertical profile  $T_1(p)$  according to  $I_V$  in the  $\text{CO}_2$  band of  $15 \mu$ , without allowing for overlapping with the  $\text{H}_2\text{O}$  bands, one can use it to determine the vertical profile  $q(p)$  according to  $I_V$  in the  $\text{H}_2\text{O}$  band of  $6.3 \mu$ . By obtaining the latter, one can define  $T_1(p)$  more accurately, with allowance for the band overlapping, and can then repeat the iteration.

The problem of determining  $q(p)$  is similar to the problem of determining  $T(p)$ , with the only difference being that equation (1) will be essentially nonlinear:  $\tau_v[p, q(p)]$  - a complex function  $q(p)$  which does not have an analytical expression. Since the mathematical method of solving equation (1) is the main problem considered below, we can utilize the approximate expression of the function  $\tau_v$  based on the band model of Elsasser:

$$\tau_v(x) = 1 - \Phi \left[ \sqrt{\frac{l_v}{2}} w_0 Q(x) \right], \quad (7)$$

where  $x = p/p_0$ ;  $w_0 = l_0 q(p_0)/g$  is the water vapor mass in a column of air reduced to normal pressure  $p_0$ ;  $l_v$  - the generalized absorption coefficient;

$$\Phi(y) = \frac{2}{\sqrt{\pi}} \int_0^y e^{-t^2} dt \quad (8)$$

-integral of probability;

$$Q(x) = \int_0^x t q(t) dt \quad (9)$$

-reduced mass of water vapor.

Let us employ the approximation method by using empirical or orthogonal functions obtained for specific humidity, in order to solve equation (1). Representing

$$q(x) = \bar{q}(x) + q'(x),$$

(where  $\bar{q}(x)$  is the mean profile of specific humidity above a given region and in a given time interval;  $q'(x)$  - profile deviation from the mean) and regarding  $q'(x)$  as a random function, we can compile a system of orthogonal functions (vectors) which provide optimum parameterization of any realization  $q'(x)$ . Figure 5 presents examples of the three first vectors of such a system, obtained according to radiosonde data above Bismarck (summer).

If it is assumed that the vertical temperature distribution  $T(x)$  and the mean specific humidity distribution  $\bar{q}(x)$  are known, then we can formulate an equation for determining  $q'(x)$ , which is assumed to be small as compared with  $\bar{q}(x)$ :

$$f_v = -B_v[T(1)] \frac{\partial \Phi_v[\bar{Q}(1)]}{\partial Q} Q'(1) - \int_0^1 B_v[T(x)] d \left\{ \frac{\partial \Phi_v[\bar{Q}(x)]}{\partial Q} Q'(x) \right\}. \quad (10)$$



Here  $f_v = I_v - \bar{I}_v$ ;  $\bar{I}_v$  is the intensity of outgoing radiation calculated according to formula (1) for  $q = \bar{q}(x)$ ;

$$\begin{aligned}\bar{Q}(x) &= \int_0^x t \bar{q}(t) dt \\ Q'(x) &= \int_0^x t q'(t) dt; \\ \frac{\partial \Phi_v[\bar{Q}(x)]}{\partial \bar{Q}} &= \frac{l_v w_0 \exp \left[ -\frac{l_v}{2} w_0 \bar{Q}(x) \right]}{[2\pi l_v w_0 \bar{Q}(x)]^{1/2}}\end{aligned}\quad (11)$$

In order to solve equation (10), which is linear with respect to  $q'(x)$ , /109 let us represent  $q'(x)$  in the following form:

$$q'_n(x) = \sum_{k=1}^n q_k \psi_k(x). \quad (12)$$

Substituting (12) in equation (10), we obtain an algebraic system of equations for determining the coefficients  $q_k$ :

$$\sum_{k=1}^n \Gamma_{vk} q_k = f_v \quad (v = 1, 2, \dots, N \geq n), \quad (13)$$

where

$$\begin{aligned}\Gamma_{vk} &= -B_v[T(1)] \frac{\partial \Phi_v[\bar{Q}(1)]}{\partial \bar{Q}} g_k(1) + \\ &+ \int_0^1 B_v[T(x)] d \left\{ \frac{\partial \Phi_v[\bar{Q}(x)]}{\partial \bar{Q}} g_k(x) \right\}; \\ g_k(x) &= \int_0^x t \psi_k(t) dt.\end{aligned}\quad (14)$$

The efficiency of the method was verified as follows. For given realizations  $T(x)$ ,  $q(x)$  and  $\bar{q}(x)$ ,  $I_v$  and  $\bar{I}_v$  were calculated according to formula (1) for several spectral sections having the width  $\Delta_v = 25 \text{ cm}^{-1}$  in the /110 interval  $v = 1241 - 1512.5 \text{ cm}^{-1}$ . The absorption coefficients  $l_v$  were taken from the study (Ref. 8). The coefficients  $q_k$  and the desired function  $q'(x)$  were then determined according to the function of  $f_v$ , which was obtained from these calculations, and the given  $T(x)$  and  $\bar{q}(x)$  described by the above method. The results derived from this calculation are given in Figure 6 for  $n = 3$  and  $N = 3$ . Attention should be called to the great divergence between the true and calculated profiles of  $q'(x)$  close to the

Earth's surface. This is apparently related to the fact that  $q'(x)$  is comparable with the mean profile  $\bar{q}(x)$ , which makes it impossible to restrict ourselves to linear terms in (10). We should also point out that, in contrast to a similar problem for the vertical temperature profile, the variations in specific humidity have less influence on the variability of the spectral pattern of outgoing radiation intensities. Actually, as follows from (1) and (7), double smoothing out of the specific humidity occurs in the calculation of  $I_v$ .

It is possible to refine the solution of the problem by applying Newton's method to the nonlinear equation (1); this method was generalized to nonlinear operators by L. V. Kantorovich (Ref. 9). Writing (1) in the form

$$F_v[q_k] \equiv B_v[T(1)] \left\{ 1 - \Phi \left( \sqrt{\frac{l_v}{2} w_0 \left[ \bar{Q}(1) + \sum_{k=1}^n q_k g_k(1) \right]} \right) \right\} + \\ + \int_0^1 B_v[T(x)] d\Phi \left\{ \sqrt{\frac{l_v}{2} w_0 \left[ \bar{Q}(x) + \sum_{k=1}^n q_k g_k(x) \right]} \right\} - I_v = 0 \quad (15)$$

and regarding (15) as a nonlinear equation with respect to the coefficients  $q_k$ , for whose first approximation  $q_k^{(1)}$  we employ the solution of system (13), we can determine the following approximations from the system

$$\sum_{k=1}^n \frac{dF_v[q_k^{(1)}]}{dq_k} [q_k^{(i+1)} - q_k^{(i)}] + F_v[q_k^{(i)}] = 0 \quad (i = 1, 2, \dots). \quad (16)$$

It can be readily seen that the coefficients of the system of equations (16) coincide with  $\Gamma_{vk}$  in the case of  $q_k^{(1)}$ . Therefore, for purposes of computational simplicity, we can employ the same coefficients in systems (16) as in system (13), only changing the free term. Figure 6 presents the results derived from solving equation (16) for  $i = 2$ . These results show that this method provides satisfactory approximations of the calculated profiles  $q'(x)$  to the actual profiles. The mean quadratic error of the solution does not exceed 10%, under the condition that the quantity to be measured is known with an absolute accuracy. If  $f_v$  is measured with a certain error  $\sigma_F$ , then the coefficient  $K_q(x) = \tau_q / \tau_F$  - which indicates the extent to which the error increases in determining the specific humidity  $\sigma_q$  - can be expressed by elements of the reversed matrix  $\Gamma_{kl}^{-1}$  of system (13) and the basis vectors  $\psi_k$ . Namely, we have

$$K_q(x) = \left[ \sum_{k=1}^n \sum_{l=1}^n \sum_{v=1}^n \Gamma_{vk}^{-1} \Gamma_{vl}^{-1} \psi_k(x) \psi_l(x) \right]^{1/2}. \quad (17)$$

The quantities  $K_q(x)$ , calculated for the solution  $q'(x)$  obtained above, are given on page 146. As was expected, the error amplification factor is at a maximum close to the Earth's surface. If the number of spectral intervals  $N$ , in which  $I_\nu$  is measured, exceeds the number of basis vectors  $n$ , then - just as in the case of temperature - the error decreases by approximately a factor of  $N/n$ .

## Conclusions

/111

Based on the fact that statistical characteristics of the vertical structure of temperature and humidity fields will be employed to solve the problem under consideration, we can formulate basic recommendations and requirements for the proposed experiment on the basis of the results obtained.

1. In order to determine the deviations of the vertical profiles for temperature and specific humidity from the mean distributions  $T(p)$  and  $\bar{q}(p)$ , the measurements must be conducted by the differential method. The radiation of a black body, equalling the radiation of the Earth for  $T(p)$  and  $\bar{q}(p)$  above the measurement region in a given time interval, must be used as the comparison standard.

2. In order to determine  $T(p)$  for the troposphere with an error exceeding the measurement error  $I_\nu$  by a factor of 3-5, it is sufficient to measure the latter in 2-3 suitably selected intervals of the  $CO_2$  absorption band of  $15 \mu$ , under the condition that the atmospheric transmission is known with an absolute accuracy. In order to decrease the error 2-3 times, it is necessary to have the measurements of  $I_\nu$  in 10-12 spectral intervals.

3. The selection of this amount of intervals for the water vapor absorption band of  $6.3 \mu$ , in which  $I_\nu$  is measured, in order to determine  $q(p)$  in the troposphere leads to a somewhat greater amplification of the measurement error (a factor of 5-8 when 3 spectral intervals are chosen, and a factor of 2-5 for 8 spectral intervals).

4. Let us assume that deviations of the temperature and humidity vertical profiles from the mean profiles must be obtained with an error of 30% of the mean quadratic deviation (this comprises  $2-3^\circ$  in terms of temperature and  $0.5 - 1 \text{ g}\cdot\text{kg}^{-1}$  in terms of specific humidity for  $T(p_0) = 300^\circ\text{K}$ ,  $\bar{q}(p_0) = 3 - 5 \text{ g}\cdot\text{kg}^{-1}$ ). The differences between the actual radiation of the Earth and the standard radiation must be measured with an error of no more than 5%, and the standard radiation must be recorded with an error of 0.1%. This experiment is technically feasible at the present time.

## REFERENCES

1. Tikhonov, A. N. Doklady AN SSSR, 151, No. 3, 501, 1963.
2. Kaplan, L. D. J. Opt. Soc. Amer., 49, No. 10, 1004, 1959.
3. Wark, D. Q. J. Geophys. Res., 66, No. 1, 77, 1961.
4. Yamamoto, G. J. Met., 18, No. 5, 581, 1961.
5. Obukhov, A. M. Izvestiya AN SSSR, Seriya Geofiz., No. 3, 432, 1960.
6. Malkevich, M. S., Tatarskiy, V. I. Kosmicheskiye Issledovaniya, 3, No. 3, 1964.
7. Kaplan, L. D. J. Quantit. Spectrosc. and Radiat. Transfer, 1, No. 2, 86, 1961.
8. Wark, D. Q., Yamamoto, G., Lienish, J. H. J. Atmos. Sci., 19, No. 5, 369, 1962.
9. Kantorovich, L. V. Trudy Matem. Instituta im. V. A. Steklova, 28, 1949.

---

### ULTRAVIOLET RADIATION SCATTERING ( $\lambda$ 1300 Å) IN THE UPPER ATMOSPHERE OF THE EARTH<sup>1</sup> (Summary)

S. A. Kaplan, V. G. Kurt

A two-layer model of the atmosphere with large optical thickness is investigated. The incident solar radiation is scattered without absorption in the first, upper layer. Simple formulas are obtained for the scattered radiation intensity for Doppler and Lorentz profiles. In the first case, the intensity is proportional to  $\sqrt{\lg N}$ ; in the second case, it is proportional to  $\sqrt{N}$ , where  $N$  is the total number of dispersion atoms in the line of sight. Scattering at the sides can provide the observed intensity increase depending on the degree of immersion in the atmosphere.

/112

---

<sup>1</sup> The article was published in the journal "Kosmicheskiye Issledovaniya", 3, No. 3, 237, 1965.

However, the absolute intensity is much less than the observed intensity. The role of absorption by molecular oxygen is taken into account in the lower layer, and it is assumed that the albedo of a single scattering process  $\Lambda$  increases linearly with an increase in optical thickness. A solution is found for the transport equation which is expressed by the Airy function. Its asymptotic expression is found.

The application of the solution to the given atmospheric model shows that the intensity begins to decrease sharply, beginning at an altitude of  $\sim 180$  km. This result closely coincides with the observational data.

---

#### UPPER ATMOSPHERE LAYERS WHICH RADIATE IN THE INFRARED SPECTRAL REGION

M. N. Markov, Ya. I. Merson, M. P. Shamilev

According to current opinions, the emissive atmosphere of the Earth represents a gas envelope with a relatively small thickness  $\sim 30$ - $40$  km. Beyond its boundaries, the gas concentration is so small that there is no significant radiation in the infrared spectral region.

These opinions have been substantiated by computations of the angular distribution of the eigen radiation of the Earth and the atmosphere, which have been performed recently by several authors (Ref. 1, 2). It should be pointed out that the result of all these computations is predetermined to a considerable extent by the formulation of the problem itself, since the assumed model of an emissive atmosphere represents, as was indicated above, a gas envelope  $40$  km thick. In addition, these calculations cannot pretend to be accurate, since at present we do not know the entire characteristics of the radiation and gas absorption spectra under the specific conditions surrounding gases at high altitudes (there has been little research on the composition, temperature distribution, and absorption function, particularly for large atmospheric thicknesses amounting to about  $1000$  km in the direction of the tangent).

The validity of existing concepts regarding the emissive atmosphere can only be demonstrated experimentally.

Throughout 1958-1963, we conducted systematic measurements of terrestrial and atmospheric radiation in cosmic space in the infrared spectral region ( $0.8 - 40 \mu$ ), from altitudes of  $25$  to  $500$  km (Ref. 3-5). The research equipment for these measurements was carried by geophysical balloons and rockets.

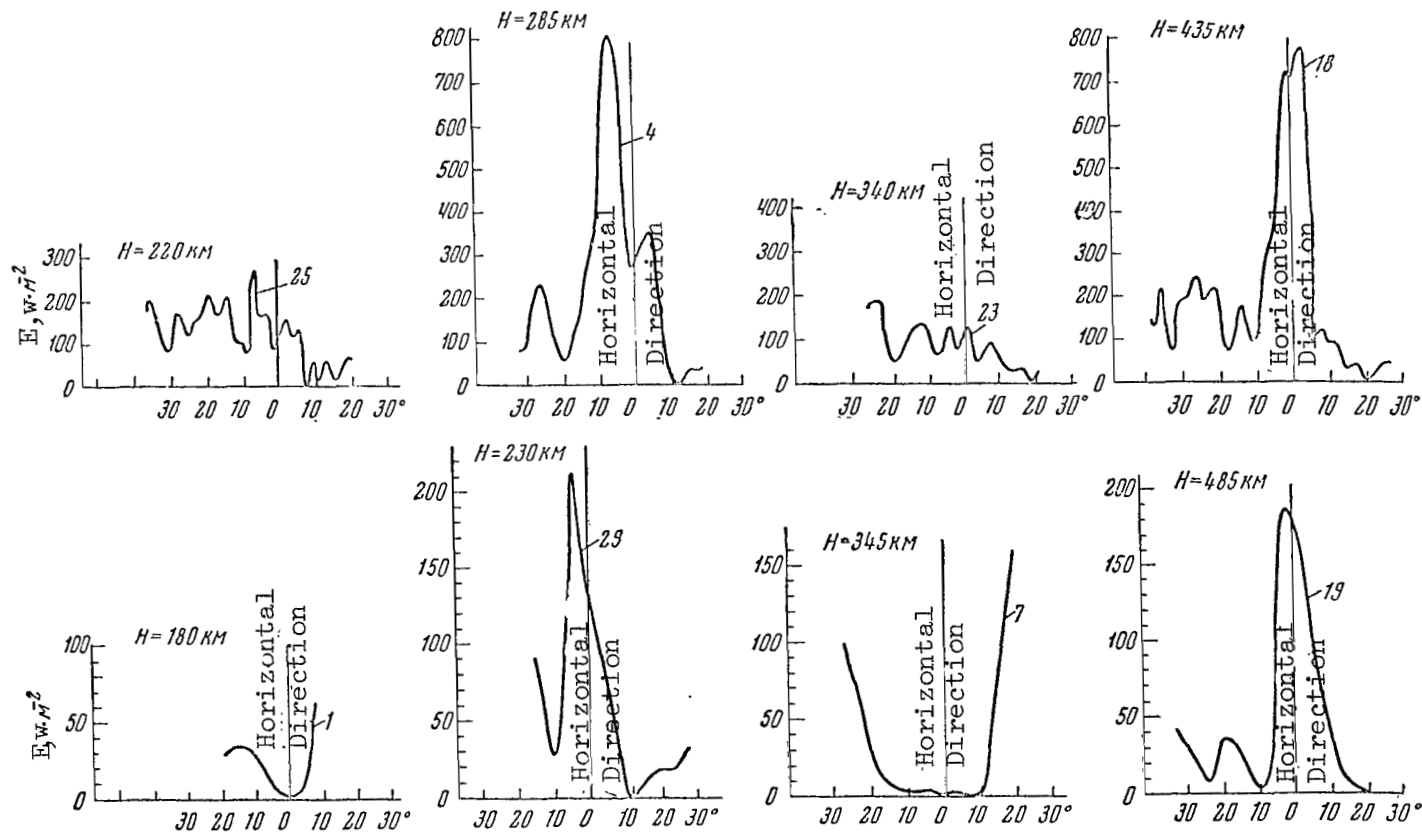


Figure 1

Sections of Angular Radiation Distribution Curves Which Are Adjacent to the Horizontal Sighting Direction at Different Altitudes, Recorded in Experiments on August 27, 1958 (Upper Group) and October 18, 1962 (Lower Group).

The following conclusions were reached from these measurements:

1. Intense infrared radiation is observed from the atmospheric layers located at altitudes above 200 km. We performed the observations during different times of the year (June, August, October) in regions which were several thousands of kilometers apart for a different equipment sighting direction with respect to compass points.

In every case, the upper atmosphere radiation had a maximum intensity in the altitudinal region of 250 - 300, 420 - 450, and about 500 km.

2. The radiation observed at these altitudes was primarily concentrated in the  $2.5 - 8 \mu$  spectral region and in the section of the atmosphere illuminated by the Sun. /114

3. The upper atmospheric radiation has a maximum intensity of  $(3-7) \cdot 10^3 \text{ w} \cdot \text{m}^2$  for sightings in the direction of the tangent, when the radiation is integrated along a line which is on the order of 1000 km long - which corresponds to isotropic radiation of  $1 \text{ cm}^3 - 10^{-3} \text{ erg} \cdot \text{sec}^{-1}$ .

4. The radiation intensity depends upon the influence of solar radiation upon the upper atmosphere, and increases during a period of maximum solar activity.

Figures 1 and 2 show sections of scanning cycles, which are adjacent to the horizontal sighting direction of the optical system for the equipment, which were obtained from different altitudes. As these figures show there are sharply expressed radiation peaks at altitudes of 250 - 300 and 420 - 450 km; these peaks were not observed at other altitudes.

Figure 3 presents curves showing the dependence of the amplitude for radiation coming from a horizontal direction upon the sighting altitude. These curves were obtained during experiments in 1958, 1962, and 1963, and present a more detailed illustration of the observed radiation distribution by altitude. We would like to point out the particular importance of the 1963 experiment, which fully corroborates the results obtained previously; this experiment again recorded radiation at altitudes of 280, 420, and in addition 500 km.

In the 1958 experiments, and particularly in 1963, throughout the entire experiment the equipment was strictly oriented in space with respect to all three axes, and was in the shade of the carrier; this eliminated any possibility of solar radiation directly affecting the equipment. In addition, the effective spectral region was confined to the  $2.5 - 40 \mu$  range in the 1963 experiments.

There should be no possibility that any structural elements of the equipment could produce an error in the recording of the parameter being studied, or that there could be a radiation effect from the carrier elements, since there could be no agreement with the observed altitudinal

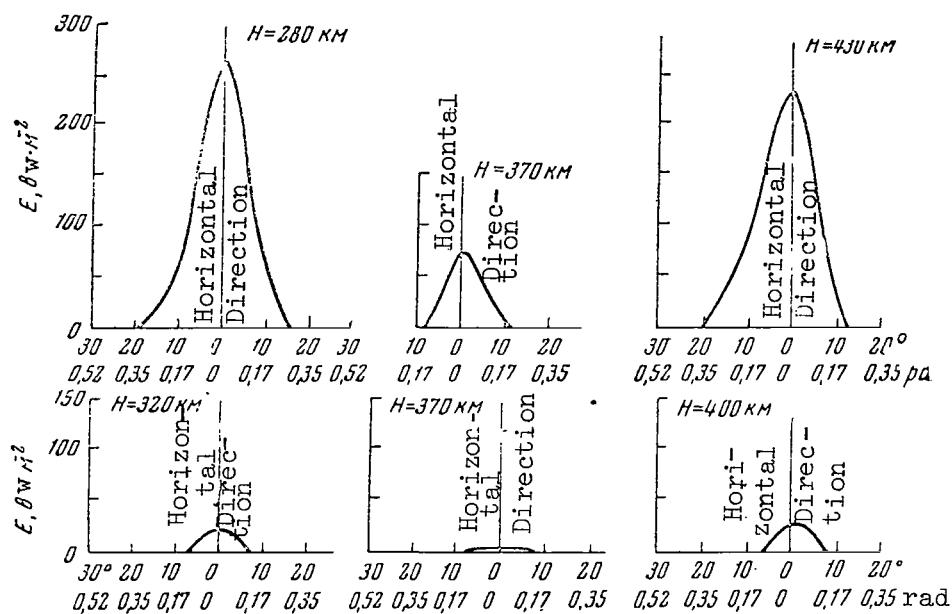


Figure 2

Sections of Angular Radiation Distribution Curves Adjacent to Horizontal Sighting Direction at Different Altitudes Recorded in Experiments on June 6, 1963 (Upper Group) and June 18, 1963 (Lower Group)

pattern of the radiation intensity. Since any influence from the outer environment upon the equipment (for example, heating or luminescence of 115 the lens mount due to recombination processes during a passage at specific altitudes) would naturally not depend on the turning angle of the equipment scanning attachments, structural features of the equipment would naturally be independent of altitude. Radiation of carrier elements could not be constant with respect to the sighting angle of the scanning system and the observational altitude for different carriers employed in our experiments between 1958-1963.

We would also like to note that during all the experiments performed with the same apparatus, except for the fact that it was carried on geophysical balloons and rose only to an altitude of 30 km, no radiation was discovered from the horizontal direction either during the daytime or at night time. However, this radiation was observed every time the apparatus was carried on different types of rockets, on high-altitude geophysical stations (HAGS), and always at the same altitudes. This clearly corroborates the reliability of the apparatus and the validity of the results obtained.



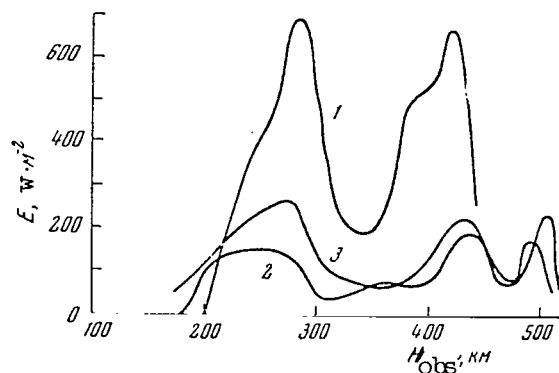


Figure 3

Altitudinal Pattern for Radiation Intensity Maxima in the Angular Region Adjacent to the Horizontal Sighting Direction. Experiments in 1958 (1), 1962 (2), and 1963 (3).

An interpretation of the results obtained lies beyond the framework of this study, since it can only be made by a careful comparison of new results which we have obtained with all other data on atmospheric properties which have been compiled up to the present.

However, we feel it is useful to perform certain calculations, in order to emphasize the possibility of combining the new data which we have obtained with other information on the atmosphere. As of the present, we do not have reliable data on the atmospheric composition at the altitudes in which we are interested (in particular, with respect to neutral compound molecules and radicals of the NO, NH type). In addition, we do not have the absorption coefficients of these gases under highly rarefied conditions and tremendous thicknesses; therefore, it is advantageous to investigate an atmospheric model which does not include absorbed gases between emissive layers. Generally speaking, an entire group of models may be postulated; however, it is considerably more difficult to find criteria for their selection.

It should be emphasized that the altitudinal and angular distributions of radiation can agree only under the assumption that the radiation is localized in definite layers (5-10 km), which are located at certain altitudes close to the upper and lower boundaries of the F ionosphere layer. We shall assume that the thickness of the emissive layers at altitudes of 280, 420 and 500 km is  $\sim 5$  km, and the effective visual angle of the equipment (with allowance for aberration and constant amplifier time) is about  $0.5^\circ$ . On the other hand, there is practically no absorption in the space between the layers. It is then possible to calculate and compile the relative intensity pattern for curves of the angular radiation distribution, assuming that the intensity is proportional to the emissive layer length with allowance for radiation dilution. Figure 4 presents the calculated curves as well as the experimental (1963) curves. These curves

were compiled in accordance with the nature of the scanning system motion for the equipment used to carry out the experiment. During the scanning, the optical system of the equipment moved up to the horizontal position, and then turned back again. Therefore, the curves obtained are symmetrical with respect to the horizontal, and correspond to different directions of motion for the optical systems during scanning. /116

It can thus be seen that there is satisfactory agreement between the calculated and experimental curves for all three observational altitudes (as well as the intermediate altitudes). The small difference between these curves can be explained by the fact that the equipment does not record the fine structure of transitional sections, and on the other hand by the approximate nature of the assumptions advanced during the calculation regarding the size of the layers, their structure, the density distribution in the layers by altitude, etc. Allowance for all of these factors can lead to more precise agreement between the calculated and experimental curves.

We performed additional computations for the model under consideration. These computations showed that for certain reasonable assumptions the experimental data provide judicious values for the temperature in the emissive layers, the number of unbalanced radiation acts, an isotropic radiation stream, etc. /117

(a) Concerning the isotropic stream of radiation detected.

For a layer thickness of 5 km, the length of the emissive gas column along the layer is about 500 km (limited by the curvature of the Earth). Thus, for a measured flux of  $\sim 10^{-2} \text{ w} \cdot \text{cm}^{-2}$ , the volumetric density of the radiation is about  $2 \cdot 10^{-10} \text{ w} \cdot \text{cm}^{-3}$  ( $10^{-3} \text{ erg} \cdot \text{sec}^{-1} \cdot \text{cm}^{-3}$ ), and the isotropic flux of one layer is  $2 \cdot 10^{-10} \text{ w} \cdot \text{cm}^{-3} \cdot 5 \cdot 10^5 \text{ cm} = 10^{-4} \text{ w} \cdot \text{cm}^{-2}$ . Thus, this flux is about 0.07% of the solar constant, and the maximum flux of all the layers can only be several tens of a percent of the solar constant (also of the radiation magnitude of the planet).

(b) Concerning the amount of unbalanced radiation processes.

Assuming that the radiation has a maximum in the spectral region around 3-5  $\mu$ , we have the value  $\sim 5 \cdot 10^{-13} \text{ erg}$  for the quantum energy. In accordance with the standard atmosphere at an altitude of 280 km, we have  $2 \cdot 10^9 \text{ particle} \cdot \text{cm}^{-3}$  (Ref. 6). Thus, 1  $\text{cm}^3$  radiates  $10^{-3} \text{ erg} \cdot \text{sec}^{-1}$ . Consequently, 1 radiation process per second corresponds to the flux which we obtained.

(c) Concerning the nature of radiation detected.

In the spectral region where radiation is primarily concentrated (2.5-8.0  $\mu$ ), there are rotational-fluctuating absorption bands of molecules comprising the atmospheric composition, particularly  $\text{H}_2\text{O}$ ,  $\text{CO}_2$ ,  $\text{N}_2\text{O}$ ,  $\text{NO}$ ,  $\text{CH}_4$ , etc. One of the assumptions regarding the radiation mechanism

stipulates that molecules of atmospheric gas are excited by the solar stream at definite altitudes, and rotational-fluctuating changes in their energy spectrum are caused by the radiation. However, we have no definite data on the neutral composition of the atmosphere at altitudes of 200-500 km. Only the ion composition is known; it comprises a small portion of the total amount of particles (for example, the concentration is about 0.1% at an altitude of 300 km [Ref. 7]). However, if we advance the assumption that the ion composition reflects the concentration of neutral particles to a certain extent, we can then draw the conclusion that NO molecules play a decisive role in radiation (at least at an altitude of 280 km). The concentration of NO ions at altitudes of about 200 km amounts to 50% of the total amount of atmospheric ions in several cases. The NO molecule has an intense absorption band at about  $5.3 \mu$  (according to data in [Ref. 8]). Thus, under these assumptions the concentration of neutral NO molecules in the lower layer can amount to  $10^9 \text{ cm}^{-3}$ , and the total number of emissive particles is on the order of  $500 \text{ km} \sim 10^{17}$  for the path length. Not even these assumptions may be advanced at present regarding the other neutral molecules of the upper atmosphere, which could radiate in the infrared region.

Rough estimates have shown that the effective temperature reaches  $\sim 2000^\circ \text{K}$  for the observed radiation intensity. It should be noted that it is difficult to determine any other temperature, which has a physical meaning with respect to the radiation intensity, since thermodynamic equilibrium (even local equilibrium) is not present under the layer conditions, and also there are no data for the NO absorption function for such large thicknesses and low pressure. The temperature can be obtained from the width of the radiation line, and for this purpose the measurements must be performed with great spectral resolving power ( $10^{-2} \text{ cm}^{-1}$ ).

We cannot exclude the assumption of a more complex mechanism by which atmospheric molecules are excited as a result of photochemical reactions, recombination processes, etc. However, at the present time there is no adequate basis for distinguishing between certain mechanisms. Further studies of the spectral composition, the latitudinal distribution, and other characteristics of the radiation detected are requisite. /118

(d) Concerning possible energy sources exciting the layers, and also indirect data substantiating these sources.

Estimates of the electromagnetic solar radiation energy in different spectral regions show that the requisite fluxes ( $\sim 1000 \text{ erg} \cdot \text{cm}^{-2} \cdot \text{sec}^{-1}$ ) cannot be obtained in the X-ray and ultraviolet spectral regions. On the other hand, the relationship with solar activity indicates that this is not due to excitation by radiation of the visible spectral region.

Thus, it must apparently be assumed that the emissive molecules are excited by corpuscular streams from the Sun. According to data by McIlwain, the corpuscular fluxes reaching an altitude of 100 km comprise several thousands of  $\text{erg} \cdot \text{sec}^{-1} \cdot \text{cm}^{-2}$ , at least during the aurorae polaris

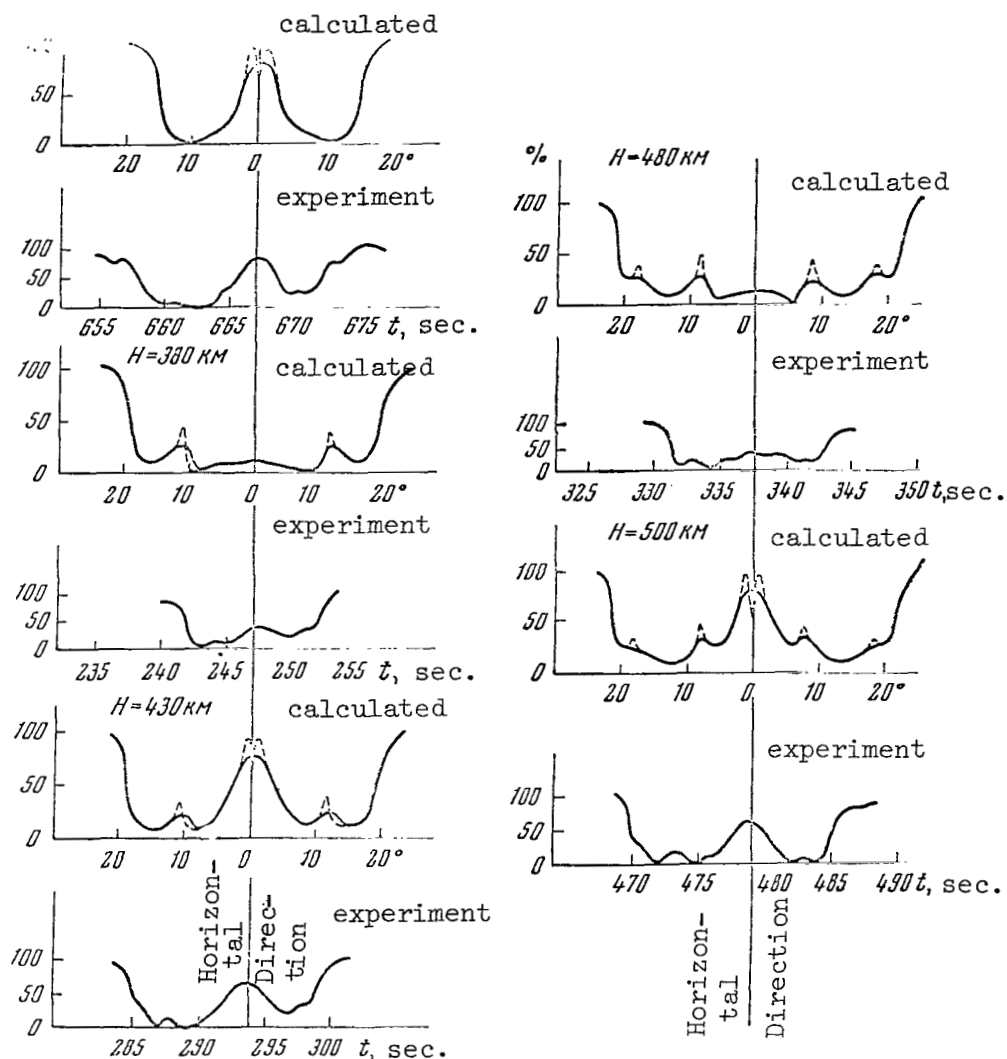


Figure 4

Calculated and Experimental Sections of Angular Distribution Curves  
(in Relative Units of Intensity) For an Experiment on June 18, 1963

(Ref. 9). At the higher regions, the influence of the radiation zones becomes possible (electron fluxes of several hundred of  $\text{erg}\cdot\text{cm}^{-2}$  were recorded in [Ref. 10]). It is interesting to note that according to the data given by C. Störmer (the book "The Aurorae Polaris") the aurorae polaris altitudes are grouped around 300-400 km in the upper atmosphere regions illuminated by the Sun (according to altitudinal observations of more than 10,000 aurorae between 1911-1944).

We have already indicated above the possible dependence of the radiation from high atmospheric layers on solar activity. Since it is natural to assume that processes on the Sun have an influence on the intensity of infrared atmospheric radiation, particularly streams of solar corpuscular

radiation reaching the upper atmosphere of the Earth, we have given the condition of the Sun and the magnetic field of the Earth below (depending on solar activity) for the days when rockets were launched.

Particles and radiation emitted by flocculi and flares occurring close to the central meridian of the solar disc have the greatest effect on the Earth's atmosphere. Therefore, the solar activity, in which we are interested, is characterized by the number and dimensions of the flocculi and flares occurring close to the center of the solar disc.

The number of flocculi was estimated for 5/31-6/1 for the launch on 6/6, and 6/11-12 for the launch on 6/18, since the corpuscular streams emitted from the flocculi region are comparatively soft, and reach the Earth in 6-7 days. Their influence on the Earth's atmosphere is primarily confined to high altitudes (1000 km and above).

The number of flares was estimated for 6/3-4 for the experiment on 6/6, and for 6/15-16 for the experiment on 6/18. This is due to the fact that particles emitted during flares are considerably harder.

Finally, ultraviolet and X-ray radiation is emitted during flares. This can be characterized by the number and intensity of flares at the launch time.

The condition of the Earth's magnetic field at launch time is characterized by the  $K_p$ -index - the planetary index of the magnetic field.

Experiment on August 27, 1958.

Sun. A storm related to a flare was observed for two days before and during the experiment; Earth.  $K_p = 4-5$ .

Experiment on June 6, 1963.

Sun. May 31-June 1 - small number of flocculi; June 4 - one very weak flare; June 6 - no flares; Earth.  $K_p = 0$  between June 4-6.

Experiment on June 18, 1963.

Sun. June 11-12 - significant number of flocculi; there were six flares for two days before this; Earth.  $K_p = 3.5$  on June 18, which indicates perturbation of the magnetic field.

The graphs shown in Figures 2-4 show that in 1958 - the year of /119 maximum solar activity - there was considerably greater radiation from the higher upper atmosphere layers than during the 1962-1963 experiments - during years of a quiet Sun. In the 1963 experiments the radiation of the upper atmosphere layers on June 18 was considerably higher than on June 6, when it was insignificant.

It can thus be stated that (naturally, taking the fact into account that there are still very few measurements) there is a correlation between the infrared radiation of the upper atmosphere and flares close to the central meridian of the solar disc.

In our opinion, the research results are very important for formulating an opinion regarding the Earth's atmosphere. It is naturally impossible to indicate all the areas where we may employ the new data on the existence of upper atmosphere emissive layers, but several of them may be clarified:

(a) Determination of the qualitative and quantitative composition of upper atmospheric gases (variable component) according to their radiation spectrum; (b) Verification of the hypothesis regarding the nature of the Earth's ionosphere; (c) Determination of temperature distribution in the thermosphere according to intensity and width of the radiation spectral lines.

#### REFERENCES

1. Kondrat'yev, K. Ya., Yakushevskaya, K. Ye. In "Iskusstvennyye Sputniki Zemli". Izdatel'stvo AN SSSR, No. 14, 1962.
2. Makgi. "Computational Model of the Earth's Atmosphere Which Radiates in the Infrared Spectral Region" (Raschetnaya model' atmosfery Zemli, izluchayushchey v infrakrasnoy oblasti spektra).
3. Liventsov, A. V., Markov, M. N., Merson, Ya. I., Shamilev, M. R. Doklady AN SSSR, 146, No. 2, 1962.
4. Aver'yanov, I. P., Kasatkin, A. M., Liventsov, A. V., Markov, M. N., Merson, Ya. I., Shamilev, M. R., Shervinskiy, V. Ye. In "Iskusstvennyye Sputniki Zemli". Izdatel'stvo AN SSSR, No. 14, p. 49, 1962.
5. Markov, M. N., Merson, Ya. I., Shamilev, M. R. Kosmicheskiye Issledovaniya, 1, No. 2, 235, 1963.
6. Kondrat'yev, K. Ya. Meteorological Studies with Rockets and Satellites (Meteorologicheskiye issledovaniya s pomoshch'yu raket i sputnikov). Leningrad, Gidrometeoizdat, 1962.
7. Mirtov, B. A. Gaseous Composition of the Earth's Atmosphere and Methods of Analyzing It (Gazovyy sostav atmosfery Zemli i metody ego analiza). Moscow, Izdatel'stvo AN SSSR, 1961.
8. Gillete, R. H., Eyster, E. H. Phys. Rev., 56, 1113, 1939.
9. In "Upper Atmosphere Research Using Rockets and Satellites". Edited by G. S. Ivanov-Kholodnyy. IL, 1961.
10. Gal'perin, Yu. I., Krasovskiy, V. I., Dzhordzhio, N. V., Mulyarchik, T. M., Bolyunova, A. D., Temnyy, V. V., Marov, M. Ya. Kosmicheskiye Issledovaniya 1, 126, 1963.

II

IONOSPHERE OF THE EARTH

The present section includes reports containing the results derived /122 from a different type of research, primarily conducted in the outer atmosphere by means of AES and rockets up to altitudes of 2000-3000 km and above. The different data characterize the electron concentration (altitudinal distribution, spectra of heterogeneous formations, fluctuations), the ion composition, their total concentration and temperature, etc. in the ionosphere. Some reports include the results derived from measuring the spectra of low-energy electron fluxes in the ionosphere, their angular distribution at different altitudes and longitudes, data on the high-energy proton distribution, etc.

A small number of reports on radiowave propagation supplements this group of problems.

The authors themselves selected the summary, as well as the data from the international literature which are presented in certain reports, the systemization of these data, and their interpretation.

The overwhelming majority of the reports are purely experimental in nature. Different methods were employed, such as the probe method (mass spectrometers, electron indicators, charged particle traps, electron multipliers, Geiger counters), and radio physical research methods, particularly employing coherent radio waves. Radio research comprises a significant portion of the studies included in this section.

Among the experimental results given in the reports, we would like to point out, for example, measurements of the outer ionosphere composition showing that during the observational period (1964) there was a rapid change from atomic oxygen ions to atomic hydrogen ions (in the 900-1200 km region) with a negligible helium content in the outer atmosphere. We would also like to point out new data on the altitudinal-heterogeneous structure of the outer ionosphere. Electron concentration maxima were found (possibly, short-lived), the complete spectra of heterogeneous formations were obtained for the first time, etc. It is interesting to note the results derived from measuring the angular distribution of low-energy electrons in different regions of the Earth, particularly in the southern anomaly region.

It is well-known that Soviet scientists were the first to obtain results on the ionosphere composition by means of mass spectrometers, on the ion concentration by means of probes ("traps"), and on the electron concentration behavior in the outer ionosphere by means of radiowaves. Soviet scientists were also the first to obtain data on streams of low-energy corpuscles. The ionosphere investigations presented at the conference have led to the discovery of several very important facts. Particularly, one fundamental fact which was noted above, is that atomic hydrogen ions represent the main ionosphere component above 1000-1200 km. These results, which are given in one of the reports, as well as other new data are on a level with present day research.



One of the most important problems of future research is the continuation of all types of experiments at great distances from the Earth's surface in order to obtain the altitudinal dependences of physical quantities which we are here discussing. Research on the region where the atmosphere of the Earth changes into the interplanetary medium is thus of fundamental importance.

Concurrent measurements of different quantities by employing different methods on one craft represent another important task. For example, in light of results which have been obtained it is absolutely requisite to perform concurrent measurements of concentration and composition of particles, the energy spectra of electrons and ions in very low energy regions - beginning from 10-100 ev - temperature, and other quantities. The time appears to be approaching when the foundation provided by experiments with AES will make it possible to formulate a theory for the formation of the ionosphere which will be more comprehensive than the theories existing today and which will encompass the main complex of phenomena occurring in the ionosphere.

# ALTITUDINAL-TIME DISTRIBUTION OF THE ELECTRON CONCENTRATION AND NONUNIFORM FORMATIONS OF THE OUTER IONOSPHERE

Ya. L. Al'pert, V. M. Sinel'nikov

## 1. Theoretical Premises

The method which we have employed in recent years to study the ionosphere by means of coherent radio waves emitted from an artificial Earth satellite (Ref. 1, 2), as well as certain results derived from these studies, are given in (Ref. 3-5). The difference, measured in these experiments, between Doppler frequency shifts  $\delta\dot{\Phi}(t)$  of two coherent radio waves at any point on the Earth's surface is directly related to the velocity components of the emitter, the electron concentration of the ionosphere, and its spatial-time changes. In general form, the formula for  $\delta\dot{\Phi}(t)$  is given, for example, in the work (Ref. 5). /123

The curves  $\delta\dot{\Phi}(t)$ , formulated on the basis of continuous recordings of the phase difference of  $\delta\Phi(t)$  - in many cases, throughout the entire observational period, or only in a certain portion of it and not at all points - have nonregular quasi-periodic variations with periods from fractions of a second to several tens of seconds (Fig. 1-3). These changes in  $\delta\dot{\Phi}(t)$  - i.e., deviations in the curve  $\delta\dot{\Phi}(t)$  from a flat pattern - are caused by the "cloudy" structure of the ionosphere - namely, by its small- and large-scale nonuniformity. In certain cases, they may be possibly caused by the nonstationary nature of the electron concentration throughout the time intervals equalling the variation periods of  $\delta\dot{\Phi}(t)$ . This can be readily seen from a general formula connecting the measured quantity  $\delta\dot{\Phi}(t)$  with quantities characterizing the electron concentration and with the velocity components of the emitter at each fixed moment of time  $t$  (see [Ref. 5]). It can be shown from analyzing this formula that, as the emitter passes along the orbit above the observational point, the velocity components of the emitter  $\dot{r}_c$  and  $\dot{z}_c$  change so that  $\delta\dot{\Phi}(t)$  has the largest positive value during the ascent of the AES. Then, decreasing smoothly, as the observational point is approached it passes close to it through the point  $\delta\dot{\Phi}=0$ , and then - /124  
increasing in terms of absolute magnitude - it reaches a maximum negative value at the moment of descent. This is achieved if  $N = N(z)$  - i.e., if  $N$  is only a function of altitude, or if no significant role is played by the quantities taking into account the dependence of  $N$  on the horizontal coordinates  $x, y$ , and the time  $t$  - i.e.,

$$\int \frac{\partial N}{\partial x} z dS, \int \frac{\partial N}{\partial y} z dS \text{ and } \int \frac{\partial N}{\partial t} dS,$$

However, it can be seen from the curves shown in Figures 1-3 that, although the general nature of the expected change in  $\delta\dot{\Phi}(t)$  is retained, the quasi-periodic changes, caused by the influence of the horizontal gradients

$N(x,y,z)$ , are superimposed upon it.

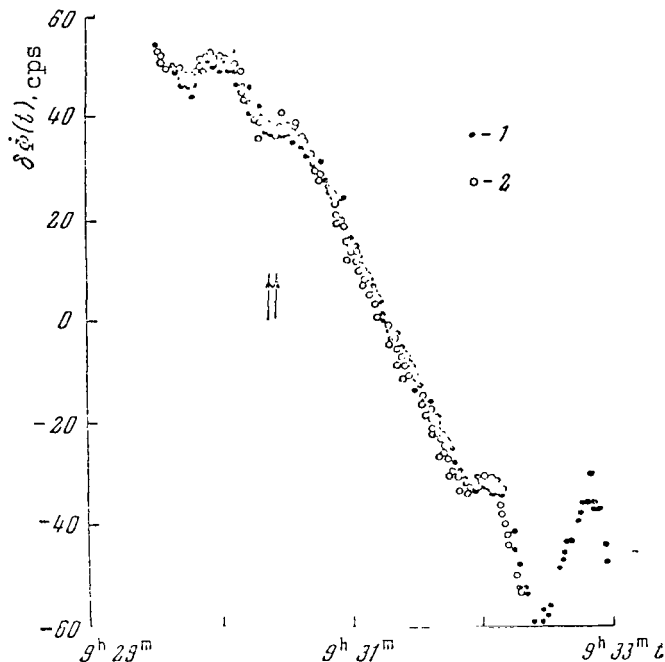


Figure 1

Comparison Of the Results Derived From Measuring the Difference  
In the Doppler Frequency Shifts  $\delta\dot{\varphi}(t)$  At Two Points In the  
Vicinity Of Moscow (1,2) According to Data From "Elektron-1"  
On March 14, 1964

When analyzing the curves  $\delta\dot{\varphi}(t)$ , we start with the following assumption, which we believe is dictated by simple physical concepts regarding the ionosphere properties: the lifetime of nonuniform formations, their diffusion at different altitudes, the drift of the nonuniformities, and regarding similar phenomena occurring in strongly-rarefied ionosphere plasma. Just as was done in previous studies (Ref. 3, 5), we assume that each quasi-periodic change in  $\delta\dot{\varphi}(t)$ , recorded in the form of a continuous recording of  $\delta\dot{\varphi}(t)$ , is primarily and most frequently caused by the local change in the electron concentration - i.e., when the emitter intercepts a nonuniform formation along the AES orbit. Then  $T_0/2$  characterizes the linear dimension  $\rho_0$  of the nonuniformity, and the deviation of  $\Delta(\delta\dot{\varphi})$  represents the change in electron concentration (see Figure 3) - i.e., the quantity  $\Delta N \sim N_d - N_0$ , where  $N_0$  is the unperturbed value of  $N$ . /125

Thus, we start with the following assumption. In the first place, we assume that along the line of sight, the gradients  $\frac{\partial N}{\partial x}$  and  $\frac{\partial N}{\partial y}$ , changing in terms of

magnitude and sign, are balanced on the average under the integral sign. This is connected with the fact that in the ionosphere one of the nonuniformities is continuously replaced by another, due to their small lifetime, and the drift of nonuniform formations occurs in different directions at different altitudes. We can thus mathematically assume that the corresponding integrals can be replaced by integrals with respect to a limited region in the vicinity of the emitter orbit. It must be kept in mind that this assumption does not exclude the fact that the local influence of the nonuniformity is not manifested along the orbit, but rather in any narrow, disturbed region of the ionosphere, which is fairly stable with respect to altitude, below the altitude of the emitter. Naturally, the validity of this assumption can be mainly demonstrated on the basis of experimental data. A general theoretical proof of this assumption - or, on the other hand, refutation of it - cannot be sufficiently valid, because it depends on the specific form of the dependence of electron concentration gradients on altitude. On the other hand, the experimental data obtained on this basis can in themselves contain several arguments which refute, or - on the other hand, which coincide with - the assumption employed. We have advanced the corresponding arguments in favor of this assumption in previous works (Ref. 3, 5). However, the most reliable proof of this assumption will be a comparison of the data obtained on the non-uniform structure of the ionosphere with the corresponding data obtained by means of other measurement methods under similar conditions.

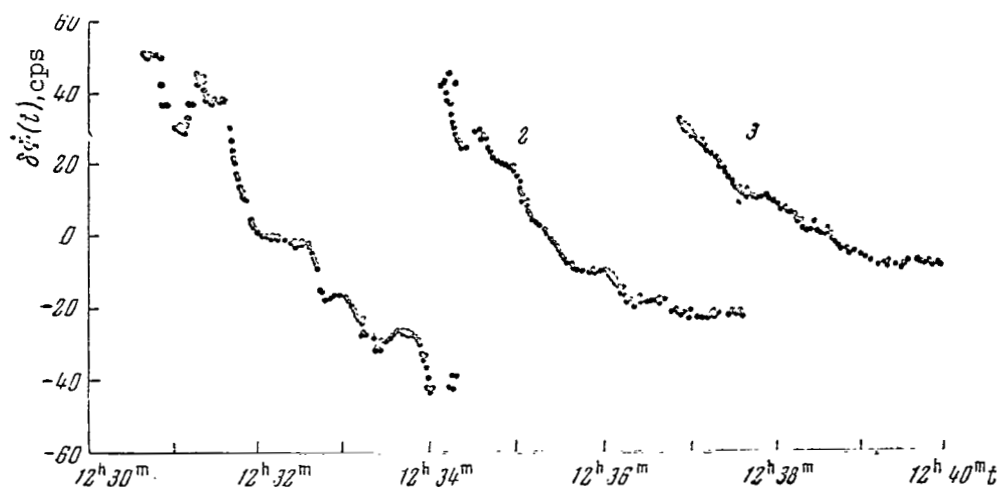


Figure 2

Dependence Of  $\delta\dot{\phi}(t)$  Obtained In Moscow (1), Sverdlovsk (2),  
And Novosibirsk (3) During One Revolution ("Elektron-1",  
March 2, 1964)

In the second place, with the processing method employed we did not distinguish between the effect of changes in  $\frac{\partial N}{\partial t}$  with time along the wave

trajectory. This is related to the fact that, in those cases when  $\int \frac{\partial N}{\partial t} dS$  causes rather rapid variations in  $\delta\dot{\phi}(t)$ , they appear on this curve as  $\delta\dot{\phi}(t)$  during the brief influence of  $\frac{\partial N}{\partial t}$ , just like the influence of a nonuniform formation. It is hardly possible to individualize these variations in time, or to determine what ionosphere regions they encompass. However,  $\int \frac{\partial N}{\partial t} dS$  /126 is a slowly changing term in the equation for  $\delta\dot{\phi}(t)$  (see [Ref. 5]), since it does not depend on the velocity component and only slightly influences the general nature of the change in the function  $\delta\dot{\phi}(t)$  with time. The nature of this change is primarily determined by the rapid change in the velocity component of the emitter when it passes above the observational point.

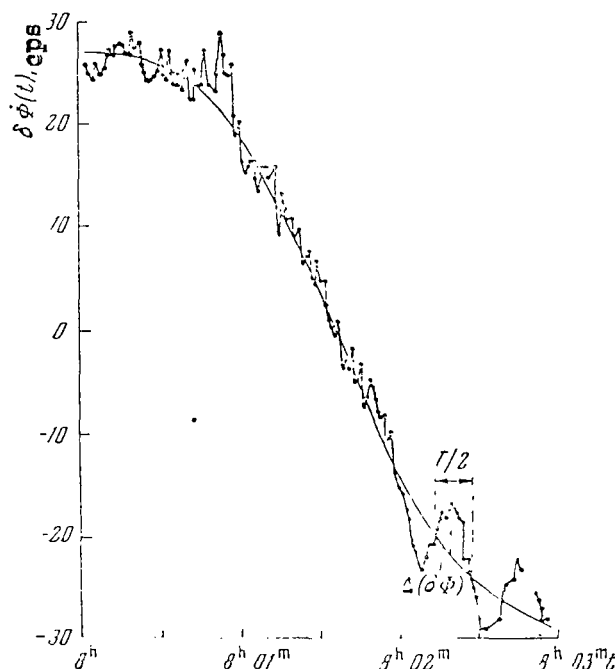


Figure 3

Example Of the Dependence Of  $\delta\dot{\phi}(t)$  With Rapid Quasi-periodic Changes. Moscow, "Elektron-1", March 19, 1964

Assuming that the quasi-periodic changes in  $\delta\dot{\phi}(t)$  are primarily caused by local changes in the electron concentration  $N_d$ , we find that the linear dimension of the nonuniform formation intercepted by the emitter is (see Figure 3):

$$l_0 = V_0 T. \quad (1)$$

Such a determination of  $\rho_0$  is chosen conditionally, keeping the fact in mind that if the wave origin is nonuniform, then its wave length is  $\Lambda = V_0 T$ , and not  $V_0 T/2$ . In addition, we can write the dependence of the electron concentration in the nonuniform formation under consideration in the following form

$$N = N_0(z) + N_d(x, y, z).$$

Not restricting ourselves to the magnitude of  $N_d$  as compared with  $N_0$ , and assuming that

$$N_d = N_{d0} \cos \frac{(z_c - z) \pi}{2\rho_z} \cos \frac{(x_c - x) \pi}{2\rho_x} \cos \frac{(y_c - y) \pi}{2\rho_y}$$

for  $\rho_0 \ll z_c$  and the isotropic nonuniformities

$$\rho_x = \rho_y = \rho_z = \rho_0/4 \ll z_c,$$

we obtain the following formula, which determines  $N_{d0}$  (see [Ref. 6]): /127

$$\Delta(\delta\Phi)_d = \frac{\omega}{c} \frac{2\pi e^2}{m} \left( \frac{1}{\omega_2^2} - \frac{1}{\omega_1^2} \right) N_{d0} \left\{ -\frac{\dot{z}_c}{\cos \varphi_c} + \left[ \frac{\rho_0}{2\pi z_c} \frac{\cos \frac{\pi}{2} \frac{x_c}{z_c}}{\pm 1 \mp \left( \frac{x_c}{z_c} \right)^2} - \right. \right. \\ \left. \left. - (\sin \varphi_0 \cos \varphi_0)^{-1} \frac{\frac{x_c}{z_c} - \sin \frac{\pi}{2} \frac{x_c}{z_c}}{\pm 1 \mp \left( \frac{x_c}{z_c} \right)^2} \right] \left( \dot{r}_c + \frac{\dot{z}_c}{\cos \varphi_c} \right) \right\}, \quad (2)$$

where the signs  $\pm$  in the denominator are selected according to the following values  $x_c/z_c \leq 1$  and  $x_c/z_c > 1$ .

In the formulation of the curves  $\delta\dot{\Phi}(t)$  we have employed the following fact. When the emitter passes above the observer at each orbital revolution, there is a point at which

$$\left( \dot{r}_c + \frac{\dot{z}_c}{\cos \varphi_c} \right) = 0. \quad (3)$$

Here  $\dot{r}_c$  and  $\dot{z}_c$  represent the radial and vertical velocity components of the AES, respectively;  $\varphi_c$  - the angle between the line of sight and the normal to the Earth's surface from the point  $c$ , where the emitter is located at a given moment. At the point where condition (3) is satisfied, the formula connecting  $\delta\dot{\Phi}$  with the ionosphere parameters is significantly simplified. In the stationary case ( $\frac{\partial N}{\partial t} \sim 0$ ), we have:

$$\delta\dot{\Phi} = \frac{\omega}{c} \frac{2\pi e^2}{m} \left( \frac{1}{\omega_2^2} - \frac{1}{\omega_1^2} \right) \left\{ -N_c \frac{\dot{z}_c}{\cos \varphi_c} + \dot{y}_c \frac{R_0}{R_c} \int_{R_0}^{R_c} \frac{\partial N}{\partial y} \frac{x}{x_c} \frac{dR}{\cos \varphi_c} \right\} \quad (4)$$

where  $\omega_1$  and  $\omega_2$  represent two of the emitter coherent frequencies ( $\omega_1 > \omega_2$ );  $\omega$  - the frequency at which the quantity  $\delta\dot{\Phi}$  is recorded (in our device  $\omega = 180.045$  Mc);  $R_0$  - radius of the earth;  $R_c = R_0 + z_c$  - radius vector connecting the center of the Earth with the point  $c$ ;  $x$  and  $x_c$  - horizontal spherical distances to the normal (radius vector  $R_c$ ) in the incident plane from each point, respectively, along the line of sight to the surface of the

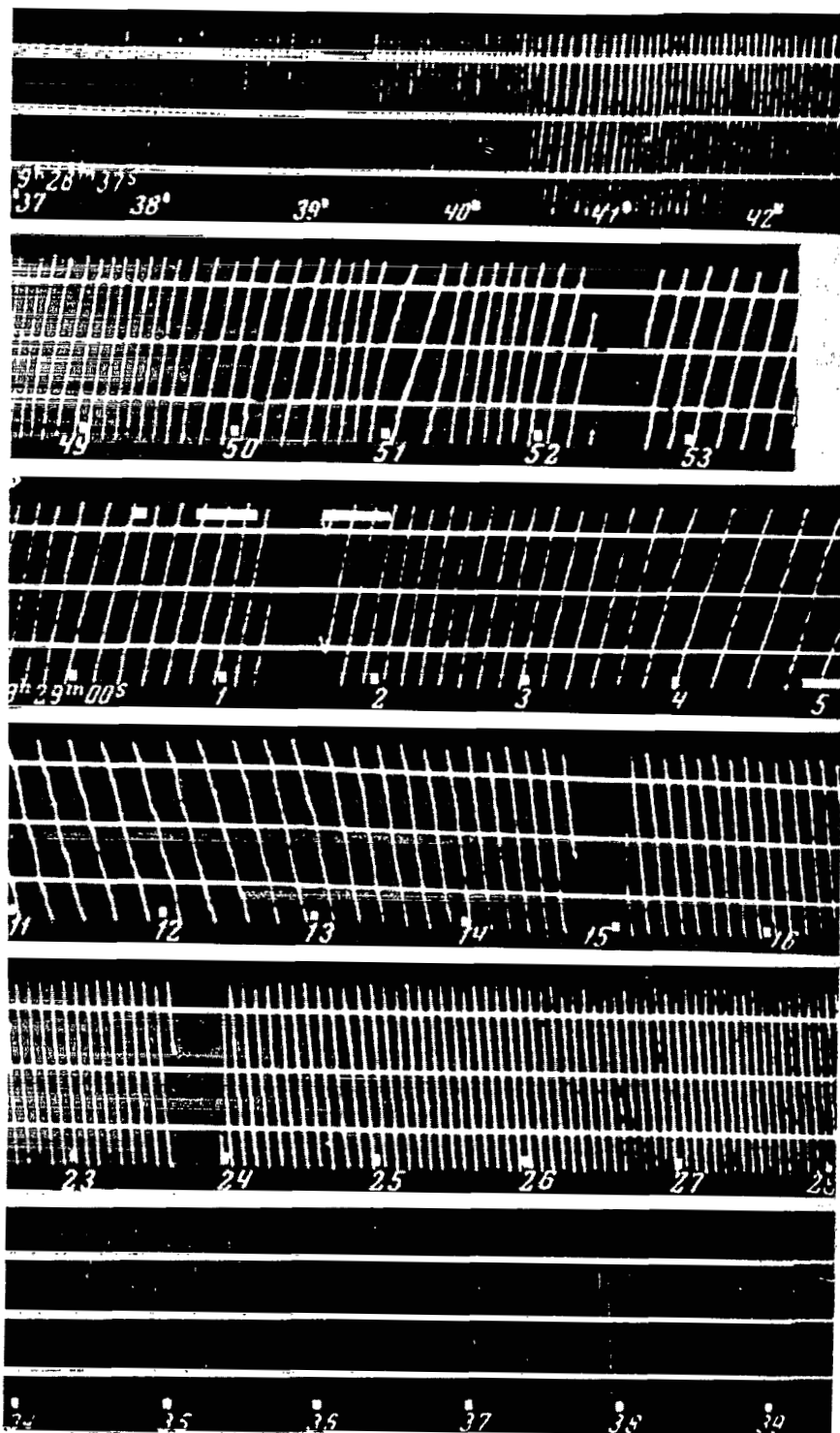


Figure 4  
 Photo-Oscillogram of  $\delta\dot{\phi}(t)$  When the AES Passed Over the Observational  
 Point In Moscow, "Elektron-1", March 18, 1964

/128

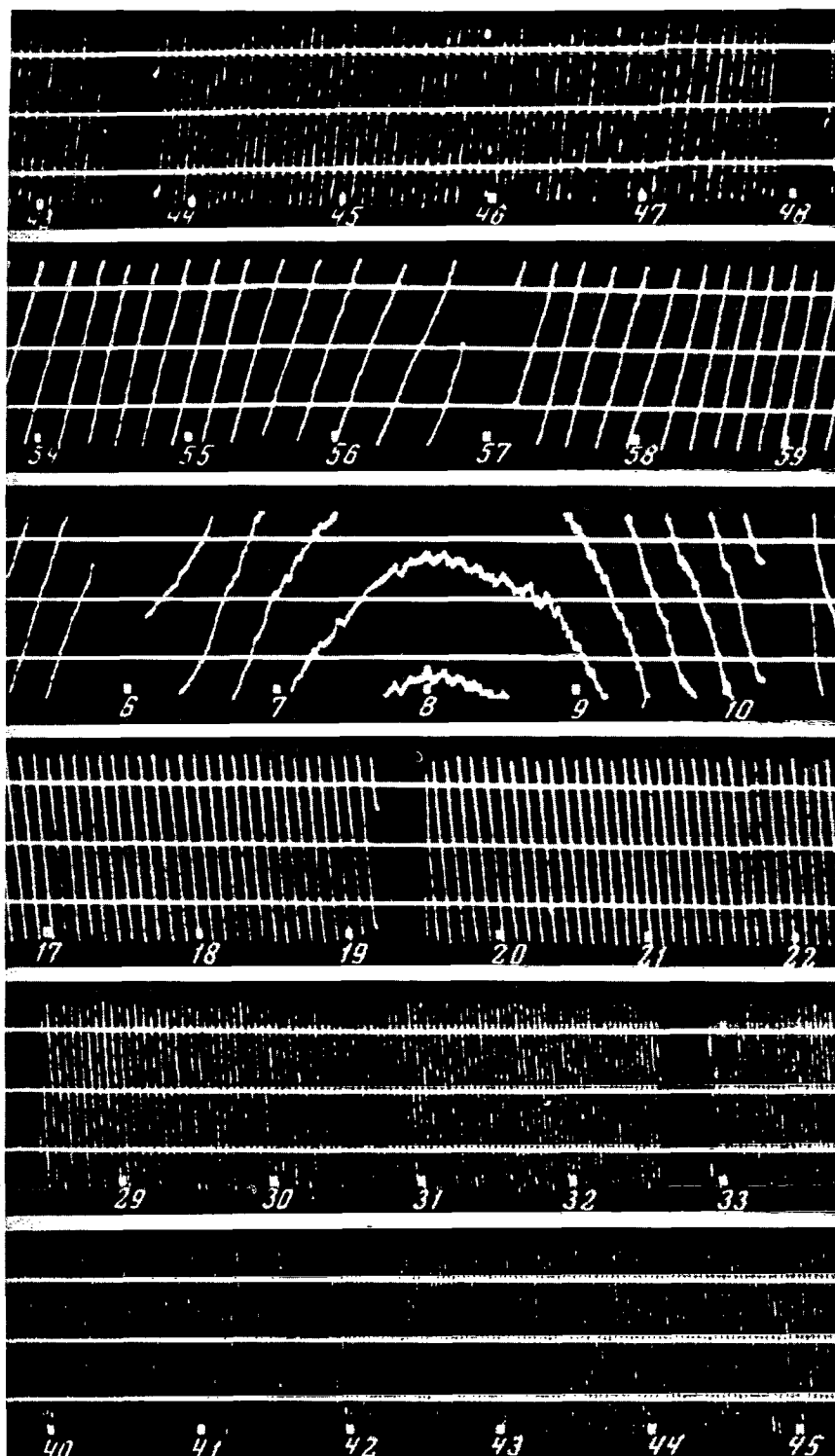


Figure 4  
(Continuation)



Earth:  $\frac{\partial N}{\partial y}(z)$  is the horizontal gradient of the electron concentration along the line of sight in a direction normal to the incident plane. If the second component is excluded from (4), which is generally assumed in many cases (see, for example, [Ref. 5]), then - at the moment when condition (3) is fulfilled at the observational point - the recorded quantity  $\delta\phi$  directly determines the local electron concentration  $N_c$  around the source, i.e., for  $\omega_2 = 20.005 M_c$  and  $\omega_1 = 90.0225 M_c$ , in our formulation we have

$$N_c (c.u^{-3}) = \delta\phi (\text{cps}) \left[ - \frac{\dot{z}_c (k.u.s^{-1})}{\cos \varphi_c} \right]^{-1} \cdot \frac{10^5}{5.7}. \quad (5)$$

Some results derived from determining the electron concentration  $N_c$  by means of a "shortened" formula (5) are given below. These results are based on  $\delta\phi$  measurements in Moscow, Sverdlovsk, Novosibirsk, and partially in Tbilisi, of emission from the radio station "Mayak" placed on the AES "Elektron-1". Altitudinal curves  $N_c(z, t)$ , which are investigated below, were constructed for the 430-1800 km altitudinal range. During the observational period from February 1 to March 27, 1964, 52 curves of  $\delta\phi(t)$  were obtained in Moscow; 78 - in Sverdlovsk; and 45 in Novosibirsk. On the basis of these curves, about 7,000 values for  $\rho_0$  were determined for the  $\rho_0 \simeq 1-400$  km range. The smallest values of  $\rho_0$ , which can be conveniently analyzed from photo-recordings, are approximately  $\sim 1$  km (this corresponds to  $T_0/2 \sim 0.1$  sec).

The maximum electron concentration deviations in nonuniform formations /130

$$\delta N = \frac{\Delta N}{N_0} = \frac{N_{d0} - N_0}{N_0} \quad (6)$$

were calculated by means of formula (2). The measurement results were processed for only 41 observational periods in Moscow for  $\rho_0 \leq 50$  km. These results are presented below.

## 2. Description of Results

Figures 1-3 present the curves for  $\delta\phi(t)$ , based on photo-oscillogram processing of  $\delta\phi(t)$ . Figure 4 presents an example of such a photo-oscillogram. Figure 1 presents a portion of a simultaneous observation period near Moscow at 2 points which were several tens of kilometers apart. The AES orbit in this case was such that for both points the times at which the condition  $(\dot{r}_c + \dot{z}_c / \cos \varphi_c) = 0$  was fulfilled almost coincided (see the vertical arrows in Figure 1, on the time axis). It can be seen from Figure 1 that the values of  $\delta\phi$  at both points (dots and crosses) very closely coincide. This agreement in the behavior of  $\delta\phi(t)$  for both Moscow points is almost always observed. The dependences of  $\delta\phi(t)$  recorded for one and the same AES revolution in Moscow, Sverdlovsk, and Novosibirsk (see Figure 2) show that, at sections of the curves  $\delta\phi(t)$  corresponding to one and the same observational time, the variation in the  $\delta\phi(t)$  behavior is almost always the same at different points. Random, quasi-periodic variations in  $\delta\phi(t)$  can be seen in Figure 3.

The dependences  $N_c(z,t)$  and  $N_c(z,t)$  in Figure 5 and 6 were formulated on the basis of the electron concentrations  $N_c$  determined by means of formula (5) according to photo-oscillograms of  $\delta\phi(t)$  recorded in Moscow, Sverdlovsk, Novosibirsk and Tbilisi. For Moscow, the observational times pertained primarily to 12-13 hours; for Sverdlovsk - to 10-14 hours; and for Novosibirsk - to 12-15 hours local time. The measurement results in Tbilisi were significantly less; they were employed to formulate the dependence  $N_c(z,t)$  for  $z = 1100 - 1800$  km. The main values of  $N_c$ , obtained at all the points, pertained primarily to points located to the north of the observational points at distances of 200-600 km (see [Ref. 7]).

The set of values for  $\rho_0$  and  $\delta N$  was processed statistically for the altitudinal regions of  $\Delta z_c = 100$  km. However, an examination of the data shows that the magnitude of  $\rho_0$ ,  $\delta N$  changes slightly through these altitudinal regions. In addition, there are few data for the altitudes  $z_c > 1200$  km. Therefore, the corresponding dependences are primarily formulated for two altitudinal regions of  $z_c = 400-800$  and  $800-1200$  km. These data are primarily recorded in a time interval of  $\pm 1$  hours with respect to midday (Ref. 6).

The dependence  $N_c(z,t)$  of the electron concentration  $N_c$  on altitude is shown in Figure 5 (see [Ref. 7]). For Moscow (dots and solid lines) and Sverdlovsk (crosses and dashed line), the curves for  $N_c(z,t)$  are somewhat distorted by the cross-averaging of individual  $N_c$  values for discrete altitudinal regions of 30-40 km. The results derived from measurements in Novosibirsk are smaller, and therefore each of the  $N_c$  values obtained for it are plotted directly in Figure 5 (triangles). In addition, the relative behavior of  $N_c(z,t)$  at an altitude below 400 km, based on observational results from the AES "Kosmos" in 1962 (crosses) (see [Ref. 5]), as well as the mean behavior of  $N(z)$  in the lower ionosphere (dot-dash line) based on data [131] from an ionosphere station, are plotted in Figure 5.

It can be seen from Figure 5 that the dependence  $N_c(z,t)$  has several alternating maxima and minima. They closely coincide with each other for all three points. The distance between the maxima and minima following one behind the other changes between 120-160 km. The deepest minimum is at an altitude of  $z_c \approx 620-630$  km. In the lower portion, the curves for  $N_c(z,t)$  have one maximum. This first maximum of  $N_c(z,t)$ , which is located above the main ionosphere maximum of  $N_{\text{max}F^2}$ , closely coincides with the maximum of  $N_c(z,t)$  which we observed previously during similar processing of  $N_c$  measurement results from the AES "Kosmos" for several days in April, 1962 (see [Ref. 5]). The general tendency of  $N_c$  to decrease with altitude (see Figure 5) - if it is described by the secant curve which averages the quasi-periodic changes in  $N_c(z,t)$  (curve a), or by the tangent to the minima of  $N_c(z,t)$  (curve b) - closely coincides in general with the individual altitudinal curves of  $N(z)$  obtained at different points for definite moments in time by means of a high-altitude rocket (Ref. 8), the AES "Alouette" (Ref. 9), and also by noncoherent radio wave scattering in the ionosphere (Ref. 10).

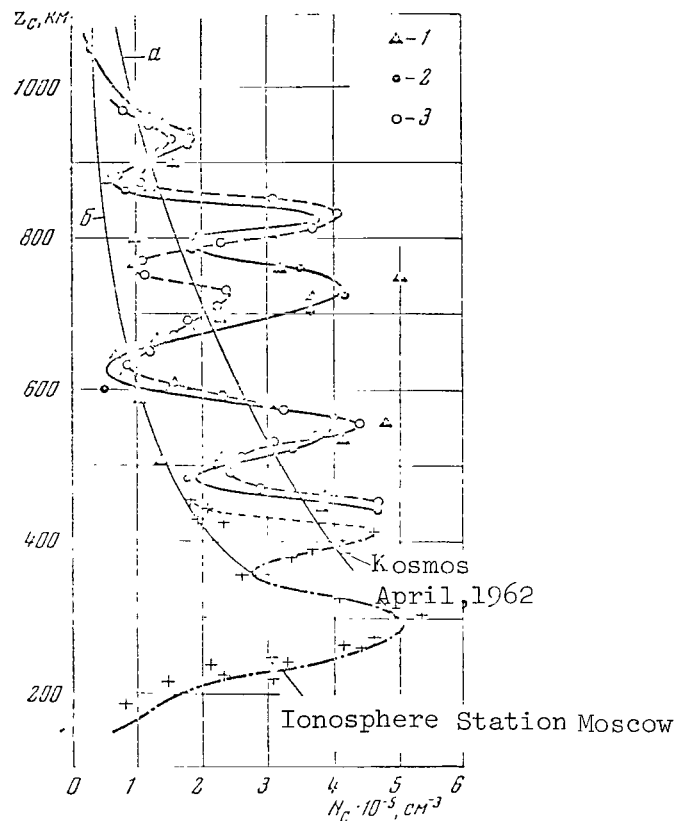


Figure 5

Dependence Of Unit Values Of the Electron Concentration  $N_c(z, t)$  On Altitude, Based On Data From "Elektron-1", February 17-March 27, 1964

1 - For Novosibirsk; 2 - for Moscow; 3 - for Sverdlovsk

The averaging of all values for  $N_c$  over large altitude regions  $\Delta z \approx 100$  km leads to an averaged, smoothed curve for  $N_c(z, t)$ , in which there is only one clearly expressed maximum above the main maximum of the ionosphere  $N_{\text{max}F_2}$  at an altitude of  $z_c \sim 800$  km, and a minimum at an altitude of 600 km. The corresponding curve is shown in Figure 6. For purposes of comparison, the individual curves for  $N(z)$  are plotted in this figure; they were obtained recently by noncoherent scattering of radio waves (Ref. 10) by means of the ionosphere impulse station on the AES "Alouette" (Ref. 9). The curves for  $N_i + (z)$ , obtained by means of a high altitude rocket (Ref. 11), are also plotted in this figure. Results derived from measurements in Tbilisi above 1100 km are utilized in this figure.

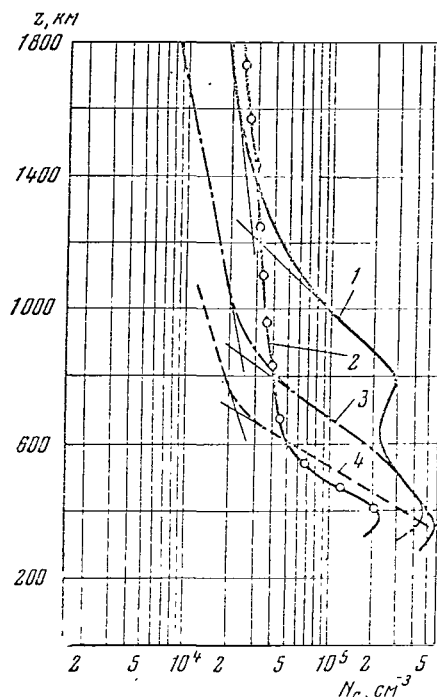


Figure 6

Smoothed Dependence of Electron Concentration  $N_e(z, t)$  According to Data from "Elektron-1", and Altitudinal Dependences of  $N_e(z)$  and  $N_i^+(z)$  Obtained in Other Experiments

1 -  $\overline{N_e(z, t)}$ , 10 hours-15 hours, February-March, 1964, "Elektron-1";  
 2 -  $N_i^+(z)$ , 1 hour 7 minutes, April 12, 1961, rocket, Cape Canaveral (Ref. 11); 3 -  $N(z)$ , 14 hours 55 minutes, September 5, 1964, noncoherent scattering, Peru (Ref. 10); 4 -  $N(z)$ , 16 hours 14 minutes, October 1, 1962, AES "Alouette", Singapore (Ref. 9).

As we can see, the altitudinal-time pattern of  $N_e(z, t)$  shown in Figure 5 for a set of individual values of  $N_e$ , corresponding not only to different altitudes  $z_c$ , but also to different coordinates of the AES and to a different time  $t$  - both for a day and a month - has led to a dependence of electron concentration on altitude which is new in qualitative terms. Along with the quasi-periodicity of  $N_e(z, t)$ , one of its important features is a deep minimum for  $z \approx 620-630$  km, located approximately in the middle portion of the entire altitude range.

Curves were constructed for the distribution of nonuniform linear dimensions on the basis of data for  $\rho_0$

$$W(\rho_0) = \frac{\sum_{i=1}^n n_i}{\sum_{\rho_0=1}^{\Delta \rho_0} \sum_{i=1}^n n_i} \quad (7)$$

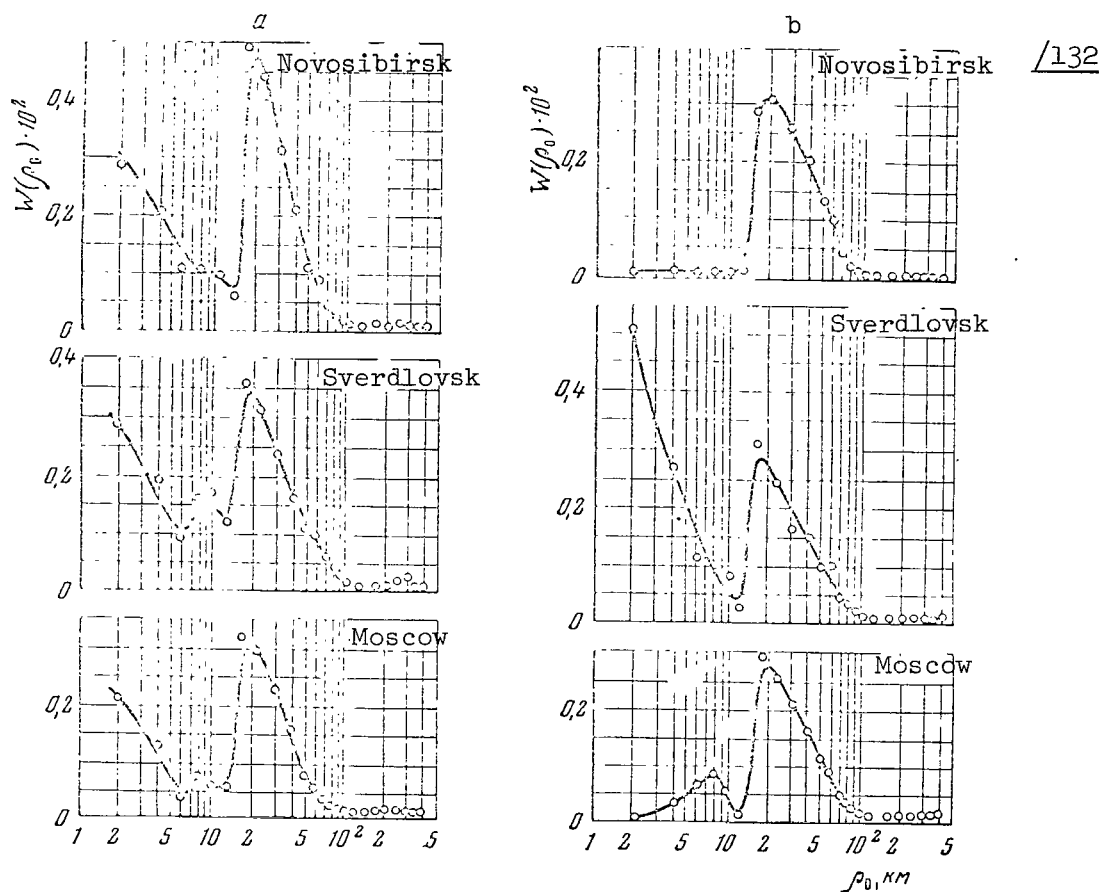


Figure 7

Spectra  $W(\rho_0)$  of Nonuniformity Dimensions in the Altitudinal Ranges

a - for 400-800 km; b - for 800-1200 km

They are given with respect to all three observational points and altitudinal ranges  $z_c = 400-800$  and  $800-1200$  km in Figure 7. When the curves for  $W(\rho_0)$  were drawn, the "weights" for  $a_i$  were taken into account - i.e., the fact that the over-all recording time of  $\delta\phi(t)$  changes for different altitudinal ranges and different observational points. It is assumed that the observational time in Moscow at an altitude of 400-800 km has the "weight"  $a_i = 1$ . All the remaining values of  $a_i$  pertain to this value.

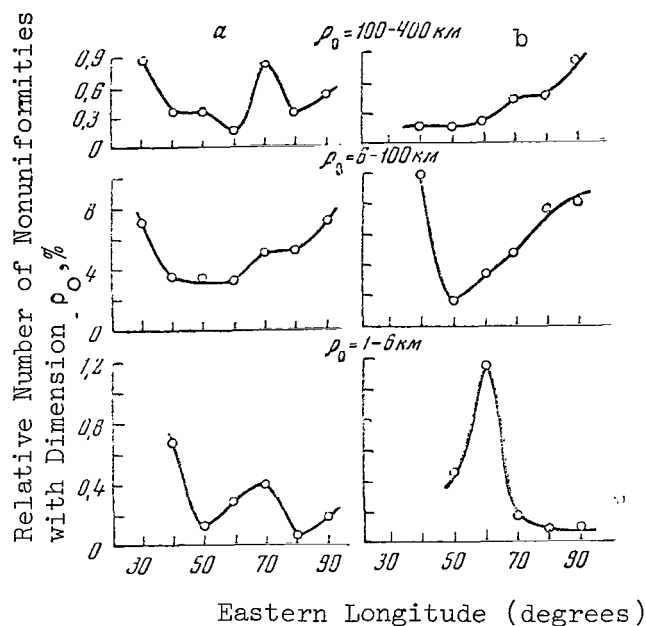


Figure 8

Dependence of Relative Number of Nonuniform Formations Having Different Dimensions  $\rho_0$  Upon Longitude At Different Altitudes  
a - for  $z \sim 400-800$  km; b - for  $z \sim 800-1200$  km.

The dependence (Figure 8) of the relative number of nonuniformities

$$\delta n_i(\lambda) = \frac{\sum_{\Delta \lambda_i} n_i(\Delta \lambda_i)}{\sum_{\Delta \lambda_i} \sum_{\Delta \rho_0} n_i(\Delta \lambda_i)} \quad (8)$$

was determined as a function of longitude, in accordance with the characteristics (which are apparent on the spectra of  $W(\rho_0)$ ) for intervals of  $\Delta \rho_0$  equalling: 1-6 km, 6-100 km, 100-400 km for discrete longitudinal ranges of:  $\Delta \lambda = (25-35), (35-45), (45-55), (55-65), (65-75), (75-85)$  and  $(85-95)^\circ E$  and the latitudinal interval of  $\varphi \approx (43-62)^\circ N$ . /134

Curves were also obtained for Moscow showing the distribution of electron concentration deviation as a function of nonuniform formation dimensions  $\rho_0$ , namely, the dependences

$$\delta N(\rho_0) = \frac{\Delta N}{N_0}(\rho_0) = \frac{\sum_{\Delta \rho_0} n_i(\Delta \rho_0)}{\sum_{\Delta \rho_0} \sum_{\delta N} n_i} \quad (9)$$

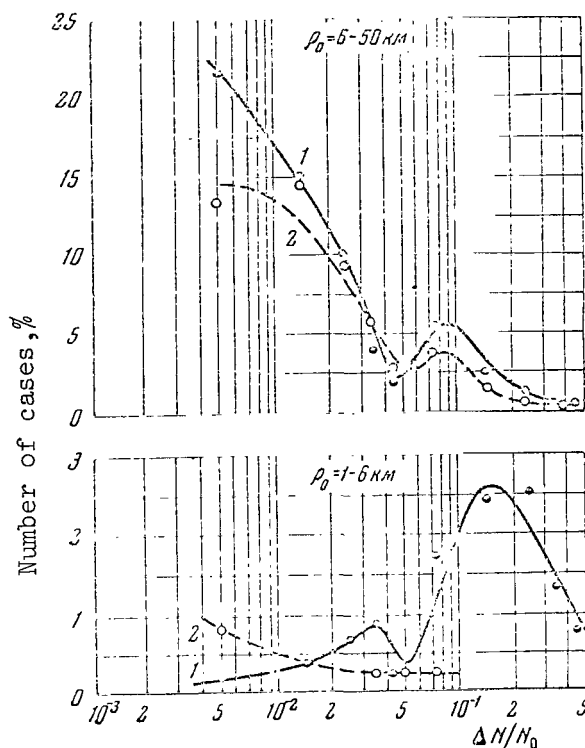


Figure 9

Distribution of Relative Fluctuation Of Electron Concentration  $\Delta N/N_0$  At Different Altitudes  $z$  For Nonuniform Formations  
1 - for  $z = 400-800$  km; 2 -  $z = 800-1200$  km.

for two altitudinal ranges (Figure 9). When the unit values of  $\Delta N = N_{do} - N_0$  were calculated by means of formula (2), the mean altitudinal dependence  $N_0(z) = \overline{N_c}(z, t)$  was employed, which was obtained in the same experiments (see Figure 6). The quantities  $\delta N(\rho_0)$  and  $\delta n_1(\lambda)$  were also determined by taking the "weights" into account (see [Ref. 6]).

### 3. Discussion Of Results

Let us briefly describe the results obtained. Naturally, the main problem is the recurrence of the ionosphere properties discovered and the subsequent verification of them. In particular, this will be accomplished after the results derived from observations on "Elektron-1" and "Elektron-3" have been processed. It is also important to examine the experimental data obtained by other methods, and to determine the relationship between the

described results and any other type of ionosphere phenomena which are anticipated, or which are already known. This will make it possible to explain them more fully. It is advantageous to point out the following facts, based on the considerations given above.

1. If for any reason - particularly, the reasons given below - there is an excess amount of electrons, as compared with the nonperturbed value of  $N_0$ , in definite local regions of the ionosphere for brief periods from time to time - or, let us say, if there is a bunching of electrons in one region, and an evacuation of electrons in the region adjacent to it, in two regions simultaneously - then this spatial law can be observed during long measurements. In this sense, it can be assumed that the dependence  $N_c(z,t)$  produces a local variability in the electron concentration, which has a constant influence in terms of altitude, but which does not necessarily have a constant influence in terms of time. Thus, if the regions of  $N_c(z,t)$  maxima are caused by an influx of electrons into this portion of the ionosphere from other ionosphere regions which are far away, then the nonperturbed distribution of  $N_0(z)$  - which is primarily observed during an individual rapid measurement of altitudinal dependence - can closely coincide with a curve which is tangent to the minima of  $N_c(z,t)$  (curve b in Figure 5).

If the maxima and minima of  $N_c(z,t)$  are interrelated and are caused by redistribution of a quantity of particles in adjacent regions - or, for instance, if they are caused by the fact that the recombination velocity increases in one region and decreases in another region - then the nonperturbed dependence of  $N_0(z)$  can be apparently described by the curve a in Figure 5, or by the curve shown in Figure 6.

2. It is possible that the quasi-periodic nature of the change in  $N_c(z,t)$  in the outer ionosphere is caused by the fact that the plasma oscillates from time to time in the region under consideration, longitudinal plasma waves arise, and standing waves having a length of 120-160 km are established between the two regions, playing the role of "reflecting boundaries". One of such "walls" may be, for example, one of the regions of temperature minima in the lower ionosphere, where the temperature gradient  $dT/dz$  greatly increases and changes sign. As is known, tidal phenomena in the ionosphere, caused by the force of gravitation of the Moon and the Sun (Ref. 12), can be explained by the influence of these "walls". It is possible that in the case of  $z \approx 1000 - 1100$  km the "reflecting boundary" from above is the region where a rapid change in the ionosphere composition is observed on the basis of recent data - the conversion from atomic oxygen initially to helium and then to hydrogen. The mass of the particles changes by a factor of 16, and this means that there is a large gradient of the mean thermal velocity of the particles  $dv_i/dz$ . The total number of "nodes" and "antinodes" must naturally depend on the nature of the "oscillation" of the plasma between the walls, as well as on the structure and thickness of the "reflecting walls" and other conditions. Waves of this type must have a hydrodynamic nature, since their length  $\Lambda \approx 120 - 160$  km is approximately 100 times greater than the mean free path of ions in this region of the ionosphere. The frequency  $\omega$  of the electron fluctuations of these waves



can be similar to the plasma frequency  $\omega_0 = \left(\frac{4\pi N_e e^2}{m}\right)^{\frac{1}{2}}$  or can lie within the region  $(\omega_0 \pm \omega_H)$  where  $\omega_H$  is the gyrofrequency of electrons.

However, there is another possible explanation of the curve for  $N_c(z, t)$ . For example, let us assume that the plasma is excited from time to time in definite ionosphere regions which are localized in terms of latitude and longitude, primarily at low altitudes, and that rapid electrons are generated. Then, being channeled along the force lines of the Earth's magnetic field, these electrons form the "zonal" structure of the ionosphere. The vertical cross section of such a "tubular" structure can lead to the altitudinal dependence of  $N_c(z, t)$  which is obtained.

3. The scheme given above, which has been presented in order to illustrate a possible explanation of the dependence of  $N_c(z, t)$  described above, as well as the majority of other similar hypotheses, assumes, as we can see that the observed dependence of  $N_c(z, t)$  is due to a perturbation of the ionosphere plasma, the excitation of plasma waves in it, the appearance of rapid electrons in these regions, and similar effects. Therefore, it must be assumed that the altitudinal-time distribution of electron concentration which is obtained is accompanied by a local disturbance of the balanced Maxwell distribution of electron velocities, by an increase in their temperature, etc. Local heating of the plasma as a whole can even be expected. The concentration of positive ions can change very little. Finally, the quasi-neutrality of the plasma is disturbed, an electric field is formed, and currents and other effects appear. Thus, for a future analysis of the distribution of  $N_c(z, t)$ , and for verification of the fact that it occurs regularly, the compilation of scientific information is necessary, and it must be determined whether this type of effect with a corresponding altitudinal distribution - or in local ionosphere regions in general - is observed in a different type of ionosphere research using AES.

4. As we have seen above, when experimental data are processed, a formula is employed in which the component describing the integral effect of the electron concentration gradient in the direction normal to the incident plane is excluded. In the flat approximation, this component of the difference in the Doppler frequency shift is

$$\delta\omega_y \sim \frac{\omega}{c} \left( \frac{1}{\omega_2^2} - \frac{1}{\omega_1^2} \right) \frac{\dot{N}_c}{z_c} \int_0^{z_c} \frac{\partial N}{\partial y} z dz \quad (10)$$

(see formula (4) and (5) as well as the work [Ref. 5]). Let us now assume /136 that the quasi-periodic changes in  $N_c(z, t)$ , calculated according to the "shortened" formula (5), are caused by the fact that the component (10) has not been taken into account. The electron concentration gradient  $\partial N / \partial y$  must then be an alternating function depending on altitude, and must change according to oscillations of the curves for  $N_c(z, t)$  (see Figure 5). Let us now assume, for purposes of brevity, that the real desired dependence of the electron concentration is the curve a, and we readily find from the observational results that the electron concentration gradient over every 60-80 km

changes on the average within the limits:

$$\frac{\partial \bar{N}}{\partial y} \geq (1-2) \cdot 10^3 \text{ electron} \cdot \text{cm}^{-3} \cdot \text{km}^{-1}. \quad (11)$$

This is a very strong effect! As we can see, it then leads to the assumption of a strato-quasiperiodic structure of the processes in the outer ionosphere. In particular, it also leads to the assumption of the presence of a complex type of horizontal waves or streams in the plasma, as well as similar phenomena, i.e., to the assumption of ionosphere properties which have been unknown up until the present.

5. The smoothed-averaged dependence of  $\bar{N}_c(z, t)$  and the curves for the equatorial region of North America (Lima in Peru) and north of the equator (Singapore) (see Figure 6) draw attention to the following facts:

In all three curves, a rapid increase in the logarithm inclination of the electron concentration  $\lg N$  can be readily seen in a certain altitudinal region, which can be noted in Figure 6 by the tangents to different branches of these curves. If it is assumed per minute that  $N(z) \sim N_0 \exp(-z/H)$ , where  $H = kT/Mg$  is the given altitude, then this change in the inclination of  $\lg N$  directly points to a rapid change in the ratio of temperature to ion mass  $T/M$ . It is found for Moscow, Peru, and Singapore that  $T/M$  increases by 9.5; 6.8; and 6 times, respectively. At the present time, it is known that above 1200-1400 km the ionosphere primarily consists of atomic hydrogen, and at altitudes of 400-600 km - of atomic oxygen  $O_1$ . This means that the inclination of the curves for  $N(z)$  will change by a factor of 16, if the temperature remains constant. The pattern of these curves thus indirectly indicates not only a significant decrease in the mass  $M$  above 800-1000 km, but also a rapid temperature increase. It is apparently correct to assume the disturbance of balanced Maxwell distribution of the particle velocities, and an intensification of the "tail" role. However, a comparison of these curves calls attention to a very significant fact. In different cases - i.e., at different periods of time - the regions of a rapid change in the inclination of the curves for  $\lg N(z)$  occur at different geographical points - i.e., changes in the composition and temperature of the ionosphere occur at different altitudes (according to Figure 6, for  $z \approx 700, 900$  and 1200 km, respectively). This is a new piece of information which, apparently, can be extracted from a similar type of analysis of the asymptotic behavior of the smoothed dependence  $N_c(z, t)$ .

It should also be noted that in the altitudinal region of  $z \approx 1200 - 1800$  km the electron concentration changes within the limits of  $(1-4) \cdot 10^4 \text{ cm}^{-3}$ . Similar values were also obtained in (Ref. 11) for the concentration of positive ions on rockets in 1961, during the night time at Blue Scout 28 N<sup>0</sup> (see Figure 6). However, all of these data exceed the concentration of positive ions at these altitude by a factor of approximately 10-20; these concentrations are given in the work (Ref. 13). This disparity provides not only a quantitative, but also a qualitative, refutation of the rapid change in the ionosphere composition - the conversion of atomic oxygen to atomic hydrogen. We shall assume that this disparity is related to an error

in the data given in (Ref. 13) (see [Ref. 14]).

6. The spectra of  $W(\rho_0)$  have the following characteristics.

At all altitudes and at all points there is an extensive and clearly-expressed maximum in the  $\rho_{\max} \approx 15-30$  km range (see Figure 7). This <sup>/137</sup> wide maximum of  $\rho_0$  encompasses two maxima regions  $\rho_{\max} = 16-18$  and  $28-32$  km, discovered previously at low altitudes  $z_c \approx 250-430$  km by means of the AES "Kosmos" (see [Ref. 3, 5]). Apparently, two maxima merge into one at these altitudes in the outer ionosphere. The distribution of  $W(\rho_0)$  also has the maximum  $\rho_{\max} \approx 7-10$  km. It is not clearly expressed. In addition, it is observed on almost all curves of  $W(\rho_0)$ .

In regions of very small  $\rho_0$  the well-known tendency of several nonuniformity dimensions to increase in the vicinity of  $\rho_{\max} \sim 2-4$  km is clearly expressed. It is very important that at altitudes of  $z_c = 800-1200$  km, and when  $z_c > 1200$  km, the nonuniformities  $\rho_0 < 5-6$  km practically disappear, in general. The result obtained in Sverdlovsk comprises an exception to this. However, a more detailed analysis of the experimental data for Sverdlovsk shows that the values of  $\rho_0 \lesssim 5-6$  km, in the case of  $z_c = 800-1200$  km, were only observed for a few days, when there was an unusually large number of nonuniformities which were small in size. The fact is not excluded that these observational periods correspond to certain conditions of ionosphere perturbation. However, we have not yet clarified the criteria for such perturbations - let us say, the excitation of a small number of non-uniform formations.

7. The distribution of  $\rho_0$  dimensions in terms of longitude shows (see Figure 8) that the number of nonuniform formations is not the same at different longitudes. There are geographical regions where it increases significantly. Thus, for example, in the  $\lambda = 70^\circ\text{E}$  region the distribution of small nonuniformities  $\rho_0 \lesssim 6$  km and of large-scale nonuniformities  $\rho_0 \approx 100-400$  km has a clear maximum in the case of  $z_c = 400-800$  km. At an altitude of  $z_c = 800-1200$  km the distribution of  $\rho_0$  is different.

8. Disturbance of the electron concentration  $\delta N$  in the nonuniformity dimension range of  $\rho_0 = 6-50$  km is observed in 22% of the cases for small values of  $\delta N \sim 0.005$  and, decreasing, it equals 1-2% for  $\delta N = 0.5$  (see Figure 9). There is thus a certain maximum for  $\delta N \approx 0.05-0.15$ . Small non-uniformities  $\rho_0 \lesssim 6$  km have, in the case of  $z_c = 400-800$  km, a more clearly expressed maximum for  $\delta N \approx 0.08-0.35$ . These maxima may possibly point to a certain regular mechanism in the excitation of nonuniform formations. In certain cases, values of  $\delta N \gtrsim 1$  are observed. In our experiments, such large disturbances of the electron concentration were determined for 30 non-uniform formations out of a total number of 1100, for which the values of  $\delta N$  were calculated. In these cases, the electron concentration  $N_{d0}$  changed within the limits of  $+(0.5-1.7) N_0$  and  $-(0.5-1.7) N_0$ , i.e., strong disturbances of the electron concentration occurred. They correspond to values of  $\rho_0 \sim 2-10$  km and altitudes of  $z_c = 400-800$  km.

In conclusion, the authors would like to express their appreciation to the following individuals for their assistance in performing these observations: N. M. Vol'f, A. M. Luchshev, V. A. Rybalkin. The authors would also like to thank L. N. Vitshas, Yu. G. Ishchuk, V. I. Krayushkinoy, F. U. Mukhamadeyevoy, A. A. Kharybinoy for processing the experimental data.

#### REFERENCES

1. Al'pert, Ya. L. Uspekhi Fizicheskikh Nauk, 64, 3, 1958; 71, 369, 1960.
2. Al'pert, Ya. L., Belyanskiy, V. B., Kutyakov, A. F. Geomagnetizm i Aeronomiya, 3, 167, 1963.
3. Al'pert, Ya. L., Belyanskiy, V. B., Mityakov, N. A. Geomagnetizm i Aeronomiya, 3, 10, 1963.
4. Mityakov, N. A., Mityakova, E. Ye., Cherepovitskiy, V. A. Geomagnetizm i Aeronomiya, 3, 816, 858, 1963.
5. Al'pert, Ya. L. Geomagnetizm i Aeronomiya, 4, 479, 1964.
6. Al'pert, Ya. L., Vitshas, L. N., Sinel'nikov, V. M. Geomagnetizm i Aeronomiya, 5, No. 4, 840, 1965.
7. Al'pert, Ya. L., Sinel'nikov, V. M. Geomagnetizm i Aeronomiya, 5, No. 2, 209, 1965.
8. Jackson, J. E., Bauer, S. T. J. Geophys. Res., 66, 3055, 1961.
9. King, J. W., Smith, P. A., Eccles, D. Radio Res. Stat., Doc. N RRS/I.M., 94, M, 112, 1963.
10. Farley, D. T., Bowels, K. L. Nat. Bur. Stand. Rep. NBS, 8489, 1964.
11. Sagalyn, R. C., Smiddy, M. J. Geophys. Res., 69, No. 19, 1809, 1964.
12. Weeks, K., Wilkes, M. V. Proc. Roy. Soc., 192, 82, 1947.
13. Gringauz, K. I. In "Iskusstvennyye Sputniki Zemli". Izdatel'stvo AN SSSR, No. 12, p. 105, 1962; see also No. 6, 108, 1961, and others.
14. Al'pert, Ya. L. Geomagnetizm i Aeronomiya, 5, No. 4, 865, 1965.

# CERTAIN RESULTS OF IONOSPHERE STUDIES USING ARTIFICIAL EARTH SATELLITES AND GEOPHYSICAL ROCKETS

V. A. Misyura, G. K. Solodovnikov,  
Ye. B. Krokhmal'nikov, V. M. Migunov

The present article presents the results derived from radiophysical /138 studies of the outer ionosphere using AES "Kosmos-11", "Electron-1" to a certain extent, and geophysical rockets. The method employed measured the difference of Doppler frequencies at coherent frequencies, as well as the method of recording the so-called rotational Doppler effect (Faraday effect) at fixed frequencies simultaneously at one or several points.

## Method For Processing Measurement Results

The difference in the Doppler frequency shifts of two coherent radio waves  $\dot{\Phi}$ , emitted by the AES, and the frequency (velocity) of rotation of the radio wave polarization plane in the ionosphere, caused by the Faraday effect  $\dot{\Phi}_F$ , were determined directly from the experiment.

When the dependence of the refraction coefficient of the ionosphere  $n(n^2 = 1 + \alpha)$  on three coordinates and time in the first approximation with respect to the magnitude of  $\alpha$  are taken into account, the expressions for them, and also the expressions for the integral quantities  $\dot{\Phi}$  and  $\dot{\Phi}_F$  corresponding to them, have the following form (Ref. 1):

$$-\frac{\lambda \dot{\Phi}}{K} = \alpha_B v_R + \frac{v_{\tau B}}{R} \int_0^R \nabla_{\tau} \alpha |_{v_{\tau B}} x_1 dx_1 + \int_0^R \frac{\partial \alpha}{\partial t} dx_1; \quad (1)$$

$$-2\lambda \dot{\Phi}_F = \alpha_B b_{LB} v_R + \frac{v_{\tau B}}{R} \int_0^R \nabla_{\tau} (\alpha b_L) |_{v_{\tau B}} x_1 dx_1 + \int_0^R \frac{\partial (\alpha b_L)}{\partial t} dx_1; \quad (2)$$

$$\frac{\lambda}{2\pi} \Phi = \Delta L = \frac{1}{2} \int_0^R \alpha dx_1 = -\frac{4.03}{f^2} N_{0L}; \quad (3)$$

$$\frac{\lambda}{2\pi} \Phi_F = \bar{b}_L \Delta L; \quad (4)$$

$$\dot{\Phi}_F = \frac{2\pi}{\lambda} \bar{b}_L N_{0L} - \frac{\bar{b}_L}{K} \dot{\Phi}. \quad (4a)$$

The following notation is introduced here:  $R$  - distance from the emitter to the receiving point;  $v_R$  and  $v_{\tau B}$  - radial emitter velocity and emitter velocity which is transverse to the radial direction;

$$\alpha = -\frac{8.06 N}{f^2}; \quad \bar{b}_L = \frac{\int_0^R \alpha b_L dx_1}{\int_0^R \alpha dx_1}; \quad b_L = \frac{f_L}{f};$$

$f$  and  $f_L$  - working frequency and longitudinal components of gyrofrequency in  $M_c$ ;  $N$  - electron concentration of the ionosphere in  $\text{electron} \cdot \text{cm}^{-3} \cdot 10^5$ ;  $\Delta L$  - phase lag of radio waves;  $N_0 L$  - total number of electrons in a tube of unit cross section along the line of observation;  $k$  - coefficient depending on the relationship between emitted frequencies; the index B pertains to the emitter. /139

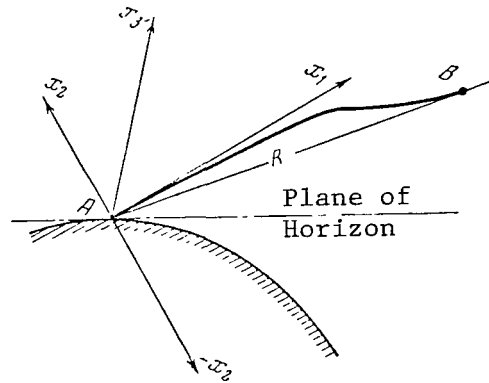


Figure 1

The coordinate system shown in Figure 1 is utilized here (the  $x_1$  axis is directed along the tangent to the line of observation at point A).

Expressions (1) and (2) can be rewritten as follows:

$$-\frac{\lambda \dot{\Phi}}{K} = \alpha_B v_R + \frac{v_{TB}}{R} I, \quad (5)$$

$$-\lambda \dot{\Phi}_F = \alpha_B b_{LB} v_R + \frac{v_{TB}}{R} I_1. \quad (6)$$

The values of  $I$  and  $I_1$  can be clearly determined from (1) and (2). They characterize the distribution of electron concentration gradients which are transverse to the line, as well as the nonstationary nature of the ionosphere.

In the case of a stationary ionosphere, the expressions for  $\dot{\Phi}$  and  $\dot{\Phi}_F$  have the following form:

$$-\frac{\lambda \dot{\Phi}}{K} = \alpha_B v_{BB} = \alpha_B v_R \cos \theta; \quad (7)$$

$$-\lambda \dot{\Phi}_F = \alpha_B b_{LB} v_{LB} = \alpha_B b_{LB} v_R \cos \theta. \quad (8)$$

Here  $v_{LB}$  is the projection of the emitter velocity on the line;  $\theta$  - is the angle between the line and the radial emitter velocity at the point where it is determined.

Comparing the equation (5) or (6) through the time interval  $\Delta t$ , in

which  $\alpha_B$  and  $I$  can be assumed to change very slightly as compared with the changes in  $v_R$  and  $v_{TB}$ , one can subsequently solve (5) and (6) by pairs with respect to  $\alpha_B$  (or  $N_B$ ) and  $I$ . A solution of each pair of equations determines the average (over the time interval  $\Delta t$ ) value of the local electron concentration  $N_B$  and the interval  $I$  successively along the orbit.

For a stationary ionosphere, the local electron concentration can be determined directly from (7) or (8). However, the fact must be taken into consideration that in the region of the parameter point (where  $v_R = 0$ ), formulas (7) and (8) are unsuitable, since in this case the quantity  $\phi$  (and, correspondingly,  $\phi_F$ ) is primarily determined by the integral term  $(\frac{v_{TB}}{R})$ .

If the difference frequency  $\dot{\phi}$  is measured directly, one can determine the integral gradient of the electron concentration  $N_{OL}$  along the line (Ref. 2). The expression for the gradient is determined by differentiating expression (3) with respect to the orbital element  $ds = vdt$ , where  $v = \frac{140}{\text{km}}$  is the satellite velocity:

$$\frac{d}{ds} N_{OL} = \frac{P}{v} \dot{\phi}. \quad (9)$$

The behavior of the gradient as a function of the satellite observational time (and, consequently, as a function of the geographical coordinates) makes it possible to a certain extent (particularly when the dependence  $N_B(t)$  is present at the same time) to formulate a judgement regarding the structure of the entire ionosphere stratum below the satellite (Ref. 1-3).

The quantity  $\phi$  obtained from the experiment can have both a regular, and a nonregular component. The nonregular component is caused by nonuniformities of electron concentration in the ionosphere, primarily those which are located along the satellite orbit (Ref. 3, 4). Therefore, it is possible to determine the nonuniformity dimensions by plotting  $F(t)$ . The same statement can be made with respect to the quantity  $\phi_F$ . Histograms of ionosphere nonuniformity dimensions were constructed from a large number of recordings, and their dependence on the time of year, the time of day, the cycle of solar activity, etc. was determined.

If  $\phi$  and  $\phi_F$  are measured simultaneously in the altitudinal region of the emitter  $z_B$ , by means of (4a) it is possible to determine  $N_{OL}$  as a function of  $z_B$  in this altitudinal region, as well as the "mean" vertical profile of the ionosphere as described below.

The method employed to determine the vertical profiles of the electron concentration for a regular ionosphere, the horizontal gradients of these profiles, and the altitudinal distribution of the integral electron concentration gradients is briefly as follows (Ref. 5).

The recordings obtained at two or more points which are spaced apart are employed. The indeterminacy in determining the total number of electrons along the line ( $N_{OL}$ ) is eliminated by employing the angle  $\phi_F$  for the

polarization plane rotation caused by the Faraday effect, or by employing the value for the phase difference  $\delta$  measured at coherent frequencies. In order to do this, it is necessary to record the Doppler and Faraday effects together. If only one quantity is measured, when data are available on the vertical sounding of the ionosphere the problem of indeterminacy is solved, if the emitter orbit intersects the ionization maximum.

The total electron concentration in a vertical column  $N_0$ , up to the altitude  $z_B$  where the geophysical rocket is located, above the point P (Figure 2) lying somewhere between the observational point A and the take-off point of the rocket, is as follows:

$$N_0 = N_{0L} \overline{\sin \beta'_B} - \int_0^{z_B} \gamma(z) (S_P - S) N(z) dz. \quad (10)$$

where  $\gamma$  is the "current" horizontal gradient of the electron concentration;  $S_P$ ,  $S$  - the arcs read off at the level  $z$  from the vertical, which is drawn at the point A, to the vertical which is drawn at the point P (the arc A'P'), and up to the points at which the arc intersects the inclined line (the arc A'T);  $\sin \beta'_B$  is determined by the expression

$$\overline{\sin \beta'_B} = \frac{\int_0^{z_B} N dz}{\int_0^{z_B} \frac{N dz}{\sin \beta'}}, \quad (11)$$

where  $N$  is the electron concentration at the altitude  $z$ .

Let us select the point P at a distance ( $r_A \varphi_P$ ) from the observational point to the Earth's surface which makes the second component in (10) equal zero. This distance is determined by the expression /141

$$\varphi_P = \frac{\int_0^{z_B} \gamma(z) S(z) N(z) dz}{\int_0^{z_B} \gamma(z) r N(z) dz}. \quad (12)$$

When the quantities  $\varphi_P$ ,  $\overline{\sin \beta'_B}$  and  $\overline{b_L}$  are calculated, the iteration method is employed (see [Ref. 5] for greater detail). If - in accordance with experimental data - the fact is taken into account that the horizontal gradient of the vertical profile of the ionosphere is caused primarily by an extended horizontal gradient in the region of the maximum F, then the following approximate expression can be employed for the first step of iteration:

$$\gamma(z) = \gamma_M \frac{N(z)}{N_M}, \quad (12a)$$



where  $\gamma_M$  and  $N_M$  represent the electron concentration gradient at the altitude of maximum and minimum electron concentration, respectively.

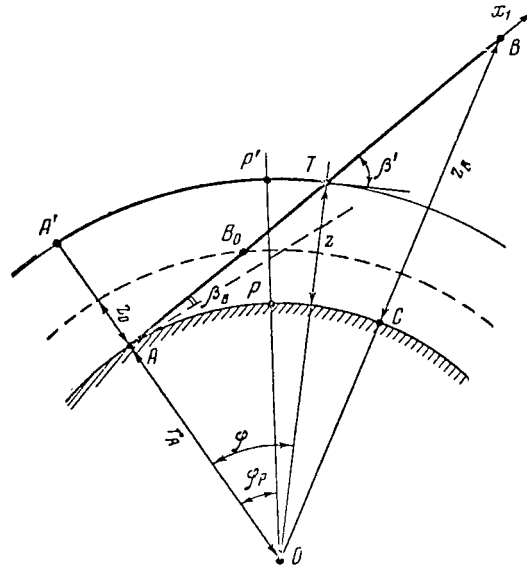


Figure 2

If (12a) is taken into consideration, expression (12) can be rewritten in the following form:

$$\varphi_P = \frac{\int_0^{z_B} r \varphi N^2(z) dz}{\int_0^{z_B} r N^2(z) dz}.$$

A numerical calculation shows that  $\varphi_P$ ,  $\overline{\sin \beta'_B}$ ,  $\overline{b_L}$  are insensitive to the ionosphere model of (Ref. 5).

Let us obtain two series of values  $\varphi_P(\varphi_{P_1}, \varphi_{P_2})$ , as well as the values of  $N_{OP_1}, P_2$  corresponding to them, as a function of the rocket altitude  $z_B$  for both observational points. In addition, let us differentiate both series of values for  $N_{OP_1}, P_2$  with respect to  $z_B$ , and let us obtain the corresponding series  $N_{P_1, P_2}$ .

The mean "equivalent" electron concentration gradients of  $\gamma$  at the corresponding level  $z_B^i$  can be determined from the expression /142

$$\gamma(z_{B_i}) = \frac{N_{P_1}(z_{B_i}) - N_{P_2}(z_{B_i})}{\Delta S_P(z_{B_i}) N_{P_1}(z_{B_i})}.$$

The values of  $\gamma(z_{B_i})$  make it possible to obtain the approximate vertical profiles in any vertical cross section between A and B, taking the gradients  $\gamma$  into account.

With values of  $N_{OL}(z_B)$  obtained only at one point, it is possible to determine certain "equivalent" vertical profiles  $N(z_B)$  making use of the relationships

$$N_0(z_B) = N_{0L} \overline{\sin \beta'_B};$$

$$N(z_B) = \frac{dN_0(z_B)}{dz_B}.$$

where  $\overline{\sin \beta'_B}$  is determined from (11). The gradients  $\gamma$  and  $\gamma_0$  cannot be determined in this case.

### Measurement Results

Observations by means of the AES "Kosmos-11" and "Elektron-1" have made it possible to determine the local electron concentration  $N_B$  along the satellite orbit. For purposes of illustration, Figure 3 ( $z_B = 346 - 300$  km,  $z_M = 276$  km,  $f_{OF2} = 5.1$  Mc) presents a typical graph for the dependence of  $N_B$  on the satellite flight time, calculated on the basis of recordings of the difference  $\delta$  in the Doppler effect at coherent frequencies, at two points which are approximately 700 km from each other. Both curves closely coincide, which points to adequate accuracy in the results obtained. The dashed line represents the magnitude of  $N_B$ , calculated with sounding data in the approximation of a parabolic-exponential ionosphere model.

Based on the local electron concentration calculated in this way, an ionosphere profile was constructed for up to an altitude of 2000 km (Figure 4), which represents a projection on the vertical of the mean (for several measurements) ionosphere profile along the satellite orbit. Naturally, it is not adequate for a vertical profile when there are horizontal gradients  $N$  (latitudinal and longitudinal, regular and nonregular).

A section in which there was a non-monotonic pattern of electron concentration was discovered above the F2 layer, which is located at an altitude of about 600 km and has an electron concentration at a maximum of 0.5-0.8 from  $N_{MF2}$ .

At one time it was pointed out in several works (for example, [Ref. 6]) that sometimes a relatively high ionization level is observed at an altitude considerably exceeding the altitude of the F2 layer, in the case of a very diffused lower portion of the F2 layer. This was observed during vertical soundings of the ionosphere. The possibility is not excluded that this entire set of observations points to the presence of a new ionosphere layer above the F2 region (see also [Ref. 3, 7, 8]).

The total number of electrons in the ionosphere, calculated according to

the profile in Figure 4, exceeds by a factor of approximately 2 the value of  $N_0$  obtained according to the parabolic-exponential ionosphere model. Calculations of  $N_0$  up to an altitude of 2000 km, directly from the profile in Figure 4 and from the concurrent solution of the equations for  $\Phi$  and  $\Phi_F$  (Ref. 5) or (4a) for  $\Phi$  and  $\Phi_F$ , provide similar values, lying within the errors of the methods employed (Ref. 1, 2, 5) (less than 10 - 20%).

/143

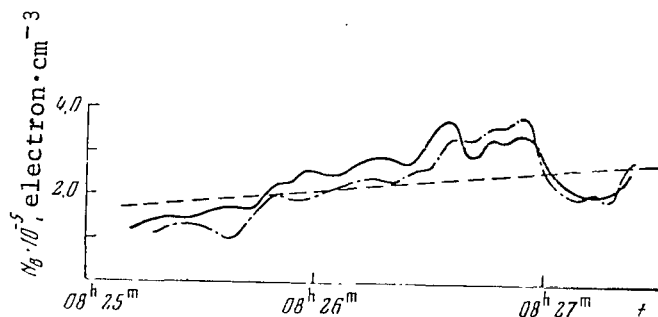


Figure 3

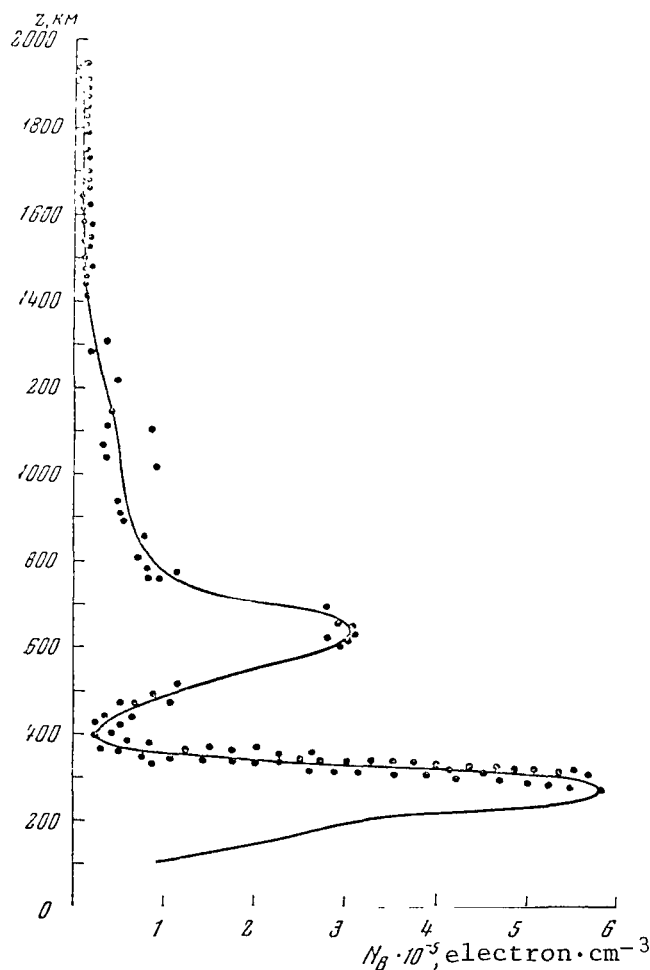


Figure 4

It is also interesting to calculate the gradient  $\frac{d}{ds} N_{OL}$  of the total electron concentration between the observational point and the satellite. Figure 5 presents the typical pattern in time of the gradients  $\frac{d}{ds} N_{OL}$  for the diurnal (a), morning (b), and nocturnal (c) satellite flights, respectively.

The values of  $\beta_B$  and R for these flights are given below:

	hours	minutes	seconds	$\beta_B$	R, km
for a:	13	3		$30^\circ.8$	453.4
	13	4		26.5	511.5
	13	4	30	19.2	656.2
for b:	6	29	30	$22^\circ.7$	1044.6
	6	30		29.5	854.2
	6	31		55.2	529.3
	6	32		70.2	446.8
	6	33		32.6	701.6
for c:	3	25		$14^\circ.5$	1547.4
	3	27		15.7	1422.8
	3	28		14.4	1550.2

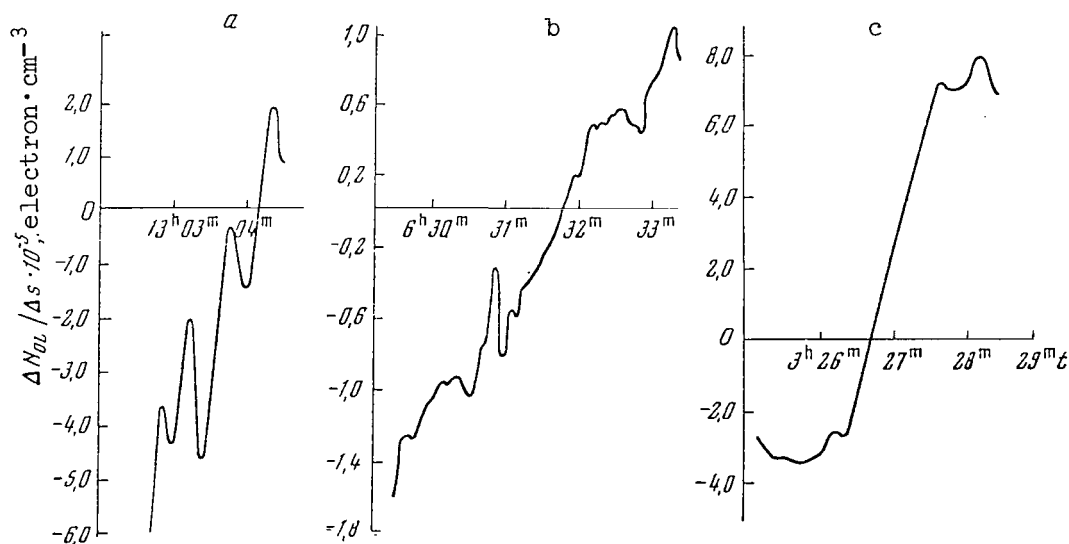


Figure 5

It can be seen that the tendency towards "quasi-periodic" nonregular changes in  $N_{OL}$  with a relatively large amplitude is more apparent for daytime

flights than it is for morning and nocturnal flights. The impression is gained that this type of "quasi-undulation" of the entire ionosphere stratum under the satellite - or the very predominant contribution to  $N_{OL}$  of the ionization of the largest "single layer" or "few-layered" nonuniformities, which are located under the satellite - corresponds to this. During morning flights (Figure 5, b) the ionosphere had a cloudy-random structure beneath the satellite and in the vicinity of it.

During the nocturnal hours, the satellite passed to the east of the observational point, from the west to the east, intersecting the transitional region between the "nocturnal" and "diurnal" ionosphere. In these cases, the magnitude of  $N_{OL}(t)$  dropped sharply (Figure 5, c).

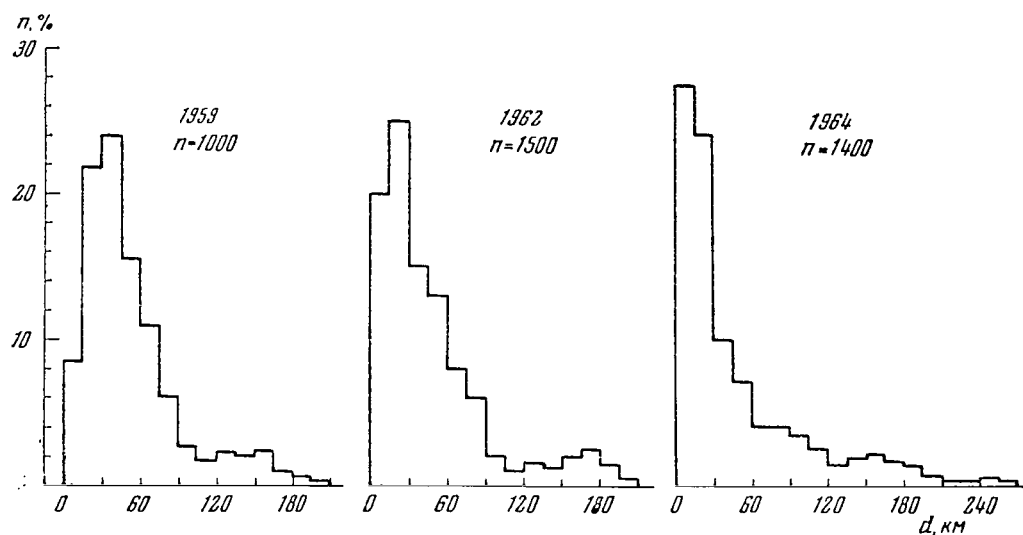


Figure 6

Histograms for the nonuniformity dimensions  $d$  (Figures 6, 7), based /145 on all of the satellite flights which we have observed, were constructed for different phases of solar activity and a different time of day. Two stable maxima were observed in the 15-30 and 150-190 km regions. It was our impression that the dimensions of large-scale nonuniformities change to a lesser extent with a change in solar activity, than they do with a change in the time of day. The second maximum appears during the transition from night time to day time, it exists in the day time, and disappears at night. The mean quadratic deviations in the electron concentration of large nonuniformities in the F2 ionosphere region closely coincide with their dimensions, but do not coincide as closely with the regular values of electron concentration at the corresponding level of the F2 region.

In Figure 8, curves 4 and 1 express the vertical profiles of the electron concentration in the ionosphere, obtained by means of a geophysical rocket (GPR) at frequencies of 48 and 144 Mc, during a vertical launch in the day

time on October 18, 1962, at mean latitudes in the Soviet Union (Ref. 5). Curve 4 represents the vertical profile above the first observational point, and profile 1 is the "mean" profile over the take-off point of the GPR. Curve 2 characterizes a certain "equivalent" profile of the ionosphere between the observational point and the take-off point of the rocket, obtained according to observational data of GPR signals at only one point. Profile 3 was obtained from the vertical soundings of the ionosphere at several points, scaled to the take-off point of the GPR. /146

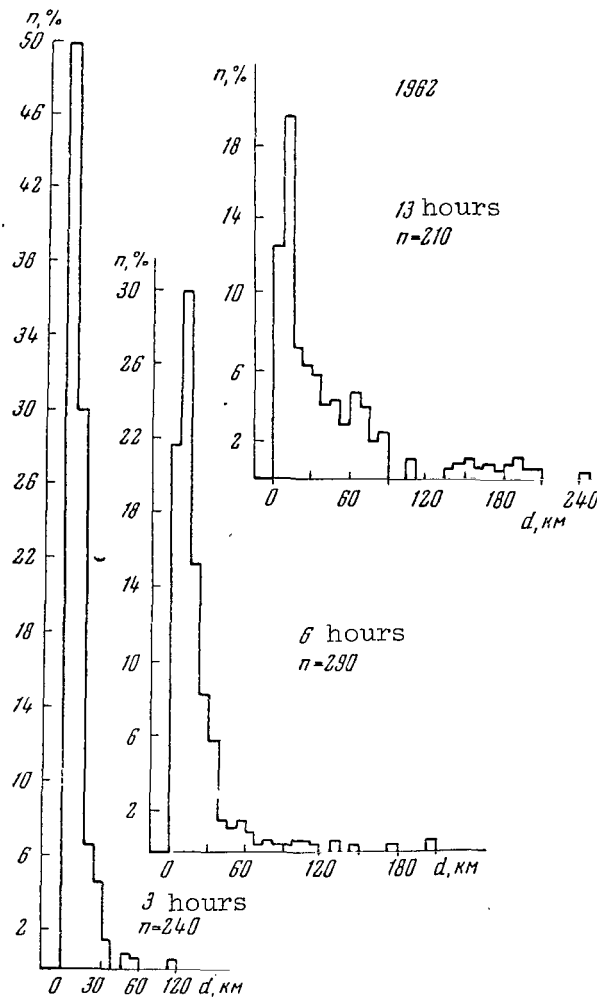


Figure 7

Figure 9 shows the normalized profiles obtained during different cycles of solar activity. We obtained curve 1 from the launch of a GPR in October, 1962, in the period below the mean solar activity. Curve 3 was obtained by K. I. Gringauz and V. A. Rudakov during launches of GPR in October, 1958, during maximum solar activity at the same latitudes (Ref. 9). Curve 5 was

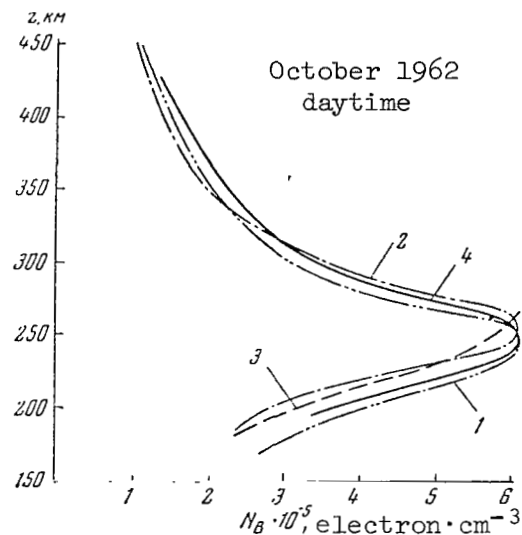


Figure 8

obtained by Ya. L. Al'pert based on signals from the first AES (Ref. 10). Profile 4 was obtained (Ref. 11) from the signals of the third AES in Khar'kov during the summer seasons of 1958-1960, primarily during the daytime. Curve 2 was obtained from AES "Kosmos-11" signals in October, 1962 (Ref. 1).

Figure 9 illustrates the tendency of the ionosphere to "flatten" during the period in which solar activity decreases, which has been observed previously by several authors (Ref. 1, 3, 5, 12, 13).

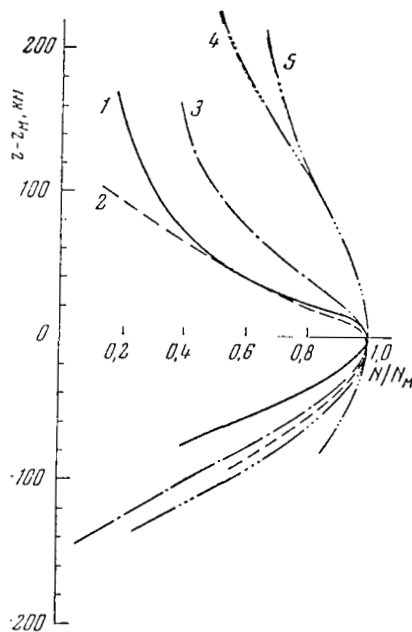


Figure 9

## REFERENCES

1. Misyura, V. A., Solodovnikov, G. K., Migunov, V. M. Kosmicheskiye Issledovaniya, 3, No. 5, 1965.
2. Misyura, V. A., Solodovnikov, G. K., Migunov, V. M. Geomagnetizm i Aeronomiya, 4, No. 6, 1964.
3. Al'pert, Ya. L. Geomagnetizm i Aeronomiya, 4, No. 3, 1964.
4. Tsedilina, Ye. Ye., Kharygina, A. A. Geomagnetizm i Aeronomiya, 4, No. 3, 1964.
5. Misyura, V. A. Osipov, D. D., Krokhmal'nikov, Ye. B., Solodovnikov, G. K. Kosmicheskiye Issledovaniya, 3, No. 5, 1965.
6. Kazantsev, A. N. Izvestiya AN SSSR, Otdeleniye Tekhnicheskikh Nauk, No. 9, 1946.
7. Sayers, J., Rothwell, P., Wager, J. H. Nature, 195, No. 4847, 1962.
8. Sayers, J. The Electron Density Profile Above the F<sub>2</sub> Region of the Ionosphere As Recorded By the Satellite Ariel.-Proc. Internat. Conf. Ionosphere, London, 1962. London, Inst. Physics and Phys. Soc., p. 23-525, 1963.
9. Gringauz, K. I., Rudakov, V. A., In "Iskusstvennyye Sputniki Zemli". Izdatel'stvo AN SSSR, No. 6, 1961.
10. Al'pert, Ya. L., Dobryakova, F. F., Chudesenko, E. F., Shapiro, B. S. 147 Doklady AN SSSR, 120, No. 4, 743, 1958.
11. Misyura, V. A. Trudy Artilleriyskoy Radiotekhnicheskoy Akademii, No. 46, 1960.
12. Rudakov, V. A. Kosmicheskiye Issledovaniya, 2, No. 6, 946, 1964.
13. Gringauz, K. I., Gorozhankin, B. N., Shyutte, N. M., Gdalevich, G. L. Doklady AN SSSR, 151, No. 3, 560, No. 7, 1963.

## IONOSPHERE STUDIES BY RECEIVING AES RADIO EMISSION ON THE EARTH

L. M. Yerukhitov, N. A. Mityakov, E. Ye. Mityakova

Beginning in 1961, research was carried out on receiving AES radio signals in the 20-90 Mc range in order to study the regular structure of the ionosphere, large-scale nonuniformities in the electron concentration, and small-scale ionosphere nonuniformities. The main results derived from



this research have been compiled in the form of articles (Ref. 1-7). In addition, the preliminary results derived from measurements by means of the AES "Elektron-1" are presented below.

1. The regular structure of the ionosphere was studied by measuring the phase difference in signals of coherent frequencies of 20 and 30 Mc ("Elektron-1" and "Elektron-3") and 20 and 90 Mc ("Kosmos-1", "Kosmos-2" and "Kosmos-11"). This was also done by studying the polarization fading of a signal at a frequency of 20 Mc (Faraday effect). The method employed in processing the experimental data is presented in the works (Ref. 1, 2, 4). The phase difference of signals having coherent frequencies  $\Phi$  is proportional to the integral electron concentration on the propagation paths of the radio waves - i.e.,  $\Phi = A \int_0^{r_c} N dr$ . Thus, changes in the phase of  $\Phi$  are

caused both by a change in the distance to the satellite, as well as by a different condition of the ionosphere on the propagation path of the radio waves when the satellite is in motion. For a flat Earth, we have

$$\Phi = A \sec \varphi \int_0^{z_c} N dz; \quad \dot{\Phi} = A \left( \frac{d}{dt} \sec \varphi \int_0^{z_c} N dz + \sec \varphi \frac{d}{dt} \int_0^{z_c} N dz \right);$$

$$\frac{d}{dt} \int_0^{z_c} N dz = N_c \dot{z}_c + \frac{\dot{z}_c}{z_c} \int_0^{z_c} \frac{\partial N}{\partial x} z dz.$$

As can be seen from the latter expression, it is not possible to distinguish the contribution which is made to the quantity  $\dot{\Phi}$  by the term  $\dot{z}_c N_c$ , which determines the local electron concentration, from the contribution

made by the term  $\frac{\dot{z}_c}{z_c} \int_0^{z_c} \frac{\partial N}{\partial x} z dz$ , which depends on the horizontal electron concentration gradients. The situation remains the same when the sphericity of the earth is considered (Ref. 2). Therefore, the method of coherent frequencies makes it possible to obtain information on only the quantities

$\int_0^{z_c} N dz$  and  $\frac{d}{dt} \int_0^{z_m} N dz$ . The electron concentration at the satellite altitude  $N_c$  can be estimated by comparing the quantities  $\int_0^{z_c} N dz$  and  $\int_0^{z_m} N dz$ , where  $z_m$  is the altitude of the F layer maximum. The quantity  $\int_0^{z_c} N dz$  can be obtained/148 by processing the recordings of the phase difference in signals of coherent frequencies, while the quantity  $\int_0^{z_m} N dz$  can be obtained from the altitudinal-

frequency characteristics of the ionosphere. In the case of a circular satellite orbit ( $\dot{z}_c \approx 0$ ) the recordings of the phase difference in signals of coherent frequencies make it possible to obtain information regarding regular, horizontal gradients of the electron concentration in the ionosphere.

Processing of polarization fadings  $\dot{\Psi}$  of AES radio signals entailed similar difficulties (Ref. 4).

The works (Ref. 3, 4) present the main observational results of "Kosmos-1", "Kosmos-2", and "Explorer-7" AES. The quantity  $\int_0^{z_c} N dz$  changed from  $0.1$  to  $1.7 \cdot 10^{13}$  electron  $\cdot$  cm $^{-2}$ , as a function of the satellite altitude and the time of day. A comparison with the data from vertical sounding makes it possible to obtain the index of the exponent  $\kappa$  on the assumption that the electron concentration above the F layer maximum decreases according to the exponential law. The mean value is  $\kappa \approx 6.2 \cdot 10^{-3} \text{ km}^{-1}$  during the daytime, which is somewhat higher than the value of  $\kappa \approx 3.5 \cdot 10^{-3} \text{ km}^{-1}$  which was assumed previously. It should be noted that the NIRFI measurements pertain to years which are close to minimum solar activity. Data have also been obtained on the regular horizontal gradients of electron concentration in the ionosphere. The quantity  $\int_0^{z_c} \frac{\partial N}{\partial x} dz$  represents  $\pm 10^4$  electron  $\cdot$  cm $^{-3}$ , while the morning satellite flights correspond to positive gradients, and the evening flights - to negative gradients. It is important we compare the contribution made to the quantity  $\dot{\Psi}$  by the term  $\frac{\dot{x}_c}{z_c} \int_0^{z_c} \frac{\partial N}{\partial x} z dz$  for AES orbits of the "Kosmos-1" and "Kosmos-2" type. The contribution made by this term frequently exceeds the contribution made by the term with  $N_c \dot{z}_c$ .

During February-March, 1964, observations were performed on the AES "Elektron-1" radio signals at coherent frequencies of 20,005 and 30,0075 Mc in order to determine the total electron concentration in the ionosphere. Observations were performed at two points. Approximately 80 phase recordings were obtained in all. At the present time, almost 9 recordings from zenith flights of AES over Gorky have been processed, and values have been obtained for the total integral of the electron concentration  $\int_0^{z_c} N dz$  up to the satellite altitude. Based on data from an ionosphere station for vertical sounding (the town of Gorky), the profiles  $N(h)$  of the ionosphere have been calculated on an electronic computer, and the quantities  $\int_0^{z_m} N dz$  ( $z_m$  - altitude of the F layer maximum) have been determined for time intervals coinciding with the satellite flight time (above the town of Gorky). A comparison of data from the AES with the data from vertical sounding makes it possible to obtain the index of the exponent  $\kappa$ , for an exponential model of the upper portion of the F layer, for each revolution, as well as the electron concentration at the location of the satellite. All of the values obtained are presented in the table. The mean value of the exponent index is  $\kappa \approx 6.2 \cdot 10^{-3} \text{ km}^{-1}$ , which closely coincides with the theoretical model of the Earth's diurnal ionosphere during a period of low solar activity (Ref. 8).

The rather sharp drop in the electron concentration above the F layer /149 maximum (the electron concentration decreases  $e$  times when the altitude changes by  $1/\mu \approx 160$  km) apparently continues up to an altitude of about 700-1000 km, where the electron concentration is  $N_c \approx 10^4$  electron·cm<sup>-3</sup>. Beyond this point, the rate at which the electron concentration changes with altitude decreases significantly. Data on  $N_c$  at altitudes of  $z > 2000$  km are presented in (Ref. 9).

Date (1964)	Time Hours, Minutes	$z_c$ , km	$\int_0^{z_c} N dz \cdot 10^{-13}$ , electron·cm <sup>-2</sup>	$\mu \cdot 10^3$ km <sup>-2</sup>
2/21	12 36	429	0.96	4.3
2/27	15 28	786	1.23	7.4
3/2	15 24	858	1.1	5.4
3/7	13 56	721	1.59	5.6
3/9	13 54	753	1.05	5.75
3/10	9 32	410	0.765	10.5
3/11	13 53	790	1.56	5.05
3/12	9 30	413	0.82	5.4
3/13	13 53	823	1.29	6

2. A study of large-scale ionosphere nonuniformities (Ref. 3, 5). Non-regular changes caused by large-scale nonuniformities in the ionosphere were clearly apparent, along with regular horizontal gradients of electron concentration, in the recording of phase difference of signals having coherent frequencies. The dimensions of these nonuniformities fluctuated from several kilometers up to several hundreds of kilometers. For nonuniformities having the dimensions of  $l \sim 100$  km, the magnitude of the gradients

$\Delta \int_0^{z_c} \frac{\partial N}{\partial x} dz \sim 10^7$  electron·cm<sup>-2</sup> does not depend, on the average, on the non-uniformity dimensions. On the other hand, in the case of  $l \sim 100$  km the magnitude of  $\Delta \int_0^{z_c} \frac{\partial N}{\partial x} dz$  increases on the average with an increase in  $l$ .

The problem of measuring the parameters of large-scale nonuniformities and the integral electron concentration of the regular ionosphere was studied by measuring the phase differences of coherent frequencies and polarization fadings in antennae spaced widely apart (Ref. 5). It was found that simultaneous measurements on antennae spaced widely apart make it possible to clarify the contribution of horizontal gradients in the quantities

$\int_0^{z_c} N dz$  and  $\frac{d}{dt} \int_0^{z_c} N dz$ . In the approximation of a flat Earth, the shift

between the Faraday fadings of the signal received at two antennae located in the direction of the magnetic parallel is fully determined by regular and nonregular ionization gradients. This makes it possible to determine the magnitude of the regular and nonregular gradient in this direction.

3. Small-scale nonuniformities of the ionosphere (Ref. 6, 7). Small-scale nonuniformities have been studied in the city of Gorky since December, 1961, based on recordings of the flickers of AES signals from "Explorer-7", "Kosmos-1", "Kosmos-2", "Elektron-1", "Elektron-3", at a frequency of 20 Mc from three antennae spaced widely apart. The altitude and dimensions of nonuniformities causing radio flickers were determined, and also the most important morphological characteristics of the nonuniformities were analyzed: the diurnal variation, and the relationship to ionosphere and magnetic perturbations. The method consisted of measuring the altitude of the nonuniformities by measuring the time shifts between similar fluctuations in the antennae spaced widely apart, and this method is described in (Ref. 6). The horizontal dimensions of the nonuniformities ( $l \approx \frac{z_h}{z_c} V_c \Delta t$ , where  $V_c$  is the horizontal component of the satellite velocity) were determined according to the specific altitude of the nonuniformities  $z_H$  and the fluctuation duration  $\Delta t$ . /150

On the basis of these measurements it was found that small-scale nonuniformities have a sharply-expressed diurnal variation, with a maximum at night. During the nocturnal hours, the nonuniformities are observed in a significant portion of the F layer up to 500-600 km. They were recorded most frequently at altitudes of 250-350 km. On the average, the altitude of nonuniformities causing the observed fluctuations is located close to the F2 layer maximum. On this basis, it can be shown that the decrease in the number of nonuniformities recorded at high altitudes during the night is not only determined by a decrease in the degree of ionosphere nonuniformity  $\Delta N/N$  with altitude in the region of these scales, but also is primarily determined by the mean altitudinal profile of the electron concentration (Ref. 7).

The dimensions of the nonuniformities are primarily on the order of 1-2 km. During periods of ionosphere disturbance, nonuniformities with dimensions of 200-600 m are also recorded. Quite frequently the nonuniformities are localized in restricted regions of the ionosphere, with horizontal dimensions ranging from several tens of kilometers up to several hundreds of kilometers. In several cases, the focusing effect of refracting nonuniformities is recorded, leading to a significant increase in the level of the signal received. These nonuniformities are primarily located at altitudes of 250-350 km.

Small-scale nonuniformities are observed less frequently during the daytime hours. As the results of the recordings from the "Elektron-1" signal have shown, during the diurnal hours nonuniformities located at altitudes of 100-200 km are observed, in addition to nonuniformities with an altitude of  $z_H \approx 200 - 300$  km. In two cases (March 5 and March 23, 1964) when

magnetosphere storms were observed, the altitudes of  $z_H$  exceeded 300-350 km. At altitudes of 100-200 km, the nonuniformity dimensions are on the order of 1 km. At altitudes of 200-300 km, nonuniformities were observed having dimensions ranging up to 4-6 km, as well as up to 400-600 m.

#### REFERENCES

1. Mityakova, E.Ye., Mityakov, N.A., Rapoport, V.O. *Izvestiya Vysshikh Uchebnykh Zavedeniy. Radiofizika*, 3, No. 6, 1960.
2. Mityakov, N.A., Mityakova, E.Ye. *Geomagnetizm i Aeronomiya*, 3, No. 5, 1963.
3. Mityakov, N.A., Mityakova, E.Ye., Cherepovitskiy, V.A. *Geomagnetizm i Aeronomiya*, 3, No. 5, 1963.
4. Mityakova, E.Ye. *Geomagnetizm i Aeronomiya*, 4, No. 4, 1964.
5. Yerukhimov, L.M., Mityakov, N.A. *Izvestiya Vysshikh Uchebnykh Zavedeniy. Radiofizika* 7, No. 3, 1964.
6. Yerukhimov, L.M. *Geomagnetizm i Aeronomiya*, 2, No. 4, 1962.
7. Yerukhimov, L.M. *Kosmicheskiye Issledovaniya*, 3, 1965.
8. Rishbeth, H. *J. Atmos. and Terr. Phys.*, 26, No. 6, 1964.
9. Benediktov, Ye.A., Getmantsev, G.G., Mityakov, N.A., Rapoport, V.O., Sazonov, Yu.A., Tarasov, A.F. *Present Collection*, p. 581.

BRIEF SURVEY OF THE RESULTS OF PHYSICAL EXPERIMENTS ON THE  
SATELLITE "KOSMOS-2" IN THE IONOSPHERE

V. V. Afonin, T. K. Breus, G. L. Gdalevich, B. N. Gorozhankin,  
K. I. Gringauz, R. Ye. Rybchinskiy, and N. M. Shyutte

On April 6, 1962, the satellite "Kosmos-2" was launched into orbit /151 at a  $49^\circ$  angle to the equator, with a perigee of  $\sim 212$  km and an apogee of  $\sim 1546$  km. Most of the experiments on the satellite pertained to ionospheric research. Other experiments (including, for example, a study of the photo-emission of electrons under the influence of solar ultraviolet radiation and changes in this emission along the satellite orbit) were related to this research. In addition to a telemetry system, operating in direct radio communication with receiving stations on USSR territory, the satellite carried a memory system which stored the data from a number of measurements over the entire orbit and which reproduced the stored information when the satellite passed over the vicinity of the radio receiving stations. The measurements connected with a portion of the experiments were reproduced only in the sectors of the satellite's orbit where there was direct radio communication with the Earth (i.e., the experimental results were not stored).

As is known, the concentration of charged particles and the chemical composition of the ionosphere region at altitudes from 500 to 1000 km were first investigated in 1958 by the third Soviet satellite. Here the ion component of the ionosphere was studied (using ion traps [Ref. 1] and an ion mass-spectrometer [Ref. 2]). All the data obtained by the third satellite referred to the orbit sectors illuminated by the sun.

The main objects of the experiments on "Kosmos-2" were:

- a) to obtain information during a different phase of solar activity on the ionosphere regions explored in the third satellite; (during a decrease in solar activity.
- b) to compile data pertaining, on one hand, to ionosphere regions not investigated by the third satellite (more than 1000 km above the Earth's surface), and, on the other hand, pertaining to nocturnal and crepuscular conditions;
- c) to obtain data on ion temperature, using for the first time a method involving honeycomb ion traps with a particularly narrow directional diagram.
- d) to study by sounding methods both the ion components of ionosphere plasma (just as in the third satellite) and its electron components in order to measure electron temperature and concentration; and
- e) to use a system of flat ion traps to determine the satellite's orientation relative to its velocity vector.

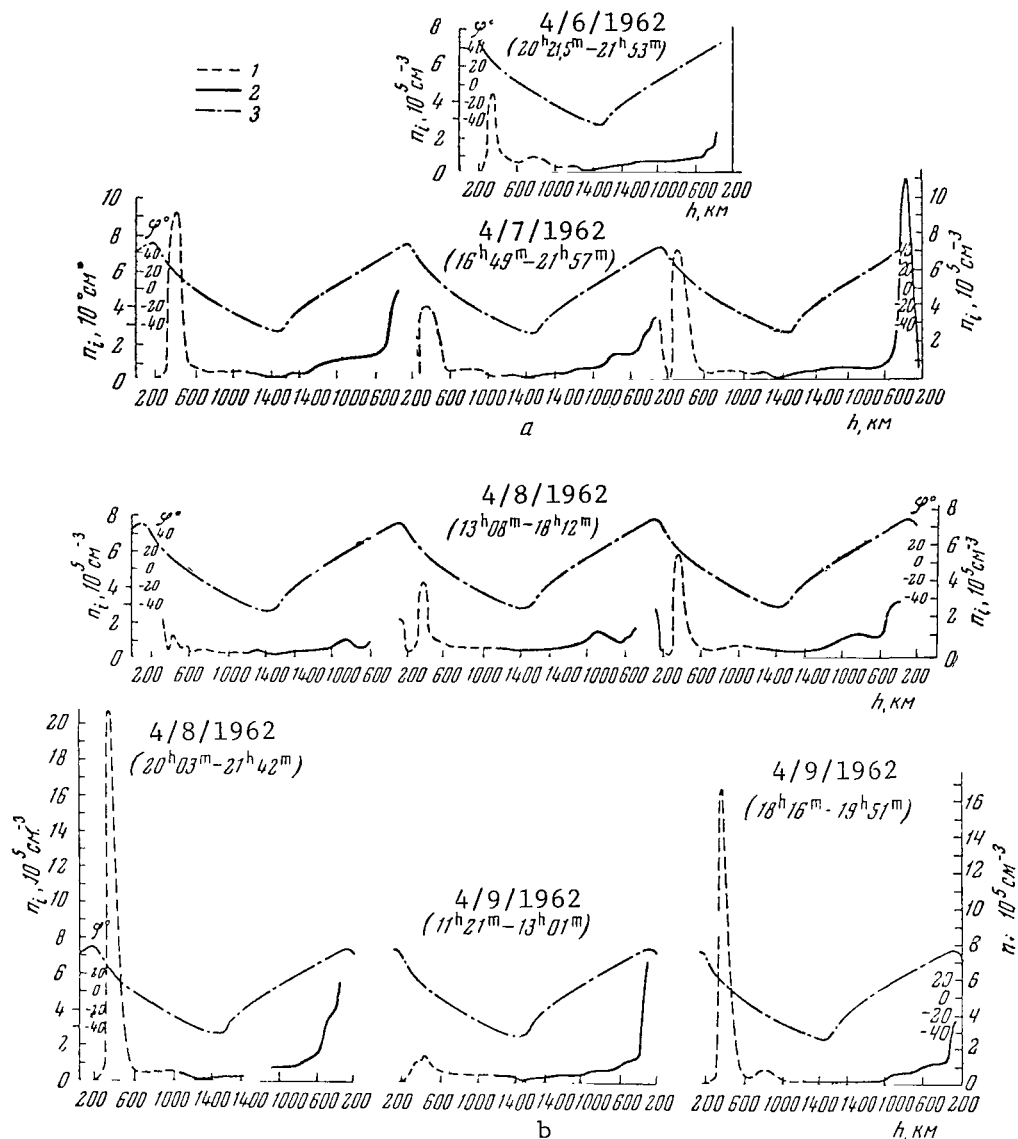


Figure 1

Dependence Of Positive Ion Concentration  $n_i$   
(Measured Along Satellite Orbit) on Altitude  $h$

1 - Nonilluminated sectors of orbit; 2 - Illuminated sectors; 3 - latitude  $\varphi$ . Moscow time.

Altitude change, from left to right.

The experiments mentioned above on photoelectron emission were conducted on the satellite, as well as certain methodological experiments to determine more precisely the influence upon the measurements of several factors, the degree of whose effect on the measurement results was not entirely clear (i.e., the influence of structural features of the ion traps and of the distance they were located from the satellite frame).

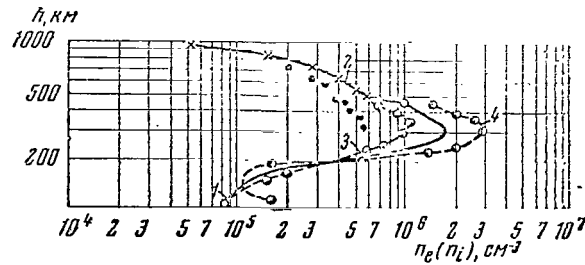


Figure 2

### Approximate Altitude Distribution Of Charged Particles At a Period Close to Maximum Solar Activity

The lower part of the graph is plotted from data obtained from one of the vertical launches of geophysical rockets (February 21, 1958, curve 1): the upper part (from 500 km and up) - from data of measurements in a portion of the third Soviet satellite orbit (May 19, 1958, curve 2). Points obtained at these altitudes at different times in 1958 from other geophysical rockets, or other revolutions of the third satellite (3, 4) are plotted close to the curve. These points characterize ionospheric variability to a certain extent.

The present brief survey cannot, of course, dwell in any detail on matters involving experimental methods or instrument design; certain indispensable information on these subjects will be given in appropriate sections of the report.

### I. Distribution of Positive Ion Concentration Along the Satellite Orbit

/152

Local positive ion concentration was related to a number of quantities which were measured, and the results were stored over the entire orbit of the satellite. On the surface of the satellite there were eight, flat, three-electrode ion traps placed, respectively, in each of the eight octants into which space may be divided. The angles between the normals to the external grids of any two adjacent traps comprised  $\leq 90^\circ$ . The external grids of the traps had the same potential as the satellite body. There /153 were also spherical three-electrode ion traps whose external grid voltages varied by a bipolar sawtooth law. These traps were separated from the satellite surface just as on the third Soviet satellite. The operating principle of the spherical traps was presented in (Ref. 3), and more fully in (Ref. 1). The internal grids in all the traps had a constant negative potential relative to their collectors, and were designed to suppress photoemission and secondary electron emission from the collectors.

Figure 1a and 1b present graphs of the changes in positive ion concentration  $n_i$  along the orbit during ten revolutions of the satellite about the Earth, based on data from the system of flat traps. The method for processing the primary data from measurements of the collector currents of the flat traps is presented in (Ref. 4). This method is based on considerations which follow from (Ref. 5) and (Ref. 1).



We should note that, although the values of  $n_i$  found with spherical traps differ somewhat from those found with flat traps, the nature of their variations along the orbit is the same.

When examining the graphs in Figures 1a and 1b, we must bear in mind that, although represented in a coordinate system  $(h, n_i)$ , they - like any other measurements of local concentrations made by the satellite - are not exact representations of the altitudinal pattern of charged particle concentration in the ionosphere for the following reasons: (a) since the horizontal velocity of the satellite is much greater than the vertical velocity, such graphs unavoidably reflect horizontal nonuniformities and latitudinal anomalies in  $n_i$ , in addition to the altitudinal behavior of  $n_i$ ; (b) local time is also continuously changing, as well as height above Earth and latitude along the orbit. It is, nevertheless, extremely interesting to compare these graphs with similar ones made during maximum solar activity in 1958.

Figure 2 presents a composite curve of the altitudinal distribution of charged-particle concentration in the ionosphere at altitudes up to 1000 km from measurement data obtained in 1958. One peculiarity of this distribution is the very slow drop in charged particle concentration as the altitude increases above the main ionization peak in the ionosphere. As may be seen from the graphs in Figures 1a and 1b, the reduction in  $n_i$  as altitude increases above the main ionization peak is the same in all the revolutions of "Kosmos-2" around the Earth - it occurs significantly faster than the 1958 data indicate (Figure 2). The curve slope in the unilluminated portion of the orbit changes rather abruptly at heights of  $\sim 600$  km (Figure 1a). Just as sharp a steepness change is observed in the illuminated portions of the orbit, but at somewhat higher altitudes. /154

Since, according to (Ref. 6), the steepness of the altitudinal pattern of charged particle concentration substantially depends on the mean ion mass, it is logical to assume that the regions of very sharp curvature change in the graphs in Figures 1a and 1b correspond to transitional regions, changing from the predominance of heavy ions at lower altitudes to the predominance of lighter ions at higher altitudes.

We must remember that there were only mass-spectrometer measurements on the third Soviet satellite in the outer ionosphere up to altitudes of  $\sim 1000$  km during a period of maximum solar activity (Ref. 2).

Equipment was employed with a range of ion mass numbers from 6 to 48 amu - i.e.,  $\text{He}^+$  and  $\text{H}^+$  ions could not be registered. Although the experimental results themselves (Ref. 2) cannot answer the question of whether there were light ions ( $\text{He}^+$  and  $\text{H}^+$ ) at these altitudes, an analysis of them in conjunction with results derived from measurements with spherical ion traps on the same satellite (Ref. 4) leads to the conclusion that at that time  $\text{O}^+$  ions were actually predominant at altitudes up to 1000 km (Ref. 2). American experiments in 1960 point to the same conclusion (Ref. 7).

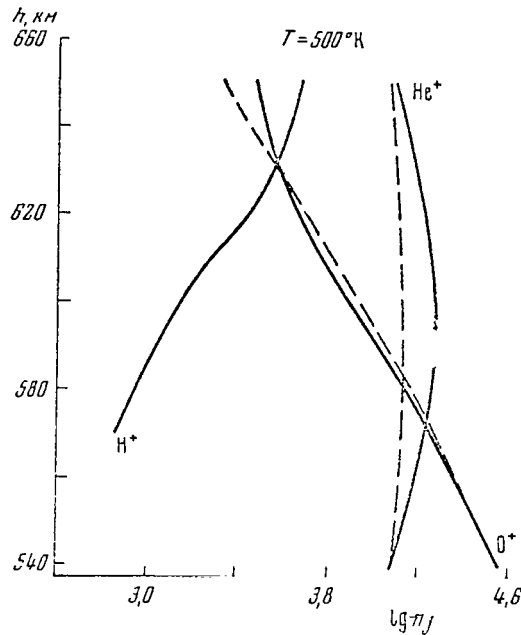


Figure 3

#### Tricomponent Model Of Transition Region

Based On Data From "Kosmos-2"

Dashed lines - theoretical curves plotted on assumption that oxygen and helium are in diffusion equilibrium;  $n_j$  - partial concentration of ions of unit mass.

If this is the case, the significant change in the nature of  $n_i$  distribution above the satellite orbit as altitude above the Earth increased in the 1958-1962 period is logically to be associated with the decrease in solar activity over this period. This decrease in solar activity cools the upper atmosphere and lowers the heavy ion ( $O^+$ ) layer, and consequently causes a transition between the regions of heavy and light ion predominance. This assumption is corroborated by the considerations in the next section of this report.

#### II. Ion Composition of Transitional Region From Heavy Ion ( $O^+$ ) to Light Ion Predominance

As already noted in (Ref. 1), analysis of the data from spherical ion traps on "Kosmos-2" makes it possible to estimate ion composition at altitudes of 520-650 km. The volt-ampere characteristics of these traps permitted total ion concentration.

$$\sum_j n_j = n_i(h). \quad (a)$$

to be determined on the basis of the point corresponding to zero potential of the external grid relative to the neutral plasma.

The sum of the ratios of partial ion concentration to corresponding mass numbers could be found from the steepness of the upper linear sector of the characteristic curve,

$$\sum_j \frac{n_j}{M_j} = F(h). \quad (b)$$

If we assume that two types of ions are present in the ionosphere region explored, then the solution of the system of the two equations (a) and (b) enables us to find the concentration distribution of both components -  $n_1$  and  $n_2$ . Two bicomponent, ionosphere models - those which are most probable for altitudes of 520-650 km - were studied. Solution of equations (a) and (b) for an assumed oxygen-hydrogen ionosphere showed that in this case the mean ion mass  $m_+$  diminishes with extraordinary slowness. This does not tally with the abrupt change in the slope of the  $n_i$  altitude distribution experimentally derived. /155

Furthermore, an oxygen-helium model was studied, which led to the relative  $\text{He}^+$  and  $\text{O}^+$  concentration distribution described in (Ref. 4).

The explanation of the  $\text{O}^+$  and  $\text{He}^+$  concentration distribution in this model encounters a number of difficulties, however, if we assume that diffusion equilibrium prevails in the region examined. At the same time there is no reason to suppose that such an equilibrium is lacking, at least for heavy ions. It may be demonstrated that a tricomponent model of the transition region ( $\text{O}^+$ ,  $\text{He}^+$ , and  $\text{H}^+$  ions) satisfies all the experimental data obtained in this region by "Kosmos-2", and moreover the heavy ions ( $\text{O}^+$ ) occur in diffusion equilibrium.

To design a tricomponent model, we must have a third equation to supplement the system of equations (a) and (b). This equation may be derived by utilizing altitude distribution  $n_i$  and formula

$$\frac{\partial n_e}{n_e} = \frac{\partial n_j}{n_j} = - \frac{m_+ g}{2kT} dz, \quad (1)$$

deduced by Mange (Ref. 6) for a quasi-neutral ionosphere ( $n_e = n_i$ ) consisting of single-charged ions on condition that  $T_i \approx T_e \approx T$ . Assuming that this condition is fulfilled and the magnitude of  $T$  is known, we may then find the mean mass  $m_+$  from equation (1):

$$\frac{\sum m_j n_j}{\sum n_j} = m_+ (h) \quad (c)$$

Simultaneous solution of equations (a)-(c) for the tricomponent case can give the concentration distribution of  $\text{He}^+$ ,  $\text{O}^+$ , and  $\text{H}^+$  with altitude.

As follows from the data in the survey reported at this conference (Ref. 8), two extreme temperature readings - 500-700 K - may be determined for the nocturnal hours ( $T_e \approx T_i$ ) in April, 1962, at equatorial latitudes (the location of the heavy-to-light ion transition region in question) and at altitudes corresponding to this region.

Figure 3 depicts the  $O^+$ ,  $He^+$ , and  $H^+$  distributions derived for the tricomponent model of an isothermic ionosphere when  $T = 500^\circ K$ . When  $T = 700^\circ K$  the distributions have the same appearance, but with the difference that transition from oxygen ion predominance to  $He^+$  predominance occurs at altitudes of  $\sim 630$  km.

The assumption that the ionosphere was isothermic was utilized, inasmuch as (Ref. 9) - the results of which were used to estimate temperatures (along with some other papers) - made it impossible to derive unambiguous /156 data on altitude temperature gradients and to judge the reliability of the gradient values contained in it. In a nonisothermic ionosphere with a gradient of  $\sim 0.5-1^\circ \text{ km}^{-1}$ , however, an intermediate model would be valid which coincided at altitudes of 500 and 650 km with the extreme models calculated for  $T = 500$  and  $700^\circ K$ .

It is to be stressed that at equatorial latitudes vertical distribution (1) corresponds to establishment of diffusion equilibrium in a volume in which diffusion takes place across the magnetic field, and therefore may give values of  $T$  distinct from longitudinal values determined from distribution along the field. The lack of data prevented this longitudinal distribution from being plotted for "Kosmos-2". The estimates which we did manage to make, however, indicate that the longitudinal temperature at an altitude of 500 km was  $\sim 700-800^\circ K$ .

As is shown by a comparison with the findings of (Ref. 10) which investigates precisely this longitudinal distribution, this result should not materially alter the qualitative picture sketched here.

The calculated tricomponent model, just as the bicomponent one described in (Ref. 4), indicates the existence of a region of helium ion predominance above the region where  $O^+$  ions predominate. It should be noted that there is fairly good agreement between the "Kosmos-2" ion composition results and data obtained by the Anglo-American satellite "Ariel-1" launched at the end of April, 1962, soon after "Kosmos-2". Nocturnal measurements at low altitudes by "Ariel-1" indicate the predominance of helium ions over the other ions in the altitude region of 500-1000 km (Ref. 9).

### III. Electron Concentration and Temperature Measurements Using Cylindrical Langmuir Probes

Measurements by Langmuir probes belong to the group of experiments whose results were not registered by the memory unit (Ref. 11). Therefore, the findings of these experiments refer only to the orbit sectors in the

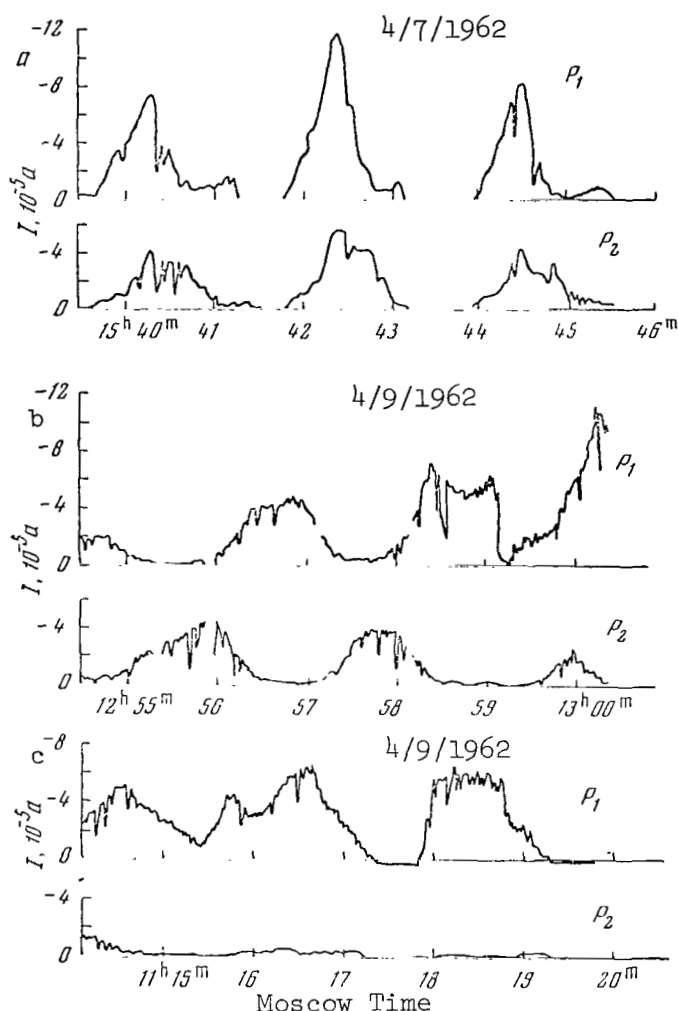


Figure 4

Envelopes Of Maximum Values Of Electron Probe Currents  
 $P_1$ ,  $P_2$  Designate First and Second Probes

~ 212 to ~ 600 km altitudinal range.

In the plane of one of the satellite cross sections perpendicular to its longitudinal axis, two cylindrical probes 1 cm in diameter and 20 cm in length were so placed near the surface that the central angle between them was  $90^\circ$ . A third probe of the same size was installed 10 cm from the satellite surface in a plane perpendicular to that of the first two. The probes were so located as to be able to detect the effect of the Earth's magnetic field on measurements. For undetermined reasons, the third probe did not function during the flight.

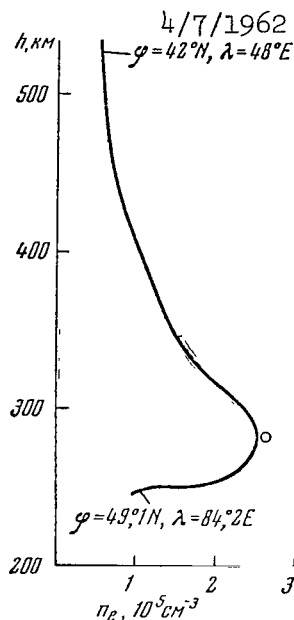


Figure 5

Dependence Of Electron Concentration  $n_e$  On Altitude  $h$ ,  
Measurement By Langmuir Probes in Sector Of Satellite  
Orbit On April 7, 1962

Circle indicates  $n_e$  value at F layer maximum as calculated from data of ionosphere stations;  $\varphi$  - latitude;  
 $\lambda$  - longitude.

Identical voltages  $V_p$  relative to the satellite frame were delivered to all the probes and varied according to a bipolar pulse law. The values both of  $V_p$  and of the probe currents were simultaneously transmitted to Earth. The classical methods described in (Ref. 12) were employed to process the probe characteristics and from them to determine electron concentration  $n_e$  and electron temperature  $T_e$ . Satellite rotation modulated the probe currents.

Figure 4 gives the envelopes of the peak electronic probe currents recorded during each period of sawtooth voltage fed to a probe. These envelopes are given for the three time periods shown in the graphs. It is evident from the graphs that maximum probe currents periodically change, 158 falling to values beneath the sensitivity level of the probe current boosters. Here in some cases the electron current maxima of both probes are congruent in time (Fig. 4a), while at other time periods a current maximum in one probe matches a current minimum in the other (Fig. 4b). There are cases where the readings of one of the probes are very small for comparatively long periods of time (Fig. 4c).

An analysis of the simultaneously-recorded ion currents in the eight flat ion traps installed on the satellite (see [Ref. 13]) showed that the minimum current values of each probe do not always correspond to the period of time the probe remains in the ion shadow formed behind the satellite (in the direction opposite the direction of its velocity). However, the variation period of the probe currents is determined by the satellite's rotation as Figure 4, for example, makes clear. We believe that these probe current changes are mainly connected with the changes in probe orientation with respect to the geomagnetic field. Depending on this orientation, the effective electron-collecting surface of the probe undergoes substantial variation, which is at its maximum when the probe axis is perpendicular to the magnetic field and minimum when this axis coincides with the direction of the magnetic field.

Figure 5 gives  $n_e$  values obtained with Langmuir probes in a sector of the satellite orbit on April 17, 1962, (satellite altitude decreased from 600 to 212 km). The same figure shows the  $n_e$  magnitude at the maximum of the F region determined from the critical frequency measured at an ionospheric station close to the projection onto the Earth of the orbit sector in which the probe measurements were made. Diurnal measurements of  $T_e$  during the flight of "Kosmos-2" gave values ranging from 1800 to 3000 °K (see table).

Figure 6 gives the simultaneously-measured probe characteristics and the time-dependence of the collector current of a "honeycomb" ion trap. Calculations based on the characteristic curves result in electron temperature values more than twice as large as the ion temperature values.

This indicates the lack of thermal equilibrium in the ionosphere at the altitudes of the F2 layer.

TABLE 1

ELECTRON TEMPERATURE  $T_e$  MEASUREMENT RESULTS USING LANGMUIR PROBES

Time						Time					
Date	Hour	Height	Lati-	Longi-	$T_e$ , °K	Date	Hour	Height	Lati-	Longi-	$T_e$ , °K
	Minute	km	tude	tude			Minute	km	tude	tude	
4/17	16 42	288	48°N	71°E	3150	4/8	13 09	299	48.27	121.01	1800
1962	16 42	285	48.4	72	3000	1962	13 09	298	48.3	121.3	2200
	18 22	343	45	32	3000		13 11	262	49.1	131.3	1800
	18 23	317	47	37	2900		14 43	528	36	59.1	2600
	18 24	297	48	43	3200		14 49	339	46.76	85.85	2700
	18 24	300	48	42	2500		14 50	336	46.9	86.5	2800
	20 08	265	48.9	27	1800						
	20 08	264	49	27.3	2500						
	20 08	262	49.1	28	2300						

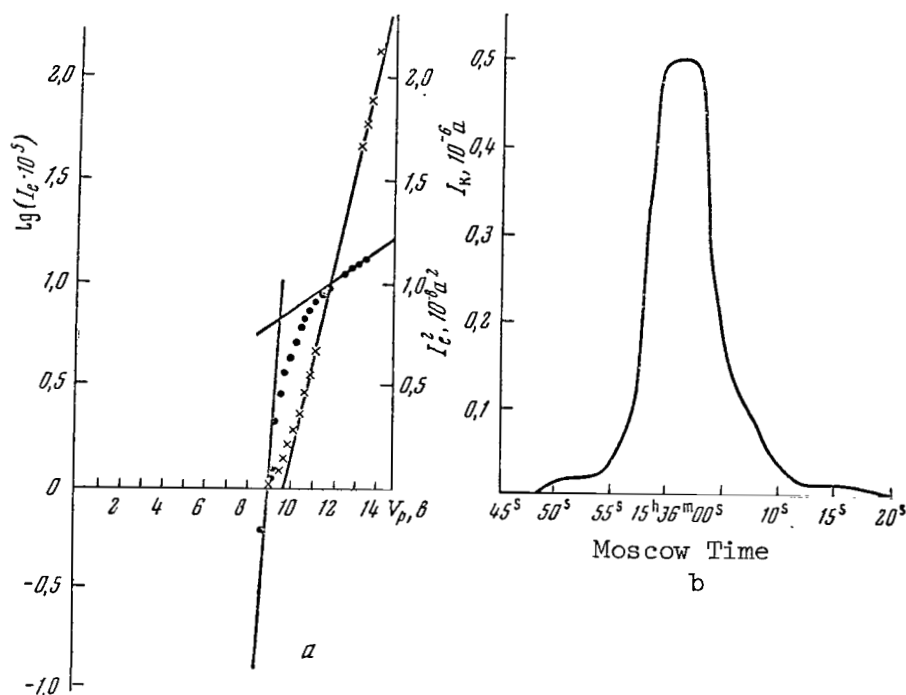


Figure 6

Experimental Recordings of Langmuir Probe Currents  
and "Honeycomb" Ion Trap Obtained Concurrently

a - Semilogarithmic characteristics and dependence of  $I_p$  on  $V_p$  for Langmuir probe; b - time-dependence of "honeycomb" ion trap collector current.

#### IV. Determining Positive Ion Temperature With Honeycomb Traps

The honeycomb-type ion trap used for the first time on "Kosmos-2" (Figure 7) is a three-electrode device consisting of a collector, an anti-photoelectron grid to suppress the photocurrent from the collector surface /160 and an external honeycomb adapter connected to the satellite frame. This adapter consists of an assemblage of contiguous hexagonal "honeycomb" tubes. It is obvious that the directional properties of such a trap are the same as with a single tube, while the collector current increases in proportion to the number of tubes. The peak current occurs when the velocity vector of the incoming stream of ions coincides with the normal to the collector. With sufficiently narrow tubes the trap can be compact and very sensitive to orientation with respect to the velocity vector. One article (Ref. 14) has been devoted to the feasibility of using a narrow tube for ionosphere measurements, and has established that neutral particle current is dependent on temperature and the angle between the velocity vector and the axis of a differentially-narrow tube.



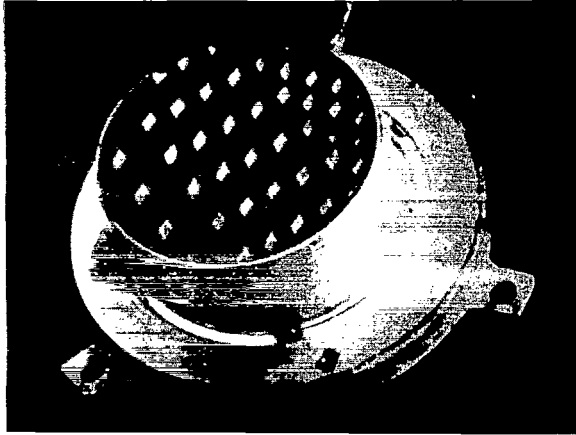


Figure 7

### Honeycomb-type Ion Trap

Given this tube shape, ion temperature  $T_i$  significantly affects the dependence of the collector current on trap orientation to the vector of the incoming ion stream. The collector current of a honeycomb trap may be represented as

$$I_c = I_{c0} F\left(\psi, \frac{R}{L}, T_i\right), \quad (2)$$

where  $I_{c0} = eSVn_i$  is trap current when  $T_i = 0$  and the velocity vector coincides with the tube axis;  $e$ , the electron charge (ions are assumed to be single-charged);  $V$ , satellite velocity;  $S$ , the sum of the cross sections of all tubes;  $F$ , the function defining the dependence of collector current on orientation and temperature;  $\psi$ , the angle between trap axis and satellite velocity vector; and  $R/L$  is the ratio of tube transverse dimension to longitudinal dimension.

To find the type of function  $F$ , the actual hexagonal tube was replaced by a right circular cylinder with a base area equal to the input aperture of the tube. When  $T_i = 0$ , function  $F$  may be easily computed analytically:

$$F(\psi, R/L, T_i = 0) = \frac{2}{\pi} \left( \arccos \frac{L}{2R} \lg \psi - \frac{L}{R} \lg \psi \sqrt{1 - (L/2R \lg \psi)^2} \right) \quad (3)$$

$$\lg \psi \leq \frac{2R}{L}. \quad (4)$$

If  $T_i \neq 0$ , the ions have velocity components perpendicular to the satellite velocity vector, with a resultant change in the form of function  $F$ . In order to ascertain the actual form of function  $F$ , we must take into account not only the thermal motion of the ions, but also the distortion

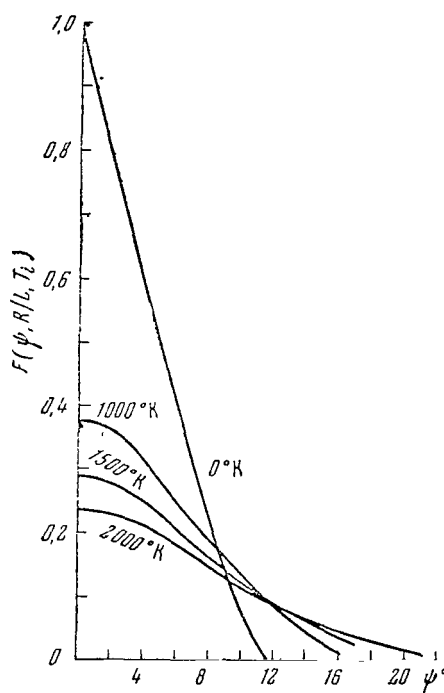


Figure 8

Calculated Curves For Function  $F(\psi, R/L, T_i)$  Which Defines Dependence Of Honeycomb-Trap Collector Current On Its Orientation  $\psi$  Relative To Velocity Vector  $V$  And Temperature  $T_i$

Calculations Made for Ions of Atomic Oxygen, Satellite Velocity  $V = 7.5 \text{ km} \cdot \text{sec}^{-1}$ , and Ratio  $R/L = 0.1057$ .

of the ion trajectory when moving in the electric fields in the space charge layer surrounding the satellite as well as within the trap. Function  $F$  was computed without regard to the effect of potentials - i.e., current was calculated for neutral particles of mass and temperature equal to ion mass and temperature. With a negative potential on the satellite frame, the presence of electrical fields results in a certain expansion of function  $F$ .

When  $T_i \neq 0$ , function  $F$  is a quintuple integral which cannot be expressed in analytic form. It was therefore calculated on an electronic digital computer. Figure 8 gives the computational results for the trap on "Kosmos-2". This same figure also displays the curve for  $T_i = 0$ . It is evident from the figure that the  $F(\psi)$  curves expand because of thermal motion. Moreover, one important feature of the  $F(\psi)$  curves is the great dependence of the values of  $F(\psi=0)$  on temperature. For example, when  $T_i = 2000^\circ\text{K}$  the maximum possible current in the trap (when the tube axes coincide with satellite velocity vector) is about four times less than when  $T_i = 0$ . The strong dependence of  $F(\psi = 0)$  on  $T_i$  is explained by the

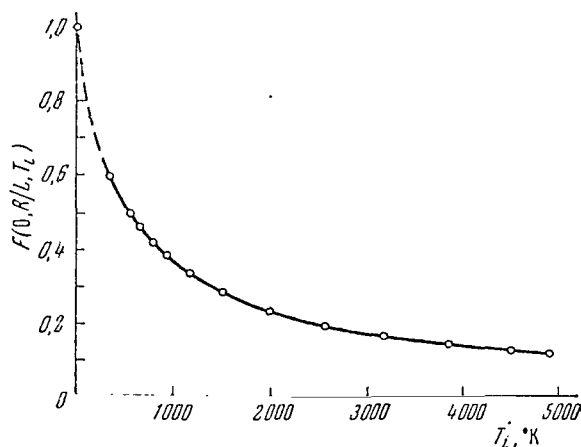


Figure 9

Calculated Dependence Of Function F On Temperature  
For  $\Psi = 0$  And the Same Parameter Values As In Figure 8

Value Of F For  $T_i = 0$  Derived by Formula (3); Other  
Values Calculated by Computer

joint effect of thermal motion and the capacity of the narrow tube to separate just those particles whose velocity vectors form a small angle with the tube axis. At a low thermal velocity the particles "enter" the tube and reach the collector without having time to reach the walls. As temperature rises, thermal velocities and the number of particles managing to reach the walls during the flight time increase, and as a result the collector current decreases. The dependence of  $F(\Psi = 0)$  on temperature is shown in Figure 9 ( $M_i = 16$  amu,  $V = 7.5$  km·sec<sup>-1</sup>,  $R/L = 0.1057$ ). /161

It can be seen from the above statements that experimental data on the dependence  $F(\Psi, R/L, T_i)$  may be employed to determine  $T_i$  (by comparing them with calculated values if  $m_i$  [ion mass],  $V$ , and  $R/L$  are known). Experimental values of honeycomb-trap collector current  $I_c$  may also be utilized to find  $T_i$  when  $\Psi = 0$ , if  $n_i$  is independently determined. This enables us to determine the experimental value of  $F(\Psi = 0)$  as the ratio /162

$$I_{c \max} / I_{c0} = I_{c \max} / eSVn_i.$$

Thus,  $T_i$  can be found by two methods - by comparing curve shapes and by employing  $I_c(\Psi = 0)$  and the values of  $F(\Psi = 0)$  given in Figure 9.

Figures 6 and 10 give examples of experimental records of honeycomb

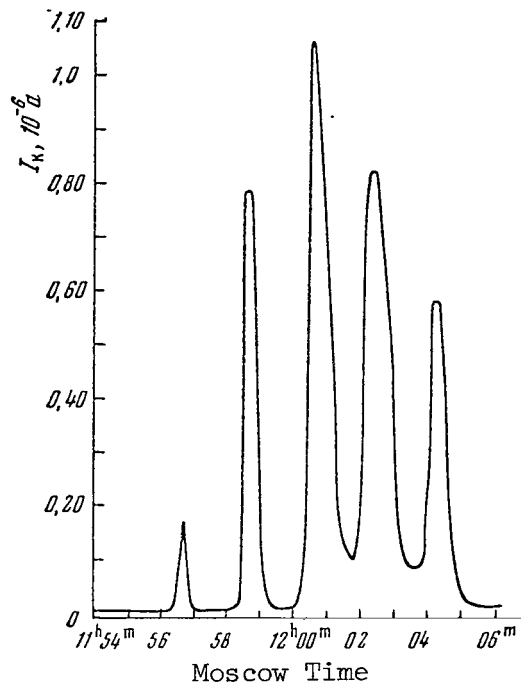


Figure 10

#### Experimental Record of Honeycomb-Trap Collector Current Obtained During Satellite Flight

trap collector currents made during the flight of "Kosmos-2".

When determining temperature by the above methods, we estimated the influence of the electric fields which were not taken into account in the calculations. With allowance for this effect, the temperature determined by the curve in Figure 6 lies between  $T_i = (1300 \pm 200)^{\circ}\text{K}$ .

#### V. Measuring Electron Photoemission Along Satellite Orbit

Use was made of so-called photoelectron analyzers of the type described in (Ref. 15) to measure electron photoemission from the metallic surfaces on "Kosmos-2". Structurally, the photoelectron analyzer was an ordinary semispherical three-electrode trap (e.g., see [Ref. 16]) whose collector in the given case was a photoelectron emitter. Three photoelectron analyzers in all were installed on the satellite, so that the normals to them formed three mutually-perpendicular directions. The voltages on the photoemitter electrodes were such that neither positive ions with thermal velocities nor electrons with thermal velocities from the surrounding medium could reach the emitter. The measurement of photoemission from a metal surface under the effect of solar radiation is of great interest in explaining the role of photoemission in establishing an equilibrium body charge. Photoemission is not very large in ionospheric regions with a great concentration of charged particles.

At altitudes where this concentration drops, however, electron photoemission from the surface of space equipment and individual instrument components may essentially affect the results derived from probe investigations of the environment.

A study of the energy distribution of photoelectrons is, moreover, a source of information on solar photon streams.

Photoemission was measured by "Kosmos-2" only in the regime of direct radiotelemetric transmission and in the altitude region of ~212-600 km. Presently existing data on absorption of ultraviolet radiation by the Earth's atmosphere refer to the region below 235 km (Ref. 17). It is thus of definite importance to obtain data on the integral absorption of solar radiation at altitudes above 200 km.

The photoemitter current is known to be proportional to the strength of the radiation stream causing it when there is no electric field braking the electrons (so-called saturation photocurrent). Therefore, without analyzing the volt-ampere characteristics derived, let us examine the variation in current saturation in the photoelectron analyzers while the satellite is moving in the altitude range from 550 to 220 km. /163

It is not difficult to measure variation in the integral stream of solar radiation with a photoemitter trained on the Sun. This problem becomes more complicated with a satellite which is not oriented toward the Sun. By analyzing the dependence of emitter saturation photocurrents on their orientation with respect to the Sun, we found that for those instants when the currents of all three emitters differed from zero the photocurrent of each "Kosmos-2" emitter could, in the first approximation, be considered proportional to the square of the cosine of the angle of radiation incidence:

$$I_{1\max} \simeq I_{0\max} \cos^2 \varphi_1;$$

$$I_{2\max} \simeq I_{0\max} \cos^2 \varphi_2;$$

$$I_{3\max} \simeq I_{0\max} \cos^2 \varphi_3;$$

that is,  $I_{0\max} \simeq I_{1\max} + I_{2\max} + I_{3\max},$

where  $I_{0\max}$  is the photoemitter current corresponding to the radiation stream falling at a  $90^\circ$  angle. Thus, with three identical photoelectron analyzers trained in three mutually-perpendicular directions, we can determine the analyzer saturation current value corresponding to normal incidence of the radiation stream on the emitter, for those moments when the current values from all the emitters differ from zero. Each emitter may be oriented in any way with respect to the Sun.

The dependence of photoemitter saturation current on altitude is shown in Figure 11. The reduction of photocurrent with altitude, evidently

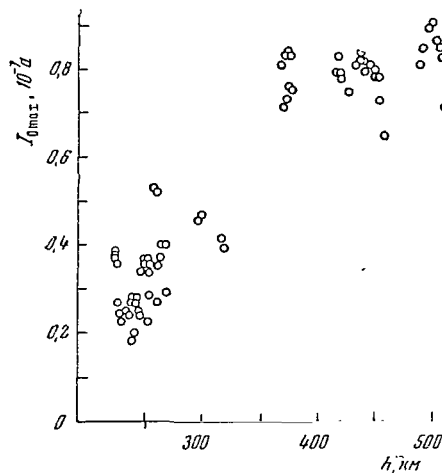


Figure 11

#### Dependence of Photoemitter Saturation Current on Altitude $h$

because of absorption of solar radiation, is in essence a photocurrent variation along the orbit, due to the increased distance along the line 1, as shown in Figure 12. Despite the essentially divergent nature of the absorption of the individual segments and lines of the solar radiation spectrum by different regions of the ionosphere (depending on composition, density, etc.), the attenuation of the integral radiation stream in a broad spectral range - as determined by the saturation current values of photoelectron analyzers in the 220-550 km altitude region - is on the whole clearly linear in nature. We should note that beginning at 293 km the angle of the Sun's elevation above the satellite horizon takes on negative values, i.e., beginning at this altitude solar radiation traverses a certain range of altitudes twice. /164

Figure 13 displays one of the volt-ampere curves obtained during the flight of "Kosmos-2", which shows the dependence of analyzer photocurrent on its internal grid voltage. The shape of this curve is essentially different from that derived during similar experiments by Hinteregger et al. (Ref. 18, 15). Under laboratory conditions, so-called calibrated volt-ampere characteristic curves were taken while irradiating an experimental model of a photoelectron analyzer with monochromatic radiation of different wavelengths. These laboratory volt-ampere characteristic curves are also depicted in Figure 13. It is evident from the figure that sector a-b of reduced slope, which is absolutely present on all in-flight characteristic curves, is lacking on the laboratory characteristic curves. This means that the solar radiation recorded by the satellite analyzers is apparently not entirely determined by radiation of the indicated wavelengths. Comparison of the laboratory characteristic curves with those of Hinteregger et al. (Ref. 15) and other experimental results obtained from irradiation of different metals with the far ultraviolet

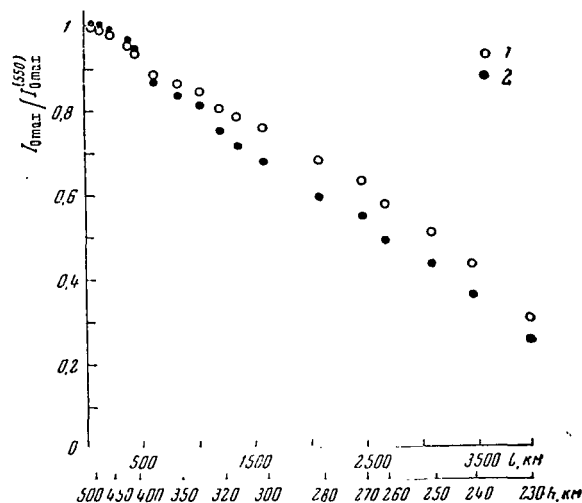


Figure 12

Relative Change in Saturation Current  $I_0 \max$   
Depending on Distance Along Line 1

$I_0^{(550)} \max$  -  $I_0 \max$  at altitude of 500 km; 1 - data from one satellite revolution of April 8, 1962; 2 - data from six satellite revolutions on April 8-9, 1962; 1 - distance along radial line figured from 550 km to satellite, h - satellite altitude above earth.

(Ref. 19), confirms the fact that there is no reason to doubt the reliability of the laboratory volt-ampere characteristic curves. At the same time, analysis of equipment functioning aboard "Kosmos-2" showed that the unusual aspect of the characteristics recorded cannot be caused by /165 equipment. All this makes us think that the shape of the volt-ampere characteristic curve is linked to the nature of the incident radiation. An indication of this may also be the fact that the sector of lesser steepness appears on the volt-ampere characteristic curves of all three photoelectron analyzers not only at a single definite value of the counter potential with respect to the emitter potential, but at different counter voltages relative to the satellite frame and to the potential of the external grid of the analyzer. The hypothesis has been advanced that in the given case a significant fraction of the photocurrent was provoked by soft x-rays. The character of the external photoeffect under the action of soft x-rays has been investigated in detail in a number of experiments (Ref. 20) which show that the photocurrent at comparatively high quanta energies has much in common with secondary emission. It has therefore been surmised that the lower portion of the volt-ampere characteristic curve, mainly up to sector a-b corresponding to photoelectrons of maximum velocities, represents primarily the spectrum of secondary electrons excited by a primary x-ray photoelectron as it traverses the slow electron outflow zone.

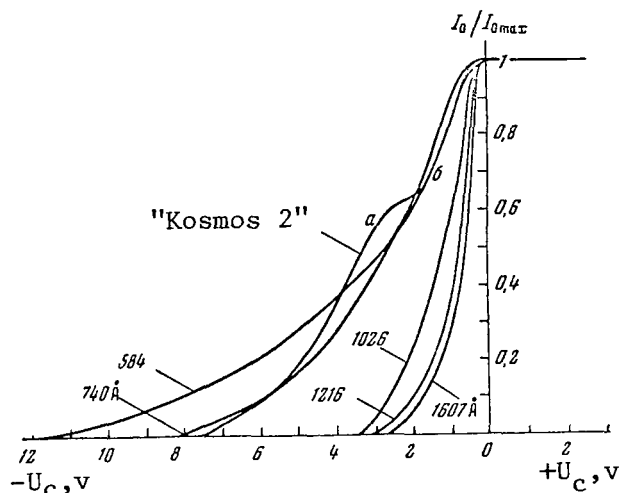


Figure 13

Photoelectron Analyzer Volt-Ampere Characteristics Derived Under Laboratory Conditions During Irradiation by Monochromatic Radiation of Various Wavelengths, and Volt-Ampere Characteristic Curve Obtained on "Kosmos-2":

$I_{0 \max}$  - saturation photocurrent with radiation incidence at  $90^\circ$  angle;  $I_0$  - photocurrent with counter potentials and  $90^\circ$  incidence of radiation,  $U_c$  - counter potential.

This hypothesis encounters serious objections, because it is rather difficult to explain the fact that during the experiments of Hinteregger et al. in 1958 and 1959, which coincided with a period of peak solar activity when the x-ray streams were more intense, no such phenomenon was detected. It may be assumed that the cause is the differing state of emitter surfaces during these experiments - to be precise, that the surface of the "Kosmos-2" emitters gave a substantially higher yield of secondary electrons. It may also be assumed that this feature of the volt-ampere curves is caused by simultaneous irradiation of the photoelectron analyzer by streams of ultraviolet radiation and corpuscular streams of energies which permit the latter to reach the emitter. The similarity of volt-ampere characteristics obtained at different altitudes, latitudes, and zenith distances, however - as well as the lack of currents recorded by analyzers in night time - indicate that this explanation encounters substantial difficulties. If, however, it is assumed that the above hypothesis is true, then this means that in the ultraviolet portion of the solar spectrum the predominant radiation has wavelengths of  $\lambda > 900 - 1000 \text{ \AA}$ . The radiation flux in the  $1216 \text{ \AA}$  region at an altitude of 500 km was estimated at  $\sim 1 \pm 0.5 \text{ erg} \cdot \text{cm}^{-2} \cdot \text{sec}^{-1}$ , while the radiation fluxes in the  $584-1000 \text{ \AA}$  region are on the order of  $\sim 10^{10} \text{ photon} \cdot \text{cm}^{-2} \cdot \text{sec}^{-1}$ .

The shape of the volt-ampere characteristic curve hardly varies as



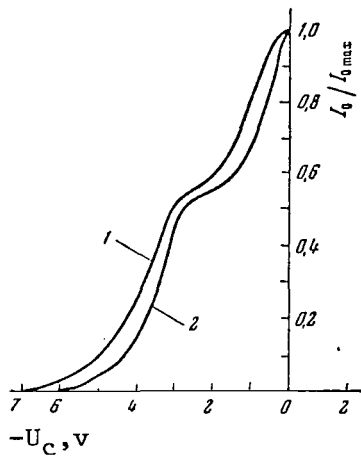


Figure 14

Volt-Ampere Characteristics of Photoemitter at  
Different Altitudes

1 -  $h = 525$  km; 2 -  $h = 300$  km;  $I_0$ ,  $I_0 \text{ max}$ ,  $U_c$  -  
as shown in Figure 13.

the satellite descends to lower atmospheric layers, and is shown in Figure 14.

It is thus obvious that in the 550-300 km altitude region the integral coefficient of solar radiation absorption is still rather large, and that radiation attenuation in this altitude region proves to be substantial when the solar rays fall obliquely.

#### VI. Determining "Kosmos-2" Orientation With Respect to Velocity Vector With Flat Ion Trap System

"Kosmos-2" used a system consisting of eight flat ion traps, described in Section I (see [Ref. 4, 5]), to determine the satellite's orientation with respect to the vector of its orbital velocity. We would like to note that in May, 1962, some time after the launching of "Kosmos-2", the British rocket Black Knight was launched in Australia with a system of 166 flat ion probes - i.e., the same physical principle (Ref. 21) - in order to determine orientation with respect to velocity vector. The collector current at some sector of a limitless flat ion trap, when the satellite frame has a negative potential, is determined by the expression (Ref. 5):

$$I_c = \alpha c S V_i n_i F(\psi, T_i) = I_{c.0} F(\psi, T_i), \quad (5)$$

where  $\alpha$  is total grid transmittance;  $S$ , collector area; and  $\psi$ , the angle between the normal to the collector and the vector of satellite velocity.

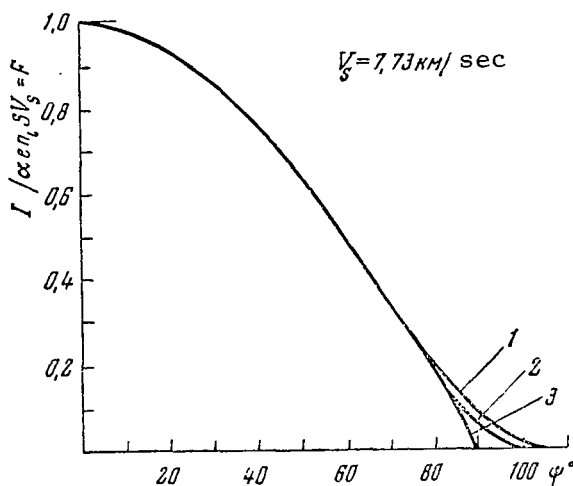


Figure 15

Dependence of Flat Ion Trap Function  $F$  on Angle  $\Psi$   
Between the Normal to Its Collector and Satellite Velocity Vector  
1 -  $T_i = 5000^\circ\text{K}$ ; 2 -  $T_i = 1800^\circ\text{K}$ ; 3 -  $T_i = 0^\circ\text{K}$

Figure 15 depicts the dependence of  $F(\Psi, T_i) = I_R / \alpha e n_i S V$  on angle  $\Psi$ , for  $T_i = 0, 1800$ , and  $5000^\circ\text{K}$  (curves 3, 2, and 1, respectively). When  $T_i = 0$  the function  $F$  coincides with  $\cos \Psi$ . When  $T_i \neq 0$  the cosinusoidal approximation may be employed in the lower range of  $\Psi$  values. It should be noted that the curves in Figure 15 refer to the flat ion trap as part of an unbounded, electrically-homogeneous plane. In our case the traps are installed on a body having finite dimensions. The edge effects must therefore not be disregarded, because at large values of angle  $\Psi$  the current of the actual trap exceeds the current in the corresponding sector of an ideal unbounded planar trap. Analysis of the flat trap collector current recordings from "Kosmos-2" demonstrates that the edge effects play a significant role. With normal incidence of the ion stream onto the trap ( $\Psi = 0$ ), the edge effects play a considerably smaller role. Taking into account the influence of ion temperature and the edge effects, we may assume that for the ion trap system aboard "Kosmos-2" the cosinusoidal approximation is valid for  $|\Psi| \leq 45 - 50^\circ$ :

$$I_c = I_{c0} \cos \psi. \quad (6)$$

This approximation was used to find velocity vector orientation with respect to the three chosen coordinate axes of the satellite. By taking advantage every instant of the current readings of the three traps, whose normals are non-coplanar, we may easily compute the velocity vector orientation with respect to the satellite frame.

To improve the accuracy with which this orientation is determined, we must solve equations of motion for the satellite as a free body and compare the solution with the trap readings. Such processing of the data from "Kosmos-2" flat trap system demonstrated that if the degree to which the sum of the squares of the direction cosines deviates from unity is

adopted as the measure of the accuracy with which velocity vector orientation is found, then this method makes it possible to find orientation within an accuracy no worse than  $\pm 3\%$ . However, this method entails a large volume of computational labor.

We must observe that the accuracy with which the velocity vector orientation was determined for the satellite in the experiments described was somewhat reduced, because of the somewhat unfortunate arrangement of the traps on the satellite surface (projecting elements of the satellite got into the way of the visual field of the traps in several directions) which slightly distorted the dependence of currents in individual traps on their orientation. If this is avoided, the accuracy with which velocity vector direction is determined can be increased. /167

### Conclusion

As is clear from the foregoing, the measurements made by "Kosmos-2" made it possible to derive interesting results regarding the structure of the ionosphere and characterizing the processes occurring within it.

In the latitude region from  $49^\circ$  N to  $49^\circ$  S and in the altitude range from  $\sim 212$  to  $\sim 1550$  km, the concentration of positive ions was measured. At altitudes from  $\sim 212$  to  $\sim 600$  km electron concentration and temperature were measured; direct computations of ion temperature were made for the first time. Data were obtained on the variations in photoemission from metals undergoing shortwave solar radiation in the altitude range close to the ionization peak of the F region of the ionosphere. These variations permitted us to estimate the integral absorption of solar ultraviolet radiation in this ionosphere region. Finally, so far as we know, the orientation of a space vehicle relative to its velocity vector was for the first time determined by means of ion sensors.

These results do not, however, exhaust the significance of the experiments made by "Kosmos-2". Their analytical results are very useful for preparing new experiments on space vehicles in the ionosphere.

### REFERENCES

1. Gringauz, K. I., Bezrukikh, V. V., and Ozerov, V. D. In: "Iskusstvennyye Sputniki Zemli", No. 6. Izdatel'stvo AN SSSR, p. 63, 1961.
2. Istomin, V. G. Ibid., No. 4, p. 171, 1961.
3. Gringauz, K. I., and Zelikman, M. Kh. Uspekhi Fizicheskikh Nauk, 63, No. 1b, 239, 1957.
4. Gringauz, K. I., Gorozhankin, B. N., Shyutte, N. M., and Gdalevich, G. L. Doklady Akademii Nauk SSSR, 151, No. 3, 560, 1963.

5. Whipple, E. C. J. Proc. IRE, 47, 2023, 1959.
6. Mange, P. J. Geophys. Res., 65, 11, 1960.
7. Bourdeau, R. E., Whipple E. C. J. Geophys. Res., 67, 467, 1962.
8. Breus, T. K., and Gdalevich, G. L. Kosmicheskiye Issledovaniya, 3, No. 6, 1965 (in press).
9. Bowen, P. I., Boyd, R. L. F., Henderson, C. L., Raitt, W. I., Willmore, A. P. Proc. Roy. Soc. A, 281, 504, 1964.
10. Angerami, I. I., Thomas, I. O. J. Geophys. Res., 69, No. 21, 4537, 1964.
11. Gringauz, K. I., Gorozhankin, B. N., Gdalevich, G. L., Afonin, V. V., Rybchinskiy, R. Ye., Shyutte, N. M. Space Res., 5, 733, 1965.
12. Mott-Smith, N. M., Langmuir, J. Phys. Rev., 28, 727, 1926.
13. Gringauz, K. I., Gorozhankin, B. N., Shyutte, N. M., Gdalevich, G. L. Space Res., 4, 473, 1964.
14. Pressman, A. Ya., and Yatsenko, S. P. Geomagnetizm i Aeronomiya, 1, No. 1, 49, 1961.
15. Hinteregger, H. E., Damon, K., Hall, L. A. J. Geophys. Res., 64, 8, 961, 1959.
16. Gringauz, K. I. Space Res., 2, 539, 1961.
17. Hinteregger, H. E. J. Geophys. Res., 66, 2367, 1961; Hall, L. A., Schweizer, W., Hinteregger, H. E. J. Geophys. Res., 68, 6413, 1963; Hall, L. A., Schweizer, W., Hinteregger, H. E. J. Geophys. Res., 75, 105, 1965; Hinteregger, H. E., Hall, L. A., Schmidtke, G. Space Res., 5, 1175, 1965.
18. Hinteregger, H. E. Space Res., 1, 304, 1960.
19. Hinteregger, H. E. Phys. Rev., 96, 538, 1954; Walker, W., Weissler, G. Phys. Rev., 97, No. 4, 1178, 1955.
20. Ganeyev, A. S., and Izrailev, I. M. Zhurnal Tekhnicheskoy Fiziki, 31, No. 3, 376, 1961; Nakhodkin, N. G., and Mel'nik, P. V. Radiotekhnika i Elektronika, 6, No. 7, 1209, 1961; 7, No. 2, 303, 1963; Rumsh, M. A., et al. Fizika Tverdogo Tela, 4, No. 1, 69, 1962.
21. Norman, K., Willmore, A. P. Planet. Space Sci., 13, 1, 1965.

# RESULTS OF IONOSPHERE RESEARCH BY ROCKETS AND SATELLITES IN 1960-1964

B. N. Gorozhankin and V. A. Rudakov

Our report is a brief survey of measurements of electron and ion concentration in the ionosphere to altitudes of approximately 2000 km. The aim of the report is not so much to communicate the specific results of various experiments as to delineate the methodological trends in the development of these measurements. The main reason for this is the inadequacy of the time allotted to the report. Moreover, the concentration of charged particles is one of the most important parameters of the ionosphere which, in particular, determines the laws of radio wave propagation therein. /168

We should also bear in mind that special reports (e.g., [Ref. 1]) are devoted to measurements of temperature and ion composition and to research on the peripheral region of the ionosphere.

The lack of time has also forced us to restrict ourselves to presenting, without a detailed discussion, only the measurement results which we view as most important.

The numerous methods of measuring  $n_e$  and  $n_i$  may be divided into two main groups:

- 1) ionospheric parameter measurements from the readings of instruments reacting to the environmental characteristics in the immediate vicinity of the sensitive element - probe methods;
- 2) measurements by radio waves emitted or received on a flying object and propagated over considerable distances - radio methods.

Some of these methods represent adaptations to new tasks of familiar methods of studying radio wave propagation and of plasma research in the laboratory. Others, however, have been specifically developed for studying the upper atmosphere by rockets and satellites.

The setup of each experiment had to allow not only for opportunities afforded by rockets and satellites, but also for the restrictions imposed by the properties of the medium, the nature of the objects' motion, the difficulties in transmitting information, etc. At present radio and probe methods alike are employed both in rockets and satellites.

## I. Rocket Measurements

We shall begin our review with rocket investigations of the ionosphere. Table I gives information on various vertical rocket launches abroad (1960-1964 period) in which ionospheric research was conducted (Ref. 2-10). The parameters measured have been appropriately designated

by the letters P and R for the measurement method used (P - for probe and R for radio methods).

TABLE I  
INFORMATION ON SEVERAL U.S. IONOSPHERE ROCKET EXPERIMENTS

Date	Greatest Height Of Region Studied, km	Parameters Measured	Measurement Method
4/12/61	1900	$n_i, T_i$	P
4/27	620	$n_e$	R
6/24	1000	$n_e$	R
10/19	1600	$n_e$	R
3/29/62	2800	$n_e, n_i$	P, R
4/30	240	$n_e, n_i$	P, R
7/2/63	850	$n_e, T_e$	P, R
6/30	5500	$n_e$	P
9/28	900	$n_e, T_e$	P, R
10/7/64	1000	$n_i, m_i$	P
10/7	1000	$n_i, m_i$	P

TABLE 2  
TABLE OF FOREIGN ROCKET LAUNCHES TO STUDY THE IONOSPHERE

Year	Country	Number of Launches	Greatest Height Reached, km
1960	U.S.	9	670
	Japan	2	190
1961	U.S.	14	6000
	Japan	5	350
1962	U.S.	8	6000
	England	5	250
1963	U.S.	14	11000
	England	7	250

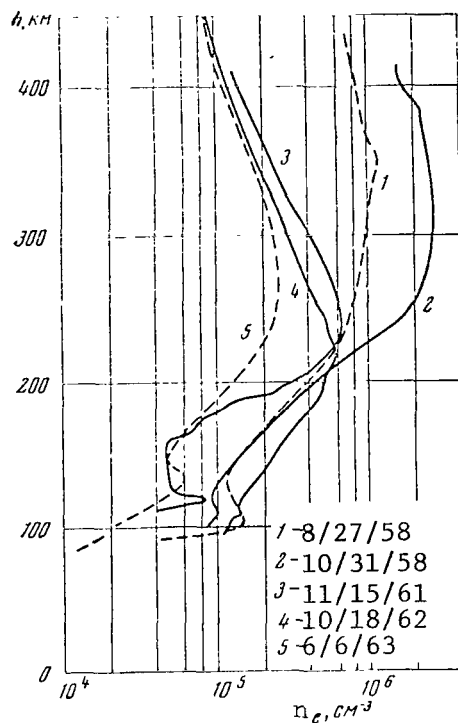


Figure 1

The radio methods, which were the first to be used in the U. S. and the USSR to measure  $n_e$  in the firing of research rockets, include the most widely-used methods of dispersion interferometry, Faraday effect observation, and pulse radio probing of the ionosphere from above. These procedures enable us directly to determine only electron concentration, but the measurement results describe substantially larger areas of the medium under study than do probe measurements. This is caused by the peculiarities of radio wave propagation. In measurements taking advantage of radio waves passing through the ionosphere, the regions over which they are averaged are measured in tens of meters, and in some cases - where the Faraday effect is used - in kilometers. The characteristics of the medium influence to a certain extent the radio measurements of local ionospheric parameters over the whole path of radio wave propagation. /169

Nevertheless, due to the great reliability of data obtained by radio methods in vertical rocket launches, these methods have been and remain the most trustworthy and accurate means of determining the altitude behaviour of  $n_e$  in the ionosphere.

Probe measurements (including, in particular, those using ion traps) make it possible to determine local concentrations of charged particles, and probe results do not depend on the state of the medium between the rocket and Earth. Probe measurements, however, involve considerable difficulties, for their results are affected by such factors as the space charge /170

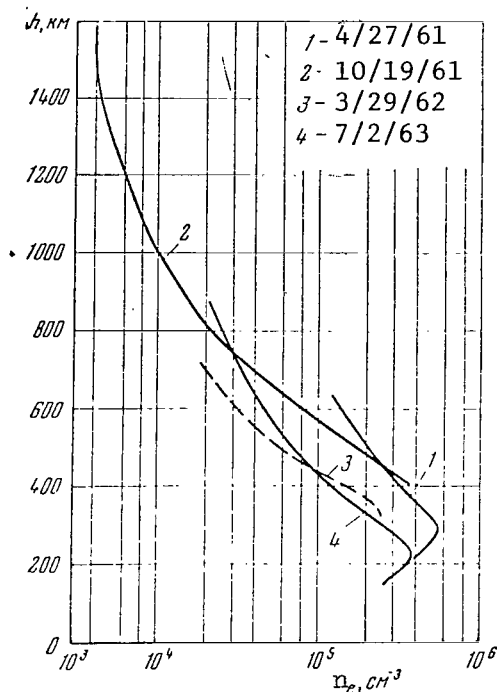


Figure 2

surrounding the rocket in flight, desorption of gases from the rocket surface, photoemission and secondary emission, and, when measuring electron concentration, the orientation of the sensor relative to the vector of the geomagnetic field.

At the relatively slow velocities of vertically-flying rockets (at least, in the upper portions of their trajectories) ion thermal velocities materially affect the determination of positive ion concentrations; therefore, ion temperature and ion mass composition must be known if the results are to be interpreted.

All of this makes rocket probe measurements complex, and demands very careful experiment preparations and, as a rule, laborious processing of experimental results.

Let us pass on to the results of rocket experiments. Figure 1 plots the distribution of electron concentration against altitude ( $n_e(h)$ - profiles) obtained by a dispersion radiointerferometer in firings of geophysical rockets by the Academy of Sciences, USSR. The solid curves refer to daytime launches, and the broken curves to morning launches. Two 1958 curves are given for purposes of comparison, as they were obtained by the same method (Ref. 11, 12).

A comparison of curves belonging to different years (see Figure 1) shows us that the main ionization peak in the years close to the solar activity minimum is several times smaller in size and 50-100 km lower in altitude than in the year near the solar activity maximum. The



concordant behavior of the curves pertaining to reduced solar activity (1961-1963), and the decrease in electron concentration above the peak in the F region, which was much more rapid in 1961-1963 than in 1958, are clearly apparent.

These deductions from a comparison of the  $n_e(h)$  - profiles in Figure 1 are in agreement with the experimental findings on ion concentration. /171 These findings indicate that, as solar activity decreases in its eleven-year cycle, ion concentration in the ionosphere is substantially reduced, and  $n_i$  decreases more rapidly as altitude increases above the peak in the F region. This information came from the ion traps installed on "Kosmos-2" (see Section II).

Figure 2 depicts the  $n_e(h)$  - profiles similarly measured during U.S. rocket flights (Ref. 3, 5, 6, 8). We should note that the curve of March 29, 1962, was derived from observations of the Faraday effect, because there was radio interference on one of the two interferometer frequencies. In the sectors compared, the curves in Figure 2 are close enough to each other, but we cannot fail to notice a perceptible difference in the slopes of these curves. In general, the curves of Figures 1 and 2 are identical in character, while the  $n_e$  values measured at different altitudes (in 1960-1963) are close to each other.

During rocket launches the altitude distribution measurements of charged particles were also carried out by various probing methods. Figure 3 illustrates such measurements with two  $n_i(h)$  distributions obtained in the U.S. with ion traps (solid curve from [Ref. 2], dotted curve from [Ref. 6]). Both distributions are nocturnal (about midnight); the difference between the behavior of the curves may, on the one hand, be attributed to differing ionospheric states during the experiments. On the other hand, this divergence may possibly result from errors introduced into the probe measurements by the diverse factors mentioned previously.

The scope of ionospheric rocket research is now great, as is illustrated by Table 2 containing incomplete data on rocket firings in several countries (Ref. 13-15). The program of the IQSY (International Quiet Sun Year) (1964-1965) calls for rocket launchings at fifteen locations in ten countries to investigate the ionosphere (Ref. 16). Because of the importance of research by vertically-launched rockets and in order that this research may be conducted by unified methods, the International Committee on Space Research (COSPAR) has published a handbook describing the recommended measurement methods and the corresponding equipment (Ref. 17).

## II. Satellite Measurements

When speaking of measurements by satellites, we must bear in mind that local measurements do not in this case give true vertical cross sections of the ionosphere, due to the presence of a horizontal component of satellite velocity which, in most cases, far exceeds the vertical component. The

TABLE 3

## IONOSPHERE RESEARCH BY SATELLITES

Date of Launch	Satellite	Country	Measured Ionosphere Parameters	Measurement Method
2/3/1960	Explorer 8	U.S.	$n_e, n_i, T_e, m_i$	T, P
10/13/1961	Discoverer 32	"	$n_i, T_i$	T
4/6/1962	Kosmos-2	USSR	$n_e, n_i, T_e, T_i, m_i$	T, P, R
4/17	Discoverer	U.S.	$n_i, T_i$	T
4/26	Ariel 1	Eng., U.S.	$n_e, n_i, T_e, T_i, m_i$	T, P
6	Air Force	U.S.	$n_i, T_e$	T
9/29	Alouette	Canada, U.S.	$n_e$	P, R
1962-1964	Kosmos series (except Kosmos-2)	USSR	$n_e$	R
4/3/1963	Explorer 17	U.S.	$n_e, n_i, T_e$	P
1964	Elektron series	USSR	$n_e$	R
8/25	OGO-1	U.S.	$n_e, n_i, m_i$	T
9/4	Explorer 22	"	$n_e$	P, R
10/9	Explorer 20	"	$n_e, m_i$	T, R

result is that horizontal gradients severely affect measurements of altitude distributions of ionosphere parameters. This is associated both with the inhomogeneous structure of the ionosphere, and with the rapid change in latitude and local sun time along the satellite's orbit.

For ionosphere study, satellites employ variants of the same methods /172 used by rockets, but substantial extra difficulty is involved in the satellite use of radiointerferometry to measure  $n_e$ .

Positive ion concentrations are measured with greater simplicity by ion traps on satellites than on rockets. Chiefly because of the great speed of a satellite, the contribution made by the thermal motion of ions to the trap collector currents may, at least in the region of heavy ion ( $O^+$ ) prevalence, be neglected. Even after the first revolution, moreover, the desorption of gas from the satellite surface becomes insignificant.

Therefore, an interpretation of measurement results becomes simpler

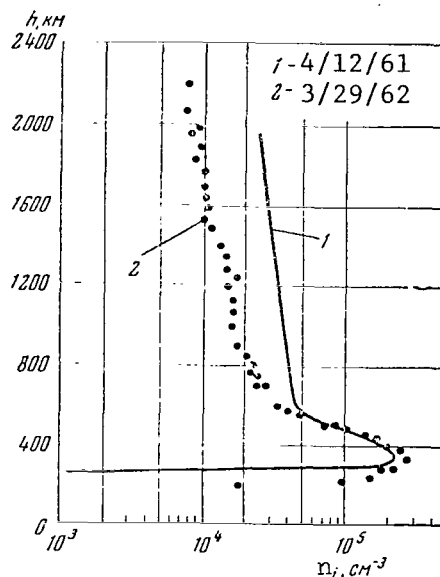


Figure 3

and their reliability greater. At the same time, if aspherical ion traps are employed on an unoriented satellite, the orientation of the traps relative to the satellite's vector velocity affects the measurements.

Successful measurements of positive ion concentrations in the ionosphere were first carried out aboard a satellite, specifically, the third Soviet satellite (1958), by means of spherical ion traps (Ref. 18). In the United States, the first successful ion trap measurements were made more than two years later (by the satellite Explorer 8, 1960) (Ref. 9). Since then ion traps have been repeatedly and successfully used in ionosphere research, as is evident, for example, from Table 3. This table is a compilation of the satellites launched in 1960-1964, which conducted (and are conducting) studies of the ionosphere (notation the same as in Table 1; the letter T denotes measurements by charged particles traps).

Figure 4 depicts an  $n_i(h)$  curve obtained by means of flat ion traps on the satellite "Kosmos-2" on April 7, 1962 (Ref. 20, 21) and an  $n_e(h)$  curve obtained by radio frequency probing by the Anglo-American satellite "Ariel-1" on May 13, 1962 (Ref. 22). The "Kosmos-2" curve refers to local daylight time and the "Ariel-1" curve - to the morning hours. Figure 4 makes it clear that the  $n_i(h)$  and  $n_e(h)$  functions were derived over a very broad latitude range (in the first case  $\Delta\varphi = 79^\circ$ , and in the second  $\Delta\varphi = 67^\circ$ ). The substantial differences in measurement conditions notwithstanding, these curves in general fairly well agree with each other. In the 800-1000 km range, however, the curves take divergent courses, the explanation for which may be that it is at these heights that the latitudes in which the measurements were made differ most from each other. /173

It was already noted in Section I that the comparison of "Kosmos-2"

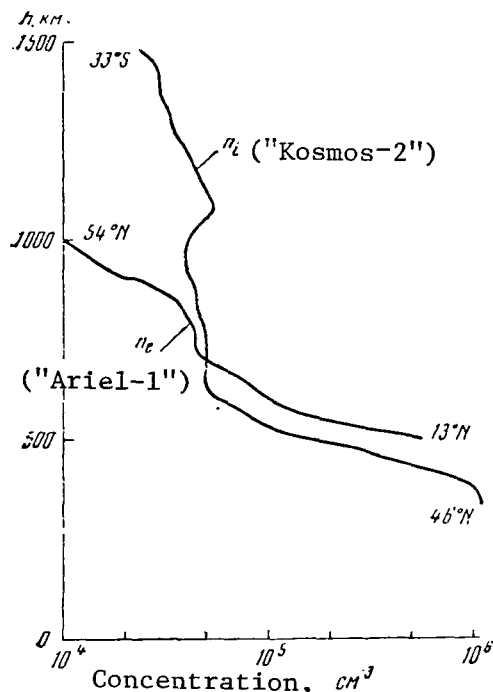


Figure 4

measurements with the results of those in 1958 on the third satellite warranted our drawing certain conclusions about the variability of  $n_i(h)$  distribution in the eleven-year cycle of solar activity. This is presented in more detail in a special report on the results of measurements performed aboard "Kosmos-2" (Ref. 21).

It is pertinent to recall here that, as mentioned above, the altitude dependences of any parameters plotted from satellite measurement data are not true altitude distributions of the parameters, but serve only to present results in a compact form. This remark only applies to measurements made by ionospheric stations installed in satellites.

An extremely promising method of ionosphere study is radio probing of the ionosphere below from satellites flying above the F region peak. The first experiments in probing the ionosphere from above were performed on American rockets in June and October, 1961 (Ref. 4, 23) for a preliminary test of the measurement methods. The Canadian-American rocket "Alouette" (see, for example [Ref. 24]) was launched on September 29, 1962 with an ionospheric station aboard. The orbit of this satellite was almost circular (height above the Earth's surface  $\sim 1000$  km, orbital inclination  $\sim 80^\circ$ ); therefore, altitude-frequency characteristics (ionograms) could be received for a protracted period to plot vertical cross-sections of the outer ionosphere. The satellite's equipment made it possible to record the ionograms every 17 sec, but there was no memory unit aboard the satellite. Information could be received from the satellite only under direct transmission conditions by special receiving stations at a restricted number of locations. /174

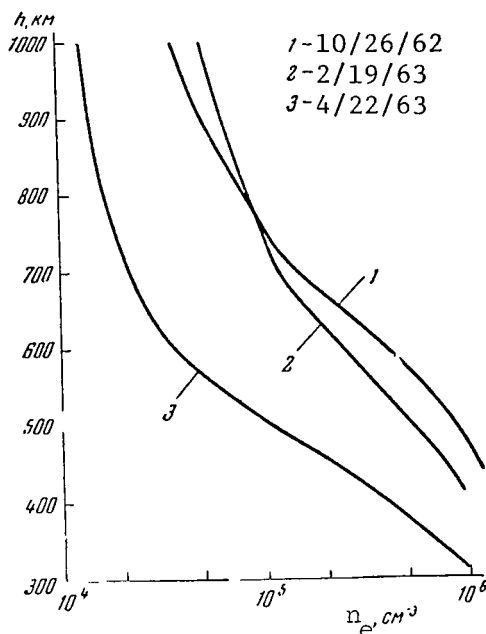


Figure 5

On August 25, 1964 the United States launched another satellite to probe the ionosphere from above - "Explorer 20". Pulse probing from this satellite took place at six fixed frequencies in the same range.

As already mentioned, direct measurements of environmental parameters by satellites is generally restricted due to the difficulty of distinguishing the vertical and horizontal changes in the quantities to be measured (i.e., the difficulty of obtaining an altitude profile). By the use of "flying ionospheric stations" (like "Alouette"), it is in principle possible to obtain a vertical cross section of electron concentration above the F region peak at any point on the satellite's orbit. We must, however, not forget that the values of  $n_e$  thus derived are average for comparatively large regions. Thus, for example, in radio probing from a satellite flying at a height of the order of 100 km above the layer under investigation, the electron concentration to be measured is averaged over a region of linear dimensions in a horizontal plane on the order of several kilometers.

By way of an example, Figure 5 represents equatorial  $n_e(h)$  - profiles derived from data received in Singapore from "Alouette" (Ref. 25). These curves show the potentialities of radio probing from above (curve 3 is daytime, curves 1 and 2 are morning).

One of the interesting results obtained by "Alouette" (October 29, 1962) is the frequent detection of regions with very great horizontal gradients at all heights investigated (see Figure 6, which shows the iso-lines of the reflected signal frequencies). In addition, regions of slightly elevated electron concentration stretching along magnetic field lines of force have been discovered (Ref. 26).

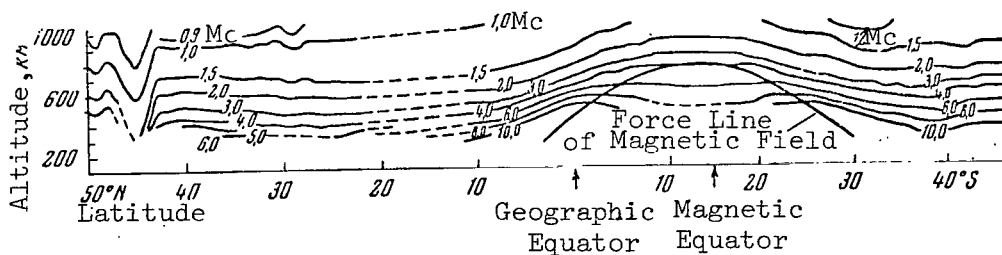


Figure 6

Only about 5% of the altitude-frequency characteristics obtained by means of "Alouette" have been processed, because of the great number of them and the laboriousness of the operation. We would like to note that altitude-frequency characteristics from "Alouette" are sent to World Center A in New York, from which any country may obtain them (Ref. 26).

In both the USSR and the U.S. (see, for example, [Ref. 27, 28] ionosphere research is being conducted by means of radio waves of different frequencies emitted by satellites; here dispersion interferometry is ordinarily used. References 29 and 30, for example, examine this method as applied to satellites.

As can be inferred from these papers, the calculation of local electron concentration  $n_e$  from data of this type of measuring leads to very large errors when satellites are employed.

A number of articles (e.g., Ref. 31-33) describe experiments conducted by a phase method during flights of the "Kosmos" series of satellites and 175 on "Elektron-1". These works attempt to determine local electron concentrations in the vicinity of the satellite, although the conclusions drawn in [Ref. 29, 30] as to the low accuracy of such estimates are entirely pertinent to these measurements. It is impossible not to draw attention also to the fact that the  $n_e$  peaks above the F layer cited in [Ref. 31-33] were not detected by other experiments measuring electron concentration.

### Conclusion

Because the ionosphere is an extremely complex, inhomogeneous, and temporally unstable medium, measurements therein, as partially noted above, encounter a series of difficulties, and all measurements to a greater or lesser degree contain an element of unreliability linked either to methodological restrictions or to interference of different kinds. To increase the reliability of the findings, it is therefore very useful to make comparisons between experimental results derived by diverse methods.

In order to make reciprocal comparisons between measurement methods, several interesting experiments were made in the U.S. using varied procedures to determine ionospheric parameters (particularly  $n_e$ ) over the same

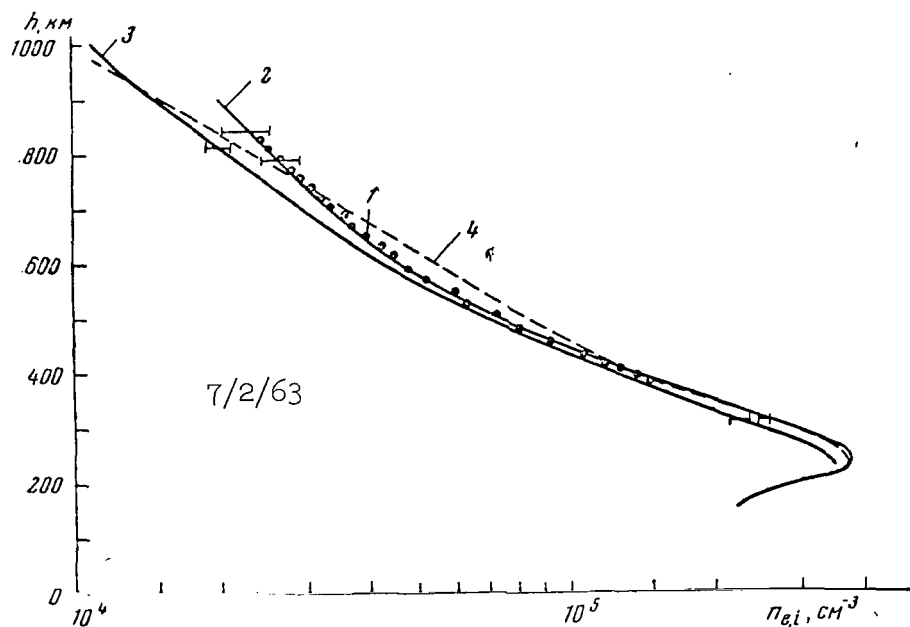


Figure 7

point. Thus, on April 18, 1963, a rocket was lofted into the region through which the ionospheric satellite "Explorer 17" was passing. Maximum height of ascent was  $h_{\max} = 320$  km, and minimum distance between rocket and satellite  $\Delta r \approx 32$  km. On July 2, 1963, a rocket was sent up 866 km and was 240 km away from "Alouette", while on September 28, 1963, the same rocket was lofted to 1030 km. On September 20, 1964, a rocket ( $h_{\max} \approx 1000$  km) was fired into the region in which "Explorer 22" passed ( $h_{\max} \approx 1000$  km).

Figure 7 gives the results of these simultaneous measurements made on September 28, 1963 with ion traps (curve 1), by dispersion interferometry during the firing of the rocket (curve 2), by a radio probe from "Alouette" (curve 3), and by the method of incoherent radio wave scattering (curve 4) (Lincoln Laboratory facility) (Ref. 8). As the figure shows, the divergence of the measurement results obtained by the above methods is very small.

This composite experiment convincingly demonstrates that all the methods used therein correctly present the true properties of the ionosphere and are therefore valid.

In experiments up till now on vertically-launched rockets, local values of  $n_e$  have been measured by radio methods to a maximum height of approximately 1600 km, which by our calculations (made for the case of dispersion interferometry) approaches the extreme heights to which these methods may be applied (2000-2500 km). Probe measurements may, in

principle, be employed at any altitude; data from probe measurements at great altitudes are presented in particular in (Ref. 1).

In conclusion, it is advantageous to draw certain conclusions which we consider essential.

High-altitude rockets are the most reliable means of obtaining altitude profiles of charged particle concentration (just as of other ionosphere parameters) and give the most accurate results. This explains their ever-increasing utilization for this purpose in various countries (including the United States).

Satellite use of radio interference methods to study the ionosphere /176 entails significant difficulties and restrictions in comparison with their use in vertically-launched rockets. The utilization of ion traps on satellites, on the contrary, leads to simplified processing of the experimental data and to more reliable results from this processing, as compared to their use on vertical rockets. Ion traps are installed on many satellites at the present time.

Let us denote some important results of studying charged particle concentration in the ionosphere by rockets and satellites.

The results of geophysical rocket launches by the Academy of Sciences, USSR, to altitudes of  $\sim 500$  km from 1958 through 1963 has demonstrated the intrinsic dependence of altitude distribution of charged particles above the F region maximum on the phase of solar activity.

A further step in ionosphere research is the organization of pulse radio probing from above, which for the first time has enabled us to obtain a clear idea of the horizontal gradients of electron concentration. The disclosure of frequently-encountered zones of very considerable horizontal gradients forbids the use of a stratified-homogeneous ionosphere model in a number of cases.

Satellite radio probing is the only satellite method permitting the derivation of altitude distributions of electron concentration  $n_e(h)$  which are practically free from the influence of horizontal gradients  $n_e$ .

#### REFERENCES

1. Bezrukikh, V. V., and Gringauz, K. I. This collection, p. 177.
2. Sagalin, R. C., and Smiddy, M. J. Geophys. Res., 69, No. 9, 1809, 1064.
3. Jackson, J. E., and Bauer, S. J. J. Geophys. Res., 66, No. 9, 3055, 1961.
4. Knecht, R. W., and VanZandt, T. E. J. Geophys. Res., 66, No. 9, 3078, 1961.



5. Bauer, S.J., and Jackson, J.E. J. Geophys. Res., 67, No. 4, 1675, 1962.
6. Donley, J.L. J. Geophys. Res., 68, No. 7, 2058, 1963.
7. Ulvick, J.C., Pfiester, W., Vancourt, R.P., Bettinger, R.T., /177  
Haycock, O.C., and Baker, K.D. Proc. IRE 50, No. 11, 2272, 1962.
8. Bauer, S.J., Bluml, L.J., Donley, J.L., Fitzenreiter, R.J., and Jackson, J.E. J. Geophys. Res., 69, No. 1, 186, 1964.
9. Huguenin, G.R., Lilley, A.E., McDonough, W.H., and Pappagionnis, M.D. Planet. Space Sci., 12, No. 12, 1157, 1964.
10. AAS News Letters, 3, No. 8, 1964.
11. Gringauz, K.I., and Rudakov, V.A. In "Iskusstvennyye Sputniki Zemli". No. 6, Izdatel'stvo AN SSSR, p. 48, 1961.
12. Rudakov, V.A. Kosmicheskiye Issledovaniya, 2, No. 6, 946, 1964.
13. Data Catalogue for Rockets and Satellites (Katalog dannyykh po raketam i sputnikam) (1957-1962). World Information Center - B, USSR, 1963.
14. Ibid. (1963). World Information Center - B, USSR, 1964.
15. Aono, Y., Hirao, K., Miyazaki, S. J. Radio Res. Lab. (Japan), 9, No. 46, 407, 1962.
16. Beinon, W.J. Nature, 204, No. 4959, 621, 1964.
17. COSPAR Information Bull., No. 17, 1964.
18. Gringauz, K.I., Bezrukikh, V.V., and Ozerov, V.D. In "Iskusstvennyye Sputniki Zemli". No. 6, Izdatel'stvo AN SSSR, p. 63, 1961.
19. Bourdeau, R.E. Space Res., 1, 554, 1961.
20. Gringauz, K.I., Gorozhankin, B.N., Shyutte, N.M., and Gaalevich, G.L. Doklady Akademii Nauk SSSR, 147, No. 3, 560, 1963.
21. Afonin, A.A., et al. Present collection, p. 151.
22. Sayers, J., Rothwell, P., Wager, J.H. Nature, 195, No. 4847, 1143, 1962.
23. Bourdeau, R.E., Chapman, S., Maeda, K. Paper Presented at XIV General Assembly of URSI (Tokyo), 1963. (Translated in "Kosmicheskiye Issledovaniya", 3, No 1, 42, 1965).
24. Thomas, J.O., Sader, A.J. J. Geophys. Res., 69, No. 21, 4561, 1964.

25. Height Distribution of Electron Concentration. I. Radio Res. Station DSRI, England, 1963.
26. Chapman, J. H. Paper presented at XIV General Assembly of URSI (Tokyo), 1963.
27. Graves, C. D. J. Geophys. Res., 65, No. 9, 2585, 1960.
28. Garriott, O. K. and de Mendonca, F. J. Geophys. Res., 68, No. 17, 4917, 1963.
29. Garriott, O. K. In: "Electron Density Profiles in the Ionosphere and Exosphere", Pergamon Press, 1962. (Translation - Moscow, Izdatel'stvo "Mir", 1964).
30. Yerukhimov, L. M., Mityakov, N. A. and Mityakova, E. Ye. Present collection, p. 151.
31. Al'pert, Ya. L. Geomagnetizm i Aeronomiya, 4, No. 3, 479, 1964.
32. Al'pert, Ya. L. Space Res., 5, 652, 1965.
33. Al'pert, Ya. L., and Sinel'nikov, V. M. Geomagnetizm i Aeronomiya, 5, No. 2, 209, 1965.

---

## THE OUTER REGION OF THE EARTH'S IONOSPHERE (FROM 2000 TO 20,000 KM)

V. V. Bezrukikh and K. I. Gringauz

This report briefly presents the state of information on the outer region of the Earth's ionosphere above 2000 km. Until recently experimental data on this ionosphere region have been very scanty. The existence of a relatively cool plasma surrounding the Earth, with particle energies of no more than one electron volt and concentrations greater than their concentration in the interplanetary environment, was discovered with charged particle traps on Soviet lunar rockets in 1959 (Ref. 1). In 1958 it was thought that a charged particle concentration matching the conditions in interplanetary space occurs at altitudes of 2000-3000 km (Ref. 2). Although as early as 1953, when studying so-called whistling atmospherics, Storey (Canada) estimated electron concentration  $n_e$  at 12,500 km as  $10^3 \text{ cm}^{-3}$ , until the Soviet moon rockets this result was ordinarily not applied to the ionosphere, but to the interplanetary medium, since before 1959 it was generally believed that  $n_e$  in interplanetary space was  $\sim 10^3 \text{ cm}^{-3}$  (Ref. 3). 178

In 1961 Al'pert et al. (Ref. 1) published the curve showing the altitudinal behavior of charged particle concentration (Figure 1). This curve was plotted from the results of measurements made at different times by various methods.

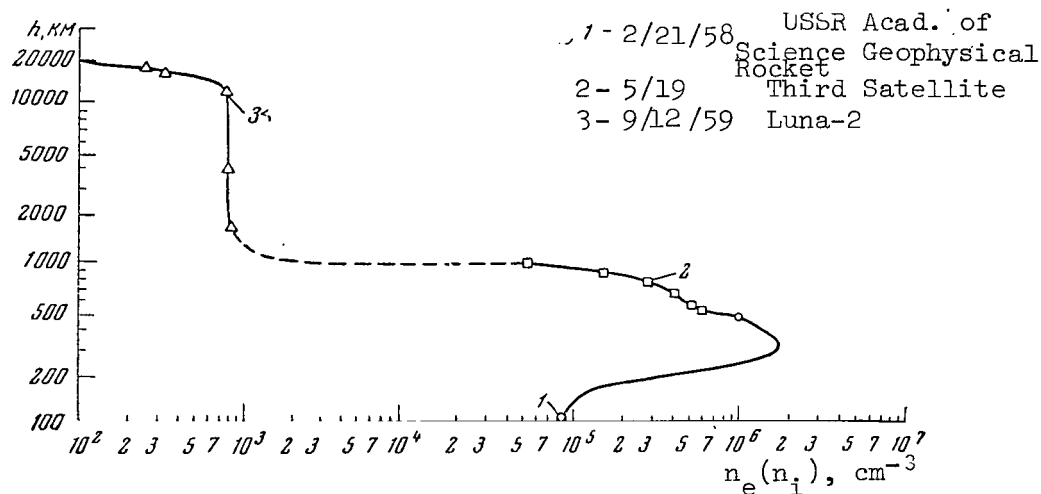


Figure 1

Data derived in 1958 by dispersion interferometry during firings of USSR Academy of Sciences geophysical rockets and by spherical ion traps on the third Soviet satellite were used to plot the curve of charged particle concentration at heights to 1000 km (Ref. 4, 5).

The concentration of charged particles at heights of more than 2000 km was obtained with three-electrode charged particle traps on the second Soviet space rocket ("Luna-2") (Ref. 6, 7). At that time these were the only experimental data on this region. It is clear from the curve (Figure 1) that in the altitude region from ~2000 to ~15000 km the value of  $n_i$  was  $\sim 10^3 \text{ cm}^{-3}$ , while at the height of 20,000 km the value of  $n_i$  was less than  $10^2 \text{ cm}^{-3}$ . Reference 1 pointed out that in the future repeated measurements of ion concentration in the peripheral portion of the gaseous envelope of the Earth should be made, the stability of its height verified, and the dependence of this height on geographical latitude checked. In the altitude range from 1000 to 2000 km in 1959, there were no data on measurements of  $n_e$  and  $n_i$ ; therefore, the portion of the curve in Figure 1 joining these heights has been left as a matter of judgment. On publication of Figure 1, it was remarked that, because of the deficiency of data on trap orientation during the flight of "Luna-2", any of the values of  $n_i$  might be less than its true reading - e.g., by a factor of two - but meanwhile it was stressed that there was no doubt as to the reality of the accelerated drop in  $n_i$  in the 1500-2000 km altitude range (Ref. 1). The conclusion that the ions recorded by the traps up to heights of ~20,000 km are low in energy and that the plasma detected consists of particles possessing thermal velocities was drawn from a comparison of the readings of charged particle traps on "Luna-2" with their external grid potentials differing by a single volt.

In (Ref. 8) it was deduced from an analysis of the data obtained that the region in question is filled with hydrogen ions - protons.

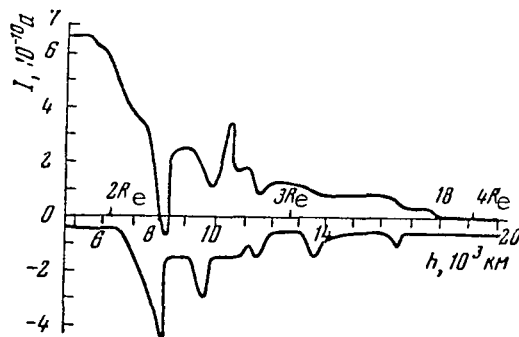


Figure 2

We will give a short list of the experiments which have studied the peripheral portion of the Earth's ionosphere since the flight of "Luna-2" in 1959. /179

In 1961 Bridge et al. (Ref. 9) by means of a modulation ion trap on the satellite "Explorer 10" observed a relatively cool stationary plasma at geocentric distances of 1.3 to 2.9  $R_e$ , i.e., at heights above the earth from  $\sim 2000$  to  $\sim 12,500$  km.

In 1962 measurements of ion concentration in the peripheral region of the ionosphere were made at great heights during the flight of the space station "Mars-1" (Ref. 10). Up to heights of 18,000 km, a trap with zero potential on its external grid registered a positive current, while a negative current flowed in a trap with a +50-v potential on this grid (Figure 2). These measurements also indicate that the earth is surrounded by an ionized gaseous envelope to heights of  $\sim 18,000$  km.

In 1963 Carpenter (U.S.) published his observational results on the propagation of whistling atmospherics (Ref. 11). He detected a sharp drop in electron concentration in equatorial latitudes at geocentric distances of 3-4  $R_e$ . Carpenter's view is that this drop, which he calls the "knee effect" is characterized by a decrease in electron concentration of no less than six times (Figure 3). Carpenter emphasizes that the "knee effect" is a constant phenomenon, although it may be observed at differing distances because of change in magnetic activity. His observations showed that the "knee" varied in position from 3  $R_e$  at  $K_p = 6$  to 4.5-7  $R_e$  under particularly quiet magnetical conditions. Carpenter's paper also noted the connection between his "knee effect" and the results of experiments with traps on "Luna-2" ("Luna-2"'s results are indicated by the small circles in Figure 3).

We would like to remark that in 1964 Carpenter continued and considerably expanded his investigations of the "knee" in the equatorial profiles.

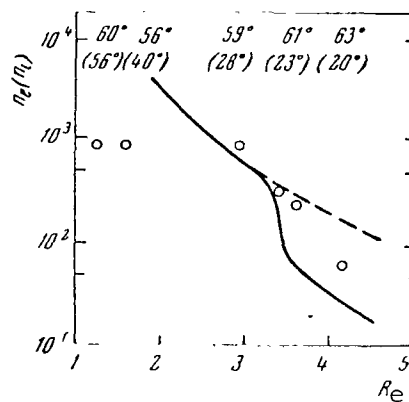


Figure 3

The reality of the "knee" effect has been completely confirmed by numerous observations. Much work has been done on studying the changes of the height of the "knee" with the time of day and in connection with geomagnetic perturbations. Unfortunately, we have at our disposal only the abstracts of the reports of Carpenter and others (Ref. 12, 13). The text of the reports has not yet, however, been published in its entirety.

At the end of 1963, a similar effect was discovered by Serbu (U.S.) on "IMP-1" ("Explorer 18") (Ref. 14). During observations of the low-energy electron streams ( $E < 5$  ev) by means of a three-electrode trap for charged particles close to the Earth, a sharp decrease in the recorded streams ( $N$ ) was found at geocentric distances of  $\sim 2.2-4 R_e$  (Figure 4). The special features of Serbu's experimental methods (in particular, the great positive, electron-attracting potential on the external grid of the trap) prevented him from converting the recorded streams into electron concentrations. There is not doubt, however, that the effect of a decrease in the stream magnitudes at the above distances is the same effect observed in the ion component of circumterrestrial plasma on "Luna 2", and also in the electron component in Carpenter's measurements. Among other scientific instruments, "Elektron-2" had a three-electrode, charged-particle trap similar to those on other Soviet space probes, beginning with the Lunniks (Ref. 1, 6, 10, 15).

/180

The satellite "Elektron-2" was lofted on January 30, 1964 into orbit with an apogee of  $\approx 11.6 R_e$  (from the Earth's center) at an angle to the equatorial plane of  $61^\circ$ . Altitude of perigee was 400 km. One of the orbit's features was that the satellite was over the tropical regions of the Earth when it traversed the altitude region from  $\sim 5000$  to  $\sim 24,000$  km.

The potential of the trap's external grid was the same as that of the satellite's frame. The trap was therefore able to record positive ions of all energies above the satellite's potential with respect to the surrounding environment.

At present, the three-electrode trap with constant potentials on the electrodes is regarded as a very coarse instrument, in comparison with traps

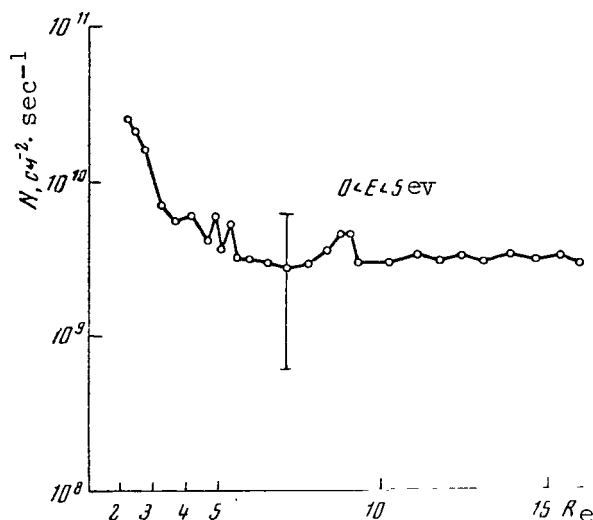


Figure 4

with varying potentials on the electrodes. Nevertheless, since the results of this experiment are comparable with those obtained earlier in 1959 on lunar rockets, and in 1962 on the space station "Mars 1", because of the identical methods and because measurements were performed during a great number of "Elektron-2" circuits about the Earth, they represent a very important stage in the study of the peripheral portion of the ionosphere in the altitude range in question.

By way of example, Figure 5 gives the trap collector current values measured on February 28-29, 1964, along the satellite's orbit. Current variations of this nature are typical of all the revolutions of the satellite. Every time that it approached the Earth there was a comparatively abrupt increase in the current created by positive ions (beginning at altitudes from  $\sim 20,000$  to  $\sim 15,000$  km). Every time that it retreated from the Earth, a current drop of a similar type was observed. These collector current variations are similar to the current decreases observed in 1959 in the charged particle traps on the Soviet lunar rockets as they receded from the Earth (Ref. 1, 5). As mentioned above, the conclusion was then drawn that the currents in traps with zero or negative potentials on the external grids were formed by ions of the Earth's plasma envelope, which is a direct continuation of the ionospheric regions previously known and consists of particles with low (thermal) energies (Ref. 6, 7).

From measurement data of the charged-particle trap-collector current in the satellite "Elektron-2" (these data pertain to several tens of satellite revolutions), we may clearly see that there is always an accelerated drop in thermal ion concentration with altitude in the Earth's plasma envelope (ionosphere). This was discovered during isolated measurements on lunar rockets at heights of 15,000-20,000 km. These altitudes are considerably lower than the minimum boundary of the magnetosphere. We would like to remark that since the current values above  $30 \cdot 10^{-9}$  amp are

[18]

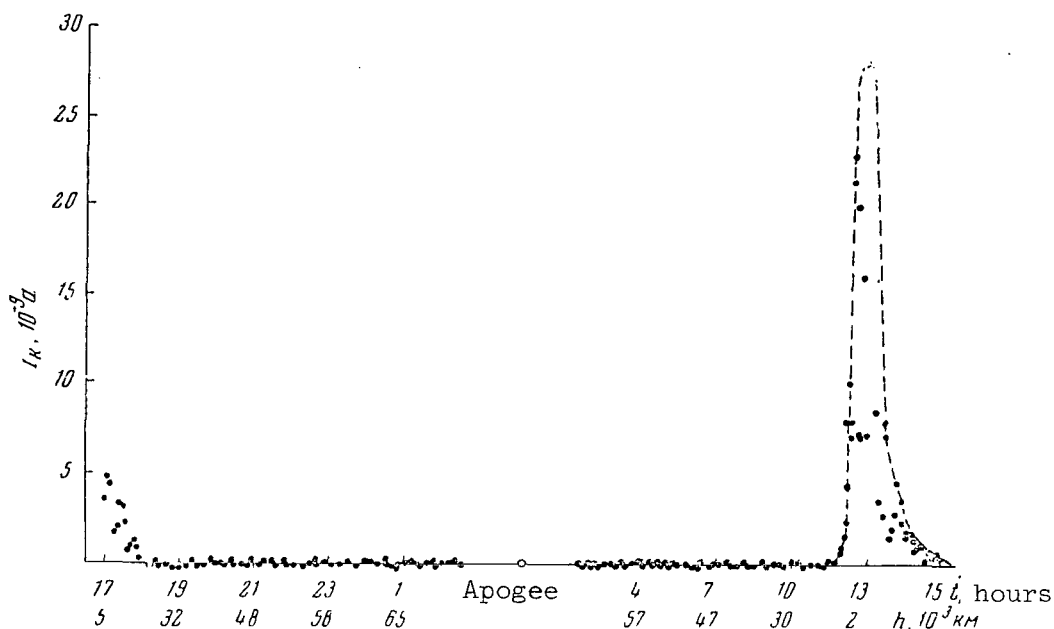


Figure 5

beyond the range limits of the amplifier, large concentrations of ions corresponding to the lower part of the ionosphere, where the satellite's perigee is located, could not be determined in this experiment.

Ion concentrations near the Earth were estimated, just as when the "Luna-2" data were processed (Ref. 1), from trap collector current magnitudes under the following basic assumptions.

(1) The assumption was made that the greatest measured collector-current value in the vicinity of a given altitude corresponds to congruence between the normal to the trap collector and the satellite's vector of velocity. In actuality, this corresponded to only the greatest approximation of these two directions to each other.

(2) The effect exerted by the satellite's electrical potential relative to the surrounding plasma on the collection of ions in the trap was not taken into consideration. The validity of this assumption at altitudes up to  $\sim 3R_e$  is corroborated by Serbu's measurements, which show that this potential at these heights is close to zero (Ref. 14). It is important to note that in the period from January 31 to February 13, 1964, when the satellite retreated from the Earth, the sector of its orbit at altitudes from  $\sim 3000$  to  $\sim 10,000$  km was not illuminated by the Sun, i.e., there was no photoelectric effect from the satellite's surface at these altitudes, and its electrical potential relative to the surrounding plasma could not be positive. In addition, as already noted in (Ref. 1), the ion current in a trap normal to the satellite's velocity vector is least sensitive to the potential value of the satellite.

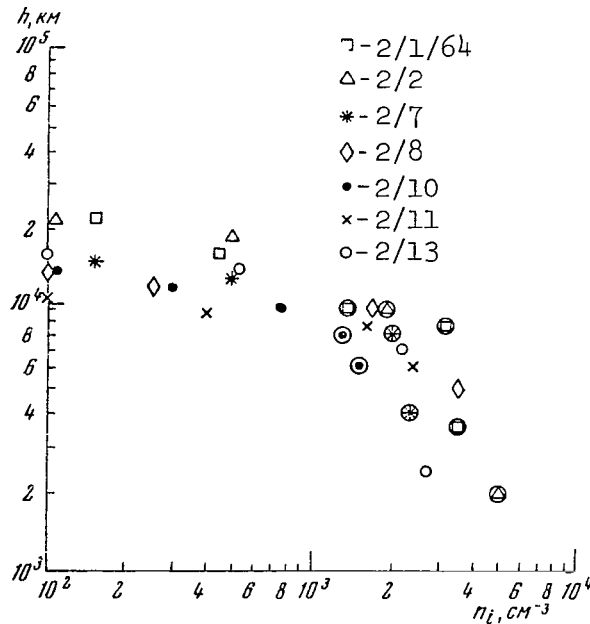


Figure 6

Figure 6 gives a number of values of  $n_i$  obtained during seven passages of the satellite near the Earth and their dates. (The encircled  $n_i$  values correspond to measurements made when the satellite was in the Earth's shadow.) These data lead to the following conclusions:

/182

(1) As pointed out in (Ref. 1, 7), the thickness of the ionosphere region in which charged particle concentration is greater than  $10^2 \text{ cm}^{-3}$  reaches 15,000-20,000 km.

(2) The altitudinal distribution of  $n_i$  within this region differs perceptibly from that cited in (Ref. 1). If the altitude dependence of  $n_i$  in Figure 6 is very similar to the distribution given in (Ref. 1) at altitudes above  $\sim 10,000$  km (see Figure 1), the  $n_i$  values pertaining to altitudes from 2,000 to 10,000 km are several times larger than the values for the same altitudes in Figure 1. The new  $n_i$  data coincide more closely with the results of the different direct measurements of electron and ion altitude distributions made in 1960 at altitudes from 1000 to 2000 km (including measurements made with ion traps on the satellite "Kosmos-2" in 1962, according to which the  $n_i$  amounts to several units per  $10^4 \text{ cm}^{-3}$  at altitudes of  $\sim 1500$  km [Ref. 16]).

It should also be noted that the altitude distributions of ion concentration  $n_i(h)$  which were obtained by "Elektron-2" in the altitude region below 10,000 km are in substantially better agreement with the electron concentration altitude distribution  $n_e(h)$  obtained by Carpenter from the data of whistling atmospherics (Figure 3).

We have already pointed out, in publications presenting the results



of  $n_i$  measurements on lunar rockets of 1959, that the determined values of  $n_i$  might be less than the true values (for example, by a factor of two)<sup>1</sup>. However, at the same time we noted the indubitable reality of an accelerated drop in  $n_i$  with altitude at  $h \geq 15,000$  km. .

Because of the divergent results of the  $n_i$  determinations on lunar rockets and on "Elektron-2", we again examined the primary results of the 1959 measurements near Earth using charged particle traps. In so doing we found that, apart from inexact information on trap orientation, the phenomenon of restricted collector current in the on-board current amplifier could affect the  $n_i$  value decrease, in comparison with the true values, in the altitude region below 10,000 km. It is impossible to ascertain with certainty whether this previously overlooked phenomenon affected the results.

When comparing the results of the lunar rockets and of "Elektron-2", we must, however, bear in mind that Obajashi (Ref. 17) - when analyzing Carpenter's results (Ref. 11) and those of the lunar rockets (Ref. 1) - formulated the hypothesis that the divergence in altitude dependences presented in (Ref. 1) and (Ref. 11) might be caused by the fact that the measurements were made over regions of differing latitude. There is /183 reason to assume that the altitude distribution of temperature depends essentially on geomagnetic latitude. Owing to the essentially anisotropic nature of thermal conductivity in the magnetosphere and the high temperature at the boundary of the magnetosphere and the solar wind, at high latitudes in the altitude region examined in this report the temperature may be considerably higher than that at equatorial latitudes. This may also cause the difference in the altitudinal behavior of  $n_i$ . The  $n_i$  distribution published on the basis of "Luna-2" data (which is distinguished by small  $n_i$  variations at heights of 2000-10,000 km) may be typical of high latitudes. These considerations of Obajashi's on the difference between the Carpenter and "Luna-3" data may be applied in their entirety to the difference between the "Luna-2" and "Elektron-2" data, since the latter - as already noted - also pertain to low latitudes.

An explanation of the discrepancy between the  $n_i(h)$  profiles obtained by "Luna-2" and "Elektron-2" will finally ensue only after similar new rocket measurements have been made in the peripheral region of the high-latitude ionosphere.

Regarding the nature of the Earth's plasma envelope, which represents the peripheral region of the terrestrial ionosphere, we may say that the water molecules entering the upper atmosphere due to evaporation from the Pacific Ocean dissociate under the ultraviolet radiation of the Sun. The hydrogen atoms thus formed are ionized by charge exchange with ions of atomic oxygen in the reaction  $H + O^+ \rightarrow H^+ + O$ . This reaction is intense in the region where collisions between the particles are still frequent enough, i.e., up to the base of the exosphere, which, depending on the phase of solar activity, is located at altitudes from  $\sim 500$  to  $\sim 1000$  km.

From the base of the exosphere, the hydrogen ions - protons - are carried upward by diffusion along the force tubes of the geomagnetic field (Ref. 18).

The question of the degree of ionization in the ionospheric region which we are examining is of interest. In 1964 V. G. Kurt estimated the concentrations of neutral hydrogen atoms in circumterrestrial space from data derived from measurements of  $I_L$  radiation ( $\lambda = 1215 \text{ \AA}$ ) scattered by neutral hydrogen (Ref. 19). These measurements were performed on "Zond-1". Some of his figures are presented below.

$R_e$	H, km	$n_0, \text{ cm}^{-3}$
1.25	1,600	$7.0 \cdot 10^2$
1.5	3,200	$3.6 \cdot 10^2$
2.0	6,400	$3.1 \cdot 10^2$
3.0	13,000	$8.5 \cdot 10^1$
4.0	20,000	$5.1 \cdot 10^1$

Here  $R_e$  is the geocentric distance in Earth radii,  $n_0$  is the concentration of neutral hydrogen atoms, and H is the distance from the Earth's surface.

A comparison of these data with the graph in Figure 1 makes it readily apparent that at the altitudes considered in our report the atmosphere of the Earth is almost completely ionized, and the concentration of neutral particles comprises only a small fraction of the ion concentration. This fraction diminishes as height increases.

In conclusion, we would like to draw attention to the engineering interest which a study of the peripheral region of the ionosphere holds for cosmonautics, in addition to its great scientific interest. When manned interplanetary crafts approach the earth, it is obviously desirable to orient the craft along the velocity vector. Very promising sensors for a system having this orientation are instruments recording the ion current, whose strength depends on the orientation of the input aperture of the instrument relative to the velocity vector of the space vehicle (since utilization of orientation sensors reacting to streams of neutral particles is precluded, because - as already noted in the report - the neutral component of the atmosphere at distances on the order of thousands of kilometers from the Earth comprises only a small fraction of the ionized component).

A study of the peripheral region of the ionosphere makes it possible to determine the size of the zone surrounding the Earth, in which a spacecraft may be oriented by ion sensors.

# REFERENCES

1. Gringauz, K. I. Space Res., 1, 539, 1962.
2. Al'pert, Ya. L., Chudesenko, E. F., and Shapiro, B. S. In "Preliminary Results of Scientific Investigations by Means of the First Soviet Artificial Earth Satellites and Rockets." ("Predvaritel'nyye Itogi Nauchnykh Issledovaniy s Pomoshch'yu Pervykh Sovetskikh Iskusstvennykh Sputnikov Zemli i Raket"). Izdatel'stvo AN SSSR, No. 1, p. 40.
3. Behr, A., Siedentopf, M. Zeitschrift für Astrophysik, 32, No. 1, 19, 1953.
4. Gringauz, K. I., Bezrukikh, V. V., and Ozerov, V. D. In "Iskusstvennyye Sputniki Zemli". Izdatel'stvo AN SSSR, No. 6, 1961.
5. Gringauz, K. I., and Rudakov, V. A. Ibid., p. 48.
6. Gringauz, K. I., Bezrukikh, V. V., et al. Doklady Akademii Nauk SSSR, 131, 1301, 1960.
7. Gringauz, K. I., Kurt, V. G. et al. Ibid., 132, 1062, 1960.
8. Gringauz, K. I., Kurt, V. G. et al. Astronomicheskiy Zhurnal, 37, 716, 1960.
9. Bridge, H. S. et al. Direct Observations of the Interplanetary Plasma, Report to Symposium in Kyoto (Japan), 1962.
10. Gringauz, K. I. et al. Space Res., 4, 621, 1964.
11. Carpenter, D. L. Report at Fourteenth General Assembly of URSI (Tokyo), 1963.
12. Angerami, J. J., Carpenter, D. L. Trans. Amer. Geophys. Union, 46, No. 1, 190, 1965.
13. Carpenter, D. L., Jewell, T. R. Trans. Amer. Geophys. Union, 46, No. 1, 190, 1965.
14. Serbu, G. P. Space Res., 5, 564, 1965.
15. Gringauz, K. I. et al. Space Research, 3, 602, 1963.
16. Gringauz, K. I., Gorozhankin, B. N. et al. Doklady Akademii Nauk SSSR, 151, 560, 1963.

17. Obajashi, T. The Report on Ionosphere and Space Research in Japan, 28, No. 3, 228, 1964.
18. Hanson, W. B., Ortenburger, J. B. J. Geophys. Res., 66, 5, 1425, 1961.
19. Kurt, V. G. Report at Fifteenth Congress of the International Astronautic Federation (Doklad na XV Kongresse Mezhdunarodnoy Astronavticheskoy Federatsii). Warsaw, 1964.

# ROCKET DATA ON THE BEHAVIOR OF ELECTRON CONCENTRATION IN THE IONOSPHERE AT ALTITUDES OF 100-300 KM

T. V. Kazachevskaya and G. S. Ivanov-Kholodnyy

The distribution of electron concentration in the ionosphere has been studied since 1946 by means of vertical firings of geophysical rockets. Up until the present, there have been about 90 successful experiments of this type both in the USSR, and abroad. The present article will attempt to draw conclusions regarding the laws followed by electron concentration changes  $n_e$  at altitudes of 100-300 km, based only on the results of direct rocket probes of the ionosphere.

For this purpose, all the results derived from rocket measurements of  $n_e$  were compared at different moments for different seasons, at altitudes of 100-130 km. The change in  $\lg n_e$  as a function of the magnitude of  $\lg f$ , which characterizes the air mass of the atmosphere (Ref. 1), was obtained. The change in electron concentration throughout the day was different for different altitudes and seasons. At all altitudes from 100 to 300 km, there was a significant change in the electron concentration as a function of season (winter-summer). The change in electron concentration depends on the phase of the solar activity cycle: at altitudes of 110-100 km, during the midday hours, the values of  $n_e$  for minimum activity are on the average 1.5-2 times lower, and at altitudes of 130-200 km they are 20-50% lower on the average, than during intense solar activity. In the E regions of the ionosphere at altitudes of 120-130 km, a variation minimum of the values obtained for  $n_e$  is observed throughout the solar cycle. /185

The linear dependence of  $\lg n_e$  on  $\lg f$  - i.e., the following type of pattern

$$n_e \propto f^{-1}. \quad (1)$$

at almost all altitudes below 200 km is of greatest interest. The inclination of the lines in the graphs for winter is approximately two times larger than for summer.

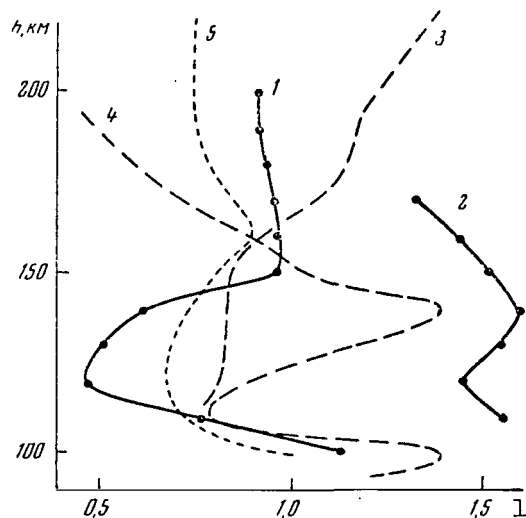


Figure 1

Change In the Parameter  $l$  With Altitude  $h$

1 - Experiment for summer ( $\lg f > 0.5$ ); 2 - Experiment for winter ( $\lg f \leq 0.4$ ); 3 - Theory according to (Ref. 2), for  $\lg f > 0.5$ ; 4 - The same as for  $\lg f < 0.5$ ; 5 - theory, according to (Ref. 3).

It is also interesting to note that at altitudes of  $>200$  km there is a decrease in  $\lg n_e$  in the midday hours (for small values  $\lg f \leq 0.4-0.5$ ). At almost all altitudes of  $\leq 200$  km, a maximum of  $\lg n_e$  can be observed for  $\lg f \approx 0.4$ . In the region of  $\lg f = 0.1-0.2$ , there is a minimum of  $\lg n_e$ . Apparently a similar picture is obtained for winter, except for the fact that it is extended 2-3 times along the abscissa axis. In the graphs for winter, there is a fairly sharply-expressed peak of  $n_e$  for small values of  $\lg f \leq 0.4$ , and a maximum is observed for  $\lg f \approx 0.6$ .

The magnitude of  $l$  [as follows from (1)] characterizes the rate at which the electron concentration changes at a given altitude throughout the day. The values of  $l$ , determined according to the inclination of rectilinear sections of the dependence of  $\lg n_e$  on  $\lg f$ , are shown in Figure 1 for summer (for high solar activity and for  $l \geq 0.5$ , as well as for winter (for  $\lg f \geq 0.4$ ).

It is interesting to note that  $l > 0.5$  at almost all latitudes, and only in the altitudinal region of 120-130 km is it close to 0.5. As is known, for the so-called simple Chapman layer which is obtained on the assumption of monochromatic radiation which ionizes the ionosphere, the rate at which  $n_e$  changes throughout the day is comparatively low. It is characterized by the value  $l = 0.5$ , since  $n_e = \sqrt{q/\alpha^f}$ , and  $q \propto f$  (here  $q$  is the rate at which ions are formed, and  $\alpha^f$  is the effective recombination coefficient which is independent of  $f$  and  $q$ ). The large magnitude of  $l$  and the dependence of  $l$  on altitude can be explained, if it is

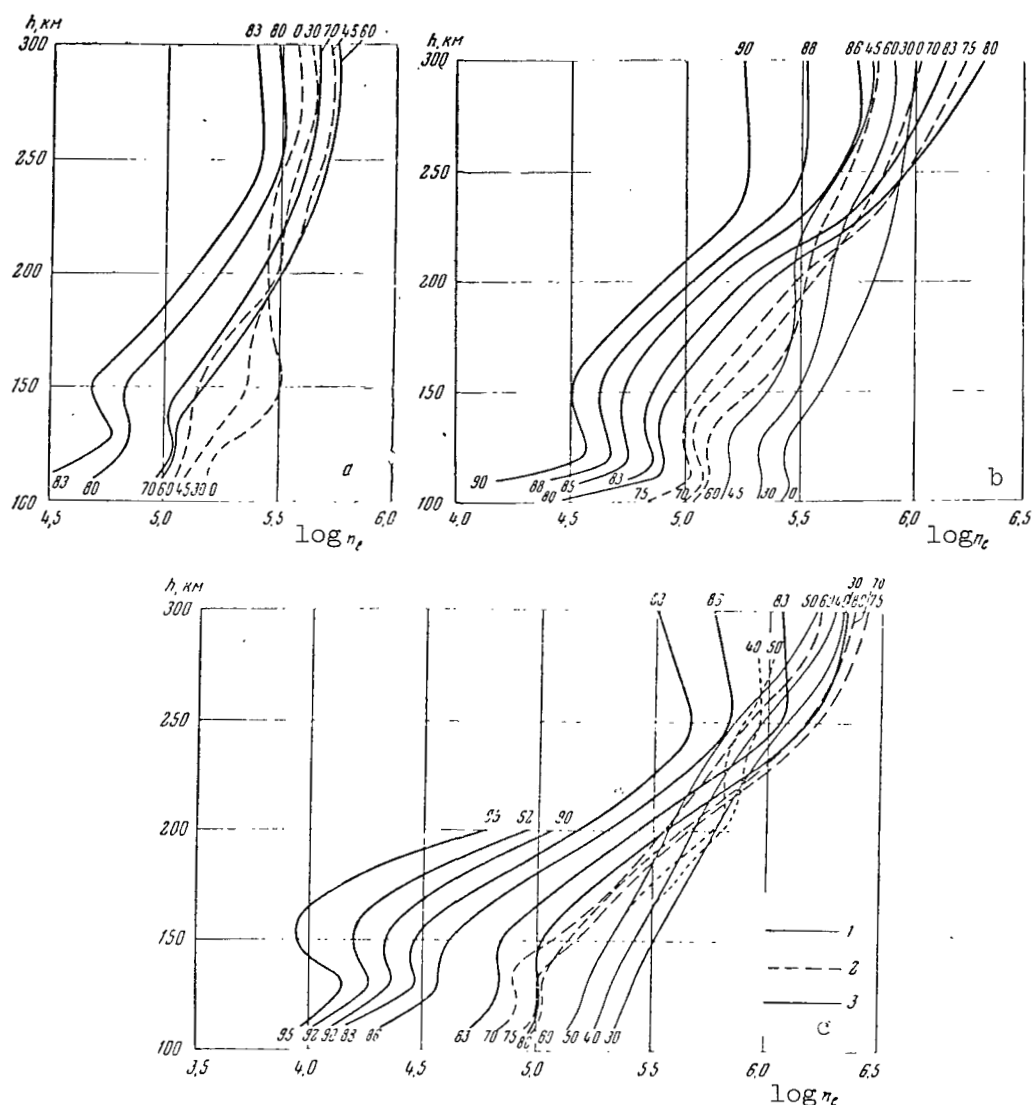


Figure 2

Mean Profiles  $n_e(h)$  Based on Rocket Data

For summer: a - for low solar activity; b - for high solar activity; c - for winter (above 200 km, a high level of solar activity). 1 - Profiles obtained; 2 - "Transitional Profiles"; 3 - Rising-descending profiles. Number of curves - zenith angle of the sun  $z_\odot$ .

assumed that the solar radiation which ionizes the ionosphere is non-monochromatic. The values of  $l$ , which we obtained on the basis of the curves for  $n_e$  as a function of  $f$ , are compared in Figure 1 with the theoretical magnitude of  $m$ , which characterizes the rate at which the

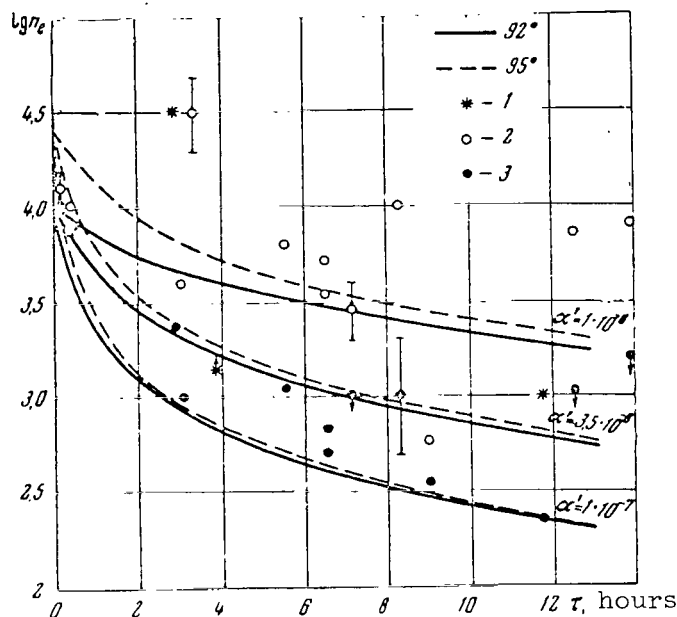


Figure 3

Electron Concentration Change Throughout the Night For Altitudes of 110 km (1), 120 km (2), and 130-160 km (3)

Curves are calculated theoretically for different recombination coefficients  $\alpha'$  (indicated in the Figure) and different initial values of  $n_e$  for sunset  $1 \cdot 10^4$  (solid line) and  $2.5 \cdot 10^4 \text{ cm}^{-3}$  (dashed line).

ion formation changes at a given altitude throughout the day:

$$q \propto f^{-m}.$$

The magnitude of  $m$  was calculated in (Ref. 2), based on the rate at which ions are formed  $q$  and the change in this rate as a function of the zenith distance of the Sun. It was assumed that the ionosphere is ionized by a wide region of the solar spectrum from 10 to 1000 Å. We also determined the values of  $m/2$ , based on data given in the work by Hinteregger and Watanabe (Ref. 3), in which the intensity and spectrum of the Sun (which differed from the values assumed in [Ref. 2]) were used to calculate  $q$ . /187

The following conclusions can be drawn on the basis of the data presented in Figure 1: just as for values of  $l$ , obtained from experimental data, theory provides a minimum value of  $m$  in the altitudinal region of 120-130 km. At altitudes below  $\sim 150$  km, larger values of  $m$  are obtained for  $\lg f < 0.5$ , which fully explains the difference in the values of  $l$  obtained from data for winter for small values of  $\lg f$  - and for summer, for large values of  $\lg f > 0.5$ . Thus, the theory which takes into account the non-monochromatic nature of ionizing solar radiation imparts fairly

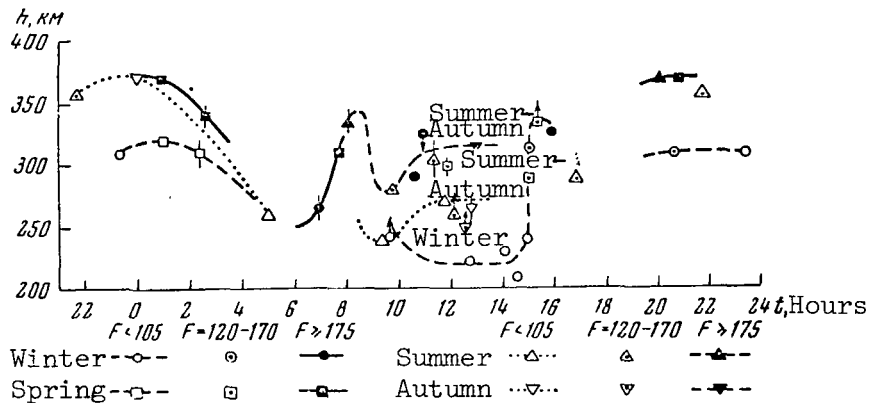


Figure 4

#### Change in F Layer Altitude Over 24 Hours

Similar seasons are connected by lines:

Winter (middle of October-February),  
Spring (March-May), Summer (June-August),  
and Autumn (September-middle of October).

closely the magnitude and nature of the change with altitude, and the rate at which the quantities  $q$  and  $n_e$  increase throughout the day.

Figure 2 presents models of a quiet ionosphere for winter and summer during high solar activity; these models were constructed on the basis of the average values of  $\lg n_e$  obtained for rocket measurements. Each curve in the figure represents the mean profile of  $n_e(h)$  at altitudes of 100-300 km for different zenith angles of the Sun  $z_\odot$ . The profiles for midday hours ( $z_\odot < 50^\circ$ ) differ from the profiles for morning and evening hours: the gradient of  $n_e$  decreases with altitude; the values of  $n_e$  below 200 km are greater - and above 200 km they are smaller - than for  $z = 60 - 80^\circ$ . As a result, a "node" is formed at an altitude of  $\sim 200$  km, where the morning-evening curves and the midday curves intersect. Thus, at an altitude of 200 km there is a minimum change in  $n_e$  throughout the day. For  $z_\odot > 70 - 80^\circ$ , there is a monotonic decrease in  $n_e$  with an increase in  $z_\odot$  at all altitudes, while the form of the profile for  $n_e(h)$  remains unchanged. The electron concentration gradient increases with altitude, not only when the Sun approaches the horizon, but also during winter it is higher than during summer and increases during the period of intense solar activity. /188

A maximum of  $n_e$  is formed on the curves for  $z_\odot > 60^\circ$  in the 100-120 km region, and also there is a "gap" in the profile of  $n_e(h)$  above the E region. Thus, as the Sun approaches the horizon there is a build up of the maximum and the gap above it.

Several important conclusions can be derived from an examination of rocket measurements of the profiles for  $n_e(h)$  during the night time. One



characteristic of the nocturnal profiles of  $n_e(h)$  is the existence of a fairly well-expressed maximum at altitudes of 100-120 km ("of the nocturnal layer E"). Above this maximum there is a significant decrease in  $n_e$  at altitudes of 125-150 km and sometimes higher, after which  $n_e$  again begins to increase. The reason for the formation of the "nocturnal layer E" and "the gap" above it has not been clarified as yet. Holmes and others (Ref. 4), after analyzing the mass-spectrometer measurements of the ion composition, concluded that this behavior of the nocturnal layer is related to an increase in the dissociative recombination coefficient with altitude - i.e., with temperature. However, this explanation contradicts existing data. The existence of an ionization source during the night time at altitudes of 100-120 km represents an alternative solution. In the description of the mean ionosphere model presented above, it was shown that a maximum is formed at altitudes of 120-130 km, as well as a gap in the profile of  $n_e(h)$  above it, in the ionosphere, due to the characteristics of the spectrum for solar ionizing radiation toward evening.

Figure 3 depicts the change in  $\lg n_e$  as a function of time  $\tau$  which transpires after the Sun has set - more precisely, after total attenuation of solar ultraviolet radiation has set in at altitudes of 110-120 and 125-150 km. Lines are used in Figure 3 to denote the decrease in  $n_e$  for a constant recombination coefficient  $\alpha'$  equalling  $1 \cdot 10^{-8}$ ,  $3.5 \cdot 10^{-8}$  and  $1 \cdot 10^{-7} \text{ cm}^3 \cdot \text{sec}^{-1}$  for two possible values of the zenith angle during sunset, 92 and 95°. It can be seen that the values of  $n_e$  in the E layer are greatly scattered, and if they decrease during the night time, then  $\alpha'_E \leq 10^{-8} \text{ cm}^3 \cdot \text{sec}^{-1}$  (under the condition that there is no nocturnal ionization source).  $n_e$  decreases during the night time considerably more rapidly with  $\alpha' = (3.5 - 10) \cdot 10^{-8} \text{ cm}^3 \cdot \text{sec}^{-1}$  in the region of the "gap" at altitudes of 125-150 km. Since the magnitude of  $\alpha'$  must decrease with altitude due to temperature increase, and since  $\alpha'$  corresponds to the diurnal value at 125-150 km, then the existence of a nocturnal ionization source, which is variable in terms of intensity, is confirmed. The attenuation of this nocturnal ionization source is characterized by a constant time  $\tau \approx (\alpha' n_e)^{-1} \geq 3 \cdot 10^4 \text{ sec}$  during the night time. It can be estimated that the strength of the nocturnal ionization source increases by a factor of ten and even 100 in the E region, during a period of intense solar activity.

/189

When the altitude variation of the E and F regions of the ionosphere is investigated, it is found that the altitude of the base of the E region depends on the season, and decreases with an increase in geomagnetic activity. The altitude of the base of the E region is lower during winter and summer than it is during autumn and spring. There may be a connection between the variation of  $h_E$  and the density variations in this region of the upper atmosphere.

Figure 4 presents the altitudinal variations of the F layer throughout 24 hours. During the night time, the altitude of  $h_F$  depends on solar activity, decreasing from the 350-370 km level during the maximum period down to 300-320 km during the minimum period. At midday, the altitude of

the F layer is greater during summer and fall than it is during winter, at 40-50 km during low solar activity and at  $\sim 20$  km during high solar activity. An unusual "sunrise-sunset" effect has been discovered: sharp variations in the altitude of  $h_F$  over a comparatively short time interval of 2-3 hours. Similar variations in  $h_F$  were estimated qualitatively based on earlier results of radio probe ionosphere stations. If consideration is given to the fact that the altitude of the F layer maximum is approximately determined by the equality between the recombination and diffusion of charged particles, it can be assumed that the complex diurnal variations in  $h_F$  are not only caused by temperature variations, but also by ionization rate variations, as well as by variations in the atmospheric composition.

#### REFERENCES

1. Chapman, S. Proc. Roy. Soc., 43, No. 26, 481, 1931.
2. Ivanov-Kholodnyy, G. S. Geomagnetizm i Aeronomiya, 2, No. 4, 674, 1962.
3. Hinteregger, H. E. and Watanabe, K. J. Geophys. Res., 67, 997, 1962.
4. Holmes, J. C., Johnson, C. J. and Young, J. M. Space Res., 5, 576, 1965.

#### ELECTRON AND ION TEMPERATURES IN THE IONOSPHERE<sup>1</sup> (Summary)

T. K. Breus and G. L. Gdalevich

Temperature is one of the main parameters characterizing the ionosphere. It makes it possible to obtain a great deal of data on the nature and magnitude of thermal sources heating the atmosphere of the Earth.

Temperature is studied by three basic methods - direct measurement on rockets and satellites, indirect determinations (for example, based on the altitude profile of ion and electron concentrations), as well as the method of inverse, non-coherent scattering.

The lack of direct measurements up until recently, as well as the ambiguity of indirect temperature determinations, has made it impossible to establish experimentally the relation between electron and ion temperatures in the ionosphere.

Earlier theoretical calculations (Ref. 1) indicated that the electron

---

<sup>1</sup> This summary will be published in its entirety in the Journal "Kosmicheskiye Issledovaniya", 3, No. 6, 1965.

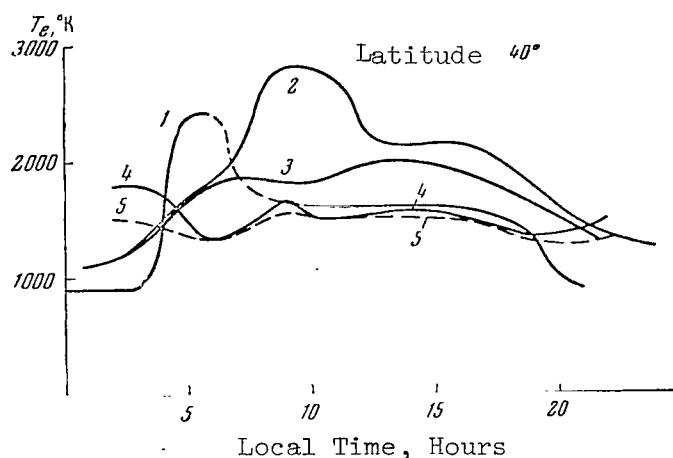


Figure 1

temperature in the F layer can differ significantly from the ion temperature. However, due to the great indeterminacy of the parameters necessary for computation (the use of understated values of these parameters) the conclusion was subsequently reached that temperature equilibrium exists (Ref. 2).

/190

Experiments on rockets and satellites have made it possible to obtain valuable information regarding the ionosphere characteristics necessary for computation, and have directly established a relationship between  $T_e$  and  $T_i$ .

On the basis of experimental data, the models of electron temperature distribution with altitude have been recalculated (Ref. 8-10). Basically they agree with the results of direct measurements of  $T_e$  and  $T_i$  during the daytime.

The present report discusses the results of direct measurements of  $T_e$  and  $T_i$  on the satellites "Explorer-8", "Explorer-17", "Alouette-1", "Ariel-1", "Kosmos-2" as well as on American and Japanese rockets (Ref. 11-17). Results obtained by the method of inverse non-coherent scattering are also discussed (Ref. 18, 19).

An analysis of these results has provided a certain clarification of the diurnal, latitudinal, and altitudinal dependences of electron temperature up to ~1200 km, since ion temperature was measured in three experiments in all and not even the results of one of them have been published (Ref. 15, 17).

Figure 1 presents the diurnal variation in  $T_e$  in the altitudinal region of 250-500 km, based on data from "Explorer-8" (curve 1), "Explorer-17" (2), "Ariel-1" (3), and "Alouette-1" (4 and 5). There is a clearly-expressed maximum during the morning hours immediately after sunrise in the majority of the curves.

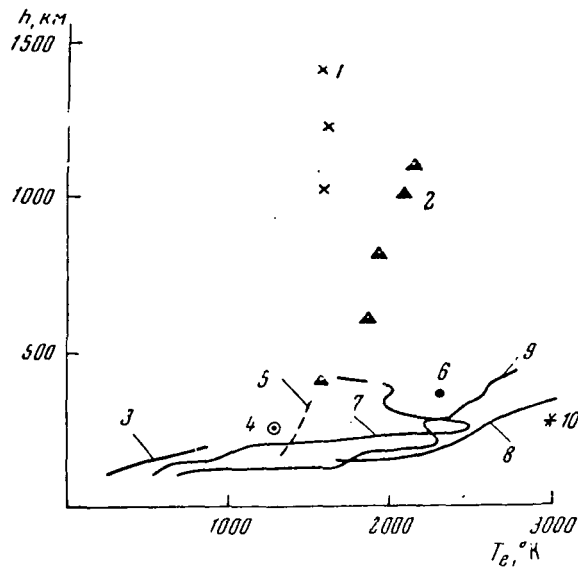


Figure 2

Figure 2 presents the daily measurements of  $T_e$  and  $T_i$  during different years in different experiments [in the Figure: 1 - based on data from "Explorer-8" (November, 1960); 2 - "Ariel-1" (April, 1962); 3 - rocket (March, 1961, Japan); 4 - "Kosmos-2" (April, 1962); 5 - U.S.A. (August, 1962); 6 - "Explorer-17" (April, 1963); 7 - rocket (March, 1963, Michigan, United States); 8 - United States (August, 1962); 9 - rocket (August, 1960, Wallops Island, U.S.A.); 10 - "Kosmos-2" (April, 1962)]. Electron temperatures measured on rockets are designated by the solid lines; measurement results for  $T_i$  are designated by the dashed line (4, 5). It can be seen from Figure 2 that the  $T_e/T_i$  ratio is significant in the region of the F layer maximum, while at the mean latitudes (where the experiments were conducted primarily) it can be greater than two.

Data from non-coherent scattering have confirmed these results, and indicate that  $T_e/T_i \approx 1.1 - 1.3$  at low latitudes above the F layer maximum, while at high latitudes it is  $\sim 1.6$ .

Up to 400 km there is a significant altitudinal temperature gradient (see Figure 2). Above 400 km the measurements performed on satellites <sup>/191</sup> are complicated by latitudinal and diurnal effects and are contradictory. Data from non-coherent scattering are ambiguous, and make it impossible to draw a definite conclusion regarding the altitudinal behavior of temperature.

Based on data from non-coherent scattering and from results obtained on "Ariel-1" and "Explorer-17", one finds that the electron temperature increases with an increase in latitude.

Future experimental studies of temperature are necessary both for

understanding the physics of the ionosphere, and for clarifying and developing theoretical models. It would be desirable to perform probe measurements, which are the most reliable, on rockets (clarification of the altitudinal behavior) and on satellites with a circular orbit (latitudinal dependence). Experiments measuring  $T_{\text{neutral}}$  should be carried out simultaneously with measurements of  $T_e$  and  $T_i$ , since - for altitudes of  $> 750$  km - the ion temperature can differ significantly from the neutral gas temperature and equal the electron temperature at altitudes of  $> 1000$  km - according to theoretical calculations.

#### REFERENCES

1. Drukarev, G. J. Phys. USSR, 10, 81, 1946.
2. Ginzburg, V. L. Theory of Radio Wave Propagation in the Ionosphere (Teoriya rasprostraneniya radiovoln v ionosfere). Gostekhizdat, 1949.
3. Hinteregger, H. E. Space Res., 1, 304, 1960.
4. King-Hele, D. G. and Walker, D. M. C. Space Res., 2, 902, 1961; Priester, W. Space Res., 2, 918, 1961.
5. Istomin, V. G. In "Iskusstvennyye Sputniki Zemli", No. 4, Izdatel'stvo AN SSSR, p. 171, 1961.
6. Pokhunkov, A. A. In "Iskusstvennyye Sputniki Zemli", No. 12, Izdatel'stvo AN SSSR, p. 133, 1962.
7. Spenser, N. W., Brace, L. H. and Garignan, G. R. J. Geophys. Res., 67, 157, 1962.
8. Hanson, W. B., Johnson, F. S. Mem. Soc. R. Sci. Liège, 4, 390, 1961.
9. Hanson, W. B. Space Res., 3, 282, 1963.
10. Dalgarno, A., McElroy, N. B. and Moffet, R. J. Planet. Space Sci., 11, 463, 1963.
11. Bourdeau, R. E., Donley, J. L. Proc. Roy. Soc., A281, 1387, 1964.
12. Brace, L. H., Spenser, N. W. J. Geophys. Res., 69, 4686, 1964.
13. King, J., Smith, P. A., Eccles, D., Fooks, G. F., Helm, H. Proc. Roy. Soc., A 281, 464, 1964; Bouer, S. I., Blumle, L. I. J. 192 Geophys. Res., 69, No. 17, 1964.

14. Bowlm, P. I., Boyd, R. L., Henderson, W. I., Raitt, W. I., Willmore, A. P. Proc. Roy. Soc., A 281, 504, 1964.
15. Gringauz, K. I., Gorozhankin, B. N., Gdalevich, G. L., Afonin, V. V., Rybchinskiy, R. Ye., Shyutte, N. M. Space Res., 5, 733, 1965.
16. Aono, J., Hirrao, K., Miyazaki, S. J. Radiat. Res. Lab., Japan, 8, 453, 1961.
17. Nagy, A. F., Brace, L. H., Garignan, G. R., Kanal, M. J. Geophys. Res., 68, No. 24, 6401, 1963.
18. Bowles, K. L., Ochs, E. R., Green, J. L. J. Nat. Bur. Stand., 66, 395, 1962; Rep. to the XV General Assembly URSI, Tokyo, 1963.
19. Evans, J. V., Loewenthal, M. Planet. Space Sci., 12, No. 10, 915, 1964.

# COMPOSITION OF THE OUTER IONOSPHERE OF THE EARTH BASED ON MEASUREMENT DATA FROM THE "ELEKTRON" SATELLITES

V. G. Istomin

The satellites "Elektron-1" and "Elektron-2" carried radio-frequency mass spectrometers (RMS) of the Bennett type (Ref. 1). The mass spectrometers operated in a regime for measuring the ion composition and were designed to study the positive ions of the outer ionosphere. Memory devices were not employed on the satellites for information obtained from the mass spectrometers, and the measurements of ion composition were only performed using "direct transmittal".

The minimum altitude at which data were obtained on the ion composition was determined by the altitude of the satellite perigee and was about 400 km. The altitude of "Elektron-1" perigee was 407 km. The initial altitude of the "Elektron-2" perigee was 460 km, but - due to regression of the orbit - it decreased approximately to 410 km.

The maximum altitude for the mass spectrometer operation was determined by the satellite coordinates when the period of communication was terminated. The maximum altitude at which measurements were made of the ion composition on "Elektron-2" was 2750 km (revolution number 2, January 31, 1964). /193

Ion composition was measured in the northern hemisphere primarily in the region from 10 to 61°N. Due to the fact that the satellite altitude above the surface of the Earth and the geographical latitude of a point, above which it was located at a given moment, were clearly related to each other, measurements on all the revolutions represent altitudinal-latitudinal cross sections of the atmosphere. Figure 1 presents the orbits of the "Elektron" satellites at the "altitude-geographical latitude" coordinates. Measurements were performed during the daytime. In the region of the perigee, the composition was studied between 9-16 hours local solar time. Measurements at altitudes of 1000-1500 km were performed between 7-20 hours local time. This is illustrated in Figure 2, which presents the sections of the "Elektron-2" orbit, at the "altitude-local solar time" coordinates, at which the ion composition was measured. It can be seen from this figure that the altitude of the "Elektron-2" perigee was not constant, but regressed from approximately 460 to 410 km (revolutions 49-60), and then it again began to rise.

The spectra obtained during optimum orientation of the mass spectrometer, with respect to the satellite velocity vector, were selected in the recordings. A minimum angle between the analyzer axis and the velocity vector, as well as the absence of "shading" from the incoming stream in the region of the analyzer input, correspond to optimum orientation. These optimum spectra, for which the ion streams of all the components were maximum, were utilized to determine the ion composition of the atmosphere. It

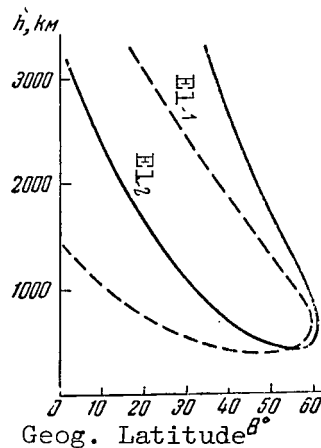


Figure 1

Orbits of the Satellites "Elektron-1" and "Elektron-2" at the "Altitude-Geographical Latitude" Coordinates (For the Northern Hemisphere)

is clear from general considerations that the least distortion in the composition of ions entering the region of the mass spectrometer input can be expected during the moment of "optimum orientation".

As is indicated by an examination of the ion trajectories in the instrument analyzer, in this case the discrimination of ions having different masses will also be minimum in this instrument.

For many reasons, it is difficult to perform a theoretical calculation of the change in a stream of ions having different masses at the collector of the radio frequency mass spectrometer as a function of the analyzer angle of attack. In the first place, difficulty is encountered in determining the thermal ion velocities and in making a definite determination of ion component temperatures. The fields outside of the analyzer, the configuration of the pulling grid field in the Debye region of the space charge, as well as the configuration and dimensions of this region, are only known in an approximate manner. Finally, the complex configuration of the satellite itself occasionally complicates the picture. If there is an adequate amount of observational material, it is possible to obtain the dependences of ion streams having different masses on the angle of attack in the experiment itself, and then to reduce all the measurements to a zero angle of attack - taking into account, when necessary, discrimination with respect to mass for this simple case.

For purposes of illustration, Figure 3 presents the dependence of ion streams having a mass number of 16, obtained on the third artificial Earth satellite, as well as a very approximate dependence which would be expected for ions having a mass number of 1. Thus, it can be seen in qualitative terms that, in the case of an angle of attack which is different from zero, the measurements must yield exaggerated values for the concentrations of lighter ions. This fact should be kept in mind when studying the results presented below for ion composition measurements.

/194



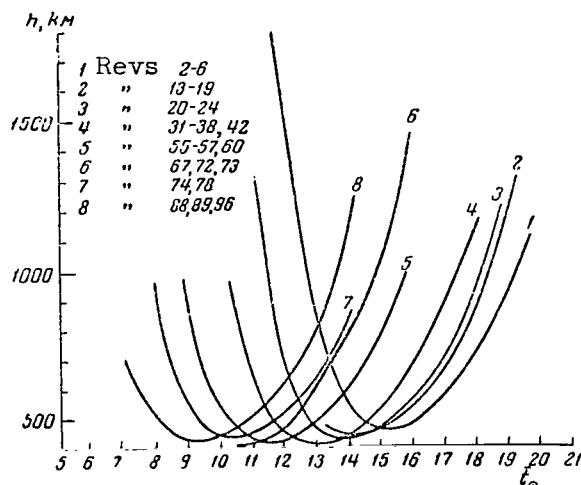


Figure 2

Sections of the "Elektron-2" Orbit at the "Altitude-Mean Solar Time" Coordinates, at Which the Ion Composition Was Measured

#### Description of the Experiment and Operational Regime of the Instruments

Radio frequency mass spectrometers were used on the "Elektron" satellites with a variable counter potential. We should recall that the magnitude of the counter potential, established in the RMS\* analyzer, is determined by the choice of the analyzer operational regime (for example, by the desired magnitude of the resolving power), and depends on the number of cascades (steps) of the RMS analyzer and on the effective value of the high-frequency potential. The relative magnitude of the counter potential  $U_{c \cdot rel}$  is determined as the proportion of the total energy increase obtained by ions in the high-frequency analyzer cascades:

$$U_{c \cdot rel} = U_c / \Delta W = U_c / 3.2,05 \cdot U_{hf \cdot eff} \quad (1)$$

Here  $U_{hf \cdot eff}$  is the effective high-frequency voltage on the analyzer grids. For a three-cascade RMS, the regimes usually employed with respect to the relative level of the counter potential range between 0.8 and 0.95. Figure 4 presents a typical graph showing the dependence of the resolving power and the ion stream of a three-cascade analyzer on the counter potential. It can be seen that the resolution  $R = M / \Delta M = 20$  is achieved for a value of  $U_{c \cdot rel}$  which equals 0.95. A decrease in the counter potential to a value of  $< 0.8$  causes spurious peaks to appear in the spectrum (so-called "harmonic" peaks) for a resolution of the main peak which is less than 10. A decrease in the resolving power is naturally accompanied by an increase in the ion stream, and consequently in sensitivity.

\* Note: RMS designates Radio Frequency Mass Spectrometer.

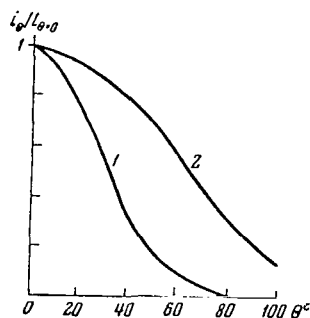


Figure 3

Relative Dependence of the Ion Current  $i_0/i_{\theta=0}$  on the Angle of Attack  $\theta$  for the Analyzer of the Radio-Frequency Mass Spectrometer

1 - for  $O^+$  ions (based on data from the third AES); 2 - for  $H^+$  ions (approximately).

The operational regime of the analyzer is determined in the satellite not only by the potentials established in the laboratory, but also depends on the relative ion energies - i.e., on the satellite velocity and on the potential  $\phi$  with respect to the plasma. The effective counter potential is determined as

$$U_{c,eff} = U_c + \phi - \Delta U_v, \quad (2)$$

The instrument regime will be established by the relationship

/195

$$U_{c,eff}/\Delta W = U_{c,eff}/3 \cdot 2.05 U_{hf,eff} \quad (3)$$

Even if the influence of the satellite potential  $\phi$  is not taken into account, the large relative velocity of the ions decreases  $U_c$  by an appreciable amount

$$\Delta U_v = 5.2 \cdot M \cdot v_s^2 [v],$$

where  $M$  is the ion mass in atomic mass units;  $v_s$  is the satellite velocity in  $\text{km} \cdot \text{sec}^{-1}$ .

For a satellite velocity of  $10 \text{ km} \cdot \text{sec}^{-1}$ , the effective counter potential for  $\text{He}^+$  and  $\text{O}^+$  ions is lowered by 2.08 and 8.3 v, respectively. As can be seen from Figure 4, such a change in the level of  $U_{c,eff}$  for the analyzer regimes employed can make the resolution substantially worse, and can also lead to the appearance of harmonics, thus making an interpretation of the results more difficult.

However, the appearance of harmonics in the spectra is not the only troublesome phenomenon. Due to the fact that the relative amplitude of the peak harmonics is a function of the counter potential, the possibility arises - according to equation (2) - of determining the magnitude of the satellite potential and its variation during the measurements. The dependence of the relative amplitude of the harmonic peak on the values of the absolute and relative counter potentials is also shown in Figure 4. It can be seen from this figure that a change (decrease) in  $U_c$  by 1 v

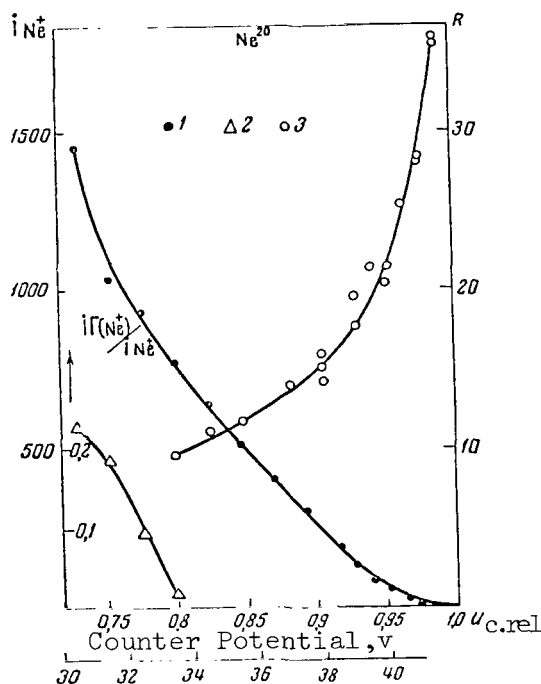


Figure 4

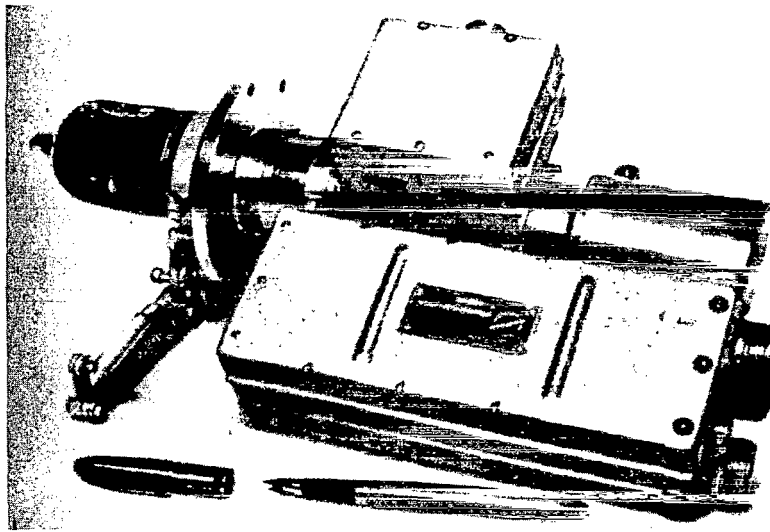
Dependence of MX-6405 Mass Spectrometer Parameters on the Counter Potential (According to the Neon-20 Peak, Laboratory Measurements)

1 - ion current (arbitrary units); 2 - relative magnitude of the harmonics; 3 - resolution (5% of the peak height)

(at the point  $U_{c,rel} = 0.8$ , which corresponds to  $U_c = 33.5$  v) increases the relative magnitude of the neon harmonic peak in the occupied spectrum of the RMS analyzer from 0.017 to 0.095. It is possible to exclude the harmonics from the mass RMS spectra obtained on the satellite by introducing an additional counter potential which changes synchronously with the scanning voltage (according to a saw-tooth law). The almost analogous effect of a synchronous change in the  $U_{c,rel}$  level can be obtained as follows from equation (3), when there is a corresponding change in the amplitude of the high-frequency voltage supplying the RMS analyzer (Ref. 1).

/196

The MX-6405 instruments located on the "Elektron" satellites have a system for supplying additional counter potential, which compensates for the influence of the satellite velocity. In addition, the satellite "Elektron-1" ("lower") contains a device which periodically switches on this system, thus making it possible to increase the mass spectrometer sensitivity. It also makes it possible to clearly determine the effect produced by using a variable counter potential system. The device for changing the regime (the regime switching block-RSB) can be clearly seen in the photograph of the MX-6405 instrument (Figure 5).



MX-6405 Mass Spectrometer Carried by the Satellite  
"Elektron-1". The Switching Regime Block RSB is  
Clearly Visible

In order to increase the effective input of the device, and consequently its sensitivity, a pulling potential of 60 v was supplied to the first analyzer grid. Due to the fact that discrimination of ions having different mass numbers can occur in the field of the first grid (which must be given particular consideration when the ions having essentially different mass numbers are analyzed), the RSB device on the "Elektron-1" satellite periodically switched on the pulling potential. A comparison of the data obtained in these two regimes makes it possible to determine the effect produced by discrimination in the field of the pulling grid of the RMS. The Table below presents the basic characteristics of the MX-6405 mass spectrometers located on the satellites "Elektron-1" and "Elektron-2", and also presents the operational regimes of the instruments.

### Results

The mass spectrometers functioned in good working order throughout their entire period of operation (data on the ion composition exist for the period from January 30 to March 12 for the "Elektron-1" satellite and for April 1, 1964 for the "Elektron-2" satellite). In spite of the fact a great number of spectra which were fully suitable for analysis were obtained from both satellites, we shall only present here the results derived from measuring the ion composition based on data from the "Elektron-2" satellite (upper).

Figure 6 presents typical spectra of ion masses obtained on the

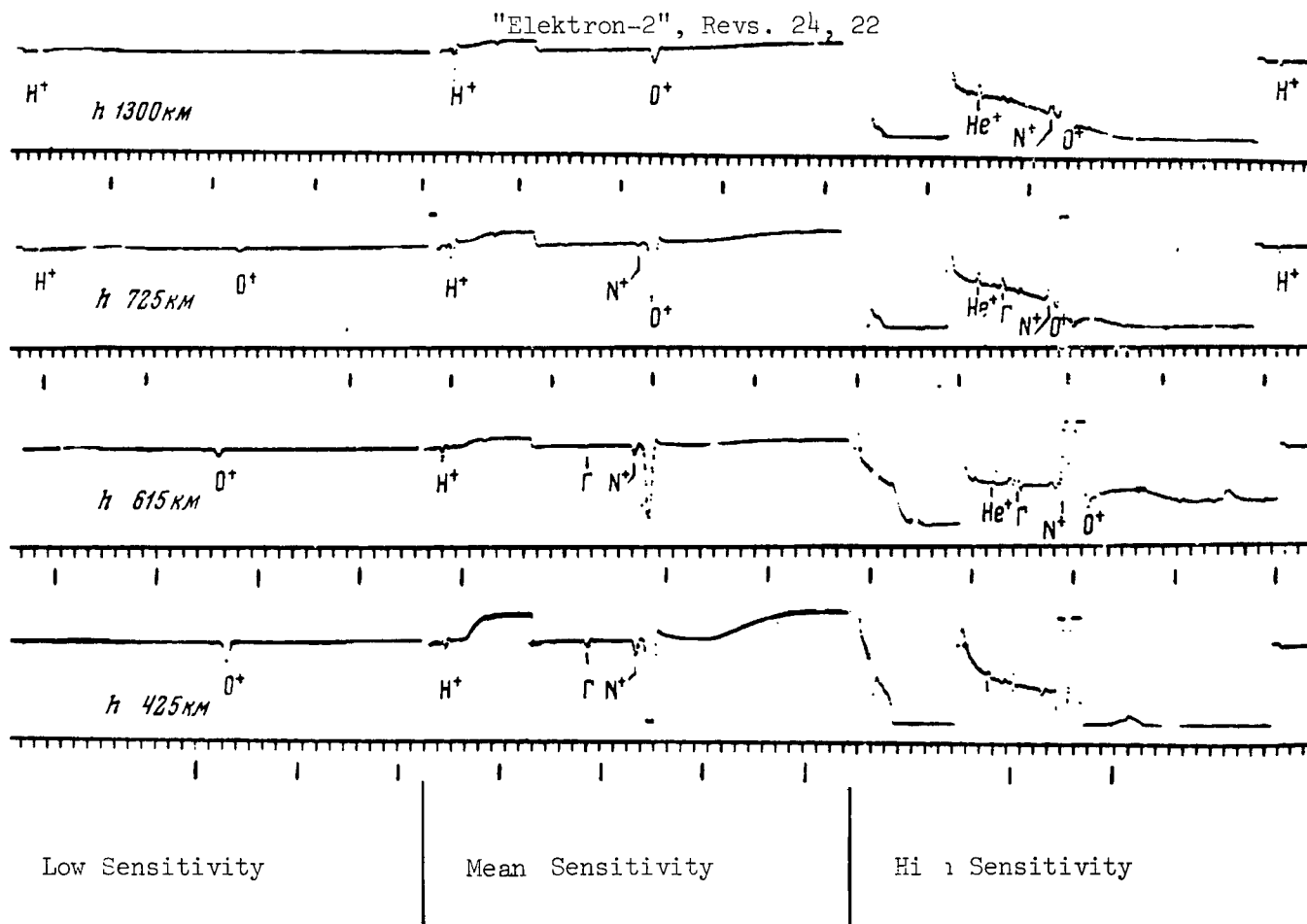


Figure 6

Mass Spectra of Ions Obtained on the Satellite "Elektron-2", Revolutions 22 and 24  
(February 19 and 21, 1964)

The mass peaks of atmospheric ions are designated by the appropriate symbols; the harmonic peak of the  $O^+$  ions, the second light harmonics, is designated by the letter  $\Gamma$ .

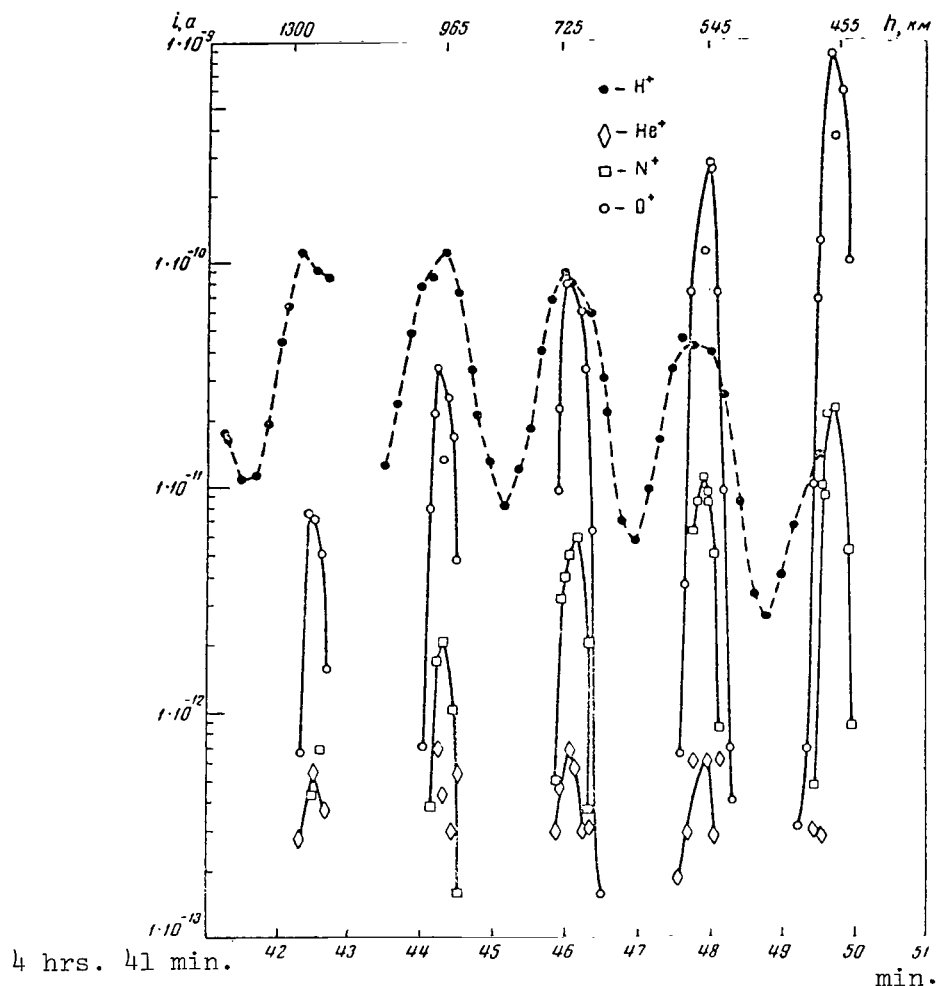


Figure 7

Ion Streams of Ionosphere Components - Hydrogen, Helium, Nitrogen and Oxygen, Recorded on the Satellite "Elektron-2", February 21 (Revolution 24)

satellite "Elektron-2" at altitudes of 1300, 725, 615, and 425 km. The spectra were obtained in the daylight hours (11, 12, 16 and 14 hours local time at latitudes of 25, 38, 60 and 56°, respectively). The first two spectra were obtained on February 21, (revolution 24), while the third and fourth spectra were obtained on February 19 (revolution 22). As can be seen from Figure 6, the subranges of light (1-2 amu) and of mean (4-34 amu) mass numbers were analyzed successively in terms of yields of low, mean, and high sensitivity on the satellite "Elektron-2". The polarity of the signal at the high-sensitivity yield is opposite that of the first two. It can be seen that mass peaks of atomic hydrogen  $H^+$  ( $M = 1$ ) and atomic oxygen  $O^+$  ( $M = 16$ ) ions are predominant in the spectra. Less intense peaks with  $M = 14$  (atomic nitrogen  $N^+$ ) and  $M = 4$  (helium ions  $He^+$ ) can also be seen in the spectra. The peak having the mass number  $M = 8$  is the so-called second light harmonics of the peak with  $M = 16$  (exact value of its mass number is  $0.485 M = 7.8$  amu). Due to the use of an alternating, counter potential regime, the second harmonics is suppressed significantly, while the first harmonics is completely absent in the spectra under

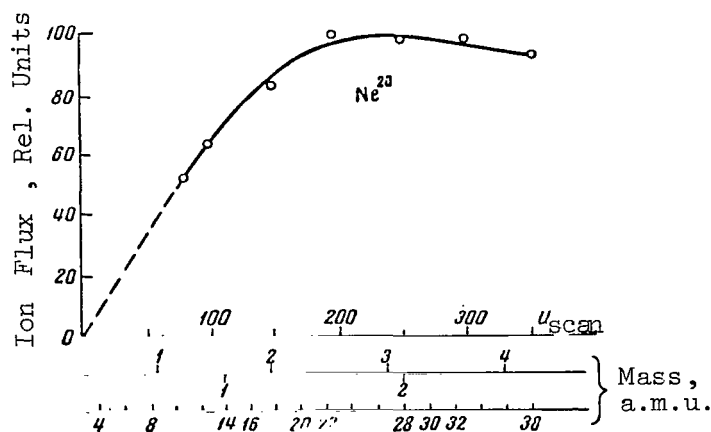


Figure 8

Discrimination Curve According to Accelerating Voltage  
for the MX-6405 Mass Spectrometer, Recorded According to the Neon-20 Peak

TABLE

Parameter	"Elektron-1" (lower)	"Elektron-2" (upper)	Dimensions
Mass Range . . . . .	1-4; 4-34	1-2; 4-34	amu
Resolving power (according to criterion of 5% peak amplitude, laboratory regime) . . . . .	20	20	
Duration of Scanning . . . . .	3.5	3.3	sec
Frequency of high-frequency voltage supplied . . . . .	12.2 4.08	16.4 4.08	Mc
Amplitude of high-frequency voltage . . . . .	8.4	8.9	v
Potential of first grid (pulling potential) . . . . .	-60 or 0	-60	v
Instrument constant . . . . .	90 10.05	162 10.05	v/amu
	0.153 0.067	0.23 0.07	sec/amu

consideration. This fact makes an interpretation of the peaks simple and unambiguous. It can also be seen in the spectra in question that even at a minimum altitude of 425 km no peaks are observed with mass numbers of  $M = 28, 30, \text{ and } 32$ .

Figure 7 presents an example of data obtained during one passage of the satellite "Elektron-2" above the USSR. The magnitudes of streams of recorded ionosphere components (amplitudes of ion peaks) are given as a function of time. The altitudes of the satellite above the Earth's surface are also given. Periodic fluctuations in the peak amplitudes in

/199

the spectra are caused by a change in the "angle of attack" of the RMS tube due to the satellite rotation. Data which are least distorted regarding the ion composition are obtained during time intervals corresponding to ion stream maxima - i.e., at moments of minimum RMS angle of attack (this is illustrated qualitatively in Figure 3).

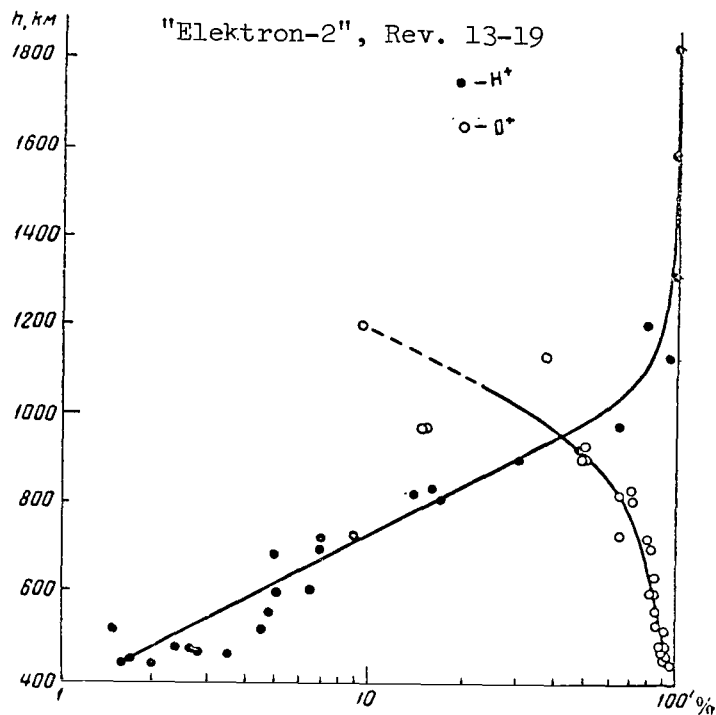
It can be seen from Figure 7 that the maximum amplitudes of the  $H^+$  peaks decrease, while the  $O^+$  and  $N^+$  peaks increase, with a decrease in altitude. It can also be seen that the ion peaks of helium  $He^+$  are small throughout the entire altitudinal region from 1300 to 455 km.

The fact alone that positive ions were recorded by an instrument placed on the satellite points to the fact that the satellite potential with respect to the unperturbed environment was, at least, not positive. This is due to the fact that the potential of hydrogen ion braking on the satellite moving at a velocity of  $10 \text{ km} \cdot \text{sec}^{-1}$  is approximately 0.5 v. Future determination of the satellite potential is possible by means of an exact measurement of the position of  $O^+$  and  $N^+$  peaks on the scale of mass numbers (Ref. 2). The mass numbers of peaks 14 and 16 (taking into account a correction for relative ion velocity, equalling the satellite velocity) differ from whole values by a magnitude of  $\Delta M_p = -0.2 \text{ amu}$ , which corresponds to a satellite potential of  $\phi = -2 \text{ v}$ . This potential is determined to an accuracy of possible quantities of the contact potential difference between the satellite frame and the tube electrodes of the mass spectrometer, which barely exceeds fractions of a volt.<sup>1</sup> Taking this into account, we can apparently assume that the mass spectrometer on the satellite "Elektron-2", for all ion components including the  $H^+$  ions, operated as a probe in the "saturation current" regime (in the region of the left section of the volt-ampere characteristic curve). This provides a basis for assuming that there must not be significant discrimination of ions having mass numbers of 1 and 4 with respect to ions with  $M = 14$  and 16 in the accelerating field of the satellite. Discrimination in the satellite field can appear when the ion direction of motion deviates from the normal to the surface at the location of the RMS analyzer, particularly in the pulling field of the first analyzer grid. One very significant effect is the "discrimination with respect to angle of incidence" of the heavier ions in the analyzer, when its axis deviates from the velocity vector of the satellite. Discrimination with respect to angle of incidence can be taken into consideration, if the angle between the analyzer axis and the satellite velocity vector is known.

Discrimination of ions in the analyzer with respect to accelerating voltage is another complicating factor. The form of the discrimination curve with respect to accelerating voltage for the MX-6405 instrument can be clearly seen in Figure 8 (the dependence is recorded based on the peak of neon-20 in the analyzer occupied spectrum under laboratory conditions). Since discrimination with respect to accelerating voltage is particularly

<sup>1</sup> The effects of "polarization" of dielectric films on the electrodes or the satellite frame can also play a significant role.





/201

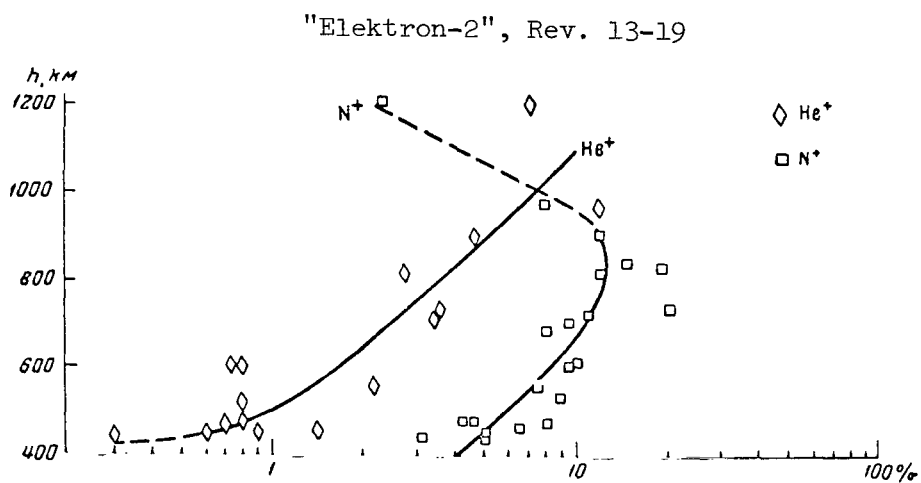


Figure 9

Change in the Relative Concentration of Atmospheric Ion Components as a Function of Altitude During the Period From February 10 to February 16, 1964 (Afternoon Hours, 14-19 Hours Local Time)

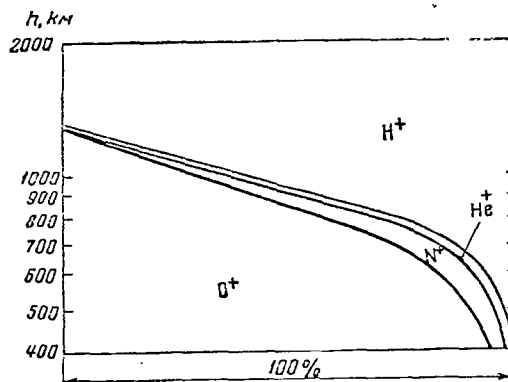


Figure 10

Diagram Illustrating Ion Composition of the Outer Ionosphere  
(February 10-16, 1964, afternoon hours)

large for ions developing at the beginning of mass number scales, and since the discrimination curve recorded for neon does not encompass the requisite region, discrimination with respect to helium ions  $\text{He}^+$  was also studied. It was found that the  $\text{He}^+$  peak amplitude, produced at the beginning of the subrange of mean mass numbers (generator frequency 4.08 Mc per hour, lower scale of masses in Figure 8) differs from the amplitude of the peak produced "in the normal way" in the range of light mass numbers (generator frequency 12.2 Mc per hour, upper mass scale in Figure 8) by a factor of 2-4 depending on the analyzer regime with respect to the counter potential. A mean discrimination factor of three was assumed in order to process the data cited here.

Apart from consideration of discrimination with respect to accelerating voltage, ion streams of hydrogen and helium lead to a nominal regime with respect to the counter potential, taking into account the satellite velocity and magnitude of additional counter potential for all the peaks. The regime

$$U_{\text{c.rel}} = U_{\text{c.eff}} / \Delta W = 0,92 \pm 0,01,$$

which was produced for ions of atomic nitrogen and oxygen was used as the nominal regime.

Figure 9 presents data on the relative concentration of  $\text{H}^+$ ,  $\text{He}^+$ ,  $\text{N}^+$  and  $\text{O}^+$  ions in the ionosphere at altitudes of from 440 to 1800 km; these data were obtained on revolutions 13-19 in the period from February 10 to February 16, 1964. These data pertain to afternoon hours (14-19 hours local time). Due to the small number of representative points obtained in a section of each revolution, and due to our indefinite information regarding the analyzer orientation with respect to the velocity vector - which would be necessary in order to obtain data free from random errors to a large degree - we must examine the results derived from measurements on several consecutive revolutions. The processing procedure consists of correcting the recorded values of  $\text{H}^+$  and  $\text{He}^+$  ion streams. The coefficients for reduction to a nominal regime for  $\text{H}^+$  and  $\text{He}^+$  were determined as 0.53 and 2.0, respectively.

The discrimination factors with respect to accelerating voltage were determined as 1.0 and 3.0. The relative concentration of the  $M^+$  component was calculated from the equation

$$[M^+] = \frac{i_{M^+}}{0.53 \cdot i_{H^+} + 6 \cdot i_{He^+} + i_{N^+} + i_{O^+}} \cdot 100 \% \quad (4)$$

where  $i_{H^+}$ ,  $i_{He^+}$ ,  $i_{N^+}$ ,  $i_{O^+}$  are streams of the corresponding components;  $i_{M^+}$  - the same streams for hydrogen, helium, nitrogen, and oxygen, multiplied by the coefficients 0.53; 6.0; 1.0, and 1.0, respectively.

In spite of the significant scatter of points on the graphs in Figure 9 (this pertains particularly to data for  $He^+$  and  $N^+$ ), the main rules followed by a change in ionosphere composition with altitude are fairly well expressed:  $O^+$  and  $H^+$  ions are the main components at all altitudes. Under given conditions, the  $O^+$  and  $H^+$  ion concentrations become equal at an altitude of 900 km. Based on data shown in the graphs of Figure 9, and taking the fact into account that molecular ions were not detected in measurements on the "Elektron" satellites, a diagram was constructed showing the outer ionosphere composition. This diagram is shown in Figure 10. The basic difference between the models (Ref. 3) existing up to the present time and the experimental data derived from probe measurements of the composition (Ref. 4, 5) consist of the fact that helium ions are not the predominant ionosphere component at any altitude, based on measurements on the satellite "Elektron-2". With an increase in altitude, the "oxygen" ionosphere changes directly into a "hydrogen" ionosphere, the so-called protonosphere. The result coincides with data from a mass spectrometer experiment conducted by Taylor and coworkers (Ref. 6). In this experiment they studied  $H^+$  and  $He^+$  ions together with the total concentration of positive ions up to an altitude of 940 km. This result also coincides with data derived by Bowles and coworkers (Ref. 7); these data were obtained by non-coherent scattering of ionosphere radio waves. /202

Unfortunately, it is not possible to acknowledge all of those individuals who assisted in the successful performance of this work, beginning several years ago. The development and preparation of the mass spectrometer was conducted under the guidance of V. A. Pavlenko and A. E. Rafal'son. I would like to thank the supervisors, M. Ye. Slutskiy and B. I. Zarkhin, who guided the execution of the work, for their great contribution in developing the mass spectrometer for the "Elektron" satellite and for their cooperation in performing the work at all subsequent stages. The coworkers of the RMS group also rendered substantial assistance: engineer A. A. Perno and technician S. V. Vasyukov. Finally, the members of the staff of G. N. Zlotin - T. A. Zaglyadimovoy and N. V. Bul'ulychevoy - made an invaluable contribution in processing the results obtained.

#### REFERENCES

1. Zarkhin, B. I., Istomin, V. G., Rafal'son, A. E., Slutskiy, M. Ye. Kosmicheskiye Issledovaniya, 3, No. 5, (in press).

2. Istomin, V. G. In "Iskusstvennyye Sputniki Zemli", Izdatel'stvo AN SSSR, No. 4, p. 171, 1960.
3. Hanson, W. B. J. Geophys. Res., 67, No. 1, 183, 1961; Bauer, S. J. Nature, 197, No. 4862, 36, 1963.
4. Bowen, P. J., Boyd, R. L. F., Raitt, W. J., Willmore, A. P. Proc. Roy. Soc., A 281, 504, 1964.
5. Gringauz, K. I., Gorozhankin, B. N., Shyutte, N. M., Gdalevich, G. L. Doklady AN SSSR, 151, No. 3, 560, 1963.
6. Taylor, H. A., Brace, L. H., Brinton, H. C., Smith, C. R. J. Geophys. Res., 68, No. 19, 5339, 1963.
7. Farley, D. T., Jr., Bowles, K. L. NRS Report 8489, Nov., 1964.

## ONE ANOMALY IN ELECTRON PITCH-DISTRIBUTIONS

O. L. Vaysberg, F. K. Shuyskaya

The satellite "Kosmos-5" carried narrow-beam charged particle sensors (Ref. 1). These sensors recorded a directional intensity of electrons with energies  $> 40$  kev in the region determined by the satellite orbital parameters, i.e., for  $L \lesssim 2.0$  and for altitudes  $h < 1600$  km. The satellite was not oriented, and rotated around its own axis, which was approximately perpendicular to the sensor axes, with a period of 3-4 minutes. We did not have data on the satellite orientation at our disposal, and therefore tried to determine it. Employing the readings of the solar orientation recorders and the sensor readings as supplementary readings, we were able to determine the orientation of these sensors for 5 revolutions. Thus, the error entailed in determining the sensor directional angle with respect to the magnetic force line did not exceed  $5-10^\circ$ , as a rule. /203

After subtracting a small signal, which was not dependent on the pitch-angle and which was caused by protons with  $\geq 20$  Mev energy, from the sensor readings, we obtained the dependence of the directional intensity of electrons with energies  $> 40$  Mev upon pitch-angle for each time the plane perpendicular to the force line was intersected by the sensors. These pitch-distributions could thus be used to obtain the specular point densities along the low section of the force line, if the electrons move along the force line with conservation of the momentum.

The processed material shows that there is satisfactory agreement between the density of specular points, obtained according to the pitch-distributions, and the electron intensities, which were observed at an angle of  $90^\circ$  to the force line and which were obtained when the satellite passed at other times through the interval  $L$  under similar conditions (similar longitudes, similar local time). However, the scatter between them was great. The widths of the pitch-distributions show that there are significant systematic changes, which exceed the total scatter and observational errors. Figure 1 shows several of these pitch-distributions. Longitudes and local observational time are given for them. /204

The pitch-distributions obtained can be divided into three groups (during the time between the launch on May 28 and the high-altitude American thermonuclear explosion on July 9, 1962, which greatly changed the radiation environment, the semimajor axis of the "Kosmos-5" orbit did not make a complete revolution, and therefore the observations do not encompass all longitudes or all times during the day):

- 1)  $-180^\circ < \lambda < -100^\circ$ ;  $T_M \approx 15$  hrs. 30 minutes - 22 hrs. 00 minutes;
- 2)  $-60^\circ < \lambda < +20^\circ$ ;  $T_M \approx 6$  hrs. 20 minutes - 13 hrs. 40 minutes;
- 3)  $+20^\circ < \lambda < +55^\circ$ ;  $T_M \approx 13$  hrs. 40 minutes - 15 hrs. 50 minutes.

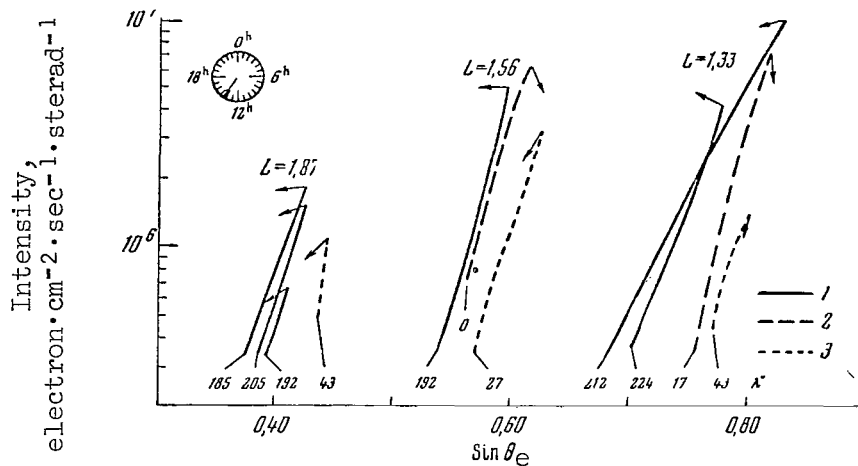


Figure 1

Pitch-Distributions of Electrons with  $E > 40$  keV Energy  
For Three Intervals  $L$  According to "Kosmos-5" Data (June, 1962)

Equatorial pitch-angles were obtained from the condition of magnetic moment conservation. The local time is indicated by an arrow above each distribution (see dial in the upper left corner). Longitudes are given below. 1 - Group I of pitch-distributions; 2 - Group II; 3 - Group III.

Figure 2 shows the specular point densities, compiled according to pitch-distributions, in  $B$ ,  $L$ -coordinates for these groups of pitch-distributions. As can be seen in Figure 2,a, wide pitch-distributions are observed in the longitudinal range to the west of the South Atlantic anomaly, and significant intensities are observed for those values of  $B$  which these electrons must overcome in the anomaly region when drifting in an electrically neutral geomagnetic field. The pitch-distributions have narrower edges in the anomaly region. However, the density of specular points does not change significantly at the anomaly output for  $B(h_{\min}) > 200$  km). Beginning with  $\lambda \approx 0$  and  $\lambda \approx 20^\circ$ , there is a contraction of the observed pitch-distributions, and the narrowest pitch-distributions are observed in the  $+20$ - $+60^\circ$  longitudinal range (Figure 2,c). As far as can be determined from fragmentary data for  $L \sim 2$ , the return to wide pitch-distributions takes place toward  $\lambda \sim 120^\circ$ .

The recording of trapped electrons in the geomagnetic field region, where they must be destroyed during a period of time which is less than one drift period, has already been reported in (Ref. 2-4). The longitudinal effect was recorded by Vernov and his coworkers in the outer zone (Ref. 5). It was later discovered at smaller  $L$  (Ref. 3, 6, 7), and the phenomenon is usually explained by scattering and particle absorption when denser atmospheric layers are penetrated. Contraction of the pitch-distributions in the observations described, which takes place at the anomaly output and which corresponds to a decrease in intensities observed

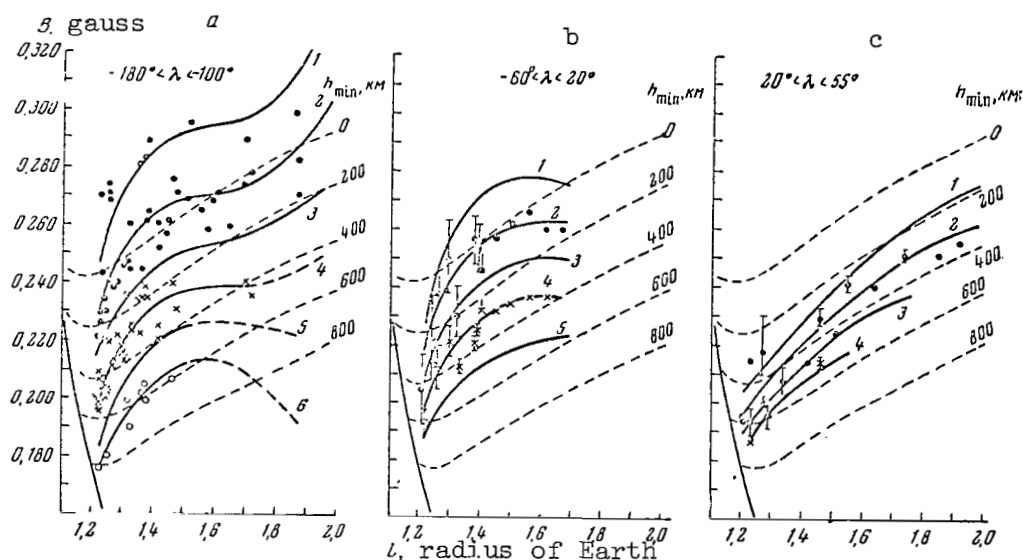


Figure 2

B, L-Distributions of Specular Point Densities Obtained According to Pitch-Distribution of Electrons With  $E > 40$  kev at Altitudes of 1000-1600 km, Under the Assumption of the Magnetic Moment Conservation, According to "Kosmos-5" Data (June, 1962)

- a - Group I of pitch-distributions; 1 -  $0.32 \cdot 10^6$ , 2 -  $0.65 \cdot 10^6$ , 3 -  $1.3 \cdot 10^6$ , 4 -  $2.6 \cdot 10^6$ , 5 -  $5.2 \cdot 10^6$ , 6 -  $10.5 \cdot 10^6$  electron  $\cdot$  cm $^{-2}$   $\cdot$  sec $^{-1}$   $\cdot$  sterad $^{-1}$ ;  
b - Group II; c - Group III.

The experimental point scatter is shown for 2, 4, and 6 levels of intensity.

in this region on other revolutions where the orientation was not known, occurs at those altitudes ( $> 600$  km) where, according to existing opinions, it cannot be explained only by scattering in the atmosphere. Based on existing theoretical assumptions (Ref. 8-10), it was assumed that the observed phenomenon is at least partially caused by the existence of electric fields in the magnetosphere. Electromotive forces, which are produced in the dynamo-region, must penetrate the capture region and distort the drift of low-energy particles, due to the high conductivity along the geomagnetic force lines. The observed systematic change in the width of the pitch-distributions for electrons with  $\sim 100$  kev energies can be caused by an electric field having a strength on the order of  $10^{-5}$  v  $\cdot$  cm $^{-1}$ . Therefore, the energy of these electrons must also change.

A harmonic analysis is presently being conducted for all existing

electron observations on the "Kosmos-5" satellite for  $L < 2.0$ , in order to clarify the relative role of the longitudinal and daily phenomena. Preliminary data show that the role of the daily phenomenon is at least no less than that of the longitudinal phenomenon in the observed variations. The daily shift with respect to B of electrons recorded coincides with the theoretical shift (Ref. 11). In addition to the systematic shift, there are also random fluctuations, whose magnitude exceeds the observational error.

#### REFERENCES

1. Krasovskiy, V. I., et al. *Geomagnetizm i Aeronomiya*, 3, No. 3, 401, 1963.
2. Mularchik, T. M., Vaisberg, O. L. *Space Res.*, 5, 500, 1965.
3. Temnyy, V. V. *Space Res.*, 5, 489, 1965.
4. Paulikas, G. A., Freden, S. C. *J. Geophys. Res.*, 69, No. 7, 1239, 1964.
5. Vernov, S. N., et al. *Geomagnetizm i Aeronomiya*, 3, No. 5, 812, 1963.
6. Vernov, S. N., et al. *Izvestiya AN SSSR, Seriya Fiz.*, 28, No. 12, 2058, 1964.
7. Imhof, W. L., Smith, R. V. *J. Geophys. Res.*, 70, No. 3, 569, 1965.
8. Gold, T. *J. Geophys. Res.*, 64, 1219, 1959.
9. Dungey, J. W. *J. Geophys. Res.*, 68, No. 11, 3540, 1963.
10. Krasovskiy, V. I. *Kosmicheskiye Issledovaniya*, 3, No. 2, 345, 1965.
11. Maeda, H. *J. Atmos. Terr. Phys.*, 26, 1133, 1964.



# VARIATIONS IN THE SOFT COMPONENT OF THE ELECTRON ENERGY SPECTRUM

T. M. Mulyarchik

The construction and operation of electron sensors carried on the satellites "Kosmos-3" and "Kosmos-5" are described in (Ref. 1-3). The curves for the sensor sensitivity are given in (Ref. 4). The readings of three sensors, which were parallel to each other and which had foils of 0.4, 0.6, and 1.1  $\text{mg}\cdot\text{cm}^{-2}$ , for different accelerating voltages (3.8, 6, 11 kv) were employed to determine the energy spectrum. An increase in the electron energy recorded due to the accelerating voltage leads to a signal increase (positive modulation) for an energy of  $\leq 30$  kev and to a signal decrease (negative modulation) for 50-150 kev energies. /206  
Electrons with energies of 35-50 kev and more than 150 kev undergo practically no modulations. The signal ratios for three sensors without accelerating voltage in the 0-40 kev region strongly depend on the recorded electron energies, and remain almost constant for  $E > 50-70$  kev.

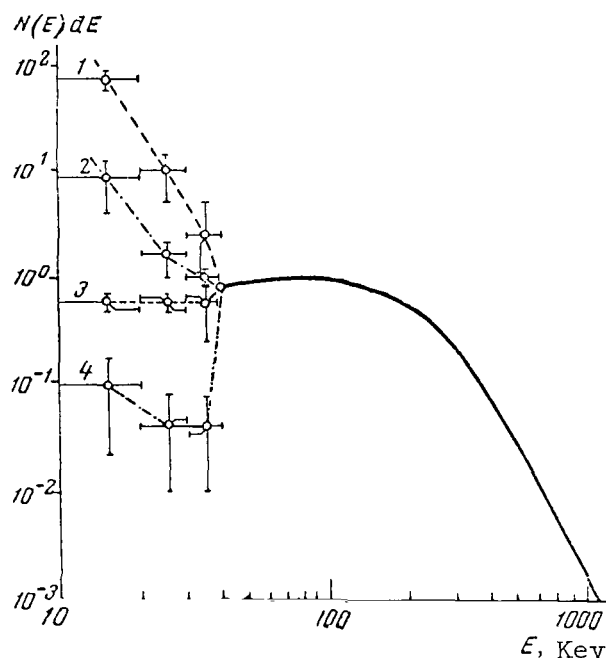


Figure 1

Example of Electron Energy Spectra Observed in Different Regions From the Satellite "Kosmos-5"  
Energy is plotted along the abscissa axis; relative differential intensities of electrons (per 1 kev) in different energy groups are plotted on the ordinate axis.

By combining the ratio of three sensor signals with the sign and magnitude of the modulation, we can determine the energy spectrum of

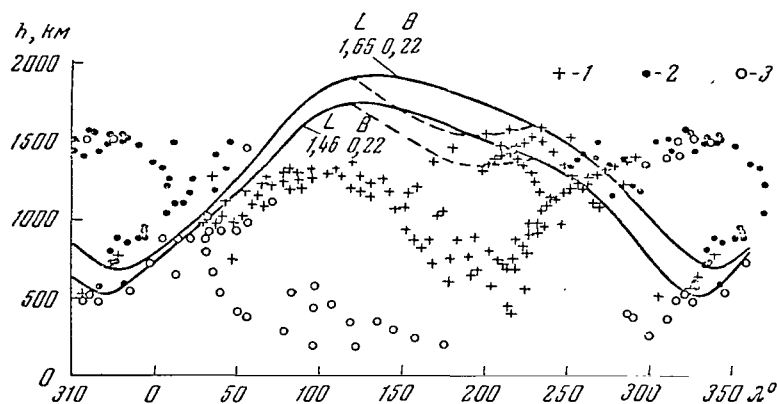


Figure 2

#### Geographic Location of Negative and Positive Modulations

1 - positive modulation, 2 - negative modulation, 3 - zero modulation. All observations for which  $L \leq 2$  are plotted. Two drift trajectories are given as an example.

electrons recorded. The energy spectrum of electrons with  $E > 50$  kev was compiled according to data in (Ref. 5), which compared all measurements for the energy spectrum of electrons with  $E > 40$  kev carried out before July 9, 1962. If it is assumed that  $N(E < 40 \text{ kev}) dE = 0$ , and  $N(E > 40 \text{ kev}) dE$  coincides with the form given in (Ref. 5), then this electron distribution would produce a negative modulation of about 7% in a sensor with foil of  $0.6 \text{ mg} \cdot \text{cm}^{-2}$ . Addition of the 30-50 kev section according to data in (Ref. 5) would lead to the recording of negative modulation with an amplitude of 4%. Positive modulation is only reached by the addition of electrons with  $E < 30$  kev.

An analysis of the sensitivity curves shows that the addition of the 10-20 kev group to the heavy component leads to a significant increase in the positive modulation amplitude and to a comparatively weak "softening" of the signal ratio for the three sensors. If the same amplitude is caused by electrons with an energy of 20-30 kev, the signal ratio of the three sensors would have to be much "softer" (Ref. 4). In every observation of positive modulation on the "Kosmos-3" and "Kosmos-4" satellites, the signal ratio of the three sensors was rather "hard" for a significant modulation amplitude, so that electrons with energies of 10-20 kev played the predominant role. Figure 1 presents examples of electron energy spectra /207 observed on "Kosmos-5" in different regions. The distribution for  $E > 40$  kev is taken from (Ref. 5), and distributions 4-1 in the 10-40 kev region are shown. These distributions give the negative modulation with an amplitude of 7%, the zero modulation and the positive modulation with an amplitude of 10 and 200%. The signal ratio of the three sensors is (3.2:1:3.0), (3.2:1:3.0), (3.2:1:2.7) and (3.2:1:1.6).

Figure 2 shows the dependence (for  $L \leq 2$ ) of the negative and positive modulation occurrence on altitude and longitude. It can be seen from the figure that the negative modulation was recorded at high invariant altitudes  $h_{\min}$  ( $h_{\min}$  - the minimum altitude of a given specular point trajectory above the Earth's surface), and the positive modulation was recorded at smaller values of  $h_{\min}$ . However, the positive modulation was only recorded when high actual altitudes (above 500-1000 km) corresponded to small values of the invariant altitude  $h_{\min}$ . Thus, electrons with an energy of approximately 15 keV, which produced a positive modulation, were recorded above central and southern Asia, the Indian Ocean, Indonesia, and the western part of the Pacific Ocean. There was a sharp relative decrease in the intensity of electrons with  $E \sim 15$  keV in the South Atlantic (change from 1 and 2 spectra to the 4 spectrum in Figure 1). The absolute intensity of the soft electrons also decreased.

The maximum intensity of soft electrons at altitudes of about 1500 km was approximately  $10^7 \text{ particle} \cdot \text{cm}^{-2} \cdot \text{sec}^{-1} \cdot \text{sterad}^{-1}$ , and their lower boundary corresponded to an intensity of  $5 \cdot 10^5 \text{ particle} \cdot \text{cm}^{-2} \cdot \text{sec}^{-1} \cdot \text{sterad}^{-1}$ .

The soft electron distribution with respect to pitch-angles was more isotropic than that for electrons with  $E > 40$  keV. However, their pitch-angle distribution remained anisotropic close to the lower boundary of the soft electron region, with a maximum close to  $90^\circ$ , so that the decrease in their intensity along a given force line below 500-1000 km was primarily related to the magnetic reflection of particles, and not to their absorption in the atmosphere at a given longitude.

Let us now examine the softest component of the energy spectrum recorded by the satellite "Kosmos-5".

Figure 2 in (Ref. 4) gives examples of signals from sensors with foils of  $0.4$  and  $0.6 \text{ mg} \cdot \text{cm}^{-2}$  under different accelerating voltages. The signal shown in Figure 2, a is primarily encountered on the illuminated section of the orbit. This signal increases when an accelerating voltage of 11 kV is switched on a sensor with a foil of  $0.4 \text{ mg} \cdot \text{cm}^{-2}$ . The signal ratio on sensors of  $0.4$  and  $0.6 \text{ mg} \cdot \text{cm}^{-2}$  thus exceeds 30, and the signal on the  $0.4 \text{ mg} \cdot \text{cm}^{-2}$  sensor decreases by a factor of 100 when the accelerating voltage decreases to 6 kV. According to the laboratory calibration, the recorded electron energy does not exceed 5 keV. The works (Ref. 3, 6) advance arguments substantiating the fact that "fresh" photoelectrons are recorded in this case; these photoelectrons are not in equilibrium with the surrounding environment and can surmount the braking potential of -40 V supplied to the screening grid of the electron sensor. /208

The intensity of these signals decreases sharply when the satellite passes into the region of dark shade. However, they have sometimes been observed for several minutes close to the terminator on the unilluminated section of the orbit. It was found in each such case that the atmosphere was illuminated on the other end of the force line at a conjugate atmospheric point. The photoelectron intensity fell below the detection limit, when the altitude of the shade on the illuminated end of the force line exceeded

300-400 km. Thus, the intensity of "crepuscular" photoelectrons depends essentially on the altitude of the observational point, and sharply decreases when the satellite passes below 250 km.

An intensity of up to  $2 \cdot 10^7 \text{ cm}^{-2} \cdot \text{sec}^{-1} \cdot \text{sterad}^{-1}$  was usually observed at an altitude of about 250 km for 1.5 hours before sunrise, under the condition that the Sun was located above the horizon at a conjugate point. As has already been indicated, the recorded electron energy exceeded 40 eV. Such electrons effectively excite several emissions of the upper atmosphere, particularly  $\lambda 3914 \text{ \AA}$   $\text{ING N}_2^+$ ,  $\lambda 6300$  and  $5577 \text{ \AA}$  [U V]. Utilizing data on the effective excitation cross sections by electron impact from (Ref. 7) and (Ref. 8), as well as the model given by Harris and Priester (Ref. 9) for  $t = 4^h$ ,  $S = 180$ , we find that the intensities of these three emissions do not exceed several Rayleighs. Thus, direct atmospheric excitation by rapid electrons, which was observed by means of "Kosmos-5", is below the detection limit of present day spectral equipment. If we take the fact into account, however, that a flux of low-energy photoelectrons exceeds the flux of electrons with  $E > 40 \text{ eV}$  by approximately one order of magnitude, the phenomenon is found to be significant. In addition, soft electron streams at altitudes of 200-300 km lead to an electron temperature increase (Ref. 7, 10). In this case predominant excitation of the red line must be observed. There have been several recent discussions (Ref. 10-14) of the possibility of an electron temperature increase and of the red line cross section excitation in the pre-morning hours by photoelectrons arriving along the force line from the illuminated atmosphere. The satellite "Kosmos-5" recorded real streams of such photoelectrons. Unfortunately, we do not have at our disposal data on the red line cross section, which could be directly compared with our measurements. However, according to (Ref. 15) the general nature of the morning behavior of the red line, particularly the "north wave" - i.e., the beginning of pre-morning intensification from the northern section of the sky - and the intensity of the pre-morning flare closely coincide with the behavior of crepuscular photoelectrons and their flux.

#### REFERENCES

1. Krasovskiy, V. I., Gal'perin, Yu. I., Temnyy, V. V., Mulyarchik, T. M., Dzhordzhio, N. V., Marov, M. Ya., Bolyunova, A. D. *Geomagnetizm i Aeronomiya*, 3, No. 3, 1963.
2. Krasovskiy, V. I., Gal'perin, Yu. I., Dzhordzhio, N. V., Mulyarchik, T. M., Bolyunova, A. D. *Kosmicheskiye Issledovaniya*, 1, No. 1, 132, 1963.
3. Mulyarchik, T. M., Vaysberg, O. L. *Space Res.*, 5, 500, 1965.
4. Mulyarchik, T. M. *Kosmicheskiye Issledovaniya* (in press).
5. Walt, M., Newkirk, L. L. *Space Res.*, 5, 458, 1965.

6. Mulyarchik, T. M. Kosmicheskiye Issledovaniya, 2, No. 2, 266, 1964.
7. Dalgarno, A. Ann. Geophys., 20, No. 1, 1964.
8. Seaton, M. I. JATP, 4, No. 6, 285, 1954.
9. Harris, I., Priester, W. J. Atm. Sci., 19, 286, 1962.
10. Hanson, W. B. Space Res., 3, 282, 1962.
11. Dalgarno, A., Walker, J. C. G. J. Atm. Sci., 21, 463, 1964.
12. Dalgarno, A., McElroy, M. B. Planet. Space Sci., 13, 163, 1965.
13. Cole, K. D. Ann. Geophys., 21, No. 1, 156, 1965.
14. Willmore, A. P. Nature, 202, 41, 1964.
15. Barbier, D. Ann. Geophys., 17, No. 1, 1961.

---

SPATIAL DISTRIBUTION OF DIFFERENT GROUPS OF TRAPPED  
CORPUSCLES BASED ON DATA FROM THE SATELLITES  
"KOSMOS-3" AND "KOSMOS-5"

V. V. Temnyy

Data obtained on the satellites "Kosmos-3" and "Kosmos-5" made it 209 possible to determine the distribution of protons having energies greater than 50 Mev, and of electrons trapped by the geomagnetic field before the high-altitude American explosion on July 9, 1962. It was found previously (Ref. 1) that the distribution of high-energy protons is characterized quite well by the B, L-coordinates introduced by McIlwain (Ref. 2). Figure 1 shows the distribution of high-energy protons in these coordinates.

Envelopes were compiled in order to study the distribution of electron streams recorded, according to the maximum value of current signals whose modulation was determined by the satellite's rotation around an axis perpendicular to the sensor axes. These envelopes determine the continuous change in trapped electron streams along the satellite's orbit, recorded in a direction which is perpendicular to the force line. The analysis of the recorded electron spectrum performed by T. M. Mulyarchik (Ref. 3) revealed the fact that these signals are primarily caused by trapped electrons with energies greater than 40 keV.

A significant scatter of experimental data, which was particularly large for small signals (the region of large B [Ref. 1]), was obtained

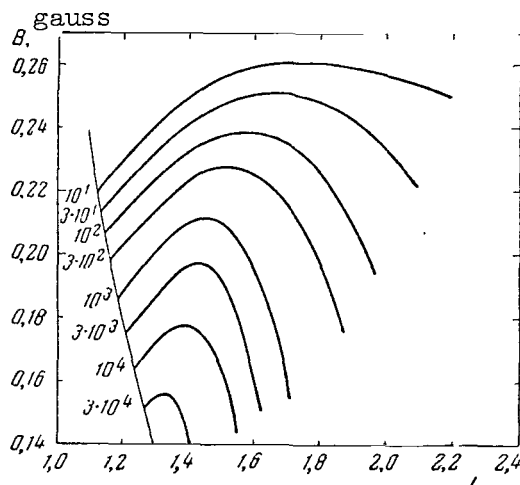


Figure 1

Distribution of Proton Streams (in  $\text{particle} \cdot \text{cm}^{-2} \cdot \text{sec}^{-1}$ )  
With Energies Greater Than 50 Mev in B, L Coordinates

when attempts were made to compile the distribution of similar intensity electrons in the B, L coordinates, which was the same as for high-energy protons.

In order to determine the nature of the scatter obtained, the dependences of omnidirectional intensity on B were compiled at seven fixed L: from 1.2 to 2.0. Some of these are shown in Figure 2. In these graphs <sup>/211</sup> the number of experimental points equals the amount of the fixed envelope L intersected by the satellite. It can be seen that significant electron streams were recorded in those drift trajectory regions which descended toward the Earth to an altitude of  $h_{\min} < 100$  km in the region of the South Atlantic anomaly. The distribution along  $L = 1.6$  of high-energy proton streams (Figure 3) serves to illustrate the fact that electron streams were recorded in those drift trajectory regions which they could not reach during adiabatic motion in the geomagnetic field. It can be seen from this figure that only a background caused by cosmic rays is recorded in the case of  $h_{\min} < 100$  km.

In the anomaly region electron streams could not be recorded in the case of  $h_{\min} < 100$  km. It is therefore interesting to examine the dependence of distribution only upon the longitude of the recording location. Figure 2 gives the geographic longitudinal regions in which experimental values were obtained. It can be seen that the largest portion of points pertaining to the anomaly region (from  $60^\circ\text{W}$  to  $60^\circ\text{E}$ ) is located to the left of the points characterizing intensities recorded in the region  $100^\circ\text{W}$  -  $150^\circ\text{E}$  at all the L investigated - from 1.2 to 2.0. This could mean that similar trapped electron streams were recorded at smaller B within the anomaly region than beyond it.

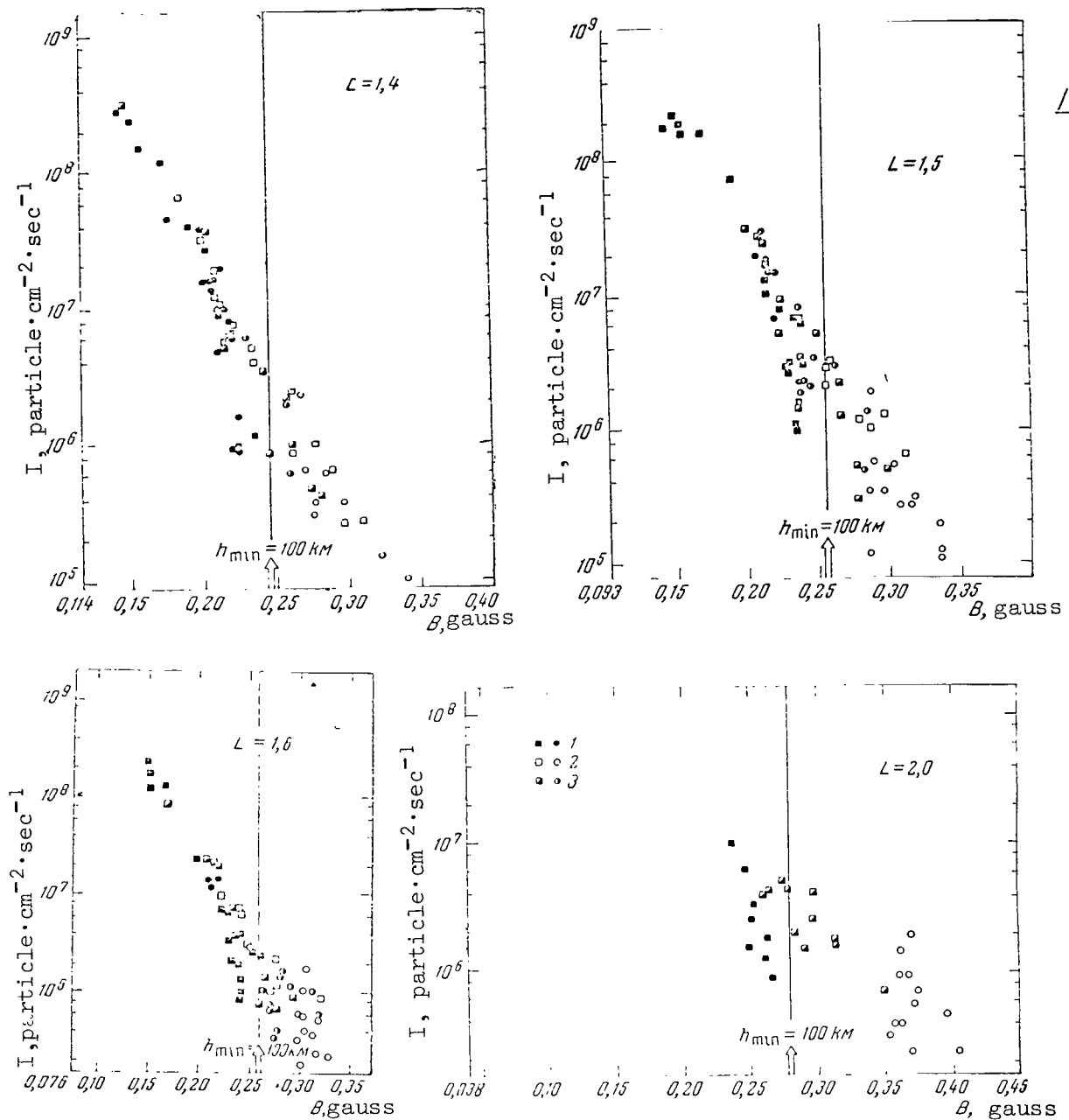


Figure 2

Distribution of Electron Streams with  $E > 40$  kev Along Four Chosen Lines L  
 1 -  $\lambda = 60^\circ\text{W} - 60^\circ\text{E}$ ; 2 -  $\lambda = 150^\circ\text{E} - 100^\circ\text{W}$ ; 3 -  $\lambda = 100^\circ\text{W} - 60^\circ\text{W}$ ,  $\lambda = 60^\circ\text{E} - 150^\circ\text{E}$ .

Squares - according to "Kosmos-5" data; Circles - according to data from "Kosmos-3".

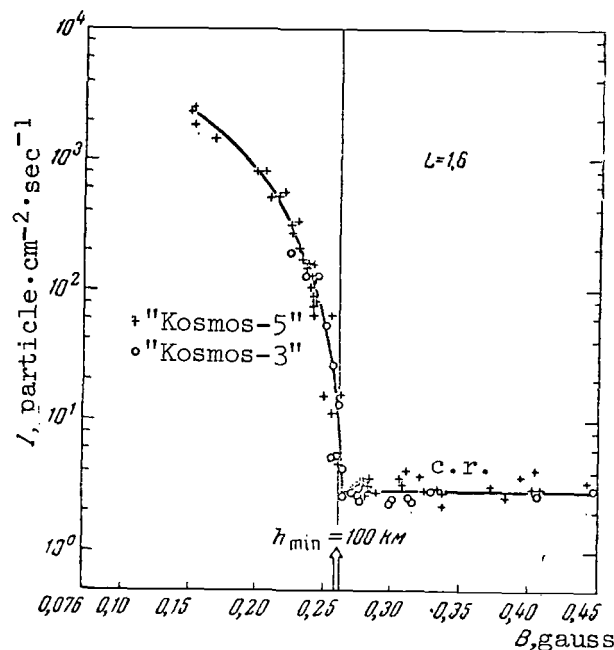


Figure 3

Distribution of Protons With  $E > 50$  Mev

c.r. - cosmic ray background (in  $\text{particle} \cdot \text{cm}^{-2} \cdot \text{sec}^{-1}$ )

The following characteristic of the distributions shown in Figure 2 was employed to determine the change in a trapped electron stream on the drift trajectory, only as a function of longitude. If  $h_{\min}$  above the Earth's surface is employed instead of  $B$ , then in the first approximation the dependences obtained would be approximately equal for all  $L$  for intensities which are less than  $5 \cdot 10^7 \text{ particle} \cdot \text{cm}^{-2} \cdot \text{sec}^{-1}$  - i.e., it can be assumed that the intensity distribution depends only on  $h_{\min}$  and the longitude  $\lambda$ . Since the electrons recorded are trapped and oscillate along the force line, instead of the geographic longitude of the recording point it is advantageous to examine  $\Delta\lambda$  - the distance in degrees along the drift trajectory from the point where the given envelope  $L$  descends into the atmosphere to the greatest extent.  $\Delta\lambda$  is obtained from data on the real field position (Ref. 4).

Figure 4 presents the averaged dependences of  $h_{\min}$  on  $\Delta\lambda$  for three chosen stream magnitudes. The experimental points are given for the flux of  $7.6 \cdot 10^5 \text{ particle} \cdot \text{cm}^{-2} \cdot \text{sec}^{-1}$ . The curves obtained reflect the distribution change along the force line: the flux increases up to  $\Delta\lambda = -100^\circ$  during motion to the east of the anomaly along  $h_{\min}$  in the direction of electron drift, and then begins to decrease during motion toward the anomaly. The picture thus obtained apparently reflects the characteristic distribution change along  $h_{\min}$ , and not sporadic fluctuations produced at different longitudes. This is due to the fact that, for example, in the



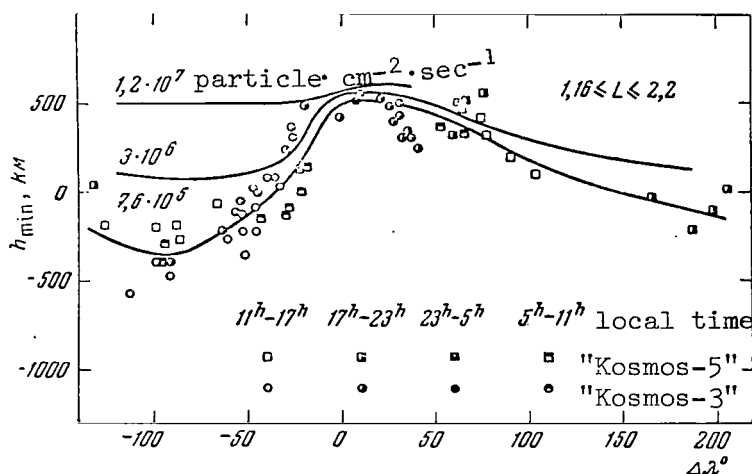


Figure 4

Change in  $h$  as a Function of Longitude for Constant Values of Electron Streams With  $E > 40$  kev

$\Delta\lambda = -100^\circ$  region not once was a flux of  $7.6 \cdot 10^5 \text{ particle} \cdot \text{cm}^{-2} \cdot \text{sec}^{-1}$  recorded for  $h_{\min} \sim 500$  km, just as in the anomaly region for the same  $h_{\min}$ . It can be seen from Figure 4 that the values obtained pertain to different intervals of local time. Due to the relatively small amount of experimental data, it was not possible to determine the daily changes in this distribution. It can only be noted that in the  $\Delta\lambda \sim -100^\circ$  region, where trapped electrons penetrate along the line to maximum B, streams were recorded in time intervals comprising 75% of the day (morning, daytime, evening) for  $h_{\min} < -200$  km. In the  $\Delta\lambda = -20^\circ - -40^\circ$  region, a flux of  $7.6 \cdot 10^5 \text{ particle} \cdot \text{cm}^{-2} \cdot \text{sec}^{-1}$  was recorded during the morning hours at smaller  $h_{\min}$  than during the daytime and evening hours.

The comparison of intensity changes given in Figure 2 and Figure 4 makes it possible to construct a model of trapped electron distribution in the B, L coordinates (Figure 5). Constant intensity is expressed in the form of a band here. The lower curve in the band pertains to the anomaly region; the upper curve pertains to the region close to  $\Delta\lambda = -100^\circ$ ; the curves for intermediate longitudes lie within the band. This distribution of electron streams indicates that the magnitude of the stream increases along identical geomagnetic latitude when there is a change from small L to  $L = 1.6$ ; the stream magnitude decreases during motion to larger L. This indicates the existence of a trapped electron stream maximum close to  $L = 1.6$ .

There is still no explanation of the mechanism leading to the recorded stream change on the drift trajectory. If it is assumed, as was done previously (Ref. 5), that along the entire drift trajectory around the Earth there is a continuous supply of trapped particles to

/213

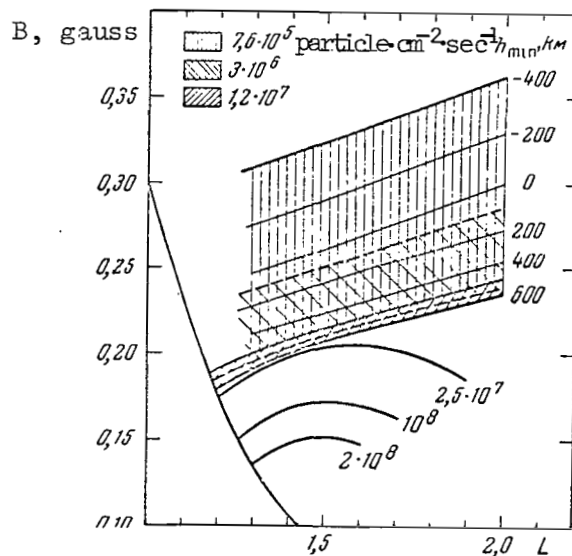


Figure 5

Distribution of Trapped Electron Streams with  $E > 40$  kev  
in B, L Coordinates, With Allowance for Longitudinal Changes

$h_{\min} < 400$  km, which predominates over absorption at those altitudes where the recording is conducted in the  $\Delta\lambda$  region to the east from zero to  $-100^\circ$ , and if it is assumed that the absorption exceeds the supply at  $\Delta\lambda$  from  $-100^\circ$  to the east up to  $\Delta\lambda = 0$ , then the "restoration" time of the zone particles can be estimated. It is on the order of  $10^7$  sec at the equator for  $L = 1.6$ .

The possible influence of the electric field, leading to the recorded particle distribution change on the drift trajectories is investigated in (Ref. 6,7).

Longitudinal stream changes on the drift trajectories only in the outer zone region ( $L > 3$ ) were obtained from measurement data on the second spacecraft-satellite (Ref. 8). Paulikas and Freden (Ref. 9) recorded the appearance of quasi-trapped electron streams for  $h_{\min} < 0$  km with energies greater than 0.9 Mev only close to  $L = 1.2$  and 2.0. The scatter in the B, L coordinates of experimental points pertaining to an electron flux of  $10^7$  particle  $\cdot$  cm $^{-2}$   $\cdot$  sec $^{-1}$ , recorded by Van Allen and Frank on the satellite "Injun-1" (Ref. 10) in the  $L < 1.32$  region, can probably also be explained by the longitudinal dependence. Recent data obtained on the satellite "Kosmos-17" characterize the longitudinal changes of electron stream distribution at  $L < 2$  after the American thermonuclear explosion on July 9, 1962 (Ref. 11).

In conclusion, I would like to thank V. N. Smirnov for assistance in

processing the results.

#### REFERENCES

1. Temnyy, V. V. COSPAR Symposium, Florence, Italy, May 1964 (in press)
2. McIlwain, C. E. J. Geophys. Res., 66, 3681, 1961.
3. Mulyarchik, T. M. Present collection, p. 205.
4. Jensen, D. C., Murray, R. W., Welch, J. A., Jr. AFSWC-TN-60-8, AFSWC-TN-60-19, 1960.
5. Temnyy, V. V. Kosmicheskiye Issledovaniya, 2, No. 5, 812, 1964.
6. Krasovskiy, V. I. Present collection, p. 11.
7. Vaysberg, O. L., Shuyskaya, F. K. Present collection, p. 203.
8. Vernov, S. N., Savenko, I. A., Shavrin, P. I., Tverskaya, L. V. Geomagnetizm i Aeronomiya 3, No. 5, 812, 1963.
9. Paulikas, G. A., Freden, S. C. J. Geophys. Res., 69, 1239, 1964.
10. Frank, L. A., Van Allen, J. A. J. Geophys. Res., 68, 1203, 1963.
11. Vernov, S. N., Chudakov, A. Ye., Vakulov, P. V., Gorchakov, Ye. V., Ignat'yev, P. I., Kuznetsov, S. N., Logachev, Yu. I., Lyubimov, G. P., Nikolayev, A. G., Okhlopkov, V. P., Sosnovets, E. N., Ternovskaya, M. V. Izvestiya AN SSSR, Seriya Fiz., 28, No. 12, 2058, 1964.

## MEASUREMENT OF SOFT ELECTRON STREAMS IN THE UPPER ATMOSPHERE AT ALTITUDES TO 500 KM

L. A. Antonova and T. V. Kazachevskaya

At present a very important problem in the physics of the upper atmosphere is the study of corpuscular radiation. The existence of electron streams in the upper atmosphere, not only in the region of the polar aurorae, but also at every latitude, is of great geophysical significance, which is associated, for example, with the problem of ionization and warming of the upper atmosphere. Of greatest geophysical interest are the streams of very soft electrons with energies of less than a tenth of a kilo-electronvolt. They possess the greatest cross section of interaction with atoms and molecules of the atmosphere and apparently carry the chief energy of the streams. /214

The existence of electrons of such energies in the upper atmosphere might explain a number of peculiarities of ionospheric behavior. However, to measure the strength and spectrum of low-energy electrons is a very difficult task, especially under the conditions of the upper atmosphere, which principally involves the very low penetrating power of the particles to be recorded. An open-type secondary-electron multiplier was chosen as the radiation detector in an experiment measuring soft electrons in the upper atmosphere. The secondary-electron multiplier very efficiently records soft electrons, permits measurement of the entire electron stream without the use of any additional absorbents, and makes it possible to measure weak electron streams and their rapid variations in time. The secondary-electron multiplier operates only at a vacuum no lower than  $5 \cdot 10^{-5}$  mm Hg, which under upper atmospheric conditions is reached at heights above 120 km. The short duration of the rocket experiment necessitated preliminary evacuation of the instrument housing containing the multiplier before the rocket was fired, so that the instrument would become degasified faster after it was opened.

Individual sectors of the electron energy spectrum were distinguished by interchanging different filters in front of the multiplier. The multiplier operated in the pulse count mode.

The experiment was conducted on October 18, 1962, at mean latitudes in the daytime. The instrument was installed in the hermetic, jettisonable AGS\* container. The axis of symmetry of the instrument input aperture lay in the equatorial plane of the container. The visual angle of the instrument was  $\pm 6^\circ$ . The container was stabilized relative to the vertical, and rotated about it with a period gradually changing from 12 to 7 sec.

The instrument in this experiment registered rather substantial noise, probably caused by dispersed light entering the instrument by multiple reflections through the slit in the filter input device. The signal was

\*Note: AGS designates High Altitude Geophysical Station.

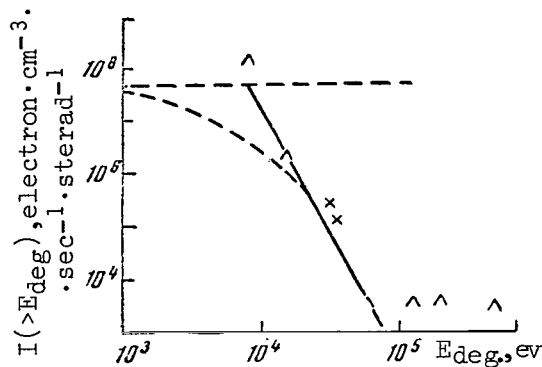


Figure 1

found to prevail over the background level for a filter representing an open window ( $d=0.1\text{ mm}$ ) and the two least dense filters (aluminum and fluoroplastic films  $\sim 7\text{ }\mu$  thick). An estimate of the average value of /215 the integral electron stream, determined from the signal through the open window, gave a value of  $\approx 5 \cdot 10^7\text{ electron}\cdot\text{cm}^{-2}\cdot\text{sec}^{-1}\cdot\text{sterad}^{-1}$  within an accuracy of 2. The mean flux of electrons having energies exceeding 30-35 keV was estimated as  $\sim 2 \cdot 10^5\text{ electron}\cdot\text{cm}^{-2}\cdot\text{sec}^{-1}\cdot\text{sterad}^{-1}$ . From these data and the upper limits of the flux for other filters, the integral electron energy spectrum (Figure 1) was plotted. In the  $\geq 10\text{ keV}$  region, it may be represented as a power function with a power exponent of  $\sim 4.5$ . A less drastic increase in intensity was observed for smaller energies, and it was concluded that the spectrum boundary on the low energy side was below  $\sim 8\text{ keV}$ .

Assuming that the spectrum boundary on the low energy side lies in the 1-8 keV region, an estimate of the entire energy flux results in values of  $\sim 0.1 - 0.5\text{ erg}\cdot\text{cm}^{-2}\cdot\text{sec}^{-1}\cdot\text{sterad}^{-1}$ . The mean flux does not depend on altitude in the measurement altitude range, nor on the angle between the velocity vector and the plane perpendicular to the magnetic line of force. Significant short-lived variations were detected.

The electron streams in the atmosphere were also measured by a method based on the principle of recording ionizing radiation by means of the thermoluminescent phosphor  $\text{CaSO}_4(\text{Mn})$  (the "Phosphor" device). The luminous compound  $\text{CaSO}_4(\text{Mn})$  has valuable properties permitting absolute measurements in the shortwave region of the spectrum below  $1350\text{ }\text{\AA}$ . Under short-wave radiation, as well as  $\gamma$ - and  $\beta$ - radiation, the  $\text{CaSO}_4(\text{Mn})$  phosphor stores energy, and when heated re-emits it in the visible region of the spectrum with a peak in the green sector. The phosphor's peak brightness when heated is - just like the total energy of this radiation (the light sum) - proportional to the energy stored by the phosphor during exposure within wide energy ranges.

The main quantity characterizing total radiation energy falling on the phosphor is the "light sum". It is experimentally measured as the integral number of quanta of visible light emitted by the phosphor during the entire heating period. The light sum gives information on the total

energy of the exciting radiation. It does not reflect the nature of the spectral distribution.

The quantum yield of the phosphor depends only on the wavelength of the radiation measured. Within wide limits (approximately five orders of magnitude), the phosphor is not saturated. An especially valuable property is that, as the investigations demonstrated,  $\text{CaSO}_4 (\text{Mn})$  is not sensitive to radiation in the spectral region of wavelengths greater than 1300 Å.

The properties described make phosphor  $\text{CaSO}_4 (\text{Mn})$  very suitable for measuring ionizing radiation. /216

Measurements with phosphor  $\text{CaSO}_4 (\text{Mn})$  were often conducted in rockets in 1948-1950 in the United States. In these experiments phosphor specimens exposed during flight were de-excited on Earth in a laboratory unit. Such measurements produced large errors, since - when the exposed samples were salvaged - some of the energy they had stored had been lost because of heating when the rocket entered the dense layers of the atmosphere.

The instrument used in our experiments differs not only in exposure, but also in the fact that de-excitation of the phosphor specimens takes place in flight. This eliminated the need for salvaging the equipment and eliminated the error pointed out in the American experiments.

The "Phosphor" device measured electron streams in the upper atmosphere for the first time during a solar eclipse (February 15, 1961).

In October, 1962, and June, 1963, phosphor measurements were again carried out. Special tubular filters with their cylindrical openings at a  $45^\circ$  angle to the intake axis were installed in front of two plates, in order to separate the electron stream. This filter completely absorbed the shortwave radiation, but electrons could get through the openings to reach the phosphor. Measurements were made while the rocket was rising to an altitude of 500 km. During the entire flight (no measurements were made below 150 km), the electron

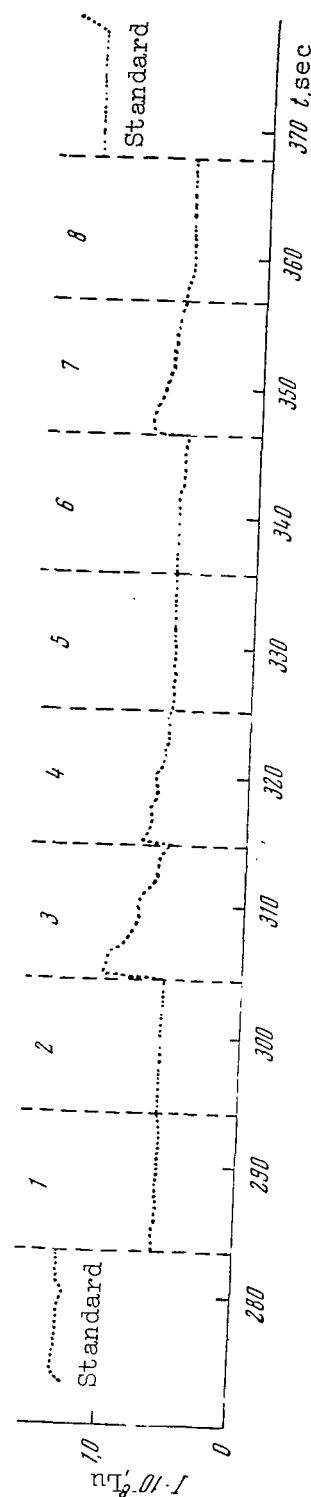


Figure 2

stream generated a reliable signal (filters 3 and 7 in Figure 2, which gives the results of primary processing). The measurement results demonstrated that the electron stream energy varied little with altitude and averaged  $0.3 \text{ erg} \cdot \text{cm}^{-2} \cdot \text{sec}^{-1}$ .

The above experiments have therefore demonstrated the efficiency of the new methods used to record low-energy electrons in the upper atmosphere and have permitted estimates of electron flux and energy spectrum at mean latitudes in the ionosphere.

#### VARIATIONS IN ATMOSPHERIC ION COMPOSITION AT ALTITUDES OF 100-200 KM (Summary)

G. S. Ivanov-Kholodnyy, A. D. Danilov

The mass-spectrometric investigations of the ion composition of the ionosphere which have been conducted up to the present in the 100-200 km region lead to a number of interesting conclusions about the variations of ion concentration associated with the time of day and solar activity. Figure 1 presents experimental data on the behavior of relative concentrations of  $[O^+]/n_e$  and  $[NO^+]/n_e$  in the course of 24 hours. The symbols corresponding to experiments made at a high level of solar activity ( $F_{10.7}^{\odot} \geq 150$ ) are enclosed in small circles. As the figures show, a difference is detected in the behavior of ion concentrations throughout one day at high and low solar activities. The noticeable similarity between the curves for altitudes  $h = 160, 180$  and  $200 \text{ km}$  increases the reliability of deductions about the behavior of the quantities  $[O^+]/n_e$  and  $[NO^+]/n_e$  with a change in zenith distance of the Sun  $z_{\odot}$  at different levels of solar activity. The principal experiments were carried out in the range  $55^{\circ} \leq z_{\odot} \leq 90^{\circ}$ ; therefore, it is this region which is theoretically analyzed in the present paper. For  $z_{\odot} < 50^{\circ}$  there is only one mass-spectrometric experiment ( $z_{\odot} = 27.5^{\circ}$ ) conducted during magnetic perturbation; therefore, the behavior of  $[O^+]/n_e$  and  $[NO^+]/n_e$  in this region is tentatively traced by the dotted lines.

The theory of the formation and disappearance of the principal ions /218 in the ionosphere leads to the conclusion that - with unchanged atmospheric composition and density in the 140-180 km region - the concentration ratio  $[NO^+]/[O_2^+]$  must not depend on altitude and  $z_{\odot}$ . A comparison of the values of  $[NO^+]/[O_2^+]$ , given for a number of experiments in Figure 2, demonstrates that on the average this ratio is actually observed to be constant within accuracy of 1.5. Curve 1 of Figure 2 refers to high solar activity; curve 2, to medium; curve 3, to low solar activity; and curve 4, to the period of magnetic perturbations. Small variations (within the limits of 1.5) nevertheless exceed the mass-spectrometric measurement errors and apparently indicate variations in the parameters of the neutral atmosphere (density, /219 composition, or temperature). A theoretical study of change in absolute and relative concentrations of charged particles in the ionosphere, as ionizing radiation intensity  $I$  or atmospheric density  $N$  changes, enables us to derive the results presented in the table.

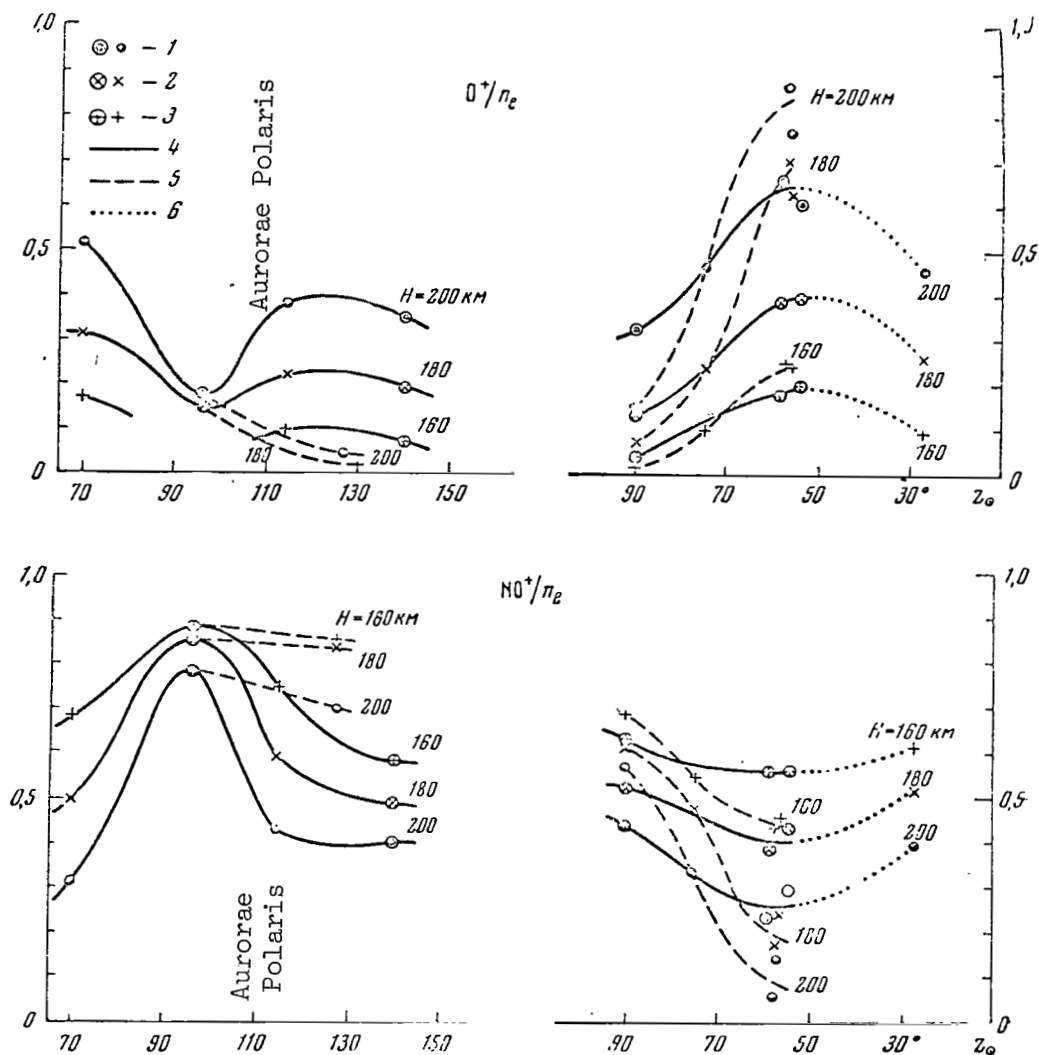


Figure 1

Diurnal Behavior of  $O^+/n_e$  And  $NO^+/n_e$   
 1 - 200 km; 2 - 180km; 3 - 160 km; 4 and 5  
 - High and Low Solar Activity; 6 - Tentative Behavior

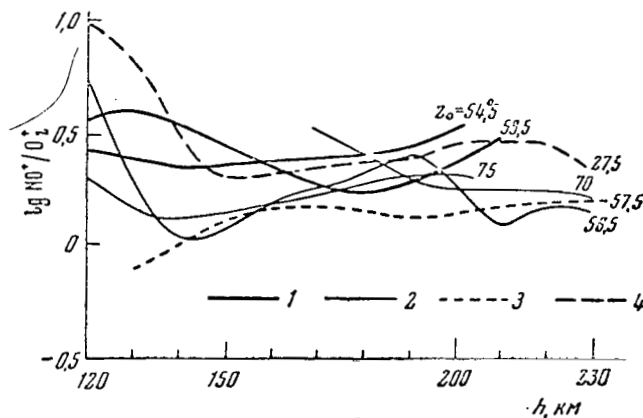


Figure 2

Change in  $\log NO^+/O_2$  With Height At Different  $z_0$



Region of Ionosphere	Concentration	Dependence on I	Dependence on N
At all altitudes	$O^+$	$\sim I$	No dependence
Upper part of Ionosphere	$O^+/n_e$	No dependence	No dependence
$[O^+] \gg [O_2^+] + [NO^+]$	$NO^+/n_e, O_2^+/n_e$	$\sim 1/I$	$\sim N$
	$NO^+, O_2^+$	No dependence	$\sim N$
	$n_e$	$\sim I$	No dependence
Lower part of Ionosphere	$O^+/n_e$	$\sim \sqrt{I}$	$\sim \sqrt{N}$
	$NO^+/n_e, O_2^+/n_e$	No dependence	No dependence
$[O^+] \ll [O_2^+] + [NO^+]$	$NO^+, O_2^+$	$\sim \sqrt{I}$	$\sim \sqrt{N}$
	$n_e$	$\sim \sqrt{I}$	$\sim \sqrt{N}$

The first half of the table corresponds to the upper ionosphere, ( $[O^+] \approx n_e$ ), where a linear law of recombination holds. The second half corresponds to the lower ionosphere, ( $[O^+] \ll n_e$ ), where the rate of electron disappearance is proportional to  $n_e^2$ . At intermediate altitudes, the dependence of electron and ion concentrations on I and N is more complex and is expressed by the formulas in this article.

Notwithstanding the fact that the electron concentration and the relative concentrations of  $O^+$  ions behave differently with  $z$  at different solar activities, the absolute concentrations of  $[O^+]$  display no appreciable dependence on the activity. This obviously indicates a simultaneous change in both I and N during the solar cycle.

Figure 3 compares the ionization rate  $q$  at the altitudes in question (as calculated by Watanabe and Hinteregger, and by Ivanov-Kholodnyy) with derivations of  $q$  based on experimental findings regarding the behavior of  $[O^+]$  with the zenith angle of the Sun. As follows from this figure, the findings of Watanabe and Hinteregger (curve 2) are closer to the experimental curve 3 than are Ivanov-Kholodnyy's data (curve 1).

Analysis of the experimental data on ion composition enables us to define the ratios more accurately which the authors previously obtained between the constants of the fundamental ion reactions in the ionosphere:

$$\gamma_{NO^+}/\alpha_{NO^+} \approx 4 \cdot 10^{-5}; \quad \gamma_{O_2^+}/\alpha_{O_2^+} \approx 2 \cdot 10^{-4}.$$

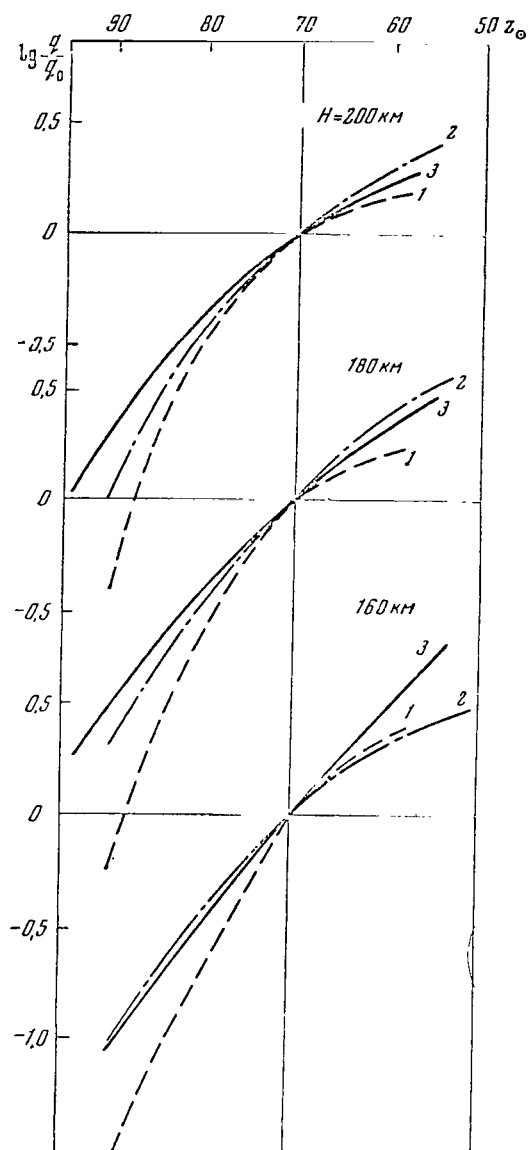


Figure 3

Relative Change in Ion-Formation Rate  $q$   
As Function of  $z_0$  at Different Altitudes

## CHARACTERISTICS OF SHORTWAVE COMMUNICATION WITH SPACECRAFTS

F. I. Berbasov, T. S. Kerblay  
Ye. M. Kovalevskaya, L. N. Lyakhova

The radio frequency which ensures good shortwave communications between two remote terrestrial points is determined on the assumption that the ionosphere is spherical and stratified and that its parameters are invariable within the limits of a single bounce. The F2 layer is taken as the principal reflecting layer in these calculations. In the vast majority of cases, these assumptions are justified. The present paper has computed a normal frequency range for shortwave radio space communications, in a manner similar to that employed for terrestrial communications. The only difference is the different arrangement of monitoring points because of the emitter's altitude of 180-250 km. The wave trajectory which occurs in normal propagation by reflections from the F2 layer is represented in Figure 1a. /220

We have considered the results derived from analyzing data on the reception on Earth of signals from transmitters broadcasting from Soviet spacecrafts at a frequency of about 20 Mc. The statistics cited in this paper refer to cases where the spacecrafts are beneath the peak of the F2 ionization region outside of the direct visibility zone.

In cases where the operating frequency has fallen within the calculated range of applicable frequencies, the probability of communication has significantly exceeded the mean value. Thus, the percentage of cases of communication with spaceship "Voskhod-1" (October, 1964) at a frequency of 20 Mc is 38% on the average, for the cases where the spacecraft was beneath the ionization peak of the F2 region. At the periods when the frequency fell into the predicted range, the percentage of communication rose to 87%. The flights of spacecrafts "Vostok-1" and "Vostok-6" took place during a decrease in solar activity in the summer months, when the maximum applicable frequencies (MAF) were in most cases below 20 Mc, so that the 20-Mc operating frequency was fundamentally higher than the upper limit of the range of applicable frequencies.

An analysis of factual findings on communications with the "Vostok" spacecrafts has showed that in most cases communication at the 20 Mc frequency was observed, in spite of its being higher than the MAF.

Table I gives the dates of the spacecraft flights, level of solar activity expressed in modified relative mean monthly figures on sunspots at these times, and average F2-4000-MAF values for diurnal and nocturnal conditions for mean and equatorial latitudes. /221

From Table I it is evident that from 1961 to 1963 the critical frequencies and MAF of the F2 layer decreased on the average, due to the decreased level of solar activity.

TABLE 1

Spacecraft	Date of Flight	Solar Activity Level	F2-4000 MAF				Percentage of Normal Propagation
			Day		Night		
			Middle Latitudes	Equatorial Latitudes	Middle Latitudes	Equatorial Latitudes	
"Vostok-1"	4/12/1961	64	22.7	24.7	11.9	25.8	70
"Vostok-2"	8/6/1961	51	18.6	18.6	12.0	20.8	36
"Vostok-3"	8/11/1962	35	18.3	17.6	11.6	19.2	25
"Vostok-4"	8/12/1962						
"Vostok-5"	4/14/1963	30	17.4	17.6	15.0	15.4	12
"Vostok-6"	6/16/1963						

Certain deviations from the monotonic frequency drop are attributed to seasonal changes in the ionosphere, since the flights took place in different months. Despite isolated deviations, Table 1 makes it clear that the ionosphere's capacity to reflect 20-Mc signals steadily decreased from 1961 to 1963.

The last column in Table 1 gives the fraction of time (relative to the entire flight time<sup>1</sup>) during which it was estimated that 20-Mc signals propagated by normal jump reflection might be expected to be received in the territory of the USSR. The operating frequency was compared only with the MAF when evaluating the propagation possibility. The magnitude of the field strength which could be expected was not considered, because incoming signal field strength would be very small in long-distance reception, particularly at times when the path was illuminated. The percentage of expected reception time given in Table 1 is slightly overestimated.

A comparison of the time, when normal propagation is possible, with the mean time of actual reception at 20 Mc, demonstrated that the actual

<sup>1</sup> Here and elsewhere in the following when figuring the time fraction during which communication occurred, the value of 100% is assumed to be the entire flight time, except for the periods that the spacecraft is within the line of sight, i.e., the time of actual communication is assigned to the whole time that communication would have to occur by ionospheric reflection.

probability of communication exceeded the normal propagation probability computed from ionospheric data. The communication probability actually derived does not diminish with the decrease in activity, but remains on approximately the same level, about 50%. The existence of communication at frequencies above the MAF cannot be due to an inaccuracy in the method of computing the MAF, since the frequency excess over the MAF reached very high values (to 8-10 Mc) in a number of cases. This made us both pay special attention to other paths of propagation which would make it possible to reflect higher frequencies, and assume that they play an important role in radio communications between spacecrafts and the Earth.

Communication at frequencies above the MAF is also sometimes detected in other terrestrial radio lines (Ref. 1); if the emitter is at a substantial altitude above the Earth's surface, the probability of communication at frequencies above the MAF rises. Figure 1 depicts possible paths of signal propagation between Earth and the spacecraft. Figure 1b-1e represent possible non-normal paths of signal propagation: reflection from  $E_s$  by jumps closest to the point of reception, and propagation along a rebound path (Ref. 2, 3) with subsequent escape by gradients (Ref. 4) or escape by dispersion (Ref. 5).

In order to determine what paths of propagation most frequently occur under actual conditions, the discrepancies in the calculated MAF and the actual radio communication frequencies ( $\Delta f$ ) were subjected to an analysis, which showed that their value essentially depends on the time of day. When the receiving station is in the illuminated hemisphere - i.e., the MAF at the monitoring station closest to the receiving point is  $\geq 20$  Mc, while the MAF in the vicinity of the spacecraft is small - the probability of communication is substantially greater than when the receiving station is not illuminated. This is particularly noticeable at great distances. Figure 2 gives the probability of different values of  $\Delta f$  during illuminated and dark periods, for distances of 6000-12,000 km. As is evident from Figure 2, the probability of large deviations of  $\Delta f$  is considerable when the point of /222 reception is illuminated.

Since the differing illumination along the path corresponds to significant horizontal gradients of electron concentration (the so-called ionosphere gradients), we may assume that when signals are propagated at frequencies above the normal MAF these gradients play an essential role.

When shortwaves are transmitted from spacecrafts beneath the peak of the F2 layer, the angles of radiowave incidence onto the reflecting layer are substantially greater than the angles of incidence attained in terrestrial communications.

Radiowaves falling onto the reflecting layer at angles  $\varphi$ , which are greater than the maximum angle of incidence  $\varphi_{\max}$  found in transmitting from the Earth, will be propagated by being reflected only from the ionosphere in a so-called rebound trajectory. As the incident angle grows larger, so also does the scaling factor of the critical frequency in the

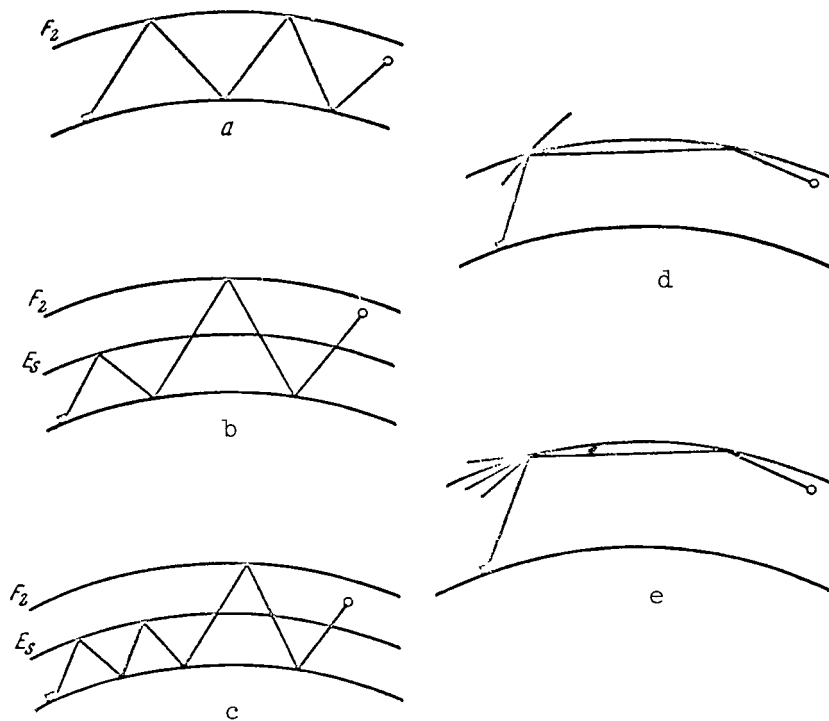


Figure 1

MAF for sloping incidence.

Propagation along rebound trajectories guarantees that the signals will travel great distances at frequencies considerably above the normal MAF. However, in order that the energy thus transmitted reaches the Earth and that reception is possible on Earth, supplementary mechanisms are needed to ensure that the waves return to Earth. These mechanisms may, first, be any type of scattering and, second, distortion of the signal path directing the energy to the Earth. The fundamental difference between these methods is that any scattering involves great energy losses compared to normal propagation, while distortion of the signal path due to a horizontal nonuniformity in the ionosphere should not result in additional signal attenuation. Even a certain signal amplification may, on the contrary, be expected since - in propagation over a rebound trajectory - each time the radio wave is reflected by the ionosphere it undergoes the focussing effect of a concave sphere and is not defocussed by the Earth's surface. Rebound trajectories have great advantages over propagation by successive reflections from the Earth and the ionosphere in cases where the trajectory passes above the Earth at a minimum altitude  $h_{\min} > 100$  km. In this case, the radiowaves bypass the principal absorbing region (the D layer and the lower portion of the E layer); therefore, it may be expected that when these waves are transmitted over long distances the field strength

/223

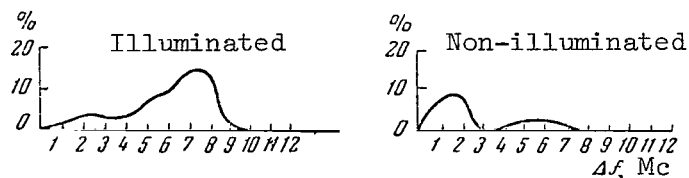


Figure 2

will be higher. Results of analyzing measurements of the field strengths of radio signals from the first and second satellites showed (Ref. 3) that, at distances greater than 6000-8000 km, the field strength exceeded that calculated for ideal transmission.

In order to corroborate the explanation of communication with a spacecraft at frequencies above the normal MAF by anomalous propagation, we examined a number of specific periods of communication with "Vostok" spacecrafts at frequencies above normal MAF. The path of the beam was computed which falls from the spacecraft onto the ionosphere at the maximum possible angle  $\varphi_{\max}^0$ , taking into consideration the ionospheric gradients at the points where the beam is reflected. The following values were calculated: distance of each bounce  $\theta_p = 2(90 - \varphi)$ ; angle of inclination\* at reflection points  $\alpha$ ; minimum altitude  $h_{\min}$  for each bounce at which the beam approaches the Earth; and MAF at each point of reflection with due allowance for the ionospheric gradient. In the cases when, at the reflection point closest to the receiving station, there was an ionospheric gradient which was adequate to give the beam a direction favorable for transmission to Earth, we could explain communication at a frequency greater than MAF. Figure 3 illustrates diagrammatically the beam path for one of the moments of communication with the "Vostok-5" spacecraft at  $f = 20$  Mc with a normal MAF of 14.5 Mc.

Besides the signal propagation path in question, an essential role in communication with spacecrafts is played by trajectories which include reflection from the  $E_s$  layer (Figure 1b, 1c). Of the possible paths of non-normal propagation shown in Figure 1, this article will consider the possibility of forecasting only two - reflection from  $E_s$  and a rebound trajectory from a gradient.

For the flight of the "Vostok-5" spacecraft\*\*, a survey of the periods

\* The slope angle was determined by methods presented in (Ref. 6) from altitude charts of equal electron concentrations, compiled by T. A. Anufriyeva under the direction of B. S. Shapiro.

\*\* In this flight the possibility of communicating by normal reflection from the F2 layer was very slight - on the order of several percents.

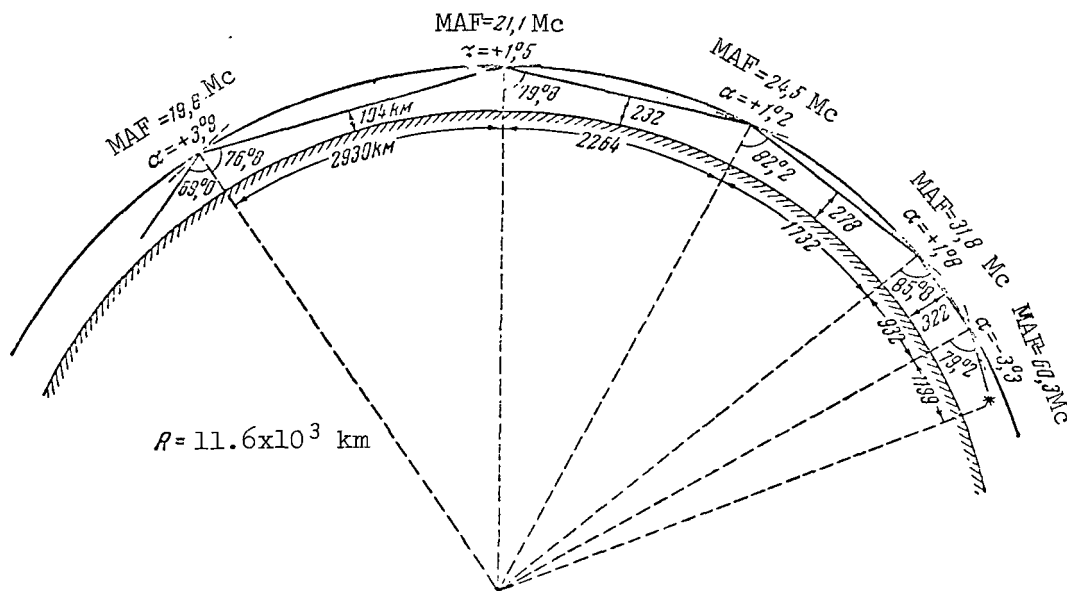


Figure 3

(in the first 17 revolutions) when communication could be effectuated was compiled: (1) by reflection from  $E_s$  in the first one or two bounces, with further reflection from the F2 layer, and (2) by the surface gradients of equal electron concentrations. The survey of communication by  $E_s$  was compiled by choosing the periods when F2-4000-MAF, in the vicinity of the spacecraft and at a distance of 4000 km (or 6000 km in the two-bounce reflection from  $E_s$ ) from the receiving station, was more than 20 Mc. It fell below 20 Mc only at a distance of 2000 km (or 4000 km). /224

Average charts of the probability that a frequency of 20 Mc would be reflected were compiled for summertime to determine the possibility of reflection from  $E_s$ . Since the  $E_s$  layer is very irregularly distributed both in time and space, it was impossible by means of hourly observations performed by a limited number of ionospheric stations to produce a picture of  $E_s$  distribution at the moment the spacecraft passed over. Therefore, average charts were utilized. It was assumed that, to propagate via  $E_s$  in one bounce, the reflection probability at the point of reflection from the  $E_s$  layer (1000 km from the receiving station) would have to be more than 50%. For reflection in two bounces, the probability at each of the two points of reflection would have to be more than 70%. During the computations it was noted that during daylight hours the probability of reflection from  $E_s$  in the vicinity of the receiving station often reaches 90%. Therefore, for each revolution a time was determined (in minutes) when communication by  $E_s$  was probable; then from actual findings on signal reception from the "Signal" transmitter, it was determined during how many



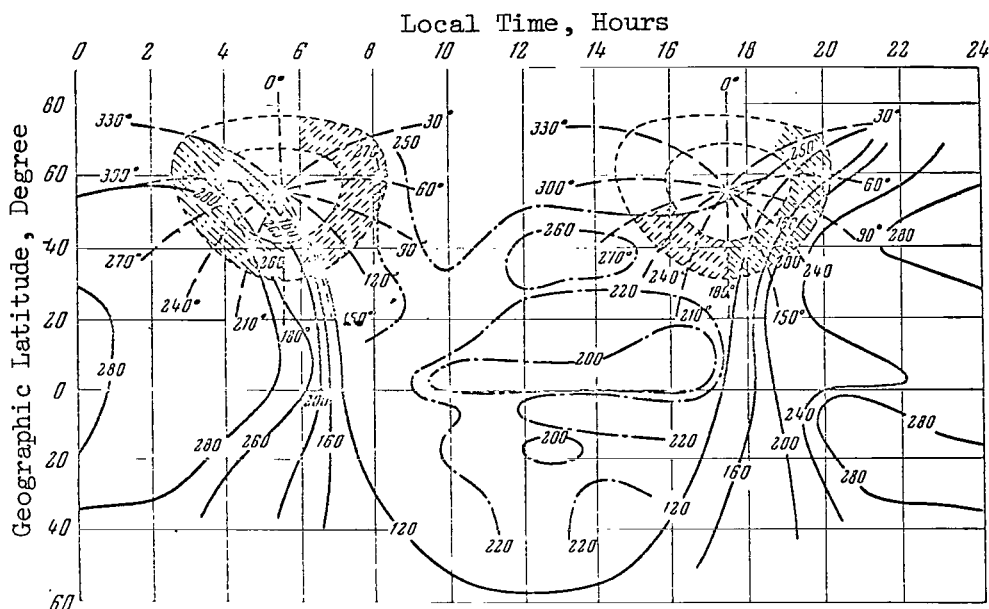


Figure 4

minutes of this period communication actually was established. In the period under investigation, communication via  $E_s$  was expected for 4 hours in all. In actual fact, communication was effectuated for somewhat more than 3 hours in these periods. Thus, the average percentage of cases in which the prediction of communication via  $E_s$  was fulfilled was 77% - i.e., it was rather high.

Propagation by gradients was surveyed as follows.

To determine the most favorable moments for the ionospheric gradients to assist in communications between a space object and Earth, we used altitude charts of equal electron concentrations. It was assumed that the various electron concentration levels had the same gradient. The chart in Figure 4 gives reflection altitudes in solid isolines for 3 Mc and broken-dotted ones for 5 Mc. By means of such charts it can be seen that, for 225 example, for a receiving station at  $\varphi = 55^\circ$  at about 6 hours, local time, the regions of favorable gradients are within the azimuths  $A = 180 - 330^\circ$ . On the other hand, between the azimuths  $A = 15 - 150^\circ$  the gradients have the opposite sign.

At 18 hours, local time, however, the most favorable conditions are created for reception on Earth of waves traveling over rebound trajectories from the northeast and east. Depending on what gradient in the neighborhood of the receiving station is sufficient to return a beam traveling a

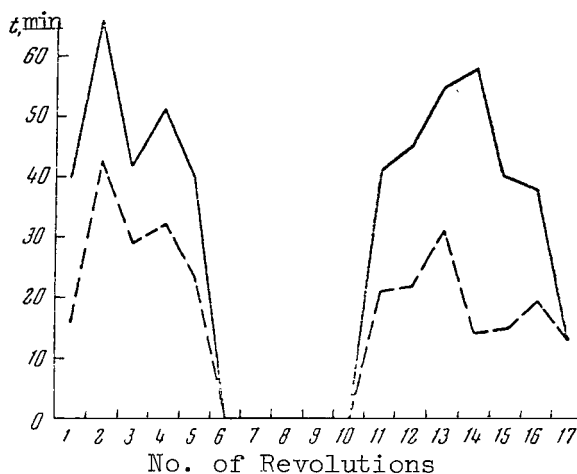


Figure 5

rebound trajectory to Earth, we derive several different time intervals during which the gradients can ensure communications. It is, moreover, necessary to take the fact into consideration that, when there is a gradual gradient in the reflecting surface along the route, the beam will gradually approach Earth after each reflection. It would, therefore, be necessary to allow for the gradient not only near the reception point, but also along the entire route. In this connection, a forecast of the periods of probable communication by means of gradients was compiled for various angles  $\alpha$  near the receiving station (from  $\alpha \geq 1^\circ$  to  $\alpha \geq 4^\circ$ ), as well as for the total angle along the entire route  $\alpha \geq 4^\circ$  (the bounces are tentatively assumed to be 2000 km). The effect of the gradients on space communication conditions is indicated by the increase in communication probability as the gradient angle near the reception point grows larger. The communication conditions as a function of the angle of the gradient are:

Angle of gradient $\alpha$ , degrees . . . . .	$\geq 1$	$\geq 2$	$\geq 3$	$\geq 4$
Performance of Communication, % of time	47	53	68	89

Figure 5 gives the total time of expected communication by  $E_s$  and by gradients (solid line) for each spacecraft orbit. The broken line shows the duration of communications during the predicted period. In the computations whose results are presented in Figure 5, it was assumed that the requisite gradient was  $\alpha \geq 3^\circ$ . It can be seen from the figure that there is satisfactory agreement between the predicted periods of propagation by  $E_s$  and by gradients, and between the actual transmission in these periods. The frequencies which can be transmitted by the above methods can exceed the normal MAF by an average of 10-20% (in isolated cases, by far more - up to 50%). Hence, by taking into consideration the reflections from  $E_s$  in the region nearest the reception point and the possible propagation over a rebound trajectory with transmission to the Earth by gradients, we may considerably raise the upper limit of the band of shortwave radio communication with spacecrafts which are below the peak of the F2 layer.

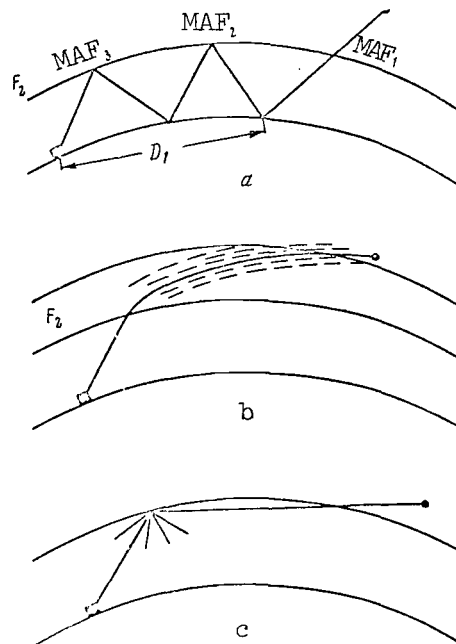


Figure 6

As has already been pointed out, the experimental data examined in the present report pertain to communications with spacecrafts below the maximum of the F2 layer. No less complex signal trajectories may occur in communications with spacecrafts whose orbits lie above the maximum of the F2 layer (Ref. 7-10). Figure 6 gives examples of various trajectories of this kind. In this case the normal distribution may be regarded as trajectories at the operative frequency exceeding the F2-MAF near the spacecraft, but reflected from the ionosphere at the following points -  $MAF_2$  and  $MAF_3 > f_{op}$  (Fig. 6a). It is obvious that, just as in the case of orbits beneath the maximum of the F2 layer, this propagation path is not unique. In addition to trajectories which take  $E_s$  and other regular layers into consideration, an essential role may be played in propagation between the Earth and the ionosphere by propagation along nonuniformities extending over the field (Figure 6b), by the occurrence of rebound trajectories (Figure 6c), and also by scattering by the Earth or the ionosphere. If we examine in detail all possible paths of propagation when the spacecraft is above the maximum of the F2 layer, we may obviously select frequencies which enable us also to obtain a satisfactory percentage of communication time for these cases.

This study of the features of shortwave communication with spacecrafts shows that, when a spacecraft is beneath the maximum of the F2 layer, higher-frequency waves may be propagated in addition to radio waves reflected from the F2 layer in the ordinary way by other propagation routes. An essential role in the propagation of frequencies above the normal MAF is played by sporadic ionization in the E layer, as well as by horizontal ionization gradients (resulting in effective gradients

of surfaces of equal electron concentration in the ionosphere). The first experiments in forecasting these effects may be regarded as satisfactory, especially if we consider that our knowledge of ionization distribution in the ionosphere, and of the day-to-day and hour-by-hour changes in this distribution, is still by no means satisfactory. Thus, these experimental data on shortwave radio communication in space point out the need to make allowances for every sort of anomalous phenomenon in the ionosphere when we compute radio communication frequencies, and the need for further study of the peculiarities of ionization distribution in the upper ionosphere, its gradients, various types of sporadic layers and nonuniformities, and their influence on shortwave radio communication.

#### REFERENCES

1. Novysh-Bylinskaya, V. N. Trudy Instituta Zemnogo Magnetizma i Radiovolnovogo Rasprostraneniya AN SSSR (IZMIRAN) No. 19/29, 71, 1961.
2. Krasnushkin, P. Ye. The Normal Wave Method in its Application to the Problem of Long-Distance Radio Communications (Method normal'nykh voln v primeneni k probleme dal'nikh radiosvyazey). Moscow, Izdatel'stvo Moskovskiy Gosudarstvennyy Universitet, 1947.
3. Kazantsev, A. N., Romanova, T. S., and Klementenko, A. Ya. Radiotekhnika i Elektronika 3, No. 9, 1107, 1958.
4. Manczarski, S. Acta Geophys. Polon., 9, No. 1/2, 82, 1961.
5. Kovalevskaya, Ye. M. Trudy IZMIRAN, No. 19/29, 85, 1961.
6. Kerblay, T. S., and Voloshinova, Z. V. Geomagnetizm i Aeronomiya, No. 1, 61, 1964.
7. Galejs, J. IRE Trans. Space Electron and Telemetry, 5, No. 4, 179, 1959.
8. Muldrew, D. B. J. Geophys. Res., 68, No. 19, 1963.
9. Chvojtkova, E. J. Atmos. and Terr. Phys., 16, 24, 1959.
10. Mija, K., Taguchi, J., Tabuchi, S. Rept. Ion. Res. Japan, 12, No. 1, 1958.

## RADIOWAVE PROPAGATION IN INTERPLANETARY AND CIRCUMSOLAR SPACE

M. A. Kolosov, O. I. Yakovlev, A. I. Yefimov

Data are presented on radiowave propagation at a 183.6 Mc frequency, emitted by "Mars-1" and received at distances of up to 50 million km on the surface of the Earth. Radiowave propagation at a distance on the order of 300 million km is also analyzed, on the basis of the data obtained by tracking radio emission of the Taurus-A source.

The assumption is advanced that when monochromatic radiowaves are propagated at such large distances their spectrum can change.

### 1. Maximum Possible Values of Monochromatic Radiowave Attenuation in Interplanetary Space

Regular measurements of the signal level from "Mars-1" were used to study the dependence of the energy stream of radiowaves received upon distance.

The study (Ref. 1) gives the corresponding dependence, where it is attributed to values obtained from the law of free radiowave propagation. The data obtained in (Ref. 1) make it possible to estimate the maximum possible attenuation of monochromatic radiowaves of 183.6 Mc frequency during propagation in interplanetary space. This value is  $4 \pm 2$  db at 50 million km. /228

The study (Ref. 2) presents data on the received signal level from "Pioneer-5", where it is pointed out that there was no significant deviation from the law of free radiowave propagation during observations of signals with a frequency of 378 Mc at distances up to 43 million km. It should be noted that experimental data given in (Ref. 2) have a large scatter. Therefore, they do not indicate the absence of radiowave attenuation, and only make it possible to determine the greatest possible attenuation which may be concealed in the experimental data scatter. Processing of these experimental data shows that attenuation of radiowaves with a frequency of 378 Mc is no greater than 2-3 db at 43 million km.

Results are presented in (Ref. 3) which were derived from repeatedly determining the effective scattering diameter of radiowaves having a frequency of 700 Mc for Venus, and the measured values of the effective scattering diameter ranged between 12-18%. When these measurements were performed, the distance changed from 40 to 65 million km. Thus, during radio location of Venus the total change in the radiowave propagation path comprised 50 million km. The maximum attenuation, which could be concealed in the effective diameter measurement errors, could not exceed 1.6 db at 50 million km in these experiments.

## 2. Attenuation of Radiowaves With a White Spectrum in Circumsolar Space

One effective method of studying circumsolar space is its transillumination by radio emission from the source Taurus-A. Since Taurus is practically located in the ecliptic plane, transillumination of circumsolar space at different angles  $\Psi$  occurs during the annual movement of the Earth around the Sun (Figure 1).

If the Taurus-A source is radiated on an interferometer, there is a decrease in the signal strength at the interferometer output for small angles  $\Psi$ . This phenomenon has been interpreted as the result of radio-wave scattering by nonuniformities in the electron concentration of circumsolar space, which leads to an increase in the source angular dimensions. Circumsolar space has been studied by means of interferometers since 1951, and the results of these experiments are given in (Ref. 4-6). Interferometer observations have shown that in the  $\lambda = 8$  m range the increase in the source angular dimensions amounts to  $\zeta = 8'$  for  $\psi = 5^\circ$ . This quantity depends on solar activity, and its maximum can reach  $\zeta = 18'$  (Ref. 6). Studies performed at different wave lengths of a meter range show that the quantity  $\zeta$  is proportional to the square of the wavelength. These studies have also made it possible to estimate the scale of the nonuniformities and to refine our concepts of the solar supercorona (Ref. 7).

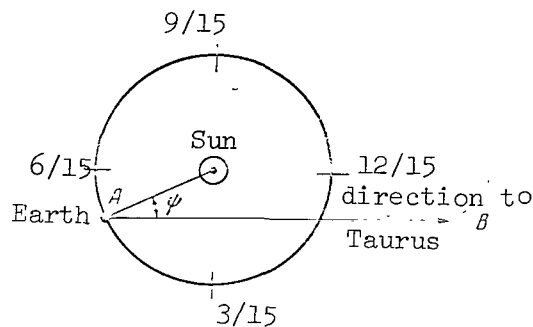


Figure 1

### Diagram of Experiment on Transillumination of the Interplanetary Medium by Radio Emission from the Taurus-A Source

Nonuniformities in the interplanetary medium can also influence radiowave propagation (Ref. 8). It is of interest to study the conditions under which radiowaves are propagated in interplanetary and circumsolar space, by observing radio emission from the Taurus-A source. In order that the changes in the source angular dimensions do not influence the measurement results, it is necessary that the width of the antenna directional diagram  $\varphi$  is much greater than the quantity  $\zeta$ . At the same time, the antenna must have a sufficiently narrow directional diagram, in order to exclude the influence of solar radio emission for small angles  $\Psi$ .

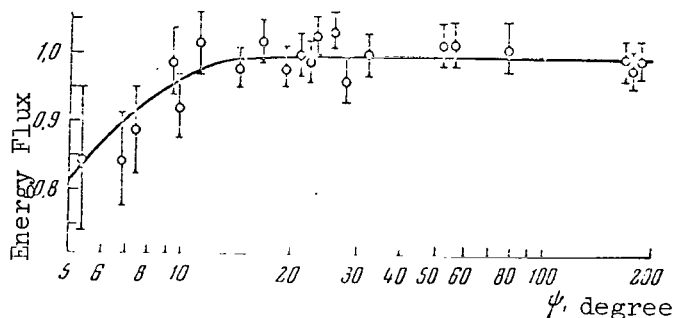


Figure 2

### Energy Flux of Radiowaves Emitted by the Taurus-A Source for Different $\Psi$ Angles

We performed measurements of the radio emission from the Taurus-A source at a frequency of 184 Mc from March to December, 1964. The width of the antenna directional diagram was such that measurements were possible for  $\Psi \geq 5^\circ$ , and the condition  $\varphi \gg \zeta$  was fulfilled very well. In order to increase the measurement accuracy, we determined the ratio of the antenna temperature, caused by emission from the Taurus-A source ( $T_T$ ), to the antenna temperature characterizing emission from Cassiopeia ( $T_C$ ). The time of day when the measurements were performed was selected so that the angles of elevation of the Taurus-A source and of Cassiopeia were more than  $35^\circ$ , and differed very little from each other. One measurement cycle, corresponding to a fixed angle  $\Psi$ , included no less than 6 measurements of  $\eta = T_T/T_C$ . At the angle  $\Psi < 13^\circ$ , there was an additional antenna temperature increase, which was caused by radio emission from the Sun. In this connection, the influence of solar emission on the results derived from measuring  $\eta$  was carefully studied. The method employed made it possible to exclude variability in antenna amplification, as well as the influence of absorption in the Earth's atmosphere; it also made it possible to decrease considerably the influence of solar radio emission on the results derived from determining radiowave attenuation in cosmic space. The maximum error entailed in determining  $\eta$  during one measurement period was no more than  $\pm 4\%$  in the case of  $\Psi > 14^\circ$ ; the errors comprised  $\pm 6\%$  for  $6^\circ < \Psi < 14^\circ$ .

Figure 2 presents the measurement results. The relative values for the energy flux of radiowaves radiated by the Taurus-A source are plotted along the vertical line; the values of the angle  $\Psi$  are plotted along the horizontal line. It follows from Figure 2 that there is no attenuation of the radiowave energy flux within the limits of error when the angle  $\Psi$  changes from  $180^\circ$  to  $10^\circ$ . In the case of  $\Psi = 10^\circ$ , radiowaves emitted by the Taurus-A source traverse a path on the order of 300 million km in the interplanetary medium lying within the Earth's orbit. The smallest distance from the radiowave trajectory to the Sun is thus about 25 million km. When the angle  $\Psi$  decreases to  $5^\circ$ , there is a small 16% decrease in the radiowave energy flux (maximum error  $\pm 8\%$ ).

Let us compare the existing experimental data with the results derived from our measurements. The energy flux attenuation is determined by the expression

$$S = S_0 \exp \left[ - \int_0^L \gamma dl \right]; \quad (1)$$

The quantity  $\gamma$  depends on distance  $R$  between the Sun and a line element  $dl$ . Let us assume that this dependence can be approximated by the law  $\gamma = \alpha R^{-n}$ , where  $\alpha$  depends on the wavelength, and it is determined by the mechanism of radiowave attenuation. If we set  $n = 2$ , then our experimental data can be closely approximated by a function of the following type /230

$$\eta(\psi) = \exp \left[ \frac{\alpha}{a} \left( \frac{\pi}{2} - \frac{\pi - \psi}{\sin \psi} \right) \right], \quad (2)$$

which is obtained by integrating (1) for  $n = 2$ . Here  $a$  is the astronomical unit. Formula (2) can be used to compare the measurement results derived by different authors for different angles  $\psi$ . It follows from the data obtained that  $\alpha = 0.7$  million km for  $\lambda = 1.6$  m. Let us determine the parameter  $\alpha$  according to data in the literature (Ref. 9-13). The table below presents the results derived from observing the energy flux attenuation of radiowaves as well as the values for the parameter  $\alpha$  calculated according to these results.

Wavelength, m	Attenuation, %	Angle $\psi$	$\alpha$ , million km	Source
11	29	$5^\circ$	0.75	(Ref. 12)
3.5	reaches 30	2.3	reaches 0.7	(Ref. 10)
1.6	$16 \pm 18$	5	0.7	This article
0.25	19	1.5	0.25	(Ref. 11)
0.21	none	1.5	--	(Ref. 9)
0.18	"	1.5	--	(Ref. 13)
0.10	"	1.5	--	(Ref. 11)

It is difficult to determine radiowave attenuation for  $\psi = 2-5^\circ$ , due to the influence of solar radiation. We must also keep the fact in mind that the measurement results presented in the table were obtained in different years during different solar activity. It follows from the table that the radiowave attenuation in the meter range does not exceed 30% in the case of  $\psi = 5^\circ$ ; there is no measureable attenuation of the radiowave energy flux in the decimeter range (in the case of  $\psi = 1.5^\circ$  the attenuation



is less than 5%). The frequency dependence of the parameter  $\alpha$  can provide information on the mechanism of radiowave attenuation in circumsolar space, but at the present time there are insufficient data with which to determine the frequency dependence  $\alpha(f)$ .

### 3. Influence of the Interplanetary Medium on Radiowave Propagation

A solar activity change must lead to an intense change in the properties of the interplanetary medium.

Observations on radio emission from the Taurus-A source (Ref. 14-16) have shown that there are irregular changes in the signal intensity. Both a sudden decrease, and a long, stable increase in the received signal level have been observed. Naturally, these facts can be explained by radiowave refraction - by the influence of electron concentration nonuniformities. However, the possibility is not excluded of attenuation or intensification of the received radiowave intensities, which are related to the influence of the irregular motion of plasma bunches. This can lead to multiple-wave propagation of radiowaves, and consequently to interference fadings during radiowave propagation in the interplanetary medium. The study (Ref. 17) indicated that these fadings were apparently observed when signals were received from "Pioneer-5".

An analysis of signals having the frequency 183.6 Mc from "Mars-1" /231 showed that there were no regular fadings, which can be readily explained by the satellite rotation. Fadings are irregular in nature, which makes it difficult to explain them entirely by the influence of ionosphere nonuniformities or by random rotations of the polarization plane due to the Faraday effect. The study (Ref. 18) presented data on signal reception at a frequency of 183.6 Mc from a distance on the order of 0.2 million km. Regular fadings were observed, which can be readily explained by the satellite rotation.

Thus, it must be assumed that the occurrence of additional fadings caused by the interplanetary medium is possible during the propagation of monochromatic radiowaves of a meter range at a distance on the order of tens of millions km.

Data are presented in (Ref. 1) which indicate a correlation between the level of the signal received from "Mars-1" and solar activity.

It should be noted that there are experimental data at the present time (Ref. 19) indicating that the distance to Venus, measured by the radio location method, is correlated with solar activity.

The signal spectrum must widen when radiowaves are propagated in a moving heterogeneous medium. During the location of Venus (Ref. 20) at

a 440 Mc frequency, it was found that the reflected signal spectrum changed with time irregularly. This change amounted to 0.5 cps, i.e., the relative spectral line width was apparently caused by the interplanetary medium and was on the order of  $\Delta f/f = 10^{-9}$  at this frequency.

#### 4. Possible Mechanism of Monochromatic Radiowave Attenuation

It can now be stipulated that the interplanetary plasma moves at a velocity of about  $500 \text{ km} \cdot \text{sec}^{-1}$  at a distance of  $\sim 150$  million km from the Sun. The electron concentration at these distances is on the order of  $10 \text{ cm}^{-3}$ . These quantities have values of  $30 \text{ km} \cdot \text{sec}^{-1}$  and  $10^3 \text{ cm}^{-3}$ , respectively, in circumsolar space at a distance of 20 million km from the Sun (Ref. 21-24). Interferometer measurements have shown that the circumsolar plasma is nonuniform, and that the nonuniformities have a wide spectrum from several tens up to several thousands of kilometers. Thus, the interplanetary and circumsolar media represent a nonuniform rapidly-moving plasma.

The spectrum of monochromatic radiowaves passing through a moving nonuniform plasma will change. This change can be caused by the following related mechanisms: Scattering by moving nonuniformities with a Doppler shift of the scattered radiowaves, scattering by plasma waves, and also random phase modulation of radiowaves passing through a nonuniform medium. These mechanisms are apparently related, and exist simultaneously. One possible mechanism for the spectrum change, caused by random modulation of the monochromatic radiowave phase will be investigated here.

During the propagation of radiowaves in a statistically nonuniform medium, the mean square of the phase fluctuation  $\overline{\Delta S^2}$  is determined (Ref. 25) by the following type of expression

$$\overline{\Delta S^2} = \frac{\sqrt{\pi}}{2} \overline{\Delta n^2} K^2 L b. \quad (3)$$

Here  $\Delta n^2$  is the mean square of the refractive index fluctuation;  $K=2\pi/\lambda$  - the wave number;  $L$  - the path length;  $b$  - the nonuniformity scale. It is assumed that the correlation function of the refractive index fluctuation is isotropic  $N(\rho) = \exp(-\rho/b)^2$ . If it is also assumed that the nonuniformities are "frozen", and their motion is caused only by solar /232 wind, then the temporal correlation function of the radiowave phase fluctuation is, according to (Ref. 25),

$$\Phi(\tau) = \exp[-(V/b)^2 \tau^2], \quad (4)$$

where  $V$  is the transverse velocity component of the solar wind. The mean quadratic value of the phase fluctuation and its temporal correlation function determines the energy spectrum  $F(\omega - \omega_0)$  of a radiowave passing

through a moving, nonuniform plasma (Ref. 26). The following expression for the energy spectrum of the phase fluctuation follows from (4):

$$G(\omega) = 2 \frac{b \sqrt{\pi}}{V} e^{-\frac{\omega^2 b^2}{4V^2}} \quad (5)$$

Let us replace the phase fluctuation spectrum obtained (5) by a uniform spectrum equivalent to the given spectrum in mean strength. The equivalent band of such a spectrum is

$$\Delta f_{\text{equi}} = \frac{V}{2 \sqrt{\pi} b}. \quad (6)$$

The energy spectrum width of radiowaves randomly modulated by phase is given by the expression (Ref. 26):

$$\Delta F = \sqrt{\frac{2\pi}{3}} V \sqrt{\overline{\Delta S^2}} \Delta f_{\text{equi}} \quad (7)$$

We should note that (7) is valid for  $\sqrt{\overline{\Delta S^2}} \gg 1$ . Utilizing the expressions for the mean square of the phase fluctuation in a nonuniform medium (3), (6), and (7), we can obtain an approximate formula for calculating the spectrum width of radiowaves passing through a moving, nonuniform plasma:

$$\Delta F \approx 97.5 \frac{V}{c} \frac{\Delta N}{f} \sqrt{\frac{L}{b}} \quad (8)$$

Here  $\Delta N$  is the electron concentration fluctuation in  $\text{m}^{-3}$ ;  $f$  - radiowave frequency in cps and  $\Delta F$  in cps. Let us estimate the possible width of the spectrum  $\Delta F$ . If we set  $f = 180 \text{ Mc}$ ,  $L = 50 \text{ million km}$ ,  $V = 500 \text{ km} \cdot \text{sec}^{-1}$ ,  $\Delta N = 10 \text{ cm}^{-3}$ , then in the case of  $b = 1000 \text{ km}$   $\Delta F \approx 2 \text{ cps}$ , and in the case of  $b = 10 \text{ km}$   $\Delta F \approx 20 \text{ cps}$ .

When the width of the receiver band  $\Delta f_{\text{re}}$  is significantly narrower than the frequency diffusion  $\Delta F$ , apparent attenuation of monochromatic radiowaves will be observed, although the total energy flux of the radiowaves will not decrease. In the case of  $\Delta f_{\text{re}} < \Delta F$ , the apparent radiowave attenuation  $\kappa$ , caused by expansion of the signal spectrum, will be

$$\kappa_{\text{db}} = 10 \lg \left( \frac{\Delta F}{\Delta f_{\text{re}}} \right) \quad (9)$$

Thus, for tenable values of the interplanetary medium parameters, attenuation of monochromatic radiowaves of a meter range is possible, caused by a change in the signal spectrum. We must keep the fact in mind that the existence of plasma waves is possible in the interplanetary and circumsolar plasma. The scattering of radiowaves by plasma

waves must also lead to a significant change in the radiowave spectrum (Ref. 27), particularly to side components in the spectrum which are removed from the carrier by the plasma frequency magnitude. In the general case, both diffusion of the main frequency, and the appearance of side components must be observed in the energy spectrum of the radiowaves. During the propagation of monochromatic radiowaves in circum-solar space, we must expect greater attenuation of meter radiowaves at the frequency  $f$ , since the electron concentration fluctuation can amount to  $10^3 \text{ cm}^{-3}$ . Radiolocation of Venus was recently carried out in the  $\lambda = 6 \text{ m}$  (Ref. 28) and  $\lambda = 7.8 \text{ m}$  (Ref. 29) ranges. During radiolocation of Venus in the meter wave range, approximately the same values were obtained for the effective scattering diameter as in the decimeter range (Ref. 30). This indicates that there is no attenuation of the radiowave energy flux. Since integration over the frequency spectrum was performed during location of Venus in the meter range, these experiments cannot indicate either the presence or the absence of attenuation of radiowaves received by a narrow-band receiver at the frequency  $f$ . /233

#### REFERENCES

1. Kolosov, M. A. et al. Radiotekhnika i Elektronika, 9, No. 10, 1735, 1964.
2. Hansen, R. S. J. Brit. Inst. Radio Engng., 22, No. 4, 329, 1961.
3. Kotel'nikov, V. A. et al. Doklady AN SSSR, 151, No. 3, 532, 1963.
4. Vitkevich, V. V. Radioastronomy. Paris Symposium (Radioastronomiya. Parizhskiy simpozium). Moscow, p. 270, 1961.
5. Khyuish, A. Radioastronomy. Paris Symposium (Radioastronomiya. Parizhskiy simpozium). Moscow, p. 263, 1961.
6. Hewish, A., Wyndham, F. D. Monthly Notices Roy. Astron. Soc., 126, No. 5, 467, 1963.
7. Vitkevich, V. V. Doklady AN SSSR, 156, No. 5, 1065, 1964.
8. Ginzburg, V. L. Doklady AN SSSR, 109, No. 1, 61, 1956.
9. Ryzhkov, N. F., Pariyskiy, Yu. N. et al. Solnechnyye Dannyye No. 7, 67, 1963.
10. Slee, O. B. Observatory, 76, 228, 1956.
11. Basu, S., Gastell, J. Nature, 197, No. 4870, 885, 1963.
12. Erickson, W. C. Astrophys. J., 139, No. 4, 1291, 1964.

13. Wyndham, F. D., Clear, K. B. Nature, 200, No. 4908, 766, 1963.
14. Slee, O. B. Monthly Notices Roy. Astron. Soc., 123, No. 3, 223, 1961.
15. Gorgolewski, S. Acta astron. (Polska), 12, No. 1, 251, 1962.
16. Hewish, A., Scoff, P. F., Wills, D. Nature, 203, No. 4951, 1214, 1964.
17. Brannan, D. J. Space Communications. N. Y., 64, 1963.
18. Kotel'nikov, V. A. et al. In "Iskusstvennyye Sputniki Zemli".  
Izdatel'stvo AN SSSR, No. 17, p. 91, 1963.
19. Priester, W. Nature, 196, No. 4853, 464, 1962.
20. Smith, W. B. Astron. J., 68, No. 1, 15, 1963.
21. Mustel, E. Space Sci. Rev., 3, No. 2, 139, 1964.
22. Hust, R. Space Sci. Rev., 1, No. 3, 522, 1963.
23. Craken, K. J. Trans. Amer. Geophys. Union, 44, No. 2, 447, 1963.
24. James, J. C. IEEE Trans. Mil. El., 8, No. 3 - 4, 210, 1964.
25. Chernov, L. A. Wave Propagation in a Medium With Random Nonuniformities (Rasprostraneniye voln v srede so sluchaynymi neodnorodnostyami).  
Moscow, 1958.
26. Levin, B. R. Theory of Random Processes and its Application to Radio  
Technology (Teoriya sluchaynykh protsessov i ee primeneniye v  
radiotekhnike). Moscow, 1960.
27. Tsytoich, V. N. Astronomicheskiy Zhurnal 46, No. 5, 992, 1964.
28. Klemperer, W. K. Astron. J., 69, No. 1, 22, 1964.
29. James, J. C. Astron. J., No. 1, 19, 1964.
30. Radio Location of Venus (Radiolokatsiya Venery). Moscow, p. 25,  
1963.

# THE PASSAGE OF ELECTROMAGNETIC WAVES HAVING SUPERLOW FREQUENCY (SLF) THROUGH IONOSPHERE PLASMA

(Summary)

V. I. Aksenov

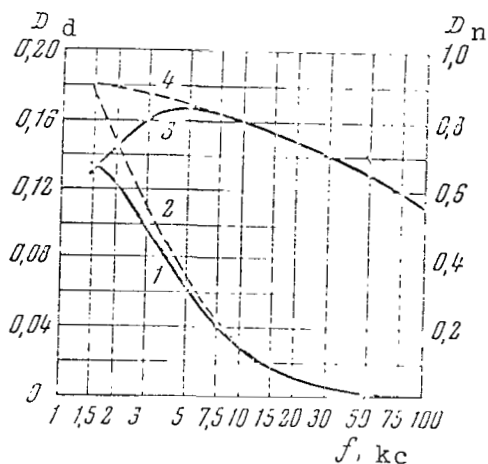
1. This study obtains a rigorous solution of the problem regarding flat, SLF electromagnetic waves passing through the plane-stratified, magnetically active ionosphere plasma in the case of longitudinal propagation (angle between the wave normal vector and direction of the outer magnetic field is zero; magnetic field is perpendicular to the layers).

On the basis of the solution found, formulas are obtained to determine the reflection and penetration factors of two characteristic waves - ordinary and extraordinary.

/234

2. The formulas obtained are used to compute the reflection and penetration factors in the 1.5-100 kc frequency range for diurnal and nocturnal ionosphere models. The concentration and effective number of electron collision dependences, which were used to perform the computations, are similar to those known in the literature (Ref. 1-3).

These computations establish the fact that an ordinary wave barely penetrates the ionosphere in the frequency range under consideration. The figure below presents the results derived from computing the dependence of the penetration factor on frequency for an extraordinary wave. The penetration factor values (which represents the ratio of the mean [in time] energy flux for a passing wave to the corresponding flux for a wave penetrating the ionosphere) were calculated for the diurnal ionosphere model at an altitude of 100 km, and for the nocturnal model at an altitude of 200 km.



Dependence of Penetration Factor on Frequency for  
Diurnal ( $D_d$ , curve 1) and Nocturnal ( $D_n$ , curve 3)  
Ionosphere Models

3. As can be seen from the figure, the factor for penetration through the diurnal ionosphere at a 1.5 kc frequency is 13%; with an increase in frequency, its value decreases monotonically to 1% at a 20 kc frequency. Electromagnetic waves with a 100 kc frequency barely penetrate the diurnal ionosphere.

4. The penetration factor is considerably larger for the nocturnal ionosphere model than it is for the diurnal model, and reaches its maximum value in the vicinity of  $f = 4$  kc frequency. The presence of this maximum may be possibly one of the reasons leading to a lower damping decrement for all spectral components of whistling atmospherics, which lie in the 3-5 kc frequency band. Storey (Ref. 4) first discovered the phenomenon of this attenuated damping in this frequency range.

5. The results of computations carried out in the geometric optics approximation (dashed line in the figure) do not coincide with a rigorous solution of the wave equation at frequencies less than 10 kc, and this divergence increases with a frequency decrease. At the 1.5 kc frequency, the penetration factor, which is found in the geometric optics approximation, is 1.3-1.4 times greater than the corresponding quantity obtained by a rigorous solution of the wave equation.

This fact must be kept in mind when results from (Ref. 2, 3) are examined. The geometric optics approximation was employed in these studies to compute the penetration factor of SLF electromagnetic waves through the ionosphere.

#### REFERENCES

1. Ratcliff, Dzh. A. Upper Atmosphere Physics (Fizika verkhney atmosfery). Fizmatgiz, 1963.
2. Fligel', D. S. Geomagnetizm i Aeronomiya, 2, No. 5, 886, 1962.
3. Fligel', D. S. Komleva, G. D. Geomagnetizm i Aeronomiya, 1, No. 1, 41, 1964.
4. Storey, L. R. Philos. Trans. Roy. Soc., A246, No. 908, 113, 1953.

III

INTERACTION OF ARTIFICIAL EARTH  
SATELLITES WITH THE IONOSPHERE



## INTERACTION OF MOVING BODIES WITH A PLASMA

### (Introductory Remarks)

Ya. L. Al'pert

In recent years there has been an increase in the number of works /237 devoted to studying the properties of an electrically charged, nonuniform cloud formed in the vicinity of a body (particularly, a moving body) located in a strongly rarefied plasma. Research in this field has recently been summed up in the works (Ref. 1, 2). However, since these works were written new theoretical results have been obtained, and several numerical computations have been performed (Ref. 3-5). It is particularly important that there has also been experimental research conducted both on AES (Ref. 6) and conducted under laboratory conditions (Ref. 7-8); to a certain extent, this research can even be compared with the theory for these phenomena. Some of these new results will be partially examined in the succeeding reports.

The current state of plasma physics, which has risen due to the launching of artificial satellites and space rockets, is similar to a certain extent to the state of solid media mechanics after the airplane was invented. Just as the development of aviation necessitated a study of the aerodynamics of a compressible gas flow around a body, the development of artificial space vehicles has necessitated the development of a theory for the kinetics of a rarefied ionosphere plasma flowing around these vehicles in space. The interaction of the vehicles with the plasma does not influence their motion, as is the case for airplanes, since the friction force caused by the plasma is small in this case. However, phenomena produced around the vehicle are, in the first place, of great independent interest. They have several features which are of general importance for plasma physics. Secondly, their study is important for the correct formulation and interpretation of many experiments which are performed on space vehicles, utilizing them as a laboratory for studying the properties of the surrounding medium.

A theoretical study of these phenomena encounters significant difficulties. This is primarily related to the plasma rarefaction. In the media under consideration, the mean free path not only of electrons  $l_e$ , but also of ions and neutral particles  $l_i$ ,  $l_n$  satisfy the inequality  $l_n \approx l_i \gg R_0$ , where  $R_0$  is the characteristic dimension of the body. Therefore, in order to describe all of the phenomena we must utilize equations of the kinetic gas theory. They are more complex than hydrodynamic equations, because a larger number of measurements - the phase space of particles - are recorded in space. In addition, they differ essentially from the problems of hydrodynamics due to the fact that particles in a plasma are charged electrically. This leads, in particular, to the necessity of allowing for the influence of

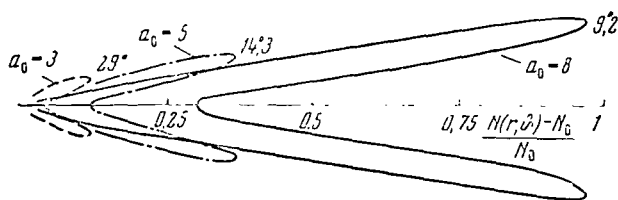


Figure 1

Angular Dependences of Relative Electron Concentration  
Distribution  $\delta N/N_0$  for Different Values of  $\alpha_0 = V_0/V_i$   
Behind a Large Body

the electric and magnetic fields on particle motion. There are three new parameters in the theory, which have the dimension of length; these parameters are missing in normal hydrodynamics, namely: the Debye radius  $D = (kT/4\pi Ne^2)^{1/2}$  ( $N$  - charged particle concentration,  $T$  - temperature), and the Larmor radii  $\rho_{Hi}$  and  $\rho_{He}$  of ions and electrons. Such a large number of parameters naturally makes the equations significantly more complex. Therefore, an important factor in solving these problems is the utilization of inequalities between these parameters which exist under real conditions; this makes it possible to clarify the qualitative picture of the phenomena and to simplify the equations to the maximum extent. /238

These problems are of particular interest for rapidly moving bodies, i.e., when the velocity of the moving bodies  $V_0$  is much greater than the thermal ion velocity  $v_i$ , which occurs when the AES moves in the ionosphere and in the vicinity of the interplanetary medium closest to the Earth. Many studies have been devoted to a theory of the phenomena thus formed. They are collected in the monograph (Ref. 1). However, several experimental data characterizing certain properties of these phenomena have also been published at the present time. Thus, for example, the angular distribution of particles behind an artificial Earth satellite has been studied (Ref. 6). An analysis of these data shows that they closely coincide with the results obtained theoretically in the angular region of approximately  $90-60^\circ$ . In the region of exponentially-small concentration values (small angles with the velocity vector) the number of particles determined experimentally is significantly greater than that given by the formulas. This is primarily related to the necessity of complete and rigorous allowance for the electric field influence on ion motion in this zone in the theory, which has not been done up to the present due to computational difficulties. We must also keep the fact in mind that close to a body the particle distribution is particularly sensitive to the form of the body and the gas composition. In particular, light hydrogen ions, even in a relatively small amount, can strongly change the particle concentration which is proportional to  $\exp[-(v_i/V_0)^2]$  in the absence of an electric field.

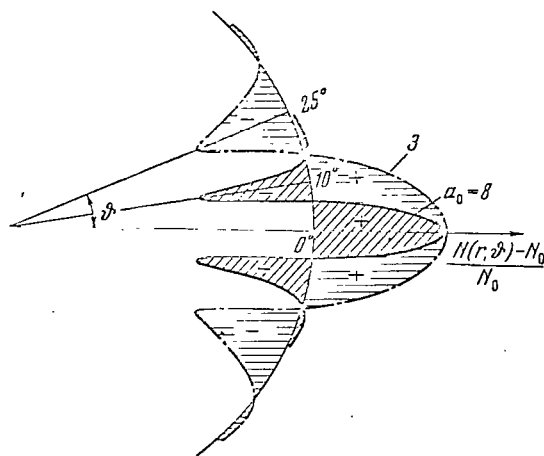


Figure 2

Angular Dependences of the Function of  $\delta N/N_0$  for a Point Body for Different Values of  $\alpha_0 = V_0/v_i$

The plus sign designates regions of charge accumulation; the minus sign designates rarefaction regions.

It can also be stated that laboratory measurements of particle distribution in the outer magnetic field close to a body and behind it, which were performed in (Ref. 8), have revealed the expected periodic distribution of particle concentration around the body axis, and closely coincide with the concentration periodicity  $N_i(\mathbf{r})$  which was obtained theoretically (Ref. 1).

The effect of the electric field on the nonuniform cloud structure is only taken into consideration in the farther zone of the moving body. The ratio  $(N(r, \theta) - N_0)/N_0$  behind the body for different values of  $\alpha_0 = V_0/v_i$  is shown in Figure 1. It can be clearly seen from this figure that there is maximum perturbation on the surface of a cone with the aperture angle  $\text{tg } \theta_{\text{max}} \sim 1.3(V_0/v_i)^{-1}$ . This surface coincides with the Mach cone for ion-sound waves. However, the nature of the concentration perturbation is different from that given in hydrodynamics. The perturbation  $N(r)$  is essentially determined by the influence of the electric field, which leads to a decrease in  $\delta N = N - N_0$  in the inner cavity of this cone, i.e., to a certain focusing of the particles along the body's axis of motion. Naturally, the cone is also very diffuse, which is related to 239 wave damping. It is interesting to note that for a small body, whose linear dimensions are smaller than the Debye radius  $D$ , the perturbation  $\delta N$  has an accumulation region around the body axis; the rarefaction region follows this, and then the change to an unperturbed value  $N_0$ . This can be seen in Figure 2, in which the accumulation regions are designated by the plus sign, and the rarefaction regions are designated by the minus sign. This particle distribution can apparently be explained by the fact that the computations were made for a point charge, so that ions are not absorbed by the body,

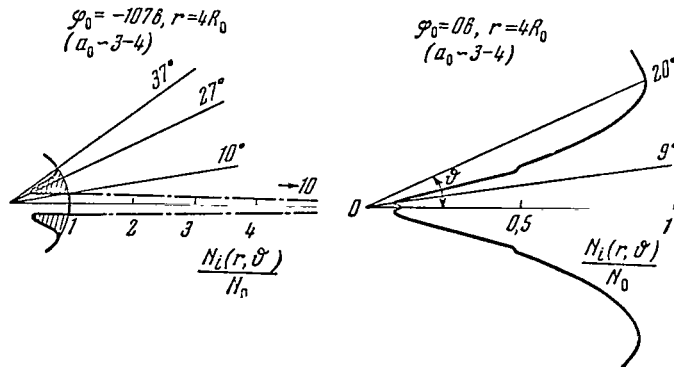


Figure 3

Results Derived from Laboratory Measurements of the Angular Distribution of Ion Concentration Behind a Body Located in an Advancing Stream of Ions With Velocities of  $\alpha_0 = V_0/v_i$  on the Surface of the Body

i.e., their number is retained. Therefore, if there is rarefaction at one point in space, then there will be accumulation at another point. However, we should note that an analogous situation occurs for large, very strongly charged bodies, when  $R_0 \gg D$ , for which ion deflection by the field will be greater than their absorption by a surface. Such a strongly charged body can focus the ions close to the axis. Moskalenko (Ref. 9) obtained such a result theoretically. This phenomenon has been recently observed in laboratory experiments (Ref. 7). Figure 3 presents the corresponding distribution curves  $N(r, v)/N_0$ , obtained fairly close to the body. It can be seen from the figure that when the body has a zero potential ( $\phi_0 = 0$ ) there is only a rarefaction region, while for  $\phi_0 = -107$  v a strongly expressed accumulation region is observed, i.e., the particles are focused. Quantitatively, these curves differ from the theoretical curves, because the measurements were conducted in the neighboring zone of the body at a distance from its center of  $r = 4R_0$  and for  $a_0 \sim 4$ .

Plasma stability in a perturbed region is a particularly important problem which is included among the theoretical problems which have not been solved up to the present time. As is known, theoretical studies have shown that the overwhelming majority of possible stationary plasma states is unstable. In our case, the situation is somewhat different, because we are dealing with directional ion motion. This must contribute to stability. Nevertheless, the problem has still not been clarified completely, and necessitates careful study, particularly if we keep in mind the influence of the outer magnetic field of the Earth, which greatly facilitates instability during the motion of a body exactly along the field.

Thus, the future development of a theory for the phenomena considered necessitates the solution of several problems, with allowance for the magnetic field, influence of the electric field in the zone adjacent to the body, as well as an investigation of the stability of the perturbed plasma

region. We should also note that in the case of a slowly moving body (body at rest), when we are speaking of a probe theory taking the magnetic field into account, there is not one complete computation which would make it possible to interpret the situation arising, for example, during probe measurements in the ionosphere or the interplanetary medium. The influence of the magnetic field must be very great in many cases. Therefore, the development of this theory is one of the urgent problems in this research area.

#### REFERENCES

1. Al'pert, Ya. L., Gurevich, A. V., Pitayevskiy, L. P. "Artificial Satellites in Rarefied Plasma" (Iskusstvennyye sputniki v razrezhennoy plazme). Izdatel'stvo "Nauka", 1964.
2. Al'pert, Ya. L. Geomagnetizm i Aeronomiya, 5, No. 1, 3, 1965.
3. Gurevich, A. V., Pitayevskiy, L. P. Geomagnetizm i Aeronomiya, 4, 817, 1964.
4. Moskalenko, A. M. Geomagnetizm i Aeronomiya, 4, No. 6, 1026, 1964; 5, 1965 (in press).
5. Panchenko, Yu. M. Geomagnetizm i Aeronomiya, 5, No. 6, 1965 (in press).
6. Smair, U. and Willmore, A. P. The Distribution of Charged Particles Near a Moving Spacecraft. Dept. of Phys., Univ. College, London, A. Preprint, 1965.
7. Hall, D. F., Kemp, R. F., and Seller, J. M. AIIA Journal, 2, No. 6, 1032, 1964.
8. Barrett, P. J. Phys. Rev. Letters, 13, No. 25, 742, 1964.
9. Moskalenko, A. M. Geomagnetizm i Aeronomiya, 4, No. 2, 261, No. 3, 509, 1964.

# BRAKING OF BODIES MOVING IN A RAREFIED PLASMA

A. V. Gurevich, A. M. Moskalenko

## 1. Interaction of Bodies With Neutral Molecules

/241

The braking of bodies moving in a rarefied plasma is caused by their interaction with neutral and charged particles, as well as with the electro-magnetic fields.

Interaction with neutral molecules and atoms naturally plays the main role for small degrees of plasma ionization. In this case, consequently, the braking of a moving body in a plasma is the same as during the motion in a neutral rarefied gas, where the particle mean free path  $l$  is much greater than the body size  $R$ . This problem, which has been investigated in several works (see, for example, [Ref. 1]) has been sufficiently studied.

For higher degrees of ionization, the interaction of the body with charged particles - electrons and ions - as well as the interaction with electric and magnetic fields in the plasma is significant. Generally speaking, in order to solve these problems it is necessary to know the complex structure of the perturbed region in the vicinity of the body moving in the plasma. Therefore, the discussion of these problems in works by previous authors (Ref. 2-9) has not always been systematic enough, and frequently was only provisional in nature. A more detailed investigation was required. The rigorous solution of several of these problems is the purpose of this article.

For purposes of completeness, let us first examine the interaction of a body with neutral molecules, atoms. The braking force  $F_n$  equals the total impulse transmitted to the body per unit of time by gas molecules, i.e., by definition

$$F_n = M \int_{(n\mathbf{v}_1 < \mathbf{v}, n\mathbf{v} > 0)} (\mathbf{v} - \mathbf{v}_1) (n\mathbf{v}_1) w(\mathbf{v}, \mathbf{v}_1, \mathbf{r}_s) f_0(\mathbf{v}_1) d^3v d^3v_1 dS. \quad (1)$$

Here  $M$  is the mass of a gas molecule;  $\mathbf{v}_1$  - its velocity before colliding with the body surface;  $\mathbf{v}$  - the velocity after collision;  $\mathbf{n}$  - the outer normal to the body surface at the collision point  $\mathbf{r}_s$ ;  $f_0(\mathbf{v}_1)$  - the distribution function of particles falling on the body surface. It is advantageous to investigate the problem in a coordinate system connected with the moving body. It can be assumed that the function  $f_0(\mathbf{v}_1)$  is a Maxwell function

$$f_0(\mathbf{v}_1) = \left( \frac{M}{2\pi kT} \right)^{3/2} N_m \exp \left\{ -\frac{M}{2kT} (\mathbf{v}_1 + \mathbf{V}_0)^2 \right\}, \quad (2)$$

where  $N_m$  is the molecule concentration;  $T$  - gas temperature;  $V_0$  - body velocity.

Finally,  $\omega(\mathbf{v}, \mathbf{v}_1, \mathbf{r}_s)$  is the scattering probability (see [Ref. 10], section 3b), i.e., the probability that a particle, falling with a velocity  $\mathbf{v}_1$  on a surface point  $\mathbf{r}_s$ , is reflected by it with the velocity  $\mathbf{v}$ . Substituting the expression for the scattering probability  $\omega$  and the function  $f_0$  in formula (1) and integrating over all velocities of particles  $d^3v_1 d^3v$  falling on the surface ( $\mathbf{n}\mathbf{v}_1 < 0$ ) and reflected from it ( $\mathbf{n}\mathbf{v} > 0$ ), and also over the entire body surface  $dS$ , we can readily calculate the braking force.

By way of an example, let us examine a sphere of the radius  $R_0$  moving in a rarefied gas at the velocity  $V_0$ . Let us assume that the law governing particle scattering on its surface is a specular law, and then according to (Ref. 11):

/242

$$\begin{aligned} F_n &= -\frac{2}{\sqrt{\pi}} N_m k T R_0^2 \int v'_1 v'_1 \exp \{ -(\mathbf{v}'_1 + \mathbf{V}'_0)^2 \} d^3 v_1 = \\ &= -N_m \pi R_0^2 k T \frac{V'_0}{V_0^3} \left\{ \Phi(V'_0) \left[ 2V_0'^4 + 2V_0'^2 - \frac{1}{2} \right] + \frac{V'_0}{\sqrt{\pi}} e^{-V_0'^2} (1 + 2V_0'^2) \right\}, \quad (3) \\ V'_0 &= \sqrt{MV_0^2/2kT} = \sqrt{\varepsilon_0/kT}, \quad \Phi(z) = \frac{2}{\sqrt{\pi}} \int_0^z e^{-x^2} dx. \end{aligned}$$

Here  $\Phi(z)$  is the probability integral. The braking force moves in a direction opposite to  $\mathbf{V}_0$ ; therefore, only the quantity  $F$  is given below.

For a small sphere velocity  $V'_0 \ll 1$ , Stokes law is valid for the braking force

$$F_n = \frac{8}{3} \frac{\sqrt{2}}{\sqrt{\pi}} N_m \pi R_0^2 \sqrt{kT} \bar{V} V_0. \quad (4)$$

For a high velocity  $V'_0 \gg 1$

$$F_n = N_m \pi R_0^2 M V_0^2 = 2N_m M \pi R_0^2 \varepsilon_0. \quad (5)$$

Particle scattering on the body surface also plays an important role. For example, for the braking of a rapidly moving sphere, in the case of elastic scattering according to the Lambert law, we have

$$F_n = \frac{13}{9} N_m \pi R_0^2 M V_0^2 = \frac{26}{9} N_m \pi R_0^2 \varepsilon_0. \quad (6)$$

Thus, the nature of particle reflection from a surface significantly influences the braking force. This becomes even more apparent, if the

braking force is divided into two sections -  $F_{1n}$  related to particles falling on the surface, and  $F_{2n}$  related to particles reflected from the body surface:

$$F_n = F_{1n} + F_{2n} = -M \int \mathbf{v}_1 (\mathbf{n} \mathbf{v}_1) f_0 d^3 v_1 dS + M \int \mathbf{v} (\mathbf{n} \mathbf{v}_1) w f_0 d^3 v d^3 v_1 dS.$$

The force  $F_{1n}$  does not depend on the nature of the particle interaction with the body surface. In the case of a rapidly moving body, we have

$$F_{1n} = N_m \pi R_0^2 M V_0^2 = 2 N_m \pi R_0^2 \epsilon_0. \quad (7)$$

For a slowly moving body we have

$$F_{1n} = \frac{8}{3} \frac{\sqrt{2}}{\sqrt{\pi}} N_m \pi R_0^2 \sqrt{k T M} V_0. \quad (7a)$$

The force  $F_{2n}$  depends significantly on the nature of particle reflection and on the form of the surface. This can be clearly seen, for example, from formulas (5) - (7a). In particular,  $F_{2n} = 0$  for specular scattering on the sphere.

We should point out that it is not possible to allow for the thermal scatter of the velocities of particles impinging on the body, when calculating the braking force of a rapidly moving body ( $V'_0 \gg 1$ ), i.e., it must be assumed that

$$f_0(\mathbf{v}_1) = N_m \delta(\mathbf{v}_1 + \mathbf{V}_0). \quad (8)$$

This simplifies the computation considerably.

## 2. Braking of a Large, Rapidly Moving Body

Let us now calculate the braking force produced by the interaction of a body with charged plasma particles - ions and electrons. We should first note that if  $T_e \ll T_i M/m$  and the body surface does not have a high positive potential  $\phi \gg kT_e/e$ , then the interaction of the body with ions plays the basic role. /243

Let us investigate a large, rapidly moving body, i.e., a body which is large as compared with the Debye radius in a plasma ( $R \gg D$ ), and a velocity  $V_0$  which is significantly greater than the thermal ion velocity  $v_i = \sqrt{2kT/M}$ <sup>1</sup>. In this case, the electric field distribution in the vicinity of the body is given in (Ref. 10).

Let us divide the braking force into two parts. The first  $F_s$  is

---

<sup>1</sup> This case occurs, in particular, during the motion of rockets and satellites in the ionosphere.



caused by particles colliding with the body surface. The second  $F_c$  is not caused by particles colliding with the body, but rather by particles interacting only with the electric field in the vicinity of the body. It is assumed that particles impinging in front of the body surface make the main contribution to the force  $F_s$ . On the other hand, particles interacting with the perturbed trail behind the body make the main contribution to the force  $F_c$ .

The force  $F_s$  is naturally determined by expression (1). It is thus assumed that in the case of a rapidly moving body the thermal ion motion can be disregarded. The influence of a weak electric field on ion motion in a quasineutral plasma in front of the body must be disregarded in the same approximation. Consequently, the function  $f_0(\mathbf{v}_1)$  at the outer boundary of a double layer is given by the expression (8):

$$f_0(\mathbf{v}_1) = N_0 \delta(\mathbf{v}_1 + \mathbf{V}_0),$$

where  $N_0$  is the ion concentration in an unperturbed plasma.

The probability  $w$  depends essentially on the nature of ion interaction with the body surface. Usually an ion is neutralized (recombined) when colliding with a surface. Let us assume that an ion moves at a velocity of  $v_{in0}$  in the direction of the inner normal to the body surface in the region of a quasineutral plasma. In a double layer, the ion velocity will increase due to the attracting electric charge of the body (it is assumed that the body reflects negatively). On the body surface, the velocity with respect to the normal is

$$v_{in} = \left[ v_{in0}^2 - \frac{2(e\varphi_0 - \beta e_i)}{M} \right]^{1/2}. \quad (9)$$

Here  $\varphi_0$  is the potential of the body surface ( $\varphi_0 < 0$ );  $e_i$  - ionization energy;  $\beta$  - numerical coefficient depending on the surface properties (the last term in (9) takes into account the work of the image force). Let us assume that an ion is recombined at the body surface. The neutral atom formed collides with the surface, and is reflected from it at a velocity  $v_d$ , depending upon the scattering law on the surface. The initial ion velocity  $v_{i0}$  changes due to collision with the surface at a velocity of  $v_d$ . For example, in the case of specular atom scattering on a body surface, the initial normal velocity component  $v_{in0}$  changes to  $-v_{in}$ , where  $v_{in}$  is determined by formula (9), and the tangential component is retained, i.e.,

$$w = \delta\{\mathbf{v} - \mathbf{v}_1 - \mathbf{n}[(\mathbf{n}\mathbf{v}) - (\mathbf{n}\mathbf{v}_1)]\} \delta\left\{\mathbf{n}\mathbf{v} - \left[(\mathbf{n}\mathbf{v}_1)^2 - \frac{2(e\varphi_0 - \beta e_i)}{M}\right]^{1/2}\right\}. \quad (10)$$

In the case of elastic diffusion scattering, according to the Lambert law we have

$$w = \frac{1}{\pi v^2} \delta\left\{v - \left[v_1^2 - \frac{2(e\varphi_0 - \beta e_i)}{M}\right]^{1/2}\right\} \frac{\mathbf{n}\mathbf{v}}{v}. \quad (11)$$

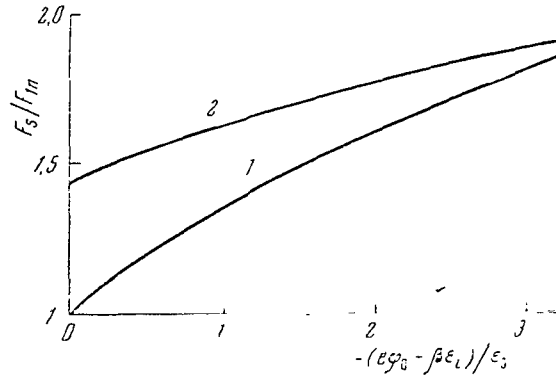


Figure 1

Dependence of the Braking Force of a Large Rapidly Moving Body on the Potential of the Body

1 - For specular ion scattering with their neutralization on the body surface; 2 - for elastic diffusion scattering of ions with neutralization.

Substituting the distribution function (8) and the expressions for the scattering probability (10) and (11) in formula (1), we can calculate the force  $F_s$ . In the case of specular scattering we have

/244

$$F_s = N_0 \pi R_0^2 \epsilon_0 \left[ 1 + (1 + a)^{1/2} - \frac{a}{2} (1 + a)^{1/2} - \frac{a^2}{2} \operatorname{Arsh} 1/\sqrt{a} \right], \quad (12)$$

where

$$a = -(\epsilon\varphi_0 - \beta\epsilon_i)/\epsilon_0,$$

for  $\alpha \ll 1$

$$F_s = 2N_0 \pi R_0^2 \epsilon_0 (1 + \alpha/2);$$

for  $\alpha \gg 1$

$$F_s = 2N_0 \pi R_0^2 \epsilon_0 \left( \frac{2}{3} \sqrt[3]{a} + \frac{1}{2} \right). \quad (13)$$

It can thus be seen that the braking force increases proportionally to  $\sqrt[3]{-\varphi_0}$  with an increase (with respect to the modulus) of the negative potential of the body surface.

In the case of diffusion (according to Lambert) scattering we have

$$F_s = 2N_0 \pi R_0^2 \epsilon_0 \left( 1 + \frac{4}{9} \sqrt[3]{1 + a} \right). \quad (14)$$

The dependence of the force  $F_s$  on the body surface potential for different scattering laws is shown in Figure 1 (curve 1 - specular scattering; 2 - scattering according to the Lambert law). It can be seen from the figure that the force  $F_s$  increases most vigorously with an increase in  $|\varphi_0|$  in the case of specular scattering.

It should be noted that total ion neutralization on the body surface was assumed above. If there is partial ion reflection from the surface with the reflection coefficient  $R_1$ , then the expressions obtained for  $F_s$  must be multiplied by  $(1-R_1)$ , and the portion of the braking force caused by reflection of non-recombined ions must be added to them. For example, for specular ion scattering on a body surface, this portion of the braking force is

$$F_s = 2N_0\pi R_0^2 \epsilon_0 R_1. \quad (15)$$

It is less than the force (12), and does not depend on the surface potential. The reason for this lies in the fact that a reflected ion in a double layer is retarded due to the influence of the electric field, and restores the additional impulse acquired when it approached the body surface. Consequently, ion recombination on the body surface is essentially indicated by the magnitude of the braking force.<sup>1</sup> Jastrow and Pearse (Ref. 2) were apparently the first ones to point this out. Interesting phenomena /245 occur due to ion recombination, if the body surface is nonuniform (Ref. 12).

Let us now discuss the braking force caused by ion interaction with the electric field. When a body moves in a plasma, an electric charge appears on its surface which produces a field in the immediate vicinity.

An electric field exists in the long trail extending behind the body. Interacting with these fields, the ions are deflected from rectilinear trajectories, due to which fact the braking force changes.

If, however, the following condition is fulfilled

$$\frac{D}{R_0} \left( \frac{e|\varphi_0|}{kT} \right)^{1/2} \ll 1; \quad \text{or} \quad \sqrt{\frac{M_0^2}{2kT}} = \sqrt{\epsilon_0/kT} \gg 1, \quad (16)$$

<sup>1</sup> A metallic body located in a plasma is usually charged negatively up to the potential  $\varphi_0 \sim -(4-5)kT/e$ . It can be seen from formula (9) that particles emitted from the body after recombination have an energy greater than  $5kT$ . The source of this energy (apart from ionization energy) is the thermal energy of plasma electrons. Actually, only rapid electrons belonging to the tail of the distribution function can fall on a negatively charged body. Due to this fact, the electron gas in a plasma cools off.

where  $D = (kT/4\pi e^2 N_0)^{1/2}$  is the Debye radius, then these corrections to the braking force are small:

$$\frac{\Delta F_i}{F} \sim \frac{kT}{MV_0^2} \ll 1. \quad (17)$$

This result is substantiated in detail in (Ref. 11), and also in (Ref. 2, 6, 8, 9).

### 3. Braking of a Small Body

Let us now examine the case of a small spherical body - sphere, whose radius  $R_0$  is much less than the Debye radius in a plasma. When the condition

$$|\varphi_0| \ll \frac{kT}{e} \frac{D}{R_0}, \quad (18)$$

is fulfilled, where  $\varphi_0$  is the body surface potential, the electric field in the vicinity of the sphere is a Coulomb field up to distances on the order of  $D$  (see [Ref. 10], section 40). In the case of  $r > D$ , the field decreases much more rapidly than the Coulomb field. In this case far removed regions ( $r \geq D$ ) make only a small contribution (on the order of, or less than,  $1/\ln(D/R_0)$ ), so that it can be assumed the electric field in the vicinity of the body is a Coulomb field, when the braking force is computed.

The body surface potential will be assumed to be negative ( $\varphi_0 < 0$ ), for purposes of simplicity. In this case, ions are attracted to the body, and electrons are repulsed.

Below we shall investigate both elastic scattering and ion recombination on a body surface, and it will be assumed that electrons are absorbed upon collision with the body. In contrast to a large body, the interaction with electrons can play a significant role in the case of a small body.

Just as was done previously, let us divide the braking force into two portions:  $F_s$  caused by particles colliding with the body surface, and  $F_c$  connected with particles interacting only with the electric field. In the case of a small body, the role of the force  $F_c$  is much more significant than in the case of a large body, which was examined above.

Let us first investigate the force  $F_s$ . It is determined, as previously, by formula (1), with the only difference being that the value  $(v-v_1)$  must be now taken not on the surface  $S$ , but at a large distance from the body ( $r \rightarrow \infty$ ), since we are interested in the total change in particle momentum resulting from its interaction with a body and with the electric field. It is

advantageous to distinguish between the components resulting from the interaction with particles falling on the body  $\mathbf{F}_{1s}$  and particles reflected by  $\mathbf{F}_{2s}$  in the force  $\mathbf{F}_s$ : /246

$$\mathbf{F}_s = \mathbf{F}_{1s} + \mathbf{F}_{2s}; \quad (19)$$

$$\mathbf{F}_{1s} = -M \int_{nv_1 < 0} (\mathbf{v}_1) |_{r \rightarrow \infty} (n\mathbf{v}_1) f_0(\mathbf{v}_1) d^3v_1 dS; \quad (20)$$

$$\mathbf{F}_{2s} = M \int_{\substack{nv_1 < 0 \\ nv_1 > 0}} (\mathbf{v}) |_{r \rightarrow \infty} (n\mathbf{v}_1) w(\mathbf{v}, \mathbf{v}_1, \mathbf{r}_s) f_0(\mathbf{v}_1) d^3v d^3v_1 dS. \quad (21)$$

The entire investigation will be based on the coordinate system connected with the body itself; the z-axis coincides with the body direction of motion. The braking force is directed along this axis.

#### 4. Interaction With Incident Ions and Electrons

On the basis of (20), the braking force by incident ions is

$$F_{1s} = M \int (v_{1z}) |_{r \rightarrow \infty} (n\mathbf{v}_1) f_0(\mathbf{v}_1) d^3v_1 dS. \quad (22)$$

We can find  $v_{1z}$  in the case of  $r \rightarrow \infty$ . Taking (Ref. 13) into consideration, we obtain

$$\begin{aligned} (v_{1z}) |_{r \rightarrow \infty} &= [-v_1 \cos(\mathbf{v}_1, \mathbf{V}_0)] = \\ &= -\sqrt{\frac{2\varepsilon_1}{M}} (\cos C_1' \cos \nu + \sin C_1' \sin \nu \cos \psi_1). \end{aligned} \quad (23)$$

The computations at this point, and also later on, are similar to those performed in (Ref. 13). Therefore, we shall primarily use the notation in (Ref. 13), and an asterisk will be used to indicate references to the formulas in this work.

The primes at  $\cos C_1$  and  $\sin C_1$  indicate that these functions are selected for incident particles. It is interesting to note that  $v_{1z}$  is expressed in the case of  $r \rightarrow \infty$  by motion constants (for points on the body surface):  $\varepsilon_1$  - energy of incoming ions;  $C_1'$  - constant characterizing orbital orientation in the half-plane of motion;  $\nu$  and  $\psi_1$  - angles characterizing the momentum moment orientation.

For  $(n\mathbf{v}_1)$  we have

$$n\mathbf{v}_1 = v_{1R_0} = -\frac{1}{M} \sqrt{2M(\varepsilon_1 - e\varphi_0) - (M_1/R_0)^2}, \quad (24)$$

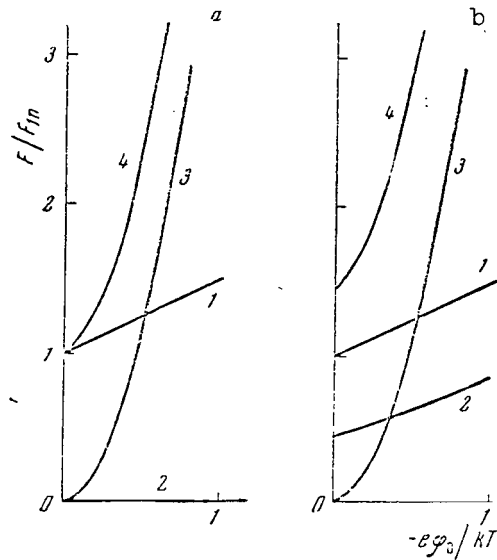


Figure 2

Dependence of Braking Force  $F_s$  of a Small, Rapidly Moving Body on the Potential

a - Specular ion scattering with neutral ionization; b - elastic ion scattering with neutralization.

and the function  $f_0(\mathbf{v}_1)$ , according to formula (12)\*, is

$$f_0 = \left( \frac{M}{2\pi kT} \right)^{3/2} N_0 \exp [Q(\epsilon_1, C_1, \psi_1)],$$

$$Q(\epsilon_1, C_1, \psi_1) = -\frac{1}{kT} [\epsilon_1 + \epsilon_0 -$$

$$- 2\sqrt{\epsilon_1 \epsilon_0} (\cos C_1 \cos \psi + \sin C_1 \sin \psi \cos \psi_1)].$$
(25)

When integration is performed in expression (22), it is advantageous to change to the variables  $\epsilon_1$  and  $\mathcal{M}_1^2$ :

$$d^3v_1 = \frac{d\psi_1 d\epsilon_1 d\mathcal{M}_1^2}{2M^2 R_0^2 \sqrt{2M(\epsilon_1 - e\varphi_0) - (\mathcal{M}_1/R_0)^2}}.$$
(26)

Taking into account (23) - (26), we obtain the following for the braking force by incident ions:

247

$$F_{1s} = \frac{N_0}{2\pi^{1/2}M(kT)^{1/2}} \int_0^{\pi} \sin \vartheta d\vartheta \int_0^{2\pi} d\psi_1 \int_0^{\infty} \sqrt{\varepsilon_1} d\varepsilon_1 \times \\ \times \int_0^{k(\varepsilon_1, \varphi_0)} (\cos C'_1 \cos \vartheta + \sin C'_1 \sin \vartheta \cos \psi_1) \exp [Q(\varepsilon_1, C'_1, \psi_1)] dM_1^2, \\ k(\varepsilon_1, \varphi_0) = 2VR_0^2(\varepsilon_1 - e\varphi_0). \quad (27)$$

We shall give the expressions for the braking force  $F_{1s}$  in two cases, when the body velocity is much greater, and much less than the ion thermal velocity (Ref. 11).

(a) The body velocity is much greater than the ion thermal velocity, i.e.,  $e\varphi_0/kT \gg 1$ .

The braking force  $F_{1s}$  is:<sup>1</sup>

$$F_{1s} = 2N_0\pi R_0^2 e_0 \left(1 + \frac{e|\varphi_0|}{e_0}\right) = F_{1n} \left(1 + \frac{e|\varphi_0|}{e_0}\right). \quad (28)$$

For  $\varphi_0 = 0$ , the braking force by incident ions  $F_{1s}$  equals the braking force by incident neutral particles  $F_{1n}$  (12), as must be the case. In the case of  $e|\varphi_0| \gg e_0$

$$F_{1n} = 2N_0\pi R_0^2 e|\varphi_0|, \quad (29)$$

i.e., the force  $F_{1s}$  does not depend on the mass of incident ions.

Figure 2 presents a graph showing the dependence of  $F_{1s}/F_{1n}$  on  $-e\varphi_0/e_0$  (curve 1).

/248

(b) The body velocity is much less than the ion thermal velocity, i.e.,  $\sqrt{e\varphi_0}/kT \ll 1$ . In this case

$$F_{1s} = \frac{8}{3} \frac{\sqrt{2}}{\sqrt{\pi}} N_0\pi R_0^2 \sqrt{kT/M} V_0 \left(1 - \frac{e\varphi_0}{2kT}\right). \quad (30)$$

Formula (30) can be written in another form (Figure 3, a,b, curves 1):

$$F_{1s} = F_{1n} \left(1 + \frac{e|\varphi_0|}{2kT}\right). \quad (30a)$$

In the case of  $\varphi_0 = 0$ , the braking force by incident ions  $F_{1s}$  equals the braking force by incident neutral particles  $F_{1n}$  (7a), as must be the case.

<sup>1</sup> The computations are presented in greater detail in (Ref. 11).

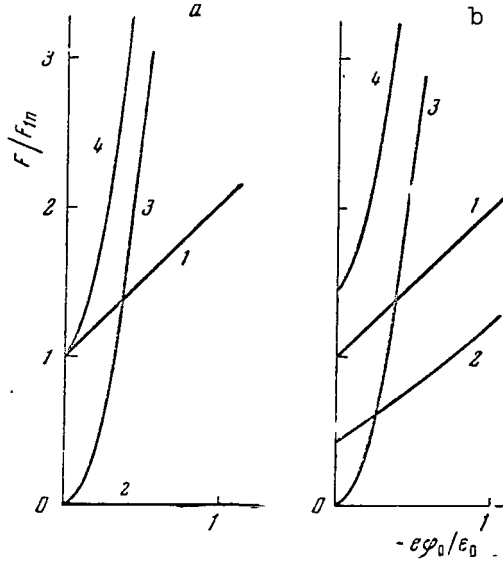


Figure 3

Dependence of Braking Force  $F_s$  of Small, Slowly Moving Body on Potential

a - Specular ion scattering with neutralization; b - elastic diffusion scattering of ions with neutralization.

If the body velocity is much greater than the electron thermal velocity, the braking force by incident electrons is as follows in the case of  $e|\varphi_0| < mV_0^2/2$  (Ref. 11):

$$F_{se} = N_0 \pi R_0^2 m V_0^2 \left(1 - \frac{2e|\varphi_0|}{mV_0^2}\right) \frac{1}{2} \left\{1 + \Phi \left[ \frac{V_0}{2v_e} \left(1 - \frac{2e|\varphi_0|}{mV_0^2}\right) \right] \right\}, \quad (31a)$$

$$v_e = \sqrt{2kT/m}.$$

and for  $e|\varphi_0| \geq mV_0^2/2$  in the approximation under consideration

$$F_{se} = 0. \quad (31b)$$

Here  $m$  is electron mass.

If the body velocity is much less than the electron thermal velocity, we obtain (Ref. 11)

$$F_{se} = \frac{8\sqrt{2}}{3\sqrt{\pi}} N_0 \pi R_0^2 \sqrt{kTm} V_0 \left(1 + \frac{e|\varphi_0|}{2kT}\right) \exp\left(-\frac{e|\varphi_0|}{kT}\right). \quad (32)$$

Comparing (31a) and (32) with (28) and (30) we find that the braking force by incident electrons is much less than the braking force by incident ions.



## Interaction With Reflected Ions

### Elastic specular scattering of ions from the body surface.

If elastic specular ion reflection from the body surface takes place, then the magnitude and direction of the momentum moment and the ion energy do not change during the reflection. We therefore have

$$w = 2M^2 R_0^2 \sqrt{2M(\varepsilon_1 - \varepsilon \varphi_0) - (\mathcal{M}_1/R_0)^2} \delta(\psi_1 - \psi) \delta(\varepsilon_1 - \varepsilon) \delta(\mathcal{M}_1^2 - \mathcal{M}^2). \quad (33)$$

In writing the probability  $w$ , we make allowance for the normalization  $\int w d^3 v = 1$ . The quantity  $v_z$  is found in the case of  $r \rightarrow \infty$  in the same way as  $v_{1z}$  is found in the case of  $r \rightarrow \infty$  [see (23)]:

$$(v_t)_{|r \rightarrow \infty} = \sqrt{\frac{2\varepsilon}{M}} H(C_1, \vartheta_1, \psi), \quad (34)$$

$$H(C_1, \vartheta_1, \psi) = \cos C_1 \cos \vartheta - \sin C_1 \sin \vartheta \cos \psi.$$

Substituting (24)-(26), (33) and (34) in (21) and integrating over  $d\psi_1 d\varepsilon_1 d\mathcal{M}_1^2$ , we have

$$F_{2s} = \frac{N_0}{2\pi^{1/2} M (kT)^{3/2}} \int_0^\pi \sin \vartheta d\vartheta \int_0^{2\pi} d\psi \int_0^\infty V \varepsilon d\varepsilon \times$$

$$\times \int_0^{k(\varepsilon, \varphi_0)} H(C_1, \vartheta, \psi) \exp[Q(\varepsilon, C_1, \psi)] d\mathcal{M}^2. \quad (35)$$

(a) The body velocity is much greater than the ion thermal velocity. /249  
For the braking force  $F_{2s}$ , we have

$$F_{2s} = -N_0 \pi R_0^2 e \varphi_0 \int_0^{a_0+2} \cos 2C_1 dt. \quad (36)$$

In the case of  $a_0 \ll 1$ , i.e.,  $e|\varphi_0| \gg \varepsilon_0$ , it thus follows that

$$F_{2s} = -F_{1n} \frac{1}{3} \frac{e|\varphi_0|}{\varepsilon_0}. \quad (37)$$

Thus, for  $e|\varphi_0| \gg \varepsilon_0$  we have the following from formulas (28) and (37)

$$F_s = F_{1s} + F_{2s} = F_{1n} \frac{2}{3} \frac{e|\varphi_0|}{\varepsilon_0}, \quad (38)$$

i.e., the reflected ions decrease the braking force by incident ions. It is thus understood that the reflected ions, when interacting with the electric field, lose their impulse, restoring its field, and consequently the body.

(b) The body velocity is much less than the ion thermal velocity. After the same computations that were performed to derive (28), we obtain

$$F_{2s} = \frac{N_0 \pi^{1/2} R_0^2 (-e\varphi_0)^3}{3(kT)^2} \frac{V_0}{v_i} \int_0^\infty a e^{-\mu a} da \int_0^{a+2} \cos 2C_1 dt. \quad (39)$$

In the case  $\mu \gg 1$ , i.e.,  $e|\varphi_0| \gg kT$  - the integral with respect to  $da$  is calculated by the Laplace method. The values of  $a$ , which are close to zero, make the main contribution to this integral. Finally, we have

$$F_{2s} = -F_{in} \frac{1}{3} \frac{e|\varphi_0|}{2kT}. \quad (40)$$

According to (38) and (40), in the case of  $e|\varphi_0| \gg kT$  we have

$$F_s = F_{in} \frac{1}{3} \frac{e|\varphi_0|}{kT}. \quad (41)$$

In this case the reflected ions also decrease the braking force by the incident ions.

#### Specular ion reflection with their neutralization on the body surface.

It will be assumed that the ion velocity does not change during reflection. However, after the ion is neutralized on the body surface its total energy changes, since a neutralized ion does not have a potential energy. We shall disregard the work of the force  $\beta e_i$  [see (9)] from this point on. Therefore,

$$w = 2M^2 R_0^2 \sqrt{2M} (\varepsilon - e\varphi_0) - (\mathcal{M}_i/R_0)^2 \times \\ \times \delta(\psi_1 - \psi) \delta(\mathcal{M}_1^2 - \mathcal{M}^2) \delta(\varepsilon - \varepsilon - e\varphi_0 R_0/r) |_{r=R_0}. \quad (42)$$

It should be noted that the potential energy at any point  $r$ , and not at points on the body surface, is included in the argument of the third  $\delta$ -function. In addition, as was indicated in (42), we must set  $r = R_0$  after integration over energy.

In the case of neutral particles,  $v_z$  can be taken on the body surface. This equals (equa. 34):

$$v_z = v_{R_0} \cos \vartheta - v_0 \sin \vartheta \cos \psi. \quad (43)$$

Here

$$v_{R_0} = \frac{1}{M} \sqrt{2M} \varepsilon - (\mathcal{M}_i/R_0)^2 \quad v_0 = \frac{\mathcal{M}}{M R_0}. \quad (43a)$$

In the same way, we can compute the pressure force by reflected particles, which coincides with the braking force for neutral particles.

/250

The reflected particle energy changes according to (35) and the argument of the third  $\delta$ -function changes from  $-e\varphi_0$  to  $\infty$ . After substituting (42), (43) and (24) - (26) in (21), and integrating over  $d\psi_1 d\epsilon_1 d\mathcal{M}_1^2$  we obtain

$$P_{2s} = \frac{N_0}{\pi^{1/2} (2MkT)^{3/2}} \left\{ \int_0^\pi \sin \vartheta \cos \vartheta d\vartheta \int_0^{2\pi} d\psi \int_{-e\varphi_0}^\infty d\epsilon \times \right. \\ \times \int_0^{k(\epsilon, 0)} \sqrt{2M\epsilon - (\mathcal{M}/R_0)^2} \exp [Q(\epsilon + e\varphi_0, C_{10}, \psi)] d\mathcal{M}^2 - \\ \left. - \int_0^\pi \sin^2 \vartheta d\vartheta \int_0^{2\pi} \cos \psi d\psi \int_{-e\varphi_0}^\infty d\epsilon \int_0^{k(\epsilon, 0)} \frac{\mathcal{M}}{R_0} \exp [Q(\epsilon + e\varphi_0, C_{10}, \psi)] d\mathcal{M}^2 \right\}, \quad (44)$$

where

$$C_{10} = \int_{R_0}^\infty \frac{\mathcal{M} dr}{r^2 \sqrt{2M\epsilon - (\mathcal{M}/r)^2}}. \quad (45)$$

Thus

$$\cos C_{10} = \sqrt{1 - \frac{\mathcal{M}^2}{2M\epsilon R_0^2}}, \quad \sin C_{10} = \frac{\mathcal{M}}{R_0 \sqrt{2M\epsilon}}. \quad (45a)$$

This value of the constant  $C_1$  was obtained due to the fact that, as was already indicated, the potential energy at any point  $r$  is included in the argument of the third  $\delta$ -function in (42). Therefore, this  $\delta$ -function indicates the potential field under the integral sign in the expression for  $C_1$  in the case of integration over  $d\epsilon_1$ . It must thus be the case that after ions are reflected and neutralized on the surface, they move along a straight line.

Let us make a substitution  $\epsilon + e\varphi_0 = E$ . Then expression (44) assumes the form

$$P_{2s} = \frac{N_0}{\pi^{1/2} (2MkT)^{3/2}} \left\{ \int_0^\pi \sin \vartheta \cos \vartheta d\vartheta \int_0^{2\pi} d\psi \int_0^\infty dE \times \right. \\ \times \int_0^{k(E, \varphi_0)} \sqrt{2M(E - e\varphi_0) - (\mathcal{M}/R_0)^2} \exp [Q(E, C_{10}, \psi)] d\mathcal{M}^2 - \\ \left. - \int_0^\pi \sin^2 \vartheta d\vartheta \int_0^{2\pi} \cos \psi d\psi \int_0^\infty dE \int_0^{k(E, \varphi_0)} \frac{\mathcal{M}}{R_0} \exp [Q(E, C_{10}, \psi)] d\mathcal{M}^2 \right\}. \quad (44a)$$

(a) The body velocity is much greater than the thermal ion velocity. After the same computations as were performed to derive (28), in the same approximation (see Figure 2, a, curve 2) we have

$$F_{2s} = 0. \quad (46)$$

This result was obtained previously in (Ref. 4) from qualitative premises. Finally, the braking force caused by ion collisions with the body surface is in this case

$$F_s = F_{1n} \left( 1 + \frac{e |\varphi_0|}{\varepsilon_0} \right). \quad (47)$$

(b) The body velocity is much less than the ion thermal velocity. If we perform the same computations as were performed to derive (30), we find that in this same approximation the braking force  $F_{2s}$  is (see Figure 3, a, curve 2)

$$F_{2s} = 0. \quad (48)$$

Finally, for the braking force caused by ion collisions with the body surface, we have /251

$$F_s = F_{1n} \left( 1 + \frac{e |\varphi_0|}{2kT} \right) \quad (49)$$

Elastic diffuse (according to Lambert) ion reflection from the body surface.

The probability  $w^*$  in this case has the form

$$w = \frac{M^2}{\pi} \frac{1}{\sqrt{2M(\varepsilon_1 - e\varphi_0)}} \frac{\sqrt{2M(\varepsilon - e\varphi_0)} (\mathcal{M}/R_0)^2}{\sqrt{2M(\varepsilon - e\varphi_0)}} \delta(\varepsilon_1 - \varepsilon). \quad (50)$$

(a) The body velocity is much greater than the ion thermal velocity. The braking force  $F_{2s}$  equals

$$F_{2s} = \frac{N_0 \pi R_0^2 (-e\varphi_0)}{a_0 + 2} \int_0^{a_0+2} \cos C_1 dt \int_0^{a_0+2} \cos C'_1 dt_1. \quad (51)$$

In the case of  $a_0 \ll 1$ , i.e.,  $e |\varphi_0| \gg \varepsilon_0$ , we thus find in the same approximation as (28):

$$F_{2s} = 0, \quad (52)$$

---

\* Translator's note: This probably is a misprint in the original foreign text. The correct term should be  $w$ .

and for  $a_0 \gg 1$ , i.e.,  $e |\varphi_0| \ll \epsilon_0$ :

$$F_{2s} = F_{1n} \frac{4}{9} \left( 1 + \frac{2e |\varphi_0|}{\epsilon_0} \right). \quad (53)$$

(b) The body velocity is much less than the ion thermal velocity. For the braking force  $F_{2s}$ , we have

$$F_{2s} = \frac{N_0 \pi^{1/2} R_0^2 (-e\varphi_0)^3}{3 (kT)^2} \frac{V_0}{v_i} \int_0^\infty \frac{ae^{-\mu a}}{a+2} da \int_0^{a+2} \cos C_1 dt \int_0^{a+2} \cos C_1' dt_1. \quad (54)$$

For  $\mu \gg 1$ , i.e.,  $e |\varphi_0| \gg kT$ , we thus find in the same approximation as (30)

$$F_{2s} = 0, \quad (55)$$

and for  $\mu \ll 1$ , i.e.,  $e |\varphi_0| \ll kT$ ;

$$F_{2s} = F_{1n} \frac{4}{9} \left( 1 + \frac{e |\varphi_0|}{kT} \right). \quad (56)$$

Diffuse (according to Lambert) ion reflection with their neutralization on the body surface.

For the probability  $w$  we have the expression

$$w = \frac{M^2}{\pi} \frac{1}{\sqrt{2M(\epsilon_1 - e\varphi_0)}} \frac{\sqrt{2M\epsilon - (M/R_0)^2}}{\sqrt{2M\epsilon}} \delta(\epsilon_1 - \epsilon - e\varphi_0 R_0/r)|_{r=R_0}. \quad (57)$$

(a) The body velocity is much greater than the ion thermal velocity. The braking force  $F_{2s}$  is

$$F_{2s} = F_{1n} \frac{4}{9} \left( 1 + \frac{e |\varphi_0|}{\epsilon_0} \right)^{3/2}, \quad (58)$$

and the corresponding dependence of  $F_{2s}/F_{1n}$  on  $-e\varphi_0/\epsilon_0$  is shown in Figure 2, b (curve 2).

On the basis of (29) and (58), we have

$$F_s = F_{1n} \left[ \left( 1 + \frac{e |\varphi_0|}{\epsilon_0} \right) + \frac{4}{9} \left( 1 + \frac{e (\varphi_0)}{\epsilon_0} \right)^{3/2} \right]. \quad (59)$$

When the influence of the field is disregarded, formula (59) coincides with (6), as must be the case.

(b) The body velocity is much less than the thermal ion velocity. /252  
The expression for the braking force in this case has the form (see Figure 3, b, curve 2):

$$F_{2s} = F_{1s} \frac{2}{9} \int_0^{\infty} z^{1/2} (z + 2\mu)^{3/2} e^{-z} dz. \quad (60)$$

In the case of  $e |\varphi_0| \gg kT$

$$F_{2s} = F_{1s} \frac{\sqrt{\pi}}{9} \left( \frac{e |\varphi_0|}{kT} \right)^{3/2}, \quad (61)$$

and in the case of  $e |\varphi_0| \ll kT$

$$F_{2s} = F_{1s} \frac{4}{9} \left( 1 + \frac{3e |\varphi_0|}{4kT} \right). \quad (62)$$

Let us now examine the force  $F_c$  caused by particles which do not collide with the body, but which only interact with the electric field produced by the body charge. Because this is a Coulomb field, we can make immediate use of the well-known expression for the braking force of a Coulomb charge in a plasma, which is usually called the dynamic friction force [see (Ref. 14, 15)]:

$$F_c = F_{ci} + F_{ce} = \frac{4N_0\pi R_0^2 (e\varphi_0)^2}{kT} \left[ G\left(\frac{V_0}{v_i}\right) \ln \frac{b_m}{b_i} + G\left(\frac{V_0}{v_e}\right) \ln \frac{b_m}{b_e} \right], \quad (63)$$

where  $G(x)$  is the function introduced by Chandrasekhar (Ref. 14):

$$G(x) = \frac{G(x)}{2x^2} = \frac{e^{-x^2}}{\sqrt{\pi}x}. \quad (64)$$

Expression (63) only takes into account particles interacting slightly with the field, which make the main contribution to the braking force  $F_c$  for large values of  $D/R_0$ . The maximum collision parameter  $b_m$  thus equals the Debye radius. The minimum parameter  $b$  equals the largest of the two quantities: The body radius  $R_0$  or the distance  $b_1$  at which the particle trajectory changes greatly under the influence of the field. For example, for ions  $b_1 = -e\varphi_0 R_0 / Mv^2$ . Thus, the Coulomb logarithm for ions  $\ln(b_m/b_1)$  in formula (63) is

$$\ln \frac{b_m}{b_i} = \ln \left\{ \frac{D}{R_0} \left[ 1 + \left( \frac{e\varphi_0}{\varepsilon_0 + kT} \right)^2 \right]^{-1/2} \right\}. \quad (65)$$

The Coulomb logarithm is determined in a similar way for electrons.

If the body velocity is much less than the ion thermal velocity, then

$$F \approx F_{ci} = \frac{4\sqrt{2}}{3\sqrt{\pi}} N_0\pi R_0^2 \sqrt{kT M} V_0 \left( \frac{e\varphi_0}{kT} \right) \ln \frac{b_m}{b_i} = F_{1s} \frac{1}{2} \left( \frac{e\varphi_0}{kT} \right)^2 \ln \frac{b_m}{b_i}. \quad (66)$$

A graph showing the dependence of  $F_{ci}/F_{ln}$  on  $-e\varphi_0/kT$  is given in Figure 3,a (curves 3).

If the body velocity is much greater than the ion thermal velocity, then

$$F_{ci} = 2N_0\pi R_0^2 \epsilon_0 \left(\frac{e\varphi_0}{\epsilon_0}\right)^2 \ln \frac{b_m}{b_i} = F_{ln} \left(\frac{e\varphi_0}{\epsilon_0}\right)^2 \ln \frac{b_m}{b_i}. \quad (67)$$

It is shown in Figure 2, b (curves 3). We should note that the force  $F_{ci}$  decreases with an increase in the body velocity in the case of  $\epsilon_0 > kT$ .

In the case of  $V_0 \gtrsim v_c (M/m)^{1/6}$ , interaction with electrons becomes decisive. Figure 4 presents a graph showing the dependence of the total force  $F_c/A$  on  $\sqrt{\epsilon_0/kT}$ . Here  $A = 4\pi R_0^2 N_0 (e\varphi_0)^2 \ln(b_m/b) / kT$ . It was thus assumed that  $b_i = b_e = b$  and the ratio  $M/m \approx 1.84 \cdot 10^3$  (hydrogen). The first maximum  $F_c/A$  occurs for  $\sqrt{\epsilon_0/kT} = 1.0$ ; the second maximum occurs for  $\sqrt{\epsilon_0/kT} = \sqrt{M/m} = 42.9$ ; the minimum  $F_c/A$  occurs for  $\sqrt{\epsilon_0/kT} = 5.0$ .  $F_c/A$  equals 0.214 at the first and second maxima;  $F_c/A$  equals 0.064 at the minimum.

The dependence of the force  $F_{ls}/A$  on  $\sqrt{\epsilon_0/kT}$  is shown in the same figure for different values of  $e|\varphi_0|/kT$ , when the body velocity is much greater than the ion thermal velocity and the ratio  $e|\varphi_0|/\epsilon_0$  is small [see (28)].  $\ln(D/R_0)$  is assumed to equal 10.

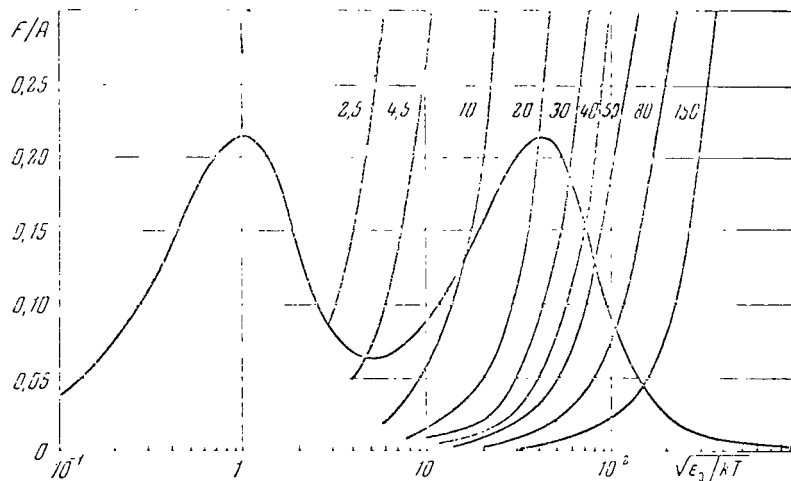


Figure 4

Dependence of Braking Force  $F_n$  on Body Velocity  
and Dependence of Force  $F_{ls}/A$  on  $\epsilon_0/kT$  for  
Different Values of  $e/\varphi_0/kT$

Figures 2 and 3 show the total braking forces of the body by incident and reflected (with neutralization) ions as well as by ions scattered by the field (curves 4). If the body velocity is much less than the ion thermal

velocity, it can be seen from Figure 3, a, b that for small  $e|\varphi_0|/kT$  ions colliding with the body surface play the main role in body braking by ions. In the case of  $e|\varphi_0|/kT \gtrsim 1$ , ions interacting only with the electric field in the vicinity of the body play the main role. Since in this case  $F_c \simeq F_{ci}$ , and the braking force by incident electrons is much less than the braking force by incident ions, it is clearly apparent that the body braking force is primarily caused by ions colliding with the body surface for small  $e|\varphi_0|/kT$ , i.e.,  $F \simeq F_s$ . In the case of  $e|\varphi_0| \gtrsim kT$ , the body braking force is primarily caused by ions interacting with the electric field, i.e.,  $F \simeq F_{ci}$ , where the force  $F_{ci}$  is given by formula (66).

If the body velocity is much greater than the ion thermal velocity, it can be seen from Figure 2, a, b that for small  $e|\varphi_0|/\epsilon_0$  ions colliding with the body surface make the main contribution to the ion body-braking force. In the case of  $e|\varphi_0|/\epsilon_0 \gtrsim 1$ , ions interacting with the electric field in the vicinity of the body make the main contribution. Thus, for small  $e|\varphi_0|/\epsilon_0$ , if condition  $\epsilon_0/kT > 0.4(e\varphi_0/kT)^2 \ln(D/R_0)$  (see Figure 4) is fulfilled, the braking force by ions colliding with the body surface is a decisive factor, i.e.,  $F \simeq F_s$ . In the case of  $e|\varphi_0| \gtrsim \epsilon_0$ , the dynamic friction force  $F_c$  makes the main contribution to the body braking force. In the case of  $\sqrt{\epsilon_0/kT} \gg (M/m)^{1/6}$ , the dynamic friction force of electrons  $F_{ce}$  makes the main contribution.

#### REFERENCES

/254

1. Schamberg, R. Aerodynamics of the Upper Atmosphere. Ed., Masson (Rand Corp.), 1959.
2. Jastrow, R., Pearse, C. A. J. Geophys. Res., 62, 413, 1957.
3. Chopra, K. P., Singer, S. F. Univ. of Maryland Phys. Dept., Tech. Rept., 97, 1958; Chopra, K. P. Rev. Mod. Phys., 33 (2), 153, 1961.
4. Brudin, C. L. AIAA Journal, 1, 2529, 1963.
5. Hohl, F., Wood, G. P. Rarefied Gas Dynamics. N. Y.-London, Acad. Press, 45, 1963.
6. Davis, A. H., Harris, I. Rarefied Gas Dynamics. N. Y.-London, Acad. Press, p. 691, 1961.
7. Beard, D. B., Johnson, F. S. J. Geophys. Res., 65, 1, 1960.
8. Wyatt, P. J. J. Geophys. Res., 65, 1673, 1960.
9. Licht, A. L. J. Geophys. Res., 65, 3493, 1960.



10. Al'pert, Ya. L., Gurevich, A. V., Pitayevskiy, L. P. Artificial Earth Satellites in a Rarefied Plasma (Iskusstvennyye sputniki v razrezhennoy plazme). Moscow, Izdatel'stvo "Nauka", 1964.
11. Moskalenko, A. M. Geomagnetizm i Aeronomiya, 5, 1965.
12. Gurevich, A. V. Geomagnetizm i Aeronomiya, 5, No. 2, 1965.
13. Moskalenko, A. M. Geomagnetizm i Aeronomiya, 4, No. 2, 260; No. 3, 509, 1964.
14. Chandrasekhar, S. Rev. Mod. Phys., 15, 1, 1943.
15. Spitzer, L. Physics of a Fully Ionized Plasma. Moscow, IL, 1957.

# ASYMPTOTIC FORM OF THE TRAIL OF A BODY MOVING IN A RAREFIED PLASMA

Yu. M. Panchenko

It is most interesting to study the structure of the trail formed behind a body A moving in a plasma (Ref. 1-4). The occurrence of a disturbed electron and ion concentration in a plasma can be reduced to solving a system of collisionless kinetic equations for the distribution function of charged particles, and the Poisson equation for a self-consistent potential. The necessity of employing kinetic equations is based on the fact that the mean free paths  $l_{i,e,n}$  in the plasma which we shall investigate, are much greater than the dimensions of the body itself  $R_0$ , as well as the characteristic dimensions of the strongly disturbed region  $\{\Omega\}$  beyond A, i.e.,

$$l_{i,e,n} \gg \{\Omega\} \gg R_0.$$

The Debye radius  $D = \sqrt{kT/4\pi e^2 N}$ , is also an important parameter in this problem, i.e., the distance at which the field of a point charge is screened. In its general form, the solution of this problem is very difficult, since the system of equations describing the disturbances is multidimensional and essentially nonlinear.

The influence of the electric field on the structure of the disturbed zone was considered in the works (Ref. 1-3) for a sphere of the radius  $R_0$ , which is much larger than the Debye radius, and for a small charged body (Ref. 1, 4) in the case of supersonic motion of bodies. However, a more comprehensive analysis of the corresponding results and numerical calculations are requisite for studying the structure of the disturbed zone. This was partially done in (Ref. 6). The distribution of particles around A has also been studied in works which have appeared recently (Ref. 7, 8).

The present study is devoted to a more detailed investigation of the trail structure in a distant zone (Ref. 11). By means of a linearized theory (Ref. 1, 2, 6), the disturbances in the concentrations of ions and neutral particles have been studied for different ratios  $a_0 = V_0/v_i$  of the body's velocity  $V_0$  to the thermal velocity  $v_i$  of ions. The corresponding results were obtained for a sphere, a cylinder, and a body whose dimensions are much smaller than the Debye radius. The solution of the corresponding system of equations in the Fourier components  $N_q$  and  $\varphi$  has the following form (Ref. 1, 2):

$$N_q = \frac{-i \int \frac{J(u)}{n(u - V_0) - i\delta} d^3u}{2 - i\delta F(u)}, \quad (1)$$

$$\varphi_q = \frac{kT}{M} N_q, \quad (2)$$

where  $N$  is the ion concentration;  $\varphi$  - the field potential;  $J(u)$  - the collision integral;  $n = \mathbf{q}/|\mathbf{q}|$  - the unit vector.

$$a = a_0 \frac{qV_0}{q}, \quad a_0 = V_0 \sqrt{M/2kT},$$

$$F(a) = \left( \sqrt{\pi} + 2i \int_0^a e^{-x^2} dx \right) e^{-a^2}. \quad (2a)$$

In (1)  $J(u)$  is the only parameter which takes into account the form and dimensions of  $A$ , its velocity  $V_0$ , the length of the region  $\Omega_1$ , and also the nature of the interaction between the space charge  $Q_{\Omega_1}$  and the plasma.

It is naturally impossible to calculate  $J(u)$  in the general case, since the electric field around the body is not known. Therefore, in each specific case definite assumptions must be formulated regarding the form of  $J(u)$ .

# 1. A WEAKLY-CHARGED SPHERE OF THE RADIUS $R_0$ , WHICH IS LARGE AS COMPARED WITH THE DEBYE RADIUS

If the sphere  $A$  is weakly charged, the electric field  $\varphi(\mathbf{r})$  of the body  $A$  is screened entirely by ions in the Debye layer, and the field  $\varphi_{\Omega_1}(\mathbf{r})$  penetrating the plasma farther than the Debye radius is small. The energy acquired by an ion located in the field  $\varphi_{\Omega_1}(\mathbf{r})$  is much less than the kinetic energy of ions with respect to the body  $e\varphi \ll MV_0^2/2$ , and it can be disregarded in comparison with  $MV_0^2/2$ . Ions with the impact parameters  $\rho$  which are smaller than  $\rho \ll R_0 + D$  are absorbed by the body.

For this reason, the influence of the electric field on the quantity  $J(u)$  can be disregarded, and it can be assumed to equal the number of ions impacting on the surface of the body, i.e.,

$$J(u) = \pi R_0^2 |u - V|/v_0 \simeq \pi R_0^2 / v_0 \left( 1 - \frac{u}{v_0} + o\left(\frac{u^2}{v_0^2}\right) \right). \quad (3)$$

The substitution of (3) in (1) yields the following for the sphere (Ref. 1, 2):

$$N_q = \frac{\pi R_0^2 N_0}{q} a_0 \frac{F(a) (1 + o(a_0^{-2}))}{2 + iaF(a)}. \quad (4)$$

The influence of the electric field is denoted by a denominator in this formula. If it is assumed that this denominator equals unity, then the right portion of (4) is a Fourier form of the corresponding expression for neutral particle concentrations.

In order to determine the disturbance of the ion concentration from  $N_q$ , it is necessary to perform reverse Fourier transformation:

$$\delta N(r) = N_i(r) - N_0 = -\frac{1}{(2\pi)^3} \int_{(q^2)} N_q e^{i\mathbf{q}\cdot\mathbf{r}} d^3q. \quad (5)$$



The angular function  $f_i(a_0, \theta)$  was calculated numerically for different values  $a_0 = 8, 7, 6, 5, 4, 3, 2$  which corresponds to the velocity of the body  $V_0 = 8, 7, 6, 5, 4, 3, 2 \text{ km} \cdot \text{sec}^{-1}$  for a plasma temperature of  $T = 1500^\circ$ .

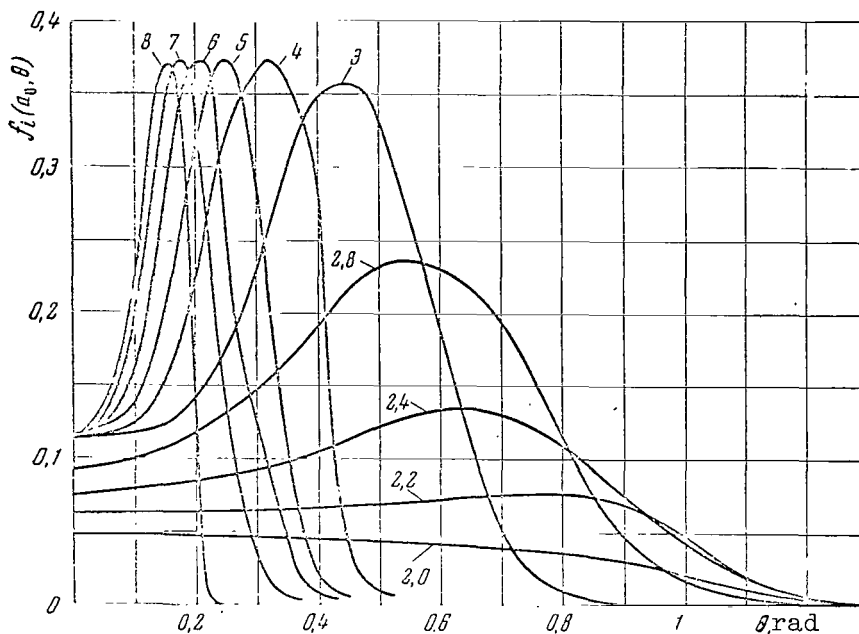


Figure 2

Figure 2 presents the results derived from calculating  $f_i(a_0, \theta)$  for different values of  $a_0$ . It can be seen from Figure 2 that the calculation of the ion concentration disturbance, taking the electric field into account, leads to an angular dependence which is new as compared to neutral particles and to a general decrease in  $\delta N_i(r)$ , as compared with  $\delta n(r)$ . The disturbance maximum is now reached at the angle  $\theta_m$  to the direction which is opposite that of the body's motion, i.e., on the surface of a cone having the angle of opening  $2\theta_m$ , which is an analog of the Mach cone in hydrodynamics. For  $a_0 = 8, 7, 6, 5, 4, 3$ , we accordingly have  $\theta_m = 0.155, 0.178, 0.21, 0.25, 0.31, 0.45$ . The disturbance has a minimum along the axis of the body's motion - i.e.,  $\delta N_i(a_0, \theta = \theta_m) < N_i(a_0, \theta = 0)$ .

It is interesting to note that for  $a_0 = 3$  and large values of  $a_0$  ( $a_0 \gg 1$ ),  $f_i(a_0, \theta)$  depends only on one parameter  $\xi = a_0 \sin \theta$ . Therefore, the curves of  $f_i(a_0, \theta)$  are the same in Figure 2 with respect to  $\xi$  for  $a_0 = 3, 4, \dots, 8$ . /257

We should note that the ratio  $f_i(a_0, \theta_m)/f_i(a_0, \theta = 0)$  (i.e., the value of  $f_i(a_0, \theta_m)$  at the disturbance maximum) to  $f_i(a_0, \theta = 0)$ , where the disturbance is at a minimum for all  $a > 3$ , is close to 3.32 - i.e.,

$$\beta_{lat} = f_i(a_0, \theta_m)/f_i(a_0, 0) = 3.22.$$

The mathematical meaning of the results obtained can be readily understood. It follows from (9) that for  $a_0 \gg 3$ ,  $f_i(a_0, \theta)$  depends not on the two parameters  $a_0$  and  $\theta$ , but on one parameter  $\xi = a_0 \sin \theta$ , since the last two terms in (9) equal zero for  $a_0 \gg 3$ . By determining the angular function in the form (9), we performed integration in (7) with respect to the contour  $C^*$ , i.e., we employed the properties of the function at the contour, where  $\Psi(a_0 \sin \theta, t)$  has its own peculiarities. When the contour  $C_R$  is traversed (Figure 1), it is possible to determine the same function  $f_i(a_0, \theta)$ , but employing the features  $\Phi(t)$ . As can be seen from (8),  $\Phi(t)$  has features only in the form of discrete poles, which lie at the same points where the function  $W(z)$  has zeros:

$$W(z) = 1 - ze^{-z^2} \int_0^z e^{x^2} dx + i \frac{\sqrt{\pi}}{2} ze^{-z^2} = 0. \quad (10)$$

By determining the roots  $z_n(10)$ , we can determine  $f_i(a_0, \theta)$  as the sum of the residues along all the poles.

The physical meaning of the obtained angular distribution for the disturbance behind the body can be readily understood.

If substitution is performed in  $W(z)$  in the form of (10):

$$z = \frac{V_0}{v_i} \cos \theta \rightarrow \frac{V_0}{v_i} \frac{\omega' + i\omega''}{k} = \beta_i,$$

then  $W(z)$  is the left side of the dispersion equation

$$\frac{T_i}{T_e} + 1 - i\beta_i F(\beta_i) = \frac{T_i}{T_e} i\beta_e F(\beta_e) \approx 0,$$

which determines the possible spectrum of longitudinal fluctuations in an electron-ion plasma, which correspond to ion sound waves (Ref. 9).

The dispersion law for such acoustic waves for  $T_i \cong T_e$  is known (Ref. 10), namely: /258

$$\omega(k) = \omega'(k) + i\omega''(k) = \sqrt{2kT_e/M} 1.48 (1 + i0.36) k.$$

Since  $\omega''(k)$  and  $\omega'(k)$  are comparable, these sound fluctuations must be greatly attenuated in a plasma having a single temperature.

Thus, for the supersonic motion of the body which is presently being examined, phenomena related to the generation of acoustic waves are possible in the distribution of ions around A, and do actually appear. The maximum perturbation of the ion concentration is observed on a surface coinciding with the Mach cone for ion-sound waves (see Figure 2) at angles of  $\theta_m = \arctg 1.30\sqrt{2kT/MV_0^2}$ . However, due to the fact that these waves are strongly attenuated, this Mach cone is less sharply expressed than in normal hydrodynamics. The kinetic energy of the body is the energy source of wave excitation, i.e., the body is damped.

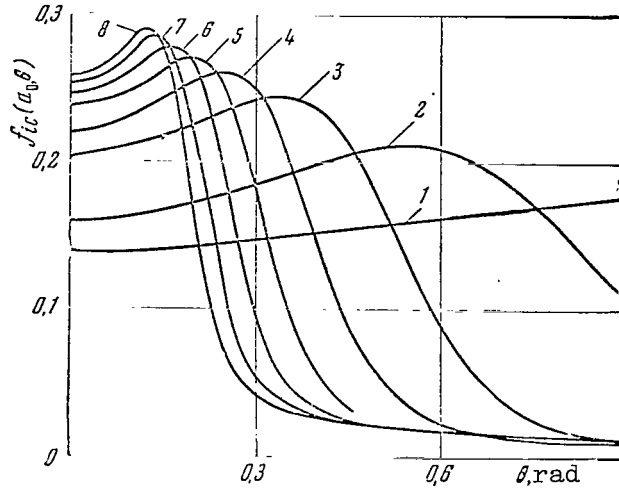


Figure 3

## 2. Perturbation in the Vicinity of a Weakly-Charged Cylinder ( $R_0 \gg D$ )

Just as in the case of a sphere, when an infinitely long cylinder  $C$  moves in a plasma, two regions can be distinguished behind it: the close region  $\Omega_1$  where the perturbation  $\delta N_1(r)$  of the ion concentration is large, and the far region  $\Omega_2$ , where  $\delta N_1(r)$  is small. Such a problem is similar to the problem for a sphere. Its solution in Fourier components has the following form:

$$N_q = \frac{1}{q} \frac{-i \int n(u - V_0) \frac{J(u)}{u - i\delta} d^2u}{1 + \frac{M}{2\pi kT} \int n(u - V_0) \frac{u}{u - i\delta} \exp\left(-\frac{Mu^2}{2kT}\right) d^2u}, \quad (11)$$

where the function  $J(u)$ , just as in the case of a sphere, is described in the form

$$J(u) = \pi R_0 |u - V_0| f_0 \cong \pi R_0 f_0 V_0. \quad (12)$$

Substituting (12) in (11), we find that

$$N_q = 2R_0 N_0 a_0 \frac{F(a)}{q(2 + iaF(a))}, \quad (13)$$

where  $F(a)$  is determined in the form of (2a). The reverse Fourier transformation

$$\delta N(r) = \frac{1}{(2\pi)^2} \int_{(q^2)} d^2q N_q e^{iqr} \quad (14)$$

at the polar coordinates  $r, \theta$  yields

$$\delta N(r) = \frac{1}{(2\pi)^2} \int_0^{2\pi} \frac{F(a_0 \cos \alpha) d\alpha}{2 + ia_0 \cos \alpha F(a_0 \cos \alpha)} \int_0^\infty e^{iqr \cos(\theta - \alpha)} dq.$$

The integral with respect to  $dq$  diverges for large  $q$ , which is related to the fact that  $N_q$  in the form of (11) is valid only for small  $q$  ( $q \ll 1/R_0 a$ ).

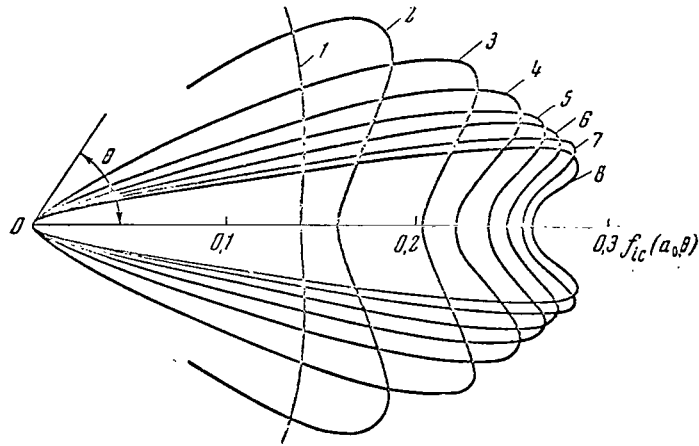


Figure 4

For large  $q$ , i.e., at small distances from  $C$ ,  $N^q$  decreases more rapidly than  $1/q$ . Therefore, in order to attribute the correct meaning to the integral with respect to  $dq$ , we must make it convergent, but must not change the behavior of the integrand for small  $q$ . In order to do this, let us go around the contour  $C^*$  (see Figure 1). After the circuit, we have

$$\int_0^\infty e^{iqr \cos(\theta-\alpha)} dq = \pi \left\{ \delta \cos(\theta-\alpha) + \frac{i}{\pi} \text{P.V.} \frac{1}{\cos(\theta-\alpha)} \right\}, \quad (15)$$

where the symbol P.V. means that the integral must be taken in the meaning of the principal value. Finally, in the region  $\Omega_2$  the ion distribution for the cylinder is: /259

$$\frac{\delta N_i(r, \theta)}{N_0} = \frac{R_0}{\pi r} a_0 f_{ic}(a_0, \theta). \quad (16)$$

Here

$$f_{ic}(a_0, \theta) = \text{Re } \Phi(a_0 \sin \theta) + \frac{1}{\pi} \text{P.V.} \int_0^\pi \frac{\text{Im } \Phi(a_0 x)}{\cos(\theta-\alpha)} d\alpha \quad (17)$$

and  $\Phi(a_0, t)$  is determined from (8). As can be seen from (16), at large distances from the cylinder the perturbation of ion concentration decreases as  $1/r$ .

The angular function  $f_{ic}(a_0, \theta)$  is calculated for the values  $a_0=8, 7, \dots, 1$ . The results are shown in Figures 3 and 4. Figure 3 is constructed in a Descartes coordinate system; the angle  $\theta$  is plotted along the abscissa, and the absolute value  $f_{ic}(a_0, \theta)$  is plotted along the ordinate. In Figure 4,  $f_{ic}(a_0, \theta)$  is formulated in a polar coordinate system. The angular /260 functions  $f_i(a_0, \theta)$  for a sphere and a cylinder in the case of  $a_0=8$  and 3 are compared in Figure 5. It can be seen from Figure 5 that  $f_i(a_0, \theta)$  and  $f_{ic}(a_0, \theta)$  have the same nature. The maximum perturbation corresponds to angles which are close to  $\theta_m$  for a sphere.



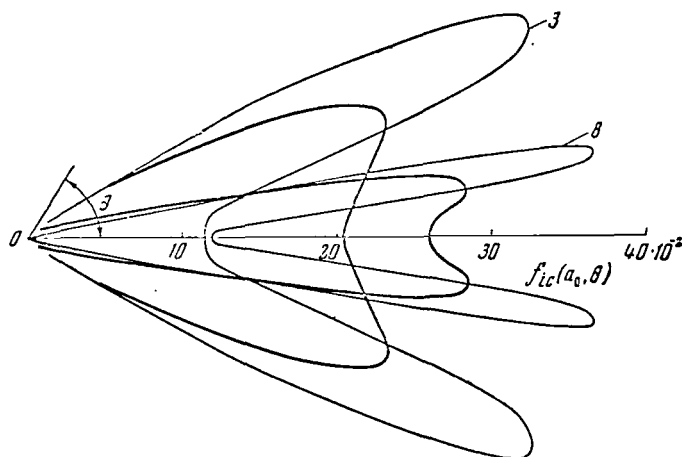


Figure 5

In contrast to the sphere A, for  $f_{ic}(a_0, \theta)$  a similarity is observed for  $f_{ic}(a_0, \theta)$  in the case of large  $a_0$  ( $a_{0c} \gg 6$ ), and has the following features:

$$\beta_{cyl} = \lim_{a_0 \gg 1} \frac{f(a_0, \theta = 0_m)}{f(a_0, \theta = 0)} \rightarrow \text{const} \sim 1,03 \quad (18)$$

$$\lim_{a_0 \gg 1} \frac{\beta_{sph}}{\beta_{cyl}} \rightarrow \pi. \quad (19)$$

The latter condition is related to the fact that when the cylinder moves it excites cylindrical ion-sound waves, while a sphere excites spherical waves, whose intensity must be  $\pi$  times greater than that of cylindrical waves. It can also be assumed from (18) and (19) that the zone  $\Omega_2$  in a moving cylinder begins approximately  $\pi$  times farther away than in a sphere.

### 3. Small Body

Let us now examine a body moving in a plasma with the charge  $Q = Ze$ . The dimensions of this body are much smaller than the Debye radius, and we shall regard it as a "point" body. More precisely, the smallness of the body is determined by means of criterion (23). We must keep the fact in mind that the solution of this problem will be valid in specific cases for bodies having finite dimensions.

The perturbation of the ion concentration was determined in the work (Ref. 5) by the perturbation method. The Fourier component  $N_q$  in the first approximation in powers of  $\frac{Ze}{kT}$  has the following form without a magnetic field:

$$N_q^{(1)} = \frac{-Z}{2(Dq)^2 + 2 + iaF(a)}. \quad (20)$$

However, it was shown in the work (Ref. 1, 2) that at large distances from the body the results of (Ref. 5) are incorrect, since in this case the 261 terms which are proportional to  $(qZe^2/kT)^2$  must also be taken into consideration. In the Fourier components, the corresponding solution is as follows:

$$N_q = \frac{-i \int \frac{J(u) - iquf_0 Z}{qvN_0} d^3v}{2(Dq)^2 + 2 + iaF(a)}. \quad (21)$$

For a point body, the function  $J(u)$  equals the number of ions scattered per unit of time by the field of the body charge.

$$J(u) = 2\pi f_0 N_0 \left\{ a_0^2 + \frac{iJ}{2(kT)^2} (V_0^2 v^2 - (V_0 v)^2) \right\} \vartheta^2(\rho) \rho d\rho. \quad (22)$$

If the charge of the body  $A$  is sufficiently small, and if

$$\frac{Ze^2}{a_0 D} \frac{1}{kT} = \varepsilon = \frac{e\varphi(D)}{a_0 kT} = \frac{e\varphi_0 D}{a_0 kT \rho_1} \ll 1, \quad (23)$$

then the field  $\varphi(r)$ , which penetrates the plasma farther than  $D$ , is small and its contribution to the scattering cross section can be disregarded. In this case, the main contribution to  $J(u)$  is only made by the values of the impact parameter  $\rho$  which are smaller than the Debye radius, where it can be assumed that it is a Coulomb field.

However, for purposes of simplification we shall not truncate the radius of action of the Coulomb forces, but rather the impact parameters  $\rho$ , assuming that the maximum value of  $\rho$  equals  $D$ . In other words, it is assumed that ions are influenced by  $\varphi(r)$  throughout all of the motion in the case of  $\rho < D$ .

The computational results finally yield (Ref. 1, 2):

$$N_q = N_q^{(1)} + N_q^{(2)} = \frac{-Z}{2(Dq)^2 + 2 + iaF(a)} - 2\pi N_0 a_0 e^2 \ln \frac{D}{\rho_1} \frac{1}{q} \frac{\left[ 1 - \left( u \frac{V_0}{V_0} \right)^2 \right] \{ (1 - 2a^2) F(a) + 2ia \}}{2(Dq)^2 + 2 + iaF(a)}, \quad (24)$$

and the perturbation  $N(r)$  is determined - just as above - by means of inverse  $N_q$  - Fourier transformation. The complete computation, however, is complex, and it is impossible to complete it analytically. Therefore, we shall first examine perturbation of ion concentration at large distances from a charged body. According to (24), the quantity  $N_q$  has an asymptotic form in the case of  $Q \rightarrow 0$ :

$$N_q = N_q^{(1)} + N_q^{(2)} = \frac{-Z}{2 + iaF(a)} - 2\pi N_0 a_0 e^2 \ln \frac{D}{\rho_1} \frac{D^2}{q} \frac{\left[ 1 - \left( u \frac{V_0}{V_0} \right)^2 \right] \{ (1 - 2a^2) F(a) + 2ia \}}{2 + iaF(a)}. \quad (25)$$

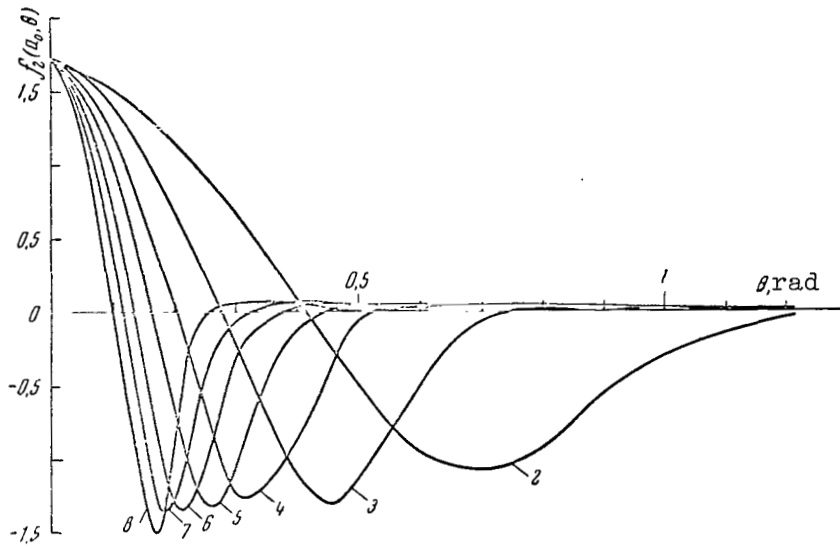


Figure 6

Introducing a spherical coordinate system with the axis along  $V_0$  and designating the angle between  $r$  and  $V_0$  by means of  $\theta$  as is usually done, we have:

$$\begin{aligned} \delta N_i(r) &= \delta N_i^{(1)}(r) + \delta N_i^{(2)}(r) = \\ &= \frac{Z}{2(2\pi)^2} \int_0^{\pi} K(a_0 t) dt \int_0^{\infty} J_0(qr \sin \theta \sqrt{1-t^2}) e^{iqr \cos \theta t} q^2 dq - \\ &\quad - \frac{N_0 a_0^2 \ln D/\rho_1}{4\pi} \int_0^{\pi} \frac{(1-t^2)(1-2a_0^2 t^2) F(a_0 t) + 2ia_0 t}{2 + ia_0 t F(a_0 t)} \int_0^{\infty} q dq \times \\ &\quad \times J_0(qr \sin \theta \sqrt{1-t^2}) e^{iqr \cos \theta t}, \end{aligned} \quad (26)$$

where

$$K(a_0 t) = [1 + 0.5iaF(a)]^{-1}.$$

The integrals in (26) with respect to  $dq$  diverge for large  $q$ , which is due to the fact that (25) is only valid for small  $q$ . Therefore, in order to attribute the correct meaning to  $\delta N(r)$ , integration with respect to  $q$  in (26) is performed along the contour  $C^*$  (see Figure 1). Taking into account the given selection of branches and integrating the first term by parts three times in (26) - and the second term, two times - we finally have:

$$\delta N(r, a_0 \theta) = \frac{-ZD^3}{r^3} f_1(a_0, \theta) - \frac{N_0 a_0^2 \ln D/\rho_1}{2\pi} \left(\frac{D}{r}\right)^2 f_2(a_0, \theta), \quad (27)$$

where

$$\begin{aligned}
f_1(a_0, \theta) = & \frac{a_0}{2\pi^2 D^3} \left[ a_0 \int_0^{\sin \theta} \operatorname{Re} K''(a_0 t) \sqrt{\sin^2 \theta - t^2} dt - \right. \\
& - 2 \cos \theta \operatorname{Im} K'(a_0) + a_0 \int_{\sin \theta}^1 \operatorname{Im} K''(a_0 t) \sqrt{t^2 - \sin^2 \theta} dt + \\
& + \cos^2 \theta \left\{ \frac{\pi}{2} a_0 \operatorname{Re} K''(a_0 \sin \theta) - a_0 \operatorname{Im} K''(a_0 \sin \theta) \ln \sin \theta - \right. \\
& - a_0 \operatorname{Im} K''(a_0) \cos \theta \ln(1 + \cos \theta) - a_0^2 \int_0^{\sin \theta} \operatorname{Re} K'''(a_0 t) \arcsin \frac{t}{\sin \theta} dt + \\
& \left. \left. + a_0^2 \int_{\sin \theta}^1 \operatorname{Im} K'''(a_0 t) \ln(t + \sqrt{t^2 - \sin^2 \theta}) dt \right\} \right], \quad (28)
\end{aligned}$$

and  $f_2(a_0, \theta)$  is determined according to (9), if we substitute  $K(a_0, \theta)$  instead of  $\Phi(a_0, \theta)$ .

The obtained expressions are only valid at large distances from the body. The first term in (27) produces a decrease in the perturbation  $\delta N_1(r, \theta)$  as  $1/r^3$ ; the second term - as  $1/r^2$ . Numerical computations were performed in order to determine the form of the angular dependence  $f(a_0, \theta)$ . The curves of the function  $f_2(a_0, \theta)$  are compiled in Figure 6 as a function of  $\theta$ , when  $a_0$  changes from 8 to  $2^{-1}$ .

The angular function of the ion concentration  $f_2(a_0, \theta)$  for a point body has the following features. In the first place, the curves in Figure 6 are similar with respect to  $\xi = a_0 \sin \theta$ . In the second place, for  $\delta N_1^{(2)}(r)$  an alternation of crowding occurs with rarefaction. On the axis which is opposite the motion of the body, there is an increase in the ion concentration as compared with  $N_0$ , which takes place by a depletion of the adjacent regions, i.e.,  $N_1(a_0, \theta = 0) > N_0$  - a "focusing" of ions occurs on the  $-V_0$  axis. Just as previously, the maximum rarefaction is achieved on a cone with the angle of opening  $2\theta_m = 2 \arctg 1.30 \sqrt{2kT / MV_0^2}$ . After the rarefaction there is a new crowding, which is small in terms of magnitude; the maximum of this crowding lies on the cone with the opening  $2\theta \simeq 4\theta_m$ . /263

The ion concentration distribution at distances on the order of, or more than, the Debye radius requires a special investigation. In this case it is necessary to determine the inverse Fourier transformation from  $N_q$  in the form of (24). The first term in (24) thus produces an increase in the perturbation at small distances from the body as  $1/r$ ; the second term - as  $\ln r$ . However, the form of the dependence of  $N(r, \theta)$  on  $r$  and  $\theta$  is complex, and we shall present it here without intermediate computations (Ref. 11).

---

<sup>1</sup> It is clear that for large  $r$  - the  $\Omega_2$  region - the second term is the main term in (27).

$$\delta N_i(r, \theta) = \delta N_i^{(1)}(r, \theta) + \delta N_i^{(2)}(r, \theta); \quad (29)$$

$$\delta N_i^{(1)}(r, \theta) = \frac{\pi}{2} \frac{Z}{D^3} \left[ \left( \frac{D}{r} \right) - I_1 - I_2 \right]; \quad (30)$$

$$\delta N_i^{(2)}(r, \theta) = -\frac{a_0 e^2}{2\pi} n_0 [I_3 + I_4 + I_5 - I_6], \quad (31)$$

where

$$I_1(r, \theta) = \int_0^1 dt \int_0^\infty dx J_0 \left( x \frac{r}{D} \sin \theta \sqrt{1-t^2} \right) \cos \left( x \frac{r}{D} \cos \theta t \right) \operatorname{Re} K(x, t);$$

$$I_2(r, \theta) = \int_0^1 dt \int_0^\infty dx J_0 \left( x \frac{r}{D} \sin \theta \sqrt{1-t^2} \right) \sin \left( x \frac{r}{D} \cos \theta t \right) \operatorname{Im} K(x, t);$$

$$I_3(r, \theta) = \sqrt{\pi} \int_0^1 dt (1-t^2) (1-2a_0^2 t^2) e^{-a_0^2 t^2} \int_0^\infty dx J_0 \left( x \frac{r}{D} \sin \theta \sqrt{1-t^2} \right) \times \\ \times \cos \left( x \frac{r}{D} t \cos \theta \right) \operatorname{Re} K(x, t);$$

$$I_4(r, \theta) = \sqrt{\pi} \int_0^1 dt (1-t^2) (1-2a_0^2 t^2) e^{-a_0^2 t^2} \int_0^\infty x dx \times \\ \times J_0 \left( x \frac{r}{D} \sin \theta \sqrt{1-t^2} \right) \sin \left( x \frac{r}{D} t \cos \theta \right) \operatorname{Im} K(x, t);$$

$$I_5(r, \theta) = 2 \int_0^1 dt (1-t^2) \left[ (1-2a_0^2 t^2) e^{-a_0^2 t^2} \int_0^{a_0 t} e^{x^2} dx + a_0 t \right] \int_0^\infty x dx \times \\ \times J_0 \left( x \frac{r}{D} \sqrt{1-t^2} \sin \theta \right) \cos \left( x \frac{r}{D} t \cos \theta \right) \operatorname{Im} K(x, t);$$

$$I_6(r, \theta) = 2 \int_0^1 dt (1-t^2) \left[ (1-2a_0^2 t^2) e^{-a_0^2 t^2} \int_0^{a_0 t} e^{x^2} dx + a_0 t \right] \int_0^\infty x dx \times \\ \times J_0 \left( x \frac{r}{D} \sqrt{1-t^2} \sin \theta \right) \sin \left( x \frac{r}{D} t \cos \theta \right) \operatorname{Re} K(x, t);$$

$$K(x, t) = (1 - ia_0 t F(a_0 t) + x^2)^{-1}.$$

In conclusion, I would like to express my appreciation to Ya. L. Al'pert, and L. P. Pitayevskiy for discussing the problems examined in the article.

#### REFERENCES

/264

1. Pitayevskiy, L. P., Kresin, V. Z. Zhurnal Eksperimental'noy i Teoreticheskoy Fiziki, 40, 271, 1961; Geomagnetizm i Aeronomiya, 1, No. 2, 194, 1961.
2. Al'pert, Ya. L., Gurevich, A. V., Pitayevskiy, L. P. Artificial Satellites in a Rarefied Plasma (Iskusstvennyye sputniki v razrezhennoy plasme). Izdatel'stvo "Nauka", 1964.

3. Al'pert, Ya. L. Geomagnetizm i Aeronomiya, 5, " , 3, 1965.
4. Gurevich, A. V. Trudy Instituta Zemnogo Magnetizma i Radiovolnovogo Rasprostraneniya (IZMIRAN), SSSR, No. 17, (27), 173, 1960; In "Iskusstvennyye Sputniki Zemli", No. 7, Izdatel'stvo AN SSSR, p. 101, 1961.
5. Kraus, L., Watson, K. Phys. Fluids, 1, 480, 1958.
6. Panchenko, Yu. M., Pitayevskiy, L. P. Geomagnetizm i Aeronomiya, 4, No. 2, 256, 1964.
7. Maslennikov, M. V., Sigov, Yu. S. Doklady AN SSSR, 159, No. 5, 1013, 1964.
8. Pashchenko, N. T. Prikladnaya Matematika i Teoreticheskaya Fizika, No. 5, 3, 1964.
9. Silin, V. P., Rukhadze, A. A. Electromagnetic Properties of a Plasma and Plasma-like Media (Elektromagnitnyye svoystva plazmy i plazmopodobnykh sred). Atomizdat, p. 100, 1961.
10. Silin, V. P., Zhurnal Eksperimental'noy i Teoreticheskoy Fiziki, 23, 649, 1959.
11. Panchenko, Yu. M. Geomagnetizm i Aeronomiya, 5, No. 6, 1965.

# PERTURBED ZONE STRUCTURE IN THE VICINITY OF A CYLINDRICAL BODY IN A PLASMA

A. M. Moskalenko

This article employs a kinetic theory to calculate the electric field and plasma perturbation in the vicinity of a charged, infinite cylinder, when the cylinder radius  $R_0$  is much greater than the Debye radius  $D$ . A similar problem has been studied for a spherical body in (Ref. 1, 2).

The expressions obtained in (Ref. 3) are employed for the concentration of attracted and repulsed particles in a cylindrical potential field when there is a fully absorbent cylindrical surface. After this, the problem is reduced to integrating the Poisson equation for the field potential  $\varphi(r)$

$$\frac{1}{r} \frac{d}{dr} \left( r \frac{d\varphi}{dr} \right) = -4\pi e [N_i(r, \varphi) - N_e(r, \varphi)] \quad (1)$$

with the boundary conditions  $\varphi(R_0) = \varphi_0$ ,  $\varphi_{r \rightarrow \infty} = 0$ , where  $r$  is the distance from the cylinder axis;  $e$  - ion charge (electron charge =  $-e$ ), and  $N_i(r, \varphi)$  and  $N_e(r, \varphi)$  - concentrations of electrons and ions, respectively. For purposes of determinacy, we assume that  $\varphi_0 > 0$ , so that electrons are the attracted particles, and ions are the repulsed particles. However, all of the investigation conducted below is completely symmetrical with respect to the charge sign of a cylinder. Particles which have finite (with respect to  $r$ ) motion are not taken into account.

Equation (1) can be rewritten as follows in dimensionless variables  $\xi = r/R_0$ ,  $\varphi^* = e\varphi/kT$ :

$$\frac{1}{\xi} \frac{d}{d\xi} \left( \xi \frac{d\varphi^*}{d\xi} \right) = \left( \frac{R_0}{D} \right)^2 \left\{ \frac{N_e(\xi, \varphi^*)}{N_0} - \frac{N_i(\xi, \varphi^*)}{N_0} \right\} \quad D = \left( \frac{kT}{4\pi e^2 N_0} \right)^{1/2} \quad (2)$$

Since a large parameter occurs before the right side of equation (2), it is clear that everywhere where  $\frac{d\varphi^*}{d\xi} \ll \frac{R_0}{D} \varphi^*$  the solution for equation (2)

coincides with the solution of the quasineutrality equation  $N_e(\xi, \varphi^*) = N_i(\xi, \varphi^*)$ , within an accuracy of small terms on the order of  $(D/R_0 \varphi^*)^2 (d\varphi^*/d\xi)^2$ . The latter condition in the vicinity of a cylinder having a large radius, for potentials  $\varphi_0$  which are not too large, is fulfilled only in a double layer having a thickness on the order of the Debye radius close to the cylinder surface. In the expression for  $N_i$   $\varphi(R_0) = \varphi_0$ , i.e., the field potential on the body surface, and in the expression for  $N_e$  in the same equation  $\varphi(R_0) = \varphi_1$ , where  $\varphi_1$  is the boundary value of the potential. The potential  $\varphi_1$  represents a solution of the equation  $N_e(\xi, \varphi^*) = N_i(\xi, \varphi^*)$  in the case of  $r \rightarrow R_0$ , i.e., in the case of  $\xi \rightarrow 1$  [see (Ref. 4)]. /265

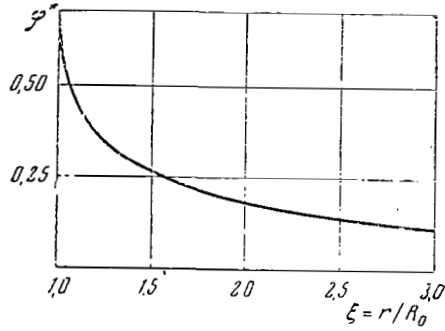


Figure 1

Field Potential Change in the Vicinity of the  
Body for  $e\varphi_0/kT \gg 1$

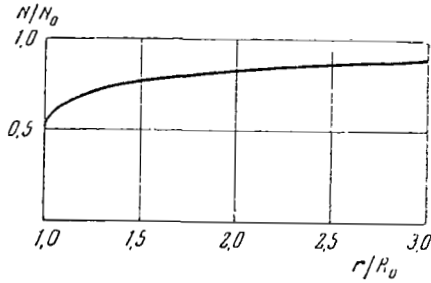


Figure 2

Particle Concentration Change in the Vicinity of the  
Body for  $e\varphi_0/kT \gg 1$

The solution of equation (2) can only be successfully obtained by the iteration method. Figure 1 presents the corresponding dependence  $\varphi^*(\xi)$ , and Figure 2 presents the dependence of ion concentration on distance from the cylinder axis.

The electron flux per unit length of the cylinder surface can be determined by the formula in (Ref. 4)

$$I_e = I_{0e} \left\{ \frac{2}{V\pi} V\overline{\varphi_{01}^* \xi_{01}^2} + e^{\varphi_{01}^* \xi_{01}^2} [1 - \Phi(V\overline{\varphi_{01}^* \xi_{01}^2})] + \right. \\ \left. + \frac{1}{2} \int_1^{\xi_{01}} (\xi_0^2 - 1) \left( 3 \frac{d\varphi^*}{d\xi_0} + \xi_0 \frac{d^2\varphi^*}{d\xi_0^2} \right) \exp \left[ \varphi^*(\xi_0) - \frac{\xi_0}{2} (\xi_0^2 - 1) \frac{d\varphi^*}{d\xi_0} \right] \times \right. \\ \left. \times \left[ 1 - \Phi \left( \frac{1}{V} \sqrt{\frac{-\xi_0^2}{2} \frac{d\varphi^*}{d\varphi_0}} \right) \right] d\xi_0 \right\},$$



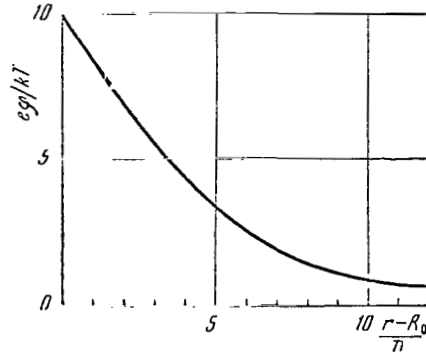


Figure 3

Dependence of Field Potential, in Double Layer  
Around a Cylindrical Body Surface in the Case  
of  $\varphi_0 = 10 \text{ kT/e}$ , Upon Distance From the Body Surface

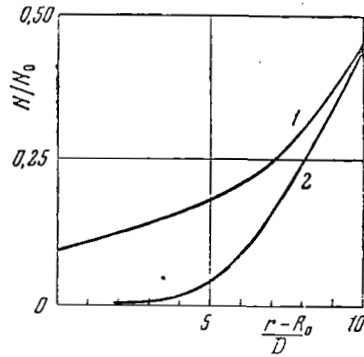


Figure 4

Dependence of Concentration of Particles Attracted (1)  
and Repulsed (2) in a Double Layer for  $\varphi_0 = 10 \text{ kT/e}$   
Upon Distance From the Body Surface

where  $I_{0e}$  is the particle flux per unit length of the cylinder surface in the absence of a field,  $I_{0e} = 2N_0R_0 \sqrt{\frac{\pi kT}{2m}}$ ;  $m$  - electron mass and  $N_0$  -

electron concentration in an unperturbed plasma, and  $\Phi(x)$  - probability integral. The ion flux per unit length of the cylinder surface, as was shown in (Ref. 3), is determined by the simple expression

$$I_i = I_{0i} \exp(-\varphi_0^*), \quad I_{0i} = 2N_0R_0 \sqrt{\frac{\pi kT}{2M}},$$

where  $M$  is the ion mass. Taking into account the expressions obtained for electron and ion fluxes, we can naturally formulate the probe characteristics - the curve showing the dependence of the flux per unit length of the cylinder surface

$$I = e(I_i - I_e)$$

upon the surface potential.

In a double layer around the cylinder surface, the electron and ion concentrations differ substantially. In this zone we must solve the total equation (1) with allowance for the following boundary conditions: In the case of  $\xi = 0$ , the field potential  $\varphi^* = \varphi_0^*$ , and in the case of  $\xi \rightarrow \infty$  the potential  $\varphi^* = \varphi_1^*$ , where  $\varphi_1$  is the field potential at the double layer boundary.

Numerical integration of this equation yields the field potential dependence on distance; Figure 3 presents this dependence for  $\varphi_0^* = 10$ . The dependence of electron and ion concentrations on distance in the double layer is given in Figure 4. It can be seen from the figure that the ion and electron concentrations decrease substantially when the cylinder surface is approached. With an increase in  $\varphi^*$ , the ion concentration decreases much more rapidly than the electron concentration. Thus, the field strength in the case of  $\varphi^* \gg 1$  is

$$E = (16\pi C)^{1/2} (N_0 kT)^{1/2} (e\varphi/kT)^{1/4}.$$

It can thus be seen that with an increase in the surface potential  $\varphi_0^*$ , the electric field strength on the cylinder surface, just as in the case of a spherical body (Ref. 1, 2), increases proportionally to  $(\varphi_0^*)^{1/4}$ , i.e., very slowly. Correspondingly, the double layer thickness - i.e., the layer on the body surface in which the electric field potential decreases considerably - increases with an increase in the surface potential proportionally to  $(\varphi_0^*)^{3/4}$ . In the case of  $\varphi_0^* \sim 1$ , the double layer thickness is on the order of the Debye radius. For very large values of the field potential on the cylinder surface  $\varphi_0^* \gtrsim (R_0/D)^{4/3}$  the double layer dimensions become comparable to the cylinder radius.

All of this investigation was conducted under the assumption that the double layer thickness is much less than  $R_0$ . This is only valid when

$$\varphi_0 \ll \frac{kT}{e} \left( \frac{R_0}{D} \right)^{4/3}.$$

The author would like to thank Ya. L. Al'pert and A. V. Gurevich for discussing the problems investigated in this article.

## REFERENCES

1. Al'pert, Ya.L., Gurevich, A.V., Pitayevskiy, L.P. Artificial Satellites in a Rarefied Plasma (Iskusstvennyye sputniki v razrezhennoy plazme). Izdatel'stvo "Nauka", 1964.
2. Gurevich, A.V. Geomagnetizm i Aeronomiya, 3, No 6, 1021, 1963.
3. Moskalenko, A.M. Geomagnetizm i Aeronomiya, 4, No 6, 1026, 1964.
4. Moskalenko, A.M. Geomagnetizm i Aeronomiya, 5, 1965.

## INTENSIFICATION OF THE OUTER ELECTRIC FIELD ON THE SURFACE OF A LARGE BODY IN THE IONOSPHERE

L. L. Goryshnik, A. N. Dyukalov

The amplification factor of a weak electric field on the surface /267  
of a large body in the ionosphere is computed.

Experiments measuring the electric field strength in the ionosphere were described in (Ref. 1-3). The half-difference of two electrostatic fluxmeter readings was utilized as the quantity characterizing the field strength; these fluxmeters were located at diametrically opposite points in the cylindrical section of a rocket. The quantity measured was thus anomalously high. The outer electric field, the directional rocket velocity, and the Earth's magnetic field can cause this asymmetry in the field strength on the rocket surface. The effect of directional rocket motion and the magnetic field of the Earth was studied in (Ref. 4).

This article studies the dependence of the field strength on the surface of a body in the ionosphere upon a weak, outer electric field. Our interest in this problem can be explained by the fact that in many of these experiments (Ref. 1) the magnetic field was perpendicular to the recorder surfaces, and consequently could not cause the great asymmetry of the field strength on the body surface. In addition, in these experiments geophysical rockets were launched on vertical trajectories, which almost entirely excluded the influence of directional velocity. Thus, only the outer electric field could cause the field strength asymmetry on the body surface in these experiments.

This entire analysis is devoted to a stationary body located in an infinite plasma, in which there is no magnetic field but there is a weak constant electric field. This field does not disturb the plasma neutrality, and leads only to the occurrence of a constant current. As is known, an isolated body located in a neutral plasma is charged up to a certain potential, and the potential difference between the body and the unperturbed plasma is determined from the condition that the total (electron and ion) current on the body equals zero.

We shall assume that the photoeffect and secondary emission can be disregarded. Then, the isolated body acquires a negative potential due to the great mobility of the electrons, and the potential difference between the body and the unperturbed plasma significantly increases the mean thermal electron energy. As a result, a space charge layer is formed close to the body, in which positively charged ions are predominant. The thickness of this layer is on the order of the Debye radius. Outside of the layer, the plasma is quasineutral.

Let us investigate the space charge region. Since the Debye radius in the ionosphere is considerably less than the characteristic size of the

rocket R, the layer can be assumed to be flat at each point.

In a one dimensional case, the Poisson equation for the potential distribution caused by the charged body within the layer assumes the form

$$\frac{d^2\Phi}{dx^2} = 4\pi e (n_e - n_i), \quad (1)$$

where  $e$  is the electron charge, and  $n_e$  and  $n_i$  - electron and ion densities at a certain point  $x$ . Setting

$$e\Phi = -U, \quad (2)$$

we obtain

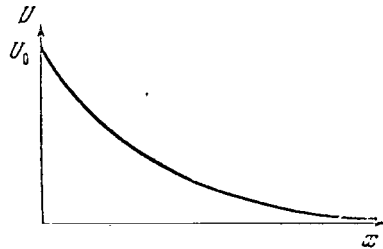
$$\frac{d^2U}{dx^2} = 4\pi e^2 (n_i - n_e). \quad (3)$$

We shall solve this equation with the boundary conditions

/268

$$\begin{aligned} U(0) &= U_0, \\ U(\infty) &= 0. \end{aligned} \quad (4)$$

The approximate potential distribution is shown in the figure.



The charged particle densities in the space charge layer are determined by the expressions

$$n_i(x) = \int_{-U}^{\infty} \frac{f_i(E) dE}{\sqrt{2M(E+U)}} \quad (5)$$

$$n_e(x) = \int_U^{\infty} \frac{f_e(E) dE}{\sqrt{2m(E-U)}}, \quad (6)$$

where  $f_i(E)$  and  $f_e(E)$  are the distribution functions of ions and electrons in the space charge layer;  $M$  and  $m$  - ion and electron masses;  $E$  - total particle energy;  $U$  - potential at the point  $x$ . For purposes of simplicity, it is assumed that the ions are singly charged. Substituting (5) and (6) in (3), we obtain the equation

$$\frac{d^2U}{dx^2} = 4\pi e^2 \left\{ \int_{-U}^{\infty} \frac{f_i(E) dE}{\sqrt{2M(E+U)}} - \int_U^{\infty} \frac{f_e(E) dE}{\sqrt{2m(E-U)}} \right\},$$

the right part of which depends only on U. Multiplying this equation by dU/dx, integrating over x, and utilizing the condition dU/dx=0 to infinity (this is a natural condition, due to the fact that we are writing a limited solution), we obtain

$$\begin{aligned} \frac{1}{2} \left( \frac{dU}{dx} \right)^2 = 8\pi e^2 \left\{ \frac{1}{\sqrt{2M}} \int_{-U}^{\infty} \sqrt{E+U} f_i(E) dE + \right. \\ \left. + \frac{1}{\sqrt{2m}} \int_U^{\infty} \sqrt{E-U} f_e(E) dE - \int_0^{\infty} \sqrt{\frac{E}{2M}} f_i(E) dE - \int_0^{\infty} \sqrt{\frac{E}{2m}} f_e(E) dE \right\}. \end{aligned} \quad (7)$$

The right part of this equation is proportional to the increase in the mean particle energy when they traverse the path from the layer boundary to the point with the potential U.

In order to determine the potential distribution in the double layer, we must solve equation (7) with the boundary conditions (4).

However, we are not interested in the potential distribution in the layer, but rather in the field strength on the body surface. For this purpose, it is sufficient to compute the right part of (7) for  $U = U_0$ . As has been already indicated,  $U_0 > kT_e$ , and therefore it can be assumed that the second term in the right part, which determines the mean electron energy on the body surface, equals zero, since there are almost no electrons close to the body. (The ratio of this term to the entire remaining terms in the parentheses is  $\sqrt{m/M}$  in order of magnitude).

Due to the fact that  $U_0 > kT_e$ , the ion energy close to the body is determined by the potential difference between the body and the unperturbed plasma, which makes it possible to disregard the thermal scatter of ion velocities and to assume that they are monoenergetic:

$$f_i(E) = MI_i \delta(E), \quad (8)$$

where  $I_i$  is the ion current density on the body at a given point on the 269 surface. Consequently,

$$\left( \frac{dU}{dx} \right)_{x=0}^2 = 16\pi e^2 \left\{ \sqrt{\frac{M}{2}} I_i \sqrt{U_0} - NP_i - NP_e \right\}, \quad (9)$$

where N is the particle density, and  $P_i$  and  $P_e$  are the mean energies of an ion and electron at the layer boundary.

Equation (9) connects the electric field strength at a point on the body surface with the ion current density at this point, with the surface potential, and with the thermal particle energies at the boundary of the layer and the plasma.

Let us now investigate the effect of a weak outer field  $E_{\perp}$ , which is such that  $\mu = \frac{eE_{\perp}\Lambda}{kT_e} \ll 1$  where  $\Lambda$  is the mean free path of each type of particle.

It is apparent from the problem symmetry that perturbation of the body potential by the weak outer field is proportional to  $\mu^2$ . Consequently, the body potential in the first order of magnitude with respect to  $\mu$  (all the investigation will be conducted with this accuracy) does not depend on the outer field, and equals

$$U_0 = \frac{kT_e}{2} \ln \frac{T_e M}{T_i m},$$

where  $T_i$  and  $T_e$  are the ion and electron temperatures. Since  $T_e$  can hardly exceed  $T_i$  in the ionosphere and since their ratio is included in the argument of the logarithm, this ratio can be disregarded and we can set

$$U_0 = \frac{kT_e}{2} \ln \frac{M}{m}. \quad (10)$$

In order to determine the ion current density and the mean energies of ions and electrons at the layer boundary, it is necessary to find the potential distribution in the quasineutrality regions. However, as estimates carried out in (Ref. 4) have shown, the field penetration beyond the double layer boundary has a slight influence on the field strength at the body surface. Consequently, we can disregard field penetration beyond the boundary of the space charge region in the approximate theory, and can assume that the plasma is unperturbed at the outer layer boundary. This means that the mean particle energy at the layer entrance equals the mean particle energy in an infinite plasma, and the correction for the latter is of the second order of smallness with respect to the field (Ref. 5).

Thus, the dependence of the field strength on the body surface upon the weak outer field is entirely determined by the dependence of the ion current density  $I_i$  at a certain point on the surface upon this outer field.

Under the condition that the field does not penetrate beyond the layer boundary and that the layer can be assumed to be flat at each point, the ion current density on the body surface equals its density at the layer boundary, i.e., (Ref. 5)

$$I_i = I_0(1 + \alpha\mu), \quad (11)$$

where  $I_0$  is the current density without the outer field, and  $\alpha$  is the numerical factor on the order of 1. Introducing the dimensionless value for the current  $j_0$  with the aid of

$$I_0 = N \sqrt{\frac{kT_e}{2M}} j_0 \quad (12)$$

and substituting (10) and (11) in (9), we obtain the following expression after normalization of  $U_0$ ,  $P_i$  and  $P_e$  by  $kT_e$ :

$$E_1^2 = \frac{8\pi e^2 N}{kT_e} (kT_e)^2 \{j_0 (1 + \alpha\mu) \sqrt{y_0 - w}\}, \quad (13)$$

where

$$y_0 = \frac{U_0}{kT_e} \text{ and } w = \frac{P_i}{kT_i} + \frac{P_e}{kT_e} \quad (14)$$

- the mean particle energy in a plasma normalized with respect to  $kT_e$ .

Extracting the root and confining ourselves to terms on the order /270 of  $\mu$ , we obtain

$$E_0 = \frac{kT_e}{D} \left\{ \sqrt{j_0 \sqrt{y_0 - w}} + \frac{\alpha j_0 \mu}{2 \sqrt{j_0 \sqrt{y_0 - w}}} \right\}, \quad (15)$$

where  $D = \sqrt{\frac{kT_e}{8\pi e^2 N}}$  is the Debye radius in an unperturbed plasma.

The field strength values at two diametrically opposed points on the body differ by the sign of  $\mu$ . Therefore, for the quantity  $E_1 - E_2$ <sup>2</sup>, measured experimentally, we obtain the following, with allowance for (10),

$$\frac{E_1 - E_2}{2} = a \frac{\Lambda}{D} E_{\perp}, \quad (16)$$

where

$$a = \frac{\alpha j_0}{2 \sqrt{j_0 \sqrt{\frac{1}{2} \ln \frac{M}{m} - w}}} \quad (17)$$

- the coefficient on the order of unity. Thus, the amplification factor of a weak outer electric field on the surface of a large body in the ionosphere is proportional to the ratio between the ion mean free path and the Debye radius in an unperturbed plasma.

The authors would like to thank S. M. Rytov for reviewing this article, and also M. L. Levin, G. L. Gdalevich, and M. V. Samokhin for valuable discussions.



## REFERENCES

1. Gdalevich, G. L. In "Iskusstvennyye Sputniki Zemli". Izdatel'stvo AN SSSR, No. 17, p. 42, 1963.
2. Imyanitov, I. M., Shvarts, Ya. M. In "Iskusstvennyye Sputniki Zemli". Izdatel'stvo AN SSSR, No. 17.
3. Imyanitov, I. M., Gdalevich, G. L., Shvarts, Ya. M. In "Iskusstvennyye Sputniki Zemli". Izdatel'stvo AN SSSR, No. 17, p. 66, 1963.
4. Gurevich, A. V. Kosmicheskiye Issledovaniya, 2, No. 2, 232, 1964.
5. Chapman, S., and Cowling, T. Mathematical Theory of Nonuniform Gases, IL, 1960.

---

### DISCRETE MODEL OF MATTER IN THE PROBLEM CONCERNING THE INTERACTION OF RAPIDLY MOVING BODIES WITH A RAREFIED PLASMA

(Summary)

M. V. Maslennikov, Yu. S. Sigov

The stationary picture of a rarefied plasma stream flowing around an axisymmetric body A is studied. The problem is solved under the following assumptions;

$$(a) \quad v_{T_e} \gg v_s \gg v_{T_i},$$

where  $v_s$  is the macroscopic stream velocity with respect to A;  $v_{T_e}$  and  $v_{T_i}$  - thermal velocities of electrons and ions, respectively.

(b) The spatial electron density  $\rho_e(\mathbf{r})$  at the point  $\mathbf{r}$  is determined by setting the self-consistent electrostatic potential  $\varphi$  and the ion density  $\rho_i$  at the same point

$$\rho_e(\mathbf{r}) = F(\varphi(\mathbf{r}), \rho_i(\mathbf{r})).$$

It is also assumed that in the vicinity of A there are no ions moving along finite trajectories, and that an ion falling on the surface A is absorbed, without changing  $\varphi\sigma$  ( $\varphi\sigma$  is the electrostatic potential on the surface of A;  $\varphi\sigma$  is the given function of a point on the surface).

/271

The ion density  $\rho_i$  is determined by the discrete plasma model, in which the particle behavior is described by the equations of classical mechanics. The self-consistent potential  $\varphi(\mathbf{r})$  is obtained from the quasilinear Poisson equation.

$$\Delta\varphi = -4\pi(\rho_i - \rho_0 F[\varphi, \rho_i]),$$

which is solved by a standard method.

Computations are performed for the case when A is a sphere whose dimensions are comparable with the Debye plasma radius. Thus,

$$F(\varphi, \rho_i) = \exp(\epsilon\varphi/kT_e),$$

where  $\epsilon$  is the electron charge;  $k$  - the Boltzmann constant,  $T_e$  the effective electron-gas temperature. In the perturbation zone beyond the body, there is an unusual "stratification" of the plasma: Along the axis of symmetry for the problem, the total charge density and  $\varphi(\mathbf{r})$  change sign repeatedly, gradually decreasing in amplitude as one recedes from the body.

# ELECTRIC FIELDS IN THE IONOSPHERE BASED ON DATA FROM DIRECT MEASUREMENTS ON GEOPHYSICAL ROCKETS

G. L. Gdalevich, I. M. Imyaninov

The entire cosmos has excellent conductivity, with large particle mean free paths. One exception to this is only a small amount of "special" regions, which include the lower layers of the Earth's atmosphere. The formation of a slowly-changing electric field in this environment produces streams of rapid particles, a temperature change, and many other effects which significantly change the characteristics of the environment. This strong dependence of the environment properties on the magnitude of stationary electric field strengths has led to the necessity of measuring the charge, as well as to several difficulties entailed in these measurements.

The difficulty encountered in these measurements is due to the fact that field strengths can arise in space which fall greatly below the measurement limits of present equipment and methods.

It is most probable that many phenomena in the ionosphere - for example, the formation of ionization nonuniformities in the F layer, the drift of nonuniformities in the ionosphere, the appearance of energetic particle streams in the upper layers of the atmosphere, etc. - owe their origin to the influence of electric fields (Ref. 1, 2). These fields can arise due to the motion of neutral streams of charged particles in a direction which is perpendicular to the magnetic field of the Earth. The streams can have both a terrestrial origin, and possibly a solar origin (Ref. 3), due to the transfer of electric fields from the interplanetary medium (Ref. 4) and due to certain other processes. A study of the electric field strength and its distribution in space must, for example, answer the question regarding the relationship of several phenomena in the ionosphere with solar activity. In particular, it must answer the question of the possible mechanism by which processes in the atmosphere are related to solar activity.

However, up until recently the field strength in the ionosphere has been determined from indirect data, such as the wind velocity in the E layer (Ref. 5), the drift velocity of ionosphere nonuniformities in the F layer (Ref. 1), the magnitude of electron temperature (Ref. 6), and /272 the night sky airglow (Ref. 7). Determinations based on these data have shown that there are stationary electric fields in the mean latitudes of the ionosphere, with a strength of  $E_{\perp}$  amounting to  $10^{-4} \text{ v} \cdot \text{cm}^{-1}$  directed perpendicularly to the magnetic force lines (Ref. 8), and with the strength  $E_{\parallel}$  amounting to  $10^{-7} \text{ v} \cdot \text{cm}^{-1}$  directed along the magnetic force lines (Ref. 6). It should be noted that such determinations are arbitrary to a certain extent, since there is not usually adequate information for performing the requisite computations. Thus, for example, there is no information on the drift velocities of nonuniformities on a planetary scale. A

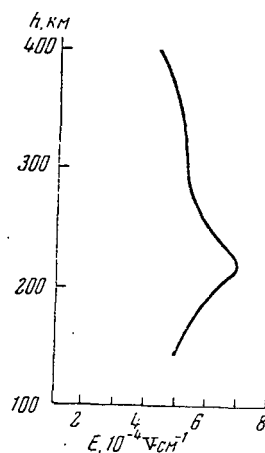


Figure 1

calculation of the field strength based on currents in the ionosphere is based on calculated values of ionosphere conductivity, while the calculated values for the layer can differ significantly from the actual values. It is more reasonable to determine the conductivity in the corresponding region, by measuring the current and strength of the electric field.

Therefore, attempts to perform experiments measuring the electric field strength directly are of great interest.

Such experiments were performed on the geophysical rockets of the AN SSSR.\* The measurements were performed by means of specially-prepared electrostatic fluxmeters (Ref. 9). Two sensors were placed at diametrically-opposed points on the cylindrical portion of the rocket surface. These sensors produced a charge which was proportional to the electric field strength where they were located. This charge was then intensified, and recorded on Earth by means of the telemetry line. The experiments directly measured the electric field strength on the rocket surface, which was caused by the eigen electric charge of the rocket and by the outer electric field in the ionosphere (Ref. 10, 11). After the data were processed and possible measurement errors were taken into account, it was found that the difference in the strengths measured by the sensors was proportional to the electric field strength in the ionosphere, while the measured difference was much greater than the outer electric field. The proportionality coefficient changed from  $10^2$  to  $10^4$ , and depended on the medium characteristics, as well as on the mutual locations of the electric and magnetic field strength vectors and of the line connecting the sensor points (Ref. 11-13).

The experiments measured one component of the field strength vector, directed either along the line connecting the sensor points and parallel to the magnetic field vector, or that giving the directional motion of the charged particles along this line, when the magnetic field strength was perpendicular to the latter and to the electric field strength. Therefore,

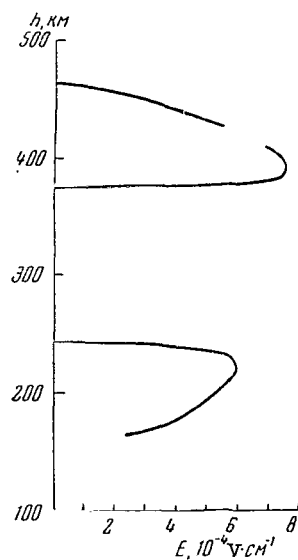


Figure 2

when determining the magnitude of the measured outer field strength, one must take its direction into consideration. Under the experimental conditions, when two sensors are used, this cannot always be done. However, in the majority of cases a comparison of the field strengths measured by both sensors makes it possible to determine the most probable direction of the outer electric field.

Figure 1 presents the results of measurements on November 15, 1961. It can be seen from this figure that the electric field strength  $E_{\perp}$  in the ionosphere amounted to  $7 \cdot 10^{-4} \text{ v} \cdot \text{cm}^{-1}$  throughout this experiment, with a field which moved from the east to the west. Figure 2 presents the results of measurements on June 6, 1963.

In comparing Figures 1 and 2, one should note that during the afternoon hours of November 15, 1961,  $E_{\perp}$  existed throughout the entire region being studied, and had a maximum at an altitude of  $\sim 200$  km. However, on June 6, 1963, during the morning hours the electric field  $E_{\perp}$  had a strength exceeding the measurement errors, only in the region of 150-230 km and 370-460 km, while the maximum value of  $E_{\perp} \sim 8 \cdot 10^{-4} \text{ v} \cdot \text{cm}^{-1}$  was observed at an altitude of 400 km.

Table 1 presents data pertaining to the observations of  $E_{||}$ . The values of  $E_{\perp}$  in Figures 1 and 2 and of  $E_{||}$  in the table were obtained on the basis of experimental data processed according to the formula presented in (Ref. 12).

The measurement results show that there are electric fields with  $E_{\perp} \approx 10^{-3} \text{ v} \cdot \text{cm}^{-1}$  and  $E_{||} \approx 10^{-5} \text{ v} \cdot \text{cm}^{-1}$  in the ionosphere. The work (Ref. 14) presents the values of  $E_{\perp} = 2 \cdot 10^{-3} \text{ v} \cdot \text{cm}^{-1}$  measured in the regions of mean latitudes. It should be noted that  $E_{||}$ , as a rule, can only be detected at altitudes of more than 200 km.

The large measured values of the electric field strength must significantly affect the ionosphere characteristics. The existence of  $E_{\perp} \approx 10^{-3} \text{ v} \cdot \text{cm}^{-1}$  in the ionosphere must lead to the drift of ionization nonuniformities with velocities of  $\sim 1 \text{ km} \cdot \text{sec}^{-1}$ . In addition, such a field must produce luminescence of the oxygen lines due to a general increase in the charged particle temperatures. It is possible that the electron and ion temperature difference discovered recently in the ionosphere may be in some way related to the influence of the electric field.

It should be noted that the electric fields having a strength of  $E_{\parallel} \approx 10^{-5} \text{ v} \cdot \text{cm}^{-1}$ , which were observed in the experiments, exist on the order of one minute, since they were recorded either on the ascending, or on the descending, branches of the rocket trajectory.

CERTAIN DATA PERTAINING TO OBSERVATIONS  
OF  $E_{\parallel} = 10^{-5} \text{ v} \cdot \text{cm}^{-1}$

Measurement Date	Altitude, km		Direction
	Ascent	Descent	
10/18/62	275-325	---	North $\rightarrow$ South
	360-380	---	North $\rightarrow$ South
	---	260-180	Vertical
6/18/63	465-485	---	South $\rightarrow$ North
	---	490-465	North $\rightarrow$ South

In one case (1960-1963) the electric field  $E_{\parallel}$  was determined during the ascent and during the descent of the rocket, although during the time between the measurements ( $\sim 120 \text{ sec}$ ) it managed to change direction.

We are now confronted by two important questions: (1) Why do such strong electric fields not cause intense heating of the ionosphere, and (2) What is the source of the strong electric fields observed.

The answers to these two questions fall outside the framework of the present brief report, but we can present certain ideas in this regard.

The phenomenon of a strong field  $E_{\parallel}$  at altitudes of more than 200-300 km in the ionosphere, having a strength - let us say of  $10^{-5} \text{ v} \cdot \text{cm}^{-1}$  - which is in operation for several seconds, and then several tens of seconds, causes the phenomenon of streams of rapid electrons leaving the 274 layer, and causes this layer to be filled up by "cold" electrons from unheated layers.

It was shown in (Ref. 6) that, if the size of the region perturbed by the electric field reaches 10,000 km in the direction of the magnetic field and 100 m in the perpendicular direction, a stream of escaping electrons is formed having particle energies of 1-10 kev. Let us examine the case when an electric field with the strength  $E_{||} = 10^{-5} \text{ v} \cdot \text{cm}^{-1}$  arises in the ionosphere region having these dimensions. The electrostatic energy of this field is:

$$w = \frac{E^2}{8\pi} V \approx 3 \text{ erg},$$

where  $V = 2.5 \cdot 10^{16} \text{ cm}^3$  is the volume of the region perturbed by the field (let us assume that the region has a cylindrical form). The energy of the field will be consumed in the acceleration of  $2 \cdot 10^8$  electrons up to energies of 10 kev, while the temperature of the remaining electrons (the total number of electrons is  $10^{22}$  particles for an electron concentration in the perturbed region of  $n_e = 4 \cdot 10^5 \text{ cm}^{-3}$ ) remains unchanged. The density of the energy flux of escaping electrons is  $4 \cdot 10^{-8} \text{ erg} \cdot \text{cm}^{-2} \cdot \text{sec}^{-1}$ , if it is assumed that they fly through the cylinder base.

High-energy charged particles having energies of  $\sim 1$ -10 kev interact only slightly with the medium, barely heating it. Therefore, it can be expected that the electric field having even a magnitude of  $E_{||} = 10^{-5} \text{ v} \cdot \text{cm}^{-1}$  does not heat the medium significantly.

Returning to the question of the source of this field, we need only note that the values of  $E_{||} \approx 10^{-5} \text{ v} \cdot \text{cm}^{-1}$  are apparently caused by a source having an extra-terrestrial derivation - most likely under the influence of the Sun.

In concluding this article, we would like to point out the following. In spite of the fact that the proposed method for measuring electric fields requires further improvement - more precise definition of the field acceleration theory and additional measurements on particle or stream concentration - experiments studying in greater detail the structure of electric fields in the ionosphere should be carried out. It should also be stressed that the examined mechanism for "acceleration" of the outer electric field at the walls of a charged object makes it possible to apply the proposed method in studies of interplanetary space, particularly in studying the question of the electric neutrality of the Earth or the Moon.

#### REFERENCES

1. Gershman, B.N., Ginzburg, V.L. *Izvestiya Vysshikh Uchebnykh Zavedeniy. Radiofizika*, 2, No 1, 8, 1958.
2. McIlwain, C.E. *J. Geophys. Res.*, 65, 2727, 1960.
3. Mitra, S.K. *Upper Atmosphere*. II, 1955.

4. Acasofu, S. J., Chapman, S. Philos. Trans. Roy. Soc., 253, 359, 1961.
5. Maeda, H. J. Geomagn. Geoelectr., 7, 121, 1955; 9, 86, 1957; Kato, S. J. Geomagn. Geoelectr., 8, 24, 1956; 9, 107, 1957.
6. Gurevich, A. V., Tsedilina, Ye.Ye. Geomagnetizm i Aeronomiya, 1, 1, 1961.
7. McGill, L. R., Rees, H., Droppleman, L. K. Planet. Space Sci., 11, 45, 1963.
8. Obayashi, T. J. Geomagn. Geoelectr., 15 No. 3, 133, 1964.
9. Gdalevich, G. L., Imyanitov, I. M., Shvarts, Ya.M. Kosmicheskiye Issledovaniya, 3, No. 1, 102, 1965.
10. Gdalevich, G. L. In "Iskusstvennyye Sputniki Zemli", No. 17, Izdatel'stvo AN SSSR, p. 42, 1963.
11. Imyanitov, I. M., Gdalevich, G. L., Shvarts, Ya.M. In "Iskusstvennyye Sputniki Zemli", No. 17, Izdatel'stvo AN SSSR, p. 66, 1963.
12. Gurevich, A. V. Kosmicheskiye Issledovaniya, 2, No. 2, 232, 1964.
13. Goryshnik, L. L., Dyukalov, A. N. Present Collection, p. 267.
14. Kavadas, A., Johnson, D. W. Space Res., 4, 365, 1964.



IV

CORPUSCULAR STREAMS AND THEIR INTERACTION  
WITH THE GEOMAGNETIC FIELD. MAGNETOSPHERE  
AND RADIATION ZONES OF THE EARTH.

As is known, the first great scientific event in circumterrestrial space research was the discovery of the so-called radiation zones of the Earth. Attempts were first made to explain them theoretically on the basis of the neutron albedo hypothesis. A certain portion of radiation zone particles are actually caused by this phenomenon. However, it was recently discovered that particles belonging to plasma streams are captured near the Earth and subsequently accelerated. /276

The accumulation of experimental data, plasma research and research on the streams arriving at the Earth (the so-called solar wind), a clarification of the geomagnetic field structure, and a study of the low-energy component of charged particles captured in the geomagnetic trap have greatly refined our concepts regarding circumterrestrial space. The close relationship between such geophysical phenomena as the aurorae polaris, magnetic storms, and the formations of the Earth's magnetosphere as well as of the Earth's radiation zone has become apparent. The interaction of solar corpuscular streams with the geomagnetic field is apparently the original dynamic process in this complex of phenomena.

In the light of present day data, the concepts of the "inner" and "outer" radiation zones are purely conditional, since the geomagnetic trap is completely occupied by charged particles.

It must be emphasized that streams of low-energy electrons have been discovered beyond the limits of the radiation zones. However, these streams could hardly be the result of radiation capture, and apparently point to the existence of the so-called outermost zone of charged particles as an isolated formation. The physics of this radiation is quite complex, and is related to solar wind flowing around the magnetosphere boundary, and possibly to the penetration of particles within the magnetosphere.

Experimental data have shown that the magnetosphere is an open formation - force lines on the nocturnal side form the so-called magnetic tail of the Earth - which does not rotate with the Earth. There is a neutral layer within the magnetic tail, where the magnetic field strength is practically zero.

This section is prefaced with a summary concerning the present state of, and problems entailed in, the study of the Earth's radiation zones. Recent experimental data obtained on the satellites "Elektron" and "Kosmos" are primarily discussed in the other articles.

All of these data may serve as a basis for extensive theoretical generalizations.

It is hoped that in the near future many enigmas of circumterrestrial space will be clarified.

# STATE OF AND PROSPECTS FOR STUDYING THE RADIATION ZONES OF THE EARTH

S. N. Vernov

Acceleration of energetically charged particles occurs in cosmic space. In certain regions of space which are very far from the Earth, the particles are accelerated up to an energy of  $10^{19}$  ev. Cosmic rays having super-high energies are thus formed. During solar flares, solar cosmic rays are created, whose maximum energy is considerably lower, namely,  $10^{10}$  ev. Finally, acceleration of particles up to an energy of  $10^7$  ev, and possibly  $10^8$  ev, also occurs at the Earth. This acceleration of particles around the Earth leads to the formation of radiation zones of the Earth. The hypothesis could be advanced that the same accelerating mechanism (of which we are still unaware) lies at the basis of all these processes. In order to determine this accelerating mechanism, it is necessary to compile the following experimental data: /277

- (1) The medium in which acceleration occurs;
- (2) The radiation produced as a result of the acceleration;
- (3) The matter in which the acceleration process takes place in time.

There are very few experimental data on cosmic rays which are formed in the depths of the Galaxy. We know very little about the medium (item 1). Surprises such as the discovery of supernovae can radically change our concepts. In general, it is still impossible to determine the manner in which the acceleration process takes place in time (item 3).

It is possible to obtain fairly detailed information regarding the formation of flares on the Sun and the generation of solar cosmic rays. It has already been determined that flares, and consequently cosmic rays, are formed where large gradients of magnetic fields exist. Rapid changes in the magnetic fields occur when the particles are accelerated. However, the data on physics of the Sun are still far from being complete, and therefore we can only formulate a hypothesis regarding the formation of solar cosmic rays.

The situation is entirely different with the radiation zones. Very detailed information can be obtained on the medium where the acceleration takes place. The construction of artificial Earth satellites has made it possible to obtain an enormous amount of experimental data. New facts which have been discovered due to the flights of the satellites have given us a key with which to interpret observations extending over several years of the ionosphere, the magnetic field of the Earth, and the aurorae polaris. As will be shown in this report, an analysis of data which have been recorded in the past makes it possible to obtain very important information regarding the state of the radiation zones 17 years ago - i.e., 10 years before they were discovered during the satellite flights.

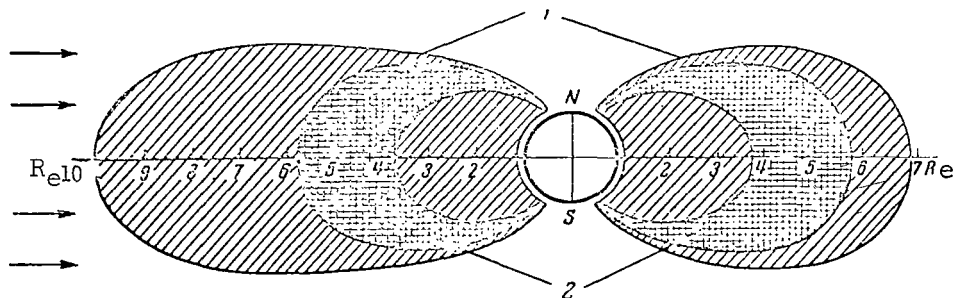


Figure 1

Distribution in Circumterrestrial Cosmic Space of Electrons  
Having Energies of  $E_e > 40$  keV and  $E_e > 500$  keV

1 - Electrosphere ( $E_e > 40$  keV); 2 - Outer Radiation Zone  
( $E_e > 500$  keV). Arrows indicate direction of solar wind.

In this report, I would like to discuss the present state of our information regarding the radiation zones. In spite of the brevity of the report, I hope to show that very detailed information has already been compiled up to the present time. The rate at which new experimental data are compiled is very fast. Therefore, the day is not far off when there will be enough information to provide a definitive answer to the question - What is the accelerating mechanism?

It is my opinion that a knowledge of the accelerating mechanism which creates the radiation zones of the Earth could be extensively applied, both in studying cosmic rays, and as applied to physics as a whole.

What information do we have at the present time on the radiation zones? /278

We know the distribution of the magnetic field both close to the Earth, and at large distances from the Earth.

We know the distribution of matter around the Earth.

Thus, although the information on the medium where the acceleration of particles occurs is still far from complete, it is nevertheless very detailed.

What is the appearance of the radiation zones consisting of particles having considerable energies (thousands and millions of electron volts)? How are these particles accelerated up to these energies close to the Earth?

We have discovered electrons and protons having different energies in the composition of the radiation zones. Data are presented below which were obtained from flights of Soviet and American satellites.

Figure 1 shows the electron distribution around the Earth. As can be seen from Figure 1, electrons having comparatively small energies (several

tens of kiloelectron volts) are distributed over a wide region, which we shall designate as the electronosphere. Apparently, the electronosphere is asymmetrical. The solar wind influences it. In accordance with the laws of electron drift in a nonhomogeneous magnetic field, the electronosphere is extended toward the Sun. In the center of this region there are electrons having relatively high energies (more than 500 kev). This region has been called the outer radiation zone of the Earth. We should point out that electron acceleration close to the Earth must be assumed in order to explain the existence of the outer radiation zone, as well as to explain the electronosphere. As can be seen from Figure 1, the spatial distribution of electrons having high and low energies is different. However, even electrons having high energies are distributed over a fairly wide region.

Figure 2 shows the proton distribution around the Earth. As can be seen from the figure, protons having comparatively small energies (from 0.1 to 5 Mev) are distributed over a very extensive region - the protonosphere. The inner radiation zone consisting of protons having high energies (more than 30 Mev) is superimposed on the protonosphere in the region which is closest to the Earth. In order to explain the protonosphere - i.e., the existence of a large number of protons having energies up to several millions of electron volts - proton acceleration close to the Earth must be assumed. The inner radiation zone arises due to the decay of neutrons which are emitted into space by the Earth's atmosphere when it is bombarded by cosmic rays. The distribution of the total radiation intensity in the radiation zones is shown in Figure 3. This figure provides a dosimetric picture of radiation around the Earth.

/279

The distribution of protons having different energies around the Earth has a very specific nature. These data are shown in Figures 4, 5. The closer they are to the Earth, the greater the proton energy in the protonosphere. This is due to the betatron acceleration of protons. At large distances from the Earth, there are protons having comparatively small energies. As they scatter toward the Earth, they enter the region of much stronger magnetic fields and are accelerated, just as in a betatron, due to an increase in the magnetic field. It can be shown by this example that certain contours of the cosmic accelerant existing at the Earth are already known at the present time. It is possible that one of the elements in the acceleration process is the transfer of particles toward the Earth - i.e., toward the region of a stronger magnetic field.

Particles in the radiation zones oscillate from the northern hemisphere to the southern hemisphere, and also drift around the Earth. Therefore, the distribution of the radiation zones at low altitudes reflects the magnetic picture of the Earth. An anomaly of the radiation zones was discovered during the flight of the second Soviet spacecraft; this anomaly coincided with the Brazilian magnetic anomaly. Figure 6 presents the results derived from measuring the radiation intensity in May, 1963, during the flight of the "Kosmos-17" AES to the East and to the West of the anomaly. We can see that the following phenomenon occurs:

/280

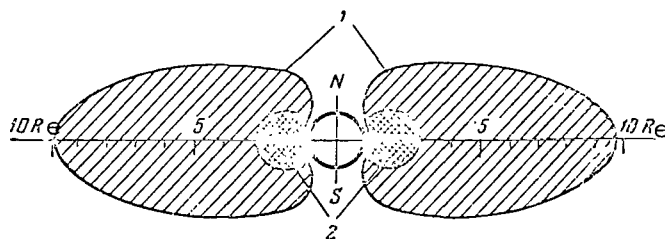


Figure 2

Distribution of Protons Having Energies of  $E_p > 30$  Mev and Energies Ranging from 0.1 to 5 Mev in Circumterrestrial Cosmic Space

1 - Protonosphere ( $5 \text{ Mev} > E_p > 0.1 \text{ Mev}$ ; at the boundary of the region  $N_p \approx 10^4 \text{ cm}^{-2} \cdot \text{sec}^{-1}$ ); 2 - Inner radiation zone ( $E_p > 30 \text{ Mev}$  at the boundary of the region  $N_p > 10^2 \text{ cm}^{-2} \cdot \text{sec}^{-1}$ ).

The intensity is not the same on different sides of the anomaly. This may be caused by the fact that the particles, as they pass through the anomaly during the longitudinal drift, simultaneously drift along the force lines toward the Earth.

Observations of particles in the radiation zones at different points above the Earth's surface showed that these particles are also discovered in regions which exclude radiation trapped by the geomagnetic field - i.e., in regions whose magnetically-linked points are located deep in the atmosphere, or even near the Earth. In other words, radiation exists whose particles move along trajectories forming an angle with the magnetic force lines which is so small that these particles must enter into the atmosphere. Thus, apart from captured radiation there must also be directly accelerated radiation, which is recorded immediately after these particles are accelerated.

As measurements performed during the flight of the American satellite "Injun-3" have shown, the intensity of directly accelerated radiation sometimes changes over a very short time interval (less than 0.1 seconds). It follows from this fact that the particles are accelerated at a distance which is small as compared with the length of the magnetic force line. This distance is less than  $10^9 \text{ cm}$ . It thus follows that electric fields must exist whose strength is greater than  $10^{-4} \text{ v} \cdot \text{cm}^{-1}$ .

Corpuscular streams emitted by the Sun influence the radiation zones, and lead to particle acceleration. The picture of the influence of corpuscular streams on the radiation zones is very complex. In a simpler form, this picture develops at the moment when an additional (short-lived) radiation zone appears at distances from the Earth which are larger than the distance of the radiation zones which always exist. Figure 7 shows the appearance of an additional radiation zone on February 16, 1964. This additional /281 zone was discovered during one of the flights of the "Elektron-2" satellite.

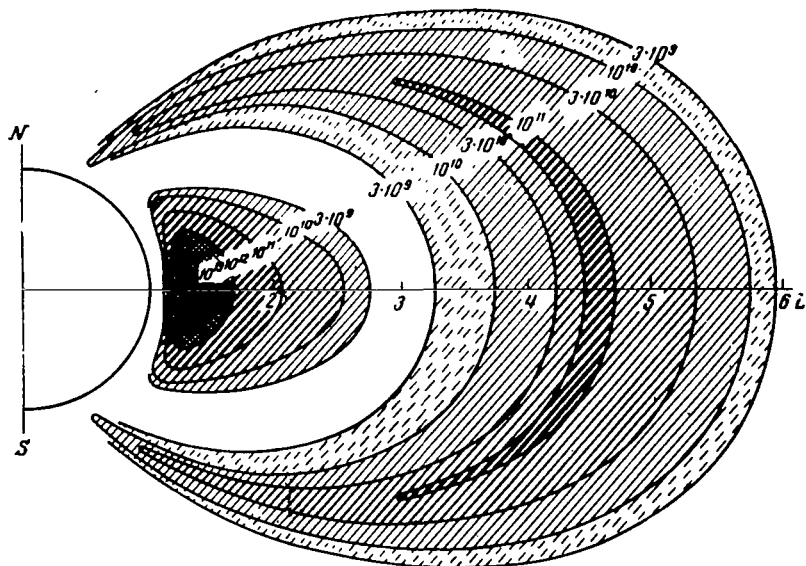


Figure 3

Liberation of Energy in a NaJ Crystal Having Dimensions of 20 x 20 mm Behind a Shielding of  $1 \text{ g} \cdot \text{cm}^{-2} \text{ Al}$  ( $\text{ev} \cdot \text{sec}^{-1}$ )

For conversion to  $\text{rad} \cdot \text{sec}^{-1}$ , the given values must be multiplied by  $7 \cdot 10^{-16}$

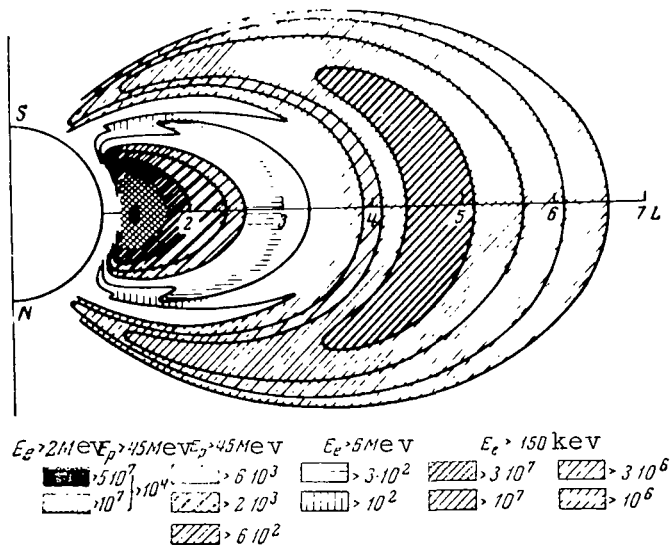


Figure 4

Spatial Distribution of Electrons and Protons Having Different Energies

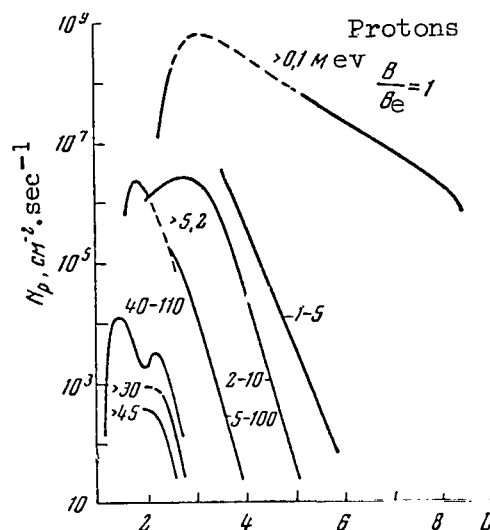


Figure 5

Dependence of Intensity of Protons Having Different Energies in Equatorial Plane on the Distance Expressed in Earth radii

Numbers on the curves designate proton energy in Mev.

O. V. Khorosheva, with the assistance of V. I. Afanas'yeva and Yu. D. Kalinin, analyzed the magnetograms corresponding to this. It was found that characteristic "coils" were observed on the magnetograms at the moment when the additional zone appeared. Data on these "coils" have made it possible to formulate a picture of the current distribution in the ionosphere. The results obtained are shown in Figure 8. It was found that a current flowing around the North magnetic pole occurred in the ionosphere when the additional radiation zone appeared. The force lines of the magnetic field of the Earth, on which this additional radiation zone appeared, passed through the ionosphere where this current was located.

Data obtained during the flights of the "Elektron" satellites disclosed a correlation between the position of the outer boundary, the radiation zones, and the "coils" on the magnetogram. It was found that when the boundary of the zone occurred at the McIlwain L coordinate from 6 to 6.5, there were no "coils" on the magnetograms. When the boundary of the zone shifted toward the Earth or away from the Earth, there were "coils" on the magnetograms, and the probability for the appearance of the "coils" was more than 70%.

V. A. Troitska analyzed data on rapid variations in the magnetic field, and found that there is a close correlation between the frequencies of these fluctuations and positions of the outer boundary for the outer radiation zone.



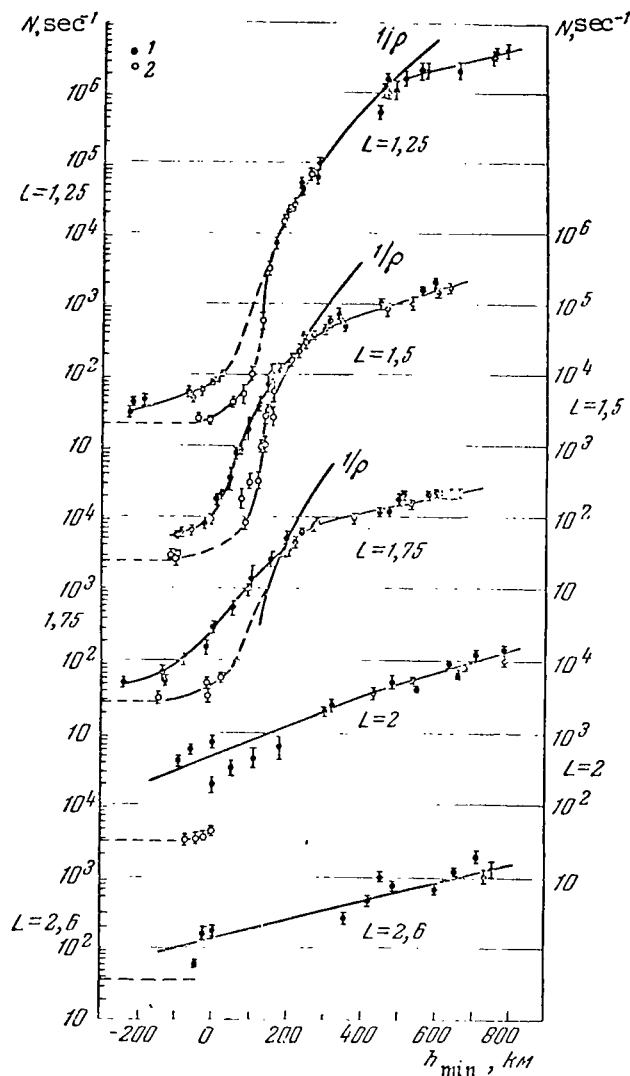


Figure 6

Intensity Dependence of Electrons Having Energies  
of Several Hundred kev in Different Magnetic Envelopes ( $L$ )  
on the Minimum Altitude of the Drift Trajectory Descent  
Toward the Earth

1 - Measurements to the West of the anomaly; 2 - toward the East,  $\rho$  - Atmospheric density. Curves are standardized with the intensity curves  $1/\rho$  at one point for each value of  $L$ .

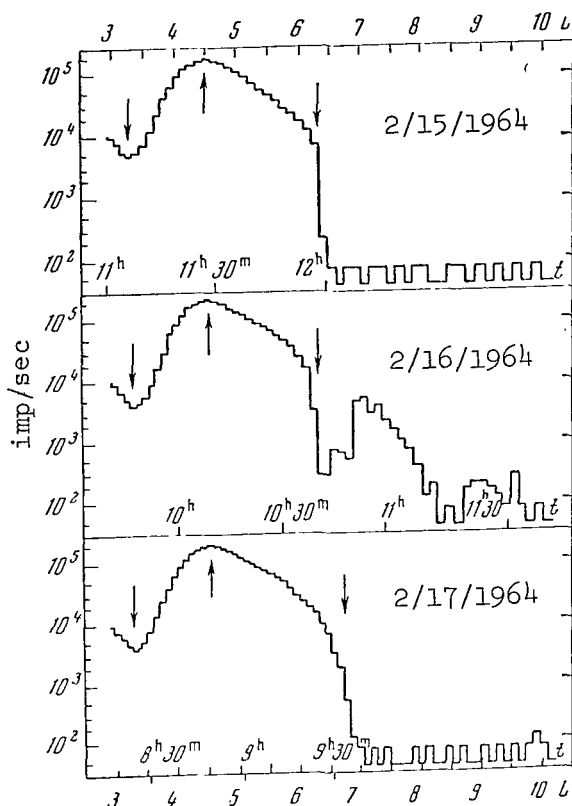


Figure 7

Illustration of the Appearance and Disappearance of an Additional Radiation Zone Sporadically Formed at Large L, as Compared to the L which Are Characteristic For the Main Radiation Zone. World Time.

There is no doubt that a concurrent analysis of data derived from direct observations of the radiation zones on satellites such as the "Elektron" type and data derived from recordings performed on the Earth of the magnetic field, the ionosphere, the auroræ polaris, etc. would provide a great deal of information.

The work of V. M. Driatskiy and his coworkers (Besprozvanova, Gorbushina, et al.) can be used as an example of the very interesting data which can be obtained by analyzing old material obtained in the Arctic. Observations of radio wave absorption in the ionosphere have made it possible to determine the appearance of solar cosmic rays and the formation of directly accelerated radiation. /283

The appearance of solar cosmic rays leads to ionization in the ionosphere of the polar cap. In this case, the ionization changes smoothly, without sharp fluctuations. The formation of directly accelerated

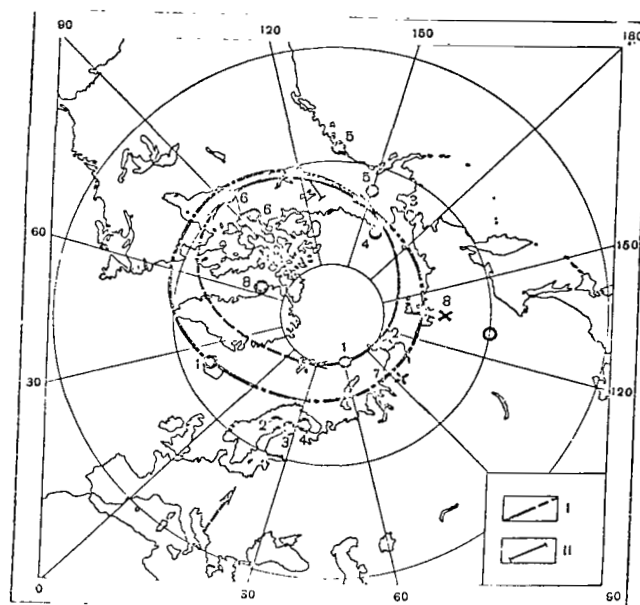


Figure 8

Distribution of a Current System (Solid Line) Based on Data From Magnetic Measurements on February 16, 1964 During the Appearance of a Sporadic Zone (see Figure 7)

The arrows indicate the current direction. The dashed lines connected with the arrows designate the assumed location of the current system in a longitudinal region where the requisite magnetic measurements are lacking. The dot-dash line designates the Fritz zone. The arrow pointing toward the pole indicates the direction of the solar rays.

1 - Tikhaya; 2 - Chelyuskin; 3 - Uelen; 4 - Barrow; 5 - College; 6 - Fort Churchill; 7 - Dickson; 8 - Tiksi (crosses); 1 - Reykjavik; 2 - Kiruna; 3 - Sadankyl; 4 - Murmansk; 5 - Sitka; 6 - Baker Lake; 7 - Resolute Bay; 8 - Thule (light circles).

radiation leads to ionization in the ionosphere in regions where it is most probable that the aurorae polaris will appear. In this case, the ionization sharply fluctuates with time. By employing these properties, one can distinguish between these phenomena. By analyzing the data derived from observations performed over several years, V. M. Driatskiy and his coworkers were able to follow the change in these phenomena with solar activity over several years.

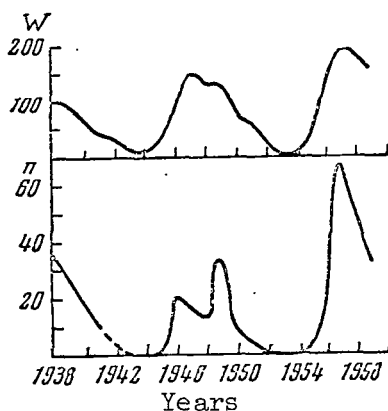


Figure 9

Secular Correlation Between Intensity of Solar Cosmic Rays ( $n$  - Number of days in Which the Third Type is Absorbed) and Solar Activity ( $W$  Wolf Number).

Figure 9 shows the dependence of solar cosmic rays on time, beginning in 1938. We can see that there is a very close correlation with solar activity. The greater the solar activity, the greater the number of cases in which solar cosmic rays appeared.

Figure 10 illustrates the dependence of directly accelerated radiation (DAR) on time, beginning in 1948. We can see that the maximum number of cases in which the DAR appears does not correspond to the maximum, but rather to the minimum, of solar activity. This fact coincides with data obtained by V. M. Driatskiy regarding the nature of the change in the so-called "pearls" with the cycle of solar activity. V. M. Driatskiy established the fact that during the years of minimum solar activity the "pearls" appear over a long time interval measurable in hours. The "pearls" correspond to periodic fluctuations in the intensity of the magnetic fields. If we compare the data on the DAR increase during years of minimum solar activity with the increase in the duration of the "pearls", we arrive at the conclusion that almost strictly periodic fluctuations /284 play a large role in particle acceleration in circumterrestrial cosmic space.

In summing up the present state of and prospects for studying the radiation zones of the Earth, we should note the following facts. Although we have abundant information on the radiation zones at the present time, it is still far from complete. These gaps in our information can be filled up somewhat by utilizing data from continuously-operating stations on the Earth, of which there are several hundred. There is no doubt that in the future continuous compilation of data from stations on the Earth and from satellites such as the "Elektron" type will completely fill out the picture, and the requisite data will be obtained at different altitudes on the

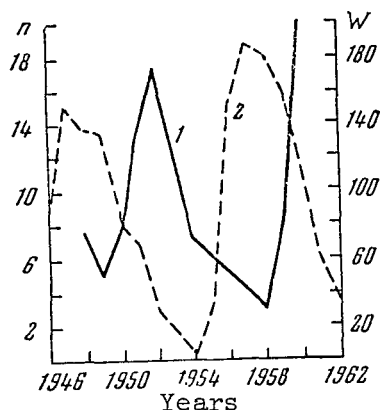


Figure 10

Dependence of Directly-Accelerated Radiation  
(n - Number of Cases in Which the Second Type  
is Absorbed) on Solar Activity (W Wolf Number)

1 - DAR (directly accelerated radiation); 2 -  
Wolf number.

composition and fluctuations of the cold and hot plasma, as well as on variations in the magnetic and electric fields at different frequencies. In this way, the entire process by which particles are accelerated in the radiation zones can be followed. As was indicated above, sometimes this acceleration process last 0.1 seconds in all. In addition, it is clear that particle acceleration takes place in the radiation zones due to a betatron mechanism, as the result of particles being transferred from the remote regions of the magnetosphere to the Earth. This acceleration process lasts very long, for at least several days.

The lack of data on the electric fields and their changes with time makes it impossible at the present time to provide a firm foundation for investigating the possible operation of different accelerating mechanisms utilizing strictly periodic fluctuations in circumterrestrial cosmic space. The principle of self-phasing can lead to the very effective operation of this mechanism, along with others.

It can be expected that the mechanisms by which particles are accelerated in the radiation zones will be discovered in the next few years. This will provide a key for understanding the enormous amount of facts which have been recorded over many years on the magnetic fields, properties of the ionosphere, the aurora polaris, etc. In addition, new methods will be found to solve the puzzle of acceleration of cosmic ray particles on the Sun and in the depths of space.

## REFERENCES

1. O'Brien, B. I. Radiation Zones and Geomagnetic Phenomena. IL, 1963.
2. Davis, L. R., Williamson, J. M. Space Res., 3, 365, 1963.
3. Vernov, S. N., Chudakov, H. Ye., et al. Izvestiya AN SSSR, Seriya Fiziki, 28, No. 12, 2058, 1964.

### PENETRATION PROCESSES INTO THE MAGNETOSPHERE OF THE EARTH, CAPTURE AND ACCELERATION OF SOLAR STREAM PARTICLES, AND THEIR ROLE IN THE DYNAMICS OF THE GEOMAGNETIC TRAP

V. D. Pletnev, G. A. Skuridin,  
V. P. Shalitov, I. N. Shvachvonov

At the present time it appears that there is a very close connection between many geophysical phenomena occurring in circumterrestrial cosmic space. Magnetic storms, the aurorae polaris, the magnetospheres of the Earth, and the radiation zones result from interconnected, dynamic processes occurring in the geomagnetic trap and at its boundaries. This complex of geophysical phenomena is called the dynamics of the geomagnetic trap. /285

As experimental and theoretical studies have shown, these geophysical phenomena are caused by the interaction of solar corpuscular streams with the magnetic field. We assume that the main result of this interaction is the penetration of solar stream particles into the magnetosphere of the Earth. Therefore, the radiation zones can be regarded as a key problem in studying circumterrestrial cosmic space. Attempts to explain the occurrence of radiation zones by a universal, cosmic accelerating mechanism operating in the cosmos are completely unfounded. The fact that the first studies of the radiation zones were performed by scientists investigating cosmic rays strongly corroborates this.

From the point of view of the processes by which solar corpuscular streams interact with the geomagnetic field, the radiation zones represent a phenomenon which is purely geophysical, and is caused by particles penetrating the magnetosphere of the Earth, as well as by the acceleration of these particles within the geomagnetic trap during the inverse phase of a magnetic storm.

The present studies investigate the interconnection between geophysical phenomena occurring in circumterrestrial cosmic space from the point of view of the dynamics of the geomagnetic trap. Preliminary ideas on this

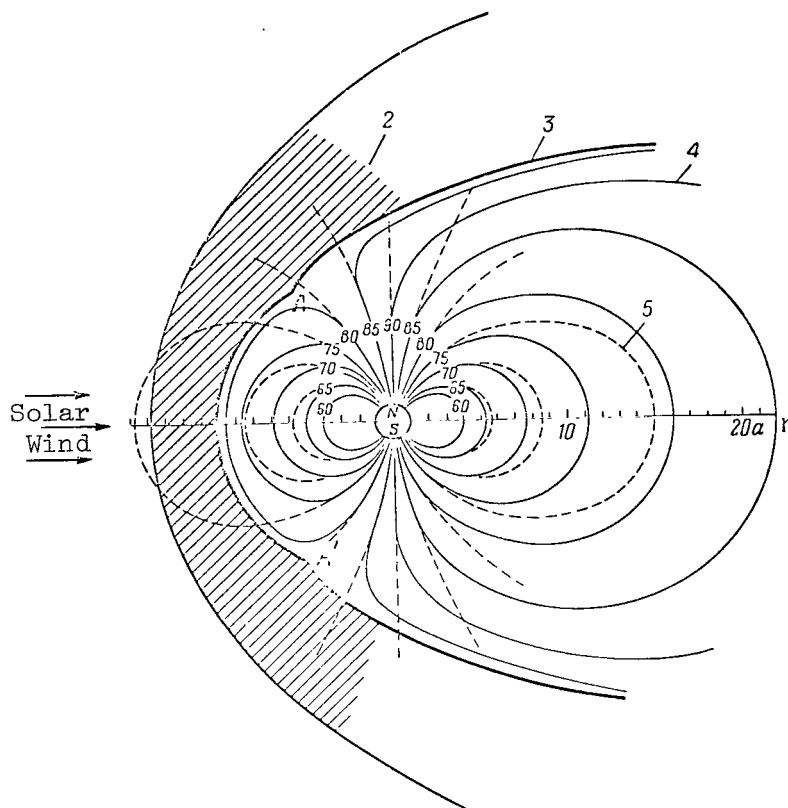


Figure 1

Magnetosphere of the Earth (In the Plane of the Noon Meridian)  
 1 - Front of a stationary shock wave; 2 - Transitional region (magnetopause); 3 - Magnetosphere boundary; 4 - Magnetic force lines of the geomagnetic field according to (Ref. 5); 5 - Magnetic force lines of the unperturbed dipole; A and A' - neutral points. Numbers in the drawing designate latitudes at which the surface of the Earth intersects the force lines.

problem have been presented in the work (Ref. 1).

An expanded version of the work (Ref. 1) was presented at seminars at the Scientific Research Institute of Nuclear Physics of Moscow State University (March 22, 1965), Institute of Terrestrial Magnetism and Radiowave Propagation of the USSR Academy of Sciences (March 31, 1965), and at the Conference on Physics of the Upper Atmosphere at the Institute of Atmospheric Physics of the USSR Academy of Sciences on April 5-7, 1965.

The results of further research on this problem were presented at the VI session of COSPAR (May, 1965) (Ref. 2).





# 1. Motion of Charged Particles in the Magnetosphere Field (Modified Problem of Störmer)

The classical method of Störmer may be employed to estimate the possibility of charged particles penetrating the magnetosphere of the Earth. As is known, the Störmer method was employed to calculate the motion of charged particles in the field of the magnetic dipole extending up to infinity. For a long period of time it was assumed that the geomagnetic field is unlimited in space and coincides with the dipole field at distances  $r$  from the center of the Earth which are greater than  $2a$ , where  $a$  is the radius of the Earth. Recent studies (Ref. 3, 4) have shown that the geomagnetic field is localized in a limited region of circumterrestrial cosmic space, due to the pressure of a corpuscular stream which is constantly in operation (solar wind). This region in which the geomagnetic field is localized is called the magnetosphere of the Earth. /286

The scalar potential of the geomagnetic field within the magnetosphere of the Earth can be represented in the form of expansion in terms of spherical harmonics (Ref. 5):

$$U = a \sum_{n=1}^{\infty} \left[ \left( \frac{a}{r} \right)^{n+1} T_n(\varphi, \lambda) + \left( \frac{r}{a} \right)^n \tilde{T}_n(\varphi, \lambda) \right] = U_0 + U_1. \quad (1.1)$$

Here  $T_n(\varphi, \lambda)$  and  $\tilde{T}_n(\varphi, \lambda)$  are the spherical functions;  $\varphi$  - geomagnetic latitude;  $\lambda$  - angle in the equatorial plane read off from the direction toward the Sun;  $U_0$  - potential of the geomagnetic field from inner sources;  $U_1$  - magnetic field potential of currents flowing along the magnetosphere surface.

In the zero approximation, we have

$$U_0 = - \frac{M_0 \sin \varphi}{r^2}, \quad (1.2)$$

where  $M_0$  is the magnetic moment of the Earth's dipole.

Figure 1 shows the force lines of the magnetic field with a potential determined by expression (1.1), taking into account the first six terms of the expansion of  $U_1$  (Ref. 5).

Within an adequate degree of accuracy, it can be assumed that the field in the central section of the magnetosphere (on the side illuminated by the Sun at the latitudinal interval of  $\pm 70^\circ$  and at the same range of the angle  $\lambda$ ) is axially symmetrical, and can be described by the potential /287

$$U = U_0 + U_1 = - \frac{M_0 \sin \varphi}{r^2} - \frac{M_1}{r_0^3} r \sin \varphi, \quad (1.3)$$

where  $r_0$  is the distance to the magnetosphere boundary along the Earth-Sun line;  $M_0 = 0.31 \text{ a}^3 \text{ gauss} \cdot \text{cm}^3$ ;  $M_1 = 0.41 \text{ a}^3 \text{ gauss} \cdot \text{cm}^3$ ;  $0 < r \leq r_0$ .

In this region, the boundary of the magnetosphere can be regarded as a portion of a spherical surface included between the neutral points ( $H=0$ ), which corresponds in space to the region where charged particles are trapped by the geomagnetic field on the diurnal side - i.e., the section of the geomagnetic trap illuminated by the Sun.

In order to study the penetration of charged particles within the magnetosphere in the boundary region indicated above, let us examine the modified problem of Störmer in an axially-symmetrical field with the potential (1.3). Just as in the classical theory of Störmer (Ref. 6), the equations of motion for a positively-charged particle in a field with the potential (1.3) can be written in a cylindrical system of coordinates  $(\rho, \lambda, z)$  in the following form:

$$\left. \begin{aligned} \frac{d^2 \rho}{dr^2} &= \frac{1}{2} \frac{\partial Q}{\partial \rho}, \\ \frac{d^2 z}{ds^2} &= \frac{1}{2} \frac{\partial Q}{\partial z}, \\ \rho^2 \frac{d\lambda}{ds} &= \frac{\rho^2}{r^3} - \alpha \rho^2 + 2\gamma, \end{aligned} \right\} \quad (1.4)$$

where

$$\begin{aligned} Q &= 1 - \left( \frac{\rho}{r^3} - \alpha \rho + \frac{2\gamma}{\rho} \right)^2, \\ \alpha &= \frac{M_1}{2M_0} \frac{1}{r_0^3}, \end{aligned} \quad (1.5)$$

$\gamma$  is the integration constant of Störmer. All the distances are measured in "Störmer units of length" -  $C_{st} = (M_0 e / m v c)^{1/2}$  (here  $e$  is the particle charge, and  $m$  is its mass).

The boundaries of regions which are excluded and allowed for particle motion are determined by the condition  $Q=0$ , or

$$\frac{\rho}{r^3} - \alpha \rho + \frac{2\gamma}{\rho} = \pm 1. \quad (1.6)$$

The results derived from numerical computations of equation (1.6) are presented below. In the problem under consideration, the form and dimensions of allowed and excluded regions depend essentially on the particle energy, while in the classical theory of Störmer such a dependence does not exist<sup>1</sup>.

For example, when the magnetosphere boundary is located at the distance  $r_0 = 10 a$ , for values of  $a > 0.1924$  - which corresponds in this

<sup>1</sup> In the classical problem of Störmer for a dipole field, excluded and allowed regions are similar in form for particles having different energies. Therefore, the introduction of a Störmer unit of length as a scale makes it possible to eliminate the clear dependence of the size of these regions on energy. In our case, this dependence remains even when the distance is measured in  $C_{st}$ .

case to protons having energies of  $E < 730$  Mev - there are only inner allowed regions which are not connected with space outside of the magnetosphere for the majority of values for the Störmer constant  $\gamma$ . Even if the magnetosphere boundary intersects the inner allowed region<sup>1</sup>, which is possible only for a very narrow range of the values for  $\gamma$ , this still does not indicate that particles may be trapped. /288

The inner allowed region which is intersected by the magnetosphere boundary will be open to particles having energies on the order of cosmic ray energies. In this region, the particle must have the diameter of a Larmor circle which is greater than the distance between the magnetosphere boundary and the inner excluded region. Therefore, after penetrating into the allowed region, the particle must necessarily go back over the magnetosphere boundary. The existence of a boundary layer helps the low-energy particles to penetrate analogous regions. /289

Figure 2 shows the allowed and excluded regions for protons having energies of 450 kev, and also shows the dependence of the allowed region size (in the equatorial plane) on the parameter  $\gamma_1 = -\gamma$ . It also shows the position of the magnetosphere boundary for  $r_0 = 10$  a.

The open allowed regions, formed as the result of the confluence of the inner and outer allowed regions, can only exist for  $\alpha < 0.1924$  (for  $r_0 = 10$  a for protons having energies greater than 730 Mev). Thus, the confluence point in the equatorial plane, which exists in the classical theory of Störmer only for  $\gamma_1 = \gamma_1^* = 1$ , is obtained as a function of energy in the  $1 \geq \gamma_1^* \geq 0.866$  range (for  $\alpha$  accordingly in the  $0 \leq \alpha \leq 0.1924$  range). The open allowed regions exist for particles with  $\gamma_1 < \gamma_1^*$ . We can thus see that in the central magnetosphere region under consideration the penetration of low-energy particles is not possible in the case of  $r_0 = 10$  a during a period which is magnetically quiet.

The examined differences between the motion of charged particles in the field of a limited magnetosphere and their motion in a field of an unlimited dipole are particularly apparent during the first phase of a magnetic storm, when the magnetosphere boundary approaches the Earth, and the field within the magnetosphere is intensified. The boundaries of excluded and allowed regions do not remain constant; as the magnetosphere boundary approaches the Earth, they also shift toward the Earth. The magnetosphere boundary intersects the inner excluded regions only for a very narrow range of values for  $\gamma_1$ .

If, for example, during the first phase of a magnetic storm the magnetosphere boundary is located at the distance  $r_0 = 6$  a, then open allowed regions exist only for protons having energies of  $E > 2.95$  Bev.

<sup>1</sup> Apparently, this effect is due to the utilization of an approximate potential (1.3), and not a precise one (1.1).

Consequently, during the first phase of a storm there is a greater possibility of solar stream particles penetrating the magnetosphere (in the central region under consideration).

We should point out that in 1959 Obayashi (Ref. 7) determined the change in allowed and excluded regions during different phases of a magnetic storm, assuming that the geomagnetic field was localized in space which was consistently limited. The results derived in (Ref. 7) also indicate that it is impossible for low-energy particles to penetrate during the first phase of a storm, while particles can readily penetrate to the depths of the trap during the main phase. However, Obayashi selected a spherical form for the cavity occupied by the geomagnetic field, which recent studies have shown to be incorrect. Therefore, the results derived from our computations for the first phase of a storm differ greatly from Obayashi's calculations.

Similar studies recently carried by Gall (Ref. 8), as well as by Akasofu, Lin, and Van Allen (Ref. 9), have not solved the problem of particle penetration within the magnetosphere. For example, Gall did not take into account the difference between the magnetosphere field and the dipole field, and assumed that the intersection of the inner allowed region by the magnetosphere boundary makes particle penetration possible. As a result, a completely invalid conclusion is reached, which states that - when the magnetosphere is greatly contracted and the field is intensified - the penetration of charged particles within the magnetosphere is facilitated. The authors of the works (Ref. 9), who employed the geomagnetic field potential in the form given by Obayashi (Ref. 7), were primarily interested in cosmic rays.

Thus, the results presented in Section 1 show that it is impossible for particles to penetrate within the magnetosphere in the central region on the diurnal side, both during a magnetically quiet period, and during the initial phase of a magnetic storm.

/290

## 2. Penetration of Charged Particles Within the Magnetosphere in the Vicinity of Neutral Points

In a real geomagnetic field, the possible penetration of charged particles is determined by two concurrent factors. One of them, which facilitates this penetration, is a decrease in the area occupied by the geomagnetic field. The other factor, which is much more important and which renders the penetration more difficult, is an increase in the geomagnetic field strength as compared with the dipole field, due to localization of the field in a limited area of space. It was shown above that, both during a magnetically quiet period and during the first phase of a magnetic storm, the second factor dominates in the central region of the magnetosphere (between neutral points) on the diurnal side. In the region of high latitudes (beyond the neutral points), the geomagnetic field strength is also greater than the dipole field strength, and

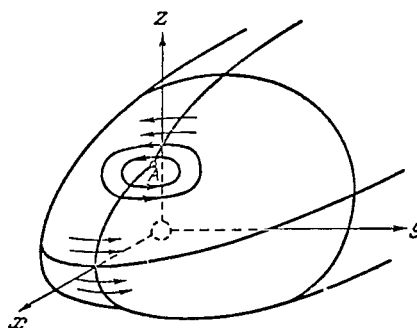


Figure 3

### Distribution of Surface Points at the Magnetosphere Boundary

particle penetration must be more difficult in this region. We should also note that the penetration of solar stream low-energy particles is rendered much more difficult by a sharp gradient of the magnetic field in a boundary layer. However, in the vicinity of the neutral points, the field strength is close to zero, both in a magnetically quiet period and during a magnetic storm. It is therefore natural to study the possible penetration of charged particles within the Earth's magnetosphere in the region of the neutral points.

The potential of a real geomagnetic field was derived by Mead (Ref. 5), taking into account the distribution of the outer boundary points which was obtained in the works (Ref. 10-13). However, this distribution of the surface current when the solar wind flows along the magnetosphere actually corresponds to a two-dimensional flow case, since the authors of the works indicated above employed the method of flat cross sections of the spatial magnetosphere form. Thus, the surface points forming the cavity boundary in each such cross section are not connected with each other, since this connection can only be obtained during a spatial investigation of the problem. As a result of such a "two-dimensional" solution, the magnetosphere boundary is broken in the region of the neutral points. Extrapolation of the solutions obtained by Spreiter and Beard in this region cannot eliminate the break either, and does not provide the correct form of the magnetosphere boundary in the vicinity of the neutral points. Therefore, the magnetic field distribution in these regions must be determined by another method.

Apparently, the surface currents are proton currents. Due to the ideal conductivity along the magnetic force lines and the large mobility of electrons as compared with protons, and also in view of the fact that the magnetic force lines are "grounded" in the ionosphere, the currents of charge separation disappear at the boundary layer (Ref. 14, 15). The surface density of the proton boundary current is as follows, according

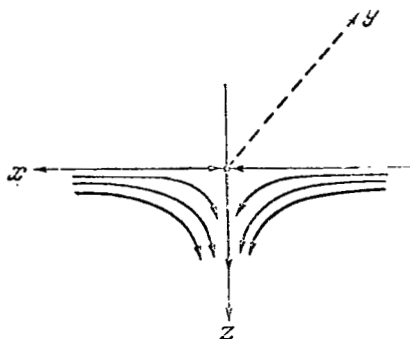


Figure 4

### Magnetic Force Lines in the Vicinity of a Neutral Point

to (Ref. 13):

$$i = \frac{M_0}{2\pi r_0^2} \cos \psi, \quad (2.1)$$

where  $\psi$  is the angle between the normal to the surface and the direction of the solar wind.

Above the neutral point A (in terms of latitude), the boundary current which intensifies the field within the magnetosphere flows in a direction which is opposite to the direction of the same current at latitudes below the neutral point (Figure 3). Due to a decrease in the sweeping effect of the field force lines on the nocturnal side (Ref. 5), when there is a shift to the evening and morning sides the surface currents must close around the neutral point. The geomagnetic field in the vicinity of the neutral point will be decreased by the field of these "circular" currents. When the radius  $l$  of the circular current approaches zero, a point which is particularly neutral is obtained, and thus the solutions match for the form of the magnetosphere boundary in the vicinity of the neutral point. We should note that the surface currents will not be purely circular. Apart from asymmetry in the noon-midnight direction, a certain elongation of the current "rings" is possible along the magnetosphere boundary in the morning-evening direction. In this case, a neutral line appears on the magnetosphere surface, and this line is the geometric location of the neutral points. The effect produced by a change in the geomagnetic field by the circular current, in the vicinity of the neutral point, will depend on the radius of the circle  $l/2$ . The larger the radius of the current circle, the larger the spatial region in which the geomagnetic field will be reduced, but the smaller will be the relative magnitude of this decrease. When there is a decrease in the circle radius, the relative change in the field strength increases, but the dimensions of the region in which the field is decreased are reduced. The effect produced by a field decrease in the center of the current circle becomes appreciable, beginning with  $l$  around 2 a. Actually,

/291

at this distance from the boundary in the direction toward the Earth, the geomagnetic field changes considerably under the influence of the boundary currents. Thus, a hollow (funnel) is formed on the magnetosphere surface; the center of this hollow is the neutral point (or the neutral line). The boundary currents flowing along the funnel walls will form a spiral, due to the fact that the particles forming the boundary current will have a velocity component along the magnetic field. This spiral current leads to a still larger expansion of the funnel.

The existence of the funnel makes it possible for particles, which are located in the region between the magnetosphere boundary and the front of a stationary solar shock wave (in the magnetopause), to pass through the boundary layer. Thus, the multiple reflection of particles from the magnetosphere boundaries, which takes place in the vicinity of the neutral point, can be disregarded (Ref. 16).

For example, let us examine a flat model of a magnetic field in the vicinity of the neutral point, as well as the motion of a charged particle in this field. The scalar potential of the magnetic field in this region, as was shown in (Ref. 17), can be written in the following form:

$$U = -\frac{A}{2}(x^2 - z^2), \quad z > 0. \quad (2.2)$$

The origin of the coordinate system employed coincides with the neutral point; the xz-plane coincides with the plane of the noon meridian; the z-axis is directed within the magnetosphere; the y-axis is a neutral line in the given model (see Figure 4).

The components of the field strength are:

$$\left. \begin{aligned} H_x &= -Ax, \\ H_y &= 0, \\ H_z &= Az. \end{aligned} \right\} \quad (2.3)$$

The coefficient  $A > 0$ ,  $A = -\partial H_x / \partial x = \partial H_z / \partial z = \text{const.}$  The equations of motion for a charged particle in this field have the following form: /292

$$\left. \begin{aligned} \ddot{x} &= Bz\dot{y}, \\ \ddot{y} &= -B(x\dot{z} + z\dot{x}), \\ \ddot{z} &= Bx\dot{y}, \end{aligned} \right\} \quad (2.4)$$

where  $B = eA/mc$ . Integration of these equations in the planes  $x = 0$  and  $z = 0$  yields <sup>1</sup> :

<sup>1</sup> These solutions are absolutely valid only for two extreme cases, when the particle moves along one of the axes Oz or Ox ( $v_n = 0$  or  $w_n = 0$ , respectively). If  $v_n \neq 0$  or  $w_n \neq 0$ , the solutions are approximately valid only for a limited interval of time, whose magnitude depends on  $v_n$  or  $w_n$ , since the particle trajectory deviates from the plane under consideration  $x=0$  or  $z=0$ . The smaller are  $v_n$  or  $w_n$ , the larger the time interval in which the solutions are approximately valid. Since in a stationary field  $v_n$  and  $w_n$  are proportional to  $\sin \theta$  ( $\theta$  - pitch angle of the particle), the solution in question has meaning for rather small  $\theta$ .

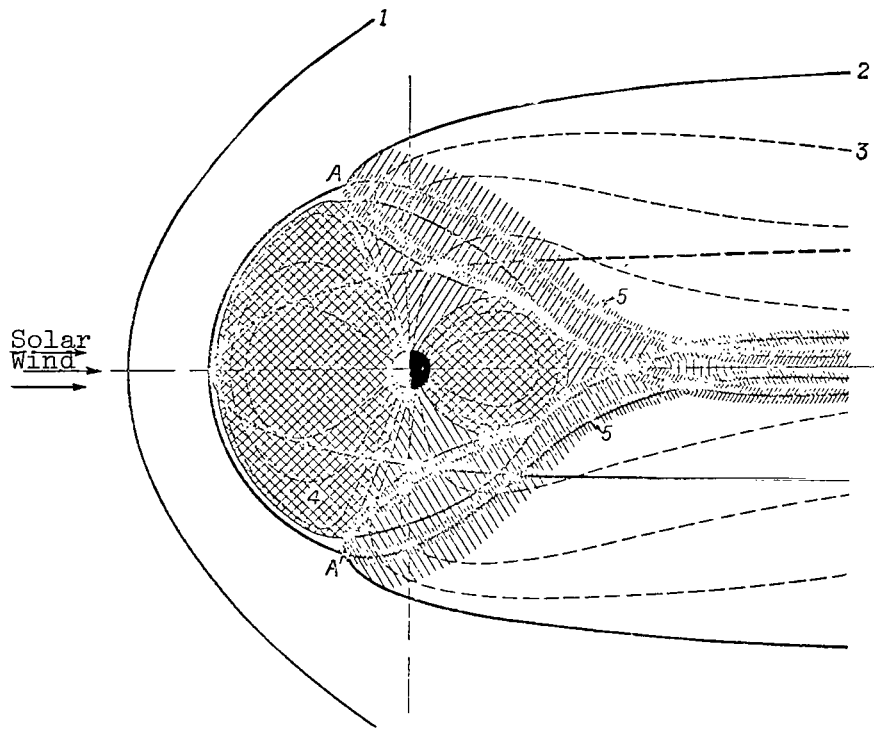


Figure 5

Diagram of Polar Drift Currents of Penetrating Particles

1 - Shock wave front; 2 - Magnetosphere boundary; 3 - Force lines of geomagnetic field; 4 - Region of geomagnetic trap (zone of trapped radiation); 5 - Polar drift currents of penetrating particles.

a)  $x=0$

$$\left. \begin{aligned} \dot{x} &= v_n \sin \left( \frac{B}{2v_s} z^2 + C_1 \right), \\ \dot{y} &= v_n \cos \left( \frac{B}{2v_s} z^2 + C_1 \right), \\ \dot{z} &= v_s = \text{const.} \end{aligned} \right\} \quad (2.5)$$

$$v_n = (x^2 + y^2)^{1/2} = \text{const}$$

b)  $z=0$

$$\left. \begin{aligned} \dot{x} &= w_s - \text{const}, \\ \dot{y} &= w_n \sin \left( C_2 - \frac{B}{2w_s} x^2 \right), \\ \dot{z} &= w_n \cos \left( C_2 - \frac{B}{2w_s} x^2 \right). \end{aligned} \right\} \quad (2.6)$$

$$w_n = (\dot{y}^2 + \dot{z}^2)^{1/2} = \text{const.}$$



Here  $C_1$  and  $C_2$  are integration constants. These solutions have a clear physical meaning, and represent two extreme cases of the particle trajectory in the vicinity of the neutral point. In the first case, the particle moves with a constant velocity  $v_s$  along the z-axis, which is the axis of the funnel and is directed within the magnetosphere (see Figure 4). Thus, the particle rotates with a constant velocity around the funnel axis in the xy - plane. It is characteristic that in this case the particle does not undergo any magnetic reflection, i.e., there is no energy of motion redistribution which is perpendicular or parallel to the field.

In the second case, the particle moves along the boundary magnetic force line (perpendicular to the z-axis) at a constant velocity  $w_s$ . It thus rotates in the xy plane at a constant velocity  $w_n$ .

Since there is absolutely no magnetic reflection, particles with  $v_s > 0$  can penetrate the funnel with no interference. This process will be most probable for particles moving in the plane  $x=0$ .

When entering the magnetosphere, the particles drift in a normal manner.

Due to the nonuniformity of the geomagnetic field, the drift velocity is given by the expression (see, for example, [Ref. 18]):

/293

$$U_1 = \frac{mv_n^2 c}{2eH^4} H \times \nabla \frac{H^2}{2}, \quad (2.7)$$

and the drift velocity produced by the curvature of the force line (Ref. 18) is

$$U_2 = \frac{mv_s^2 c}{eH^4} H \times (H \nabla) H. \quad (2.8)$$

Here  $v_n$  is the velocity component which is perpendicular to  $H$ ;  $v_s$  is the velocity component parallel to  $H$ .

It should be noted that during a magnetically quiet period, the intensity of low-energy charged particles in the magnetopause, close to the boundary of the magnetosphere, amounts to  $5 \cdot 10^{10} \text{ cm}^{-2} \cdot \text{sec}^{-1}$  for protons having energies of 60-100 ev,  $\sim 10^8 \text{ cm}^{-2} \cdot \text{sec}^{-1}$  - for protons having energies of several kev, and  $\sim 10^8 \text{ cm}^{-2} \cdot \text{sec}^{-1}$  - for electrons having energies greater than 200 ev (Ref. 19, 20).

During a magnetically-perturbed period, the stream intensity of such particles considerably increases. Due to this fact, intense polar drift currents of penetrating particles arise within the magnetosphere (Figure 5). Thus, the density of the drift current equals (Ref. 18):

$$j_n = \frac{c}{8\pi p_m} H \times \{ \nabla p_n + [(p_s - p_n)/p_m] (H \nabla) H / 8\pi \}, \quad (2.9)$$

where  $p_s = mnv_s^2$  is the pressure of a particle stream along the magnetic force line;  $p_n = \frac{1}{2} mnv_n^2$  - the pressure of a particle stream which is perpendicular to the force line;  $p_m = H^2/8\pi$  - the magnetic pressure.

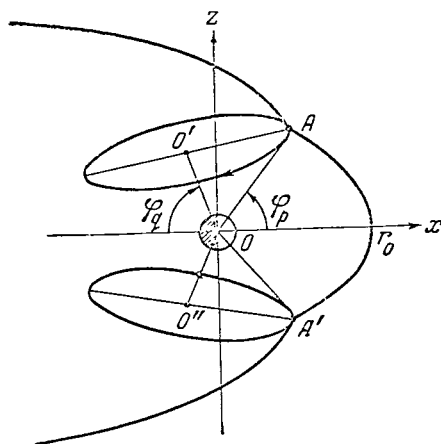


Figure 6

### Model of Circular Drift Currents of Penetrating Charged Particles

The protons drift to the west (to the morning side), and the electrons /294 drift to the east (to the evening side). Since the magnetosphere field is asymmetric with respect to the plane of the morning and evening meridians (the magnetic field is smaller on the nocturnal side of the magnetosphere than it is on the diurnal side), in addition to field gradient components which produce the drift around the polar axis there is a field gradient component which shifts the drift current to the plane of the geomagnetic equator. The drift current thus flows outside of the geomagnetic trap (i.e., region where the radiation is trapped), flowing around it. On the nocturnal side this current shifts to the equatorial plane and produces a "neutral layer" of the field and the plasma dividing the northern and southern portions of the magnetosphere tail. The magnetosphere tail results from the alignment of the magnetic field force lines on the nocturnal side of the magnetosphere, due to a decrease in the geomagnetic field by the field of a penetrating particle current. It should be noted that the geomagnetic field strength in the regions of the magnetosphere which are on the outside with respect to the drift current (in the regions of the magnetic force lines passing through the polar caps) will be increased both by the boundary currents and by the drift current of penetrating particles.

The drift currents of penetrating particles may also represent the outer source of the aurorae polaris excitation. The zones where the charged particles of the drift currents pour out into the dense atmospheric layers correspond to zones of the aurorae polaris maximum. Due to the inclination of the drift currents toward the equatorial plane, these zones from which the particles pour out will actually be distributed at latitudes which are lower on the nocturnal side than on the diurnal side. They must have an oval form, and the width of the zone from which the particles pour out will be greater on the nocturnal side than on the

diurnal side. The amount of particles which are poured out will also be greater on the nocturnal side than on the diurnal side, due to the alignment of the force lines in the magnetosphere tail.

Due to contraction of the field on the solar side and intensification of the circular boundary currents, during a magnetic storm the particles penetrate to deeper layers of the magnetosphere, and these particle streams are more intense than during a magnetically quiet period.

According to the work (Ref. 18), the force of the drift current can be determined by formulas for the dipole field, selecting the particle distribution ( $\sim \sin^{\epsilon+1}\theta$ ) with respect to the pitch angles in such a way that the particle density in the high latitudinal region is slightly greater than the density in the equatorial region. At an arbitrary point on the force line  $n(\varphi)$  the particle density can be expressed by the particle density on the same line at the equatorial point  $n(0)$  in the following way:

$$n(\varphi) = n(0) \left( \frac{H(0)}{H(\varphi)} \right)^{\epsilon/2}, \quad (2.10)$$

where  $H(0)$  is the field strength at the equator of this force line. If the current is concentrated at high latitudes, then the corresponding dipole force lines will have larger  $L$  (on the order of 100). Then  $H(\varphi)/H(0) \sim 10^4$  and for  $\epsilon = -1.1$   $n(\varphi)/n(0) \sim 10^2$ . Assuming that the particle density decreases by one or two orders of magnitude during a shift along the radius vector by one radius of the Earth, and assuming that  $nE \approx 500 \text{ kev} \cdot \text{cm}^{-3}$  for the entire spectrum of particles penetrating the magnetosphere from the magnetopause, according to formula (72) from the work (Ref. 18) we can obtain the current force: /295

$$I \approx 10^7 - 10^8 a. \quad (2.11)$$

This quantity is 1-2 orders of magnitude greater than in the model of the equatorial circular current (Ref. 18).

The change in the geomagnetic field strength close to the surface of the Earth by the field of the drift current was calculated according to the following simple model. The drift current was assumed to be circular, the northern and southern circles were "fixed" at the neutral points (Figure 6), and the radius and inclination of the circles were varied.

Let us present a few of the computational results. For

$$\begin{aligned} r_p &= 0.1 = r_0; & \varphi_p &= 60^\circ; & r_q &= OO' = 0.6r_0; \\ I &= 2 \cdot 10^7 a; & \varphi_q &= 85^\circ \text{ and } 80^\circ; & r_0 &= 6a \text{ and } 10a \end{aligned}$$

(for the notation, see Figure 6) Table 1 gives the field strength of currents (in gammas) at the equator of the Earth on the diurnal side ( $H_1(0)$ ), on the nocturnal side ( $H_2(0)$ ), and at the pole ( $H_p$ ).

The current field strength given in the Table is proportional to the force of the current  $I$ , which allows conversion for any values of  $I$ .

TABLE 1

$r_0$	10a		6a	
$\varphi_q^\circ$	85	80	85	80
$H_1(0)$	90	100	150	165
$H_2(0)$	140	150	235	245
$H_p$	120	130	200	215

The magnetic field of the drift currents decreases the horizontal component of the geomagnetic field at the mean and low latitudes, and increases the vertical component in the polar regions.

We should note that field asymmetry on the diurnal and nocturnal sides is not observed for every inclination of the current circles toward the equatorial plane.

For the example in question, the magnetic moment of the current is  $0.4 M_0$  ( $M_0$  is the magnetic moment of the Earth's dipole) in the case of  $r_0 = 6a$ .

An intense drift current of penetrating particles greatly changes the geomagnetic field in the region where it is located, as a result of which the characteristics of the current itself are greatly changed. The work (Ref. 21) demonstrated the fact that an outer neutral line which is parallel to the current can appear, due to the intense drift current in the geomagnetic field. In our case, this line shifts from the current toward the equator. Due to the appearance of this neutral line, the hollow on the magnetosphere boundary widens in the vicinity of the neutral point, thus presenting an additional possibility for charged particles to penetrate the magnetosphere from without, in the region of lower latitudes. Streams of these particles intensify the drift current. In addition, as was shown in the work by Dungey (Ref. 22), the reverse effect of a field changed by the current will lead to a sharp intensification of the current itself.

Under the influence of a penetrating particle current, the magnetic force lines, which define the geomagnetic trap at high latitudes, will be aligned. Thus, in addition to a latitudinal shift toward the equator, 296 the drift current of penetrating particles will descend along the aligned magnetic force lines.

Similar effects, but on a smaller scale, will take place on the nocturnal side, where the drift current will also enter the region in space

occupied by the geomagnetic trap. Due to this fact, the neutral layer in the magnetosphere tail will begin at smaller geocentric distances, and the magnetosphere boundary will approach the Earth on the nocturnal side.

The geomagnetic field decreases more appreciably at the mean and low latitudes as the drift currents approach the Earth. The time required for these currents to be established corresponds to the first phase of a magnetic storm. The intensification of the currents due to additional penetration by outer charged particles causes the main phase of the storm to develop. The greatest depth to which the currents descend corresponds to the maximum of the main phase.

Drift of penetrating charged particles in the geomagnetic field leads to separation of the protons and electrons, and to the formation of morning proton branches and evening electron branches of the current. A similar charged separation occurs at the magnetosphere boundary. However, as was shown in the works (Ref. 14, 15), the field of this separation is balanced by particles from the ionosphere, due to the ideal conductivity along the magnetic force lines. At the same time, the penetrating electrons, which have greater mobility than the protons, will penetrate more deeply along the force line under the influence of this field of the charge distribution. Therefore, the electron branch of the current will be diffused along the magnetic force lines. As a result, the magnetic effect of the morning (proton) branch of the current will be stronger than the evening branch (electron), which is indicated in the diurnal variations of magnetic perturbation intensities.

The inclination of the Earth's axis to the ecliptic plane causes one of the drift currents to have greater intensity than the other. This is indicated in the seasonal variations of magnetic storm intensity. In summer the magnetic storms must be more intense than during winter.

Due to the more rapid descent of drift currents on the diurnal side during a magnetic storm, the zones from which the particles pour out will move downward in a latitudinal direction more rapidly on the diurnal side than on the nocturnal side. The latitudinal asymmetry of these zones, which was pointed out previously, at the surface of the Earth will decrease.

According to the calculations of Chapman and Akasofu (Ref. 21), the fluctuational amplitude of protons in a drift current which is perpendicular to the neutral line will be approximately ten times greater than the amplitude of similar fluctuations of electrons having the same energy. Consequently, the protons will penetrate more deeply into the boundary region of the geomagnetic trap. This must lead to a separation of the proton and electron fields in the zones from which particles pour out. As has already been stated, as one recedes from the penetration region the electron and proton branches of the drift current become separated. Therefore, electrons and protons (in one and the same spatial region) must pour out concurrently only on the diurnal side. Proton aurorae polaris must occur primarily on the morning side, while electron aurorae polaris must primarily occur on the evening side.

However, during a magnetically quiet period this effect may be suppressed, due to the drift of particles which have poured out around the polar axis, since the process of the particles pouring out will be much less intense than during a magnetic storm. According to the theory discussed above, the maximum particle penetration, and consequently the most intense pouring out, will occur during the first phase and during the early main phase of a storm. During the main phase maximum, the steady, intense drift current of penetrating particles will prevent both penetrating particles and particles of the current itself from pouring out.

/297

In our opinion, the following data provide experimental corroboration of the picture just presented for the penetration of charged particles within the magnetosphere.

1. The intensity of magnetic perturbations, both during world wide storms and during polar storms, is greatest at high latitudes, which correspond to the regions which we have proposed for particle penetration.

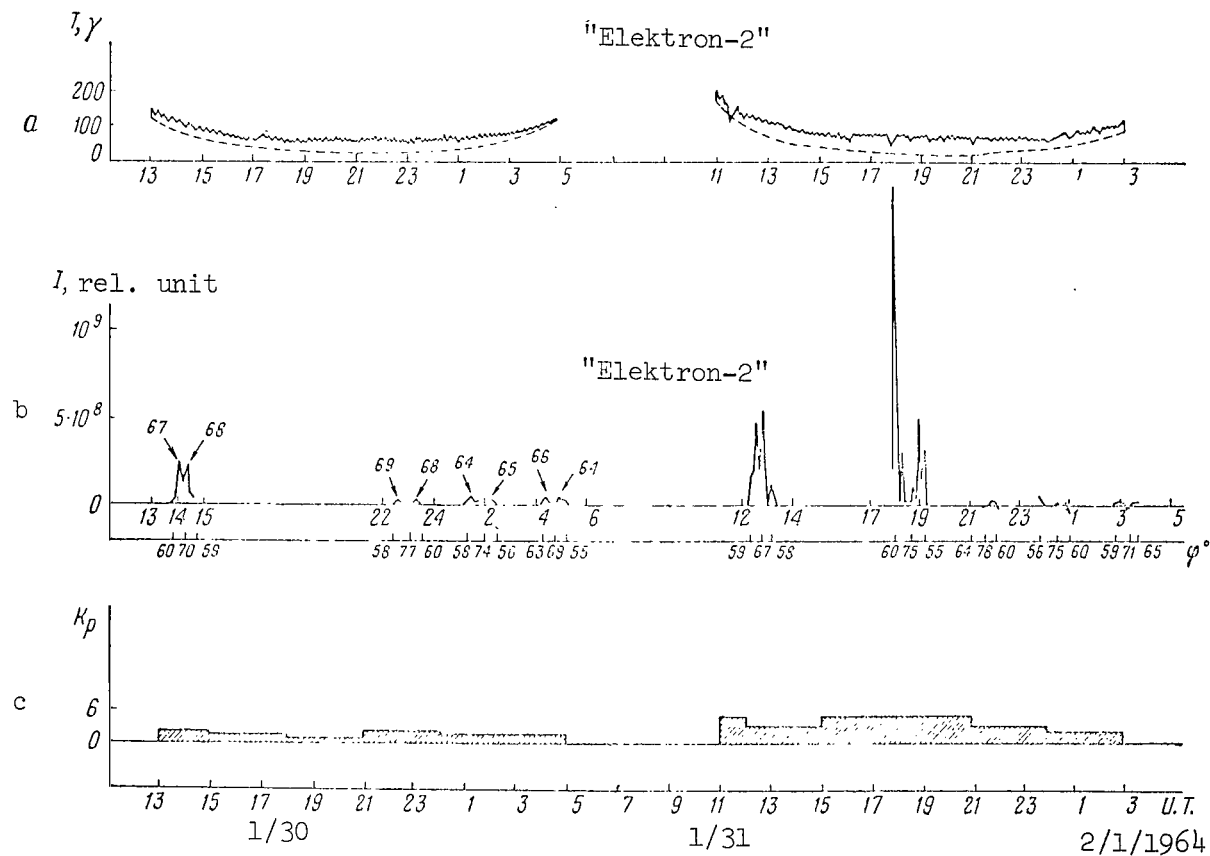
2. The horizontal component of the field within the geomagnetic trap decreases during the main phase of a storm, and the vertical component of the field increases in the region of the polar caps (beyond the neutral points).

3. During a storm intense geomagnetic perturbations are accompanied by strong aurorae polaris, and also by a sharp increase in radio emission absorption along the aurorae polaris zone and by an increase in electron streams in the lower atmospheric layers in the aurorae polaris zone (Ref. 21). We relate this to charged particles pouring out of the polar drift currents.

4. In the opinion of the authors, the position of the zones in which the aurorae polaris may be best observed, the behavior of these zones during magnetic storms (Ref. 23), and the fact that the aurorae polaris are observed at anomalously low latitudes during strong magnetic storms corroborate the general theoretical picture which has been formulated for particle penetration within the Earth's magnetosphere.

5. In my opinion, the asymmetry which was recently pointed out (Ref. 24) in the change of the horizontal component of the geomagnetic field at low and mean latitudes during magnetic storms can be explained by the openness of the drift current on the nocturnal side, and also by its inclination toward the equatorial plane.

6. Measurements of the geomagnetic field and of low-energy charged particles, which were performed on the satellites "Elektron-1" and "Elektron-2" (Ref. 25-27), indicate that there is a good correlation between intense currents of low-energy particles and the variations of the geomagnetic field in the high-latitudinal regions of the magnetosphere. Figures 7-9 present the results derived from geomagnetic measurements on the satellite "Elektron-2" (Ref. 25), as well as the results derived from



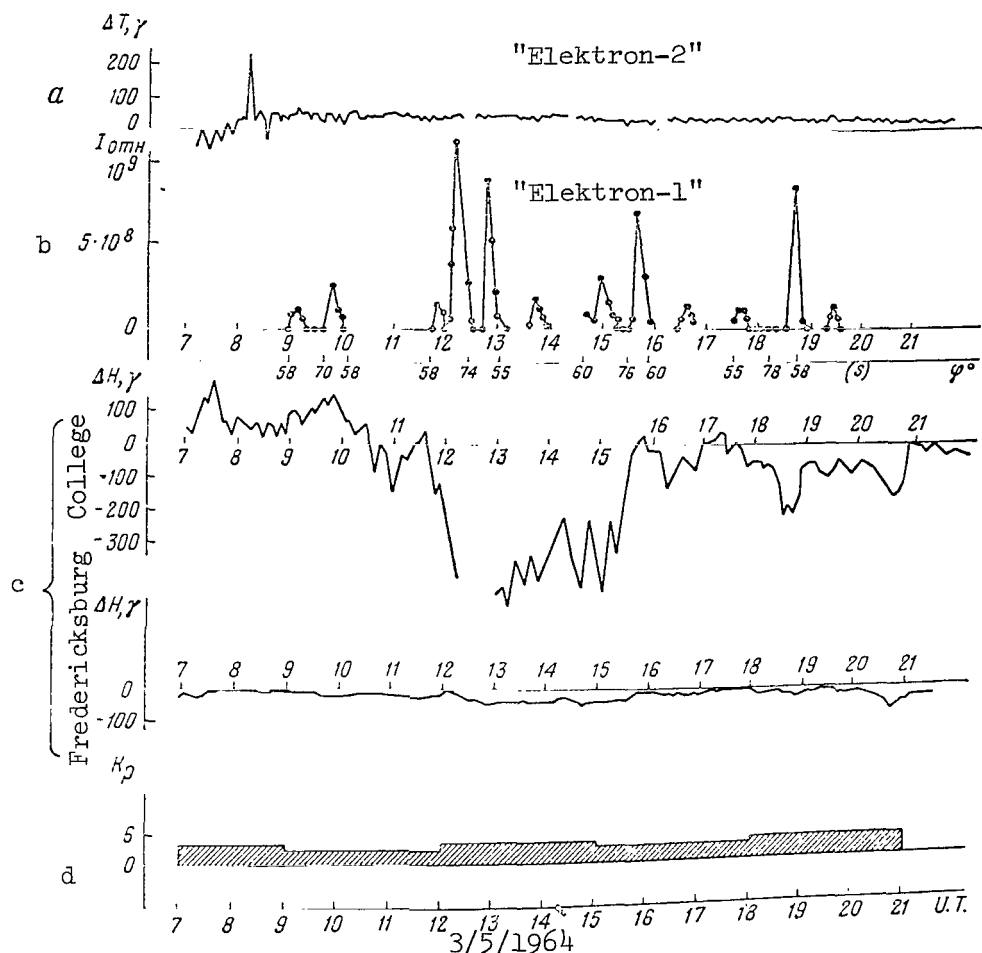


Figure 8

Difference Between the Geomagnetic Field Strength Measured on the Satellite "Elektron-2" and Theoretical Values of This Strength (Ref. 25), March 5, 1964

(a); Intensity measurements of a stream of electrons of  $E \geq 20$  kev (Ref. 26) on the satellite "Elektron-1". The geomagnetic latitudes  $\varphi$  are shown (b); Change in the horizontal component of the geomagnetic field at the College and Fredericksburg stations (c);  $K_p$  - index (d).

measuring the intensity of streams of low-energy electrons on the satellite "Elektron-1" (Figures 7-8) (Ref. 26) and on the satellite "Elektron-2" (Figure 9) (Ref. 27).

From our point of view, the occurrence of streams of low-energy particles at high latitudes (Figure 7, 8), which corresponds with high-latitude polar perturbations and with the  $K_p$ -index, can be explained



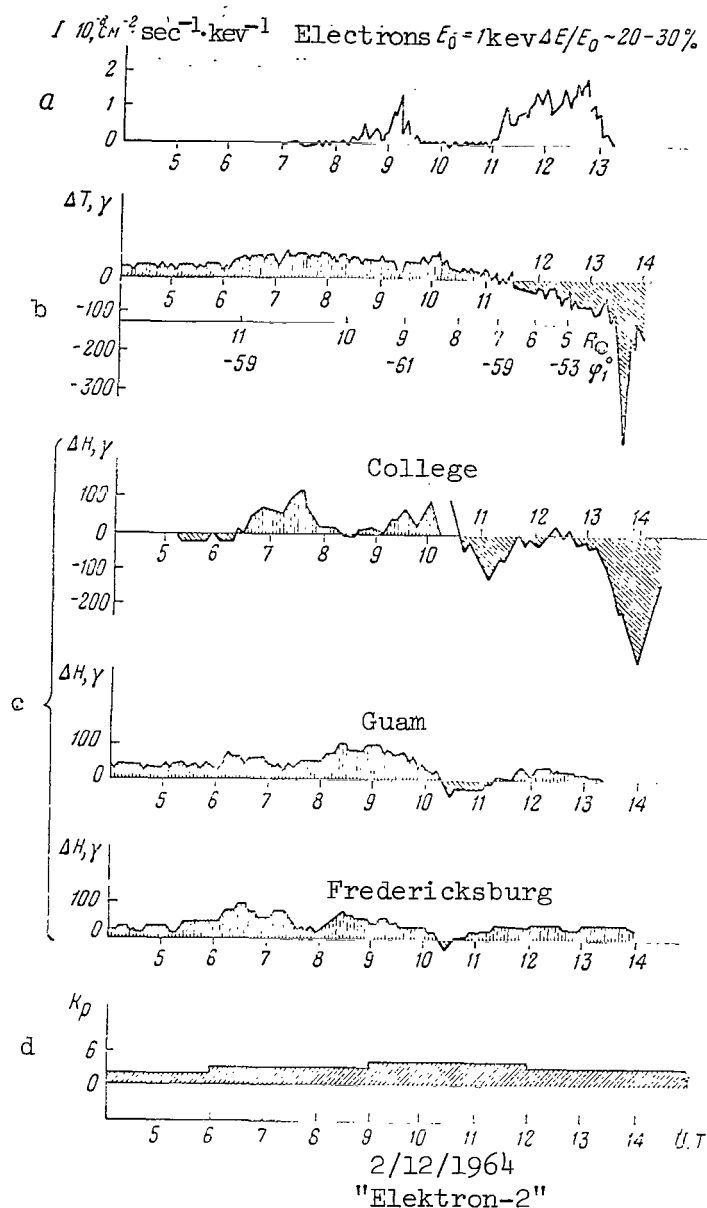


Figure 9

Measurements of Electron Flux Intensity  $E = 1 \text{ kev}$  on "Elektron-2" (Ref. 27), February 12, 1964 (a); Difference Between Geomagnetic Field Strength Measured on "Elektron-2" and Theoretical Values. Geocentric distances and Geographical Observational Latitudes are Shown (Ref. 25) (b); Changes in Horizontal Component of Geomagnetic Field at the College, Guam, Fredericksburg stations (c);  $K_p$ -Index (d).

by the penetration of charged particles within the magnetosphere.

We would like to point out Figure 9 in particular, which shows the anomalous change in the geomagnetic field strength in the region where a penetrating stream of electrons was recorded. In our opinion, this corresponds to a decrease in the geomagnetic field strength in the region of the penetration current. It should be noted that similar anomalous effects were observed several times, and always on revolutions passing at high geomagnetic latitudes on the morning side. On revolutions which passed through the region of low latitudes on the evening side, these phenomena were not discovered. We should recall that, according to our model, the morning branch of the drift current is more intense than the evening branch.

The final result derived from studying the geomagnetic field on "Elektron-2" is of interest (Ref. 25). With an increase in the magnetic perturbation, the region in which the difference between the measured and calculated geomagnetic field strength  $\Delta T = 0$  passes through zero, beyond which the influence of the field of outer sources on the geomagnetic field is substantial, is discovered in space at smaller geocentric distances and at lower latitudes. Thus, the shift in the region  $\Delta T = 0$  to smaller distances and lower latitudes only takes place in every observed case during the main phase of a storm, while the region  $\Delta T = 0$  retains its position in space during the initial phase.

In our opinion, this indicates that polar drift currents are established toward the end of the first phase of a storm, and that the geomagnetic field decreases strongly with the field of these drift currents during the main phase of a magnetic storm. /299

7. In model experiments ([Ref. 28, 29] and others), when a plasma current flows around the dipole field, plasma penetration into the magnetosphere is observed through the neutral points. This is particularly apparent in Figure 10, a, which was taken from the work (Ref. 28); this Figure shows a plasma current flowing into the tail on the "nocturnal" side. Figure 10, b, (Ref. 28) shows the manner in which particle penetration changes when the dipole axis is inclined toward the direction of the incoming stream. The drift current formed by positively-charged particles flows along the "morning" side into the tail of the magnetosphere (Figure 10, c).

8. "Explorer-10" (Ref. 30) first observed the effect produced by the magnetosphere boundary approaching the Earth on the nocturnal side during a magnetic storm. Measurements on "Explorer-14" in 1963 made it possible to study the behavior of the magnetic tail of the Earth in detail (Ref. 31). They showed, for example, that on the magnetically quiet day of January 27, 1963, in the plane of the geomagnetic equator the aligned force lines of the tail began on the nocturnal side of the Earth at distances which were greater than 10  $a$  from the center of the Earth (Figure 11, a). In this same region of space on January 30, 1963 during a magnetic storm with  $K_p=4$  /301

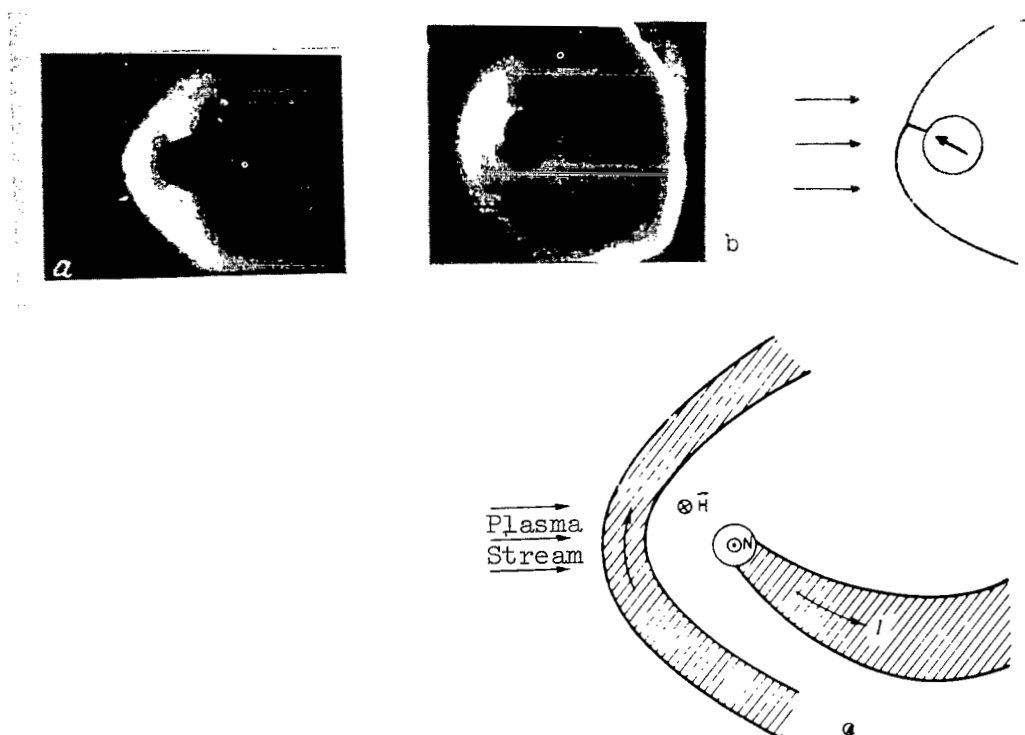


Figure 10

Photograph from the work (Ref. 28) showing the Penetration of Charged Particles Through the Neutral Points Within the Magnetosphere (Model Experiment). The axis of the dipole is perpendicular to the direction of motion of the plasma stream (a). The penetration diagram illustrates the case when the dipole axis is inclined to the plasma stream. Penetration of particles is observed at a neutral point extending toward the stream (b). Distribution of the currents in the experiment (Ref. 28) (c).

the magnetic tail began at a geocentric distance of 8 a (see Figure 11, b). It can also be seen from Figure 11, b, that the drift current of penetrating particles which create the magnetic tail of the Earth leads to alignment of the force lines during a magnetic storm in the region of the geomagnetic trap at high latitudes.

These results fully substantiate the theoretical concepts presented above regarding the distribution of drift currents of penetrating particles on the nocturnal side and their effect upon the geomagnetic field.

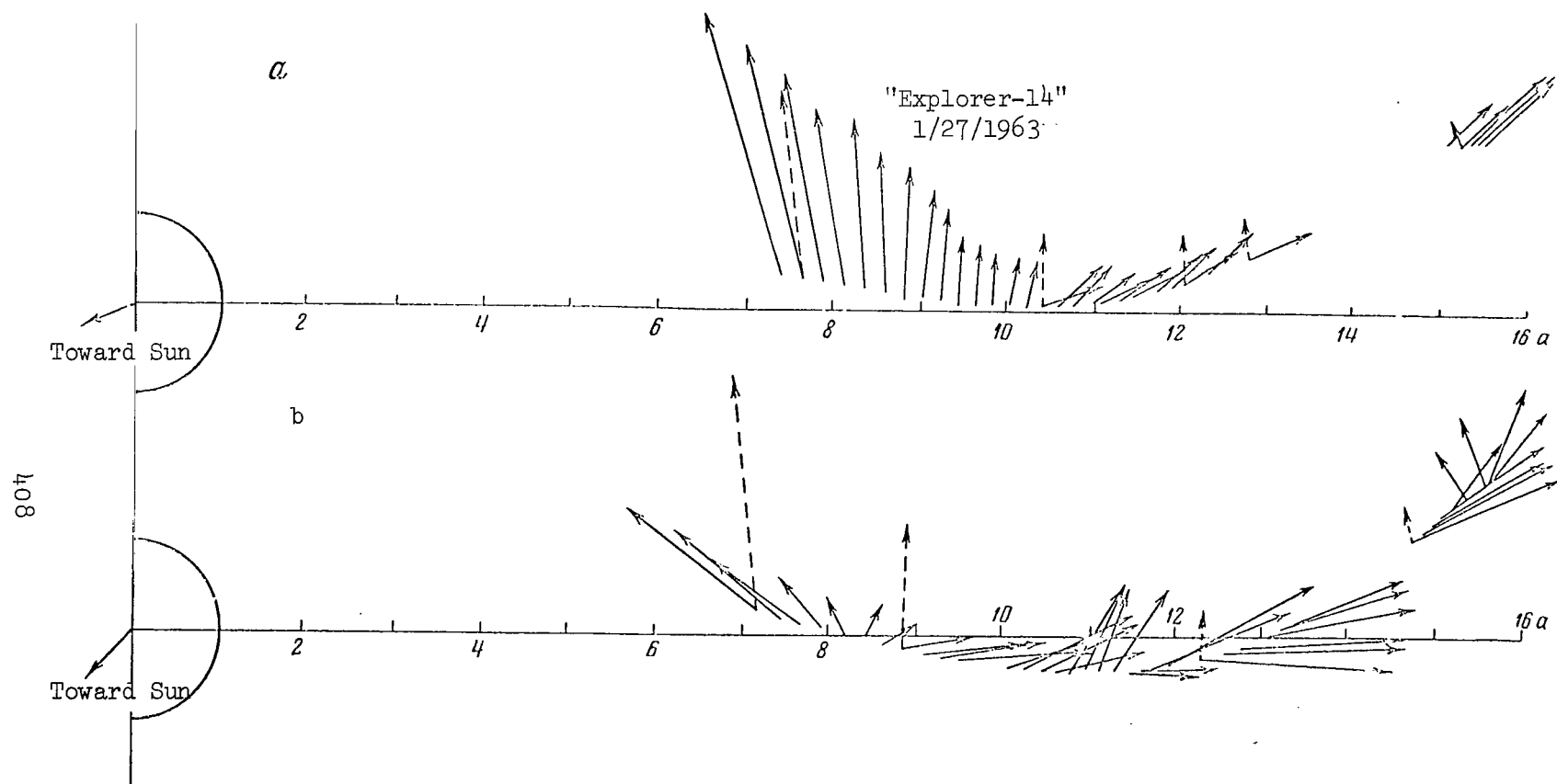


Figure 11

Geomagnetic Field Strength Measurements in the tail of the Magnetosphere (Ref. 31)

a - Magnetically quiet day; b - Day with  $K_p = 4$

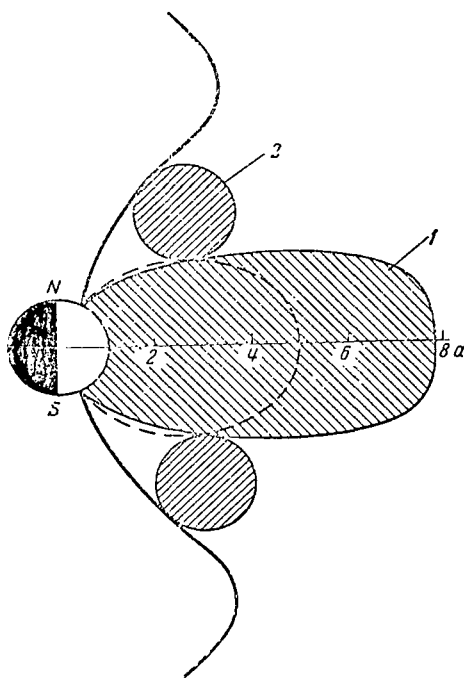


Figure 12

Meridional Cross Section of the Magnetosphere,  
Whose Field is Transformed by the Outer Pressure  
and by the Field of the Drift Current of Penetrating Particles

1 - Geomagnetic trap boundary on the diurnal side during the main phase of a storm; 2 - Transverse cross section of drift currents. Dotted line designates magnetic force line of unperturbed dipole with  $L = 5 a$ .

### 3. Capture of Charged Particles in the Geomagnetic Trap and Their Acceleration During the Inverse Phase of a Magnetic Storm

As has already been indicated, during the main phase of a storm the field in the geomagnetic trap is deformed due to the influence of a penetrating particle current. This deformation is as follows. The force lines of the field which define the geomagnetic trap at the high latitudes become aligned and approach the equator. Thus, high-latitudinal regions of the geomagnetic trap, which were previously inaccessible, are opened up to the penetrating particles.

The effect of this "lateral contraction" of the magnetic trap during the main phase of a storm will be particularly intense, if the outer boundary of the geomagnetic trap - which is located at a smaller distance from the Earth during the first phase of a storm than during a magnetically-quiet period - remains at this same distance during the main phase. The 303

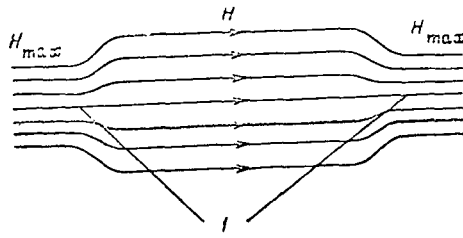


Figure 13

Diagram of Normal Magnetic Trap of Charged Particles  
Used in Plasma Physics

1 - Magnetic mirrors.

total magnetic stream within the geomagnetic trap decreases simultaneously, which results from the fields of polar drift currents being superimposed on the magnetic field within the trap.

Let us examine a penetrating particle drifting along the boundary of the geomagnetic trap (see Figure 12). Let us assume that a shift in the boundary force line toward the equatorial plane causes this particle to enter the region through which the dipole force line passes in a normal, unperturbed state - for example, with  $L = 5a$ .

However, the total magnetic stream  $\Phi$ , which passes through the drift ring of the particle and which is the third adiabatic invariant, does not equal the stream  $\Phi_0$  passing through the same drift ring in a field unperturbed by the storm (dipole). If the particle drifts along the surface with  $L = 5a$  in an unperturbed field, then the stream  $\Phi_0 \gg \Phi$ . In the example under consideration, calculations show that in a perturbed field  $\Phi = \Phi_0$  for a dipole line with  $L = 3a$ .

After the abrupt termination of the solar stream causing the storm, sharp restoration of the geomagnetic field is initiated. Since the solar stream is a perturbing factor, the restoration of the field is initiated outside, from the magnetosphere boundary. As a result, the boundary returns to its unperturbed state  $r_0 = 10a$ . The neutral points shift latitudinally toward their initial position  $\varphi = \pm 72^\circ$ . A rupture thus occurs between the stream of particles entering through the neutral points and the stream of particles penetrating during the main phase of the storm. The drift currents of penetrating particles are trapped in the magnetosphere regions which are outside the geomagnetic trap. The field of the geomagnetic trap will be restored more slowly closer to the Earth than on its boundary. During this restoration process, "lateral extension" of the geomagnetic trap will occur, leading to deeper penetration of the trapped particles within the trap and to acceleration of these particles.

In order to understand the manner in which the charged particles penetrate the depth of the trap, as well as the manner in which they are trapped and accelerated, let us examine a trap (see Figure 13) in which the plasma heats up under laboratory conditions (we shall call this a straight trap).

If adiabatic, lateral- or, as it is called, radial-contraction of this trap occurs in such a way that the first, second, and third adiabatic invariants of the charged particle motion in the magnetic field are retained, then the particles will approach the trap axis, and their energy /304 and density will increase. The acceleration of charged particles in a contracted trap is betatronic. The mechanism for this acceleration is well-known (Ref. 33). During adiabatic, radial contraction, betatronic acceleration leads to an increase in the velocity component of the particle which is perpendicular to the magnetic force line, and to an increase in the particle pitch angle.

If not only radial contraction of the trap occurs, but also contraction along the axis, then the energy and density of the charged particles increase to still a greater extent, since additional Fermi acceleration occurs due to convergence of the magnetic mirrors. As a result of the Fermi acceleration, the particle pitch angle decreases (Ref. 33).

We should also note that in adiabatic contraction the total magnetic stream  $\Phi$  must remain constant through the drift orbit of the particles around the trap axis, since it is an adiabatic invariant. Due to the invariant nature of  $\Phi$ , during contractions the particle will be located at one and the same surface of the force lines, but this drift surface will approach the trap axis. Particle acceleration in this type of trap has been studied extensively in plasma physics.

The behavior of the geomagnetic trap is different during the inverse phase of a storm, because its field - when the strength is both decreased and increased - is not transformed due to expansion or contraction, but due to the superposition of an additional outer field of the drift currents. Therefore, the geomagnetic trap is contracted when the field strength decreases and is expanded when the field strength increases. This provides a basis for calling such a trap an inverse trap.

The physical processes in an inverse trap, which are related to a change in energy, density, and pitch angles of the charged particles, barely differ from processes in a straight trap, and can be described by the same formulae which are extensively used in plasma physics.

However, one principal difference lies in the fact that the total change in the size of the inverse trap field when it is expanded corresponds, in terms of the physical results, to the change in the size of the direct trap field when it is contracted.

For example, if the magnetic stream through the cross section of the

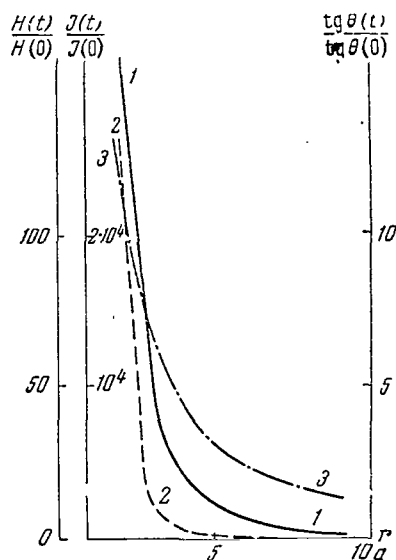


Figure 14

Change in Magnetic Field Strength in the Equatorial Plane During the Inverse Phase of a Storm (1);  
Change in intensity of charged particle streams during the inverse phase of a storm in the equatorial plane (2);  
change in  $\text{tg } \theta$  at different distances from the Earth in the equatorial plane (3).

drift surface of penetrating particles equals  $\Phi$  for  $L = 3a$  at the end of the main phase of a storm, then during the inverse phase the acceleration of particles and the increase in their density in the geomagnetic trap will be the same as in a direct trap during contraction from  $L = 10a$  to  $L = 3a$ . The mean relative increase in energy  $W$  during this contraction - if it is assumed that it is uniform both along the radius and along the axis - will equal (Ref. 32):

$$\frac{\bar{W}(t)}{\bar{W}(0)} = \left( \frac{V(t)}{V(0)} \right)^{2/3} = \left( \frac{n(t)}{n(0)} \right)^{2/3}. \quad (3.1)$$

Here  $V$  is the area occupied by the field;  $n$  - the particle density. In our example,  $W(t)/W(0) = 11$  and  $n(t)/n(0) = 37$ . This effect adequately explains the experimentally-observed increase in the intensity of high-energy particle streams by one order of magnitude in the outer zone during the inverse phase of a storm. /305

betatronic acceleration due only to radial contraction at any point on the geomagnetic trap is given by the expression

$$\frac{W_{\perp}(t)}{W_{\perp}(0)} = \frac{H(t)}{H(0)} = \beta. \quad (3.2)$$

The change in particle density is also proportional to  $\beta$ . The change in  $\text{tg } \theta$ ,



where  $\theta$  is the pitch angle, is

$$\frac{\operatorname{tg} \theta(t)}{\operatorname{tg} \theta(0)} = \beta^{1/2}. \quad (3.3)$$

Figure 14 presents graphs of the relative change in the geomagnetic field within the geomagnetic trap (curve 1) in the equatorial plane at different distances from the center of the Earth. It also gives the change in intensity of a particle stream  $J$  (curve 2) and  $\operatorname{tg} \theta$  (curve 3), corresponding to these field changes. The quantities  $J(t)/J(0)$  and  $\operatorname{tg} \theta(t)/\operatorname{tg} \theta(0)$  are found for a storm in which the force line encompassing the magnetic stream  $\Phi = \Phi_0$  for  $L = 3a$  is the boundary force line of the geomagnetic trap during the main phase. Thus, the particle spectrum of the radiation zone formed will depend on the distance  $R$  from the center of the Earth; the greater is  $R$ , the smaller is the maximum energy of the trapped particles.

We should note that a rigorous calculation also requires the consideration of the axial contraction due to the ascent of the specular points. The change in the longitudinal particle energy due to axial contractions is

$$\frac{W_{\parallel}(t)}{W_{\parallel}(0)} = \frac{\mathcal{L}(0)}{\mathcal{L}(t)} = k^2, \quad (3.4)$$

and the decrease in the pitch angle is characterized by the expression

$$\operatorname{ctg} \theta(t) = \sqrt{\frac{W_{\perp}(t)}{W_{\parallel}(0)}} = k. \quad (3.5)$$

Here  $\mathcal{L}$  is the distance between the specular points of the particle along the magnetic force line.

We should point out that the coefficient  $k$  is small during purely radial contraction, and becomes significant only in the case of very great contraction ( $\beta \sim 1000$ ), when  $k \approx \beta^{1/2}$ . In addition, particles falling on one and same force line, but at different points along it, acquire different energies as a result of the acceleration, since  $\beta$  will change along the force line.

Thus, the graphs shown in Figure 14 can be analyzed and show the minimum relative acceleration for particles located in the equatorial plane. A rigorous computation of trapped particle distribution in the geomagnetic trap, as well as their energy spectrum, is only possible by solving the so-called "contraction equations". These equations connect the particle trajectory in a magnetic field which is modified during the main phase of a storm with the particle trajectory in a field unperturbed by a storm. These equations are due to the retention of the first, second, and third adiabatic invariants  $\mu = \text{const}$ ,  $J = \text{const}$ ,  $\Phi = \text{const}$  ( $\mu$  - the magnetic moment of the particle,  $J$  - the longitudinal invariant). /306

Due to the adiabatic invariant nature of  $\mu$ , we have

$$\frac{W(0, s_0)}{H(0, s_0)} = \frac{W(t, s'_0)}{H(t, s'_0)}, \quad (3.6)$$

where  $2s_0$  is the distance along the force line between the specular points at the initial moment of time ( $s_0 \equiv s_0(0)$ ),  $2s_0^t$  - the same distance at the moment of time  $t$  ( $s_0^t \equiv s_0(t)$ ). The value of  $s_0^t$  is found from the second contraction equation which is due to the retention of  $J$ :

$$\sqrt{H(0, s_0)} \int_0^{s_0} \sqrt{1 - \frac{H(0, s)}{H(0, s_0)}} ds = \sqrt{H(t, s_0^t)} \int_0^{s_0^t} \sqrt{1 - \frac{H(t, s')}{H(t, s_0^t)}} ds'. \quad (3.6)$$

Here  $s$  is the arc length of the magnetic force line read off from the equator at the initial moment of time ( $s \equiv s(0)$ );  $s'$  - the same length at the moment of time  $t$  ( $s' \equiv s(t)$ ).

The distribution of the magnetic field strength along the force line depends on the distance of the given force line from the center of the trap (in the geomagnetic field from the center of the Earth) after contraction. For example, the function  $H(t, s')$  can be given for the geomagnetic field, if  $R_0^t$  is known - the equatorial distance of the given force line from the trap axis after contraction of the trap field. This distance can be found from the equation resulting from the retention of  $\Phi$ .

If  $\Phi = \text{const}$ , then in the equatorial plane we have

$$\int_0^{R_0} R H(0, R) dR = \int_0^{R_0^t} R' H(t, R') dR', \quad (3.7)$$

where  $R_0 = R(0)$ ,  $R_0^t \equiv R_0^t(t)$ .

Due to the restoration of the geomagnetic field during the inverse phase of a storm, a current of penetrating particles will be dissipated; this dissipation is related to charged particles pouring out into dense atmospheric layers, and to the distribution of particles which have not poured out (trapped) over a large volume of the geomagnetic trap. The time required for total dissipation of the current - i.e., the time required for total penetration of the geomagnetic trap field in the region occupied by the current - corresponds to the inverse phase of the storm. The dissipation of drift currents of penetrating particles can be computed by solving the equations of a self-consistent field.

As has already been indicated, protons in a drift current have much larger fluctuation amplitudes with respect to the neutral line than do electrons having the same energy. Therefore, protons will be the first to be trapped by the restored field of the geomagnetic trap, and as a result their relative energy increase  $W(t)/W(0)$  will be much greater than it is for electrons. It is apparent that this effect will be particularly strong for the high-energy portion of protons in the drift current. Therefore, the maximum of trapped protons must be located at a smaller distance from the center of the Earth than is the electron maximum. However, this does not prevent penetrating electrons from penetrating the geomagnetic trap to very great depths, but to do this they must have an energy acceleration which is much greater than the energy of protons in the drift current.

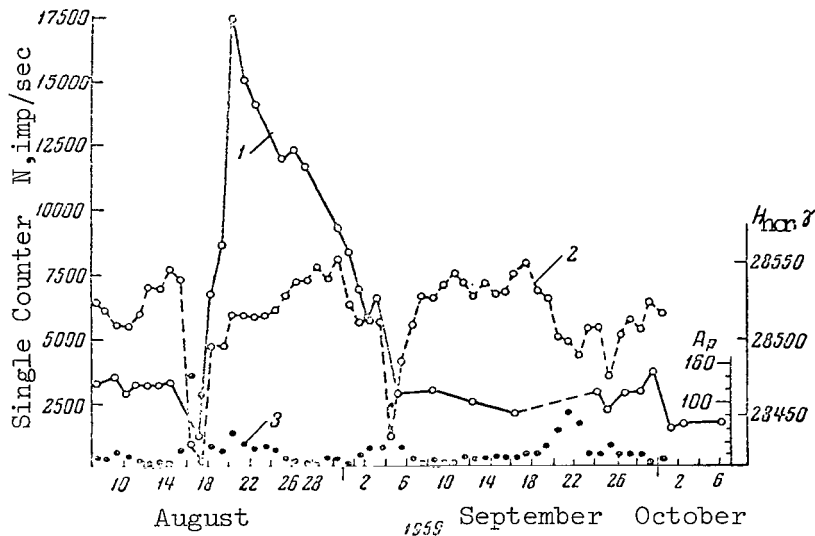


Figure 15

Intensity of a Stream of Electrons of  $100 \text{ kev} < E < 1000 \text{ kev}$  in the Region of the Outer Radiation Zone Maximum in the Vicinity of the Geomagnetic Equator During a Magnetic Storm [According to the Data from "Explorer-6" (Ref. 35)],  $\varphi = \pm 10^\circ$  (1); Simultaneous Measurements of Magnetic Field Strength According to Data Obtained on Earth (2);  $A_p$ -index (3).

The appearance of a second (electron) maximum corresponds to the final /307 stage in the field restoration, when the field has penetrated the region containing the main mass of particles in the drift current. In this case, the particles have much smaller energies, and the maximum is located farther from the Earth than the first maximum (proton).

The distances of these maxima from the center of the Earth, and also the largest energy acquired by the particles, are related to the intensity of the magnetic storms. For example, if the geomagnetic trap boundary during the main phase of a storm passes through the region intersected by the force line with  $L = 5a$  during a magnetically quiet period, just as in the example which we discussed above (page 411), then the first (proton) maximum appears after the storm at the distance  $R_0 = 3a$  from the center of the Earth. The second (electron) maximum appears at the distance  $R_0 = 5a$ . Naturally, these maxima will be somewhat blurred with respect to  $R$ , due to gradual penetration of the restored geomagnetic field in the region of the drift current.

It follows from the statements given above that the energy spectrum of particles captured by the geomagnetic trap, as well as the distribution of these particles within the trap will be determined by the following factors: (a) By the initial energy spectrum of penetrating particles;

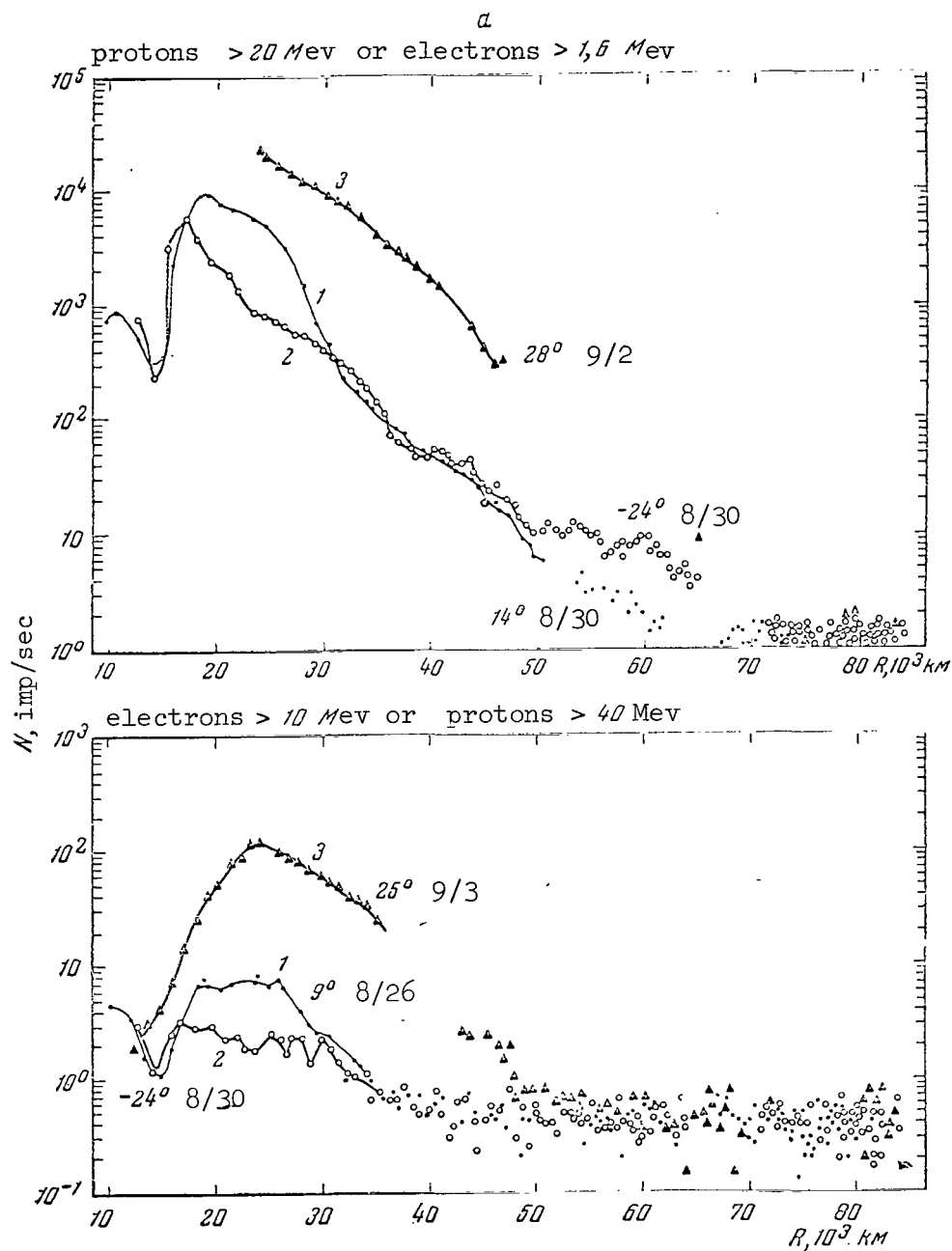


Figure 16

Measurement of Particle Streams in the Outer Zones  
During Magnetic Storm (Data from "Explorer-12") (Ref. 36)

a - High-energy particles: 1 - before the  
storm, 2 - main phase, 3 - later inverse phase

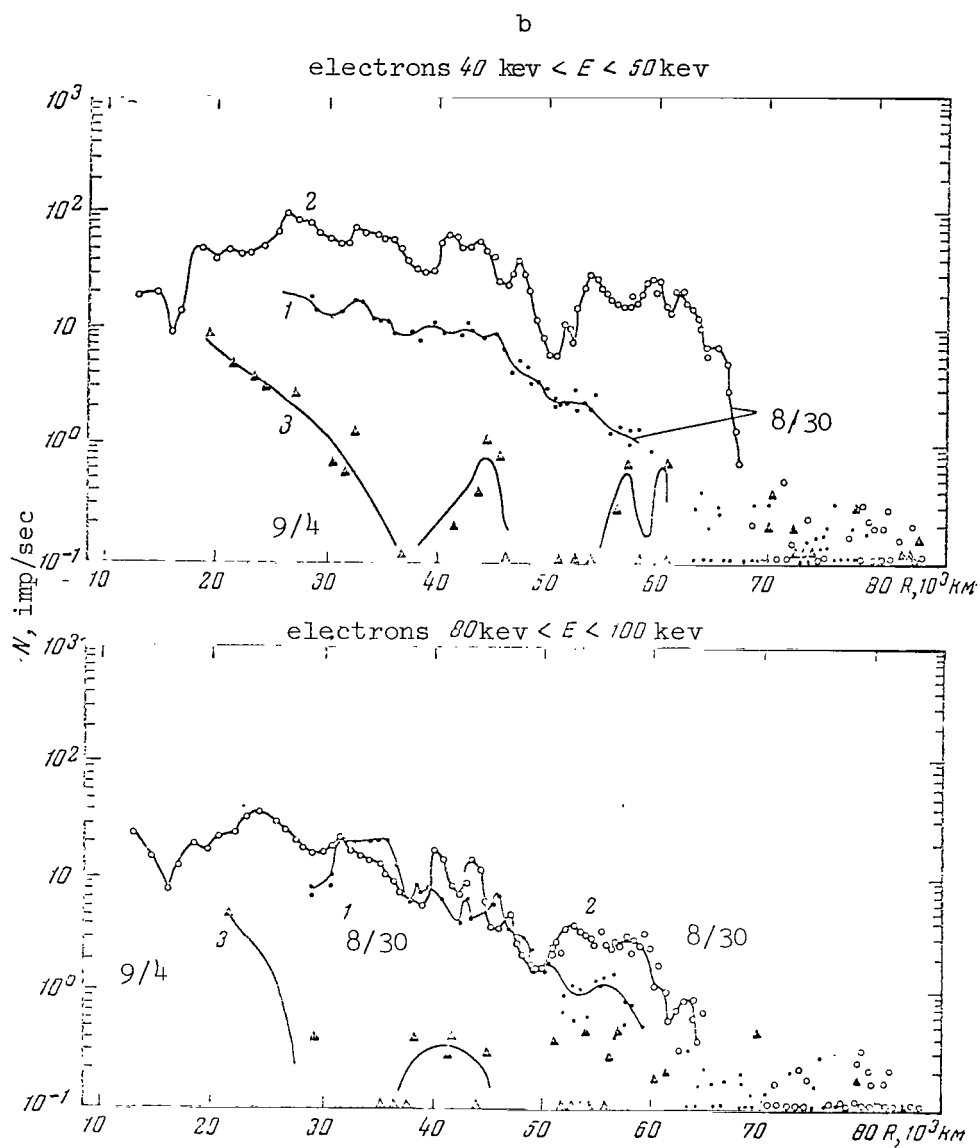


Figure 16

Measurement of Particle Streams in the Outer Zones  
During Magnetic Storm (Data from "Explorer-12") (Ref. 36)

b - Low-energy particles; 1 - early main  
phase, 2 - main phase, 3 - later inverse  
phase.

(b) By the intensity of the specific magnetic storm producing the particle penetration, and the corresponding field change; (c) By the distribution of the specular points of penetrating particles along a specific magnetic force line; (d) By the equatorial distance of a given force line from the center of the Earth.

The distribution of charged particles within the geomagnetic trap will also depend on the penetration rate of the restored geomagnetic field in the region where the drift current is located.

We should note that deviations from the spectrum of adiabatic acceleration can occur which are related to the perturbation of  $J$  and  $\Phi$  for certain groups of particles, due to a rather sharp restoration of geomagnetic field during the inverse phase of a storm. The nonconservation of  $J$  and  $\Phi$  must lead to particle diffusion in much deeper regions of the geomagnetic trap than with an adiabatic change in the field. As a result of this diffusion, the electrons and protons can penetrate to the region  $L < 3$  even when adiabatic acceleration permits penetration up to the maximum depths of  $L \sim 3$ . /308

Experimental studies have shown that in recent years, when solar activity has decreased, an outer proton zone has appeared with a maximum at the magnetic envelope  $L = 3a$  (Ref. 34). Based on measurements performed on "Elektron-1" and "Elektron-2", the outer electron zone maximum shifts by one Earth radius as compared with the period of a perturbed Sun (with  $L = 4$  at  $L = 5$ ); the maximum electron energy in the region of the zone maximum apparently decreases. /309

The theoretical picture presented above of the intensity change of trapped radiation in the geomagnetic trap during a magnetic storm closely coincides also with the results derived from experimental studies. Figure 15 shows the intensity in the outer radiation zone during several magnetic storms during August-October, 1959, based on measurements performed on "Explorer-6" (Ref. 35). It can be seen that the intensity of high-energy radiation sharply decreased during the main phase of a strong magnetic storm on August 18 in the outer zone. During the inverse phase of the storm, it increased by almost one order of magnitude, as compared with the magnetically quiet period. /310

Figure 16 presents the results derived from similar measurements on "Explorer-12" (Ref. 36) during a magnetic storm on August 30-September 3, 1961. The stream intensity of high-energy particles in this case also sharply decreased during the main phase of the storm, and increased by more than one order of magnitude during the inverse phase (Figure 16, a). However, equipment on "Explorer-12" also recorded streams of relatively low-energy charged particles (protons  $40 \text{ keV} < E < 50 \text{ keV}$ ; electrons  $80 \text{ keV} < E < 100 \text{ keV}$ ). These results are of particular interest. It can be seen from Figure 16, b, that during the later main phase the intensity of particle streams in this energy range sharply increased in the region of the outer radiation zone, while it decreased during the inverse stage.

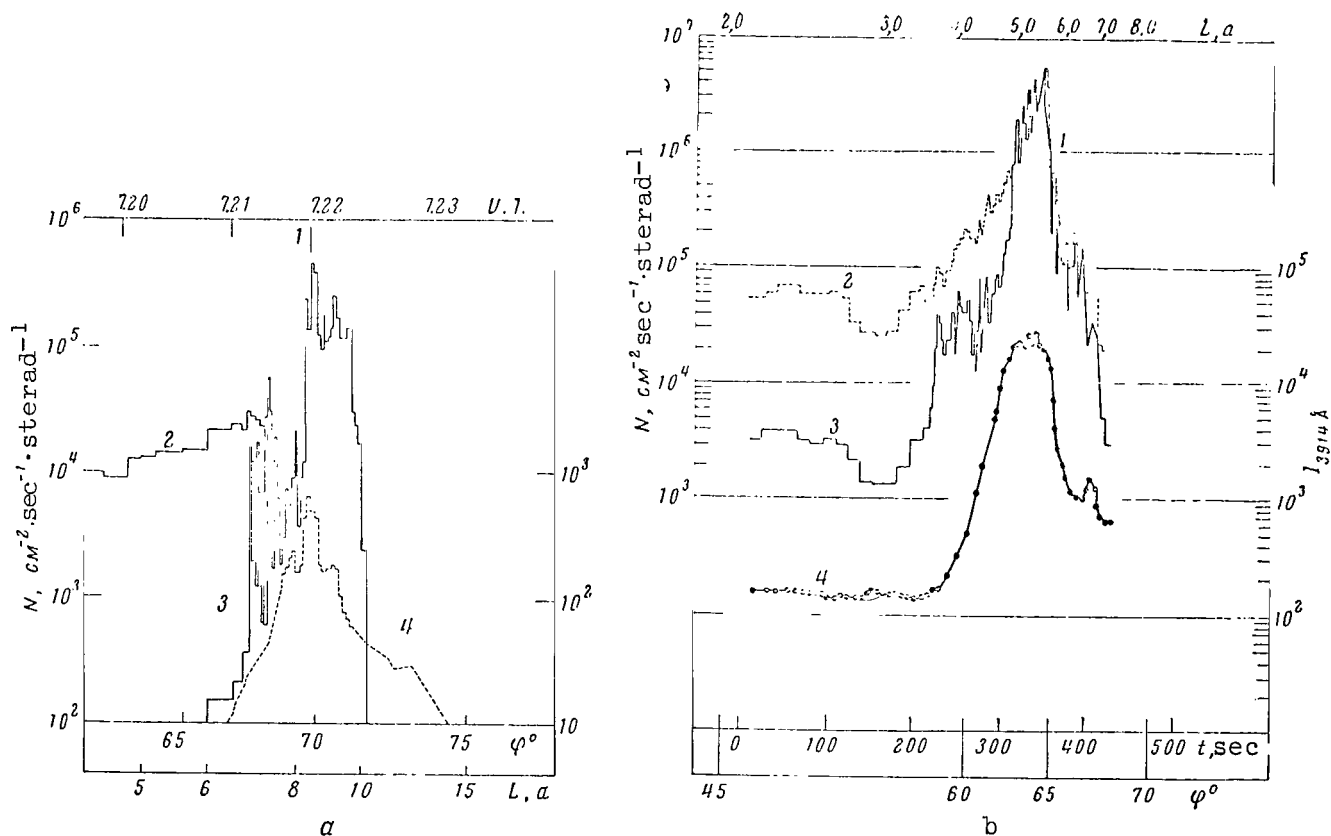


Figure 17

Distribution of Low-Energy Electrons in the Region of the Aurorae Polaris Maximum Based on Data From Measurements on "Injun-3"

a - In a magnetically-quiet period (Ref. 37); 1 - Maximum of low-energy electron streams; 2 - Trapped electrons,  $E > 40$  keV; 3 - Emitted electrons,  $E > 40$  keV; 4 - Radiation of the Aurorae Polaris  $\lambda 3914 \text{ \AA}$ .

b - During a magnetic storm on January 31, 1963 (Ref. 37); 1 - Particles of the Aurorae Polaris; 2 - trapped electrons,  $E > 40$  keV,  $\alpha = 90^\circ$ ; 3 - Emitted electrons,  $E > 40$  keV,  $\alpha = 50^\circ$ ; 4 - Radiation  $N_2^+$ .

The occurrence of these particles during the main phase of the storm can be explained by their penetration into the geomagnetic trap, while their disappearance during the inverse phase can be explained by betatronic acceleration.

The measurements performed on the artificial satellite "Injun-3" at low altitudes in the region of high latitudes are particularly interesting (Ref. 37). Figure 17, a, shows the distribution of low-energy electrons producing the auroræ polaris in a magnetically quiet period. A minimum zone between regions containing these electrons and electrons captured by the geomagnetic trap is particularly apparent. This zone passes approximately along the force line of the unperturbed dipole with  $L = 8a$ .

We can explain the outer maximum of low-energy electrons in the region  $8a < L < 10a$  by a current of electrons penetrating through the neutral points; this current is diffused along the force line. We should point out that the size of the region  $\Delta L \approx 2a$  occupied by this current coincides with the theoretical estimates. During a magnetic storm of mean intensity, as was shown in the example which we discussed, the current maximum of penetrating electrons must be located at a distance corresponding to the line of an unperturbed dipole with  $L = 5a$ . However, the most energetic electrons can reach the magnetic surface with  $L = 3a$  (page 414).

It can be seen from Figure 17, b, that the results of measurements on "Injun-3" (Ref. 37) during a magnetic storm on January 31, 1963, with  $K_p = 5$  fully coincide with the theoretical picture presented above for the acceleration and capture of charged particles during the inverse phase of a magnetic storm. Unfortunately, "Injun-3" moved at low altitudes at which - in our opinion - it would be impossible to measure the drift current maximum of penetrating protons. The intensity distribution of penetrating protons would have to have an inverse dependence on  $L$ , according to the theoretical picture presented above.

Measurements performed on "Explorer-7" in 1959 during a strong magnetic storm ( $K_p = 8$ ) revealed a similar, but much more intense, intrusion of a penetrating electron current up to the magnetic envelopes with  $L = 3.1a$  (Ref. 38). In our opinion, the outer electron maximum must begin with  $L \approx 3a$ , while the largest electron energy in the region of this maximum must considerably exceed the electron energy at the maximum for  $L = 5a$ . As is known, in 1959 (the year of maximum solar activity) the satellite "Explorer-6" (Ref. 35) discovered the so-called  $E_2$  zone of high-energy electrons located at the distance  $R = 3a$  from the center of the Earth.

According to the theoretical concepts presented above, the outer proton zone must be "submerged" in the inner radiation zone of the Earth during such large changes in the geomagnetic field.

The behavior of streams of electrons captured by the geomagnetic

/312



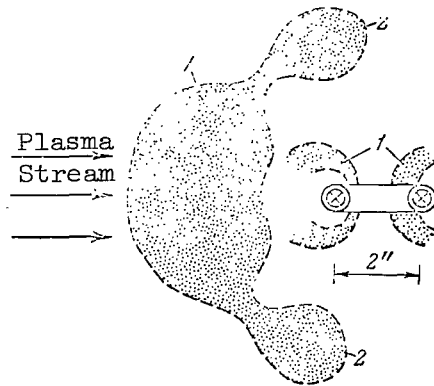


Figure 18

Model Experiment (Ref. 29)

1 - Regions Corresponding to the radiation zones;  
2 - Regions filled by penetrating particles.

trap on the diurnal side was studied during measurements performed on the polar satellite 1963 38C (Ref. 39). The results of these measurements show that the intensity of electron streams within the geomagnetic trap in the  $2.5 \leq L < 9$  range is directly proportional to the magnetic activity. In addition, a correlation was also found between the electron energy spectrum and the magnetic activity. However, with respect to our theory the results derived from measuring the time required (from the beginning of the magnetic storm) for intense streams of trapped electrons to appear are of the greatest interest (see Table 2).

TABLE 2

L	Elapsed time, days		L	Elapsed time, days	
	$E_e =$ =280 kev	$E_e =$ =1.2 Mev		$E_e =$ =280 kev	$E_e =$ =1.2 Mev
2.5	4.3	--	5.5	3.2	4.0
3.0	0.3	--	6.0-		
3.5	1.0	3.0	7.0	3.2	--
4.0	2.1	3.0	7.5	3.5	--
4.5	2.8	3.5	8.0	3.8	--
5.0	3.2	3.8	9.0	4.0	--

In the specific example, which we have investigated theoretically, for the acceleration and capture of charged particles during a magnetic storm of mean magnitude, the first streams of trapped charged particles must also appear at the magnetic envelope with  $L = 3$  at the beginning of the inverse phase of the magnetic storm. According to our theory, the time which has elapsed before trapped particles appear on the envelopes with large  $L$  is proportional to the magnitude of  $L$ . This theoretical conclusion is corroborated experimentally in Table 2.

It is characteristic that the appearance of intense streams of trapped particles coincides, according to the experimental data (Ref. 39), with the inverse phase of the storm, while the most energetic electrons appear at the end of the inverse phase.

/313

It should be pointed out that the comparatively low altitude of the polar satellite trajectory (1100 km) provides no basis for assuming that the behavior of trapped particles at this altitude will differ greatly from their behavior in the equatorial region of the geomagnetic trap. The measurement results on "Explorer-4" and "Explorer-6" indicate that trapped particles have a similar behavior throughout the entire geomagnetic trap (both at high and low altitudes) during a magnetic storm.

A model experiment (Ref. 29) on the flow of a plasma stream around a magnetic dipole field also provides indirect corroboration of our theory. In this experiment the plasma penetrated to the vicinity of the neutral points, and charged particles were also trapped and accelerated by the magnetic trap. Figure 18 clearly illustrates the connection between drift currents of penetrating particles and a magnetic trap filled with particles of these currents. It is characteristic that analogs were obtained not only of the outer, but also of the inner, radiation zones of the Earth.

The authors would like to express their appreciation to Sh. Sh. Dolginov, Ye. G. Yeroshenko, L. N. Zhuzgov, K. I. Gringauz, O. L. Vaysberg, I. A. Savenko, and B. I. Savin for providing us with their experimental results, and also for discussing the theory we have formulated. The authors would also like to thank Ya. L. Al'pert, B. R. Chirikov, M. Z. Khokhlov, B. A. Tverskiy, V. I. Krasovskiy, Yu. I. Gal'perin, V. V. Temnyy, and other individuals who have discussed this study in preparation for its publication. The authors also express their appreciation to L. A. Kazenova for helping to prepare the material and to formulate this article.

#### REFERENCES

1. Pletnev, V. D., Skuridin, G. A., Shalimov, V. P., Shvachunov, I. N. Kosmicheskiye Issledovaniya, 3, No. 2, 1965.

2. Pletnev, V. D., Skuridin, G. A., Shalimov, V. P., Shvachukov, I. N.  
Report to the Sixth COSPAR Symposium (Doklad na 6-m simpoziume  
COSPAR). Buenos Aires, May, 1965.
3. Obayashi, T. J. Geophys. Res., 69, No. 5, 861, 1964.
4. Coleman, P. G., Jr. XIII-th Internat. Astronaut. Congr., V. 1,  
Springer-Verlag, Wien - N. Y., p. 233, 1964.
5. Mead, G. D. J. Geophys. Res., 69, No. 7, 1181, 1964.
6. Störmer, C. The Polar Aurora. Oxford, 1955.
7. Obayashi, T. Reports of Ionosphere and Space Research in Japan,  
V. XIII, p. 201, 1955.
8. Gall, R. J. Geophys. Res., 69, No. 19, 4157, 1964.
9. Akasofu, S. J., Lin, W. C., and Van Allen, J. A. J. Geophys. Res.,  
68, No. 19, 5327, 1963.
10. Spreiter, J. R. and Briggs, B. R. J. Geophys. Res., 67, No. 1, 37,  
1962.
11. Beard, D. B. J. Geophys. Res., 65, No. 11, 3559, 1960.
12. Midgley, J. E. and Davis, L. J. Geophys. Res., 67, No. 2, 499, 1962.
13. Mead, G. D. and Beard, D. B. J. Geophys. Res., 69, No. 7, 1169, 1964.
14. Beard, D. B. Rev. Geophys., 2, No. 2, 335, 1964.
15. Sigov, Yu. S., Tverskoy, B. A. Geomagnetizm i Aeronomiya, 3, No. 1,  
43, 1963.
16. Blum, R. J. Geophys. Res., 69, No. 9, 1765, 1964.
17. Morozov, A. I., Solov'yev, L. S. In "Voprosy Teorii Plasmy", No. 2,  
Gosatomizdat, p. 3, 1963.
18. Akasofu, S. J. and Chapman, S. J. Geophys. Res., 66, No. 5, 1321, 1961.  
(Russian translation. In "Radiation Zones of the Earth", II, p. 149,  
1962.
19. Gringauz, K. I., Kurt, V. G., Moroz, V. I., Shklovskiy, I. S. In  
"Iskusstvennyye Sputniki Zemli", No. 6. Izdatel'stvo AN SSSR, p. 108,  
1961.
20. Serbu, G. R. Space Res., 5, 564, 1965.

21. Akasofu, S. J., Chapman, S. Phil. Trans. Roy. Soc. London, A253, No. 1031, 359, 1961.
22. Dungey, J. W. Philos. Mag., 44, 725, 1953.
23. Feldstein, Ya. I. Tellus, No. 2, 1964.
24. Akasofu, S. J. and Chapman, S. Planet. Space Sci., 12, No. 6, 607, 1964.
25. Dolginov, Sh. Sh., Yeroshenko, Ye. G., Zhuzgov, L. N. Geomagnetizm i Aeronomiya, 5, No. 5, 1965. /314
26. Bolyunova, A. D., Vaysberg, O. L., Gal'perin, Yu. I., Potapov, B. P., Temnyy, V. V., Shuyskaya, F. K. Kosmicheskiye Issledovaniya, 3, No. 3, 1965.
27. Vernov, S. N., Mel'nikov, V. V., Savenko, I. A., Savin, B. I., Shavrin, P. I. Izvestiya AN SSSR, Seriya Fiziki, No. 9, 1965. (In press.)
28. Kawashima, N., Fukushima, N. Planet. Space Sci., 12, No. 12, 1187, 1964.
29. Bostick, W. H., Bufield, H., Brettschneider, M. J. Geophys. Res., 68, No. 18, 5315, 1963.
30. Heppner, J. P., Ness, N. F., Skillman, T. L., Searce, C. S. J. Geophys. Res., 68, No. 1, 1, 1963.
31. Cahill, L. J., Jr. Report at the Sixth COSPAR Symposium, Buenos Aires, May, 1965.
32. Post, R. F. In "Physics of a Hot Plasma and Thermonuclear Reactions" (Fizika goryachey plazmy i termoyadernyye reaktsii). Atomizdat, p. 548, 1959.
33. Danzhi, Dzh. Cosmic Electrodynamics (Kosmicheskaya elektrodinamika). Moscow, Gosatomizdat, 1965.
34. Davis, L. R., Williamson, J. M. Space Res., 3, 365, 1963.
35. Fan, C. Y., Meyer, P., Simpson, J. A. J. Geophys. Res., 66, No. 9, 1961. (Russian translation. In "Radiation Zones of the Earth", IL, p. 85, 1962).
36. Freeman, J. W., Jr. J. Geophys. Res., 69, No. 9, 1691, 1964.
37. O'Brien, B. J., and Taylor, H. J. Geophys. Res., 69, No. 1, 45, 1964.

38. O'Brien, B. J., Van Allen, J. Y., Roach, F. E., Gartlein, C. W.  
J. Geophys. Res., 65, No. 9, 2759, 1960.
39. Williams, D. J. and Smith, A. M. J. Geophys. Res., 70, No. 3, 541,  
1965.

# ANOMALOUS DIFFUSION OF CHARGED PARTICLES IN THE RADIATION ZONES OF THE EARTH

B. A. Tverskoy

## Introduction

An analysis of the experimental data shows that the radiation zones /314 contain several groups of rapid particles which differ in terms of their composition, energy spectrum, spatial distribution, and variations in time. The following four groups of particles can be distinguished.

1. Soft electrons having energies of  $\epsilon < 50 - 100$  kev. These electrons do not have a clear maximum, and their mean temporal intensity changes very little throughout the entire region of the magnetosphere in which consistent capture is possible (i.e., the drift orbits are closed within the limits of the magnetosphere). In the case of  $L \lesssim 3.5$  the time variations are small, while in the case of large  $L$  significant intensity changes are observed which are related to the magnetic storms. During a storm the intensity always increases sharply (sometimes by two orders of magnitude and more), while during prolonged periods of low magnetic activity this intensity decreases monotonically (Ref. 1-3). Leakages of these electrons are apparently caused by intense (clearly non-Coulomb) scattering in the ionosphere (Ref. 3-6).

2. Heavy electrons in the outer zone having energies of  $> 200$  kev form a sharp peak for  $4 < L < 6$  (Ref. 2). In the case of  $L < 3$  and  $> 7$ , the intensity is 1-2 orders of magnitude lower than at the maximum. During prolonged periods of low magnetic activity, the electron distribution of this group strives toward a certain stable profile, while the spectrum sharply decreases in the case of  $\epsilon \gtrsim 800$  kev (Ref. 7). Sometimes the spectrum is extended toward the large energies, and with significant intensity electrons are recorded having energies of  $\sim 1 - 2$  Mev (Ref. 1, 2, 8, 9). The time variations are complex, and are not always directly related to the storms. A study of the artificial radiation zones (Ref. 2, 10) has shown that electrons having energies of  $\sim 200$  kev - 2 Mev are scattered in the ionosphere with a characteristic time of  $\sim 30$  days. In the case of  $L \gtrsim 3.5$ , the leakage intensity sharply increases during a storm. /315

3. Protons of the inner zone have energy greater than 40 - 50 Mev, and are located in envelopes with  $L \lesssim 2.5$ . The spectrum approximately corresponds to the spectrum of albedo neutrons of cosmic rays, and the intensity is very stable.

4. Protons of the outer zone. In contrast to prevailing opinions, we include in this group not only protons having energies of  $\sim 100$  kev - 1 Mev, but also harder protons (up to 20 Mev, and even partially up to 40 Mev). It is known that the observed intensities and the spectra of these protons

cannot be explained by neutron decay (Ref. 11-13). The spatial structure is characterized by a shift in the maximum toward the Earth, and by an increase in the steepness of the drop at the outer boundary with an energy increase. Time variations are only observed at large L ( $L \gtrsim 4$ ).

At the present there is common agreement on the nature of proton sources in the inner zone (decay of albedo neutrons of cosmic rays). However, the formation of the outer proton zone has not been fully clarified as yet. The remaining three groups are caused by certain acceleration processes in the magnetosphere.

A comparison of the properties of soft and hard electrons shows that there are electromagnetic fluctuations in the magnetosphere which accelerate electrons up to energies of  $\sim 50 - 100$  kev and which scatter electrons of larger energies. Waves in which the electric field  $E$  is somewhat smaller than the magnetic field  $h$  have this property. In a nonrelativistic case, the electric force  $eE$ , which produces the energy change, can be greater than, or on the order of, the Lorentz force  $\frac{v}{c} h$  ( $v$  - particle velocity), which leads to pure scattering. However, in the case of  $v \rightarrow c$  the scattering will essentially predominate over the acceleration. It can be shown that  $E = \frac{v}{c} h$ , when the particle velocity  $v = v_f$  ( $v_f$  - phase velocity of the wave). Since acceleration takes place up to significant energies ( $\sim 50$  kev),  $v_f$  cannot be too small. Therefore, if the plasma fluctuation spectrum is taken into account, the acceleration of soft electrons and the scattering of hard electrons are most probably caused by electron fluctuations of the frequency  $\omega \leq \omega_H$  ( $\omega_H$  - cyclotron frequency of the electrons), whose phase velocity in the magnetosphere amounts to  $\sim 5 \cdot 10^9$  cm·sec<sup>-1</sup>.

It will be shown in this report that the basic mechanism by which protons and electrons are accelerated in the outer zone, and also the mechanism by which the inner zone is formed, is the transfer of particles across the drift envelopes. The possible role of these processes in the dynamics of trapped radiation was already pointed in 1959-1960 (Ref. 14-16). However, it was only in 1963 that sufficient experimental data had been accumulated to discover these effects qualitatively. An analysis has shown that particle transfer can play a decisive role in the formation of radiation zones. A theory was developed for such processes which permitted a quantitative comparison with experimental data (Ref. 16-21). Finally, data compiled from investigations on satellites in the "Elektron" series made it possible to verify and to refine certain basic aspects of the theory. At the present time this theory provides a reliable, quantitative description of many properties of the radiation zones.

## 1. Particle Transfer Across the Drift Envelopes (General Theory)

If a group of charged particles is located in a magnetic field upon which non-stationary perturbations are imposed, then under definite conditions intense mixing of the particles can occur - or, as it is called,

anomalous diffusion. This effect has been studied extensively. In the case of the magnetosphere, this effect was first studied by Parker in 1960. Parker showed that the sudden commencement of magnetic storms leads to anomalous diffusion, and he employed the model of Chapman-Ferraro and statistics on magnetic storms to estimate the magnitude of this effect (Ref. 15). The works (Ref. 16-21) developed a general theory for anomalous diffusion in the magnetosphere, the basic premise of which (the potentiality of a perturbed field in the region of the radiation zones) has now been corroborated by magnetic measurements in near space (Ref. 22, 23).

Particle transfer across the drift envelopes is connected with perturbations of the third adiabatic invariant (in the case of a dipole field, this is the parameter of the magnetic envelope  $L$ ). Therefore, the time scale of perturbation  $t_0$  must be less than, or on the order of, the period of the particle longitudinal drift  $t_\varphi$ . In addition, it follows from the law of generalized moment conservation  $[r(\mathbf{P} + \frac{e}{c} \mathbf{A})]$  ( $r$  is the particle radius vector,  $\mathbf{P}$  - its impulse,  $\mathbf{A}$  - the vector potential of the electromagnetic field) that the particles move in an inverse direction during perturbations which are symmetrical with respect to the magnetic axis of the Earth. Consequently, an asymmetric perturbation component is necessary for irreversible transfer.

If the perturbation is small, the investigation can be confined to one asymmetric component  $\mathbf{h}$ . The requirements formulated above make it possible to clearly distinguish the dependence of  $\mathbf{h}$  on the coordinates. As observations of the satellite "Explorer-12" have shown (Ref. 22), magnetic perturbations in the magnetosphere increase comparatively slowly in time ( $t_0 \sim 1 - 4$  minutes). This fact receives confirmation from magnetic and plasma measurements in interplanetary space: it has been found that the perturbation front in the solar wind is  $\sim 10^5$  km wide, which - at a velocity of  $\sim 10^3$  km·sec $^{-1}$  - leads to the indicated time of  $t_0$ , which coincides with the propagation time of weak perturbations. Thus, in the magnetosphere shock waves are not formed, the plasma contracts or expands adiabatically and remains cold, and the field perturbation is potential. Measurements have shown that, both in the unperturbed and the perturbed case, the field of outer currents flowing along the magnetosphere boundary decreases comparatively slowly as the Earth is approached. It thus follows that even close to the magnetosphere boundary on the diurnal side field expansion in series, with respect to spherical functions, rapidly converges. Therefore, the asymmetric harmonics with the minimum  $n$  will make the main contribution to  $\mathbf{h}$ . If the fact is taken into account that the mean shift with respect to the force line will equal zero in the case of an electric field  $E_\varphi$ , which is antisymmetric with respect to the equatorial plane, then all the harmonics with  $n = 1$  and the harmonics  $n = 2, m = 2$  can be disregarded. We thus obtain:

$$\mathbf{h} = -h(t) \nabla \frac{r^2}{2R_E} \sin 2\theta \cos \varphi \quad (1)$$



( $r, \theta, \varphi$  - are the spherical coordinates with the origin at the center of the Earth and with the polar axis along the magnetic axis).

As observations have shown, this type of magnetic perturbations has the form of single impulses. The amplitude of  $h(t)$  in (1) characterizes perturbations at the equator of the Earth. As was shown in (Ref. 21), the perturbations produce similar changes in  $L$  in all the particles located on one and the same force line. Therefore, it is sufficient to examine particle motion with reflection points in the equatorial plane.

If the magnetic drift is small ( $t_0 \ll t_{\varphi}$ ) during the first phase of the perturbation, the shift with respect to  $L$  is determined by the electric field  $E_{\varphi}$ , which is proportional to  $L^2 \cos \varphi$  in the equatorial plane ( $\mathbf{E} = -\frac{1}{c} \frac{\partial A}{\partial t}$ , and the vector potential of the perturbation  $A$  depends on  $r = R_e L$ , just as does the scalar potential). The velocity of the

electric drift  $L \sim \frac{E_{\varphi}}{H} \sim L^5 \cos \varphi_0$ , since  $H \sim \frac{1}{R_e}$ , and  $E_{\varphi} \sim \cos \varphi$ . Thus, the mean longitudinal shift of particles with a given initial  $L$  is zero, and the root-mean-square shift  $\Delta L^2 \sim L^9$  - and diffusion is produced. The corresponding term in the transport equation is proportional to  $h^2$ , and therefore the equation of motion must be solved within an accuracy of terms on this order of magnitude inclusively. The mean shift  $\Delta L$ , which is square with respect to  $h$ , must be determined. Let us examine a particle stream through the envelope  $L = \text{const}$ . It can be readily seen that, due to the strong dependence of  $\Delta L$  on  $L$  ( $\delta L \sim L^5$ ), the particles entering this envelope ( $L_0 > L$ ) move along orbits which are somewhat farther away from  $L$  than are those of outgoing particles; it also follows that  $\delta \Delta L \approx \frac{\partial \Delta L}{\partial L} \Delta L \sim L^9$ . Thus, the mean shift is proportional to  $h^2 L^9$ , and is directed toward the Earth.

In order to compute  $\overline{\Delta L^2}$  and  $\overline{\Delta L}$  quantitatively, it is necessary to determine the electric field  $\mathbf{E}$  within an accuracy of terms  $\sim h^2$  inclusively. It is composed of the vortex field  $\mathbf{E}_s = -\frac{1}{c} \frac{\partial A_0}{\partial t}$  ( $A_0$  - the vector potential of perturbation satisfying the condition  $A_{0r} = 0$ ) and of the potential polarization field of the plasma  $\mathbf{E}_p$ . In view of the high conductivity of the plasma, the sum  $\mathbf{E}_s + \mathbf{E}_p$  must not have components along the force lines of the field. This condition determines  $\mathbf{E}_p$ . Electric fields during magnetic perturbations were studied in detail in (Ref. 21), taking into account the skin effect, charge separation in the ionosphere, and non-dipole components of the geomagnetic field. It was found that these corrections can play a significant role only in the case of  $L < 1.3 - 1.4$ . The adiabatic restoration of the field to an unperturbed state was taken into account in solving the equation of motion in (Ref. 21).

These results make it possible to determine the particle stream, averaged over many perturbations, through the drift envelope with the

/317

parameter  $L$ . The perturbation time  $t_0$  is large as compared with the periods of Larmor rotation and oscillation along the force line. Therefore, a change in particle energy when  $L$  changes will be caused by the conservation of the magnetic moment and longitudinal action. The work (Ref. 19) studied the corresponding energy change and showed that within a high degree of accuracy the quantity

$$J = pL^{3/2} \quad (2)$$

is retained for particles with reflection points at the magnetic latitudes  $\lambda < 30^\circ$ , even when  $L$  changes by a factor of 2-3 (here  $p$  is the impulse measured in units of  $Mc$ ;  $M$  is the particle mass). In the case of  $\lambda = 0$  the law (2) expresses the conservation of the magnetic moment. A similar result was obtained in the nonrelativistic approximation in (Ref. 24).

Since the majority (70-90%) of particles in the zones have reflection points in the indicated latitudinal region, when the distribution is computed close to the equatorial plane the distribution function  $\theta = \theta(L, J, t)$  can be introduced, so that the quantity

$$dv = \theta(L, J, t) dJ dL \quad (3)$$

gives the number of particles with  $J$  in the interval  $(J, J + dJ)$  which are included between the envelopes  $(L, L + dL)$ .

The intensity of particles with the impulse  $> p$  is determined according to the given function of  $\theta$  in the following way:

$$S = \frac{\alpha}{w_0 L^2} \int_{pL^{3/2}}^{\infty} v(J, L) \theta(L, J, t) dJ, \quad (4)$$

where  $w_0 L^2$  is the size of the layer between two envelopes which are 1 cm apart in the equatorial plane;  $v(J, L)$  - particle velocity with given  $J$  and  $L$ ;  $\alpha$  - the coefficient depending slightly on the angular velocity distribution in the equatorial plane (for isotropic distribution  $\alpha = 1$ , and for the distribution  $\sim \sin^4 \theta$   $\alpha = 1.5$ ; the angular distribution does not normally exceed these limits).

A particle stream through the envelope with the parameter  $L$  is expressed by  $\theta$  in the following way:

$$dF = -D_0 L^{10} \left( \frac{\partial \theta}{\partial L} + \frac{2.6}{L} \theta \right) dJ. \quad (5)$$

The first term describes diffusion and the second term describes a regular stream. Due to an arithmetic error, the coefficient for the second term, given in (Ref. 21), is somewhat exaggerated (3.5 instead of 2.6):

$$D_0 = \frac{1}{8T} \left( \frac{h_0}{H_e} \right)^2 \quad (6)$$

( $h_0$  is the magnitude of the jump  $h(t)$ ;  $H_e$  - the unperturbed field at the equator of the Earth;  $T$  - the time between two consecutive perturbations, while averaging is performed over many perturbations). Generally speaking,  $D_0$  can depend on the period of particle drift  $\tau_\psi$ . However, this dependence - as well as the order of magnitude of  $D_0$  - can be determined with only a low degree of accuracy from magnetic data. It would be much more realistic to compare the theory with the experimental data on the structure and dynamics of the radiation zones. The result given in (Ref. 15) follows from (6) when  $h_0$  is computed according to the model of Chapman-Ferraro.

Let us assume that particle leakages are caused by ionization losses and magnetic scattering. The equation for  $\theta$  then has the following form:

$$\begin{aligned} \frac{\partial \theta}{\partial t} = \frac{\partial}{\partial L} \left[ D_0 L^{10} \left( \frac{\partial \theta}{\partial L} + \frac{2.6}{L} \theta \right) \right] + \frac{1}{\tau_c} \frac{\partial}{\partial J} \left( \frac{J^2 - L^3}{J^2} L^{3/2} \theta \right) - \\ - \frac{\theta}{\tau_S(L, J)} + Q(L, J, t). \end{aligned} \quad (7)$$

the term with  $\partial/\partial J$  describes ionization losses. The quantity

$$\tau_c = \frac{Mmc^3}{4\pi e^4 N \ln q} \quad (8)$$

( $M$  - particle mass;  $m$  - electron mass;  $e$  - its charge;  $c$  - speed of light;  $N$  - density of cold electrons;  $\ln q$  - logarithm of Debye screening) determines the time of ionization losses of a particle with the impulse  $Mc$ , and can depend on  $L$  through  $N_0$ .

The time required for magnetic scattering  $\tau_S(L, J)$  for electrons having energies of  $\sim 200$  kev - 2 Mev for  $2 < L < 4$  is on the order of  $3 \cdot 10^6$  seconds; in the case of  $L \geq 3.5$ , this time increases greatly during storms. Magnetic scattering plays no role in the dynamics of protons. The quantity  $Q(L, J, t)$  in (7) is the density of particle sources. Equation (7) differs from that presented in (Ref. 21) due to the allowance for magnetic scattering.

Let us examine the basic solutions (7). The most important characteristic of transfer processes is the time required for perturbation propagation in an envelope with the parameter  $L$ . The study (Ref. 21) determined the self-similar solution of the equation

$$\frac{\partial \theta}{\partial t} = D_0 \frac{\partial}{\partial L} L^{10} \left( \frac{\partial \theta}{\partial L} + \frac{2.6}{L} \theta \right), \quad (9)$$

corresponding to the jump-like change in conditions at infinity in the case of  $t = 0$ . It was found that the solution takes the form of a diffusion wave with a steep inner front, whose coordinate  $L_f$  is

$$L_f \approx (100 D_0 t)^{1/4}. \quad (10)$$

It can be shown that a similar solution holds for a continuous change in conditions at infinity according to the law  $t^n$ . In the case of  $n \leq 3$ , the form of the wave and the position of its front are determined by the same relationships as in the case of a jump, and the amplitude increases  $\sim t^n$ . /319

Thus, the time

$$\tau_D(L) = (100 D_0 L^4)^{-1} \quad (11)$$

is the main characteristic of transfer processes. It can be shown that the role of losses can be compared with the role of transfer, when  $\tau_D(L)$  equals the loss time. If a certain zone is formed by particle diffusion from the magnetosphere boundary, an intensity maximum will be observed at this point.

The general solution of equation (9), with allowance for the sources, can be obtained by means of Green's function:

$$G(x, x', t - t') = \frac{x'^{1.5}}{2(t - t') \sqrt{x'}} \exp \left\{ -\frac{x^2 + x'^2}{4(t - t')} \right\} \cdot I_{0.8} \left[ \frac{xx'}{2(t - t')} \right] \quad (12)$$

( $x = 1/4L^4$ ,  $x' = 1/4L'^4$ ,  $I_{0.8}$  - the Bessel function of an imaginary argument on the order of  $I_{0.8}$ ). The problem with the initial condition  $\Theta|_{t=t_0} = \Theta_0(L, J)$  has the following solution:

$$\Theta(J, x, t) = \int_0^x G(x, x', t - t_0) \Theta_0(x', J) dx', \quad (13)$$

and the problem with the source  $Q = \begin{cases} Q(x, J, t) & (t > 0) \\ 0 & (t < 0) \end{cases}$ ,

$$\Theta(J, x, t) = \int_0^x \int_0^\infty G(x, x', t - t') Q(x', J, t') dx' dt'. \quad (14)$$

The function (12) is obtained for the solution of (9) by Laplace transformation with respect to  $t$  and by subsequent use of the Fourier-Bessel theorem. A similar result was obtained in (Ref. 15); however, the order of  $I$  was different, since the mean shift was not taken into account in (Ref. 15).

We should note that, if the time of magnetic scattering  $\tau_s$  does not

depend on  $L$ , Green's function can be obtained by multiplying (12) by  $e^{-t/\tau_S}$  in order to make a comparison with the allowance for scattering.

Let us now interpret the experimental results. Since the main features of the transport theory are most readily apparent in the structure of the outer proton zone, it is advantageous to employ these data to define the magnitude of the main parameter of the theory  $D_0$  more accurately.

## 2. Protons of the Outer Zone and Determination of $D_0$

During flights of the satellite "Explorer-12" in the radiation zones of the Earth, protons were discovered having energies from 100 keV to several MeV. On the basis of the first publication (Ref. 11), it can be concluded that the acceleration of these protons is most probably caused by the betatron effect. As was shown in (Ref. 11), the proton spectrum has an exponential nature ( $S \sim e^{-\epsilon/\epsilon_0}$ ). In the case of  $L = 6.1$   $\lambda_{\text{geom}} = 6.5^\circ$ , the mean energy is  $\epsilon_0 = 64$  keV; in the case of  $L = 5.0$   $\lambda_{\text{geom}} = 10^\circ$   $\epsilon_0 = 120$  keV; and in the case of  $L = 2.8$   $\lambda_{\text{geom}} = 38^\circ$   $\epsilon_0 = 400$  keV. It can be readily seen that close to the equatorial plane ( $L = 6.1$  and  $5.0$ )  $\epsilon_0 \sim L^{-3}$ , and changes proportionally to the magnetic field strength. For  $L = 2.8$   $\epsilon_0$  must be  $\approx 700$  keV in the equatorial plane. However, in the case of  $\lambda_{\text{geom}} = 38^\circ$  the acceleration is much less effective than in the case of  $\lambda_{\text{geom}} \rightarrow 0$ . A considerable change in the field from  $\sim 40$   $\gamma$  at the magnetosphere boundary up to  $\sim 1500$   $\gamma$  in the case of  $L = 2.8$  leads to considerable energy dependence on the magnetic latitude of the reflection point. Computations based on the scheme in (Ref. 19) show that in the case of  $\lambda_{\text{geom}} = 38^\circ$  the magnitude of  $\epsilon_0$  must be  $\approx 360$  keV. /320

Thus, if it is assumed that the field is 40 - 50  $\gamma$  at the magnetosphere boundary, the mean energy  $\epsilon_0$  at the boundary must be  $\sim 20$  keV. This quantity is close to the energy of solar wind protons passing through the shock wave at the magnetosphere boundary.

If it is assumed that: (a) the spectrum of protons trapped at the magnetosphere boundary has the form  $S \sim e^{-\epsilon/\epsilon_0}$ ; (b) the outer proton zone is caused by transfer and betatron acceleration; (c) the formation of the inner boundary is primarily related to ionization losses (losses by charge transfer are small, due to a high degree of ionization); (d) the density of the cold plasma  $N_0$  in the case of  $2 \leq L \leq 4$  depends slightly on  $L$ , and the parameter  $D_0$  depends slightly on  $\tau_\phi$  - then based on data from (Ref. 11) we can calculate the distribution of protons having any energy and can concurrently determine the magnitude of  $D_0$ . These assumptions appear to be completely reasonable. A comparison of the theoretical curves with the experimental curves will provide the most reliable

verification of these assumptions.

In the given formulation, the problem can be reduced to solving the equation

$$D_0 \frac{\partial}{\partial L} L^{10} \left( \frac{\partial \Theta}{\partial L} + \frac{2,6}{L} \Theta \right) + \frac{1}{\tau_c} L^{7/2} \frac{\partial \Theta}{\partial J} \frac{\partial}{J^2} = 0 \quad (15)$$

with the boundary conditions

$$\Theta|_{L=L_0} = A \exp \left( -\frac{J^2}{J_0^2} \right), \quad \Theta|_{L \rightarrow \infty} = 0, \quad (16)$$

where  $L_0 \approx 9$  is the boundary value of  $L$  at which the geomagnetic dipole field would equal 40 - 50  $\gamma$ ,  $J_0 = 2 e_0(L_0)L_0^3$ . In the nonrelativistic case  $L^3 \gg J^2$ , which makes it possible to simplify the term describing ionization losses in (7).

The problem can be reduced to numerical computation of a specific integral by Laplace transformation with respect to  $J^3$ . At large distances where the ionization losses are unimportant,

$\Theta \sim L^{-2,6} \exp \left\{ -\frac{J^2}{J_0^2} \right\}$ . The maximum is determined by the relationship

$\tau_D(L_m) = \tau_c \frac{p^3}{3} \left( \tau_c \frac{p^3}{3} - \text{the time required for ionization braking of a particle with the impulse } p \right)$ .

Specific computations were performed for  $\epsilon > 500$  kev. The parameters  $D_0$  and  $A$  can be determined by comparing the theory with the results presented in (Ref. 2) and (Ref. 11). Theoretical curves for  $\epsilon > 100$  kev, 1 Mev, 1.7 Mev and 2 Mev close to the equatorial plane were constructed on the basis of these data (Figure 1, a).

/321

Satellites in the "Elektron" series performed detailed measurements on proton intensity with  $\epsilon > 1$  Mev and  $\epsilon > 2$  Mev (Ref. 25). It is of particular interest to compare the results obtained independently from theoretical and experimental measurements. The work (Ref. 2) presents data on the intensity of protons with  $\epsilon > 500$  kev in the case of  $L = 2.8; 3.2$  and  $3.6$ . Additional results, obtained on "Explorer-12" ( $\epsilon > 1.7$  Mev) are given in (Ref. 26). In order to compare the spatial pattern which is provided by theoretical and experimental studies, the measurement results were multiplied by certain coefficients, so that theory and experiment concurred at the maximum. The following conditional notation is employed in Figure 1a: 1 -  $S_{> 100 \text{ kev}}$  (Ref. 11); 2 -  $3S_{> 500 \text{ kev}}$  (Ref. 2); 3 -  $2S_{> 1 \text{ Mev}}$  (Ref. 25); 4 -  $S_{> 1.7 \text{ Mev}}$  (Ref. 26); 5 -  $S_{> 2 \text{ Mev}}$  (Ref. 25). It can be seen from the figure that the spatial intensity pattern provided by theoretical and by experimental results almost coincides. In the case of  $\epsilon > 500$  Mev and 1 Mev, the difference in absolute values by a factor of 2-3 lies within the limits of

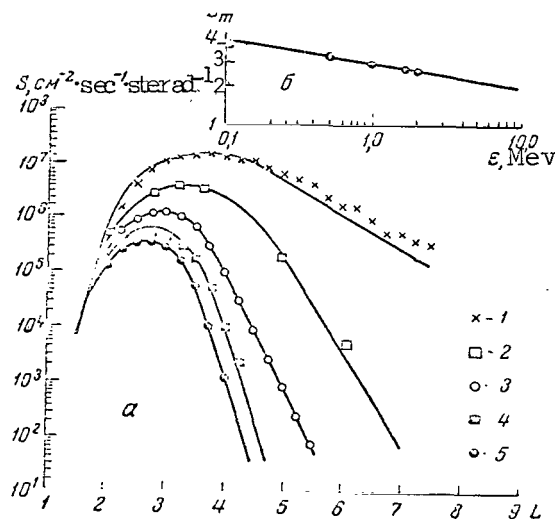


Figure 1

orientational effects and errors in absolute calibrations of the equipment. If  $D_0$  and  $N_0$  do not depend on  $L$ , the relationship  $\epsilon \sim L_m^{16/3}$  must be fulfilled. Figure 1, b illustrates the fulfillment of this law. All deviations in the case of  $\epsilon = 100$  kev point to the fact that  $N_0$  is approximately 1.5 times smaller in the case of  $L \approx 4$  than it is in the case of  $L \approx 2.5 - 3$ . Assuming that for  $L = 3 - 2.5$   $N_0 = 1500 \text{ cm}^{-3}$  we find that  $D_0 = 6 \cdot 10^{-14} \text{ sec}^{-1}$ . Apparently, the actual value of  $N_0$  differs very little from the value given above, and the value of  $D_0$  is sufficiently reliable. The value obtained for  $D_0$  considerably exceeds previous estimates based on data from statistics on magnetic storms (Ref. 15), and also based on certain features of the outer zone structure of relativistic electrons (Ref. 21). It closely coincides with magnetic data on single impulses (Ref. 22).

The close agreement between theory and experiment in the proton energy range from 100 kev to  $\sim 3$  Mev indicates that  $D_0$  barely depends on the period of longitudinal drift, at least in the case of  $7 \text{ min} < \tau_\gamma < 100 \text{ min}$ . The most plausible explanation of this fact may be found in the fact that the transfer is caused primarily by sudden impulses (by rapid changes in the field with subsequent prolonged restoration).

Experimental data were recently published (Ref. 22) making it possible to compute  $D_0$  directly from the results of magnetic measurements, with a much higher degree of accuracy than was the case previously. According to (Ref. 22), the dependence of the field jump on the longitude of  $\varphi$  at the equator of the Earth has the form  $h_0 = \eta(1 + 0.45 \cos \varphi)$  in the case of sudden impulses. The constant

$\eta$  can have both signs, and in the majority of cases amounts to 20-40  $\gamma$  in terms of absolute magnitude, and the impulses appear with a frequency of  $\sim 1.5$  times per day. If we subtract the screening current field of the normal field component at the surface of the Earth, we find that the jump magnitude of the asymmetric field component for outer currents at the equator of the Earth is  $h_0 = 3/5 \cdot 0.45 \eta = 0.27 \eta$ . Consequently,  $D_0 = 1/8T(h_0/H_e = 3 - 15 \cdot 10^{-14} \text{ sec}^{-1}$ , which closely coincides with computational results based on data on the structure of the outer proton zone. A very important conclusion (Ref. 22) - to the effect that the pattern of magnetic perturbations during sudden impulses has the same form in space and on the surface of the Earth - facilitates a study of the variation of  $D_0$  with the solar cycle based on data from Earth stations.

Thus, this group of theoretical and experimental results completely corroborates the important role of anomalous diffusion in the dynamics of the radiation zones of the Earth. It also corroborates the initial assumptions regarding the nature of magnetic perturbations and, consequently, expression (5) for a particle stream; these results also make it possible to reliably determine the numerical value of the parameter  $D_0$ .

/322

Since the effectiveness of the transfer is much higher than was previously assumed, the possibility is not excluded that a certain portion of protons having energies of 10 - 100 Mev is also formed due to particle transfer from the magnetosphere boundary. If a proton has an energy of 200 kev in a field of strength  $H = 40 \gamma$ , when it is deflected toward an envelope with  $L = 1.5$  ( $H \approx 10^4 \gamma$ ) it is accelerated up to 50 Mev. However, it is more expedient to investigate this problem in connection with the dynamics of the inner zone, to which the following section is devoted.

### 3. High-Energy Protons

Soon after the radiation zones of the Earth were discovered, the hypothesis was advanced that high-energy protons of the inner zone ( $\epsilon \sim$  tens-hundreds of Mev) are formed due to the decay of albedo neutrons of cosmic rays (Ref. 27). However, it was found later that this hypothesis encounters several difficulties. The use of magnetic scattering (Ref. 28-30) to provide a qualitative explanation of the sharp intensity drop for  $L > 1.5$  requires exaggerated amplitudes of magnetic pulsations with frequencies of  $\gtrsim 1$  cps. It was shown (Ref. 13) that in the case of  $\epsilon < 30 - 40$  Mev the proton spectrum is much softer than would be expected from the neutron hypothesis, and the intensity is much greater in the case of  $\epsilon \sim 10$  Mev. An explanation of this phenomenon by the influence of solar protons on the polar cap is far from satisfactory quantitatively (Ref. 31). Finally, it was shown in (Ref. 10) and (Ref. 12) that for  $\epsilon \leq 40$  Mev there is a sharp deviation from the neutron hypothesis in the equatorial plane region.



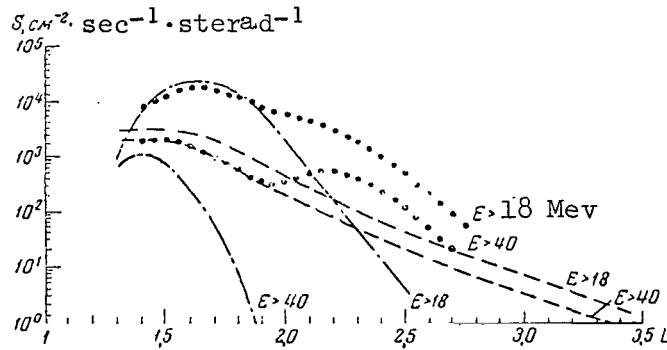


Figure 2

The concept of anomalous diffusion seems to provide a quantitative explanation of these contradictory facts. It was shown in (Ref. 16-21) that particle transfer across drift envelopes can rapidly eliminate the products of neutron decay, and can thus explain the sharp intensity drop with an increase in  $L$ . The asymptotic law obtained in (Ref. 16-21) for the intensity drop  $S \sim L^{-10}$  is fulfilled fairly well at geomagnetic latitudes of  $> 20^\circ$  for  $\epsilon > 30 - 40$  Mev (see the analysis of data presented in [Ref. 32, 33] in [Ref. 21]).

An analysis of the subsequent experimental results leads to the conclusion that protons having energies of  $> 50 - 60$  Mev are primarily caused by neutron decay and by elimination due to anomalous diffusion. If it is assumed that the quantity  $D_0$  retains the value obtained above  $\sim 10^{-13} \text{ sec}^{-1}$  for these energies, then data presented in (Ref. 34) can be used to determine the structure of the outer boundary of the inner zone in the equatorial plane as a function of the threshold energy of the recording apparatus<sup>1</sup>. The corresponding results for  $\epsilon > 18$  and 40 Mev are given in Figure 2 (dashed curves). The points near which the conversion to the asymptotic law  $S \sim L^{-10}$  takes place are determined from an equation for ionization loss time  $\tau_c = \frac{p}{3}$  ( $p$  - impulse in units of Mc) and for diffusion time  $\tau_D(L) = (100D_0L^8)^{-1}$ . It is assumed that the density of a cold plasma  $N_0$  is  $1.5 \cdot 10^3 \text{ cm}^{-3}$ .

Protons having energies of  $< 20 - 30$  Mev, and partly of 40 Mev, are not basically connected with neutron decay, and represent the hard tail of the outer proton zone. It can be seen from the results presented in (Ref. 11) that in the case of  $L = 5$  there is a large number of protons

<sup>1</sup> An analysis of the data in (Ref. 22) shows that this assumption is valid for  $\tau_{\text{op}} \geq 1$  minutes; it is possible that  $D_0$  remains large up to  $\tau_{\text{op}} \sim 10$  sec due to resonance with eigen hydromagnetic oscillations of the magnetosphere.

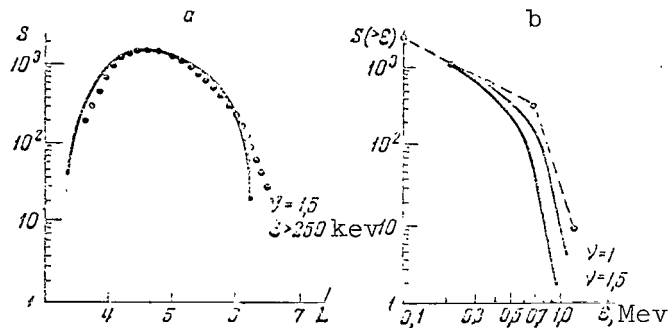


Figure 3

with  $\epsilon \geq 1$  Mev; their spectrum falls within the framework of Maxwell distribution with the same  $\epsilon_0$  as for small energies. It is apparent that these protons can scatter into the depths of the magnetosphere, and can be accelerated until the ionization loss rate equals the diffusion rate. It can be readily seen from the relationships  $p(L) = p_{L=5} \left(\frac{5}{L}\right)^{3/2}$  and  $\frac{1}{3} p^3(L) = (100D_0 L^3)^{-1}$  that for  $N_0 = 1.5 \cdot 10^3 \text{ cm}^{-3}$

/323

and  $D_0 = 6 \cdot 10^{-14}$  seconds these protons drift toward envelopes with  $L \approx 1.4$ , and are accelerated up to  $\sim 40$  Mev. Figure 2 presents the expected distribution of protons in the outer zone with energies of  $> 18$  and  $> 40$  Mev in the equatorial plane (dot-dash curves). For purposes of comparison, the experimental data from (Ref. 10) and (Ref. 12) are plotted by dots. Experiment and theory do not diverge significantly in the case of  $L < 2$ . However, in the case of  $L \approx 2.3$  additional peaks can be seen on experimental curves. It can be shown that the intensity distribution in these peaks corresponds to the diffusion wave produced due to capture at the magnetosphere boundary of protons with the spectrum  $S \sim e^{-\epsilon/\epsilon_0}$  in 1956-1959 where  $\epsilon_0 \approx 150$  keV.

The total number of protons captured during this period per  $1 \text{ cm}^3$  close to the boundary must be  $\sim 10^{-5} \text{ cm}^{-3}$ . If the fact is taken into consideration that there was an intense maximum of solar activity in 1955-1959, these ideas regarding the nature of additional maxima are completely reasonable.

Thus, a theory of anomalous diffusion can explain the structural features of the inner zone. It is thus found that protons having energies of  $\leq 40$  Mev are primarily formed to betatron acceleration during transfer from the magnetosphere boundary, and consequently represent a continuation of the outer proton zone. The neutron mechanism plays a basic role only for energies of  $> 50$  Mev, and in this case the outer boundary of the zone is formed by anomalous diffusion. It can be expected that there will be  $\alpha$ -particles having energies of  $\sim 1.0$  Mev, also caused by anomalous diffusion, in the case of  $L \sim 1.5-2$ .

#### 4. Hard Electrons of the Outer Zone

Primary attention was directed to electrons of the outer zone in the works (Ref. 16-21), and it was shown that many phenomena related to the diffusion processes also belong to this group of particles. Although the assumption (Ref. 16-21) of a low diffusion rate and, consequently, a long lifetime of electrons has not been corroborated, many results from these works remain in force. It was thus shown in (Ref. 16-21) that the spectrum becomes harder with a decrease in  $L$ . This has now received reliable confirmation from experiments. The steady profile of the outer zone, which was determined in (Ref. 21), can be transferred without any significant changes to the case of rapid diffusion and rapid leakages (the Coulomb loss time must only be replaced by the magnetic scattering time).

/324

Figure 3, a, presents the distribution, calculated according to this model, of the readings from the outer Geiger counter carried on satellites of the "Elektron" series during a prolonged period of low magnetic activity. This counter primarily recorded braking radiation of electrons with  $\epsilon > 250$  kev. The lifetime of the electrons was assumed to be  $\sim 10^6$  sec. The theoretical result closely coincides with the experiments (Ref. 7).

As was noted in the introduction, irreversible electron acceleration ceases at energies of  $\sim 100$  kev. If it is assumed that the minimum field on the diurnal boundary of the magnetosphere is  $40 \gamma$  during magnetically quiet days, then in the case of betatron acceleration the electron spectrum must be sharply truncated for the impulse  $p_0 = p_b \sqrt{H/H_b}$ , where  $p_b \approx 0.7$  is the electron impulse with  $\epsilon = 100$  kev,  $H$  - the field at the observed point, and  $H_b = 40 \gamma$ . The smaller is  $L$ , the larger is the boundary energy. Thus, in the case of  $L = 4$  - where the most complete electron energy spectrum can be recorded due to the absence of an altitudinal pattern - a sharp drop must occur for  $\epsilon \approx 800$  kev, which closely coincides with the experiments (Ref. 7) (Figure 3, b).

It is well-known that in 1961-1963 the electron spectrum was significantly harder, and in the case of  $\epsilon > 1.5$  Mev the intensity frequently amounted to  $\sim 10^6 \text{ cm}^{-2} \cdot \text{sec}^{-1}$  (Ref. 1, 2, 9). During this period the intensity distribution of these electrons had, as a rule, a very similar form (in particular, it was for this reason that the value for  $D_0$  was too low in [Ref. 21]). According to data in (Ref. 7), the absence of this intensity in 1964 means that this peak of relativistic electrons is not stationary. The study (Ref. 2) traced the development of this peak throughout a prolonged period of low magnetic activity. The authors stated that they observed a non-stationary, diffusion wave. This conclusion closely coincides with computations based on equation (13). Apparently, the diffusion waves of relativistic electrons, which were observed at the end of 1962, were caused by an impulsive injection of electrons in far-removed envelopes.

There are two possibilities for the creation of this zone: either a

shift in the irreversible acceleration boundary toward larger energies, or a sharp decrease in the field at the magnetosphere boundary. In the first case, an intensity of  $\sim 10^6$  of electrons with  $\epsilon > 300$  kev must be formed at the magnetosphere boundary. The subsequent transfer of a portion of these electrons to smaller L leads to their acceleration up to relativistic energies.

Based on data in (Ref. 22), the field frequently decreased to 20-30  $\gamma$  at the magnetosphere boundary in 1961. It can be assumed that during strong storms the field drops even more (let us say, to 10-15  $\gamma$ ). In the latter case, it is sufficient that electrons are accelerated to energies of  $\sim 100$  kev in a field of  $\sim 10$   $\gamma$ , in order that they may be accelerated to 1-2 Mev during subsequent diffusion in the region  $L \sim 4 - 5$ .

/325

Since diffusion in this region requires  $\sim 10$ -30 days, it is possible that data on the field at the magnetosphere boundary may make it possible in the future to predict the period of radiation danger in the outer zone<sup>1</sup>.

Thus, theoretical and experimental studies performed in 1963-1964 show that anomalous diffusion plays a very important role in the dynamics of the radiation zones of the Earth. The theory of anomalous diffusion fully solves the problem of the origin of the outer proton zone, and on this basis makes it possible to overcome difficulties related to different anomalies of the high-energy proton spectrum. The concept of particle transfer across the drift envelopes, with allowance for magnetic scattering, makes it possible to understand the main features of the dynamics and structure of the outer electron zone. It is possible that the transfer effect plays a significant role in the formation of the current ring during magnetic storms.

#### REFERENCES

1. Freeman, J. J. Geophys. Res., 69, 1961, 1964.
2. Frank, L., Van Allen, J., Hills, J. J. Geophys. Res., 69, 2171, 1964.
3. Maehlum, B., O'Brien, B. J. Geophys. Res., 68, 997, 1963.
4. O'Brien, B. J. Geophys. Res., 67, 3687, 1962.
5. O'Brien, B. J. Geophys. Res., 69, 13, 1964.

---

<sup>1</sup> However, it should be kept in mind that the magnitude of  $D_0$ , which is averaged over  $\sim 10$  days, can strongly fluctuate, particularly during a period of strong magnetic perturbation.

6. Winkler, J., Bhavsar, P., Anderson, K. J. Geophys. Res., 67, 3717, 1962.
7. Vernov, S. N., Kuznetsov, S. N., Logachev, Yu. I., et al. Present Collection, p. 394.
8. Rosser, W. J. Geophys. Res., 68, 3131, 1963.
9. Frank, L., Van Allen, J., Macagno, E. J. Geophys. Res. 68, 3543, 1963.
10. McIlvain, C. Science, 142, 355, 1963.
11. Davis, L., Williamson, J. Space Res., 3, 365, 1963.
12. McIlvain, C., Fillius, R., Valerio, J., Davé, A. J. Geophys. Res., 69 (in press).
13. Naugle, J. E., Kniffen, D. A. J. Geophys. Res., 68, 9065, 1963.
14. Kellogg, P. Nature, 183, 1295, 1959.
15. Parker, E. J. Geophys. Res., 65, 3117, 1960.
16. Tverskoy, B. A. Transactions of the All-Union Conference on Cosmic Rays (Trudy Vsesoyuznoy Soveshchaniya po fizike kosmicheskikh luchey), 1963, Izdatel'stvo AN SSSR (in press).
17. Ibid, 1963. Izdatel'stvo AN SSSR, 1964 (in press).
18. Tverskoy, B. A. Transactions of the International Conference on Physics of Cosmic Rays in India (Trudy Mezhdunarodnogo sov. po fizike kosmicheskikh luchey v Indii), 1963, (in press).
19. Tverskoy, B. A. Geomagnetizm i Aeronomiya, 4, 224, 1964.
20. Ibid, 4, 436, 1964.
21. Krymov, Yu. S., Tverskoy, B. A. Geomagnetizm i Aeronomiya, 4, 397, 1964.
22. Nishida, A., Cahill, L. J. Geophys. Res., 69, 2243, 1964.
23. Cahill, L., Amazeen, P. J. Geophys. Res., 68, 1835, 1963.
24. Nakada, M., Dungey, J., Hess, W. J. Geophys. Res., 70 (in press).
25. Vernov, S. N., Logachev, Yu. I., Sosnovets, E. I., et al. Present Collection, p. 394.
26. Kellogg, P. J. Proc. Conf. Cosmic Rays in India, 1963.

27. Vernov, S. N., Chudakov, A. Ye. Uspekhi Fizicheskikh Nauk, 70, 585, 1960.
28. Welch, J., Whittaker, W. J. Geophys. Res., 64, 909, 1959.
29. Wentzel, D. J. Geophys. Res., 66, 359, 1961.
30. Drogdt, A. J. Geophys. Res., 66, 1641, 1961.
31. Yershkovich, A. I. Dissertation for the Institute of Atmospheric Physics (Dissertatsiya in-t fiziki atmosfery), AN SSSR, 1964.
32. Van Allen, J. In "Radiation Zones of the Earth," II, 1962.
33. McIlwain, C. J. Geophys. Res., 66, 3681, 1961.
34. Hess, W., Canfield, E., Lingenfelter, R. J. Geophys. Res., 66, 666, 1961.

---

The Formation of Radiation Zones as a Result of  
Particle Drift in the Depths of the Magnetosphere

A. Ye. Antonova, A. I. Yershkovich, V. P. Shabanskiy

As measurements on the satellite "Relay-1" have shown, the intensity of trapped protons having energies of  $E_p > 34$  Mev changes during magnetic storms as the particles drift toward the Earth (Ref. 1). With a disturbance of the third invariant, this drift can result from a sudden change in the azimuthal symmetry of the geomagnetic field, with its subsequent slow restoration (Ref. 2). Another possible mechanism is particle drift toward the Earth under the influence of hydromagnetic waves (Ref. 3).

Let us assume that the first and second invariants are conserved during particle drift. When the particles move toward envelopes with a small McIlwain  $L$  parameter, the particles will be accelerated betatronically. In order to obtain a spatial distribution of particle intensity, it is necessary to solve an equation of continuity, assigning definite mechanisms to the formation and destruction of particles. Let us first determine the effectiveness of an albedo neutron source, assuming for purposes of simplicity that the particles drift instantaneously toward the envelope under consideration  $L_1$ . This assumption means that all the particles, which are formed during the  $\beta$ -decay of albedo neutrons per unit of time in the magnetosphere in the case of  $L \geq L_1$ , are assumed to be transferred with allowance for energy change within this envelope (in the region  $L \leq L_1$ ). Since the velocity of a proton formed during neutron decay is  $v_p \approx v_n$  (where  $v_n$  is the neutron velocity), the average number of protons having the energy  $E_p \geq E_1$ , produced per unit volume per unit of time within an envelope having the parameter  $L_1$ , is

$$\frac{dN_p(E_1, L_1)}{dt} \approx \frac{1}{V_1} \int_{L_1}^{L_0} dV \int_{E_{\min}}^{\infty} \frac{S(E, L) dE}{t_n v_n} (cM^{-3} \cdot \text{sec}^{-1}), \quad (1)$$

where  $S(E, L)dE$  is the differential spectrum of albedo neutrons;  $t_n \approx 1013$  sec - the mean neutron lifetime;  $L_0 \approx 10$  - corresponds to the mean position of the magnetosphere boundary;  $V_1$  - the size of the inner magnetosphere section which is defined by the envelope  $L_1$ . For prerelativistic particles with large pitch angles, we approximately have  $E(L) \cdot L^3 = \text{const}$  (it is assumed that the geomagnetic field is a dipole field), and thus  $E_{\min} = E_1 (L_1/L)^3$ . The albedo neutron spectrum given in (Ref. 4) was employed for the computations. The dashed line in Figure 1 designates the function  $dN_p/dt$  for protons having a kinetic energy of more than 1.7 Mev ( $E_1 = 1.7$  Mev). In the envelope of  $L \approx 3$ , the lifetime of protons with respect to the ionization losses (this is the slowest of the postulated loss mechanisms) is  $T_1 \approx 4 \cdot 10^8$  sec. An approximate calculation using formula (1) shows that the proton intensity produced by albedo neutron decay in this envelope is

$$I_p \approx \frac{dN}{dt} \cdot v_p \cdot T_1 \approx 3 \cdot 10^3 cM^{-2} \cdot \text{sec}^{-1}.$$

This is approximately one order of magnitude smaller than the values obtained during the experiments of Davis and Williamson (Ref. 5). For  $E_1 = 97$  kev, the divergence is several order of magnitude (Ref. 5, 6). Thus, the albedo neutron source does not play an important role in the formation of the Davis protonosphere. /327

The effectiveness of a neutron source for the formation of a relativistic electron zone (with no allowance, however, for the electron spectrum of  $\beta$ -decay) was determined in a similar manner in the work (Ref. 3). If we take the spectrum of  $\beta$ -electrons into account, we obtain

$$\frac{d}{dt} N_e(E_1, L_1) \approx \frac{1}{V_1} \int_{L_{\min}}^{L_0} n(L) dV \int_{E_{\min}}^{2.53} F(E) dE (cM^{-3} \cdot \text{sec}^{-1}), \quad (2)$$

where

$$n(L) = 1.1 \cdot 10^{-13} \left(\frac{L}{4}\right)^{-2.7} cM^{-3} \cdot \text{sec}^{-1} \quad (3)$$

is the integral density of albedo neutron decay in the magnetosphere (Ref. 4)

$$F(E) dE = 0.613 \cdot (E^2 - 1)^{1/2} \cdot E \cdot (2.53 - E)^2 dE \quad (4)$$

is the electron spectrum of  $\beta$ -decay normalized per unit (here  $E$  is the total electron energy in units of  $m_e c^2$ ;  $m_e$  is the rest mass of an electron;  $c$  is the speed of light). Since  $(E^2 - 1) L^3 \approx \text{const}$  in the case of betatron

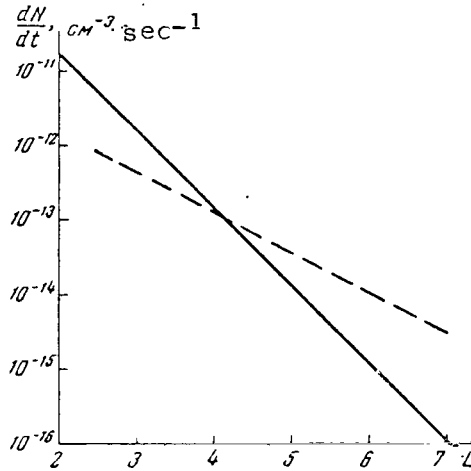


Figure 1

Function of  $dN/dt$  for Protons With a Kinetic Energy of More Than 1.7 Mev (dashed line) and for Electrons with a Kinetic Energy of More Than 1.6 Mev (solid line), computed According to Formulas (1) and (2), Respectively.

acceleration of relativistic electrons with large pitch angles, we have

$$(E_{\min}^2 - 1)L^3 = (E_1^2 - 1)L_1^3;$$

$$L_{\min} = L_1 \left( \frac{E_1^2 - 1}{2.53^2 - 1} \right)^{1/3}.$$

The function of  $dN_e/dt$  is shown in Figure 1 by the solid line for electrons having a kinetic energy of more than 1.6 Mev ( $E_1 = 4.13$ ). It is known that at the maximum of a relativistic electron zone ( $L \sim 4$ ) the intensity  $I_e$  of electrons having this energy is on the order of  $10^5 \text{ cm}^{-2} \cdot \text{sec}^{-1}$  (Ref. 7). Lifetimes of  $T \sim I_e / c \left( \frac{dN_e}{dt} \right) \approx 2 \cdot 10^7 \text{ sec}$  are requisite for such an intensity caused by neutron  $\beta$ -decay (see Figure 1). These lifetimes are three orders of magnitude smaller than the lifetime with respect to ionization losses for  $L \sim 4$ . Consequently, when the electrons drift fairly rapidly toward the Earth, the albedo neutron source can produce the observed intensity of relativistic electrons during a period of time which is much smaller than the lifetimes determined by ionization losses.

Let us investigate a particle whose reflection point lies close to the plane of the geomagnetic equator. Just as in (Ref. 2), let us introduce the dimensionless quantity

$$J = \frac{pL^{3/2}}{mc}, \quad (5)$$



where  $p$  and  $m$  are the impulse and rest mass of the particle, respectively. If the second invariant equals zero, it follows from the conservation of the first invariant that  $J = \text{const}$  in the case of drift (in the absence of losses). Calculations performed in (Ref. 8) show that  $J$  is retained with sufficient accuracy, if the particle reflection points lie at latitudes of  $\leq 30^\circ$ . Let  $f(L, J)dLdJ$  be the number of particles in a force tube with the diameter  $L$  in the interval  $(L, L + dL)$  and  $J$  - in the interval  $(J, J + dJ)$ . Then in the stationary case the equation of continuity in the space  $(L, J)$  has the following form: /328

$$\frac{\partial}{\partial L} \left( f \frac{dL}{dt} \right) + \frac{\partial}{\partial J} \left( f \frac{dJ}{dt} \right) + Q = 0, \quad (6)$$

where  $Q$  is the density of the source, and  $\frac{dL}{dt}(L, J)$  and  $\frac{dJ}{dt}(L, J)$  are the coefficients (of the rate of change) determined from physical considerations.

Since the neutron source is not powerful enough to create the observed proton streams, let us assume that the proton zone results from the drift toward the Earth of protons occupying the layer between the magnetosphere boundary and the front of a stationary shock wave, and that  $Q = 0$  within the magnetosphere (in the case of  $L < L_0$ ). If we do not attribute proton drift and losses to a specific mechanism, we can assume that

$$\frac{dL}{dt} = \alpha J_p^m L^q, \quad (7)$$

$$\frac{dE_p}{dt} = \beta J_p^n L^k, \quad (8)$$

where, according to (5),  $J_p = \frac{v_p}{c} L^{3/2}$ ,  $E_p = \frac{J_p^2}{2L^3}$  (with the exception of formula (26), the proton energy  $E_p$  is measured in units of  $m_p c^2$  both here and below).

The solution of the corresponding Cauchy problem ( $f(L = L_0) = \varphi(J_p)$ ) for equation (6) in the case of  $Q = 0$  and the conditions of (7) and (8) has the following form

$$f(L, J_p) = \varphi \left\{ \left[ J_p^{m-n+2} + a(L) \right]^{\frac{1}{m-n-2}} \left( \frac{L}{L_0} \right)^{-q} \cdot \frac{[J_p^{m-n+2} + a(L)]^{\frac{n-1}{m-n+2}}}{J_p^{n-1}} \right\}, \quad (9)$$

where

$$a(L) = \frac{3}{\alpha} \frac{m-n+2}{q-k-4} (L^{k-q+4} - L_0^{k-q+4}), \quad q \neq k+4. \quad (10)$$

Let us assume that the proton spectrum has the following form at the magnetosphere boundary  $L_0$ :

$$f(L = L_0) = \varphi(J_p) = C_1 \exp(-AJ_p^2). \quad (11)$$

If we now turn to proton energies, then (11) designates the spectral dependence of the type  $\exp(-E_p/E_0)$  and  $A = \frac{1}{2E_0 L_0^3}$ . Using (11), we can find the following from (9):

$$f(L, J_p) = C_1 \left(\frac{L}{L_0}\right)^{-q} \frac{[J_p^{m-n+2} + a(L)]^{\frac{n-1}{m-n+2}}}{J_p^{n-1}} e^{-A(J_p^{m-n+2} + a)^{\frac{2}{m-n+2}}} \quad (12)$$

A spectrum similar to (11) was observed by Davis and Williamson (Ref. 5, 6) within the magnetosphere not only in envelopes which were rather far removed (where the energy losses are small as compared with the drift velocity and where, consequently, it can be assumed that  $a = 0$  in [12]), but also in the region of the proton zone maximum ( $L \sim 3$ ). Consequently, in order that the spectrum (12) coincide with the experimental data (Ref. 5, 6) we must assume that  $m = n = 1$  - i.e., we must assume that the drift velocity  $\frac{dL}{dt}$  (and the rate of energy losses  $\frac{dE_p}{dt}$  are proportional to the proton impulse or to their Larmor radius). /329

Since the drift effects are manifested only in second order perturbation theory with respect to  $\delta B/B$  (where  $B$  is the geomagnetic field strength), it can be readily shown that  $\frac{dL}{dt} \sim B^0$ , i.e.,  $q = 8.5$ . We thus have

$$\frac{dL}{dt} = \alpha J_p L^{8.5}, \quad (7a)$$

$$\frac{dE_p}{dt} = \beta J_p L^k. \quad (8a)$$

We find the following from (12)

$$f(L, J_p) = C_1 \left(\frac{L}{L_0}\right)^{-8.5} \cdot \exp(-A J_p^2) \cdot \exp[-A a(L)]. \quad (13)$$

The volume  $dV$  of the geomagnetic field lune, defined by envelopes having the parameters  $L$  and  $L + dL$  when the magnetic stream is constant through its transverse cross section, changes proportionally to  $L^{4.25} dL$ . Therefore the intensity of particles having the energy  $> E$  is

$$I(>E, L) = \frac{1}{L^{4.25}} \int_{J(E)}^{\infty} f(L, J) v(J) dJ. \quad (14)$$

Since  $v_p = \frac{cJ_p}{L^{3/2}}$ , from (13) and (14) we find that

$$I_p(>E_p, L) = \frac{C_1 c L_0^{8.5}}{2A} L^{-14.25} \exp\left(-\frac{E_p L^3}{E_0 L_0^3}\right) \exp[-A a(L)], \quad (15)$$

where, according to (10)

$$a(L) = \frac{23}{\alpha(4.5-k)} (L^{k-4.5} - L_0^{k-4.5}) \quad k \neq 4.5. \quad (16)$$

If it is assumed that  $L_0 = 10$ , then the measurements in (Ref. 6) give<sup>1</sup>

$$E_0 \approx \frac{15 \text{ keV}}{9.4 \cdot 10^3 \text{ keV}} \approx 1.6 \cdot 10^{-5}; \quad A = \frac{1}{2E_0 L_0^3} \approx 31.3.$$

The position of the proton intensity maximum is determined from (15) by differentiation with respect to  $L$ :

$$L_{\max}^{k-4.5} = \left( 2A \frac{3}{\alpha} \right)^{-1} (3AE_p L_{\max}^3 + 14.25). \quad (17)$$

In the case of  $k > 4.5$ , the maximum shifts toward larger  $L$  when the energy increases, which contradicts the experimental data. Selecting values of  $L_{\max}$  for any two values of proton energy  $E_p$  from the experimental data, we can determine  $k$  and  $\beta/\alpha$  from (17). Let us assume that  $L_{\max} = 3.5$  for protons having an energy of 97 keV (Ref. 6) and  $L_{\max} = 3.2$  for protons having an energy of 500 keV (Ref. 9). From (17) we then find that  $k = 2.5$  and  $\beta/\alpha = 2.75$ . For these values of  $k$  and  $\beta/\alpha$ , we can determine the position of the maxima for protons having different energies from (17):  $L_{\max} = 2.85; 2.8; 2.5; 1.75; 1.5$  for protons with energies of  $> 1.7; > 2; > 5; > 40$  and  $> 100$  MeV, respectively.  $L_{\max} \sim E_p^{-1/12}$  approximately from 97 keV to 5 MeV;  $L_{\max} \sim E_p^{-1/6}$  between 5 and 40 MeV. The intensity distribution of protons having different energies, calculated according to (15) and (16) for values of  $\beta/\alpha = 2.75; k = 2.5; L_0 = 10$ , is shown in Figure 2 for protons having energies greater than 0.097; 0.4; 0.5; 1.0; 1.7; 2.5 and 6 MeV.  $C_1 = 5.75$  was selected for normalization to the absolute intensity of protons having energies of  $> 97$  keV ( $\sim 2 \cdot 10^7 \text{ cm}^{-2} \cdot \text{sec}^{-1} \cdot \text{sterad}^{-1}$  in the case of  $L = 3.5$ ) (Ref. 6). The crosses designate experimental points for protons having energies greater than 97 keV and 1.7 MeV, obtained on the satellites "Explorer-12", "Explorer-14", and "Explorer-15" (Ref. 5, 6). The triangles correspond to proton measurements having energies of  $> 500$  keV performed by the Van Allen group (Ref. 9). The asterisks pertain to experiments on the satellite "Kosmos-41" (Ref. 10) (proton energies of  $> 400$  keV), and the vertical dashes correspond to observed intensity variations. The small circles designate experimental points obtained on the "Elektron" series of satellites (Ref. 11) (energies greater than 2 and 5 MeV). /330

We should call attention to the fact that the Davis spectrum  $\sim \exp \left( - \frac{E_p L^3}{E_0 L_0^3} \right)$  (Ref. 11) fully determines the spatial intensity

<sup>1</sup> As is known, the volume element of the geomagnetic field  $dV^* = L^2 \cos^7 \lambda dL \cdot d\lambda \cdot 2\pi$ , where  $\lambda$  is the geomagnetic latitude. It follows from a constant magnetic stream that  $dL \sim L^2$ . Therefore, the lune volume with a constant "diameter"  $dL$  at the equator is proportional to  $L^4 dL \int_0^{\lambda_m} \cos^7 \lambda d\lambda$ , where  $\lambda_m$  is the geomagnetic latitude of the specular point. In the case of  $\lambda_m \leq 30^\circ$ , the conservation of the first two invariants yields  $\lambda_m \sim L^{1/4}$  (Ref. 8). Therefore, the lune volume defined by the envelopes of  $L$  and  $L + dL$  is proportional to  $dV \sim L^{4.25} dL$  in the case of  $\lambda_m \leq 30^\circ$ .

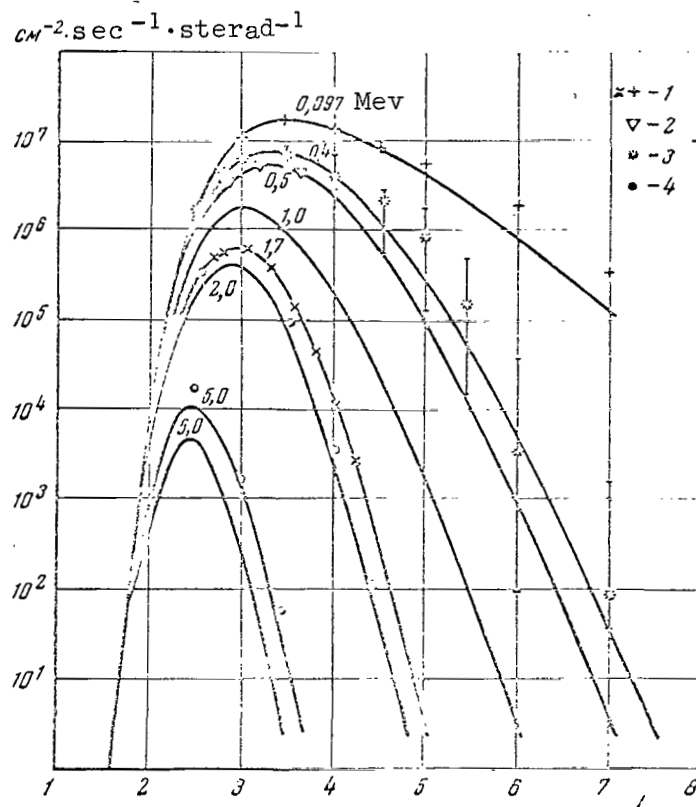


Figure 2

Intensity Distribution of Protons having Different Energies Computed According to (15) and (16) for the values

$$\beta/\alpha = 2.75 \text{ m}_p/\text{m}_e, k = 2.5; L_0 = 10; C_1 = 5.75$$

- 1 - Experimental points according to (Ref. 5, 6);  
 2 - According to (Ref. 9); 3 - According to (Ref. 10); 4 - According to (Ref. 11).

distribution of protons having any energy if this distribution is known for protons having a definite energy. However, we only employed the experimental values of  $L_{\max}$  for protons having energies greater than 97 and 500 kev and the spectral dependence (11), in order to determine all unknown parameters of the theory  $m$ ,  $n$ ,  $k$  and  $\beta/\alpha$ . Therefore, the satisfactory agreement with the experimental data which is illustrated in Figure 2 is due to our assumptions regarding radial proton drift, which is described by the equation of continuity (6).

Equation (15) also makes it possible to determine the proton stream at the magnetosphere boundary. In the case of  $C_1 = 5.75$  and  $L_0 = 10$ , we find

$$I_p(>E_p) \approx 5 \cdot 10^3 e^{-\frac{E_p}{E_0}} \text{ c.u.}^{-2} \cdot \text{sec}^{-1} \cdot \text{sterad}^{-1}. \quad (18)$$

Thus, the expected intensity of protons having energies of  $\geq 10$ -15 kev at the magnetosphere boundary is on the order of  $2 - 3 \cdot 10^4 \text{ cm}^{-2} \cdot \text{sec}^{-1}$ . This estimate does not contradict the measurements performed by Bader (Ref. 12) on the satellite "Explorer-12" (a stream of protons with energies from 100 ev to 20 kev  $< 10^6 \text{ cm}^{-2} \cdot \text{sec}^{-1}$ ). This estimate is not unexpected, since the solar wind protons having a mean energy on the order of several kev must be thermalized in the region between the magnetosphere boundary and the front of a stationary shock wave.

Let us now assume that the radial drift and "magnetic" electron scattering are described by the relationships (7) and (8) with the same parameters  $m$ ,  $n$ ,  $k$  and  $\beta/\alpha$  as for protons (just as previously, we obviously have  $q = 8.5$ ; this value, which is determined theoretically, does not depend on the mass of the charged particle):

$$\frac{d\bar{L}}{dt} = \alpha J_e L^{8.5}, \quad (19)$$

$$\frac{d\bar{E}_e}{dt} = \beta J_e L^{2.5}, \quad (20)$$

where for relativistic particles  $J_e = \frac{p_e L^{3/2}}{m_e c} \approx E_e L^{3/2}$  (the electron energy  $E_e$  is measured in units of  $m_e c^2$ ).

In the region of the relativistic electron zone maximum, the density of the sources  $Q = 0$ , since relativistic electrons cannot be formed directly during  $\beta$ -neutron decay, but drift into the maximum region from magnetic envelopes which are farther away  $L_c \geq L \geq L_c$ . The solution of the Cauchy problem for equation (6) has the following form in the case of  $Q = 0$  and under the conditions of (19-20):

$$f(L, J) = \varphi\left\{\left(J_e + a\right)\right\} \cdot \left(\frac{L}{L_c}\right)^{-8.5} \frac{J_e + a(L)}{J_e}, \quad (21)$$

where

$$a(J) = \frac{3}{3.52} (L^{-3.5} - L_c^{-3.5}). \quad (22)$$

In order to define the boundary condition  $f(L = L_c) = \varphi(J_e)$ , let us solve the equation of continuity (6) in the region  $L_c \geq L \geq L_c$  with the source  $Q(L, J)$  which is determined by the density of albedo neutron decay, but without losses (the intensity maximum is formed for those values of  $L$  at which the drift rate  $\frac{dL}{dt}$  is on the order of the loss rate  $\frac{dE}{dt}$ ; as follows from (19) and (20), in the case of  $L \gg L_{\max}$  the loss rate is negligibly small as compared with the drift rate). From (6), we obtain

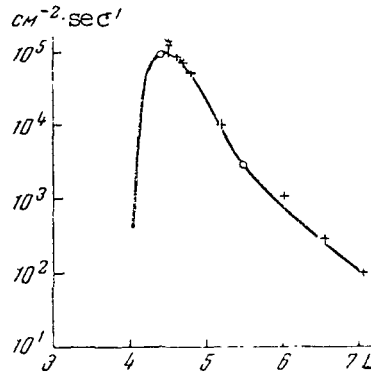


Figure 3

Spatial Intensity Distribution of Electrons with Energies of More Than 1.6 Mev Calculated as from (21)-(25)

Crosses designate experimental points from (Ref. 7) ("Explorer-14"); Circles designate measurements on the second Soviet cosmic rocket (Ref. 13);

The stars designate measurements from (Ref. 14) ("Explorer-12").

$$f(L_c, J_e) = \varphi(J_e) = (\alpha J_e L_c^{5.5})^{-1} \int_{L_c}^{L_0} Q(L, J_e) dL. \quad (23)$$

Employing the equations (3) and (4), we find that the number of electrons formed per unit of time in a force tube with the parameter  $L$ , in the  $(L, L + dL)$  range, and  $J_e$  in the  $(J_e, J_e + dJ_e)$  range, approximately equals

$$Q(L, J_e) dL dJ_e \approx 2.8 \cdot 10^{-12} J_e^2 L^{-3} \left( 2.53 - \frac{J_e}{L^{1/2}} \right)^2 dL dJ_e. \quad (24)$$

The relationships (21)-(24) facilitate the determination of  $f(L, J_e)$  in 332 the case of  $L \leq L_c$ ; it is sufficient to replace  $L_c \rightarrow L$  in (23) in order to determine  $f(L, J_e)$  in the case of  $L > L_c$ . According to (14), the intensity of relativistic ( $v_e \approx c$ ) electrons having energies of  $> E_e$  is

$$J_e(> E_e, L) = \frac{c}{L^{4.25}} \int_{J_e(E_e)}^{J_{\max}} f(L, J) dJ, \quad (25)$$

where  $J_{\max} = E_{\max} \cdot L_0^{3/2} = 2.53 \cdot L_0^{3/2}$ . According to (21)-(25),  $L_0 = 10$ ,  $L_c = 7$ ;  $E_e = 4.13$  was selected for the computations (electrons having a kinetic energy of  $> 1.6$  Mev). The selection of  $L_c = 7$  was imposed by the considerations already mentioned, namely for  $L \leq 7$  it can be assumed that  $Q(L, J) = 0$ , since the  $\beta$ -decay electrons - drifting in the maximum region ( $L \sim 4$ ) - cannot be accelerated up to an energy of 1.6 Mev. In the case of  $L > 7$ , energy losses as compared with the drift rate can be disregarded.

Figure 3 presents the spatial intensity distribution of electrons having energies greater than 1.6 Mev; this distribution was computed according to (21)-(25). The crosses designate the experimental points obtained by the Van Allen group on the satellite "Explorer-14" (Ref. 7). The small circles correspond to measurements on the second Soviet cosmic rocket (Ref. 13), and the asterisk designates measurements on the satellite "Explorer-12" (Ref. 14). It can be readily seen (see, for example, (7a)-(8a)) that - when measuring the energy of both protons and electrons in units of  $m_e c^2$  (and, correspondingly, the proton impulse - in units of  $m_e c$ ) - we obtain  $\frac{\beta}{\alpha} = 2.75 \frac{m_p}{m_e} = 5.1 \cdot 10^3$  (instead of the previous value of  $\beta/\alpha = 2.75$ ). Therefore,  $\beta/\alpha = 5.1 \cdot 10^3$  was selected to determine the electron intensity profile shown in Figure 3.

Thus, the same assumptions with respect to the nature of drift and loss (drift rate and energy loss rate are proportional to the impulse, or to the Larmor radius of the particles - (7a), (8a), (19), (20)) for the same ratio of  $\beta/\alpha$  provide for the formation of intensity maxima of the proton and electron zones of similar energies in the L-envelopes close at hand. Drift, arising from perturbations of the third invariant due to a sudden change in the azimuthal symmetry of the geomagnetic field (Ref. 2), does not depend on the particle mass or energy, and therefore it does not have this property. In order that the theory (Ref. 2) may coincide with experimental data on the intensity maxima position of the proton and electron zones (with energies on the order of 1 Mev), it must be assumed that the loss mechanisms are different for protons and electrons. Radial particle drift under the influence of hydromagnetic waves propagated toward the Earth does not depend on particle mass or energy either (as a computational refinement by the author has shown [Ref. 3]). Therefore, this cannot be the only mechanism leading to the formation of electron and proton zones having similar energies.

Computations employing (21)-(25) for different values of electron energy  $E_e$  (but for the fixed ratio  $\beta/\alpha$ ) have shown that the intensity maximum position of relativistic electrons barely depends on their energy:  $L_{\max} \sim E_e^{-\sigma}$ , where  $\sigma \approx (3 - 5) \cdot 10^{-2}$ . This corresponds to the measurement results (see, for example, [Ref. 11]). /333

In contrast to the proton source, whose strength was determined from experimental data (see [18]), the source of relativistic electrons (density of albedo neutron decay in the magnetosphere) is assumed to be preset. Therefore, electron intensity measurements make it possible to find not only the ratio  $\beta/\alpha$  (which determines the intensity maximum position), but also the drift rate - i.e.,  $\alpha$ , since intensity  $I_e \sim 1/\alpha$  - [see (21)-(25)].  $\alpha = 8 \cdot 10^{-16}$ , and consequently  $\beta = 4 \cdot 10^{-12}$ , was selected for normalization to the absolute stream of electrons having energies of  $> 1.6$  Mev in the region of the zone maximum ( $I_e \approx 10^5 \text{ cm}^{-2} \cdot \text{sec}^{-1}$  for  $L \approx 4.5$  [Ref. 7]). Thus, by utilizing (7a), (8a), (19), (20), we can determine the magnetic scattering time  $T_M \left( \frac{dE}{dt} \sim \frac{E}{T_M} \right)$ , and the drift time  $T_d$  per 1 Earth radius

$\left(\frac{dL}{dt} \sim \frac{1}{T_d}\right)$  for protons and electrons, respectively:

$$T_d^e = \frac{1}{\alpha E_e L^{10}}; \quad T_d^p = \frac{1}{\alpha \left(2 \frac{m_p}{m_e} E_p\right)^{1/2} L^{10}}; \quad (26)$$

$$T_M^e = \frac{1}{3L^4}; \quad T_M^p = \sqrt{\frac{E_p}{2 \frac{m_p}{m_e} \beta L^4}} \frac{1}{\beta L^4}.$$

In (26) the electron and proton energies are given in identical units of  $m_e c^2$ . The table below gives these times for protons and electrons having different energies for  $\beta/\alpha = 5.1 \cdot 10^3$ ,  $\alpha = 8 \cdot 10^{-16}$ . For purposes of comparison, the lifetime  $T_i$  with respect to ionization losses is also given. Small times of  $T_M^p$  for  $L \geq 3$  indicate that protons may be "discharged" into the atmosphere. In the case of  $L \leq 3$   $T_M^p > T_i$  for electrons and protons having energies on the order of 1 Mev. For protons with energies of the order of 30 Mev,  $T_M^p > T_i^p$  in the case of  $L \leq 2$ . Consequently, the assumption of magnetic proton scattering (which is proportional to their Larmor radius) does not contradict the prevailing assumption that the inner zone of energetic protons (with energies of  $\sim 30$ -100 Mev) results from  $\beta$ -decay of albedo neutrons, and that the main mechanism leading to their destruction is ionization losses. However, the possibility is not excluded that the drift of solar protons having energies on the order of several hundred of kev, in an envelope with the parameter  $L \sim 1.5$ , can lead to the formation of a considerable amount of energetic protons within the zone. However, this determination requires measurements of the solar proton spectrum having energies which are several hundred of kev outside of the magnetosphere.

TABLE

L	Electrons			Protons					
	E <sub>e</sub> = 1.6 Mev			T <sub>d</sub>		T <sub>M</sub>		T <sub>i</sub>	
	T <sub>d</sub>	T <sub>M</sub>	T <sub>i</sub>	E <sub>p</sub> = 1 Mev	E <sub>p</sub> = 30 Mev	E <sub>p</sub> = 1 Mev	E <sub>p</sub> = 30 Mev	E <sub>p</sub> = 1 Mev	E <sub>p</sub> = 30 Mev
1.5	5.2 · 10 <sup>12</sup>	4.1 · 10 <sup>10</sup>	6.0 · 10 <sup>8</sup>	2.5 · 10 <sup>11</sup>	4.6 · 10 <sup>10</sup>	1.1 · 10 <sup>9</sup>	6.1 · 10 <sup>9</sup>	2.0 · 10 <sup>7</sup>	3.3 · 10 <sup>9</sup>
2.0	2.9 · 10 <sup>11</sup>	1.3 · 10 <sup>10</sup>	1.4 · 10 <sup>9</sup>	1.4 · 10 <sup>10</sup>	2.6 · 10 <sup>9</sup>	3.5 · 10 <sup>8</sup>	1.9 · 10 <sup>9</sup>	4.6 · 10 <sup>7</sup>	7.5 · 10 <sup>9</sup>
3.0	5.0 · 10 <sup>9</sup>	2.6 · 10 <sup>9</sup>	6.0 · 10 <sup>9</sup>	2.5 · 10 <sup>8</sup>	4.5 · 10 <sup>7</sup>	6.9 · 10 <sup>7</sup>	3.8 · 10 <sup>8</sup>	2.0 · 10 <sup>8</sup>	3.3 · 10 <sup>10</sup>
4.0	2.8 · 10 <sup>8</sup>	8.2 · 10 <sup>8</sup>	2.5 · 10 <sup>10</sup>	1.4 · 10 <sup>7</sup>	2.5 · 10 <sup>6</sup>	2.2 · 10 <sup>7</sup>	1.2 · 10 <sup>8</sup>	8.3 · 10 <sup>8</sup>	1.4 · 10 <sup>11</sup>
6.0	4.9 · 10 <sup>6</sup>	1.6 · 10 <sup>8</sup>	2.2 · 10 <sup>11</sup>	2.4 · 10 <sup>5</sup>	4.4 · 10 <sup>4</sup>	4.3 · 10 <sup>6</sup>	2.4 · 10 <sup>7</sup>	7.2 · 10 <sup>9</sup>	1.2 · 10 <sup>12</sup>



# REFERENCES

1. McIlwain, C. E. Redistribution of trapped protons during a magnetic storm. Univ. California at San Diego, April, Preprint, 1964.
2. Tverskoy, B. A. Geomagnetizm i Aeronomiya, 4, No. 3, 436, 1964.
3. Shabanskiy, V. P. Geomagnetizm i Aeronomiya 4, No. 6, 1108, 1964.
4. Hess, W. N., Canfield, E. H., Lingenfelter, R. E. J. Geophys. Res., 66, No. 3, 665, 1961.
5. Davis, L. R. Symposium on plasma physics in space. Catholic Univ. America, Washington, June, 1963.
6. Davis, L. R., Williamson, J. M. Space Res., 3, 365, 1963.
7. Frank, L. A., Van Allen, J. A., Macagno, E. J. Geophys. Res., 68, No. 12, 3543, 1963.
8. Krymov, Yu. S., Tverskoy, B. A. Geomagnetizm i Aeronomiya, 4, No. 2, 397, 1964.
9. Frank, L. A., Van Allen, J. A., Hills, H. K. J. Geophys. Res., 69, No. 11, 2171, 1964.
10. Vernov, S. N., Savenko, I. A., Tel'tsov, M. V., and Shavrin, P. I. Present Collection, p. 460.
11. Vernov, S. N., Chudakov, A. Ye., Vakulov, P. V., Gorchakov, Ye. V., Kuznetsov, S. N., Logachev, Yu. I., Sosnovets, E. N. Present Collection, p. 394.
12. Bader, M. J. Geophys. Res., 67, No. 13, 5007, 1962.
13. Vernov, S. N., and Chudakov, A. Ye., Uspekhi Fizicheskikh Nauk, 70, No. 4, 585, 1960.
14. O'Brien B. J., Van Allen, J. A., Laughlin, C. D., Frank, L. A., J. Geophys. Res., 67, No. 1, 397, 1962.

## INTERPLANETARY PLASMA (SOLAR WIND)

(Summary)

K. I. Gringauz

1. In 1958-1959, there were two models of the interplanetary plasma: A statistical model - Chapman (Ref. 1), and a dynamic model - Parker (Ref. 2). It followed from the Parker theory that:

/334

(a) The plasma in interplanetary space must exist in the form of streams which are constantly moving from the Sun at velocities of:  $\sim 10 \text{ km} \cdot \text{sec}^{-1}$  close to the solar corona at a distance of 1 a.u.  $\sim (5-10) \cdot 10^2 \text{ km} \cdot \text{sec}^{-1}$ ;

(b) The particle motion must be similar to radial motion;

(c) The interplanetary magnetic field, frozen into the plasma, must have a magnitude on the order of unity per  $10^{-5}$  gauss close to the Earth. Its force lines must be in the form of spirals, whose form depends on the particles' velocity.

According to Parker's computations performed in 1958-1959, plasma streams close to the Earth's orbit must be on the order of  $10^{11} \text{ cm}^{-2} \cdot \text{sec}^{-1}$  which corresponds to a concentration of  $\sim 10^3 \text{ cm}^{-3}$  for a stream velocity of  $\sim 10^3 \text{ km} \cdot \text{sec}^{-1}$ , which is the same as that given by the Chapman model.

2. The interplanetary plasma outside of the geomagnetic field was first recorded in experiments with charged particle traps on the second Soviet lunar rocket (1959) (Ref. 3). Subsequent observations were performed on the third lunar rocket (1959) and the interplanetary station "Vener-1" (February, 1961) (Ref. 4, 5). It was found that the magnitude of the streams ranges between  $10^8 \text{ cm}^{-2} \cdot \text{sec}^{-1}$  to  $10^9 \text{ cm}^{-2} \cdot \text{sec}^{-1}$ , and a relationship was found between the magnitudes of solar plasma streams and geomagnetic perturbations. The satellite "Explorer-10" (March, 1961) first performed direct measurements of the proton velocities in solar plasma streams (ranging between 400-700  $\text{km} \cdot \text{sec}^{-1}$ ) (Ref. 6).

/335

3. All of the experiments based on direct observations of the interplanetary plasma before 1962 were fragmentary in nature, and their observational periods lasted a comparatively short period of time. Therefore, it was not possible to confirm the fact that the solar plasma streams recorded always existed - i.e., they pertained to the "solar wind" of Parker. It was only the almost continuous, four-month observations of the solar plasma streams on the American interplanetary station "Mariner-2" (1962) which finally pointed to the definite conclusion that solar plasma streams always exist and that their velocity is close to that postulated by Parker's theory (Ref. 7).

4. An analysis of the Doppler frequencies in the spectrum of signals reflected during solar radio location, performed at Harvard Radioastromical Observatory (USA), showed that the solar corona expands at a rate of approximately  $15 \text{ km} \cdot \text{sec}^{-1}$  close to the Sun (Ref. 8). This fact, along with direct measurements of the velocity of solar plasma streams close to the Earth's orbit, substantiates the validity of the assumption that the solar corona expands at a rate which increases as the distance from the corona increases.

5. Magnetic measurements in interplanetary space have confirmed the solar origin of interplanetary magnetic fields, as well as their spiral-like structure postulated by Parker's theory. As was indicated by this theory, the magnitude of the interplanetary magnetic field was found to be  $10^{-5}$  gauss (Ref. 9, 10).

6. In addition to "Luna-2", "Luna-3", and "Vener-1", the solar plasma streams were also observed on the Soviet interplanetary stations "Mars-1" (1962) and "Zond-2" (1964). Both the ion stream magnitudes and their energy spectra were measured. All of the measurement data on these Soviet space vehicles point to a correlation between the magnitudes of the solar wind streams and the  $K_p$ -indices characterizing the intensity of geomagnetic perturbations (Ref. 11). This conclusion differs from the conclusion reached by the authors performing observations on "Mariner-2"; in their opinion there is a good correlation between the velocities of solar wind streams and the  $K_p$ -indices, but there is no such correlation between the magnitudes of the streams and the  $K_p$ -indices (Ref. 7). It can be assumed that this is related to the difference in the observational method (measurements were performed on charged particle traps on Soviet space vehicles, while an electrostatic analyzer was employed on "Mariner-2"). Based on observational data from the satellite "IMP-1" (Ref. 12) and from the station "Zond-2" (Ref. 11), the fluxes of solar wind ions can change between  $2 \cdot 10^7 \text{ cm}^{-2} \cdot \text{sec}^{-1}$  to  $10^9 \text{ cm}^{-2} \cdot \text{sec}^{-1}$ .

7. The existing experimental data pertaining to the plasma and to the magnetic field in interplanetary space indicate that Parker's theory correctly describes the main features of the phenomena observed, although individual details of this theory must be reexamined.

8. The solar wind represents a factor which determines all of the basic processes in the interplanetary medium and many of the most important geophysical phenomena. Thus, the structure of the interplanetary magnetic field depends on the solar plasma streams (and, consequently, the trajectory of cosmic rays). These streams determine the form of the magnetosphere and apparently control geomagnetic and ionosphere storms. Solar wind also plays an important role in the physics of the planets - laboratory experiments irradiating different metals and rocks with proton streams provide a basis for assuming that many special physical properties of the lunar surface are caused by the direct influence of the solar wind upon it (Ref. 12, 13).

Therefore, future experiments studying the solar wind represent one of the most important problems of physical investigations in space.

#### REFERENCES

1. Chapman, S. J. Atmos. Terr. Phys., 15, 43, 1959.
2. Parker, E. H. Astrophys. J., 128, 664, 1958.
3. Gringauz, K. I., Bezrukikh, V. V., Ozerov, V. D., Rybchinskiy, R. Ye. Doklady AN SSSR, 131,6,1301,1960.
4. Gringauz, K. I. Space Res., 2, 539, 1961.
5. Gringauz, K. I., Bezrukikh, V. V., Balandina, S. M., Ozerov, V. D. Rybchinskiy, R. Ye. In "Iskusstvennyye Sputniki Zemli". Izdatel'stvo AN SSSR, No. 15, p. 98, 1963.
6. Bridge, H. S., Lazarus, A. J., Lyon, E. F., Rossi, B., Sherb, F. Space Res., 4, 1133, 1963.
7. Snyder, C. W., Neugebauer, M. Space Res., 4, 89, 1964.
8. Maxwell, A., Defouw, R. J., Commings, P. Planet. Space Sci., 12, No. 5, 435, 1964.
9. Ness, N. F., Searce, C. S., Seek, J. B. J. Geophys. Res., 69, 3531, 1964.
10. Ness, N. F., Wilcox, J. M. Phys. Rev. Letters, 13, 461, 1964.
11. Bezrukikh, V. V., Gringauz, K. I., Rybchinskiy, R. Ye., Musatov, L. S., Khokhlov, M. Z. Doklady AN SSSR, 163, 4, 1965.
12. Wehner, G. K., Kenknight, C. F., Rosenberg, D. Planet. Space Sci., 11, No. 11, 1257, 1963.
13. Rosenberg, D., Wehner, G. K. J. Geophys. Res., 69, 15, 3307, 1964.

COMPARISON OF SIMULTANEOUS MEASUREMENTS OF THE MAGNETIC FIELD AND  
POSITIVE ION STREAMS WITHIN THE EARTH'S MAGNETOSPHERE, PERFORMED  
ON THE SATELLITE "ELEKTRON-2"

K. I. Gringauz, Sh. Sh. Dolginov, V. V. Bezrukikh,  
Ye. G. Yeroshenko, L. N. Zhuzgov, L. S. Musatov,  
E. K. Solomatina, U. V. Fastovskiy

The satellite "Elektron-2" was launched into orbit on January 30, 1964, with an apogee  $11.6 R_e$  (from the center of the Earth) at a  $61^\circ$  angle to the plane of the equator. Figure 1 shows the position of the satellite's orbit in an ecliptical coordinate system, in three projections and for three flight periods (see page 465 I - January 31-February 1, 1964; II - March 28-29, 1964; III - May 5, 6, 1964). The X-axis is directed toward the Sun; the Z-axis is directed toward the north pole of the ecliptic. /336

The scientific equipment carried on the satellite "Elektron-2" included a charged particle trap and magnetometers, along with other instruments.

The three-electrode trap was similar to charged particle traps carried on the Soviet space rockets since 1959 (Ref. 1); the potential of its outer grid equalled the potential of the satellite frame. In this way the trap could record positive ions having energies exceeding the satellite potential with respect to the surrounding medium, which produced a positive current in the trap collector circuit. The trap could also record streams of electrons having energies greater than 100 eV (higher than the inner grid potential), which produced negative currents in the same circuit. In addition, the trap recorded photoelectrons from the inner grid also in the form of negative currents in the collector circuit. Thus, if the total current in the collector circuit was positive, this corresponded to the recording of positive ion streams.

The magnetometer, whose readings are employed in this report, was a three-component device with orthogonal ferroprobe recorders with a measurement range of  $\pm 120\gamma$  ( $1\gamma = 10^{-5}$  oe) for each component. The magnetometer sensitivity threshold for each component was  $2\gamma$ . Due to the rotation of the container, it was possible to control and to determine the correction for absolute zero of the field within an accuracy of  $3\gamma$ . The constant sensitivity of the apparatus was checked every hour by calibration of the magnetometer channels during the flight (Ref. 2). The present report presents the results derived from comparing data from several measurements performed with the charged particle trap and the magnetometer on "Elektron-2", as well as the  $K_p$ -indices characterizing the geomagnetic field perturbation based on data from simultaneous measurements performed at magnetic observatories on the Earth. This comparison indicates that there is a correlation between changes in the magnetic activity on the Earth's surface and changes in the geomagnetic /338

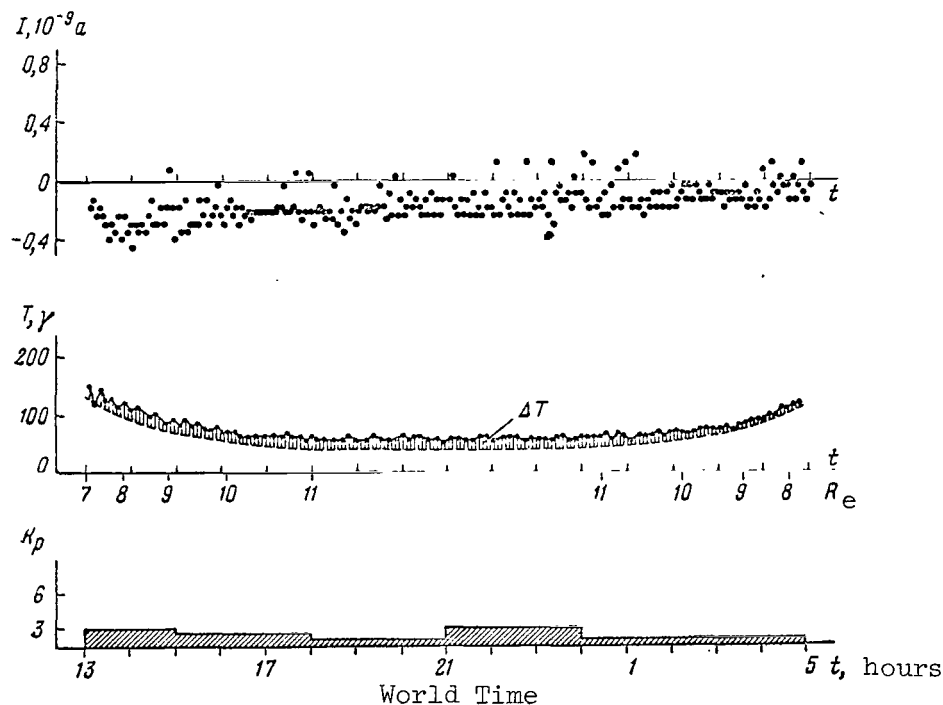


Figure 1

field strength and positive ion streams at great distances from the Earth, within its magnetosphere, during the initial flight period of the satellite. This comparison also indicates that there is no correlation beyond this point, up to the end of the flight.

The nature of the correlation is illustrated by data obtained during magnetically quiet days (January 30, 31, 1964; Figure 1), during magnetically perturbed days (January 31-February 1, 1964; Figure 2), and during the period when the magnetically quiet state changed into a magnetically perturbed state (February 11-12, 1964; Figure 3) at distances of 6-11.6  $R_e$  as the satellite approaches and recedes from the Earth. The geographic latitudes corresponding to the projections of these orbital sections on the Earth range between  $24^\circ\text{S}$  to  $60^\circ\text{S}$ . The range in which the longitude changes in these orbital sections is  $\sim 160^\circ$ . The following conclusions can be drawn from examining the results shown in Figures 1-3.

1. During the magnetically quiet days of January 30-31, 1964 ( $K_p < 3$ ) primarily negative currents were recorded (with a very small number of positive values), corresponding to small magnitudes of the positive ion streams. The magnetometer thus recorded a field which was fairly regular in terms of magnitude and which exceeded the theoretical value by  $\Delta T \sim 20\gamma$ . This field changed very little over the entire orbital section /339 under examination. In the region of the apogee,  $\Delta T$  was about 40% of the calculated field determined as the eccentric dipole field. The regular nature of the magnetograms indicates that the "Elektron-2" orbit was entirely within the magnetosphere.

2. Only positive currents were recorded in the trap collector circuit, amounting to  $4 \cdot 10^{-10} \text{a}$ , during a magnetically perturbed day ( $3 \leq K_p \leq 5$ ) on the orbital section under consideration. These currents could be caused

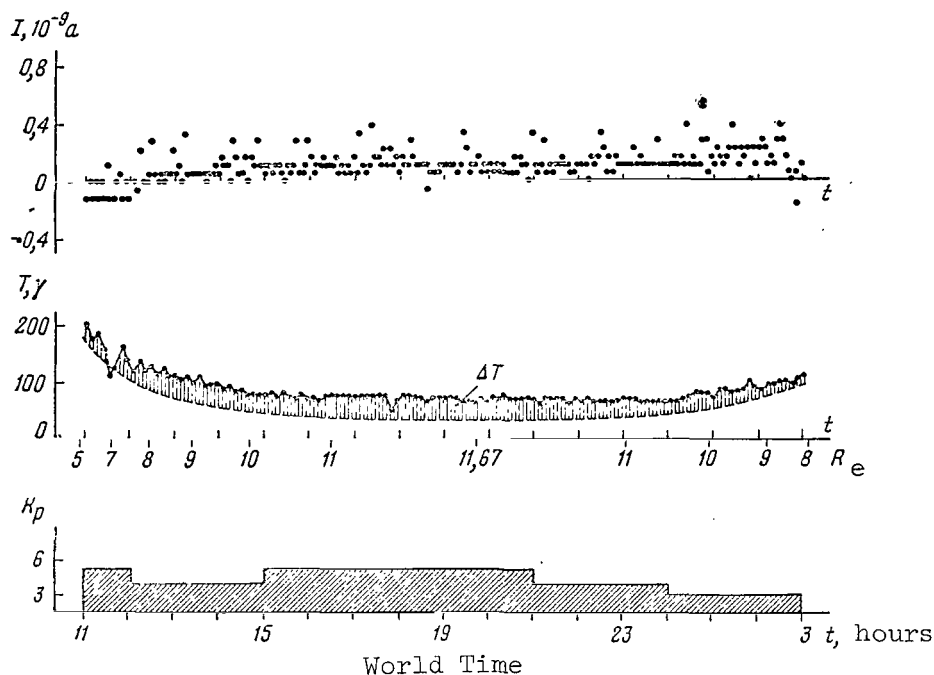


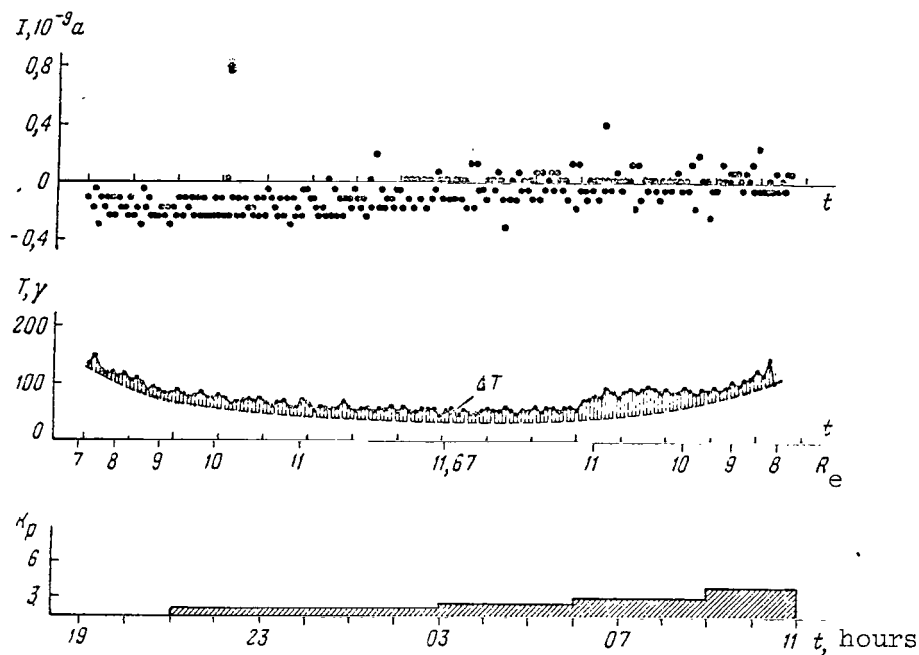
Figure 2

by ion fluxes exceeding  $2 \cdot 10^8 \text{ cm}^{-2} \cdot \text{sec}^{-1}$  (which corresponds in order of magnitude to solar plasma fluxes outside of the magnetosphere [Ref. 3-5]).

The magnetometer recorded a field with  $\Delta T \sim 40 \gamma$ , which is 100% of the calculated field in the apogee region. The significant field fluctuations thus discovered coincide with variations of the geomagnetic field on the Earth during the same period.

The beginning of February 12, 1964, was characterized by low magnetic activity ( $K_p < 3$ ). At 6 hours 5 minutes, all of the observatories on the Earth noted a perturbation with a sudden commencement. The magnetic activity index rose up to 3, and equalled 4 at 9 hours. At 6 hours the satellite reached apogee. The magnetometer, which recorded a value of  $\Delta T$  which was characteristic for quiet days at the beginning of the day, indicated a fairly rapid field increase at about 6 hours. After this time,  $\Delta T$  reached values which are characteristic for a perturbed day.

Up to 3 hours, the trap collector currents were primarily negative, which is characteristic for a magnetically quiet period. From approximately 3 hours on, the amount of positive currents recorded began to increase, which indicates an increase in the positive ion streams. In the period between 9 hours and 11 hours, when  $K_p = 4$ , primarily positive currents were recorded, corresponding to ion fluxes on the order of  $10^8 \text{ cm}^{-2} \cdot \text{sec}^{-1}$ , which is characteristic for a magnetically perturbed period.



World Time  
Figure 3

It should be noted that on February 12, 1964, the increase in positive ion streams anticipated a magnetic field increase by approximately 3 hours. The magnetic field increase close to the satellite and on the Earth began simultaneously in the first approximation - in any event, with very small intervals - and took place at a much faster rate than that at which the trap changed from recording negative collector currents to recording positive currents.

Several observations performed previously by means of magnetometers on space rockets and satellites (Ref. 6-8 and others) established a correlation between the magnetic field variability in cosmic space and the magnetic activity indices on the surface of the Earth, as well as a similarity between the form of the field changes in cosmic space and on Earth in a great many cases. In experiments based on direct measurements of solar plasma streams outside of the geomagnetic field, a correlation was found between the intensity and velocity of particles in these streams and geomagnetic perturbations on the Earth (Ref. 3, 5).

Positive ion streams in the outer magnetosphere regions were observed on the American satellite "Explorer-12", which was launched on August, 1961, on an orbit which was inclined by  $33^\circ$  to the equator, with an apogee of  $\sim 13 R_e$  toward the Sun (Ref. 9-11). The electrostatic analyzer on this satellite did not record streams of protons with energies of  $< 20$  kev, exceeding the equipment sensitivity threshold ( $6 \cdot 10^6 \text{ cm}^{-2} \cdot \text{sec}^{-1}$ ). The scintillation counter recorded streams of protons with energies of



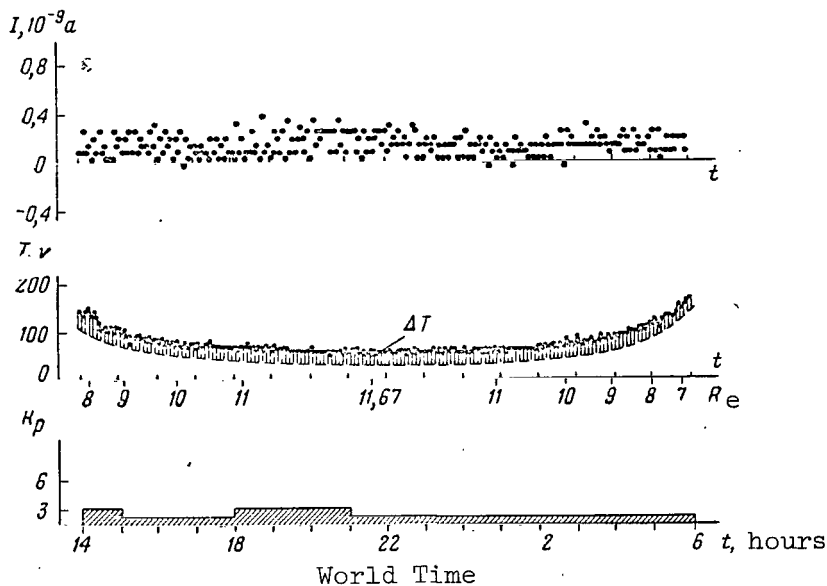


Figure 4

0.1 Mev and 4.5 Mev (representing the proton component of the outer radiation zone). The maximum intensity of these fluxes was  $6.7 \cdot 10^6 \text{ cm}^{-2} \cdot \text{sec}^{-1} \cdot \text{sterad}^{-1}$  and was located at a geocentric distance of  $\sim 3.5 R_e$ . The zone boundary was located at distances of up to  $11 R_e$ . During a magnetic storm, the maximum intensity of these streams increased by approximately a factor of three (Ref. 11). During a magnetic storm on September 30, 1961, this apparatus observed omnidirectional proton streams outside of the Earth's magnetosphere (close to the satellite apogee), with the largest intensity of  $2 \cdot 10^5 \text{ cm}^{-2} \cdot \text{sec}^{-1} \cdot \text{sterad}^{-1}$ .

However, on certain days during the initial flight period of the satellite there was no correlation between positive ion streams, on the one hand, and the values of  $\Delta T$  and  $K_p$ , which we discussed above. Figure 4 shows measurements performed on February 15-16, 1964, from which it can be seen that increased streams of positive ions occurred at low values of  $\Delta T$  and at low values of  $K_p$ .

Figure 5 presents the mean (during the observational period) values of the trap collector currents at distances between  $6 R_e$  and  $11.6 R_e$ , the mean values of  $\Delta T$  according to the magnetometer, and the  $K_p$ -indices in February, 1964. As can be seen, the correlation indicated above was observed on almost every day during this period, and only in two cases was there no correlation (February 3, 1964 and February 15-16, 1964).

Similar comparisons for the majority of revolutions in March, April, and May, 1964, revealed no correlation in the sense of Figure 1 - namely, during magnetically quiet days the trap collector currents had large positive readings, while the values of the  $K_p$ -indices and of  $\Delta T$  were small

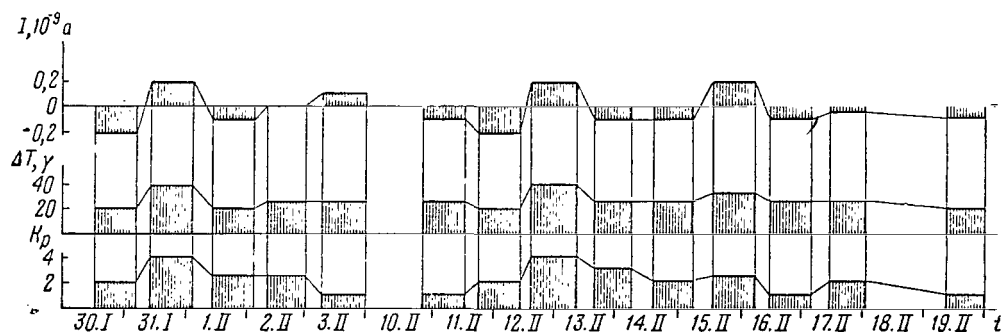


Figure 5

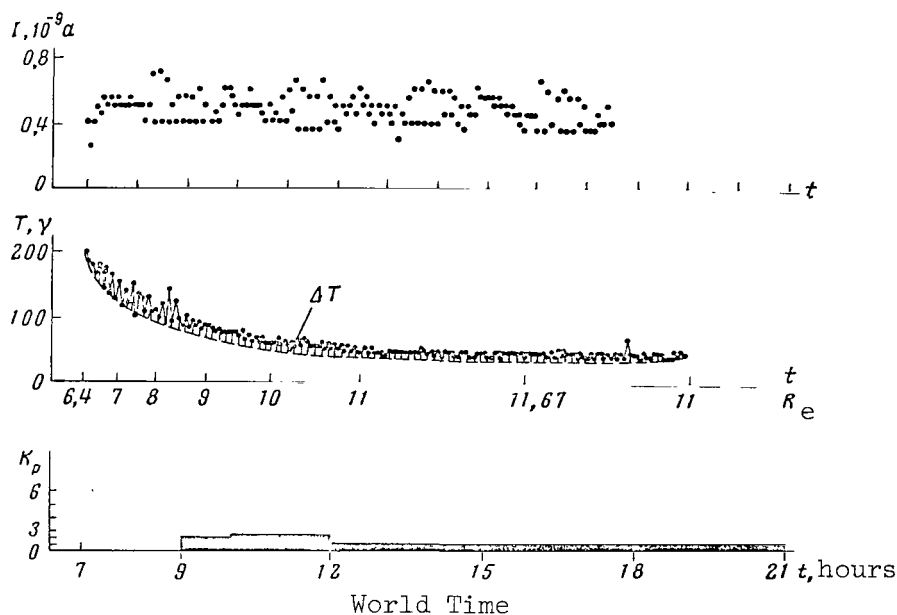


Figure 6

(see, for example, Figure 6 for April 24, 1964). These large positive readings of the collector currents were observed up to the end of the flight of "Elektron-2". In principle, we cannot exclude the possibility that the lack of correlation was caused by abnormal operation of the equipment over a period of time. Another possibility is a change in the physical conditions in the surrounding medium related to the "Elektron-2" orbit changing to the nocturnal side (Figure 1 on page 466), and also related to the change in the position of the neutral points of the magnetosphere region below the Sun, with respect to the Earth-Sun line. On the other hand, there is no basis for assuming that the positive correlations discovered in February are random. They could be related to important elements in the magnetic perturbation mechanism.

In contrast to the observations indicated above on "Explorer-12", the observation of positive ion streams in February, 1964, which are

described in this report, pertain to the region lying beyond the outer radiation zone, but within the magnetosphere, although the distance between the satellite and the Earth is approximately the same in both cases. (This is related to the different inclination to the equator of both satellite orbits).

It is still not clear whether the streams observed by charged particle traps on the satellite "Elektron-2" are caused by the solar wind penetrating to the depths of the magnetosphere, or whether they are formed from particles of the circumterrestrial plasma which are accelerated by a mechanism which no one has studied as yet.

#### REFERENCES

1. Gringauz, K. I., Bezrukikh, V. V. et al. Doklady AN SSSR, 131, 1301, 1960.
2. Dolginov, Sh. Sh., Yeroshenko, Ye. G., Zhuzgov, L. N., Pushkov, N. V. In "Iskusstvennyye Sputniki Zemli". Izdatel'stvo AN SSSR, No. 5, 1960.
3. Gringauz, K. I. Space Res., 2, 539, 1961.
4. Gringauz, K. I., Bezrukikh, V. V. et al. Space Res., 3, 1962.
5. Bonetti, A., Bridge, H. S. et al. Space Res., 3, 1962.
6. Neugebauer, M., Snyder, C. W. Space Res., 4, 1963.
7. Antsilevich, M. G., Shevnin, A. D. Doklady AN SSSR, 135, 298, 1960.
8. Greenstadt, C. W. Nature, 191, 329, 1961.
9. Davis, L. R., Williamson, J. M. Space Res., 3, 1963.
10. Bader, M. J. Geophys. Res., 67, No. 13, 5007, 1962.
11. Hoffman, A., Davis, L., Williamson, J. M. J. Geophys. Res., 67, No. 13, 5001, 1962.

INVESTIGATION OF THE EARTH'S MAGNETOSPHERE IN THE RADIATION ZONE REGION  
(3-6 $R_e$ ), FEBRUARY-APRIL, 1964

Sh. Sh. Dolginov, Ye. G. Yeroshenko, L. N. Zhuzgov

Direct measurements of the geomagnetic field strength made during the first space rocket flights in the Earth's outer magnetosphere and its boundary region (Ref. 1-5) gave the first information on external sources of the magnetic field in the region in space where their action is comparatively great and comprises a perceptible portion of the magnetic field strength at these distances determined by sources within the Earth. These first direct experiments on measuring geomagnetic field strength and radiation make it possible to distinguish the magnetically most active regions at a distance of 10-15  $R_e$ , where the geomagnetic field makes direct contact with geoeffective corpuscular solar radiation, and of 3-5  $R_e$ , where processes take place which are responsible for the development of successive stages of magnetic storms. /342

Studies made by the satellites "Explorer-10", "Explorer-12", and "Explorer-18" (Ref. 5-7) disclosed experimental findings favoring the assumptions that the magnetosphere has an abrupt boundary or "magnetopause", a transitional region, and a shock front boundary.

Experimental findings from the flights of space rockets (Ref. 8-10) and long-lived satellites (Ref. 11-15) made it possible to define more accurately the composition and morphological features of the external radiation zone on magnetically-quiet and magnetically perturbed days. Information obtained on the external zone distribution of protons having comparatively small energies of 150 keV to 4.5 MeV (Ref. 16-17) was of extreme importance.

The space of the radiation zone, especially the region of the maximum, was explored to a lesser degree. Our information on the magnetic field at distances of 3-5  $R_e$  had been practically limited to the first probe measurements (Ref. 1, 2, 5). The experiments conducted had, in particular, furnished no systematic or definite information on the magnetic effects of the proton and electron components of trapped radiation on quiet days, or on the existence and location of the extra-ionospheric current ring of magnetic storms (Ref. 18-19). The experimental findings on the topology and morphology of the magnetosphere boundary region at mean latitudes were likewise inadequate. The investigation of these problems comprised a considerable portion of the scientific program of the magnetic and radiation studies on the "Elektron" satellites.

## 1. Orbit and Metrological Features of the Equipment

The satellite "Elektron-2" was lofted into orbit on January 30, 1964. The orbital inclination to the Earth's equatorial plane was  $61^{\circ}$ . Its apogee was  $11.67 R_e$  ( $R_e$  designates the Earth's radius). The satellite's initial period of revolution was 22 hr, during which information on the magnetic field in the range from 3 to  $11.6 R_e$  arrived for almost 20 hr. Figure 1 presents the orbital position and change during the active operation of "Elektron-2". In the initial period, the satellite reached apogee on the morning side of the Earth, moving in an ascending revolution from the nocturnal to the morning side and approaching the Earth on the morning-diurnal side. Orbital apogee subsequently shifted to the nocturnal side. The forward revolutions began on the evening side of Earth and the reverse revolutions ended on the morning side. In the next operational period of the satellite the orbit's apogee was displaced to the nocturnal /343 side. The forward revolutions began on the evening side, while the reverse revolutions ended on the nocturnal-morning side.

During the satellite's flight from January 30, 1964 to May 5-6, 1964, information was obtained on 40 revolutions in space from 3 to  $11.6 R_e$ . The measurements were made by two three-component magnetometers with a measurement range of  $\pm 1200 \gamma$  and  $\pm 120 \gamma$  for each component (Ref. 15).

The sensitivity threshold of these magnetometers under real measurement conditions may be taken to be 10 and  $2 \gamma$ , respectively. The channels of each three-element magnetometer were interrogated practically simultaneously by the memory unit commutators of the radiotelemetry system. Most of the time the magnetometers were interrogated once per two minutes; one other measurement regime consisted of one measurement per eight minutes.

The time-stability of the equipment was checked under laboratory conditions, and the temperature coefficients and corrections to absolute zero were determined for every magnetometer channel. The instruments were calibrated every hour during flight.

The initial data received directly from the satellite were the values of the field components from the readings of both magnetometers.

The present article analyzes only the scalar field values  $T$  calculated from the three magnetometer channels. We must dwell in somewhat more detail on magnetogram accuracy. The error of a single magnetometer reading may, after the telemetry data are decoded, reach a value of  $\Delta T = \Delta X \cos \alpha + \Delta Y \cos \beta + \Delta Z \cos \gamma$ , where  $\alpha, \beta, \gamma$  are the angles between the magnetometer axis and the total field vector. Under unfavorable conditions this error may, depending on magnetometer sensitivity, reach  $3.5 \gamma$ . For the second instrument with a ten times wider range, it may reach-35 .

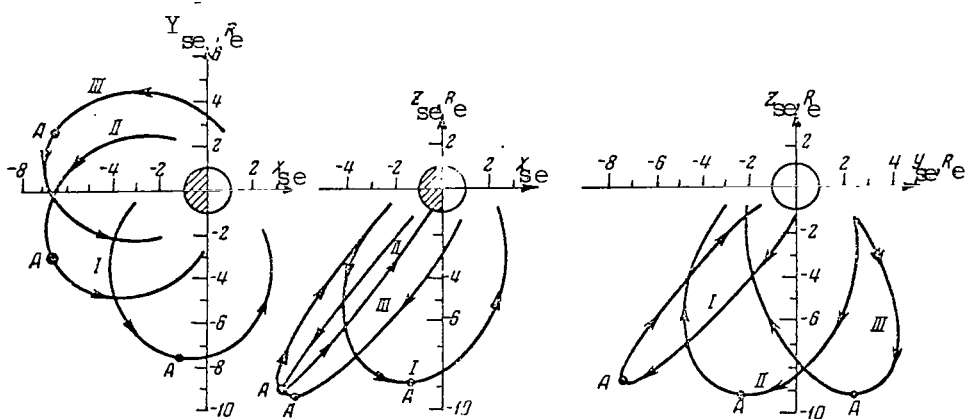


Figure 1

### Change in Orbit of Satellite "Elektron-2"

When estimating average field level, we may use a group of readings as a function of the coordinates, and average them graphically. This permits us to eliminate random telemetry errors with an accuracy depending on the number of points in the averaging period. Then the difference between the  $T_{\text{change}}$  graph and the true graph of the modulus of vector  $T$  will be specified by the systematic error in measuring corrections to absolute zero ( $X_0, Y_0, Z_0$ ). The stability of the magnetometer zero may be monitored by modulation effects (Ref. 2) with a sensitivity of  $\sim 2 \gamma$  in the modulus of  $T$  for a sensitive instrument, and of  $\sim 20 \gamma$  for a coarse instrument. Stability control of the coarse magnetometer zero was also made by comparison with readings of the sensitive magnetometer in a region of space where not one of the instruments was off-scale. The absolute systematic error of the  $T$  magnetogram modulus in the operating /344 sections of the sensitive magnetometer does not exceed  $2 \gamma$ , and of the course magnetometer -  $20 \gamma$ .

### 2. Nature of the Magnetometric Information

The solid curve in Figure 2 represents a typical magnetogram from measurements at a distance of  $3-11 R_e$ . The broken curve represents the computed geomagnetic field values with allowance for six harmonics of the Gaussian series\*. In the trajectory sections from  $3$  to  $7 R_e$ , the magnetograms were plotted from the coarser magnetometer readings, and in trajectory sections from  $7-11.6 R_e$  - from the sensitive manometer readings.

The difference between the sum of the six harmonics and an eccentric dipole at distances of  $\sim 3 R_e$  does not exceed  $8 \gamma$ . At greater distances,

\* The computations were made according to a field synthesis program compiled by T. L. Vinnikova from coefficients extrapolated for the period of 1964 by N. P. Ben'kova and L. O. Tyurmina.

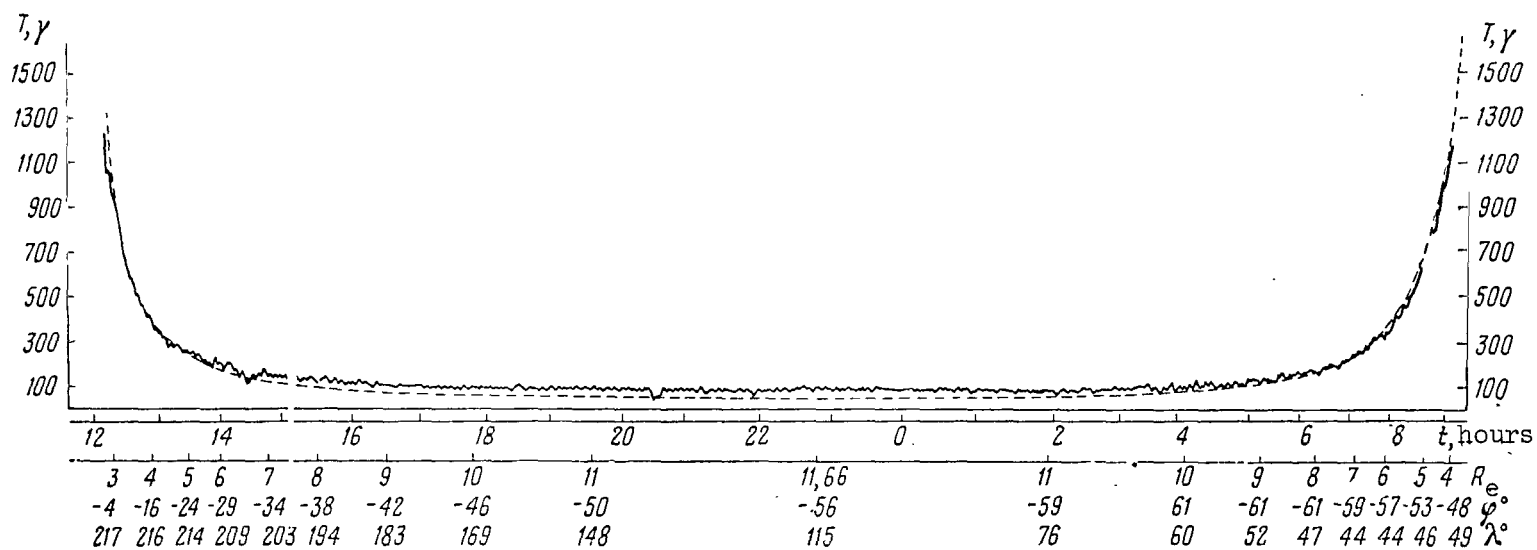


Figure 2

Typical Magnetograms of Observed (Solid Curve) and Calculated Values (Broken Curve) of Scalar Magnetic Field Strength Along the Trajectory of "Elektron-2". Moscow time, Geocentric Distance  $r$  in Earth Radii, and Geographic Latitude and Longitude are Plotted Along the Horizontal Axis.

this discrepancy is negligibly small. The  $\Delta T$  curves are analyzed and compared below. Along the trajectory the  $\Delta T$  have certain features in common which are maintained on magnetically-quiet and magnetically-perturbed days: Their measured values on the forward revolutions are less than the calculated ones at distances from 3 to 5  $R_E$ . When the Earth was approached on the reverse revolutions, the measured values became less than the calculated at distances of  $\sim 7 R_E$  in the initial operational period of "Elektron-2". At  $\sim 6 R_E$  in all subsequent revolutions this sign was maintained right down to distances of  $\sim 3 R_E$ . In the remaining space, the  $\Delta T$  values were positive, i.e., the measured values were greater than the calculated field values.

Beyond the above-listed possible errors in experimental and computed magnetograms, it is natural to link the obtained  $\Delta T$  values with the effect of the magnetic field's external sources. Bearing the fact in mind that the experimental findings were made at great distances from the Earth's surface, we believe it is reasonable to limit the possible external magnetic field sources to: (1) currents in the geomagnetic field boundary region about which a stream of ionized solar plasma flows, (2) currents in the external radiation zone, and (3) interplanetary fields and corpuscular stream fields.

Without any previous model to explain the most probable contribution of each above-listed source to the  $\Delta T$  values obtained, in order to distinguish between the field sources, it is reasonable to compare the absolute values of  $\Delta T$  at various distances and the degree of variability in  $\Delta T$  at various distances when magnetic activity changes.

Figure 3 gives the average three-hour positive values of  $\Delta T$  on successive revolutions (top curve) and the  $K_p$  indices of magnetic activity (bottom curve).

The variations in the positive  $\Delta T$  at distances of 7-11.6  $R_E$  during moderate magnetic disturbances amount to 200% of field magnitude at these distances. The correlation between variations in positive  $\Delta T$  values and  $K_p$  indices is sufficiently clear.

The negative  $\Delta T$  observed at distances of 3-6  $R_E$  amount at the most to 10% of the dipole field strength at these distances; in absolute magnitude, this is three to four times more than the scalar  $\Delta T$  values at great distances.

To clarify the degree of correlation between the variations in negative values of  $\Delta T$  and the  $K_p$  indices at short distances, where the field changes rapidly with change in distance, the areas were estimated which were delimited by the curves of negative  $\Delta T$  values and of the  $\Delta T = 0$  lines in the successive phases of forward and reverse revolutions (Figure 4). These areas are proportional to the "negative magnetic fluxes". It was found that these fluxes on the forward revolutions (low-latitude trajectory phases) are loosely correlated with variations in the index of



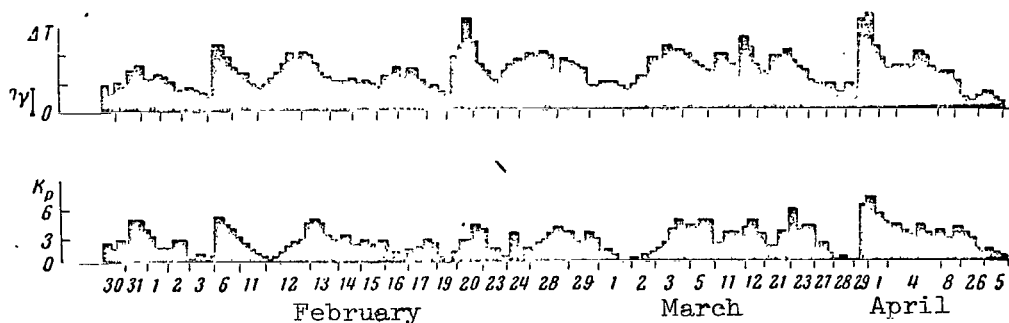


Figure 3

Comparison of Variability of Three-Hour  $\Delta T$  Value Between Measured and Computed Values (Top Curve) and of  $K_p$  Index of Magnetic Activity for February-April, 1964

magnetic activity. On the reverse revolutions (high-latitude trajectory phases) they vary noticeably as magnetic activity varies. The variability of the "negative magnetic streams", however, is percentagewise substantially less than the variability at distances of 7-11.6  $R_e$ .

A comparison of the sign of the absolute values of negative  $\Delta T$  at distances of 3-6  $R_e$ , and of positive  $\Delta T$  at 6-11.6  $R_e$ , and a comparison of their degree of variability with the change in activity permits the assumption that they are due to different sources. However, there is no doubt that these different sources make a definite contribution both to the negative and the positive values of  $\Delta T$  which were observed. This study will only examine observations at distances of 3-6  $R_e$ , where the  $\Delta T$  differences are negative.

### 3. $\Delta T$ Values at Distances of 3-6 $R_e$

(a) Figure 4 gives the  $\Delta T$  values observed in 38 successive revolutions. They are arranged in three columns, in each of which the  $\Delta T$  values on the forward revolutions are plotted on the left, and the values on the reverse revolutions are plotted on the right. The date and number of the revolution are designated by figures; the indicator at the left gives the scale on the  $\Delta T$  axis in gammas.

It should first be noted that during the "Elektron-2" measurements (February-May, 1964) there was no opportunity to observe positive values of  $\Delta T$  at these distances, where in all cases the measured values were less than the computed values at these distances.

The largest  $\Delta T$  values on ordinary days were detected at distances of  $\sim 3 R_e$ . They amount to  $\sim 100$ -150  $\gamma$ . The  $\Delta T$  pattern at distances nearer to the Earth - which is extremely important in understanding the nature

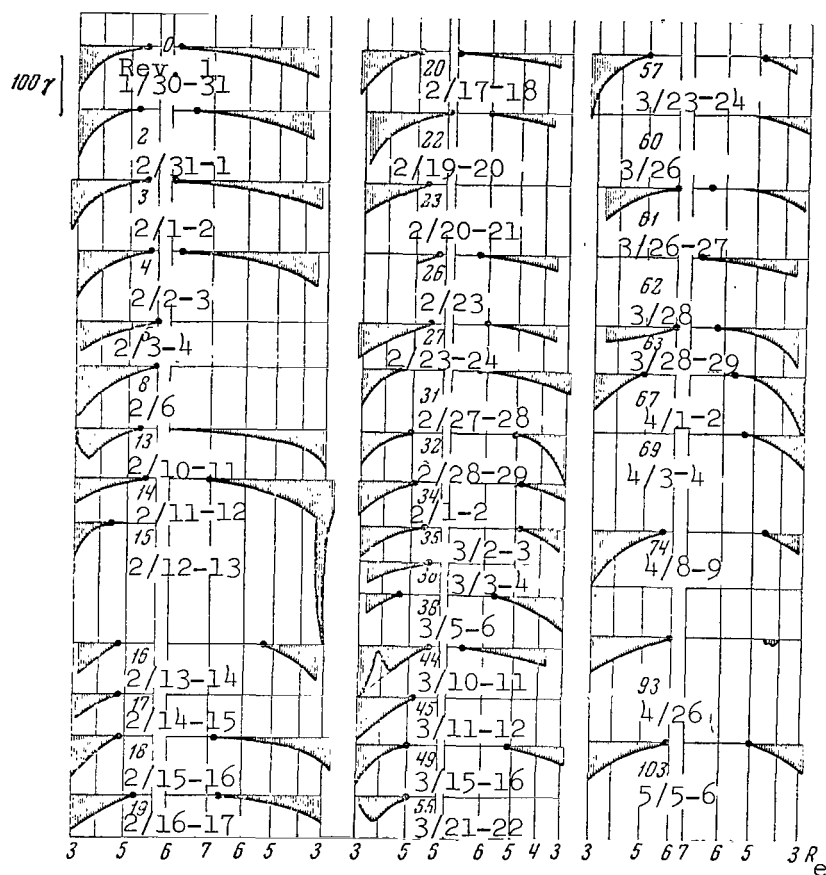


Figure 4

Difference of  $\Delta T$  Between Measured and  
Computed Field Values at Distances of 3-6  $R_e$

of the effect - has not been studied, as in this region the field is above the instrument measurement range. Only in a few instances were diminishing  $\Delta T$  readings discovered at distances of 3-4  $R_e$ , which indicates that the  $\Delta T$  curves have extremal values.

In the initial flight period of "Elektron-2" a certain asymmetry was seen in the  $\Delta T$  curves on the forward and reverse revolutions; the  $\Delta T$  curves on the reverse revolutions are flatter. Later on no such asymmetry in the curve pattern was consistently detected. /347

(b) As the Earth is left behind,  $\Delta T$  becomes smaller and in certain regions  $\Delta T = 0$ . With further withdrawal from the Earth, the value of  $\Delta T$ , as already mentioned, changes sign. When the Earth is approached on the reverse revolutions, there is an area where  $\Delta T = 0$ .

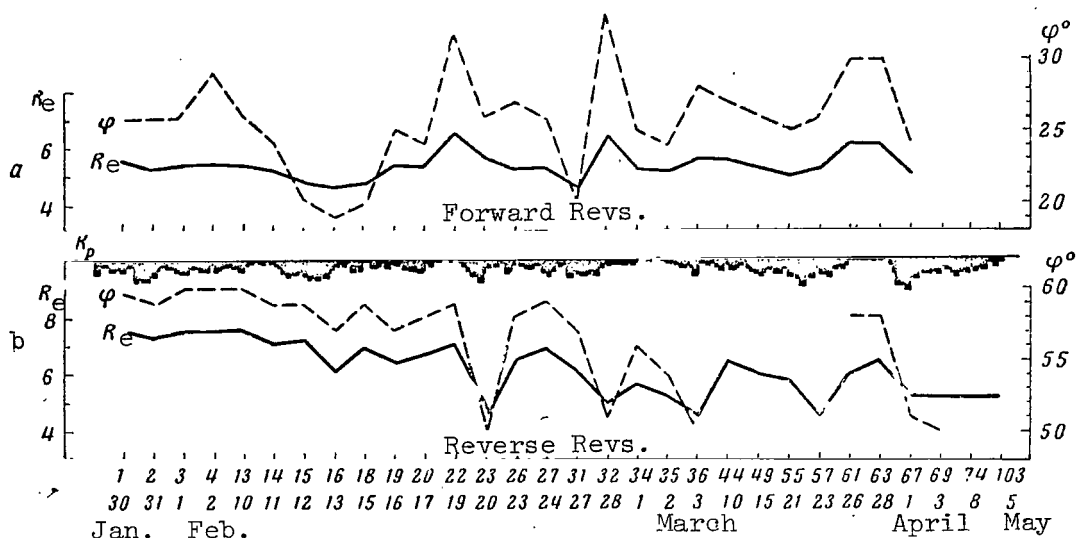


Figure 5

Geocentric Distances  $R_e$  and Geographical Latitudes  
of the  $\varphi$ -Regions where  $\Delta T = 0$

Horizontal axis gives dates and revolution numbers.

The geocentric distances (points joined by solid curve) and the geographic latitudes (broken curves) where  $\Delta T = 0$  are plotted on the vertical curve in Figures 5a,b. The revolution numbers to which the observations refer are plotted on the horizontal axes. The upper curve is that of the forward revolutions, the lower - that of the reverse revolutions. The figure also gives the three-hour  $K_p$  index values and the corresponding observational days. It must be remembered that the observation times at the points where  $\Delta T = 0$  on the forward and reverse revolutions are 16-18 hours apart.

Our attention is first of all attracted by the quite distinct dependence of the  $R_e$  and  $\varphi$  coordinates of the  $\Delta T = 0$  regions on magnetic activity. The value of  $\Delta T$  is observed to equal zero on the forward revolutions, on the average, at distances of  $5 R_e$  and at latitudes of  $26^\circ S$ . This is observed on reverse revolutions on the average at distances of  $6 R_e$  and at latitudes of  $58^\circ S$ . As perturbation in the region  $\Delta T = 0$  increases,  $\Delta T$  is discovered to equal zero at smaller geocentric distances and lower latitudes. As magnetic activity in the region subsides,  $\Delta T = 0$  at greater geocentric distances and higher latitudes.

/348

(c) The regions of  $\Delta T = 0$  on the reverse revolutions display a systematic seasonal drift. The radial distances of the  $\Delta T = 0$  region shifted from  $7.5 R_e$  at the end of January, 1964 to  $5 R_e$  at the end of April, 1964. The latitudes changed from  $\varphi = 59^\circ$  to  $52^\circ S$ .

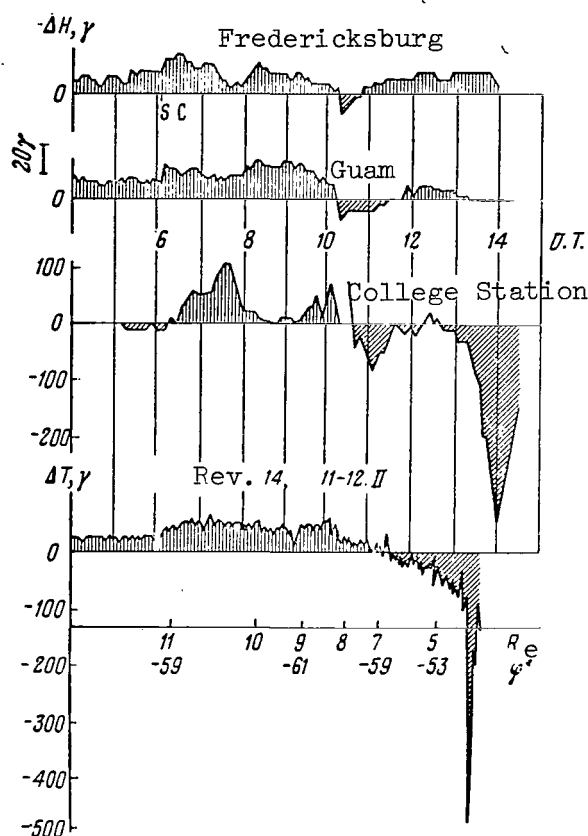


Figure 6

Effect of Magnetic Perturbation at a Distance of  $3-4 R_e$   
 During the Storm of February 11-12, 1964 (Bottom Curve)  
 and on the Surface of the Earth

(d) The regions of negative  $\Delta T$  (from the  $\Delta T$  maximum to  $\Delta T = 0$ ) on the forward and reverse revolutions are approximately 160 longitudinal degrees apart. This indicates the circular nature of the effect.

(e) The above features of  $\Delta T$  distribution at distances of  $3-6 R_e$  are characteristic of each day in the period under investigation. There were no large magnetic storms in this period. At the same time, particularly great discrepancies between the measured and the calculated field values were recorded at  $3-4 R_e$  during three moderate magnetic perturbations. The measured field values proved to be 300-400  $\gamma$  less than the calculated in a sharply delimited space of  $\sim 0.2-0.5 R_e$  at distances of  $\sim 3.5 R_e$ .

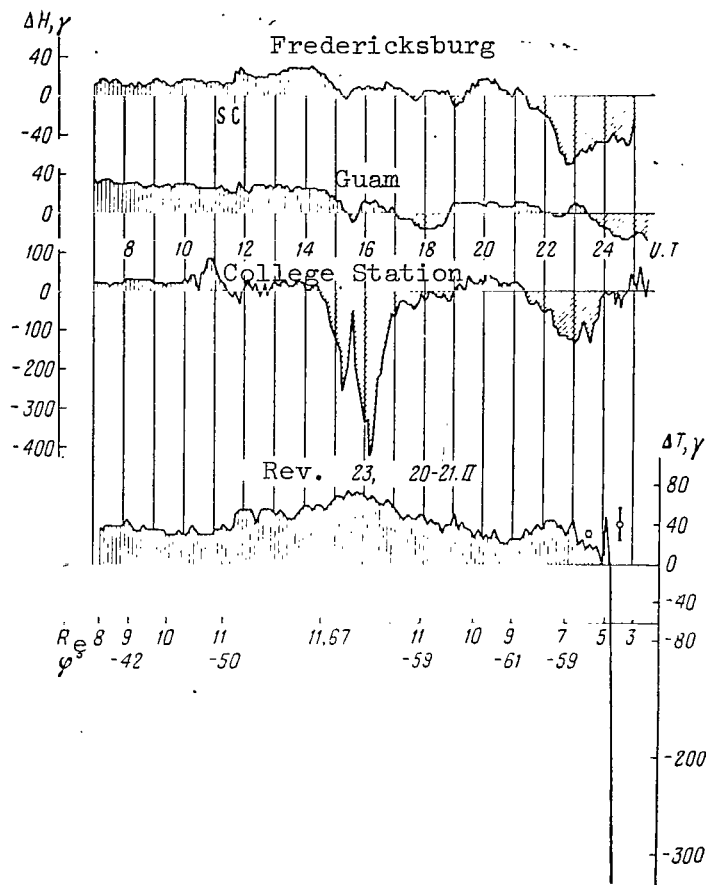


Figure 7

Effect of Magnetic Perturbation at Distance of 3-4  $R_E$  During Storm of February 21, 1964 (Bottom Curve) and on Surface of the Earth

(f) All the above-mentioned cases of severe field depression at 3-4  $R_E$  occurred during magnetic storms, but when compared morphologically with terrestrial data each of these effects had its own characteristic features.

The first of these cases was recorded during the magnetic storm of February 12, 1964 several hours after its sudden commencement, but long before development of the storm's main phase (Figure 6). This event coincided with the start of a polar substorm development at 13 hours 30 minutes UT (College Station data). On-board data indicated that this phenomenon lasted  $\sim 12$  minutes (six readings), and the maximum amplitude was  $\Delta T = -450\gamma$ . However, in this case the substantial field decrease was apparently not of an annular nature, the stability of which would have

lasted at least 2 hours. This ensues from the fact that 2 hours later, when the satellite was at these same distances on the ascending limb of the next revolution ( $\varphi = 4^\circ \text{S}$ ), no similar depression was detected. The main phase of the storm began to develop at low and middle latitudes 15 hours after this event.

/350

Two other cases were recorded while the main phase of the storm was developing. The on-board magnetograms indicated the main phase primarily by the fact that the geocentric distances of the  $\Delta T = 0$  regions decreased to  $4.5 R_e$ , whereas the  $\Delta T = 0$  region on the reverse revolutions is usually observed at  $6-7 R_e$ .

The severe field depression effect during the main phase of the storm of February 20-21 was represented at distances of  $4.3 R_e$  by a single point (because of information breakdown, Figure 7). However, this reading ( $\Delta T = -330 \gamma$ ) may be considered rather reliable, because the three measured field components are reduced in value.

During development of the main phase of the March 4 storm, a significant field reduction ( $\Delta T = -450 \gamma$ ) was noted at  $3.5 R_e$ , and is represented by two readings (Figure 8). This time depression of the field also coincided with development of a polar substorm. It was impossible in the next two cases, however, to determine whether the phenomenon were annular in nature during the main storm at  $3.5 R_e$  (because of lack of information on succeeding revolutions).

#### 4. Magnetic Field of Trapped Radiation

The magnetic field of a radiation zone is connected (Ref. 20-22) with three ordered movements of protons and electrons in the geomagnetic field:

/351

- a) rotation of particles in planes perpendicular to the lines of force,
- b) oscillations along lines of force between specular reflection points,
- c) east-west drift of protons and electrons.

The fact that the particles move around curved lines of magnetic force plays an important role, while the radiation density has maxima in the space of the outer magnetosphere.

The maximum density of protons of  $>0.15$  Mev energy occurs at a distance of  $\sim 3.5 R_e$ , where flux intensity is  $\sim 5 \cdot 10^8$  proton. $\text{cm}^{-2} \cdot \text{sec}^{-1}$  (Ref. 17, 23, 24). In a quiet period, the intensity varies within 30%. The maximum of protons of  $\sim 1.2$  Mev energy is found at  $\sim 3.0 R_e$ , where intensity is  $2.5 \cdot 10^6$  proton. $\text{cm}^{-2} \cdot \text{sec}^{-1}$  (Ref. 25, 26). The energetic protons display their greatest variability in a magnetically perturbed period (Ref. 23). The maximum of the zone of electrons having

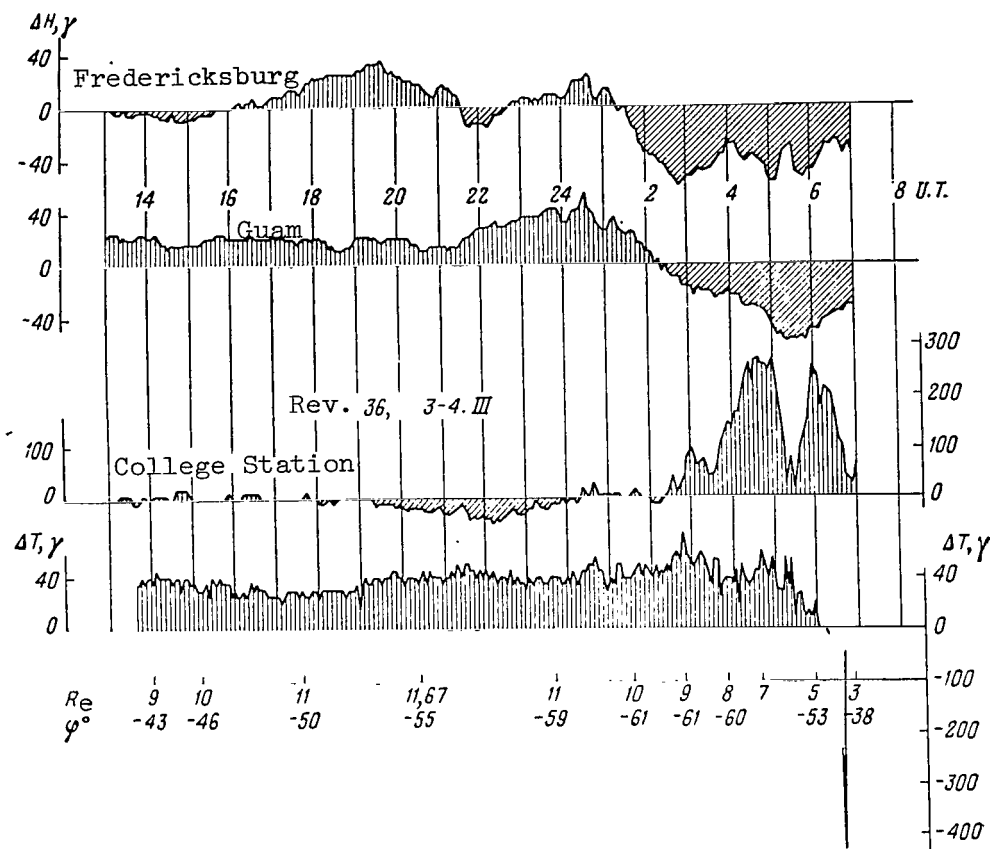


Figure 8

Effect of Magnetic Perturbation at 3-4  $R_e$  During Storm of March 3-4, 1964 (Bottom Curve) and on Surface of the Earth

$\sim 50$ - $100$  keV energies is located at  $4.5$ - $5 R_e$  (Ref. 25). During years of maximum solar activity, it is located at a distance of  $\sim 3.5 R_e$  (Ref. 8). The flux of electrons with energies of  $\sim 50$ - $100$  keV is  $5 \cdot 10^7$  electron  $\cdot \text{cm}^{-2} \cdot \text{sec}^{-1}$ . The flux of energetic electrons ( $1.6$  MeV) is  $3 \cdot 10^5$  electron  $\cdot \text{cm}^{-2} \cdot \text{sec}^{-1}$  (Ref. 25, 26). The efficiency of particles in creating a magnetic field is determined by their number, energy, and pitch-angle distribution.

The magnetic fields of specific models of radiation zones have been calculated in (Ref. 27-29).

Figure 9 gives the  $\Delta T$  values of the magnetic field in the equatorial plane resulting from the action of the external radiation zone protons (Ref. 27). With a maximum particle density of  $0.6$  proton  $\cdot \text{cm}^{-3}$  and average particle energy of  $500$  keV, the value of  $\Delta T$  on the Earth's surface is  $-38 \gamma$ . At a distance of  $4 R_e$  it is  $-72 \gamma$ , which is approximately 15% of the dipole field at this distance. Beyond  $7 R_e$ , the proton zone increases the Earth's field by  $+20 \gamma$ .

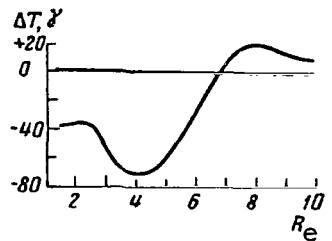


Figure 9

### Computed Values of Magnetic Effect of a Quiet Protonosphere (Ref. 27)

In an evaluation of the quiet protonosphere magnetic field (Ref. 28), the following values were assumed: particle density -  $\sim 0.46 \text{ proton} \cdot \text{cm}^{-3}$ , and average proton energy -  $\sim 300 \text{ kev}$ . In comparison with the values adopted in Ref. 27, the pitch angles and distances from zone maximum to the center of the Earth were slightly altered. Under these conditions, the magnetic field of  $\Delta T$  on the Earth's surface proved to be  $-14\gamma$ ;  $-23\gamma$  at  $3.5 R_e$ ; and  $+2.5\gamma$  beyond  $7 R_e$ .

(Ref. 29, 30) compute the  $\Delta T$  field based on models of the external radiation zone in 1958-1959. With a "smoothed out model" of the external zone of radiation, the  $\Delta T$  field at  $\sim 4 R_e$  proved to be  $-100\gamma$ , while at  $8 R_e$  it was  $+3\gamma$ . Here it was assumed that electron density at the outer zone maximum was  $5 \text{ electron} \cdot \text{cm}^{-3}$ . With a model of the outer radiation zone with a steeper front for the density rise on the internal side of the zone turned toward the Earth, the  $\Delta T$  of the zone at  $\sim 4 R_e$  reaches  $-250\gamma$ .

The results of Section 3 will be easier to discuss, if the above information is supplemented by the features of outer zone morphology and the dynamics of the outer zone in a magnetically active period (Ref. 25, 26).

At present, more and more corroboration is being provided for the view that the protons and electrons forming the outer radiation zone have diffused inward into the magnetosphere from its boundaries.

/352

The intensity of the soft electrons of the outer zone displays a positive correlation with the  $K_p$  index of magnetic activity. Their intensity during the initial storm phase rises by a factor of up to 100, showing greater increase at large values of  $L$ . With small  $L$  values, this increase in intensity is observed for large values of  $K_p$ .

The intensity of the high-energy 1.6 Mev electrons decreases in the initial period of the storm. For several days after the initial storm phase, this intensity increases, first at  $L = 5$  and then at small values of  $L$ , while the increasing intensity front apparently shifts into the interior of the magnetosphere at a rate of  $\sim 0.02 R_e \cdot \text{day}^{-1}$ . The intensity



of the low-energy electrons is thus reduced (Ref. 14, 31).

At distances of  $<5 R_e$ , there is no perceptible dependence of electrons on local time. At great distances, such a dependence is rather noticeable. On the nocturnal side, the 50-keV electron boundary on the average is at  $L = 7-8 R_e$ , while on the morning side it is located at  $L = 10-11 R_e$  (Ref. 25). It has been found that during the initial phase of a magnetic storm the external boundary of the 50-keV electron zone approaches the Earth. During the recovery phase, it retreats from the Earth.

## 5. Discussion of Experimental Results

Section 3 of this article examined the results of magnetic measurements in the region in space which is conventionally called the space of the outer radiation zone. In our study the boundaries chosen were the regions delimited, on one hand, by the measurement range of the equipment and, on the other, by the regions where  $\Delta T = 0$ .

There is at present still no adequate analysis of the radiation instrument findings, so as to throw light on the nature of the regions where  $\Delta T = 0$ , but a number of the laws which they obey permit us to assume, to a certain degree, that this boundary of the region under consideration reflects certain physical properties of the magnetosphere.

We feel it necessary to discuss the accuracy of the magnetograms in this region of space. It is known that magnetometers on the satellites ("Explorer-12", "Explorer-14") which had flown in this region of space for a long time before the launching of "Elektron-2" had, in principle, made it possible to conduct measurements at distances of  $3-4 R_e$ . However, as a rule the magnetic data obtained during the experiments were published for a distance no closer than  $5 R_e$ , where the  $\Delta T$  values are always positive.<sup>1</sup>

The group of methodological control procedures used in the given experiment allow us to assume that the magnetogram error in this region of space is 6-8 times less than the maximum  $\Delta T$  effects measured at  $3-4 R_e$ .

(a) On the basis of these estimates, it may be assumed that the measured field values at distances of  $3-5 R_e$  were always less than those to be expected under the assumption that all the field sources are within the Earth - at least in the observational period with the above-described position of the orbit relative to the Sun. These  $\Delta T$  field deviations at  $\sim 3 R_e$  reach 10% of the dipole field at these distances.

---

<sup>1</sup> (Ref. 32) gives two magnetograms obtained during measurements by "Explorer-14" on the nocturnal side, where  $\Delta T$  values at distances of  $5-8 R_e$  are negative.

(b) If the external sources are assumed to be responsible for the deviations observed, it may naturally be assumed that among the possible /353 sources a contribution to the observed magnetic effects may be made by the closest sources: the protons and electrons of the outer radiation zone whose maximum intensity is located at distances of 3-4  $R_e$  from the Earth's center.

From the above survey of the sparse computations of the magnetic effects of trapped radiation, it may be easily seen that the models adopted explain the sign of the  $\Delta T$  values observed.

The Chapman-Akasofu model (Ref. 27) gives values which differ by 30-50% from those obtained by "Elektron-2". The Hoffmann-Bracken model (Ref. 28), which explains 20-30% of the observed effects, is in the worst agreement numerically. If it is taken into account that neither the first nor the second model allows for the distribution of low-energy ( $< 150$  kev) protons, about which there is inadequate information, or for the electron component of trapped radiation, then the conformity between the calculated magnetic effects of trapped radiation and the observed  $\Delta T$  values at distances of 3-5  $R_e$  may be regarded as sufficiently close.

Thus, without excluding the possibility that other magnetic field sources may also affect these distances, we may at the same time conclude that, during a magnetically quiet period, it is sufficient to allow for the influence of the trapped radiation of outer zone protons and electrons in order to explain the observed  $\Delta T$  values. The annular nature of the effect, its occurrence at a quiet period, and the character of its distribution with respect to trapped radiation maximum are other qualitative arguments in favor of this view.

(c) The regions where  $\Delta T = 0$  are convenient indices of magnetospheric dynamics far from its boundaries in the regular field region. As follows from the experimental data described in Sections 3 and 4, the nature of the change in geocentric distances of the  $\Delta T = 0$  regions and of the outer boundary of the electron zone is quite similar: the  $\Delta T = 0$  regions and the external boundary of the electron zone (e.g., of  $\sim 50$ -kev electrons) are detected at shorter geocentric distances as the magnetic activity  $K_p$ -index increases - and, conversely, at longer geocentric distances as the  $K_p$ -index decreases. However, the boundary of electrons having  $\sim 50$  kev energy does not coincide with the  $\Delta T = 0$  regions. Apparently, the position and intensity of the electron component are only responsible to a certain degree for the position of the  $\Delta T = 0$  regions. We have as yet been unable to determine to what degree the  $\Delta T = 0$  regions could be explained by the distribution of the features of other trapped radiation components.

(d) It is of interest to determine what causes the variability of the  $\Delta T = 0$  regions. Since the above-mentioned annular current models indicate the existence of regions where  $\Delta T = 0$ , it was natural to try to discover a connection between the magnetic activity indices and the change

in "negative magnetic flux" intensity. They are proportional to the areas delimited by the  $\Delta T$  curves and the  $\Delta T = 0$  line (Figure 4). The correlation between variations in "negative magnetic flux" intensity and U-dimensional magnetic activity should adequately indicate the change in annular current intensity. No such correlation could be discovered on the forward revolutions.

It is very possible that "negative magnetic flux" variability could not be noticed every day because of limited measurement accuracy at these distances. Bearing in mind, however, that magnetogram accuracy at these distances is  $\sim 20\gamma$ , we may conclude that these changes must be small, or otherwise they could be distinguished. Nevertheless, the most drastic changes in geocentric distances  $R_g$  and latitude  $\varphi$  of  $\Delta T = 0$  regions, /354 observed on the forward and reverse revolutions on February 13, February 20, March 3, and March 23, 1964, (Figure 5) took place during the main phases of moderate magnetic perturbations (Figures 6, 7, and 8 give the magnetograms pertaining to some of these events). It should, therefore, be noted that the activity boundary shift at low latitudes which is familiar on the Earth during magnetic perturbations (aurorae at low latitudes when the perturbations increase in intensity) was explained precisely by the annular current effect.

As already mentioned, the "negative magnetic fluxes" on the reverse revolutions are fairly definitely correlated with the  $K_p$ -indices of magnetic activity. Since the  $K_p$ -index variations are in excellent correlation with changes in the positive values of  $\Delta T$  (Ref 33), which in turn display their greatest variability during the initial phase of a storm, the "negative magnetic flux" variability on the reverse revolutions may be in great measure connected with processes in the boundary region. The perceptible seasonal dependence of geocentric distances and geographic latitudes of the  $\Delta T = 0$  regions, which is observed only on the reverse revolutions, substantiates the above statements.

The seasonal drift in  $\Delta T = 0$  region coordinates on the reverse revolutions may be associated with the shift in these revolutions from the morning side, at the beginning of February, to the nocturnal side at the end of April. It is obvious that the observed effects could also be manifested during a shift of the differently deformed magnetosphere relative to the orbit. Thus, the change in  $\Delta T = 0$  region coordinates is connected both with annular current changes and with a change in the magnetospheric boundary region. Under different conditions, other causes are more easily found, which represent different aspects of the same process.

(e) As already mentioned, the seasonal pattern of  $\Delta T = 0$  coordinates on the reverse revolutions consists of a decrease in the geocentric distances and the geographic latitudes, but similar changes are experienced by the  $\Delta T = 0$  regions when the perturbation increases. From February to the end of April, the position of the magnetic axis changed in relation to the Sun-Earth line and, in particular, the orbit "shifted" to the nocturnal side. If the seasonal drift in  $\Delta T = 0$  coordinates is tied in with the changes

mentioned, then it must be assumed that this shift to the nocturnal side was equivalent to an increase in the "perturbation". It is not yet clear whether the observed effects are related to such facts as, for example, the closer location of the radiation zones on the nocturnal side (Ref. 25) and the greater closeness of the oval zone boundary of the polar aurorae on the nocturnal side of Earth (Ref. 34).

(f) Attention may also be directed to the fact that the flatter shape of the negative  $\Delta T$  curves on the reverse revolutions, as compared to the forward revolutions during the initial period of observation (Figure 5), agrees with the flatter pattern of the low-energy electron profiles on the reverse revolutions as compared with the forward revolutions (Ref. 25). Subsequently, the asymmetry of the radiation and  $\Delta T$  profiles on the nocturnal and diurnal sides, which was obvious in the beginning, became less apparent.

(g) The large field deformations discovered at distances of  $3.5 R_E$  during the flight of the satellite "Elektron-2" on February 12, February 20, and March 4, 1964, during the development of polar storms and the main storm phase again indicate the special activity of this magnetosphere region during magnetic storms.

We have already noted that the absence of information on the subsequent revolutions prevents the  $3.5 R_E$  region from being examined at other longitudes during the main phase of a magnetic storm. This examination would be decisive for an understanding of the observed field deformation and its role in the mechanism of the magnetic storm. For the time being, we must direct our attention to the fact that greater and greater field deformations were detected only on the reverse, high-latitude revolutions. Another feature of the observed effects is their significantly limited /355 nature in space (or time). If, moreover, we consider that great field deformations had also been observed long before development of the magnetic storm's main phase (February 12, 1964), but always during polar substorms, then the simplest procedure is to conclude that in all the indicated cases the local field deformations are associated with penetration into the magnetosphere of an "active agent", which is also responsible for the polar storms detected. Such a "penetration" is apparently a necessary condition for development of the main phase, as it is known that the bigger the substorms, the more intense is the main phase of the storm (Ref. 35). Further comparisons of the magnetic measurements pertaining to the described effects and of simultaneous radiation measurements may possibly enable us to define the nature of the "active agent" more accurately.

### Conclusion

The satellite "Elektron-2" enabled us to make systematic measurements of the magnetosphere at distances of  $3-6 R_E$  in the space of the outer radiation belt. These measurements indicate that there is a quiet-day outer magnetic field associated with the protons and electrons of the radiation zones. This conclusion is based on a comparatively limited period of observation.

Further investigations by the satellite "Elektron-4" at other orbital positions relative to the Sun-Earth line should more accurately define to what degree the observed effects may be associated with this radiation zone. It also seems that the features of magnetosphere dynamics noted far from the magnetosphere boundary region, and the effects observed during polar storms, have a bearing on uncovering the puzzling mechanism of magnetic storm development.

The authors deem it a pleasant duty to express their gratitude to those who have greatly assisted them in analyzing the material, in preparing the experiment, and in carrying it out.

#### REFERENCES

1. Dolginov, Sh. Sh., and Pushkov, N. V. Doklady Akademii Nauk SSR, 128, 77, 1959.
2. Dolginov, Sh. Sh., Yeroshenko, Ye. G., et al. In "Iskusstvennyye Sputniki Zemli", No. 5, Izdatel'stvo AN SSSR, p. 16, 1960.
3. Sonett, C. P., Smith, E. J., Sims, A. R. Space Res., 1, 921, 1960.
4. Smith, E. J., Coleman, D. J., et al. J. Geophys. Res., 65, 1858, 1960.
5. Heppner, J. P., Ness, N. F. et al. J. Geophys. Res., 68, 1, 1963.
6. Cahill, L. J., Amazeen, P. G. J. Geophys. Res., 68, 1835, 1963.
7. Ness, N. F. et al. J. Geophys. Res., 69, 3531, 1964.
8. Vernov, S. N., Chudakov, A. Ye., Uspekhi Fizicheskikh Nauk, 70, 585, 1960.
9. Van Allen, J. A., Frank, L. A. Nature, 183, 430, 1959.
10. Gringauz, K. I., Kurt, V. G., et al. Astronomicheskiy Zhurnal, 37, 716, 1960.
11. Fan, C. Y., Meyer, P., Simpson, J. A. J. Geophys. Res. 66, 2607, 1961.
12. Forbush, S. E., Pizella, G., Venkatesan, D. J. Geophys. Res., 67, 3651, 1962.
13. Arnoldy, R. L., Hoffman, R. A., Winckler, J. R. J. Geophys. Res., 65, 1361, 1960.
14. Vakulov, P. V., Gorchakov, Ye. V., Logachev, Yu. I. The Earth's Radiation Belts from Research by Artificial Soviet Satellites and Space Rockets in 1957-1959 (Radiatsionnyye poyasa Zemli po issledovaniyu na sovetskikh iskusstvennykh sputnikakh i kosmicheskikh raketakh v 1957-1959 gg.). Izdatel'stvo "Nauka", 1965.

15. Aleksanyan, L. M., Zhuzgov, L. N., Yeroshenko, Ye. G., and Fastovskiy, U. V. Space Studies (Kosmicheskiye issledovaniya). (In press).
16. IGY Bulletin. Trans. Amer. Geophys. Union, 43, 221, 1962.
17. Davis, L. R., Williamson, J. M. Space Res., 3, 365, 1963.
18. Dolginov, Sh. Sh., Pushkov, N. V. Kosmicheskiye Issledovaniya, 1, No. 1, 1963.
19. Cahill, L. J. IEE Trans. Nuclear Science, N 3, 1963.
20. Dessler, A. J., Parker, E. N. J. Geophys. Res., 64, 2239, 1959.
21. Akasofu, S. J., Chapman, S. J. Geophys. Res., 66, N 5, 1961.
22. Apel, J. R., Singer, S. F., Wentworth, Advances in Geophys., 9, 132, 1962.
23. Davis, L. R., Hoffman, R. A., Williamson, J. M. Trans Amer. Geophys. Union, 45, N 1, 83, 1964.
24. Krasovskiy, V. I. Report at the Sixth Symposium of the Committee on Space Research (Doklad Na 6-M Simpoziume COSPAR). Buenos Aires, May, 1965.
25. Vernov, S. N., Chudakov, A. Ye. et al. Ibid.
26. Frank, L. A., Van Allen, J. A. J. Geophys. Res., 69, 4923, 1964.
27. Akasofu, S. J., Cain, J. C., Chapman, S. J. Geophys. Res., 66, 4013, 1961.
28. Hoffmann, R. A., Bracken, P. A. Magnetic Effects of the Quiet Time Proton Belt. Preprint, 1964.
29. Apel, J. R. Geomagnetic Field Perturbations Due to Trapped Particles. Preprint, 1960.
30. Singer, S. J. Trans. Amer. Geophys. Union, 38, 175, 1957.
31. Freeman, J. W. J. Geophys. Res., 69, 1962, 1964.
32. Cahill, L. J. Trans. Amer. Geophys. Union, 45, N 1, 1964.
33. Yeroshenko, Ye. G. Present Collection, p. 356.
34. Feldstein, Y. J. Tellus, 16, 2, 1964.
35. Akasofu, S. J., Chapman, S. J. Geophys. Res., 68, 125, 1963.

STUDY OF THE EARTH'S MAGNETOSPHERE AT A  
DISTANCE OF 7-11.7  $R_e$  ON THE "ELEKTRON" SATELLITES

Ye. G. Yeroshenko

The strength of the geomagnetic field and the plasma were measured /356  
during flights of the first cosmic rockets (Ref. 1-3) in the outer magnetosphere of the Earth and its boundary region. These measurements produced the first experimental data on the physics of the boundary region of the magnetosphere, where the solar wind and corpuscular streams interact with the magnetosphere of the Earth. The most recent studies, performed on the satellites "Explorer-10", "Explorer-12", and "Explorer-14", presented data (Ref. 3-5) on the topology of the magnetosphere and its boundary region on the nocturnal and diurnal sides at pre-equatorial latitudes. The data from these experiments confirm the theoretical premises regarding a physical boundary of the magnetosphere and its asymmetry in the Earth-Sun direction (Ref. 6, 7), the existence of a transitional region, and the existence of a shock front (Ref. 8). There are still insufficient experimental data on the topology and morphology of the magnetosphere boundary region at the mean and high latitudes.

It is also necessary to conduct observations during minimum magnetic activity, when sporadic magnetic perturbations which are isolated in time can be followed more closely by a group of magnetic and radiation measurements.

A considerable portion of the scientific program on magnetic and radiation studies on the "Elektron" satellites has been concerned with these problems.

The satellites "Elektron-2" and "Elektron-4" carried two, three-component ferroprobe magnetometers. The measurement limits of the field components on the first magnetometer were  $\pm 1200 \gamma$ , and on the second magnetometer -  $\pm 120 \gamma$  ("Elektron-2") and  $\pm 240 \gamma$  ("Elektron-4").

The present report presents results derived from magnetic measurements of the outer magnetosphere of the Earth at distances of 7-11.7  $R_e$  from  $35^\circ$  S to  $60^\circ$  S. The measurements were performed by sensitive equipment for 2 minutes, or for 8 minutes. A special device made it possible to calibrate the sensitivity of the equipment each hour. As processing results have shown, the magnetometer sensitivity remained within nominal limits throughout the entire operation of the satellite. The error in the field component measurements (with allowance for telemetry error) did not exceed  $\pm 2 \gamma$  for the sensitive equipment. The error of one reading in the scalar magnitude of the total vector  $T_{\text{meas}}$ , determined from three measured components, was no more than  $\pm 3 - 4 \gamma$ . /357

Graphic averaging employing a group of readings may be used to determine the mean field level. This excludes random telemetry errors;

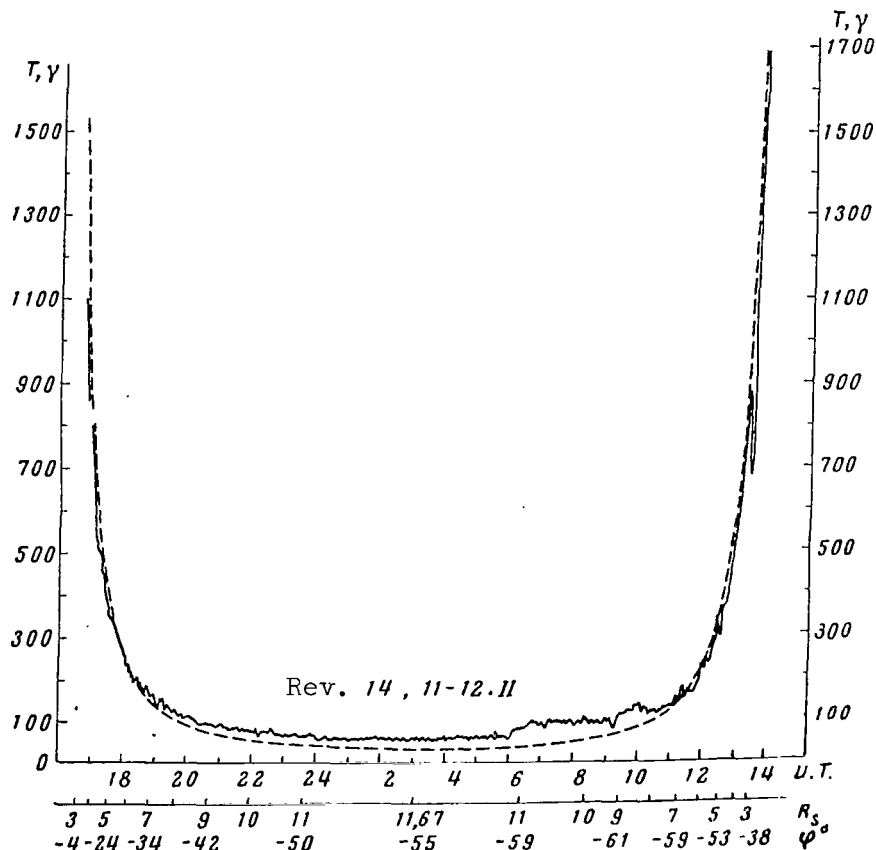


Figure 1

Photo of T Magnetogram From the Satellite "Elektron-2"

the accuracy will depend on the number of points in the averaging period. The systematic absolute error, determined in this way, of the modulus magnetogram  $T_{\text{meas}}$  does not exceed  $\pm 2 \gamma$  in portions of the sensitive magnetometer operation. The measurement errors given above pertain to data on the "Elektron-2" satellite.

Due to the satellite rotation, it was possible to control the change in the magnetometer eigen zero deviation from absolute zero (Ref. 9). All of the data obtained from the satellite "Elektron-2" from February to June, 1964, have indicated that the drift of the zero point of the sensitive magnetometer was no more than  $\pm 5 - 6 \gamma$  per month.

#### Orbit of the "Elektron-2" Satellite and the Region of Magnetosphere Exploration

Figure 1 of the preceding article (page 465) depicts the projection of the satellite orbit in a solar-ecliptic coordinate system in three



planes. The direction toward the Sun coincides with the positive direction of the  $X_{ne}$  axis, the  $Z_{ne}$  axis directed toward the North Pole of the ecliptic, and the  $Y_{ne}$  axis is directed so that a right-handed coordinate system is formed. Figure 1,a shows the orbit projection in the ecliptic plane, and its change from the initial satellite operational period to the final period. Figure 1,b and c shows the orbit projections in the meridional plane and the plane which is perpendicular to it (view from the Sun). The inclination of the orbit plane to the ecliptic plane is about  $50^\circ$ , and the geocentric distance of the apogee is  $11.67 R_e$  ( $R_e$  designates the radius of the Earth).

The orbit position in a solar-ecliptic coordinate system was changed so that the apogee sections were closer to the morning side during the initial period, and then shifted to the nocturnal side of the Earth. At the beginning of February, the angle between the normal to the orbit plane and the direction toward the Sun was  $\sim 105^\circ$ . In the first ten days of April, this angle increased to  $140^\circ$ . Thus, the magnetosphere asymmetry in the Earth-Sun direction can be more readily detected during the initial period than at a later time. It can be seen from Figure 1, a that during the initial period the satellite left the nocturnal side on forward revolutions and rotated on inverse revolutions to the morning-diurnal side. Later on, the forward revolutions began on the evening side, and the inverse revolutions passed to the nocturnal side.

The lower boundary of the magnetosphere region which was explored was determined by the measurement range of the crude magnetometer and extended up to geocentric distances of  $\sim 3 R_e$ . Measurements on the sensitive magnetometer were performed from approximately  $7 R_e$ , and continued up to apogee. The readings of the three recorders of both magnetometers, which represented sinusoidal curves due to the satellite rotation, indicated that the regular nature of the field did not change throughout the operation of "Elektron-2" at distances from 3 to  $11.67 R_e$ . This indicates that the magnetosphere boundary was located above the satellite apogee.

#### General Nature of Magnetometer Information

Reference data used to analyze the field are: (1) magnetograms of scalar magnitude of the total vector  $T_{meas}$ , calculated according to the measured values of 3 components - solid line in Figure 1; (2) theoretical curves of the total vector  $T_{teor}$ , calculated with allowance for 48 coefficients of Gaussian series<sup>1</sup> - dashed curve in Figure 1. /358

Magnetic data obtained on board the spacecraft were analyzed and compared with data obtained on Earth primarily on the basis of the curve  $\Delta T$ ,

<sup>1</sup> Calculations were performed on the basis of a program of field synthesis, formulated by T. L. Vinnikova using coefficients extrapolated to 1964 by N. P. Ben'kova and L. O. Tyurmina.

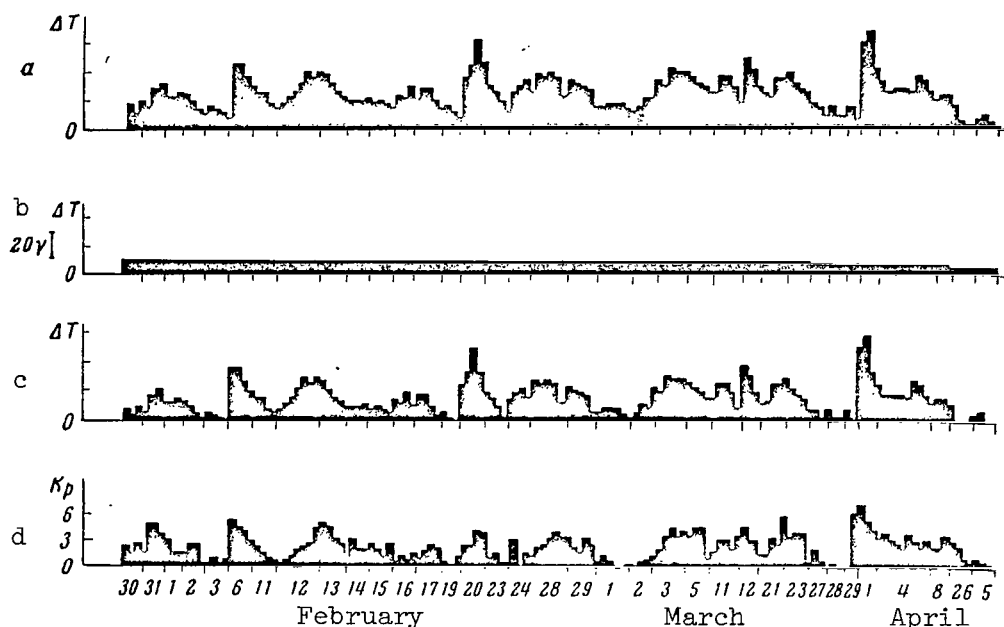


Figure 2

Three-Hour Values of  $\Delta T$  Based on Data From  
 "Elektron-2" at Distances of 7-11.7  $R_E$  During February-April

representing the difference between the measured and calculated values of the scalar field quantity. As can be seen from Figure 1, the measured values of the total vector were lower than the theoretical values on the sections between 3 and 5.5  $R_E$  on a forward revolution, and between 7.5 and 3  $R_E$  on a reverse revolution. In the remaining portion of the orbit, the measured values exceeded the theoretical values -  $\Delta T$  was positive. The curve  $\Delta T$  had the same pattern from revolution to revolution throughout the entire period of the satellite.

Maximum values of negative  $\Delta T$  were observed at distances of  $\sim 3 R_E$ , where they reached 100-150  $\gamma$ , which amounted to 10% of the dipole field at these distances. The mean positive value of  $\Delta T$  changed as a function of magnetic activity between 7 and 70  $\gamma$ , which amounted to 20 to 200% of the dipole field in these sections of the orbit.

As has already been noted, the present article analyzes the positive values of  $\Delta T$  observed at distances of 7-11.7  $R_E$ . The variability of the outer magnetosphere during magnetically quiet days, and during magnetically perturbed days, is revealed when the mean values of the value of  $\Delta T$  and the indices of magnetic activity are examined. It is also apparent when the magnetograms of  $\Delta T$  on board the spacecraft and the magnetograms on the Earth are compared during the corresponding days. /359

A close correlation is revealed by comparing the value of  $\Delta T$

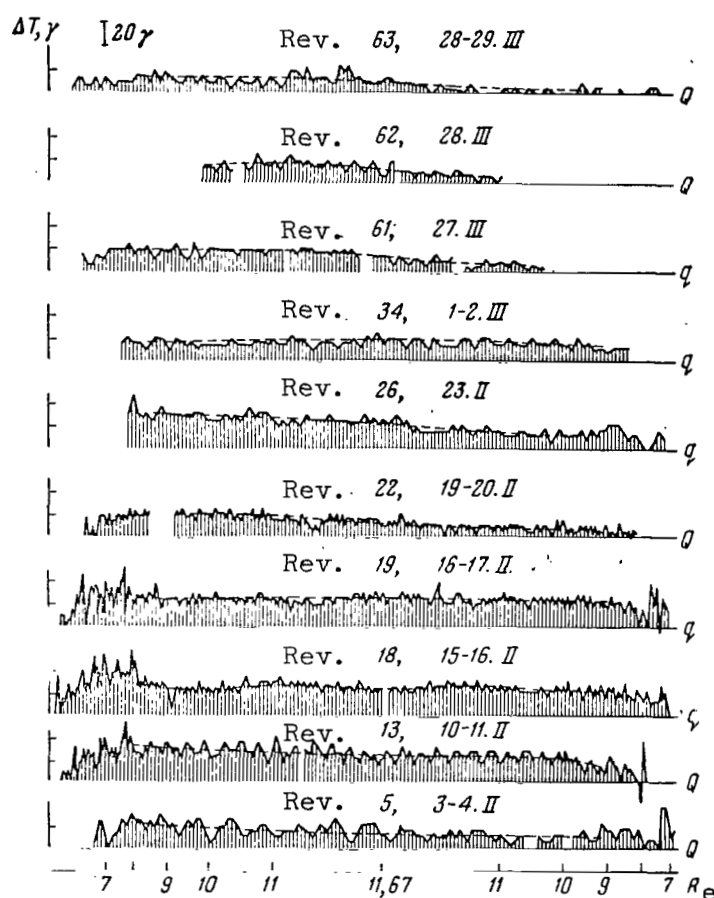


Figure 3

### Positive Values of $\Delta T$ During International Quiet Days

averaged over three-hour intervals, with the  $K_p$ -indices of magnetic activity throughout the entire observational period (Figure 2): the difference  $\Delta T$  increases with an increase in  $K_p$ . If the regular portion passing along the points with a minimum  $K_p$ -index (Figure 2,b) is subtracted from the group of three-hour values of  $\Delta T$  (Figure 2,a), this correlation becomes more apparent (Figure 2,c). The regular portion of  $\Delta T$  decreases smoothly within the limits of 8  $\gamma$  during February-April.

### Variability of the Field During Magnetically Quiet Days

Figure 3 presents the different curves of  $\Delta T$  measured during magnetically quiet days during February-March, 1964. We should first of all point out that the magnetograms on board the spacecraft were quite sensitive to gradations in the degree of "quietness", designated by the indices  $Q$  and  $q$ .

The data presented in the Table clearly illustrate this, where the mean values of  $\Delta T$  are compared with the quietness indices and with the  $K_p$ -indices.

As can be seen from Figure 3, the changes in values of  $\Delta T$  follow definite patterns on quiet days, which is particularly apparent on revolutions with the minimum value of the  $K_p$ -index. On forward revolutions, the value of  $\Delta T$  is somewhat larger from 7  $R_e$  and approximately up to apogee than it is on the trajectory sections from apogee and up to 9-8  $R_e$  on reverse revolutions. Thus, on the 61st, 62nd, and 63rd revolutions  $\Delta T$  first amounted to 15-17  $\gamma$  on the average, and on reverse revolutions - about 5-7  $\gamma$ . This phenomenon occurred on each quiet day throughout the entire period of February-April.

It should be noted that, as the satellite moves along the orbit, it passes the sections under consideration when the geographical latitude changes from  $-35^\circ$  to  $-55^\circ$  on forward revolutions, and from  $-55^\circ$  to  $-61^\circ$  on reverse revolutions. Thus, the longitude of the point below the satellite changed within the limits of  $160^\circ$ . /360

On each revolution the change in  $\Delta T$  may be connected with the change in the satellite position, if it is assumed that the outer source of the magnetic field, causing the change in  $\Delta T$ , depends on latitude and longitude.

TABLE

Rev. No.	Date (1964)	$\Delta T_{av}$ , $\gamma$	Index of Quiet Day	$\Sigma K_p$ According to a 28-Number Scale	Rev. No.	Date (1964)	$\Delta T_{av}$ , $\gamma$	Index of Quiet Day	$\Sigma K_p$ According to a 28-Number Scale
5	2/3-4	14	Q	13	34	3/1-2	16	q	21
13	2/10-11	18	Q	23	61	3/26-27	10	q	18
18	2/15-16	24	q	26	62	3/28	10	Q	2
19	2/16-17	22	q	39	63	3/28-29	10	Q	21
22	2/19-20	10	Q	10	91	4/24	7	Q	20
26	2/23	22	q	40					

If we keep the fact in mind that this change in  $\Delta T$  occurs at very large distances from the maximum of the outer radiation zone, it is more plausible to connect the observed phenomenon with physical processes determined by the solar wind flowing around the magnetosphere. As is known, theoretical models considering these phenomena predict the dependence of the observed values of  $\Delta T$  on latitude and longitude (Ref. 10). /361

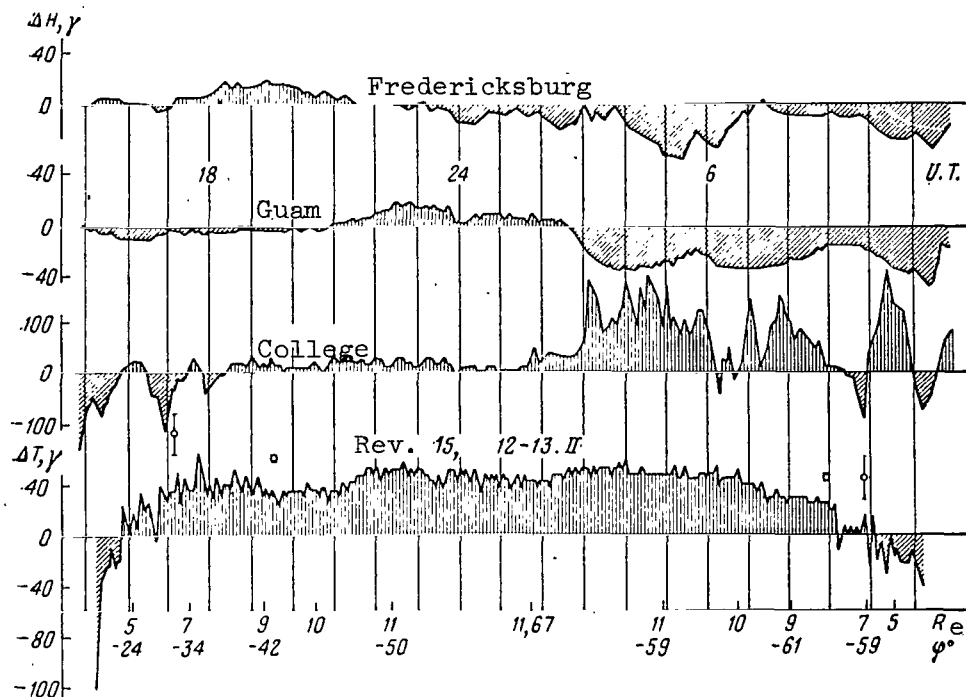


Figure 4

Magnetograms of  $\Delta T$  and  $\Delta H$  (from Stations on the Earth)  
on February 12-13, 1964

It follows from the theoretical analysis presented in (Ref. 10) that in the region of the outer magnetosphere changes in the observed value of  $\Delta T$  as a function of latitude exceed by a factor of 3-4 the corresponding changes in terms of longitude. Based on this fact, we may assume that the pattern of the curves of  $\Delta T$  may be primarily explained by a latitudinal effect on each revolution during quiet days. However, we must not overlook the fact that when the local time of the satellite changes within 5 hours the diurnal pattern must be indicated by the value of  $\Delta T$ , although this effect apparently does not exceed 20-30% of  $\Delta T$ . In addition, on quiet days there is a gradual decrease in the value of  $\Delta T$  - from 15-18  $\gamma$  at the beginning of February to 5-7  $\gamma$  at the end of April, if the values of  $\Delta T$  are compared close to the apogee sections (see the Table). This is corroborated by the smooth decrease in the regular portion of the three-hour values of  $\Delta T$ , which was pointed out above.

The seasonal pattern of  $\Delta T$  - i.e., the gradual decrease in the value of  $\Delta T$  from revolution to revolution - is probably related to the change in the orbital position with respect to the position of the Sun. As has already been pointed out, throughout this period the orbit shifted to the nocturnal side, and the apogee portions receded from the cavity boundary from the diurnal side and shifted toward the periphery of the nocturnal magnetosphere. On quiet days, different factors may cause the

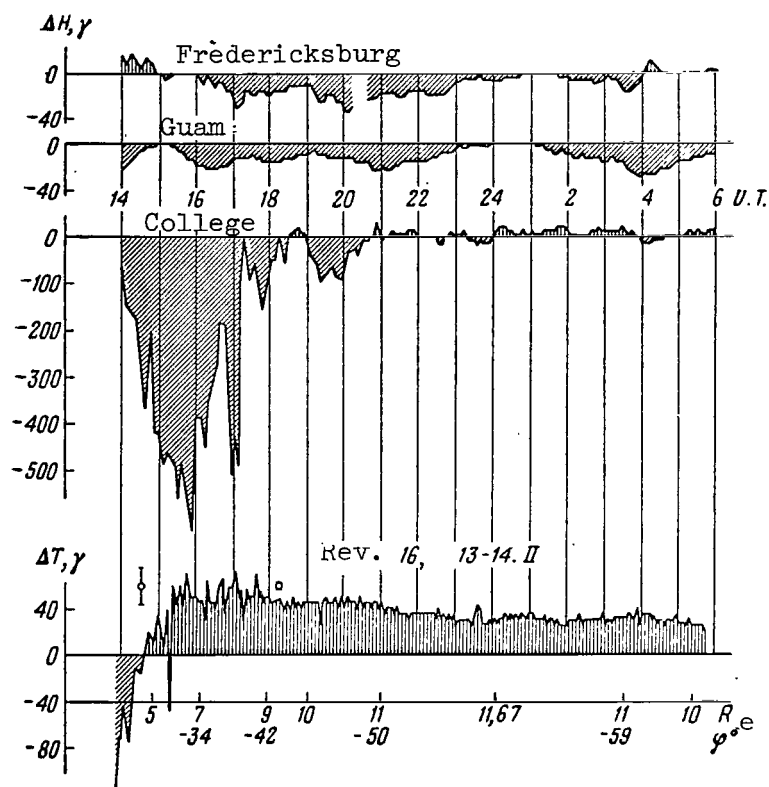


Figure 5

Magnetograms of  $\Delta T$  and  $\Delta H$  (From Earth Stations) on  
February 13-14, 1964

decrease in  $\Delta T$  in this spatial region: A decrease in the effect of currents in the boundary region due to a change in the orbital geometry in space; possible seasonal change in intensity of the currents themselves, and a change in the interplanetary magnetic fields.

#### Variability of the Field During Magnetically Perturbed Days

It was possible to examine the morphology of the magnetosphere change on perturbed days in the initial operational period of the satellite during two moderate magnetic storms. The magnetograms on board the satellite and the magnetograms on Earth were compared for two storms with a sudden commencement (SSC) on February 12-13 and February 20-21, 1964, for individual polar perturbations on January 31 and April 8. Since the horizontal component is the most variable element during a storm, magnetograms  $H$  from stations on the Earth, from which the quiet diurnal variation was excluded, were compared with data from the spacecraft. Due to the fact that the direction of the perturbed field vector (based on data from

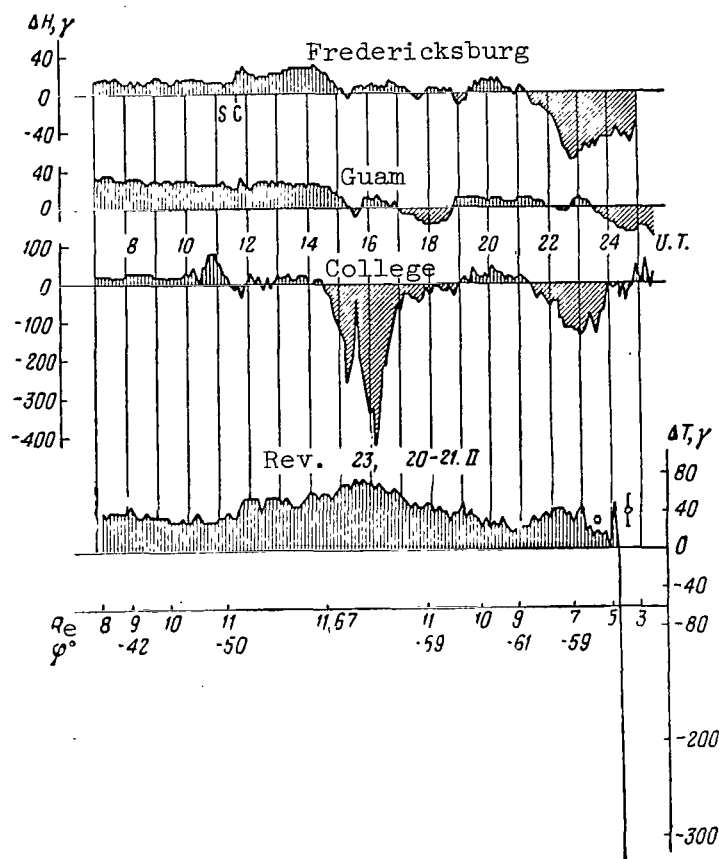


Figure 6

Magnetograms of  $\Delta T$  and  $\Delta H$  (From Earth Stations)  
on February 20-21, 1964

the spacecraft) was not known, it was impossible to determine the actual value of the perturbed field. It is apparent that its effect was at least equal to, or greater than, the observed effect.

#### Magnetic Storm on February 12-13

The sudden commencement of a magnetic storm (SSC) was noted from data on low- and mean-latitude observations on February 12, 1964, at 6 hours 6 minutes UT. After the sudden commencement, which was observed at stations on the Earth, the magnetograms on board the spacecraft (see Figure, page 473) indicated a smooth increase in  $\Delta T$  for approximately 30 minutes up to a maximum value of  $\sim 50$   $\gamma$ . At 6 hours 6 minutes UT, on February 12 a brief, short-lived jump was recorded, which was similar to the characteristic SSC signal at the stations on the Earth. The magnetogram on board the spacecraft did not reveal this, although at 6 hours 6 minutes UT there was a magnetometer reading.

/362

On the subsequent revolution (Figure 4), the increased value of  $\Delta T$ , which was characteristic for a perturbed day, remained throughout the entire period. Two blurred maxima of  $\Delta T$  should be pointed out here. One of these maxima corresponded to the maximum of positive values for  $\Delta H$  at low-latitudinal stations (about 22-23 hours UT on February 12) - i.e., the initial phase maximum. The second maximum of  $\Delta T$  coincided in time with the development of a polar sub-storm and the main phase at low latitudes at 4-6 hours UT on February 13. The termination of the polar sub-storm and a large negative coil of  $\Delta H$  (Figure 5) corresponded, just as in the preceding case, to an increased value of  $\Delta T$  (on a forward revolution). Beginning at 21 hours UT, there was a gradual decrease in  $\Delta T$  in the magnetogram on board the spacecraft. /363

#### Magnetic Storm on February 20-21

A magnetic storm with a sudden commencement (SSC) was observed at 11 hours 37 minutes UT on February 20, 1964. After the appearance of the SSC at stations on the Earth, there was an increase in  $\Delta T$  for approximately 16 minutes up to a value of 50  $\gamma$  (Figure 6) in the magnetogram on board the spacecraft (measurements were performed for 8 minutes). Between 15 hours and 16 hours UT, there was one increase in  $\Delta T$  up to a value of 70  $\gamma$ . During this same period (15-16 hours UT) the development of a polar sub-storm was observed (based on data from the College station). According to data from the spacecraft, the development of the main phase of this storm was characterized by the fact that positive values of  $\Delta T$  were observed up to 5  $R_e$  on the reverse revolution, while in all other cases positive  $\Delta T$  were observed up to a distance of 8-7  $R_e$  on reverse revolutions. /364

The comparison presented above of data obtained on board the spacecraft and on the Earth clarifies the following characteristic behavior patterns of positive  $\Delta T$  during a magnetically perturbed period:

- (1) There was no sharp field jump in the magnetograms on board the spacecraft when there was a sudden commencement of a magnetic storm;
- (2) The increase in  $\Delta T$  is always correlated in time with the development of the initial phase of the storm and with polar sub-storms;
- (3) A change in  $\Delta T$  at distances of 7-11.7  $R_e$  during the main phase of the storm does not coincide in sign with the change in  $\Delta H$  on the Earth at low and mean latitudes. This does not contradict the assumption that the current system causing the main phase is far from the apogee sections, where the effect of the main phase is not manifested in the magnetograms on board the spacecraft.



## Fine Structure of Polar Magnetic Perturbation Effects Based on Satellite Data

Two aspects of the formation and development of a polar magnetic perturbation are usually investigated: (1) The intrusion of particles into the upper atmospheric layers; (2) the formation of a polar ionosphere current system, which indirectly causes magnetic perturbation (Ref. 11). In this connection, it is of great interest to analyze individual polar perturbations and their appearance in the outer magnetosphere based on satellite observations.

During certain polar perturbations, magnetograms on board the satellites reported a sharp and short-lived decrease in the positive difference  $\Delta T$ . A satellite magnetogram recorded a negative "coil" of  $\Delta T$  which lasted  $\sim 15$  minutes with an amplitude of 50  $\gamma$  (Figure 7) at 17 hours 50 minutes UT on January 31. This coil coincided in time, but not in duration with the negative coil of  $\Delta H$  at a network of North Pole observatories. When this phenomenon was compared with visual observations of the aurorae polaris at a network of Soviet stations, it was found that at 18 hours UT the aurora was centered either at those stations where it had not appeared before, or at other stations - the change from quiet forms of a homogeneous type arc to mobile, ray-like forms.

On January 31, a satellite magnetogram recorded one case of a decrease in the positive value of  $\Delta T$ , corresponding in time to the negative polar coil  $\Delta H$  at 11 hours 30 minutes UT. However, this phenomenon was recorded on a crude instrument, and due to the large amount of error it was difficult to determine the sharp fronts of the coil of  $\Delta T$  or an accurate value of the amplitude. When this case is compared with data from visual observations of aurorae polaris at certain stations, the appearance of aurorae was also observed close to this time. A similar phenomenon in the form of a sharp negative peak  $\Delta T = 40 \gamma$ , lasting 5-8 minutes, was recorded on a satellite magnetogram during a polar magnetic perturbation on April 8, on the background of an increased value (which was normal for a perturbed day) of positive  $\Delta T$ .

Along with this, several cases occurred when, during the development of similar polar perturbations, a satellite magnetogram also recorded a characteristic smooth increase in  $\Delta T$ , and no negative coils of  $\Delta T$ .

The morphological features of the negative coils of  $\Delta T$  examined here (on satellite magnetograms) suggest that such phenomena apparently have a rather sharp spatial limitation. The spatial-time nature of these deviations in  $\Delta T$  may be related to the diamagnetic effect of a plasma penetrating the inner regions of the magnetosphere.

/365

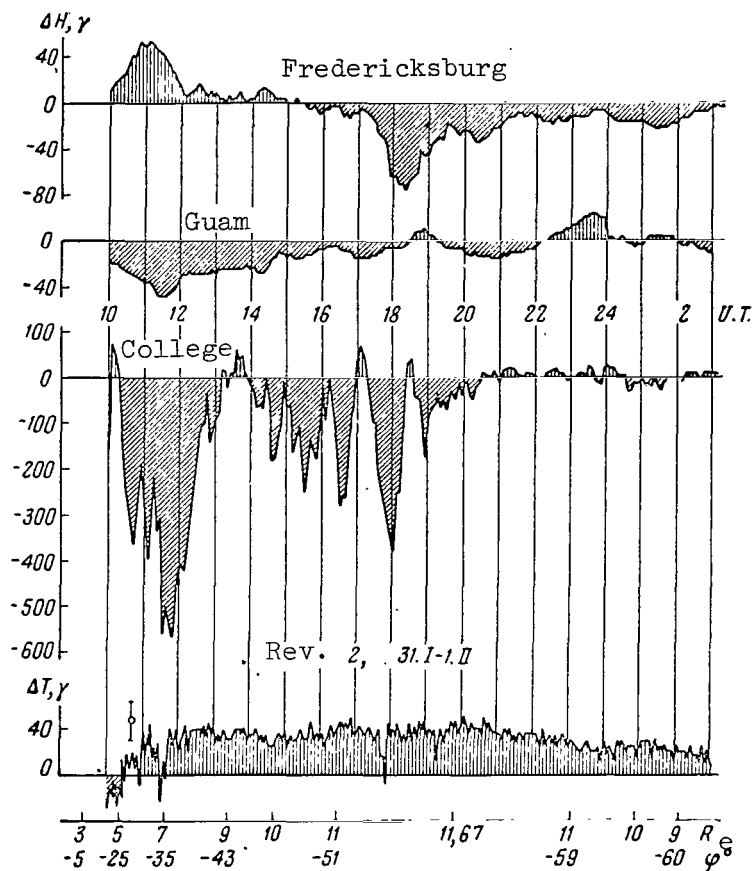


Figure 7

Magnetograms of  $\Delta T$  and  $\Delta H$  (From Earth Stations)  
From January 31-February 1, 1964

Intersections of the Magnetosphere Boundary  
According to Observations on "Elektron-4"

As has already been indicated, the magnetic data from the satellite "Elektron-2" established the fact that the magnetosphere boundary is located above the satellite apogee. This result coincides with the asymmetrical model of the magnetosphere whose farther boundary is located on the nocturnal side.

The apogee portions of the "Elektron-4" orbit ( $r_A = 11.4 R_e$ ) reached the diurnal side during the initial operational period (July 10-22, 1964), as can be seen from Figure 8. "Elektron-4" magnetograms pertaining to a magnetically quiet period also revealed the regular nature of the field, which indicates that during this period the magnetosphere boundary was above  $11.4 R_e$ . However, during a magnetic storm on July 17-20, 1964, the intersection of the magnetosphere boundary was established by magnetograms on

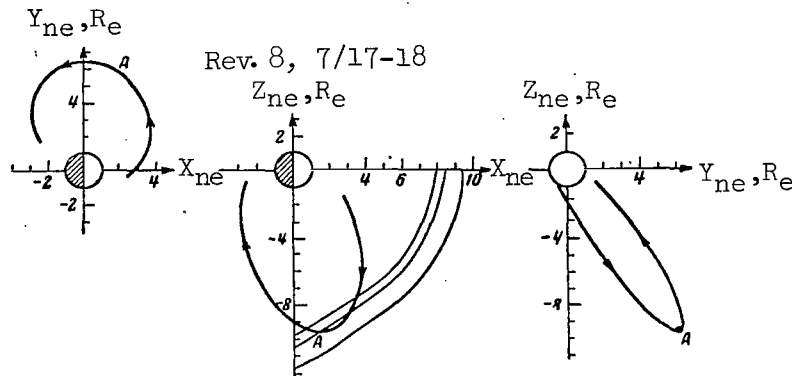


Figure 8

Orbital Position of "Elektron-4" During the Initial Operational Period

"Elektron-4".

The time at which the magnetosphere boundary was intersected was established by the perturbation of the regular nature of the field. The nonregular nature of the field was primarily manifested by the fact that the sinusoidal nature of the readings from all three manometer recorders was disturbed. This indicated a rapid and nonregular change in the direction of the field. The amplitude of the scalar value of the field vector also changed irregularly from 8 to 35  $\gamma$ . Several consecutive measurements when the magnetosphere boundary was intersected pointed to the fact that the geocentric distance of the magnetosphere boundary changed as the degree of magnetic activity changed during the storm. Figure 9 shows the apogee section of the "Elektron-4" orbit (during July 17-20). There are two possible positions of the magnetopause here (according to [Ref. 12]): The first position - for  $r_f = 8 R_e$  ( $r_b$  is the geocentric distance of the magnetosphere boundary at the equator from the solar side); the second position - for  $r_b = 8.55 R_e$ . The following symbols are used to designate the times at which the boundary was intersected (based on data from "Elektron-4") for different days: The small circles - July 17; the crosses - July 18; the triangles - July 19; and the squares - July 20. On forward revolutions; the geocentric distance of the magnetosphere boundary changed from  $9.6 R_e$  during the first day of the storm to  $9.3 R_e$  - on the second day of the storm. It then gradually increased to  $10.4 R_e$  after this time. The geocentric distance of the magnetopause changed within narrower limits on reverse revolutions - from  $11.1 R_e$  to  $11.3 R_e$ . As can be seen from Figure 9, this migration of the boundary closely coincides with the theoretical model of the magnetosphere cavity under consideration.

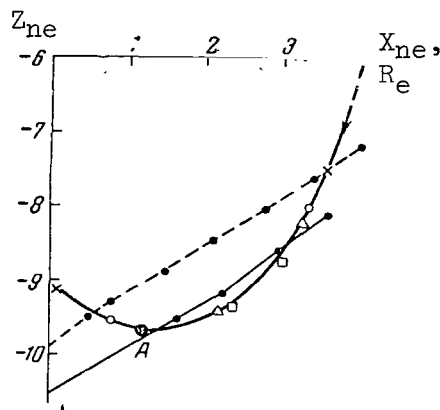


Figure 9

Change in Geocentric Distance of Magnetosphere  
Boundary During a Storm on July 17-20, 1964  
(Based on Data From "Elektron-4")

#### Conclusion

The following conclusions can be drawn from the comparison of satellite magnetograms of  $\Delta T$  (at distances of 7-11.7  $R_e$ ) with data derived on Earth.

1. There is a close correlation between changes in mean values of  $\Delta T$  at these distances and between changes of the  $K_p$ -index of magnetic activity on the surface of the Earth.

2. It is possible to distinguish the regular portion of the field of  $\Delta T$  by utilizing the mean value of  $\Delta T$  for a group of quiet days. This field displayed a smooth decrease within the limits of 8  $\gamma$  during February-April, 1964. Such a decrease in the field may be related to a change in the orbital position with respect to the Earth-Sun line, which may be due to a change in the influence of the solar wind and the interplanetary magnetic fields. /367

3. A diurnal variation in  $\Delta T$  is observed at each revolution during a quiet day within the limits of 12  $\gamma$ . This variation may be due to diverse deformation of the field by the solar wind, if the latitudinal and longitudinal effects of surface currents on the magnetosphere boundary are kept in mind.

4. During magnetic storms with a sudden commencement, the satellite magnetograms did not record a sharp change in the field; only a smooth increase in the positive value of  $\Delta T$  was observed (for 15-20 minutes).

5. Any magnetic perturbation was indicated in the satellite magnetograms in the form of an increase in the positive value of  $\Delta T$  (at

distances of 7-11.7  $R_e$ ). These changes in  $\Delta T$  coincide in sign with the change in  $\Delta H$  during the initial phase of the storm at low and mean latitudes. The increase in the duration of  $\Delta T$  on the satellite corresponds to the duration of polar sub-storms and the time required for the initial phase to develop.

6. A change in  $\Delta T$  on the satellite at these distances during the main phase of the storm does not coincide in sign with the deviation in  $\Delta H$  on the Earth at low and mean latitudes. This indicates that the source of the main phase is located below these distances (7-11.7  $R_e$ ).

7. Along with the large-scale changes (in time) of positive values of  $\Delta T$ , during individual polar magnetic perturbations there were short-lived negative deviations of  $\Delta T$  with sharp fronts (for 5-15 minutes). These phenomena coincided with the appearance and development of the aurora polaris. The nature of these short-lived changes in  $\Delta T$  apparently has a sharply-defined spatial character.

8. The results derived from processing magnetic data from "Elektron-2" indicated that the magnetosphere boundary was located above the satellite apogee.

9. A preliminary analysis of magnetic measurements during the initial operational period of "Elektron-4" (at distances of 8-11.4  $R_e$ ) shows that at least during the magnetic storm the satellite intersected the magnetosphere boundary on the diurnal side. These results coincide with the asymmetrical model of the magnetosphere.

#### REFERENCES

1. Dolginov, Sh. Sh., Yeroshenko, Ye. G., et al. In "Iskusstvennyye Sputniki Zemli". Izdatel'stvo AN SSSR, No. 5, p. 16, 1960.
2. Sonett, C. P., Sims, A. R., Abrams, I. J. J. Geophys. Res., 67, 1191, 1962.
3. Heppner, J. P., Ness, N. F. et al. J. Geophys. Res., 68, 1, 1963.
4. Cahill, L. J., Amazeen, P. G. J. Geophys. Res., 68, 1833, 1963.
5. Cahill, L. J. Trans. Amer. Geophys. Union, 45, N 1, 231, 1964.
6. Zhigulev, V. N., Romishevskiy, Ye. A. Doklady AN SSSR, 127, 1001, 1959.
7. Piddington, J. G. Planet. Space Sci., 9, 305, 1962.
8. Kellogg, P. J. J. Geophys. Res., 67, 3805, 1962.
9. Aleksanyan, L. M., Zhuzgov, L. N., Yeroshenko, Ye. G., Fastovskiy, U.V. Kosmicheskiye Issledovaniya. (In Press).

10. Mead, G. D. J. Geophys. Res., 69, 1181, 1964.
11. Akasofu, S. J., Chapman, S. Philos. Trans. Roy. Soc. London,  
A 253, N 1031, 359, 1961.
12. Mead, G. D., Beard, D. B. J. Geophys. Res., 69, 1169, 1964.

# STRUCTURE OF THE SOLAR CORPUSCULAR STREAM AND ITS INTERACTION WITH THE MAGNETOSPHERE OF THE EARTH

Yu. D. Kalinin, E. I. Mogilevskiy

1. When determining the manner in which the solar corpuscular stream transmits energy to the magnetosphere of the Earth, one must have information regarding the corpuscular stream structure in order to understand the "probe" measurements of the magnetic field and the plasma in the interplanetary medium and circumterrestrial space which were made by cosmic rockets and AES. The number  $A = \frac{\epsilon_M}{\epsilon_K} = \frac{H^2}{4\pi\rho V^2} > 1$  or  $\gg 1$  holds in the solar atmosphere (in the active region where a geoeffective corpuscular stream is generated), in the interplanetary medium, and in a large portion of the Earth's magnetosphere. This means that the dynamics of the plasma are determined by the field, not only by its magnitude, but also by its structure, the geometry of the field throughout the entire volume, and its possible changes.

Observations of primarily the magnetic vector, performed on "Mariner-2" and "IMP-1" and others, were used as the basis for two assumptions.

(a) The magnetic field (and probably the plasma) of the corpuscular geoeffective stream corresponds to a stream model consisting of several discrete, large-scale plasmoids ("M-elements") having an eigen quasi force-free magnetic field<sup>1</sup>. This stream structure is a direct result of observed magnetic fields on the Sun and of the mechanism by which the corpuscular stream is generated in the active regions.

(b) The existing schemes for the interaction of the solar corpuscular stream with the magnetosphere of the Earth must be reconsidered, since "probe" observations of the magnetic vector on the periphery of the magnetosphere and in the region closest to the Earth indicate that the magnetic field of the stream plays a significant role (if not a decisive role) in the process by which the corpuscular stream acts upon the magnetosphere.

2. Measurements of the magnetic fields in the active regions of the Sun at the level of the chromosphere have shown (Ref. 1, 2) that between the field vector  $H$  and the velocity vector  $V$  the following relationship holds

$$H = \beta(r) V. \quad (1)$$

An analysis leads to the conclusion that if the parameter  $\beta$  equals

$$\beta = \frac{a}{|H|} \exp\left(-\frac{\lambda^2}{2} r\right), \quad (2)$$

<sup>1</sup> For purposes of brevity, we shall call this a force-free field.

then the field in the chromosphere has a force-free structure - i.e.,  $[\text{rot } \mathbf{H}, \mathbf{H}] = 0$ . Observations, pointing to the validity of relations (2), lead to the conclusion that the force-free fields in the chromosphere may be connected by a force tube with the photosphere, where there is primarily a force field. Isolated force-free fields have also been observed, which are not connected with the photosphere field. examination of the mechanism by which corpuscular streams are generated leads to the conclusion that only discrete plasmoids with eigen force-free magnetic fields (M-elements) can leave the active region.

We must now clarify the meaning of the term, force-free magnetic fields, which we are employing here and which we shall continue to employ in this report. In all cases it is assumed that there is a force magnetic field and a current with a source in a specific limited volume which is usually small (or on a specific surface). In the case of a normal chromosphere (coronal) force-free field, the force source is located below the photosphere. For an isolated plasmoid with almost infinite conductivity, on a specific surface a slowly-decreasing current and a force field, formed previously when the plasmoid field broke away from the active region field, can be studied<sup>1</sup>. The force-free magnetic field  $\mathbf{H}$  is directly connected with this force-field in a limited volume (surface), so that the relationship  $[\text{rot}, \mathbf{H}, \mathbf{H}] = 0$  holds in the entire remaining limited volume of the plasma. The force-free magnetic field, being the most stable, breaks up, thus remaining as a force-free field. The dissociation of the force-free field may be related to both dissipative processes (Joule current losses, etc.) and to the formation of convective instabilities, as well as to other types of instabilities. Thus, for the case  $\text{rot } \mathbf{H} = \alpha \mathbf{H}$ , where  $\alpha = \text{const}$ , the field is unstable according to (Ref. 5), and the time required for the instability to develop is determined by the relationship

/369

$$t_0 \approx 3 \cdot 10^{-9} l_0 n^{1/2} H^{-1} \text{ sec},$$

where  $l_0$  is the characteristic dimension of the volume under consideration (where the field  $\mathbf{H}$  is a force-free field);  $n$  - the plasma concentration per  $\text{cm}^3$ . It can be readily seen that on the scale of solar activity phenomena in the chromosphere and the corona, where  $l_0 \gtrsim 10^9 - 10^{10} \text{ cm}$ ,  $n \lesssim 10^{11} - 10^8 \text{ cm}^{-3}$ ,  $H \sim 10^2 - 10 \text{ oe}$ , the time required for the instability to develop  $t_0$  (in this unfavorable case) is on the order of  $\gtrsim 10^5$  seconds. In the interplanetary medium,  $t_0$  increases by at least two orders of magnitude for M-elements. Thus, if the characteristic time  $t$  of the phenomena we are considering [generation and escape of M-elements in the chromosphere and the corona ( $t \lesssim 10^3 \text{ sec}$ ), M-elements of corpuscular streams moving from the Sun to the Earth ( $t \lesssim 10^5 - 10^6 \text{ sec}$ )] is smaller than  $t_0$ ,

<sup>1</sup> We should note that the formation of such separated magnetic fields, which very frequently are of large magnitude, with plasmoids is frequently observed during chromosphere flares (Ref. 3) and in active prominences (Ref. 4).



the magnetic field can be approximately regarded as a stationary, e-free formation.

3. The over-all macroscopic structure of the corpuscular stream, consisting of individual M-elements, has the following features.

(a) Each plasmoid with an eigen magnetic field is an independent element of the stream, which moves in a radial direction and which retains angular momentum around the Sun. Therefore, the chain of M-elements is distributed along the isochrone, i.e., the Archimedes spiral whose tangent inclination is determined by the radial velocity. The size of each element increases with time, so that the magnetic field of the stream extends into the surrounding, rarefied collisionless plasma, primarily in the direction of the magnetic force lines of the corresponding plasma stream at a velocity of  $V \simeq \langle V_A \rangle \simeq 2.5 \cdot 10^7 \text{ cm} \cdot \text{sec}^{-1}$ .

A supersonic shock magnetic plunger will extend ahead of the M-element boundary and its dimensions can be estimated according to (Ref. 6):

$$\delta \simeq \frac{m_i}{m_e} \frac{c}{\Omega_i} (M_A - 1)^{-2},$$

where  $m_i$  is the mean mass of a stream ion (we have  $m_i \simeq 3/2 m_H$ );  $m_e$  - the electron mass;  $\Omega_i = \left( \frac{4\pi n e^2}{m_i} \right)^{1/2}$  - ion plasma frequency;  $M_A$  - Mach - Alfvén number. In our case, we have  $\delta \lesssim 2 \cdot 10^{11} \text{ cm}$ . The existence of a collisionless shock wave (and not a magnetic plunger), going ahead of the corpuscular stream plasma, was discussed in the works (Ref. 7, 8).

(b) The interplanetary medium surrounding the M-elements (a quiet solar wind connected with the thermal dissipation or with constant expansion of the solar atmosphere) moves in a radial direction from the Sun at a velocity of  $\lesssim 3 \cdot 10^7 \text{ cm} \cdot \text{sec}^{-1} < V_{r, \text{stream}} \simeq 4-6 \cdot 10^7 \text{ cm} \cdot \text{sec}^{-1}$ , and carries along the over-all magnetic field of the Sun, according to (Ref. 9). Due to the presence of an orthogonal field component, interaction occurs between two magnetized streams moving at a relative velocity. This interaction is similar to the interaction in the problem of plasma flow between two cylindrical walls in a magnetic field having a field component which is perpendicular to the plasma flow (Ref. 10). /370  
The problem is complicated by the fact that the motion is pre-Alfvén motion close to the moving boundary of the M-element, where the field is relatively large ( $H \gtrsim 15-20 \text{ } \gamma$ ). At greater distances, the number  $M_A < 2$ , and on the far periphery it can be greater than two. The second complication arises from the necessity of allowing for conductivity anisotropy (the Hall currents become important here). Gas-hydrodynamic flow was computed in order to determine the distribution of the transverse velocity component of the surrounding quiet wind which is carried along (Ref. 10). The final result is shown in Figure 1, from which it can be concluded that the maximum radial velocity in the plasma medium which is carried along is achieved at a considerable distance from the M-elements.

There is clear asymmetry in the velocity distribution of the plasma carried along, which coincides qualitatively with the radial velocity distribution of the plasma and of the magnetic field, according to measurements on "Mariner-2". We should note that in the usual model of a corpuscular stream (the so-called "magnetic bubble" [Ref. 11-13] or the continuous "flow of magnetized plasma" [Ref. 14-16]), it is difficult to obtain this distribution of the field and the plasma velocity. The kinetic energy transmitted by the M-element, by means of the magnetic field, to the surrounding plasma on the entire path from the Sun to the Earth (for  $t \approx 3.7$  days in the case of  $V_r \approx 5 \cdot 10^7 \text{ cm} \cdot \text{sec}^{-1}$ ) does not exceed 10% of the M-element energy which equals  $\geq 10^{29}$  erg.

(c) There must apparently be a magnetic field which is curved along the isochrone throughout the entire extensive (in the  $\geq 2 \cdot 10^{13} \text{ cm}$  cross section) "peripheral" portion of the corpuscular stream, beyond the limits of the M-elements. If the model under consideration is valid, the direction of this magnetic field must correspond to the magnetic polarity of the M-element sequences. In accordance with the present scheme for stream generation on the Sun, the latter retain a polarity corresponding to the effective magnetic dipole polarity of the active region. Thus, throughout the entire stream periphery, the magnetic force lines may be directed either from the Sun (if the corpuscular stream in the given solar cycle (No. 19) has left the active region of the N-hemisphere), or toward the Sun (if the corpuscular stream is generated in the S-hemisphere). The structure of the corpuscular stream field was analyzed in the second, <sup>a</sup> 371 more comprehensive publication of data on the magnetic vector measurements performed on "Mariner-2" during the perturbed period between October 7 and October 10, 1962 (Ref. 17) (see below). We need only note that, as can be seen from Figure 2, throughout the entire initial (from 13 hours 30 minutes - the beginning of information - to 14 hours 40 minutes - the boundary ahead of the magnetic plunger) and extensive peripheral regions (from 7 hours 50 minutes, on October 8, to 11 hours 20 minutes on October 9 - the end of information) the field vector projection in the ecliptic plane was directed toward the Sun, and was distributed along the isochrone corresponding to  $\langle V \rangle \sim 3.6 - 6 \cdot 10^7 \text{ cm} \cdot \text{sec}^{-1}$ . A comparison of the geomagnetic perturbation on October 7-9 with the active regions on the Sun (Ref. 18) shows that in this case the corpuscular stream could only leave the active region ( $\phi_0 = 8^\circ \text{N}$ ,  $L_0 = 258^\circ$ ) of the Sun in the northern hemisphere, which corresponds to the force line directions toward the stream periphery with S-N-polarity of M-stream elements.

Magnetic vector observations performed on "IMP-1", when it remained beyond the boundary of the magnetosphere and of the shock wave front, may be used to determine the prolonged (for several days) retention of the magnetic force line directions toward the periphery of the corpuscular streams and the shift in the field direction (from the Sun or toward the Sun), depending on which hemisphere (N or S) the corpuscular stream leaves from. The study (Ref. 19) discovered a direct connection between the interplanetary field and the magnetic fields on the Sun, and - based

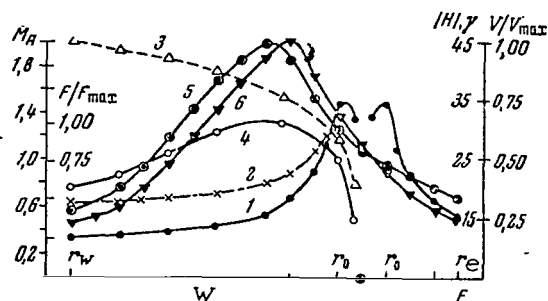


Figure 1

### Distribution of Main Corpuscular Stream Parameters Based on its Transverse Cross Section

The distances from the stream axis are given along the horizontal and are designated by double circles;  $r_0$  - characteristic dimension of the M-element; E - eastern section of the stream; W - western portion of the stream;  $|H|$  - force-free field modulus (1 - non-deformed field, 2 - allowance for deformation of the accompanying plasma);  $M_A$  - Mach-Alfven number (3);  $F/F_{\max}$  - relative force related to magnetic viscosity and formed when the accompanying plasma is carried away (4);  $V/V_{\max}$  - relative radial velocity of the plasma (5 - calculated, 6 - mean curve for four corpuscular streams observed on "Mariner-2").

on extensive observational material compiled over several months - the authors determined the direction of the interplanetary field from the Sun or toward the Sun (along the isochrone, see Figure 1 in [Ref. 19]). /372  
The length of time ( $\geq 4$  days) during which one magnetic field direction is maintained is determined in this same study by a cross-modulation analysis (see Figure 2 [Ref. 19]) of the interplanetary field direction with respect to the selected polarity of the magnetic fields on the Sun. It can be readily seen that the prolonged retention of the interplanetary field direction does not correspond in any way (as the authors have verified) to the normal, approximately daily (and by no means more!) polarity shift of the magnetic fields of active regions in the center of the solar disc.

We investigated the magnetic vector directions in the interplanetary medium for all 13 days encompassed in the publication of magnetic observations performed on "IMP-1" (more than 3,000 determinations of the magnetic vector) (Ref. 20, 21). Due to the low solar activity during these observations (December, 1963-February, 1964), a comparison may be made between the predominant directions of the magnetic fields, according to "IMP-1" measurements, and the active regions in the N- or S-hemisphere, which are responsible for the so-called M-streams. In almost all of these cases it

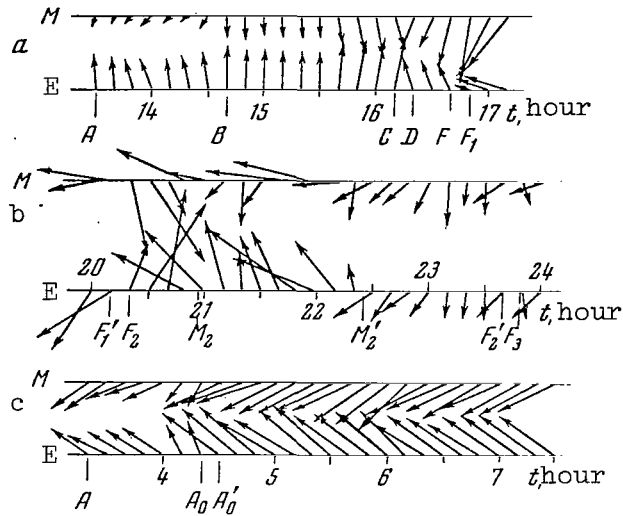


Figure 2

#### Vectors of the Magnetic Field Observed on "Mariner-2"

(M - in a plane perpendicular to the ecliptic, E - in the ecliptic plane; Direction toward the Sun on the right) for three periods.

a - October 7, 1962; A - beginning of information, BC - assumed shock front, DF - intermediate zone,  $F_1$  - boundary of the first M-element; b - October 7, 1962;  $F_1'$  - boundary of the first M-element,  $F_2$  - boundaries of the second M-element,  $F_2$  -  $M_2$  - region of boundary force field,  $M_2'$  - region above core of M-element,  $F_3$  - boundary of the third M-element; c - October 9, 1962, region of western stream periphery; A - beginning of period,  $A_0$ ,  $A'_0$  - characteristic changes in direction of vector oriented along the isochrones in the region of maximum radial plasma velocity. World time.

may be assumed that the Earth is located at the far-removed or close periphery of the corpuscular streams. Corroboration is thus provided for the rule stating that magnetic force lines are directed from the Sun at the periphery of a corpuscular stream from the N-hemisphere, and from regions in the S-hemisphere they are directed toward the Sun. This can be seen from the data presented in Figure 3.

It should be noted that a change in the opposite direction of the force lines for the stream field - which would be expected from the corpuscular stream model of the "expanding bubble" type (Ref. 11-13) - does not agree with the observations on "IMP-1". A change in direction according to this model could not occur more frequently than 0.5 - 1 days (for a radial stream velocity of 400 - 800 km·sec<sup>-1</sup>), which

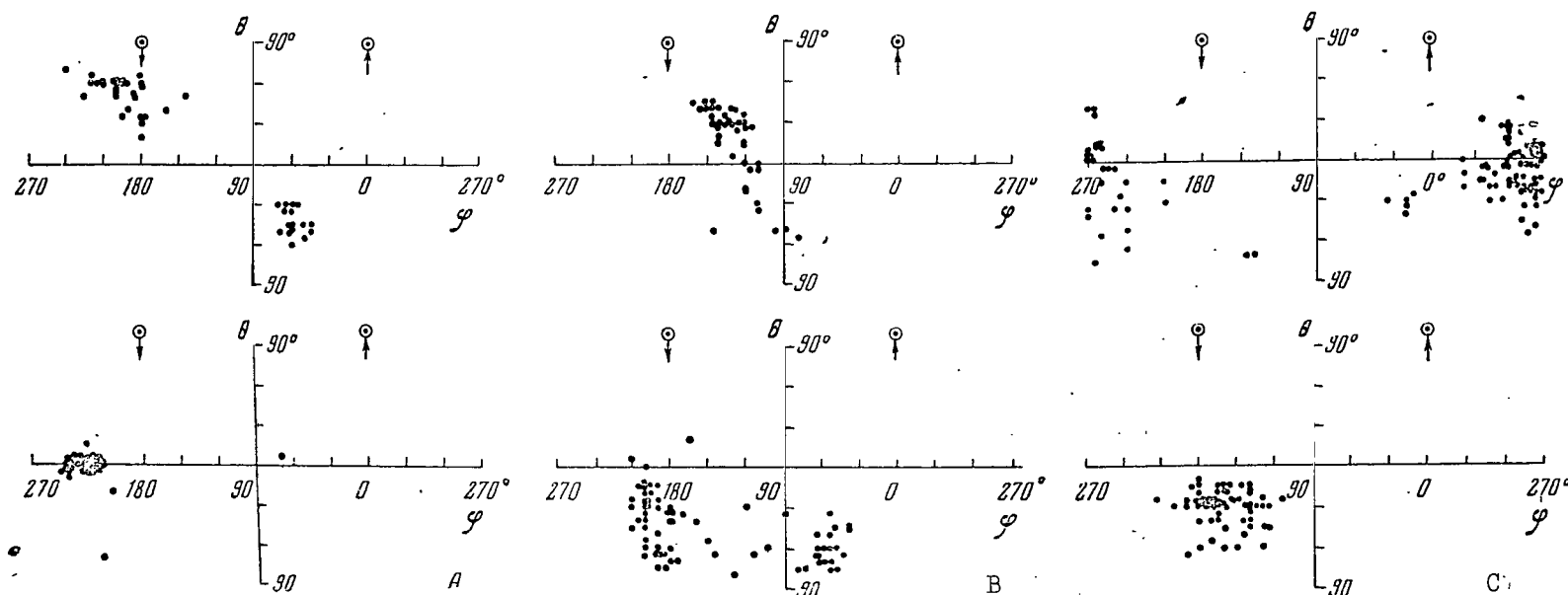


Figure 3

Relationship of Controlling Field Vector Angles on "IMP-1" ( $\theta$  - in a Plane Perpendicular to the Ecliptic,  $\varphi$  - in the Ecliptic Plane)

$\theta = 0^\circ$ ,  $\varphi = 0^\circ$  - direction toward the Sun;  $\theta = 0^\circ$ ,  $\varphi = 180^\circ$  - direction from the Sun;  $\theta > 0$  - toward the North,  $\theta < 0$  - toward the South. Upper series - December 19-20, 1963, lower series - January 20, 21, 1964; A - on the boundary and within the magnetosphere, B - in the transitional region (between the magnetosphere boundary and the shock wave front), C - in the interplanetary medium, on the periphery of the corpuscular stream. This notation was used in Figures 7-11.

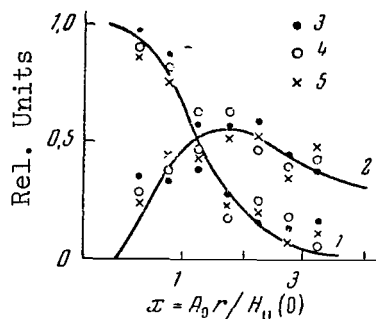


Figure 4

Comparison of Calculated Model for Force-Free  
Field With Field Component Values  $H_{||}$  and  $H_{\perp}$   
Measured on "Mariner-2"

The relative distances from the M-element axis  
are plotted on the abscissa axis; relative values  
are plotted on the ordinate axis.

1 -  $H_{||}/H_0(0)$ ; 2 -  $H_{\perp}/H_{||}(0)$ ; 3 - first element;  
4 - second element; 5 - third element.

strongly contradicts the observations. For a stream model of the "continuous flow" type, reversal of the magnetic field direction cannot be expected in general. Thus, experimental data on the peripheral stream region closely coincide with the stream model which we have considered. As has already been indicated (Ref. 22), the entire outer region (associated with the motion of M-elements) of a corpuscular stream with a rarefied plasma where the force-free magnetic field has a quasi cylindrical form with amplitude modulation of the field reflecting the closed fields of far-removed M-element chains - represents the phenomenon which is usually called "the perturbed solar wind".

The fact that the magnetic field on the stream periphery is not simply an extended field which is connected with the Sun is also shown by analyzing the stability of this type of plasma stream. Close to the Sun, where the customary magneto-hydrodynamic approximation is employed, a magnetized corpuscular stream is of necessity agitated at a distance of  $\sim 2 - 3R_0$ , as has been shown in (Ref. 23). Far from the Sun, the plasma jet stream in the outer field (the active region field) has of necessity rotary instability (Ref. 24). However, observations on "Mariner-2" from October 7-9, 1962, point to modulation of the field vector magnitude and direction on the stream periphery (and not rotation!), which reflects closed magnetic fields of far-removed M-elements. In this case (a direct connection between the stream periphery field and the M-elements), there is no rotary instability.

4. The first incomplete publication (Ref. 25) of data derived from measurements on "Mariner-2" of the magnetic vector, for 7 hours of

observations on October 7, 1962, during a perturbed period, was used to formulate a spatial model of the central section of a corpuscular stream (Ref. 26). Two structural M-elements of the stream may be distinguished, in which the magnetic field has a force-free nature. A similar analysis based on the more comprehensive publication of data derived from field and plasma measurements on "Mariner-2" (Ref. 17) has made it possible to formulate the field structure of individual M-elements. Allowance was thus made for the "nonaxial passage" of "Mariner-2" through the corpuscular stream (Ref. 7). With this fact taken into account, it was possible to distinguish three sections in which the field was recorded (from 16 hours 50 minutes to 20 hours 10 minutes, from 20 hours 20 minutes to 23 hours 40 minutes on October 7, 1962, and from 23 hours 50 minutes on October 7 to 2 hours 50 minutes on October 8, 1962), where the field structure corresponded to the field of a force-free toroid. /374 .

Data presented in Figure 4 corroborate this assumption. The components  $H_{||}$  and  $H_{\perp}$ , recalculated for the mean quantities, for three plasmoids (in relative quantities) were compared with the theoretically calculated quantities of the force-free field components. The satisfactory agreement between the calculated and experimental values of the field components (just like the energy criterion employed for this purpose in [Ref. 26]) corroborates the fact that M-elements with force-free magnetic fields are observed in the solar stream. The field values at the boundary of the M-elements were not taken into account in these computations because, judging from the sharp rotation of the field vector (see, for example, the region  $F_1F_2$  in Figure 2), there must be a force boundary current at these locations. This may also be verified by analyzing the detailed measurements presented in (Ref. 25) of the radial velocity component of the plasma at eight energy levels of the plasma electrostatic analyzer. The variation in the plasma velocity recording, which is given in Figure 11 in (Ref. 25), during the perturbation examined from 14 hours on October 7 to 6 hours on October 8 may be employed to formulate the relative "spectrum" of plasma velocities (energy) for several moments in time. Figure 5 presents examples of these "spectra" for times corresponding to peripheral stream regions, and for a region corresponding to the M-element boundary. The appearance of a second maximum on the "spectrum" curve may serve as an indication of the occurrence of a "force current" in this region.

The studies (Ref. 7, 8) advanced the assumption that the magnetic field is simply a turbulent stream field, according to measurements on "Mariner-2" in the zone where it is largest. In our opinion, such an interpretation of measurements on "Mariner-2" encounters several difficulties and contradicts the observations. Employing the concepts of the interstellar gas turbulence (Ref. 27), which in the last analysis are applicable for the interplanetary medium, one can determine, for example, the inner scale of turbulence, i.e., the extremely small characteristic size of the ionized gas under consideration, beyond whose boundaries the motion is turbulent. Employing the known relationships of (Ref. 27), we find that for a concentration of  $n \sim 10 \text{ cm}^{-3}$ , a field of  $H \sim 10^{-4} \text{ oe}$ , a reduced magnetic viscosity of  $\nu'_m \approx 10^{19} \text{ cm}^2 \cdot \text{sec}^{-1}$  (as is known, the largest

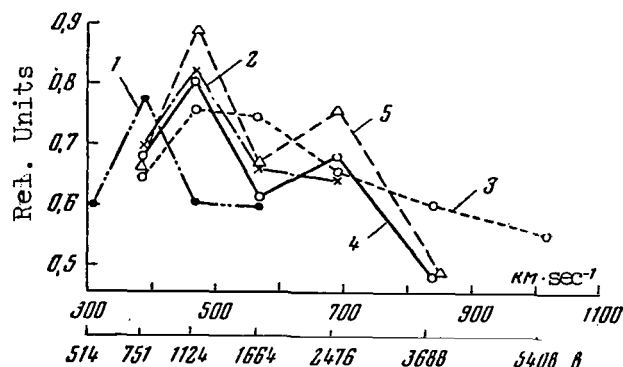


Figure 5

"Spectra" of Radial Plasma Velocities Based  
on Measurements on "Mariner-2"

The velocities (in  $\text{km}\cdot\text{sec}^{-1}$ ) and the electrostatic analyzer potential values corresponding to them (in volts) are plotted on the abscissa axis; relative values are plotted on the ordinate axis.

1 - for 14 hours, October 7; 2 - for 16 hours, October 7; 3 - for 2 hours, October 8; 4 - for 20 hours 15 minutes, October 7; 5 - for 16 hours 45 minutes, October 7, 1962. Curves 1-3 pertain to the stream periphery; 4,5 - to the M-element boundaries where "force currents" flow.

magnitude of magnetic viscosity in a direction which is perpendicular to the field must be chosen), and for a gas velocity of  $\sim 5 \cdot 10^7 \text{ cm}\cdot\text{sec}^{-1}$ , the characteristic inner turbulence scale is  $\geq 10^{13} \text{ cm}$ . This exceeds by almost three orders of magnitude the size of field nonuniformities in a corpuscular stream, if it is assumed that they result from turbulence. If all observed changes in the magnetic field were related to turbulence, then (in the case of developed isotropic turbulence) for the characteristic functional  $L = H_{\perp}^2 - H_{\parallel}^2$  we would have to obtain a constant quantity along the measurement trajectory  $|L| \approx H^2$  and  $\delta L < 0$  which determines the turbulence instability. For a force-free field satisfying the condition  $\underline{j} = \alpha \underline{H}$  where  $\alpha = \text{const}$ , the values of  $L$  must everywhere equal zero. An estimate, performed for the three M-elements under consideration observed by "Mariner-2", has shown that  $0 \leq L < H_{\parallel}^2$ . This indicates that the field is not turbulent (because  $\delta L > 0$ ) and is stable on the average, and that the parameter  $\alpha$  is a function of the coordinates in the case of a force-free field structure<sup>1</sup>. The large-scale structural nature of the magnetic

<sup>1</sup> This assumption was formulated in computations of a force-free field in (Ref. 26) when measurements on "Mariner-2" were analyzed.



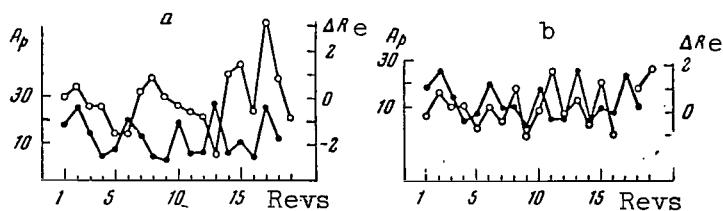


Figure 6

Connection Between Deviations in the Magnetosphere Boundary Positions and the Shock Wave Front From the Corresponding Mean Positions and the Level of Geomagnetic Perturbation

a - based on data pertaining to the entrance of "IMP-1" into the magnetosphere from a turbulent region.  $\Delta R_e$  (light circles) - deviation in the corresponding boundary from its mean position indicated in Figure 28 in (Ref. 20), scale in Earth radii - on the right;  $A_p$  (dark circles) - index of geomagnetic perturbation, scale in units of  $A_p$  - on the left. The number of revolutions for "IMP-1" from the work (Ref. 20) is given below.

field within the limits of the M-elements by no means excludes the occurrence of an unstable field in the collisionless plasma of a corpuscular stream. The fact must also be taken into account that within the limits of the M-elements, where  $A = \epsilon_M / \epsilon_K > 1$  (in the coordinate system connected with the M-element), the magnetic field geometry of the M-element is a decisive factor in the stability and over-all structure of a plasmoid. Therefore, continuously - recurring field instabilities peculiar to a magnetized, rarefied plasma (Ref. 6) will appear and will extend along the field, without changing the over-all macroscopic structure peculiar to a corpuscular stream. In particular, this represents one approach to solving the problem of the corpuscular stream structure (based on experimental data), where the measured magnetic field vector is the main decisive parameter. We would like to point out that in all the "probe" measurements in the interplanetary medium magnetic measurements providing the total magnetic vector at a given point yield the greatest amount of information, whereas only the parameters of primarily only one radial component are measured for a plasma. These assumptions remain in force to a significant extent, based on an analysis of measurements on "IMP-1".

5. It can be concluded from the information presented above regarding the structure of the corpuscular solar stream that the magnetic field of a stream, by means of which a portion of the energy of

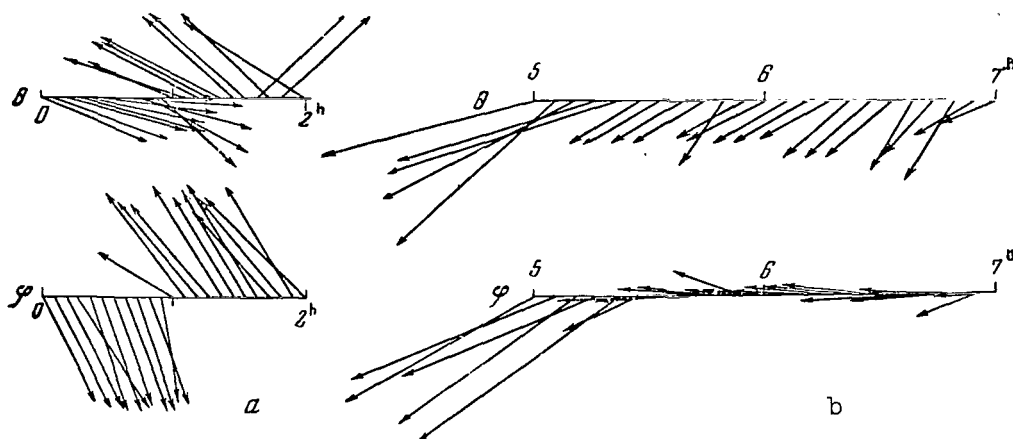


Figure 7

## Field Vectors on "IMP-1"

Time (world time) is given on the horizontal axes. a - December 20, 1963, the Earth is located in a stream from the active region in the S-hemisphere of the Sun (region of tangential discontinuity); b - January 21, 1964, the Earth is located in a stream from the active region in the N-hemisphere of the Sun (region of stationary shock wave). Sun is on the right.

a moving solar plasma is transmitted to the magnetosphere, must play a significant role (if not a decisive role) in the process by which energy is transmitted from a solar stream to the magnetosphere. This group of problems was discussed in the works (Ref. 22, 28, 29). Unfortunately, the extensive literature on the interaction of a corpuscular stream with the Earth's magnetosphere does not, as a rule, examine the role of the interaction of the stream magnetic field in this process. This problem /376 is complicated by the fact that several phenomena observed by means of satellites and rockets (a stationary shock wave on the diurnal side, non-linear phenomena, plasma heating, etc. between the shock wave front and the magnetosphere boundary, etc.) can be explained both by the flowing of a supersonic plasma stream around the Earth, and by "the impact" (or by the relatively rapid change at the magnetosphere boundary) of the magnetic field against the rarefied plasma (see, for example, the laboratory studies (Ref. 30) on magneto-hydrodynamic pinching and heating of a plasma). However, it is difficult (if not impossible) to understand the existing "probe" measurements of the magnetic field at the boundary of the Earth and within the magnetosphere, if allowance is not made for the decisive role of the magnetic field in the solar stream - magnetosphere interaction. This can clearly be seen from the following statements.

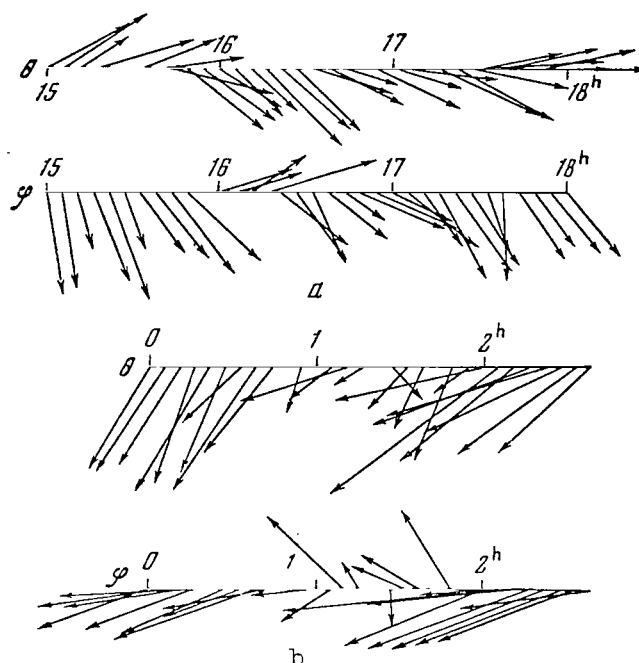


Figure 8

Field Vectors Based on Data From "IMP-1" in the Region Between the Magnetosphere Boundary and the Shock Wave Front

Time (world time) is plotted on the horizontal axes.  
 a - December 19, 1963, the Earth is located in a stream from the active region in the S-hemisphere of the Sun; b - January 21, 1964, the Earth is located on the periphery of a stream from the active region in the N-hemisphere of the Sun (Sun is on the right).

(a) The deviations from the mean positions of the observed boundaries of the magnetosphere and a shock wave front, determined on "IMP-1" (Ref. 20), can be compared with the index of geomagnetic perturbation  $A_p$  at times which are close to the satellite intersection of the boundaries on the ascending or descending portion of a revolution. This comparison, which is shown in Figure 6, demonstrates the fact that changes in the magnetosphere boundary coincide with geomagnetic perturbation, since for the shock wave front position there is an anti-correlation (see revolutions No. 5-14) for those azimuths of the satellite trajectory axis which are close to the average (passing along the isochrone) direction of the stream magnetic field in the ecliptic plane. In our opinion, the latter fact points to the decisive role of the magnetic field of a stream in determining the position of the shock wave front, since all the remaining parameters

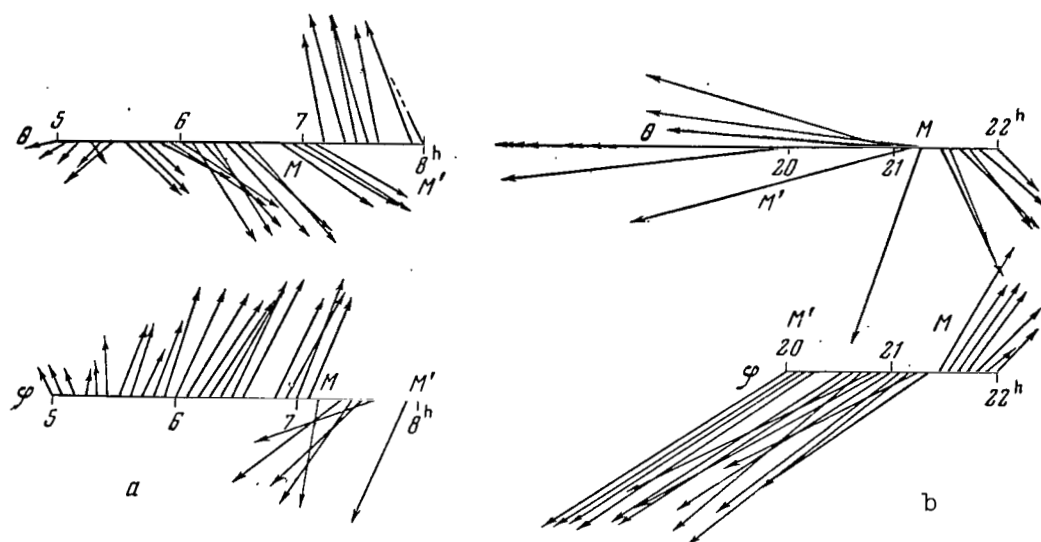


Figure 9

Field Vectors on "IMP-1" in the Region Between the Magnetosphere Boundary (M) and the Shock Wave Front in the Magnetosphere (MM')

Time (world time) is plotted along the horizontal axes.  
 a - December 20, 1963 (vector lengths are reduced four times as compared with the vector length in Figure 9,b), the Earth is located in a stream from the active region in the S-hemisphere of the Sun; b - January 21, 1964, the Earth is located on the periphery of a stream from the active region in the N-hemisphere of the Sun (Sun is on the right).

of the interaction process at these azimuths do not have any distinctive features.

(b) One very characteristic phenomenon can be observed on "IMP-1" magnetograms published for a few geomagnetically perturbed periods (Ref. 20): With the approach of the stream magnetic field (when the magnetic field increases by a factor of 2-3 in the interplanetary medium) a characteristic tangential discontinuity appears, instead of a shock wave, and the "turbulent" transitional zone disappears. This can be clearly seen, for example, by comparing the data from "IMP-1" for December 20, 1963, and January 21, 1964 (see Figure 7,a and 7,b). It can thus be concluded that during the approach of the stream magnetic field there is a pre-Alfven flow around the magnetosphere of the Earth. Since the plasma will not pass through the tangential discontinuity, the stream magnetic field must play a decisive role in the transfer of energy to the magnetosphere.

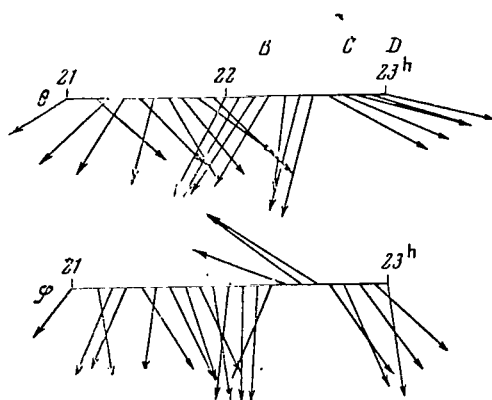


Figure 10

Field Vectors Based on Data From "IMP-1" on December 19, 1963 in the Interplanetary Medium (AB), at the Assumed Boundary of a Stream (BC), Leaving the Active Region in the S-Hemisphere of the Sun, Within the Stream (CD).

Time (world time) is plotted along the horizontals. Sun is on the right.

(c) Figures 3 and 8,a and 8,b show the relationships between the magnetic vector angles and the AES-Sun lines ( $\theta$  and  $\varphi$ ) based on measurements on "IMP-1". These relationships show the dependence of the angles in the transitional zone at the magnetosphere boundary on the direction of the stream magnetic field (this dependence is traced for all the observational days at our disposal).

378

The measured magnetic field vectors over the entire magnetogram (see Figure 8,a and 8,b) are formulated for two characteristic days (December 19, 1963 and January 21, 1964). These days can be used to compare the solar phenomena with the observations far beyond the magnetosphere boundaries, and an opinion can thus be formulated regarding the continuation of the Earth's magnetosphere on the periphery of corpuscular streams leaving the active regions of the N- (for January 20, 1964) and S- (for December 19-20, 1963) hemispheres. The difference between phenomena at the magnetosphere boundary (Figure 9,a and 9,b), which indicate the deep penetration of the stream field, follows from this. It can thus be seen that in the transitional zone and close to the magnetosphere boundary there is a characteristic rotation of the field vector. This is similar to what must be observed when a magnetic plunger moves in a magnetized plasma (simple Alfvén rarefaction waves, rotational discontinuity and shock waves). At the same time simple contraction waves are lacking which would have to exist if the leading stream plasma plays a decisive role. This provisional, but important, conclusion regarding the nature of instabilities in the transitional zone requires verification by additional observational data on the field and plasma in a transitional region, particularly

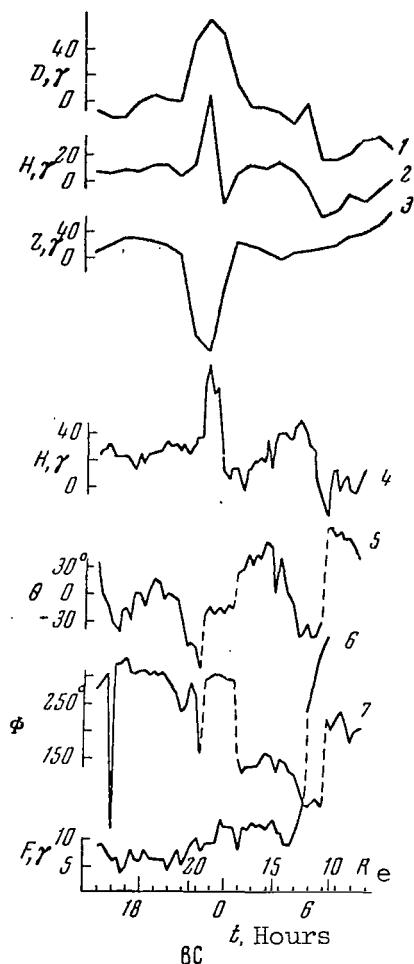


Figure 11

Magnetogram Recordings on the Earth Showing the  
Magnetosphere of the Earth Passing Through the Stream Boundary (BC)

1-3 - data from the Murmansk Observatory; 4 - variation H in the  
Leningrad Observatory; 5-7 - traces from magnetogram on "IMP-1".  
World time.

during geomagnetic perturbations.

(d) At the present there are a large number of observations of the magnetic field in the interplanetary medium and at the magnetosphere boundary, which point to a direct correlation between field variations observed in the interplanetary medium and on the surface of the Earth. This was established by observations on "Pioneer-5" (Ref. 31), "Explorer-12" (Ref. 32), "Mariner-2" (Ref. 22) and others. From this point of view, one of the observations of a sudden commencement of a geomagnetic perturbation on December 2, 1963, performed on "IMP-1" at a distance of  $\sim 2 \cdot 10^9$  cm (i.e., far beyond the magnetosphere boundary

/379

and for  $\sim 3$  minutes at observatories on the Earth, is of great interest.

An attempt may be made, as is frequently done, to explain the correlation (in any event, with reference to rapid field changes with frequencies of  $\omega \gtrsim 10^{-2} \text{ sec}^{-1}$ ) between extraterrestrial and terrestrial field variations by the propagation of transverse hydromagnetic or shock waves from the magnetosphere boundary toward the Earth. However, the simple propagation of hydrodynamic waves toward the Earth can be complicated by the following factors:

(a) Due to the decomposition instability of Alfvén waves (Ref. 33) in the magnetosphere and beyond its boundaries, the possibility of total agreement (with phase retention) between extra-magnetosphere and terrestrial field variations becomes unlikely;

(b) According to computations in (Ref. 34), hydromagnetic waves can reach the surface of the Earth only under strictly limited conditions. The presence of an Alfvén velocity maximum in the lower magnetosphere excludes the possibility of the propagation toward the Earth of "slanting" bundles of low-frequency, hydromagnetic waves.

A comparison of observations of field variations on "IMP-1" with field recordings at magnetic observatories provides additional data on the agreement between  $D_1$ -variations and coil-like perturbations during slightly perturbed periods and the field change recorded by "IMP-1".

For example, between 22 hours 18 minutes and 22 hours 42 minutes on December 19, 1963, on "IMP-1", which was located at a distance of about  $18 R_E$  at this time - i.e., it was far beyond the magnetosphere boundaries and the shock wave front - changes in the angles  $\theta$  and  $\varphi$  were observed (Figure 10), which can be interpreted as the boundary of a corpuscular stream passing by "IMP-1". As this lasted for several minutes on the magnetograms of observatories on Earth (Figure 11), sharp changes were noted in elements of terrestrial magnetism. On January 7, 1964, when "IMP-1" was at a distance of about  $30 R_E$  - i.e., in the interplanetary medium - changes in the angles  $\theta$  and  $\varphi$  on "IMP-1" (and simultaneous small changes in the field vector modulus  $F$ ) closely coincided with changes in geomagnetic elements based on data from observatories on the Earth. /380

Thus, comparisons of "probe" and terrestrial observations clearly indicate the decisive role played by the stream magnetic field in the transfer of perturbations to the Earth's magnetosphere. These comparisons indicate that there is direct agreement between the  $D_1$ -variations of the geomagnetic field and the field variation beyond the boundaries of the Earth's magnetosphere. We would like to point out that when the scheme presented in (Ref. 28) for the interaction of the stream magnetic field with the magnetosphere of the Earth is further developed quantitatively, it will explain both the features of the stream field influence indicated above, and the acceleration (complete or partial) of the plasma

in the upper magnetosphere accompanying geomagnetic variations. Allowance must thus be made for the properties of a strongly-magnetized, collisionless plasma of the magnetosphere, resolving penetration, and propulsion in the form of a magnetic plunger of the solar stream field which is outside of the magnetosphere.

In conclusion, the authors would like to express their deep appreciation to V. I. Afanas'yeva, under whose guidance a great deal of material from magnetic observatories on the Earth was utilized in this study, and who also supervised the compilation of illustrations utilizing these data and data from "IMP-1".

#### REFERENCES

1. Ioshpa, B. A., Mogilevsky, E. I., Obridko, V. N. Space Res., 4, 789, 1964.
2. Mogilevsky, E. I., Shelting, B. D. Proc. Internat. Sympos. of Galileo Milano, 1964 (in press).
3. Zirin, H. Astrophys. J., 140, N 3, 1216, 1964.
4. Ioshpa, B. A. Geomagnetizm i Aeronomiya, 3, No. 6, 1125, 1963.
5. Voslamber, D., Callebaut, D. K. Phys. Rev., 128, N 5, 2016, 1962.
6. Sagdeyev, R. Z. In "Voprosy Teorii Plazmy". Atomizdat, No. 4, p. 20, 1964.
7. Sonett, C. P., Colburn, D. S., Davis, Jr., L., Smith, E. J., Coleman, Jr. P. J. Phys. Rev. Letters, 13, N 5, 153, 1964.
8. Ivanov, K. G. Geomagnetizm i Aeronomiya, 1965, (in press).
9. Parker, E. N. Interplanetary dynamical processes. N. Y.-London Internat. Publ, 1963.
10. Kalikhman, L. Ye. Elements of Magnetic Gas Dynamics (Elementy magnitnoy gazodinamiki). Atomizdat, 1964.
11. Gold, T. J. Geophys. Res., 64, N 11, 1665, 1959.
12. Piddington, J. H. Phys. Rev., 112, N 2, 589, 1958.
13. Gold, T. Astrophys. J., Suppl. 4, 406, 1960.
14. Mustel', E. R. Astronomicheskii Zhurnal, 38, No. 1, 28, 1961.
15. Marochnik. L. S. Astronomicheskii Zhurnal, 38, No. 3, 409, 1961.



16. Ivanov, K. G. Geomagnetizm i Aeronomiya, 1965 (in press).
17. Smith, E. J., Davis, L., Coleman, P. J., Sonett, C. P., Smith, E. J. Space Phys., 387, 1964.
18. Afanas'yeva, V. I., Geomagnetizm i Aeronomiya, 4, No. 1, 34, 1964.
19. Ness, N. F., Wilcox, J. M. Phys. Rev. Letters, 13, N 15, 461, 1964.
20. Ness, N. F., Searce, C. S., Seek, J. B. J. Geophys. Res., 69, N 17, 3531, 1964.
21. Ness, N. F. The Magnetohydrodynamic Wake of the Moon. Preprint. 1964.
22. Afanas'yeva, V. I., Kalinin, Yu. D., Mogilevskiy, E. I. Geomagnetizm i Aeronomiya, 4, No. 4, 722, 1964.
23. Dokuchayev, V. P. Astronomicheskii Zhurnal, 39, No. 6, 1009, 1962.
24. Kadomtsev, B. B. In "Voprosy Teorii Plazmy". Atomizdat, No. 2, p. 132, 1963.
25. Snyder, C. W., Neugebauer, M. Space Res., 4, 89, 1964.
26. Mogilevskiy, E. I. Geomagnetizm i Aeronomiya, 4, No. 2, 213, 1964.
27. Kaplan, S. A., Pikel'ner, S. B. The Interstellar Medium (Mezhzvezdnaya sreda). Fizmatgiz, 1963.
28. Mogilevskiy, E. I. Geomagnetizm i Aeronomiya, 3, No. 6, 1001, 1963.
29. Afanas'yeva, V. I., Zhulin, I. A., Kalinin, Yu. D., Mogilevskiy, E. I. Geomagnetizm i Aeronomiya, 4, No. 6, 1127, 1964.
30. Kolb, A. C., Griem, H. R., Lupton, W. H., Phillips, D. T., Ramsden, S. A., McLean, E. A., Faust, W. R., Swart, M. Space Res., 2, 553, 1962.
31. Coleman, P. J., Sonett, C. P., Judge, D. L., Smith, E. J. J. Geophys. Res., 65, N 6, 1856, 1960.
32. Patel, V. L., Cahill, L. F., Jr. Phys. Rev. Letters, 12, N 9, 213, 1964.
33. Galeyev, A. A., Orayevskiy, V. N. Doklady AN SSSR, 147, No. 1, 71, 1962.
34. Sugiura, M. Propagation of Hydromagnetic Waves in the Magnetosphere. Preprint, 1964.

# RECORDING CHARGED PARTICLES WITH AN ENERGY OF 0.1-10 KEV WITH A SPHERICAL ELECTROSTATIC ANALYZER

S. N. Vernov, V. V. Mel'nikov, I. A. Savenko,  
B. I. Savin, and T. I. Pervaya

The first investigations of low-energy charged particles in space <sup>/381</sup> were made with the simplest charged-particle traps (Ref. 1, 2). Subsequent improvement in instrumentation resulted in traps with a special grid to which is applied an a.c. braking potential permitting such traps to measure the differential energy spectrum (Ref. 3). A start has been made on using electrostatic analyzers in conjunction with differential traps to analyze the energy spectrum of low-energy particles (Ref. 4-8). The main element of the analyzer is a spherical or cylindrical deflecting capacitor to whose plates constant voltages are delivered. Particles whose energy lies in a given range can pass through the gap in this type of capacitor. Thus, the feasibility of measuring a differential spectrum is implicit in the very design of the electrostatic analyzer. The potentials on the analyzer deflection plates, in contrast to those on trap electrodes, is significantly less than the respective energy of the particles to be analyzed. This makes it possible to reduce the difficulties associated with designing high-voltage sources. The recording unit of the electrostatic analyzer is protected against direct sunlight.

The present report discusses the design and characteristics of spherical electrostatic analyzers, and also the results of experiments on the satellites "Kosmos-12", "Kosmos-15", and "Elektron-2" (Ref. 6, 9).

## Equipment

Figure 1 shows the analyzer installed on "Kosmos-12" and "Kosmos-15". "Elektron-2" carried two analyzers of a similar type.

The deflecting capacitor plates are supplied with symmetrical voltages which can be switched on during flight in accord with a given program.

The energy  $E_0$  at the passband maximum in the deflecting capacitor geometry shown in Figure 1 is linked with the plate potential differential by the expression  $U(v) = 0.4 E_0(\text{ev})$ .

Following are the characteristics of the "Kosmos-12" and "Kosmos-15" analyzers: Luminosity at passband maximum  $I_0 \sim 0.7 \text{ cm}^2 \cdot \text{sterad}$ ,  $\Delta E/E_0 \sim 30\%$ , geometric factor  $G \sim 0.1 \cdot E_0 \text{ cm}^2 \cdot \text{sterad} \cdot \text{kev}$ , and minimum recordable combined current strength  $I_{\min}(E_0) \sim 1 \cdot 10^7 \text{ l/E}_0 \text{ cm}^{-2} \cdot \text{sec}^{-1} \cdot \text{kev}^{-1}$ . <sup>/382</sup>

On "Kosmos-15" and "Kosmos-12" the analyzer was adjusted for electrons or ions of 1-kev energy. At one of the commutator positions which switches the potentials on the spheres, the spheres are connected to the frame. To prevent ionospheric thermal ions from entering the operational

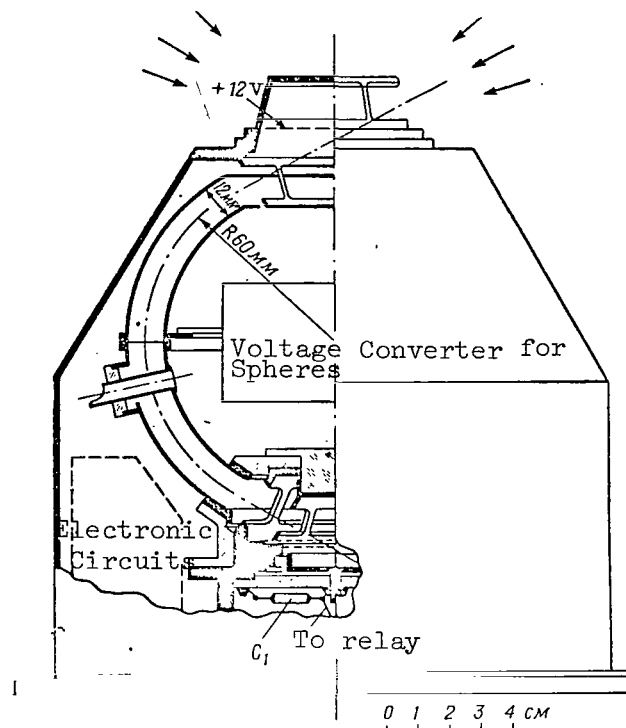


Figure 1

Cross Section of Spherical Electrostatic Analyzer  
Used on Satellites "Kosmos-12" and "Kosmos-15"

Arrows indicate direction of motion of particles  
received by analyzer.

area, the inlet of the analyzer on "Kosmos-15" was covered with a grid with a +12v bias relative to the satellite frame. A Faraday cylinder of duraluminum fastened to a polished plexiglas insulator was used as the particle collector in the analyzer. The inner surface of the Faraday cylinder was ribbed to decrease the outflow of secondary electrons. The bottom of the collector is surrounded by the metal shielding sections of the instrument. The collector inlet window is covered with two grids; the nearer one is connected to the instrument housing, and the further one is kept at -20 v potential relative to the frame. It was experimentally verified that -20 v potential is adequate to suppress secondary electrons from the Faraday cylinder. The grids also attenuate capacitance coupling between collector and spheres, to which high-voltages are periodically switched on. The current of particles falling onto the collector was measured by an electrometric circuit, using the principle of charge accumulation on capacitor  $C_1$  during period  $t$  and conversion of the accumulated charge into a number of pulses (Ref. 10).

The satellite "Elektron-2" contained an instrument consisting of /383

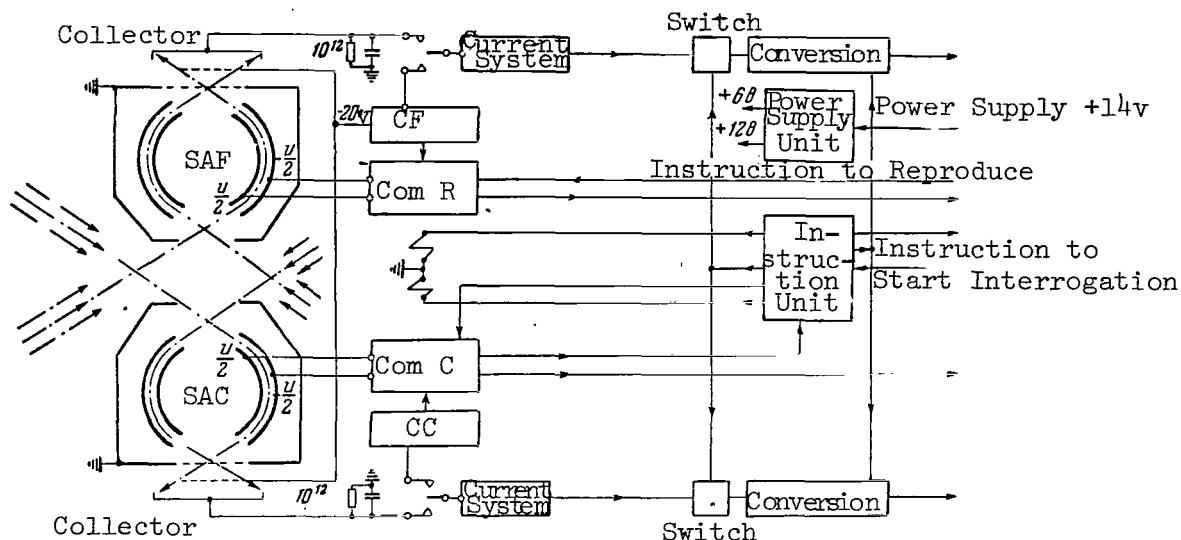


Figure 2

### Block Diagram of Analyzers of Satellite "Elektron-2"

SAF - 0.1-1 kev analyzer; SAC - 1-10 kev analyzer;  
CF, CC - high-voltage converters; ComR, ComC - low-voltage commutators.

two identical spherical analyzers, having the same geometry and operating on the same principle as those on "Kosmos-12" and "Kosmos-15". Figure 2 gives the block diagram of the "Elektron-2" instrument. The system for converting the accumulated charge into binary code had a logarithmic characteristic (Ref. 11).

The "Elektron-2" analyzers were adjusted to particle energies of 0.1, 0.2, 0.4, 1.0, 2.5, 5.0, and 10 kev. The minimum recordable strength (isotropy being assumed) was  $\sim 1 \cdot 10^7 / E_0 \text{ cm}^{-2} \cdot \text{sec}^{-1} \cdot \text{kev}^{-1}$ , which in comparable units is more than one order of magnitude lower than the sensitivity threshold of the analyzer used on the American satellite "Explorer-12" (Ref. 4).

### Results

#### "Kosmos-12", "Kosmos-15" (Ref. 6, 7)

At night the charged particle fluxes of energy  $E_0 = 1 \text{ kev}$  in the  $\Delta E/E_0 \sim 30\%$  range do not generally exceed  $1 \cdot 10^7 \text{ cm}^{-2} \cdot \text{sec}^{-1} \cdot \text{kev}^{-1}$ . On the diurnal side of the Earth the electron and ion fluxes having an energy of 1 kev are no more than several units of  $10^7 \text{ cm}^{-2} \cdot \text{sec}^{-1} \cdot \text{kev}^{-1}$  and are concentrated in definite regions. The observed collector signal is produced chiefly by photoelectrons knocked out of the grids by diffuse ultraviolet; it has sloping maxima which can be explained by the penetration of sunlight into the gap between the spheres, and conforms to

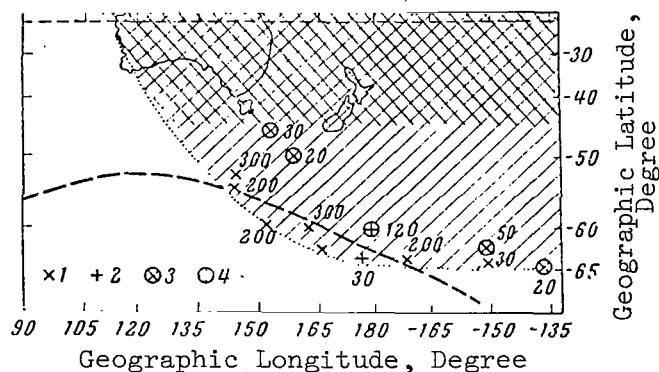


Figure 3

Region of Elevated Intensity of Electrons Having 1 keV Energy in the Area of Maximum Southern Isochasm, From "Kosmos-12" and "Kosmos-15"

#### Analyzer Data

The region of the Earth's shadow is shown for "Kosmos-12" by lines from upper left to lower right, and for "Kosmos-15" by lines from lower left to upper right.

1 - Tuned to electrons; 2 - tuned to ions - "Kosmos-15"; 3-4 - the same for "Kosmos-12"; Figures by the symbols indicate potential differences in the storage capacitor. To convert into intensity in units of  $\text{cm}^{-2} \cdot \text{sec}^{-1} \cdot \text{keV}^{-1}$ , these figures must be multiplied by  $6 \cdot 10^5$ . Broken line indicates position of maximum southern isochasm.

the tapering angular sensitivity diagram of the analyzer. The shape of the peaks and the signal level between them are not uniform, which may be attributed to the contribution of the charged particle streams.

In the region south of New Zealand ( $180 \pm 30^\circ \text{E}$ ,  $60-65^\circ \text{S}$ ) during every flight "Kosmos-12" and "Kosmos-15" recorded electron fluxes of 1 keV energy and an intensity of up to  $1.2 \cdot 10^8 \text{cm}^{-2} \cdot \text{sec}^{-1} \cdot \text{keV}^{-1}$ . The region where these electrons are of elevated intensity is the area of maximum southern isochasm (Figure 3).

#### "Elektron-2" (Period From January 30 to February 20)

Inside the magnetosphere, an extensive spatial region of heightened electron intensity with energies from 0.1 to 10 keV has been discovered outside of the trapped electron zone of energy  $\geq 150$  keV. The region of heightened electron intensity was recorded on practically every revolution, both in the ascending phase of the trajectory (around midnight local time) and in the descending phase (local satellite time near 7:00 a.m.). The electron fluxes in this region reached values of  $\sim 10^9 \text{cm}^{-2} \cdot \text{sec}^{-1} \cdot \text{keV}^{-1}$  with an energy of 0.2 keV and  $\sim 5 \cdot 10^7 \text{cm}^{-2} \cdot \text{sec}^{-1} \cdot \text{keV}^{-1}$  for 10 keV. The absolute flux values, cited here and at a later point, are given with a

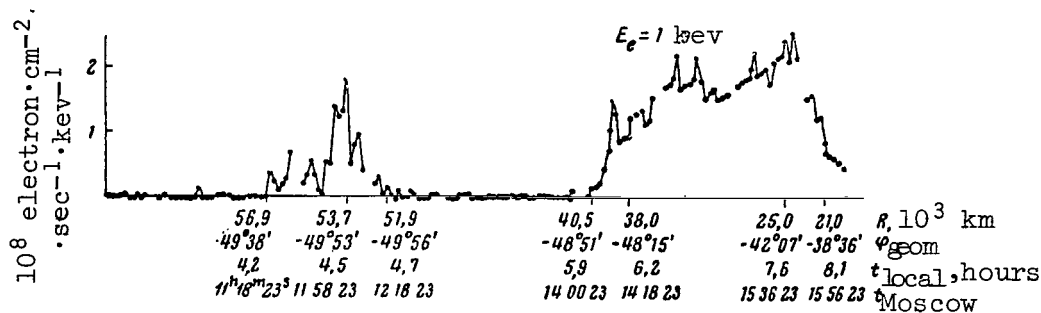


Figure 4

### Intensity of Electrons with Energies of 1 keV in Descending Phase of 14th Revolution (February 12)

mean-square error of  $\pm 50\%$ . The region extends farther for electrons with energies of  $\leq 1$  keV than for those of  $\sim 10$  keV. A tendency for the electron spectrum to soften is noted as the Earth is left behind. The electron streams in the region, and the size of the region, undergo substantial changes with characteristic periods on the order of several days, which are positively correlated with geomagnetic activity. To illustrate, Figures 4 and 5 show analyzer data in the descending phases of the 14th (February 12) and 19th (February 17) revolution. The analyzer readings have been converted into intensity of isotropic electron flux, and have been corrected for the background. The background originated from photoelectrons knocked out of the grids by diffuse solar ultraviolet radiation. Figure 6 gives the fluctuations of the maximum recorded electron intensity in the region between January 30 and February 20. The protracted existence - several days - of the heightened intensity region indicates that the low-energy electrons observed have been trapped in the geomagnetic field. The same figure indicates the boundaries of the elevated intensity region of electrons having 1-10 keV energy reduced to the plane of the magnetic equator along dipole force lines. The boundary chosen was the point at which electron intensity equalled half the maximum intensity in the region. It is evident from Figure 6 that in dipolar coordinates the position and extension of the region on the nocturnal side differs from the position and extension on the morning side. The region begins on the nocturnal side at  $L \sim 3-7$ , and terminates at  $L \sim 7-14$ . The corresponding values of  $L$  on the morning side are 5-13 and 12-20. This morning-night asymmetry may indicate distortion of the Earth's dipole field at great distances on the morning side. The region of heightened electron strength recorded on the nocturnal side is apparently an extension of the so-called "outermost zone".

During several flights, in the region of the orbital apogee sporadic rises were detected in electron intensity with energies of  $\leq 1$  keV. Such a rise was first recorded in the descending trajectory phase of the 14th revolution of February 12, and lasted approximately from 8 hours 20 minutes to 9 hours 20 minutes UT (Figure 4). It is to be noted that at 6 hours before this rise the sudden commencement of a magnetic storm had been

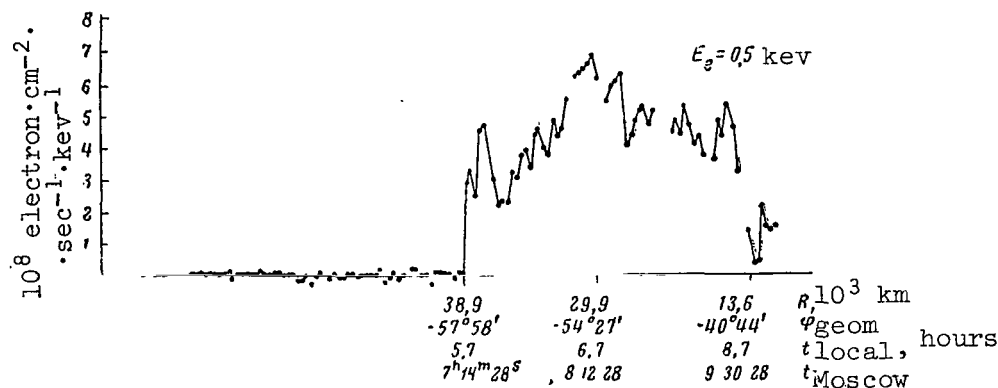


Figure 5

### Intensity of Electrons of 0.5 keV Energy in the Descending Phase of the 19th Revolution (February 17)

recorded. After detection of this intensity rise, the satellite passed through the previously-mentioned region of low-energy trapped electrons. By comparing the intensity and extent of the region on February 11 and 12, we can see that they increased after the storm of February 12. There was an especially severe rise in intensity on the nocturnal side (Figure 6). It is possible that there is a correlation between the appearance of the sporadic electron stream, extension of the region, and electron intensity therein. On February 19 and 20 a sporadic stream of electrons of 200 eV energy was also noticed. The fluxes reached  $\sim 5 \cdot 10^8 - 10^9 \text{ cm}^{-2} \cdot \text{sec}^{-1} \cdot \text{kev}^{-1}$ . The data for the preceding day show that this sporadic stream had apparently begun as early as February 18, but that its intensity was  $< 10^8 \cdot \text{cm}^{-2} \cdot \text{sec}^{-1} \cdot \text{kev}^{-1}$ . Figure 7 shows the flux of February 19. The coordinates of the trajectory 1387 phases, where sporadic fluxes were recorded, are given in the Table.

TABLE

Date (1964)	Start of Recording			End of Recording		
	R, 10 <sup>3</sup> km	φ <sub>geom</sub>	t <sub>local</sub> , hours	R, 10 <sup>3</sup> km	φ <sub>geom</sub>	t <sub>local</sub> , hours
2/12	56.9	-49° 5	4.2	51.9	-50°	4.7
2/19	64.6	-53.4	1.1	63	-71.6	4
2/20	67	-54.8	1.4	68	-61	2

The Table makes it clear that sporadic streams were recorded at southern geomagnetic latitudes of  $\varphi_{\text{geom}} < 50^\circ$  between the midnight and morning meridians at radial distances  $> 9 R_e$ . The readings of the on-board

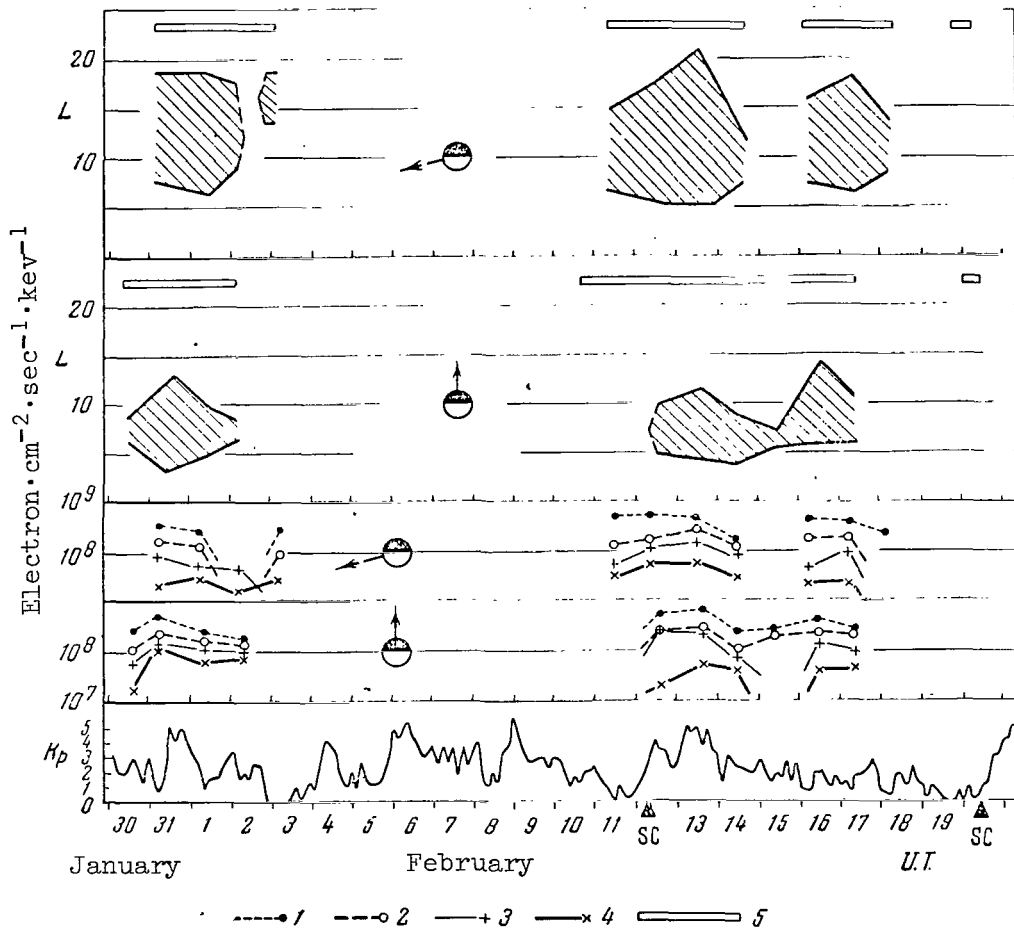


Figure 6

Extension of Elevated Intensity Region and Maximum Fluxes  
in the Region From January 30-February 20

1 - Electrons of  $E_e = 1$  kev; 2 - 2.5 kev; 3 - 5 kev; 4 - 10 kev; 5 - period when there was information on analyzer operation.

magnetometer, as well as present concepts of the structure and dimensions of the magnetosphere, indicate that the satellite "Elektron-2" did not fly beyond the limits of the magnetosphere - i.e., the sporadic streams were detected inside the magnetosphere on force lines going toward the nocturnal side and remaining there during the daily rotation of the Earth. The fluxes of positive ions with energies from 0.1 to 10 kev do not, according to the analyzer data aboard "Elektron-2", exceed  $\sim 5 \cdot 10^7 \text{ cm}^{-2} \cdot \text{sec}^{-1}$ .



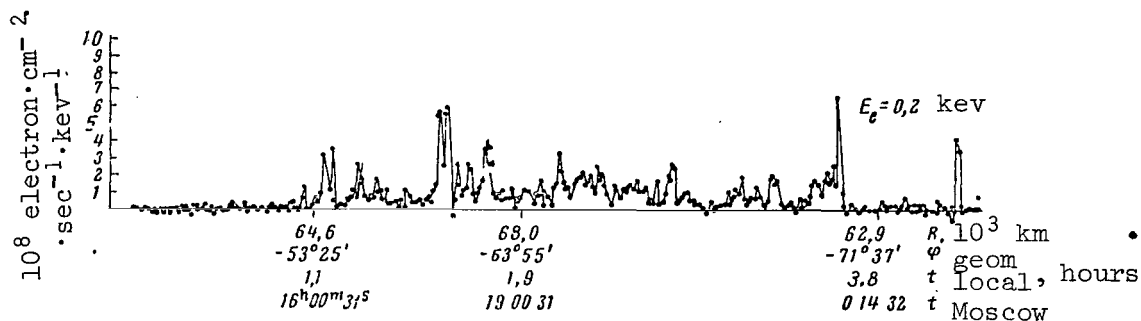


Figure 7

Sporadic Electron Stream of 0.2 keV in Region of Orbital Apogee on 22nd Revolution of February 19

#### REFERENCES

1. Gringauz, K. I., Bezrukikh, V. V., and Ozerov, V. D. In "Iskusstvennyye Sputniki Zemli", No. 6, Izdatel'stvo AN SSSR, p. 63, 1961.
2. Gringauz, K. I., Bezrukikh, V. V., Ozerov, V. D., and Rybchinskiy, R. Ye. Doklady Akademii Nauk SSSR, 131, 1301, 1960.
3. Bridge, H., Egidi, A., Lazarus, A., Lyon, E. and Jacobson, L. Space Res., 5, 969, 1965.
4. Bader, M. J. Geophys. Res., 67, No. 13, 5007, 1962.
5. Neugebauer, M., Snyder, C. W. Science, 138, No. 3545, 1095, 1962.
6. Mel'nikov, V. V., Savenko, I. A., Savin, B. I., and Shavrin, P. I. Geomagnetizm i Aeronomiya, 5, No. 1, 148, 1965.
7. Mel'nikov, V. V., Savenko, I. A., Savin, B. I., Shavrin, P. I. and Markelova, T. N. Geomagnetizm i Aeronomiya, 5, No. 3, 1965.
8. Savenko, I. A., Mel'nikov, V. V., Savin, B. I., and Shavrin, P. I. Izvestiya Akademii Nauk SSR, No. 9, 1965 (in press); Report at the All-Union Conference on Cosmic Rays (Doklad na Vsesoyuznoy konferentsii po kosmicheskim lucham). Apatity, August 1964.
9. Mel'nikov, V. V., Savenko, I. A., and Savin, B. I. Geomagnetizm i Aeronomiya, 1, No. 6, 981, 1961.
10. Goryunov, N. N., Savin, B. I., and Sosnovets, E. N. Kosmicheskiye Issledovaniya, 3, No. 1, 172, 1965.
11. Mineyev, Yu. V., Savin, B. I., Sanin, A. A., and Gadalov, A. N. Geomagnetizm i Aeronomiya, 5, No. 3, 1965.

PHYSICAL PICTURE OF THE FORMATION OF AN ARTIFICIAL RADIATION ZONE DURING THE HIGH-ALTITUDE, AMERICAN THERMONUCLEAR EXPLOSION ON JULY 9, 1962

Yu. I. Gal'perin

As has already been reported (Ref. 1, 2), the satellite "Kosmos-5" /388 employed a device which was designed for measuring soft corpuscular radiation in the upper atmosphere to record the burst of  $\gamma$ -radiation far beyond the visibility limits of the explosion region. With allowance for the altitude of the screening layer  $\delta$  for  $\gamma$ -radiation, the radius of a spherical plasma cloud  $r_{\min}$  - with the center at the point with the coordinates  $\varphi_0, \lambda_0, h_0$ , at which its boundary would coincide with the lower boundary of the visibility zone from the satellite (with the coordinates  $\varphi_c, \lambda_c, h_c$ ) - can be found according to the formulas

$$\left. \begin{aligned} r_{\min} &= -(R_e + h_0) \cos(\theta_0 - \mu) + (R_e + \delta), \\ \cos \theta_0 &= \sin \varphi_0 \sin \varphi_c + \cos \varphi_0 \cos \varphi_c \cos(\lambda_c - \lambda_0) \end{aligned} \right\} \quad (1)$$

$$\cos \mu = \frac{R_e + \delta}{R_e + h_c}; \quad R_e - \text{Radius of the Earth} \quad (2)$$

By employing the computed quantity  $\delta = 64$  km we obtain  $r_{\min} \approx 770$  km for the satellite coordinates, according to (Ref. 1), and the explosion point  $h_0 = 400$  km above Johnston Island (Ref. 3). In order to interpret the burst of  $\gamma$ -radiation, it is very important to know whether the cloud expansion radius of the plasma, resulting from the explosion, exceeds the quantity  $r_{\min}$  - i.e., whether the cloud penetrates the zone of visibility. Let us examine the experimental data on the plasma cloud diameter in the geomagnetic field. Such data can be primarily obtained from observations of artificial aurorae polaris accompanying the explosion.

Photometric observations of the aurorae polaris luminescence in the pre-equatorial regions of the southern hemisphere (Ref. 3) have shown that immediately after the explosion intense luminescence appeared in the band along the geomagnetic meridian of Johnston Island with a width of  $\pm 5^\circ$  longitude. This luminescence could be caused by direct excitation by particles dispersed from the plasma cloud and absorbed in the atmosphere at an adjoining point. Several factors could cause this luminescence: as a result of excitation by energetic photoelectrons formed under the influence of shortwave radiation of the explosion beyond the limits of the plasma cloud. It could also result from discharge in the adjoining region of the ionosphere under the influence of the electric field produced in the force tube containing an expanded plasma cloud and transferred to an adjoining point due to the high electroconductivity of the upper atmosphere along the field, etc. However, in all the mechanisms the diameter of the luminescent region is not less than the cloud diameter (although a very interesting fine structure is observed within the aurorae polaris - for example, narrow rays which are similar to the natural aurorae polaris). It thus follows that the plasma cloud radius

in the horizontal direction along the east-west line does not exceed  $\sim 600$  km.

It is most important to clarify the propagation boundary of a cloud of charged particles moving along the L-envelopes. These data were obtained by measurements performed on the satellites "Traak" and "Ariel" (Ref. 3, 4) by analyzing the intensity distribution in the "second" artificial zone of relativistic electrons injected by fission fragments remaining in the upper atmosphere into the explosion region, after dissipation of the plasma cloud. Since the lower boundary of the artificial zone  $h_{\min} \sim 200$  km above the Johnston Island penetrated only to an altitude of  $\sim 1000$  km, the lower spatial region could only be occupied by "recent"  $\beta$ -decays (Ref. 3, page 64). This made it possible to obtain data on the distribution of fission products during the first and second days after the explosion. It was found that the intensity of the "second" artificial zone sharply decreased for  $L > 1.18$ , since there was a wide intensity maximum between the "second" and main zone (Ref. 3, 4). These results were confirmed by measurements on the satellite "Kosmos-5". The envelope  $L = 1.18$  penetrated to an altitude of  $\sim 700$  km above Johnston Island. Since it would not be expected that these particles would drift due to circulation of the upper atmosphere during the first days, the data presented above indicate that the radius of the force tube containing the main portion of fission products did not exceed  $\sim 300$  km above Johnston Island, the maximum value of  $L \approx 1.18$  (Ref. 4).

/389

Finally, the work (Ref. 5) published a photograph of the luminescent region in the upper atmosphere in the oxygen line  $5577 \text{ \AA}$  above Johnston Island three minutes after the explosion, taken from a distance of  $\sim 1000$  km. The position of magnetic force lines and the explosion point were indicated. Luminescence lasting this period of time could only be caused by  $\beta$ -decays of radioactive explosion products, and consequently the position of the luminescence region reflected the diffusion of fission products in the atmosphere. It can be seen in the photograph that the luminescence continued only in a force tube having a radius of no less than  $400$  km close to the explosion point. These direct data thus closely coincide with the conclusions indicated above, which were obtained by analyzing the measurements of the "second" artificial zone.

Direct observations thus show that the finite radius  $r_k$  of the plasma cloud did not exceed  $600$  km, and possibly even less. The obtained maximum radius of the cloud was less than the finite radius  $R_k$  of the plasma cloud extension in a vacuum (Ref. 6). This indicates considerable energy dissipation of the plasma extending into the ionosphere close to the F-region maximum. The indicated value of  $r_k < r_{\min}$  and, consequently, the cloud as a whole was located below the horizon for the satellite "Kosmos-5". (Therefore, the term " $\gamma$ -glow" was used as a metaphor in (Ref. 1) to designate the burst of  $\gamma$ -radiation).

Nevertheless, fission products undoubtedly penetrated to higher altitudes (and larger  $L$ ), since the radiation zone which was formed extended no less than up to  $L \sim 3.5$  - according to data derived from the satellite "Kosmos-5" (Ref. 2) - and no less than up to  $L \sim 6.5$  - according to data from the satellite "Ariel" (Ref. 4). Figure 1 presents the results derived from formulating model distributions of the counter recording rate on "Kosmos-5", which coincided in the lower sections with measurements on "Kosmos-5" and which were extrapolated to the equatorial plane based on the following: (a) intensity measurements in the artificial zone in 1964 by means of the satellites "Elektron-1" and "Elektron-3", and (b) measurements of the rate at which intensity decreased ("lifetime") on the satellites "Kosmos-5", as well as on "Injun-1" and "Injun-3" (Ref. 7), "Explorer-15", and "Relay-1" (Ref. 8), "Elektron-1" and "Elektron-3" (Ref. 9), and computations (Ref. 3, page 98; Ref. 10). For purposes of comparison, this figure presents the results derived from measuring hard electrons of ( $E \gtrsim 4.5$  Mev) on the satellite "Explorer-15" (Ref. 8). This is a low estimate, since it was assumed that particle concentration in a force tube above approximately  $h_{\min} = 500$  km is constant - i.e., the distribution is isotropic.

As can be shown, the volume  $U(L)dL$  of a radiation zone having the thickness  $dL$  above a certain  $h_{\min}$  is:

$$U(L)dL = \left(4/3\pi R_e^3\right) \cdot \frac{3}{35} \cdot L \cdot \sqrt{\frac{l-1}{l}} \left(16 + \frac{8}{l} + \frac{6}{l^2} + \frac{5}{l^3}\right) dL, \quad (3)$$

where

$$l = L^2 \frac{R_e}{R_e + h_{\min}}.$$

Figure 2 shows a graph of the function  $U(L)$ , together with the model distribution of the recording rate  $\dot{N}_{\text{equa}}$  for 7/9/1962. Figure 2 also presents the total content of electrons trapped in the zone  $nU$  and  $n = \dot{N}_{\text{equa}} \cdot Kc$ , where  $l/K$  is the effectiveness of the counter for the  $\beta$ -spectrum of fission products ( $K = 2 \cdot 10^3 \text{ particle} \cdot \text{cm}^{-2} \cdot \text{imp}^{-1}$ ,  $c$  is the speed of light)<sup>1</sup>. Integration of the quantity  $nU$  over  $L$  gives the total amount of electrons injected into the zone. /390

It was found from the integration that approximately one hour after the explosion there were  $\sim 1.5 \cdot 10^{25}$  electrons having energies of  $> 20$  kev in the artificial zone. It was found that this amount of electrons in the zone was due to the decomposition at the corresponding altitudes (above  $\sim 1200$  km over Johnston Island, i.e., within the limits of visibility from the satellite "Kosmos-5") of fragments from approximately

<sup>1</sup> We have disregarded the possible softening of the fission electron spectrum with an increase in  $L$  (Ref. 3, page 7), since measurements on the satellites "Elektron-1" and "Elektron-3" (Ref. 9) showed that that there is a very intense electron component having a natural origin in this region, which was not excluded from the results (Ref. 3, page 8).

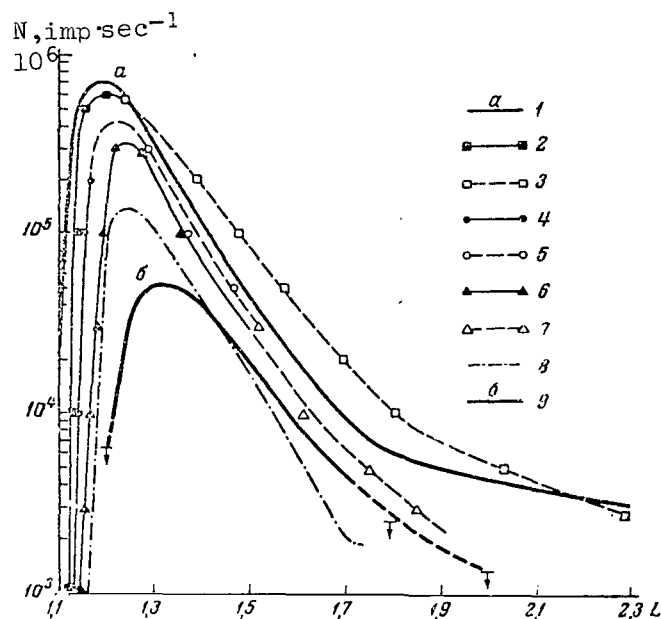


Figure 1

Recording Rate Distribution  $N$  ( $\text{imp} \cdot \text{sec}^{-1}$ ) of a Geiger Counter on the Satellite "Kosmos-5" With Respect to  $L$  in the Equatorial Plane - Model and Measurements (see text) and Measurements on the Satellites "Explorer-15" and "Elektron-1", Normalized to the Same Intensity of the  $\beta$ -Spectrum of Fission

I - Based on data from "Kosmos-5" (1962): 1 - measurements ( $L \lesssim 1.25$ ) and model ( $L \lesssim 1.25$ ), July 9; 2 and 3 - measurements and model on July 10, respectively; 4 and 5 - measurements and model on July 17-19, respectively, 6 and 7 - measurements and model on August 12-October 16, respectively.

II - Based on data from "Explorer-15": 8 -  $E > 4.5$  Mev, January 1, 1963.

III - Based on data from "Elektron-1": 9 -  $E > 1.1$  Mev, February, 1964.

---

$10^{25}$  fissions (Ref. 2) while during the explosion there were apparently about  $2 \cdot 10^{25}$  fissions (Ref. 3, page 25).

The burst of  $\gamma$ -radiation can be measured to obtain the upper limit of time required for these fission fragments to penetrate far beyond the plasma cloud limits. It is most important that for  $\sim 3$  seconds after the explosion there were products of exactly  $\sim 10^{25}$  fissions in the zone of visibility from the satellite "Kosmos-5" (Ref. 2). The quantitative agreement between data on the number of injected fission fragments, based on measurements of the radiation zone and on measurements of the burst of " $\gamma$ -glow", fosters the conclusion that both of these phenomena - " $\gamma$ -glow"

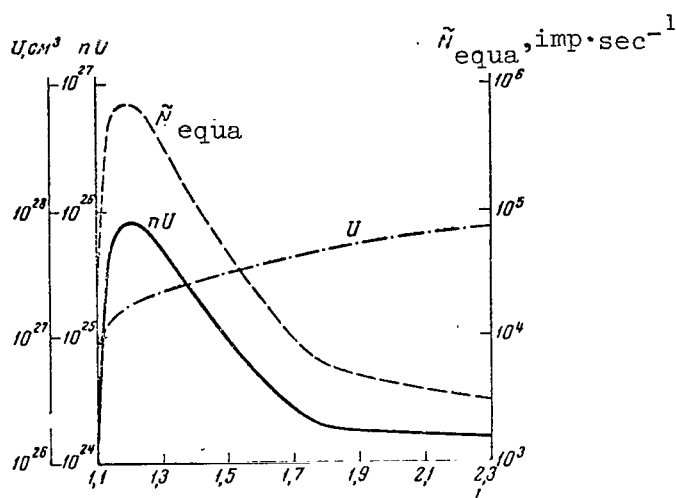


Figure 2

Function  $U(L)$  and also Total Number of Electrons in the L-Envelope  $n(L)$   $U(L)$ . For purposes of Comparison, the Original Model of Intensity Distribution in the Equatorial Plane  $N_{\text{equa}}$  is Given

and the radiation zone - have one and the same cause - decomposition of a small portion of the radioactive fission fragments in the geomagnetic field, beyond the limits of the cloud formed by the explosion. The following mechanisms may possibly lead to the ejection of particles beyond the cloud limits (Ref. 2) (Figure 3). /391

A. The diamagnetic ejection of plasma clusters due to the instability at the plasma-field boundary. In actuality, this boundary curves toward the field, and cannot therefore be stable (Ref. 11). Due to the considerable relaxation and expansion time, the plasma clusters will be additionally ejected toward a decrease in the geomagnetic field - i.e., upward, similarly to the processes of diamagnetic ejection of plasma clusters in the solar chromosphere (Ref. 12); /392

B. The free scattering into the magnetosphere of fission fragments neutralized during the initial stages of the explosion cloud expansion - i.e., up to the stage of "inertial scattering". This mechanism was postulated in (Ref. 4) in order to explain the bursts of the recording rate for approximately 20 seconds after the explosion, which were observed on the satellite "Ariel";

C. The free scattering into the magnetosphere of fission products neutralized due to the recharging of plasma cloud ions with neutral atmospheric particles. Since the number of neutral particles on the fission fragment path, and also the degree of ionization in the atmosphere after

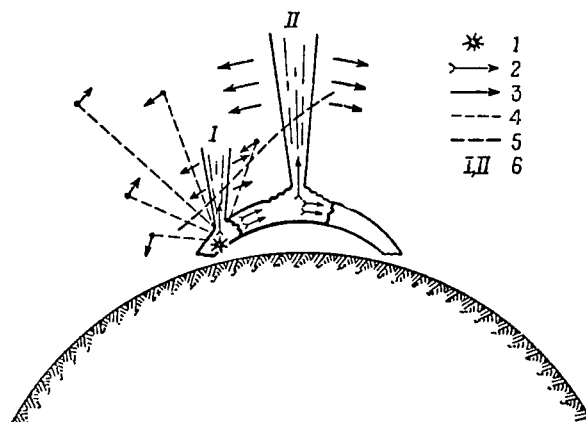


Figure 3

Schematic Drawing of Fission Fragment Distribution  
in the Upper Atmosphere After an Explosion

1 - explosion point; 2 - plasma motion; 3 - trapped particle motion; 4 - neutral particle motion; 5 - line of the horizon for "Kosmos-5"; 6 - eruptive plasma ejections.

the explosion, depends sharply on the velocity vector angle of an ion with a vertical (of the zenith angle  $z$ ), the main portion of recharged ions must move close to the horizontal plane with respect to the explosion point, and must have a certain distribution with respect to velocity  $v_0$ .

It must be taken into account that  $\beta$ -decomposition of each of two fission fragments requires 15 seconds on the average, and the fragment then becomes an ion and is "captured" by the magnetic field. A portion of the fragments thus descends into the dense atmosphere and is absorbed, which causes an additional increase in the intensity of  $\gamma$ -radiation for 10-20 seconds. On the other hand, a certain relative increase in the intensity of  $\gamma$ -radiation must take place for 1-2 minutes, due to the satellite approaching the explosion cloud, and due to the drift to the west - toward the satellite - of ionized fragments captured in the trap after  $\beta$ -decomposition. However, neither of these phenomena is significant for the first  $\sim 200$  seconds. By way of an example, Figure 4 compares the observed counter recording rate  $N$  on "Kosmos-5" during "gamma-glow" with the calculated pattern  $F_v(\Delta t)$  of  $\gamma$ -radiation intensity of fission fragments ejected at the time  $t_0 = 9$  hours 00 minutes 09.0 seconds UT (Ref. 3) with an identical velocity of  $v_0 = 1000 \text{ km} \cdot \text{sec}^{-1}$  and with a  $z$  distribution which is proportional to  $B(z)$  - the Bemporad function, which must be characteristic for recharged fragments. Consideration was only given to the change in the dilution factor due to the cloud expansion (the first 15 seconds) and due to the relative convergence with the

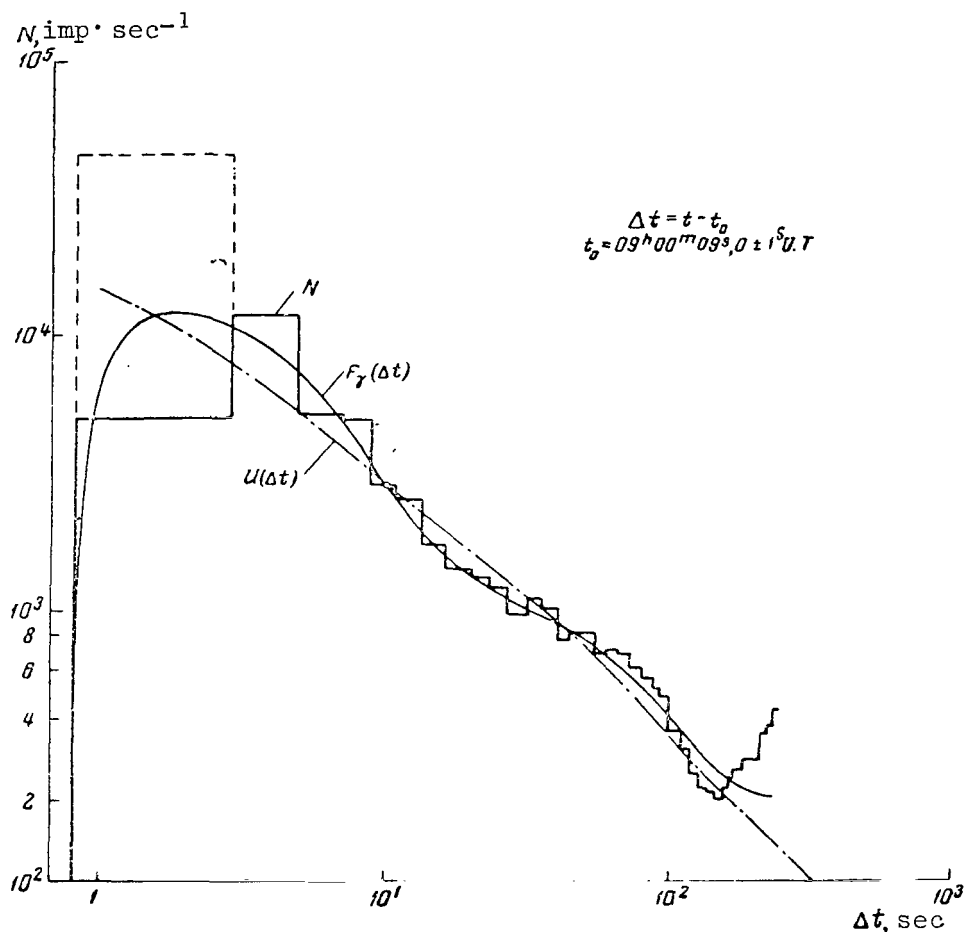


Figure 4

Comparison of the Calculated Variation in Intensity of  $\gamma$ -Radiation from the Time for Overcharged Fission Fragments With a Velocity of  $v_0 = 1000 \text{ km} \cdot \text{sec}^{-1}$  With Observations of "Y-Glow" on July 9, 1962

satellite (for 1-2 minutes). The departure of particles from the zone of visibility, the particle distribution with respect to  $v_0$ , and the effects of  $\gamma$ -radiation scattering in the atmosphere were ignored. Therefore, a comparison of the fine details is arbitrary to a certain extent. However, the qualitative nature of the dependence of  $\gamma$ -radiation intensity on time (the proportionality of  $u(\Delta t)$ , with the exception of the first few seconds [Ref. 2]) depends very slightly on  $v_0$ .

Mechanisms A and B indicated above contribute to the ejection of fission fragments, which may also make a certain contribution to the observed intensity. The aurorae polaris rays, which are directed upward from the equatorial region of the explosion force tube and which are related to the penetration of the plasma, have been actually observed



(Ref. 3).

In conclusion, we would like to express our appreciation to V. I. Krasovskiy, S. B. Pikel'ner, A. S. Strelkov, and Yu. V. Kukushkin for their valuable discussion of the results.

#### REFERENCES

1. Gal'perin, Yu. I., Bulyunova, A. D. Kosmicheskiye Issledovaniya, 2, No. 5, 763, 1964; Space Res., 5, 446, 1965.
2. Gal'perin, Yu. I. Kosmicheskiye Issledovaniya, 3, No. 3, 426, 1965.
3. Operation "Sea Star" (Operatsiya "Morskaya Zvezda"). Atomizdat, 1964.
4. Durney, A. C., Elliot, H. E., Hynds, R. J., Quenby, J. S. Nature, 195, 1245, 1962; Preprint, 1964.
5. U.S. National Report to V COSPAR. Florence, May 1964.
6. Rayzer, Yu. P. Prikladnaya Matematika i Teoreticheskaya Fizika, No. 6, 19, 1963.
7. Hess, W. Space Res., 4, 60, 1964.
8. McIlwain, C. E. Science, 142, 355, 1963; Preprint, March, 1964.
9. Bulyunova, A. D. et al. Present Collection, p. 406; Space Res., 6, 1965 (In press).
10. Walt, M., Newkirk, L. L. Space Res., 5, 458, 1965; J. Geophys. Res. 69, No. 19, 3947, 1964.
11. Artsimovich, L. A. Controlled Thermonuclear Reactions (Upravlyayemyye termoyadernyye reaktsii). Fizmatgiz, 1961.
12. Lifshits, M. A., Pikel'ner, S. B. Astronomicheskiy Zhurnal, 41, No. 3, 464, 1964.

RADIATION RESEARCH ON THE SATELLITE "KOSMOS-17"  
(Summary)

P. V. Vakulov

The AES "Kosmos-17" carried equipment to study radiation of the Earth's radiation zones and primary cosmic radiation at altitudes up to 800 km. The equipment included two scintillation counters and one gas discharge counter.

One of the scintillation counters was located on the outer frame of the satellite and used two thresholds to record electrons with energies greater than 50 and 180 kev and protons with energies greater than 600 kev. Two other thresholds were used to record only protons with energies greater than 5.4 and 8.5 Mev. A second scintillation counter, and also a gas discharge counter, with a thickness of about  $1 \text{ g}\cdot\text{cm}^{-2}$  Al were located under the frame.

The data obtained may be divided into two classes: (1) radiation recorded in the radiation zones, and (2) radiation outside of the radiation zones (cosmic rays and radiation related to them genetically).

Large electron fluxes produced by the American high-altitude nuclear explosion Starfish were recorded in the inner radiation zone. The mean lifetimes of these electrons were determined for different magnetic envelopes. The absolute fluxes of these electrons, as well as the energy spectrum of trapped protons and their fluxes in the inner zone, were obtained.

The regions in space where the satellite recorded trapped radiation were determined. It was found that these regions closely coincide with the regions determined theoretically by an analysis of the L,B-maps.

# RESULTS DERIVED FROM STUDYING THE GEOMETRIC POSITION AND PARTICLE COMPOSITION OF RADIATION ZONES OF THE EARTH BASED ON DATA FROM THE SATELLITES "ELEKTRON-1" AND "ELEKTRON-2"

S. N. Vernov, A. Ye. Chudakov, P. V. Vakulov,  
Ye. V. Gorchakov, S. N. Kuznetsov, Yu. I. Logachev,  
A. G. Nikolayev, E. N. Soskovets, I. A. Rubinshteyn,  
V. G. Stolpovskiy, V. A. El'tekov

The artificial Earth satellites "Elektron-1" and "Elektron-2" were /394  
launched on January 30, 1964 on orbits having the following parameters:

	"Elektron-1" (Low)	"Elektron-2" (High)
Apogee Altitude . . . . .	7.14 thousand km	68.2 thousand km
Perigee Altitude . . . . .	406 km	460 km
Period of Rotation . . . . .	2 hours 48 minutes	22 hours 30 minutes
Inclination Angle of the Orbital Plane . . . . .	61°	61°

The orbits with respect to the Sun were located so that the time when the satellites passed through the apogee corresponded to approximately three hours am local time. The satellites intersected the outer boundary of the radiation zones as they receded from the Earth (forward revolution) at approximately midnight, and as they approached the Earth (reverse revolution) they intersected at 7-8 hours local time. After this the apogee of the satellites shifted to the evening side: for "Elektron-1" at a velocity of ~ 8 minutes per day, and for "Elektron-2" - ~ 4 minutes per day.

Geomagnetic coordinates are used in Figure 1 to show the regions of circumterrestrial space in which data were obtained on the radiation zones. In spite of the fact that the inclination angle of the orbital plane for both satellites toward the plane of the geographic equator was large (61°), during certain revolutions the satellite "Elektron-2" passed through the entire outer radiation zone at small geomagnetic latitudes which did not exceed 20°. The maximum geomagnetic latitudes which the satellites reached on different revolutions changed between 50-72°. The trajectory of the satellite "Elektron-2" was distinguished by the fact that the satellite flew almost along a line of constant L on certain revolutions. Thus, the magnetic field strength B changed by approximately a factor of 2-3, which made it possible to obtain the accurate altitudinal pattern /395 of trapped radiation. In addition, at certain times the satellites passed through the radiation zone region almost simultaneously, which made it possible to study the momentary distribution of particles along the force line. The existence of two satellites with such essentially different

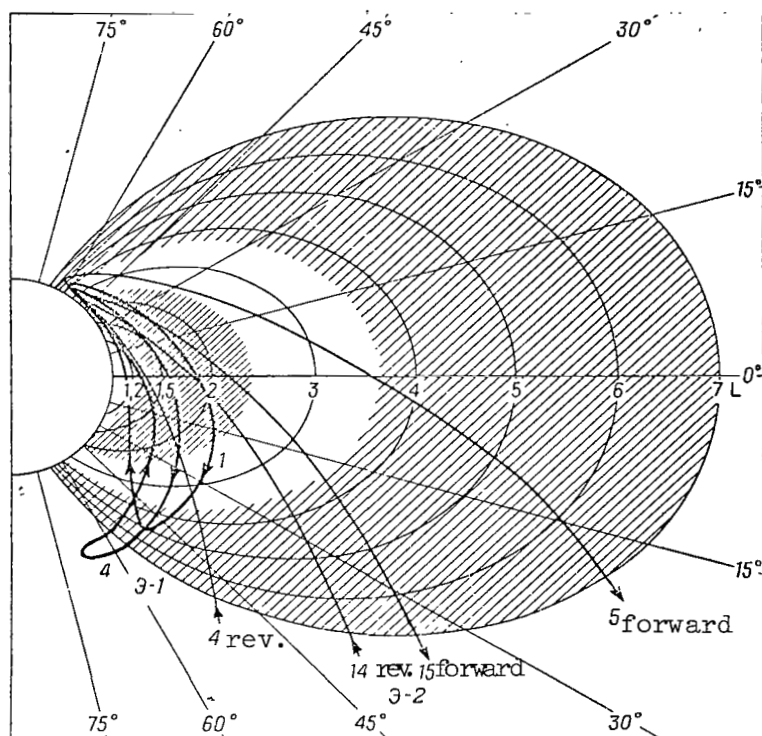


Figure 1

### Trajectory of Satellites "Elektron-1" and "Elektron-2" in Geomagnetic Coordinates

The revolutions closest to the equator and farthest away from the equator are shown for each satellite.

(Number and direction are shown around the satellite.) (N-above)

orbits made it possible to formulate a comprehensive picture of the radiation zones during the 1-2 days of flight.

Apparatus. Several devices which were similar to those employed previously (Ref. 1, 2) were used to study the radiation zones on the satellites.

Figures 2 and 3 show the type of sensors and energy thresholds for recording particles from each of the sensors. In terms of radiation sensor composition, the equipment on "Elektron-1" and "Elektron-2" was completely identical, the only difference being the magnitude of the individual energy thresholds. Due to this fact, it was possible to compare the results obtained at different points in space, and at points where the orbit was intersected, and to control the operation of equipment on both the satellites concurrently. Scintillation, gas discharge, and semi-conductor counters were used as sensors. Figure 4 shows a

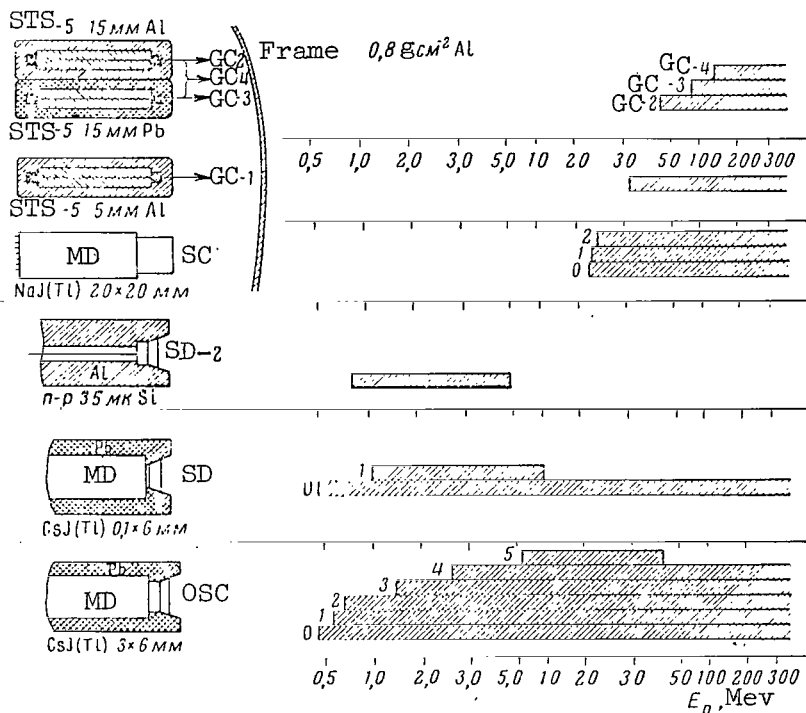


Figure 2

Proton Detectors and Energy Thresholds Above Which Protons May be Recorded

block diagram of the apparatus. All of the gas discharge counters GC and the scintillation counter SC were located within the satellites. An outer scintillation counter OSC, a scintillation proton detector SD-1 and a semi-conductor detector SD-2, were placed outside of the satellite. /397 The SC device and one counter GC-1 operated constantly, and the remaining sensors were divided into two groups which were switched on in succession by commands from the Earth.

All of the electronic components contained semi-conductor elements. Some of these components were employed previously, and were described in the work (Ref. 1). Impulses were accumulated during the time between interrogations of the memory device MD on trigger chains. One of these chains is shown in Figure 5. One feature of this circuit lies in the fact that it has a variable number of preliminary conversion triggers - i.e., the number of triggers before the first interrogation trigger. The number of triggers increases automatically as the impulse recording rate increases. This made it possible to considerably expand the range of measured recording rates using a small number of binary outputs for telemetry (7-8).

Information on radiation was passed to the memory device. A certain amount of information was also obtained by means of the transmitter "Signal".

The rotational periods of the satellites were  $\sim 40$  and  $\sim 120$  sec for "Elektron-1" and "Elektron-2", respectively. When the results are analyzed,

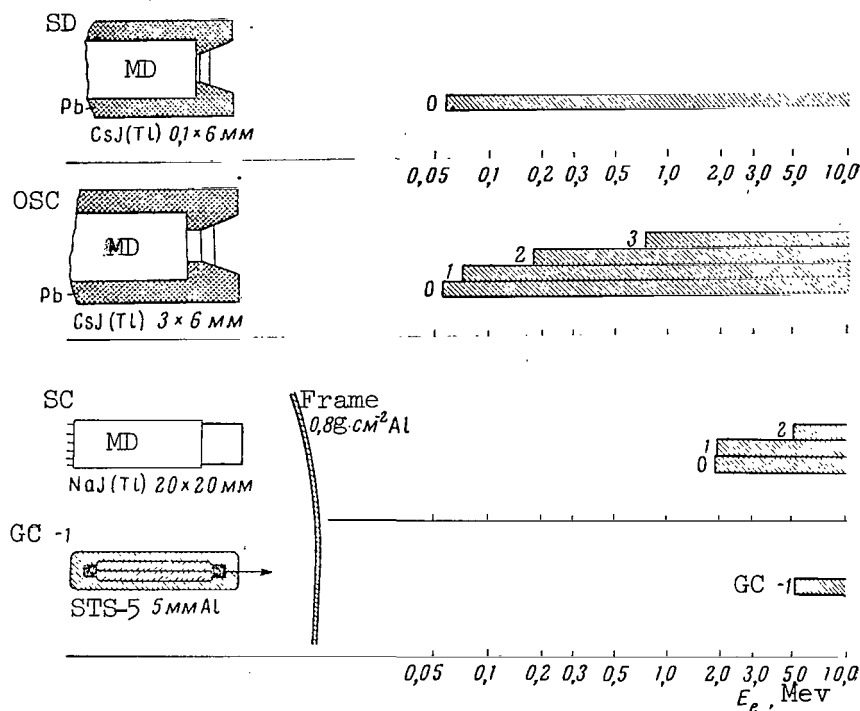


Figure 3

### Electron Detectors and Energy Thresholds Above Which Electrons May be Recorded

we shall discuss the directional intensities of particles averaged over the time between two memory cycles.

Experimental results. This report will primarily investigate the results obtained on the quiet state of the radiation zones during the first month of the satellites' operation, i.e., February, 1964. This was facilitated by the fact that 1964 was a year of minimum solar activity, when there were very few happenings on the Sun and when it was possible to study the unperturbed state of the zones between these happenings. Individual reports (Ref. 3-5) have presented results on the time changes in the intensity in the radiation zones and outside of the zones, as well as data on cosmic rays. /398

The analysis of the entire group of data will include an investigation of the inner zone from small  $L$  to  $L = 2.5$ , the intermediate region from  $L = 2.5$  to  $L = 4.0$ , and the outer radiation zone in the case of  $L > 4$ . The values of  $L$  presented here (the McIlwain parameter) characterize the boundaries encompassing the zone of spatial distribution of trapped radiation, and are apparently typical for the period of minimum solar activity.

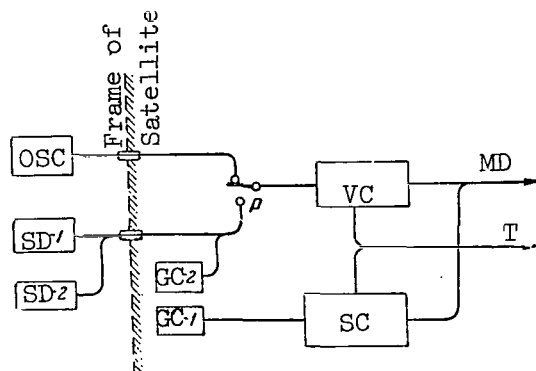


Figure 4

Block Diagram of Apparatus on the Satellites  
"Elektron-1" and "Elektron-2"  
(VC = voltage converter; T = transmitter)

Inner Zone. One unusual feature of the inner zone is the presence of protons having energies up to several hundreds of Mev and, after high-altitude nuclear explosions, electrons having energies of several Mev. However, the results pertaining to the artificial zones will not be discussed in detail in this article. We would only like to note that the maximum of the artificial zone in February, 1964 was located at  $L = 1.35$  and the flux of electrons having energies of  $> 2$  Mev at the maximum was  $\sim 10^7 \text{ cm}^{-2} \cdot \text{sec}^{-1} \cdot \text{sterad}^{-1}$ .

The distribution of protons having different energies along the equator (Figure 6) was compiled, utilizing the counter recordings and the parameter of SC-2. The parameter SC-2 (proton energy of  $> 30$  Mev) has been processed up to  $L = 2$  at the present time. The curves for  $E_p > 45$  and  $E_p > 70$  Mev were obtained from the readings of the gas discharge counters GC-1 and GC-2. The parameter SC-1 was used to exclude the recording of quanta of braking radiation by these counters. It was found that 50% of the recordings for the counters GC-1 and GC-2 was caused by braking radiation of electrons. The curve for  $E_p > 110$  Mev was obtained by readings of the GC-3 counter. The contribution of braking radiation to the reading of this counter was small, since in the  $L \approx 2$  region the main quanta energy of electron braking radiation, determined by the parameters SC-0 and SC-1, is about 350 kev for  $L = 2$ , and decreases down to 100 kev for  $L = 2.6$ . The GC-3 counter recorded braking radiation of this energy with very poor efficiency ( $< 10^{-4}$ ).

The number of electrons and their mean energy sharply increases for  $L < 2$ . This makes it difficult to analyze the counter readings. Therefore, the difference curve between GC-1 and GC-2 is given for  $L < 2$ , which pertains to protons having energies between 45-70 Mev. Actually, for a mean quanta energy of braking radiation of  $\sim 500$  kev and above, the GC-1 and GC-2 counters will record these quanta with approximately the same efficiency. Consequently, the difference between the counter readings can be explained by protons of 45-70 Mev. For purposes of

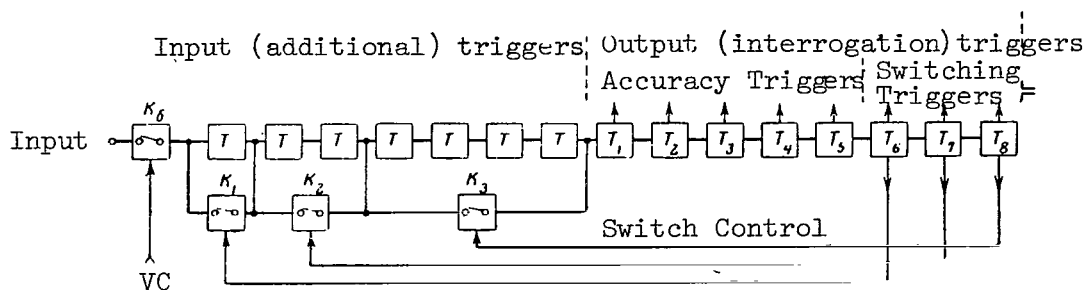


Figure 5

Diagram of Conversion Chain With Variable Number of Triggers  
Up to the First Interrogation Trigger

comparison, data from "Explorer-15" are given in this same figure (Ref. 6). It can be seen from the figure that there is a maximum at  $L = 1.45$ , and a plateau at approximately  $L = 2.2$  in the distribution of protons having high energy. If the integral spectrum of protons is represented in the form  $N(> E) \sim E^{-\gamma}$ , then the index  $\gamma$  - and, consequently, the hardness of the spectrum - changes with a change in  $L$ . For  $L = 2$   $\gamma = 1.8$  in the energy range between 30-45 Mev, and  $\gamma = 1.25$  between 70-110 Mev. In the case of  $L = 2.2$   $\gamma = 2.5$ , and in the case of  $L = 2.4$   $\gamma = 4.0$ . The form of the spectrum for  $L = 2.2$  and  $L = 2.4$  agrees with the results of McIlwain (Ref. 7). There is no divergence for  $L = 2$  up to a proton energy of 45 Mev. In the case of  $E_p > 45$  Mev, the proton spectrum for  $L = 2$  becomes harder, according to our data. If it is assumed that the GC-3 recording is half caused by braking radiation quanta, then the spectrum will be harder.

/399

The conclusion can be drawn on the basis of the results obtained that there are apparently two mechanisms leading to the formation of high-energy protons: One of them produces protons having an energy mainly up to  $\sim 50$  Mev; the second produces protons having an energy above 50 Mev. This second mechanism begins to operate from  $L = 2$  toward smaller  $L$ , and it is very probable that this is due to protons from albedo neutron decay.

Region of intermediate  $L$ . For the region of intermediate  $L$  ( $2.5 < L < 4$ ), it is characteristic to have a maximum in the distribution of low-energy protons and a minimum in the distribution of electrons having energies of several hundred kev. There is also a zone of electrons having energies up to 6 Mev in this region, but the origin of this zone has still not been clarified.

(a) Low-energy protons. Low-energy protons in the radiation zones are understood to mean protons having an energy less than 10 Mev.



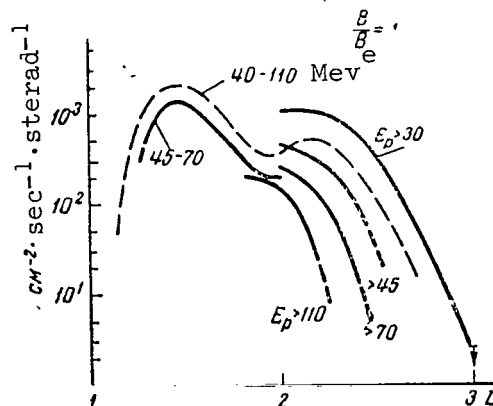


Figure 6

### Distribution of High-Energy Protons Along the Geomagnetic Equator

The mean directional stream is plotted along the ordinate axis.  
Dashed lines indicate the result obtained on "Explorer-15"

Figure 7, a, b, c, and d present the distribution of protons having different energies for the equator and geomagnetic latitudes of 30, 36, and  $43^\circ$  ( $B/B_e = 1; 3; 5$  and  $10$ , respectively). The mean directional stream is plotted along the ordinate axis in  $\text{cm}^{-2} \cdot \text{sec}^{-1} \cdot \text{sterad}^{-1}$ . For purposes of comparison, the dotted curve shows the results derived by McIlwain when measuring a proton stream perpendicular to the magnetic force line in the energy range  $1.1-14$  Mev (Ref. 7). It can be seen from Figure 7 that there is a considerable shift in the position of the proton stream maximum as a function of energy: The maximum shifts toward smaller  $L$  when the energy increases. The position of the curve maximum for  $1.1-14$  Mev in the equatorial plane seems somewhat strange to us. It can be seen from the figures that the proton spectrum depends on  $L$ , and becomes softer with an increase in  $L$ . A flux of protons having energies of  $> 2$  Mev is  $\sim 4.5 \cdot 10^5 \text{ cm}^{-2} \cdot \text{sec}^{-1} \cdot \text{sterad}^{-1}$  at the equator. The distribution maximum of these protons is located at  $L = 2.8 \pm 0.2$ . The altitudinal pattern of protons with an energy of  $> 2$  Mev depends on  $L$ , and on the latitude for each fixed  $L$ . The altitudinal pattern for a given  $L$  cannot be represented in the form of the function  $N \sim (B/B_e)^{-m}$ . The index  $m$  increases with an increase in latitude. In the case of  $L = 3$  at the equator  $m \approx 1$ , and gradually increases from  $m = 4$  at a latitude of  $\sim 45^\circ$ . For the plane of the geomagnetic equator, the index  $m$  depends on the value of  $L$ . When  $L$  changes from 2 to 3, the magnitude of  $m$  decreases from  $m \approx 2$  to  $m \approx 1$ . In the interval  $3 < L < 4$ , the altitudinal pattern depends slightly on  $L$ , and on the average  $m = 0.8 \pm 0.2$ .

Computations performed by B. A. Tverskoy (Ref. 8) and V. P. Shabanskiy et al. (Ref. 9) show that this spatial distribution and proton spectrum can be explained by employing the different mechanisms of proton transfer from the boundary to the depths of the magnetosphere.

(b) Zone of energetic electrons. Figure 8 shows two flights of the

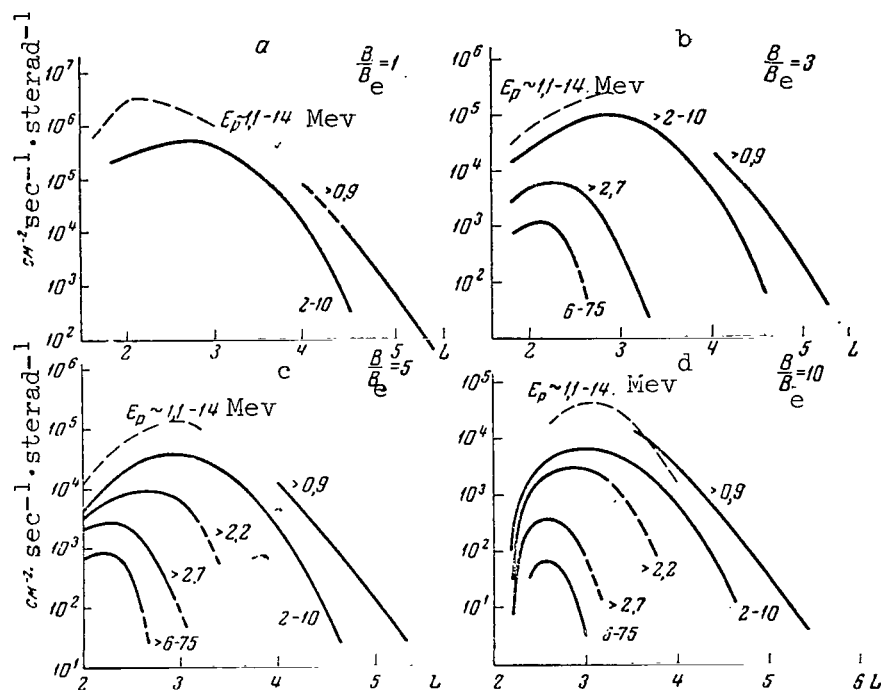


Figure 7

Distribution of Protons Having Energies of  $\sim 1$  Mev as a Function of  $L$

- a - in the plane of the magnetic equator ( $B/B_e = 1$ );
- b - for the geomagnetic latitude of  $30^\circ$  ( $B/B_e = 3$ );
- c -  $36^\circ$  ( $B/B_e = 5$ ; d -  $43^\circ$  ( $B/B_e = 10$ )).

The dashed line indicates a proton stream of 1.1-14 Mev perpendicular to the force line, based on data from "Relay-1".  $B_e$  - magnetic field strength toward the equator.

satellite "Elektron-1" through the  $2 < L < 3$  region on January 30, and January 31, 1965. During each of these flights, the GC-1 counter operated behind a shielding of 5 mm Al. On the first revolution on January 30, 1965, the GC-2 counter also operated behind a shielding of 15 mm Al. During the second revolution on January 31, 1965, the outer scintillation counter was switched on, and the figure shows the recording of the parameter OSC-4 ( $E_p > 2.7$  Mev). In the first case, the counter GC-2 - and in the second case, the channel OSC-4 - showed hardly any recording increase at the point where there was a maximum in the GC-1 recording. This maximum was located at approximately  $L = 2.75$ . If this maximum can be explained by protons, then the proton energy could not exceed 70 Mev (GC-2 threshold). Then the channel OSC-4 should also show an increase in the recording for  $L = 2.75$ . However, it can be seen from Figure 8 that OSC-4 decreases monotonically, and no maximum is observed on this channel. The situation was the same on the satellite "Elektron-2", but the maximum in the GC-1 recording is less apparent

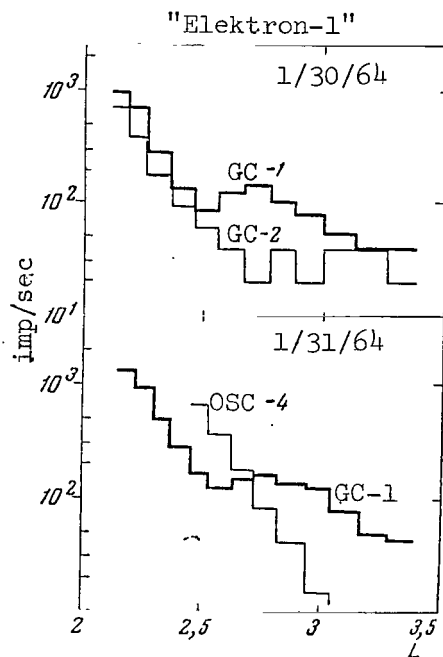


Figure 8

Example of "Elektron-1" Flights Through  
a Zone of Electrons Having Energies up to 6 Mev

there, since the trajectory of this satellite passed close to the equator. Due to this fact, the background from braking radiation of low-energy electrons increased. A comparison of the different parameters fosters the conclusion that this zone, which is  $\sim 0.4 R_e$  wide at the equator, is formed from high-energy electrons up to 6 Mev. The GC-1 counter can record electrons having this energy with an efficiency of  $\sim 50\%$  in a direct passage. The contribution made by braking radiation to the readings of both counters (GC-1 and GC-2) must be almost the same. Consequently, electrons directly penetrating through the GC-1 shielding make the difference between GC-1 and GC-2. Then the mean directional flux of electrons having the energy  $\sim 6$  Mev at the equator  $L = 2.75$  is  $\sim 10^2 \text{ cm}^{-2} \cdot \text{sec}^{-1} \cdot \text{sterad}^{-1}$ , within an accuracy of a factor on the order of two orders of magnitude. This maximum cannot be explained by electrons having energies of  $E_e > 4.3$  Mev (GC-1 records these electrons with 10%-efficiency, and their flux would be  $\sim 5 \cdot 10^2 \text{ cm}^{-2} \cdot \text{sec}^{-1} \cdot \text{sterad}^{-1}$ ). Electrons with these energies could not cause the parameter SC-2 to operate. This channel has an electric threshold of 3.5 Mev on "Elektron-1", and a threshold of 4.0 Mev on "Elektron-2", and in the latter case there is a plateau which is barely noticeable in the recording for  $L = 2.75$ . During the first revolutions of the satellite "Elektron-1", a clear maximum at  $L = 2.75$  was recorded on the SC-2 channel, just as was the case on the GC-1 counter. Later on, when the sensitivity of the scintillation counter decreased by about 20%, the SC-2 channel of the satellite "Elektron-1" became insensitive to the

/401

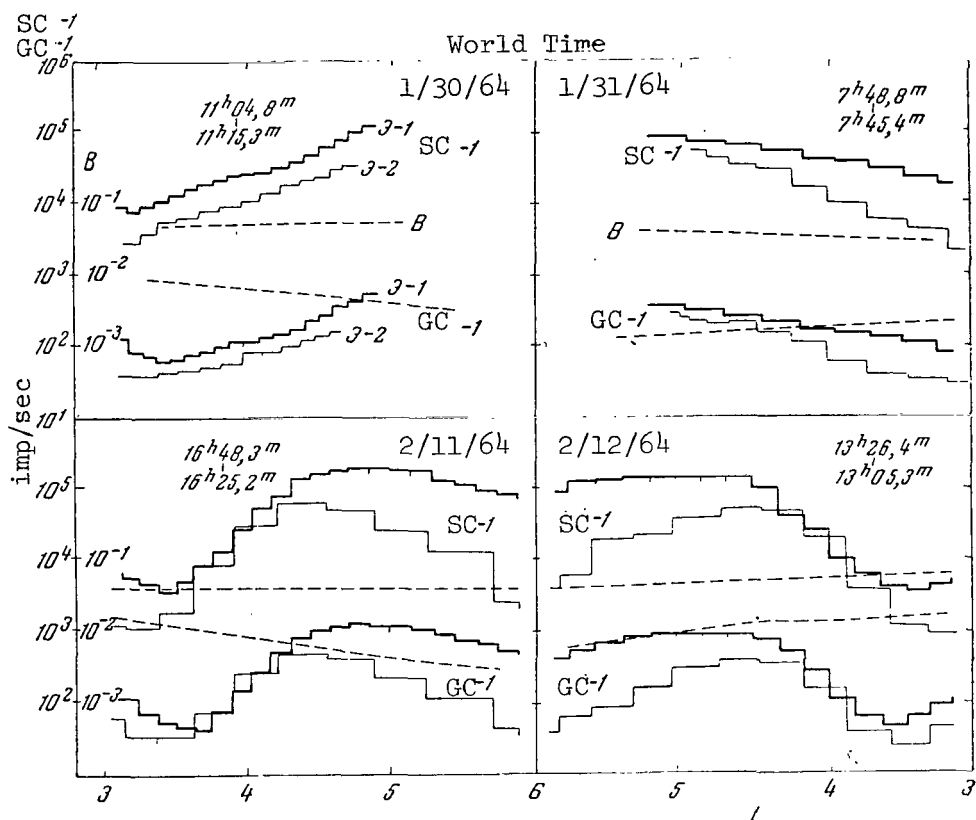


Figure 9

# Almost Simultaneous Flights of the Satellites "Elektron-1" and "Elektron-2" Through a Region of Intermediate L

The dashed line indicates the magnetic field B along the trajectory of each satellite as a function of L. The times at which one of the L-envelopes is intersected are shown. Each step corresponds to the two-minute duration of the memory cycle. Forward revolutions (receding from the Earth) are shown on the left; reverse revolutions (approaching the Earth) are shown on the right.

observed radiation, although a clear maximum was recorded on the GC-1 counter. Thus, the difference between the threshold energies is less than 1 Mev, and the observed phenomenon is practically excluded. This determines the upper energy limit of electrons recorded,  $\sim 7$  Mev. The origin of this zone is still not clear, although it is possible that it was formed during a magnetic storm on September 23, 1963 (Ref. 10).

(c) Space between the zones. The spatial region  $3 < L < 4$  is characterized by the fact that it contains a minimum in the intensity distribution of electrons having energies of several hundred kev. The concept of the "space" arose historically, when primarily a hard radiation component was measured during the first satellite flights. Later

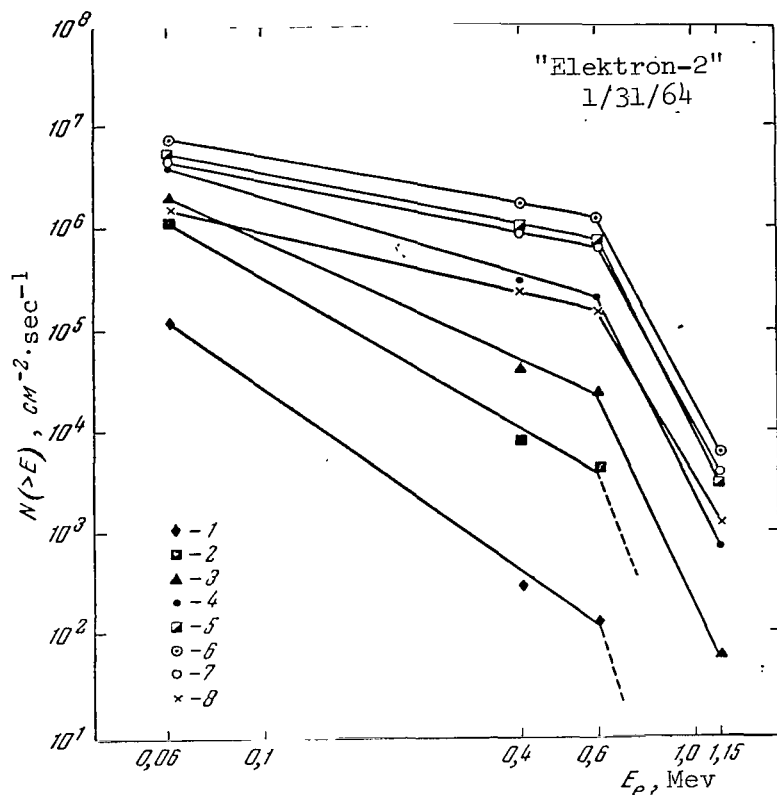


Figure 10

Spectrum of Electrons in the Outer Zone at Different L-Envelopes, Recorded by the Outer Scintillation Counter OSC on the Satellite "Elektron-2" on January 30, 1964, from the Morning Side in the Geomagnetic Latitude Range of 35-50°

1 - L = 11; 2 - L = 9; 3 - L = 8; 4 - L = 7; 5 - L = 6; 6 - L = 5;  
7 - L = 4.5; 8 - L = 4

studies showed that this minimum is insignificant for electrons having smaller energies ( $\sim 40$  kev), and the depth of the trough depends greatly on the geomagnetic perturbation. Figure 9 shows approximately simultaneous flights of "Elektron-1" and "Elektron-2" through the radiation zones during the evening and morning hours. Forward revolutions are shown on the left (the satellite recedes from the Earth), and reverse revolutions are shown on the right. The dotted line designates the magnetic field strength B along the trajectory of each satellite, as a function of L. The times are given when the satellites intersected practically one and the same L-envelopes. The time given above pertains to the satellite "Elektron-1". In spite of the fact that the latitudes differed by approximately 20° during each flight, there was very little difference between the intensities recorded by both satellites in the

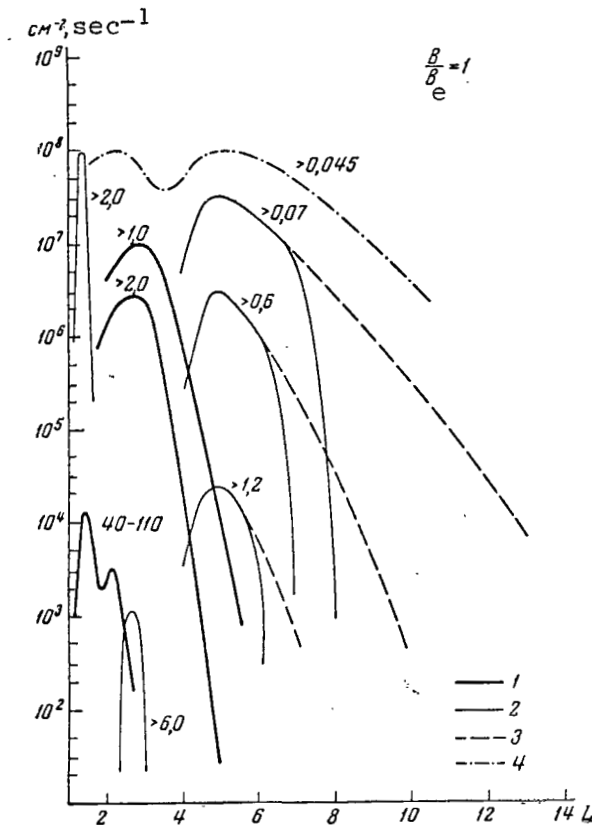


Figure 11

Streams of Electrons and Protons Having Different Energies in Mev in the Equatorial Plane

1 - protons; 2 and 3 - electrons at zero hours and 8 hours, respectively; 4 - electrons based on data from "IMP-1" at 8 hours.

$L \approx 4$  region. During these almost simultaneous flights of the satellites "Elektron-1" and "Elektron-2" through the outer radiation zone, the altitudinal pattern of electrons recorded by the GC-1 counters in the  $L \approx 4$  region was considerably weaker than in the remaining regions of the outer radiation zone. Thus, for electrons having an energy of  $\sim 150$  kev and above, the  $L \approx 4$  region is characterized by the fact that there is practically no altitudinal variation with time here.

Outer radiation zone. When the outer radiation zone was studied in preceding years, when there was great solar activity, it was difficult to study the stable state of the zone, because individual magnetic perturbations were imposed on each other. During a year of minimum solar activity, it is possible to study the zone in an unperturbed state. Thus, in February, 1964, two moderate magnetic storms with a sudden commencement were recorded, and one recurrent storm was recorded. The average time

between these events was approximately 7 days. According to the catalog of international quiet days, in February there were about 10 magnetically-quiet days. There was a particularly quiet period after the storm on February 12, 1964, approximately between February 15-19, 1964. An analysis of the data showed that the outer zone had a fairly stable form for certain restricted time intervals on the order of 4-6 days. There was a very sharp decrease in intensity by 2-3 orders of magnitude on the nocturnal side within the limits of  $\Delta L \sim 0.2 - 0.3 R_e$ . On the morning side, there was no such sharp relationship, and it was here, beyond the boundary of the zone, that the level was received of braking radiation quanta having an energy of  $> 30$  kev, which exceeded the background by a factor of 10. It was established that there is no significant difference in the position of the zone maximum on the nocturnal and morning sides of the Earth, but the position of the outer boundary strongly depends on the local time. The maximum of the outer zone in February, 1964, was located on the average at  $L = 4.5-4.8$ . The boundary from the nocturnal side was located at  $L = 6.5-7.5$ , and from the morning side - at  $L = 10-11$ .<sup>1</sup> All of the small intensity changes during the quiet periods occurred primarily in the case of  $L > 6$ .

/402

The parameters of SC-1 from both satellites, recording braking radiation quanta having an energy of  $> 30$  kev, were employed to determine the altitudinal pattern of the electrons. The simultaneous flights (within an accuracy of several minutes) of the satellites through the outer zone at different latitudes were selected. The altitudinal intensity pattern changed very slightly within a wide L-range, and could be represented in the form of  $N(B) \sim (B/B_e)^{-m}$ , on the average, where

/403

$$m \simeq 0,5^{+0,3}_{-0,2}.$$

The OSC devices were used to obtain the electron spectrum in the outer zone. The contribution of protons having an energy of  $> 1$  Mev to the electron channel recordings for  $L > 4$  could be disregarded, in view of the fact that they rapidly decreased with an increase in L (see above). In addition, at latitudes of  $> 30^\circ$  the number of protons was also small, as compared with the electrons, due to their sharper altitudinal behavior. Figure 10 presents electron spectra for different L-envelopes, obtained during the first reverse flight of the satellite "Elektron-2" on January 31, 1964. The figure gives the spectra from  $L = 4$  to  $L = 11$  in the geomagnetic latitude range of  $35-50^\circ S$ . The mean electron flux, obtained under the assumption that the electron flux was isotropic within the limits of the angle  $2\pi$ , is plotted along the ordinate axis. It can be seen from the figure that the electron spectrum becomes softer with an increase in L. In the energy region above 600 kev, there is a sharp break in all of the spectra, and the spectrum becomes softer. Between 70-600 kev, all of the spectra lie on a straight line, and consequently, they can be represented in the form  $N(>E) \sim E^{-\gamma}$ . In the case of  $E > 600$  kev (since there are

/404

<sup>1</sup> Larger L ( $> 6-7$ ) were computed in the dipole approximation in the present article.

only two points here), the power law may also be employed. The index  $\gamma$  decreases from  $\gamma = 3$  for  $L = 11$  to  $\gamma = 1$  in the case of  $L \leq 6$  in the energy range of 70-600 keV; thus, the spectrum is hardest in the  $L \leq 6$  region. If an attempt is made to represent the spectrum in the form  $N(>E) \sim e^{-E/E_0}$  for  $L = 5$ , then between 70-600 keV  $E_0 \approx 290$  keV. This quantity is somewhat lower than in (Ref. 11), where at  $L = 5$   $E_0 \approx 340$  keV. Thus, up to an energy of  $\sim 600$  keV the electron spectrum of the outer zone closely coincides with the results derived by other authors. The divergence in the case of  $E > 1.2$  MeV can be explained if it is assumed that particle generation at the magnetosphere boundary is directly related to solar activity, and that the majority of electrons forming the outer zone - similarly to protons (Ref. 8, 9) - drift within the magnetosphere from its boundary. Thus, if electrons having an energy of 200-300 keV are generated, their energy reaches a value of  $\sim 1$  MeV when these electrons move to  $L \sim 5$ . The report (Ref. 4) investigates all of the strongest occurrences of non-regular electron streams beyond the zone boundary from the morning and evening sides during February, 1964. Not one case was recorded, in which the electron energy exceeded 400 keV. During satellite flights on March 10 and March 15, 1964, after a recurrent storm on March 4-5, 1964, it was found that there were electrons with an energy of  $> 1.2$  MeV in the zone. The electron spectrum was similar to the spectrum cited in (Ref. 11). The conclusion may be drawn from the statements given above that the electron spectrum in the outer radiation zone undergoes considerable variations. The spectrum apparently becomes softer, on the average, during years of a quiet Sun. However, high-energy electrons may sometimes appear after large magnetic perturbations.

## CONCLUSIONS

Figure 11 presents the over-all picture of the hard component distribution of radiation zones of the Earth, compiled from data obtained from the satellites "Elektron-1" and "Elektron-2". This picture makes it possible to sum up all of the information presented above and to draw the following conclusions.

1. A zone of artificially-injected electrons is located very close /405 to the center of the Earth. In February, 1964, the maximum of the zone was located at  $L = 1.35$ . A flux of electrons having an energy of  $> 2$  MeV at the maximum comprises  $\sim 1 \cdot 10^7 \text{ cm}^{-2} \cdot \text{sec}^{-1} \cdot \text{sterad}^{-1}$ .

2. At the maximum of the inner zone, the mean directional flux of protons having an energy of 45-70 MeV is  $\sim 1.5 \cdot 10^3 \text{ cm}^{-2} \cdot \text{sec}^{-1} \cdot \text{sterad}^{-1}$  for  $L = 1.45$ . For  $L = 2.2$  there is a change in the integral spectrum for energies of  $E_p > 50$  MeV. The spectrum becomes harder in this energy region, and can apparently be explained by the theory of albedo neutrons.

3. The spatial distribution of protons having an energy between 1 and several MeV is different from the electron distribution. The proton



distribution follows a definite law as a function of their energy. The mean directional flux of protons having an energy of  $> 2$  Mev is  $\sim 4.5 \cdot 10^5 \text{ cm}^{-2} \cdot \text{sec}^{-1} \cdot \text{sterad}^{-1}$  in the equatorial plane for  $L = 2.8$ . The index of the altitudinal pattern changes from  $m = 2 \pm 0.1$  for  $L = 2$  to  $m = 0.8 \pm 0.2$  for  $L = 4$ . The majority of protons in this energy range is apparently formed by the drift of protons across the force lines of the magnetic field.

4. A zone of high-energy electrons was discovered at  $L = 2.75$ . The width of the zone at the equator was  $\Delta L \sim 0.4$  Earth radii. The mean directional flux of electrons having an energy of  $> 6$  Mev is  $\sim 10^2 \text{ cm}^{-2} \cdot \text{sec}^{-1} \cdot \text{sterad}^{-1}$ .

5. A minimum was observed in the distribution of electrons having an energy of  $> 150$  kev in the  $3 < L < 4$  region. The altitudinal intensity pattern in this region changed greatly with time, and became negligibly small at certain periods of time.

6. The maximum of the outer zone, both on the nocturnal and on the morning side, was located on the average at  $L = 4.8$ . The mean index of the altitudinal pattern was  $m = 0.5_{-0.2}^{+0.3}$  in a wide region of  $L$ . On the nocturnal side, there was a sharp boundary at  $L = 7 \pm 0.5$ . On the morning side, there was no sharp boundary, and there was a monotonic decrease in intensity. The mean directional flux of electrons having an energy of  $> 70$  kev at the outer zone maximum was  $\sim 5 \cdot 10^6 \text{ cm}^{-2} \cdot \text{sec}^{-1} \cdot \text{sterad}^{-1}$  and could change by more than one order of magnitude. The electron energy spectrum between 70-600 kev coincides with the results derived by other authors. In the energy region of  $> 1$  Mev, the electron spectrum became, on the average, softer as compared with preceding years.

#### REFERENCES

1. Vakulov, P. V., Goryunov, N. N., Logachev, Yu. I., Sosnovets, E. N. *Geomagnetizm i Aeronomiya*, 1, 6, 1961.
2. Vakulov, P. V., Gorchakov, Ye. V., Logachev, Yu. I. *Kosmicheskiye Luchi*, no. 6, 1965.
3. Kuznetsov, S. N., Sosnovets, E. N., Stolpovskiy, V. G. Present collection, p. 420.
4. Vernov, S. N., Chudakov, A. Ye., et al. Present Collection, p. 433.
5. Vernov, S. N., Chudakov, A. Ye., et al. Present Collection, p. 425.
6. McIlwain, C. E., *Science*, 142, 355, 1963.
7. Fillius, R. W., McIlwain, C. E. The Anomalous Energy Spectrum of Protons in the Earth's Radiation Belt. Preprint, 1964.

8. Tverskoy, B. A. Report to the Sixth COSPAR Symposium (Doklad na 6-m simpoziume COSPAR). Buenos Aires, May, 1965.
9. Antonova, A. Ye., Yershkovich, A. I., Shabanskiy, V. P. Present Collection, p. 326.
10. McIlwain, C. W. Redistribution of Trapped Protons During a Magnetic Storm. Preprint, 1964.
11. Frank, L. A., Van Allen, J. A. J. Geophys. Res., 69, 23, 1964.

PRELIMINARY RESULTS DERIVED FROM CORPUSCLE  
INVESTIGATIONS ON THE SATELLITE "ELEKTRON-1"

A. D. Bolyunova, O. L. Vaysberg, Yu. I. Gal'perin,  
B. P. Potapov, V. V. Temnyy, F. K. Shuyskaya

The satellite "Elektron-1" carried two soft corpuscle indicators, /406 which were designed to study the spatial distribution of three main types of charged particles trapped by the geomagnetic field: Soft and hard electrons and soft protons. The first indicator I-1, which was similar to that carried by the satellites "Kosmos-3" and "Kosmos-5" (Ref. 1, 2), could record electrons beginning at  $\sim 1$  kev, since it had a electrostatic accelerating attachment with high voltage which changed stepwise, up to  $+11$  kv. The thickness of its aluminum foil was  $0.6 \text{ mg} \cdot \text{cm}^{-2}$ . The second indicator I-2, with foil of  $0.4 \text{ mg} \cdot \text{cm}^{-2}$ , was designed to record protons having energies greater than  $\sim 150$  kev. A magnetic attachment, which prevented electrons with  $H_p \lesssim 5000$  gauss $\cdot$ cm (energy less than  $1.1$  Mev) from reaching a fluorescent screen, was placed in its field of vision. The screen of both indicators was completely the same outside of the field of vision. The angular field of vision of both recorders amounted to  $1/30$  sterad. Therefore, they recorded a signal which greatly depended on the indicator orientation in the geomagnetic field in an anisotropic radiation field. The scatter of the points on the graphs presented below was caused to a significant extent by changes in the indicator orientation and partially by the inaccuracy of the B, L-coordinates employed. The preliminary results derived from analyzing the data obtained by averaging the signals measured at different indicator orientations are given below. These data have not yet been compared with simultaneous measurements performed by other equipment on the satellites "Elektron-1" and "Elektron-2". It was subsequently decided to perform more exhaustive studies on the basis of detailed computations of the B, L-coordinates and the orientation.

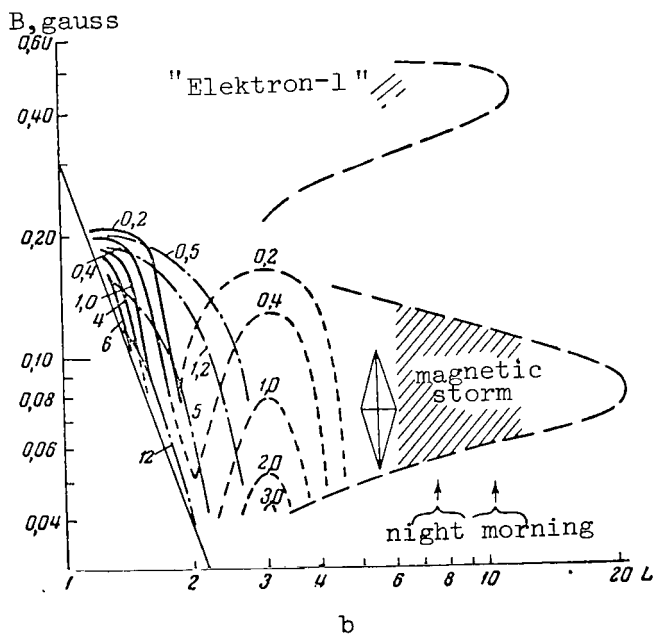
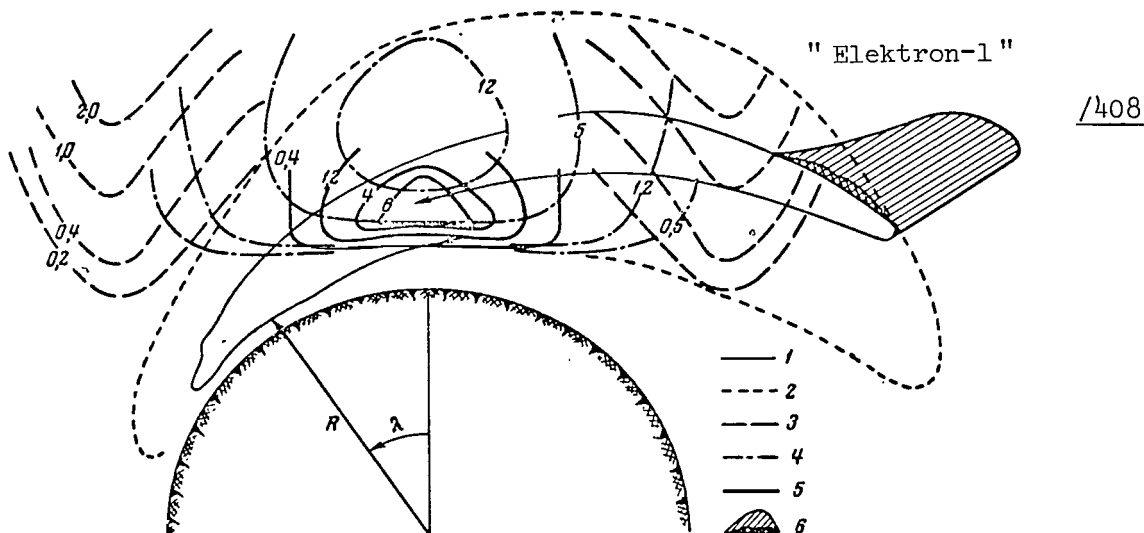
As is known, an overwhelming portion of electrons in the natural radiation zones have energies which are less than  $1$  Mev. However, after the American high-altitude thermonuclear explosion on July 9, 1962, a large amount of heavy electrons having energies of several Mev appeared in the upper atmosphere (Ref. 3, 4). Although these indicators were not designed especially for recording and analyzing heavy electrons, they also recorded considerable streams of this new component in the radiation zones. In such cases, the readings of both indicators were approximately the same. The indicator screenings made it possible for electrons having energies of more than  $\sim 1.1$  Mev to penetrate the recorder in a wide angular range. Therefore, when such electrons were recorded, the signal changed from point to point very smoothly in spite of their anisotropic distribution with respect to pitch-angles in the magnetic field - in contrast to the recording of soft corpuscles. In this way, it was possible to distinguish between cases when heavy electrons were recorded, and cases when protons having small energies were recorded.

Let us first examine the distribution of the signals obtained by the indicators in the invariant B, L- or R,  $\lambda$ -coordinates. The signals of the proton indicator I-2 were greatly concentrated toward the equator at  $L \sim 1.2-1.3$ , and rapidly decreased to  $L \sim 2$ . It was clear from the nature of the recording (weak dependence of signals on pitch-angle) that penetrating particles were being recorded here at a substantial solid angle. Since penetrating protons with energies of tens of Mev up to  $L \sim 1.6$  made an insignificant contribution to the signal of our indicators,<sup>1</sup> it is apparent that relativistic electrons of an artificial radiation zone were recorded in this region. At  $L \gtrsim 2$ , the I-2 indicator signals again increased, reaching a maximum at  $L \approx 3$ , and then again decreased to  $L \sim 4$ . The I-1 electron indicator signals thus became smaller than the I-2 proton indicator signals. This definitely indicates that the I-2 indicator primarily recorded protons having small energies of less than 0.5 Mev. Figure 1 also shows the lines of equal intensity for soft protons. For  $L \gtrsim 5$ , a proton stream was usually below the recording threshold of our indicators. /407

The slight dependence of the I-1 indicator sensitivity on electron energy in the  $\gtrsim 20$  kev region made it possible, in the first approximation, to regard its readings as the magnitude of the integral electron stream of  $E \gtrsim 20$  kev, in the absence of accelerating voltage. Consequently, the difference between the readings of the two indicators in the  $1.20 < L \lesssim 2.5$  region only determined the intensity of electrons with energies ranging from  $\sim 20$  kev up to 1.1 Mev.

In the  $L \sim 1.4-2.0$  region, the I-1 electron indicator readings considerably exceeded the proton indicator readings, which indicates that electrons were recorded having energies of  $E < 1.1$  Mev. Their distribution in the B, L-coordinates, which is also shown in Figure 1, differs considerably from the distribution of hard electrons in an artificial zone. The readings of the two indicators were almost proportional in the region of the proton zone center ( $L \approx 3$ ), and the flux of electrons with energies of  $E > 20$  kev did not usually exceed  $3 \cdot 10^8 \text{ particle} \cdot \text{cm}^{-2} \cdot \text{sec}^{-1}$ . (This maximum estimate was obtained on the assumption that the entire I-1 indicator signal was caused by electrons. It will be shown below that the flux of electrons in this region is much smaller.) At  $L \gtrsim 5$ , the electron stream increased on the average, but fluctuated very greatly. Figure 1 shows the magnitude of the dispersion for B for points of equal electron intensity  $E \gtrsim 20$  kev at high latitudes, since a representation of their averaged intensities in the usual B, L-coordinates concealed very interesting variations with local time, geomagnetic activity, etc.

<sup>1</sup> This contribution is known from measurements performed with similar indicators on the satellites "Kosmos-3" and "Kosmos-5" (Ref. 5). We have not attempted to interpret the signals in those magnetosphere regions where this contribution could exceed 20% of the recorded signal.



b  
Figure 1

Distribution of Lines of Equal Indicator Signals

a - In invariant  $R$ ,  $\lambda$ -coordinates; 1-Rev. 10; 2-boundary of measurement region; 3-isolines of soft proton intensity in units of  $5 \cdot 10^7 \text{ particle} \cdot \text{cm}^{-2} \cdot \text{sec}^{-1}$  (preliminary data); 4-isolines of electron intensity  $E < 1.1 \text{ Mev}$  in units of  $10^8 \text{ particle} \cdot \text{cm}^{-2} \cdot \text{sec}^{-1}$ ; 5-isolines of electron concentration  $E > 1.1 \text{ Mev}$  in units of  $10^{-3} \text{ particle} \cdot \text{cm}^{-3}$ ; 6-intensity variation during magnetic storm.

b - The same in invariant  $B$ ,  $L$ -coordinates (disregarding the magnetosphere asymmetry). The boundary values of  $L$  are also indicated, above which there were usually no signals. The rhombus designates the dispersion of  $B$  values for identical  $I-1$  indicator readings.

Disregarding the daily magnetosphere asymmetry, Figure 1 also shows the boundary of the B, L-coordinate region intersected by the orbit of the satellite "Elektron-1". It can be seen that the satellite intersected the magnetic force lines, passing through the north and south zones of the aurorae polaris, when the orbital angle of inclination to the equator was  $i = 61^\circ$ . Thus, in January-March it penetrated the southern zone of the aurorae polaris from 21 to 8 hours local time, at altitudes of 5,000-7,000 km, and it penetrated the northern zone of the aurorae polaris at altitudes of 400-500 km from 9 to 20 hours local time.

Let us now examine in turn the data obtained from these signals on the distribution of the types of charged particles indicated above, which are caught in the trap of the geomagnetic field.

### 1. Artificial Zone of Heavy Electrons Close to the Equator

The distribution of the mean concentration of relativistic electrons ( $E > 1.1$  Mev) close to the equator for  $L < 1.5$ ,  $B > 0.08$  gauss can be obtained from Figure 1 by multiplying the given values by  $10^{-3}$ . A comparison of the intensities measured at the beginning of 1964 with the intensities observed directly after the explosion on the satellite "Kosmos-5" (Ref. 4) shows that the form of the artificial zone changed considerably, primarily due to the relatively great attenuation at low altitudes and at large latitudes. The omnidirectional intensity in the center of the artificial zone close to the equatorial plane ( $L = 1.3$ ) decreased by approximately one order of magnitude, and amounted to  $\sim 2 \cdot 10^8 \text{ electron} \cdot \text{cm}^{-2} \cdot \text{sec}^{-1}$ , while at altitudes below approximately 1000 km it decreased by no less than a factor of 100 (Figure 2). The data /409 obtained closely coincide with measurements in the artificial radiation zone which were performed by McIlwain and his coworkers on the satellites "Explorer-15" (Ref. 6) (with allowance for the correction given in [Ref. 7]) and "Relay-1" (Ref. 8). Such a picture for the decrease in the artificial zone intensity for  $L \lesssim 1.3$  agrees formally with the computations of the Coulomb scattering effects by the solution of the Fokker-Planck equation (Ref. 3, 9).

On the other hand, the large elastic scattering cross section for hard electrons leads to the fact that the altitudinal particle distribution is practically in balance with the atmosphere, if the other mechanisms by which relativistic particles are redistributed at low latitudes are actually unimportant. Therefore, the data obtained on the intensity behavior with altitude in an artificial zone make it possible to determine, similarly to the proton measurements (Ref. 10), the altitude of the homogeneous atmosphere  $H$  for density. However, in contrast to hard protons, the time required to establish equilibrium distribution along the force line is small, even at high altitudes (Ref. 3, 9). The information obtained on the altitude of the homogeneous atmosphere  $H$  at high altitudes is given in the table. Since electrons are diffused downward on the

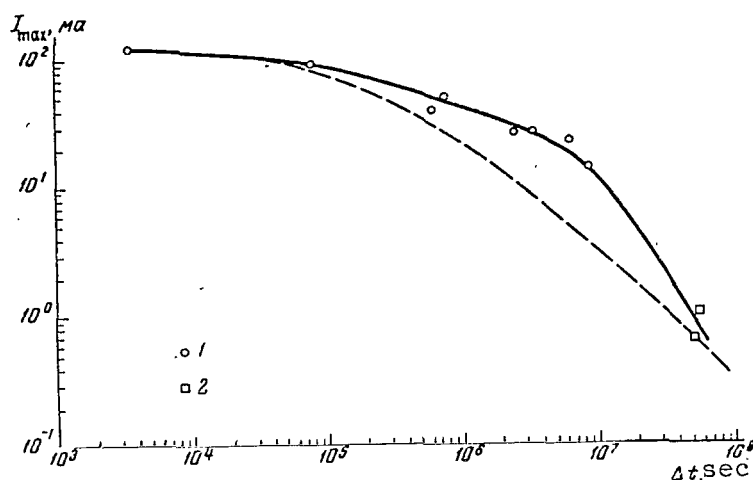


Figure 2

Intensity Decrease at the Point Where the Center of the Artificial Zone was Located Directly After the Explosion

( $L = 1.20 \pm 0.04$ ,  $B = 0.194 \pm 0.006$  Gauss)

1 - "Kosmos-5"; 2 - "Elektron-1" The computational results are shown by the dashed line (see [Ref. 5], p. 111)

average, the values obtained for  $H$  represent an upper estimate. They pertain to 1963, but somewhat exceed the corresponding values computed by the models of Anderson and Francis (see [Ref. 9]) and Harris-Priester (Ref. 11). A more detailed analysis of the particle concentration distribution and a refinement of the method for computing  $H$ , with allowance for the Coulomb scattering effects, make it possible to determine more accurately the temperature and the mean molecular weight in the exosphere at these altitudes, on the basis of these data.

These results show that the lifetime of an artificial zone at low latitudes ( $L \lesssim 1.3$ ) is unusually large. During the last period, it is primarily determined by only the density of particles in the exosphere of the Earth (although the role of other factors cannot be excluded, such as the electric drift of particles, variation of the magnetic field, etc.). If this is valid, then the duration of an artificial radiation zone at low latitudes must be calculated in tens of years. It can only 410 be hoped that the most powerful world-wide magnetic storms, or special future experiments to bring about compulsory departure of these particles from the geomagnetic field trap, will accelerate the process by which the background of hard radiation is restored to the level existing before the beginning of nuclear explosions in the atmosphere at high altitudes in 1958 (Ref. 12).

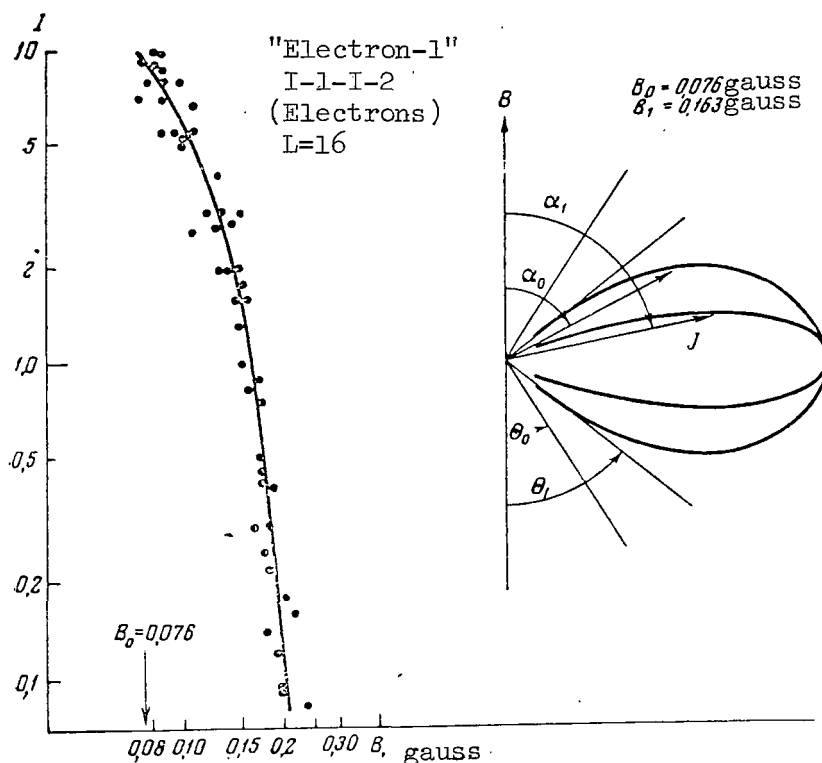


Figure 3

Dependence of a Stream of Trapped Electrons of  $20 \text{ kev} < E < 1.1 \text{ Mev}$  on the Strength of the Field  $B$  at the Force Line  $L = 1.6$  (On the Left), and the Dependences Thus Obtained of Electron Intensity Distribution on the Pitch-Angle  $J(\alpha)d\alpha$  at Two Selected Points on the Force Line:  $B_0 = 0.076 \text{ Gauss}$  (at the Equator) and  $B_1 = 0.163 \text{ Gauss}$

Pitch-angles, corresponding to  $h_{\min} \approx 0$ , are designated by  $\theta_0$  and  $\theta_1$ .

TABLE

$h, \text{ km}$	$H, \text{ km}$		
	"Elektron-1"	Model (Ref. 9) (Mean Daily)	Model (Ref. 11) ( $T = 19 \text{ hours}$ , $S = 70$ )
800	$320 \pm 10$ *	110	176
1000	$320 \pm 10$	230	198
1200	$370 \pm 32$	340	229
1500	$500 \pm 25$	440	320
1800	$760 \pm 185$	560	476

\* The mean quadratic deviation is indicated. Systematic error, related to inaccurate measurements and to approximations utilized to compute  $H$ , can be significantly larger (see the text).



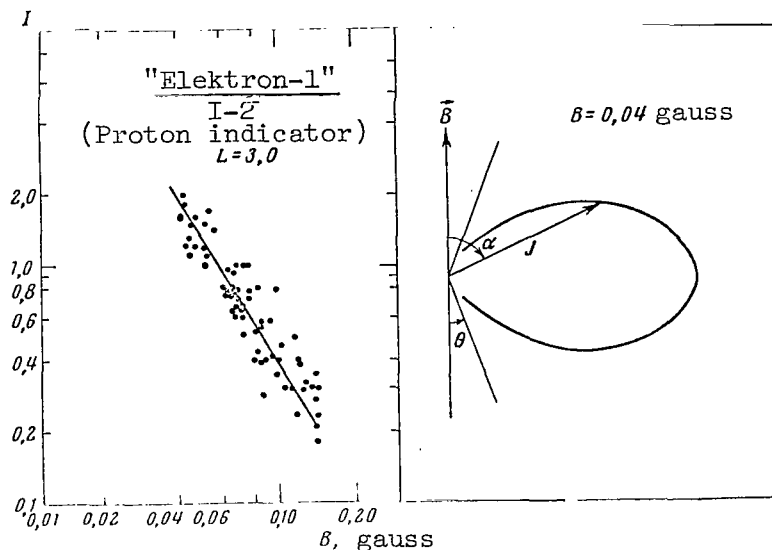


Figure 4

The Dependence (Similar to Figure 3) for Soft Protons at the Line  $L = 3.0$ , and the Corresponding Distribution at the Point  $B = 0.04$  Gauss

## 2. Electrons Having a Natural Origin at Low Latitudes

Let us now examine the results derived from measuring electrons having an energy of  $\lesssim 1.1$  Mev. Measurements (by means of electrostatic attachments modulated to electron energy) performed on the satellites "Kosmos-3" and "Kosmos-5" before the formation of an artificial radiation zone at low latitudes (Ref. 13), and a comparison between these data and indicator readings on the satellite "Elektron-1", lead to the conclusion that the energy of the main portion of electrons measured here is 20-200 kev.

The intensities of soft electrons with an energy of  $\sim 15$  kev, which were measured at low latitudes in the eastern hemisphere with similar indicators on the satellite "Kosmos-5" (Ref. 13), were below the sensitivity threshold of our apparatus on the satellite "Elektron-1". It must be noted that soft electron measurements on the satellite "Elektron-1" are particularly provisional, since - in addition to the indeterminant nature of orientation - measurements of the soft electron component at low latitudes are greatly complicated by the high intensity of penetrating electrons of the artificial radiation zone.

Figure 3 presents an example of the electron intensity dependence  $E < 1.1$  Mev on the pitch-angle for  $L = 1.6$  at the equator ( $B_0 = 0.076$  gauss) and at the point  $B_1 = 0.163$  gauss, formulated by recalculating

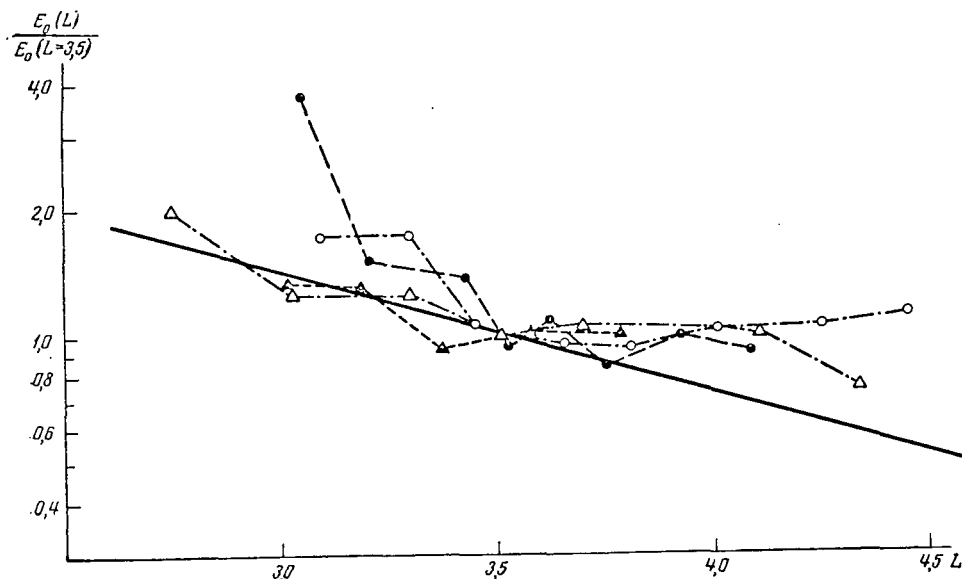


Figure 5

Change in Trapped Proton Spectrum as a Function of L During Several Revolutions Based on Data From "Elektron-1"

The dashed lines on the graph indicate relative values of the parameter  $E_0$  for the proton spectrum in the form  $N(E)dE \sim \exp(-E/E_0)dE$ . For purposes of comparison, a similar dependence obtained from measurement data on the satellite "Explorer-12" is shown by the solid line.

the measurements of averaged directional intensity at different points along a magnetic envelope. A comparison of the measurement data on the satellite "Kosmos-5" before the explosion on July 9, 1962 (Ref. 14) leads to the conclusion that the intensity gradient along the magnetic force line and, consequently, the nature of the anisotropic distribution of these particles in the magnetic field coincides with the results obtained before the explosion on July 9, 1962 - when it could be assumed that the electron zone at low latitudes was a natural zone. A detailed comparison in the overlapping regions of the B, L-coordinates ( $1.4 \lesssim L \lesssim 2$ ) shows /411 that the intensity gradients  $d \ln I / dB$  differ by a factor of less than 1.5. The electron fluxes, measured on the satellite "Elektron-1", may possibly even have decreased somewhat (but no more than twice), as compared with measurements on "Kosmos-5" with a similar indicator. The low relative accuracy of this comparison is primarily related to the indeterminate nature, existing at the present time, of the indicator orientation on the satellite "Elektron-1". The distribution of the mean-energy electron component sharply differs from the distribution described above of relativistic electrons in the artificial zone, and also from the distribution of  $E < 450$  kev electrons, obtained in 1963 on the satellite "Relay-1" (Ref. 8). This agrees with the conclusion that the energy of electrons which we recorded was considerably less than 0.5 Mev.

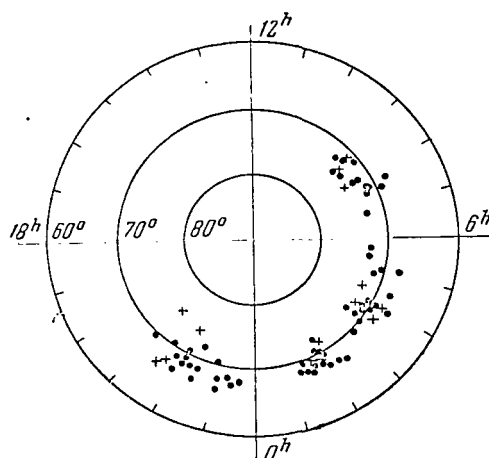


Figure 6

Dependence of  $\Phi_{\text{bound}}$  on Local Time.

Dots stand for  $K_p < 2$ ; Crosses stand  
for  $K_p \geq 2$

Thus, these measurements characterize the distribution of electrons having an energy of 20-200 keV and having primarily a natural origin, since the lifetime of electrons with these energies, which were injected on July 9, 1962, is short.

One characteristic of the distribution of these mean-energy electrons in the geomagnetic field is the significant decrease in their intensity in the region  $L \gtrsim 2$ . They have a particularly low intensity at  $L \sim 3$ , where the center of the soft proton zone is located, and which we shall now examine.

### 3. Soft Proton Zone

/412

The orbit of the satellite "Elektron-1" only allowed measurements in this zone far from the equator, at latitudes of 30-50°. The purpose of our measurements was to obtain information on soft proton streams (with energies of hundreds of keV) above the mean and high latitudes, and to compare them with the results derived from measuring soft protons obtained by Davis and Williamson on the satellite "Explorer-12" (Ref. 15) in 1961 primarily at lower latitudes. Due to the considerable anisotropy of their distribution in the geomagnetic field, the expected intensity along the "Elektron-1" orbit was approximately one order of magnitude below that at the equator.

Assuming that the change in the proton energy spectrum within  $20^\circ < \alpha_0 < 30^\circ$  (where  $\alpha_0$  is the pitch-angle at the equator) is insignificant, we can formulate the dependence of proton intensity on  $B$  for fixed

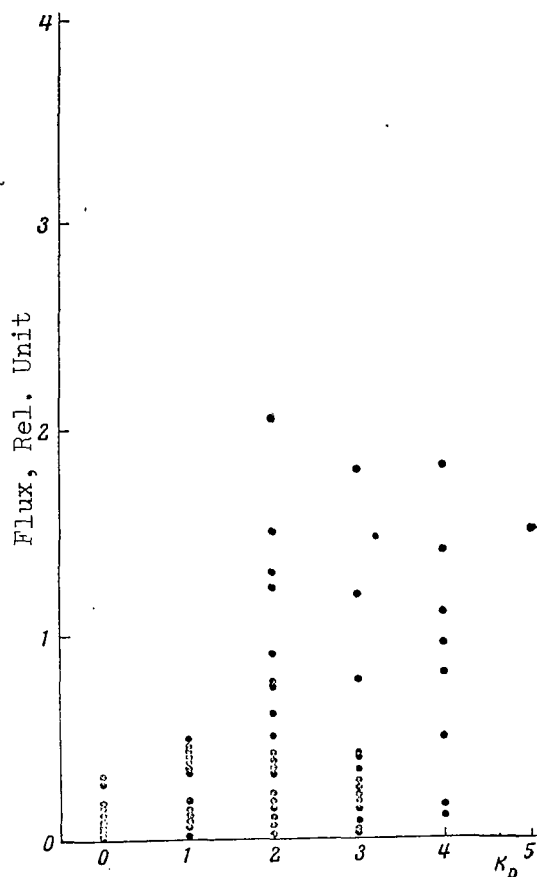


Figure 7

Comparison of Electron Flux Magnitude, Based on I-1 Data ( $E > 20$  kev, at the Envelope  $L \sim 7$ ) With Three-Hour Values of the Planetary Magnetic Index  $K_p$

The Electron fluxes increased significantly only during magnetically perturbed periods.

values of  $L$ . An example of this dependence for  $L = 3.0$ , and the corresponding anisotropic distribution of soft protons at the measurement point closest to the equator  $B = 0.04$  gauss, is shown in Figure 4. The anisotropy of the distribution can be approximately described by the formula  $J(\alpha) = J_0 \sin^n \alpha$ , where  $n = 3.4 \pm 0.8$ . For purposes of comparison, it can be shown that the value of  $n$ , obtained in (Ref. 15) for this point, is 3.0.

While the I-2 proton indicator in this region definitely recorded only protons, electrons having an energy of  $< 1.1$  Mev could make a certain contribution to the signal of the I-1 electron indicator. If it is assumed that the I-1 indicator signal is primarily caused by electrons with  $E < 1.1$  Mev, then the proton energy in the zone must be no more than 250 kev, and their flux for  $L = 3$  and  $B = 0.04$  gauss must be no less than  $10^9 \text{ particle} \cdot \text{cm}^{-2} \cdot \text{sec}^{-1}$ . Such a large value for the flux and the form of the

spectrum at the  $\Phi = 32^\circ$  latitude is very improbable. If it is assumed, on the other hand, that the I-1 indicator signal (and the I-2 indicator signal) is due primarily to protons in this region, then - by representing the proton energy spectrum, according to (Ref. 15), in the form  $N(E)dE \sim \exp(-E/E_0)dE$  and utilizing measurement data obtained on "Elektron-1" - one can obtain the characteristics of the proton spectrum softening with an increase in latitude. The value of  $E_0$  can be determined by the ratio between the signals of the two indicators. These data /413 are plotted in Figure 5 for several revolutions. The measurement results obtained on "Explorer-12" are also plotted in this Figure (Ref. 15). The figure shows that the data obtained on "Elektron-1" coincide with the results derived from measuring the proton spectrum on "Explorer-12" only when the electron flux of  $> 20$  kev is considerably less than  $3 \cdot 10^8 \text{ particle} \cdot \text{cm}^{-2} \cdot \text{sec}^{-1}$ .

The maximum proton flux, recorded at  $L = 3$ ,  $\Phi = 32^\circ \text{S}$  within an accuracy of the factor  $\sim 2$ , equalled  $1.5 \cdot 10^8 \text{ particle} \cdot \text{cm}^{-2} \cdot \text{sec}^{-1}$ . Extrapolation to the equator of the distribution obtained at latitudes of  $\Phi > 32^\circ$  depends on the behavior of  $n$ , which can decrease considerably in the pre-equatorial region. In particular, a distribution with a maximum at an intermediate latitude and a minimum at the equator (the form of the intensity dependence on the pitch-angle at the equator is similar to a butterfly in this case) is even possible. Nevertheless, it is apparent that the density of the soft proton energy close to the equator must be no less than several percents of the density of the geomagnetic field energy at the equator. A decrease in the recorded proton signal at  $L > 3$  can be caused not only by a decrease in the total proton flux, but also by the softening of their spectrum, for which a significant portion of the protons have an energy which is less than the threshold for the I-2 indicator.

The picture of the intensity distribution of soft protons within an accuracy of our measurements was formulated between January 30 and March 5, 1964. It approximately coincides with the results obtained by "Explorer-12" (Ref. 15) in 1961, but there are certain systematic discrepancies, which may be caused by the inaccurate determination, indicated above, of the absolute omnidirectional intensity under the flight conditions of "Elektron-1". /414

#### 4. Electrons at High Latitudes

At  $L \gtrsim 4$ , the I-1 indicator again began to record electron signals (which considerably exceeded the I-2 indicator signals) in the region of the apogee, simultaneously with a decrease in the soft proton intensity. This electron region extended up to the zone of the aurorae polaris. In the majority of cases, the signal change did not exceed 1.5 times when accelerating voltage was supplied; this indicates that the mean electron energy was greater than 20 kev. During magnetically quiet days, the I-1 recorder signal corresponded to an electron intensity which amounted to

$5 \cdot 10^6 \text{ particle} \cdot \text{cm}^{-2} \cdot \text{sec}^{-1} \cdot \text{sterad}^{-1}$  ( $E > 20 \text{ kev}$ ). The flux maximum was observed at  $L \sim 5-6$ , and fell below  $10^6 \text{ particle} \cdot \text{cm}^{-2} \cdot \text{sec}^{-1} \cdot \text{sterad}^{-1}$  at  $L \sim 7-8$  during departure from the zone ( $T_{\text{local}} \sim 21-4 \text{ hours}$ ) and  $L \sim 9-11$  when the zone was entered ( $T_{\text{local}} \sim 4-8 \text{ hours}$ ). At low altitudes in the northern hemisphere, where trapped particles existed for a short period of time, the I-1 signal was below the sensitivity threshold when there were no magnetic perturbations - i.e., the electron intensity was smaller than  $10^6 \text{ particle} \cdot \text{cm}^{-2} \cdot \text{sec}^{-1} \cdot \text{sterad}^{-1}$  ( $E > 20 \text{ kev}$ ). There was no observed dependence of the signal magnitude on longitude for  $L \sim 5-6$ .

At larger values of  $L$  - i.e., at geomagnetic latitudes  $\Phi$  which were larger than a certain value of  $\Phi_{\text{bound}}$  - the I-1 indicator signal usually fell to values which were smaller than the sensitivity threshold. Figure 6 presents the dependence of the boundary geomagnetic latitude  $\Phi_{\text{bound}}$  on local time, corresponding to this flux value. /415

It can be seen that the values of  $\Phi_{\text{bound}}$  fall within the aurorae polaris zone. Since the satellite intersected the aurorae polaris zone at a local time of 21-8 hours at high altitudes, only a portion of a circle was described. Its form indicates that the capture region boundary shifted from the geomagnetic pole to the nocturnal side of the Earth, by apparently no less than  $5^\circ$ . The magnitude of this shift and the circle radius ( $\sim 20^\circ$ ) coincide with data on the position of the "instantaneous zone of the aurorae polaris", obtained by O. V. Khorosheva (Ref. 16), and with the results obtained on the satellite "Injun-3" (Ref. 17).

The intensity of soft electrons in the outer zone region ( $L \gtrsim 5$ ) changed with time when the magnetic activity increased, sometimes increasing up to  $\sim 2 \cdot 10^8 \text{ cm}^{-2} \cdot \text{sec}^{-1} \cdot \text{sterad}^{-1}$  (January 31, 1964) ( $E > 20 \text{ kev}$ ), and showing a statistical dependence on the magnetic index  $K_p$  (Figure 7). During magnetically perturbed days, there was considerable electron intensity (up to  $\sim 3 \cdot 10^7 \text{ particle} \cdot \text{cm}^{-2} \cdot \text{sec}^{-1} \cdot \text{sterad}^{-1}$ ) also at higher geomagnetic latitudes up to  $\Phi \approx 73^\circ$  ( $L = 13$ ).

## 5. Intensity Variations During Magnetic Storms

Very significant soft electron fluctuations at high altitudes were recorded during magnetic storms on January 31 and March 5, 1964.

The fact is very important that the intensity fluctuation amplitude considerably exceeded the intensity variation along the force line. These fluctuations, consequently, could not be caused by redistribution of electrons with respect to pitch-angles while their number remained the same.

Considerable signal variations during periods of high magnetic activity are apparently related to both spatial nonuniformities of anomalous electron intensity and to time fluctuations, similarly to the distribution of the aurorae polaris. At this same geomagnetic

latitude, the intensities measured during the same revolution can differ by almost two orders of magnitude. In several cases, considerable streams of softer electrons were observed during this period, whose mean energy did not exceed 20 kev. Figure 8 shows flux measurements of electrons with  $E > 20$  kev during magnetic storms on January 31 and March 5, 1964. The same figures present changes in the horizontal component of the magnetic field based on data from the Voyeykovo Observatory (Leningrad).

During a storm on March 5, signals were recorded from soft electrons at altitudes of 400-500 km in the northern hemisphere, whose flux amounted to  $10^7 \text{ particle} \cdot \text{cm}^{-2} \cdot \text{sec}^{-1} \cdot \text{sterad}^{-1}$ . With allowance for a possible electron stream having smaller energies, such a particle stream could cause the aurorae polaris with an intensity of 10 kilo-Rayleighs at  $\lambda = 5577 \text{ \AA}$  for  $\sim 20$  seconds, if the electron reserves in the magnetosphere are determined by the intensity recorded during a magnetically quiet period ( $5.0 \cdot 10^7 \text{ particle} \cdot \text{cm}^{-2} \cdot \text{sec}^{-1}$  with  $E > 20$  kev). At the same time, data from observations on the Earth indicate that there was a significant aurorae polaris for several hours. Thus, the absence of "sufficient reserves" of electrons in the geomagnetic trap at high altitudes directly refutes the hypothesis of aurorae polaris formation due to electron discharge from a radiation zone.

It is apparent that during this aurorae polaris a considerable portion of the electrons, while exciting luminescence, invade the atmosphere from directly outside (and not from the capture region). Actually, the aurorae polaris are observed in a region which is close to the pole, where it is impossible for corpuscles to be captured in the trap. The crosses in Figure 6 show the positions of the "boundary" of particle stream recordings from high latitudes during perturbed periods. It can be seen that at individual moments a considerable electron stream is observed at higher latitudes than during a magnetically quiet period. On the other hand, intensity variations in the soft proton zone during magnetic storms on January 31 and March 5 were small, or were completely absent. Thus, during the storm of March 5, only a very insignificant drop in soft proton intensity, within the limits of error, was observed for the entire  $2 < L < 4$  region (no less than a factor of two).

#### Conclusion

/417

Thus, radiation distribution in the trap of the geomagnetic field along the orbit of "Elektron-1" in January-March, 1964, can be summarized as follows (Figure 1).

At low latitudes ( $L < 2$ ) close to the equator, the predominant factor in particle stream magnitude is electrons - those having a natural origin with an energy of 20-200 kev and a flux of up to  $2 \cdot 10^9 \text{ particle} \cdot \text{cm}^{-2} \cdot \text{sec}^{-1}$  and those artificially injected during the explosion on July 9, 1962, with an energy of several Mev and a flux of up to  $2 \cdot 10^8 \text{ particle} \cdot \text{cm}^{-2} \cdot \text{sec}^{-1}$ . In this same region, there are trapped protons with energies of tens and hundreds of Mev, and with a

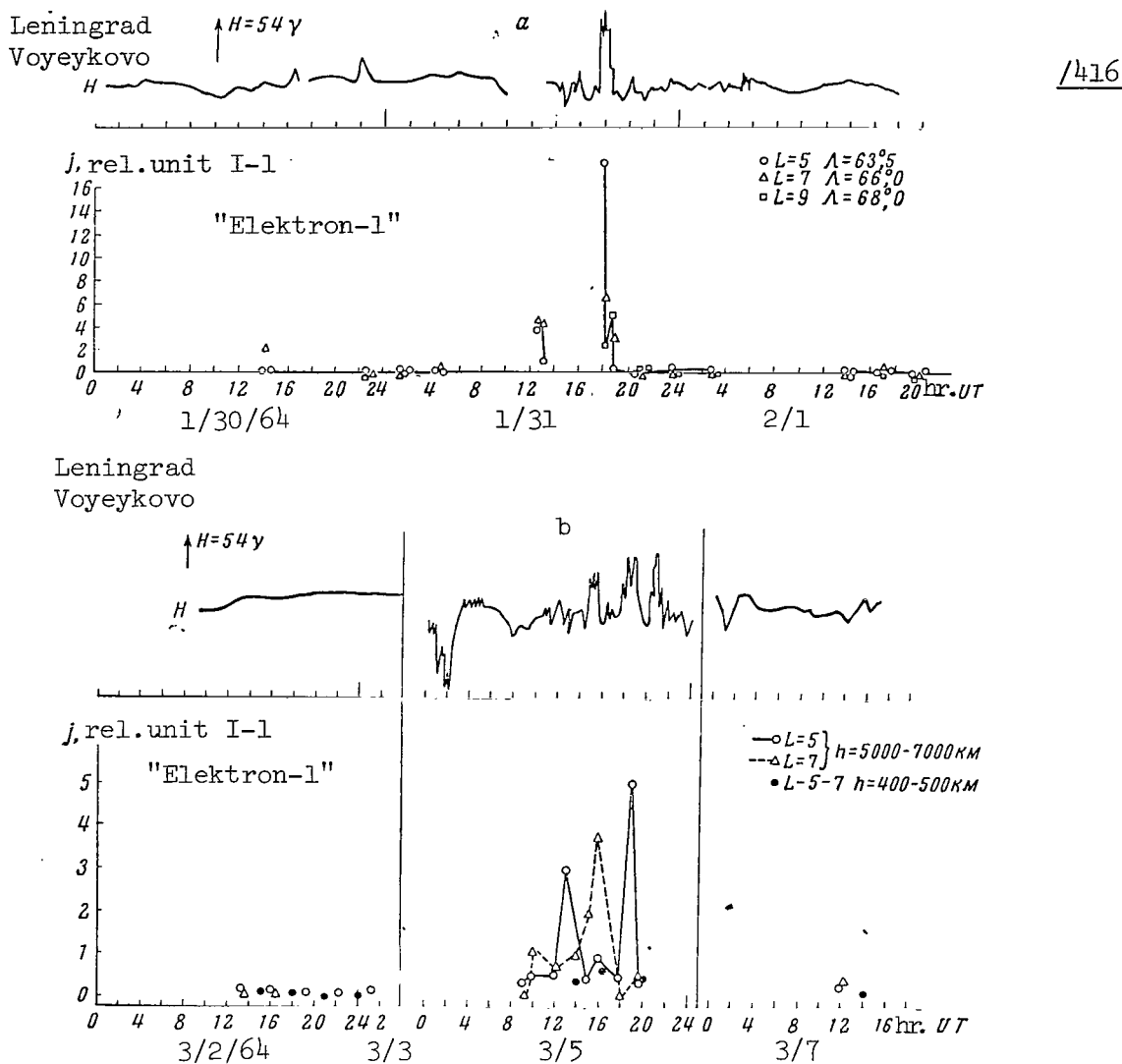


Figure 8

A Comparison of an Outer Zone Electron Stream ( $L > 5$ )  
With the Pattern of the Horizontal Component of the  
Magnetic Field  $H$  Based on Data From the Voyeykovo Observatory

a - during a magnetic storm on January 31, 1964 (there  
are no data between 10-14 hours); b - similar picture  
during a magnetic storm on March 4-5, 1964.

flux of up to  $\sim 5 \cdot 10^4$  particle  $\cdot$  cm $^{-2}$   $\cdot$  sec $^{-1}$  ( $E > 50$  Mev).

At mean latitudes ( $2 < L < 4$ ), there was a sharp increase in  
the stream of soft protons having energies of several hundred keV  
and up to no less than  $\sim 10^8$  particle  $\cdot$  cm $^{-2}$   $\cdot$  sec $^{-1}$  at latitudes of



$\Phi = 30-50^\circ$  and no less than  $\sim 3 \cdot 10^8$  close to the equatorial plane at  $L \sim 3$ . Their spectrum was moderated toward high latitudes.

At higher latitudes, there were both protons and electrons, and the electron component having a small energy ( $E \gtrsim 20$  kev) was very unstable, particularly when geomagnetic activity increased.

The boundary of the capture zone in the geomagnetic field during a magnetically quiet period coincided with the outlines of the "instantaneous" aurorae polaris zone reflecting daily magnetosphere asymmetry.

As can be seen from these data, our concepts of particle composition, their flux, and even the amount of the so-called radiation zones have undergone radical changes as compared with the initial stages of research on these phenomena.

In conclusion, we would like to thank V. I. Krasovskiy, T. M. Mulyarchik, N. V. Dzhordzhio, M. L. Bragin, G. N. Zlotin, I. N. Kiknadze, I. D. Dmitriyeva, T. N. Zaglyadimova, A. K. Nazarova, and G. A. Bordovskiy for their great assistance in the work and for valuable discussions.

#### REFERENCES

1. Krasovskiy, V. I. et al. Geomagnetizm i Aeronomiya, 3, No. 3, 401, 1963.
2. Gal'perin, Yu. I., Krasovskiy, V. I. Kosmicheskiye Issledovaniya, 1, No. 1, 126, 1963.
3. Operation "Sea Star" (Operatsiya "Morskaya zvezda"). Atomizdat, 1964.
4. Gal'perin, Yu. I., Bolyunova, A. D. Kosmicheskiye Issledovaniya, 2, No. 5, 763, 1964.
5. Baysberg, O. L., Shuyskaya, F. K. Present Collection, p. 203.
6. McIlwain, C. E. Science, 142, 355, 1963.
7. West, H. I., Jr., Mann, L. G., Bloom, S. D. Space Res., 5, 423, 1965.
8. McIlwain, C. E., Fillius, R. W., Valerio, J., Dave, A. Preprint, March, 1964.
9. Walt, M., Newkirk, L. Space Res., 5, 458, 1965; J. Geophys. Res., 69, No. 19, 3947, 1964.
10. Gal'perin, Yu. I., Temnyy, V. V. Space Res., 5, 1965 (in press).

11. Harris, I., Priester, W. Theoretical Models for the Solar-Cycle Variation of the Upper Atmosphere. NASA TN D-1444, 1962.
12. Shklovskiy, I. S., Krasovskiy, V. I., Gal'perin, Yu. I. Izvestiya AN SSSR, Seriya Geofiz., No. 12, 1799, 1959.
13. Mulyarchik, T. M. Present Collection, p. 205.
14. Temnyy, V. V. Present Collection, p. 209.
15. Davis, L. R., Williamson, J. M. Space Res., 3, 365, 1962; Nakada, M. P., Dungey, J. W., Hess, W. N. Space Res., 5, 399, 1965.
16. Khorosheva, O. V. In "Aurorae Polaris and Night Airglow" (Polyarnyye siyaniya i svecheniye nochnogo neba", No. 10, p. 126, Izdatel'stvo AN SSSR, 1963.
17. Frank, L. A., Van Allen, J. A., Craven, J. D. J. Geophys. Res., 69, No. 15, 1964.

POSSIBLE EXISTENCE OF A SOFT ELECTRON COMPONENT IN THE  
OUTER RADIATION ZONE AND ITS VARIATIONS

V. V. Bezrukikh, K. I. Gringauz,  
L. S. Musamov, E. K. Solomatina

The present report presents a portion of the results derived from /418 measuring charged particle streams on the satellite "Elektron-2" by means of a charged particle trap. This portion of the results was obtained when the satellite passed through the outer radiation zone during the initial stage of its flight. The results obtained on other sections of the orbit are described in the works (Ref. 1, 2) and are also discussed at the present conference. The studies (Ref. 1, 2) contain a brief description of the apparatus. We would like to note at this point that the electric potential of the outer grid of a three-electrode trap, which served as a sensor, equalled the satellite frame potential. The potential of the grid inside the frame was 100 v. Due to this fact, negative currents in the trap collector system could be created by electron streams with energies of  $E_e \geq 100$  ev.

When determining the electron fluxes by the negative collector current recorded, one must keep the fact in mind that when the trap was illuminated by the solar ultraviolet, its inner grid emitted photoelectrons which fell on the collector.

In the initial processing stage, whose results are given in this report, the authors were not able to distinguish between, and separate from the primary data, those measurements which corresponded to the

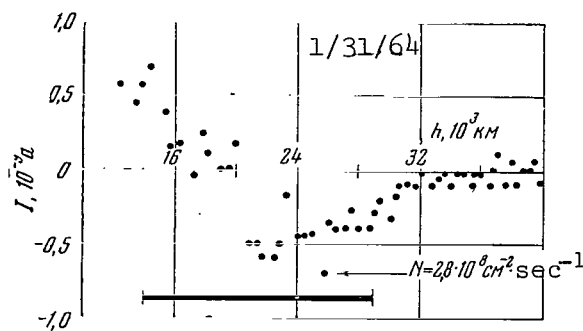


Figure 1

trap position in the shaded section of the satellite. Therefore, in order to allow for the influence of the photocurrent from the inner grid when determining the recorded electron fluxes, photocurrent data were used from experiments with similar traps on previous cosmic rockets. The magnitudes of the electron fluxes, which will be given later, represent the lower limits of their possible values, since positive ions which decrease the observed negative current could fall into the trap, in addition to electrons.

When "Elektron-2" passed through the outer radiation zone, negative collector currents were recorded in the trap, whose magnitude changed considerably from revolution to revolution. On certain revolutions, practically no negative currents were observed. At the same time, the radiation counters carried on the same satellite (Ref. 3) indicated that the energetic particles recording rates (with  $E > 100$  kev) were fairly stable - i.e., they fluctuated by 10%. This phenomenon is illustrated in Figures 1-3. These figures show the collector currents of the trap corresponding to the outer radiation zone on the ascending sections of the satellite orbit. The dark horizontal lines designate the altitude region corresponding to the outer radiation zone based on the counter data. The largest soft electron flux  $N$  in the outer radiation zone, during the period between January 30 and February 17, 1964, was recorded on January 31, 1964, and amounted to  $\sim 3 \cdot 10^8 \text{ cm}^{-2} \cdot \text{sec}^{-1}$ . The experimental results derived during this period substantiate the assumption that this magnitude of the soft electron flux exceeds, by no less than one order of magnitude, the flux of energetic electrons trapped in the outer radiation zone and consequently recorded by the radiation counter. These results can be assumed to prove the existence of a soft component of electron streams in the outer zone, whose variability in time is much greater than the variability of high-energy particle streams. The comparatively stable readings of particle counters in the outer zone with  $E > 100$  kev indicate that the collector currents, recorded by the trap in this same zone and changing greatly from revolution to revolution, are formed by electrons having energies which do not exceed 100 kev.

The region containing the soft electron streams recorded by the trap always extends beyond the limits of the outer radiation zone boundary.

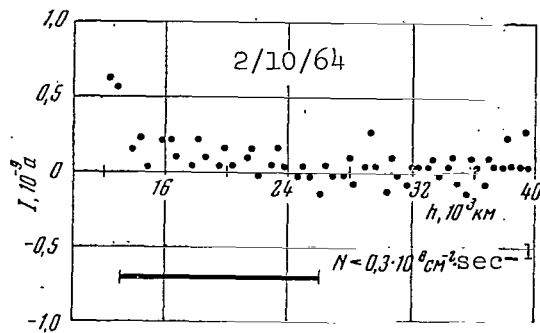


Figure 2

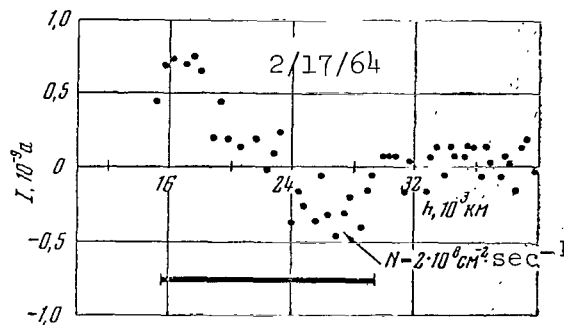


Figure 3

We would like to note that experimental results on "Elektron-2" (Ref. 4) revealed sporadic radio emission, whose intensity was largest at a frequency of 725 kc. The development of radio emission and its intensity closely coincide with the presence of soft electron streams, to which the present article is devoted.

The existence of and properties of a soft electron component in the outer radiation zone requires further study.

The authors would like to thank S. N. Vernov, Yu. I. Logachev, E. N. Sosnovets, Ye. A. Benediktov, G. G. Getmantsev, and H. A. Mityakov, who kindly made it possible for us to examine the results of their experiments before publication.

#### REFERENCES

1. Bezrukikh, V. V., Gringauz, K. I., Present Collection, p. 177.
2. Gringauz, K. I., Dolginov, Sh. Sh., et al. Present Collection, p. 336.
3. Vernov, S. N., Logachev, Yu. I., et al. Present Collection, p. 502.
4. Getmantsev, G. G., Tarasov, A. F., Benediktov, Ye. A., Sazonov, Yu. A. Present Collection, p. 581.

# TIME CHANGES IN THE OUTER RADIATION ZONE OF THE EARTH BASED ON DATA FROM THE "ELEKTRON" SATELLITES

S. N. Kuznetsov, E. N. Sosnovets, V. G. Stolpovskiy

Variations of the outer radiation zone have been studied by many authors both at high, and low altitudes. /420

In August-September, 1959, the outer radiation zone variations were studied by the satellite "Explorer-6" (Ref. 1, 2). It was found that the outer radiation zone has two maxima located, respectively, at  $L \approx 2.5-3.3$  and  $3.1-4$  at different times. The space between the outer and inner zones is located at  $L \approx 2-2.5$ ; the outer boundary of the zone is located at  $L \approx 6.7-7.5$ . During magnetic perturbations, the intensity changed by one order of magnitude. Polar geomagnetic perturbations and intensification of the aurorae polaris brightness correspond to a change in the zone boundary position and to variations in the Geiger counter recording rate when the satellite approached the zone boundary.

Between October, 1959, and December, 1960, the outer radiation zone was studied by the satellite "Explorer-7", flying at an altitude of  $\sim 1000$  km (Ref. 3). It was found that during magnetically quiet days the outer zone maximum was located at  $L \approx 4$ , and the zone maximum shifted to  $L \approx 3$  when the magnetic perturbation increased. The deviation of the magnetic field at equatorial stations from the quiet day level,  $v$ , (a current ring field) was used as the measure of geomagnetic perturbation. It was also found that for  $L \geq 4$  the coefficient for the correlation between  $\lg v$  ( $\lg v \approx K_p$ ) and the intensity at an envelope was approximately  $-0.4-0.5$ . When  $L$  decreased to  $2.5$ , the correlation coefficient changed to  $+0.4$ . Data on "Explorer-6" and "Explorer-7" were obtained by Geiger counters which directly recorded electrons with  $E \geq 2.9$  and  $1.6$  Mev. Low-energy electrons were recorded according to braking radiation.

Beginning in August, 1961, up to 1963, the radiation zones were studied by the satellites "Explorer-12" and "Explorer-14", flying at distances of  $14 R_e$  in the equatorial plane, and by the satellites "Injun-1" and "Injun-3", flying at an altitude of  $\leq 1000$  km. Generalization of the existing data produced the following picture of zone structure (Ref. 4).

On the diurnal side, the zone extends to a distance of  $10 R_e$ , and on the nocturnal side - to a distance of  $7 R_e$ . Beginning at several thousand kilometers up to the outer boundary of the outer radiation zone, the flux of electrons with  $E > 40$  kev equals  $10^8 \text{ cm}^{-2} \cdot \text{sec}^{-1}$ , within an accuracy of the factor 2-3. Electrons with  $E > 1.6$  Mev have a maximum in the region of  $4-5 R_e$ .

At high latitudes, the zone terminates on the diurnal side at  $\lambda_{\text{geom.}} \approx 75^\circ$ , and on the nocturnal side - at  $\lambda_{\text{geom.}} \approx 69^\circ$  (Ref. 5). The

flux of electrons with  $E > 40$  kev increases with an increase in magnetic activity (Ref. 6, 7). There is no correlation between the behavior of high-energy electrons and a change in magnetic activity.

It is thus apparent that, when data from the "Elektron" satellites are processed, it is necessary to establish a concrete connection between geomagnetic perturbations and phenomena occurring in the zones, in addition to studying the zone variations in time.

Data obtained between January 30-February 23, 1964, have now been processed provisionally. The present article employs the parameters of SC-1, GC-1, and OSC-1, given in Figures 4 and 5 in (Ref. 9). When studying the outer radiation zone, we employed the McIlwain coordinates computed in the dipole approximation, although they could be erroneous due to distortion of the Earth's magnetic field by the solar wind. However, when data from the satellite "Explorer-18" ("IMP-1") (Ref. 8) /421 and from the satellite "Elektron-2" (February 16, 1964) on the zone structure on the morning side of the Earth were compared, it was found that the zone boundary begins at one and the same  $L \approx 10$  close to the equator and at the geomagnetic latitude  $\sim 50^\circ$ .

An irregular stream beyond the zone boundary was recorded by both satellites at one and the same  $L$  (in spite of the fact that the satellites recorded electrons of different energies). Consequently, it is possible to employ  $L$ , B-coordinates on the morning side of the Earth - at least up to  $L \approx 14$  during magnetically quiet periods. It can be expected that the distortion of  $L$ -envelopes is also insignificant on the nocturnal side of the Earth.

This article studies the outer radiation zone variation on the nocturnal side of the Earth. The outer radiation zone occupies the region  $L \approx 3.5-7$  from the nocturnal side of the Earth and  $L \approx 3.5-10$  - from the morning side of the Earth. The outer zone maximum is located at  $L \approx 4.2-5.2$ . "Elektron-2" recorded the outer zone maximum at somewhat larger  $L$  than did "Elektron-1" (Ref. 9).

During magnetically quiet periods, the form of the zone did not change from its maximum to  $L \approx 6$ . The main changes occurred in the zone at  $L > 6$ .

The "Elektron" satellites studied the intensity variations in the recordings of different equipment at the zone maximum, variations in the position of the zone maximum, and its boundaries. The connection between these variations and geomagnetic perturbations was also investigated.

Figure 1 presents data on the change in electron intensity at the zone maximum, and on the change in the magnetic activity index ( $K_p$ -index and  $\bar{K}$ -index - the mean index of magnetic activity according to the College and Murmansk Stations - are plotted). It can be noted that the recording rate of the scintillation detector and the Geiger counter rate

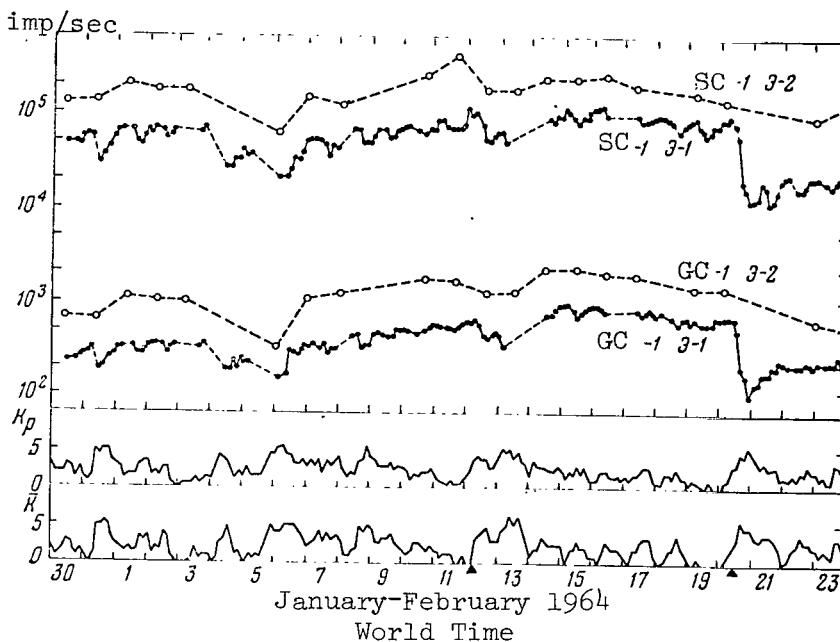


Figure 1

decreased with an increase in magnetic activity. However, the detector recording rates sometimes increased during great magnetic activity (for example, on February 6, 1964, 12 hours UT). During magnetic storms with a sudden commencement, the intensity decreased, which began almost immediately after the sudden commencement and terminated during the maximum development of the main phase of the storm. The intensity may thus decrease by one order of magnitude.

The non-monotonic intensity decrease during the storm on February 12-13, 1964, can be explained by the developmental features of this storm (a decrease in magnetic perturbation between the sudden commencement and the main phase of the storm). After the intensity decrease, during the magnetic activity decrease the intensity increased by a factor of approximately two at the zone maximum during one day. This phenomenon was observed after a polar storm on January 31, 1964, and after a storm on February 12-13 and February 20, 1964. This phenomenon may be used to form an opinion regarding the magnitude of reversible variations in the zone. After this, the zone intensity changed much more slowly.

The position of the outer zone maximum changes slightly with a change in magnetic perturbation (see Figure 2, which shows variations in the maximum position and in the outer zone boundary based on data from the "Elektron" satellites). However, during magnetic storms on February 12-13 and February 20, 1964, the zone maximum moved to smaller  $L \approx 3.8-4$ . The zone boundary was more sensitive to changes in the magnetic environment. The zone boundary may be regarded as the point at which the GC-1 counter recording exceeded the background recording by more than 5 impulses, which corresponds to a stream of electrons with

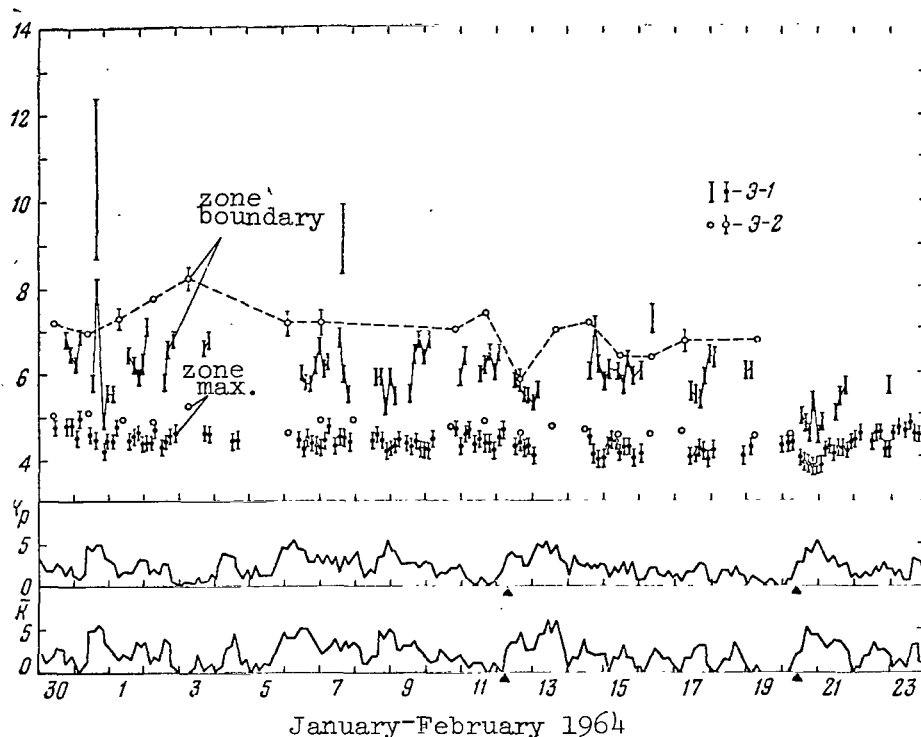


Figure 2

$E > 100 \text{ kev} \sim 10^5 \text{ cm}^{-2} \cdot \text{sec}^{-1}$ . As was shown in (Ref. 10), this leads to an insignificant error in determining the zone boundary on the nocturnal side of the Earth. With an increase in the magnetic activity, the zone boundary moves to smaller  $L$ , both at high and low altitudes. Thus, the motion of the zone boundary corresponds more closely with  $K_p$ , determined by the high-latitude stations. However, the coefficient equals approximately 40%, which coincides with the data in (Ref. 3). When the magnetic activity increased, the zone boundary was sometimes observed at large  $L$ . This phenomenon is apparently related to the occurrence of irregular electron streams beyond the zone boundary, which directly touch the zone and which we cannot distinguish from the zone. For example, on January 31, 1964, at approximately 18 hours UT, for  $K_p = 5$  the zone boundary - according to "Elektron-1" data - was located at  $L \approx 8$ , and up to  $L \approx 12.4$  there were powerful irregular streams with an intensity of  $10^7 \text{ cm}^{-2} \cdot \text{sec}^{-1}$  for electrons with  $E > 100 \text{ kev}$ . Since the satellite "Elektron-2" intersected the zone boundary in the eastern hemisphere, the stations Kheysa, Dickson, Chelyuskin, Tiksi, and Uelen were selected for a detailed analysis of the magnetic environment when the satellite intersected the zone boundary. The analysis was performed between January 30 and February 16. The analysis data are shown in Figure 3.  $L$ , at which the zone boundary was located, is plotted on the abscissa axis. The probability that the magnetic field will be perturbed at the moment when the satellite intersects the zone boundary is plotted on the ordinate axis. There were two types of perturbation at these stations: Either magnetic bays were observed (it is assumed that magnetic bays indicate the presence of aurorae polaris near the station [Ref. 11]), or trains of



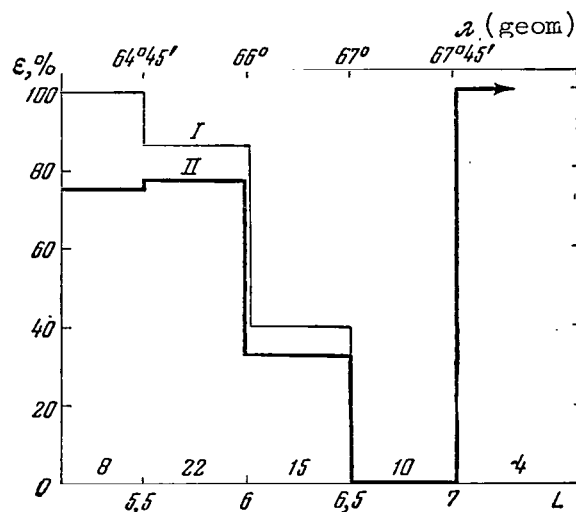
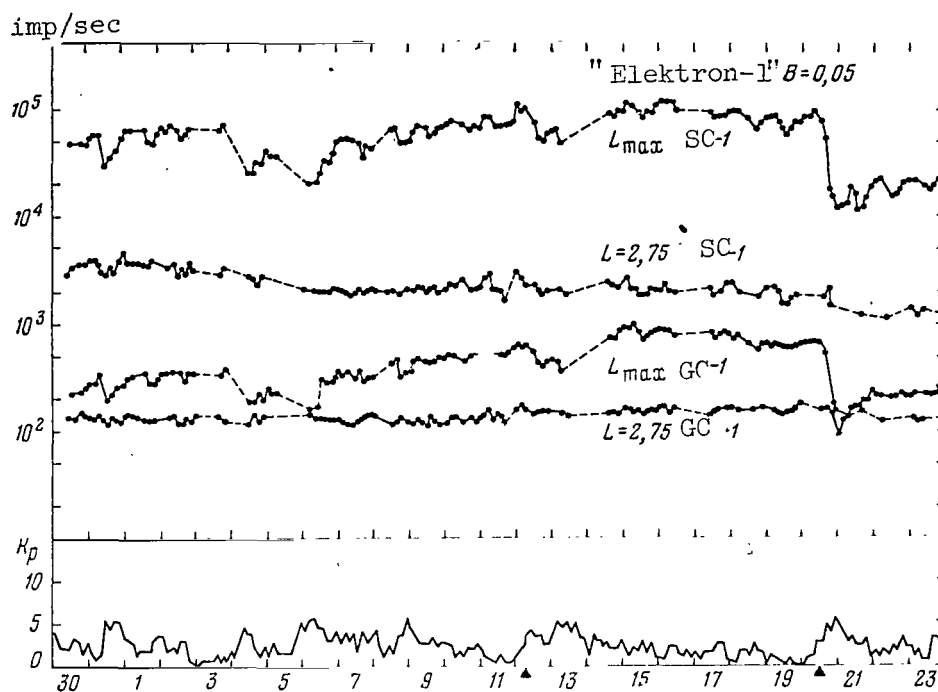


Figure 3

magnetic field fluctuations were observed with an amplitude of several tens of gammas and with a period of several minutes lasting  $\sim 0.5$ -1 hour. Line I gives the probability for the appearance of both types of perturbation for a given boundary position. Line II gives the probability for the appearance of bays. The numbers above each histogram interval indicate the number of cases when the zone boundary was located at a given interval of  $L$ . In the case of  $L > 7$ , only bays were observed; however, there were four such cases. The zone boundary was determined for electrons with energies of  $> 100$  kev. The aurorae polaris produced electrons with  $E \approx 10$  kev. It can be seen that both soft and harder electrons pour out close to the zone boundary. "Injun-1" established the fact that during magnetic storms, when the zone boundary moves to smaller latitudes, there is intense ionosphere absorption of radio noise close to the zone boundary. This radio noise is apparently caused by electrons which are pouring out (Ref. 12). The "Elektron" satellites discovered that this pouring out process occurs close to the boundaries in a quiet environment. During magnetic storms, the zone moves most sharply toward small  $L$ . During the magnetic storm on February 20, 1964, the zone boundary on the /424 nocturnal side was located at  $L \sim 4.5$  (see Figure 2). At 20 hours 51 minutes UT, the zone boundary moved to  $L \sim 5.5$ , and during the next passage it was again at  $L \sim 4.5$ . Not one of the stations indicated above observed magnetic storms or significant field fluctuations at this time. This means that the pumping of particles into the zone and their discharge could take place for  $< 3$  hours close to the zone boundary.

It is clear from the statements given above that the outer radiation zone is very sensitive to the magnetic environment. The space between the outer and inner zones apparently demarcates the magnetosphere regions in which trapped radiation behaves differently. In order to verify this assumption, the time variations at the outer zone maximum and at  $L \approx 2.75$  were compared close to the space between the zones where a high-energy electron zone was discovered (Ref. 9) (see Figure 4). The SC-1 counter



January-February 1961

Figure 4

records primarily electrons with  $E > 6$  Mev. It can be seen that, in spite of significant fluctuations in the outer zone of both the GC-1 and the SC-1, the BC-1 recording at  $L \approx 2.75$  barely changed throughout the observational period.

The monotonic decrease in the SC-1 recording at  $L \approx 2.75$  can be explained by an increase in the electric threshold by a factor of approximately 2 throughout the period, since close to this space the mean electron energy is much less than at the outer zone maximum.

Thus, the "Elektron" satellites have established the scale of time variations in the radiation zones during a quiet Sun year, and have found a connection between certain variations and geomagnetic phenomena.

#### REFERENCES

1. Fan, C. Y., Meyer, P. Simpson, J. A. J. Geophys. Res., 66, N 9, 2607, 1961.
2. Arnoldy, R. L., Hoffman, R. A., Winkler, J. R., Akosofu, C. J. J. Geophys. Res., 67, N 10, 3673, 1962.
3. Forbush, S. E., Pizzella, G., Venkatesan, D. J. Geophys. Res., 67, N 10, 3651, 1962.

4. Frank, L. A., Van Allen, J. A., Nacagno, E. J. Geophys. Res., 68, N 12, 3543, 1963.
5. O'Brien, B. J. J. Geophys. Res., 68, 989, N 4, 1963.
6. O'Brien, B. J. J. Geophys. Res., 69, N 1, 13, 1964.
7. Frank, L. A., Van Allen, J. A., Hills, H. K. J. Geophys. Res., 69, N 11, 2171, 1964.
8. Anderson, R. A., Harris, H. K., Paoli, R. J. Energetic Electron Fluxes in and Beyond the Earth's Outer Magnetosphere. Preprint 1964.
9. Vernov, S. N., Chudakov, A. Ye., Vakulov, P. V., Gorchakov, Ye. V., Kuznetsov, S. N., Logachev, Yu. I., Nikolayev, A. G., Rubinshteyn, I. A., Sosnovets, E. N., Stolpovskiy, V. G., El'tekov, V. A. Present Collection, p. 394.
10. Vernov, S. N., Chudakov, A. Ye., Vakulov, P. V., Kuznetsov, S. N., Logachev, Yu. I., Sosnovets, E. N., Stolpovskiy, V. G. Present Collection, p. 425.
11. Bless, R. C., Gartlein, C. W., Kimball, D. S., Spragne, G. J. Geophys. Res., 64, 949, 1959.
12. Machlum, B., O'Brien, B. J. J. Geophys. Res., 68, N 4, 997, 1963.

## IRREGULAR HIGH-ENERGY ELECTRON STREAMS NEAR THE BOUNDARY OF THE RADIATION ZONES OF THE EARTH

S. N. Vernov, A. Ye. Chudakov, P. V. Vakulov, S. N.  
Kuznetsov, Yu. I. Logachev, E. N. Sosnovets, V. G. Stolpovskiy

When satellites having an apogee altitude of  $\sim 10 R_E$  and greater studied the radiation zones, it was found that electron streams are frequently observed beyond the outer zone boundary, which are irregular in time and which fluctuate greatly in magnitude. The first systematic investigations of the region beyond the radiation zone boundaries was carried out on the American satellites "Explorer-12" and "Explorer-14" from the end of 1961 to August, 1963. These satellites performed measurements primarily from the diurnal side, and produced the following results (Ref. 1-6). /425

1. There is a sharp boundary of trapped electrons with an energy of  $> 40$  kev on the diurnal side at a distance of  $10-11 R_E$ . The electron intensity decreases from  $10^7-10^8 \text{ cm}^{-2} \cdot \text{sec}^{-1}$  to  $\sim 10^4 \text{ cm}^{-2} \cdot \text{sec}^{-1}$  at a distance of  $\sim 0.2 R_E$ . On the nocturnal side, the boundary extends to  $6-7 R_E$ .

2. The abrupt electron decrease coincides with the boundary of the regular magnetic field (magnetosphere). Beyond this boundary, the direction and magnitude of the magnetic field change considerably.

3. The region beyond the magnetosphere boundary, which extends to  $2-3 R_E$ , is called a transitional region. Electron streams are frequently observed in this region with an energy of  $> 40$  kev and magnitude between  $\sim 5 \cdot 10^3 \text{ cm}^{-2} \cdot \text{sec}^{-1}$  and  $\sim 10^5 \text{ cm}^{-2} \cdot \text{sec}^{-1}$ .

4. There is a positive correlation between the appearance of electron bursts and geomagnetic perturbation.

Thus, for example, in 31 out of the 63 flights of the satellite "Explorer-14" electron streams were observed beyond the radiation zone boundary, while there were no streams observed in the remaining flights. For the first case, the mean  $K_p$ -index was  $\sim 2.5$ ; for the second case - 1.5 or less. Thus, even 6 years after the solar activity maximum (1963), the probability for the occurrence of irregular streams is  $\sim 50\%$ . It can be assumed that during years of maximum solar activity the transitional region is almost always occupied by electrons having an energy of  $> 40$  kev. However, this phenomenon only makes it more difficult to clarify the nature of the particles, since the different solar phenomena occur too frequently, and one event is superimposed on another. /426

In this respect, the studies performed on the Soviet satellites "Elektron-1" and "Elektron-2", which were launched in a year of minimum solar activity (1964), provided better results than preceding experiments.

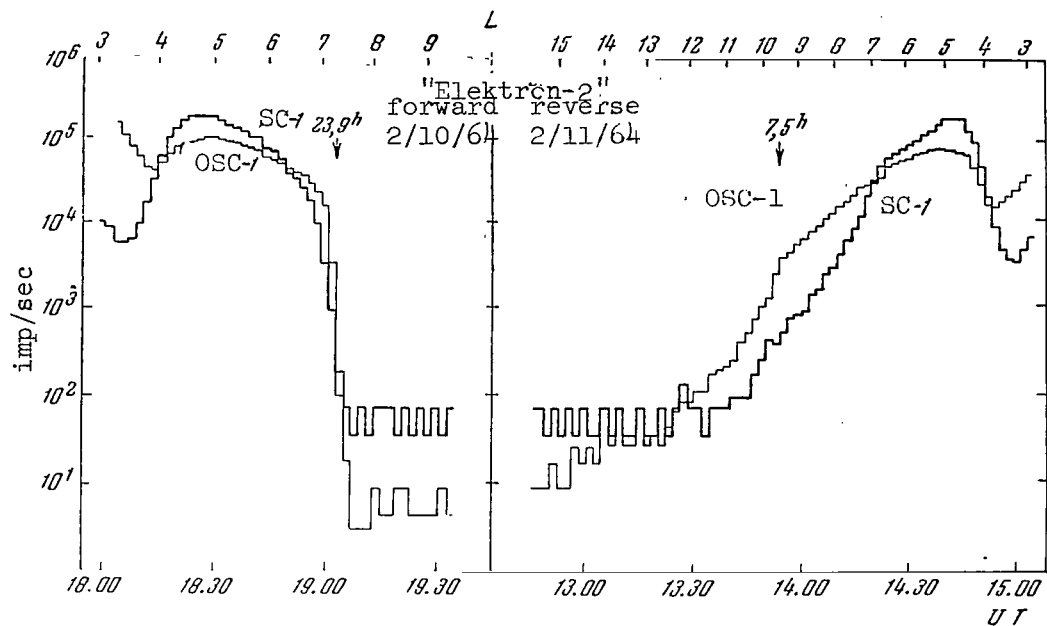


Figure 1

Example of "Elektron-2" Flight Through the Zone  
Boundary From the Nocturnal and Morning Sides  
The direct recording of electrons with  $E_e > 70$  kev  
(OSC-1) is compared with the recording of braking  
radiation of the electrons (SC-1) with  $\epsilon_\gamma > 30$  kev.

The two-satellite system has the advantage that it is thus possible to study simultaneously radiation at two different points in space. The satellites "Elektron-1" and "Elektron-2" were launched so that their apogee, during the first period after launch, occurred at approximately 3 hours am local time. On forward revolutions (from perigee to apogee) the radiation zone boundary was intersected exactly at midnight, and on reverse revolutions it was intersected at 7-8 hours in the morning.

This report presents the results pertaining to the first month in which the satellites were in operation. The spectrum of electrons recorded beyond the zones is considerably softer than in the zones themselves. Therefore, those detectors which had the greatest sensitivity (SC-1, GC-1, OSC-0, OSC-1, SD-0) were primarily used to analyze the results. Detailed information on the apparatus carried on board the satellites is given in (Ref. 7) (see page 535 of the present collection). The inner scintillation counter (SC) recorded individual events with an energy liberation of  $> 30$  kev. The Geiger counter (GC-1) could record only electron braking radiation which penetrated the satellite frame having a thickness of  $\sim 1 \text{ g} \cdot \text{cm}^{-2} \text{ Al}$ . Two scintillation counters (OSC and SD) were located on the outside of the satellite. These counters could record electrons penetrating directly into a crystal through the foil of  $\sim 2 \text{ mg} \cdot \text{cm}^{-2} \text{ Al}$ . Ionization in the crystal was measured in both instruments, /427

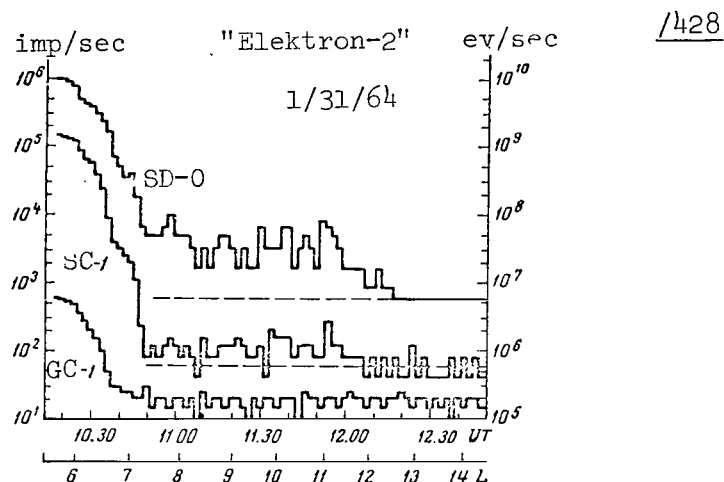


Figure 2

Irregular Stream of Electrons Beyond the Zone Boundary  
on January 31, 1964 During a Polar Storm

SD-0 - Energy liberation in the CsJ(Tl) 0.15×6 mm crystal behind a shielding of 2 mg·cm<sup>-2</sup>Al (ev·sec<sup>-1</sup>); SC-1 - counter readings of  $\gamma$ -quanta > 30 kev behind a shielding of  $\sim 1$  g·cm<sup>-2</sup>Al; GC-1 - Geiger counter behind a shielding of  $\sim 2.35$  g·cm<sup>-2</sup>Al

and electrons having an energy above the given energy could be recorded in the OSC device. The most sensitive channel of the OSC recorded electrons having an energy exceeding  $\sim 70$  kev.

When the data pertaining to the midnight meridian were analyzed, it was found that the electron intensity decreases by 2-3 orders of magnitude in a narrow radial distance range at the outer zone boundary. Since the OSC operated throughout a revolution, it was not possible to determine the zone boundary at each revolution directly from electrons of  $E_e > 70$  kev. However, on those revolutions where the OSC was in operation, it was found that the zone boundary determined by electrons with  $E_e > 70$  kev practically coincided with the boundary given by the parameter SC-1 (Figure 1) which recorded  $\gamma$ -quanta of  $> 30$  kev. Since the electron intensity on the nocturnal side fell very abruptly, it does not matter what is assumed to be the boundary. As can be seen from Figure 1, there is no such sharp intensity decrease for the morning side and, generally speaking, it is not clear which point can be assumed to be the zone boundary. The counter readings of  $\gamma$ -quanta (SC-1) were employed for further analysis, and the zone boundary was assumed to be the point at which the SC-1 recording was  $5 \cdot 10^2$  imp·sec<sup>-1</sup>, which was approximately ten times greater than the background. A comparison of the OSC-1 and SC-1 results shows that the latter recorded electrons with an energy of  $\sim 100$  kev with an efficiency of  $\sim 10^{-3}$ . The counter recording of primary cosmic radiation was  $\sim 50$  imp·sec<sup>-1</sup>. In order to make a reliable determination of a supplementary electron stream,

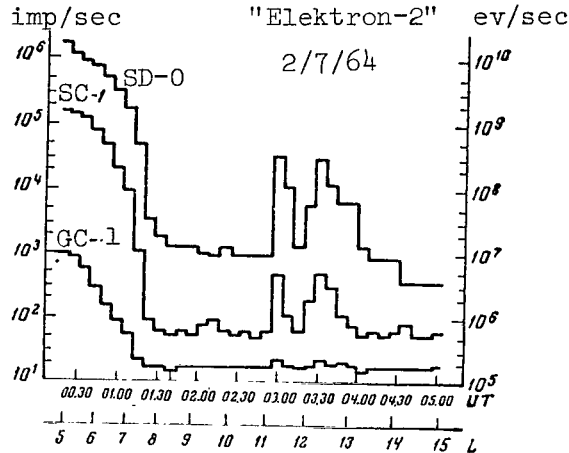


Figure 3

Electron Burst at a Distance of About 50,000 km on  
February 7, 1964 at Three Hours World Time

it was necessary that the recording exceeded this background by approximately a factor of 2 - i.e.,  $100 \text{ imp} \cdot \text{sec}^{-1}$ . The crystal surface was  $4.7 \text{ cm}^2$  and, consequently, the minimum flux of recorded  $\gamma$ -quanta with an energy of  $> 30 \text{ kev}$  was  $\sim 10 \text{ quantum} \cdot \text{cm}^{-2} \cdot \text{sec}^{-1}$ , under the condition that the detector was comprehensive enough. The corresponding minimum flux of electrons with an energy of  $\sim 100 \text{ kev}$  was  $\sim 10^4 \text{ el} \cdot \text{cm}^{-2} \cdot \text{sec}^{-1}$ .

On the basis of the criterion advanced above for determining the zone boundary, it was established that during quiet days the radiation zone terminated at  $L = 6.5-7.5$  on the nocturnal side of the Earth. On the morning side, the zone boundary extended on the average to  $L = 9-10$ . (Here  $L$  is the conditional McIlwain parameter computed in the dipole approximation and expressed in Earth radii).

Figure 1, which shows an example of an "Elektron-2" flight through the zone during a quiet day, uses arrows to designate the boundary position on the nocturnal and morning sides. The similar difference in the boundary position on the nocturnal and morning sides coincides with the results derived in previous works (Ref. 1-6).

Figures 2-5 present several cases in which electron streams were recorded beyond the zone boundary. Figure 2 shows a flight on January 31, 1964 during a polar storm, which began at 9 hours 23 minutes UT. It is interesting to note here that in the wide spatial region from  $L = 7$  to  $L = 12$  the flux magnitude - although it fluctuated - remained on one and the same level on the average. On the Earth's surface this would correspond to the geomagnetic latitude region from  $\sim 68^\circ$  to  $73.5^\circ$ .

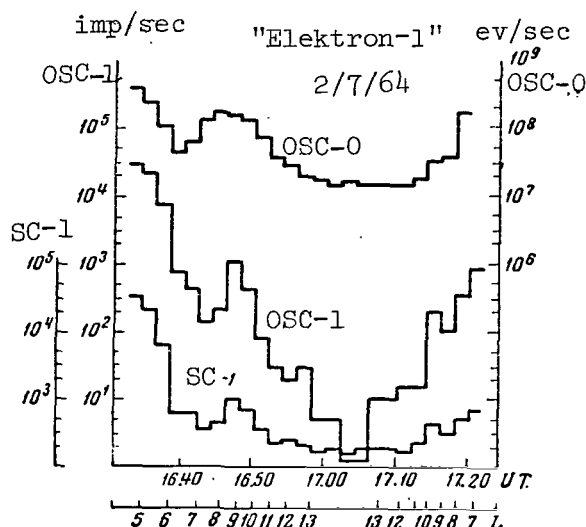


Figure 4

Stream of Electrons at Large Geomagnetic Latitudes  
of  $50^\circ$  on February 7, 1964

OSC-0 - Ionization in a CsJ(Tl)  $3 \times 6$  mm crystal behind  
a shielding of  $2 \text{ mg} \cdot \text{cm}^{-2}$  Al ( $\text{ev} \cdot \text{sec}^{-1}$ ); SC-1 and OSC-1,  
see the captions for Figures 1 and 2.

Figure 3 shows a flight on February 7, 1964, when an electron stream was recorded at a distance of  $\sim 50$  thousand km from the surface of the Earth. Two electron bursts can be seen very clearly here, and the braking radiation recording increased by approximately one order of magnitude.

Figure 4 shows an irregular stream recorded on "Elektron-1" also on February 7, 1964, but during a different period of time. The OSC device operated on this revolution, and the parameter of OSC-1 recorded electrons penetrating the crystal directly through a foil of  $2 \text{ mg} \cdot \text{cm}^{-2}$  Al. It is interesting to note that the OSC-0 ionization maximum shifted somewhat with respect to the maximum of the OSC-1 and SC-1 recording channels. This can apparently be explained by the fact that the energy composition of the stream was heterogeneous and the electron spectrum was very soft at the first moment. It can also be seen from the figure that the satellite intersected the stream on the reverse revolution. However, if the maximum was located at  $L = 8-9$ , according to the SC-1 and OSC-1 parameters, on the forward revolution, then on the reverse revolution it was located at  $L = 9-10$ . It is possible that this is related to time changes, but it may also be assumed that this shift in the maximum was caused by inaccurate information on the drift envelope of electrons as they move around the Earth.

Figure 5 illustrates the clearest recording of electron bursts on February 16, 1964. This flight pertained to an unperturbed day, and when



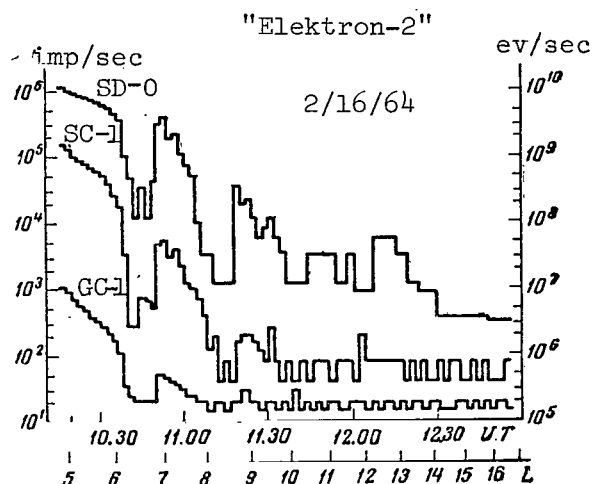


Figure 5

Irregular Stream of Electrons in a Wide Region of  
Radial Distances from  $L \approx 6.5$  to  $L \approx 13.5$ ;  $K_p = 2$

Notation is the same as in Figure 2.

the streams were observed  $K_p = 2$ . The spatial region in which a perturbation was observed extended from  $L \approx 6.5$  to  $L \approx 13.5$ .

The American satellite "Explorer-18" flew simultaneously with the satellites "Elektron-1" and "Elektron-2". Unfortunately, the study (Ref. 8) does not give the exact flight time of the satellite through the region in which we are interested. Nevertheless, we have tried to compare our measurements with the "Explorer-18" data during one of the flights. Figure 6 presents the result of this comparison. Although the satellites flew at different latitudes, the distribution of electrons with  $E_e > 45$  kev, according to "Explorer-18", and the distribution of electrons with  $E_e > 70$  kev, according to "Elektron-2", were quite similar. The small difference can be apparently explained by the different flight time through this zone.

The Table presents information on the most interesting non-stationary stream recorded between January 30 and February 23, 1964.

Figure 7 presents the general picture of the radiation zone boundary and the occurrence of irregular streams, based on data from "Elektron-2". This same figure plots  $K_p$ -indices and  $\Delta T$ , showing the extent to which the real magnetic field of the Earth - measured on "Elektron-2" - differs from the dipole field. These data were kindly given to us by Sh. Sh. Dolginov and Ye. G. Yeroshenko.

It can be seen from the figure that the occurrence of irregular streams outside of the zones of the Earth coincides with an increase in

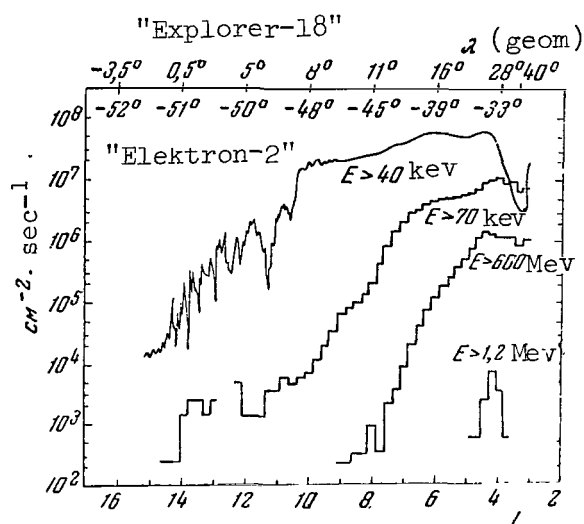


Figure 6

Cross Section of the Zone and Profile of Electron Streams at Different Latitudes, Based on Data From "Elektron-2" and "Explorer-18"

TABLE

Date	Satellite	Crossing the Stream Maximum						Projection on northern Hemisphere		$N_{\max}$ ( $E > 100$ kev) $\text{cm}^{-2} \cdot \text{sec}^{-1}$
		t, hr.	UT min	k, km	$\varphi_{\text{geogr}}$	$\lambda_{\text{geogr}}$	L	$\varphi_{\text{geogr}}$	$\lambda_{\text{geogr}}$	
1/31	"Elektron-1"	18	20	7100	-51°	+122°	10	78°	+122°	$2 \cdot 10^5$
2/7	"Elektron-2"	3	00	46900	-39.5	-30	11.2	63	-60	$7 \cdot 10^4$
		3	30	50000	-41.5	-36	12.3	65	-65	$7 \cdot 10^4$
2/13	"Elektron-1"	16	46	7100	-48	+125	8.8	77	+125	$4 \cdot 10^5$
		17	15	6300	-61	+175	9.7	70	-138	$5 \cdot 10^4$
	"Elektron-1"	3	02	6400	-61	13	6.3	58	-44	$1 \cdot 10^5$
		3	06	6200	-60	23	6.4	59	-40	$2 \cdot 10^4$
2/16	"Elektron-2"	10	10	35700	-58	-57	14.4	64	-70	$1.5 \cdot 10^5$
	"Elektron-2"	10	52	28200	-26	-170	7	63	-133	$10^7$
2/16	"Elektron-2"	11	24	33600	-31	-174	8.8	69	-140	$10^5$
		2	49	6800	-60	-16	5.7	54	-60	$10^6$

\*The satellite apparently intersected the same point twice.

the geomagnetic field perturbation both on the surface of the Earth, and at distances of  $\sim 30\,000$  km from the Earth. The question of the nature of these streams then arises. It is evident that, when the magnetic perturbation increases at large distances from the Earth, accelerating processes /431

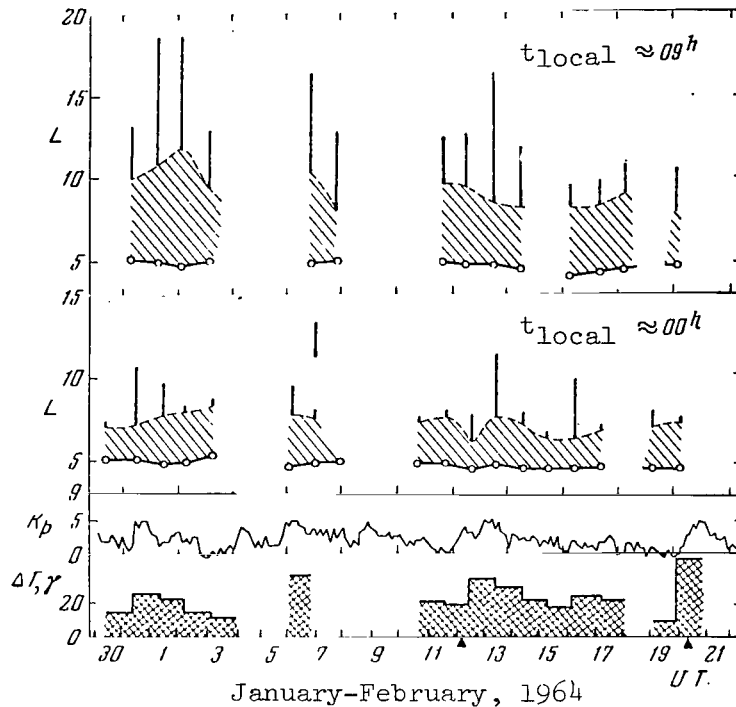


Figure 7

Position of Outer Zone Maximum and its Boundary on the Morning and Evening Side of the Earth

The vertical lines designate the sections of the "Elektron-2" trajectory where the SC-1 reading exceeded  $100 \text{ imp} \cdot \text{sec}^{-1}$ ;  $\Delta T$  - the amount by which the measured magnetic field exceeds the dipole field.

come into operation, which cause electrons to appear with an energy of up to 100 keV.

According to data obtained on the satellite "Injun-3" (Ref. 9), when the accelerating mechanism is in operation electrons are formed with such pitch-angles that they are reflected at a high altitude above the Earth's surface. In those regions where the accelerated particles can be held back by the magnetic field of the Earth, part of them is captured.

Figure 8 shows a picture of the outer radiation zone, based on a recording of x-ray  $\gamma$ -quanta with  $E_\gamma > 30 \text{ keV}$  on three consecutive flights. During the first flight the zone had a sharp boundary at  $L \approx 6.3$ ; beyond this point, the counter recorded a background. During the second flight, the zone boundary was also located at  $L \approx 6.3$ , but beyond the boundary there were irregular streams which occupied a region up to  $L \approx 10$ . During the third flight, the zone boundary was discovered at  $L \approx 6.8$ . This

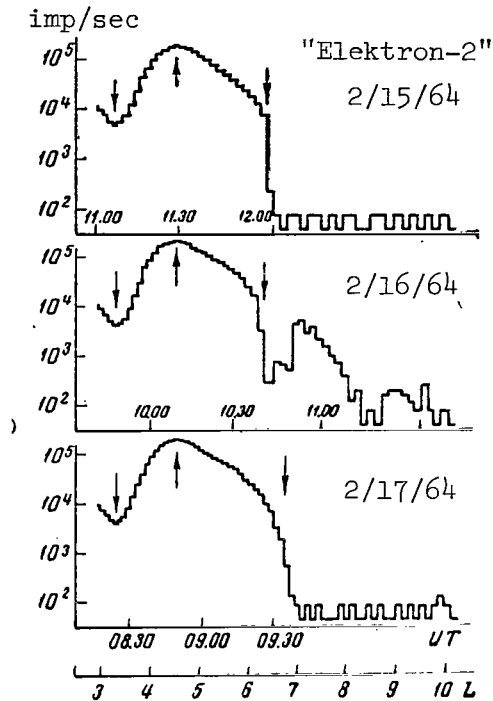


Figure 8

Three Consecutive Flights Through the Outer Zone Boundary  
From the Nocturnal Side Before, During, and After the  
Appearance of an Irregular Electron Stream

picture can be explained by the fact that irregular streams were either scattered deep within the magnetosphere - and a portion of the electrons was captured close to the zone boundary - or accelerating processes developed in the interval between the second and third flights close to the zone boundary, producing trapped electrons at  $L \approx 6.8$ .

Since all of the recorded phenomena were observed in high geomagnetic latitude regions, it is interesting to trace the connection between these phenomena and the terrestrial observations of such geophysical phenomena as the aurorae polaris and magnetic bays. The possibility is not excluded that particles with lower energies are produced along with streams of electrons with  $E_e > 40$  kev. Thus, the satellites "Explorer-12" (Ref. 2, 4) and "Elektron-2" (Ref. 10) recorded electron fluxes with energies of 1-10 kev up to  $10^9$ - $10^{10}$  el·cm<sup>-2</sup>·sec<sup>-1</sup>. An electron spectrum beginning with  $E_e > 500$  ev was obtained for a stream of electrons observed on February 16, 1964. Data on the electron streams between 0.5-10 kev were kindly furnished by B. I. Savin. If the spectrum is represented in an exponential form

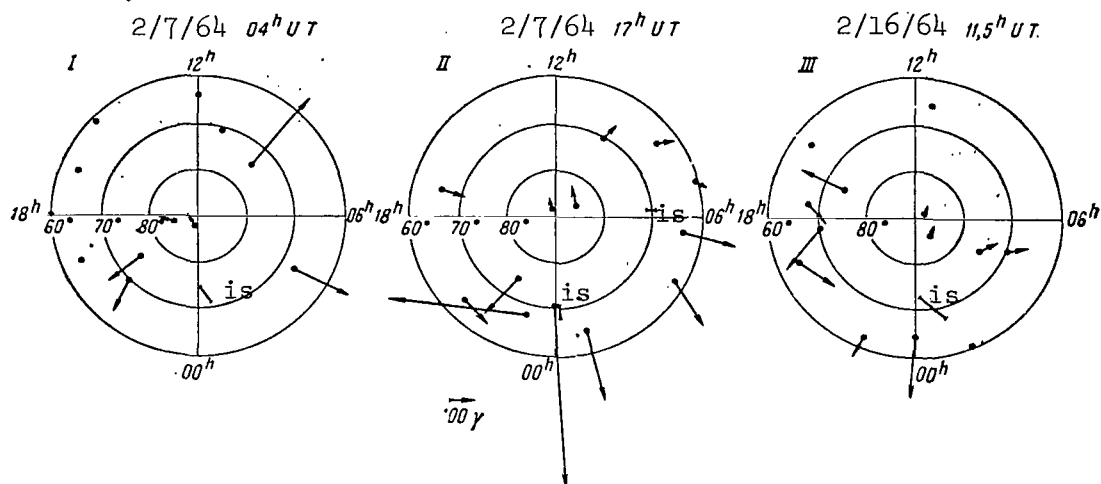


Figure 9

Distribution of Magnetic Perturbations in the Northern Polar Cap on February 7 and February 16, 1964

The polar cap projection is constructed in geomagnetic coordinates. The points designate the stations at which magnetic perturbations were observed at a given moment.  
(is = irregular streams)

$$N(>E) \sim e^{(-E/E_0)}, \quad N(>0,5 \text{ kev}) = 2 \cdot 10^9 \text{ cm}^{-2} \cdot \text{sec}^{-1},$$

then in the 0.5-10 kev range,  $E_0 \sim 4$  kev; 10-40 kev,  $E_0 \sim 10$  kev; 40-150 kev,  $E_0 \sim 30$  kev.

Moving along the force lines of the field, these particles can enter the lower atmospheric layers and cause perturbations there. It is known that magnetic bays may be related to the discharge of electrons into the atmosphere (Ref. 11) at  $L \approx 6-7$  and the aurorae polaris are observed during the existence of these bays (Ref. 12). We analyzed three cases in detail, which are shown in Figures 3, 4, and 5.

/432

Investigations were carried out, based on the stations at which the magnetic bays were observed. According to present day opinions, these bays are caused by ionosphere currents. The currents are formed during the aurorae polaris. The direction of the current and its position may be determined by the sign of the perturbation (i.e., whether the current flows into the region to the south or to the north of the station). Figure 9 shows the perturbation distribution.

A list of stations is presented below, which were utilized to formulate the perturbation distribution at the polar cap:

Thule	Uelen
Resolute	Tiksi
Baker Lake	Chelyuskin
Fort Churchill	Dickson
Minuk	Kheysa
Sitka	Murmansk
College	Reykjavik

Figure 9 was compiled for the maximum development of bays accompanying the appearance of irregular streams. It can be seen that the projection of the observed stream in the northern hemisphere falls within the latitudinal region of maximum magnetic perturbations. The magnetic perturbations correspond to an electron stream in the westerly direction. An electron stream in the westerly direction was observed in Case I - on the morning side of the Earth, in Case II - on the nocturnal side of the Earth, and in Case III - on the evening side of the Earth. There was no current vortex in the opposite direction on the diurnal side of the Earth. In Case II and III, a current stream in a south-east direction branched off at lower latitudes from the main stream proceeding in a westerly direction, on the evening side of the Earth.

It must be emphasized that the electron streams being studied were observed in the southern hemisphere on the nocturnal side, and the distribution of magnetic perturbations was formulated for the northern polar cap. The concurrent occurrence of these events apparently indicates closed force lines of the Earth's magnetic field up to a latitude of  $75^\circ$ . No definite conclusion may be drawn regarding the connection between the aurorae polaris and the existence of non-stationary electron streams beyond the zone boundary, due to the lack of constant, detailed observations of the aurorae polaris. However, due to the existence of the magnetic bays, it may be <sup>/433</sup> assumed with great probability that such a connection exists. The possibility is not excluded that a certain portion of the particles formed at large distances from the Earth scatter in a radial direction across the force lines of the magnetic field. When a particle retains the first invariant of motion, its energy will increase as the Earth is approached, and consequently observation of irregular electron streams may possibly clarify the nature of particles populating at least the outer radiation zone.

#### REFERENCES

1. Rosser, W. G. V., O'Brien, B. J., Van Allen, J. A., Laughlin, C. D. J. Geophys. Res., 67, 4533, 1962.
2. Freeman, J. W., Van Allen, J. A., Cahill, L. J. J. Geophys. Res., 68, 2121, 1963.
3. Cahill, L. J., Amazeen, P. G. J. Geophys. Res., 68, 1835, 1963.

4. Freeman, J. W. J. Geophys. Res., 69, 1961, 1964.
5. Frank, L. A., Van Allen, J. A., Nacagno, E. J. Geophys. Res., 68, 3543, 1963.
6. Frank, L. A., Van Allen, J. A., J. Geophys. Res., 69, 4925, 1964.
7. Vernov, S. N., Chudakov, A. Ye., Vakulov, P. V., Gorchakov, Ye. V., Kuznetsov, S. N., Logachev, Yu. I., Nikolayev, A. G., Rubinshteyn, I. A., Sosnovets, E. N., Stolpovskiy, V. G., El'tekov, V. A. Present Collection, p. 394.
8. Anderson, K. A., Harris, H. K., Paoli, R. J. Energetic Electron Fluxes in and Beyond the Earth's Outer Magnetosphere. Preprint, 1964.
9. O'Brien, B. J. J. Geophys. Res., 69, No 13, 1964.
10. Vernov, S. N., Vel'nikov, V. V., Savenko, I. A., Savin, B. I. Present Collection, p. 381.
11. Barkus, J. R., Brown, R.R. In "Radiation Zones and Geophysical Phenomena", p. 216, IL, 1963.
12. Bless, R.C., Gartlein, C.W., Kimball, D.S., Spragne, G. J. Geophys. Res., 64, 949, 1959.

---

PULSATIONS OF THE MAGNETIC FIELD ACCORDING TO MEASUREMENTS  
ON THE SATELLITE "ELEKTRON-3".

(Summary)

S. N. Vernov, A. Ye. Chudakov, P. V. Vakulov,  
Ye. V. Gorchakov, Yu. I. Logachev, A. G. Nikolayev,  
I. A. Rubinshteyn, E. N. Sosnovets, M. V. Ternovskaya

The satellite "Elektron-3", which was launched on July 11, 1964, carried apparatus for recording magnetic field pulsations. The magnetic field pulsations were recorded by a coil with a ferrite core located outside of the frame, close to its outer surface. Signals from the coil fell on two amplifying channels; the pass band of one of them was 1-10 cps, the pass band of the other - 30-300 cps.

The number of impulses between interrogations, whose amplitude exceeded  $\sim 1$ ,  $\sim 5$ ,  $\sim 25\gamma$ , was recorded on both channels. The memory system was set up in such a way that impulses were recorded during the time between 7 interrogations on each of the six interrogation channels, after which the channel system was shut off and was insensitive to further impulses, due to the short length of the conversion chains. In order to decrease the influence of interference, the circuit was also blocked during interrogation of the instrument readings by the memory device. A very small portion of the information obtained has been processed as of the present. It was found that coarse channels (threshold  $\geq 25\gamma$ ) during the time between interrogations did not record even one impulse, as a rule, while the most sensitive channels

( $\geq 1\gamma$ ) recorded more than 7 impulses every two minutes.

/434

Channels having mean sensitivity ( $\geq 5\gamma$ ) recorded the number of impulses in the measureable range: On the order of 2-3 on the low-frequency channel, and on the order of 1 on the high-frequency channel.

Thus, the number of magnetic field pulsations with an amplitude of  $\geq 5\gamma$  in the frequency region 1-10 cps is, generally speaking, greater than in the 30-300 cps region.

It should also be noted that the pulsation intensity has a tendency to increase in certain geographic regions. As a rule, the pulsation intensity increase on the low-frequency channels is not accompanied by an increase in the recording rate on the high-frequency channel.

#### STUDY OF THE EARTH'S OUTER RADIATION ZONE AT LOW ALTITUDES DURING SPACECRAFT-SATELLITE FLIGHTS AND THE "KOSMOS" AES FLIGHTS BETWEEN 1960 AND 1963

S. N. Vernov, V. Ye. Nesterov, N. F. Pisarenko,  
I. A. Savenko, L. V. Tverskaya, P. I. Shavrin

The second and third cosmic spacecraft-satellites, as well as certain satellites in the "Kosmos" series, carried radiometers which included scintillation and gas-discharge counters. Detailed information on the radiometric apparatus on these satellites is given in (Ref. 1-3).

The results derived from these studies are given below, pertaining to longitudinal intensity behavior, position of the outer radiation zone maximum, time variations, the space between radiation zones, and escapes from the outer radiation zone based on measurements at low altitudes (200-400 km above the Earth's surface).

#### 1. Apparatus and Experiment Conditions

The Table presents the composition and some brief characteristics of the recorders.

The crystals of the inner scintillation counters were strongly screened on all spacecrafts. About 82% of the total solid angle of these counters was shielded by a layer of matter of more than  $8 \text{ g}\cdot\text{cm}^{-2}$ . The remaining 18% of the solid angle had screening between  $5-8 \text{ g}\cdot\text{cm}^{-2}$ . However, all of this section was covered in addition by equipment and armature whose exact thickness cannot be calculated. Thus, the inner scintillation counter could record electrons from the outer radiation zone only through braking radiation. We should note that this greatly decreased the dependence of the recording on the satellite orientation with respect to the geomagnetic field force lines.



## APPARATUS

Within the Satellite	Outside the Satellite
Scintillation counter with NaJ (Tl), d = 30 mm, h = 14 mm crystal. Recording is performed with threshold of 25 kev and anode current. Two STS-5 gas discharge counters.	Scintillation counter with CsJ (Tl), d = 30 mm, H = 2.2 mm crystal. Anode current is recorded. Minimum screening of $2 \text{ mg} \cdot \text{cm}^{-2}$ Al.
Scintillation counter with NaJ (Tl), d = 30 mm, h = 14 mm crystal. Recording is done with threshold of 25 kev and anode current. STS-5 gas discharge counter.	Scintillation counter with CsJ (Tl), d = 30 mm, h = 2.2 mm crystal. Anode current is recorded. Minimum screening of $2 \text{ mg} \cdot \text{cm}^{-2}$ Al.
Scintillation counter with CsJ (Tl) d = 30 mm, h = 20 mm crystal. Recording is done with threshold of 60 kev and anode current. Two STS-5 counters.	Scintillation counter with CsJ (Tl), d = 30 mm, h = 20 mm crystal. Recording is done with threshold of 60 kev and anode current. Minimum screening of $2 \text{ mg} \cdot \text{cm}^{-2}$ Al.
Scintillation counter with CsJ (Tl), d = 30 mm, h = 20 mm crystal. Recording is done with threshold of 30 kev and anode current. Two STS-5 counters.	Scintillation counter with CsJ (Tl), d = 30 mm, h = 20 mm crystal. Recording is done with threshold of 45 kev and anode current. Minimum screening of $180 \text{ mg} \cdot \text{cm}^{-2}$ .
Scintillation counter with NaJ (Tl), d = 30 mm, h = 20 mm crystal. Recording is done with threshold of 15 kev and anode current. STS-5 counter.	Scintillation counter with CsJ (Tl), d = 30 mm, h = 20 mm crystal. Recording is done with threshold of 60 kev and anode current. Minimum screening of $180 \text{ mg} \cdot \text{cm}^{-2}$ .
Scintillation counter with CsJ (Tl), d = 30 mm, h = 20 mm crystal. Recording is done with threshold of 160 kev and anode current. Two STS-5 counters.	Scintillation counter with CsJ (Tl), d = 26 mm, h = 4 mm crystal. Minimum screening of $2 \text{ mg} \cdot \text{cm}^{-2}$ Al. Recording is done with threshold of 75 kev.
Scintillation counter with CsJ (Tl), d = 30 mm, h = 20 mm crystal. Recording is measured with a threshold of 30 kev and anode current. Two STS-5 counters.	Spherical electrostatic analyzer.
Scintillation counter with CsJ (Tl), d = 30 mm, h = 20 mm crystal. Recording is done with threshold of 100 kev and anode current. Two STS-5 counters.	Spherical electrostatic analyzer.

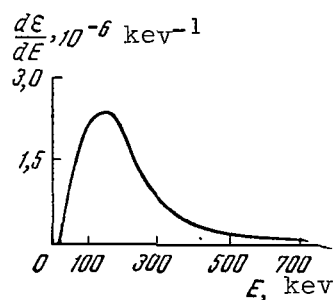


Figure 1

The outer scintillation counters on the spacecrafts could directly record, in addition to braking radiation, electrons with an energy greater than 100 keV with a minimum screening of  $2 \text{ mg} \cdot \text{cm}^{-2}$ , and above 600 keV with a minimum screening of  $180 \text{ mg} \cdot \text{cm}^{-2}$ .

Apart from the recording rate of impulses with an amplitude exceeding a certain threshold value, the scintillation counters made it possible to measure the anode current which was proportional to the mean liberation of energy in the crystal. The readings of other recorders in the radiometric apparatus (Geiger counters and spherical analyzers) are not employed in this study. Figure 1 illustrates the probability of recording outer radiation zone electrons with the inner scintillation counter of the radiometric apparatus, computed under the assumption that a stream of electrons, with the energy spectrum given in (Ref. 4), fall on the aluminum sphere with a wall thickness of  $5 \text{ g} \cdot \text{cm}^{-2}$ , within which the counter is located. /436

It can be seen from this figure that the inner scintillation counters of the radiometric apparatus primarily recorded electrons having energies between 50-300 keV. The curve in Figure 1 was obtained without allowance for the resolution of the scintillation counter and under the assumption that the efficiency with which  $\gamma$ -radiation was recorded equalled unity for every energy. Precise allowance for these factors does not change the conclusion formulated above.

During the operational period of the satellites listed in the Table information was obtained on the more than 300 cases in which they entered the outer radiation zone in both hemispheres. Detailed data on the geographic distribution of this information are given in the dissertation (Ref. 5).

## II. Longitudinal Behavior

The apparatus on the third artificial Earth satellite (Ref. 6) made it possible to determine the outer radiation zone position at altitudes of 300-600 km in the northern hemisphere, in the  $30$ - $120^\circ\text{W}$  longitudinal range. In the southern hemisphere, the outer zone was recorded at an altitude of 1500 km in the  $30$ - $180^\circ\text{E}$  region (Ref. 7). "Explorer-7" transmitted information on the outer zone also in a limited longitudinal range (Ref. 8). Studies performed on the second and third Soviet cosmic

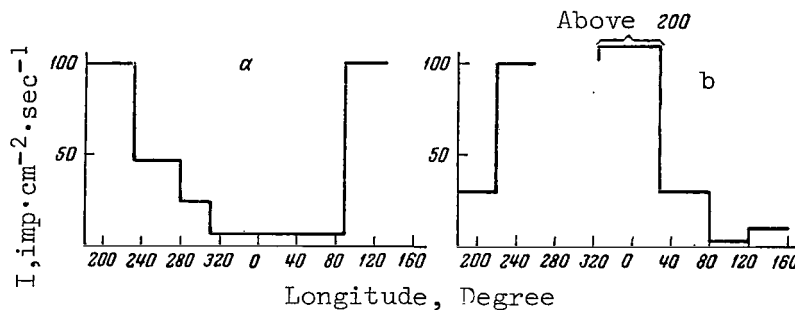


Figure 2

spacecrafts in August and December, 1960, first made it possible to study the outer radiation zone position in detail close to the Earth, at all longitudes in the geographic latitudinal range of  $\pm 65^\circ$ . Regions were discovered at all longitudes in which the increased radiation intensity could not be explained by the latitudinal effect of cosmic rays.

It was shown in (Ref. 9-11) that all of these regions were caused by the outer radiation zone of the Earth, except for the region on the eastern coast of Brazil. Since there are presently no doubts regarding the validity of this statement, it is not necessary to provide corroboration for it.

It should be noted that, when the spacecrafts entered sections of the outer (and inner) radiation zone, there was a sharp increase in the background recordings of the apparatus carried by the spacecrafts to study heavy nuclei (Ref. 12) and x-ray radiation of the Sun (Ref. 13).

Longitudinal dependence will be used to designate the intensity change with longitude for fixed values of the parameter  $L$  and the altitude above the Earth's surface. The intensity dependence on longitude with fixed  $L$  and  $B$  will be called longitudinal behavior. The longitudinal behavior results from the non-dipole nature of the geomagnetic field, which is particularly significant at low altitudes. If the line of equal values of  $B$  at all longitudes lies at one altitude for the central dipole, then the altitude of the line for equal  $B$  depends on longitude for a real geomagnetic field. Due to this fact, when drifting longitudinally the particles enter the region with a very different atmospheric density. For purposes of illustration, let us say that the altitude of the specular points in the southern hemisphere changes as a function of longitude by more than 1000 km, while the atmospheric density changes  $e$  times when the altitude changes by 50 km (Ref. 14). Since the atmospheric density at low altitudes is large, the mean lifetime of a particle, with respect to downward diffusion, can be less than the drift period with respect to longitude - which leads to the occurrence of longitudinal behavior. Finally, a trivial reason for the longitudinal behavior is the drift towards the Earth of the drift trajectory in any longitudinal range.

An analysis of the maxima distribution of the inner scintillation counter recording on the second spacecraft showed that, in spite of

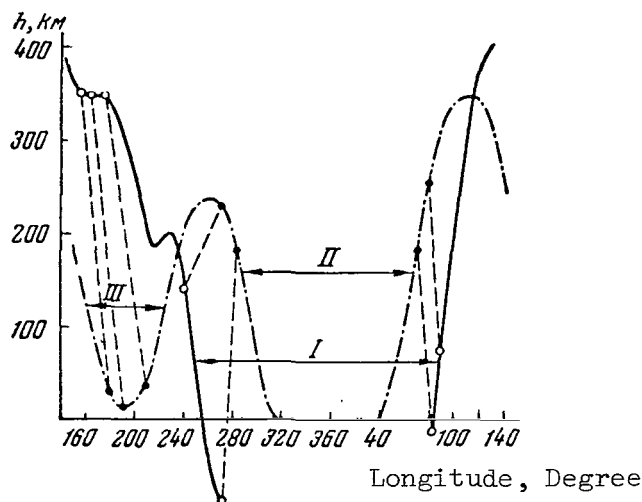


Figure 3

significant time variations, there is a clear longitudinal intensity dependence in the outer zone. This dependence can be roughly determined by averaging the counter readings for fixed  $L$  in the longitudinal range of  $50-75^\circ$ . The result derived from averaging data from the second spacecraft for  $L \approx 3.7$  (mean flight altitude 320 km) is shown in Figure 2 for the northern (a) and southern (b) hemispheres. The mean intensity at those longitudes for which there is information is plotted along the ordinate axis in the figure. /437

The nature of the longitudinal dependence obtained in Figure 2 can be explained quite well by the structure of the real magnetic field. Figure 3 shows the altitudes of drift trajectories ( $L = 3$ ,  $B = 0.52$ ) in the southern (solid curve) and in the northern (dash-dot curve) hemispheres as a function of geographic longitude (read off from Greenwich to the east) (Ref. 15). The conjugate points are connected by dashed lines. Three negative geomagnetic anomalies can be clearly distinguished by the drift trajectory patterns; the South Atlantic (see I in Figure 3), the North Atlantic (II), and the anomaly with its center in the region of the Bering Sea (III), which we call the Bering Anomaly. The South Atlantic anomaly and the Bering Anomaly are important for the outer zone. The North Atlantic Anomaly region is connected to the South Atlantic Anomaly, where the specular points are located much lower (see Figure 3). Therefore, the South Atlantic Anomaly plays the predominant role at these longitudes.

A comparison of Figures 2 and 3 leads to the conclusion that the regions of the negative anomalies represent regions of maximum radiation intensity at a given altitude. The longitudinal intensity dependence outside of the anomalies is determined by the difference between the altitudes of the specular points in both hemispheres. The intensity is much less in the region adjoining the anomaly.

In order to clarify the role of the South Atlantic Anomaly, let us trace the longitudinal intensity dependence for fixed  $L$ . The maximum value of  $L$  for drift envelopes which are intersected by the satellite at all

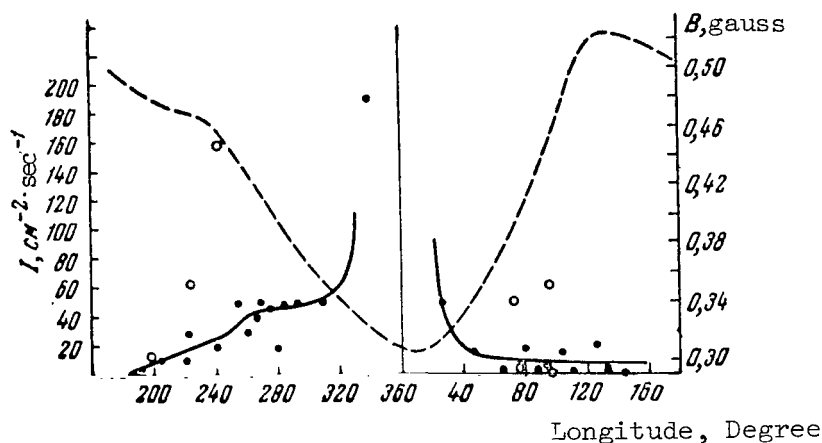


Figure 4

longitudes is 2.5, which corresponds to the gap between the zones.

The solid curve, which approximates the experimental points (black circles), in Figure 4 represents the intensity dependence on longitude for the drift surface  $L = 2.5$  at an altitude of 320 km in the southern hemisphere (Ref. 16). The dashed lines gives the dependence of the magnetic field strength  $B$  on longitude on the same drift surface for the same altitude. Curve 1 in Figure 5 represents the behavior of one of the drift trajectories for  $L = 2.5$  in the southern hemisphere. The experimental points, through which this trajectory passes at an altitude of 320 km, occur at longitudes of 280 and 70°. The region between these points may pertain to the anomaly. For purposes of comparison, curve 2 gives the drift trajectory of adjoining specular points in the northern hemisphere.

It can be seen from Figure 4 that in the longitudinal region of 260-320° increased intensity  $\sim 40-50 \text{ imp}\cdot\text{cm}^{-2}\cdot\text{sec}^{-1}$  is observed to the west of the anomaly for  $L = 2.5$ . We should point out that there was not one point in this region at which background was recorded. The situation is quite different in the longitudinal region to the east of the anomaly, beginning at 50-60°. For the same value of  $L$ , points are observed with an intensity which barely differs from the background (the background is subtracted for the data on the graph), as well as points with an intensity of about  $20 \text{ imp}\cdot\text{cm}^{-2}\cdot\text{sec}^{-1}$ . Thus, the intensity in this region is considerably less, on the average, than to the west of the anomaly. As can be seen from the pattern of the dependence  $B$  on longitude, on the same drift surface (dotted curve in Figure 4) the  $B$  are identical, and the intensities are different, within a wide longitudinal range to the east and to the west of the anomaly. This points to the existence of a longitudinal pattern along the given drift surface. This is a natural result, which is completely understandable. It can be seen from Figure 5 that the drift trajectories, which penetrate the anomaly at an altitude of 320 km to the west and to the east, drift near the

/439

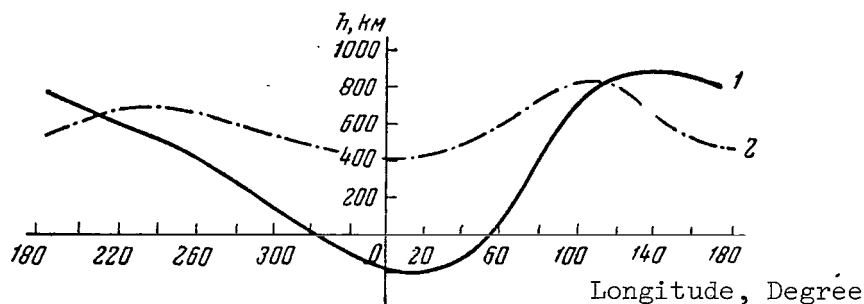


Figure 5

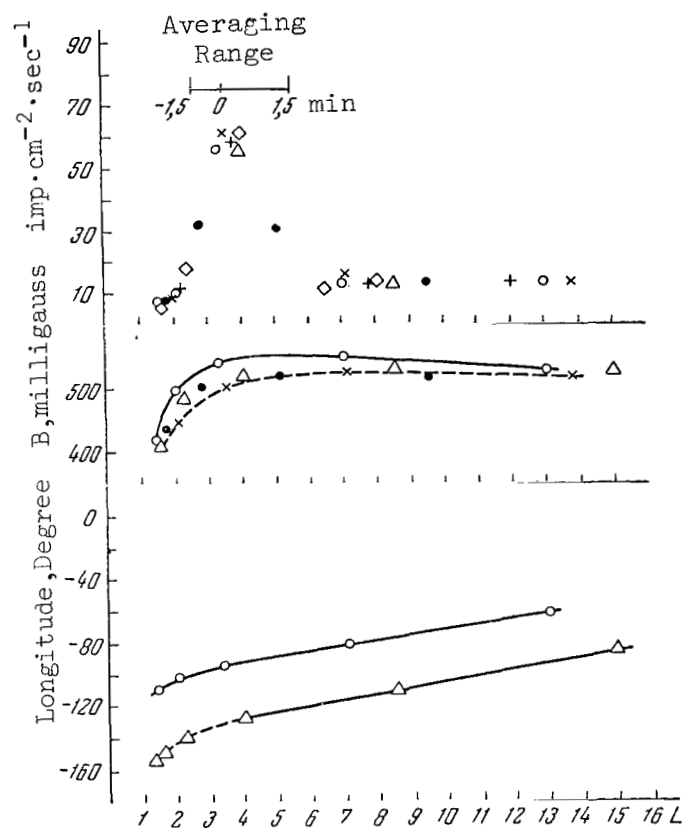
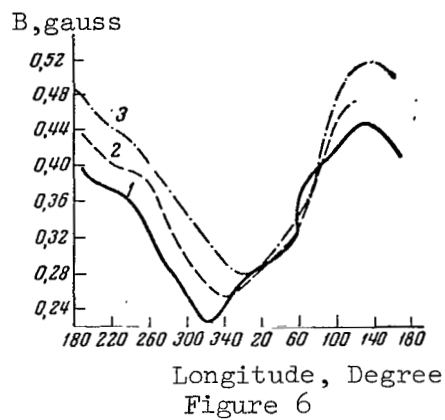
Earth. Therefore, when the anomaly is left behind, there are almost no intensities at the points to the east of the anomaly at an altitude of 320 km, and the particles proceed to scatter to these altitudes from higher altitudes during the longitudinal drift.

As has been already pointed out, the drift envelopes with  $L > 2.5$  were not intersected at all longitudes of the satellite trajectory. However, in spite of the inadequate amount of information, it can be determined that the same characteristic is manifested for large  $L$  as it is for  $L = 2.5$ : The intensity along the line of different  $L$  at an altitude of 320 km is greater to the west of the anomaly than it is to the east. For purposes of illustration, Figure 4 uses white circles to plot the intensity values for  $L = 3.4$  (the outer zone maximum, as will be shown below, was located close to  $L = 3.7$  at this time).

The characteristics of the intensity distribution within the anomaly are given below and in Figure 6.

	1.3			1.6			2.1			2.9		
Longitude, degree . . . .	311	236	349	320	336	353	333	346	359	339	360	16
$I, \text{imp} \cdot \text{cm}^{-2} \cdot \text{sec}^{-1}$ . . . .	50	153	16	100	344	110	120	178	85	200	600	300

In spite of the fact that these data pertain to the gap between the zones, they clarify the influence of the South Atlantic Anomaly on the intensity distribution in the outer radiation zone. Figure 6 presents curves showing the dependence of  $B$  on longitude for different drift surfaces at an altitude of 320 km (1 -  $L = 1.3$ ; 2 -  $L = 1.6$ ; 3 -  $L = 2.1$ ). The largest recording in the anomaly region is made in the region of the minima for these curves. Based on data presented above, it can be seen that there is a significant shift in the intensity maximum for  $L$  which differ in longitude, which corresponds to the shift of the curves in Figure 6. The inner zone maximum occurs in the  $L = 1.5$ - $1.6$  region. An analysis of the intensity distribution along the drift envelopes shows that at low altitudes there is a smooth intensity change with longitude. Three longitudinal regions can be clearly distinguished in the southern hemisphere: A peak in the anomaly ( $320$ - $50^\circ$ ), a low-intensity region ( $60$ - $220^\circ$ ), and a plateau to the west of the anomaly



(260-320'). The connection between the intensity distribution in the anomaly and the characteristics of the real geomagnetic field can be traced.

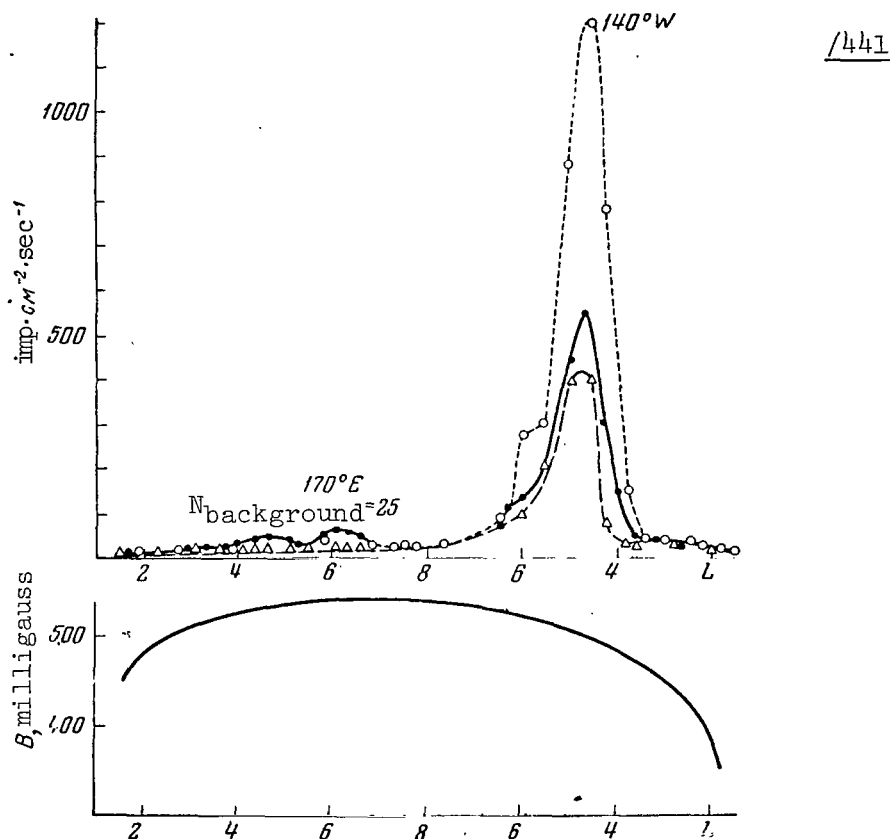


Figure 8

In the northern hemisphere increased intensity is observed in the region of the Bering anomaly ( $120^{\circ}$ - $240^{\circ}$ ), while at the other longitudes the intensity barely differs from the background. The existence of the Bering Anomaly must also lead to a longitudinal behavior; however, the influence of the South Atlantic Anomaly is much stronger.

### III. Position of the Maximum

The occurrence of a sharply expressed intensity maximum at a certain value of  $L = L_{\max}$  is a characteristic indication of the outer radiation zone. Generally speaking, the position of  $L$  depends on the detector with which the zone profile is recorded (the intensity dependence on  $L$  [Ref. 5] is called the profile). In particular, the detector for electrons having an energy of  $\gtrsim 40$  kev does not have a sharply expressed maximum (Ref. 17).

Figure 7 gives the intensity recorded by the inner scintillation counters on the second and third spacecrafts on trajectory revolutions which were no more than  $70^{\circ}$  apart with respect to longitude.



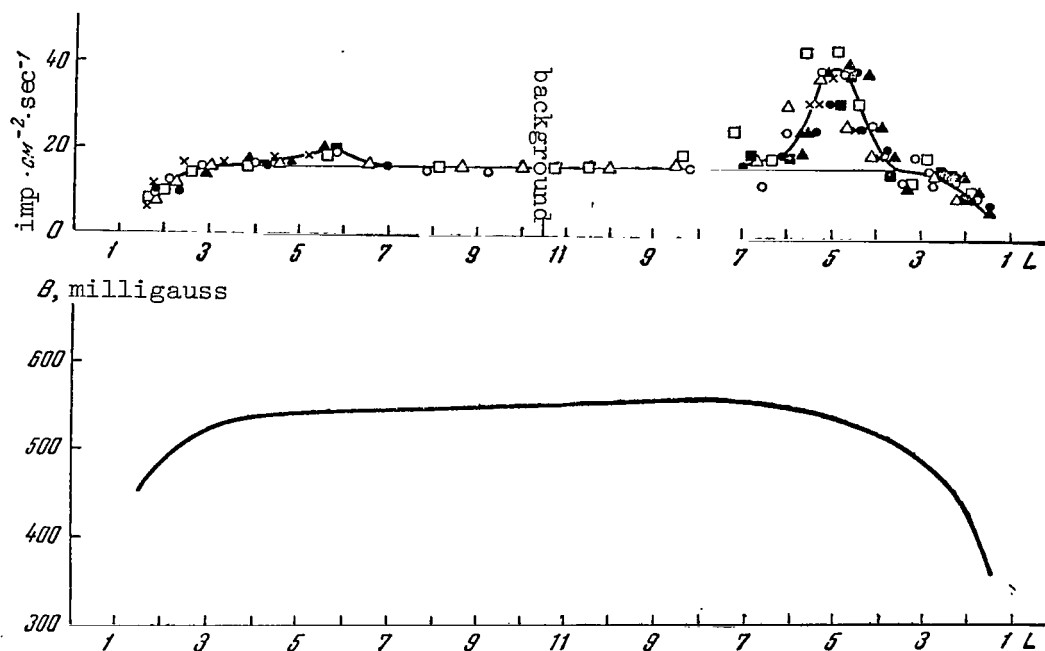


Figure 9

The middle section of the graph in Figure 7 shows the dependence of B on L along certain revolutions (data pertaining to different revolutions are designated by different signs in this and subsequent graphs), while the lower section shows the longitudinal dependence on L for two revolutions in a given longitudinal range. In spite of the relatively large range over which the data are averaged in time (3 minutes) on the spacecrafts, it can clearly be seen in Figure 7 that the intensity in the outer radiation zone is described by a characteristic profile with  $L_{\max}$  in the  $L = 3.7$  region. In the case of  $L > 6$ , the intensity corresponds to the level of the cosmic ray background. /442

The fact the intensity recorded on the third spacecraft is not less than that recorded on the second spacecraft - in spite of the low flight altitude - can apparently be explained by the fact that the flight of the third spacecraft passed through a strong magnetic storm.

Figures 8 and 9 give similar data for the satellites "Kosmos-12" and "Kosmos-15", respectively, obtained within a comparatively small longitudinal range. These data indicate that the smallest intensity is obtained in the case of "Kosmos-15", and the largest intensity is obtained in the case of "Kosmos-12", in the given longitudinal range (this is related to the difference in the trajectory altitude above the Earth and to the different recording thresholds). The data presented in Figures 8 and 9 were averaged over 1 minute, on the average; therefore, the outer zone profiles can be described very clearly, and  $L_{\max}$  can be determined without any difficulty. It can be seen from

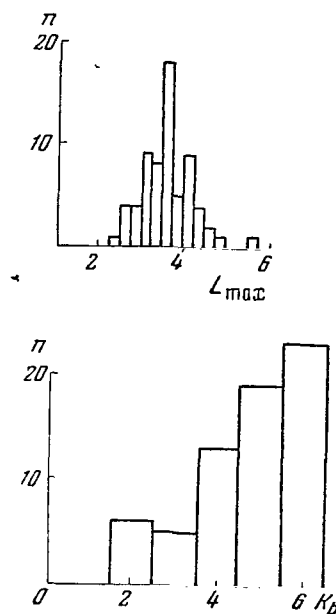


Figure 10

Figures 8 and 9 that the outer zone profile has a characteristic triangular form with a halfwidth of  $\Delta L \approx 1.2$ . Thus, on the trajectory section intersecting the zone from the north to the south, the intensity differed very little from the background; on the section intersecting the zone from the south to the north, the intensity was always significant. This can be explained by the altitudinal difference of adjoining points in opposite hemispheres.

If we are not interested in the absolute intensity, but rather in the position of the point  $L_{\max}$  characterizing the location of the outer zone in space, we then obtain the following interesting result. Figure <sup>443</sup> 10 presents a diagram showing the spatial position of the outer radiation zone maximum based on data from the second and third spacecrafts-satellites (August and December, 1960). Figure 11 shows the same diagram for the "Kosmos" satellites (see the Table). The upper graphs in these figures give the distribution with respect to  $L$  of the outer zone maximum position, and the lower graphs give the distribution of the corresponding three-hour planetary  $K_p$ -indices. A comparison of Figures 10 and 11 fosters the conclusion that  $L_{\max}$  shifts, on the average, toward small  $L$  when the  $K_p$ -index increases. This conclusion was already formulated in the works (Ref. 18,19). The possibility is not excluded that, during a change to the solar cycle minimum, the most probable value of  $L_{\max}$  shifts toward larger  $L$ , as compared with 1959-1960, in the sense that the value of  $L_{\max}$  corresponding to a certain given value of the  $K_p$ -index is smaller in 1960 than in 1962, on the average. In any event, observations performed on the spacecrafts and the satellite "Explorer-7" have shown that the outer radiation zone maximum

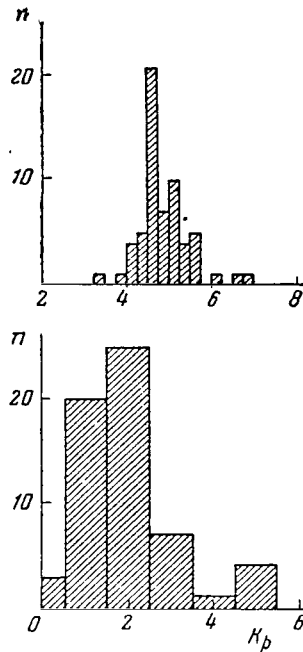


Figure 11

in 1959-1960 was located at  $L \leq 4.5$  for all values of magnetic perturbation. Its most probable position shifted from  $L = 4$  to  $L = 3$  with an increase in perturbation. Observations on the "Kosmos" satellites in 1962-1963, as well as results given in (Ref. 20) for September and October, 1962, have shown that both during quiet days and during magnetically perturbed days the outer zone maximum is observed in the region of  $L = 4-6$  at low altitudes. This conclusion is valid for high altitudes. If  $L_{\max}$  of the outer zone was  $\sim 3.5$  during the flight of the space rockets (Ref. 21) in 1959, then  $L_{\max} \geq 4$  during the flight of "Explorer-15" in 1962-1963 for electrons with an energy of  $\leq 0.5$  Mev.

#### IV. Gap Between the Zones

As is known, there is a region containing a relative minimum of energetic electrons between the inner and outer radiation zones - the so-called gap, or space, between the zones.

The minimum intensity point between the zones ( $I_{\min}$ ) shifted from  $L \sim 2.2$  in 1959-1960 to  $L = 2.8$  in 1962-1963, according to the shift in  $I_{\max}$  indicated above. An interesting feature of the radiation zone structure was thus revealed - the occurrence of additional maxima in the gap, i.e., in the  $2 \lesssim L \lesssim 3$  region.

Figure 12 presents the curves showing the intensity of the scintillation counter recording on "Kosmos-4" (curve 1), "Kosmos-7" (curve 2),

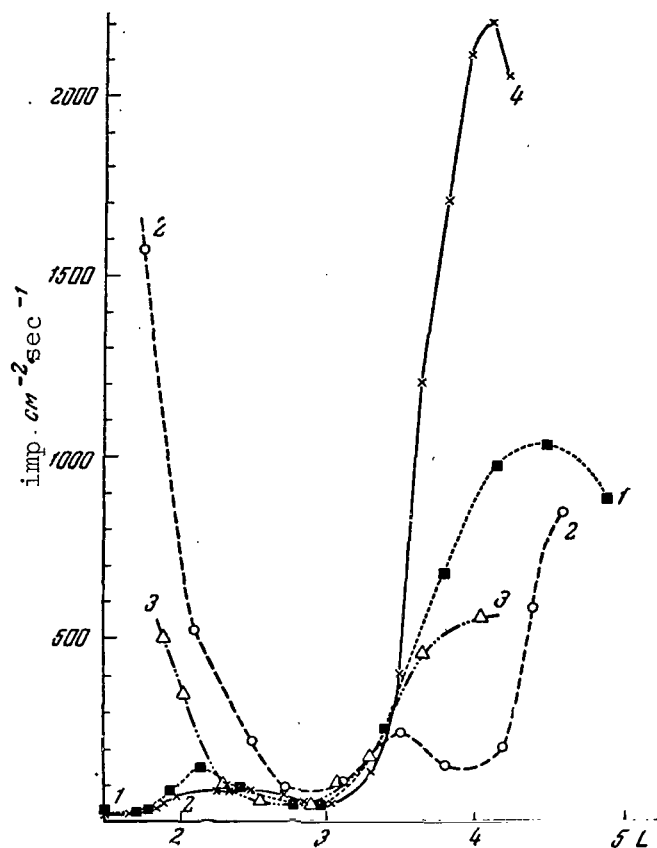


Figure 12

"Kosmos-9" (curve 3), and "Kosmos-12" (curve 4) for the spacecraft trajectory revolutions which were no more than  $20^\circ$  apart in terms of longitude. As can be seen from Figure 12, there is a recording maximum in the  $L \lesssim 2$  region, whose magnitude in the given longitudinal range comprises 5-20% of the main maximum magnitude for  $L \geq 4$ . These maxima were recorded by all of the satellites, including the spacecrafts, and are given in the Table. The fact that curve 2 in Figure 12 has no clearly expressed additional maximum can be explained by the fact that the high altitude nuclear explosion on July 9, 1962, led to an intensity increase in the  $L \lesssim 2.5$  region, and thus concealed the presence of an additional maximum in the space between the zones. Additional maxima in the case of  $L \approx 2$  were discovered in the work (Ref. 20), where the assumption was advanced that these maxima may be explained by the effect of whistling atmospherics ("whistlers"), which cause the particles to pour out of the radiation zone (see also [Ref. 23]). The location and magnitude of the additional maxima do not reveal a significant correlation with magnetic activity. Figure 13 presents the scintillation counter readings on "Kosmos-12" for three trajectory revolutions (1-3), which were no more than  $11^\circ$  apart in terms of longitude (profile of the gap between the zones).

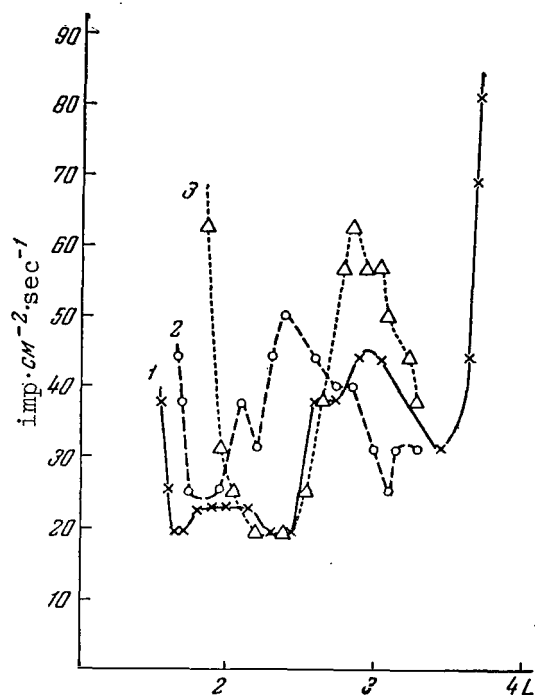


Figure 13

In spite of the fact that the magnetic index  $K_p = 1$  for all three curves, the position and magnitude of the maxima differ considerably.

/445

Additional maxima are clearly apparent on revolutions intersecting lines of equal  $L$  at small angles. In other cases, they are concealed, due to the large range over which  $L$  is averaged. (Nevertheless, for example, in Figure 8 in the  $2 < L < 3$  region in the right section of  $L$  the scatter of the intensity values can be explained by the presence of additional maxima). It should be noted that additional recording maxima in the  $2 < L < 3$  region are also observed sporadically for electrons with an energy of  $\geq 40$  kev (Ref. 24).

The discovery of additional maxima in the gap between the radiation zones is of great interest in clarifying the mechanism of escape from the radiation zones and in clarifying the existence of the gap itself.

## V. Intensity Variations

As can be seen, for example from Figure 7, the profile of the outer radiation zone has a spherical form in the majority of cases, so that it may be characterized by the following parameters: (a) By the position of the maximum  $I_{\max}$ ; (b) by the maximum intensity  $I_{\max}$ ; (c) by the halfwidth of  $\Delta L$  (i.e., by the width corresponding to the intensity level  $0.5 I_{\max}$ ). Generally speaking, all of these parameters depend on the detector threshold, with which the zone profile is determined. Finally, there is undoubtedly a connection between the quantities given above and the geomagnetic environment.

Reversible changes in the spatial location, the energy spectrum, and the angular distribution of outer zone electrons can occur with a change in magnetic perturbation. Thus, during observations by a threshold detector at a fixed point  $L$ , the comparatively small changes in these characteristics may produce significant changes in the recording rate which is registered. It can be seen from Figure 9, for example, that when  $L$  changes by 20% the recording rate changes by one order of magnitude. Therefore, in order to determine the scale of changes occurring in the outer zone, one must not analyze the intensity changes, in our opinion - for a fixed value of  $L$ , as was done in the works (Ref. 8) and (Ref. 20) - but must trace the changes in  $I_{\max}$ ,  $I_{\max}$  and  $\Delta L$ .

Figure 9 clearly illustrates the nature of the intensity variations recorded in the outer zone by the scintillation counters on the "Kosmos" satellites. The intensity  $I_{\max}$  may change by a factor of 2-3 over a period of several days in a certain narrow longitudinal range (in the given case, in the  $140^\circ\text{W}$  region). A comparison of the results derived from the second and third spacecrafts with data obtained by the satellites "Kosmos-4", "Kosmos-7", and "Kosmos-9" shows that variations of the same scale are observed for much longer periods of time. Thus,  $I_{\max}$  is characterized by a certain quasi-uniformity --- deviations from a certain mean value are observed no more than 2-3 times. Such variations may be explained by reversible changes in the geomagnetic field (Ref. 5).

Along with the type of  $I_{\max}$  variations described above, sharp intensity increases are sometimes observed in a wide region of  $L$ , as was the case on the satellite "Kosmos-7" on July 31, 1962, and on "Kosmos-12" on December 26, 1962. These phenomena were observed during a period of increased geomagnetic activity, and may be interpreted as a brief discharge of electrons into the atmosphere, similar to that recorded in the work (Ref. 17). With regard to high-altitude thermonuclear explosions, as can be seen from Figure 12, the high-altitude explosion on July 9, 1962, did not lead to a significant intensity change in the case of  $L > 2.5$ , at least for 20 days after the explosion.

In principle, observations performed at low altitudes make it possible to determine the magnitude of particle escape from the zone, and the strength of the injection sources, which is very important for clarifying the mechanism leading to the formation of the radiation zones.

We shall designate the lifetime of electrons in the outer zone by  $T = Q/q$ , where  $Q$  is the total particle reserves within a given force tube with the cross section of  $1 \text{ cm}^2$  at the flight altitude;  $q$  is the discharged stream which is recorded. It is possible to determine  $Q$  from results obtained at high altitudes. The loss of  $q$  can be determined from intensity measurements at low altitudes.

If  $I_0$  is the measurement intensity in the equatorial plane,  $S$  is the cross section of the geomagnetic field force tube in this plane (we shall assume that the tube cross section is  $1 \text{ cm}^2$  at the measurement altitude), then we obtain the following expression for the lifetime (Ref. 5):

$$T = 2 \left( \frac{I_0}{I} \right) \frac{S\tau}{\cos \alpha_{\min}},$$

where  $I$  is the intensity averaged over longitude at the measurement altitude;  $\tau$  - lifetime of electrons at the measurement altitude,  $\cos \alpha_{\min} = 0.2$  within an accuracy of two for a measurement altitude of 350 km.

The intensity  $I_0$  in the equatorial plane was measured on the satellite "Explorer-14" (Ref. 25). It was established that in a quiet geomagnetic environment the integral electron spectrum in the energy range between 40-1600 keV has the form of  $1/E$ . The mean electron intensities in the case of  $L \sim 4$  are  $3 \cdot 10^7$ ,  $3 \cdot 10^6$  and  $3 \cdot 10^5 \text{ cm}^{-2} \cdot \text{sec}^{-1}$ , respectively, for energies of  $> 40 \text{ keV}$ ,  $> 230 \text{ keV}$ , and  $> 1.6 \text{ MeV}$ . However, during magnetic perturbations variations in  $I_0$  by one order of magnitude are observed. The intensity  $I$  can be obtained by utilizing Figures 1 and 2. The mean recording  $80 \text{ cm}^{-2} \cdot \text{sec}^{-1}$  corresponds, in the case of the spectrum (Ref. 4) for electrons with an energy of  $> 100 \text{ keV}$ , to an intensity of  $1.6 \cdot 10^5 \text{ cm}^{-2} \cdot \text{sec}^{-1}$ . For electrons with an energy of  $> 100 \text{ keV}$ , this leads to a lifetime of  $T = 5 \cdot 10^5 \text{ sec}$ , and for electrons with an energy above 600 keV a value of  $I = 2 \cdot 10^3 \text{ cm}^{-2} \cdot \text{sec}^{-1}$  - which corresponds to  $T = 5 \cdot 10^7 \text{ sec}$  - is obtained on the average, based on data from the outer scintillation counter on "Kosmos-7". The values of  $\tau$ , computed according to (Ref. 26), were employed to calculate  $T$  by the formula given above. In spite of the comparatively large indeterminate nature of the lifetime estimates given above, it can be concluded with sufficient accuracy that the lifetime of electrons with energies on the order of hundreds of keV in the outer radiation zone, on the one hand, is much greater than the lifetime of 40-keV electrons ( $\sim 10^4 \text{ sec}$ ), obtained from measurements

on the satellites "Injun". On the other hand, this lifetime is many orders of magnitude smaller than the lifetime calculated from the hypothesis of a neutron mechanism ( $10^{11}$ - $10^{12}$  sec).

### Conclusion

The data given above indicate that the term: "radiation zone" may be validly applied in its "classical" meaning to electrons trapped by the geomagnetic field and having energies of hundreds of kev. The outer radiation zone formed by these electrons has the profile  $I(L)$  with a clearly expressed maximum  $I_{\max}$  for  $L = L_{\max}$ . The space between the inner and outer radiation zones is also clearly apparent. The longitudinal intensity behavior of such electrons at low altitudes can be explained quite well by the characteristics of the real geomagnetic field.

/447

Variations in the position of  $L_{\max}$  are related to geomagnetic perturbation. In the majority of cases, variations in the intensity  $I_{\max}$  may be explained by reversible changes in the geomagnetic field. The lifetime of these electrons at  $L \sim 4$  has been estimated as much greater than the lifetime of one drift revolution.

The structure and dynamics of the radiation zone of electrons having energies of  $> 10^5$  ev differ greatly from that of electrons having energies of  $\geq 40$  kev, which was discovered on the "Injun" satellites (Ref. 17) (Ref. 37). If we employ the terminology of O'Brien for the dynamics of electrons with  $E \geq 40$  kev, and if we employ the model of "splash catcher", then the model of "a leaky bucket" is more valid for a zone of electrons with energies of  $> 10^5$  ev.

It thus follows that a sharp distinction must be drawn between the electron components having different energies when studying the radiation zones. This conclusion is corroborated by results obtained at high altitudes (Ref. 22, 25). The term "outer radiation zone" applies to electrons with an energy exceeding 100 kev in the region in space between  $L = 3-8$ . The term "inner radiation zone" is usually applied to protons with energies of tens and hundreds of Mev which are trapped by the geomagnetic field within  $L < 2$ . The spatial region  $2 < L < 3$ , as was noted above, is called the gap.

Electrons and protons of smaller energies are observed in an extensive region of the  $L$  parameter. The terminology for them has not yet been formulated. The expressions "outermost zone", "Davis zone", "protonosphere", "electronosphere", etc. are employed. But the terms "outer radiation zone" and "inner radiation zone" have been firmly established in the sense indicated above.

It should be noted that electrons of energies  $> 10^5$  ev comprise a small portion of electrons in the spectrum which are recorded in the outer radiation zone. Their total energy is inadequate to produce such



geophysical phenomena as the aurorae polaris. However, such electrons represent an unusual indicator of the geophysical environment, and their study is extremely important for clarifying the mechanism of magnetic storms and the aurorae polaris.

#### REFERENCES

1. Papkov, S. F., Pisarenko, N. F., Savenko, I. A., Shavrin, P. I., Tupikin, A. F. In "Iskusstvennyye Sputniki Zemli". Izdatel'stvo AN SSSR, No. 9, p. 78, 1961.
2. Savenko, I. A., Shavrin, P. I., Nesterov, V. Ye., Pisarenko, N. F., Tel'tsov, M. V. Kosmicheskiye Issledovaniya, 1, No. 1, 172, 1963.
3. Pisarenko, N. F. Dissertation Nauchno-Issledovatel'skiy Institut Yadernoy Fiziki (NIIYaF), Moskovskiy Gosudarstvennyy Universitet (MGU), 1964.
4. Walt, M., Chase, L. F., Jr., Cladis, J. B., Imhof, W. L. J. Geophys. Res., 66, 2297, 1964.
5. Shavrin, P. I. Dissertation NIIYaF MGU, 1964.
6. Vernov, S. N., Chudakov, A. Ye., Vakulov, P. V., Logachev, Yu. I. in "Iskusstvennyye Sputniki Zemli". Izdatel'stvo AN SSSR, No. 2, p. 61, 1958.
7. Gorchakov, Ye. V. In "Iskusstvennyye Sputniki Zemli". Izdatel'stvo AN SSSR No. 9, p. 66, 1961.
8. Forbush, S. E., Pizzella, G., Venkatesan, D. J. Geophys. Res., 67, 3651, 1962.
9. Vernov, S. N., Savenko, I. A., Shavrin, P. I., Nesterov, V. Ye., Pisarenko, N. F. In "Iskusstvennyye Sputniki Zemli". Izdatel'stvo AN SSSR, No. 10, p. 34, 1961.
10. Savenko, I. A., Pisarenko, N. F., Shavrin, P. I., In "Iskusstvennyye Sputniki Zemli". Izdatel'stvo AN SSSR, No. 9, p. 71, 1961.
11. Vernov, S. N., Savenko, I. A., Shavrin, P. I., Nesterov, V. Ye., Pisarenko, N. F. In "Iskusstvennyye Sputniki Zemli". Izdatel'stvo AN SSSR, No. 13, p. 67.
12. Kurnosova, L. V., Kolobyanina, T. M., Logachev, V. I., Razorenov, L. A., Sirotkin, I. A., Fradkin, M. I. In "Iskusstvennyye Sputniki Zemli". Izdatel'stvo AN SSSR, No. 8, p. 90, 1961; Ginzburg, V. L., Kurnosova, L. V., Logachev, V. I., Razorenov, L. A., Sirotkin, I. A., Fradkin, M. I. In "Iskusstvennyye Sputniki Zemli". Izdatel'stvo AN SSSR, No. 10, p. 22, 1961.

13. Mandel'shtam, S. L., Tindo, I. P., Voron'ko, Yu. K., Vasil'yev, B. N. Shurygin, A. I. In "Iskusstvennyye Sputniki Zemli". Izdatel'stvo AN SSSR, no. 11, p. 3, 1961.
14. Nicolet, M. Aeronomy, 11, 1961.
15. Vernov, S. N., Savenko, I. A., Shavrin, P. I., Tverskaya, L. V., Tverskoy, B. A. Kosmicheskiye Issledovaniya, 2, No. 6, 1964.
16. Vernov, S. N., Savenko, I. A., Shavrin, P. I., Tverskaya, L. V. Geomagnetizm i Eronomiya, 3, No. 5, 812, 1963.
17. O'Brien, B. J. J. Geophys. Res., 67, 3687, 1962.
18. Forbush, S. E., Venkatesan, D., McIlwain, C. E. J. Geophys. Res., 66, 2275, 1961.
19. Vernov, S. N., Yeroveyeva, V. N., Nesterov, V. Ye., Savenko, I. A., Shavrin, P. I. Kosmicheskiye Issledovaniya, 2, No. 2, 289, 1964.
20. Paulikas, G. A., Freden, S. C. J. Geophys. Res., 69, 1239, 1964.
21. Vernov, S. N., Chudakov, A. Ye. Uspekhi Fizicheskikh Nauk, 70, 4, 585, 1960.
22. McIlwain, C. E. Science, 142, 355, 1965.
23. Dungy, J. W. Planet. Space Sci., 11, 591, 1963.
24. O'Brien, B. J., Laughlin, C. D., Van Allen, J. A., Frank, L. A. J. Geophys. Res., 67, 1209, 1962.
25. Frank, L. A., Van Allen, J., Hills. J. Geophys. Res., 69, 2171, 1961.
26. Cristifilos, N. C. J. Geophys. Res., 64, 8, 1959.
27. O'Brien, B. J. J. Geophys. Res., 69, 13, 1964.

# STUDY OF THE INNER AND ARTIFICIAL RADIATION ZONES OF THE EARTH AT LOW ALTITUDES IN 1960-1964

V. Ye. Nesterov, N. F. Pisarenko, I. A. Savenko,  
M. V. Tel'tsov, P. I. Shavrin, K. N. Sharvina

## Introduction

/448

An analysis of data obtained from the radiometric apparatus carried on spacecrafts and artificial Earth satellites has revealed a region with high radiation intensity around the coast of Brazil (Ref. 1-3) (see the Table)

TABLE

Satellite	Launch Date	Perigee and Apogee, km	Energy Threshold of Scintillation Counter, kev
Second spacecraft	8/19/60	306-339	25
Third spacecraft	12/1/60	187-265	25
"Kosmos-4"	4/26/62	298-330	60
"Kosmos-7"	7/28/62	210-369	30
"Kosmos-9"	9/27/62	301-353	15
"Kosmos-12"	12/22/62	211-405	30
"Kosmos-15"	4/22/63	173-371	100

A comparison of the recording rates of Geiger and scintillation counters, as well as an analysis of energy liberation in the scintillation counter crystal in this region, has fostered the conclusion that the radiation includes protons with energies greater than 50 Mev.

/449

The presence of high-energy protons was explained by the inner zone dropping to low altitudes in the region of the negative magnetic anomaly (Ref. 1, 2). It was thus possible to study the inner radiation zone at low altitudes in the anomaly, where particle destruction must be at its greatest. In addition, because the artificial radiation zone which was formed from the high-altitude thermonuclear explosion on July 9, 1962, was centered at low altitudes, primarily in the region of the Brazilian magnetic anomaly, it was possible to study the artificial zone.

It is of great interest to study the radiation zones in the region of magnetic anomalies because information may be obtained on the mechanisms

of particle loss and formation, which is of great importance in formulating a theory for the radiation zones. Therefore, after the discovery of the Brazilian anomaly a great amount of research was devoted to radiation in the anomaly. However, these studies dealt primarily with the spatial distribution of artificial radiation zone electrons at low altitudes (Ref. 4-6), and to a lesser extent with protons and electrons in the inner zone (Ref. 5, 7-10, 12). Since the inner radiation zone is camouflaged by artificially injected electrons in the anomaly region, it is of interest to study in greater detail the experimental data obtained before the high-altitude nuclear explosion of July 9, 1962. In this connection, this study presents certain supplementary results derived from measurements performed in 1960 on the second and third spacecrafts. The study also presents data pertaining to the artificial radiation zone, obtained from the scintillation counters carried on the satellites "Kosmos-4", "Kosmos-7", "Kosmos-9", "Kosmos-12", "Kosmos-15".

## Measurement Results

### 1. Longitudinal Behavior of Protons and Spatial Distribution of Inner Zone Particles

Experimental data obtained from scintillation counters carried on the second and third spacecrafts and the satellite "Kosmos-4", pertaining to the region of the Brazilian magnetic anomaly, were processed in the McIlwain BL-coordinates. The trajectory coordinates of these satellites in the longitudinal range of  $80^{\circ}\text{W} - 40^{\circ}\text{E}$  and the latitudinal range of  $65^{\circ}\text{S} - 0^{\circ}$  were changed into B, L coordinates by means of interpolation graphs constructed from tables of adiabatic invariants (Ref. 14).

The scintillation counters with a NaJ crystal, which were carried on board the second and third spacecrafts, had a minimum shielding of  $3 \text{ g}\cdot\text{cm}^{-2}$ , which corresponds to the direct passage of protons with energies greater than 50 Mev and electrons with energies greater than 6 Mev. Low-energy electrons were recorded with an efficiency of less than 1% according to the braking radiation. The energy threshold of these counters was 25 kev. The counters were interrogated by the memory device every three minutes. The recording rates were converted to a surface unit under the assumption that the radiation recorded was isotropic. The intensity, which was averaged over a three-minute interval, pertained to the middle of the interval. The usual representation of the results in the form of contours of different intensities in the B, L coordinates assumes that the intensity does not depend on longitude. As will be seen below, this assumption is not valid in the region of the magnetic anomaly. As they drift around the Earth, particles in the anomaly region approach the Earth and may be absorbed in the denser atmospheric layers. The intensity at points lying on the same magnetic envelope L, for different B, was plotted as a function of  $h_{\min}$  - the minimum altitude at which the line for points with the same values of B passed in the anomaly region. /450

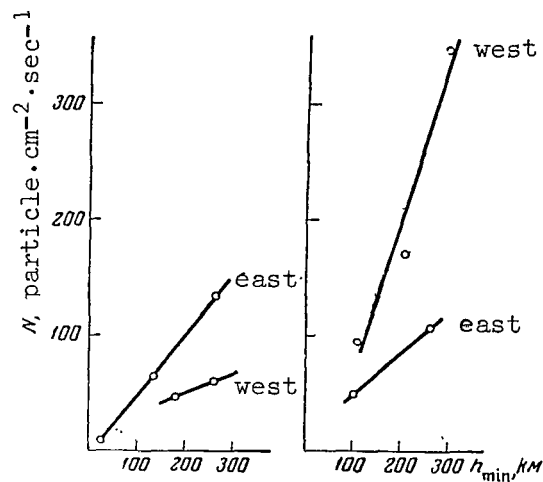


Figure 1

Particle Intensity Dependence, Measured by the Scintillation Counter on the Second Spacecraft, on  $h_{\min}$  for  $L = 1.3$  - on the Left; for  $L = 1.6$  on the Right.

Figure 1 represents an example of this formulation, where the particle intensity distributions are expressed as a function of  $h_{\min}$  for  $L = 1.3$  and  $1.6$ . As can be seen from the figure, the intensities at points lying to the west and to the east of the anomaly differ considerably, although they occur on one drift trajectory of the specular points. Similar graphs were constructed for all values of  $L$  from  $1.2$  to  $2.1$ , with an interval of  $0.1$ .

An analysis of all the graphs showing the intensity recorded by the scintillation counter on the second spacecraft shows that particle intensity is greater to the east of the anomaly than it is to the west of the anomaly, at the magnetic envelopes  $1.2 \leq L \leq 1.4$ . At the  $1.5 \leq L \leq 2.1$  envelopes, the situation is reversed. It is known that electrons drift from the west to the east in the terrestrial magnetic field; the protons drift from the east to the west. Therefore, it may be stated that at  $1.2 \leq L \leq 1.4$  the measured particle intensity is primarily caused by protons, and at  $1.5 \leq L \leq 2.1$ , it is primarily caused by electrons.

The intensity decrease in protons with energies greater than  $50$  Mev at the  $L \leq 1.4$  magnetic envelopes, at an altitude of  $320$  km to the west, is unexpected, and cannot be explained by ionization losses of proton energies during the drift period around the Earth.

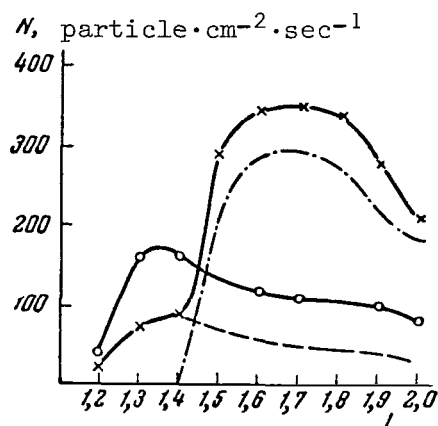


Figure 2

Spatial Distribution of Particle Intensity as a Function of  $L$  at a Minimum Altitude of 300 km  
Circles designate points to the east of the anomaly; crosses - to the west.

At the measurement point, a proton with an energy of 100 Mev has a gyration radius of less than 70 km. The lowest orbital points of these protons descend to an altitude equalling the difference between the minimum altitude for given  $L$  and  $B$  and the gyration radius - i.e., in the case of  $h_{\min} = 250$  km, to an altitude of 180 km. The drift time of protons located in these envelopes is  $\tau_g \approx 0.5$  min. around the Earth, and the drift time in the anomaly is approximately  $1/6$  of this quantity - i.e., 5 seconds. During this time, a 100-Mev proton traverses a path of  $7 \cdot 10^{10}$  cm, which is approximately  $50 \text{ mg} \cdot \text{cm}^{-2}$  for a gas density of  $7 \cdot 10^{-13} \text{ g} \cdot \text{cm}^{-3}$  at an altitude of 180 km. Even this value is very small as compared with the range of a 100-Mev proton. In actuality for part of the time the proton is located at altitudes greater than 180 km, i.e., it penetrates a still smaller thickness.

The intensity decrease of protons to the west of the anomaly at the  $L \leq 1.4$  envelopes could be caused by unequal screening of the scintillation counter due to a different orientation of the second spacecraft to the west and to the east of the anomaly. However, the eastern and western experimental points were compiled both for direct and reverse revolutions, and it is difficult to assume that, each time the satellite had such an orientation, the recorded intensity to the west was smaller than the intensity to the east. Errors may also be introduced when the intensity is averaged over a three-minute interval, but an examination of the experimental points at a minimum altitude of about 300 km does not substantiate the assumption that the error amounts to 100%. Thus, the possibility of a recording rate decrease to the west of the anomaly is most probably not the reason for the longitudinal dependence of proton intensity which was discovered. However, the possibility cannot be excluded that this longitudinal dependence at small  $L$  is

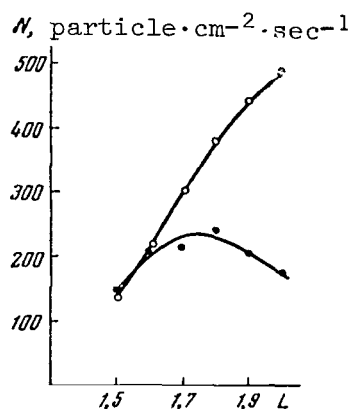


Figure 3

A Comparison of Electron Intensities Based on Data From the Scintillation Counters on the Second and Third Spacecrafts

Dots pertain to the second spacecraft; circles to the third.

related to a discrepancy between the real magnetic field in the anomaly region and the assumed system of B, L-coordinates.

The spatial intensity distribution of particles recorded by the scintillation counter was compiled as a function of L for  $h_{\min} = 300$  km, based on data from the second spacecraft (Figure 2). It can be seen from the figure that the proton distribution maximum at  $h_{\min} = 300$  km is located at  $L = 1.3-1.4$ , and that for  $L = 1.45$  the longitudinal behavior changes sign as a result of the constantly increasing electron contribution.

It can be shown that, for those L where primarily electrons are recorded, the electron contribution to the east of the anomaly at a minimum altitude of 300 km must be insignificant, under the condition that there is no electron stream from above. Actually, since the drift time around the Earth of electrons with energies of hundreds of kev can be counted in tens of minutes, as they move from the west to the east in the anomaly they penetrate a considerable thickness. For example, an electron with an energy of 500 kev, having specular points on a circle of constant values of B and L with a minimum altitude of 300 km, traverses a path of  $0.1 \text{ g}\cdot\text{cm}^{-2}$ , which approximately corresponds to the range of such an electron.

Thus, if it is assumed that primarily protons make a contribution to the particle intensity recorded to the east of the anomaly at  $L \leq 1.45$ , then the proton distribution to the west at large L may be formulated, by extrapolating the distribution of protons with  $L < 1.4$  to a value of  $L \leq 1.45$  (the dotted curve in Figure 2). The dashed

curve in this figure gives the approximate distribution of electrons in the inner radiation zone in the anomaly region at a minimum altitude of 300 km.

If it is assumed that the electron intensity at the given minimum altitude is inversely proportional to the gas density at the same altitude, then the magnitude of a standard atmosphere - by determining it as the altitude at which the electron intensity decreases by a factor of 2.7 - can be determined from the graphs showing the dependence of electron intensity on minimum altitude. The magnitude of a standard atmosphere determined in this way changes from 150 km for  $L = 1.6$  to 300 km for  $L = 2.0$ . The magnitude of a standard atmosphere determined by satellite braking (Ref. 13) at an altitude of about 300 km was 40-50 km for 1960. The fact that the magnitude of a standard atmosphere, determined by the electron intensity change with altitude, was much greater than the magnitude of a standard atmosphere given in the work (Ref. 13) indicates that the particle intensity at envelopes of  $L = 1.6-2.0$  is not determined by the atmosphere. /452

## 2. Time Variations in the Inner Radiation Zone in the Anomaly Region

Data from the scintillation counters carried on the third spacecraft and the satellite "Kosmos-4" were processed by a method similar to that presented above. The trajectory of the third spacecraft passed considerably below the trajectory of the second spacecraft (see the Table). Therefore, fewer data were obtained on the radiation trapped by the geomagnetic field in the anomaly region. It is known that a strong magnetic storm was recorded on November 30-December 1, 1960, during the flight of the third spacecraft; this caused a particle intensity increase in the region of the South Atlantic, in spite of the decrease in the satellite's altitude (Ref. 2).

Data from the third spacecraft only make it possible to formulate the particle intensity distribution to the west as a function of  $L$ , for  $L \geq 1.5$  and a minimum altitude of 200 km. In order to make a comparison with these results, the same distribution was formulated based on data from the second spacecraft (Figure 3). It can be seen from the figure that the magnetic storm of November 30-December 1, 1960, did not change the electron intensity at  $L = 1.5-1.6$  envelopes, and it increased by a factor of 2-3 at  $L \geq 1.6$ .

Measurements of proton intensity at low altitudes at different times in the solar cycle make it possible to determine the variations caused by an atmospheric density change. A comparison of the proton intensities recorded by the scintillation counters on the second spacecraft and the satellite "Kosmos-4", at  $L = 1.2-1.3$ ,  $h_{\min} = 300$  km and a measurement altitude of 320 km to the east of the anomaly, shows that the intensity increased in April, 1962, by approximately 3 times, as compared with August, 1960.



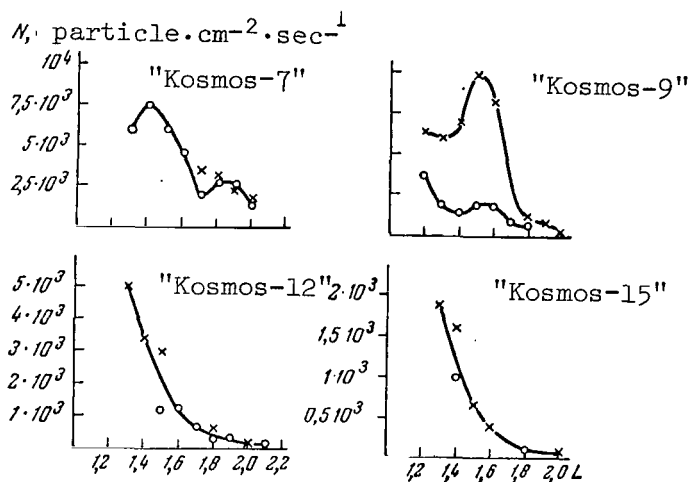


Figure 4

Spatial Distribution of Artificial Zone Electrons as a Function of  $L$  at a Minimum Altitude of 250 km, Based on Data From Scintillation Counters on the Satellites "Kosmos-7", "Kosmos-9", "Kosmos-12", and "Kosmos-15"

Circles designate points to the east of the anomaly; crosses - to the west.

### 3. Spatial Distribution and Lifetime of Artificial Zone Electrons

The study (Ref. 11) presented the geographic distribution of radiation intensity in an artificial zone determined by the Geiger counters on the satellites "Kosmos-7" and "Kosmos-15". This study gave the distribution of artificial zone electrons in the  $B$ ,  $L$  coordinates based on data from the scintillation counters of the satellites "Kosmos-7", "Kosmos-9", "Kosmos-12", and "Kosmos-15". The scintillation counters on these satellites were located behind a minimum shielding of  $3 \text{ g} \cdot \text{cm}^{-2}$ , and primarily recorded artificial zone electrons based on the braking  $\gamma$ -radiation. Their energy thresholds are shown in the Table. Particle intensity recorded by the scintillation counters carried on these satellites is plotted in Figure 4 as a function of  $L$  for a minimum altitude of 250 km. The circles designate points lying to the east of the anomaly; the crosses designate points to the west of the anomaly. The electron lifetime was determined for each value of  $L$  from 1.2 to 2.0, with an interval of 0.1 and  $h_{\min} = 250 \text{ km}$ . The scintillation counter readings obtained on the satellite "Kosmos-4", were assumed to be background, and were subtracted from the readings of the other counters. At those points where it was possible, the lifetime was determined both for electrons recorded to the west, and for electrons recorded to the east. The lifetime differences for both were within the limits of measurement accuracy. The electron lifetime  $\tau$ , determined as the time during which intensity decreases by

/453

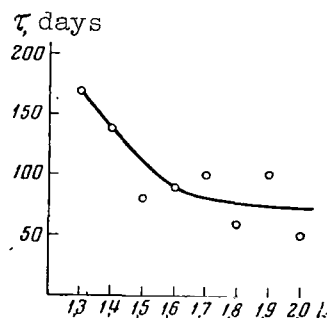


Figure 5

#### Dependence of Lifetime of Artificial Zone Electrons on L in the Anomaly Region

2.7 times at a given L and  $h_{\min} = 250$  km, is plotted in Figure 5 as a function of L. As can be seen from Figure 5, it decreased from 170 days for  $L = 1.3$  to approximately 70 days for  $L = 2.0$ .

#### Conclusion

The discovery of the Brazilian anomaly during the flight of the second spacecraft in 1960 led to a great number of studies, due to the possibility of obtaining direct information on particle loss from the radiation zones.

A supplementary analysis of experimental data obtained during the flights of the second and third spacecrafts, and also satellites in the "Kosmos" series, has led to the following results:

1. A longitudinal behavior of the scintillation counter recording rate, which is different from the longitudinal behavior of electron intensity at large L, has been detected in the region of the Brazilian anomaly at magnetic envelopes with  $L = 1.2-1.4$ . The recording rate at  $L = 1.2-1.4$  to the east of the anomaly is 2 times greater than to the west, on the same drift trajectories. This fact points either to a longitudinal behavior of proton intensity which contradicts existing concepts of the proton component in the inner zone, or to a difference between the real magnetic field at small L in the anomaly and the magnetic field employed for computing B and L. /454

2. The spatial distribution of protons and electrons in the inner zone has been obtained in the region of the Brazilian magnetic anomaly at an altitude of 300 km.

3. The spatial distributions of artificial radiation zone electrons have been obtained at a minimum altitude of 250 km in July, September,

December, 1962, and in April, 1963.

4. The lifetime of electrons in the artificial radiation zone has been determined in the region of the Brazilian magnetic anomaly at a minimum altitude of 250 km. In the case of  $L = 1.3$ , the lifetime is 170 days, and decreases to approximately 70 days for larger  $L$ .

#### REFERENCES

1. Vernov, S. N., Savenko, I. A., Shavrin, P. I., Pisarenko, N. F.  
In "Iskusstvennyye Sputniki Zemli". Izdatel'stvo AN SSSR, No. 10,  
p. 40, 1961.
2. Vernov, S. N., Savenko, I. A., Shavrin, P. I., Nesterov, V. Ye.,  
Pisarenko, N. F. Geomagnetizm i Aeronomiya, 2, No. 1, 41, 1962.
3. Ginzburg, V. L., Kurnosova, L. V., Logachev, V. I., Razorenov, L. A.,  
et al. In "Iskusstvennyye Sputniki Zemli". Izdatel'stvo AN SSSR,  
No. 10, p. 20, 1961.
4. Hess, W. N. J. Geophys. Res., 68, No. 3, 667, 1963.
5. Vernov, S. N., Nesterov, V. Ye., Savenko, I. A., Shavrin, P. I.,  
Sharvina, K. N. Kosmicheskiye Issledovaniya 2, No. 3, 485, 1964.
6. Vernov, S. N., Chudakov, A. Ye., Vakulov, P. V., Gorchakov, Ye. V.,  
et al. Izvestiya AN SSSR, Seriya Fiz., 28, No. 12, 1964.
7. Mihalov, J. D., Mozer, F. S., White, R. S. J. Geophys. Res., 69,  
No. 19, 4003, 1964.
8. Mann, L. J., Bloom, S. D., West, H. J., Jr. Space Res., 3, 1963.
9. Sewarel, F. D., Kornblum, H. N., Jr. Preprint 1963.
10. Gal'perin, Yu. I., Krasovskiy, V. I., Dzhordzhio, N. V., Mulyarchik,  
T. M., Bolyunova, A. D., Temnyy, V. V., Marov, M. Ya. Kosmicheskiye  
Issledovaniya, 1, No. 1, 126, 1963.
11. Vernov, S. N., Nesterov, V. Ye., Pisarenko, N. F., Savenko, I. A.,  
Savun, O. I., Shavrin, P. I., Sharvina, K. N. Kosmicheskiye  
Issledovaniya, 2, No. 3, 492, 1964.
12. Freden, S. C., Paulinas, J. A., J. Geophys. Res., 69, No. 7, 1259, 1964.
13. King-Hele, D. G., Janice, M. Proc. Roy. Soc. A270, No. 1343, 562, 1962.
14. Jensen, D. C., Murray, R. W., Welck, J. A., Jr. Tables of Adiabatic  
Invariants for the Geomagnetic Field 1955 O.A.F.S.W.S.-TN-60-8.  
Kirtland Air Force Base. New Mexico; 1960.

# OUTER RADIATION ZONE OF THE EARTH AND BURSTS OF X-RAY RADIATION IN THE STRATOSPHERE

S. N. Vernov, L. L. Lazutin,  
A. N. Charakhch'yan, T. N. Charakhch'yan

It may be assumed that trapped electrons leave the outer radiation zone as a result of perturbations occurring in it. When entering the upper atmosphere in an air layer of approximately 10-100 mg, these electrons produce photons of braking radiation which are propagated in the depths of the atmosphere. A clarification of the mechanism by which electrons are emitted from the radiation zone is of great theoretical interest. But, as will be seen below, this phenomenon is quite complex, and no satisfactory explanation has been found for it as of the present.

During observations in 1959 above Murmansk during bursts of cosmic <sup>455</sup> rays in the stratosphere, a large number of short range particles with a range of less than 7 mm Al - electrons and photons at depths of up to 50-80 g·cm<sup>-2</sup> - were recorded in addition to solar protons (Ref. 1). These results were obtained during simultaneous measurements employing a telescope with a filter of 7 mm Al and a single counter with a wall thickness of 0.05 g·cm<sup>-2</sup>. In measurements performed on May 12, July 12, and July 15, 1959, the recording rate of the single counter exceeded the recording rate which was expected from the telescope data by several times. Table 1 presents the results derived from measuring the recording rate of the single counter and the expected recording rate.

TABLE 1

Measurement Date (1959)	Measurement Time, Hours Minutes	Pressure, g·cm <sup>-2</sup>	Recording, Minutes <sup>-1</sup>	
			Measured	Expected
5/12	13 23	23	900	320
7/12	13 42	17	2950	1440
	13 11	52	82	48
7/15	13 20	21	13200	2200
	13 01	57	2180	60

After a comparison of the radiation intensity at two pressures for July 15, it followed that the absorption coefficient of short range particles in the stratosphere is ~16 g·cm<sup>-2</sup> which corresponds to a range of photons with energies of ~1 Mev.

A large intensity for photons in the stratosphere with energies of 2-3 Mev was discovered on July 15, 1959, by Brown directly from a scintillation counter (Ref. 2). However, the phenomenon to which protons are related in the stratosphere is not clear: To electrons from the outer radiation zone, or to short range particles carried by corpuscular streams accompanying chromosphere flares on the Sun.

Winckler recorded low-energy photons (about 50-100 kev) by means of large balloons over Minneapolis (Ref. 3). He arrived at the following conclusions. During strong magnetic storms radiation is observed almost 60% of the time. For a period of relatively weak perturbations of the magnetic field, radiation is observed less than 1% of the time the apparatus remains in the air. Radiation was observed primarily during nocturnal hours. There is a good correlation between X-ray radiation and the aurorae polaris with a radial structure. The integral flux of electrons producing X-ray radiation in the upper atmosphere is  $10^9$ - $10^{12}$  electron $\cdot$ cm $^{-2}$  during normal flares lasting one hour. During strong aurorae polaris, the intensity peak reaches  $10^9$  cm $^{-2}$   $\cdot$  sec $^{-1}$  (Ref. 3).

Anderson studied X-ray radiation in the aurorae polaris zone using balloons at four points (Ref. 4). He obtained data primarily by means of scintillation counters at altitudes corresponding to a pressure of 3-10 g $\cdot$ cm $^{-2}$ . During random flights in the aurorae polaris zone at geomagnetic latitudes of 64-69° (Fort Churchill, Flin-Flon, College) X-ray radiation of  $\sim$  50 kev was observed approximately 60% of the time that the apparatus remained in the air; at a geomagnetic latitude of 56° (Minneapolis) radiation was observed  $\sim$  5% of the time, and close to the geomagnetic pole (Resolute Bay) X-ray radiation was not observed at all. The radiation was anisotropic in space. Sometimes the recorded radiation differed by more than one order of magnitude, in terms of intensity at points which were 300 km apart.

For the aurorae polaris zone, bursts of X-ray radiation were observed during weak magnetic activity. Strong fluctuations in radiation intensity were characteristic in these cases. The mean intensity of electrons pouring out of the zone is several units of  $10^6$  cm $^{-2}$   $\cdot$  sec $^{-1}$ , according to data given by Anderson. This number is close to that obtained by data from the satellite "Injun-1" by O'Brien at an altitude of 800-1000 km (Ref. 5). Satellite studies at altitudes of about 1000 km showed that the energy spectrum for electrons pouring out and for trapped electrons with energies of 40-120 kev fluctuates greatly. The differential spectrum index changes from 0 to 7 (Ref. 6). A similar conclusion regarding the variability of the energy spectrum for X-ray photons can be reached on the basis of stratosphere observations, although some authors assume a spectrum having a definite form. /456

Thus, Winckler (Ref. 3) assumes that the differential spectrum of electrons pouring out is characterized by the index 4-5. Anderson (Ref. 4) gives  $\gamma \approx 7$  for the spectrum index. Figure 1,a gives the integral energy photon spectra for two magnetic storms on September 25 and

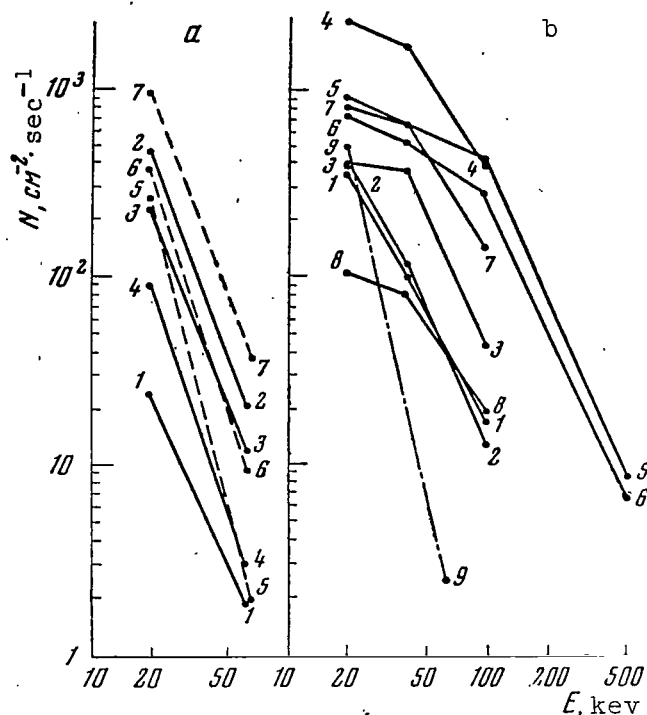


Figure 1

Integral Energy Spectra of Photons at a Pressure of  $7-10 \text{ g}\cdot\text{cm}^{-2}$   
a - 9/25/61 1 - 5 hours 10 minutes; 2 - 7 hours 15 minutes; 3 - 9 hours 15 minutes; 4 - 9 hours 45 minutes. 10/1/61 5 - 8 hours 45 minutes; 6 - 9 hours 20 minutes; 7 - 11 hours. 9/17/63, 1 - 4 hours; 2 - 3 hours 50 minutes; 3 - 7 hours 20 minutes; 4 - 9 hours 20 minutes; 5 - 11 hours 10 minutes; 6 - 11 hours 20 minutes; 7 - 10 hours 40 minutes; 8 - 12 hours 30 minutes; 9 - based on data in (Ref. 4).

October 1, 1961. The photon intensity  $N$  is plotted along the ordinate axis; the photon energy  $E$  is plotted along the abscissa axis. The data presented are taken from the work of Winckler, Bhavsar, and Anderson (Ref. 7), which gives the results derived from scintillation counter measurements at "International Falls" in Canada. Measurement times are given below the figure. In these cases, the integral spectrum index changes from 1.8 to 4.2 in the energy range of 20-60 keV. A hard spectrum of X-ray photons was recorded by Anderson, when the so-called micro-shocks were observed, lasting 0.25 seconds. Within 30-60 keV, the integral spectrum index in these cases was  $\gamma \sim 1.0$  (Ref. 8). It follows from the data given by Anderson that the photon intensity in the bursts does not decrease with a decrease in solar activity. This can be seen from the measurement data 457 at Flin-Flon for 1961, 1962, and 1963 which are given in Table 2. After studying radiation in the aurorae polaris zone, the Sparmo Organization at Kiruna (Sweden) (Ref. 9) also found that the radiation spectrum in 1963

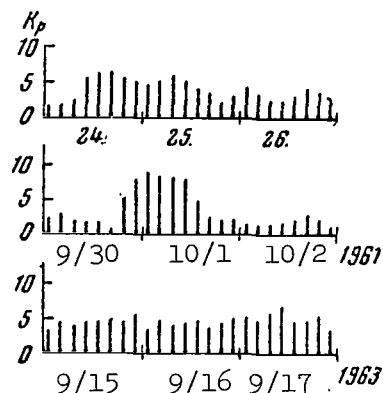


Figure 2

Values of the  $K_p$  Index

Data in the upper graph pertain to September, 1961.

was harder than in 1961.

Figure 1,b gives the photon energy spectrum for cases in which the pouring out process took place when, on September 17, 1963 at Kiruna (Ref. 9), a large photon intensity was observed during several bursts lasting 10-15 minutes up to several hours. It can be seen that on September 17, 1963 the pouring out process was somewhat more intense than during the examples on September 25 and October 1, 1961. The energy spectra in these cases are characterized by small indices. The integral spectrum index in the energy range of 20-40 kev changes from 0.3 to 1.7, and in the energy range of 40-100 kev it changes from 0.3 to 2.4. Two bursts were recorded when protons having energies greater than 500 kev were present. An increase in the recording level of a single counter (Ref. 10) was recorded in the stratosphere above Apatity at about 8 hours on September 17. For additional radiation, the absorption range corresponds to photons with energies of  $\sim 300$  kev, and an approximate photon intensity of  $200 \text{ cm}^{-2} \cdot \text{sec}^{-1}$  close to the atmosphere boundary. September 17, 1963, did not differ from September 25, 1961 with respect to magnetic perturbation, which can be seen from the  $K_p$ -index values for these days given in Figure 2.

TABLE 2

	1961	1962	1963
Total time apparatus remains in the air, hours . . . . .	70	52	80
Length of time $\gamma$ -rays are observed, % . . . . .	40	90	65
Mean flux of $\gamma$ -rays, $\text{cm}^{-2} \cdot \text{sec}^{-1}$ . . . . .	10	18	17
Mean electron flux, $\text{cm}^{-2} \cdot \text{sec}^{-1}$ . . . . .	$2 \cdot 10^6$	$3.6 \cdot 10^6$	$3.4 \cdot 10^6$

Thus, bursts of X-ray radiation did not become less rare close to the solar activity minimum, and the energy spectrum of photons became harder.

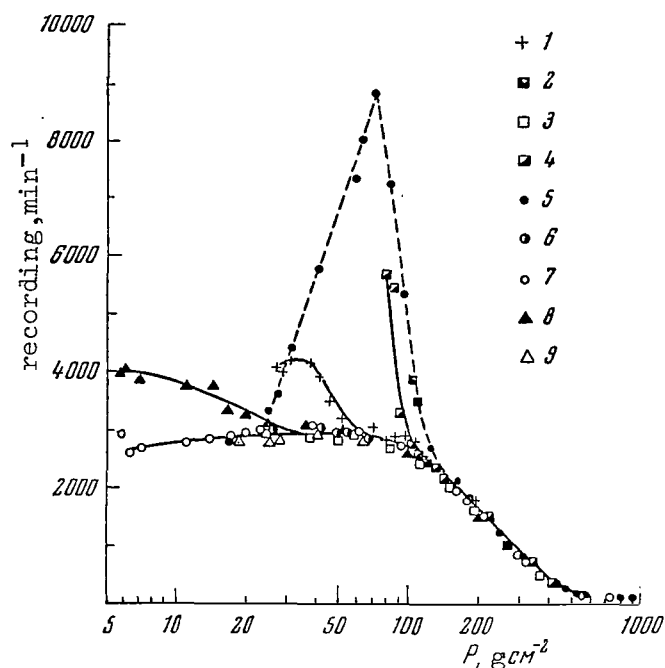


Figure 3

Dependence of a Single Counter Recording Rate on Pressure  $P$  on January 1 and 3, March 5, and April 28, 1964

1 - January 1, 7 hours 2 minutes, Murmansk; 2 - January 3, 7 hours 1 minute, Murmansk; 3 - January 3, 6 hours 44 minutes, Mirnyy; 4 - January 3, 14 hours 13 minutes, Murmansk; 5 and 6 - March 5, 7 hours 13 minutes, Murmansk (above and below, respectively); 7 - March 5, 6 hours 36 minutes, Mirnyy; 8 - April 28, 6 hours 43 minutes, Murmansk; 9 - April 28, 6 hours 43 minutes, Mirnyy.

This is an important conclusion. This may explain the more frequent recording of radiation propagated to considerable depths in the atmosphere.

Somewhat unusual cases, in which the total ionizing radiation in the stratosphere increased (Ref. 11) - reaching a pressure of about  $150 \text{ g}\cdot\text{cm}^{-2}$  - were recorded in the first half of 1964 above Murmansk. These cases were recorded above Murmansk, but were not discovered during simultaneous measurements above Mirnyy.

Data, which were obtained in the second half of 1964 and which have now been processed, indicate an even greater radiation propagation flux, of up to  $300\text{-}400 \text{ g}\cdot\text{cm}^{-2}$ . The results for 1964 are unique, since we did not observe such cases previously, beginning with 1957. It can be assumed that this new phenomenon is not only related to radiation of the Earth's radiation zone, but also to processes which are characteristic for a solar activity minimum.

/458



Figure 3 presents experimental data pertaining to some of these cases. The rate at which discharges are recorded in the counter is plotted along the ordinate (the GDC-1, wall thickness corresponds to the range for electrons of  $\sim 250$  kev).

It can be seen from the behavior of the points 5 (for measurements of March 5) that when the radio probe rises upward, beginning at a pressure of about  $150 \text{ g}\cdot\text{cm}^{-2}$ , the level of recorded radiation sharply increases. This continues to a pressure of about  $70 \text{ g}\cdot\text{cm}^{-2}$ . With a further pressure decrease, at which the measurements were performed, the intensity of the recorded radiation sharply decreases and reaches an almost normal value at pressures of about  $18 \text{ g}\cdot\text{cm}^{-2}$ . The radiation intensity at these pressures was normal when the radio probe was launched (curve 6). It is difficult to explain the break in the curve at pressures of about  $70 \text{ g}\cdot\text{cm}^{-2}$  by something penetrating the stratosphere, in addition to a sharp decrease in the outer radiation level. Therefore, it can be concluded from the data on the second branch of the curve (at pressures of  $< 70 \text{ g}\cdot\text{cm}^{-2}$ ) that the radiation source was almost completely stopped for about 30 minutes.

Two measurements on January 3 over Murmansk also point to a radiation increase in approximately the same pressure ranges as on March 5.

The observed cases of increased radiation in the stratosphere correspond to recurrent magnetic storms (a  $K_p$ -index value of 2-4 on these days), and to large ionosphere perturbations. For the aurorae polaris zone, <sup>459</sup> they correspond to radiowave absorption in the F2 layer of the ionosphere (Ref. 12). According to data at Apatity, considerable absorption of galactic radio noise was recorded on the radiometer in every case, with the exception of Jan. 1. In addition, no chromosphere flares or radio emission bursts on the Sun were recorded during these measurements (Ref. 13). Measurements performed on the satellite "Elektron-1" on the intensity of galactic cosmic radiation beyond the outer radiation zone on March 5, 12, and 24 indicated that the intensity was no different from other days. Cosmic ray intensity on March 5 was even 5% lower than on March 4 (Ref. 14). This indicates that the excess radiation recorded in the stratosphere was not related to cosmic ray flares on the Sun, and was most probably the result of electrons pouring out of the outer radiation zone of the Earth.

Based on the fact that the radiation recorded in the stratosphere was due to photons of braking radiation from outer radiation zone electrons, it is possible to determine the effective photon energy from the measured absorption curve of recorded radiation, and thus to determine the order of magnitude of primary electron intensity. These results are given in the last column of Table 3. The effective photon energy was close to 1 Mev on January 3, March 5, and June 25. It is interesting to note that on June 25 a radiation intensity increase was also recorded above Apatity in the stratosphere; when the radio probe above Qlen was located at a pressure of  $29 \text{ g}\cdot\text{cm}^{-2}$ , the apparatus above Apatity was located at a pressure of  $15 \text{ g}\cdot\text{cm}^{-2}$ . A comparison of the excess radiation intensity at these two pressures shows that the range of radiation absorption is  $\sim 16 \text{ g}\cdot\text{cm}^{-2}$ .

TABLE 3

Date (1964)	Observational Time, Hours, Minutes	Pressure Range, $\text{g}\cdot\text{cm}^{-2}$	Effective Photon Energy, Mev	Photon Flux of Braking Radiation close to the Atmospheric Boundary, $\text{cm}^{-2}\cdot\text{sec}^{-1}$	Electron Flux at the Atmospheric Boundary, $\text{cm}^{-2}\cdot\text{sec}^{-1}$
1/1	8 18 -8 44	27-50	0.30	$9\cdot 10^3$	$3\cdot 10^6$
3/1	7 57 -8 04	80-120	1	$3\cdot 10^4$	$3\cdot 10^6$
3/5	8 06 -8 57	25-143	1	$3\cdot 10^4$	$3\cdot 10^6$
3/12	8 45 -9 07	10-13	0.04	$7\cdot 10^3$	$2\cdot 10^7$
3/24	13 38 -13 44	8-19	0.08	$10^3$	$10^6$
4/28	7 06 -7 36	6-25	0.3	$4\cdot 10^2$	$10^5$
6/25	8 49 -8 54	14-29	1	70	$7\cdot 10^3$

The cases which we recorded are most likely instances in which electrons poured out very strongly.

According to measurements on the satellites "Elektron-1" and "Elektron-2", the maximum number of electrons with energies exceeding 1 Mev does not exceed  $3\cdot 10^4 \text{ cm}^{-2}\cdot\text{sec}^{-1}$  in the outer zone (Ref. 15). The concept of trapped electrons pouring out in the outer radiation zone cannot be used to explain the powerful radiation recorded in the stratosphere due to electrons from the zone, since the primary electron intensities obtained are several orders of magnitude greater than the expected intensities. On the basis of his data, Anderson came to the conclusion that the mean intensity of electrons pouring out, determined by means of balloons, was such that the outer zone would have to vanish for several hours.

Thus, data on electrons pouring out of the outer radiation zone of the Earth force one to draw the conclusion that X-ray radiation in the stratosphere is, in many cases, due to an additional stream of electrons /460 which are formed during non-stationary processes of electron acceleration occurring in the Earth's magnetosphere. The effectiveness of this process intensifies as the solar activity decreases.

## REFERENCES

1. Charakhch'yan, A.N., Tulinov, V.F., Charakhch'yan, T.N. Zhurnal Eksperimental'noy i Teoreticheskii Fiziki, 41, 735, 1961.
2. Brown, R.R., D'Arcy, R.G. Phys. Rev. Letters, 3, No. 8, 390, 1959.
3. Winckler, J.R. Univer. Minnesota Technical Report, CR-40, July, 1961.
4. Anderson, K.A. Department of Physics and Space Sciences Laboratory, University of California. Preprint UCB, April, 1964.

5. O'Brien, B.J. J. Geophys. Res., 67, 3687, 1962.
6. O'Brien, B.J., Laughlin, C.D., Van Allen, J.A., Franks, L.A. J. Geophys. Res., 67, 1209, 1962.
7. Winckler, J.R., Bhavsar, P.D., Anderson, K.A. J. Geophys. Res., 67, 3717, 1962.
8. Anderson, K. A., Milton, D. W. Department of Physics and Space Science. Preprint UCY, May 1964.
9. Pfoetzer, G., Ehmert, A., Bewersdordt, A., Kremser, C., Rossberg, L. Riedler, W., Trefall, H., Legrand, J. R. Technical Report AFEOAR Grant, 62-98, August, 1964.
10. Lizutin, L. L. Geomagnetizm i Aeronomiya, 4, 1965 (in press).
11. Charakhch'yan, A. N., Golenkov, A. Ye., Charakhch'yan, T. N. Geomagnetizm i Aeronomiya (in press).
12. Kosmicheskiye Dannyye. Dekadnyy Obzor IZMIRAN, No. 10, 16, 17, 21, 1964.
13. Solnechnyye Dannyye, No. 1, 3, and 4, 1964.
14. Vernov, S. N., Chudakov, A. Ye., Vakulov, P. V., Logachev, Yu. I. Zatsepin, V. I., Okhlopov, V. P. Present collection, p. 502.
15. Vernov, S. N., Chudakov, A. Ye., Vakulov, P. V., Logachev, Yu. I., Kuznetsov, S. N., Sosnovets, E. N., Nikolayev, A. G. Present collection, p. 394.

#### MEASUREMENT RESULTS ON THE SATELLITE "KOSMOS-41" IN THE OUTER RADIATION ZONE

S. N. Vernov, I. A. Savenko, M. V. Tel'tsov, P. I. Shavrin

The satellite "Kosmos-41" was launched on August 22, 1964, onto an orbit with an apogee of 39,855 km and a perigee of 394 km, which was inclined to the equatorial plane at an angle of  $65^\circ$ . It carried a radio-metric apparatus for studying radiation trapped in the magnetic field of the Earth. Table 1 gives the composition of the apparatus. A detailed description of the apparatus may be found in the studies (Ref. 1, 2).

Figure 1 shows the proton intensity change  $N_p$  with an energy of 0.4-7 Mev (curves for September 3, 19, 21 and October 9, 1964), as well as the magnetic field strength  $B$  (curve 1) and the satellite altitude above the Earth's surface  $h$  (curve 2) as a function of the parameter  $L$  (Ref. 3). In this section of the satellite's trajectory, the angle between the n-p-counter axis and the magnetic force line is  $\sim 60^\circ$ , i.e., protons with pitch-angles of  $30-90^\circ$  were recorded. The recording of the second

n-p-counter, which recorded protons of 3-8 Mev, was always lower than, or on the level of, the measurement range - i.e.,  $\leq 3 \text{ cm}^{-2} \cdot \text{sec}^{-1} \cdot \text{sterad}^{-1}$  - at  $L = 3.5-10$  for the indicated values of  $B$  on this trajectory section during the period from the end of August to the end of December, 1964. It can be seen from Figure 1 that at  $L = 3.5$  the intensity of protons with energies of 0.4-3 Mev was  $2 \cdot 10^5 \text{ cm}^{-2} \cdot \text{sec}^{-1} \cdot \text{sterad}^{-1}$ .

TABLE 1

/461

Type of Detector	Shielding	Geometric Factor	Type and energy of particles recorded
Semi-conducting n-p-counter with sensitive layer of $8 \text{ mg} \cdot \text{cm}^{-2}$ . . .	$200 \text{ mkg} \cdot \text{cm}^{-2}$	$0.07 \text{ cm}^2 \cdot \text{sterad}$	$0.4 \leq E_p \leq 7 \text{ Mev}$
" " . . . . .	$20 \text{ mg} \cdot \text{cm}^{-2} \text{ Al}$	$0.07 \text{ cm}^2 \cdot \text{sterad}$	$3 \text{ Mev} \leq E_p \leq 8 \text{ Mev}$ During Forward passage
Cylindrical (NaJ (Tl) scintillator . .	$\text{min } 0.18 \text{ g} \cdot \text{cm}^{-2} \text{ Al}$	$6.8 \text{ cm}^2 (\text{isotropic})$	$E_e > 600 \text{ kev}$ $E_p > 100 \text{ Mev}$
Gas Discharge counters STS-5 .	$\text{min } 0.15 \text{ g} \cdot \text{cm}^{-2} \text{ Al}$ + steel	$4.3 \text{ cm}^2 (\text{isotropic})$	$E_e > 500 \text{ kev}$ $E_p > 9 \text{ Mev}$
Si-ZBG I . . . . .	$\text{min } 0.84 \text{ g} \cdot \text{cm}^{-2} \text{ Al}$ + steel	$0.1 \text{ cm}^2 (\text{isotropic})$	$E_e > 2 \text{ Mev}$ $E_p > 25 \text{ Mev}$
Si-ZBG II . . . . .	$\text{min } \sim 3 \text{ g} \cdot \text{cm}^{-2}$	$0.1 \text{ cm}^2 (\text{isotropic})$	
End-window gas discharge counters:			
SBT-9 No. 1 .	$\sim 1 \text{ mg} \cdot \text{cm}^{-2} \text{ mica}$	$0.1 \text{ cm}^2 \cdot \text{sterad}$	$E_e > 25 \text{ kev}$ $E_p > 0.5 \text{ Mev}$
SBT-9 No. 2 .	$\sim 1 \text{ mg} \cdot \text{cm}^{-2} \text{ mica}$ and magnetic shielding	$0.1 \text{ cm}^2 \cdot \text{sterad}$	$E_e > 120 \text{ kev}$ $E_p > 0.5 \text{ Mev}$
SBT-9 No. 3 .	$20 \text{ mg} \cdot \text{cm}^{-2} \text{ Al}$ , $\sim 1 \text{ mg} \cdot \text{cm}^{-2} \text{ mica}$ and magnetic shielding	$0.1 \text{ cm}^2 \cdot \text{sterad}$	$E_e > 120 \text{ kev}$ $E_p > 3 \text{ Mev}$

If the proton intensity decrease with increasing  $L$  is represented by the expression  $L^{-n}$ , then  $n$  equals 30 for a very abrupt proton intensity decrease (September 19). In addition to information from the satellite trajectory sections indicated above, we have data from the descending trajectory section in the geomagnetic equator region. In this case, the satellite moved almost along the magnetic force line, and the n-p-counter axis formed a  $\sim 30^\circ$  angle with the magnetic force line. Thus, it was possible to record a proton intensity change at one and the same  $L$ , but for considerably different values of  $B$ . The difference in the measurement time at high latitudes and in the equatorial region was about

8 hours. Data are given below from such measurements on September 1, 1964, at  $L = 5$  at two points A and B of the satellite trajectory (Table 2).

TABLE 2

	A	B
$h$ , thousand km	6.6	26
$\Lambda$	$49^\circ N$	0
$B$ , gauss	$5.4 \cdot 10^{-2}$	$0.25 \cdot 10^{-2}$
$\bar{\theta}$	$60^\circ$	$30^\circ$
$N_p$ , $\text{cm}^{-2} \cdot \text{sec}^{-1} \cdot \text{sterad}^{-1}$	$10^4$	$3 \cdot 10^4$

( $\Lambda$  - geomagnetic latitude;  $\theta$  - angle between the n-p-counter axis and the magnetic force line;  $N_p$  - intensity of protons with an energy of 0.4-3 Mev).

If it is assumed that the pitch-angle distribution of protons in the equatorial plane satisfies the expression  $P = \sin^{\alpha+1} \theta$ , where  $\alpha = 2$  (this closely coincides with experimental data [Ref. 4]), then the coefficient 6 must be introduced for normalizing the intensity at the point B, and the intensity ratio  $N_p(B)$  becomes equal to 18. We thus find that

$\overline{N_p(A)}$   
 $k \approx 1$ , representing the altitudinal pattern as  $(B/B_{\text{equa}})^{-k}$ . /463

If it is assumed that this altitudinal behavior for protons having the energy given above is valid for small  $L$ , then at  $L = 3.5$  our detector could record a proton flux of  $\sim 6 \cdot 10^6 \text{ cm}^{-2} \cdot \text{sec}^{-1} \cdot \text{sterad}^{-1}$  in the geomagnetic equatorial plane.

Figure 2 presents, in the same form as in Figure 1, data derived from recording outer radiation zone electrons during September, 1964. Curves 5 and 6 represent the recording rate of the gas discharge counters Cu-ZBG I and II, respectively (in  $\text{cm}^{-2} \cdot \text{sec}^{-1}$ ), which differ only in their shielding. Curve 4 represents the change in the mean anode current of the photomultiplier with a crystal of NaJ(Tl) in  $\text{Mev} \cdot \text{sec}^{-1}$ . Protons with an energy of  $E_p > 10$  Mev, electrons with  $E_e > 600$  kev with direct passage in the crystal and electrons having lower energy caused by braking radiation may make a contribution to the scintillation detector current. For purposes of comparison, Figure 2 presents a curve for the detector recording rate of protons with an energy of 0.4-7 Mev (curve 3). It can be seen from the behavior of the curves that the maximum intensity of outer radiation zone electrons is recorded at  $L = 5$ . In addition, the more abrupt decrease (with an increase in  $L$ ) in the recording rates of the gas discharge counters

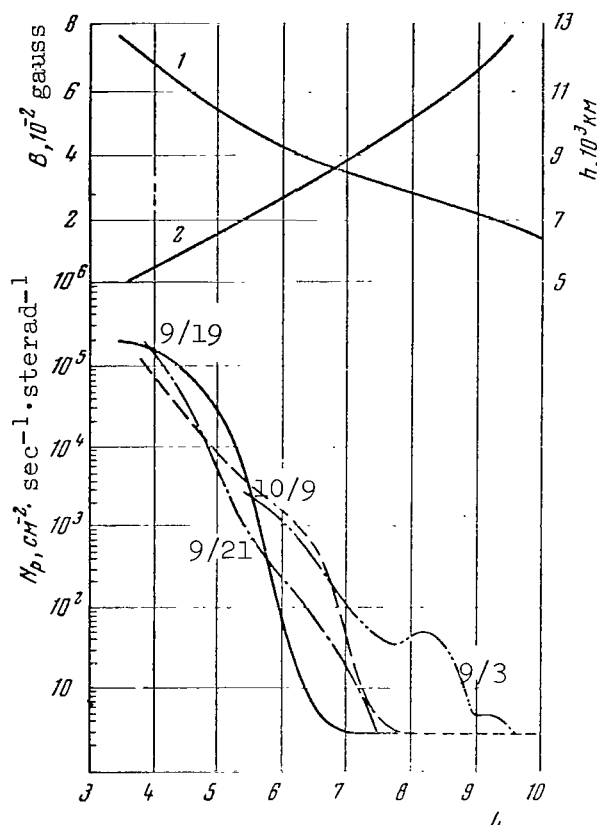


Figure 1

recording energetic electrons, as compared with the photomultiplier current, indicates that the spectrum of outer zone electrons shifts to a low-energy region with an increase in  $L$ . It should be noted that the ratio of electron intensities recorded in trajectory sections A and B by the Si-ZBG gas discharge counters is 20 in the case of  $L = 5$ .<sup>1</sup>

The processing of data from other satellite crossings at the same geomagnetic latitudes and distances from the Earth shows that changes in the configuration and intensity of the outer section of the proton zone are related, as a rule, to changes in the outer electron radiation zone.

The lower portion of Figure 3 uses dots to indicate the intensities of protons recorded in the same spatial region as for Figure 1 at different  $L$ ; the upper portion of the Figure shows the intensities of outer radiation zone electrons based on data from the Si-ZBG I between August 28 and October 10, 1964. For purposes of illustration, Figure 3 presents curves for the intensity changes of electrons and protons for September 4 and 19.

<sup>1</sup> Normalization is not required in this case, since the radiation recording by the Si-ZBG gas discharge counters is almost isotropic.

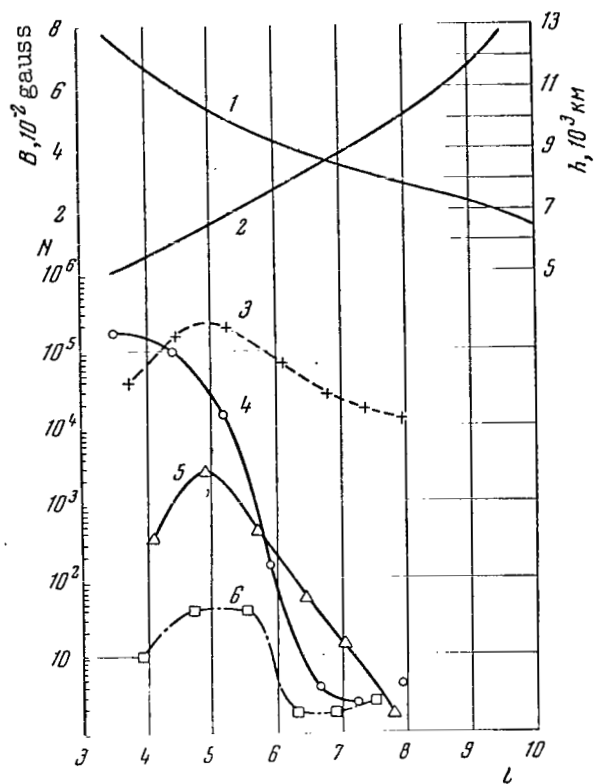


Figure 2

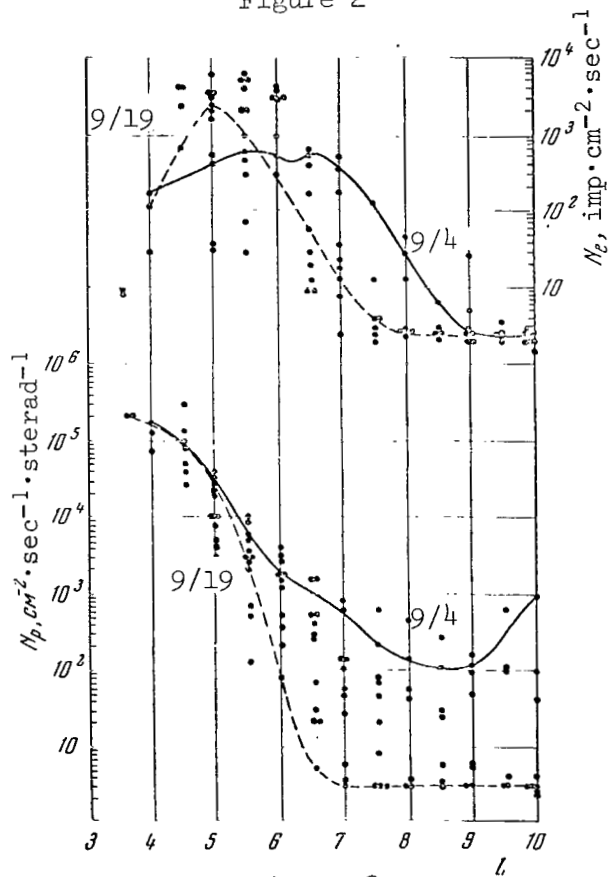


Figure 3  
627

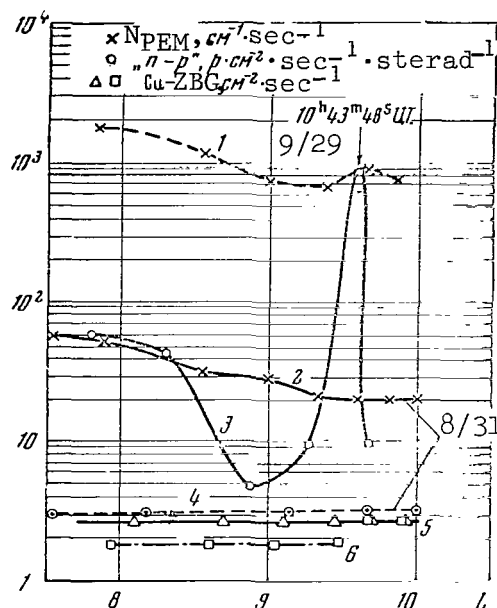


Figure 4

It should be noted that the greatest variation in electron intensity occurs in the  $L = 5-7$  region for fixed  $L$ . There is a change in the position of the maximum as well as a change in the maximum intensity, and the variations increase with an increase in  $L$  for proton intensities up to  $L = 10$ . These variations and their intercorrelation will be investigated in greater detail, with allowance for the specific geomagnetic environment.

In certain cases, the semiconductor detector recorded a sharp increase in the low-energy proton flux at large  $L$ . Curve 3 in Figure 4 represents such a peak of electron intensity recorded on September 29, 1964, at  $L = 9.5$ . In comparison with the normal proton intensity in this region of space (curve 4 for August 31, 1964), the intensity increased by three orders of magnitude. The scintillation detector recording with a 90-kev threshold (curve 1) was somewhat higher than usual (curve 2) for September 29, and it increased by a factor of 3 in the region of the proton peak. The Si-ZBG I, II detectors (curves 5 and 6) indicated no changes, and their recording exactly coincided with the usual recording. A small storm with a gradual commencement was recorded by stations on the Earth between zero hours UT on September 28 and 3 hours on September 29, and the K-index doubled on September 29 (Ref. 5).

Figure 1 also presents anomalous phenomena occurring at the outer protonosphere boundary (the curve for September 3). A smoother proton intensity peak was observed here at  $L \approx 8.5$



## REFERENCES

1. Savenko, I. A., Tel'tsov, M. V., Maduyev, V. L., Savun, O. I. Geomagnetizm i Aeronomiya (in press).
2. Maduyev, V. L., Savenko, I. A., Tel'tsov, M. V. Geomagnetizm i Aeronomiya, (in press).
3. McIlwain, C. E. J. Geophys. Res., 66, 3681, 1961.
4. Davis, L. R., Williamson, J. M. Proceedings of the Third International Space Science Symposium W. H. P. Co., p. 365-375, 1963.
5. "Cosmic Data" ("Kosmicheskiye dannyye"). Ten-year Survey, No. 36, September 21-30, 1964. Moscow, IZMIRAN, 1964.

## STUDY OF RADIATION INTENSITY IN THE RADIATION ZONES OF THE EARTH ON THE "KOSMOS-17" AES

(Summary)

G. A. Kirdina, Yu. M. Kulagin, A. B. Malyshev,  
M. N. Nazarova, P. M. Svidskiy, I. S. Yudkevich

Data are presented which were derived from recording charged particle streams in the Earth's radiation zones by Geiger and scintillation counters in the 260-780 km altitudinal range between May 22 and May 30, 1963.

B, L-coordinates are used to represent the results derived from Geiger counter measurements of penetrating particle streams (electrons with an energy of  $E_e > 2.7$  Mev, protons with an energy of  $E_p > 30$  Mev) in the inner radiation zone. A comparison of the simultaneous measurements by scintillation counters and by Geiger counters having different screening showed that in the  $1.15 \leq L \leq 1.6$  range the main portion of recorded intensity was due to penetrating electrons injected during the high-altitude nuclear explosion of July 9, 1962. The maximum flux of electrons with an energy of  $E_e > 2.7$  Mev was  $5 \cdot 10^5 \text{ cm}^{-2} \cdot \text{sec}^{-1}$  in the region with  $L = 1.2-1.25$  and  $B = 0.19$  gauss. Primarily protons with an energy of  $E_p \geq 30$  Mev were recorded in the drift envelopes with  $L = 1.6-2.5$ . The flux of these protons increased by approximately one order of magnitude as compared with 1958. This increase can be explained by decreased solar activity during the 11-year solar cycle.

During magnetically quiet days, the intensity maximum in the outer zone was recorded at  $L = 4.7-4.8$ . During a period of increased magnetic activity, the maximum position shifted toward smaller L. /465

In the gap between the zones, there was a narrow region ( $L \sim 2.5-2.7$ ), in which electrons with an energy of  $0.1 \leq E_e \leq 1.5$  Mev were recorded. The radiation intensity in this region and its maximum position depend greatly on the level of magnetic activity.

Stable corpuscular streams were discovered under the lower boundary of the inner zone at drift envelopes with  $L \geq 1.05$ ; these were apparently streams of soft electrons with energies of 50-100 kev, which were connected with the radiation zones of the Earth. The total distribution of these streams indicates that the corpuscles recorded were captured in the geomagnetic trap. The fluxes reached values of  $10^5-10^6$   $\text{cm}^{-2} \cdot \text{sec}^{-1}$ , and could not be classified as sporadic phenomena.

# THE PROBLEM OF CORPUSCULAR RADIATION IN PRE-EQUATORIAL REGIONS AT LOW ALTITUDES

(Summary)

I. A. Savenko, P. I. Shavrin, L. V. Tverskaya

During flights of the Soviet spacecrafts and satellites in the "Kosmos" series, it was found that there are significant electron streams even close to the geomagnetic equator at low altitudes (300-400 km) (Ref. 1). It may be assumed that this intensity is due to the decay of cosmic ray albedo neutrons. Since the drift orbits rapidly rise upward to the east of the Brazilian geomagnetic anomaly, these electrons could be trapped and could be stored for one drift revolution. If the latitudinal and pitch-angle region is determined (as a function of longitude  $\lambda$ ) in which stable capture is possible, then the intensity accumulated over the time  $t$  may be readily computed.

The computation shows that a definite altitude, at which stable electron capture with  $Y_0 = 0$  becomes possible, corresponds to each electron energy value. Table 1 presents the capture altitudes, calculated for 4D and 6D Nicolet models (Ref. 2), for electrons having different energies with a  $90^\circ$  pitch-angle at the equator. The 4D model corresponds to the minimum of solar activity; the 6D model corresponds to maximum solar activity.

TABLE 1

E, kev	Capture Altitude, km	
	4D	6D
200	480	750
300	410	650
400	340	490
500	310	420
600	280	370

TABLE 2

E, kev	$\gamma^\circ$				
	300 km	400 km	500 km	600 km	700 km
200	--	--	4	10	12
300	--	--	10	12	12
400	--	9	11	12	12
500	--	10	12	12	12
600	6	11	12	12	12

The range for pitch-angles, at which capture takes place, expands as the drift trajectory rises above the capture altitude for electrons with a  $90^\circ$  pitch-angle at the equator. However, beginning at altitudes which exceed the critical altitude by  $\sim 100$  km, the range width becomes almost constant ( $|\gamma| \leq 12$ ). Table 2 presents pitch-angle ranges ( $\gamma$ ) for electrons having different energies at different altitudes (computed according to the 4D model). /466

According to (Ref. 3),  $\sim 30\%$  of electrons from neutron decay correspond to a pitch-angle range of  $12^\circ$ ; consequently, the intensity of the sources  $q$  is  $\approx 3 \cdot 10^{-12} \text{ cm}^{-2} \cdot \text{sec}^{-1}$ .

TABLE 3

$\lambda^\circ$	$\lambda_0^\circ$	t, sec	$\text{cm}^{-2} \cdot \text{I}, \text{sec}^{-1}$	$\lambda^\circ$	$\lambda_0^\circ$	t, sec	$\text{cm}^{-2} \cdot \text{I}, \text{sec}^{-1}$
290	332	$1.1 \cdot 10^4$	$1.9 \cdot 10^3$	154	54	$3.3 \cdot 10^3$	$6 \cdot 10^2$
268	350	$9.4 \cdot 10^3$	$1.7 \cdot 10^3$	128	66	$2 \cdot 10^3$	$3.6 \cdot 10^2$
224	18	$6.9 \cdot 10^3$	$1.3 \cdot 10^3$	100	100	0	0

Table 3 presents the results derived from computing the expected intensity values at an altitude of 500 km (model 4D). Here  $\lambda$  is the observational longitude;  $\lambda_0$  - the longitude at which the accumulation of electrons with energies of  $> 300$  kev begins at the drift envelope passing through  $\lambda$ ; t - the corresponding drift time from  $\lambda_0$  to  $\lambda$  (accumulation time); I - intensity at the point  $\lambda$ .

Intensity on the ascending branch of the drift orbit is small, since the electrons rapidly move upward from the given altitude. The greatest intensity is expected above the Pacific Ocean and South America (i.e., on the western edge of the Brazilian anomaly, where the accumulated particles descend to the observational altitude).

Thus, the neutron mechanism is powerful enough to create an intensity of  $\sim 10^3 \text{ cm}^{-2} \cdot \text{sec}^{-1}$  during the longitudinal drift.

#### REFERENCES

1. Savenko, I. A., Shavrin, P. I., Pisarenko, N. F. Nesterov, V. Ye., Tel'tsov, M. V., Yerofeyeva, V. I. Kosmicheskiye Issledovaniya, 2, No. 1, 150, 1964.
2. Nicolet. Aeronomy. Translation from the English. "World press", 1964.
3. Hess, W. H., Canfield, E. H., Lingenfelter, R. E. J. Geophys. Res., 66, No. 3, 665, 1961.
4. Van Allen. In "Radiation Zones of the Earth", Moscow, p. 14, 1962

#### INTERACTION OF SOLAR WIND AND GEOMAGNETIC FIELD

(Summary)

M. V. Samokhin

This report is devoted to summarizing the domestic and foreign theoretical studies on the form of the magnetosphere boundary, the transitional turbulent layer, and the shock wave produced during super-Alfven flow around the geomagnetic cavity. The introduction presents a list of artificial satellites and rockets employed to study the magnetosphere, as well as the main measurement results. Both approximate and accurate methods are employed to determine the form of the magnetosphere (the approximate method of Beard connected with simplification of the boundary conditions, a strict solution for the two-dimensional region, and the moment technique). The shock wave form is determined by a different physical model - for example, the problem of supersonic flow around a spherical body having a radius equalling the magnetosphere radius at the point where the stream stops, is investigated. The measurements and computations coincide satisfactorily for the solar side of the magnetosphere. /467

STRUCTURE OF THE BOUNDARY LAYER BETWEEN A  
RAREFIED PLASMA AND A MAGNETIC FIELD  
(Summary)

Yu. S. Sigov

The stationary problem of the microstructure of the boundary between a magnetic field and a fully ionized gas is solved in flat geometry (Chapman-Ferraro model). The behavior of electrons and ions is described by collisionless kinetic equations. /467

The proposed method entailing numerical solution of a nonlinear equation system for a self-consistent electromagnetic field makes it possible to obtain the over-all spatial picture of the boundary layer for arbitrary particle distribution functions - assuming there is no electric neutrality within the boundary layer.

Computations performed on an IBM computer have provided quantitative estimates of the main physical characteristics of the transitional layer: spatial scales, extreme values of charges and currents, electrostatic potential jumps, etc.

The discussion covers problems related to the energy balance in the boundary layer and energy re-distribution between heavy and light components of the plasma. Oblique incidence of a plasma stream on a "magnetic wall" is examined. It is found that a change in the angle of incidence can lead to a sharp rearrangement of the self-consistent electrostatic field, while the spatial picture of the magnetic field changes to a much smaller extent. The relativistically-invariant form in which the solution is carried out produces results for a wide particle energy range in the plasma.

THE OUTERMOST ZONE OF CHARGED PARTICLES

K.I. Gringauz, M.Z. Khokhlov

This report examines the results derived from studying zones of charged particles with comparatively low energies (from  $\sim 100$  ev to  $10^{-40}$  kev) located beyond the outer radiation zone (including new data obtained from the satellite "Elektron-2" and the space rocket "Zond-2").

As is known, the radiation zones of the Earth were discovered in /468 1958 when experiments studying cosmic rays were performed. These experiments employed devices which could only record comparatively high-energy particles, beginning with tens of kev, and the impression was initially gained that conditions which are characteristic for interplanetary space exist beyond the

boundary of the trapped radiation zones.

Experiments with charged particle traps (Ref 1) on Soviet lunar rockets disclosed that there is a zone in which electrons accumulate close to the geomagnetic equator beyond the outer radiation zone. In this zone, the concentration and fluxes of electrons considerably exceed the concentration and fluxes of electrons in the outer radiation zone. According to data from the rocket "Luna-2", this zone extends on the order of 40,000 km. In (Ref 2) the appearance of intense ( $\sim 10^8 \text{ cm}^{-2} \cdot \text{sec}^{-1}$ ) low-energy particle fluxes beyond the outer radiation zone was interpreted as the result of solar plasma streams interacting with peripheral regions of the Earth's magnetic field. The mechanism cited in (Ref 3) was examined as one of the possible processes by which the solar plasma is thermolyzized. Other different mechanisms for solar plasma electron acceleration were later investigated (Ref 4,5). However, the main idea that the outermost zone was formed as the result of certain boundary effects, due to the interaction of solar plasma streams with the Earth's magnetic field, completely retained its validity.

Although more than five years have passed since this zone was discovered by the Soviet lunar rockets, a considerable portion of the studies devoted to it appeared only after 1962, and the terminology pertaining to this zone has still not been established. At first it was called the "third radiation zone" (Ref 6,7). In order to emphasize the difference between the physical features of this zone and the radiation zones, it was proposed in 1961 (Ref 8) that this zone - where low-energy charged particles exist and which is located between the zone of trapped radiation and the unperturbed solar wind - be called the outermost belt of charged particles (see also [Ref 9,10]), or more recently the outermost zone of charged particles (Ref.11). Other designations - particularly the name "auroral radiation" which was proposed in (Ref 12) for streams of soft charged particles beyond the outer boundary of trapped radiation - are less suitable in our opinion.

## 1. Experimental Data

The table below presents in chronological order (according to launch date) the space vehicles which obtained data on streams of soft electrons and protons beyond the radiation zones. The observational method is given, as well as the values of the angle  $\lambda_{es}$  (see Figure 7), corresponding to the observational times.

The orbits of the majority of the space vehicles, which are listed in the table, pass close to the ecliptic plane. Only "Mars-1" and "Elektron-2" observed electron streams with  $E_e > 100 \text{ ev}$  beyond the trapped radiation boundaries at high latitudes (and great distances from the Earth).

## 2. Observations at Low Latitudes

Due to insufficient space, we shall confine ourselves to briefly examining only several characteristic examples of soft electron stream recordings.

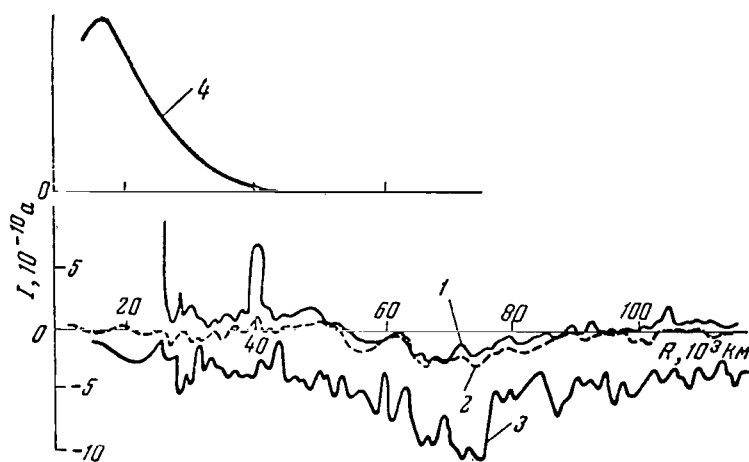


Figure 1

Collector Currents of Integral Charged Particle Traps (Ref. 1) and Recording Rate of Hard Radiation (Ref. 20)

1 - Upper boundary of collector currents in traps with a retarding grid potential of  $\varphi = -10, -5$  and  $0$  v; 2 - lower boundary of the same currents; 3 - upper boundary of currents in a trap with  $\varphi = 15$  v; 4 - recording rate in relative units.

Figure 1 presents collector current recordings from integral charged particle traps carried on the space rocket "Luna-2" launched /469 on the nocturnal side. The same figure presents data from the readings of counters for more energetic particles carried on the rocket (Ref. 20). As can be seen from the figure, in the case under consideration the zone of intense fluxes of soft electrons lies almost entirely outside of the zone in which energetic particles were recorded. These zones overlapped considerably during the experiments on the rocket "Luna-1" launched on the diurnal side.

It should be noted that the "Luna-2" trajectory passed close to the geomagnetic equator, and intersected it at the distance  $\sim 8.5 R_E$ .

Figure 2 shows the intensity behavior of electron streams recorded /471 on the diurnal side by means of an integral trap carried on the satellite "Explorer-18" (Ref. 16). Just as in the case of "Luna-1", electron streams were observed on both sides of the trapped radiation boundary (on the diurnal side close to the geomagnetic equator, the trapped radiation boundary coincides with the magnetosphere boundary). Due to the fact that the apogee of the "Explorer-18" orbit was a great distance from the Earth, it also recorded the outer boundary of the thermolyzed solar plasma zone which was identified with the shock wave front. Streams

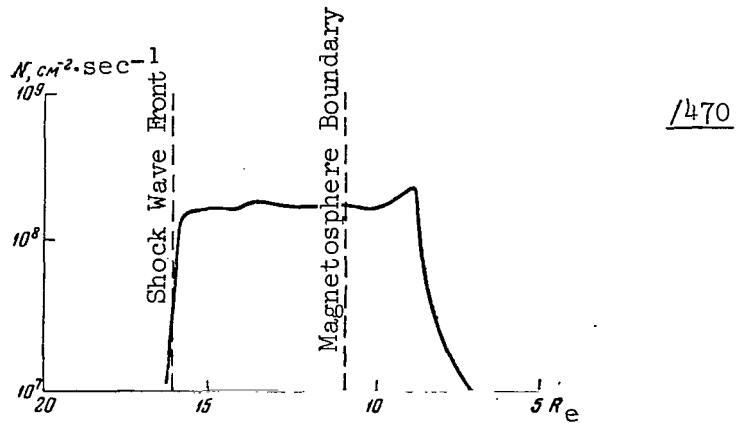


Figure 2

Streams of Electrons With  $E_e > 100$  ev Based on Data  
From the Integral Trap on "Explorer-18" (Ref. 16)

TABLE

Apparatus	Launch Date	Source	$\lambda_{es}$	Measurement Method
"Luna-1"	1/1/59	[Ref. 6]	285°	Integral trap (electrons with $E_e > 200$ ev)
"Luna-2"	9/12/59	[Ref. 1]	135	" "
"Explorer-12"	9/16/61	[Ref. 13, 14]	285-360 and 225	Integral detector CdS ( $E_e > 200$ -500 ev)
"Mars-1"	9/1/62	[Ref. 15]	200	Integral trap ( $E_e > 100$ ev)
"Explorer-18"	11/27/63	[Ref. 16, 17]	270-360	" " Modulation trap ( $E_i \sim$ kev ions, 65-210 ev electrons)
"Elektron-2"	1/30/64	[Ref. 18]		Electrostatic analyzer ( $E_i \sim$ kev ions)
		--	290 and 210	Integral trap ( $E_e > 100$ ev electrons)
"Zond-2"	11/30/64	[Ref. 19]		Electrostatic analyzer (ions and electrons with $E \sim 100$ ev-10 kev)
		[Ref. 11]	230	Integral trap (electrons with $E_e > 70$ ev)



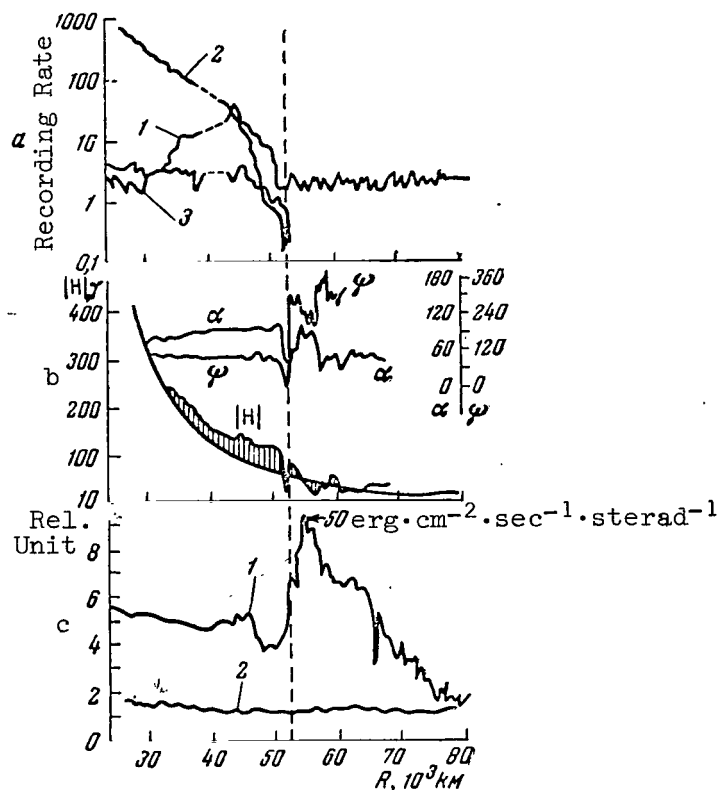


Figure 3

Readings from Equipment on the Satellite "Explorer-12"  
During Intersection of the Magnetosphere Boundary on  
November 13, 1961 (Ref. 13)

- a - Recording of hard radiation: 1 -  $40 \leq E_e \leq 50$  keV,  
2 -  $E_e \geq 16$  MeV,  $E_p > 20$  MeV, 3 -  $80 \leq E_e < 100$  keV;
- b - Magnetometer readings;  $\alpha$  - angle between H and direc-  
tion of the satellite's axis of rotation,  $\psi$  - angle  
between the planes, one of which contains H and the  
satellite's axis of rotation, and the second of which  
contains the axis of rotation and the Sun-satellite  
line;
- c - total energy detector readings of CdS-1; background - 2.

of protons (Ref. 17) (they were recorded with an electrostatic analyzer in [Ref. 18]) with energies of up to  $\sim 5$  keV, as well as omnidirectional electron streams in the 65-210 eV range (Ref. 17), were recorded throughout the entire transitional region beyond the magnetosphere boundary with a modulation trap. For protons in the transitional zone, the intensity of streams originating from the Sun was almost double the intensity of streams coming from the opposite direction.



Figure 4

#### Constant Component of Collector Current of Modulation Trap on the Interplanetary Station "Zond-2"

Figure 3 presents the data obtained on "Explorer-12" when the satellite intersected the magnetosphere boundary on the side below the Sun on November 13, 1961 (Ref. 13). There was a small maximum in the readings of the CdS total-energy detector close to the boundary within the magnetosphere, as well as an intensity maximum of fluxes of electrons with an energy of 40-50 kev. Immediately beyond the magnetosphere boundary (determined by the magnetic field jump and by the beginning of the turbulent field region beyond it) there was a sharp increase in the stream of energy recorded by the CdS crystal up to  $\sim 50 \text{ erg} \cdot \text{cm}^{-2} \cdot \text{sec}^{-1}$ . An indirect determination of the electron flux and the electron energy gave, respectively,  $10^{10} \text{ cm}^{-2} \cdot \text{sec}^{-1}$  and 2.5 kev. Measurements were performed during a magnetic storm and for unperturbed conditions which were not typical, on the average. The work (Ref. 14) analyzes all other cases in which electron streams were observed beyond the magnetosphere boundary. After each successful (the CdS crystal was not exposed to solar radiation reflected by the Earth) intersection of the magnetosphere boundary, electrons were observed, whose flux exceeded the threshold value of  $\sim 1 \text{ erg} \cdot \text{cm}^{-2} \cdot \text{sec}^{-1}$  (the region in which electron streams were recorded is shown in Figure 8).

Streams of electrons with an energy of  $\sim 0.5$ -40 kev were again recorded by means of the same total-energy detector on the nocturnal side (Ref. 14). It was not possible to determine the energy more accurately. There are discrepancies in the electron flux determination. In (Ref. 10) the flux is estimated as  $\sim 10^8$ - $10^9 \text{ cm}^{-2} \cdot \text{sec}^{-1}$ , while in (Ref. 14) a value of  $\sim 10^{12} \text{ cm}^{-2} \cdot \text{sec}^{-1}$  is given. There is no direct connection observed between the nocturnal and diurnal regions of electron fluxes, based on data obtained on "Explorer-12" (Ref. 13, 14).

The trajectory of the cosmic rocket "Zond-2" passed above the nocturnal side of the Earth, approximately at the point where the nocturnal region of electron streams was observed on "Explorer-12". Figure 4 shows the behavior of the collector current constant component of the modulation trap carried on the satellite, up to a geocentric distance of  $\sim 7.3 R_e$ , at which the first measurement period was terminated (Ref. 11). In this

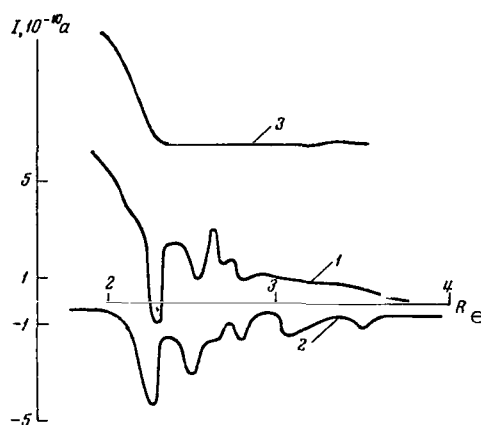


Figure 5

Collector Currents of Integral Charged Particle Traps (Ref. 15) and Recording Rate of Hard Radiation (Ref. 21) on the Interplanetary Station "Mars-1"

1 - Potential of retarding grid  $\varphi = 0$ ; 2 -  $\varphi = 50$  v; 3 - recording rate in relative units.

trajectory section, no proton streams were recorded by the modulation portion of the circuit. The electron flux amounted to  $\sim 3 \cdot 10^8 \text{ cm}^{-2} \cdot \text{sec}^{-1}$  when the measurement period ended, which was a considerable quantity.

### 3. Observations at High Geomagnetic Latitudes

As has already been indicated, only "Mars-1" and "Elektron-2" observed intense electron fluxes of low energies ( $E_e \sim 100$  ev) at high latitudes (and at great distances from the Earth).

The trajectory of the interplanetary station "Mars-1" passed above 472 the nocturnal side of the Earth close to the meridional plane, passing through the Earth-Sun line. Figure 5 shows the collector current recordings for two integral traps on this station, according to (Ref. 15). Curve 3 in Figure 5 describes the change in the rate at which the more energetic particles were recorded (Ref. 21). A comparison of curves 1 and 2 shows that in this case the peripheral ionosphere region was intersected, as well as the outermost zone of charged particles. It should be noted that the zone containing soft electron streams lies between the force lines of the geomagnetic dipole corresponding to the geomagnetic latitudinal range of  $\sim 63-73^\circ$  (Figure 6), in which the zone of maximum aurorae polaris recurrence is located.

"Elektron-2" was the first satellite to study low-energy charged

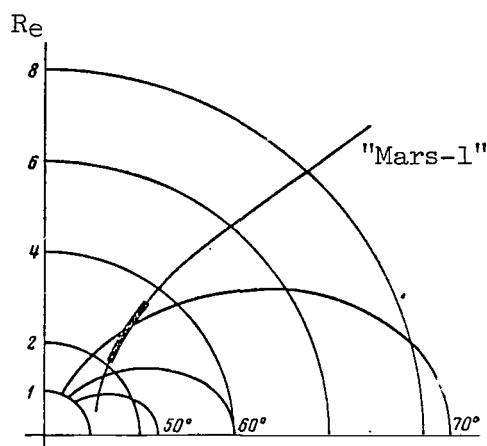


Figure 6

Location of the "Mars-1" Trajectory With Respect to the Force Lines of an Ideal Geomagnetic Dipole

The dark section of the curve indicates the region where soft electron streams were recorded (Ref. 15)

particles at great distances from the Earth at high latitudes and to carry out these studies systematically for a long period of time. Electron streams were recorded by an electrostatic analyzer carried on the satellite (Ref. 19) and an integral charged particle trap (Ref. 22). When the data obtained are compared, the fact should be kept in mind that primary data are given for the trap (collector current), while for the analyzer the magnitude of recorded streams - i.e., the photocurrent magnitude in the collector circuit - had been already computed. Attention should be called to the satisfactory, qualitative agreement between data obtained from two different devices. Intense electron streams with energies of up to 10 kev were systematically observed, according to data from the electrostatic analyzer, outside of the trapped radiation region ( $L > \sim 7.5$ ). It should be noted that electron streams were not always observed, according to data from the integral trap. We must recall that the collector current for the "Elektron-2" trap was determined by the difference between the fluxes falling on the collector, having a value determined by the satellite potential, and electrons having an energy of  $E_e > 100$  ev. The minimum collector current which could be recorded corresponded to a flux of  $3 \cdot 10^7 \text{ cm}^{-2} \cdot \text{sec}^{-1}$  (see [Ref. 22] for more details on this point). The measurement results indicate significant instability of the outermost charged particle zone, which coincides with the instability of the soft electron component of the outer radiation zone (Ref. 22). Just as was found in experiments on other space vehicles/473 the soft electron stream zones partially overlapped the trapped radiation zones.

#### 4. Spatial Distribution of Soft Electron Streams

Figure 7a and b shows the spatial distribution of soft electron streams and proton streams observed on different space vehicles at great distances from the Earth (in a projection on the ecliptic and on the meridional plane perpendicular to it; the  $X_{se}$  axis is directed toward the Sun; the so-called solar-ecliptic coordinate system is employed).

The trajectory sections, on which streams of soft charged particles were recorded, formed two regions - nocturnal and diurnal regions - close to the ecliptic plane (Figure 7,a).

1. The diurnal region is located along the magnetosphere boundary towards the Sun. The outer boundary of this region coincides with the shock wave front, behind which unperturbed solar plasma streams are located ("Luna-1", "Explorer-12", "Explorer-18"). According to data from the integral charged particle traps, electron streams were recorded on both sides of the magnetosphere boundary. However, the energy spectrum of soft electrons observed on different sides of the boundary is apparently different: Electrons are more energetic inside of the magnetosphere than they are outside of it.

2. The nocturnal stream region ("Luna-2", "Explorer-12", "Zond-2") is not connected with the diurnal region, judging from observational data close to the ecliptic plane. According to "Explorer-12" data, on the morning side there is a zone of trapped electron streams of  $E_e \sim 40$  kev in the space between the diurnal and nocturnal regions; this zone is apparently an extension of the outer radiation zone (Ref. 26). It is not absolutely clear whether there is such a space on the evening side. The trapped radiation region boundary is drawn symmetrically with respect to the OX axis in Figure 8,a.

The results derived from high-latitudinal measurements on "Mars-1" and "Elektron-2" (Figure 7,b) provide a basis for assuming that the nocturnal and diurnal regions are connected together by the high-latitudinal regions, and thus the outermost zone of charged particles represents a single formation of a very complex configuration. The separation of the soft electron streams recorded on "Elektron-2" into two regions - nocturnal and morning regions - is apparently related to seasonal changes in electron stream intensities (see section 6).

As of the present time, there has been no case in which a space vehicle, carrying sensors for electrons with energies on the order of hundreds of ev and several kev and launched in any direction, intersected the outer radiation zone boundary and did not find soft electrons beyond it. Since the outer boundary of the trapped radiation zone is closed, it must be assumed that the zone - where soft electron streams occur and which is located beyond this boundary - is also a single whole. However, this does not mean that the plasma streams have identical physical properties and a similar origin in the diurnal and nocturnal regions.

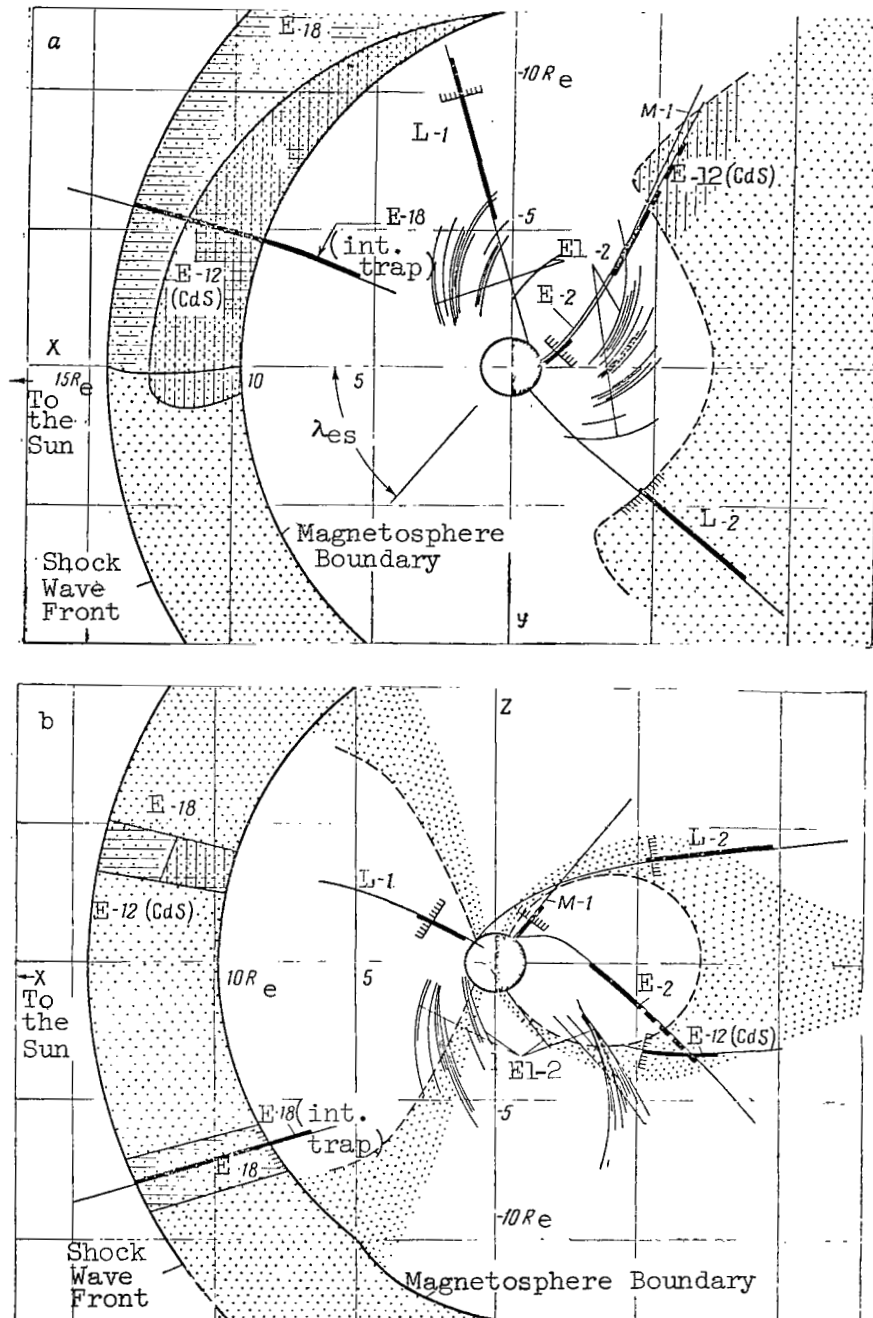


Figure 7

Distribution of Charged Particles Observed on Different Space Vehicles, in the Projection on the Ecliptic Plane (a) and on the Meridional Plane (b) in a Solar-Ecliptic Coordinate System /474

The trajectory sections on which streams were recorded are indicated by the solid lines and by the shading. Only those trajectory sections on which streams were recorded (based on data from the integral trap) are shown for "Elektron-2". The approximate trapped radiation boundaries (dashed line and the comb-like symbol) are plotted from (Ref. 20, 21, 23-26). The magnetosphere boundaries are plotted from (Ref. 17, 27, 28). The assumed position of the outermost zone of charged particles is shown by the dots.

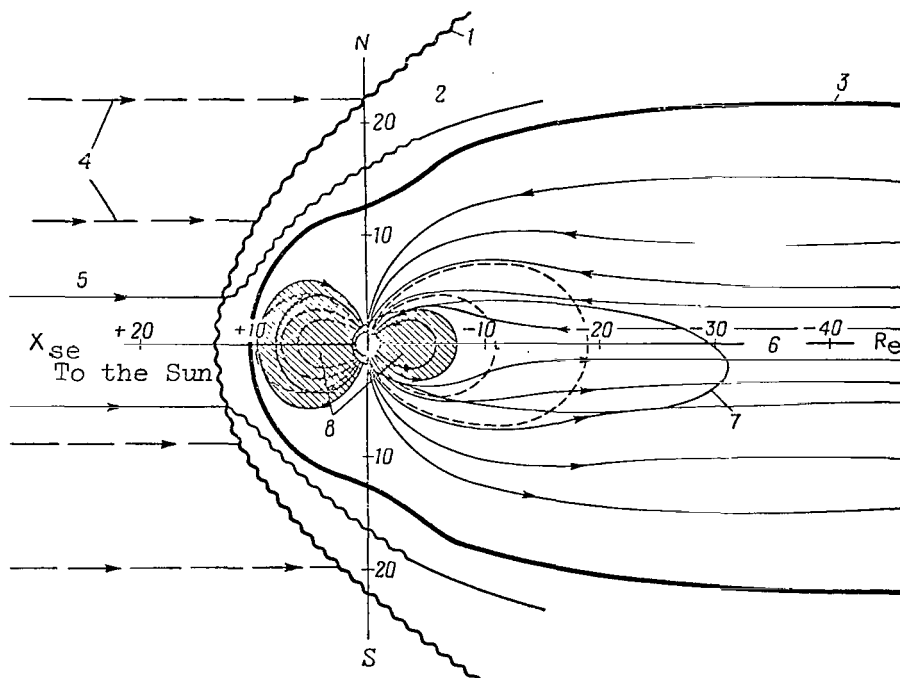


Figure 8

Structure of the Magnetic Field in the Tail Section of the Magnetosphere, According to Measurements on "Explorer-18" (Ref. 40)

1 - Shock wave front; 2 - turbulent region; 3 - magnetosphere boundary; 4 - solar wind; 5 - interplanetary magnetic field; 6 - neutral layer; 7 - 41st orbit of "Explorer-18"; 8 - magnetic field force lines based on data from theoretical computations (dashed line) and based on experimental data (solid lines). The shading designates the region occupied by the radiation zones of the Earth.

The region of soft electron streams is located closer to the Earth on the nocturnal side than it is on the diurnal side, which closely coincides with the position of the trapped radiation boundary (Ref. 24, 25, 29). The stream regions on the nocturnal side, which were discovered on "Luna-2" and "Explorer-12", are located symmetrically with respect to the Earth-Sun line. There is a certain divergence between the stream magnitudes given by data obtained on "Luna-2" and "Explorer-12":  $2 \cdot 10^8 \text{ cm}^{-2} \cdot \text{sec}^{-1}$  - on "Luna-2" (Ref. 1), and  $10^8 - 10^9 \text{ cm}^{-2} \cdot \text{sec}^{-1}$  - on "Explorer-12" (Ref. 10), in spite of the fact that the trap on "Luna-2" had a much larger scanning angle. No observations were performed in the intermediate midnight region.

/475

A zone of thermolyzed plasma beyond the magnetosphere boundary was not observed either at high latitudes, since up to the present no satellites or space rockets have intersected the magnetosphere boundary at high latitudes.

## 5. Connection Between Spatial Distribution of Soft Electron Streams and Magnetic Field Structure

The connection between the diurnal and nocturnal regions of the soft electron stream zone probably depends on the structure of the Earth's magnetic field at great distances from the Earth, particularly on the field structure above the nocturnal side of the Earth and in the magnetosphere tail. In particular, the connection between these regions may be entirely different, depending upon whether the magnetosphere is open or closed in the antisolar direction.

Different authors maintain different points of view regarding the form of the magnetosphere on the nocturnal side (Ref. 30-38). There are still very few experimental data with which to solve this important question. However, magnetic field measurements on "Explorer-14" (Ref. 39) and on "Explorer-18" (Ref. 40) in 1964 offer strong arguments in favor of the open magnetosphere model. In January, 1964, "Explorer-14" was located on the nocturnal side of the Earth (the angle between the Earth-satellite and Earth-Sun directions was approximately  $140-150^\circ$ ). As the satellite receded from the Earth, beginning at  $\sim 9-10 R_E$ , the field lost its dipole nature, and remained constant in terms of direction and magnitude ( $H \sim 30-50 \gamma$ ) up to the orbit apogee ( $\sim 15 R_E$ ). In this region, the field was directed toward the Earth and toward the Sun, i.e., the field behavior was like that required in an open model or at least in a magnetosphere which is greatly extended in the antisolar direction. It should be noted that the data presented in (Ref. 39) are still provisional. However, they closely coincide with earlier magnetic measurements on "Explorer-10" (Ref. 41), and with recent magnetic measurement data on "Explorer-18" (Ref. 40). The data given in (Ref. 40), which greatly exceed those given in (Ref. 39, 41), confirm the fact that the magnetic field completely loses its dipole nature beyond  $8-10 R_E$  on the nocturnal side; the force lines are extended, and are almost parallel (Figure 8).

The discovery of a magnetically neutral layer on the nocturnal side is a completely new factor (Ref. 40). Repeated changes in the magnetic field direction by  $180^\circ$  were observed approximately close to the geomagnetic equatorial plane, and it was close to zero in a narrow layer ( $\sim 600$  km). Measurements were performed up to  $\sim 31 R_E$ , and the magnetic field in the magnetosphere tail was  $10-15 \gamma$ .

Figure 9 shows the current system providing the field structure in the "tail" section of the magnetosphere, which is open in the antisolar direction. This was taken from the study (Ref. 32). In order that the field structure observed in the experiments of (Ref. 40) be valid, the existence of a fairly dense plasma in the magnetically neutral layer must be assumed. Based on the necessity of static equilibrium in the transverse cross section of the magnetosphere nocturnal section and taking into account the features of electron streams recorded on different space vehicles, the study (Ref. 38) reaches the conclusion that soft electron streams, observed close to the geomagnetic equator on "Luna-2" and

/477



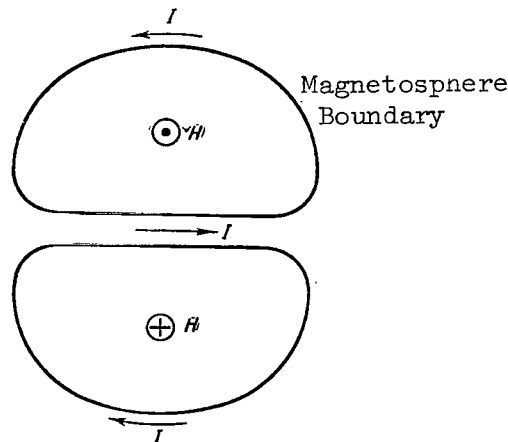


Figure 9

Current System in the Tail Section of the Magnetosphere  
According to (Ref. 32)

"Explorer-12", are located in a magnetically neutral layer. It must be kept in mind that the assumption is advanced in (Ref. 38) that all of the energy of the electrons observed goes into forming plasma pressure in a transverse direction to the magnetic field. The assumption of electron motion in a direction parallel to the magnetic field would increase the estimate of requisite electron fluxes given in (Ref. 38). It is possible that the phenomenon of counter glow is related to the occurrence of this layer (Ref. 38, 42, 43).

If the magnetosphere is open in the antisolar direction, then all of the force lines from the polar regions, passing around the trapped radiation zone on the nocturnal side, represent parallel bundles extending "to infinity" in the antisolar direction, between which the magnetically neutral layer is located. The force lines, moving along the surface of these bundles and washed by the solar wind flowing around the magnetosphere, form two circles on the surface of the Earth (around the northern and southern magnetic poles) along the high-latitudinal boundaries of the trapped radiation zones (naturally, the trapped radiation can only be located on closed force lines). This circle corresponds approximately to the zones of maximum aurorae polaris recurrence. The energetic electrons, which are formed at the magnetosphere boundary and at the magnetically neutral layer when the solar wind interacts with the geomagnetic field, can penetrate the depth of the magnetosphere along these force lines up to the aurorae polaris zones. From this point of view (in accordance with the considerations presented previously) (Ref. 12), the regions of soft electron streams discovered on the nocturnal and diurnal sides of the Earth comprise a single formation with a complex configuration. They are apparently closely related to the aurorae polaris zones.

If the magnetosphere is closed, it is possible for the thermolyzed solar plasma to penetrate directly into neutral point regions located on

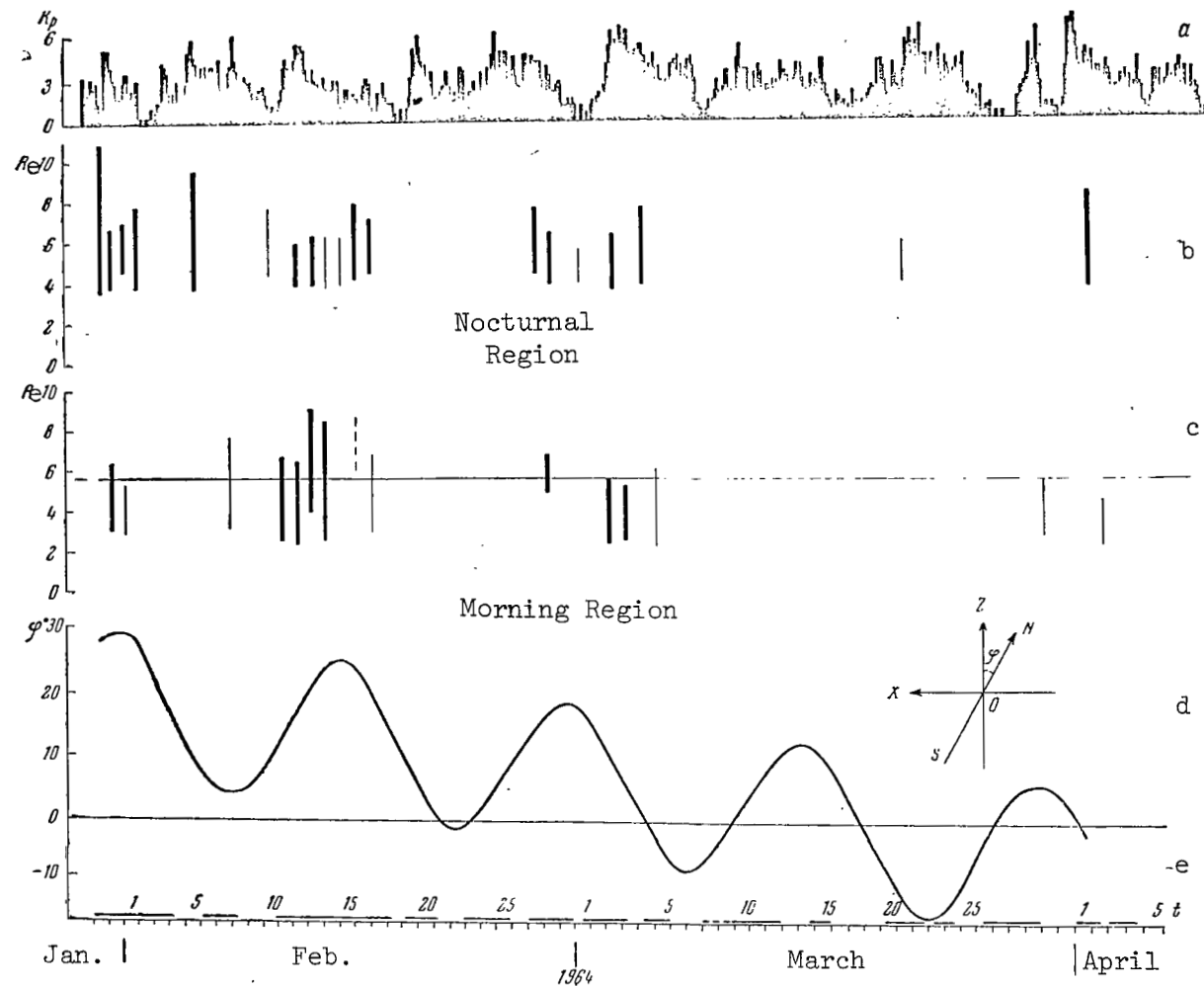


Figure 10

Comparison of Cases in Which Soft Electron Streams Were Recorded, Based on Data from "Explorer-2" (Integral Trap) With  $K_p$ -Indices and Orientation of the Geomagnetic Dipole Axis ( $\phi$ )

a -  $K_p$ -Indices; b - geocentric distances at which streams were recorded during the nocturnal orbital sections; c - the same as b, but on morning orbital sections; d - orientation of the dipole axis ( $\phi$ ); XZ - meridional plane of the solar ecliptic coordinate system; SN - projection of the geomagnetic dipole axis on this plane; e - time intervals corresponding to reception of information.

the magnetosphere boundary above the diurnal side of the Earth (see, for example, [Ref. 44-46]). Their position naturally depends on the nature of the interaction of solar plasma streams with the geomagnetic field, as well as on the interplanetary field structure.

The study (Ref. 46) examines the possibility of plasma penetration to the neutral points, with the penetrating charged particles subsequently drifting across the magnetic field force lines and passing through the nocturnal portion of the magnetosphere.

The opinions postulated in (Ref. 46) are corroborated by the measurement results, presented in section 6, from the satellite "Elektron-2", which intersected the magnetic field force lines close to the southern neutral point during the initial portion of its flight in the morning sections of the orbit.

Other explanations may be assumed for the origin of the soft electron stream zone on the nocturnal side of the Earth - for example, the magnetosphere model (Ref. 31, 33, 37) in which low-energy particles perform complex, convective motions in the outer magnetosphere region. However, the magnetic field structure on the nocturnal side, which is postulated in these studies, does not coincide with direct observational data.

Allowance must probably be made for soft electron streams resulting from certain local mechanisms by which charged particles are accelerated in the peripheral regions of the Earth's ionosphere; these are usually investigated in connection with the origin of the outer radiation zone (Ref. 47, 48).

## 6. Time Variations (Based on "Elektron-2" Data)

/478

Observations of soft electron streams by means of the three-electrode integral trap of charged particles on the satellite "Elektron-2" make it possible to reach a tentative conclusion regarding a relationship between the intensity of the soft electron streams observed, the orientation of the Earth's magnetic dipole axis with respect to the direction toward the Sun, and geomagnetic activity.

Figure 10 presents time changes of the  $K_p$ -indices during the initial stage of the satellite's flight (which, according to [Ref. 49] and [Ref. 11], coincide with the velocity and intensity of solar plasma streams). This figure also gives the geocentric distances at which soft electron streams were recorded on the nocturnal (b) and morning (c) sections of the "Elektron-2" orbit, as well as the angle  $\varphi$  close to the geomagnetic latitude of the sub-solar point of the magnetosphere<sup>1</sup>.

<sup>1</sup> The  $\varphi$  values are computed for the times when the satellite was located at geocentric distances corresponding to the horizontal line in Figure 10, c ( $R \sim 5.7 R_e$  - is approximately the mean section of the morning region in which soft electron streams were recorded during the initial portion of the satellite's flight).

When examining this figure, one must keep the fact in mind that we do not have continuous data on the magnitudes of the trap collector currents; the time intervals corresponding to the reception of information are shown (Figure 10, e) by the heavy sections of the line. We should also recall that, in addition to electron streams, positive ions can penetrate the trap, due to which fact the negative collector currents recorded permit a determination of only the lower boundaries of the electron stream magnitudes.

It can be seen from the data presented above that soft electron streams were recorded on the morning sections of the satellite's orbit primarily when the southern magnetic pole had a maximum inclination toward the Sun, i.e., when the conditions were most favorable for penetration of the thermolyzed solar plasma through the southern neutral point (if such a penetration takes place).

The same periodicity in the occurrence of the streams is observed on the nocturnal side, but with a change in time. The periodicity in the stream recordings was even more apparent on the nocturnal side than it was on the morning side, where the number of recordings and the stream intensities were smaller than on the nocturnal side. Days with increased geomagnetic perturbation represent isolated exceptions to this.

It should be emphasized that the data given above are only tentative, particularly because they are based on very few observational statistics. A concurrent analysis of all results derived from observing soft electron streams must be carried out in the future (including observations carried out simultaneously by means of an electrostatic analyzer [Ref. 19]).

We would like to point out that the data given above, showing a connection between soft electron stream recordings on the satellite "Elektron-2" and the orientation of the geomagnetic dipole axis, are of great importance - particularly in explaining the nature of solar plasma penetration into the Earth's magnetosphere and occupying the geomagnetic trap. In this connection, we would like to note that, for example, the study (Ref. 50) has already indicated a possible connection between certain daily and seasonal variations of geomagnetic activity and the change in the orientation of the geomagnetic dipole axis with respect to the direction toward the Sun.

#### 7. Brief Comments on the Origin of Soft Electrons Beyond the Radiation Zone Boundaries

/480

The diurnal region of the charged particle zone is separated from the unperturbed solar wind by the shock wave front formed when the supersonic stream of solar plasma (solar wind) encounters the geomagnetic field. Electrons in this zone have energies on the order of hundreds of ev and kev (up to 10-40 kev), while the solar wind electrons have energies on the order of 10 ev. The energy of the solar wind protons, which have energies on the order of hundreds of ev and kev, is apparently transferred to the electrons close to the magnetosphere boundary. This assumption was already

advanced in 1962 regarding the outermost zone (Ref. 2). The mechanism of electron acceleration when plasma clusters move in a heterogeneous magnetic field was postulated as one of the possible mechanisms for the acceleration of solar wind electrons (Ref. 3).

One of the other possible mechanisms for electron acceleration is related to the fact that solar wind protons, having an energy which is three orders of magnitude greater than that of electrons, can correspondingly penetrate deeper into the geomagnetic field. Spatial separation of the charges producing the electric field must take place, which, in its turn, "pulls" the electrons toward the protons with their corresponding acceleration (Ref. 4).

We must keep the fact in mind that "Explorer-18" recorded electrons with an energy of  $\sim 30$  keV in a narrow layer, apparently on the shock wave front (threshold value of the counters employed) (Ref. 18). Their intensity was determined as  $\sim 10^5 \text{ cm}^{-2} \cdot \text{sec}^{-1}$ . There is apparently an adequately effective mechanism for electron acceleration on the shock wave front. It is interesting to note that, as the satellite orbit recedes from the sub-solar point, the region in which energetic electrons are formed - which is concentrated at small angles of  $\lambda_{\text{es}}$  in a narrow layer close to the outer boundary of the transitional zone - expands considerably. It is relevant to assume that low-energy electrons are formed during the acceleration process.

Certain possible mechanisms for electron acceleration in the transitional zone are examined in (Ref. 5, 51).

The origin of streams on the nocturnal side is more complex. In particular, this is due to the fact that, as measurements have shown, the outer boundary of the trapped radiation zone is located in the depths of the magnetosphere in this case, and is not directly contiguous to solar plasma streams. As has already been indicated earlier, it is possible that the occurrence of these streams on the nocturnal side is related to the plasma penetration through the magnetic field neutral points. (Ref. 46). Particle acceleration in the magnetically neutral layer, due to instabilities in this layer which lies between flat, anti-parallel magnetic fields, can also be of importance for an open magnetosphere or for a greatly extended magnetosphere (Ref. 52-54).

In conclusion we would like to note that the data presented above point to the great geophysical importance of the outermost charged particle zone. The close connection between this zone and the structure of the geomagnetic field peripheral regions and its orientation with respect to the direction of solar plasma streams and the interplanetary magnetic field, as well as the connection between the zones of maximum aurorae polaris recurrence (at least spatially) and solar and geomagnetic activity, corroborate the assumption that a study of the outermost charged particle zone can provide a key with which to understand many important problems which have not been solved as yet. For example, these problems include the nature of the solar plasma penetration into the Earth's magnetosphere

and the occupation of the geomagnetic trap.

However, we must keep the fact in mind that fluxes of soft electrons and protons have still not been measured sufficiently, and their energy spectrum is far from clear. Therefore, one of the important problems /481 of future space research is a careful study of soft charged particle streams in the outermost zone, particularly at high latitudes where the diurnal and nocturnal sections of this zone are combined, close to the magnetic field neutral points on the diurnal side, and in the magnetically neutral layer of the zone's nocturnal section. These measurements must be carried out simultaneously with measurements on the same space vehicles of the magnitude and direction of the Earth's magnetic field, and streams of energetic particles. These must then be compared with data on solar and geomagnetic activity.

#### REFERENCES

1. Bezrukikh, V. V., Gringauz, K. I., Ozerov, V. D., Rybchinskiy, R. Ye. Doklady AN SSSR, 131, 1301, 1960.
2. Shklovskiy, I. S., Moroz, V. I., Kurt, V. G. Astronomicheskii Zhurnal, 37, 931, 1960.
3. Veksler, V. I. Doklady AN SSSR, 3, 84, 1958.
4. Bernstein, W., Fredriks, R. W., Scarf, F. L. J. Geophys. Res., 69, 1201, 1964.
5. Kaufman, R. J. Geophys. Res., 68, 371, 1963.
6. Gringauz, K. I., Kurt, V. G., Moroz, V. I., Shklovskiy, I. S. Astronomicheskii Zhurnal, 37, 716, 1960.
7. Gringauz, K. I., Rytov, S. N. Doklady AN SSSR, 135, 48, 1960.
8. Gringauz, K. I. Space Res., 2, 539, 1961.
9. Gringauz, K. I. J. Geophys. Res., 69, 1007, 1964.
10. Van Allen, J. A. J. Geophys. Res., 69, 1011, 1964.
11. Bezrukikh, V. V., Gringauz, K. I., Khokhlov, M. Z., Musatov, L. S. Rybchinskiy, R. Ye. Doklady AN SSSR, 163, No. 4, 1965.
12. Dessler, A. J., Juday, R. D. Planet. Space Sci., 13, 63, 1965.
13. Freeman, I. W., Van Allen, J. A., Cahill, L. I. J. Geophys. Res., 68, 2121, 1963.

32. Axford, W. I., Hines, C. O. *Canad. J. Phys.*, 39, 1433, 1961.
33. Hones, E. W. *J. Geophys. Res.*, 68, 1209, 1963.
34. Alfven, H. A. *Space Sci. Rev.*, 2, 862, 1963.
35. Dessler, A. J. *J. Geophys. Res.*, 69, 3913, 1964.
36. Axford, W. I., Petschek, H. E., Siscoe, G. L. *J. Geophys. Res.*, 70, 1231, 1965.
37. Shabanskiy, V. P. *Kosmicheskiye Issledovaniya*, 3, 221, 1965.
38. Ness, N. F. The Earth's Magnetic Tail, the Second Benedum Conf. on Earth Magnetism. Pittsburgh, Nov. 1964.
39. Cahill, L. I. *Trans. Amer. Geophys. Union*, 45, 231, 1964.
40. Ness, N. F., Searce, C. S., Seek, I. B. *J. Geophys. Res.*, 69, 3531, 1964.
41. Heppner, J. P., Ness, N. F., Searce, C. S., Skillman, T. L. *J. Geophys. Res.*, 68, 1, 1963.
42. Shklovsky, I. S. *Planet. Space Sci.*, 1, 63, 1959.
43. Brandt, I. C. *Astrophys. J.*, 134, 1961.
44. Bobrov, M. S. *Astronomicheskiy Zhurnal*, 37, 410, 1960.
45. Kawashima, N., Fukushima, N. *Planet. Space Sci.*, 12, 1187, 1964.
46. Pletnev, V. D., Skuridin, G. A., Shalimov, V. P., Shvachunov, I. N. *Kosmicheskiye Issledovaniya*, 3, 336, 1965.
47. Krasovskiy, V. I. Report to the IGY Assembly (Doklad na Assambleye MGG). Moscow, 1958.
48. Vernov, S. N. Present collection, p. 277.
49. Snyder, C. W., Neugebauer, H., Rao, U. R. *J. Geophys. Res.*, 68, 6361, 1963.
50. Mishin, V. M., Platonov, M. L. *Geomagnetizm i Aeronomiya*, 4, 717, 1964.
51. Gintzburg, M. A. *Phys. Rev. Letters*, 14, 625, 1965.
52. Sweet, P. A. *Proc. IAU Symposium Electrodynamical Phenomena in Cosmos No. 6*, Stockholm, 1956.

53. Furth, H. P., Killen, I., Rosenbluth, M. N. *Phys. Fluids*, 6, 459, 1963.

54. Furth, H. P. *Phys. Fluids*, 6, 48, 1963.

Note. After the conference had ended, the authors of this report learned of a new publication pertaining to observations of electron streams with energies of 10 kev beyond the trapped radiation zone boundary at low altitudes (up to 2700 km), performed on the American satellite "Injun-3" (I. A. Fritz, D. A. Gurnett *J. Geophys. Res.*, 70, 2485, June 1, 1965). As the authors have shown, these results closely coincide with observational results obtained at high altitudes on the Soviet space vehicles "Luna-2" (Ref. 1, 6) and "Mars-1" (Ref. 15), as well as with the results obtained on "Explorer-12" (Ref. 14). As was assumed, these soft electrons penetrate the aurorae polaris zone.



V. COSMIC RAYS

The study of cosmic rays occupies an exceptionally important place /484  
in modern physics and astronomy. One may recall that it was precisely during the study of cosmic rays that major discoveries were made and, for example, such particles were first detected as the positron,  $\mu$ - and  $\pi$ -mesons, and several hyperons. Thus, all of high-energy and elementary-particle physics is indissolubly connected with cosmic rays. The same may be said of radioastronomy and gamma-astronomy and, properly, of astrophysics as a whole, for it is now a matter of general knowledge that cosmic rays, along with the stars and interstellar gas, comprise the most important constituent elements of the universe.

The development of powerful accelerators has somewhat reduced the amount of cosmic ray research into the physics of elementary particles, in the energy range to 30 Bev, since large energies have not yet been achieved in accelerators. At the same time, there are particles in cosmic rays of energies reaching  $10^{10}$ - $10^{11}$  Bev. There is no doubt but that particles of similar and even significantly smaller energy,  $E \leq 10^3$  Bev, will be studied for an indefinite period only in cosmic rays. Moreover, the relative reduction of the "nuclear physics" role in the study of cosmic rays is substantially counterbalanced by the tremendous growth in volume and importance of research on cosmic ray astrophysics.

In the field of cosmic ray research, both in its nuclear physical and astrophysical aspects, the future categorically belongs to satellites and space rockets. Primary cosmic rays may penetrate only through an air layer of tens of grams or even a few grams without energy loss and "envelopment" by secondary products impeding observations. Therefore, equipment must, as a rule, be lifted to an altitude of more than tens of kilometers. This problem may be partially solved by balloons, the use of which undeniably has played, and still is playing, an essential role. But it is just as undeniable that balloons are now no longer able, and from now on will be even less able, to compete with satellites and space rockets with respect to prolonged and continuous recording of different phenomena, complexity and weight of lofted equipment, maximum reduction of the shielding layer over the apparatus, and so on. More detailed substantiation will be provided for this in the articles in the present section. These articles, moreover, present certain results of cosmic ray study which have already been obtained by satellites.

It is possible that in the future the scale of cosmic ray investigation by satellites and rockets will grow larger and larger. It is, therefore, an urgent necessity to make a thorough analysis of the potentialities, problems, and results of the corresponding investigations. The material called to our readers' attention will assist in achieving this goal.

PROBLEMS OF AND PROSPECTS FOR THE STUDY OF HIGH AND  
ULTRAHIGH-ENERGY COSMIC RAY PARTICLES  
(Summary)

N. L. Grigorov, I. D. Rapoport,  
I. A. Savenko, and G. A. Skuridin

High- and ultrahigh-energy cosmic ray particles are of great interest to two fields of science - the physics of high energy particles and astrophysics. /485

Primary cosmic rays are known to have a broad energy distribution, which can be described in the first approximation by the exponential law  $N(E)dE \sim E^{-\gamma}dE$ , where  $\gamma \approx 2.7$  when  $10^{10} \lesssim E \lesssim 10^{15}$  ev, and  $\gamma \approx 3$  when  $E \gtrsim 10^{15}$  ev. At the present time, this spectrum has been traced to energies  $E \approx 10^{19}$  ev, i.e., the composition of cosmic rays contains particles with energies many orders of magnitude higher than those obtainable in the most powerful accelerators.

Notwithstanding the fact that cosmic ray particles have long been utilized to study interaction processes at high and ultrahigh energies, it has been impossible in most cases up to the present to obtain sufficiently precise quantitative results by means of cosmic rays. The difficulties in deriving accurate experimental quantitative results have been associated until recently with the small streams of high-energy cosmic ray particles on mountain tops and at sea level (where most of the research has mainly been conducted). This has prevented measurements with the necessary statistical accuracy. There was, moreover, no method of measuring the energy of an individual cosmic ray particle (in the  $10^{11}$ -ev energy region and above), and, because of the power-law nature of the spectrum and fluctuations in the phenomena under study, the measurement results did not yield to a single interpretation.

It was for these reasons that up till now such theoretically important matters have remained practically unresolved, as the behavior of an effective cross section of proton interaction with protons, protons with complex nuclei, and nuclei with nuclei in the  $10^{11}$ - $10^{13}$ -ev energy region; the dependence of the mean multiplicity of secondary particles produced  $\bar{n}$  on energy  $E_0$  of the primary particle, on mass of the primary particle, and on mass of the target nucleus; the dependence of the degree of inelastic interaction on energy of the primary particle, its mass, and mass of the target nucleus; and the laws of fluctuation governing the various interaction characteristics.

Both theory and experiment indicate a very loose dependence of these interaction characteristics on primary particle energy  $E_0$ . Therefore, in order to choose between existing hypotheses on the basis of experimental data, experiments must be performed within an accuracy of several percents, and an energy range of 2-3 orders of magnitude must be covered.

In the area of astrophysical cosmic ray problems, there have been no solutions as yet to such basic questions as the mechanism of particle acceleration to huge energies, the processes responsible for cosmic ray generation, and processes involving the propagation of high- and ultrahigh-energy particles in the Galaxy. Hopes for the solution of these problems are primarily related to accurate measurement of the energy spectrum and chemical composition of the primary rays in the  $10^{12}$ - $10^{15}$  ev energy range and above. They are also related to a study of the energy spectrum and charge composition of the primary cosmic ray electron component in the energy region to  $10^{10}$ - $10^{11}$  ev, and to the study of high-energy  $\gamma$ -quanta (measurement of  $\gamma$ -quanta intensity, study of their energy distribution, study of the distribution of  $\gamma$ -quanta sources over the celestial sphere, and the search for local  $\gamma$ -quanta sources). /486

Most of the problems which have not yet been solved, both in the field of nuclear interactions of very high-energy particles and in the astrophysics of high- and ultrahigh-energy cosmic rays, require that the energy of each cosmic ray particle be measured before they can be solved.

The invention of the ionization calorimeter (Ref. 1) put into experimenters' hands an instrument which solves the problem of measuring the energy of an individual particle. This instrument, based on measurement of the complete energy release of the primary particle as it is being absorbed in a thick block of matter, enables us to solve most of the above problems (the methods of solving them are set forth in detail in [Ref. 2]).

Because fluxes of primary high-energy cosmic ray particles are three to four orders of magnitude greater than a flux of particles having the same energy on mountain tops, an ionization calorimeter on an AES can be used to study the diverse processes of high- and ultrahigh-energy particle interaction with nuclei with great statistical accuracy. In particular, an ionization calorimeter one square meter in area can measure the effective cross sections of inelastic interactions of different types of particles (protons,  $\alpha$ -particles, heavy nuclei) with nuclei of different atomic weights with a statistical accuracy of  $\sim 0.5$ -5% in the  $10^{11}$ - $10^{13}$ -ev energy range, can study with great precision the dependence of  $\bar{n}$  on  $E_0$ , and can investigate the energy characteristics of nucleon interaction with nucleons and complex nuclei in the energy range to  $10^{14}$  ev (Ref. 2).

Utilization of the ionization calorimeter in conjunction with various recording instruments (nuclear photoemulsions, scintillation chambers, Cherenkov gas counters) makes possible the detailed study of the elementary interaction processes of particles with energies of  $10^{12}$ - $10^{13}$  ev, the investigation of the cosmic ray electron component up to high energies, and an extensive search for local high-energy sources of  $\gamma$ -quanta in the universe (Ref. 2). A large ionization calorimeter ten square meters in area, when carried beyond the boundary of the atmosphere, can be used to

examine the composition and energy spectrum of primary cosmic rays directly in the region of enormous energies up to  $10^{16}$  ev.

#### REFERENCES

1. Grigorov, N. L., Murzin, V. S., and Rapoport, I. D. Zhurnal Eksperimental'noy i Teoreticheskoy Fiziki (ZhETF), 35, 506, 1958.
2. Grigorov, N. L., Rapoport, I. D., Savenko, I. A., and Skuridin, G. A. Kosmicheskiye Issledovaniya, 2, 724, 1964.

#### PROBLEMS OF AND PROSPECTS FOR PRIMARY COSMIC RAY RESEARCH

V. L. Ginzburg, L. V. Kurnosova, L. A. Razorenov,  
S. I. Syrovatskiy, M. I. Fradkin

The purpose of this report is to discuss problems involving research into primary cosmic rays, including  $\gamma$ -radiation. We can only present the appropriate material in a relatively brief form. (Ref. 1-4) present a more detailed discussion of all the problems touched. There is a correlation between the study of various components of cosmic rays, but for 487 purposes of convenience this report is divided into three sections. In Section I, we will deal with the proton-nuclear component; in Section II with the electron-positron component of cosmic rays, and, finally, in Section III with cosmic  $\gamma$ -rays and X-rays.

#### I. Nuclei and Protons

Since the proton-nuclear component of primary cosmic rays is basic in terms of intensity and transferable energy, it has been most fully investigated. There is, however, another entire group of questions which have not been clarified up until now; the solution of these problems is important, both with regard to the origin of cosmic rays and to the study of conditions in interstellar and circumsolar space. Let us examine these problems in somewhat greater detail.

##### I.1. Energy Spectrum of Protons and Nuclei in Energy Range Below 100 Mev/Nucleon

(Ref. 5-6) have pointed out the existence of a significant flux of low-energy protons where the flux increased as the energy decreased. Measurements were made on quiet days (i.e., of solar activity), and the conclusion was therefore drawn that the low-energy protons discovered are of a solar origin, accumulated and retained in the vicinity of the Sun. The measurements in (Ref. 7), however, which were made during the same period by the satellite "Explorer-7", gave no indications of this type of particle at great altitudes (Figure 1).

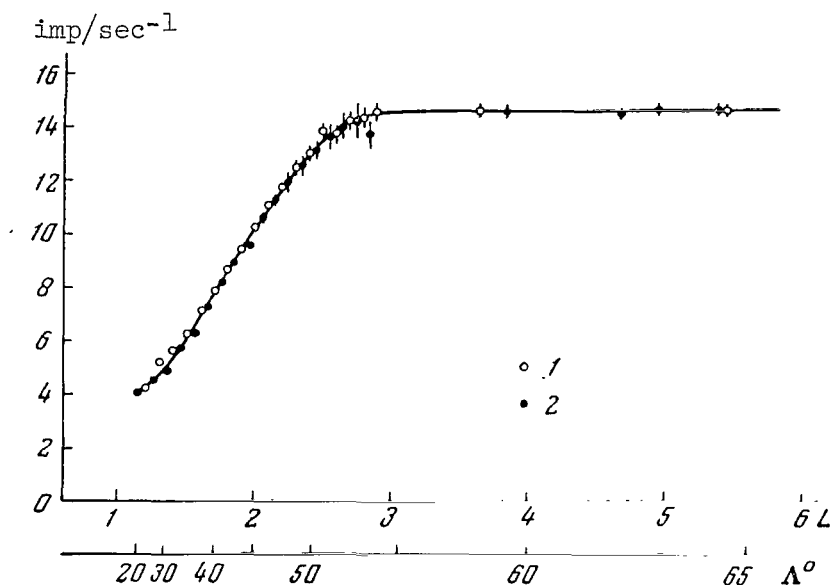


Figure 1

Latitudinal Effect of Cosmic Rays From Measurements by Satellite "Explorer-7" in November, 1959-December, 1960

Ordinate axis - rate of recording; abscissa axis - invariant  $L$  (in Earth radii) and corresponding latitude  $\Lambda = \arccos \frac{1}{\sqrt{L}}$ ; 1 and 2 - measurements over southern and northern hemispheres, respectively.

Previously published works (Ref. 8-12) report the absence of soft protons and, from an analysis of the method used in (Ref. 5 and 6) for 488 introducing corrections for the secondary particle contribution, conclude that these measurements in (Ref. 5 and 6) agree with the statement that there are no low-energy protons. It can be seen from this example that the role the atmosphere plays in the study of particles of comparatively low energies is very great: The conclusion varies essentially depending upon the manner in which the correction is introduced. In this respect, the most decisive results are those given in (Ref. 12), obtained by the far-removed satellite "Explorer-18" ("IMP-1").

Protons were measured in the 15-75 Mev energy range. Their flux was  $19 \text{ proton m}^{-2} \cdot \text{sec}^{-1} \cdot \text{sterad}^{-1}$  (approximately 1% of the entire cosmic ray flux), while the energy spectrum in this energy range had the form  $N(E) \sim E^{1.8}$ , i.e., the proton flux diminishes as the energy decreases. The spectral form of the more complex nuclei is still a completely open question. Here there are only isolated measurements of the  $\alpha$ -particle flux (Ref. 10, 11) and measurements having low statistical accuracy (of 20 nuclei in all) of nuclei in the L, M, and H groups (Ref. 13).

## I.2. Ratio Between Fluxes of Various Nuclear Groups in the Low-Energy Region

The above-mentioned paper (Ref. 13) found that the ratios of the fluxes of different nuclear groups (L, M, H) in the 55-550 Mev/nucleon range are close to the measurements made by other authors in the  $E < 500$  Mev/nucleon range. It is not extraneous to mention here that data in the literature indicate an energy dependence of these ratios (particularly of the L/M ratio). Although, as is evident from Table I, this relationship is not clearly pronounced (within the error limits, the L/S ratios may be regarded as identical; S represents all nuclei with  $Z \geq 6$ ), its nature is very important for determining the applicability of any particular theory on cosmic ray origin (see [Ref. 22] for greater details). From the experimental standpoint, this matter has not been clarified, and further experiments are required.

TABLE 1

$E_{\text{kin}}, \text{Gev} \cdot \text{nucleon}^{-1}$	L/S	Author and Source
$> 1$		
$\gtrsim 2$	$0.18 \pm 0.04$	O'Dell et al. (Ref. 14)
$> 1.5$	$0.20 \pm 0.04$	Foster et al. (Ref. 15)
$\gtrsim 0.5$		
$> 0.7$	$0.19 \pm 0.03$	Badhwar (Ref. 16)
$> 0.7$	$0.23 \pm 0.03$	Koshiba et al. (Ref. 17)
$> 0.5$	$0.31 \pm 0.09$	McDonald et al. (Ref. 18)
$> 0.4$	$0.27 \pm 0.07$	Fichtel (Ref. 19)
$< 1$	$0.32 \pm 0.06$	Foster et al. (Ref. 15)
$> 0.5$	$0.31 \pm 0.10$	Ginzburg et al. (Ref. 1)
$> 0.8$	$0.28 \pm 0.08$	Balasubrahmanyam et al. (Ref. 20)
$< 0.7$		
$< 0.7$	$0.38 \pm 0.05$	Koshiba et al. (Ref. 17)
$< 0.7$	$0.30 \pm 0.04$	Ayzu et al. (Ref. 21)
$0.4 \leq E_{\text{kin}} \leq 0.8$	$0.28 \pm 0.08$	Balasubrahmanyam et al. (Ref. 20)
$0.2 < E_{\text{kin}} < 0.7$	$0.41 \pm 0.08$	Badhwar (Ref. 16)

To eliminate the effect of the Earth's atmosphere and magnetic field, the measurements pertaining to subsections I.1 and I.2 should be performed by distant Earth satellites or interplanetary stations receding far from the limits of the Earth's magnetosphere. The measurement method may establish energy losses  $dE/dx$  and total energy  $E$ ; the feasibility of

/489

these measurements is determined by the fact that nuclear ranges in the 150-300 Mev/nucleon range are not too small ( $6 \text{ g}\cdot\text{cm}^{-2}$  for C with  $E \sim 150 \text{ Mev/nucleon}$ ) and at the same time within the measuring element limits ( $40 \text{ g}\cdot\text{cm}^{-2}$  for Li with  $E \sim 300 \text{ Mev/nucleon}$ ).

### I.3 Isotope Composition of Primary Cosmic Rays

In its significance for the theory of cosmic ray origin, the question of their isotopic composition is similar to the familiar "lithium, beryllium, and boron problem" which has been satisfactorily solved in the last few years. The important factor is that the distribution of one (stable) isotope in nature differs, by a factor of thousands and even of millions, from that of another isotope of the same element. We shall illustrate this with data on several elements:

Isotope . . . . .	$\text{H}^1$	$\text{H}^2$	$\text{He}^3$	$\text{He}^4$	$\text{C}^{12}$	$\text{C}^{13}$
Natural distribution, %	99.99	0.01	$1.3 \cdot 10^{-4}$	99.9999	98.9	1.1

Thus, the nuclei of  $\text{He}^2$ ,  $\text{He}$ , for example, are just as rare in nature as those of Li, Be, B. Therefore, in the primary acceleration of particles to the energies of cosmic rays, it is expected that only those isotopes will appear which have the greatest distribution. Since cosmic ray particles pass through an appreciable quantity of matter (from the number of Li, Be, and B nuclei discovered it follows that the path covered by the cosmic rays is 3 to 5  $\text{g}\cdot\text{cm}^{-2}$ ) before reaching the Earth, not only will  $\text{H}^1$ ,  $\text{He}^4$ ,  $\text{C}^{12}$  nuclei be formed as fragments from the fission of nuclei, but also the rare nuclei of  $\text{H}^2$ ,  $\text{He}^3$ ,  $\text{C}^{13}$ , etc. Thus, by measuring the isotopic composition we will obtain still another parameter for constructing a quantitative theory of cosmic ray origin.

There is very little information on the proton-to-deuteron flux ratio. (Ref. 23) states that the ratio of the deuteron to the proton flux (in the 92-175 Mev/nucleon energy range) is close to zero. This value is matched by the findings of (Ref. 24) -  $I_d/I_p \lesssim 3\%$  for the energy range of 130-202 Mev (protons) and 82-166 Mev/nucleons (deuterons). In the latter case, the deuteron flux was measured: It was  $4.2 \cdot 10^{-3} \text{ particles}\cdot\text{m}^{-2}\cdot\text{sec}^{-1}\cdot\text{sterad}^{-1}\cdot\text{Mev}^{-1}$ . The measurements in (Ref. 25) gave a value approximately four times greater for the 56-200 Mev/nucleon energy range: According to these findings  $I_d \approx (17.6 \pm 6.8) \cdot 10^{-3} \text{ particles}\cdot\text{m}^{-2}\cdot\text{sec}^{-1}\cdot\text{sterad}^{-1}\cdot\text{Mev}^{-1}$ , which corresponds to  $I_d/I_p \sim 12\%$ . The data of (Ref. 26), given at a conference in India, indicate an  $I_d/I_p$  ratio of less than 10% (with  $E_p \sim 20 \text{ Gev}$ ). (Ref. 12) cites a value of 8% as the upper limit for the deuteron-to-proton flux ratio in the 25-80 Mev/nucleon range.

The experimental data on measurement of the  $\text{He}^3/(\text{He}^3 + \text{He}^4)$  ratio are slightly more numerous (Table 2). However, as the Table shows, the data are not in very good agreement with each other, although there is reason (Ref. 34) to believe that the low values of the  $\text{He}^3/(\text{He}^3 + \text{He}^4)$  ratio derived in (Ref. 29, 31, and 32) are tied in with the cutoff of a sizeable fraction



of the  $\text{He}^3$  nuclei by the Earth's magnetic field at the observational point. In this case, all the remaining data will agree with the value of 0.2-0.3 for the  $\text{He}^3/(\text{He}^3 + \text{He}^4)$  ratio.

Despite a certain inconsistency, all the figures in Table 2 give a  $\text{He}^3/(\text{He}^3 + \text{He}^4)$  ratio value which is 10,000 times greater than that corresponding to the distribution in nature. However, in order that /490 these figures may be effectively utilized for numerical calculations, they must be known with greater certainty and accuracy.

TABLE 2

$\text{He}^3$ $\text{He}^3 + \text{He}^4$	E, Mev/nucleon	Author and Source
0.41±0.09	200-400	Appa Rao (Ref. 27)
0.38±0.09	200-400	Appa Rao (Ref. 28)
0.31±0.08	160-355	Appa Rao (Ref. 28)
0.08±0.08	200-300	Ayzu (Ref. 29)
0.20±0.05	160-370	Appa Rao (Ref. 30)
0.10±0.05	155-320	Ayzu (Ref. 31)
0.06±0.03	260-360	Hildebrand et al. (Ref. 32)
0.22±0.06	{ 180-280 $\text{He}^4$ 120-230 $\text{He}^3$	Foster, Mulvey (Ref. 33)

A few words about the possibility of detecting unstable isotopes. /491 Detection of such isotopes would indicate a solar origin of the corresponding particles in the solar system, or mechanisms by which particles are retained and accumulated in the solar system. In fact, the half-lives of almost all light radioactive isotopes are insignificantly short, in comparison with the time required for cosmic ray particles to travel from the center of the Galaxy to the solar system ( $T_{\text{cr}} \sim 3 \cdot 10^7$  years). For example, the half-life of  $\text{H}^3$  is  $\tau = 12.1$  years; that of  $\text{C}^{14}$  is 5000 years. Unstable isotopes will therefore decay practically "instantaneously". Only the  $\text{Be}^{10}$  isotope is an exception. Its half-life is  $\tau = 2.5 \cdot 10^6$  years. During time  $T_{\text{cr}}$ , a substantial portion of the slow  $\text{Be}^{10}$  nuclei decay according to the formula  $\text{Be}^{10} \rightarrow \text{B}^{10} + \beta^-$  (when  $T_{\text{cr}} = 10^7$  years, 1/16 of these nuclei formed will remain when  $T_{\text{cr}} = 2.5 \cdot 10^7$  years, this fraction decreases to 1/1000). The relativistic nuclei may not, however, decay in time  $T_{\text{cr}}$ , with the result that the relative content of Be nuclei (e.g., the Be/B ratio) will grow with the increase in energy. According to the calculations of (Ref. 35), this ratio varies from 0.33 to 0.62 with the transition from energies of several hundred Mev/nucleon to energies at which  $\text{Be}^{10}$  decay may be disregarded. Measurement of the relative abundance of Be nuclei in cosmic rays will make it possible to determine the lifetime of cosmic rays in the Galaxy independently.

TABLE 3

$E_{kin}$ , Mev/nucleon	$p v$ , Mc/nucleon	Parameter	Isotopes						
			H <sup>1</sup>	H <sup>2</sup>	H <sup>3</sup>	He <sup>3</sup>	He <sup>4</sup>	C <sup>12</sup>	C <sup>13</sup>
100	440	$r, g \cdot cm^{-2}$	10	20	30	7,5	10	3,3	3, <sup>c</sup>
		$I(z)/I_p(1)$	3,38	3,38	3,38	13,5	13,5	121	121
		$H\rho, 10^6 oe \cdot cm$	1,47	2,93	4,40	2,20	2,93	2,93	3,17
150	550	$r, g \cdot cm^{-2}$	20	40	60	15	20	6,7	7,1
		$I(z)/I_p(1)$	2,59	2,59	2,59	10,4	10,4	93	93
		$H\rho, 10^6 oe \cdot cm$	1,83	3,67	5,50	2,75	3,67	3,67	3,98
200	640	$r, g \cdot cm^{-2}$	33	66	99	24,7	33	11	11,7
		$I(z)/I_p(1)$	2,12	2,12	2,12	8,5	8,5	76	76
		$H\rho, 10^6 oe \cdot cm$	2,13	4,26	6,40	3,20	4,26	4,26	4,61
300	800	$r, g \cdot cm^{-2}$	65	130	195	48,7	65	22	23,3
		$I(z)/I_p(1)$	1,68	1,68	1,68	6,7	6,7	60	60
		$H\rho, 10^6 oe \cdot cm$	2,67	5,33	8,00	4,00	5,33	5,33	5,77
400	950	$r, g \cdot cm^{-2}$	100	200	300	75	100	33	35
		$I(z)/I_p(1)$	1,47	1,47	1,47	5,9	5,9	53	53
		$H\rho, 10^6 oe \cdot cm$	3,17	6,33	9,50	4,75	6,33	6,33	6,86
500	1030	$r, g \cdot cm^{-2}$	150	300	450	112	150	50	54
		$I(z)/I_p(1)$	1,35	1,35	1,35	5,4	5,4	49	49
		$H\rho, 10^6 oe \cdot cm$	3,60	7,20	10,80	5,40	7,20	7,20	7,80
700	1340	$r, g \cdot cm^{-2}$	250	500	750	187	250	83	90
		$I(z)/I_p(1)$	1,18	1,18	1,18	4,7	4,7	42	42
		$H\rho, 10^6 oe \cdot cm$	4,47	8,93	13,40	6,70	8,93	8,93	9,67
900	1560	$r, g \cdot cm^{-2}$	350	700	1050	262	350	117	127
		$I(z)/I_p(1)$	1,03	1,03	1,03	4,3	4,3	39	39
		$H\rho, 10^6 oe \cdot cm$	5,20	10,40	15,60	7,80	10,40	10,40	11,27

Three independent parameters (e.g.,  $pc$  in addition to  $dE/dx$  and  $E$ ) must be measured to determine isotopic composition. Up until now isotopic composition has been established only in emulsions. However, it seems possible to perform such measurements by employing another method. For example, the use of scintillation counters (determining  $dE/dx$ ) and the magnetic field (measuring  $pc$ ) plus the measurement of the range will make it possible to analyze isotopic composition. The feasibility of distinguishing isotopes is apparent from Table 3, which gives data on range  $r$ , of the relative ionization

$$I(z) / I_p \quad (1)$$

and the curvature  $\rho$  in the magnetic field  $H$  for a number of isotopes.

#### I.4. Antiprotons

During the interaction of cosmic ray protons and interstellar matter, antiprotons, among other particles, must and will be formed. If we do not touch upon the hypothesis of "antimatter" and its penetration into circumsolar space from other regions of the Galaxy, then nuclear interactions are the sole source of antiprotons. The fraction of antiprotons to be expected in the primary cosmic ray flux may be estimated. Such an estimate has been conducted in (Ref. 36), and the corrected value of the maximum fraction of antiprotons given in (Ref. 1) is 0.05%. Existing experimental data give values of no more than 0.1% for the fraction of antiparticles (antiprotons and "antinuclei") in (Ref. 21 and 37) and no more than 0.23% in (Ref. 38). These figures refer to antiparticles which might have been destroyed if arrested in an emulsion (not a single such case has been recorded).

It is of interest to search for fast antiprotons. Definite possibilities are afforded by the use of a magnetic analyzer (of course, with simultaneous measurement of other parameters). The development of such an analyzer for performing measurements on satellites is becoming feasible because of the development of superconductive wires. We may at present speak of the development of superconducting magnets with a magnetic field strength of 30-50 koe and dimensions of 1-2 m. Using a magnet with these characteristics, we can measure impulses on the order of  $10^{13}$  ev with up to 100% accuracy, and impulses on the order of  $10^{11}$  ev with up to 1% accuracy. Such an instrument would make it possible not only to distinguish between 492 particles by charge sign (protons and antiprotons, electrons and positrons), but also to obtain particle impulse spectra, to perform analysis of masses, and to settle other questions involving cosmic ray composition. It must, however, be emphasized that the detection of fast antiprotons in cosmic rays, even with a magnetic field, is a very complex task, for the expected number of these particles is negligibly small, and the whole effect may "drown" in the mass of phenomena caused by other particles (e.g., by electrons, the number of which is approximately 100 times greater than the expected number of antiprotons).

#### I.5. Superheavy Nuclei

Information on nuclei of  $Z > 30$  is very fragmentary and sparse. Photoemulsions have recorded isolated cases of nuclei of  $Z > 34$ , and even of  $Z \sim 41$ , but no flux evaluations based on such measurements have been successfully made. An experiment (Ref. 39) conducted aboard AES-3 in ten days recorded one case of a nucleus with a very high charge passing through the instrument; this gives the ratio

$$I_{Z>30-40} / I_{Z>15} \sim (1-3) \cdot 10^{-4}.$$

as a certain estimate of the flux.

More precise definition of this quantity is of undoubted interest, but this task is not a simple one, from the experimental point of view. Even if the ratio  $I_{Z>30}/I_{Z>15} \sim 10^{-4}$  (and not ten times less) holds, an enormous detector would be required to record only 5-10 nuclei in a day (the instrument should have a geometric factor of  $\Gamma \sim 3000 \text{ cm}^2 \cdot \text{sterad}$ , but those ordinarily used to solve these problems have  $\Gamma \sim 30-100$ ).

#### I.6. Time Changes in Flux of the Primary Nuclear Component

It is well-known that registration of variations in cosmic ray intensity is an effective method of studying conditions in interplanetary (and in some cases also in interstellar) space, and also processes leading to the acceleration of charged particles on the Sun and to emission of corpuscular streams. Simultaneous recording of a common cosmic ray component and of its individual components (various nuclei groups) undubitably affords greater possibilities for a more detailed analysis of these processes, and may furnish criteria for the validity of some particular hypothesis explaining these phenomena. Although variations of diverse nature may evidently be studied by a single instrument, it is convenient when presenting the material to take a separate look at particle generation on the Sun and modulation of galactic cosmic rays.

##### Particle Generation on the Sun

Data on the generation of cosmic rays on the Sun during very powerful solar flares have been available for a long time (Ref. 40). Regular flights to great altitudes in the stratosphere in the last decade have enabled us to detect flares with the power of low-energy protons (Ref. 41, 42). The last few years have recorded cases of nuclei generation with cosmic ray energies on the Sun. A number of experiments conducted in the USSR (see survey [Ref. 1] and report [Ref. 43]) have discovered heavy nuclei of a solar origin with an energy of more than 600 Mev/nucleon. In (Ref. 44) an American group reported on the registration of low-energy nuclei generated during solar flares. There is reason to assume that under various conditions diverse acceleration mechanisms operate on the Sun, and in some cases result in the generation and emission of basically heavy, high-energy 493 nuclei, and in others in the generation of cosmic rays whose chemical composition is similar to that of the Sun. In connection with the question of a heavy nuclei flux increase without simultaneous increase in proton flux, we would like to point out (Ref. 45). It compares the fluctuations in nuclear strength recorded in space (Ref. 46) with those recorded by neutron monitors on the Earth's surface. It is found that in the "impact zones" slight increases in the neutron-monitor counting rate are detected, which exceed the limits of statistical error and which are correlated with nuclei flux increases in space. At the same time, outside the "impact zone" (in the "background zone") no such effects are observed.

## Modulation Effects

While there are rather extensive experimental data on the modulation effects of the entire cosmic ray component, information on modulation variations of nuclear intensity is very scanty. There are data on long-period fluctuations in the nuclear component intensity (associated with the eleven-year cycle of solar activity). Many authors (Ref. 47, 48) have pointed out an inverse correlation between cosmic ray nuclear intensity and solar activity. Measurements conducted in the last few years by Soviet artificial satellites and space rockets have enabled this pattern to be traced during the last solar minimum period, and information was obtained on the intensity fluctuation not only of  $\alpha$ -particles, but also of heavier nuclei (for more details see [Ref. 49]). The intensity of  $\alpha$ -particles during Forbush decreases was irregularly recorded; the computed number of these observations is familiar (Ref. 50, 51). It is, moreover, clear that in the explanation of the Forbush-decrease mechanism, simultaneous measurements of the fluxes of different components (protons,  $\alpha$ -particles, heavier nuclei) play a prime role (it should be stressed that protons and nuclei with  $Z \geq 2$  with the same energy per nucleon possess different hardness).

The receipt of information on fluctuations in cosmic ray nuclear intensity requires constant measurements outside the atmosphere (and, in some cases, outside the magnetosphere) of the Earth. Due to the smallness of the nuclear component flux, the equipment must possess great illuminating power. We may illustrate this by pointing out that a device with  $\Gamma \approx 1500 \text{ cm}^2 \cdot \text{sterad}$  (three detectors each with  $\Gamma \sim 500 \text{ cm}^2 \cdot \text{sterad}$ ) will make it possible to measure fluxes of protons,  $\alpha$ -particles, and nuclei of  $Z \geq 6$  for 1 min. with a statistical accuracy of 0.7-2, 2-5, and 11-35%, respectively. The volume of a single detector (cube-shaped) will be approximately 11 liters. The use of several detectors is due to the necessity of being able to separate true variations in intensity from variations in the equipment. The best information on variations in the primary cosmic ray flux would be given by instruments installed on long-lived, distant artificial Earth satellites or on the natural satellite, the Moon.

### I.7. Gradient of Cosmic Ray Intensity in the Solar System

The problem of modulatory variations is closely related to the form of the energy spectrum of primary cosmic rays in the low-energy region. The almost complete absence of galactic cosmic rays having a hardness of less than approximately 1 Gev in the Earth's orbit (the so-called high-latitude truncation) and the change in the magnitude of this threshold hardness, <sup>/494</sup> during the transition from the period of maximum solar activity to the minimum period, provide a basis for assuming that this effect is likewise associated with the action exerted on the cosmic rays by the magnetoelectric conditions in interplanetary space which are determined by fluxes from the Sun. In accordance with this, a certain gradient should be observed in the cosmic ray intensity in interplanetary space (at least during years of a solar maximum).

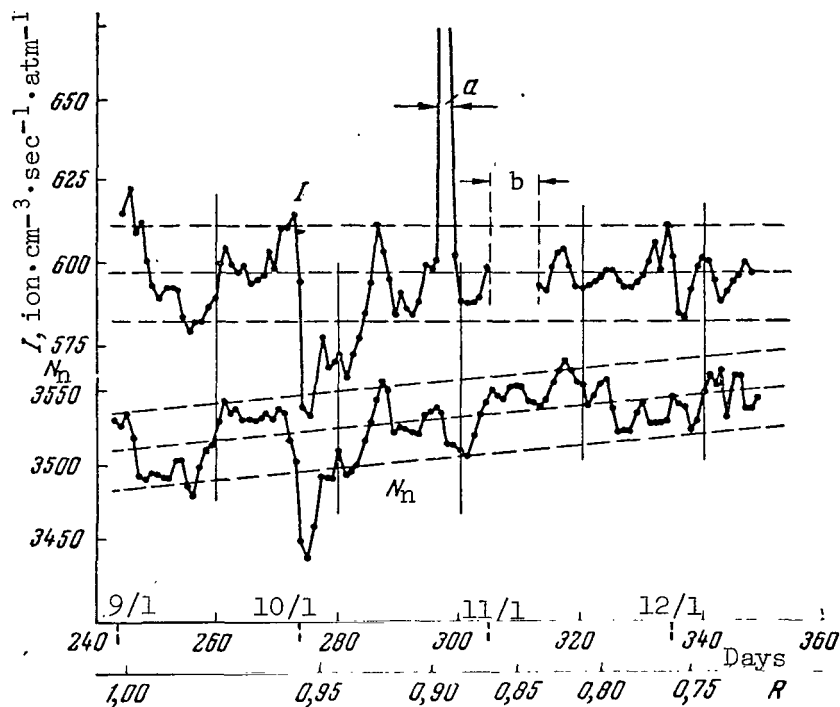


Figure 2

Ionization I Measured by Chamber Aboard "Mariner-2" and Readings of Neutron Monitor  $N_n$  at Deep River for the Same Period (September-December 1962)

Along abscissa axis (beneath) - distance R from Sun (in astronomical units), a - solar flare, b - period when device was shut off.

The experiments conducted by space rockets "Pioneer-5" (Ref. 52) and "Mariner-2" (Ref. 53, 54) flying toward Venus, and by the interplanetary station "Mars-1" (Ref. 55) flying toward Mars, did not give enough reliable information on the gradient of the total intensity. This problem is difficult to solve, because at such distances the gradient, if indeed there be one, is slight, and the fluctuations in intensity associated with solar activity are great.

As an example, we may cite the data received by "Mariner-2" (Figure 2). It is clear from the figure that ionization measured by the ionization chamber aboard the rocket did not vary during passage from the orbit of the Earth to that of Venus; intensity measured by the terrestrial neutron monitor at Deep River went up 3% in that period. Since, according to data of the authors in (Ref. 54), the readings of the ionization chamber beyond atmospheric limits rigorously coincide with those of the neutron monitor at Deep River, the authors conclude that the increase detected on Earth is

completely compensated by the decrease in intensity as the orbit of Venus 495 is approached. They thus derive a gradient value of 12% per astronomical unit.

It is desirable to measure the gradient not only towards the Sun and from the Sun, but also perpendicular to the ecliptic plane, since in the latter direction the magnetoelectric environment will apparently vary more drastically, since the Sun chiefly emits the streams in the plane of the ecliptic.

## I.8. Anisotropy

Let us pause briefly on the matter of cosmic ray anisotropy. We shall not discuss the anisotropy of ultrahigh-energy particles (greater, say, than  $10^{14}$  ev) which can be studied from extensive atmospheric showers. From theoretical estimates based on cosmic-ray particle diffusion in the Galaxy, we may expect an isotropy reaching  $(6-13) \cdot 10^{-2}\%$  for protons and  $(12-15) \cdot 10^{-2}\%$  for nuclei (see Ref. 2)\*. An indication that anisotropy of the entire component exists for protons of energy  $E > 50$  Gev was obtained in (Ref. 57) by analyzing data on variations in the meson component in 1954-1955. There are no other experimental findings which show anisotropy of a stream of particles with these energies and, in particular, there are no experiments to detect anisotropy in nuclei heavier than protons.

As was indicated in (Ref. 58) (for the influence of the Sun's magnetic field), we may in principle expect anisotropy to appear in particles of low energy close to the threshold energy of high-latitude truncation, if this truncation is connected with magnetic field action. This anisotropy will be "local" in nature (occurring in the solar system) and to some degree similar to the effect of east-west asymmetry on Earth.

## II. Electron-Positron Component of Primary Cosmic Rays

The importance of the primary electron problem has been repeatedly indicated in the literature, and we will here refer to the book (Ref. 2) which contains a detailed bibliographical list. We shall only briefly discuss information on the existing experimental studies and on problems which have not yet been solved.

### II.1 Flux and Energy Spectrum of Electron-Positron Component

After the publication of (Ref. 59) in 1950-1951, it was almost ten years before there were reports on attempts to measure the electron

---

\* (Ref. 2) did not take into account plasma effects which may lead to a decrease in degree of anisotropy (see [Ref. 56]).

intensity in primary cosmic rays. Table 4 gives the results of electron flux measurements which were published after 1961.

As is apparent, the experiments are very small in number and the statistical certainty of the results is small. As an example, it may be explained that (Ref. 60) classified only eleven showers as electron showers, while (Ref. 62) lists eighteen such events. All these experiments made by balloon indicate that secondary particles formed in the air layer above the device or arriving at the measurement spot along a magnetic force line from the opposite hemisphere (atmospheric albedo) may make a significant contribution. It is therefore advisable that experiments studying electrons be conducted by distant satellites (outside the Earth's magnetosphere). /496

TABLE 4

$E_e$ , Mev	Electron Flux		Method Employed	Source
	Absolute value $\text{cm}^{-2} \cdot \text{sec}^{-1} \cdot \text{sterad}^{-1}$	Ratio to Proton flux, %		
>500	32±10	(3±1)	Wilson Cloud Chamber	(Ref. 60)
25 < $E_e$ < 100	28-30	--	Scintillation-shower device	(Ref. 61)
100 < $E_e$ < 1300	35-110	1.7-5		
>1300	0-80			
>4500	6.6	1.1-1.5	Cylindrical scintillation chambers	(Ref. 62)

## II.2. Ratio Between Positron and Electron Fluxes

Apart from the question of the electron component energy spectrum, it is very important and interesting to determine the ratio between the number of electrons and positrons in a primary cosmic ray stream. It is known that positrons may appear in cosmic rays only as the end product of unstable particle decay; these particles are formed during the nuclear interaction of cosmic rays and interstellar matter. Therefore, the charge composition of the electron-positron component will enable us to judge the relative contribution of direct acceleration and "secondary" processes ( $\pi$   $\pm$ -meson decay, etc. [Ref. 64]) to the electron-positron component.

As of the present, only a single work (Ref. 63) has determined the ratio of the positron and electron fluxes in primary cosmic rays. The



measurements were made with scintillation chambers, between two rows of which a permanent magnet with a field strength of 6000 gauss was placed. Electrons (positrons) up to a hardness of 2 Gev could be measured. Table 5 gives findings on three energy ranges (to 1 Gev).

TABLE 5

$E_e$ , Mev	Number of Particles Recorded						$e^+/(e^++e^-)$
	$e^+$			$e^-$			
	1st Flight	2nd Flight	Total	1st Flight	2nd Flight	Total	
50-100	4	5	9	13	7	20	$0.31 \pm 0.12$
100-300	19	13	32	24	27	51	$0.38 \pm 0.07$
300-1000	15	8	23	52	65	117	$0.16 \pm 0.04$

The experiment in (Ref. 63) has comparatively good statistical accuracy, and shows that in the energy range to 1 Gev a large portion of the electrons are of "primary" origin: They apparently result from direct acceleration\*. This result agrees qualitatively with the calculations in (Ref. 64) of the quantity of "secondary" electrons formed in the Galaxy during the interaction of cosmic rays. It is clear, however, that this isolated experiment must not be regarded as a full and final solution of the problem. It is particularly necessary to conduct this type of research in a broader energy range. /497

It is apparent that the above-described magnetic analyzer of superconductive wire is the ideal instrument for solving the problem of the ratios between fluxes of electrons and protons.

Experiments of the type described in (Ref. 63) furnish information on positrons in the vicinity of the Earth (or of the Earth's orbit when measurements are made by a satellite). As for the regions farther removed from us, only the recording of  $\gamma$ -radiation can furnish us information on the positron content there. As is easily seen, positrons, if they exist in cosmic rays, will in time either leave the Galaxy or, slowing down, become destroyed, emitting two  $\gamma$ -quanta, each with an energy of 510 kev. By recording these monochromatic  $\gamma$ -quanta, we can derive information on the total number of positrons in different directions. The flux of such  $\gamma$ -quanta to be expected is weak (see Section III), and therefore a detector with a

\* From available information, the authors of (Ref. 63) now believe that the positrons and electrons which they recorded in the  $E_e < 500$  Mev energy range may be of atmospheric origin to a considerable extent.

very high energy resolution is needed to record them. An n-p sensor of germanium, which possesses a sufficiently fine  $\gamma$ -quanta detectivity, may be utilized as this detector.

### III. Cosmic Gamma- and X-Ray Radiation

New prospects in the study of cosmic rays in remote areas of the universe have unfolded due to the recently developed gamma- and X-ray astronomy. If we are speaking of  $\gamma$ -rays with energies of  $E \geq 50$  Mev, they can be generated only by cosmic rays. Therefore, measurement of the intensity, and spectral and spatial distribution of such  $\gamma$ -rays can provide invaluable information about cosmic rays, especially if we take the fact into consideration that the  $\gamma$ -radiation in question is propagated linearly and practically without absorption to a distance up to the photometric radius of the universe.

Softer electromagnetic radiation ( $E < 50$  Mev) may in great measure be caused by subcosmic particles (particles of energy  $E < 100$  Mev) or simply be gas heated to a high temperature. The latter belongs to X-ray radiation (we will conventionally designate photons of energy  $E < 100$  kev as X-ray). Since we will have at our disposal practically no independent information on subcosmic particles in interstellar and intergalactic space, when examining the low-energy photon region we will have in mind only the portion of gamma and X-ray radiation originating from cosmic rays. This group of questions is discussed in detail in (Ref. 3). We will cite below only the results derived from calculating the expected intensity for the most important processes of gamma- and X-ray generation. We shall also point out the areas of experimental and theoretical research into the problem, which, in our opinion, are the most promising.

The principal mechanisms generating continuous gamma-radiation are:

(1) The decay of  $\pi^0$ -mesons which are formed during the nuclear collisions of cosmic rays with matter (interstellar gas). The overwhelming portion of  $\gamma$ -rays formed in this process have an energy of  $E_\gamma > 50$  Mev, and their energy spectrum is close to that of cosmic rays.

(2) The braking radiation of the relativistic electrons and positrons /498 comprising the electron component of cosmic rays. The energy spectrum of this radiation reflects that of the electron component of cosmic rays. When a substantial quantity of subcosmic electrons is present, we may expect an appreciable intensity of  $\gamma$ -rays with energies of  $E_\gamma < 50$  Mev. The spatial distribution of braking radiation, as in the case of ion  $\gamma$ -rays, is stipulated by the distribution of interstellar gas. In the case of the Galaxy, it is sharply anisotropic (the maximum in the direction of the galactic center).

(3) Compton  $\gamma$ -rays which are formed by X-ray electrons during the scattering of thermal photons (stellar radiation). This radiation has a flatter energy spectrum than that of the electron component of cosmic rays, and extends far into the low-energy region. The spatial distribution

of the radiation reflects the density distribution of light photons in space. For the Galaxy, in particular, it is essentially more isotropic than the radiation stemming from the two previously examined processes.

Table 6 gives evaluations of the intensity of  $\gamma$ -rays produced by these mechanisms in the Galaxy (in different directions and averaged over direction) and in the Metagalaxy (for further details see [Ref. 3]).

TABLE 6  
INTENSITY OF  $\gamma$ -RADIATION  $I_\gamma(> E_\gamma)$  (In  $\text{cm}^{-2} \cdot \text{sec}^{-1} \cdot \text{sterad}^{-1}$ )

$E_\gamma$	Radiation Mechanism	Galaxy			Metagalaxy
		toward center	toward pole	average	
1 Gev	$\pi^0 \rightarrow \gamma + \gamma$	$2 \cdot 10^{-5}$	$2 \cdot 10^{-7}$	$5 \cdot 10^{-7}$	$3 \cdot 10^{-4} \xi_{\text{cr}}$
	Braking	$5 \cdot 10^{-6}$	$5 \cdot 10^{-8}$	$1.3 \cdot 10^{-7}$	$8 \cdot 10^{-6} \xi_e$
	Compton	$3 \cdot 10^{-6}$	$3 \cdot 10^{-6}$	$3 \cdot 10^{-6}$	$2 \cdot 10^{-3} \xi_e$
50 Mev	$\pi^0 \rightarrow \gamma + \gamma$	$3 \cdot 10^{-4}$	$3 \cdot 10^{-6}$	$8 \cdot 10^{-6}$	$5 \cdot 10^{-4} \xi_{\text{cr}}$
	Braking	$10^{-4}$	$10^{-6}$	$3 \cdot 10^{-6}$	$1.6 \cdot 10^{-4} \xi_e$
	Compton	$1.3 \cdot 10^{-5}$	$1.3 \cdot 10^{-5}$	$1.3 \cdot 10^{-5}$	$9 \cdot 10^{-3} \xi_e$

Note:  $\xi_{\text{cr}}$  and  $\xi_e$  are coefficients of proportionality between cosmic ray and electron component intensities in the Metagalaxy and Galaxy.

At present only the upper boundary of the average intensity with respect to direction

$$I_\gamma(> 50 \text{ Mev}) \leq 3,5 \cdot 10^4 \text{ photon} \cdot \text{cm}^{-2} \cdot \text{sec}^{-1} \cdot \text{sterad}^{-1} \quad (1)$$

has been experimentally ascertained (Ref. 65). This value is substantially higher than the expected intensity for the Galaxy. Therefore, both an increase in measuremental accuracy and a determination of the relationship between the radiation and the galactic coordinates are needed to isolate the galactic component of  $\gamma$ -radiation, and to determine its nature. The experimental upper boundary (1) now makes it possible to draw an important inference regarding cosmic rays in metagalactic space. The intensity of the electron component of metagalactic cosmic rays, as is clear from Table 6, cannot exceed 1/30 of the relativistic electron intensity in the Galaxy. This result agrees with the general conclusion that there is a relatively small concentration of cosmic rays in the Metagalaxy (for further details, see [Ref. 2]).

The next important area of gamma-astronomy is the detection of radiation from discrete sources, primarily such vigorously generated and quickly developing phenomena as supernovae, radiogalaxies, and quasars (super-giant stars). Existing attempts to detect high-energy gamma-radiation ( $E_\gamma \sim 10^{13}$  ev) from such sources have proved unsuccessful; this also agrees with the theoretical estimates of the intensity expected in this  $E_\gamma \sim 1$  Gev energy range, which also result in the very small values of  $F_\gamma(E_\gamma > 1 \text{ Gev}) \approx 10^{-8} - 10^{-12}$  photon  $\cdot$  cm $^{-2}$   $\cdot$  sec $^{-1}$ . However, exceptions and certain surprises are quite possible here. Thus, for example, a high concentration of relativistic electrons is to be expected for the supergiant 3C 273-B, if its optical radiation has a magnetically braking nature. If the size of this source is  $r = 2 \cdot 10^{16}$  cm, as might be assumed from the observed brightness fluctuations, then the thermal radiation density near its surface will reach a value of  $W_p \approx 5 \cdot 10^{13}$  ev  $\cdot$  cm $^{-3}$ . Under these conditions, the Compton scattering of the relativistic electrons ensures a measurable  $\gamma$ -ray flux on Earth (Ref. 3, 66):

$$F_\gamma(3 \cdot 10^6 < E_\gamma < 10^8 \text{ ev}) \approx 5 \cdot 10^{-6} \text{ photon} \cdot \text{cm}^{-2} \cdot \text{sec}^{-1} \quad (2)$$

The supergiant radius may in fact prove to be  $10 - 10^3$  times greater, and the  $\gamma$ -ray flux the same number of times smaller.

No less valuable information may, in principle, be derived from measurements of  $\gamma$ -ray intensity in the 0.1-10 Mev range, although this information may to a considerable degree pertain to subcosmic particles. Of the processes caused by cosmic rays, we would like to point out the  $\gamma$ -rays generated during positron annihilation, and the nuclear  $\gamma$ -rays formed during the collision of cosmic rays with interstellar gas nuclei. Nuclear  $\gamma$ -ray intensity is small, and the important fact is that it is distributed along numerous lines in the  $\gamma$ -spectra of nuclei which are propagated to the greatest extent in the interstellar medium. This may hinder the isolation of nuclear  $\gamma$ -rays against the background caused by subcosmic particles. In this respect, the experimental detection, already mentioned above (see subsection II.2), of the  $E_\gamma = 0.51$  Mev line caused by annihilation of the arrested positrons is most promising. The preponderant portion of positrons is annihilated after being retarded to thermal velocities; these velocities also determine the effective width of this line. The isolation of such a narrow line will permit a substantial reduction in the possible effect of continuous background from other processes. In a stationary model, which assumes that in the last  $10^9$  years the Galaxy has not essentially changed and that all processes therein took place at the same rate as at present, the expected intensity of the annihilation  $\gamma$ -quanta directed toward the galactic center is

$$I_\gamma(E_\gamma = 0.51 \text{ Mev}) = (1,2 - 300) \cdot 10^{-6} \text{ photon} \cdot \text{cm}^{-2} \cdot \text{sec}^{-1} \cdot \text{sterad}^{-1} \quad (3)$$

Here the lesser value matches the period of diffusion escape from the Galaxy  $T_e \approx 10^8$  years, while the greater value corresponds to a closed model of the Galaxy where it is postulated that all positrons formed are retained in the Galaxy until their annihilation ( $T_e > 10^9$  years).

Let us now briefly discuss the potentialities and prospects of X-ray astronomy. We would first of all like to note that the reception of X-ray radiation is the sole method of detecting neutron stars, which represent an important stage in the development of matter in the universe.

Magnetic braking X-ray radiation of very high-energy electrons can be directly linked to cosmic rays, more accurately, to their electron component. This type of radiation has apparently now been discovered /500 for the Crab Nebula. This indicates that very efficient mechanisms for accelerating electrons to energies of  $E \sim 10^{13}$  ev, and possibly more, exist in that nebula. If electrons of energy  $E \sim 10^{14}$  ev enter interstellar space and possess sufficient power, their magnetic braking radiation in the interstellar magnetic fields may provide a rather strong X-ray "background". Thus, the study of the X-ray radiation of discrete sources, as well as the over-all X-ray radiation of the galaxy, is already furnishing, and no doubt will furnish more, valuable information on superhigh-energy electrons in the universe.

The results enumerated and the conceivable paths by which gamma- and X-ray astronomy may develop present only the first rough sketch of the possibilities opening up before this branch of astrophysics. We can scarcely doubt that the picture will be substantially clarified in the future and will contain richer information:

#### REFERENCES

1. Ginzburg, V. L., Kurnosova, L. V., Razorenov, L. A., and Fradkin, M. I. Uspekhi Fizicheskikh Nauk (UFN), 82, 585, 1964; Space Science Review, 2, 778, 1963.
2. Ginzburg, V. L., and Syrovatskiy, S.I. The Origin of Cosmic Rays (Proiskhozhdeniye kosmicheskikh luchey). Izdatel'stvo AN SSSR, 1963.
3. Ginzburg, V. L., and Syrovatskiy, S.I. UFN, 84, 201, 1964.
4. Kurnosova, L. V., Razorenov, L. A., and Fradkin, M. I. Report to the Cosmic Rays Conference (Doklad na Soveshchaniy po kosmicheskim lucham). Apatity, 1964.
5. Vogt, R. Phys. Rev., 125, 366, 1962.
6. Meyer, P., Vogt, R. Phys. Rev., 129, 2275, 1963.
7. Lin, W. C., Venkatesan, D., Van Allen, J. A. J. Geophys. Res., 68, 4885, 1963.
8. Brunstein, K. A. Phys. Rev., 133, B1520, 1964.

9. Fichtel, C. E., Guss, D. E., Kniffen, D. A., Neelakantan, A. J.  
Geophys. Res., 69, 3293, 1964.
- 9a. Fichtel, C. E., Guss, D. E., Stevenson, D. G. R., Waddington, C. J.  
Phys. Rev., 133, B818, 1964.
10. Ormes, J., Webber, W. R. Phys. Rev. Letters, 13, 106, 1964.
11. Freier, P. S., Waddington, C. J. Phys. Rev., 13, 108, 1964.
12. McDonald, F. B., Ludwig, G. H. Phys. Rev. Letters, 13, 783, 1964.
13. Yagoda, H., Fukui, K. et al. Nuovo Cimento, 34, 854, 1964.
14. O'Dell, F. W., Shapiro, M. M., Stiller, B. J. Phys. Soc. Japan, 17,  
Suppl. A-111, 23, 1962.
15. Foster, F., Debenedetti, A. Nuovo Cimento, 28, 1190, 1963.
16. Badhwar, G. D. J. Geophys. Res., 70, No. 5, 1005, 1965.
17. Koshiba, M., Lohrmann, E., Aizu, H., Tamai, E. Phys. Rev., 131, 2692,  
1963.
18. McDonald, F. B., Webber, W. R. J. Geophys. Res., 67, 2119, 1962.
19. Fichtel, C. E. Nuovo Cimento, 19, 1100, 1961.
20. Balasubrahmanyam, V. K., McDonald, F. B. J. Geophys. Res., 69,  
3289, 1964.
21. Ayzu, Kh. et al. Transactions of the International Conference on  
Cosmic Rays (Trudy mezhdunarodnoy konferentsii po kosmicheskim  
lucham). Izdatel'stvo AN SSSR, 3, p. 110, 1960.
22. Ginzburg, V. L., and Syrovatskiy, S. I. Report to Conference on  
Cosmic Rays (Doklad na Soveshchaniy po kosmicheskim lucham).  
Apatity, 1964.
23. Appa Rao, M.V.K., Lavakare, P.J. Nuovo Cimento, 26, 740, 1962.
24. Badhwar, G. D. J. Geophys. Res., 69, 4435, 1964.
25. Hasegawa, H., Nakagawa, S., Tamai, E. Proc. Int. Conf. on Cosmic  
Rays. (India), 3, 1964.
26. Ganguli, S. N., Kameshwar Rao, N., Swami, M. S. Proc. Int. Conf. on  
Cosmic Rays (India), 3, 1964.

27. Appa Rao, M. V. K. Phys. Rev., 123, 295, 1961.
28. Appa Rao, M. V. K. J. Geophys. Res., 67, 1289, 1962.
29. Aizu, H. J. Phys. Soc. Japan, 17, Suppl. A-111, 52, 70, 1962.
30. Appa Rao, M. V. K., Dahanayake, R., Kaplon, M. F., Lavakare, P. J.  
Proc. Int. Conf. on Cosmic Rays (India), 3, 1964.
31. Aizu, H. Proc. Int. Conf. on Cosmic Rays (India), 3, 1964.
32. Hildebrand, B. et al. Proc. Int. Conf. on Cosmic Rays (India),  
3, 1964; Shapiro, M. M., Hildebrand, B., O'Dell, W. F., Silberberg,  
R., Stiller, B. Space Res., 3, 1097, 1963.
33. Foster, F., Mulvey, J. H. Nuovo Cimento, 27, 93, 1963.
34. Webber, W. R. Handbuch der Physik. Preprint, 46/2, 1965. /501
35. Badhwar, G. D., Daniel, R. R., Vijayalakshmi, B. Progr. Theor. Phys.  
28, 607, 1962.
36. Fradkin, M. I. Zhurnal Eksperimentl'noy i Teoreticheskoy Fiziki  
(ZhETF), 29, 147, 1955.
37. Haskin, D. M. et al. Proc. Moscow C. R. Conf., 3, 123, 1960.
38. Grigorov, N. L., et al. In "Iskusstvennyye Sputniki Zemli".  
Izdatel'stvo AN SSSR, 10, p. 96, 1961.
39. Kurnosova, L. V., Rozorenov, L. A., and Fradkin, M. I. In  
"Iskusstvennyye Sputniki Zemli". Izdatel'stvo AN SSSR, 2, p. 70,  
1960.
40. Dorman, L. I. Cosmic Ray Variations and Space Research (Variatsii  
kosmicheskikh luchey i issledovaniye kosmosa). Izdatel'stvo  
AN SSSR, 1963.
41. Charakhch'yan, A. N., Tulinov, V. F., and Charakhch'yan, T. N.  
ZhETF, 39, 249, 1960.
42. Winckler, J. R. J. Geophys. Res., 65, 1331, 1960.
43. Kurnosova, L. V., Razorenov, L. A., Logachev, V. K., and Fradkin,  
M. I. Present collection, p. 501.
44. Fichtel, C. E., Guss, D. E. J. Phys. Soc. Japan, 17, Suppl. A-11,  
321, 1962.

45. Vladimirskiy, B. M. Report to Conference on Cosmic Rays (Doklad na Soveshchanii po kosmicheskim lucham). Apatity, 1964.
46. Kurnosova, L. V., Razorenov, L. A., and Fradkin, M. I. In "Iskusstvennyye Sputniki Zemli". Izdatel'stvo AN SSSR, No. 6, p. 132, 1961.
47. Duke, P. J. Transactions of the International Conference on Cosmic Rays (Trudy Mezhdunarodnoy konferentsii po kosmicheskim lucham). Izdatel'stvo AN SSSR, 3, p. 101, 1960.
48. Stevenson, G. R., Waddington, C. J. Phil. Mag., 6, 517, 1961.
49. Blokh, Ya. L., Dorman, L. I., Kurnosova, L. V., Logachev, V. I., Platonov, G. F., Razorenov, L. A., Sinitsina, V. G., Suslov, A. A., and Fradkin, M. I. Present collection, p. 514
50. Meyer, P. J. Geophys. Res., 65, 3881, 1960.
51. Freier, P. S., Waddington, C. J. Proc. Int. Conf. on Cosmic Rays (India), 2, 246, 1964.
52. Fan, C. Y., Meyer, P., Simpson, J. A. Phys. Rev. Letters, 5, 272, 1960.
53. Van Allen, J. A., Frank, L. A. Science, 138, 1097, 1962.
54. Neher, H. V., Anderson, H. R. J. Geophys. Res., 69, 1911, 1964.
55. Vakulov, P. V., et al. Space Res., 4, 1964.
56. Ginzburg, V. L., and Syrovatskiy, S. I. Astronomicheskiy Zhurnal (in press).
57. Dorman, L. I., and Inozemtseva, O. I. In "Kosmicheskiye Luchi". Izdatel'stvo AN SSSR, No. 4, p. 209, 1961.
58. Janossy, L. Z. Phys., 104, 430, 1938.
59. Critchfield, C. L., Ney, E. P., Oleksa, S. Phys. Rev., 85, 461, 1952.
60. Earl, J. A. Phys. Rev. Letters, 6, 125, 1961.
61. Meyer, P., Vogt, R. Phys. Rev. Letters, 6, 193, 1961.
62. Agrinier, D., Koechlin, Y., Parlier, B., Boella, G., Degli Antoni, G., Dilworth, C., Scarsi, L., Sirone, G. Phys. Rev. Letters, 13, 377, 1964.
63. De Shong, J. A., Hildebrand, R. H., Meyer, P. Phys. Rev. Letters, 12, 3, 1964.



64. Ginzburg, V. L., and Syrovatskiy, S.I. Astronomicheskiy Zhurnal, 41, 430, 1964.
65. Kraushaar, W. L., Clark. G. W. Phys. Rev. Letters, 8, 106, 1962.
66. Ginzburg, V. L., Ozernoy. L. M., and Syrovatskiy, S.I. Doklady AN SSSR, 154, 557, 1964.

# EXPERIMENTAL STUDIES OF THE COMPOSITION OF PRIMARY COSMIC RAYS

(Summary)

L. V. Kurnosova, L. A. Razorenov,  
V. I. Logachev, M. I. Fradkin

This report presents the main results derived from investigations using satellites and rockets between 1958 and 1963 when studying the nuclear component of cosmic rays. The values for streams of different nuclei groups are given, obtained from measurements by integral and differential Cherenkov counters. The upper estimate for the ratio of nuclei streams with  $Z \geq 30-40$  to  $Z \geq 15$  is 0.01-0.03%. The ratio of 502 a stream of light nuclei of the L group to a nuclei stream of the group  $S=M+H$  is given. The ratio is  $31.0 \pm 9.6\%$ . The result derived from studying the latitudinal intensity dependence of nuclei streams of different groups indicates that the energy spectra of different nuclei groups coincide in the energy region where the particles are influenced by geomagnetic phenomena.

The report discusses the short-lived increases in nuclei streams related to chromosphere solar flares, which were first discovered during the flight of the second space rocket. The existence of short-lived increases in the nuclei streams of cosmic rays indicates that processes take place on the Sun in which the nuclei are accelerated up to kinetic energies exceeding  $0.5 \cdot 10^9$  ev/nucleon. Two mechanisms are apparently in operation on the Sun. One of them, which is the most extensive, leads primarily to acceleration of protons - or, in any event, does not lead primarily to acceleration of heavy nuclei. The second mechanism leads primarily to the acceleration of heavy nuclei (the case on 11/12/59 at 11 hours 27 minutes UT).

## STUDIES OF PRIMARY COSMIC RADIATION ON THE SATELLITES "ELEKTRON-2" AND "ELEKTRON-4"

S. N. Vernov, P. V. Vakulov, V. I. Zatsepin,  
Yu. I. Logachev, V. P. Okhlopov, A. Ye. Chudakov

This report will examine experimental data on primary cosmic radiation, obtained on the satellites "Elektron-2" and "Elektron-4" from primarily one gas discharge counter screened by  $2.3 \text{ g} \cdot \text{cm}^{-2}$  Al. The operational length of the counter was approximately 5 cm; the diameter was 1 cm. The surface of the counter on the satellite "Elektron-4" exceeded the surface of the counter on "Elektron-2" by a factor of 1.06. The threshold

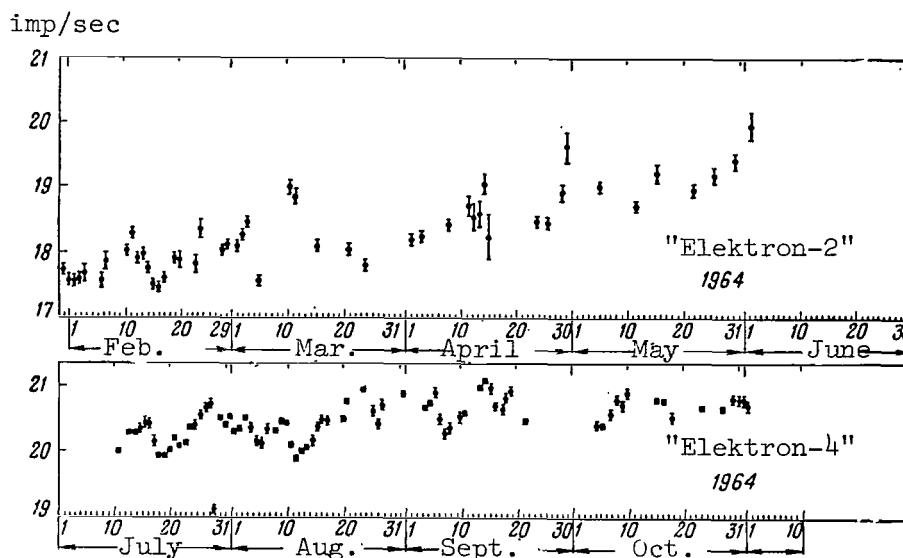


Figure 1

Gas Discharge Counter Recording Rates Behind a Shielding of  $2.3 \text{ g} \cdot \text{cm}^{-2}$  Al Based on Data From the Satellites "Elektron-2" and "Elektron-4"

The effective surface of the counter on "Elektron-4" exceeds by a factor of 1.06 the counter surface of the "Elektron-2" satellite.

energy for recording protons by this counter was 45 Mev.

The "Elektron" satellites also carried counters which were screened by  $4 \text{ g} \cdot \text{cm}^{-2}$  Al and  $17 \text{ g} \cdot \text{cm}^{-2}$  Pb (threshold energies for protons of 70 and 110 Mev, respectively).

The "Elektron-2" and "Elektron-4" satellites were launched on January 30 and July 11, 1964, respectively. These satellites had an altitude at apogee of about 68,000 km. For the greater portion of the time, they were located outside of the radiation zones of the Earth and recorded cosmic radiation.

The mean recording rate of the counter employed was about  $20 \text{ imp} \cdot \text{sec}^{-1}$ , which provided a statistical accuracy of up to 0.1% during the 20 hours the satellites remained beyond the radiation zones of the Earth on each revolution.

Figure 1 gives the recording rates recorded by this counter between January 30 and November 1, 1964. Data between January 30 and June 1 were obtained by a counter carried on the satellite "Elektron-2". Data between July 11 and November 1 were obtained by a counter carried on the satellite "Elektron-4".

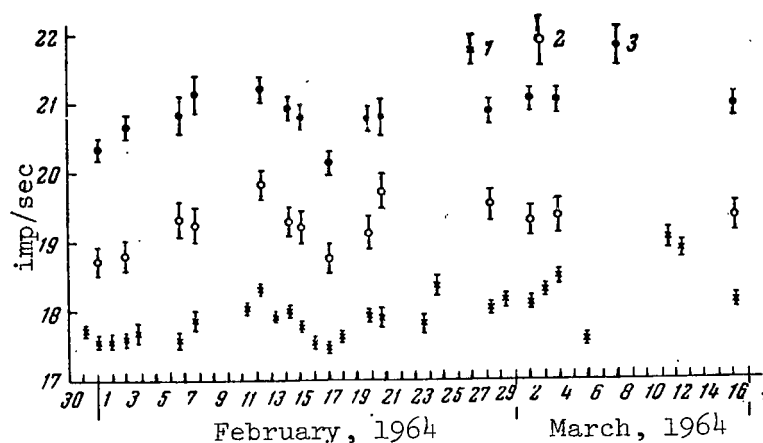


Figure 2

Gas Discharge Recording Rates Behind a Shielding of  
 $2.3 \text{ g} \cdot \text{cm}^{-2}$  Al (1),  $4 \text{ g} \cdot \text{cm}^{-2}$  Al (2),  $17 \text{ g} \cdot \text{cm}^{-2}$  Pb (3)  
 Based on Data From "Elektron-2"

Recording Rates obtained during an averaging period  
 of 20 hours.

During the flight of the "Elektron" satellites, the supply voltage remained stable in an interval which could not lead to a change in the counter recording rates; neither could the temperature fluctuations lead to observed changes in the recording rate. The correctness of the observed variations was confirmed by other gas discharge counters carried on the "Elektron" satellites. The coefficients of the correlation between the indices of all the counters were about 0.8-0.9 (Figure 2).

In addition to demonstrating the validity of the observed changes, 503 the good correlation between the readings of the three different counters behind different screenings also gave the lower energy limit of the particles responsible for the recorded variations. The particle intensity under the absorber did not decrease with an increase in the absorber thickness, but - on the contrary - even increased somewhat. This means that the primary stream did not include a significant amount of particles with energies between 50-110 Mev, and that in fact the primary stream was cut off at energies greater than 110 Mev. This is indicated by the intensity increase with an increase in the absorber thickness. This increase is 504 undoubtedly due to particle multiplication in the filter, and indicates a rather high mean particle energy in the primary stream.

It can be seen from Figure 1 that there are two types of cosmic ray intensity variations: Slow variations related to the 11-year cycle of solar activity, and rapid variations with a characteristic time on the order of two weeks.

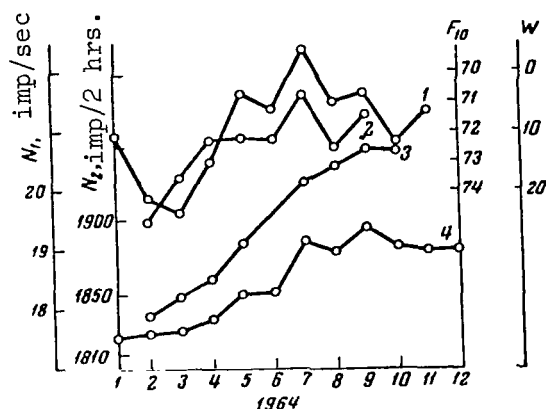


Figure 3

Comparison of Mean Monthly Values of Cosmic Ray Intensities  $N_1$ , Based on Data From the Satellites "Elektron-2" and "Elektron-4" (Gas Discharge counter with Screening of  $2.3 \text{ g} \cdot \text{cm}^{-2}$  Al, Curve 3) With Readings  $N_2$ , of a Neutron Monitor (City of Apatity, Curve 4), the Number of Solar Spots  $W$  (Curve 2), and a Stream of Solar Radio Emission  $F_{10}$  on a  $10.7 \text{ cm}$  Wave (Curve 1).

11-year variations of cosmic ray intensity. During the first half of 1964, the intensity of a primary stream of cosmic rays continued to increase. During the second half of 1964, the intensity increase slowed down, and in October there was a tendency for it to decrease. The mean rate at which the intensity increased between February-May was 2% per month. During July and August, the rate of increase was 1% per month, while in September and October the intensity remained constant. This intensity increase in a primary stream of cosmic rays closely coincides with the intensity increase of the neutron component which extended through 1964. For example, the correlation coefficient with data from the Fort Churchill monitor was 0.7-0.85 during different periods of 1964. The correlation coefficient with data from the Deep River neutron monitor was 0.61 in the first half of the year, and 0.70 in the second half of the year (Ref. 1). Thus, the cosmic ray intensity changes recorded on the satellites closely coincide with the data obtained on the Earth from neutron monitors.

The slow intensity increase throughout 1964 is undoubtedly related to the 11-year cycle of solar activity. As was already indicated, the rate at which the primary stream intensity increased was 2% per month in the first half of 1964, and 0.4% per month according to data from the Deep River neutron monitor. These figures do not contradict the spectrum of the 11-year variation published in (Ref. 2).

A clarification of the phase shift between solar activity and cosmic ray intensity is of great importance. Certain information in this regard may be obtained from Figure 3, which presents the change in the mean monthly values of cosmic ray intensities, the relative number of solar

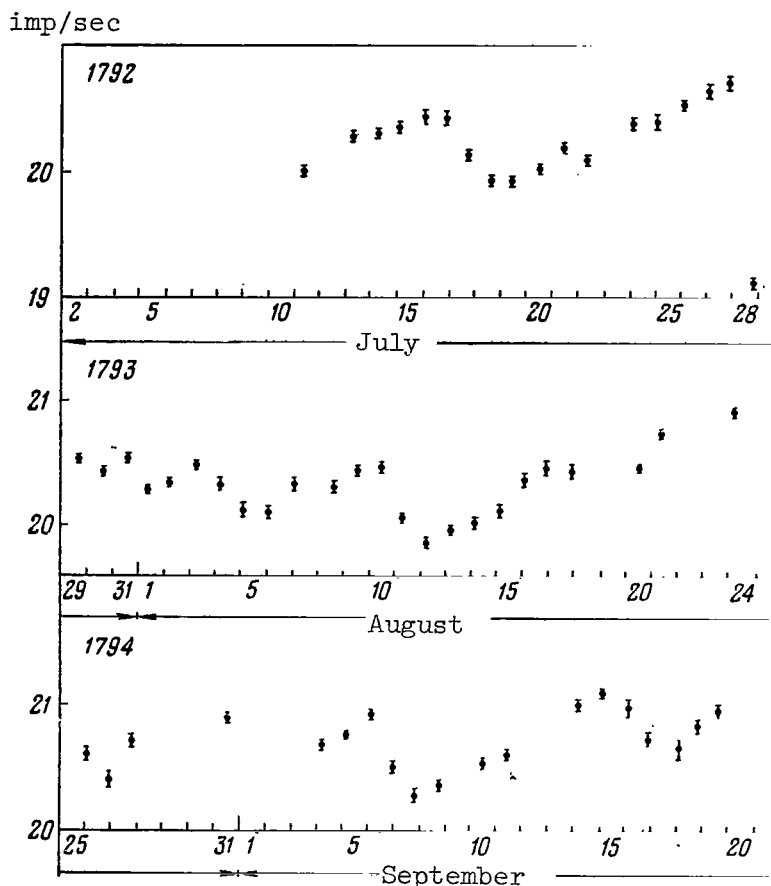


Figure 4

Gas Discharge Recording Rates Behind a Shielding of  $2.3 \text{ g} \cdot \text{cm}^{-2} \text{ Al}$   
For Solar Rotations 1792, 1793, and 1794.

spots, and a stream of solar radio emission on a 10.7 cm wave (Ref. 3). 505  
It can be seen from Figure 3 that the minimum number of solar spots occurs in July, 1964. In succeeding months, the number of solar spots began to increase. The cosmic ray intensity apparently reached a maximum in September, since data for October indicate a certain tendency to decrease. However, it is premature to draw a categorical conclusion regarding the initial intensity decrease of cosmic rays based on these premature data.

Thus, the maximum intensity of cosmic rays is at least two months behind the minimum of solar activity.

Intensity Variations with a characteristic time of about two weeks.  
These time variations have a clearly expressed cyclical nature with a period of about two weeks and an amplitude of about 1.5%. It is interesting to note that a wave of this type, with a period of approximately 14 days and an amplitude of about 2.5%, was recorded in April, 1963 during

the flight of the automatic interplanetary station "Luna-4" (Ref. 4). However, on the whole the intensity fluctuations are not regular in nature. The nature of this variation is still unclear. An analysis of the data points, to a certain extent, to the occurrence of a 27-day wave, both in the first and in the second half of 1964.

In this connection, the data from the counter screened behind  $2.3 \text{ g} \cdot \text{cm}^{-2}$  Al were analyzed with respect to solar revolutions. There was no clearly expressed recurrence of the intensity change from revolution to revolution, although for several revolutions - for example, for the revolutions 1792, 1793, and 1794 shown in Figure 4 - the general tendency for the intensity to change was expressed fairly clearly.

/506

The large coefficients for the correlation between our data and the data from monitors on the Earth took place not only for long periods of time, but also for short periods. Thus, the coefficients for the correlation with data from the Fort Churchill and Deep River monitors were 0.7-0.85 during a period on the order of 1-2 months (Ref. 1). In this connection, and also in view of the fact that there was no apparent connection with solar rotation, the assumption may be advanced that the variations discussed are not related to solar rotation, but are caused by the same mechanism as the 11-year intensity variations of cosmic rays. It must be assumed that the intensity increase of cosmic rays does not occur monotonically as solar activity decreases, but is accompanied by short increases and decreases related to the change in the conditions of cosmic ray propagation, or to the change in the size of the region of effective cosmic ray scattering on the scale of the solar system.

#### REFERENCES

1. Solar-Geophysical data, No.2-12, 1964.
2. Vernov, S. N., Chudakov, A. Ye., Vakulov, P. V., Gorchakov, Ye. V., Ignat'yev, P. P., Kuznetsov, S. N., Logachev, Yu. I., Lyubimov, G. P., Nikolayev, A. G., Okhlopkov, V. P., Sosnovets, E. N., Ternovskaya, M. V. Izvestiya AN SSSR, Seriya Fizika, 28, No. 12, 1964.
3. Solnechnyye Dannyye, No. 1-9, 1964.
4. Vernov, S. N., Chudakov, A. Ye., Vakulov, P. V., Gorchakov, Ye. V., Logachev, Yu. I., Lyubimov, G. P., Nikolayev, A. G. Kosmicheskkiye Issledovaniya, 2, No. 4, 1964.

# STUDY OF COSMIC RAYS DURING FLIGHTS OF SPACECRAFTS-SATELLITES AND THE "KOSMOS" AES

R. N. Vasilova, V. Ye. Nesterov, N. F. Pisarenko,  
I. A. Savenko, P. I. Shavrin

In several of the "Kosmos" satellites individual STS-5 gas discharge counters, which were of the same type and were designed to measure charged particle streams, were carried within the satellites under identical conditions. It was previously shown (Ref. 1) that the contribution from radiation zone particles to the STS-5 recording rate was not significant at any point, except for the Brazilian magnetic anomaly. Thus, the recording was due to primary cosmic rays, secondary particles (atmospheric albedo), and particles resulting from cosmic ray multiplication in the satellite.

This made it possible to employ the STS-5 counter recording rate to study time variations in the cosmic rays, and to determine the position of the cosmic ray equator.

Cosmic ray intensity changes between August, 1960 and April, 1963. The Table below presents the satellites carrying the STS-5 counters, and 507 gives their orbital parameters and measurement times.

Satellite	Perigee Altitude, km	Apogee Altitude, km	Measure- ment Time	STS-5 Recording Rate at High-Latitudinal Plateau, $\text{imp} \cdot \text{cm}^{-2} \cdot \text{sec}^{-1}$
Second spacecraft- satellite . . . .	306	339	8/19/60	$3.25 \pm 0.15$
Third spacecraft- satellite . . . .	187	256	12/1/60	$3.25 \pm 0.15$
"Kosmos-4" . . . .	298	330	4/26-29/62	$4.44 \pm 0.05$
"Kosmos-9" . . . .	301	358	9/27-10/1/62	$4.44 \pm 0.17$
"Kosmos-12" . . . .	211	405	12/22-30/62	$4.08 \pm 0.25$
"Kosmos-15" . . . .	173	371	4/22-27/63	$4.26 \pm 0.14$

Figure 1 shows the dependence of the STS-5 counter recording rate on the magnetic hardness threshold for all satellites listed in the Table.

The magnetic hardness threshold was determined according to Quenby and Wenk (Ref. 2) for the surface of the Earth, and was converted to the



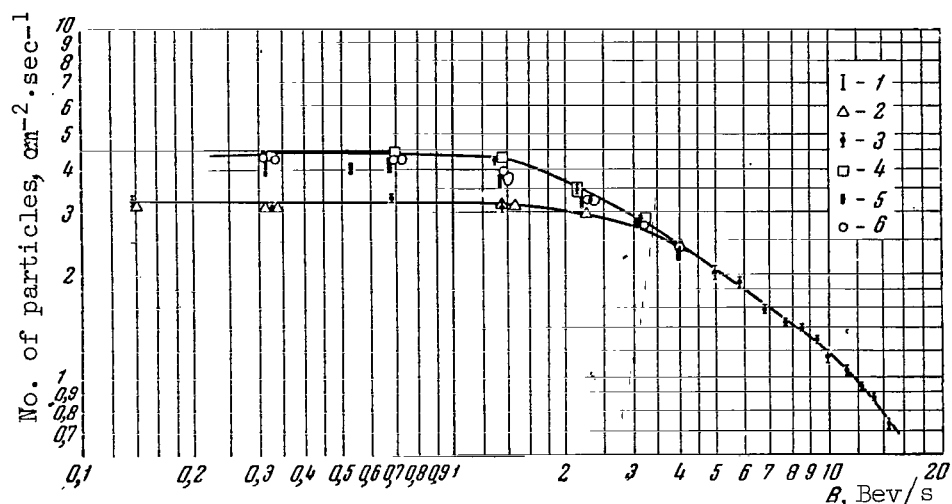


Figure 1

Dependence of Cosmic Ray Intensity on Hardness  
Threshold for Second and Third Spacecrafts-Satellites  
and the Satellites "Kosmos-4", "Kosmos-9", "Kosmos-12", and "Kosmos-15"

- 1 - Second spacecraft-satellite; 2 - third spacecraft-satellite;  
3 - "Kosmos-9"; 5 - "Kosmos-12"; 6 - "Kosmos-15".

altitude of the satellite's flight by the formula

$$\frac{P_h}{P_0} = \left( \frac{r_e}{r_e + h} \right)^2,$$

where  $P_0$  is the threshold hardness on the surface of the Earth in Bev/s;  $P_h$  - threshold hardness at the altitude  $h$  in Bev/s;  $r_e$  - radius of the Earth in km;  $h$  - satellite altitude above the surface of the Earth in km. Since the counters were not completely identical and their operation was not controlled during the flight, we made use of the fact that cosmic ray intensity did not change in the pre-equatorial region throughout the period of solar activity, in order to determine their relative efficiency. All of the counters were compared with the counter carried on the satellite "Kosmos-4".

The Table presents the STS-5 counter recording rates on different satellites, with allowance for counter differences. They are reduced to an altitude of 300 km.

The last column of this Table gives the STS-5 recording rates on the high-latitudinal plateau. The recording rate increased from 3.25 in December, 1960 to 4.44 imp·cm<sup>-2</sup>·sec<sup>-1</sup> in April, 1962, and it then remained on this level until April, 1963. Figure 2 gives the time behavior of

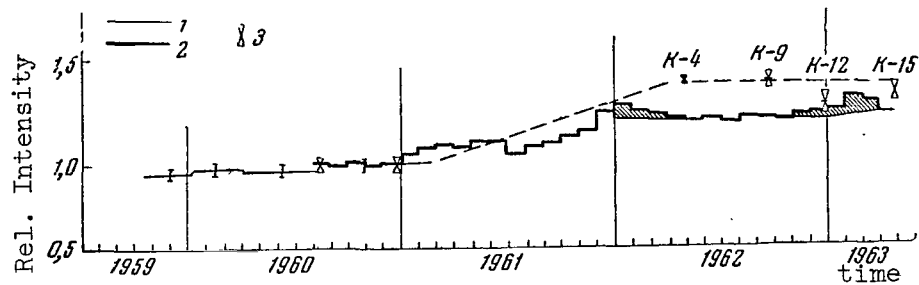


Figure 2

### Time Behavior of Cosmic Ray Intensity on the High-Latitudinal Plateau

1 - "Explorer-7"; 2 - stratosphere measurements of A. N. Charakhch'yan and coworkers; 3 - Measurements on spacecrafts-satellites and spacecrafts "Kosmos-4"; 4 - "Kosmos-9", "Kosmos-12", "Kosmos-15"  
The vertical criss-cross cross section indicates error.

cosmic ray intensity on the high-latitudinal plateau based on measurements performed on satellites and on sounding balloons. According to the satellites and sounding balloons, the cosmic ray intensity was assumed to be one between August-December, 1960. Satellite data between 1959-1960 were obtained on "Explorer-7" (Ref. 3), and these data were averaged over this period, with the exception of magnetically perturbed periods. The crosses indicate the measurement periods on the spacecrafts-satellites and on the satellites "Kosmos-4, 9, 12, 15". With the exception of "Kosmos-12", all these satellites flew during magnetically quiet periods. The heavy solid line gives the recording rates of one counter in the stratosphere (Ref. 4).

2. Spectrum of additional radiation particles. It can be seen from Figure 2 that between 1960 and 1962 there were particles with a small impulse. By subtracting the curve pertaining to spacecrafts-satellites from the curve pertaining to "Kosmos-4", one can obtain the integral hardness spectrum of additional radiation. It is shown in Figure 3, a.

This same figure gives the integral spectrum of additional radiation based on data from "Kosmos-17" (Ref. 5) and from stratosphere measurements (Ref. 4). It can be seen from the figure that the satellite data closely coincide, but differ from the stratosphere data.

Figure 3,b gives a rough picture of the differential spectrum. It can be seen that particles appeared in the energy range of 0.25-3 Bev. Generally speaking, this spectrum must be distorted by multiplication in the satellite mass. However, a comparison with the same spectrum obtained by comparing the gas discharge counter recording rates on the satellites "Kosmos-17" and "Explorer-7" (Ref. 5) shows that the spectra closely coincide. This

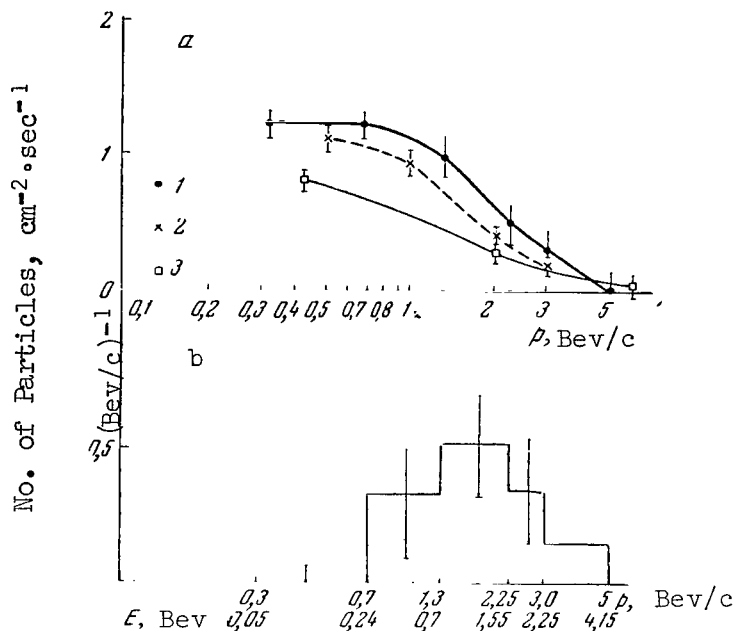


Figure 3

Integral Hardness Spectrum of Additional Cosmic Radiation (a) Appearing Between August, 1960, and April, 1962. (1 - comparison of "Kosmos-4" with Spacecrafts-Satellites; 2 - comparison of "Kosmos-17" with "Explorer-7"; 3 - Stratosphere data), and Differential Spectrum (b) Based on Data from the "Spacecrafts-Satellites and "Kosmos-4".

indicates that multiplication and absorption are of no importance in this energy range.

Brief conclusions. The above data, derived from measuring the time variations of cosmic rays on satellites and from measuring the cosmic ray equator, indicate that such a simple and reliable instrument as the gas discharge counter, when carried on a satellite, can monitor the cosmic ray intensity.

#### REFERENCES

1. Basilova, R. N., Vernov, S. N., Nesterov, V. Ye., Pisarenko, N. F. Savenko, I. A., Shavrin, P. I. Kosmicheskiye Issledovaniya, 2, No. 2, 280, 1964.
2. Quenby, J. J., Wenk, G. T. Philos. Mag., 7, No. 81, 1962.
3. Lin, W. C., Venkatesan, D., Van Allen, T. A. J. Geophys. Res., 68, No. 17, 1963.

4. Charakhch'yan, A. N., Charakhch'yan, T. N. Geomagnetizm i Aeronomiya, 3, 304, 1963; Report to the All Union Conference on Cosmic Rays (Doklad na Vses. sov. po kosmicheskim lucham). Apatity, 1964.
5. Vernov, S. N., Chudakov, A. Ye., Vakulov, P. V., Gorchakov, Ye. V., Logachev, Yu. I., et al. Izvestiya AN SSSR, Seriya Fiz., 28, No. 12, 1964.
6. Simpson, T. A., Fenton, K. B., Katzman, T., Rose, D. C. Phys. Rev., 102, 1648, 1956; Rothwell, P., Quenby, T. Nuovo Cimento, Suppl. II, 5, 1957.

# RECORDING COSMIC RAYS ON THE "KOSMOS-17" AES (Summary)

S. I. Avdyushin, R. M. Kogan, M. N. Nazarova,  
N. K. Pereyaslova, I. Ye. Petrenko, P. M. Svidskiy

The cosmic radiation intensity was measured outside of the radiation zones of the Earth at altitudes of 260-780 km by scintillation and Geiger counters in May, 1963. The detector shielding angle was  $2\pi \sim 1 \text{ g}\cdot\text{cm}^{-2}\text{Al}$ ; in the remaining portion of the solid angle,  $\sim 20\text{-}25 \text{ g}\cdot\text{cm}^{-2}$ . /510

The dependence of the radiation intensity on the invariant coordinate  $L$  was obtained. With a change in  $L$ , the charged particle flux recorded by the counters changed from  $0.5 \text{ particle}\cdot\text{cm}^{-2}\cdot\text{sec}^{-1}$  in the equatorial region to  $3.0 \text{ particle}\cdot\text{cm}^{-2}\cdot\text{sec}^{-1}$  at high latitudes. The flux of gamma-quanta in the energy range between 0.1-3 Mev changed from 9 to  $22 \text{ quanta}\cdot\text{cm}^{-2}\cdot\text{sec}^{-1}$ .

The boundary of the high-latitudinal plateau of cosmic ray intensity lay at  $L = 3.0$ . A comparison with data from "Explorer-17" (1959) points to an enrichment of the cosmic ray spectrum in the 0.9-1.5 Bev range. The cosmic ray equator compiled for altitudes of 400-600 km barely differs from the equator for altitudes of 200-300 km, based on data from "Kosmos-7" and others.

A system of five scintillation counters and four Geiger counters, included in a coincidence circuit of different multiplicity was used to record showers, which were produced when the cosmic particles interacted with the satellite material and which had divergence angles of more than  $60^\circ$  and a particle density of  $n \gtrsim 10^{-2} \text{ particle}\cdot\text{cm}^{-2}$  at the measurement point.

Values were obtained for the recording rate of the three-, four-, and five-fold coincidences in the scintillation counters; the three- and four-fold coincidences in the Geiger counters, and also the mixed coincidences of 6 multiplicity (three Geiger counters and four scintillation counters). All of the experimental data can agree, if it is assumed that the shower distribution with respect to the particle density  $n$  (gamma quanta and charged particles) has the form  $f(n)dn = Ae^{-\lambda n}dn$ ,

where  $A = 1.3 \cdot 10^2 \text{ cm}^{-2} \cdot \text{sec}^{-1}$ ,  $\lambda = 26 \text{ cm}^2$ . The ratio between the number of gamma quanta and the number of charged particles does not depend on  $n$ , and is  $\alpha = 11.3$ .

The fact that a number of showers do not have a latitudinal behavior indicates that the showers recorded are primarily generated by particles with energies greater than 30 Bev. At the same time, the total number of recorded showers indicates that the energy threshold for their generation does not exceed 60 Bev.

When the showers are recorded, the spectrum of energy liberation in the scintillation detector yields the mean energy of gamma quanta in the shower composition  $E_{\text{av}} = 4.6 \text{ Mev}$ . Under the condition that the contribution made by the showers comprises 0.3 of the total recording rate of a single Geiger counter, a comparison of the recording rates for detectors having a different surface yields an estimate of the particle density  $n = 0.01$  for the equatorial region, the number of showers  $N_s = 15 \text{ showers} \cdot \text{cm}^{-2} \cdot \text{sec}^{-1}$ , and the separation angle of particles in the shower  $\theta = 15\text{-}20^\circ$ . Thus, in this case we are dealing with fairly diverging showers.

# IONIZING RADIATION INTENSITY BASED ON MEASUREMENTS ON "ZOND-1" /511

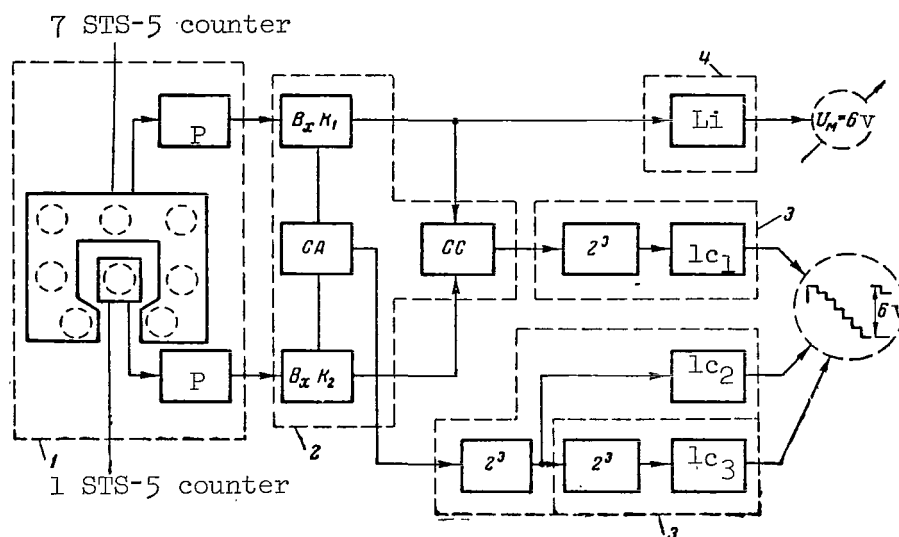
## (Summary)

S. I. Avdyushin, N. K. Pereyaslova, I. Ye. Petrenko

When cosmic ray intensities are measured at great distances from the Earth, the effect of shielding, albedo from the atmosphere, and the magnetic field of the Earth is completely excluded. The magnetic field has a particularly strong influence on the low-energy component of cosmic rays, whose variation is connected with magnetic field changes in the solar system and with the solar activity.

The present report gives the results derived from measuring cosmic radiation intensity beyond the Earth's magnetosphere on the space station "Zond-1".

A device designed to measure the intensity was carried within the space station, close to its frame, behind a shielding of  $\sim 10 \text{ g} \cdot \text{cm}^{-2}$ . The thickness of the shielding layer was not the same on both sides; the maximum thickness was  $\sim 150 \text{ g} \cdot \text{cm}^{-2}$ . Eight STS-5 Geiger counters represented the ionizing radiation detectors. The counters were arranged so that one central counter was shielded by the others. The block diagram of the equipment is shown in the figure. The equipment recorded the total intensity of the shielding counters' recording, the number of anti-coincidences, and the number of coincidences between the central counter and any of the shielding counters. The total radiation flux recorded by the detector was  $3.37 \pm 0.40 \text{ cm}^{-2} \cdot \text{sec}^{-1}$ .



Block Diagram of the Equipment

1 - Counter Unit; 2 - Coincidence (CC) and anti-coincidence (CA) Unit; 3 - Conversion Unit; 4 - Logarithmic intensimeter Unit (LI)  
(P = preamplifier;  $B_{xK_{1,2}}$  = threshold discriminator; lc = logarithmic converter)

The Table below presents the results derived from measuring a flux of cosmic rays, obtained at different times on different space vehicles.

It can be seen from the results presented in the Table that the flux, obtained on "Zond-1", was approximately 25% less than the flux obtained on the space stations "Mars-1" and "Luna-4", although it was comparable with the flux measured on "Mariner-2". There was a considerable increase in <sup>512</sup> the cosmic ray flux as compared with 1959 (first and second space rockets), which coincides with the cosmic radiation intensity change as a function of the solar activity change in the 11-year cycle.

Measurement time, year	Distance from Sun, a.u.	Shielding, $g \cdot cm^{-2}$	Flux, $cm^{-2} \cdot sec^{-1}$	Space Vehicle
1959	$\sim 1$	$\sim 1$	$2.38 \pm 0.1$	First and second space rockets (Ref. 1, 2)
1962	0.7	$< 1$	$3.20 \pm 0.024$	"Mariner-2" (Ref. 3)
1962	1-1.24	$\sim 1$	$4.5 \pm 0.1$	"Mars-1" (Ref. 4)
1963	1	$\sim 1$	$4.45 \pm 0.1$	"Luna-4" (Ref. 4)
1964	0.97	$\geq 10$	$3.37 \pm 0.40$	"Zond-1"

A more detailed comparison of the results obtained by "Zond-1" and the other results given in the Table is rendered more difficult by the significant difference in the radiation detector shieldings.

The number of anti-coincidences was also obtained in this experiment. The anti-coincidence recording rate (reduced to unit of counter surface) was  $1.3 \pm 0.2 \text{ cm}^{-2} \cdot \text{sec}^{-1}$ . An analysis of the data, which takes into account the magnitude of the total recording rate, the anti-coincidence recording rate, and the detector geometry, shows that an overwhelming portion of the anti-coincidences recorded is caused by gamma quanta with energies of  $\lesssim 1 \text{ Mev}$ . The gamma quanta are apparently formed when primary cosmic particles interact with the station material. The lack of data on the spectral distribution of the gamma quanta recorded makes it impossible to determine the gamma radiation flux with sufficient accuracy. However, it can be stated that this flux is several tens of quanta per  $1 \text{ cm}^2$ , since the efficiency of the Geiger counters is  $\sim 1\%$  in the energy range of gamma radiation under consideration.

Data on the number of anti-coincidences also indicate that the charged particle flux, determined from the recording rate of a single Geiger counter, can be overestimated due to gamma radiation. If the anti-coincidence recording rate is taken into account, we then obtain a quantity of  $2.1 \pm 0.6 \text{ particle} \cdot \text{cm}^{-2} \cdot \text{sec}^{-1}$  for the charged particle flux.

In conclusion, we would like to point out that the error entailed in these values, which is large as compared with data given by other authors, is primarily due to insufficient statistical readings because of the small measurement period.

#### REFERENCES

1. Vernov, S. N., et al. Doklady AN SSSR, 125, No. 2, 1959.
2. Vernov, S. N., et al. In "Iskusstvennyye Sputniki Zemli". Izdatel'stvo AN SSSR, No. 5, 1960.
3. Anderson, H. R. J. Geophys. Res., 69, No. 13, 1964.
4. Vernov, S. N., et al. Kosmicheskiye Issledovaniya, 2, No. 4, 1964.

EFFECTS OF SOLAR AND GEOPHYSICAL PHENOMENA IN PRIMARY  
RADIATION, RECORDED BY EQUIPMENT ON THE ARTIFICIAL  
EARTH SATELLITE "KOSMOS-19"

(Summary)

Yu. G. Shafer, B. M. Kuzhevskiy,  
A. G. Kulagin, N. G. Skryabin

/513

The study presents the results derived from analyzing experimental material obtained on the artificial Earth satellite "Kosmos-19" during the period of minimum solar activity between July 6 and December 31, 1963, for a magnetic hardness threshold of 3.5 Bev at an altitude of 350-450 km.

The equipment developed for measuring cosmic ray intensity consisted of an ionization chamber of an unshielded and shielded gas discharge counter and a counter telescope.

1. The 27-day variations in cosmic ray intensity were studied in this period by periodogram analysis. It was found that during minimum solar activity the cosmic ray intensity, with a magnetic hardness of more than 3.5 Bev, does not undergo 27-day variations. This coincides with the results obtained by equipment on the Earth and obtained by balloons (Ref. 1).

2. During very powerful magnetic storms from August 17-27, the equipment carried on the satellite indicated a sharp decrease in the recording rate (Forbush effect). The magnitude of the effect was 8% based on data from the shielded counter, and 9.2% based on data from the unshielded counter. The Forbush effect was observed simultaneously by a neutron monitor at Yakutsk and at the Resolute station. It should be noted that the effect of a magnetic storm on the cosmic ray intensity recorded by the equipment on the satellite was the same as that recorded by equipment on the Earth. The beginning and duration of the phenomenon coincide with similar phenomena on the surface of the Earth.

3. An increase in the recording rate, as compared with mean monthly data, was noted by three devices (unshielded counter, shielded counter, and counter telescope) was observed between August 12-21. The phenomenon increased the statistical error by a factor of 5-10.

The recording rate increase was noted 10-13 hours after chromosphere flares were observed on the Sun. Assuming that the effect upon cosmic ray intensity is related to solar particles, one can determine the corpuscular stream velocity. It is  $3200-4200 \text{ km} \cdot \text{sec}^{-1}$  (Ref. 2).

4. An equal intensity line was compiled based on data from the equipment on the satellite. A comparison with equal intensity lines obtained in (Ref. 3) shows that there was an intensity increase of 3%



between 1957 and 1963. The mean quadratic error of the result is no greater than 2%. Such a small cosmic ray intensity change during this period is related to the large threshold hardness of the particles recorded.

#### REFERENCES

1. Dorman, L. I. Cosmic Ray Variation and a Study of the Cosmos (Variatsiya kosmicheskikh luchey i issledovaniye kosmosa). Izdatel'stvo AN SSSR, 1963.
2. Krzhivskiy, L. Byull. Astron. Institutov Chekhoslovakii, 16, No. 1, 1965.
3. Vernov, S. N., Grigorov, N. L. In "Iskusstvennyye Sputniki Zemli". Izdatel'stvo AN SSSR, No. 1, 1958.

#### RESULTS DERIVED FROM STUDYING THE COSMIC RAY NUCLEAR COMPONENT ON THE SATELLITE "ELEKTRON-2"

Ya. L. Blokh, L. I. Dorman, L. V. Kurnosova,  
V. I. Logachev, G. F. Platonov, L. A. Razorenov,  
V. G. Sinitsina, A. A. Suslov, M. I. Fradkin

The purpose of studies on the nuclear component of primary cosmic rays, which were performed on the satellite "Elektron-2", was to observe different groups of nuclei streams for a long period of time, and to determine their changes as a function of solar activity during the International Quiet Sun Year. The satellite "Elektron-2" was located at great distances from the Earth for a significant amount of time. This made it possible to measure the fluxes under conditions when the Earth's magnetic field had no effect on their magnitude. /514

The equipment used consisted of two recorder units: A power transformer and stabilizer unit and a radioelectronic unit. One of the recorder units was located on the outside of the satellite, directly in cosmic space; the other was located within the satellite frame. The outer recorder unit contained a Cherenkov and a scintillation counter. The Cherenkov counter of the outer unit recorded nuclei with  $Z \geq 2$  and very heavy nuclei with a charge of about 30. In addition, nuclei with  $Z \geq 2$  were recorded by a "telescope" which was formed by the Cherenkov counters and the scintillation counters of the outer unit. The Cherenkov counter, which was located in the inner unit, recorded nuclei with  $Z \geq 2, \geq 5, \geq 15$ . Both the integral Cherenkov counters and the telescope recorded cosmic ray nuclei with energies of  $\geq 600$  Mev/nucleon. The inner

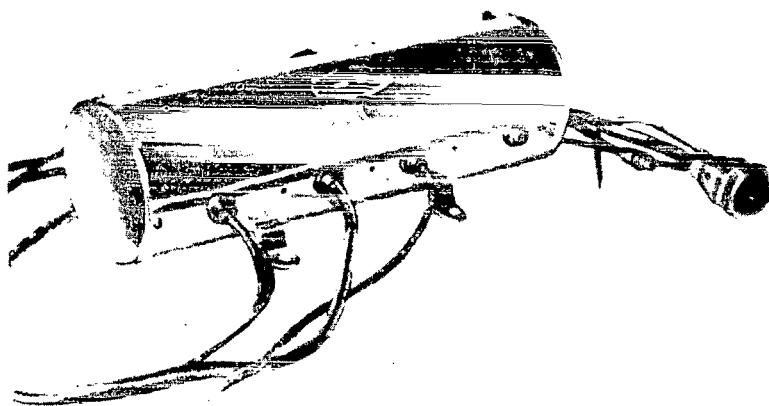


Figure 1

### Outer Recorder Unit

counter was shielded by a layer of about  $1.5 \text{ g}\cdot\text{cm}^{-2}$ . Both detectors of the outer unit were shielded by an aluminum layer of  $\sim 0.6 \text{ g}\cdot\text{cm}^{-2}$ . Figure 1 shows a photograph of the outer recorder unit. Figure 2 gives the arrangement of the detectors in the unit. The inner unit containing the Cherenkov counter and the electronic systems pertaining to it is shown in Figure 3.

The power supply for the equipment came from a solar battery on board the satellite through the transformer and stabilizer. The power transformer unit (Figure 4) and the radioelectronic unit of the outer recorder were located within the satellite frame, where a fairly stable 515 temperature regime could be ensured.

Figures 5 and 6 show the principal circuits of the outer and inner recorder units. Figure 7 shows the circuit of the outer recorder electronic unit. The counters were calibrated with the impulse created by a singly charged particle passing through the detector. Its magnitude was determined by recording, under laboratory conditions, the amplitude distribution curve of impulses produced by cosmic ray particles. The thresholds in different channels were established in accordance with the magnitude obtained for the mean impulse created by a singly charged particle. The dependence of the thresholds on temperature was measured in a very wide range before the equipment was placed on the satellite.

Verification of the counter linearity is of very great importance. Since the range, where the multiplier intensifies the input impulse amplitude linearly, can depend on the duration of this impulse, the linearity of the PEM\* must be verified for fairly short light impulses. Brief flashes can be obtained by utilizing, for example, a diode on a silicon carbide base.

\* Note: PEM designates Photoelectron Multiplier.

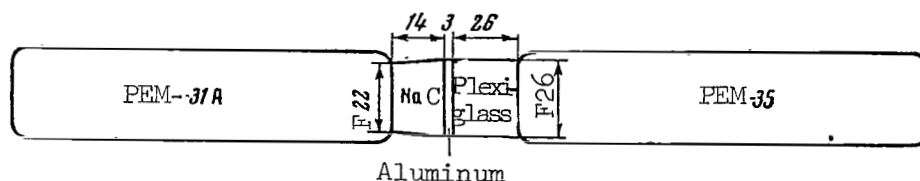


Figure 2

#### Detector Arrangement in Outer Unit

In view of the fact that the Cherenkov counter had to record nuclei in a large range  $Z$ , the light characteristics of the PEM-35 were recorded. There was a change in the dependence of the electric impulse magnitude at the anode on the magnitude of the flash, which would correspond to flashes produced by nuclei from  $Z = 4$  to  $Z = 21$  passing through the counter. A similar dependence was recorded for the seventh dynode, which corresponds to  $6 \leq Z \leq 28$ .

The ratio between the impulse magnitude at the anode and the impulse magnitude at the dynode was determined from the data obtained.

When the characteristics were recorded, a diode with a circular contact on a silicon carbide base SiC was used as the light source (Figure 8). The electric impulse at the diode was supplied from a short-impulse generator at the hydrogen thyatron TGI 1-50/5. The generator made it possible to obtain impulses having an amplitude between 100-2000 v, with a duration of 30-100 nsec. The light diode was located directly at the PEM photocathode.

/516

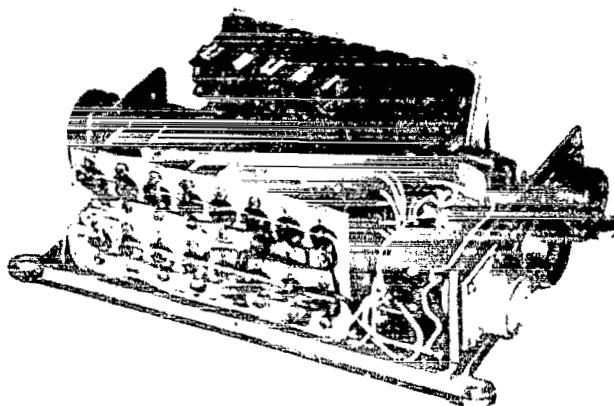


Figure 3

#### Inner Block Containing Cherenkov Counter

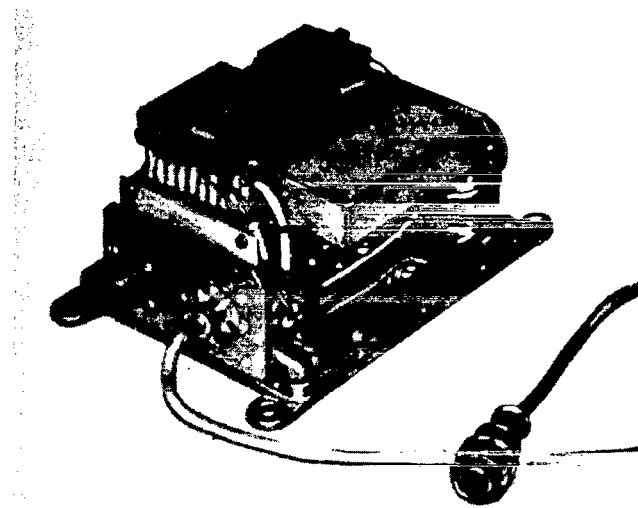


Figure 4

#### Unit of Power Transformers and Stabilizers (Without a Cover)

Figure 9 shows the dependence of the impulse amplitude at the anode (curves 1 and 2) and at the dynode (curves 3 and 4) of the PEM-35 on the magnitude of the flash. Curves 1 and 3 pertain to a flash duration of 100 nsec; curves 2 and 4 pertain to a duration of 30 nsec. Deviation of curve 1 from the linearity was due to PEM saturation. Curves 2 and 4 are linear throughout the entire flash region studied. The curves were calibrated with the impulse created by cosmic  $\mu$ -mesons (40 mv). It can be seen from curve 1 that the PEM is linear up to  $Z = 21$ . Point A, representing the maximum flash duration of 30 nsec, corresponds to  $Z = 15$ .

Utilizing the data given in Figure 9, one can obtain the dependence of the impulse amplitude ratio at the anode to the impulse amplitude at the dynode on the magnitude of the flash. The mean value of this ratio is 32. We can thus estimate the impulse magnitude at the seventh PEM dynode from cosmic  $\mu$ -mesons, and can calibrate the dynode curves. The estimates <sup>518</sup> show that point B on the dynode curve 3 (Figure 9) corresponds to  $Z = 28$ , and the point C on curve 4 corresponds to  $Z = 8$ .

The effective geometric factor (luminosity) of the integral Cherenkov counter can be calculated from definite assumptions (Ref. 1). The magnitude of the geometric factor depends on its dimensions and the magnitude of the threshold established. The computation was performed for particles coming from the "upper" half-space. The geometric factor of the inner integral Cherenkov counter for recording nuclei with  $Z \geq 2$ ,  $\geq 5$  and  $\geq 15$  was, respectively, 26, 30, and 33  $\text{cm}^2 \cdot \text{sterad}$ . As has already been indicated, the satellite "Elektron-2" carried a telescope consisting of a



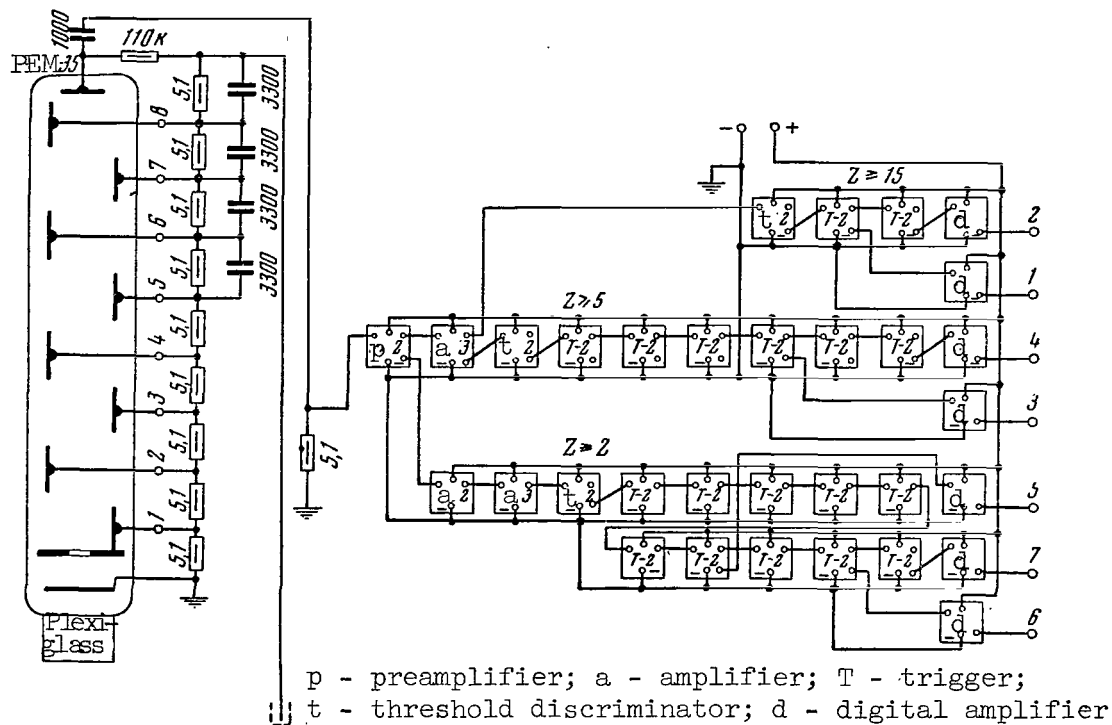


Figure 6

#### Principal Electron Circuit of Inner Cherenkov Counter (Г)

1 and 2 - outputs to recording channel of RTS\* for nuclei with  $Z \geq 15$ ;  
3 and 4 - the same for nuclei with  $Z \geq 5$ ; 5, 6, and 7 - the same for  
nuclei with  $Z \geq 2$ .

amplitude distribution introduced by the photomultiplier. The form of the amplitude distribution is approximated by a Gaussian curve. It is thus found that the geometric factor depends on the threshold established, and slightly depends on the halfwidth of the distribution curves.

A great deal of rich information was obtained on streams of different nuclei groups when the equipment was in operation. Preliminary processing of data from the first revolution of the satellite "Elektron-2" makes it possible to compare the fluxes of different nuclei groups, measured in 1959 on the second and third space rockets, in 1960 on spacecrafts-satellites, and at the end of 1962 on the interplanetary station "Mars-1", with these fluxes during an extreme solar activity minimum... For heavy nuclei with  $Z \geq 15$ , this comparison has been made for the first time with sufficient statistical material. These data point to an increase in the fluxes of all nuclei groups by a factor of 1.7-2.

Figure 10 shows the relative number of solar spots characterizing the

\*Note: RTS = Radio Telemetry System

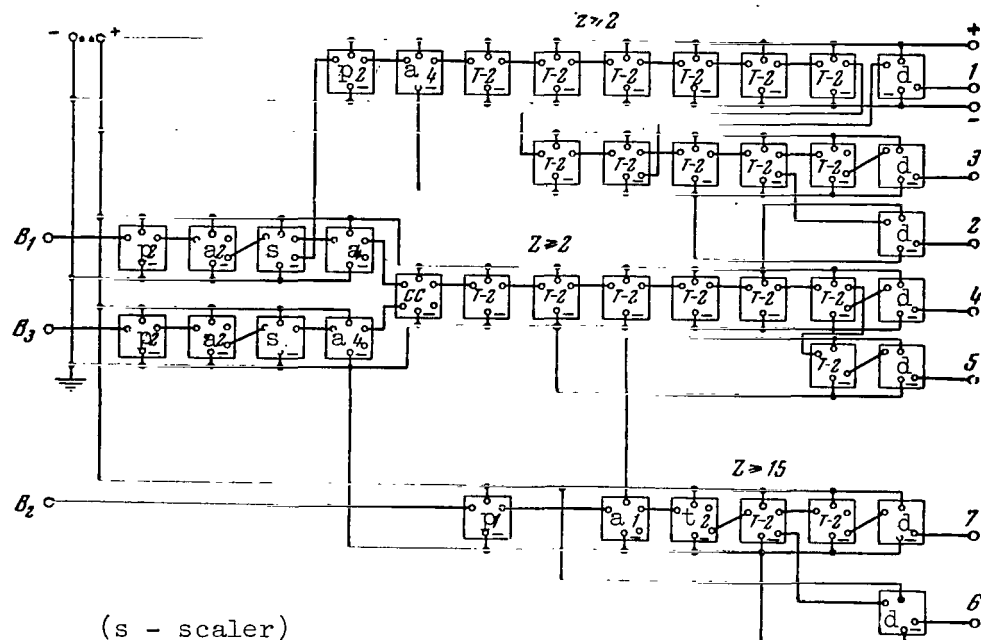


Figure 7

Principal Circuit of the Electronic Unit for the Outer Recorder (B)  
 $B_1$  and  $B_2$  - input from collector and dynode of Cherenkov counter PEM;  $B_3$  -  
input from collector of scintillation counter PEM; 1-3 - output to recording  
channel of RTS for nuclei with  $Z \geq 2$ ; 6, 7 - the same for very heavy nuclei;  
4 and 5 - outputs to telescope recording channel RTS.

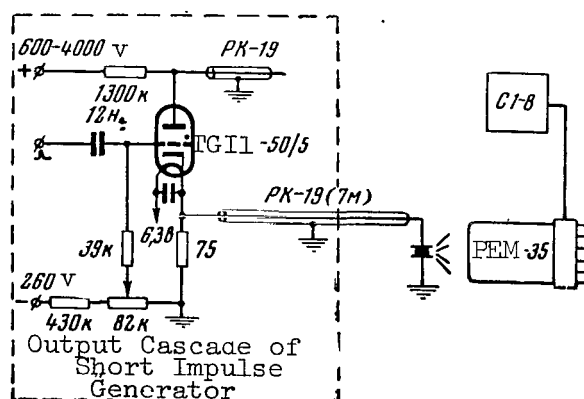


Figure 8

Diagram For Recording PEM Characteristics by Means of Light Diode

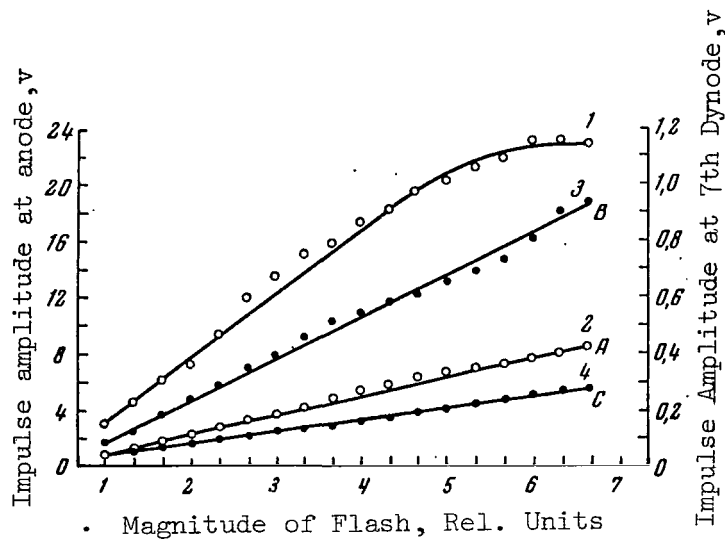


Figure 9

Dependence of Impulse Amplitude at Anode (Curves 1 and 2) and Dynode (Curves 3 and 4) of the PEM-35 on Magnitude of the Flash. Curves 1 and 3 pertain to a flash duration of 100 nsec, and curves 2 and 4 pertain to a duration of 30 nsec.

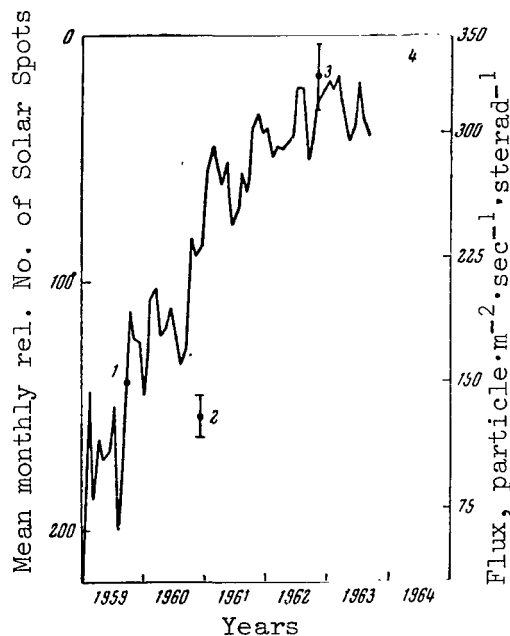


Figure 10

Relative Number of Solar Spots (Curve) and Magnitude of Nuclear Flux with  $Z \geq 2$  During Different Years (Points)  
 Data: 1 - Second space rocket; 2 - third spacecraft-satellite;  
 3 - interplanetary station "Mars-1"; 4 - the satellite "Elektron-2".



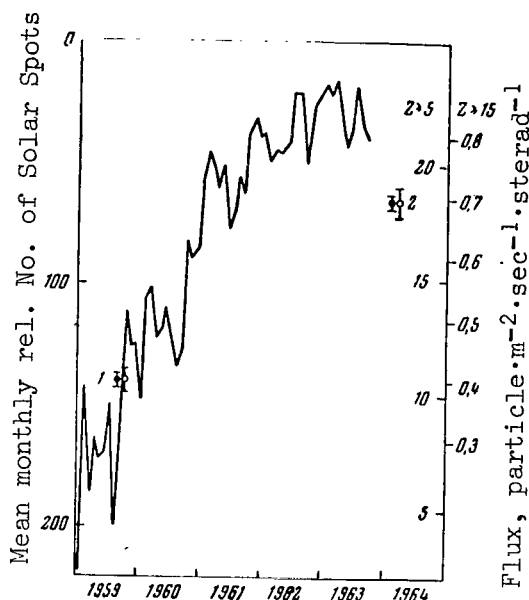


Figure 11

Relative Number of Solar Spots (Curve) and Magnitude of Nuclei Fluxes With  $Z \geq 5$  (Dark Circles) and with  $Z \geq 15$  (Light Circles) During Different Years

Data: 1 - second space rocket; 2 - the satellite "Elektron-2"

solar activity, as well as the flux of nuclei with  $Z \geq 2$  during different years. The mean monthly relative number of solar spots (Wolf number) is plotted downward on the left vertical scale; the flux of nuclei with  $Z \geq 2$ , primarily of  $\alpha$ -particles, is plotted on the right vertical scale. Point 1 refers to measurements on the second space rocket; 2 - to measurements on the third spacecraft-satellite; 3 - to data from the interplanetary station "Mars-1"; 4 - to data derived from processing results obtained on the first revolutions of "Elektron-2". Points 3 and 4 pertain to a period of minimum solar activity. It can be seen from the figure that there is a negative correlation between the number of solar spots and the nuclei flux.

Points 1 and 4 were obtained with such statistical accuracy that the errors were overlapped by the points in the figure. The fact that the measurements were performed by recorders having the same luminosity made it possible to perform a reliable comparison of the fluxes during different years.

/521

The relative number of solar spots and the fluxes of nuclei with  $Z \geq 5$  and  $\geq 15$  are compared for different years in Figure 11.

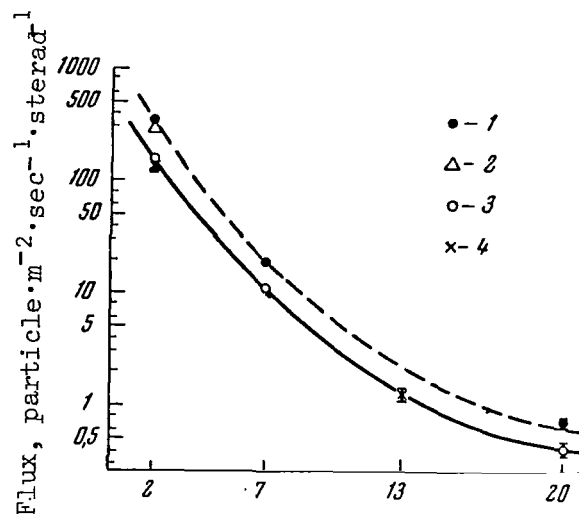


Figure 12

Dependence of Flux on Mean Effective Charge of Nuclei Recorded  $Z_{\text{eff}}$  Between 1959-1962 (Solid Curve) and During Minimum Solar Activity (Dashed Line)

Data: 1 - The satellite "Elektron-2" (1964); 2 - interplanetary station "Mars-1" (1962); 3 - second space rocket; 4 - third spacecraft-satellite. The dashed line indicates mean recording rates per revolution.

The Table below presents preliminary data<sup>1</sup> on fluxes obtained by the inner recorder on "Elektron-2" on one of the revolutions. These data are compared with the fluxes measured during other flights.

Figure 12 shows the dependence of the flux of the mean effective charge of the nuclei recorded. The upward shift of all curves during the solar minimum (data from "Mars-1" and "Elektron-2"), as compared with its position in 1959-1960, can be clearly seen.

The generation of solar cosmic ray nuclei during chromosphere flares was first discovered during the flights of the Soviet space rockets and the spacecrafts-satellites (Ref. 2). The prolonged observation of nuclei fluxes, which was performed by equipment carried on

/524

<sup>1</sup> The fluxes based on data from "Elektron-2" and the second space rocket were obtained by utilizing the luminosities calculated on the assumption that the Cherenkov counter recorded particles coming from the leading hemisphere (see [Ref. 1]). Allowance for the contribution made by particles coming from the trailing hemisphere increases the luminosity, which leads to a decrease in the absolute values of the fluxes.

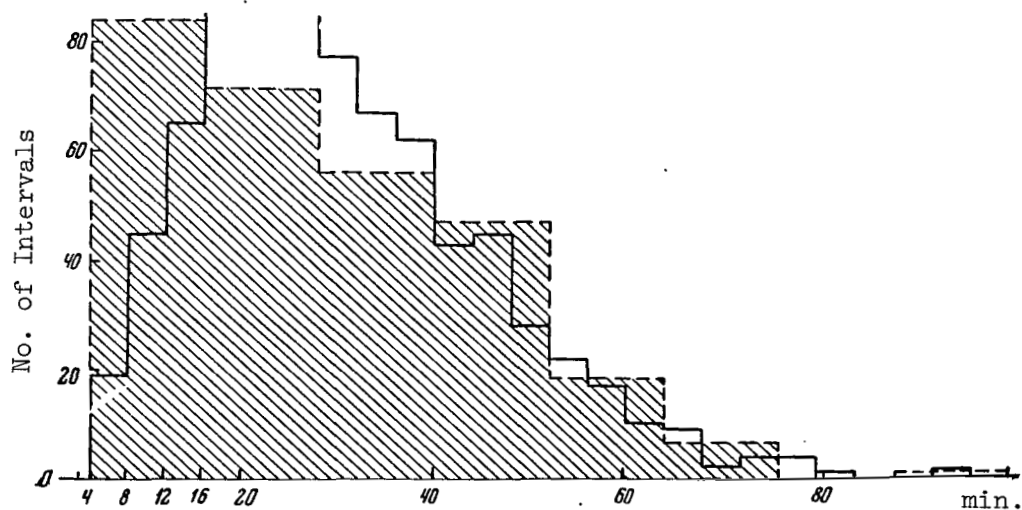


Figure 13

Distribution of Time Intervals Between Counter Readings for Nuclei With  $Z \geq 15$  According to the Duration of These Intervals. The shaded area designates the same distribution compiled for the period encompassing solar flares and bursts.

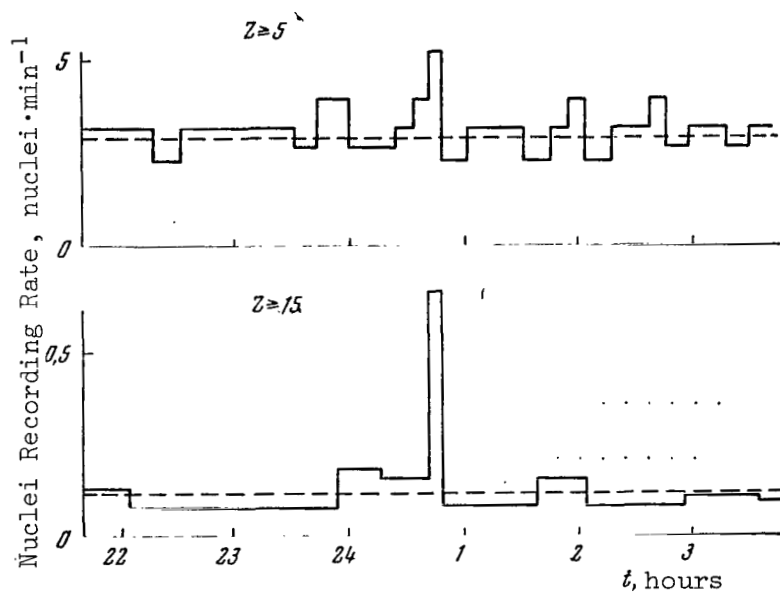


Figure 14

An Example of Simultaneous Intensity Increase for Nuclei With  $Z \geq 15$  and  $Z \geq 5$ , Recorded on February 11, 1964, at Zero Hours 42 Minutes. World Time.

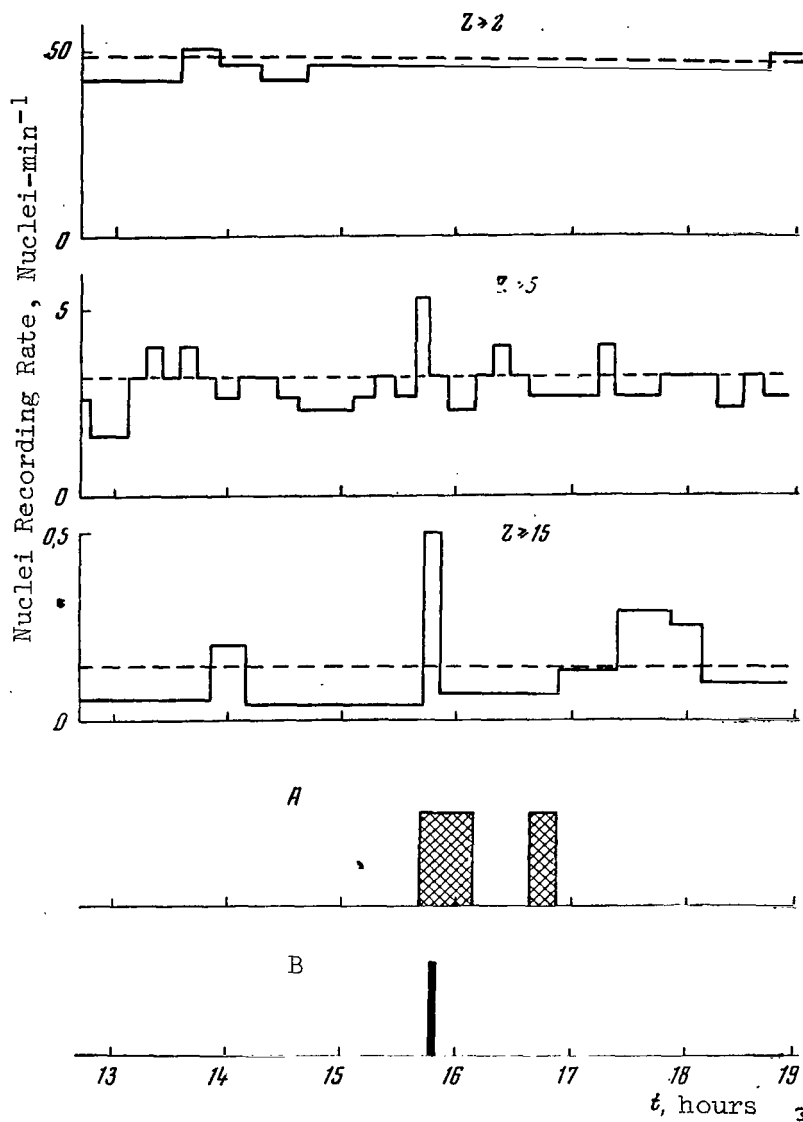


Figure 15

Example of Brief Intensity Increase for Nuclei with  $Z \geq 15$  and  $Z \geq 5$ ,  
 Recorded on January 30, 1964.  
 The dashed line designates mean recording rates per revolution. The  
 lower part of the figure shows a chromosphere flare of class 1-(A)  
 and a type III burst in the 20-42 Mc range (B). World Time.

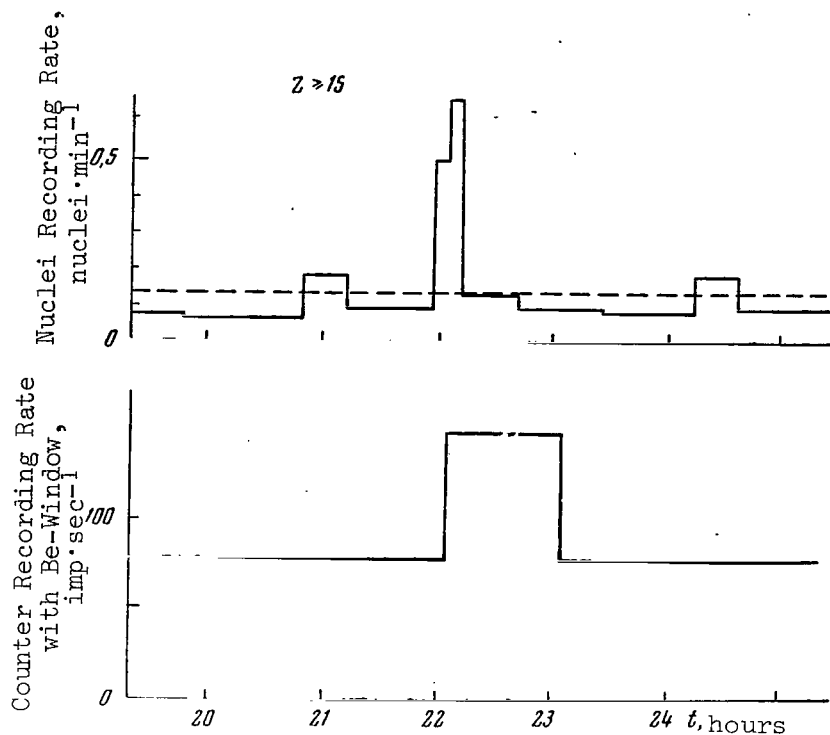


Figure 16

Example of Brief Intensity Increase for Nuclei With  $Z \geq 15$ , Recorded on January 31, 1964 at 22 Hours. World Time. Dashed line designates mean value per revolution. The lower section of the figure shows the recording rate increase of the X-ray radiation counter with a beryllium window, recorded during the same flight.

Space Vehicle	Nuclei Flux·particle·m <sup>-2</sup> ·sec <sup>-1</sup> ·sterad <sup>-1</sup>		
	$Z \geq 2$	$Z \geq 5$	$Z \geq 15$
"Elektron-2"	$343.4 \pm 1.4$	$18.3 \pm 0.3$	$0.69 \pm 0.06$
Second space rocket	$150.6 \pm 1.3$	$10.6 \pm 0.3$	$0.4 \pm 0.05$
Third spacecraft-satellite. . . . .	$129.2 \pm 12.9$	$9.8 \pm 0.7$	--
"Mars-1" . . . . .	$333 \pm 21$	--	--

the satellite "Elektron-2", revealed new data on the temporal changes in the intensity of cosmic ray generation during low solar activity.

At the present time, only a portion of the material obtained has been processed, and therefore the data presented are provisional in nature.

A portion of the material obtained was processed statistically for nuclei with  $Z \geq 15$ . The distribution of the time intervals, during which the recorder counted four nuclei, was compiled according to the interval duration.

Figure 13 shows this distribution by the solid, step-like line. The interval duration in minutes is plotted along the abscissa axis; the number of observed intervals having corresponding duration is plotted along the ordinate axis. The maximum of the distribution curve corresponds to the mean interval during which four nuclei are recorded, i.e., the mean intensity. The curve width characterizes the statistical scatter.

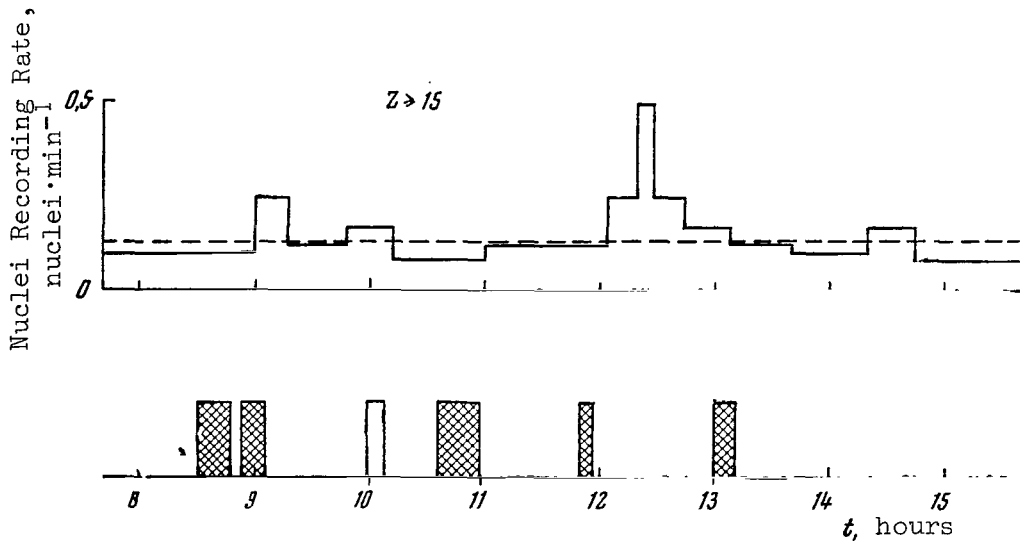


Figure 17

Example of Brief Intensity Increase for Nuclei with  $Z \geq 15$   
Dashed line - mean value per revolution. The lower section shows chromosphere flares of class 1-. The shaded section designates flares arising in one and the same region.

World Time.

Material obtained approximately during the observational months was employed to compile the curve. A similar distribution was then compiled for the same material, which was obtained during solar flares and bursts. For this purpose, data pertaining to 20-minute periods after the beginning of each flare or burst were summarized. Thirty-eight solar flares and bursts were employed in all.

The distribution thus obtained was normalized to the distribution for all of the material with respect to the times used in both cases (normalization factor  $\sim 52$ ). The dashed line in Figure 13 shows the distribution corresponding to the period of an active Sun.

As can be seen from the figure, the form of both distributions is somewhat different. In the case of distribution pertaining to the active period, there is a larger amount of short time intervals than in the case of total distribution. This corresponds to a brief intensity increase in the nuclei recorded during flares and bursts. However, the difference between distribution curves is not very great, since such intensity increases were far from being observed in all the flares.

In order to determine the probability of random divergence in the distributions formulated, a statistical analysis was performed. The Pearson criterion made it possible to reject the hypothesis of random divergence in the form of the distribution curves, with a probability of no more than 15% error. The use of the superposed-epoch method was rendered more difficult by the fact that the time of the nuclei intensity increase can change in various ways with respect to the beginning of the solar flare in different cases.

The fact must also be kept in mind that the intensity of galactic cosmic rays can decrease during the flares. A significant increase in the nuclei intensity during a class I flare is very unusual. It is possible that the increases are related to other solar activity phenomena (for example, to rapid processes or a special type of burst). For purposes of illustration, we shall present several cases in which there were brief increases in the recorded intensity of heavy nuclei.

Figure 14 shows an example of a simultaneous intensity increase for nuclei with  $Z \geq 15$  and  $\geq 5$ , recorded on February 11 at 00 hours 42 minutes UT. The dashed line gives the mean nuclei recording rates per revolution. In this case, the intensity of nuclei with  $Z \geq 2$  did not increase.

The recorded intensity of nuclei with  $Z \geq 15$  increased by a factor of approximately 5. However, due to the comparatively small luminosity of the equipment, the number of nuclei recorded during the increase was not much greater than the mean number during the same period of time. Therefore, in this case the increase may be explained by statistical fluctuation. /526

Estimates have shown that about one such case may be expected during a period of time equalling the time utilized in the processing, due to fluctuations.

There is undoubtedly an increase in the nuclei flux, if any solar activity phenomena are recorded at the same time.

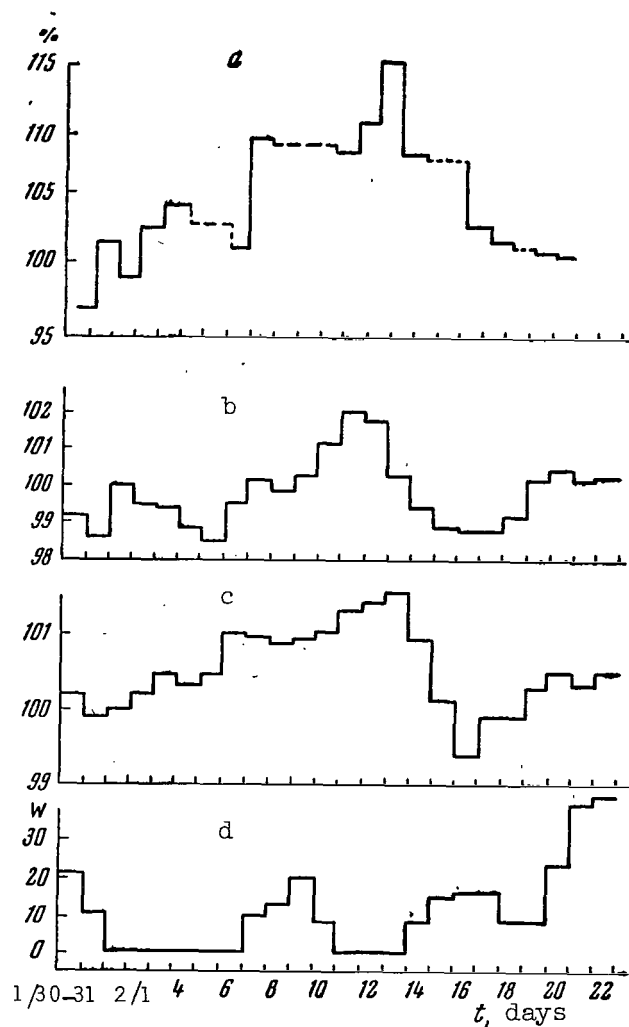


Figure 18

Recording Rate Change for Nuclei With  $Z \geq 2$  in the  
First Half of February, 1964.

Dashed line shows sections where no information was received, or where the data has not yet been processed. For these sections, a recording rate is assumed which equals the mean value for two adjacent sections.

a - nuclei with  $Z \geq 2$  ( $E_{\min} > 600$  Mev/nucleon); b - data from neutron monitor (Krasnaya Pakhra); c - data from neutron monitor (Climax, altitude of 3400 m); d - number of solar spots.



Figure 15 shows such a case for nuclei with  $Z \geq 15$  and  $\geq 5$ , recorded on January 30, 1964 during a class 1- chromosphere flare. The flare was accompanied by the third type of radio emission burst in the 20-42 Mc frequency range.

/527

In this case, a statistical fluctuation in the number of nuclei recorded can hardly be used as an explanation for the increase. Actually, the probability for a random conformity between this increase and the third type of radio emission burst is  $< 2 \cdot 10^{-2}$ . In other words, such a random agreement can only be expected during a period of time which exceeds that employed in the experiment by a factor of 50.

Figure 16 shows the case of a brief intensity increase for nuclei with  $Z \geq 15$  recorded on January 31, at 22 hours UT.

According to measurement data in (Ref. 3), in the same period there was an increase in the recording rate of X-ray radiation counters having beryllium and aluminum windows. This increase lasted about one hour. Data from the counter with the beryllium window are presented in the lower part of the figure. The probability of such an increase in the nuclei recorded intensity, caused by statistical fluctuation, is such that only one case can be expected throughout the entire period of time utilized in the experiment.

However, the agreement between the phenomenon recorded and the intensity increase in X-ray radiation compels us to conclude that in this case the increase is not random in nature, but is related to solar activity.

Figure 17 shows an example of a brief intensity increase for nuclei with  $Z \geq 15$ , which is not accompanied by an intensity increase for nuclei with  $Z \geq 5$  and  $\geq 2$ . In this case, there is no clear correlation between the phenomenon observed and a flare or burst. However, attention should be called to the fact that the brief increase in nuclei intensity was recorded after several weak chromosphere flares.

We would like to point out that it is very probable that cases of brief increases in the equipment recording rate may occur, due to statistical fluctuations, during prolonged observations. However, the fact that these cases coincide with the occurrence of solar activity, or the fact that there is agreement between the recording rate increases in two channels simultaneously, greatly decreases the possibility of their random occurrence.

A more detailed analysis of all the cases recorded will be given at a later point.

In conclusion, we would like to discuss changes in the mean recording rate during long periods of time. This type of data is presently being processed, and we can only present certain data pertaining to a period of

extreme minimum solar activity during the first half of February, 1964. Figure 18 shows the change in the recording rate for nuclei with  $Z \geq 2$  recorded by the outer counter. This same figure gives the readings from the neutron monitor of the Instituta Zemnogo Magnetizma i Radiovolnogo Rasprostraneniya (IZMIRAN) of the USSR Academy of Sciences in Krasnaya Pakhra and from the neutron monitor at Climax (altitude, 3400 m above sea level). The readings obtained on February 1 were 100% in every case. The lower part of the figure shows the number of solar spots for each day. Figure 18 illustrates the fact that between February 10-13 the readings of the IZMIRAN neutron monitor were 2% higher than on February 1, while the readings of the neutron monitor at Climax were approximately 1% higher. There were no solar spots between February 11-13. No chromosphere flares or bursts of radio emission were recorded on these days (between February 1-6, individual small flares and bursts were observed, when there were no solar spots). The Cherenkov counter readings for nuclei 528 with  $Z \geq 2$  reached a maximum on February 12-13; as compared with February 1, they had increased by approximately 10-15%. This increase was apparently related to the restoration of cosmic ray intensity during a period of weak solar activity in the first half of February.

#### REFERENCES

1. Dragun, G. S., Kurnosova, L. V., Logachev, V. I., Razorenov, L. A., Sirotkin, I. A., Fradkin, M. I. In "Iskusstvennyye Sputniki Zemli". Izdatel'stvo AN SSSR, No. 9, p. 86, 1961.
2. Ginzburg, V. L., Kurnosova, L. V., Razorenov, L. A., Fradkin, M. I. Uspekhi Fizicheskikh Nauk, 82, 585, 1964.
3. Tindo, I. P. Present collection, p. 533.

/529

VI

SUN

# X-RAY RADIATION OF THE SUN <sup>1</sup>

## (Summary)

S. L. Mandel'shtam

This represents a resumé of the main results derived from experimental and theoretical studies of X-ray radiation of the Sun in the spectrum region below 100 Å. /531

X-ray radiation of a quiet Sun extends to the shortwave spectral region up to several angstroms. This radiation is thermal in nature. In the shortwave section  $\lambda \leq 15\text{-}20$  Å, the radiation primarily has a continuous spectrum and is caused by recombination radiation for C, N, O ions and other elements included in the corona composition. In the 30-100 Å region, line radiation of these ions comprise about 2/3 of the stream, while continuous electromagnetic radiation and recombination radiation - caused by the interaction of corona electrons with hydrogen and helium ions - comprises about 1/3.

X-ray radiation, just like radio-frequency radiation, can be divided into a quasi-constant component radiated by unperturbed corona regions and a slowly-changing component radiated by the active regions (hotter and denser) in the solar corona. In the shortwave section of the X-ray region  $\lambda < 20$  Å, the contribution which is made by the quasi-constant component is very insignificant, and the radiation flux is primarily determined by the slowly-changing component. The radiation flux changes within very wide limits, depending on the number, dimensions, density, and temperature of the active regions. In the spectral region of 2-10 Å, it changes in order of magnitude from  $10^{-5}$  to  $10^{-3}$  erg·cm<sup>-2</sup>·sec<sup>-1</sup> while in the 8-20 Å region it changes from  $10^{-4}$  to  $10^{-2}$  erg·cm<sup>-2</sup>·sec<sup>-1</sup>. In the long-wave section of the X-ray region  $\lambda = 40\text{-}100$  Å, the contributions made by the quasi-constant and slowly-changing components are comparable, and the radiation flux changes within quite small limits - in order of magnitude from 0.1 to 0.5 erg·cm<sup>-2</sup>·sec<sup>-1</sup>.

Based on data from X-ray radiation measurements, the temperature of the active corona regions can amount to  $T_e \approx 2 - 2.5 \cdot 10^6$  K; the temperature of unperturbed regions amounts to  $T_e \approx 1 - 1.3 \cdot 10^6$  K. The electron density in the active regions exceeds the mean electron corona density by a factor of 5-10. The regions primarily generating X-ray radiation have angular dimensions of  $\sim 1\text{-}2'$ . They coincide with regions of increased radio-frequency radiation in centi- and decimeter bands, and are located above the strong calcium flocculi in the solar chromosphere. Apparently, these regions of increased heating penetrate the entire solar atmosphere above the photosphere right up to the corona, and can exist for a long /532 period of time - on the order of several solar days.

<sup>1</sup> This is a brief abstract of the report. The report was compiled on the basis of work by B. N. Vasil'yev, I. A. Zhitnik, L. P. Malyavkin, V. P. Prokudinaya, I. P. Tindo, A. I. Shurygin, Ye. P. Fesitov.

The present state of the theory now makes it possible to calculate the X-ray radiation fluxes within an accuracy of the coefficient 2 - 3, by utilizing the radiospectroheliograms of the Sun in the centimeter band. In principle, this makes short-range forecasts of X-ray radiation from a quiet Sun possible.

During chromosphere flares and other sporadic processes on the Sun, there are sharp changes in the X-ray radiation of the Sun. The stream of radiation increases, particularly in the shortwave section of the spectrum, and it is shifted toward the shortwave boundary of the spectrum.

Flares of X-ray radiation can be divided into two classes. Flares of class I are characterized by a comparatively long duration which can amount to several minutes, and usually last as long as the optical flare. The shortwave spectral boundary is shifted to approximately  $1 \text{ \AA}$ , and there is a great increase in the radiation energy close to this boundary (the total energy increase of X-ray radiation during a flare is not very great). Just as in the case of a quiet Sun, during a flare the radiation is thermal, and is caused by the corona plasma being heated in the region of the flare up to a temperature on the order of  $3 \cdot 10^6 - 10^7 \text{ }^\circ\text{K}$ .

Class II X-ray flares represent brief bursts lasting several tens of seconds, and arise during the initial stage of certain optical flares. During these flares, hard protons are formed having energies of  $1 \cdot 10^5 - 5 \cdot 10^6 \text{ ev}$ . This radiation probably has a thermal nature, and represents braking radiation or acceleration radiation of directional streams of accelerated electrons. These electrons may possibly be the result of instabilities arising in the corona plasma. The generation of accelerated particles can apparently occur during these flares. Particularly, so-called proton flares closely coincide with X-ray flares (in terms of ionosphere effects). Two cases have also been observed in which X-ray flares coincided with bursts of a heavy nuclei stream with  $Z > 15$ .

As regards X-ray radiation of a quiet Sun, it can be assumed that the main features of this radiation have been clarified to a sufficient extent, both from an experimental and from a theoretical viewpoint. Additional compilation of experimental data and a more precise definition of individual questions are necessary. As regards X-ray radiation of the Sun during flares, the situation is completely different. In order to make further progress on this problem, it is necessary to develop a general theory of flares and to compile more accurate methods for performing experimental studies. In particular, in order to make a distinction between "thermal" and "non-thermal" flares, it is necessary to study the line X-ray spectrum of the corona and the polarization of X-ray radiation during flares. A concurrent study must also be made during the flares of X-ray and corpuscular radiation of the Sun. A study of these problems may possibly reveal a method for warning cosmonauts of radiation danger.

## IMAGE OF THE SUN IN THE FAR SHORTWAVE REGION OF THE SPECTRUM (Summary)

I. A. Zhitnik, V. V. Krutov, L. P. Malyavkin, S. L. Mandel'shtam

An image of the Sun in the shortwave spectral region 170-400 Å was 533 obtained by means of a device located on a geophysical rocket, which was fired to an altitude of 500 km on June 6, 1963. It was found that regions of increased shortwave radiation intensity are located above the faculae fields, and remain on the Sun for at least a solar day.

---

## MEASUREMENT OF SOLAR X-RAY RADIATION INTENSITY BY MEANS OF THE SPACE STATION "ELEKTRON-2"

I. P. Tindo

Significant variations in a stream of soft X-ray radiation from a "quiet" Sun, as well as brief "bursts" of intensity, were studied during the flight of the space stations "Elektron-2" and "Elektron-4" at the beginning and in the middle of 1964.<sup>1</sup>

The radiation receivers in these experiments consisted of end-window Geiger photon counters, with windows made of beryllium<sup>2</sup> and aluminum<sup>3</sup> foil having a density of 25 and 2.7 mg·cm<sup>-2</sup>, respectively.

A significant portion of the "Elektron-2" orbit lay beyond the boundary of the outer radiation zone, in the region of space having a comparatively small stream of penetrating corpuscular particles. As will be shown below, the background radiation far from the boundary of the radiation zone was close to the level of the cosmic radiation background, and the stream of solar X-ray radiation could be measured with a high sensitivity.

In order to determine the level of interference from corpuscular particles, control counters were employed having an aluminum window, and in addition the counters were covered with gold and silver foil (0.77 and 1.05 mg·cm<sup>-2</sup>, respectively). The sensitivity of these aluminum counters to soft X-ray radiation was decreased by approximately two orders of magnitude due to the additional foil, while the sensitivity to

---

<sup>1</sup> Results of the experiments performed on the space station "Elektron-4" are being processed at the present time.

<sup>2</sup> Ye. S. Turlysova and I. A. Prager helped in the construction of the beryllium counters.

<sup>3</sup> Ye. P. Bogatova and V. G. Chaykovskiy helped in constructing the aluminum counters.

penetrating radiation was practically unchanged (Ref. 1).

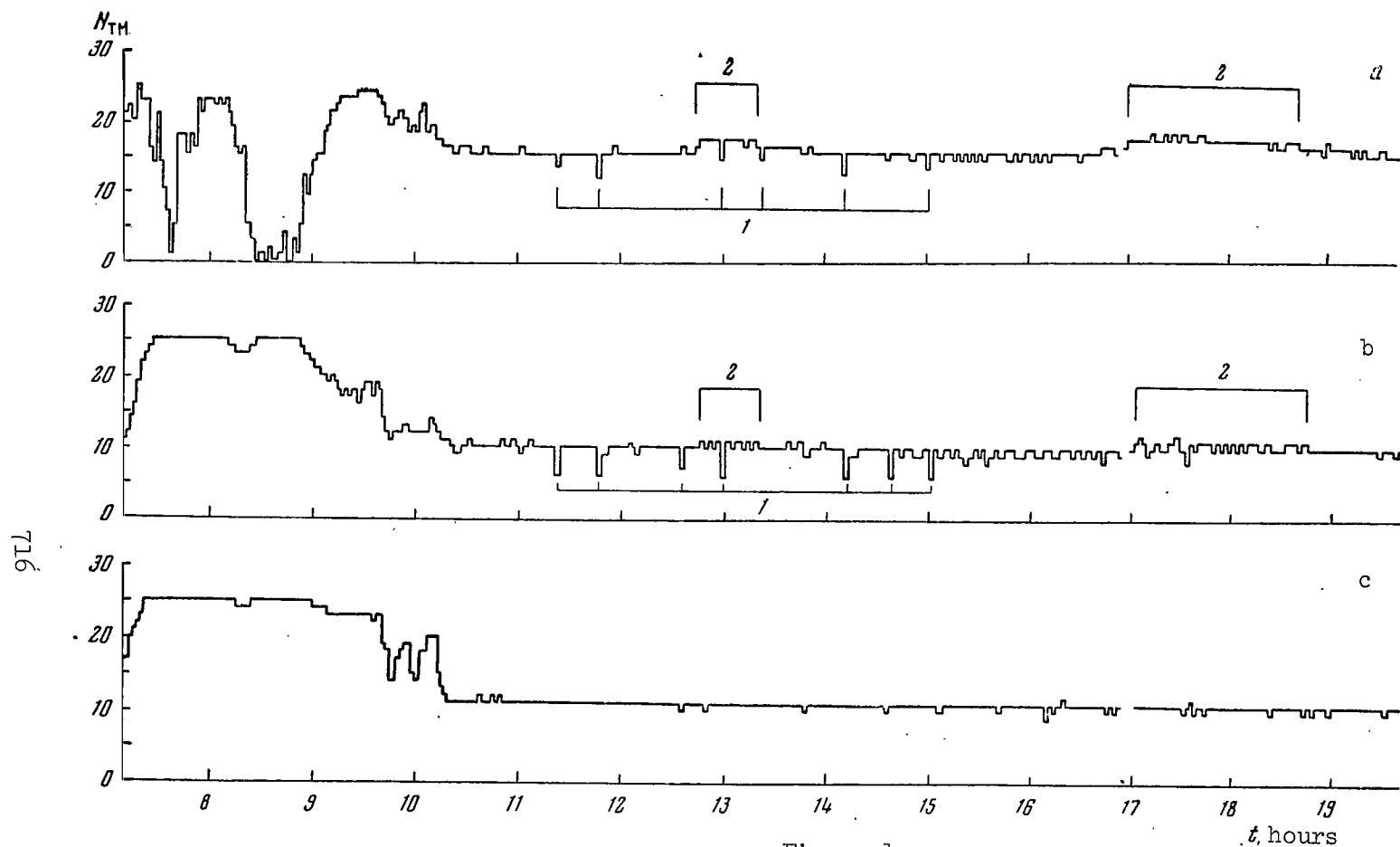
The counters were mounted in two recorder units, one of which was placed on the platform of an independent slave system which kept the counters constantly oriented on the Sun throughout the flight (Ref. 2). The second pickup block was mounted securely on the outside of the instrument capsule. In order to make sure that the Sun was in the counters field of vision, a photorecorder - a silicon phototransformer which was sensitive to visible light - was placed in each block. /534

The radioelectronic system of the device recorded the maximum rate at which impulses were recorded from each group of counters during the exposure time, which comprised 2 or 8 minutes in different orbit revolutions. The averaging time (integration) in determining the maximum recording rate was about 2 seconds. The recording rate was fixed by an electronic system within the limits of 1 out of 30 discrete levels, distributed according to the dynamic range of  $1-10^4$  impulse $\cdot$ sec $^{-1}$  - distributed equidistantly in a logarithmic scale. This recording system provided for an approximately constant relative measurement accuracy throughout the entire band: with an error of not more than 35% of the measurable quantity, when a relatively small amount of information transmitted to the memory device was retained. A detailed description of the individual units in the radioelectronic block of the device, which was developed by B. N. Vasil'yev, is given in the work (Ref. 3).

Figure 1 shows a typical example of the readings from the device obtained on the ascending branch of the third revolution of the space station "Elektron-2". As can be seen from the picture, the sections of a high recording rate, corresponding to great interference from particles of the radiation zones, occupy only an insignificant portion of the revolution<sup>1</sup>. The boundary of the outer zone, which was determined from our readings, closely coincided with the results of simultaneous measurements performed by a special apparatus designed to study corpuscular radiation (Ref. 4). In the revolution section located above the zones, the recording rate in the period from January 30 to March 16, 1964, changed within comparatively narrow limits - from 30 to 500 impulse $\cdot$ sec $^{-1}$  for a beryllium counter, and from 10 to 300 impulse $\cdot$ sec $^{-1}$  for an aluminum counter. The fluctuations in the recording rate in this section of the revolution, which are shown in Figure 1, are partially related to the influence of the discrete encoding device (fluctuations per  $\pm 1$  logarithmic unit), and partially related to normal fluctuations in the recording rate.

In addition to these "equipment" effects, recurrent minima of the recording rate (points 1 in Figure 1) are observed, occurring when the counters were in the shade as the station rotated. Finally, there were

<sup>1</sup> There was a decrease in the recording rate of the beryllium counter up to zero close to the intensity maximum of the outer radiation zone. This decrease was caused by strong "off-scale reading". When less intense solar x-ray radiation was measured, this phenomenon did not occur.



Sample of Instrument Recordings on January 1, 1964

The numbers of the code, which were written by the peak memory device, and which correspond approximately to the logarithm of the impulse recording rate, are plotted along the ordinate axis. a - beryllium; b - aluminum; c - control counters. World time. Apogee of the station for the Sun-Earth-station angle  $\gamma-135^\circ$ .



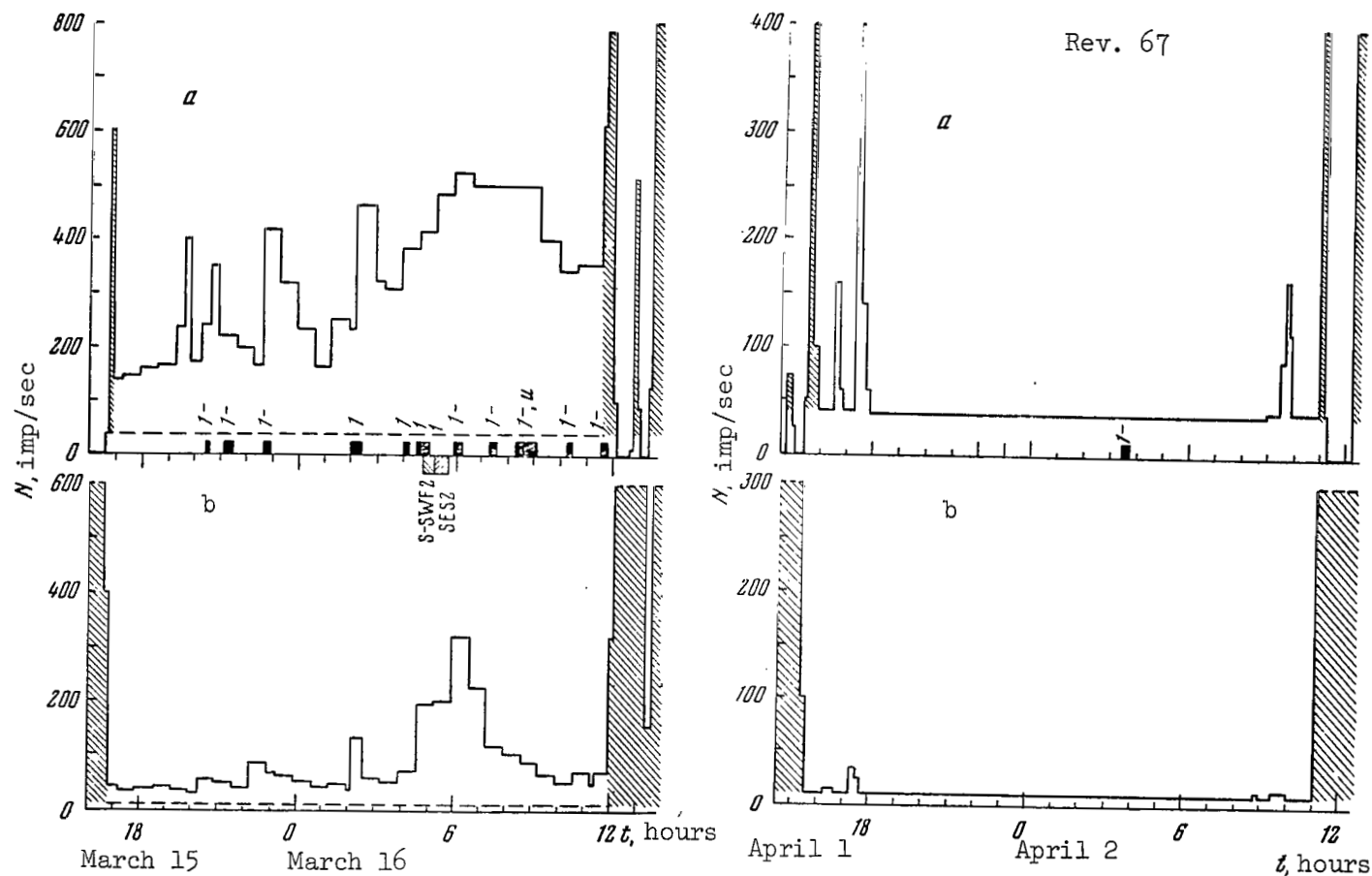


Figure 2

Recording Rate of Beryllium, Aluminum, and Control Counter on the 3, 22, 49, and 67th Revolutions  
(On the 67th Revolution, the Counters Were Constantly Shaded)

a - beryllium; b - aluminum; c - control counters. World time. The beginning and end of chromosphere flares (squares), the class of the flare, and data on the ionosphere effects (S-SWF, SES) are given on the abscissa axis of graph a. The shaded portions correspond to large interference from radiation zone particles and the dashed line corresponds to the level of the cosmic background.

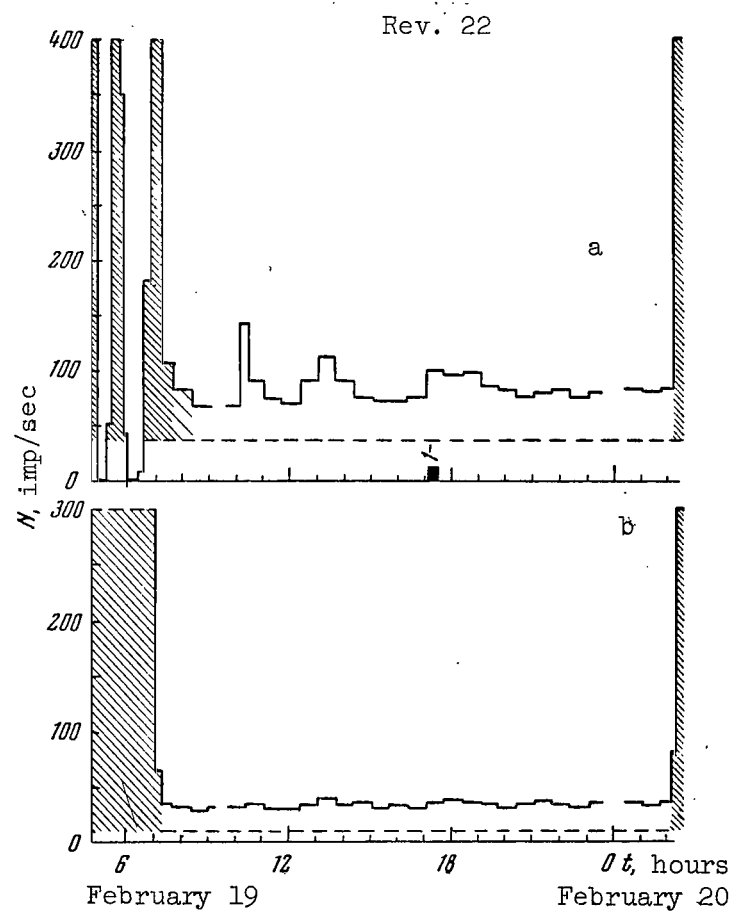
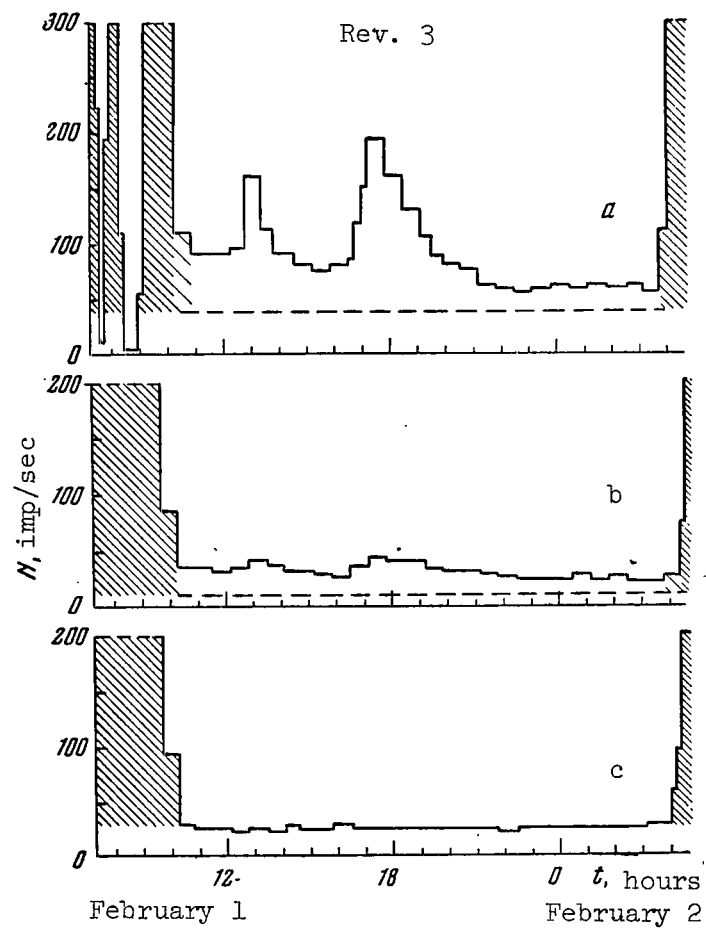


Figure 2 (continued)

longer increases in the recording rate (points 2 in Figure 1), which were caused by bursts of X-ray solar radiation or by penetrating particles of sporadic corpuscular streams. The points corresponding to exposures during which the Sun did not once enter the counters' field of vision (points 1 in Figure 1) were employed to determine the background level.

Figure 2 presents the averaged, typical curves for the recording rate for the third, twenty-second, and forty-ninth revolutions, pertaining to periods of different solar activity. As was indicated by the data obtained, the beryllium counters operated normally throughout the entire active operation of the station. The aluminum counter of the orientable block operated normally throughout the entire flight. An analysis of the recordings from the control counters showed that one of the two (connected in "parallel") counters changed into self-maintained discharge after two weeks of flight. Therefore, in the following period it was not possible for us to distinguish between corpuscular streams based on readings from the control counters of our device. Nevertheless, the general form of the curves shown in Figure 2 is as follows. The sharp boundary of the outer radiation zone and the absence of a clear dependence of the rate at which impulses were recorded on the position of the station in the orbit, the relative constancy of the mean recording rate in the remaining portion of the revolution, and finally the recording of significant bursts of intensity also close to the apogee - all of this leads to the assumption that in the following period in the overwhelming majority of cases the interference level was small, and X-ray solar radiation was recorded. This conclusion received confirmation during measurements from the second half of March to the beginning of May. During this period, beyond the boundary of the outer zone the recording rate of beryllium and aluminum counters when they were shaded did not usually rise above a level which was comparable with cosmic ray background, except for two cases in which particles were recorded from the outermost quasi-stationary zone on April 1 and April 2, 1964. These are shown in Figure 2 (revolution 67). /538

Electron streams having energies of  $E \geq 70$ -100 keV were measured on the space station "Elektron-2" by means of a special apparatus by S. N. Vernov, Yu. I. Logachev, E. N. Sosnovets et al. (Ref. 4). These measurements made it possible to directly determine the possible level of interference during the subsequent operational period of our device. According to these measurements, beyond the limit of the outer radiation zone a flux of electrons having the indicated energies is usually no greater than  $4 \cdot 10^2$ - $10^3$  electron $\cdot$ cm $^{-2}$  $\cdot$ sec $^{-1}$ . Assuming that the energy spectrum of electrons is as follows

$$N_{E \geq E_0}(E) = KE^{-\alpha},$$

we find that their contribution to the recording rate must not exceed the quantities shown in Table 1.

TABLE 1

$\alpha$	1	2	4	8
Be-counter ( $E \geq 200$ kev), impulse $\cdot$ sec $^{-1}$ . . . . .	20	10	3	0.2
Al-counter ( $E \geq 50$ kev), impulse $\cdot$ sec $^{-1}$ . . . . .	0.6	1.2	5	80
Ratio of Recording Rates (Be/Al) . . . . .	33	8	0.6	$2.5 \cdot 10^{-3}$

The recording rate ratios actually measured outside of these zones (after the cosmic ray background was deducted) fluctuated from 3-8, i.e., if it is assumed that the readings are caused by the recording of corpuscular particles, then their spectrum would correspond to  $\alpha \approx 3$ . However, the absolute recording rates corresponding to the recording of electrons can only comprise a few percent of the total recording rate measured experimentally - i.e., the counters record only X-ray radiation of the Sun and the cosmic ray background. It may also be noted that this low interference level caused by corpuscular streams is primarily due to the fact that the space station "Elektron-2" at large distances from the Earth traveled at high geomagnetic latitudes ( $\varphi_m \sim 60-70^\circ$ ). Measurements of a stream of electrons having energies of  $E \geq 45$  kev, which were recently carried out on the satellite "IMP-1" and which encompassed distances up to  $31.5 R_e$  at a low geomagnetic latitude, showed that in this portion of circumterrestrial space in the  $\gamma = 0$  direction (i.e., the local "midnight") there was a significant quasi-constant flux up to  $10^4$  electron $\cdot$ cm $^{-2} \cdot$ sec $^{-1}$ . This flux contained individual "islands" with a flux of up to  $10^6$  electron $\cdot$ cm $^{-2} \cdot$ sec $^{-1}$ , which were sharply defined in terms of latitude and whose frequency of appearance decreased as the craft receded from the Earth (Ref. 5).

When analyzing the results obtained beyond the boundary of the radiation zones, we determined the level of radiation from a "quiet" Sun during the period of January 30-March 16, 1964. For this purpose, we selected the mean recording rate during one day from 20 to 21 hours, in order to facilitate a comparison with data from radiospectroheliograms obtained simultaneously. The method of utilizing these data for forecasting the X-ray radiation level has been described in several works (Ref. 6, 7). In individual cases, when active processes were observed on the Sun during a period of 20-21 hours, the magnitude of the recording rate in the closest "quiet" period was employed. Figure 3, a and b, presents the results obtained after the cosmic background level was deducted. As these graphs show, even when there were no active formations on the disc, the intensity of radiation with  $\lambda < 18 \text{ \AA}$  and  $\lambda < 10 \text{ \AA}$  did not drop to zero, even though it decreased to almost the threshold sensitivity of the

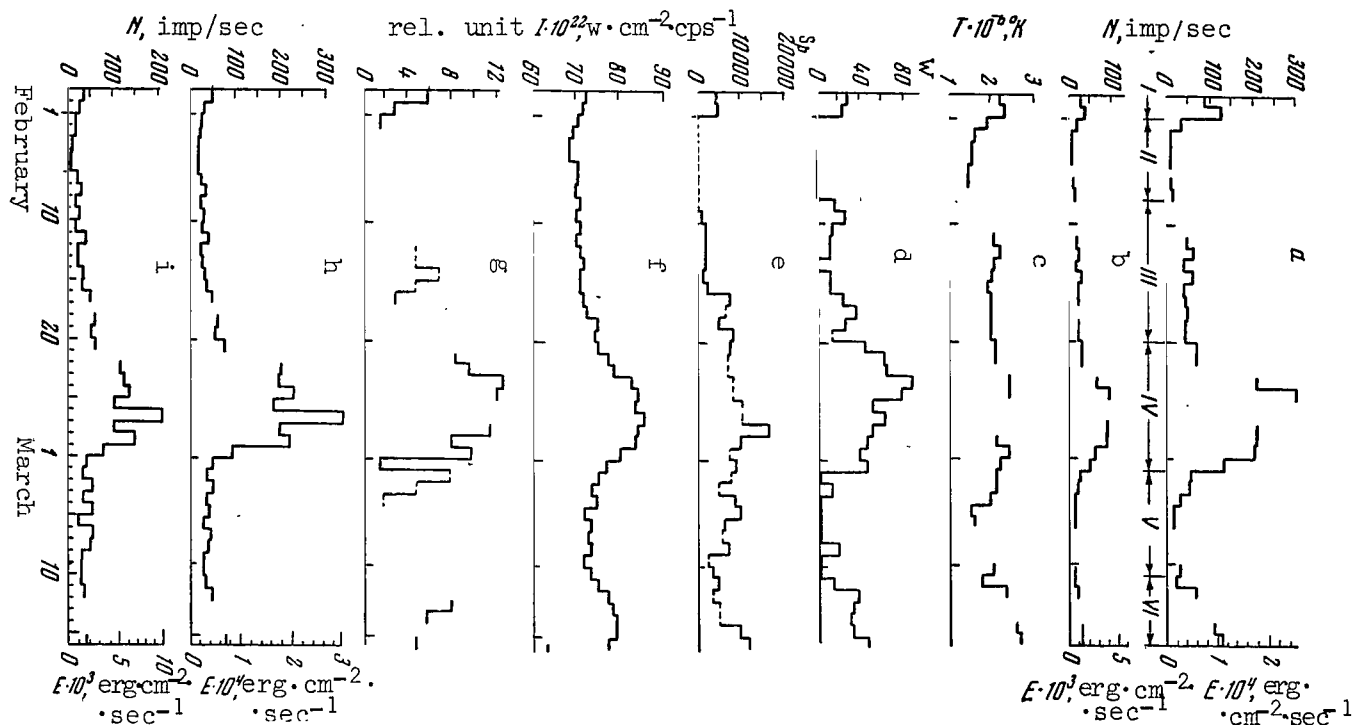


Figure 3

Stream of X-Ray Radiation from a "Quiet" Sun During the Period  
from January 31 to March 16, 1964

a, b - Recording rate of beryllium and aluminum counters, and the radiation stream determined from these data in the spectral regions of 2-10 and 8-18 Å respectively; c - Effective "color" temperature (based on counter data); d - Wolf number (Ref. 8); e - Total Area of Flocculae (Data from [Ref. 8] indicated by solid line and data from [Ref. 9] indicated by dashed line) in  $10^{-6}$  fractions of the hemisphere area; f - Radio-frequency radiation stream in the 10.7 wave (Ref. 9); g - Radiation stream from local radio sources on the solar disc at the  $\lambda = 6.6$  cm wave, in percentages of the integral stream (according to the special report of G. B. Gel'freykh); h,i - expected calculated recording rate of beryllium and aluminum counters.

TABLE 2

Recording Time of X-Ray Solar Radiation During the Period From January 30 to March 16, 1964

Date	Observational Time Hours, Minutes	Date	Observational Time Hours, Minutes	Date	Observational Time Hours, Minutes	Date	Observational Time Hours, Minutes	Date	Observational Time Hours, Minutes
1/30	12 00-24 00	2/6	03 40-20 40	2/14	13 30-24 00	2/20	06 00-24 00	3/2	12 40-24 00
1/31	00 00-06 40 12 10-24 00	2/7	01 15-19 05	2/15	00 00-06 35 12 00-24 00	2/21	00 00-00 35 02 50-19 00	3/3	00 00-07 10 13 25-24 00
2/1	00 00-04 35 10 15-24 00	2/11	00 00-13 35 17 40-24 00	2/16	00 00-06 35 12 00-24 00	2/24	00 30-18 40 18 35-24 00	3/4	00 00-05 50 08 40-24 00
2/2	00 00-04 00 08 35-24 00	2/12	00 00-11 35 16 10-24 00	2/17	00 00-05 50 09 35-24 00	2/28	00 00-12 20 16 35-24 00	3/6	00 00-03 50 01 25-19 20 23 20-24 00
2/3	00 00-03 00 07 50-24 00	2/13	00 00-09 30 15 20-24 00	2/18	00 00-04 30 07 25-24 00	2/29	00 00-10 50 14 45-24 00	3/12	00 00-17 40
2/4	00 00-00 10	2/14	00 00-09 00	2/20	00 00-02 10	3/2	00 00-08 30	3/15	16 50-24 00 3/16 00 00-11 35

apparatus employed. For purposes of comparison, Figure 3 presents certain other quantities illustrating the correlation with the intensity of solar X-ray radiation, as well as curves h and i representing the expected calculated recording rate of Be- and Al-counters, constructed on the basis of data from radiospectroheliograms according to the method described previously (Ref. 6, 7).

The period of our observations was broken down into several intervals according to the general level of solar activity. These intervals can be clearly seen in the recordings of X-ray counters (see Figure 3, a and b): I - January 30-31, on the western edge of the solar disc a large group of spots was observed No. 9, a radio emission region No. 10, and the flocculae related to them (Ref. 8); II - February 1-7, a quiet period, there were no spots or flocculae on the disc; III - February 8-12, new groups of spots appeared on the disc; February 13 there were no spots or pores on the disc; February 14 and February 16 groups No. 10 and No. 9, as well as the radio emission group No. 17, again appeared on the eastern edge; IV - February 20, a rapidly-developing group No. 18 appeared; groups of spots were observed in the following days up to March 1; V - from March 2 up to March 10 there were no spots on the disc (except for March 3 and March 8), and only flocculae remained which were visible on the disc until March 5; VI - on March 11, a new period of activity commenced, which was related to the radio emission region No. 23, the large group of spots No. 18, etc.

A comparison of the graphs a, b, d in Figure 3 shows that the intensity of X-ray radiation with  $\lambda = 2 - 10 \text{ \AA}$  coincides in its general features with the relative number of solar spots during the period investigated. The radiation recorded by the aluminum counter ( $\lambda = 8-18 \text{ \AA}$ ) was somewhat "colder" as compared with this index of activity.

This correlation was sometimes disturbed in particular details, for example on February 1 and March 2, when groups of spots appeared behind the western edge of the disc, while the level of X-ray radiation still remained high. This effect could be expected, if we take into account the difference in altitude of coronal condensations, in which X-ray radiation primarily occurs, and photosphere spots.

A comparison with the total flocculae area determined simultaneously shows that this activity index does not coincide as well with the intensity of X-ray radiation. Thus, from March 4 to March 12 the counters recorded a low level of radiation when there were significant groups of flocculae on the solar disc.

As can be seen from Figure 3, f, the integral (with respect to the disc) stream of radio emission at the 10.7 cm wave changes in its general features parallel with the stream of X-ray radiation, although in significantly narrower limits, particularly as compared with data from the short-wave beryllium counter. This conclusion coincides with the results of our previous studies, and also with the studies of other authors (Ref. 10, 11), and leads to the assumption of increased temperature in the coronal

condensations in which thermal X-ray radiation occurs. The conclusion is also confirmed in Figure 3,c, which shows the effective color temperature change of radiation determined by the recording rate ratio of the beryllium and aluminum counter. The temperature values obtained lie within /541  $(1.5-2.5) \cdot 10^6$  °K for the entire observational period. The data from the radiospectroheliograms show that during the active days only one (or two) regions make the main contribution to radiation each time. In this case, it can be assumed that the electron condensation temperature is close to the effective temperature measured by the counters  $(\sim 2 - 2.5) \cdot 10^6$  °K.

As would be expected, the variations in the radiation flux of local radio sources, measured with the large Pulkova radio telescope at the 6.6 cm wave<sup>1</sup>, closely coincide with the curve showing the change in X-ray radiation intensity which occurs in the regions of "hot condensations" which are related to groups of spots and floccular fields. However, at very short waves ( $\lambda = 6.6$  cm) the acceleration component apparently makes a significant contribution, whereas it has been determined that X-ray radiation of a quiet Sun has purely a thermal nature (Ref. 7, 10). This fact limits the possible degree of similarity between graphs a, b, and g in Figure 3. We have previously pointed out (Ref. 6, 7) the close correlations between a stream of X-ray radiation and the structure of the radio image at the 9.1 cm wave. This correlation can be clearly seen when the experimental and calculated curves of Figure 4, a, b, h and i are compared. In order to obtain agreement with the experimental results, we assume that an electron temperature of  $T_e$ : 1.0; 1.50; 1.75 and  $2.5 \cdot 10^6$  °K must be attributed to regions on the solar disc having the following brightness temperature at the 9.1 cm wave:  $T_B \leq 30, 30 < T_B \leq 60, 60 < T_B \leq 150$  and  $T > 150 \cdot 10^3$  °K. When the radiation flux was calculated, the emission rates  $Y = \int n_e^2 dV$  were employed; these rates were determined by radio data (Ref. 9). Such a determination of the emission rate assumes that thermal X-ray radiation and radioemission are produced in one and the same regions of the corona, and this determination is valid if the optical thickness is  $\tau \ll 1$  in both cases. The possibility is not excluded that the inclusion of other active region characteristics for determining the temperature  $T_e$  - for example, data on the increase in a group of spots (Ref. 11) - would make it possible to obtain still more precise correlation with the flux of the "slowly-changing" component of X-ray solar radiation.

It is interesting to compare the energy flux simultaneously determined on the space station "Elektron-2" and on the satellite "SR-IV" (USA) during the period from February 14 to February 22, 1964 (Ref. 12)

Based on data from our measurements, during this period the flux in the spectral region 0-10 Å was  $E(0-10) \leq 1 \cdot 10^{-5} \text{ erg} \cdot \text{cm}^{-2} \cdot \text{sec}^{-1}$ ; in the 0-20 Å region, the flux was  $E(0-20) \approx 2 \cdot 10^{-3} \text{ erg} \cdot \text{cm}^{-2} \cdot \text{sec}^{-1}$ . Preliminary

---

<sup>1</sup> According to the special report of G. B. Gel'freykh.



TABLE 3

BURSTS OF X-RAY RADIATION BASED ON DATA FROM BE- AND AL-COUNTERS

/543

Date (1964)	X-Ray Bursts				Optical Observations		Interference Level		De- vice	
	Time; Hours, Minutes		Mean Increase in Recording Rate , impulse·sec <sup>-1</sup>		Time; hours, Minutes		Type and Class of Phenom- enon	Recording Rate, impulse·sec <sup>-1</sup>		
	Be- gin- ning	Dura- tion	Be	Al	Begin- ning	Dura- tion				
1/31	05 32	01 14L	109	11				5	3	1;2
2/1	03 38	16	122	6				15	5	1
	16 45	02 32	76	10				15	5	1
2/11	19 38	01 02	70	16						
2/14	14 06	18	108	7	14 10	17	Ch1			
2/17	10 14	22	116	4				5	3	2
2/20	08 56	02 32	64	8	10 14	10	Ch1-			
	16 48	01 28	80	7	18 02	06E	Ch1-			
2/23	03 36	03 04	122	39	05 00E	03 00L	Ch1-	5	3	2
	06 40	01 36	240	125	06 45E	01 45	Ch1	5	3	2
	17 44	01 04	152	52	18 18	24	Ch1	5	3	2
2/24	03 36	03 36	142	155				5	3	2
	10 00	16	130	72	10 08E		Ch1-	5	3	2
	15 20	16	130	72				5	3	2
2/27	23 18	36	102							
2/28	01 50	20	109							
	09 50	18	110	6	09 39	07	Ch1			
2/28	10 20	45	110		10 41	09L	Ch1-			
	20 38	03 20	110	4	23 30	35	Er <sup>2</sup>	5	3	2
3/4	02 56	12	100							
3/5	11 10	06	114	3	11 15E	09L	Ch1-	5	3	2
3/12	09 57	40	168	25	09 54E	50L	Ch1	5	3	2
	14 29	16	195	33				5	3	2
	15 09	16	260	53	15 13E		Ch1	5	3	2
	15 49	16	140	33				5	3	2
3/15	19 19	10	146							
	19 36	16	220							
	20 20	40	130		20 27	09L	Ch1-			
	21 18	38	130		21 08E	22L	Ch1-			
	22 35	02 00	320		22 39E	16L	Ch1-			
3/16	01 26	34	104							
	02 07	01 02	320		02 01	21	Ch1			
	03 45	24	260		03 59	10	Ch1			
	04 43	04 46	340		04 31	25	Ch1			

Continuation of TABLE 3

BURSTS OF X-RAY RADIATION BASED ON DATA FROM BE- AND AL-COUNTERS

X-Ray Bursts					Optical Observations			Interference Level		De- vice
Date (1964)	Time; Hours, Minutes		Mean Increase in Recording Rate, impulse·sec <sup>-1</sup>		Time; hours, Minutes		Type and Class of Phenom- enon	Recording Rate, impulse·sec <sup>-1</sup>		
	Be- gin- ning	Dura- tion	Be	Al	Begin- ning	Dura- tion				
					04 46	12	Ch1			
					07 17	13	Ch1-			
					08 11	41	Ch1			

NOTATION: E - phenomenon began earlier; L - phenomenon terminated later, or continued longer; Ch - chromosphere flare; Er- eruptive prominence on the limb; 1 or 2 in the last column mean:

1 - Interference level was determined from readings of the control counter on the device,

2 - interference was determined from data of the scintillation counter (electrons with  $E \geq 70 - 100$  kev [Ref. 4]).

results from American measurements, performed with less sensitive apparatus, have shown that the radiation intensity was below the detection threshold, i.e.,  $E(0 - 8) < 2 \cdot 10^{-4}$  and  $E(0 - 20) < 0.9 \cdot 10^{-3}$  erg·cm<sup>-2</sup>·sec<sup>-1</sup>.\*

\* When the magnitude of the stream was determined from equipment readings in the work (Ref. 12), it was assumed that the spectral distribution of the energy corresponds to a "grey" emitter with  $T_{\text{color}} = 2 \cdot 10^6$  °K. In our study, we used the spectrum of a plasma thermal radiation with  $T_e = 2 \cdot 10^6$  °K. The absolute counter effectiveness employed in the calculations may be exaggerated when part of the photoelectrons are captured by the electronegative component of a gas filling. At the present time, experimental verification of this effect is being conducted.

This does not contradict the results of our observations. The significant increase in radiation intensity with  $\lambda < 20 \text{ \AA}$  in the period from February 23 to March 1, 1964, which is clearly apparent in Figure 3, b, was also determined by the American researchers (Ref. 12).

While the equipment was in operation, a large number of "bursts" was observed in the intensity of X-ray radiation; these bursts lasted from several minutes up to several hours.<sup>1</sup> The intensity changes were more significant in the shortwave region of the spectrum recorded by the beryllium counter, but the "bursts" were significant in the recordings of the aluminum counter. Table 2 presents the time intervals in which these measurements were performed. Gaps in the observations are due to interference from the radiation zones or are due to the absence of telemetry information. Table 3 presents data on sporadic radiation intensity increases caused by a significant increase in the recording rate of the Be-counter during the period from January 30 to March 16, 1964. This Table also presents the results derived from simultaneous optical observations (Ref. 8, 9). The times presented in Table 3 for the beginning and duration of X-ray bursts are known within an accuracy of  $\pm 2$  (or  $\pm 8$ ) minutes, in conformity with the period during which the memory device was interrogated. These times were determined from the recordings of the beryllium counter, since the "bursts" in the recording rate of the aluminum counter were smaller, and the corresponding times were therefore not always accurately determined. Table 3 also presents the duration of the bursts and the mean increase in the recording rate of both counters during the time in which it appeared above the quiet level. The subsequent table columns contain data on the beginning, duration, type, and class of the phenomena recorded by observatories on the Earth. Finally, the last columns indicate the upper limit of the interference level from streams of energetic electrons, which could distort the counter readings; this upper limit was determined from data derived from the sensors on the station "Elektron-2". A preliminary analysis shows that only in 9 cases during the period from January 30 to February 16, when the station was located outside of the outer radiation zone (but comparatively close to its boundary), were the recording rate maxima definitely caused by streams of energetic electrons ( $E \geq 200 \text{ kev}$ ) being recorded. These maxima are given in Table 4, and the last column of this table indicates the cases when corpuscular streams were recorded simultaneously by the apparatus of S. N. Vernov et al. (Ref. 4). In other cases, the

---

<sup>1</sup> We could not analyze single bursts - lasting 2 (8) minutes - due to individual random errors in the encoding; these errors were possible due to the fact that the inputs of the recording system were not blocked when the telemetry was interrogated.

TABLE 4  
RECORDING OF PARTICLES

Date (1964)	Data from X-ray Device, Hours, Minutes		Based on Data from (Ref. 4), Hours, Minutes
	Beginning	End	Time of Maximum
1/31	11 16	12 02	
2/2	9 55	10 08	
	3 00	3 50	3 15
	5 40	5 50	
2/7	7 15	7 25	
	17 20	17 30	17 15
2/13	9 45	10 20	10 10
2/16	10 50	11 08	10 52
	11 18	11 32	11 24

intrusion of corpuscular streams having small energies into circumterrestrial space was not accompanied by a significant change in the counter recording rates. This was the case, for example, during 3-9 hours on February 12, and 8 hours 30 minutes on February 20, when powerful streams were discovered from the readings of the ion trap and the magnetometer on the station "Elektron-2", and when magnetic storms "with a sudden commencement" were simultaneously recorded on the Earth (Ref. 13). /545

For all the "bursts" shown in Table 4, there are data derived from a patrol of chromosphere flares which was performed by observatories on the Earth. About one-half of the recording rate maxima given in the table coincide in time with the periods of small chromosphere flares of class I - and I. The maximum phase of the flare beginning at 21 hours on February 28 coincided with the development of an eruptive prominence on the edge of the disc. The remaining "bursts" of X-ray radiation were not accompanied by significant phenomena in the optical region. Only one burst of X-ray radiation, which was recorded simultaneously with the development of a

class 1- chromosphere flare beginning at 18 hours, 22 minutes, on February 23, was accompanied by a burst of type III (Ref. 9).

In two cases (12 hours, 45 minutes on January 31, and 8 hours, 27 minutes on March 2) unusual phenomena were observed in the radio-frequency region when the station "Elektron-2" passed close to the boundary of the outer zone, where it was difficult to determine the interference level.

An examination of Table 3 shows that the observed "bursts" of X-ray radiation lasted for a long period of time which was comparable to, and sometimes significantly exceeded, the time required for simultaneous chromosphere flares to develop. The possibility is not excluded that several of the "bursts" actually represent a series of consecutive processes lasting a shorter period of time. The averaged "color" radiation temperature of the "bursts", determined on the basis of the ratio for recording rate increases in the Be- and Al-counters, was usually no greater than  $10^7$  °K. It is interesting to determine the possible size of the emissive region, under the assumption of a thermal mechanism in the burst radiation. Assuming that  $T_e \sim 4 \cdot 10^8$  °K,  $n_e \approx 10^9$  electron·cm<sup>-3</sup>, we can obtain the observed magnitude of the stream  $E(2 - 10) \sim 5 \cdot 10^{-4}$  erg·cm<sup>-2</sup>·sec<sup>-1</sup> from a region having a size of  $10^{28}$  cm<sup>3</sup>. Making the conditional assumption that the emissive region is in the form of a cube, we obtain its apparent angular dimension of  $\sim 1'$ , which is typical for so-called sporadic condensations which usually exist on the Sun for several hours.

In connection with the problem of the generation of relativistic particles on the Sun, considerable interest is afforded by two bursts of X-ray radiation intensity, one of which began at 22 hours, on January 31- the other began at 2 hours, 15 minutes, on February 14. In both cases, the recording rate increase of the beryllium counter was about 100 impulse·sec<sup>-1</sup>. According to data from the measurements of L. V. Kurnosova et al., which were performed on the station "Elektron-2", these bursts were accompanied by a significant increase in a stream of heavy nuclei with  $Z \geq 15$  (Ref. 14).

In accordance with the computational results, it can be expected that "bursts" of X-ray radiation, whose intensity is similar to those listed in Table 3, must not cause significant ionosphere effects (Ref. 15). Actually, during our observation period from January 30 to March 16, 1964, only four fadings were recorded: one at 20 hours, 25 minutes on February 13, which did not pertain to any chromosphere flare, and also three fadings related to flares of class 1: at 8 hours 25 (E) minutes on March 11, at 21 hours, 32 (E) minutes on March 12, and at 4 hours, 46 minutes on March 16 (Ref. 9). According to data from our measurements, the first two flares were only accompanied by a negligible increase in the radiation flux [ $E(2 - 10) \sim 1 \cdot 10^{-5}$  erg·cm<sup>-2</sup>·sec<sup>-1</sup>]. The latter flare corresponds to a significant intensity burst; however, as can be seen from Figure 2 (revolution 49), a class 1- flare followed by a trail behind it produced a more powerful burst.

In addition to comparatively large intensity "bursts", a large portion of which are presented in Table 3, about 100 smaller recording rate maxima were recorded while the equipment was in operation. In almost /546 all of these cases, optical observations did not reveal any active processes on the Sun. On the contrary, only in five cases of chromosphere flares (class 1-) did the recorders detect any increase in the flux of X-ray radiation. These data show that the patrolling of X-ray bursts, particularly in the case of  $\lambda < 10 \text{ \AA}$ , is one of the most sensitive methods for discovering active processes on the Sun - at least during a minimum year, when the integral (with respect to the disc) flux of X-ray radiation (the "slowly-changing component") is small.

During the period from February 23-24, flares of X-ray radiation were also recorded by photometers of the American satellite "SR-4" (Ref. 12). In particular, according to these data at 7 hours, 04 minutes, on February 23, a flux of radiation with  $\lambda > 8 \text{ \AA}$  exceeded the sensitivity threshold of the photometer and increased up to  $1 \cdot 10^{-3} \text{ erg} \cdot \text{cm}^{-2} \cdot \text{sec}^{-1}$  in a few minutes time. According to our data, at this moment an intensity maximum was also observed corresponding to the flux  $E(0-8) \geq 2 \cdot 10^{-4} \text{ erg} \cdot \text{cm}^{-2} \cdot \text{sec}^{-1}$  ( $T_e \sim 2 \cdot 10^6 \text{ }^\circ\text{K}$ ). According to our data, the beginning of the flare could be traced from 06 hours, 40 minutes ( $\pm$  08 minutes), which closely coincides with the beginning of the class 1- chromosphere flare at 6 hours, 45 minutes E. According to our data, the increased radiation level was retained up to 8 hours, 10 minutes, while the visible flare terminated at 8 hours, 30 minutes.

Another report will present a more detailed analysis of the data obtained.

The author would like to express his appreciation to S. L. Mandel'shtam for supervising the work, and also to S. N. Vernov, E. Sosnovets, G. B. Gelf'reykh for the use of their observational material.

#### REFERENCES

1. Mandel'shtam, S. L., Voron'ko, Yu. K., Tindo, I. P., Shurygin, A. I., Vasil'yev, B. N. Doklady AN SSSR, 142, No. 1, 77, 1962.
2. Kalashnikov, V. A., Kuz'min, V. P., Zhivoglotov, V. N., Aleksandrov, A. V. Kosmicheskiye Issledovaniya (in press).
3. Vasil'yev, B. N. Kosmicheskiye Issledovaniya (in press).
4. Vernov, S. N., Chudakov, A. Ye., Vakulov, P. V., Sosnovets, E. N., Kuznetsov, S. N., Stolpovskiy, V. G., Logachev, Yu. I. Present Collection, p. 425.

5. Anderson, K. A., Harris, H. K., Paoli, R. J. Energetic Electron Fluxes in and Beyond the Earth Magnetosphere. Series 5, Issue 50, Phys. Dept. and Space Sci. Lab. Univ. Calif. Berkley, Calif. 1964.
6. Tindo, I. P., Shurygin, A. I. Kosmicheskiye Issledovaniya, 3, 262, 1965.
7. Mandel'shtam, S. L., Prokudina, V. S., Tindo, I. P., Fetisov, Ye. P. Kosmicheskiye Issledovaniya (in press).
8. Solar Data. January-March, 1964 (Solnechnyye Dannyye. Yanvar' - Mart 1964).
9. Solar and Geophysical Data. HAO Boulder, CRPL-F, part B, No. 234-236, Feb.-Apr. 1964.
10. Shklovskiy, I. S. Astronomicheskiy Zhurnal, 41, No. 4, 676, 1964.
11. Neupert, W. M. Space Res., 4, 1964.
12. Creplin, R. W. Proc. COSPAR Simpos. Florence, Italy, 1964 (in press).
13. Gringauz, K. I., Dolginov, Sh. Sh., Bezrukikh, V. V., Yeroshenko, Ye. G., Zhuzgov, L. N., Musatov, L. S., Solomatina, E. K. Doklady AN SSSR, 159, 172, 1965.
14. Kurnosova, L. V., Mandel'shtam, S. L., Razorenov, L. A., Tindo, I. P., Fradkin, M. I. Kosmicheskiye Issledovaniya (in press).
15. Creplin, R. W., Chubb, T. A., Friedman, H. J. Geophys. Res., 67, 2231, 1962.

# COSMIC RAY GENERATION ON THE SUN

A. N. Charakhch'yan, T. N. Charakhch'yan

From the data derived from cosmic ray measurements on the surface of the Earth alone, it might be thought that cosmic ray generation on the Sun is a rare event occurring once in three or four years, but in actual fact this is not so. This may be seen from the table, where  $m_{str}$  is the ratio of primary cosmic-ray intensity during several bursts to ordinary intensity, derived from measurements in the stratosphere, and  $m_{de}$  is the percentage deviation of terrestrial equipment (neutron monitor) readings during the same bursts. It is apparent that the terrestrial equipment readings are practically zero in a number of cases, because of the tremendous increase in the number of primary cosmic rays in the stratosphere. /547

TABLE

Date of Chromosphere Flare	Time (Universal) hr-min	$m_{str}$	$m_{de},\%$	Date of Chromosphere Flare	Time (Universal) hr-min	$m_{str}$	$m_{de},\%$
3/17/58	10 25	35	< 2	9/3/60	00 40	70	3
7/7/58	00 58	40	< 1	11/12/60	13 22	1200	130
5/11/59	20 55	40	< 1	11/15/60	02 07	500	80
7/10/59	02 00	200	< 1	11/20/60		7	5
7/14/59	04 00	200	< 1	7/18/61	09 30	140	12
7/16/59	21 00	2800	5	7/20/61	15 50	13	3
5/4/60	10 15	35	10				

## Cosmic-Ray Bursts in the Stratosphere

Bursts of cosmic rays in the stratosphere were detected in the USSR, and independently in the United States, in 1958 during experiments in the stratosphere above Murmansk, Minneapolis, and Fort Churchill. Intensity of the primary component of the cosmic rays in the Murmansk metering data was approximately 2500 times greater than usual on March 3 and 40 times greater on March 17 and August 8, 1958. There were doubts at first as to whether the recorded events were actually due to cosmic ray generation on the Sun, but these doubts were dismissed the following year. In July, 1959, three powerful chromosphere flares of the highest class (3+) appeared on the Sun, following one after the other every few days. The same



sequential nature was recorded in cosmic ray bursts in the stratosphere producing increases in the primary cosmic ray component of approximately 200, 800, and 2800 times (Ref. 1). Similar results were obtained by Winckler in experiments over Minneapolis (Ref. 2). Cases are known, however, where it is difficult to find a solar chromospheric flare matching a recorded cosmic-ray burst. These cases are discussed below.

The behavior of a cosmic-ray burst and of its accompanying phenomena is as follows. In most cases the cosmic-ray bursts are detected several hours after a chromospheric flare on the Sun, while approximately a day after the flares magnetic storms, ionospheric perturbations and, in some cases, polar aurorae begin. At the start of a magnetic storm, or somewhat later, there is a drop in intensity of high-energy cosmic rays. This phenomenon is customarily called the Forbush decrease. There are cases, however, where cosmic-ray bursts in the stratosphere are not accompanied by geophysical phenomena. This is ordinarily true of chromospheric flares at the edge of the solar disc whose corpuscular streams by-pass the Earth.

/548

Research into cosmic-ray bursts is of great interest in connection with the general problem of cosmic ray generation and the study of physical occurrences on the Sun. This research is also of practical significance for purposes of protecting astronauts in space from dangerous radiation during flares.

The question of radiation protection of astronauts against cosmic-ray bursts during flights in interplanetary space may, in principle, be solved on the basis of the data amassed on duration, amplitude, and energy spectrum of particles in the bursts. Supported by these data, we may say that guaranteed protection against solar cosmic rays requires protective shieldings, but this would lead to excessive weighting of space vehicles. It is therefore extremely important for space flights in the immediate future that ways be sought to forecast cosmic-ray bursts and to predict the power of the burst and the nature of its propagation in interplanetary space. This is a new task whose successful solution requires comprehensive and systematic study of solar activity by astronomical, radioastronomical, and cosmic-ray methods.

### Study of Proton Energy Spectrum in Bursts

One method of studying the energy spectrum of primary protons in a burst is to measure absorption of these protons in the upper atmospheric layers (Ref. 3). The stratosphere intensity of cosmic rays having a galactic origin reaches a maximum at altitudes of 16-22 km. At higher altitudes this intensity significantly decreases. During bursts the stratospheric intensity of cosmic rays at high latitudes has no maximum, but continuously increases with altitude. Subtracting the measured number of particles at different altitudes before bursts from that during bursts, we can plot a so-called absorption curve - the number of recorded particles as a function of stratosphere pressure. During bursts radiosondes are more

frequently sent into the stratosphere, every two or three hours in some cases. This furnishes information on changes in the primary radiation spectrum and intensity with time. The graphs in Figure 1 illustrate the type of absorption curves derived from certain measurements during the bursts of May 4 and September 3, 1960. The number of double coincidences is plotted on the ordinate axis, and the pressure is plotted along the abscissa axis.

The small difference in slope of the absorption curves derived at different times during the bursts is remarkable, although primary proton intensity changes substantially in time. It is also surprising that these curves are close to each other even for independent bursts.

The data shown in Figure 1 were derived from measurements before the corpuscular streams of the chromospheric flare, during which the cosmic rays were generated, began to arrive on Earth. Figure 2 gives the results of measuring absorption curves in the period after capture by corpuscular streams of the Earth during the flares of May 12, July 12, and July 15, 1959. The slopes of the straight lines drawn through the experimental points also differ very little, but spectrum steepness is substantially greater in this case.

By studying similar absorption curves in other flares and converting them to the proton energy spectra, we arrived at the following important conclusion. The indices of proton differential energy spectra in the representation  $N/\epsilon^\gamma$ , in the proton energy region of several hundred Mev, cluster around a value close to  $\gamma \approx 3.0$  in measurements of corpuscular fluxes before their arrival on Earth from a chromospheric flare which generated cosmic rays. The spectrum exponents in post-arrival flux measurements cluster around the value  $\gamma \approx 6.0$ . The inference drawn was that a spectrum with the index  $\gamma \approx 3.0$  is due to protons leaving the Sun and diffusing freely in the interplanetary medium, while the spectrum with the index  $\gamma \approx 6.0$  is due to an extra proton stream borne by the magnetic traps of fast protons. It must be assumed that these protons are present in solar corpuscular streams in order to explain the increase in proton spectrum steepness in the second series of experiments (Ref. 4). /549

We will pause on the reasoning underlying this conclusion. Solar cosmic-ray protons, spreading diffusely in space, arrive on Earth about 20 to 30 hours earlier than do the corpuscular streams of the chromospheric flare causing this burst of cosmic rays. Long before the arrival of corpuscular streams on Earth, circumsolar space is filled with solar cosmic rays, but something happens at the instant the Earth enters the corpuscular streams. The abrupt softening of the energy spectrum - enrichment of the spectrum with low-energy protons and simultaneous increase in total proton flux - is hard to explain in any other way than by supposing that circumterrestrial space contains fresh radiation involving the chromospheric flare's corpuscular streams. We are dealing with corpuscular streams of a solar flare during which cosmic rays have been generated. We may therefore imagine this picture: Part of the cosmic ray protons generated during the chromospheric flare leave the Sun and, diffusing in the interplanetary /550

medium, reach the Earth. The index of the energy spectrum for these protons is  $\gamma \approx 3.0$ . Another part of the protons, being trapped by the magnetic clouds of corpuscular streams, cannot go out freely into interplanetary space. These particles, captured by unusual magnetic traps, are carried away into interplanetary space along with the corpuscular streams themselves. An investigation of this phenomenon clearly is also of great practical significance with respect to the irregular concentration of radiation in space.

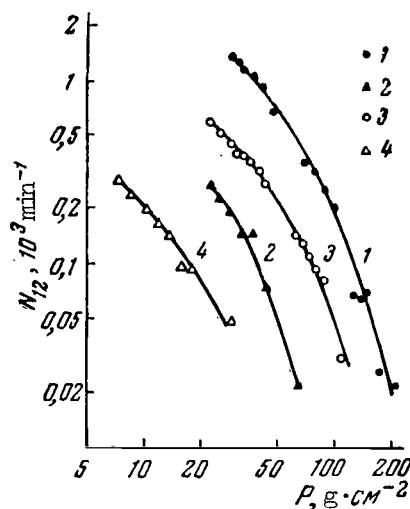


Figure 1

Number of Coincidences  $N_{12}$  as Function of Pressure (1960).

1 - September 3, instrument launch 0700 hr; 2 - September 4, instrument launch 11 hrs 56 mins; 3 - May 4, instrument launch 15 hrs; 4 - May 5, instrument launch 10 hr 20 min.

The constancy of energy spectra from flare to flare -  $\gamma \approx 3.0$  in the first series of experiments and  $\gamma \approx 6.0$  in the second - is striking. This means that the formation of proton energy spectra, and consequently their acceleration in flares, has a stable character and does not depend on the various sorts of perturbation constantly occurring in the atmosphere of the Sun. Neither does it depend on the strength and diverse characteristics of chromosphere eruptions.

We have until now spoken of the spectrum of protons having energies of several hundred Mev. But what happens to the spectrum in the energy range above several hundred Mev? It is found that the slopes of energy spectra in this energy region vary for different bursts. The spectra are deflected at  $\gamma \approx 6.0$ . The proton energies, where this change in spectrum steepness sets in, differ in different bursts. Qualitatively, the existence of such a phenomenon follows from the simple fact that there is no proportionality in burst amplitudes recorded in the stratosphere

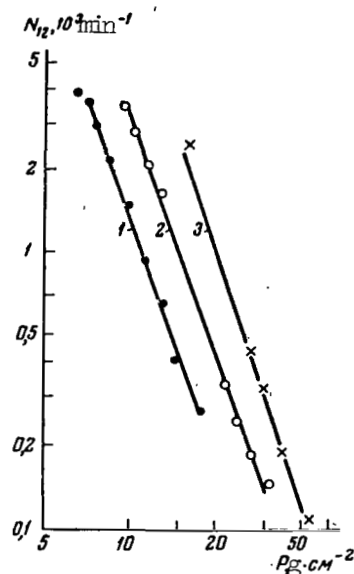


Figure 2

Measured Number of Double Coincidences  $N_{12}$  as a  
Function of Pressure (1959)  
1 - May 12, instrument launch 12 hours; 2 - July  
12, instrument launch 11 hours 45 minutes; 3 -  
July 15, instrument launch 12 hours.

and near sea level (Ref. 4).

It is natural that the energy range of particles generated by the Sun is somehow limited on the high-energy side, and the physics of the phenomenon is evidently such that this limitation in specific cases is different for different flares. The phenomenon under discussion is illustrated by the data on integral spectra shown in Figure 3. The date, place, measurement time in hours after start of the corresponding flare, and normalization factor  $K$  - by which the data must be divided to get absolute proton intensity - are given below.

Date	Time in hrs.	K	Observation Site
1 - 5/4/60	3.5	12.5	Murmansk
2 - 11/15/60	6	1	Murmansk
3 - 11/15/60	6	1	Moscow
4 - 7/18/61	8	0.85	Fort Churchill
5 - 9/3/60	7	0.7	Murmansk
6 - 9/3/60	12	1	Murmansk
7 - 9/3/60	13	1	Fort Churchill
8 - 7/12/61	6	8	Murmansk
9 - 7/12/61	10	8	Murmansk
10 - 7/12/61	14	8.5	Fort Churchill

/551

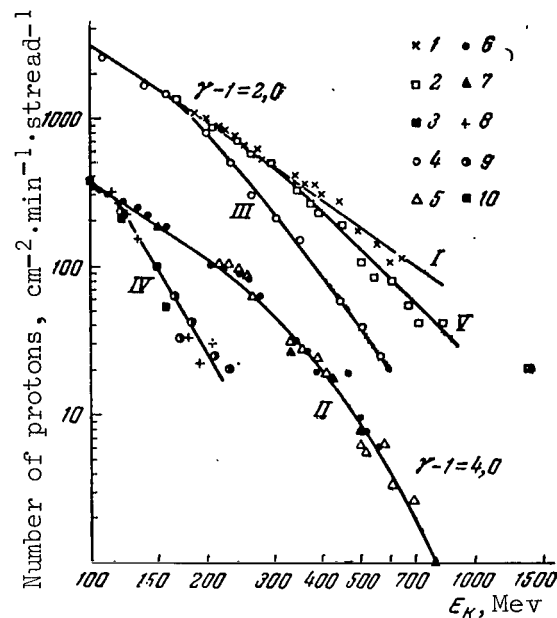


Figure 3

### Integral Spectra of Protons

As may be seen in Figure 3, the integral spectrum slope for the burst of May 4, 1960 (I) corresponds to the index  $\gamma - 1 = 2.0$  up to proton energies around 700 Mev. In the burst of November 15, 1960, this value is maintained only to energies of 500 Mev (Curve V). In the burst of September 3, 1960, the spectrum deflection begins at proton energies of 200-300 Mev (curve II), in that of August 18, 1961, at energies of 200 Mev (curve III), and in the August 12, 1961, burst this break in the energy spectrum probably sets in at energies below 100 Mev (curve IV). This statement may be supplemented by stating that, if the spectrum becomes steeper at proton energies appreciably less than 100 Mev, it is not very probable that such cases of cosmic ray generation will be recorded in the stratosphere. This may possibly explain the fact that not all recorded cases of galactic radio-noise absorption, caused by the invasion of the upper atmospheric layers by slow protons of solar origin, correspond to cosmic-ray bursts which are recorded in the stratosphere. It is, of course, very interesting to study the described spectrum deflection phenomenon in different bursts as an aspect of research into characteristics of chromospheric flares which generate cosmic rays.

Diffusion of Solar Cosmic Ray Protons in the Interplanetary Medium. Data on Coefficient of Diffusion. Field Strength in Magnetic Nonuniformities.

The length of time required for generation and shaping of the cosmic ray energy and charge spectrum on the Sun is tens of minutes,

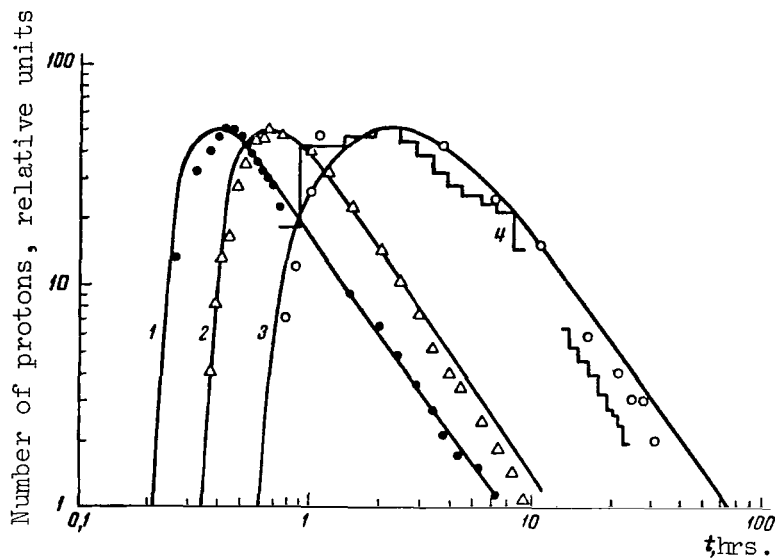


Figure 4

#### Solar Cosmic Ray Intensity as a Function of Time

1 - Ionization chamber data according to Shmidt (Ref. 5); 2 - Neutron monitor data in Chicago, (Ref. 6); 3 and 4 - data from stratosphere measurements above Murmansk (Ref. 3) and Fort Churchill (Ref. 7), respectively.

in any case less than several hours, but the lifetime of these cosmic rays in interplanetary space is several days. This fact leads us to the conclusion that cosmic-ray propagation in interplanetary space is diffuse in nature. The medium through which cosmic-ray particles diffuse consists of magnetic nonuniformities, about whose existence in interplanetary space there is apparently no doubt. Let us determine to what degree this concept corresponds to the experimental data. It may be seen from Figure 4 that solar cosmic-ray intensity varies as a function of time. Along the abscissa axis is laid off time calculated from the beginning of the chromospheric flare in question. The maxima of these measurement findings are intercorrelated. The solid lines are computed from a formula providing a solution of the diffusion equation for homogeneous space of spherical symmetry. The parameter, which we vary in the formula in order to describe all three experimental findings, is the coefficient of diffusion  $D$ . The values used for  $D$  are curve 1 -  $5.2 \cdot 10^{22} \text{ cm}^2 \cdot \text{sec}^{-1}$ ; curve 2 -  $3 \cdot 10^{22} \text{ cm}^2 \cdot \text{sec}^{-1}$ ; and curve 3 -  $5.5 \cdot 10^{21} \text{ cm}^2 \cdot \text{sec}^{-1}$ . Naturally, such a simple diffusion model can make no pretense of completeness, but to reveal the basic features of the phenomenon this simplification is clearly justified. Based on the data regarding the diffusion coefficient magnitude and the assumption that it is matched by the different effective proton impulses registered in an ionization chamber, by a neutron monitor and in the stratosphere, equalling approximately 15, 5, and 0.5 Bev/oe, we proceed to the deduction

that the proton scattering range in interplanetary space depends on an impulse approximately like  $\sqrt{p}$  (Ref. 8).

The diffusion model also makes it possible to find the kinetic energy borne by protons generated in flares. It is found that this energy for a moderate solar flare is  $\sim 10^{29}$  erg.

#### Cosmic Rays Bursts Generated on the Back Side of the Solar Disc. Radial Solar Magnetic Fields.

If, in addition to the magnetic nonuniformities in which proton scattering occurs, interplanetary space also contains a radial solar magnetic field, the diffuse propagation of protons from the Sun in interplanetary space will be anisotropic in nature. Therefore cosmic ray bursts originating on the back side of the Sun, if they are recorded on Earth at all, show amplitudes lower than those of bursts originating on the Sun's visible side. The experimental findings described in detail in (Ref. 4) actually demonstrate that the amplitudes of cosmic ray bursts originating on the visible side of the Sun are almost tens of times stronger than those on the side which is not visible.

#### REFERENCES

1. Charakhch'yan, A. N., Tulinov, V. F., Charakhch'yan, T. N. ZhETF , 39, 249, 1960.
2. Winckler, J. R. Radiation Res., 14, No. 5, 521, 1961.
3. Charakhch'yan, A. N., Tulinov, V. F., Charakhch'yan, T. N. ZhETF , 41, 735, 1961.
4. Charakhch'yan, A. N. UFN , 83, No. 1, 35, 1964.
5. Dorman, L. I. Variations in Cosmic Rays (Variatsii kosmicheskikh luchey). Gostekhizdat, 1957.
6. Neyer, P., Parker, E. N., Simpson, J. A. Phys. Rev., 104, 768, 1956.
7. Hofman, D. J., Winckler, J. R. Space Res., 3, 662, 1963.
8. Charakhch'yan, A. N., Charakhch'yan, T. N. Geomagnetizm i Aeronomiya, 5, No. 2, 1965.

VII  
VARIOUS PROBLEMS



## INTERPRETATION OF RADIATION DATA FROM METEOROLOGICAL SATELLITES

K. Ya. Kondrat'yev

The utilization of meteorological satellites is of great interest, /555 because they make it possible to enlarge the volume of meteorological information received significantly. Expansion of information is very important for improving weather forecasts by the use of presently existing methods, but it is even more essential to the development of our concepts regarding patterns of weather-forming processes.

The use of satellites to obtain meteorological information, i.e., data on the fields of the basic meteorological elements (atmospheric pressure, temperature, humidity, cloudiness, etc.) in the lower layers of the atmosphere, is an exceptionally complex assignment. In any instance the source of information which may be obtained by equipment aboard the satellite is clearly only the radiation field of the Earth's surface and atmosphere, since no other physical characteristics can be directly measured from the satellite.

Perhaps the simplest situation is the one involving television and photography. Television or photographic cloud-cover pictures are a very graphic means of analyzing the patterns of weather-forming processes from data obtained by satellites, which contain meteorological information on a planetary scale. It is for this very reason that satellite nephoanalysis - which is at present the chief method of utilizing satellite meteorological findings in the weather bureau - has been so extensively and fruitfully developed.

It is at the same time obvious that there are wider possibilities in satellite meteorology. Having at our disposal varied information on the radiation field of the Earth as a planet, we can very materially enrich meteorological information in comparison to the information given by television or photography. The purpose of this brief survey offered for the reader's attention is to clarify those answers to the problem of interpreting radiation data from meteorological satellites which are suitable (approved) in some degree for practical use. It must be emphasized that the bibliography on this problem, which is given in this article, makes no pretense of completeness. A description of the works published before 1962 may be found in the author's monograph (Ref. 1) and more exhaustive lists of the literature may be found in the pertinent bibliographical publications.

### 1. Energetics of Atmospheric Processes

/556

One of the fundamental problems in long-term weather forecasts is the necessity of accounting for energetics of large-scale atmospheric processes. This primarily requires detailed investigations of the patterns of heat

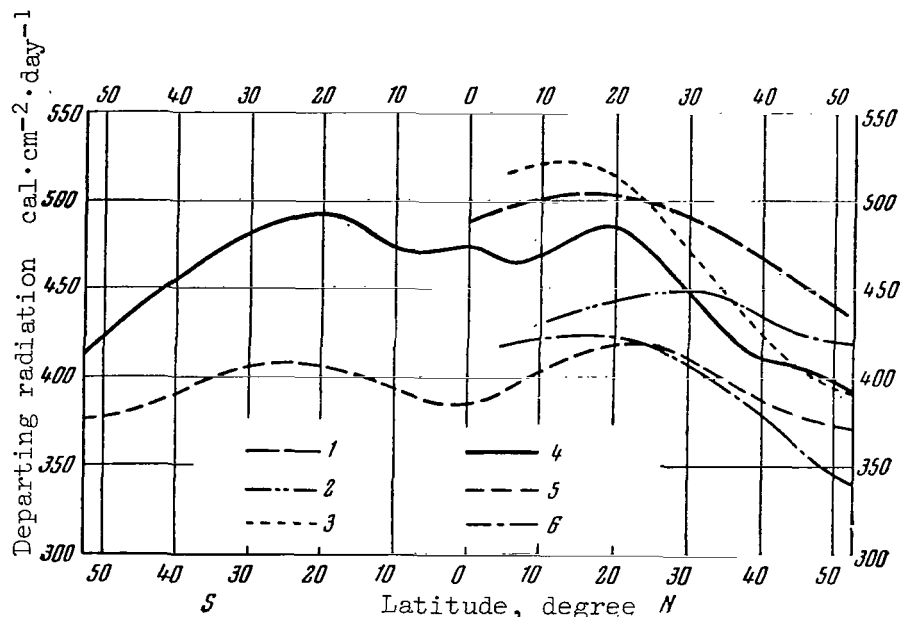


Figure 1

Mean Latitudinal Distribution of Departing Long-wave Radiation from "Tiros-2" Data for 26 Hours, Compared to Theoretically Calculated Data

1 - Khotton (annual average); 2 - Ret'yen (winter);  
3 - London (winter); 4 - "Tiros-2" (November-January);  
5 - Simpson (November-December); 6 - Baur and Philipps (January).

redistribution due to radiation processes: the Earth receives energy only from the Sun and loses it to space only by radiation. An investigation of the distribution of the radiation budget  $R_s$  of the terrestrial surface-atmosphere system over the planet's surface becomes very important here. The radiation budget may be defined as

$$R_s = Q_0(1 - A_s) - F_\infty.$$

Here  $Q_0$  is the arrival of solar radiation outside the atmosphere;  $A_s$ , albedo of the terrestrial surface-atmosphere system;  $F_\infty$ , departing long-wave radiation. Since the magnitude of the solar constant determining the value of  $Q_0$  is sufficiently well-known, we have only to obtain experimental data on albedo and departing radiation. This can be done only with satellites.

Although the accuracy of satellite measurements of departing radiation and albedo (particularly the latter) is still very inadequate, the first experimental data characterizing  $R_s$  and space and time variability  $A_s$ ,  $F_\infty$  have been successfully obtained in the last few years. These data distinctly (in close conformity to information derived from theoretical computations) show that the departing long-wave radiation has a minimum near the

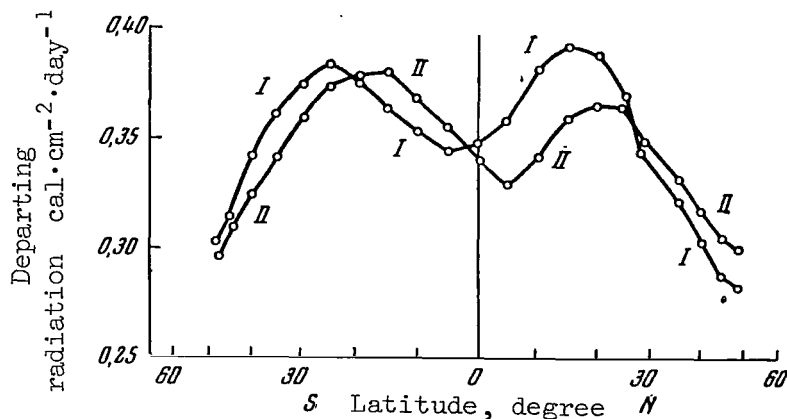


Figure 2

Latitudinal Variation in Departing Long-wave Radiation from "Tiros-4" Data (Hemispherical Sensors)

1557

Area averaged,  $48^{\circ}\text{N}-48^{\circ}\text{S}$ . Departing radiation in periods: Period I -  $500 \text{ cal}\cdot\text{cm}^{-2}\cdot\text{day}^{-1}$  (February 8-April 10, 1962); Period II -  $501 \text{ cal}\cdot\text{cm}^{-2}\cdot\text{day}^{-1}$  (April 11-June 10, 1962).

equator, almost symmetrical maxima in the subtropic zones, and then monotonically falls off toward the poles. Results of this sort have been obtained, for example, by Winston and Rao (Refs. 2, 3) ("Tiros-2", five-channel radiometer, Figure 1) and also by Suomi and House (Ref. 4) ("Tiros-4", hemispherical departing-radiation sensors, Figure 2).

The main factors in the departing-radiation latitudinal distribution are cloudiness and Earth surface temperature. Thus, for example, the peak values of departing radiation in the subtropic zones are caused by the high terrestrial surface temperature and comparatively slight cloudiness. The rather considerable discrepancy between measured and calculated results is noteworthy.

The latitudinal dependence of albedo is almost the mirror image of variability in departing radiation. The cause of this is cloudiness (Figure 3 from [Ref. 4]). The broken lines in Figure 3 describe the possible effect of measurement errors. The average latitudinal radiation budget distribution of the terrestrial surface-atmosphere system is asymmetrical with respect to the equator. Therefore, the transition from a positive budget in low latitudes to a negative budget in high latitudes occurs in different latitudinal belts of the Northern and Southern hemispheres (Figure 4 from [Ref. 4]).

1558

Astling and Horn (Ref. 5) used measurement data from the meteorological

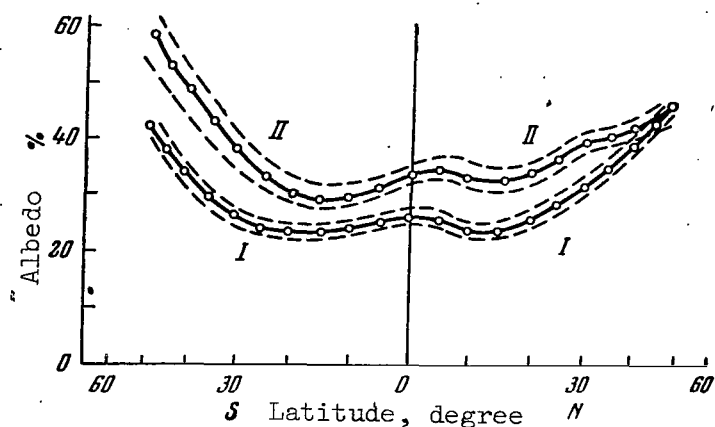


Figure 3

Latitudinal Variation in Albedo from "Tiros-4"  
Data (Hemispherical Sensors)

Area averaged,  $48^{\circ}\text{N}-48^{\circ}\text{S}$ . Albedo in periods:

Period I - 28.9%, reflected radiation  $598 \text{ cal}\cdot\text{cm}^{-2}\cdot\text{day}^{-1}$  (February 8-April 10, 1962);

Period II - 37.2% reflected radiation  $500 \text{ cal}\cdot\text{cm}^{-2}\cdot\text{day}^{-1}$  (April 11-June 10, 1962).

satellite "Tiros-2" gathered on twenty-seven days between November 26, 1960, and January 6, 1961, to plot the average latitudinal distribution of departing long-wave radiation for the entire surface of the Earth and for the continents and oceans separately. The measurement data adequately encompass the latitude zone between  $50^{\circ}\text{N}$  and  $50^{\circ}\text{S}$ , with the exception of part of Central Asia and the northern part of South America, including adjacent water areas of the Pacific and Atlantic Oceans. The original data for each day (no less than ten values used) were averaged over squares of  $2.5^{\circ}$  latitude with one side on the equator, and then were employed to compile maps of geographical distribution of departing radiation for each of the twenty-seven days. All the measurement data pertain to angles of no less than  $56^{\circ}$  relative to the nadir. The averaged meridian profiles of the departing radiation are calculated by taking the departing radiation values from the charts mentioned (7269 points), where the mean latitudinal radiation values are figured for latitude belts  $5^{\circ}$  wide.

The departing-radiation profile derived from all the measurement data reflects, as in the aforementioned (Ref. 2, 3), a minimum near the equator, maxima in the warm and relatively cloudless subtropic zones, and a decrease in departing radiation with a further rise in latitude. The absolute values of departing radiation proved to be less - particularly in the  $5^{\circ}\text{N}-10^{\circ}\text{S}$  zone - than those found earlier from data measured by the satellite "Explorer-7"

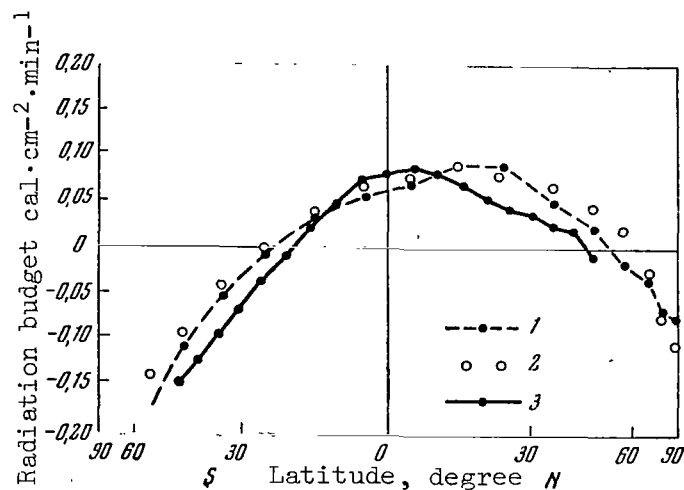


Figure 4

Latitudinal Variation in Radiation Budget from Data of "Tiros-4" (Hemispherical Sensors)

1 - Simpson (March-May, 1928); 2 - London (fall and spring, 1957); 3 - "Tiros-4" (March-May, 1962).

and actinometric radiosondes. This discrepancy can apparently be attributed to inaccurate allowance for the effect of darkening toward the edge of the planet's disc in processing the "Tiros-2" data (departing radiation measured at a large angle with respect to the nadir turn out to be underestimated, compared to the corresponding "subsattellite" values, due to a darkening phenomenon). This inference is corroborated by the underestimation of the departing-radiation values, averaged over all the measurement data, which is revealed by a comparison with the average values obtained by selecting data pertaining to nadir angles of less than  $26^\circ$ . Since, however, even the "subsattellite" departing-radiation values from the "Tiros-2" data are less than those from "Explorer-7", it is assumed that one reason for the divergence is also the difference in equipment calibration on these satellites. According to the data for nadir angles of less than  $26^\circ$ , the departing-radiation values in the zones of subtropical maxima ( $15-25^\circ\text{N}$ ,  $10-35^\circ\text{S}$ ) are about  $480 \text{ cal}\cdot\text{cm}^{-2}\cdot\text{day}^{-1}$ . /559

A substantial difference between the meridian profiles of departing radiation belonging to continents and oceans was detected. If an abrupt departing-radiation minimum is observed in the  $5^\circ\text{N}-15^\circ\text{S}$  latitude band over the continents, over the oceans this minimum is more weakly marked and shifts in a latitudinal range of  $5-10^\circ$ . Apparently the shift in the minimum region over the continents to the south was due to cloudiness associated with the intratropical convergence zone. Another important difference occurs in subtropical regions and involves the effect of the

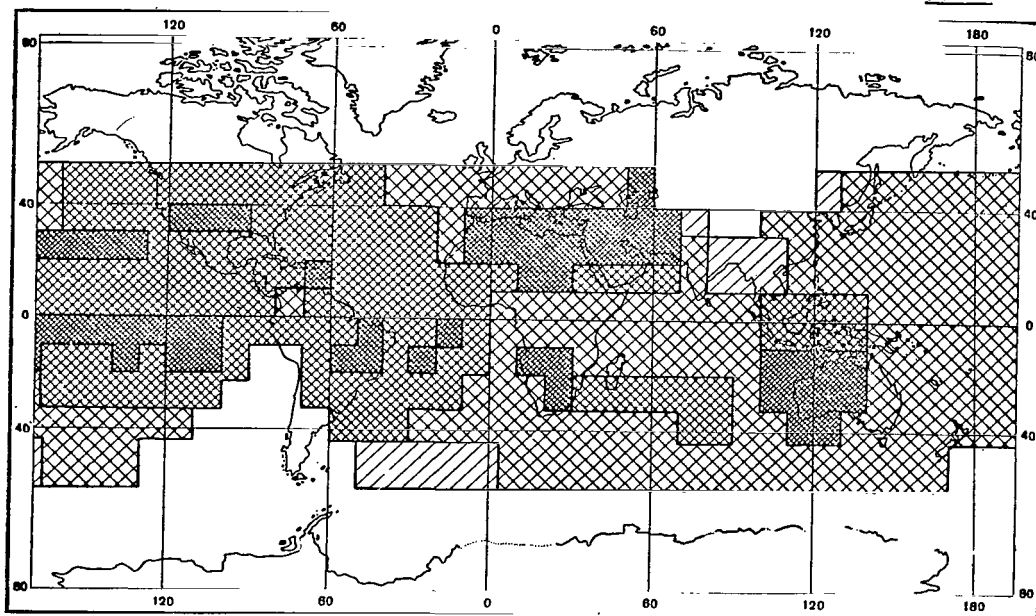


Figure 5

Planetary Distribution of Effective Temperatures  
Measured by "Tiros-3" (Channel No. 2) in the  
Period from July 12 to September 10, 1961

Darkest shading -  $T > 295^{\circ}\text{K}$ ; Lightest shading -  
 $T < 255^{\circ}\text{K}$ .

underlying surface temperature in these relatively cloudless regions: over the oceans (small temperature variation) the departing-radiation values in both hemispheres are approximately  $500 \text{ cal}\cdot\text{cm}^{-2}\cdot\text{day}^{-1}$  in subtropical zones; the corresponding values over the continents are  $540 \text{ cal}\cdot\text{cm}^{-2}\cdot\text{day}^{-1}$  (summer hemisphere, high temperatures) and  $475 \text{ cal}\cdot\text{cm}^{-2}\cdot\text{day}^{-1}$  (winter hemisphere, low temperatures).

The data obtained in (Ref. 5) on variability in the departing radiation relative to the average values shows that the variability is more sharply pronounced over the continents. An attempt to use the data of "Tiros-2" to estimate the average value of departing radiation and albedo for the Earth as a whole - while employing calculated values for the high latitudes - has led to an average planetary departing-radiation value of  $0.311 \text{ cal}\cdot\text{cm}^{-2}\cdot\text{min}^{-1}$ , and an albedo of 0.38. It should be noted that the albedo value usually adopted is 0.34, while the "Explorer-7" data resulted in a value of 0.33. This discrepancy can be attributed to the limited (in time) volume of data employed. Therefore, there is an obvious necessity of compiling

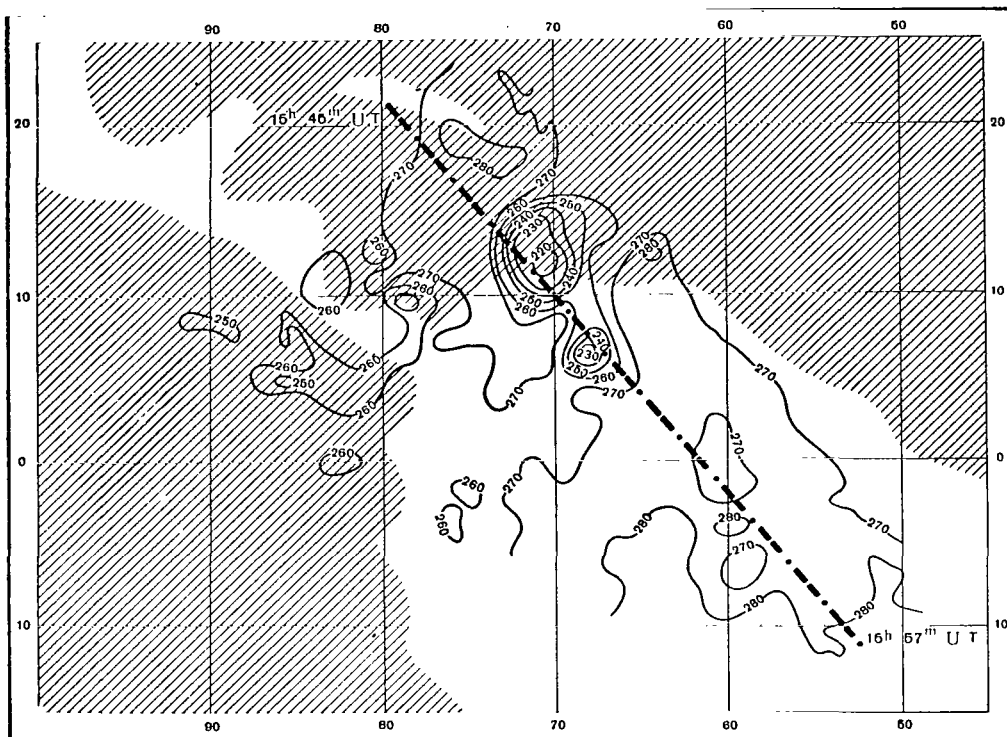


Figure 6

Synoptic Radiation Chart. Geographic Distribution of  
Departing Radiation in Atmospheric Transmittance Window ( $7.5-13.5 \mu$ )

132nd revolution, July 21, 1961; 15:45-16:02 Greenwich time.

further satellite observations.

## 2. Identification of Cloudiness

Thermal (infrared) radiation is known to be determined by the temperature of the emitting object. The general rule that the upper cloudiness boundary is colder than the Earth's surface opens up opportunities of identifying the cloud cover by measurement data on departing infrared radiation. To illustrate this deduction, let us adduce the results obtained, for example, by Rasool (Ref. 6), who processed measurement data on departing radiation in the atmospheric transmittance window (wave length of  $8-12 \mu$ ) as obtained from the "Tiros-3" meteorological satellite from July to September, 1961, to study cloud cover distribution on the night side of the Earth (Figure 5). It was found that the geographic distribution of the effective radiation temperature in this window, averaged over squares of  $10^\circ$  latitude by  $10^\circ$  longitude, and from 06 to 18 hours local time, clearly

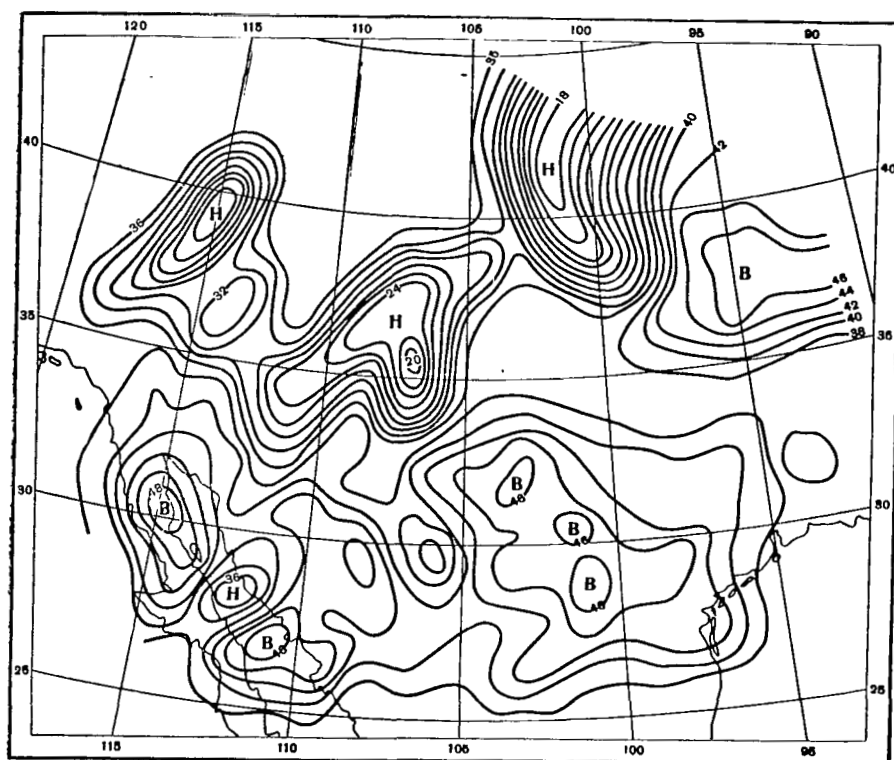


Figure 7

Geographic Distribution of Departing Radiation in Transmittance Window ( $7.5-13.5\mu$ ); November 27, 1960, about 15 hours, Moscow time.

/561

reflects the features of planetary cloudiness distribution: (1) a belt of relatively low temperature near the equator matches the zone of elevated cloudiness observable in this region; (2) subtropical bands of high effective temperatures on both sides of the equator characterize the relatively unclouded subtropical zones; (3) the exceptionally low effective temperatures in regions of Eastern Pakistan and India indicate great cloudiness there with a high upper boundary.

It is well known that cloud distributions represent good indicators of weather-forming processes. This means that the most typical meteorological systems should be easily identifiable from the radiation field distribution. There are at present extensive data confirming this inference and providing a basis for speaking of the development of a new research discipline, which may be called radiation synoptics.

One of the clearest examples, illustrating the appearance of hurricane "Anna" in a radiation field of different wavelengths, has been analyzed



by Bandeen et al. (Ref. 7). These authors studied properties of the departing-radiation field in various spectral regions in the locale of hurricane "Anna" from data measured by the five-channel radiometer of "Tiros-3" on July 12, 1961. It was found that the hurricane stood out very distinctly in the field of infrared departing radiation as a zone of profound minimum radiation, caused by cloudiness with a high and cold upper limit in the hurricane's center. This may be clearly seen in Figure 6, which represents the field of departing radiation in the atmospheric transmittance window at  $7.5\text{--}13.5\ \mu$ . Figure 6 also indicates the effective (radiation) temperatures corresponding to different isolines. It can be seen that the temperature at the hurricane's center falls to  $220^\circ\text{K}$ .

V. G. Boldyrev (Ref. 8) has studied an example of "radiation" analysis of a synoptic situation on United States territory on November 27, 1960. This example (Figure 7) demonstrates that in the case in question three minima of departing radiation cover the center of the cyclone, and the maximum region in the Gulf of Mexico corresponds to a cloudless zone. Winston and Rao (Ref. 3) have shown that the departing longwave radiation field closely represents the features of weather-forming processes in different regions of the globe. Intratropical convection zones, for example, are clearly apparent. In the temperate latitudes of the Northern Hemisphere, the regions of minimum departing-radiation values correspond to regions of cyclones and fronts, while their maximum regions coincide with the location of cold anticyclones in the west-east transfer zone and of subtropical anticyclones to the south of this zone. /562

A very interesting and successful experiment to obtain infrared images of the cloud cover on the nightside of the Earth was effected with the satellite "Nimbus-A" carrying a scanning radiometer of high resolving power, with peak sensitivity around 4-microns at the transmittance "window".

In view of the possibility of obtaining infrared images of cloud covers, it is of interest to examine the conditions under which the solution of this problem is simple and, on the other hand, to delineate the cases in which an interpretation of the data may be erroneous. This may be the case in inversion stratification of the atmosphere, when the Earth's surface may be colder than the upper cloud limit or when the terrestrial surface-cloud temperature contrasts are very small. Such situations are typical of high latitudes, particularly in wintertime. To analyze such situations, the author and N. Ye. Ter-Markaryants (Ref. 9) studied the annual pattern of temperature differences  $\Delta T$  between the Earth's surface and the upper cloud boundary in different climatic zones and different cloud layers. Figure 8 illustrates this with data referring to Moscow. This figure clearly shows how complex the problem of identifying cloudiness from measurement data on departing longwave radiation may be in winter.

As M. S. Malkevich has shown (Ref. 10), an important role in obtaining reliable results in such cases may be played by measurement data on /563

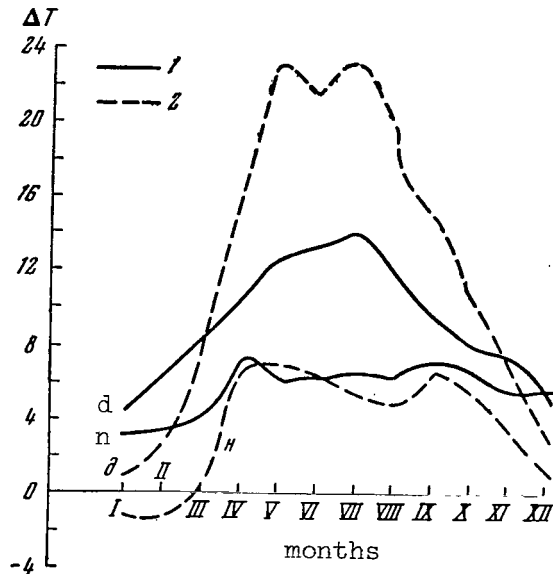


Figure 8

Annual Course of Temperature Differential at Surface  
of Earth and Upper Cloud Boundary

1 - Lower level clouds; 2 - Upper level clouds (d- day;  
n- night).

infrared departing radiation, both in the transmittance window and in absorption bands. The brightness contrasts between the atmospheric window and the absorption band will obviously be greatest at the surface of the Earth and should diminish with increased cloud height, as is evidenced in Figure 9. Even should terrestrial-surface and upper-cloud-limit temperatures be identical, the use of these contrasts helps to distinguish the clouds from the surface of the Earth.

### 3. Cloud Temperature and Altitude, Troposphere Humidity

Radiation from the Earth's surface (or from the upper cloud limit) makes the chief contribution to departing radiation in transmittance "windows". Therefore, the measurement data on departing radiation in the "windows" makes it possible to ascertain surface temperature. The correction of measurement results which exclude the effect of the atmospheric layer above the radiating surface is of very great significance. The airplane measurements of V. L. Gayevskiy and Yu. I. Rabinovich (Ref. 10) demonstrated that these corrections may go as high as  $15^{\circ}$  in 8-12-micron windows, for the water vapor content in 3.6 cm of atmosphere (these experiments gave substantially smaller correction values than did theoretical computations). It was found that correlation graphs could be plotted

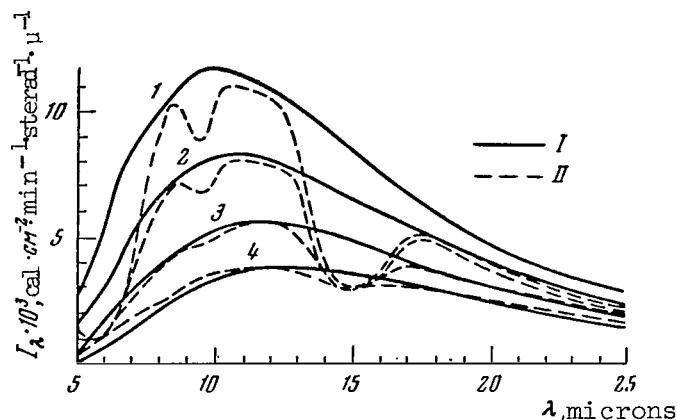


Figure 9

Spectral Distribution of Absolutely Black Radiation from Cloud Apexes (I) and Longwave Departing Radiation (7-32 microns) with Upper Cloud Boundary  $z_0$  at Different Altitudes (II)

1 -  $z_0 = 0$ , Earth's surface,  $T = 273^\circ\text{K}$ ; 2 - lower-level clouds,  $T = 273^\circ\text{K}$ ; 3 - middle-level clouds,  $T = 250^\circ\text{K}$ ; 4 - upper-level clouds,  $T = 223^\circ\text{K}$ .

showing the dependence of corrections on the effective (radiation) surface temperature with the use of only one parameter - moisture content in the atmospheric layer. Thus, knowing moisture content we may determine the correction and the true surface temperature from the measured effective temperature (allowance for the effect of ozone, which is required in interpreting satellite measurement data, may be made by employing the findings of theoretical calculations).

Another method of allowing for the intermediate atmospheric layer, <sup>/565</sup> based on the introduction of a so-called transfer function, has been suggested by M. S. Malkevich (Ref. 10). A transfer function is defined as the ratio of true surface radiation to radiation of an absolutely black body at the temperature of the surface, and is dependent only on the amount of water vapor in the atmospheric layer.

Determination of the upper cloud-boundary temperature makes it possible to find cloud altitude, if there is any information on the vertical temperature profile. Fritz and Winston (Ref. 11) have developed a method for solving such a problem based on the use of isotherm charts for the 700, 500, and 300-mb levels prepared by the National Weather Analysis Center of the United States. The surface chart can be plotted from the data of ordinary weather observations. The results thus derived have in many cases proved to be quite satisfactory.

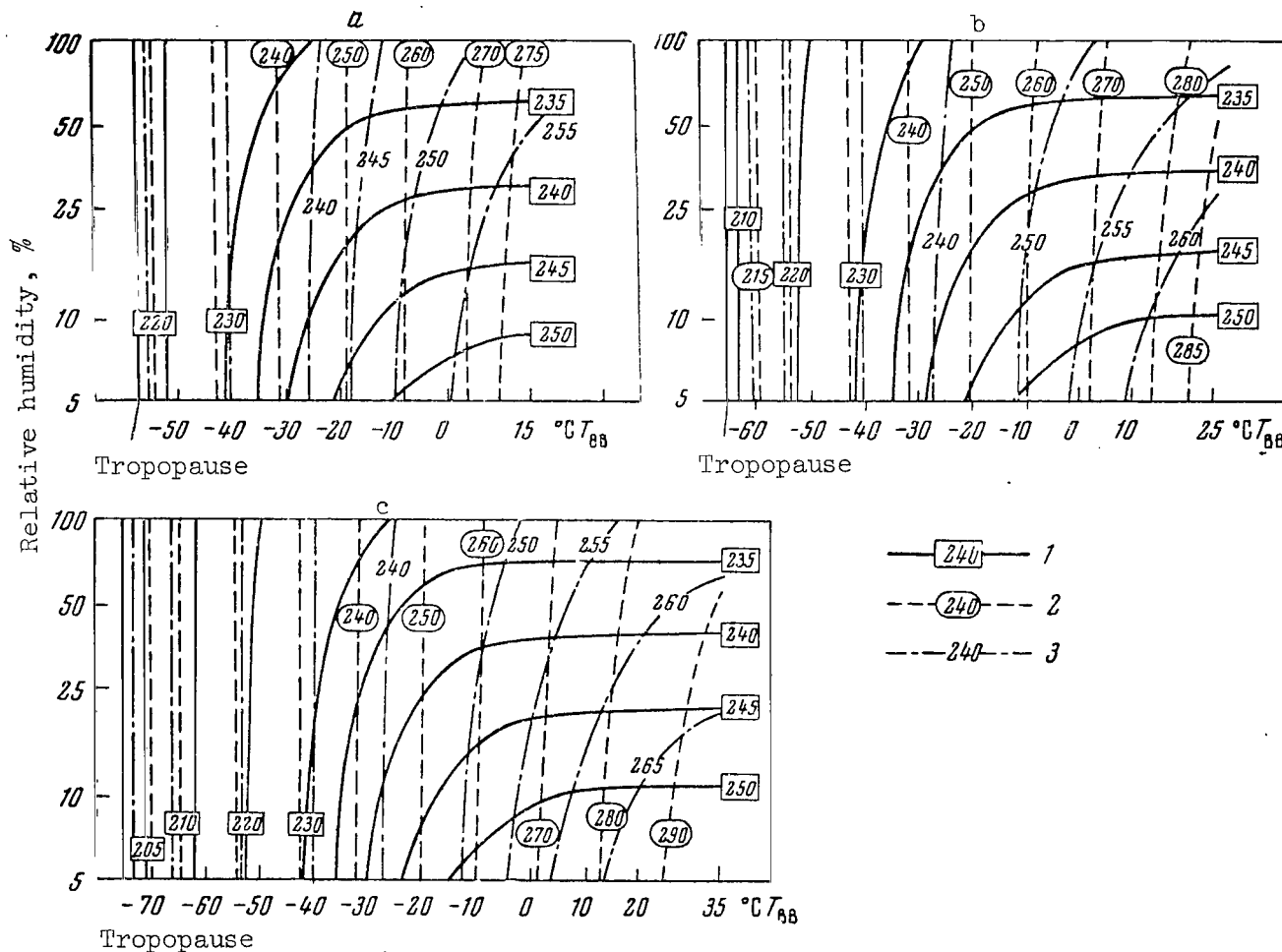


Figure 10

Nomograms for Computing Underlying Surface Temperature and Relative Humidity  
 Diagrams for: a - standard atmosphere 1 (Air Research and Development Command);  
 b - subtropical atmosphere 2; c - tropical atmosphere 3.

1 - Channel No. 1 (5.6-6.8 microns); 2 - Channel No. 2 (7.5-13.5 microns);  
 3 - Difference in readings (12-32.5 microns)

Möller (Ref. 12) proposed a simple method of determining Earth-surface (or upper cloud-limit) temperature and relative humidity. This method is based on the use of observational data from the "Tiros" satellites.

Having at our disposal calculations of the departing radiation for the spectral regions 5.8-6.8 microns (channel No. 1 of the "Tiros" five-channel radiometer), 8-13 microns (channel No. 2), 7.5-32.5 microns (channel No. 4), 12-32.5 microns (difference of readings between channels No. 4 and 2), we may plot isolines of computed departing-radiation (or effective-temperature) values in the coordinate system of surface temperature-relative humidity (Figure 10a-c). If relative humidity is plotted on the ordinate axis and surface temperature on the abscissa axis, then the isolines pertaining to channel No. 2 are practically parallel to the ordinate axis. Having measured departing radiation (effective radiation temperature), we may therefore use the mentioned diagram to find the surface temperature reading. After that, with the known surface-temperature value at our disposal, we may determine relative humidity of the top half of the troposphere from the isolines for channel No. 1. The difference in radiometer readings between channel No. 4 and channels No. 1, 2 gives the relative humidity value of the lower part of the troposphere.

Raschke (Ref. 13) showed that the above isolines should be plotted for the various atmosphere models pertaining to definite latitudinal belts and should be then applied to specific observational conditions (Figure 10 gives diagrams for standard, subtropical, and tropical atmospheres). Let us examine an instance where the method proposed by Möller is applied.

Let us assume that the following effective-temperature values have been derived from observational data:

Channel	$T_{\text{eff}}, ^\circ\text{K}$
1	$237.5 \pm 2.5$
2	$272.5 \pm 2.5$
(4-2)	$257.5 \pm 2.5$

Making use of the set of three diagrams constructed by Raschke for the three atmospheric models, we can compile a table.

As is evident, when changing from model 1 to model 3, the surface temperature decreases slightly, while relative humidity rises.

If we assume that in the case under consideration the Earth's surface is covered with clouds, we will then, by adopting values of  $10^\circ\text{C}$  for the upper cloud-boundary temperature, obtain the upper boundary located at 566 the following levels, depending on the atmosphere model chosen:

Atmosphere Model	Level of Upper Cloud Limit (pressure, mb)
1	930
2	770
3	650

This table shows that the atmosphere model selected when determining cloud altitude is very important. Rasool (Ref. 6) suggested a method for determining cloud altitude which resembles this in concept. In order to obtain a numerical interpretation of measurement data, Rasool computed the effective temperatures in the transmittance window for ten cloudless atmospheric models belonging to ten latitudinal belts  $10^\circ$  wide, ranging from  $50^\circ\text{N}$  to  $50^\circ\text{S}$ . Similar calculations have also been made for differing cloudiness conditions (varying degree and altitude of clouds). From the computational data mentioned, the dependence of effective temperature differences and Earth-surface temperatures on degree of cloudiness have been plotted for various atmospheric moisture contents (cloud altitude serves as a parameter of the dependence). With information on Earth-surface temperature, degree of cloudiness, and atmospheric moisture content, these data may be used for approximately evaluating cloud temperature (and altitude of upper boundary) from data on effective temperature measured by satellites. The use of climatic data for temperatures of the underlying surface has enabled us to study the latitudinal dependence of the difference between effective temperature measured and the surface temperature for day and night.

Using the known latitudinal distribution of daytime cloudiness (obtained by satellite television data) and using the above-mentioned relationships, we can derive information on the average latitudinal distribution of the upper nighttime height of the cloud boundary, and on the latitudinal distribution of degree of cloudiness. A comparison of the average daytime and nighttime latitudinal distributions of degree of cloudiness shows that in the Southern Hemisphere the nighttime cloudiness is significantly greater than during the daytime. In the Northern Hemisphere, on the contrary, the nighttime values are approximately 20% less than the daytime in the  $20\text{--}40^\circ$  latitude zone. It must, however, be stressed that these results were obtained on the assumption that cloud altitude for the given latitudinal zone does not change from day to night (which may be regarded as debatable).

V. L. Gayevskiy and L. N. Guseva (Ref. 10) have discussed the possibilities of determining upper boundary altitude of the cloud cover from 567 data on cloud radiation temperature measured from a satellite, when vertical temperature distribution is unknown and therefore a certain average value of the vertical temperature gradient must be employed. For this purpose, computations have been made of the vertical temperature gradient in

TABLE

Channel	Atmosphere Model	Surface Temperature, °C	Relative Humidity, %
1 and 2	1	+9	40
	2	+8	45
	3	+7	55
2 and (4-2)	1	+7	-
	2	+6.5	-
	3	+6	22

the layer from the Earth's surface to the level of the upper cloud limit, using data from airplane soundings in the Leningrad region (923 cases examined in all). It has been shown that in 80% of the cases the vertical temperature gradient is from 0.4 to 0.75 degrees per 100 meters, and only when there were stratified clouds was this range significantly wider (from -0.1 to 0.9 deg/100 m). If it is assumed that the vertical temperature gradient is 0.55 deg/100 m, then the error in determining the altitude of clouds whose upper limits are at 7 and 3 km will be 1 and 0.5 km, respectively, and will be greatest for stratified clouds. It has been noted that, based on the measuremental findings on cloud-surface radiation temperature, its values may differ by 3-10°C from the actual air temperature at this level. Such great differences restrict the application of the examined method for determining altitude of upper cloudiness boundary. The above errors may be considered in line with reality only for clouds whose thickness is not less than 400 m. Such clouds may be distinguished by means of satellite photographs of the cloudiness. The terrestrial surface temperature readings may be found from satellite data on radiation in the spaces between clouds.

As Rao and Winston (Ref. 3) have shown, one serious obstacle to finding upper-boundary temperature and altitude of clouds occurs when clouds of different levels are simultaneously observed. It is also possible to ascertain the upper-boundary altitude of cloudiness from data on solar radiation absorption due to the 0.76-micron oxygen absorption band in the atmosphere layer above the cloud. Such a method has, however, not yet been tested in practice.

#### 4. Vertical Movements

Cloudiness fields as a rule, but by no means in all cases, coincide with zones of ascending temperature movements, while descending streams are most often observed in cloudless regions. Therefore, the derivation of information on cloudiness makes it possible at the same time to characterize

the field of vertical movements, at least in broad outline. This was convincingly demonstrated by Sh. A. Musaelyan (Ref. 10), who discovered a linear connection between coefficients of the Fourier series which define the fields of vertical movements in cloudiness.

Shenk (Ref. 14), after deriving a correlative relationship between surface temperature under a cloudless sky and departing radiation in the 8-12 micron transmittance window, utilized measurement data on the difference between departing-radiation fluxes under cloudless and cloudy skies to determine the characteristic temperature differences between surface of the Earth and upper cloud limit and, hence, the vertical temperature gradient. Since the vertical temperature gradient is the index of the nature of vertical movements, the opportunity therefore arises of deriving information on vertical movements from measurement data on departing radiation. Since, furthermore, vertical movements are associated with the meridian component of atmospheric circulation, it is also possible to determine this value. It is essential that the correlation between the difference in departing-radiation fluxes and vertical velocity be linear. For levels of 700, 500, and 300 mb the correlation coefficient is, respectively, 0.768, 0.569, and 0.564. The poorer correlation for the higher levels is caused by less computational accuracy in these instances. A linear correlation has also been detected between the difference in departing-radiation fluxes and the magnitude of the meridional component of wind velocity. /568

The simplest cases of satellite meteorology involving the determination of various meteorological parameters from measurement data on departing radiation have been mentioned above. At present the feasibility is being extensively discussed of more thorough utilization of observational data and, in this connection, the effectuation of new experimental programs to derive information on the vertical profiles of temperature, water vapor, and ozone; on wind fields and atmospheric pressure, location of aerosol layers, etc. All these problems, however, are still in the development stage.

#### REFERENCES

1. Kondrat'yev, K. Ya. Weather Satellites (Meteorologicheskkiye sputniki). Gidrometeoizdat, 1963.
2. Winston, J. S., Rao, P. K. Monthly Weather Rev., 90, No. 8, 1962.
3. Winston, J. S., Rao, P. K. Monthly Weather Rev., 91, No. 10-12, 1963.
4. House, F. B. The Earth's Radiation Heat Budget as Seen by Tiros-4 Satellite. Radiation Sympos. Leningrad, August 5-12, 1964.
5. Astling, E. C., Horn, L. H. J. Atmos. Sci., 21, No. 1, 1964.



6. Rasool, S. J. J. Atmos. Sci., 21, No. 2, 1964.
7. Bandeen, W. R., Conrath, B. J., Nordberg, W., Thompson, H. P. A Radiation View of Hurricane Anna from the Tiros-3 Meteorological Satellite. Proc. First Internat. Sympos. Rocket and Satellite Meteorol. H. Wexler and J. E. Caskey (Eds), Jr., North-Holl. Publ. Co., Amsterdam, 1963.
8. Boldyrev, V. G. Meteorologiya i Gidrologiya, No. 10, 1962.
9. Kondrat'yev, K. Ya., and Ter-Markaryants, N. Ye. Trudy Glavnoy Geofizicheskoy Observatorii, No. 170, 1965.
10. Trudy Glavnoy Geofizicheskoy Observatorii, No. 166, Gidrometeoizdat, 1964.
11. Fritz, S., Winston, J. S. Monthly Weather Rev., 90, No. 1, 1962.
12. Möller, F. Arch. Meteorol. Geophys. and Bioklimatol., 12, No. 1, 1962.
13. Möller, F., Raschke, E. J. Atmos. Sci., 21, No. 2, 1964.
14. Shenk, W. E. J. Appl. Meteorol., 2, No. 6, 1963.

## RADIATION SAFETY PROBLEMS IN SPACE FLIGHTS

V. Ye. Nesterov, N. F. Pisarenko,  
I. A. Savenko, P. I. Shavrin

The matter of radiation safety in space flights is one of the important problems arising in the conquest of space. Despite the large number of experiments in this general area in recent years, there has been insufficient study of many aspects of this problem.

As the reader knows, radiation danger in space is caused by three basic types of ionizing radiation:

primary cosmic radiation,  
radiation of the Earth's radiation belts, and  
radiation generated during major chromospheric flares on the Sun.

Let us take a more detailed look at each of these types of radiation.

### Primary Cosmic Radiation

According to Soviet space rocket data (Ref. 1, 2) the intensity of galactic cosmic radiation in space fluctuates from 2 to  $4.5 \text{ particle} \cdot \text{cm}^{-2} \cdot \text{sec}^{-1}$  depending on the eleven-year cycle of solar activity. In years of maximum solar activity the dosage from this radiation is 15 mrad per day, 569 or about 5 rad per year. In the period of minimum solar activity this dose increases by a factor of 2 to 2.5. The amount of this dose depends slightly on the shielding provided by the spaceship frame, due to the powerful penetrating capacity of primary radiation.

When, however, the components of primary radiation hit such a large object as the human body a "multiplication" of the incident beam will be observed in the large object. If we approximately stipulate that the interaction of primary radiation with the human body is similar to that with the Earth's atmosphere, then the altitudinal dependence of ionization in the atmosphere may be used to evaluate the average tissue dose increase in the body. This factor leads to a dosage increase of at least two times. In order to convert from a physical dose in rads to a biological dose in rems, the former must be multiplied by an RBE (relative biological effectiveness) coefficient. The RBE coefficient for primary radiation is not at present precisely known, but it is clearly substantially greater than unity. Its possible value according to the data of different authors, varies from 4 to 7.

The possible value of a dose of primary cosmic radiation thus will amount to 10-25 rad per year or (RBE = 4) to 40-100 rem per year, depending on the period of solar activity. Existing medical rules permit an irradiation dose of no more than 5 rem per year (Ref. 3). It is

interesting to note that 92% of the biological dose is derived from the heavy component ( $Z \geq 10$ ) of primary radiation.

Thus, the question of evaluating radiation danger from primary cosmic radiation is now passing from physicists to radiobiologists and medical men. With its extreme importance to long-lived orbiting space stations and flights on the Earth-Mars-Earth and Earth-Venus-Earth trajectories, it is essentially reduced to the possibility or impossibility of chronic irradiation of participants in such a space flight by doses of 1-2 rad or 4-8 rem per month.

### Radiation Zones of the Earth

The energetic proton component and hard electrons of the Earth's radiation zones have remained until recently a source of grave radiation danger to flights in circumterrestrial space. In space vehicle flights on elliptical and circular orbits with an apogee from 300 to 2000 km, practically the entire dose will be collected in the region of the Brazilian anomaly in the Western Hemisphere.

A detailed study of the radiation environment in the radiation zones was carried out during 1960-1964 with equipment installed on more than 30 spacecrafts and satellites of the "Kosmos" series and the "Elektron" scientific space stations.

The result of this research was the compilation of charts showing the planetary distribution of absorbed dosages and radiation fluxes at different altitudes, as well as a determination of the total doses which would be registered within the spacecraft during flights along the various orbits. The table below gives some results of these measurements. These data have been converted to January, 1965, and refer to elliptical orbits; perigee altitude in all cases was 300 km, and orbital inclination was  $65^\circ$ . The dosage for circular orbits must be increased by a certain factor close to 2.

The tabulated data show that radiation formed in the radiation zones after the atmospheric nuclear explosions of 1962, in addition to primary 570 cosmic radiation and the proton component of the radiation belts, makes a substantial contribution to the instrument readings. By the end of 1963, the number of artificially trapped injected particles had diminished approximately by a factor of ten. By the end of 1964, this quantity at altitudes above 1000 km had apparently further decreased by no more than a factor of 1.5, while at lower altitudes the intensity had fallen significantly.

The tabular findings were utilized in evaluating the radiation situation on the flight trajectory of spacecraft "Voskhod-2". The flight orbit reached 495 km at apogee and 173 km at perigee with an inclination of  $65^\circ$ . According to these data, the dose within the spacecraft should have been

50 to 70 mrad per day. On-board measurements in flight gave an absorbed radiation dosage for both cosmonauts (P. Belyayev and A. Leonov) of 60 mrad. The metered values were in good agreement with the calculated values. Both cosmonauts received the very same dose.

TABLE

Number in Order	Apogee Altitude, km	Daily dosage by natural radiation zones and cosmic radiation, rad	Daily dosage by natural and artificial radiation zones and cosmic radiation, rad
1	300	0.012	0.012
2	400	0.025	0.025
3	500	0.050	0.070
4	600	0.070	0.150
5	700	0.100	0.300
6	800	0.200	0.600
7	900	0.300	1.000
8	1000	0.700	1.800
9	1500	--	6.000
10	2000	--	30.000

The study of the radiation zones at great altitudes and, principally, a more detailed determination of the spatial location of the energetic proton and electron components represent a very urgent task. It must be noted that the experimental findings received from the "Elektron" satellites are of great scientific and practical significance in settling questions of radiation safety in spacecraft flights near Earth. These were the first data enabling us to compile charts of the planetary distribution of radiation up to distances of 60,000 km.

It is extremely important to note that, besides the dose which can be received inside the spaceship and which comes chiefly from the hard component of trapped radiation, the danger is very grave when the cosmonaut in a spacesuit operates in zones where there are even softer radiation components. Thus, electron fluxes of an average energy of hundreds of kev in the magnetosphere reach values of  $1 \text{ erg} \cdot \text{cm}^{-2} \cdot \text{sec}^{-1}$ , and can in time amount to  $100 \text{ erg} \cdot \text{cm}^{-2} \cdot \text{sec}^{-1}$  in the aurorae polaris regions. Such irradiation can damage the spacesuit material and endangers the life of a cosmonaut outside the spacecraft.

The main radiation danger during long space flights involves radiation generated during large-scale chromospheric flares. This phenomenon, discovered during the last solar activity cycle, has been studied very little in many respects. The time behavior of the different energetic radiation components, the spectra and integral fluxes, the angular distributions, and several other characteristics have been quite inadequately investigated.

All of this prevents a definite determination of the level of possible radiation injury in flight during a burst. In the most powerful flares (February 23, 1956, May 10, 1959, August 10-16, 1959, November 12-15, 1960) the possible irradiation dosages for a man in a spacecraft behind several grams of shielding per square centimeter is 100 to 1000 rad.

From the findings available at present, a table of solar flare characteristics has been compiled for the last solar activity cycle to enable us to determine the degree of radiation danger and the probability of radiation injury when entering a burst.

During maximum solar activity, the probability that a spacecraft will hit upon a period of major solar flare occurrence - for example, like the flare of November 12-15, 1960 - is about 15%. In a period of minimum solar activity this probability is substantially reduced. We are at present observing a solar activity minimum. Subsequently, solar activity will rise and reach its peak in 1968-1970.

The probability of a space vehicle entering a flare may be reduced in practice by forecasting radiationally dangerous solar flares, but, because of a lack of experimental data, forecasting methods are at the very beginning stages of development. Forecasting of large-scale chromospheric flares can at present cover only a period on the order of 2 or 3 days with a probability of no more than 50%. The development of a reliable method for predicting radiationally dangerous solar flares over a longer period, on the basis of current observations of sun-spot magnetic fields or penumbras of these spots is apparently improbable.

One of the important problems in the near future is therefore to seek and develop additional new methods of long-term forecasting. Thus, space flights in the next five years will require strict attention to the problem of radiation safety.

It should be particularly noted that the present lack of information on radiationally dangerous solar flares makes it impossible to draw any definite inferences or to make any recommendations about protecting the spacecraft crew from solar cosmic-ray action during prolonged flights - i.e., the radiation safety of these flights cannot be guaranteed with sufficient reliability. All of this urgently requires prompt solution of the following basic tasks in the field of space-flight radiation safety.

1. Careful study of spectra for  $Z$  (especially when  $Z \geq 10$ ), and also a determination of the nuclear interaction of these components with matter, are requisite when investigating primary cosmic radiation.

2. An investigation of radiation zones demands that a study also be made of the dynamics of trapped radiation, particularly the origin and time behavior of the energetic electron component and of processes occurring during the interaction of solar plasma and the Earth's magnetosphere, including - which is very important - the polar aurorae. /572

3. Finally, a study of solar flares and the corpuscular and electromagnetic radiation thus generated.

a. Thorough investigation of the energy and charge spectra of corpuscular radiation generated in solar flares. Familiarity with the spectrum permits more precise determination of the dose absorbed inside the spacecraft, selection of proper design, or other methods of protecting the crew. It is possible that existing estimates of degree of dosage during flares are too high. In this case, a knowledge of corpuscular radiation spectra may result in reducing present requirements. These data are particularly important, since the possible dose magnitudes are either on the borderline or somewhat in excess of critical values; any increase in precision, even by low factors, is extremely important here.

b. Study of the time-development nature of solar flares and the corpuscular streams associated with them. This problem involves a study of the propagation of solar-generated particles into space between the Sun and the Earth. Solar cosmic-ray isotropy during the various solar perturbation periods and short-term forecasting of solar cosmic-ray occurrence are of extreme importance in this problem.

c. Development of methods for long-term forecasting of radiationally dangerous solar flares. The establishment of a correlation between the nature of the corpuscular radiation in such flares and diverse heliophysical characteristics observed immediately preceding the flares is very important in this regard. We may possibly be successful in discovering the heliophysical forerunners of radiationally-dangerous solar flares, and this would significantly advance long-term forecasting.

Solution of the problems which have been posed requires the formulation of extensive experiments on artificial Earth satellites to study the Sun. It is particularly important that the artificial satellite research be tied in with a wide heliophysical and optical measurement network on the Earth, as well as with a network measuring solar radio emission.

#### REFERENCES

1. Vernov, S. N., Chudakov, A. Ye., Vakulov, P. V., Logachev, Yu. I., and Nikolayev, A. G. Doklady Akademii Nauk SSSR (DAN SSSR), 130, 517, 1960.

2. Vernov, S. N., Chudakov, A. Ye., Vakulov, P. V., Gorchakov, Ye. V., Logachev, Yu. I., Lyubimov, G. P., Nikolayev, A. G. Kosmicheskiye Issledovaniya, 2, 633, 1964.
3. Medical Rules for Working with Radioactive Materials and Sources of Ionizing Radiation (Sanitarnyye pravila raboty s radioaktivnymi veshchestvami i istochnikami ioniziruyushchikh izlucheniye). Atomizdat, Moscow, 1960.

---

## STUDY OF METEORIC MATTER

T. N. Nazarova

Meteoric matter which is a constituent of the solar system has the appearance of a multitude of solid bodies having a diameter from several tens of kilometers to several microns. As they move through interplanetary space, meteoric bodies are invisible from the Earth, since their reflection of sunlight is too faint. Only the total reflection and diffusion effect created by a great number of particles is accessible to the earthbound observer in the form of weak luminescence of zodiacal light. Individual meteor particles become visible to the terrestrial observer only when - invading the Earth's atmosphere, becoming red hot, and vaporizing - they produce short-lived flashes and form shafts of ionized gas in their wake, while meteoric bodies which remain after passage through the atmosphere fall onto the Earth's surface. /573

For this reason an investigation of meteoric matter from the Earth is conducted by photometric study of zodiacal light and of the F-component of the solar corona. This gives the spatial density of particles having the mass  $m < 10^{-6}$  g in interplanetary space. Optical and radar observations of the phenomena attending the motion of a meteoric body in the Earth's atmosphere allow us to measure the velocity vector, mass, density, composition, and spatial density of particles of mass  $m > 10^{-4}$  g and to extend these findings to the space surrounding the Earth's orbit. The collection and investigation of meteorites which have fallen to Earth provide information on composition, age, and rate of accretion of meteorites. Thus, up to the present time observations of meteoric particles from Earth have enabled us to obtain rather complete data on particles having a mass greater than  $10^{-4}$  g. However, extrapolation of these data to particles of smaller mass is not admissible in all cases (in particular, the nature of spatial density change of particles as their mass decreases) (Ref. 1-3).

With the advent of research rockets and artificial Earth satellites, it has been possible to record individual particles having a mass down to approximately  $10^{-13}$  g both near Earth and in interplanetary space. The scientific equipment installed on rockets and satellites registers the spatial density of meteoric particles, their momentum or energy and mass, (on the condition that particle velocity is given) (Ref. 4). In spite of the nonuniformity and restricted volume of the experimental material, Soviet and American measurements at altitudes of 100-300 km have demonstrated the existence of a dense dust envelope about the Earth (Ref. 6).

Independent confirmation of the increased density of dust particles in the vicinity of the Earth is given by observing the luminescence of the twilight sky. For particles of  $m = 10^{-8}$  g at an altitude of  $H=100-300$  km the number  $N$  of impacts per square meter per second is  $3 \cdot 10^{-2} - 7 \cdot 10^{-1}$ , and at altitudes of 400-2000 km  $N \sim 10^{-3} \text{ impact} \cdot \text{m}^{-2} \cdot \text{sec}^{-1}$ . Extreme estimates of matter in the zodiacal cloud made photoelectrically give  $10^{-4} - 10^{-5} \text{ m}^{-2} \cdot \text{sec}^{-1}$ . Figure 1 gives the average combined curve of the number of impacts of sporadic meteoric particles with masses from  $10^{-7}$  to  $10^{-11}$  g, plotted by Alexander et al. from American and Soviet rocket and satellite measurements (Ref. 5, 7, 8). Findings by "Elektron-2" are entered in this graph (Ref. 10). There is a difference between the Soviet and American studies for the assumed dependence of impulse on particle mass and velocity recorded by the sensors. The American works use  $I = mv$  and the Soviet,  $I = A \frac{mv^2}{2}$ , where  $m$  and  $v$  are mass and velocity of the meteoric particle.

Apparently the difference between the numerical value of the coefficient and the velocity values adopted for the calculations results in final values which are in good agreement within the limits of measurement accuracy.

Meteoric particle density is subject to fluctuations in time and space. There are individual bunchings of particles with nonuniform spatial density. The linear dimensions of these bunchings fluctuate widely, reaching millions of kilometers. The satellite "Elektron-2" during observations from January 30 to March 10, 1964, with an exposure time of 1,778,460 sec, recorded three bunchings of meteoric particles, 1575 representing formations with linear dimensions from 3 to 5 million kilometers. The first one, recorded on January 30-31, 1964, was dense enough for the direction of its motion to be determined (Figure 2).

A geometric examination of the problem showed that the angle between the velocity vector direction of the bunching and of the Earth was about  $42^\circ$ . If it is assumed that the bunching had a maximum possible velocity of  $42 \text{ km} \cdot \text{sec}^{-1}$  at the Earth's distance from the Sun, then the average relative encounter velocity of meteoric particles and sensors was about  $61 \text{ km} \cdot \text{sec}^{-1}$ . The average number of impacts in this case was  $1.1 \cdot 10^{-1} \text{ impact} \cdot \text{m}^{-2} \cdot \text{sec}^{-1}$ . As in our previous work, we estimated the mass of the recorded particles from the ratio  $I \sim \frac{mv^2}{2}$ , of impulse ( $I$ ) received by the sensor, particle mass ( $m$ ) and velocity  $v$ , assuming  $v = 61 \text{ km} \cdot \text{sec}^{-1}$ . Of the



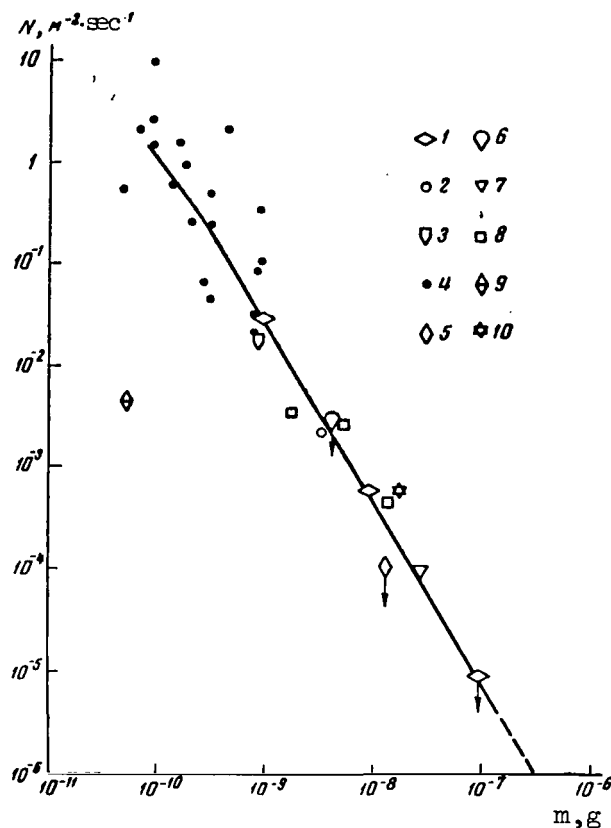


Figure 1

Average Combined Curve of Meteoric Particle Distribution by Mass in Vicinity of Earth From Rocket and Satellite Observations.

1 - "Explorer-8" (U.S.); 2 - "Vanguard-3" (U.S.); 3 - "Explorer-1" (U.S.); 4 - rockets (U.S.); 5 - third satellite (USSR); 6 - first space rocket (USSR); 7 - second space rocket (USSR); 8 - automatic interplanetary station (USSR); 9 - "Pioneer-1" (U.S.); 10 - "Elektron-2" (USSR).

185 particles recorded in this bunching, 166 had  $4.4 \cdot 10^{-9} \text{ g} \geq m \geq 1.3 \cdot 10^{-9} \text{ g}$ ; 10 had  $10^{-8} \text{ g} \geq m \geq 4.4 \cdot 10^{-9} \text{ g}$ ; 7 had  $3.3 \cdot 10^{-8} \text{ g} \geq m \geq 10^{-8} \text{ g}$ ; and two had  $m > 3.3 \cdot 10^{-8} \text{ g}$ .

It can be seen that it is impossible to characterize the distribution of the particles in this bunching by mass by using the single formula  $f(M) \frac{1}{M^n}$ , where  $n = \text{const}$ ; for  $m_1$  and  $m_2$  the value  $n > 2$ , for  $m_2$  and  $m_3$   $n < 2$ , and for  $m_3, m_4$   $n < 2$ . In the period before March 10, 1964, while

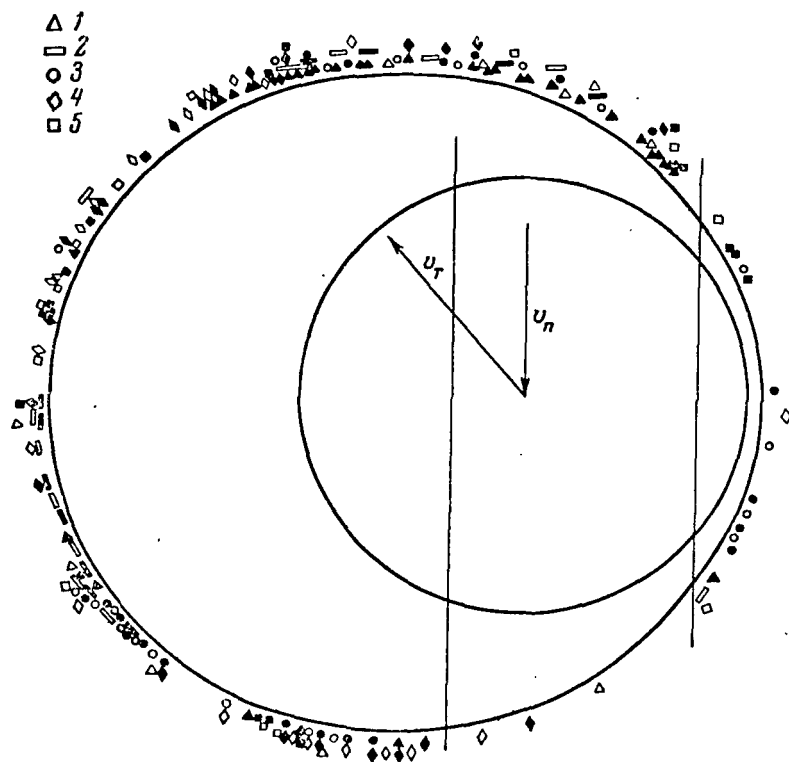


Figure 2

Bunching of Meteoric Particles on January 30-31, 1964

1 - first revolution; 2 - second; 3 - third; 4 - fourth,  
5 - fifth.

the equipment was functioning there were two more meteoric particle bunchings recorded on February 11-13 and February 23-25. Since in this period a small number of impacts were recorded (in one case -10, and the other -24) it seemed impossible to ascertain the possible bunching directions of motion. The particle velocity adopted was  $v = 15 \text{ km} \cdot \text{sec}^{-1}$ , which we ordinarily use for sporadic meteoric particles.

The number of impacts recorded of particles with the mass  $6.5 \cdot 10^{-8} \text{ g} \geq m \geq 2 \cdot 10^{-8} \text{ g}$  per square meter per second in these cases was  $N_2 = 2.4 \cdot 10^{-3} \text{ m}^{-2} \cdot \text{sec}^{-1}$  and  $N_3 = 5.8 \cdot 10^{-3} \text{ m}^{-2} \cdot \text{sec}^{-1}$ . From February 29 to March 10, 1964, four more meteoric particle impacts were registered, two in about 22 hours from February 29 to March 1 and two on March 5 in approximately 14 hours. The average  $N$  for particles with  $6.5 \cdot 10^{-8} \text{ g} \geq m \geq 2 \cdot 10^{-8} \text{ g}$  in the February 3 - March 10, 1964, period was  $7.5 \cdot 10^{-4} \text{ impact} \cdot \text{m}^{-2} \cdot \text{sec}^{-1}$ , which fits well into the combined curve plotted by Alexander et al. (U.S., 1962).

Bunchings of micrometeor particles which did not coincide with streams known on the Earth had also been observed earlier. Near Earth on May 15, 1958, equipment aboard the third satellite recorded from 4 to 11 impact.  $\cdot m^{-2} \cdot sec^{-1}$  of particles with the mass  $2 \cdot 10^{-7} g \geq m \geq 6 \cdot 10^{-8} g$  (for  $v = 15 km \cdot sec^{-1}$ ). The mass of a particle in this bunching may have been on the order of  $5 \cdot 10^{-10} g$  on the assumption that its velocity was  $70 km \cdot sec^{-1}$ . From November 31, 1962, to January 30, 1963, at a distance of 23-45 million kilometers from the Earth, the interplanetary station "Mars-1" recorded an elevated density of meteoric particles - 104 impacts in 4 hours 13 minutes 30 seconds. (After January 30, 1963, the equipment for registering meteoric particles no longer functioned.) The station had apparently encountered a stream of meteors which could not be successfully identified with any known on the Earth.

With the satellite "Explorer-1" American investigators also observed a "stream of sporadic meteors" unrecorded on Earth (Ref. 9). From preliminary reports the spacecraft "Mariner-4" flying toward Mars (1965) in one phase of its trajectory recorded an elevated density of meteoric particles, possibly belonging to a bunching similar to that recorded by the station "Mars-1". Thus, there are many meteoric streams and bunchings which are unknown on Earth in interplanetary space, and it is still impossible to predict them. The occurrence of extended (up to millions of kilometers) and dense formations, where one meteoric body can occur in a cube with a side of several tens of meters, is dangerous for spacecrafts remaining in space for a long period of time, as it may cause surface erosion, optical damage, and rupture of fine structural elements. /576

Future prolonged and systematic research of different regions in interplanetary space by means of space vehicles will make it possible to expand and refine our information regarding the solid component of interplanetary matter, to widen the circle of meteoric streams with which we are acquainted, and possibly to predict the probability of spacecrafts encountering them in the future.

#### REFERENCES

1. Levin, B. Yu. Physical Theory of Meteors and Meteoric Matter in the Solar System (Fizicheskaya teoriya meteorov i meteornoye veshchestvo v solnechnoy sisteme). Izdatel'stvo AN SSSR, 1956.
2. Whipple, F. L. Nature, 189, 127, 1961.
3. Whipple, F. L. J. Geophys. Res., 68, 4929, 1963.
4. Alexander, W. M., McCracken, C. W. Review of Direct Measurements of Interplanetary Dust from Satellites and Probes. Paper Presented at the COSPAR meeting, May, 1962.
5. Isakovich, M. A., Roy, N. A. In "Iskusstvennyye Sputniki Zemli". Izdatel'stvo AN SSSR, No. 2, p. 81, 1951.

6. Moroz, V. I. In "Iskusstvennyye Sputniki Zemli". Izdatel'stvo AN SSSR, No. 12, p. 151, 1962.
7. Nazarova, T. N. In "Iskusstvennyye Sputniki Zemli". Izdatel'stvo AN SSSR, No. 12, p. 141, 1962.
8. Nazarova, T. N. Kosmicheskiye Issledovaniya, 1, No. 1, p. 169.
9. Dubin, M., McCracken, C. W. Astr. J., 67, 248, 1962.
10. Nazarova, T. N., Rybakov, A. K. Report to the Sixth COSPAR Symposium (Doklad na 6-m simpoziume COSPAR). Buenos Aires, May, 1965.

# MEASUREMENT OF SCATTERED $L_{\alpha}$ - RADIATION IN THE VICINITY OF THE EARTH AND IN INTERPLANETARY SPACE

V. G. Kurt

The space vehicle "Zond-1", which was launched on April 2, 1954, carried apparatus for measuring scattered ultraviolet radiation. This equipment consisted of two photon counters with windows made of lithium fluoride and NO-filling, as well as a two-channel intensimeter with logarithmic outputs in a recording rate range from 3 to  $10^4$  impulse $\cdot$ sec $^{-1}$ . Both counters were screened with lead ( $3.5 \text{ g}\cdot\text{cm}^{-2}$ ) throughout their entire surface, with the exception of the window having a surface area of  $0.7 \text{ cm}^{-2}$ . The photon counters had identical collimators which limited the field of vision to  $1.15 \cdot 10^{-2}$  sterad. A filter made of calcium fluoride was placed before one of the counters, in order to cut off radiation having a wave length shorter than  $\lambda 1225 \text{ \AA}$ . The long-wave boundary of the counters was located at about  $\lambda 1350 \text{ \AA}$ . The counters were assembled in series, and were supplied with high voltage ( $\sim 900 \text{ v}$ ) from a general voltage transformer. There were also two emitter repeaters, along with the photon counters. The counters were standardized for  $L_{\alpha}$  - radiation by means of an ionization /577 chamber and a thermoluminescent phosphor (Ref. 1):

Close to the Earth "Zond-1" moved at an angle of approximately  $90^\circ$  to the Earth-Sun line, rotating around an axis directed toward the Sun. The optical photometer axis described a cone with an angle of opening of  $160^\circ$  (Figure 1). At a distance ranging from 37 to 47 thousand km, four complete photometer cross sections of the hydrogen corona of the Earth were obtained. The photometer axis thus passed at a distance of 8700 km from the center of the Earth. In addition to these four cross sections, data pertaining to the distance of 180 thousand km, as well as to 15 million km, were obtained. In the latter case, it can be assumed that the equipment recorded only radiation from the interplanetary medium. An analysis of these observations will be given later. Let us introduce the following notation in order to change from the observed quantities to the surface brightness as a function of the distance from the center of the Earth:

- $R_e$  - radius of the Earth;
- $R_0$  - distance of the object to the center of the Earth;
- $\rho$  - shortest distance from the center of the Earth to the optical axis of the photometer, measured in units of  $R_e$ ;
- $y$  - Distance along the line of sight;
- $2\alpha$  - Angle of opening for the cone whose generatrix is used to direct the optical axis of the equipment;
- $\omega$  - Angle of rotation of the object, calculated from the position at which the photometer axis is located at a minimum distance from the Earth;
- $\gamma$  - "Sun-object-center of the Earth" angle; /578
- $\xi = 180^\circ - \gamma$ ;
- $\zeta$  - Angle between the photometer axis and the direction of the object toward the center of the Earth.

It can be seen from Figure 2 that

$$\rho = R_0 \sin \zeta. \quad (1)$$

Thus, for  $\omega = 0, \pi$  we have

$$\zeta = \alpha - \xi \quad \text{and} \quad \zeta = \alpha + \xi \quad (2)$$

respectively.

By determining the coordinates of the points  $N(x, y, z)$  and  $T(X, Y, Z)$ , one can readily obtain the expression for  $\cos \zeta$ :

$$\cos \zeta = \frac{Xx + Yy + Zz}{|ON| R_0} \quad (3)$$

or

$$\cos \zeta = \cos \xi \cos \alpha + \sin \xi \sin \alpha \cos \omega. \quad (3a)$$

In our case  $\xi = 68^\circ$  and  $\alpha = 80^\circ$ .

Substituting the value of  $\zeta$  from (3a) in (1), we can determine the dependence of  $\rho$  on  $\omega$  (Figure 3). We should note that the function  $\rho(\omega)$  has four extremes when  $\omega$  changes from 0 to  $2\pi$ . It can be seen that  $\rho(\omega)$  will be a symmetrical function with respect to  $\omega = \pi$ . On the cross section  $0 \leq \omega \leq \pi$ , we thus have two minima for  $\omega = 0, \pi$  and one maximum close to  $\omega = \pi/2$ . We should note that - beginning with  $\omega = 0.18\pi$  to  $\omega = 1.82\pi$  - the function of  $\rho$  is two-valued, i.e., two values of  $\omega$ :  $\omega_1$  and  $\omega_2$  correspond to the same value of  $\rho$ . In the second case, the perpendicular drawn from the center of the Earth intersects the continuation of the optical axis of the equipment.

The observed surface brightness  $B(\rho)$  is determined by the integral

$$B_{1,2} = \int_{\pm y_0}^{\pm \infty} F(R) dy \quad (4)$$

(index 1 corresponds to  $+y_0$ , while 2 -  $y_0$ ), where  $y$  is calculated at both sides of the point N, and  $F(R)$  is the volumetric luminescence equalling, in its turn

$$F(R) = \frac{\pi F_s}{4\pi} \sigma_0 \left( \frac{2\Delta\lambda_D}{\Delta\lambda_s} \right) n(R). \quad (5)$$

Here  $\pi F_s$  is the stream in the line  $L_\alpha$  from the Sun;  $\sigma_0$  - the effective scattering cross section in the center of the line;  $\Delta\lambda_D$  - the Doppler halfwidth of the scattered radiation line;  $\Delta\lambda_s$  - the width of the solar emission line  $L_\alpha$ ;  $n(R)$  - the concentration of neutral hydrogen. The assumption is thus introduced that the concentration is a function of only the distance from the center of the Earth, and does not depend - for example - on the zenith distance of the Sun, the geographical latitude, etc. /579

In addition, by selecting two values of  $B(\rho)$  corresponding to the same  $\rho$ , but different  $\omega$ , one can readily show that

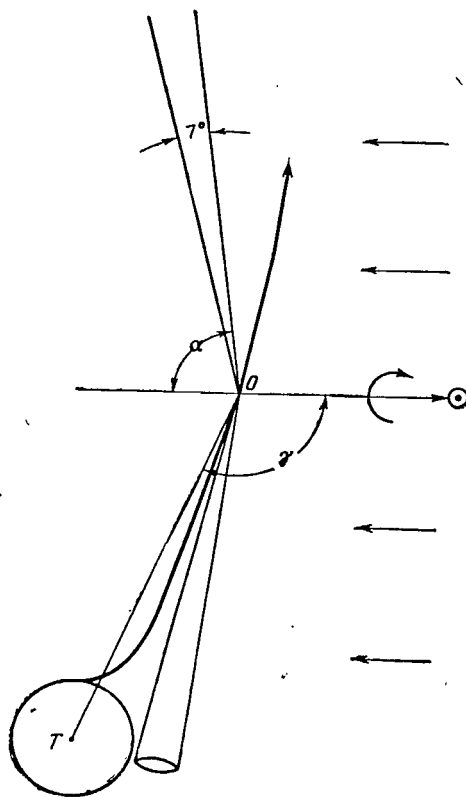


Figure 1

$$B_1(\rho) + B_2(\rho) = I(\rho), \quad (6)$$

where

$$I(\rho) = \int_{-\infty}^{\infty} F(R) dy. \quad (7)$$

In actuality, we have

$$\int_{-y_0}^{\infty} F(R) dy + \int_{+y_0}^{\infty} F(R) dy = \int_{-y_0}^0 F(R) dy + \int_0^{\infty} F(R) dy + \int_{y_0}^{\infty} F(R) dy.$$

Since  $\int_{y_0}^0 F(R) dy = \int_0^{-y_0} F(R) dy$ , expression (8) will be

$$2 \int_0^{\infty} F(R) dy = \int_{-\infty}^{+\infty} F(R) dy. \quad (8a)$$

Thus, for the angle interval  $0.18\pi \leq \omega \leq \pi$  it is possible to obtain the dependence  $I(\rho)$  from the observations. For the region  $0 \leq \omega \leq 0.18\pi$ , we have the quantity  $B_1(\rho)$ , and  $B_2(\rho)$  ( $\rho \leq 3.5$ ) can be readily obtained by

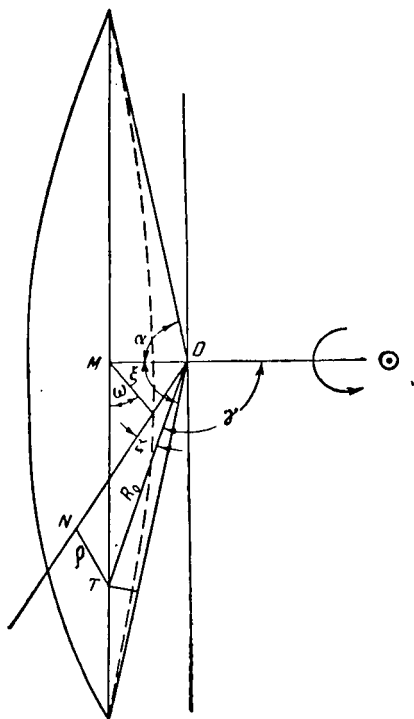


Figure 2

extrapolation. Since an overwhelming number of hydrogen atoms are located within the sphere of radius  $R_0$ , the quantity  $B_2(\rho)$  must depend comparatively slightly on  $\rho$ , or on  $\omega$ , which is well illustrated in Figure 4. For  $y_0 = 6.5$ , both values of  $B_1$  and  $B_2$  are equal. Figure 4 also shows the dependence  $I(\rho)$ . The values of  $B_1$  and  $B_2$  were obtained from observations by averaging all four recordings pertaining to the mean distance  $R_0 = 42000$  km. All the values of  $B(\omega)$  were employed for the best averaging, and it was assumed that  $B(\omega) = B(\omega + \pi)$ . In the case of  $\rho = \omega$ , the value of  $I(\rho)$  was obtained from observations in the case of  $R_0 = 1.5 \cdot 10^7$  km. In order to obtain  $n(R)$ , it is necessary to solve the integral equation of Abel (Ref. 7), the solution of which has the following form:

$$F(R) = -\frac{1}{\pi} \int_R^{\infty} \frac{\frac{dI}{d\rho}}{\sqrt{\rho^2 - R^2}} d\rho. \quad (9)$$

For  $I(\rho)$ , we employed the following type of dependence which was chosen empirically:

$$I(\rho) = \sum_i \frac{K_i}{\rho^{m_i}}, \quad (10)$$

$$I(\rho) = 10^7 \left( \frac{6.5}{\rho^{2.77}} + \frac{12.8}{\rho^{0.53}} \right) \text{quantum} \cdot \text{cm}^{-2} \cdot \text{sec}^{-1} \cdot \text{sterad}^{-1}.$$



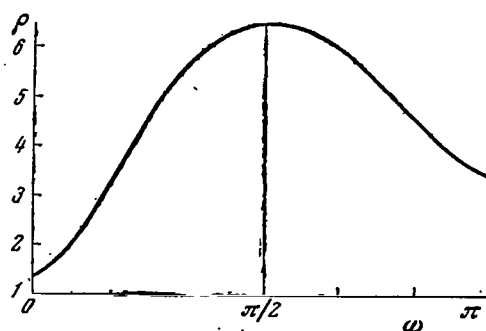


Figure 3

We should point out that (10) represents experimental data only within the limits by which  $\rho$  changes from 1.25 to 6.5. In the case of the solar corona (Ref. 2), we have

$$F(R) = \frac{\Gamma(1,5)}{\pi} \sum_i \frac{m_i K_i}{R^{m_i+1}} \frac{\Gamma\left(\frac{m_i+1}{2}\right)}{\Gamma\left(\frac{m_i}{2}+1\right)} \quad (11)$$

where  $\Gamma$  is the gamma function.

Substituting the values of  $m_i$  and  $K_i$  in (11), we obtain the expression for  $F(R)$  and then the expression for  $n(R)$  from (5): /580

$$n(R) = 10^2 \left( \frac{6,7}{R^{3,77}} + \frac{4,0}{R^{1,53}} \right) \text{cm}^{-3}. \quad (12)$$

Naturally, this formula is not applicable for  $R > 6.5$ . Integrating the expression (12) with respect to  $R$  up to infinity, we obtain the expression for  $N$ :

$$N(R) = 10^{11} \left( \frac{1,3}{R^{2,77}} + \frac{4,0}{R^{0,53}} \right) \text{cm}^{-2}. \quad (13)$$

In order to change from  $F(R)$  to  $n(R)$  and  $N(R)$ , according to formula (5) it was assumed that the temperature of scattered atoms is  $10^3$  °K,  $\sigma_0 = 2 \cdot 10^{-13} \text{cm}^2$ ;  $\Delta\lambda_D = 1.6 \cdot 10^{-2} \text{Å}$ ,  $\Delta\lambda_S = 1 \text{Å}$  and  $\pi F_S = 2 \cdot 10^{11} \text{quantum} \cdot \text{cm}^{-2} \cdot \text{sec}^{-1}$ . The value  $T = 10^3$  °K pertains to the illuminated side of the Earth, and for the period of minimum solar activity in 1964 it is hardly too low. The Table below presents the values of  $n(R)$  and  $N(R)$  calculated according to formulas (12) and (13). Since the optical thickness is small (0.1-0.3) in the case of  $R = 1.25$ , the change from  $I(R)$  to  $F(R)$  and  $n(R)$ , which was performed above, can be effected by the formulas (5) and (9).

Let us now discuss the results which have been obtained. Donahue (Ref.3) has compiled the most plausible model for the distribution of neutral hydrogen, which is presented in the last column of the following Table. His distribution differs from the distribution obtained experimentally primarily due to a larger gradient. If the experimental data are described by a power law with the index  $n$  at large distances ( $R > 3R_e$ ), then the results of the study (Ref. 3) correspond to  $n = -3.3$ . In addition, for  $R < 2R_e$  the model

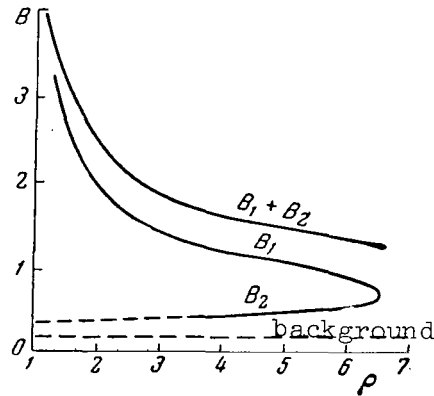


Figure 4

TABLE

R	$R, 10^3 \text{ km}$	$n, \text{ cm}^{-3}$	$N, \text{ cm}^{-2}$	$n(\text{according to [Ref. 3]})$
1.25	8.1	$6.5 \cdot 10^2$	$4.30 \cdot 10^{11}$	$2.5 \cdot 10^4$
1.50	9.6	3.6	3.62	$8.0 \cdot 10^3$
2.00	12.8	1.9	3.10	$2.4 \cdot 10^3$
2.50	16.0	1.2	2.70	$9.5 \cdot 10^2$
3.00	19.0	0.84	2.42	$4.5 \cdot 10^2$
3.50	22.4	0.65	2.20	$2.6 \cdot 10^2$
4.00	25.6	0.51	2.06	$1.5 \cdot 10^2$
4.50	28.8	0.42	1.90	$9.5 \cdot 10$
5.00	32.0	0.36	1.82	$6.0 \cdot 10$
5.50	35.1	0.31	1.75	$4.0 \cdot 10$
6.00	38.3	0.26	1.69	$3.0 \cdot 10$
6.50	41.6	0.22	1.63	$2.2 \cdot 10$

of Donahue leads to much larger values of the hydrogen concentration. Equal values are obtained in the case of  $R = 6.6 R_E$ . At large distances from the Earth, the theoretical model provides concentrations which are lower than those values which we found. If it is assumed that the counter sensitivity does not change, then even at distances greater than 180,000 km, there is a significant amount of hydrogen. The change in intensity from 180,000 to  $15 \cdot 10^5 \text{ km}$  is  $1.5 \cdot 10^7 \text{ quantum} \cdot \text{cm}^{-2} \cdot \text{sec}^{-1} \cdot \text{sterad}^{-1}$ . When relating this quantity to the distance  $\sim 2 \cdot 10^5 \text{ km}$  we find that the mean hydrogen concentration at a distance of  $\sim 250,000 \text{ km}$  is on the order of  $1 \cdot 10 \text{ cm}^{-3}$ .

We should point out that we did not know the orientation of the equipment with respect to the Earth at the time the brightness was measured at a distance of 180,000 km. Therefore, we cannot draw any conclusions regarding the presence of an extended hydrogen "tail" at the Earth (Ref. 4). After analyzing the observations at a distance of

/581

$15 \cdot 10^6$  km, we can draw the main conclusion that there is no significant concentration of interplanetary hydrogen toward the ecliptic plane. The surface brightness at this distance is  $1.5 \cdot 10^{-4} \text{ erg} \cdot \text{cm}^{-2} \cdot \text{sec}^{-1} \cdot \text{sterad}^{-1}$ , which coincides fairly well with the data given by Morton and Purcell (Ref. 5). They obtained the value of  $4.1 \cdot 10^{-4} \text{ erg} \cdot \text{cm}^{-2} \cdot \text{sec}^{-1} \cdot \text{sterad}^{-1}$  by means of a filtering method. Taking into account the indeterminacy in the standardization both of our data, and of the measurements performed by Morton and Purcell, a difference of no more than three should be assumed. Accordingly, the concentration of neutral hydrogen in interplanetary space decreases threefold, calculated by Patterson, Jackson and Hanson (Ref. 6) on the basis of these observations. This amount is approximately  $10^{-2} \text{ cm}^{-3}$  at a distance of 1 to 45 au, which is almost independent of distance.

#### REFERENCES

1. Babichenko, S. I., Karpinskiy, I. P. et al. Kosmicheskiye Issledovaniya, 3, No. 3, 237, 1965.
2. Baumbach, S. Astron. Nachrichten, 267, 273, 1938.
3. Donahue, T.M. Preprint, January 16, 1963.
4. Brandt, J.C. Astrophys. J., 134, 394, 1961.
5. Morton, D.C., Purcell, J.D. Planet. Space Sci., 9, 455, 1962.
6. Patterson, T.N., Johnson, F.S., Hanson, W.B. Planet. Space Sci., 11, 767, 1963.

RESULTS OF RADIO EMISSION STRENGTH MEASUREMENTS  
AT 725 AND 1525 KC BY EQUIPMENT ON THE SATELLITE "ELEKTRON-2"

Ye. A. Benediktov, G. G. Getmantsev, N. A. Mityakov,  
V. O. Rapoport, Yu. A. Sazonov, and A. F. Tarasov

The extension of the range of radio-astronomical measurements toward medium and long waves involves the necessity of conducting appropriate measurements aboard artificial Earth satellites and rockets (Ref. 1, 2). It is obviously advisable to conduct these measurements on AES of relatively great apogee, so that the effect of the Earth's ionosphere on the results will be reduced to a minimum. In this sense, the experimental conditions on "Elektron" were very favorable, because at apogee the satellite receded to almost seventy thousand kilometers, and ionospheric influence on the measurement results was completely eliminated. On approaching perigee, "Elektron-2" "plunged" into the ionosphere. Based on the variation in the radio emission level received at the output of the receiving equipment, the profiles of electron concentration in the ionosphere could be determined in a rather extensive altitude range.

The measurement conditions on "Elektron-2" were also favorable, in the sense that the satellite was in operation for a relatively long period of time. Prolonged measurements made possible the discovery of sporadic radio emission at both frequencies: 725 and 1525 kc.

1. Radio Receiving Equipment and Measurement Method

Description of Equipment. Radio emission is received with receivers tuned to the fixed frequencies of 725 and 1525 kc. Both receivers have a common antenna which assumes the form of an oscillator, one of whose branches is a metal rod 3.75 m long and the other, the satellite frame with all its projecting parts. The capacitance  $C_a$  between the oscillator branches is 46 pf. Antenna radiation resistance  $R_\Sigma$  is 0.033 ohm at 725 kc, and 0.146 ohm at 1525 kc.

/582

The antenna is connected to receiver inputs by a coaxial feed whose capacitance, together with the connecting jacks, is 64 pf.

The circuit of the radio receivers uses direct amplification with three stages of HF amplification and two of the LF type. The d.c. voltages from receiver outputs, proportional to the signals to be measured, are fed to the telemetering system. The receivers are provided with an AVC system which extends the range of voltages which can be measured. The receiver passband widths at high frequency are, respectively, 3.9 and 7.4 kc; the range of measurable voltages is 0.2-10  $\mu$ v, and the time constant of the receiver output loops is  $\sim 1$  sec.

To suppress radio interference from satellite equipment, its common power-supply circuit contains a band filter with attenuation on the order of 80 db at the receivers' operating frequencies. The lack of radio interference was experimentally verified in the 0.5 - 1.5 Mc range with a special, high-sensitivity receiver.

Method of Measuring Strength of Radio Emission. Radio-emission strength  $I$  is

$$I = \frac{2kT_{\text{eff}}}{\lambda^2}, \quad (1)$$

where  $T_{\text{eff}}$  is the effective temperature averaged over the celestial sphere,  $k$  is Boltzmann's constant, and  $\lambda$  is the wavelength. Radio-emission temperature  $T_{\text{eff}}$  in turn is found from the formula

$$u_a = 4kT_{\text{eff}}R_{\Sigma}\Delta f, \quad (2)$$

where  $u_a$  is the emf induced in the antenna,  $R_{\Sigma}$  is antenna radiation resistance, and  $\Delta f$  is the receivers' passband width.

As is clear from formula (2), the amplitude characteristics of the receivers' output voltages and antenna radiation resistance must be known if radio-emission strength is to be determined from the output voltages. These parameters were measured when the equipment was calibrated on Earth. The receivers' amplitude characteristics were corrected during satellite flight according to their output voltages when operating with an internal noise generator. The amplitude characteristics of the receivers were recorded for several days before launching by means of a G2-1 (GShN-1) noise voltage generator, which was connected to their input over a capacity of 46 pf. This generator with the capacitance in series was a dummy antenna.

Noise generator voltage  $u_a$  was determined from formula

$$u_a^2 = \frac{u^2 \Delta f}{n \Delta f_g}, \quad (3)$$

where  $u^2$  is the square of the effective voltage as measured by a thermocouple at attenuator input,  $n$  is the power reduction of the generator attenuator, and  $\Delta f_g$  is the width of the generated noise spectrum. Recording of the receiver's amplitude characteristics was reduced to measuring the dependence of their output voltages on  $n$ , since  $u^2$  was kept constant. /583

It follows from formulae (2) and (3) that

$$T_{\text{eff}} = \frac{u^2}{4kn\Delta f_g R_\Sigma} \quad (4)$$

Effective radio-emission temperature was ascertained directly from this formula.

Antenna capacitance was experimentally measured on the satellite's dummy antenna by varying the frequency of a transmitter whose oscillatory circuit was switched in between the rod and the satellite frame. To eliminate antenna field distortion, the transmitter was placed inside the dummy housing. The change in transmitter frequency when the rod antenna was connected was determined by a special receiver 30 meters away from the dummy. Antenna radiation resistance  $R$  was found by formula

$$R_\Sigma = 800 \left( \frac{l_{\text{eff}}}{\lambda} \right)^2, \quad (5)$$

where  $l_{\text{eff}}$  is the length of the equivalent symmetrical dipole with uniform current distribution.

Effective length  $l_{\text{eff}}$  was experimentally established as follows.

The satellite's dummy antenna and an auxiliary rod antenna were placed on a metallized platform 50 x 50 meters square. An IP-12 field voltage meter was used to measure the emf induced in both antennae by a radio-broadcasting station operating at 825 kc. A 2-pf capacitance was switched on in series to the IP-12 input to eliminate the effect of antenna impedance on the measurements. The rod length was chosen so that the emf induced for both antennae were equal. It was found that the dummy satellite antenna during reception was equivalent to a rod 5.3 meters long, and that consequently,  $l_{\text{eff}} = 2.65$  m. Error in measurements of radio-emission strength was determined chiefly by inaccuracies introduced when measuring receiver amplitude characteristics and antenna radiation resistance. The noise generator and telemetering system contribute to the error in measuring amplitude characteristics. Systematic errors in measurements using the G2-1 noise generator were eliminated by supplementary measurements. The appropriate corrections were made when establishing  $T_{\text{eff}}$ .

Based on our estimates, the resultant error in the absolute values of cosmic radio-emission strength is  $\pm 30\%$  at a frequency of 1525 kc and  $(+30, -50)\%$  at 725 kc, while the ratio of radio-emission strength at the two frequencies is found with an error of  $\pm(15 \text{ to } 20)\%$ .

## 2. Description of Primary Measurement Results

The incoming signal levels at 725 kc and 1525 kc ("Elektron-2") and at 1110 and 2293 kc ("Elektron-4") are recorded by the telemetry system of the satellites as the output voltage of the measuring radio-receivers. At a certain time interval (approximately one hour), the input loops of the receivers are regularly switched from the antenna to the calibrated noise signal source to check the stability of equipment amplification. When the measurement results are processed, the output voltages are converted into effective temperature of radio-emission in conformity with the parameters of the radio-receiving equipment.

Twenty sections of incoming signal-level records pertaining to flights of "Elektron-2" near apogee were processed to find the effective temperature readings of the celestial sphere at the frequencies of 725 and 1525 kc. Figure 1 gives  $T_{\text{eff}}$  values successively obtained for two hours during one such flight of the satellite. The dots correspond to  $T_{\text{eff}}$  at  $f = 1525$  kc, and the crosses to  $T_{\text{eff}}$  at  $f = 725$  kc. The circles designate calibration points matching signals of the noise generator periodically connected to the receivers. As is evident from Figure 1, there is a certain point scatter resulting both from errors of an engineering nature, and possibly from a shift of the directional pattern of the receiving antenna over the celestial sphere because of satellite rotation. The path of "Elektron-2" and "Elektron-4" near perigee passed through the upper part of the F-layer of the ionosphere where plasma frequencies  $f_0$  were close to the operating frequencies of the receiving equipment. Therefore, near perigee there might be expected a reduced output signal level due to ionosphere influence on the receiving antenna parameters. The results of observations on "Elektron-2" and "Elektron-4" confirm this hypothesis. Figure 2a gives a typical example of the experimental relationship of the change in level of the signal being recorded at  $f = 1525$  kc during one of the flights of the satellite "Elektron-2", on the descending limb of its orbit when it entered the F-layer of the ionosphere. The incoming signal levels at  $f = 1525$  kc are indicated by dots. The calibration points, as in Figure 1, are encircled. The crosses note the signal levels at  $f = 725$  kc. Substantial attenuation of the signal at  $f = 1525$  kc during this flight began, as is apparent from Figure 2a, at altitudes of  $\sim 4000$  km. At the moment when the satellite was at an altitude on the order of 500 km, the output signal level proved to be close to that of the eigen noise of the equipment, and consequently practically no cosmic radio-emission was received by the antenna system. Figure 2b shows the dependence of signal level on altitude of satellite flight at  $f = 1525$  kc for one of the sectors on the ascending limb of the trajectory. It is clearly apparent that, as the altitude of the satellite increases, the signal level approaches the usual unperturbed level of cosmic radio-emission.

/584

Similar recordings have also been obtained at frequencies of 1110 and 2293 kc ("Elektron-4"). In a number of cases, however, the drop in signal level on the satellite's entry into the ionosphere was masked by sporadic radio-emission generated in the ionosphere, or by noise from a terrestrial origin which, generally speaking, cannot be entirely prevented. At  $f = 725$  kc the radio-emission generated in the ionosphere was in most flights so strong that it proved to be practically impossible to ascertain the electron concentration profile from observational results at 725 kc. This is illustrated by Figure 2. The drop in signal level at  $f = 725$  kc, which began at altitudes of  $\sim 12,000$  km, came to an end at  $h \sim 6000 - 8000$  km. At lower altitudes the signal fluctuated severely, reaching very large values in comparison to the normal level of cosmic radio-emission.

Sporadic radio-emission arising in the ionosphere was repeatedly recorded by "Elektron-2" and "Elektron-4" as individual spikes and as a general rise in signal level; it was detected both in flights through the upper ionosphere and outside of it at great altitudes. Sporadic high-intensity radio-emission was most often recorded at the 725 kc frequency. Figure 3 shows the typical appearance of the signal-level recording at  $f = 725$  kc with sporadic radio-emission. The time scale of the observations is plotted on the horizontal axis of Figure 3; on the ordinate axis, the effective temperature of the radio-emission is plotted. In the altitude range from 15,000 to 30,000 km in Figure 3, we observed a general rise in the level of radio-emission; at altitudes on the order of 586 50,000 km there were isolated peaks with a clearly ascertainable level of cosmic radio-emission in between them. At the frequency of 1525 kc, sporadic emission was observed much less frequently. It differed from the 725 kc radio-emission level in that at 1525 kc a general rise in the radio-emission level is noted as a rule. Figure 4 gives an example of sporadic radio-emission at  $f = 1525$  kc.

### 3. Frequency Intensity Spectrum of Cosmic Radio-Emission

The results derived from measuring the strength of cosmic radio-emission at 725 and 1525 kc ("Elektron-2") and provisional values of this emission at 1110 and 2293 kc ("Elektron-4") are shown in Figure 5 (curve 7). The same figure also presents the results obtained by other authors in 587 measuring the strength of cosmic radio-emission (this graph, supplemented by the findings of the other authors, is borrowed from [Ref. 3]). [1 - the Mullard Radio-Astronomical Observatory (terrestrial measurements); 2 - Chapman, Molozzi; 3 - Ellis et al. (terrestrial measurements), upper symbols refer to region of maximum, and lower to region of minimum radio-emission; 4 - Radio-Astronomical Observatory of the University of Michigan; 5 - measurements by the satellite, "Alouette" (mean strength values); 6 - Korobkov (terrestrial measurements); 7 - measurements by the "Elektron" satellites.



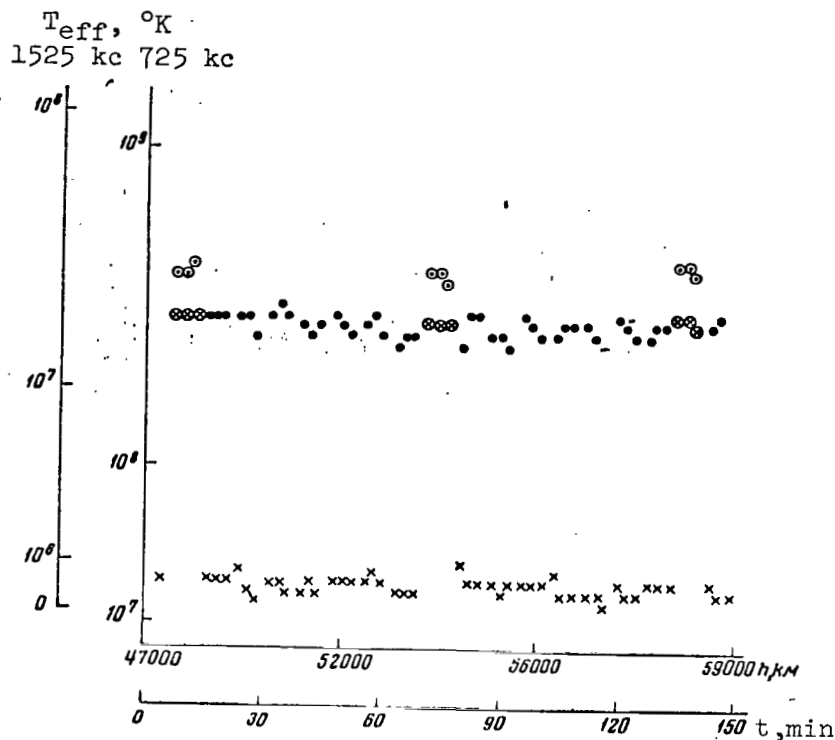


Figure 1

Figure 5 shows that the scatter of experimental values of radio-emission strength derived by various authors is rather substantial, and that the spectral indices found from diverse data differ noticeably from each other. We would like to remark in this connection that the earlier measurements of the frequency spectrum of low-frequency cosmic radio-emission were made either on Earth, or on relatively low AES and rockets within the Earth's ionosphere. The ionospheric effect is, of course, taken into consideration in the data shown in Figure 5, but such allowance cannot always be made with the necessary accuracy. The inhibiting influence of the ionosphere in measurements of the cosmic radio-emission level in (Ref. 3-5) was also evidenced by the fact that the measurements were made at frequencies  $f > 1.2$  Mc (Ref. 3) and  $f > 1.5$  Mc (Ref. 4), which are greater than ionospheric plasma frequencies at altitudes on the order of 1000 - 2000 km.

The measurements made by "Elektron-2" and "Elektron-4" of the cosmic radio-emission strength at 725, 1525, 1110, and 2293 kc are entirely free of the inhibiting influence of the Earth's ionosphere, since at apogee the satellites had retreated almost 70,000 km from the Earth. The frequency of 725 kc is, so far as the authors know, the lowest frequency at which the cosmic radio emission strength can be successfully measured.

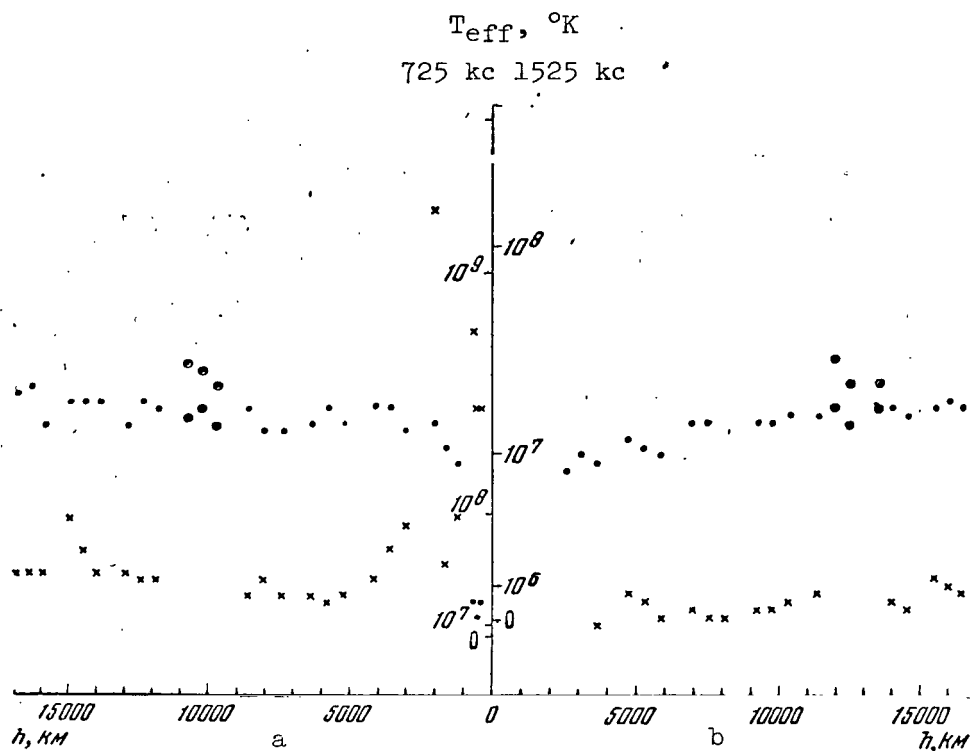


Figure 2

The measurement results are given below.

f, kc	725	1110	1525	2293
$I \cdot 10^{21}$ , watt $\cdot$ m $^{-2}$ $\cdot$ cps $^{-1}$ $\cdot$ sterad $^{-1}$	5.1	8.4	8.7	10.2
$T_{\text{eff}} \cdot 10^{-7}$ °K	3.2	2.2	1.2	0.64

As already mentioned in Section 1, the random error in measuring the absolute values of radio-emission strength at the above frequencies in the experiments described is estimated at approximately  $\pm 30\%$ . This error includes the random scatter of radio-emission values corresponding to various flights of the satellite (data on 20 flights were used to determine the mean strength values), errors in calibrating radio-receiver amplification, inaccuracies in establishing the receiving antenna radiation resistance, and several other factors. The ratio of radio-emission strength at two fixed frequencies, which in the last analysis determines the values of the spectral index of the radio-emission, is known with somewhat greater accuracy:  $\pm(15-20)\%$ . The frequency spectrum of cosmic radio-emission, plotted from "Elektron" satellite measurement data, is denoted in Figure 5 by the broken line. Assuming that the radio-emission strength is  $I \propto f^\alpha$  and utilizing the results of the "Elektron" measurements, we may find the value of spectral index  $\alpha$ , which is 0.05 at the

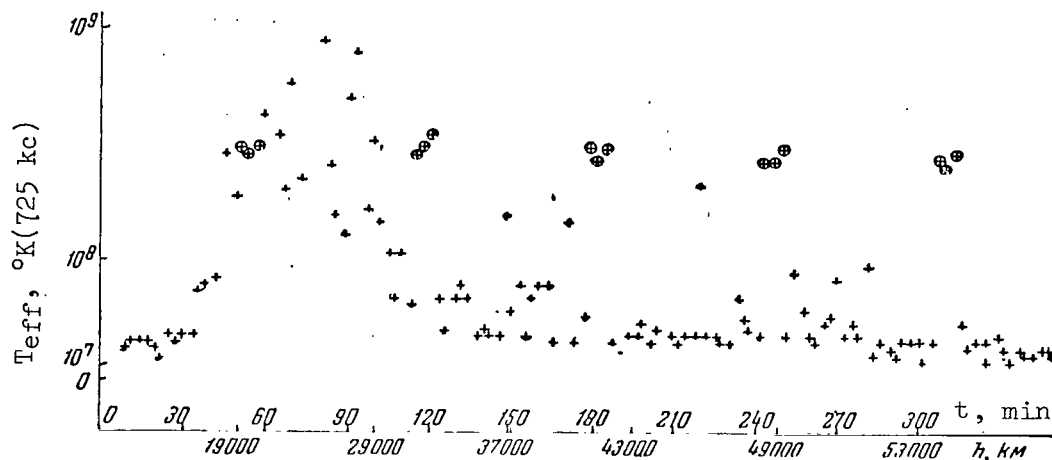


Figure 3

frequency  $f = 1.5$  Mc. This spectral index value is close to the  $\alpha$  of the measurements by "Alouette" (Ref. 4) and is considerably less than the values of  $\alpha$  for the measurements in (Ref. 3, 5). As is apparent from Figure 5, at frequencies  $f \lesssim 3 - 5$  Mc the spectral index increases as frequency decreases. In Figure 5 the frequency spectrum curve, measured in 1964 at a number of fixed frequencies in the 6 - 40 Mc range by Yu. S. Korobkov (Ref. 6)<sup>1</sup> is also designated by the dashed line.

The entire complex of data on the low-frequency sector of the cosmic radio-emission spectrum presented in Figure 5 indicates that the strength of cosmic radio-emission at frequencies  $f \lesssim 3 - 5$  Mc grows smaller as frequency diminishes. Turning to an interpretation of the bend in the cosmic radio-emission spectrum at  $f \lesssim 5$  Mc, let us point out that the most probable reason for the spectrum curvature is radio-emission absorption in the ionized interstellar gas concentrated in the region of the galactic plane (Ref. 2 - 5). This reason is most probable due to the fact that other factors (reabsorption of radio-emission by relativistic electrons, the index of refraction of the interstellar medium not being equal to unity, distortion of the energy spectrum of relativistic electrons because of

<sup>1</sup> It must be borne in mind, however, that data from measurements by the "Elektron" satellites define the average values of radio-emission strength over the celestial sphere, while the measurements in (Ref. 6) refer to a  $30^\circ \times 30^\circ$  region of the celestial sphere with its center at  $l^1 = 98^\circ.5$ ,  $b^1 = -5^\circ.3$ .

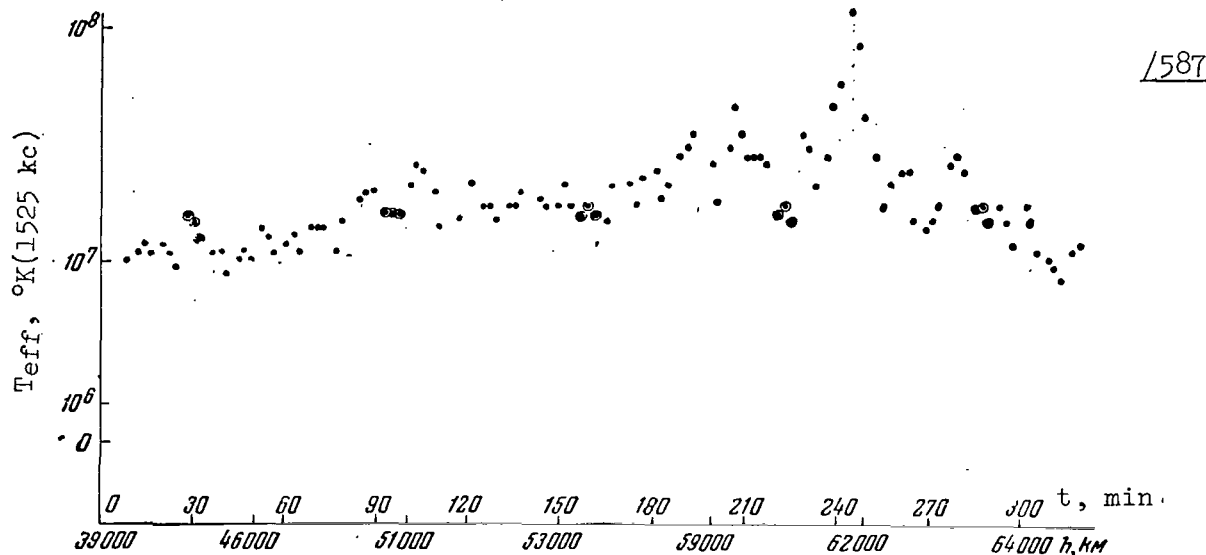


Figure 4

ionization energy losses by particles, and several others) must lead to a relatively slower bending of the frequency spectrum at frequencies on the order of, or less than, one megacycle (Ref. 7). The possibility is, of course, not excluded that cosmic radio-emission in the medium-wave range is principally of metagalactic origin, and that in primary metagalactic radio-emission there is an observed bend in the frequency spectrum. There are no clear data concerning this at present. If, however, we assume that the bend in the frequency spectrum is actually caused by the absorption of cosmic radio-emission in ionized interstellar gas, then we may evaluate the concentration of ionized gas from existing experimental data.

Figure 6 presents a set of theoretical frequency spectrum curves whose behavior at low frequencies is determined by radiowave absorption. The curves are plotted for the following model: The solar system is located in the plane of symmetry of an unbounded radiowave-absorbent layer of thickness  $2a$  (a planar sub-system of the Galaxy). Radio-emission comes both from sources uniformly distributed in the most radiowave-absorbent layer, and from the space surrounding the absorbent layer (the 589 galactic corona, Metagalaxy). The values of the optical thickness  $\tau = \mu a$  of the radiowave-absorbent layer in radiowave propagation perpendicular to the layer are plotted on the axis of the abscissa in Figure 6. The spectral density, averaged by integration over the total solid angle, of

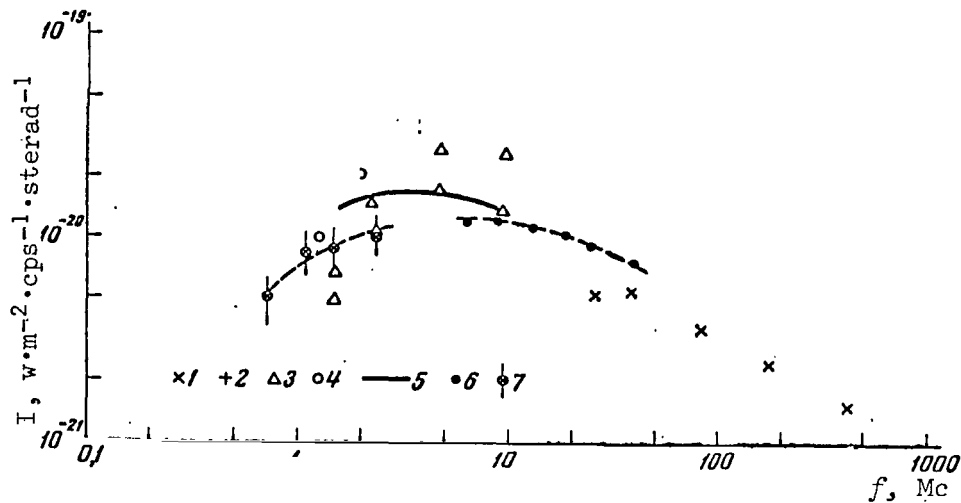


Figure 5

received radio-emission strength  $W$  is plotted in relative units on the ordinate axis. The different curves match different values of the parameter  $p = a_{p_{\text{layer}}} / I_{\text{halo}}$ , which describes the ratio between the emissive capacities of the planar sub-system of the Galaxy ( $p_{\text{layer}}$  - emissive capacity per unit volume of the layer) and the space surrounding this sub-system ( $I_{\text{halo}}$  - strength of radiation per unit of solid angle). Since the maxima of all the curves correspond to values of  $\tau$  which are very close to each other, Figure 6 gives all the curves with maximum values of 1. The curves are plotted on the assumption that the frequency spectrum of the primary (unabsorbed) radio-emission of the halo and of the planar sub-system is proportional to  $f^{-0.5} \propto \tau^{\frac{1}{2}}$  (Ref. 3)<sup>1</sup>. Experimental findings from measurements by "Elektron-2" and "Elektron-4" are plotted in the same figure (the radio-emission intensity reduced to unity in Figure 6 at the spectrum peak is assumed to equal  $1.3 \cdot 10^{-20}$  watt·m<sup>-2</sup>·cps<sup>-1</sup>·sterad<sup>-1</sup>). Assuming that  $f \approx 3$  Mc satisfied the radio-frequency spectrum

<sup>1</sup> The curves in Figure 6 are plotted from the relationship

$$\tau^{-1} \left\{ 1 + \left[ \left( \frac{a_{p_{\text{layer}}}}{I_{\text{halo}}} \right) \tau - 1 \right] \left[ e^{-\tau} - \tau \int_{\tau}^{\infty} \frac{e^{-y}}{y} dy \right] \right\} \tau^{\frac{1}{2}}.$$

When  $\tau = \mu a \rightarrow \infty$  the radio-frequency strength determined by this expression strives to zero, while when  $\tau \rightarrow 0$  it is determined by the original frequency spectrum without allowance for radio-emission absorption.

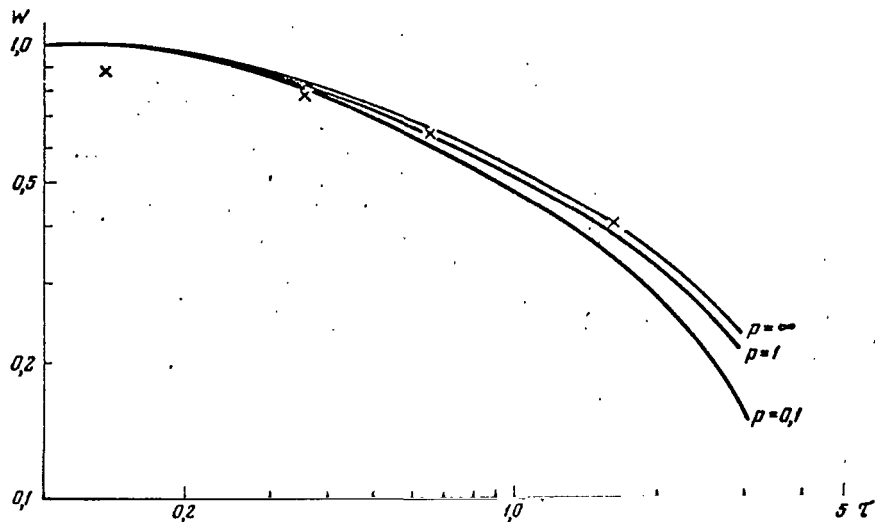


Figure 6

peak and that  $\tau_{\max} = \mu a \approx 0.1$ , and setting  $a \approx 100$  nc, we can find  $\mu$  and consequently the ionized gas concentration in the radiowave-absorbent layer. For the electron temperature  $T_e \approx 10^4$  degrees, the value of  $N_e$  proves to be  $0.12 \text{ cm}^{-3}$ .\*

If the bend in the cosmic radio frequency spectrum is in fact /590 linked to radio-emission absorption in the ionized gas of a planar galactic sub-system, then low-frequency radio emission must possess one extremely interesting property - unusual and very strong anisotropy in the angular distribution of radio-emission over the celestial sphere (Ref. 8). The anisotropy can be readily understood if we consider that nonthermal cosmic radio-emission is synchrotronic in origin and associated with the radiation of relativistic electrons moving in the interstellar magnetic field.

\* For another distribution model of the radiowave-absorbent gas - where the solar system is at the center of an absorptive sphere of radius  $a$ , and where the sources of radio-emission are isotropically distributed both inside and outside of the sphere - the theoretical frequency spectra curves have their maximum at  $\tau_{\max} \approx 0.5$ . For this model the existing experimental data give a value of  $N_e \approx 0.3 \text{ cm}^{-3}$ . As a comparison of the theoretical and experimental frequency spectra demonstrates, it is not possible at present to choose definitively a certain model for ionized gas distribution in the planar sub-system of the Galaxy.

The strength of synchrotronic radio-emission is known to be proportional to  $H_{\perp}^{(\gamma+1)/2}$ , where  $H_{\perp} = H \sin \theta$  is perpendicular to the velocity vector of the radiating particle of the magnetic field component;  $\theta$  is the angle between particle velocity and direction  $H$ ;  $\gamma$  is the power exponent in the energy spectrum of the relativistic electrons. Because of radio-wave absorption, the level of the incoming radio-emission at sufficiently low frequencies must be determined by sources arranged in a quasi-spherical region whose radius  $a$  is found from the condition  $\tau = \mu a \approx 1$ . When the frequency drops, the radius of the region becomes less than 100-150 nc - i.e., less than half the thickness of the planar galactic subsystem, and we may assume that within this region the interstellar magnetic field is homogeneous with respect to direction. Because of the above cited dependence of synchrotronic radio-emission strength on the angle  $\theta$ , and because radiation of the relativistic particles is directed along their velocity vector, the level of the incoming radio-emission may be expected to be greatly dependent on angular orientation of the receiving antenna with respect to the lines of force of the interstellar magnetic field. In measurements on AES, the anisotropic effect indicated will be substantially smoothed out, since the antenna systems of the AES in the medium-wave range are elementary dipoles and have a wide directional pattern. Nonetheless, the corresponding effect may be even more significant. Estimates made for the case of  $\gamma = 3$  show that the ratio of the maximum signal which should be recorded to the minimum signal must be 1.6 - i.e., in principle, there may be a substantial effect.

In the recordings of cosmic radio-emissions obtained during measurements by the AES "Elektron-2" and "Elektron-4", there are in many cases a number of periodically-recurring phenomena characterizing radio-emission level variations which could in principle be regarded as manifestations of the above effect. Such phenomena are also apparent, in particular, in the sector of the radio-emission recording at 1525 kc shown in Figure 1. Unfortunately, the authors have been unable to make a detailed comparison between the observed fluctuations in radio-emission strength and data on the angular orientation of the AES antenna with respect to the direction of the interstellar magnetic field in the region of the solar system. The nature of radio-emission level fluctuations still remains open.

#### 4. Determining the Ionosphere Electron Concentration Profile from Cosmic Radio Emission at 1525 kc

When the satellite enters the ionosphere, the receiving properties of the antenna vary depending on the degree of electron concentration. The consequences are that at altitudes below 5000 km, the receiver output voltage is perceptibly reduced at the frequency of 1525 kc, while near perigee ( $h < 1000$  km) a complete "cutoff" of cosmic radio emission sets in (Figure 2)\*. The reduction in received signal level may be used to

\* Similar effects are also observed at 725, 1110, 2293 kc. At 725 kc, the drop in level at relatively low altitudes was frequently masked by sporadic radio emission.

compute the electron concentration in the region of the satellite (e.g., see [Ref. 3]). Antenna capacitance and radiation resistance vary depending on the characteristics of the medium.

Let us examine the equivalent circuit of the input loops of the receiver (Figure 7). The figure has the following notation:  $u_a$  - the equivalent antenna noise voltage;  $R_\Sigma$  - antenna radiation resistance;  $C_a$  - antenna capacitance (capacitance in vacuum  $C_{a0}$  - 46 pf);  $C_c$  = 64 pf - cable capacitance;  $C_{c1} = C_{c2}$  - 78 pf - capacitance of circuits  $L_1 C_{c1}$  and  $L_2 C_{c2}$ ;  $C_1 = C_2$  = 39 pf - coupling capacitance;  $u_2$  - grid voltage of the 1525 kc receiver input tube. Inductances  $L_1$  and  $L_2$  are so chosen that the input circuit of the receivers has resonance frequencies of 725 and 1525 kc.

Using Thevenin's theorem for the case  $R_\Sigma \ll 1/\omega C_a$ , we may write

$$\frac{u_2}{u_a} = \frac{a \frac{C_a}{C_{a0}}}{b + \frac{C_a}{C_{a0}}}, \quad (6)$$

where  $C_a/C_{a0}$  is the ratio of antenna capacitance in the medium to capacitance in a vacuum, while  $b$  has the value  $b = 2.75$  for these parameters of the input circuit. Equivalent antenna noise voltage is

$$u_a = \sqrt{4kT_{\text{eff}}\Delta f R_\Sigma}, \quad (7)$$

where  $k$  is Boltzmann's constant;  $T_{\text{eff}}$ , effective temperature of cosmic radio emission; and  $\Delta f$ , receiver band. Radiation resistance  $R_\Sigma$  in the medium is distinguished from antenna radiation resistance  $R_{\Sigma 0}$  in vacuo. If we introduce the attenuation function of radio emission received by the antenna  $\Gamma = (u_2/u_{20})^2$  as the ratio of signal powers at the receiver input tube grid when the satellite is in the ionosphere and beyond it, then - as is readily apparent - we have

$$\Gamma = \frac{(b+1)^2}{\left(b + \frac{C_a}{C_{a0}}\right)^2} \left(\frac{C_a}{C_{a0}}\right)^2 \frac{R_\Sigma}{R_{\Sigma 0}}. \quad (8)$$

If we do not allow for ionospheric plasma anisotropy caused by the magnetic field, then

$$\frac{C_a}{C_{a0}} = \epsilon; \quad \frac{R_\Sigma}{R_{\Sigma 0}} = \sqrt{\epsilon}, \quad (9)$$

where  $\epsilon = 1 - v$  - dielectric constant of the medium;  $v = \frac{\omega_0^2}{\omega^2} = \frac{4\pi e^2 N}{m\omega^2}$ ;  $N$  - electron concentration;  $e$  and  $m$  - electron charge and mass. Using the



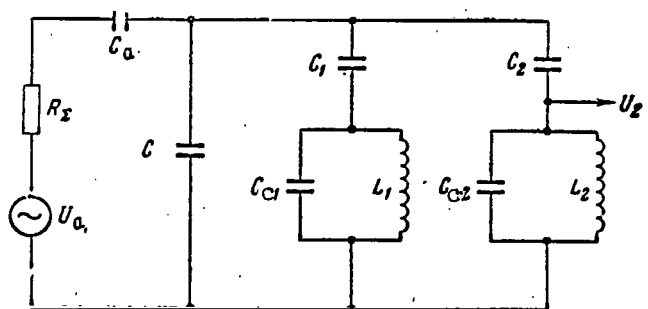


Figure 7

dependence  $\Gamma(N)$ , we may calculate the electron concentration along the satellite's orbit when the receiver output voltage drops as the satellite enters the ionosphere. Since the ionosphere is in fact an anisotropic medium, we must estimate the effect of the Earth's magnetic field on antenna capacitance and radiation resistance.

The dielectric constant in an anisotropic medium is a tensor. According to Kaiser (Ref. 9), we may write the capacitance of a thin antenna as

$$\frac{C_a}{C_{a0}} = \frac{\alpha_{11}(\cos^2 \varphi + K^2 \sin^2 \varphi)^{1/2}}{1 + a \ln \left[ \frac{2(\cos^2 \varphi + K^2 \sin^2 \varphi)}{K + K(\cos^2 \varphi + K^2 \sin^2 \varphi)^{1/2}} \right]}, \quad (10)$$

where  $\alpha_{11} = 1 - \frac{v(1-is)}{(1-is)^2 + u}$ ,  $\alpha_{33} = 1 - \frac{v}{1-is}$  are tensor components  $\epsilon_{ik}$ ;  
 $K^2 = \alpha_{33}/\alpha_{11}$ ;  $a = (\ln \frac{2l}{r})^{-1}$ ,  $l$  and  $r$  are antenna length and radius;  $\varphi$  is the angle between the magnetic field  $H$  and the antenna;  $u = \frac{\omega_p^2}{\omega^2} \frac{H}{\omega^2}$ ;  $\omega_H = \frac{|e|H}{mc}$  is the gyrofrequency; and  $v_{\text{eff}} = s\omega$  is the effective number of electron collisions.

The degree of capacitance  $C_a$  depends on antenna orientation to the Earth's magnetic field. It is essential that for weak anisotropy ( $u \ll 1$ ) the expression for  $C_a/C_{a0}$  differ little from the isotropic case, e.g., when  $u < 0.17$  and  $v < 0.5$  (at the frequency of 1525 kc, this corresponds to altitudes of  $h > 2000$  km), the corrections for the  $N$  values computed from formulas (8) and (9) amount to less than 20% when  $\varphi = 0$  (antenna along the field  $H$ ) and less than 10% when  $\varphi = \pi/2$  (antenna perpendicular to field  $H$ ). At altitudes of  $h < 2000$  km where  $u \lesssim 1$ , the corrections become larger, and significant receiver output voltage fluctuations are observed when the antenna changes its orientation to the Earth's magnetic field.

The influence of the magnetic field on antenna radiation resistance is likewise small in the case of anisotropy. Moreover, as is apparent from formulas (8) and (9), the dependence of attenuation function  $\Gamma$  on the parameters of the medium is chiefly determined by the change in antenna capacitance in the medium. The change in radiation resistance  $R_\Sigma$  in the case in which we are interested ( $u \lesssim 0.17$ ,  $v \lesssim 0.5$ ) has little effect on the receiver output voltage; in the first approximation, this effect is taken into account by the expression for  $R_\Sigma$  in the isotropic case (9).

When determining antenna capacitance  $C_a$ , we neglected the effective number of collisions, assuming that  $v_{\text{eff}} \ll \omega$ . Kaiser (Ref. 9) notes that if the mean free electron path  $l_e$  exceeds antenna size  $l$ , the quantity  $v_{\text{eff}} = v_e/l$  in formula (9) must be replaced by  $v'_{\text{eff}} = v_e/l$ , where  $v_e$  is the mean electron thermal velocity. At altitudes of  $h > 1000$  km, the mean free electron path is  $l_e > 1$  km, and therefore the value of  $v'_{\text{eff}}$  must be used. At the electron temperature  $T_e \approx 4 \cdot 10^3$  °K we have  $v'_{\text{eff}} \approx 10^5$ , which is considerably less than the receiver operating frequency of 1525 kc. Since antenna capacity is determined by the local characteristics of the medium, the measurements of electron concentration can be complicated by plasma perturbations caused by the satellite charge and by hydrodynamic perturbations due to satellite motion. /593

The plasma perturbations associated with the satellite charge are localized at a distance on the order of the Debye radius  $D$  from the surface of the satellite. At an altitude of  $h \approx 3000$  km, the value  $D \approx 4$  cm, i.e., it is substantially less than the size of the system. The satellite charge effect may thus be neglected in the first approximation. Hydrodynamic perturbations of the medium lead to plasma densification in front of the satellite, and to a region of rarefaction behind it (e.g., see [Ref. 10]). These perturbation regions, however, occupy a small volume in comparison to  $l^3$ , where  $l$  is the system's maximum dimension, and the probability of finding the antenna in the perturbation regions as the satellite rotates is obviously not too great.

These calculations demonstrate that the formulas for the isotropic case may be utilized to determine electron concentration from data on the reduced level of cosmic radio emission. This is particularly true because the large scatter of experimental points will give rise to a fundamental error when determining the attenuation function of cosmic radio emission  $\Gamma$ . The absolute error in measurements of electron concentration  $N$  is approximately  $\pm (1 - 2) \cdot 10^3 \text{ electron} \cdot \text{cm}^{-3}$ .\*

---

\* Near perigee, part of the celestial sphere was screened by the Earth. If the temperature of cosmic radio emission is distributed unevenly over the celestial sphere, then this may in principle lead to various values of  $T_{\text{eff}}$  when the satellite is at apogee or near perigee. At 1525 kc, the background inhomogeneity of cosmic radio emission is obviously not large, and may be neglected in the first approximation. It may be noted that the orbital plane of "Elektron-2" almost coincides with the equatorial plane of the Galaxy. The bearing from the Earth's center to apogee corresponds approximately to  $270^\circ$  of galactic longitude (in the  $l^\perp$  system).

Figures 8 and 9 give profiles of electron concentration  $N$  computed by the above method as a function of altitude  $h$  along the satellite orbit. The numbers assigned the curves in the figures match the satellite flight dates given in Table I. This table also gives the change of eastern geographical longitude for each flight from point  $\lambda_1$ , corresponding to minimum height of  $N(h)$  on the graph, to point  $\lambda_2$ , corresponding to the concentration  $N = 10^3 \text{electron} \cdot \text{cm}^{-3}$ .

The left side of Figure 8 corresponds to the descending portion of the satellite's path and the right, to the ascending portion. Figure 9 gives the results from processing only the ascending portion of its path.

TABLE 1

Curve No.	Date (1964)	$\lambda_1^\circ$	$\lambda_2^\circ$	Curve No.	Date (1964)	$\lambda_1^\circ$	$\lambda_2^\circ$	Curve No.	Date (1964)	$\lambda_1^\circ$	$\lambda_2^\circ$
1	30.I	168	196	10	11.II	291	282	19	14.II	138	155
2	31.I	42	34	11	12.II	102	115	20	15.II	158	175
3	27.II	66	73	12	12.II	307	297	21	16.II	181	193
4	28.II	289	277	13	13.II	118	135	22	1.III	115	131
5	3.III	143	173	14	13.II	321	317	23	5.III	199	212
6	4.III	34	12	15	16.III	83	89	24	3.IV	95	108
7	3.II	272	275	16	16.III	292	275	25	15.III	54	71
8	3.II	104	94	17	2.II	243	265	26	21.III	185	190
9	11.II	79	95	18	10.II	66	71	27	23.III	200	227

In order to give the over-all picture of the position of the satellite in space, Table 2 gives the geographic latitudes for the altitude range in 595 which we are interested, both for the ascending ( $\varphi_1$ ) and descending ( $\varphi_2$ ) phases of the orbit.

TABLE 2

$h, \text{km}$	$\varphi_1^\circ$	$\varphi_2^\circ$	$h, \text{km}$	$\varphi_1^\circ$	$\varphi_2^\circ$	$h, \text{km}$	$\varphi_1^\circ$	$\varphi_2^\circ$
1 000	31	57,5	7 000	-21	13	13 000	-38	-5
2 000	13,5	46	8 000	-25	9	14 000	-40	-7
3 000	3	36	9 000	-28	5	15 000	-42	-9
4 000	-5	29	10 000	-31	2	16 000	-43	-11
5 000	-11,5	23	11 000	-34	-1	17 000	-45	-12,5
6 000	-16,5	17,5	12 000	-36	-3	18 000	-46	-14,5

Electron concentration at an altitude of 2000-3000 km amounts to  $N = 10^4 \text{electron} \cdot \text{cm}^{-3}$  and, as a rule, falls smoothly to  $N \approx 10^3 \text{electron} \cdot \text{cm}^{-3}$

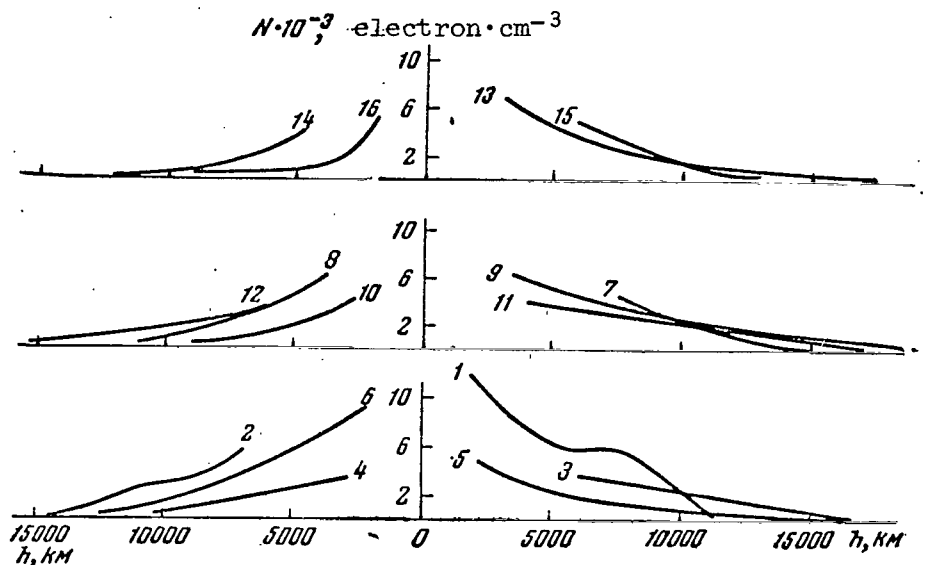


Figure 8

at altitudes of 10,000 - 15,000 km<sup>1</sup>. A few curves (18, 20, 21) have a flat segment at altitudes of 6000 - 15,000 km with a value of  $N \approx (2 - 4) \cdot 10^{-3} \text{ electron} \cdot \text{cm}^{-3}$ . The path of curve 17 differs sharply from the other curves by a minimum at 9000 km and a maximum at 13,000 - 16,000 km. The position of this peak corresponds to the intersection of the geomagnetic equator by the satellite at the geographic longitude of 270°. This agrees with the results of pulse probing by the satellite "Alouette" (Ref. 11), which indicate an elevated ionospheric density near the geomagnetic equator in the same longitude regions at altitudes of  $h > 800$  km.

It should be noted that curve 1 refers to the trajectory section immediately after the satellite is launched into orbit. The elevated value of electron concentration in this sector of the orbit, as compared to the other cases, may apparently be explained by the liberation of gas from the satellite surface.

#### 5. Sporadic Radio Emission from the Earth's Atmosphere

As was pointed out in Section 2, during the flight of "Elektron-2", sporadic radio emission was recorded at 725 and 1525 kc with a strength considerably above that of cosmic radio emission. In this section we shall examine the characteristics of this radio emission in more detail, as well as several possible ways to interpret it.

<sup>1</sup> (Ref. 12) published the measurement results of positive ion concentration in approximately the same altitude range by Soviet space rockets in 1959.

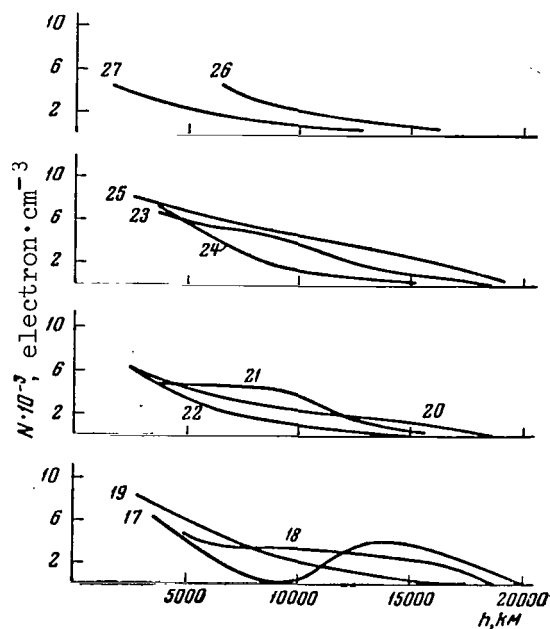


Figure 9

Figure 3 gives a characteristic recording of the strength of sporadic emission at 725 kc, and makes it clear that radio emission strength fluctuates greatly, changing from a level determined by the strength of cosmic radio emission to a value two or three orders of magnitude greater than this level. This radio emission was observed in all sectors of the satellite orbit, while its average strength decreased somewhat with an increase in altitude.

The sporadic radio emission at 1525 kc had a different nature (Figure 4). At this frequency, an over-all rise in strength was detected which at times exceeded the cosmic background by one order of magnitude. Sporadic radio emission at this frequency was recorded much less frequently than at 725 kc. In cases where sporadic radio radiation was recorded at a frequency of 1525 kc, sporadic radiation was always detected at a frequency of 725 kc. However, there was no detailed correlation between changes in strength at the operating frequencies of 725 and 1525 kc. This fact indicates that the spectral width of the radio emission burst is on the order of, or smaller than, the interval between the operating frequencies. /596

The effective temperature of sporadic radio emission at 725 kc was on the average one order of magnitude greater than at 1525 kc. In order to determine more accurately the characteristics of the radio emission observed, we compared sporadic radio emission with other geophysical

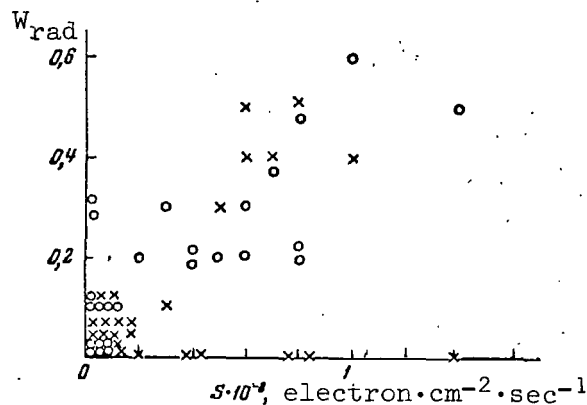


Figure 10

phenomena. We discovered no clear connection between this emission and such factors as variations in the planetary  $K_p$ -index, presence of sporadic  $E_s$ -layers in the polar region, and solar radiation in the optical or radio ranges. A comparison of data on radio emission with data on the presence of soft electrons in the region of the radiation zones<sup>1</sup> made it apparent that there is a clear correlation between the presence of soft electrons and the occurrence of sporadic radio emission.

Figure 10 presents a graph for dependence of the probability of sporadic radio emission at 725 kc (circles) and 1525 kc (crosses) on the magnitude of an electron stream having energies greater than 100 ev in the radiation zones. Electron stream magnitude was defined as the maximum value of the stream recorded when the satellite intersected the radiation zones. The probability of radio-emission was defined as the ratio of the number of reference points (where heightened radio emission was recorded) to the total number of reference points. If the satellite intersected the radiation zone in the ascending portion of the trajectory, then this probability was determined for the entire ascending phase of the trajectory to apogee; the descending phases of the path were handled in a similar manner.

The figure shows that the probability of sporadic radio emission at 725 kc is proportional to magnitude of the stream. At 1525 kc, the probability dependence on flux magnitude remains the same, but in several cases when there were soft electron streams, no radio emission was detected at 1525 kc. As will be indicated below, this may probably be attributed to the dependence of sporadic radio-emission strength on longitude. /598

<sup>1</sup> K. I. Gringauz kindly gave us prepublication data on electron streams of greater than 100-ev energy, derived from measurements by "Elektron-2".

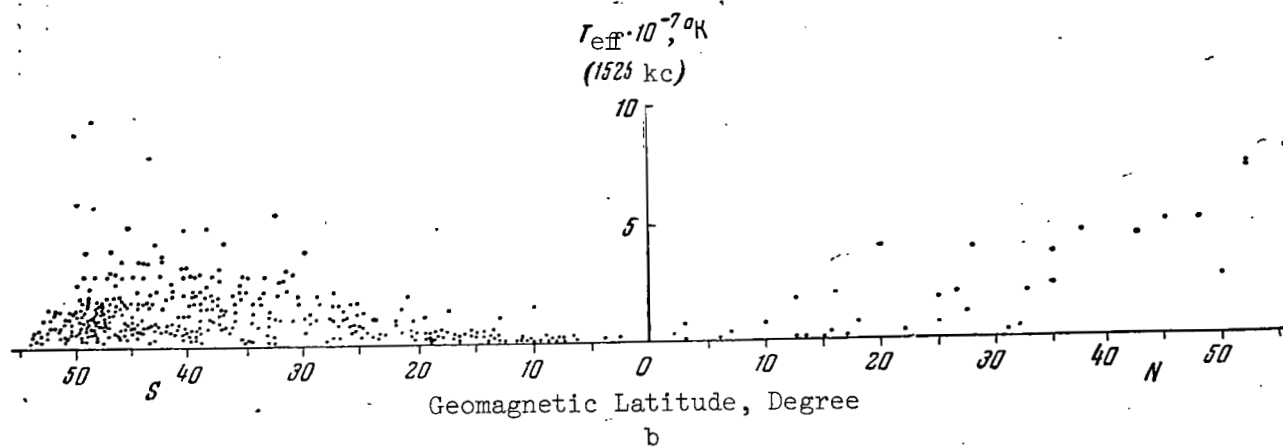
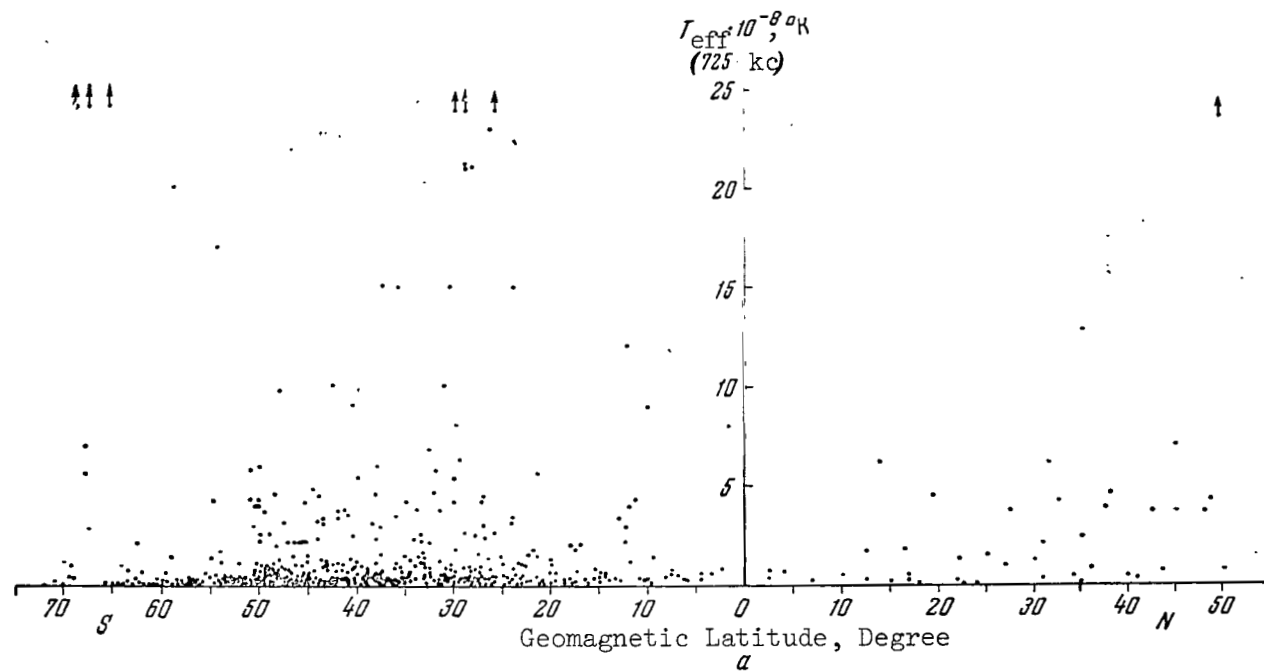


Figure 11

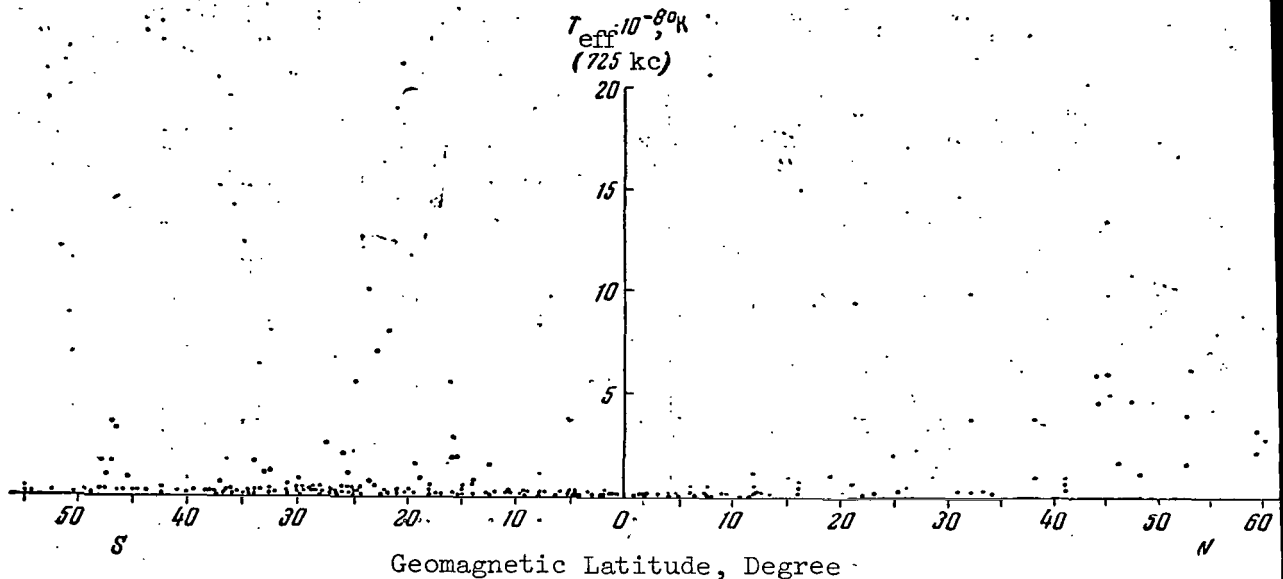


Figure 12

The experimental facts presented (sharply decreasing radiation spectrum, more frequent appearance of radio emission at the lower frequency, correlation of radiation with soft electron streams) suggest that radio emission arises from the interaction of electron streams with the plasma of the Earth's upper atmosphere. Since the trajectories of the electron streams are determined by the Earth's magnetic field, it is advantageous to know the intensity distribution of sporadic radio emission as a function of the geomagnetic coordinates of the Earth. Figures 11 and 12 give this distribution at 725 and 1525 kc as a function of geomagnetic latitude. Figure 11 plots the distribution for relatively high altitudes. This distribution was obtained by using the trajectory sections encompassing the descending node and the entire apogee portion of the trajectory almost to the ascending node. Figure 12 shows sporadic radio emission distribution at 725 kc for trajectory sections including the perigee region, as well as regions in the vicinity of the ascending and descending orbital nodes.

Figure 13 gives the longitudinal distributions of radio emission strength at 725 and 1525 kc.

Before proceeding to a more detailed analysis of these distributions, we must turn our attention to the following facts. The time spent by the satellite at various latitudes is different. Table 3 gives the relative operational time of the receiving equipment as a function of geomagnetic



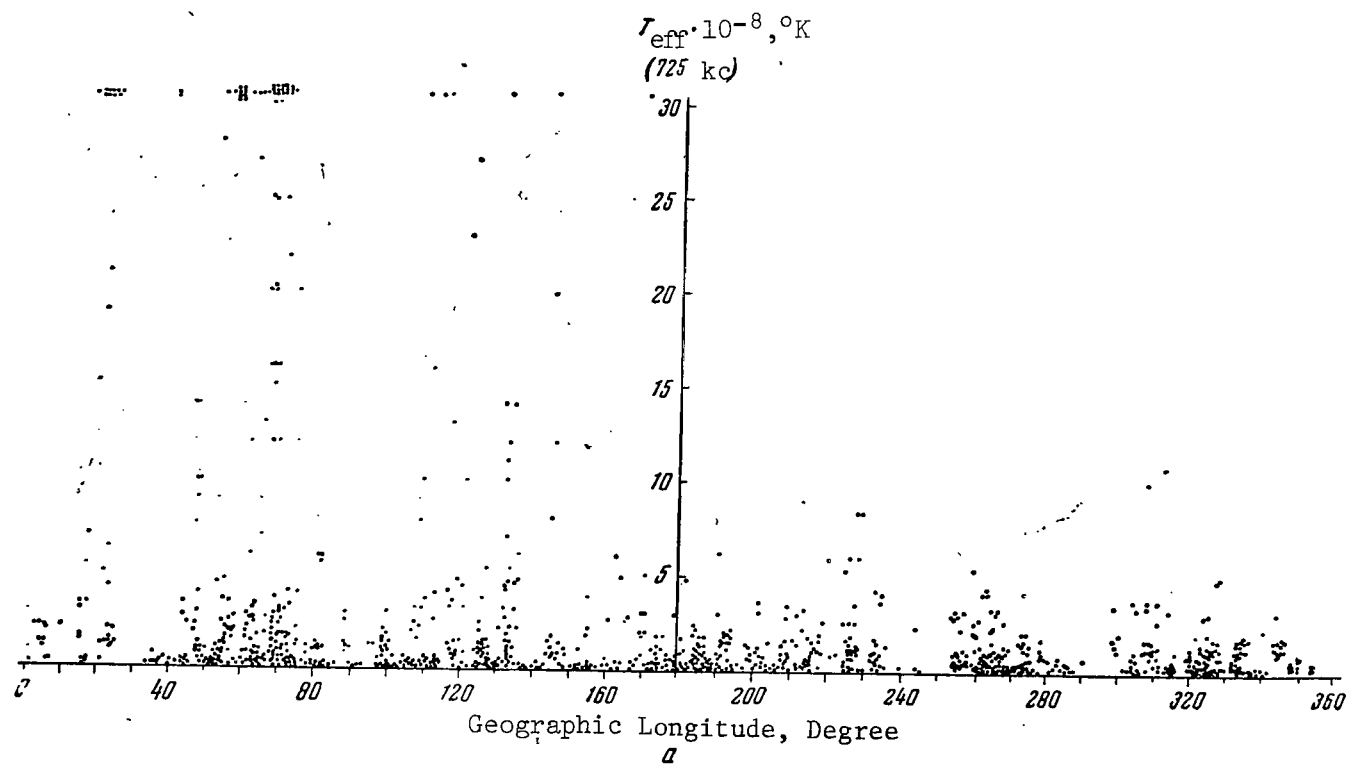


Figure 13a

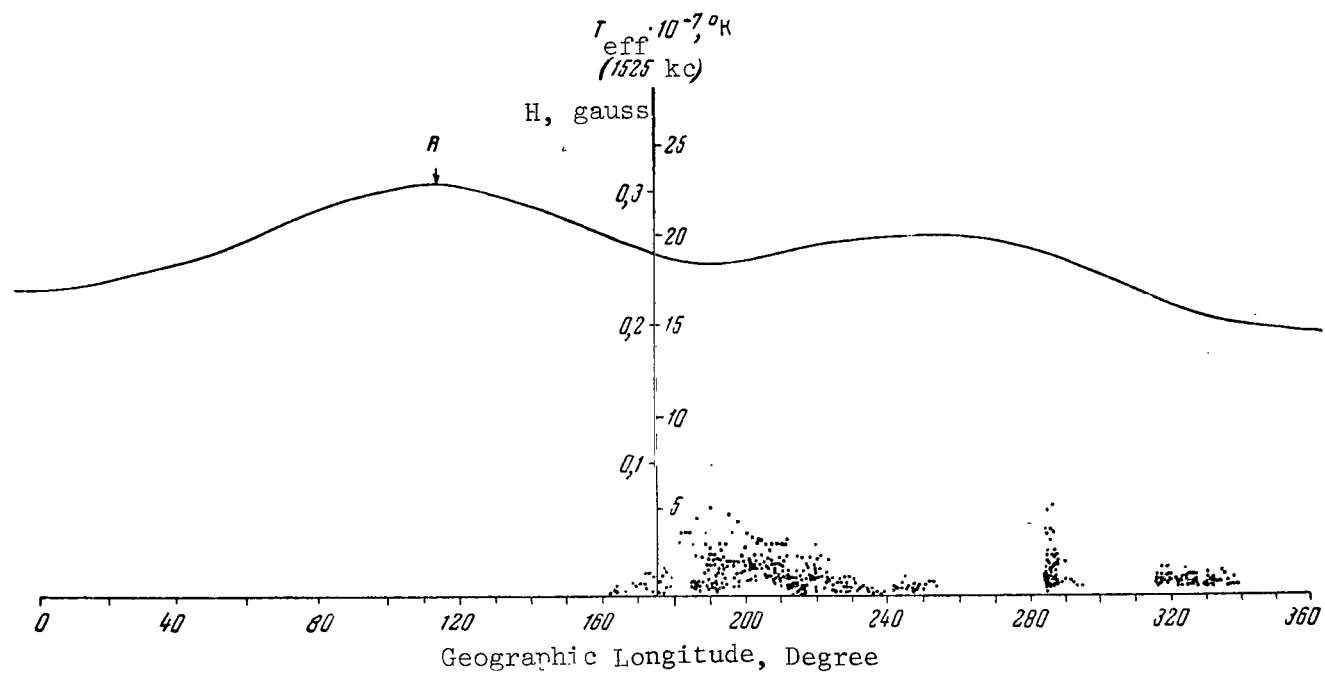


Figure 13b

latitude for the revolutions which were used for plotting the dependence of sporadic radio emission strength on latitude.

The trajectories of the different revolutions at the geomagnetic coordinates differ substantially from each other.

Figure 14 gives the trajectory of revolutions in the geomagnetic latitude-longitude plane in the southern hemisphere for the revolutions which were used to derive the latitudinal distribution of the radio emission (Figure 11). The dates of the flights whose trajectories are represented in Figure 14 are given below.

February 1964 . . . . . 1 2 3 11 12 13 14 15 17 19 20 21 28  
 Number of Rev. . . . . 1 2 3 4 5 6 7 8 9 10 11 12 13

When plotting the longitudinal dependence, we used a somewhat larger number of satellite flights than when plotting the latitudinal dependence. As is apparent from the figures, the radio emission strength in all cases has a minimum in the region of the geomagnetic equator. Radio emission strength for comparatively high altitudes increases with geomagnetic latitude, reaching a maximum at latitudes of 30-50°; then as latitude increases, the strength diminishes. /602

TABLE 3

North Geo- magnetic Latitude	Operating Time %	South Geo- magnetic Latitude	Operating Time %
40-50°	0.17	0-10°	1.44
30-40	0.25	10-20	2.6
20-30	0.43	20-30	4.4
10-20	0.62	30-40	7.2
0-10	0.79	40-50	26.5
		50-60	29.3
		60-70	21.6
		70-80	4.7

It therefore follows from the type of distribution that there is radio emission whose "directional diagram" peak lies in the 30-50° belt of geomagnetic latitude (in Figure 14 this region is marked off by broken lines).

To plot the longitudinal distribution of radio emission, it would be

best to use data on this emission in a narrow band of geomagnetic latitudes, but the number of experimental findings is clearly inadequate to derive this distribution. To compile longitudinal distribution, we took advantage of data on radio emission at all latitudes. While sporadic radiation at  $f = 1525$  kc was detected in the  $160-340^\circ$  longitudinal range, it was observed at  $f = 725$  kc at all longitudes, with a certain predominance in the  $0-180^\circ$  range. Figure 13b, in addition to the longitudinal distribution of radio emission at 1525 kc, gives the relationship of magnetic field strength for  $45^\circ$  south geomagnetic latitude and an altitude of 1600 km. The regions of peak radiation strength at 1525 kc are near those regions where the magnetic field has its minimum value.

Let us discuss the possibilities of interpreting sporadic radio emission. First of all, we must ascertain that the radiation being recorded has nothing to do with the reception of signals from sources on the Earth's surface, or of noise from on-board equipment.

It seems to us extremely improbable that noise from on-board equipment was received, for the satellite had no generators at frequencies near the operating frequencies of the receivers. Pulse noise should, /603 moreover, have a considerably more uniform spectrum than that which was observed in the experiment. Moreover, as indicated in Section 1, during the tests on Earth, no noise was discovered coming from the on-board equipment. It is also advisable to investigate the possibility of "Elektron-2" receiving noise coming from the Earth's surface (radio station signals, atmospheric and industrial interferences, et.). For this purpose, the conditions under which radio waves propagate through the ionosphere in the Earth's magnetic field must be analyzed. This matter is rather complex, as we are dealing with the propagation of radiowaves of frequencies close to the gyromagnetic frequency  $f_H$  and the plasma frequency  $f_0$  of the ionosphere when  $f_H$  and  $f_0$  depend on altitude. Ye. A. Benediktov (Ref. 13) qualitatively examined the propagation conditions in which we are interested.

Let us first of all examine the conditions of radiowave penetration through the ionosphere at mean latitudes at a frequency of  $f_1 = 725$  kc. The findings presented in (Ref. 13, 14) enable us to show that at an ionospheric F-layer critical frequency greater than  $\sqrt{f_1^2 + f_1 f_H} \approx 1.2$  Mc, radiowaves of 725 kc cannot pass through the ionosphere. Existing data show that F-layer critical frequencies may be less than 1.2 Mc only in exceptional cases in the pre-morning hours in isolated regions of the globe. It is thus very improbable that the observed sporadic radio emission at 725 kc is caused by noise from the Earth's surface.

Radio emission at  $f_2 = 1525$  kc will, of course, pass through the ionosphere without essential attenuation, if the F-layer critical frequencies are less than  $f_2 = 1525$  kc. Since, as a rule, these frequencies are greater than 1.5 Mc, it is also improbable that radio interference from the Earth's

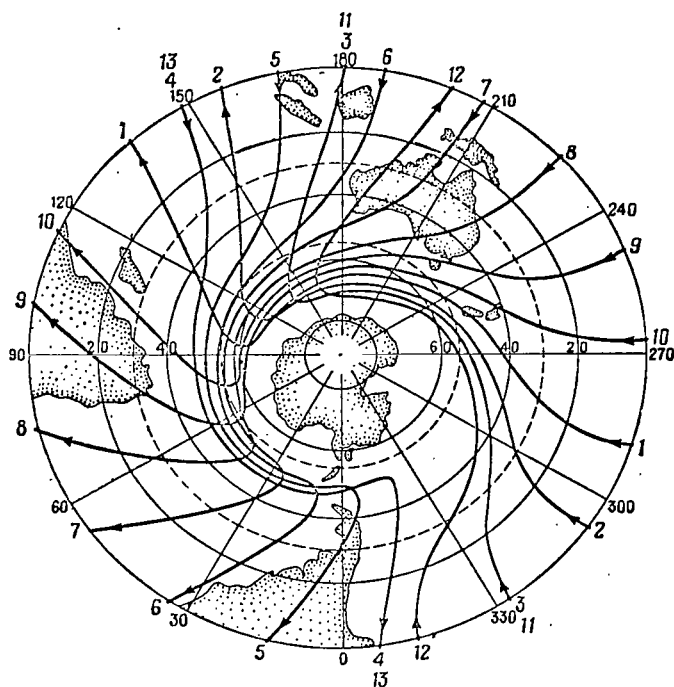


Figure 14

surface will penetrate the ionosphere at  $f_2 = 1525$  kc. Radiowaves of frequency  $f_2$  passing through the ionosphere, due to the interaction of normal waves in the ionosphere, is possible - first, when the F-layer critical frequency lies within  $\sqrt{f_2^2 + f_2 f_H} = 2 \text{ Mc} > f_{OF} > 1.5 \text{ Mc}$ . Secondly, the radiowaves which have passed through the ionosphere will be greatly attenuated by the two z-transitions above and below the maximum of the F-layer. It should also be noted that even if conditions permitting the passage of terrestrial radio interference through the ionosphere can be realized in isolated regions of the Earth's ionosphere, this noise has to be recorded in the AES as unitary bursts of short duration. In actual fact, however, as was already noted above, in many cases an overall rise in level is characteristic of the radio emission at 725 and 1525 kc. The author therefore believes that it is improbable that sporadic radio emission results from noise reception from the Earth's surface. Let us examine other possible ways of explaining this recorded radio emission.

The mechanisms of nonthermal radio emission usually examined are generally braking radiation, synchrotron radiation, magnetic braking radiation, and the Cherenkov effect. In addition to these mechanisms, in our case it is also possible that an emf is induced in the receiver antenna by shot noise generated when the energetic particles of a stream pass near the antenna<sup>1</sup>. Effectuation of the last mechanism requires a detailed

<sup>1</sup> This mechanism was pointed out to us by A. A. Andronov.

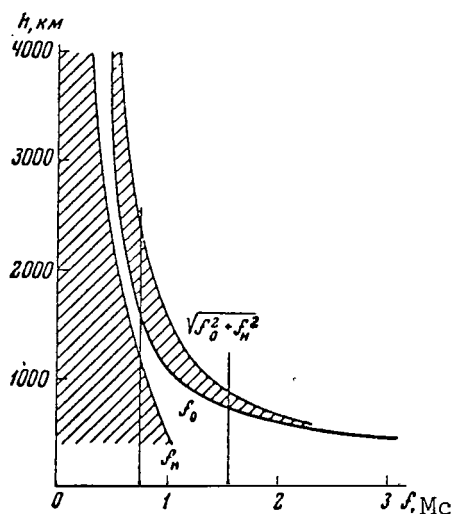


Figure 15

correlation between any parameters of sporadic radio emission and the degree of electron stream intensity, but no such correlation was detected. Therefore, it is impossible to use this mechanism to explain the observed radio emission. It is also impossible to explain it by means of the braking and synchrotron mechanisms of electron radiation in vacuo, since the spectrum of the radio emission produced by these mechanisms is considerably smoother than that observed in the experiment. /604

If the sharply decreasing spectrum of radio emission is to be explained, the radiowaves must be generated in the vicinity of some frequencies characteristic of the given medium. In our case these frequencies of the medium are the Langmuir frequency of the upper ionospheric plasma  $f_0$  and the gyro-frequency  $f_H$ . Radiowaves may in this case be generated at frequencies whose refractive index values in medium  $n$  are large. The division of the radiation into Cherenkov and magnetic braking radiation is conditional, and in the following we shall employ the term "plasma radiation" for this radio emission. As is known (Ref. 15), radiowave generation on the plasma branch of the refractive index dispersion curve in a plasma, with a magnetic field, is possible in the frequency range

$$0 < f \min \{f_0, f_H\}, \max \{f_0, f_H\} < f < \sqrt{f_0^2 + f_H^2}.$$

In this case, an ordinary wave is generated in the lower-frequency sector, and an extraordinary wave is generated in the high-frequency sector.

Figure 15 depicts the typical dependence of  $f_H$  and  $f_0$  on altitude. The shaded regions in the figure correspond to areas of radiowave generation. The function  $f_0(h)$  is taken from data in Section 4 of this article, as well as from (Ref. 11, 16). The magnetic field is regarded as a dipole field. As the figure shows, the regions of radio emission at 725 kc and 1525 kc are substantially scattered with respect to altitude. Radio emission

at 725 kc is generated at altitudes of 1600-2400 km (region of extraordinary component generation); at 1525 kc - at  $h \approx 700-900$  km. It is difficult to estimate radio emission strength in the generation region because of the indefinite nature of our information on corpuscular streams, nor is it entirely clear whether incoherent generation of radiowaves occurs, or whether collective effects may take place.

The calculations in (Ref. 17) demonstrate, however, that rather large radio emission strengths are also possible for incoherent emission of radiowaves.

If the plasma mechanism of radio emission is effectuated, the problem arises of radiowaves leaving the ionosphere. Here it seems more probable that the radio emission generated in the region of /605  
 $\max \{f_0, f_H\} < f < \sqrt{f_0^2 + f_H^2}$  will leave the confines of the ionosphere, since in this case only one transformation of an extraordinary into an ordinary wave is required. The low-frequency region, however, demands two conversions - the ordinary into an extraordinary wave, and vice versa.

Conversion of an extraordinary into an ordinary wave may be realized either in the region of  $f_0/f \approx 1$  with small angles between the direction of wave propagation and direction of magnetic field, or in thermal non-uniformities of the plasma, or because of electron concentration gradients in the  $f \approx f_0$  region (Ref. 15).

From the fact that radio emission is connected with the strength of soft electron streams, we may draw the conclusion that it is soft electron streams which produce radiowave generation in the ionosphere. However, this conclusion requires supplementary verification, since there has been no detailed comparison of sporadic radio emission and variations in the hard electron component of the radiation zones.

The latitudinal distribution of radio emission is apparently associated with the penetration of electron streams into the Earth's ionosphere principally in the  $30-50^\circ$  latitudes. Distribution of this radiation by longitude may be explained by the varying depth of stream penetration into the ionosphere. This is connected with the asymmetry of the Earth's magnetic field. In fact, as is evident from Figure 13b, the regions of maximum strength of sporadic radio emission at the frequency of 1525 kc coincide in longitude with the areas of minimum magnetic field values.

We would like to draw attention to the fact that if radio emission occurs in the region  $\max \{f_0, f_H\} < f < \sqrt{f_0^2 + f_H^2}$ , then in principle this radiation may reach the surface of the Earth (Ref. 13). It is possible that it was precisely this radio emission which was recorded in Reber's experiments (Ref. 18).

In conclusion, we should note that the sporadic radio emission observed in the experiment conducted has certain features in common with the sporadic radio emission from Jupiter in the decameter range.

The authors are grateful to all their fellow-workers who participated in preparing the experiment and in processing the measurement results. They express their appreciation to Yu. V. Abramov, A. A. Andronov, B. N. Voykin, V. L. Ginzburg, V. V. Zheleznyakov, V. S. Karavanov, Yu. I. Logachev, G. A. Skuridin, and V. Yu. Trakhtengerts for assisting in the work at different stages of the experiment preparation and for discussion of the results derived.

#### REFERENCES

1. Getmantsev, G. G., Ginzburg, V. L., and Shklovskiy, I. S. *Uspekhi Fizicheskikh Nauk*, 66, No. 2, 157, 1958.
2. Benediktov, Ye. A., Getmantsev, G. G., and Ginzburg, V. L. "Iskusstvennyye Sputniki Zemli". No. 7, Izdatel'stvo AN SSSR, p. 3, 1961.
3. Walsh, D., Haddock, F. T., Schulte, H. F. Report for the COSPAR 6th Plenary Meeting and 4th International Space Science Symposium, Warsaw, Poland, June, 1963.
4. Hartz, T. R. *Nature*, 203, No. 4941, 173, 1964.
5. Ellis, G. R., Waterworth, M. D., Bessel, M. *Nature*, 196, No. 4859, 1079, 1962.
6. Korobkov, Yu. S. *Izvestiya Vysshikh Uchebnykh Zavedeniy. Radiofizika*, 7, No. 5, 982, 1964.
7. Razin, V. A. *Ibid.*, 3, No. 6, 921, 1960.
8. Getmantsev, G. G. *Kosmicheskiye Issledovaniya*, 3, No. 3, 495, 1965.
9. Kaiser, T. R. *Planet. Space Sci.*, 9, 639, 1962.
10. Al'pert, Ya. L., Gurevich, A. V., and Pitayevskiy, L. P. Artificial Satellites in a Rarefied Plasma (*Iskusstvennyye Sputniki v razrezhennoy plazme*). Izdatel'stvo "Nauka", 1964.
11. Lockwood, G. E. K., Nelms, G. L. *J. Atmos. Terr. Phys.*, 26, No. 4, 569, 1964.
12. Gringauz, K. I., Kurt, V. G., Moroz, V. I., and Shklovskiy, I. S. *Doklady Akademii Nauk SSSR*, 132, No. 5, 1062, 1960.
13. Benediktov, Ye. A. *Izvestiya Vysshikh Uchebnykh Zavedeniy. Radiofizika*, 3, No. 1, 33, 1960.
14. Denisov, N. G. *Radiotekhnika i Elektronika*, 4, No. 3, 388, 1959. /606



15. Zheleznyakov, V. V. Radio Emission of the Sun and Planets  
(Radioizlucheniye Solntsa i Planet). Izdatel'stvo "Nauka", 1964.
16. Bourdeau, R. E., Chapman, S., Maeda, K. Ionospheric Research by  
Means of Rockets and Satellites. 14th General Assembly of URSI,  
Tokyo, Japan, September, 1963.
17. Benediktov, Ye. A., Rapoport, V. O., and Eydman, V. Ya. Geomagnetizm  
i Aeronomiya, 2, No. 4, 708, 1962.
18. Reber, G. J. Geophys. Res., 63, No. 1, 109, 1958.

## EXPERIMENTS UNDER THE PROGRAM OF THE WORLD MAGNETIC SURVEY

Sh. Sh. Dolginov, V. I. Nalivayko,  
A. V. Tyurmin, M. N. Chincevoy

### 1. The World Magnetic Survey

Measurements of the Earth's magnetic field were first made in immediate proximity to the Earth at altitudes of 230-800 km over an extensive region of the globe - the territory of the Soviet Union (Ref. 1, 2). A comparison of the measured geomagnetic field values with those calculated from magnetic charts of Soviet Union territory revealed that they differ by from 0.1 to 1.0% (Ref. 3). /606

In 1959 the magnetic field was measured by the satellite "Vanguard-3" in an altitude range from 500 to 3500 km over separate regions of the United States, Latin America, and Australia (Ref. 4). Comparison of the "Vanguard-3" measurements with those calculated from different versions of the geomagnetic field analytical concepts also revealed that they differ by up to 1.5% (Ref. 5). The discrepancies between measured and calculated geomagnetic field values are connected with errors in the original charts and in their analytical conception. The above-mentioned satellite geomagnetic field measurements were made over comparatively well-studied regions of the globe. The major portion of the Earth has been studied to a much lesser extent, especially the Pacific Ocean.

It should be borne in mind that charts compiled from minute and reliable measurements no longer reflect true field distribution after some time has passed, because the Earth's magnetic field undergoes slow secular changes. Their most important features are a decrease in the Earth's total magnetic moment and a systematic westward drift of the field. Thus, in the last hundred years the Earth's magnetic moment has decreased 5%, and the magnetic pole of the dipole portion of the field has shifted  $5^\circ$  to the west along a parallel.

The secular pattern of the magnetic field is a very complex, and by no means well-investigated, physical phenomenon. It differs in various regions of the globe, changing with time in the very same place, and depends on the level of magnetic and solar activity. In isolated places the secular pattern attains values of 150 $\gamma$  per year (Ref. 6). One of the basic restrictions on investigating the secular pattern is the slight degree to which it has been studied over the greater part of the globe. There have been no repeated measurements of the magnetic field over four-fifths of the terrestrial surface. Large regions have not generally been examined with magnetic instruments. A study of the patterns of secular pattern has enormous significance for a study of the Earth's internal structure, and the nature and origin of the geomagnetic field. It is of great practical value as well, for it would facilitate a prediction of the geomagnetic field variation over the surface of the Earth and would make it possible to render magnetic charts more accurate.

The matter of the World Magnetic Survey was first discussed at a /607 session of the International Union of Geodesy and Geophysics in Toronto in 1957, and more thoroughly in Moscow at the 1958 conference of KSAZh\*. It is proposed that a general magnetic survey of the Earth be accomplished by the different means available and, consequently, at different levels from the Earth's surface: by ground instruments, aeromagnetometers, measurements on a nonmagnetic ship, magnetometers towed behind vessels and placed in nonmagnetic balloon baskets, and, finally, by survey from artificial Earth satellites. The last method is the quickest. It facilitates a solution of not all, but the principal, problems of the World Magnetic Survey project. Measurements from satellites were provided, in particular, by the Soviet National Program in the World Magnetic Survey project.

## 2. Magnetic Surveys from a Satellite

The basis for the feasibility of conducting a magnetic survey from a satellite lies, first of all, in the fact that, at the minimum altitudes available for a sufficiently protracted and safe sojourn by an artificial Earth satellite, the geomagnetic field, decreasing at a rate proportional to the cube and higher powers of the distance from the Earth's center, retains its main characteristic features. The strong regional anomalies stretching for 300-400 km appreciably contribute to the magnetic field at an altitude of 250-300 km. Thus, according to calculations in (Ref. 7), a magnetic anomaly 450 km long, with a strength on the Earth's surface of up to 3000 $\gamma$ , has a strength of about 200 $\gamma$  at an altitude of 200 km.

Owing to the difference between the periods of a satellite's revolution and the period of the Earth's rotation about its axis, a satellite with an active lifetime of about 15 days may be used to conduct a fairly detailed survey of the globe. In fact, with a satellite period of rotation of  $\sim 90$  min., each revolution will be approximately  $22.5^\circ$  apart in the equatorial plane, assuming that the orbit is fixed with respect to the stars. Because of the asphericity of the Earth, the satellite's orbit will shift  $4.5^\circ$  westward per day when inclination is  $50^\circ$ . Hence, in five days the  $22.5^\circ$  distance will have been filled with revolutions having an interval of about  $4.5^\circ$ . In ten days the distance between revolutions in the equatorial plane will be  $2.2^\circ$ . Revolutions 4.8 days apart in time will have  $\varphi$  and  $\gamma$  values which are close to each other. Thus, with an active life of about 15 days, it is possible to obtain adequate information and to repeat measurements at points with similar  $\varphi$  and  $\gamma$  coordinates. If, however, the satellite moves at comparatively short distances from Earth, the flight altitude above the surface will change rather rapidly, and repeated measurements at the very same points in space are practically impossible. Nevertheless, a prolonged operational period would be preferable for a more

---

\* Translator's Note: This abbreviation probably designates CSAG (Comité Spécial de l'Année Géophysique).

reliable study of the influence of the external sources of the Earth's variable magnetic field. For further analysis of the data, an orbit close to a circular one is the most advantageous.

The problem of the World Magnetic Survey may, in one experiment, be solved with an orbit inclined  $\sim 85^\circ$  to the equatorial plane. With the indicated minimum time of active satellite life, it is efficient to have a minimum number of 180 readings per revolution. With an orbit inclined  $49^\circ$  to the equatorial plane, the magnetic survey covers about 75% of the Earth's surface. These conditions hold when small satellites of the "Kosmos" series are used. Surveying from a satellite thus gives a practically simultaneous picture of magnetic field-strength distribution from uniform experimental data evenly distributed over the surface.

### 3. Magnetometric Equipment of Satellites "Kosmos-26" and "Kosmos-49"

/608

Proton magnetometers were used in the small satellites of the "Kosmos" series. Measurement of the magnetic field by proton magnetometers is reduced to measuring the free precession frequency of protons in the terrestrial field being metered. Precession frequency of protons possessing a magnetic moment and spin is, as we know, defined by the Larmor relationship  $\omega = \gamma_p H$ , where  $\gamma_p$  is the gyromagnetic relation and  $H$  the strength of the field under measurement.

In 1954 Packard and Varian (Ref. 8) described a convenient method for observing free nuclear precession, making it possible to measure weak magnetic fields with great accuracy. An auxiliary field of polarization  $H_0$  (on the order of 100 oe) at a  $90^\circ$  angle to the measured field  $H$  is applied for a short time to the specimen - fluid (water, alcohol) with a high content of the protons to be found in the magnetic field  $H$  to be measured. Under the action of field  $H_0$  the specimen acquires a macroscopic magnetization of intensity  $I_n = \chi_n H_0$ , where  $\chi_n$  is nuclear susceptibility. After field  $H_0$  is shut off, the macroscopic magnetic moment begins to precess freely around field  $H$  with a frequency of  $\omega = \gamma_p H$ . The magnitude of the macroscopic moment gradually decreases. Relaxation time is about 3 sec. This time is enough for measuring the voltage frequency induced by the precessing moment of the specimen in the sensor signal coil - which is also an excitation coil - now connected to an amplifier. The alternating emf induced in the coil will be  $E = K \chi_n \gamma_p H_0 H \sin^2 \theta e^{-t/T_2}$ , where  $K$  is a constant depending on coil parameters, space factor, and circuit quality;  $\theta$ , the angle between  $H$  and  $H_0$ ;  $t$ , the time from the moment of cutting off field  $H_0$ ; and  $T_2$ , relaxation time.

The nuclear precession method possesses a number of remarkable properties:

- (1) field measurements are reduced to measuring frequency;
- (2) magnetometer readings are given on an absolute scale;

(3) sensor and channels shaping the signal are in principle free from zero creep;

(4) measurement results with a stationary sensor do not depend on orientation of the sensor in the field to be measured;

(5) measuring accuracy depends only on accuracy of the frequency meter and signal-to-noise ratio.

The following difficulties arise in measurements on a revolving object.

1. When the coil rotates together with the object at angular velocity  $\dot{\phi}$  around an axis perpendicular to the axis of the coil, field  $H$  will be measured with an error of  $\Delta H = 3.7 \dot{\phi}$ , where  $\Delta H$  is expressed in gammas and  $\dot{\phi}$  in  $\text{rad} \cdot \text{sec}^{-1}$  (Ref. 9).

2. Although precession frequency does not depend on orientation, the signal strength is proportional to  $\sin^2 \theta$ , and with small  $\theta$  the signal may be close to zero.

A proton magnetometer, as is known, was installed on the satellite "Vanguard-3" (Ref. 4). Only the units shaping and amplifying the nuclear precession signal were installed on the satellite. The magnetometer conducted 50 measurements of the magnetic field per day. The nuclear precession signal modified the transmitter carrier frequency. After reception of the signal by the ground station, it was carefully purified by narrow-band filters and measured with accurate frequency meters. This instrument thus permitted measurements only in a zone where the satellite was directly visible - in regions of a limited number of ground stations. Since the frequency of free nuclear precession in the measured field range varies from 850 to 2100 cps, field measurement over the entire orbit with a standard memory unit is possible only during on-board measurement of free precession frequency and storage of the measurement results in the form of a coded number. /609

Reliable operation of the on-board frequency meter is possible when the signal-to-noise ratio is advantageous, which is achieved in the proton magnetometer in a narrow band in the signal-shaping channel. In order that the magnetometer may operate over the entire orbit, however, this channel must have a wide enough band. This conflict was resolved by using an instrument with automatic range switching.

Among these different switching variations, preference was accorded a magnetometer model in which range retuning is accomplished by a logic circuit which analyzes the nuclear precession signal (proposed by V. I. Nalivayko). In this model the optimum signal must be sought by a mechanical switch in the first measurement period. The optimum position is remembered, and range subsequently is changed by shifting to a range on one side or the other. This self-tuning magnetometer idea was included in the instrument design. The construction was also based on circuit solutions of the PM-5 portable precision proton magnetometer. The measurement range in the PM-5

magnetometer was changed by a hand switch. Precession frequency was measured with an accurate frequency meter which was part of the magnetometer.

In the development process a more efficient version was suggested. In this version the optimum signal was searched for in every polarization cycle of the meter. This made each discrete field measurement independent, which is important because during measurement on unoriented objects the nuclear precession signal may be small or zero when there are small angles between the sensor axis and field direction. One limitation of this method lies in the fact that part of the useful signal is lost every time that a search operation occurs. However, it was possible to overcome this limitation, and the advantages of the method are obvious. This version was proposed by M. M. Chincev.

This principle was employed in the magnetometer with PM-4 index. During part of the free nuclear precession period, the instrument automatically seeks the optimum signal, analyzes it, and if the signal is big enough interrupts the search and gives the command to measure the frequency. The optimum position is meanwhile remembered, and thereafter frequency search is accomplished from this state. The frequency measured at the optimum signal is stored in octal code in the channels of the radio-telemetric system memory unit.

Figure 1 represents the block diagram of the PM-4 magnetometer whose functional elements provide the presented sequence of metrological operations. At an external command, the instrument turns on the polarization current for 2 sec and then connects the sensor coil to amplifier input. The search for optimum signal begins - the entire measurement range is broken down into eleven subranges. The electronic commutator switches them in order. When the commutator comes to the subrange at which there is a precession signal, this signal is amplified to a degree which is sufficient to stop the electronic commutator by means of the stop-search circuit. When the frequency search circuit interrogates the subranges and discovers a signal on one of them, the search is interrupted. However, measurement can occur only after readout of 32 periods of nuclear precession from the amplifier output. This makes it possible to distinguish signal from noise. In case of interference, the scaling circuit is not charged, and the search continues. If there is a signal on one of the subranges, the detector scaling circuit is necessarily charged, search stops, and the frequency-meter input opens. With cessation of search, the number of the subrange /610 where the signal was detected is remembered. In the following measurement cycle, the search begins with this subrange. The frequency meter measures the frequency and stores it in the binary numerical system. The registered number, coded in a stepped voltage of from 0 to 6 v, is delivered to the six channels of the telemetering system.

Two magnetometers with sensors oriented at a  $90^\circ$  angle were installed on each of the "Kosmos" satellites. The instruments were turned on

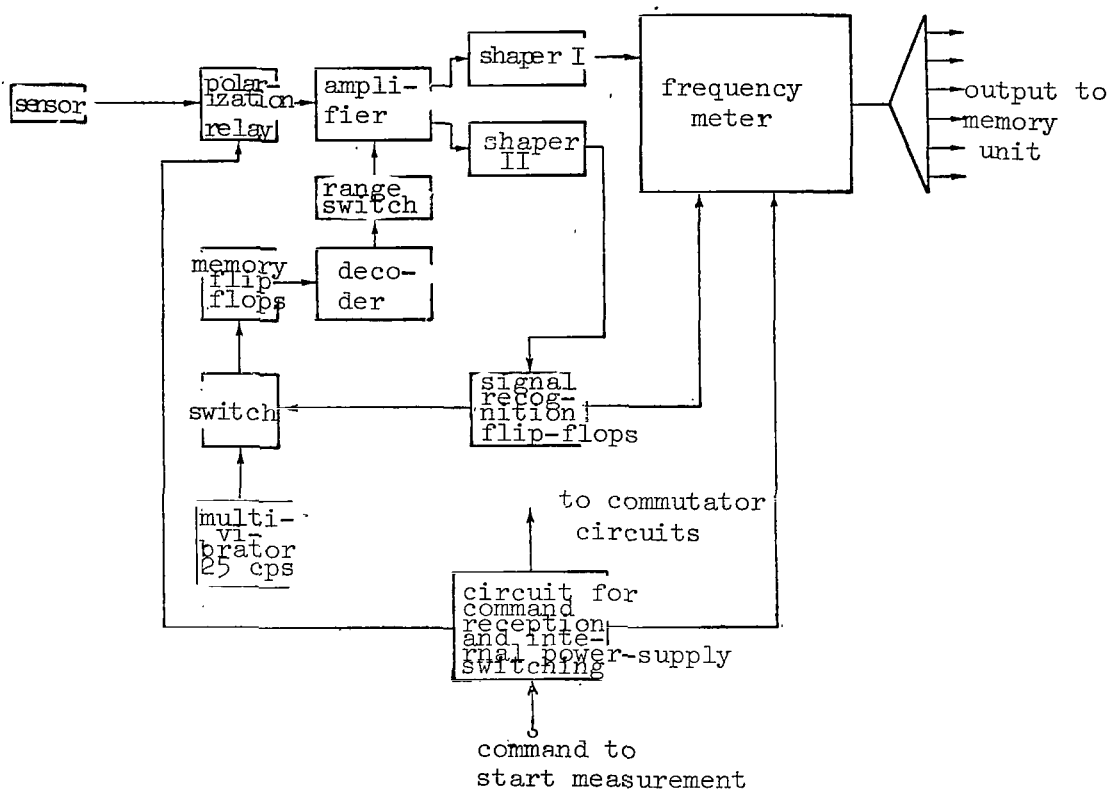


Figure 1

Block Diagram of PM-4 Proton Magnetometer

alternately from an accurate program- and timing-device at intervals of 32 sec. Time markers correlated the on-board readouts of each instrument with absolute time. The magnetometer sensors were a distance of about 3.3 m from the center of the satellite, where there were magnetic parts. The magnetic influence of the satellite at this distance was compensated by a system of permanent magnets creating a sufficiently homogeneous field at the sensor locations. A short series of investigations of the PM-4 instruments in the observatory, under conditions of search for an unknown imposed field of an annular system, showed that measurement accuracy of the magnetometer was 2-3  $\gamma$ . Although - with signal-to-noise ratios below the threshold value - the frequency meter was closed and measurements were improbable, less accurate readings are nevertheless not eliminated with weak signals. Discovery and rejection of poor readouts is possible, since they are rather rare and result in large geomagnetic field gradients which would not be expected at great altitudes.

Measures were taken so that, during separation of the satellite from

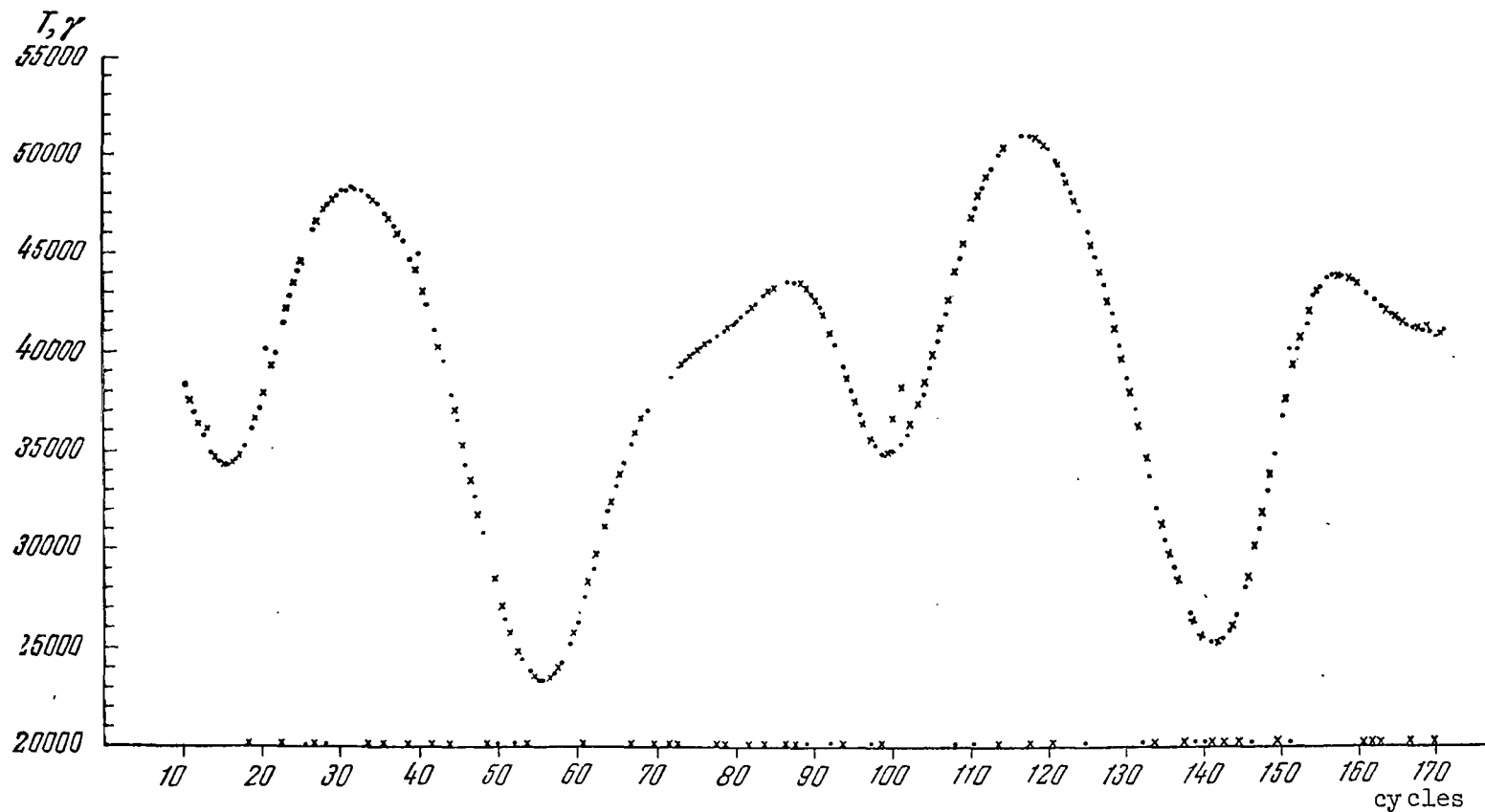


Figure 2

Typical Magnetogram Received from Satellite "Kosmos-49"

Crosses and dots on time axis designate "forbidden" readings where, because of disadvantageous orientation, signal-to-noise ratio was small and frequency meter measured no frequencies. False readings may also be seen which are easy to distinguish from reliable ones.



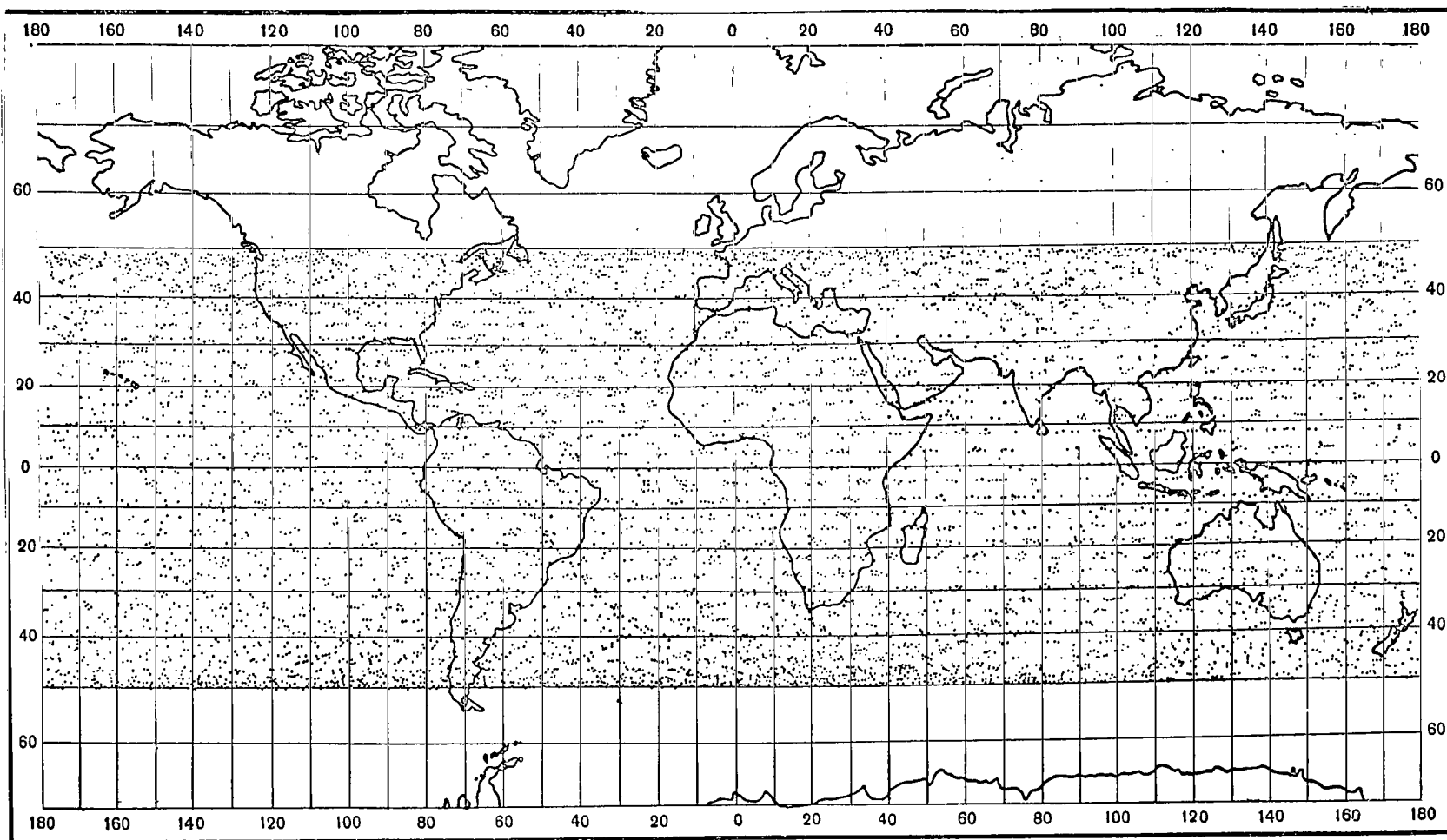


Figure 3

Chart of Magnetic Research in 270-404 km Range

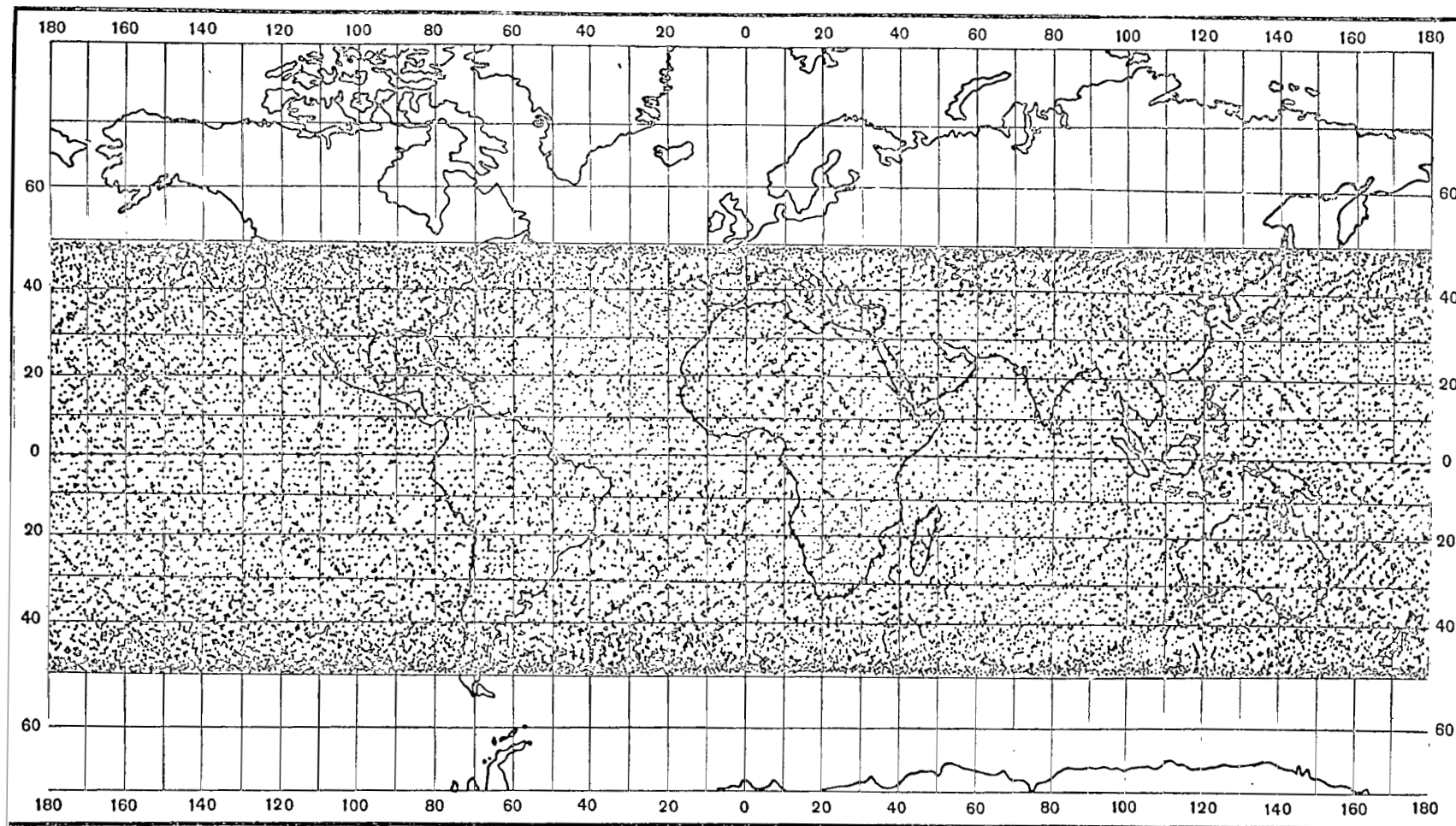


Figure 4

Chart of Magnetic Research in 270-490 km Range

its carrier, the satellite did not acquire large angular velocities, which, as mentioned above, result in errors in measuring nuclear precession frequency.

#### Information on Magnetic Field and Plans for Scientific Data Processing

/614

Between March 18 to 30, 1964, and October 24 to November 6, 1964, the Earth's magnetic field was measured in a latitudinal band of  $+49^\circ$  from the equator, in the altitudinal range of 270-403 km ("Kosmos-26") and 270-490 km ("Kosmos-49").

Figure 2 gives a typical magnetogram of magnetic field strength along the path of one revolution of the satellite "Kosmos-49". The crosses designate readings of the PM-4-2 magnetometer, and dots - those of the PM-4-1 magnetometer. The moments when a magnetometer was not emitting information in a disadvantageous orientation are noted by dots and crosses on the time axis. The magnetogram also shows instances of unreliable readings. They differ drastically from normal readings. Figure 3 gives a chart of magnetic research from "Kosmos-26", and Figure 4 a similar chart from "Kosmos-49". At every point designated on the chart, measurements were received on the scalar magnitude of the Earth's magnetic field strength.

The experimental material obtained facilitates scientific research in the following areas:

1. Investigation of the Earth's magnetic field structure, definition of coefficients of a Gaussian series analytically representing the geomagnetic field.
2. Determination of the geomagnetic field secular pattern by comparing coefficients of the Gaussian series with similar coefficients for other periods. The foundation of an absolute network for studying global secular pattern in the future.
3. Plotting the residual field (measured minus the dipole field) for an altitude of 350 km and comparing it with gravitational field anomalies found by satellites.
4. Study of the variable field phenomena in the ionosphere.

The authors deem it their pleasant duty to express their sincere gratitude for participation in initial processing of the experimental data to G. N. Zlotin, I. N. Kiknadze, R. E. Brodskaya, A. R. Freydin, R. D. Kuznetsova, I. P. Ivchenko, A. V. Klimovskiy, N. Yu. Protsenko, V. N. Fursenko, H. V. Chistova, M. N. Yakushenko, T. D. Grishina, and A. K. Nazarova. The authors take this opportunity to express their appreciation to the individuals and organizations who assisted in conducting the experiments.

#### REFERENCES

1. Dolginov, Sh. Sh., Zhuzgov, L. N., and Shushkov, N. V. In "Iskusstvennyye Sputniki Zemli". No. 2 Izdatel'stvo AN SSSR, No. 2, p. 50, 1958.
2. Dolginov, Sh. Sh., Zhuzgov, L. N., and Senyutin, V. A. Ibid., No. 4, p. 135, 1960.
3. Dolginov, Sh. Sh., Zhuzgov, L. N., Pushkov, N. V., Tyurmina, L. O., and Fryazinov, I. V. Geomagnetizm i Aeronomiya, 1960.
4. Heppner, J. P., et al. Space Res., 1, 982, 1960.
5. Cain, J. C., Shapiro, J. R., Stolarik, J. D., Heppner, J. P. J. Geophys. Res., 67, 5055, 1962.
6. Orlov, V. P. Geomagnetizm i Aeronomiya, 1, No. 2, 1961.
7. Ponomareva, I. A. Report at the All-Union Conference on Geomagnetism and Earth Currents (Doklad na Obshchesoyuznom soveshchani i po geomagnetizmu i zemnym tokam). Moscow, April 13, 1965.
8. Packard, M., Varian, R. Phys. Rev., 93, 941, 1954.
9. Laurence, J., et al. J. Geophys. Res., 61, No. 3, 1956.

## INFLUENCE OF SATELLITES ON RADIATION INTENSITY IN THE RADIATION ZONES

P. V. Vakulov

The radiation zones of the Earth represent charged particle streams /615 (primarily electrons and protons) trapped by the geomagnetic field. The radiation intensity in the radiation zones is so great that it entails serious danger not only for cosmonauts, whose spacecrafts will intersect these zones in the future when going to other planets in the solar system or in circumterrestrial flights at altitudes greater than 500 km. These dangers also exist for individual units of the space vehicle equipment (solar batteries, semiconductor devices, photographic material, optical systems, etc).

The radiation intensity in the radiation zones has increased to an even greater extent at the present time, due to the artificial radiation zones produced by high-altitude nuclear explosions in 1962. The American high altitude explosion "Seastar" ("Starfish") which was conducted on July 9, 1962 produced an extremely powerful artificial radiation zone in the equatorial region. Experimental data indicate that the artificial radiation zone produced by this explosion will exist for several decades (Ref. 1, 2).

The following question may be posed: Is there no possibility of reducing the particle fluxes in the radiation zones? The satellites themselves present one such possibility. Actually, when bombarding the satellite, the radiation zone particles are destroyed, and due to this fact the number of particles in the zones is reduced. Since the number of particles absorbed by the satellite is proportional to its surface, a fairly large satellite passing through the radiation zones can substantially decrease the intensity in those regions of the radiation zones which it intersects. This possibility was pointed out by S. F. Singer (Ref. 3), who called this the "cosmic snowstorm" method. However, several qualitative statements, as well as quantitative computations, which this author advanced (Ref. 3) were based on invalid assumptions. This makes it impossible to utilize the expression he obtained for quantitative determinations of the "cosmic snowstorm" effect.

In order to make a quantitative estimate of this effect, it is necessary to distinguish the limited area in which the satellite will "sweep out" (more precisely, absorb) the trapped particles. In the given case, that area in which very few particles enter will be called the limited area. The envelope, along which trapped particles drift, whose thickness is on the order of the Larmor radius of these particles is such a minimum limited area. If even a comparatively small satellite (a diameter of about 10 m) were continuously located on one and the same envelope, it would "sweep out" the main portion of trapped particles in this envelope comparatively rapidly (over a period of several months). However, it is impossible to produce a satellite

which is always located on a given envelope. Even a satellite which is launched in the equatorial plane on a circular orbit will intersect several magnetic envelopes, due to the eccentricity of these envelopes; this is primarily caused by the shift of the magnetic dipole axis of the Earth.

On the whole, the minimum limited area which a satellite can constantly occupy is no less than  $10^{26} \text{ cm}^3$ , taking into account the inclination of the geomagnetic dipole axis.

On the basis of the statements presented above, let us now determine what portion of the total number of radiation zone particles will be absorbed by the satellites. Let us also investigate what size the satellite must be in order that there be an appreciable decrease in the particles, if only in individual regions of the radiation zones. /616

Let us assume that there is a mean flux of trapped particles  $\bar{j}$  in a certain closed area having the volume  $V$ . The mean concentration of these particles per unit volume is then

$$\bar{n} = \frac{\bar{j}}{v},$$

where  $v$  is the trapped particle velocity. The total number of trapped particles in the given volume  $V$  is

$$N = \bar{j}V/v.$$

A number of particles

$$dN = \bar{j}s dt.$$

will pass through a body having the surface  $s$  located in this area during the time  $dt$ .

If it is assumed that all of the particles falling on the surface will be absorbed, then the relative loss of particles will be determined as

$$\frac{dN}{N} = -\frac{sv}{2V} dt.$$

The multiplier 2 appears here, due to the fact that particles will be absorbed only in one hemisphere. It follows from this expression that the total number of particles in the volume under consideration, when there is no injection, will change in time according to the exponential law

$$N = N_0 \cdot e^{-\frac{t}{\tau}},$$

where the quantity  $\tau = 2V/sv$  designates a constant time - the time during which the number of particles (and, consequently, intensity) decreases  $e$  times.

In order to best represent the order of magnitude of all the quantities, let us examine a specific example as applied to radiation zone electrons having energies greater than several hundreds of kev. The fluxes of such electrons are the largest, particularly in the pre-equatorial regions of the magnetosphere, and they have a maximum influence due to the great penetrating capacity of the braking radiation produced by electrons when bombarding the satellite frame. The velocity of these electrons is close to the speed of light, i.e.,  $v \approx c$ .

Let us assume that a spherical satellite having the radius  $r$  is launched in the equatorial plane on a circular orbit with an altitude of  $\sim 2000$  km. This satellite will absorb particles falling on its surface from an area having the size

$$V \approx 10^{26} \text{ cm}^3 = 10^{11} \text{ km}^3.$$

The area under consideration includes the maximum intensity region of the artificial radiation zone produced by the explosion "Starfish".

Utilizing the expression obtained previously and advancing the hypothesis that the constant lifetime of electrons in the area under consideration is about three months ( $10^7$  seconds), we can determine the required satellite size, assuming that it has a spherical form.

Assuming that

$$\tau = \frac{2V}{4\pi r^2 c},$$

$$r = \sqrt{\frac{2V}{4\pi \tau c}} \approx 7 \cdot 10^3 \text{ cm} = 70 \text{ m}.$$

Thus, a satellite having a diameter of  $\sim 150$  m lowers the lifetime of electrons in the region of the artificial radiation zone maximum to three months; at the present time, the mean lifetime of electrons in these regions is assumed to be approximately 10 years. /617

This satellite will also decrease the lifetime of protons in the inner radiation zone. However, the velocity of these protons is several times less than the speed of light, and therefore their lifetime will be much greater than the electron lifetime.

So many satellites have been launched as of the present, that their influence on the intensity in radiation zones must be fairly large. Rough estimates have shown that the existing satellites, together with the rockets-carriers accompanying them into orbit, can decrease the lifetime of trapped particles by several years at altitudes of  $\sim 1000$  km.

The influence on the radiation zones of the satellites already launched could be even greater. However, many satellites (particularly the

large ones) pass at low altitudes, and therefore pass under the zones in the majority of cases. Only in individual revolutions do they enter the radiation zones in the region of the Atlantic magnetic anomaly, where the zones descend to the lowest point in the direction of the Earth's surface.

However, taking into account the increasing rate at which satellites are launched as well as the increase in their size and weight, one can assume that over a period of decades the radiation intensity in the radiation zones, at altitudes on the order of thousands of kilometers, will be primarily determined by particle loss due to the influence of these numerous satellites.

It must be pointed out that a satellite which is several hundreds of meters in size and which weighs several hundreds of tons must be developed in order to substantially decrease the radiation intensity throughout the entire inner radiation zone, by the method presented above. Generally speaking, although this lies within the realm of probability (for example, to produce several tens of satellites of 10 t), it is only justified if these satellites are used for many other purposes (radio relaying, intermediate launching satellites, etc.).

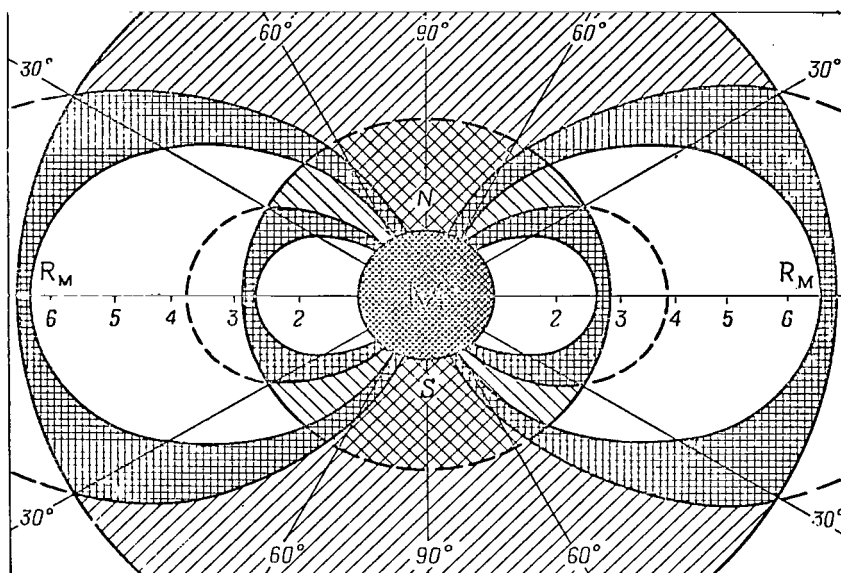
If there are no satellites on the Earth which are sufficiently large as yet, there are two satellites on Mars; they are located comparatively close to this planet and have transverse dimensions of about 10 km. If Mars has a magnetic field which is comparable to the magnetic field of the Earth in order of magnitude (and, consequently, if it has radiation zones), then these satellites must substantially change the structure of the Mars radiation zones. If it is assumed that the radiation zones of Mars are similar in size to the Earth's radiation zones (this means that the magnetic moment of Mars is approximately eight times less than the Earth's magnetic moment), then the size of Mars' radiation zones is  $V_M \approx 10^{13} \text{ km}^3 = 10^{28} \text{ cm}^3$ . Utilizing the expression obtained previously, we obtain  $\tau \approx 10^5 \text{ sec} \approx 1 \text{ day}$ .

Thus, if the orbit of even one of the Mars satellites has the most favorable location (i.e., an elliptic orbit with a perigee of  $\sim 7 R_M$  with a low apogee, and a small angle of inclination of the orbital plane to the equatorial plane), then the mean lifetime of trapped particles in the Mars radiation zones would be several days in all. Therefore, the radiation zones of Mars would be several orders of magnitude weaker than Earth's radiation zones.

However, as is known, Mars' satellites (Phobos and Deimos) have almost circular orbits with an identical orbital angle of inclination  $\sim 30^\circ$ , and a distance from the center of Mars of  $R_p \approx 2.8 R_M$  and  $R_D \approx 7 R_M$ .

Therefore, in actuality the Mars satellites will "sweep out" the radiation zones only in individual regions. The meridional cross section of these regions is shown in the figure. The regions with double shading characterize the "shade" regions, i.e., those regions from which trapped particles will be definitely "swept out". Due to the relatively small size





Structure of Mars' Hypothetical Radiation Zones  
(Meridional Cross Section)

Double-shaded sections indicate regions where there will be almost no trapped radiation.

of these regions, the lifetime of particles will be several hours in all. This means that there will be practically no trapped radiation in these regions. The regions designated by the single shading indicate regions where the "sweeping out" of particles will take place only if the magnetic dipole axis of Mars is displaced from the rotational axis of the planet. The size of these regions will increase proportionally to the angle of inclination of Mars' magnetic dipole. /618

Thus, if there is a magnetic field on Mars, and consequently radiation zones, then these zones will consist of two sharply defined areas.

#### REFERENCES

1. McIlwain, C. E. Science, 142, No. 3590, 355, 1963.
2. Vakulov, P. V. Dissertation, Moscow, 1965.
3. In "Radiation Safety During Space Flights" (Radiatsionnaya bezopasnost' pri kosmicheskikh poletakh). Izdatel'stvo "Mir", Moscow, p. 164, 1964.

Scientific Translation Service  
4849 Tocaloma Lane  
La Canada, California

*"The aeronautical and space activities of the United States shall be conducted so as to contribute . . . to the expansion of human knowledge of phenomena in the atmosphere and space. The Administration shall provide for the widest practicable and appropriate dissemination of information concerning its activities and the results thereof."*

—NATIONAL AERONAUTICS AND SPACE ACT OF 1958

## NASA SCIENTIFIC AND TECHNICAL PUBLICATIONS

**TECHNICAL REPORTS:** Scientific and technical information considered important, complete, and a lasting contribution to existing knowledge.

**TECHNICAL NOTES:** Information less broad in scope but nevertheless of importance as a contribution to existing knowledge.

**TECHNICAL MEMORANDUMS:** Information receiving limited distribution because of preliminary data, security classification, or other reasons.

**CONTRACTOR REPORTS:** Technical information generated in connection with a NASA contract or grant and released under NASA auspices.

**TECHNICAL TRANSLATIONS:** Information published in a foreign language considered to merit NASA distribution in English.

**SPECIAL PUBLICATIONS:** Information derived from or of value to NASA activities. Publications include conference proceedings, monographs, data compilations, handbooks, sourcebooks, and special bibliographies.

**TECHNOLOGY UTILIZATION PUBLICATIONS:** Information on technology used by NASA that may be of particular interest in commercial and other nonaerospace applications. Publications include Tech Briefs; Technology Utilization Reports and Notes; and Technology Surveys.

*Details on the availability of these publications may be obtained from:*

SCIENTIFIC AND TECHNICAL INFORMATION DIVISION  
NATIONAL AERONAUTICS AND SPACE ADMINISTRATION

Washington, D.C. 20546